TEMPERATURE AND DISLOCATION STRESS FIELD MODELS OF THE LEC GROWTH OF GALLIUM ARSENIDE

by

CARLOS ENRIQUE SCHVEZOV

Lic. en Fisica, Universidad Nacional de Rosario, Argentina, 1975

M.A.Sc. in Metallurgy, University of British Columbia, Canada, 1983

A THESIS SUBMITTED IN PARTIAL FULFILLMENT OF

THE REQUIREMENTS FOR THE DEGREE OF

DOCTOR OF PHILOSOPHY

in

THE FACULTY OF GRADUATE STUDIES

(Department of Metallurgical Engineering)

We accept this thesis as conforming
to the required standard

THE UNIVERSITY OF BRITISH COLUMBIA

October 1986

© Carlos Enrique Schvezov, 1986

In presenting this thesis in partial fulfilment of the requirements for an advanced degree at the University of British Columbia, I agree that the Library shall make it freely available for reference and study. I further agree that permission for extensive copying of this thesis for scholarly purposes may be granted by the head of my department or by his or her representatives. It is understood that copying or publication of this thesis for financial gain shall not be allowed without my written permission.

Department of Metals and Materials Engineering

The University of British Columbia
1956 Main Mall
Vancouver, Canada
V6T 1Y3

Date December 15, 1986

DE-6(3/81)

ABSTRACT

The temperature fields and resulting stress fields have been calculated for a growing GaAs crystal produced by the LEC process. The calculations are based in a finite element numerical thermoelastic stress analysis. The calculated temperature fields have been compared to reported experimental measurements with good agreement. The stress fields have been used to calculate the resolved shear stresses, in the growing crystal, from which the dislocation density and distribution were determined.

Using the model the effects of a range of growth and environmental parameters on the dislocation density and distribution were determined. Theses parameters include crystal length, crystal diameter, cone taper, boron oxide thickness, gas pressure, solid/liquid interface shape, vertical temperature gradients and others. The results show that the temperature distribution in the gas surrounding the crystal, and the boron oxide thickness, were critical factors in determining the dislocation density and distribution in the crystal. The crystal radius, crystal length and interface curvature also strongly influenced the dislocation configuration. After crystal growth, the dislocation density at the end of the crystal was strongly influenced by the cooling procedure adopted. The dislocation distribution on cross-sections of the crystal exhibited two-fold, four-fold and eight-fold symmetry depending on growth and cooling conditions and position in the crystal.

TABLE OF CONTENTS

		Page
ABSTRACT		II
TABLE OF CONTENTS		III
LIST OF FIGURES		XI
LIST OF TABLES		XXV
LIST OF SYMBOLS		XXVI
ACKNOWLEDGEMENTS		XXX
CHAPTER 1		
INTRODUCTION		1
CHAPTER 2		
THE GROWTH OF BULK GaAs CRYSTALS		4
2.1	The Liquid Encapsulated Czochralski Technque (LEC)	4
2.2	Classification of Defects in LEC grown GaAs crystal	7
2.3	Dislocations in LEC-GaAs	8
2.4	Effect of Dislocations on Properties of GaAs Devices	11
CHAPTER 3		
THE ORIGIN OF DISLOCATIONS IN LEC GaAs CRYSTALS		12
CHAPTER 4		
DISLOCATION DENSITY AND CRYSTAL GROWTH		17

4.1 Stresses in the Crystal Due to Thermal Gradients..... 17

4.1.1 Crystal Dimensions..... 18

4.1.2 Thermal Conditions During Crystal Growth..... 20

4.2 Alloy Addition to the GaAs..... 22

CHAPTER 5

MODELS OF DISLOCATION GENERATION IN GaAs..... 29

5.1 Stress Fields..... 29

5.2 Calculation of Dislocation Densities..... 36

CHAPTER 6

OBJECTIVES..... 40

CHAPTER 7

FORMULATION OF THE MODELS..... 43

7.1 Model of crystal growth..... 45

7.1.1 Temperature Field..... 45

7.1.1.1 Governing Equations..... 45

7.1.1.2 Finite Element Equations..... 48

7.1.2 Stress Field Model..... 53

7.1.2.1 Governing and Element Equations..... 53

7.1.2.2 Requirements for the interpolation functions.... 57

7.1.2.3 Formulas for Stress Calculations..... 59

7.1.2.4 Linear Elements..... 60

7.1.2.5 Quadratic Element..... 61

7.1.3 Von Mises and Resolved Shear Stresses..... 63

7.2 Modelling for Cooling After growth..... 67

7.3 Analytical Solutions..... 71

7.3.1 Analytical QSS Temperature Field..... 71

7.3.2 Analytical solutions for the Stress Field..... 73

7.3.2.1 Plane Strain Approximation..... 73

7.3.2.2 Axisymmetric Solutions..... 74

CHAPTER 8

EVALUATION OF THE MODELS..... 76

8.1 Programming and Input Parameters..... 76

8.1.1 Input Parameters..... 86

8.1.2 Numerical Evaluation of the Analytical Solutions..... 93

8.2 Comparison of Model Predictions with Analytical Solutions..... 93

8.2.1 Temperature Field..... 93

8.2.2 Stress Fields..... 97

8.3 Comparison of Model Predictions with Temperature Measurements..... 107

8.4 The Temperature Model for Cooling - Programming and Convergency..... 115

CHAPTER 9

RESULTS AND ANALYSIS..... 120

9.1 Cone Angle..... 121

9.1.1 Effect of Cone Angle on Stress Symmetry..... 133

9.1.2 Effect of Thermal Conditions..... 146

9.1.3 Effect of the Heat Transfer Coefficient..... 155

9.1.4 Effect of Non-linearity in the Temperature Profile..... 161

9.2 Crystal Length..... 170

9.2.1 Effect of crystal Length on Stress Symmetry..... 175

9.3 Crystal Radius..... 190

9.3.1 Effect of Radius on Stress Symmetry..... 197

9.4 Growth Velocity 199

9.5 Thermal Conditions..... 202

9.5.1 Radius 27.5 mm 205

9.5.1.1 Boron oxide thickness 21.0 mm..... 205

9.5.1.2 Boron oxide thickness 40.0 mm 207

9.5.2 Radius 40.0 mm 217

9.5.2.1 Boron oxide thickness 21 mm 217

9.5.2.2 Boron oxide thickness 40 mm 217

9.5.2.3 Boron Oxide thickness 50 mm 221

9.6 Gas Pressure and Composition 227

9.7 Curvature of the Solid-Liquid Interface..... 235

9.7.1 Convex interface..... 236

9.7.1.1 Crystal Length..... 236

9.7.1.2 Effect of Encapsulant Thickness and Gradient..... 245

9.7.1.3 Effect of crystal Radius 251

9.7.2 Concave Interface..... 253

CHAPTER 10

RESULTS FOR COOLING AFTER GROWTH..... 257

10.1 Ambient Temperature 1000°C 258

10.1.1. Argon..... 258

10.1.1.1 Initial Gradient GC = 70°C/cm 258

10.1.1.2 Initial Gradient GC/2 = 35°C/cm 269

10.1.1.3 Initial Gradient GC/4 = 17.5^{o}C/cm..... 276

10.1.2. Boron Oxide 278

10.2 Ambient Temperature 800°C/cm 283

10.3 Analysis of the Results for Cooling 283

CHAPTER 11

SUMMARY AND CONCLUSIONS 290

REFERENCES 306

APPENDIX I

EFFECT OF DISLOCATIONS ON GaAs AND DEVICES 320

I.1 Effect of Dislocation on Properties 320

I.2 Dislocations and Fermi Level 327

APPENDIX II

Integration by Parts of the Element Equation for the Temperature Field 330

APPENDIX III

Evaluation of the Matrix Elements for the Temperature Field 332

APPENDIX IV

Evaluation of Stiffness Matrix Elements for Linear Elements 338

APPENDIX V

Quadratic Element Calculations 340

APPENDIX VI

Calculation of Resolved Shear Stresses 353

APPENDIX VII

Temperature Field During Cooling 362

APPENDIX VIII

Analytical Solution of the Temperature Field 367

APPENDIX IX

Plane Strain Analytical Stresses 372

APPENDIX X

ANALYTICAL ASISYMMETRIC SOLUTIONS FOR STRESSES 375

X.1 Axisymmetric Temperature Field 375

X.2 Analytical Axisymmetric Solution for $\theta = -\rho^2$ ... 385

APPENDIX XI

COMPUTER PROGRAMS..... 390

XI.1 Mesh Generator 390

XI.2 Finite Linear Element Program for the Temperature Calculations during Growth 394

XI.3 Finite Linear Element Program for the Stress Calculations 402

XI.4 Finite Quadratic Element Program for the Stress Calculations 412

XI.5 Program for the Calculations of the MRSS-CRSS in (010) Sections 425

XI.6 Program for the Calculations of MRSS-CRSS in (001) Sections 428

XI.7 Program for the Numerical Evaluation of Temperatures During Cooling 432

APPENDIX XIII

XII.1 Program for the Numerical Evaluation of Analytical Axisymmetric Temperature Fields 437

XII.2 Program for the Numerical Evaluation of Analytical Analytical Axisymmetric Stresses for Radial Temperature Fields 439

XII.3 Program for the Numerical Evaluation of Analytical Axisymmetric Stresses for Axisymmetric Temperature Fields 441

APPENDIX XIII

TEMPERATURE AND STRESS PLOTS FROM THE COMPUTER PROGRAMS OUTPUT (GROWTH) 444

XIII.1 Cone Angle
CL, 10 mm ; R, 20 mm ; B, 10 mm ; AP, 30 atm. ; BG, 100°C/cm ; AG, 50°C/cm 444

XIII.2 Crystal Length
R, 27.5 mm ; B,21 mm ; AP, 30 atm. ; CA, 30° ... 521

XIII.3 Crystal Radius
R, 40 mm ; B, 21 mm ; CA, 30° ; AP, 30 atm. 575

XIII.4 Growth Velocity
R 27.5 mm ; CL, 55 mm ; CA, 30° ; B, 21 mm 617

XIII.5 Thermal Condition R, 27.5 mm
CL, 55 mm ; CA, 30° ; AP, 30 atm. 624

XIII.6 Thermal Conditions R, 40 mm
CL, 80 mm ; CA, 30° ; AP, 30 atm. 655

XIII.7 Argon Pressure, 2 atmospheres.
R, 27.5 mm ; CL, 55 mm ; CA, 30° ; B, 21 mm 690

XIII.8 Curvature of the Solid/Liquid Interface
CA, 30° ; AP, 30 atm. 703

APPENDIX XIV

TEMPERATURE AND STRESS PLOTS FROM THE COMPUTER PROGRAMS OUTPUT (COOLING) 761

XIV.1 Ambient Temperature 800°C, Argon 761

XIV.2 Ambient Temperature 1000°C 799

LIST OF FIGURES

Fig. 2.1 Schematic of a LEC pulling chamber 5

Fig. 3.1 Transmission X-ray topography in GaAs - (a) and (b) undoped ; (c) Te-doped, (110) axial section[113] 13

Fig. 4.1 Radial dislocation density profiles across wafers obtained from the front, middle, and tail of a crystal. The radial profiles are "W" shaped, and the average EPD increases from the front to the tail..... 19

Fig. 4.2 Mean density of "grown-in" dislocations in GaAs single crystals (20-25 mm in diameter) grown by the Czochralski LEC Technique, as a function of dopant concentration : (1) Te, (2) Sn, (3) In, (4) Zn..... 23

Fig. 4.3 Hypothetical distribution of the dopant (In) along the pulling axis of the ingot. The indium concentration oscillates around a mean value which is proportional to the distance from the top of the ingot..... 26

Fig. 5.1 (a) and (b) - Isotherms and shear stress topography in two gallium arsenide single crystal grown under different conditions .
(c) - Distribution of Shear Stresses τ_1, τ_2, τ_3 and (d) - dislocations density over the cross-sections over galium arsenide single crystals... 30

Fig. 5.2 T R S S contours for the top wafer of a <001> GaAs boule..... 33

Fig. 5.3 Distribution of the calculated dislocation density in a gallium arsenide single crystal being grown in the <111> direction for slip systems with Burgers dislocation vectors perpendicular..... 34

Fig. 7.1 Flow chart of the model used to derive the stress fields..... 44

Fig. 7.2 Crystal configuration and coordinate system used in the mathematical model..... 47

Fig. 8.1 Flow chart of the computer program to calculate the temperature field in the crystal using a finite element method..... 78

Fig. 8.2 Flow chart of the computer program for the stress calculations using finite linear and quadratic elements..... 81

Fig. 8.3 Flow chart of the mesh generator computer program..... 84

Fig. 8.4 Flow chart of the computer program to calculate and plot RSS in a vertical (010) plane..... 87

Fig. 8.5 Flow chart of the computer program to calculate and plot RSS in a (001) plane..... 88

Fig. 8.6 Estimated radiative and convection heat transfer coefficients for GaAs/B_2O_3 (l), He (g), N_2 (g) and A (g) as a function of ambient temperature. The numerical labels are the product of the carrier concentration X crystal diameter in units of cm^{-2} 90

Fig. 8.7 Total heat transfer coefficient h, in B_2O_3 and argon as a function of the ambient temperature T_a (1) Total heat transfer coefficient in B_2O_3. (2) Total heat transfer coefficient in argon pressurized at 30 atm..... 90

Fig. 8.8 Temperature dependence of the critical stress for dislocation generation in GaAs ; (1) Te-doped material, $n = 2 \times 10^{18}$ cm^{-3} ; (2) Te-doped material, $n = 7 \times 10^{17}$ cm^{-3} ;

(3) Zn-doped material, $p = 9 \times 10^{18}$ cm^{-3} ;
(4) undoped material..... 92

Fig. 8.9 A comparison of finite element and analytical calculated temperature curves for h = $0.3\ cm^{-1}$ 94

Fig. 8.10 A comparison of finite element and analytical calculated temperature curves for h = $0.6\ cm^{-1}$ 95

Fig. 8.11 Mesh employed in the calculations of the temperature fields shown in Fig. 8.9 and 8.10. Number of nodes = 45. Number of elements = 64..... 96

Fig. 8.12 Calculated radial stresses as a function of r/r_o for radial temperature fields (1) Finite element with averaged element (2) Finite element with nodal temperatures (3) Analytical-plane strain (4) Analytical-axisymmetric..... 98

Fig. 8.13 Calculated azimuthal stresses as a function of r/r_o for radial temperature fields (1) Finite element with averaged element temperatures (2) Finite element with nodal temperatures (3) Analytical-plane strain (4) Analytical-axisymmetric..... 99

Fig. 8.14 Calculated axial stresses as a function of r/r_o for radial temperature fields (1) Finite element with averaged element temperatures (2) Finite element with nodal temperatures (3) Analytical-plane strain (4) Analytical-axisymmetric..... 100

Fig. 8.15 Four steps in the mesh refinement used to analyse the convergency of the finite element stress calculations. (a) NN = 15, NE = 16 (b) NN = 45, NE = 16 (c) NN = 45, NE = 64. (d) NN = 153, NE = 256 (b) Quadratic elements. (a), (c) and (d) linear elements..... 102

Fig. 8.16 Calculated radial stresses as a function of r/r_o for different numbers of nodes and sizes of element (1) Finite element with averaged

element temperature (2) Finite element with nodal temperatures. L = Linear element, Q = Quadratic element..... 103

Fig. 8.17 Calculated radial stresses as a function of r/r$_o$ for axisymmetric thermal fields (1) Finite element with averaged element temperatures (2) Finite element with nodal temperatures (3) Analytical-plane strain (4) Analytical-axisymmetric..... 105

Fig. 8.18 Position of thermocouples in GaAs crystal. B = Boric oxide layer, argon pressure 3.04 MPa. Reference 218..... 108

Fig. 8.19 Temperatures measured with thermocouples 2, 3 and 4 in Figure 8.18 as a function of the relative position of the thermocouples with the interface. Reference 218..... 110

Fig. 8.20 Measured and calculated temperatures along the crystal axis at four crystal lengths..... 111

Fig. 8.21 Measured and calculated temperatures adjacent to the outside surface of the crystal at four crystal lengths. The measured ambient temperature is also shown..... 112

Fig. 8.22 Measured and calculated axial temperature gradients along the crystal axis at four crystal lengths..... 113

Fig. 8.23 Flow chart of the computer program for the numerical evaluation of the analytical temperature fields during cooling of the crystal..... 117

Fig. 8.24 (a) Typical temperature field obtained during cooling units are 10^3 °C. (b) and (c) Von Mises stress contours (MPa) for the temperature field given in (a). (b) NN = 451, NE = 800. (c) NN = 1105, NE = 2048..... 118

Fig. 9.1 Von Mises Stress contours (MPa) in vertical planes for five cone angles. (a) 7.1°, (b) 30°, (c) 45°, (d) 54.7°, (e) 65°. Cone surface in (d) coincides with a (111) plane. Crystal radius, 20 mm ; crystal length, 10 mm ; B_2O_3 thickness, 10 mm ; B_2O_3 gradient, 100°C/cm ; argon pressure, 30 atm. ; argon gradient, 50°C/cm..... 123

Fig. 9.2 Maximum resolved shear stress (MRSS) contours in MPa, in vertical (010) planes for five cone angles. (a) 7.1°, (b) 30°, (c) 45°, (d) 54.7°, (e) 65°. Cone surface in (d) coincides with a (111) plane. Conditions are the same as in Figure 9.1 128

Fig. 9.3 Total resolved shear stress (TRSS) contours in MPa for the 45° cone angle crystal. Compare the large stress levels of the TRSS with the stress levels for same crystal shown in Figure 9.1(c) for the VMS and Figure 9.2(c) for the MRSS..... 131

Fig. 9.4 Contours of the MRSS (MPa) in excess of : (a) CRSS (yield) ; (b) CRSS (MB) ; (c) CRSS (MBTe). Shaded regions indicate areas in which the MRSS is less than the CRSS..... 132

Fig. 9.5 Slip mode distribution in the (010) plane for the 45° cone angle crystal corresponding to the MRSS distribution shown in Figure 9.2(c)..... 134

Fig. 9.6 Contours in MPa of the MRSS in excess of (a) CRSS (Yield) ; (b) CRSS (MB) and (c) CRSS (MBTe). In most of the crystal the MRSS is larger than the critical values. The bump shaped contours (A) give complex stress distributions in perpendicular cross-sections..... 137

Fig. 9.7 MRSS contours (MPa) in cross-sections perpendicular to the crystal axis for five cone angles. (a) 7.1°, (b) 30°, (c) 45°, (d) 54.7°, (e) 65°. Section (a-d) are 7.5 mm from the interface and section (e) is 8.0 mm from the interface. The horizontal direction corresponds to the [100] direction and the vertical direction corresponds to the [010] direction..... 141

Fig. 9.8 Contours of the MRSS-CRSS (Yield) (MPa) for the 65° cone angle crystal. MRSS contours are shown in Figure 9.7(e). At high cone angles MRSS levels are larger than CRSS at the centre and outside part of the wafer..... 142

Fig. 9.9 Stress contours (MPa) in cross-section 2.5 mm from the interface. (a) and (b) in a 7.1° cone angle crystal. (c) in a 45° cone angle crystal. (a) MRSS contours. (b) and (c) MRSS-CRSS (Yield). For the 7.1° cone angle there is eight-fold symmetry at the centre in (a) which is not seen in (b) because stress levels are less than CRSS. For the 45° cone angle there is four-fold symmetry..... 145

Fig. 9.10 Slip mode distribution in a (001) plane corresponding to the MRSS distribution shown in Figure 9.7(c) for the 45° cone angle crystal at 7.5 mm from the interface. The eight-fold distribution of the mode at the edge of the section is associated with the eight-fold symmetry of the MRSS..... 147

Fig. 9.11 Temperature distribution as a function of external temperature gradient for a 45° cone angle crystal. Thermal gradients in the boron oxide are : (a) 50°C/cm, (b) 100°C/cm, (c) 200°C/cm and (d) 400°C/cm. Temperatures are given in 10³°C. For low gradients isotherms are nearly flat and slightly convex. For larger gradients isotherms are curved and concave..... 149

Fig. 9.12 Stress contours (MPa) in a (010) plane for a 45° cone angle crystal grown with a 50°C/cm gradient in the boron oxide. (a) MRSS contours does not show the bump shaped stress distribution below the shoulder in (a). The MRSS-CRSS (Yield) is positive only in a few regions in (b)..... 151

Fig. 9.13 (a) MRSS contours and (b) MRSS-CRSS (Yield) contours for a 200°C/cm gradient in the boron oxide. Units are in MPa. MRSS stress are large below the shoulder in (a). The MRSS-CRSS is greater than zero in most of the crystal in (b). 152

Fig. 9.14 (a) MRSS contours. (b) MRSS-CRSS (Yield) contours. (c) Slip mode distribution. Gradient

in the boron oxide is 400°C/cm. In (a) contours are similar to those obtained for a 200°C/cm gradient. Stress levels have doubled. In (b) only a small area in the seed developed stresses less than the CRSS. In (c) the mode distribution is similar to that shown in Figure 9.5 for a 100°C/cm gradient..... 154

Fig. 9.15 MRSS contours in MPa in a cross-section at 7.5 mm from the interface for the crystal shown in Figure 9.14(a). The symmetry is similar to that shown in Figure 9.7(c) for a 100°C/cm gradient..... 156

Fig. 9.16 Temperature profiles at the surface of 45° cone angle crystals for three diferent conditions. Curve H corresponds to the temperatures calculated using the original heat transfer coefficient values. In curves H / 1.3 and H x 1.3 the original heat transfer coefficient values were divided and multiplied by 1.3 respectively..... 158

Fig. 9.17 Stress contours in MPa derived from the temperature field obtained using heat transfer coefficient values 1.3 larger than original values. (a) MRSS contours. (b) MRSS-CRSS (Yield)..... 159

Fig. 9.18 Stress contours in MPa derived from the temperature field obtained using heat transfer coefficient values 1.3 times smaller than original values. (a) MRSS contours. (b) MRSS-CRSS (Yield). Variations of only 20 % are observed in the maximum MRSS values between (a) and Figure 9.17(a)..... 160

Fig. 9.19 MRSS (MPa) contours for a crystal growing under four different conditions given in Table 9.3. (a) Run #1 ; (b) Run #2 ; (c) Run #3 ; (d) Run #4. From (a) to (b) the AMRSS doubles. In (d) the bump shape below the shoulder does not appear..... 165

Fig. 9.20 MRSS (MPa) contours in a (001) plane at a distance of 5.0 mm from the interface in the crystal shown in Figure 9.19(d) (run #4).

The four-fold symmetry with a slight two-fold symmetry is observed..... 167

Fig. 9.21 MRSS-CRSS (Yield) contours (MPa) for the four growth conditions shown in Table 9.3 and MRSS contours shown in Figure 9.19 (a) Run #1 ; (b) Run #2 ; (c) Run #3 ; (d) Run #4 169

Fig. 9.22 MRSS (MPa) contours for five crystal lengths. (a) 13.75 mm ; (b) 27.5 mm ; (c) 55.0 mm ; (d) 82.5 mm ; (e) 110.0 mm . Crystal radius is 27.5 mm..... 172

Fig. 9.23 MRSS-CRSS (yield) (MPa) for five crystal lengths. (a) 13.75 mm ; (b) 27.5 mm ; (c) 55.0 mm ; (d) 82.5 mm ; (e) 110.0 mm . Crystal radius is 27.5 mm..... 174

Fig. 9.24 Slip mode of the MRSS for the five crystal lengths shown in Figure 9.22 (a) 13.75 mm ; (b) 27.5 mm ; (c) 55.0 mm ; (d) 82.5 mm ; (e) 110.0 mm . Crystal radius is 27.5 mm..... 176

Fig. 9.25 MRSS-CRSS (Yield) (MPa) in a (001) plane at a distance of 8.25 mm from the cone at four crystal lengths. (a) 13.75 mm ; (b) 27.5 mm ; (c) 55.0 mm ; (d) 82.5 mm. Crystal radius 27.5 mm..... 182

Fig. 9.26 MRSS-CRSS (Yield) (MPa) in a (001) plane at a distance of 49.5 mm from the cone at two crystal lengths. (a) 55.0 mm ; (b) 82.5 mm. Crystal radius 27.5 mm..... 185

Fig. 9.27 MRSS-CRSS (Yield) (MPa) in a (001) plane at a distance of 77.0 mm from the cone at two crystal lengths. (a) 82.5 mm ; (b) 110.0 mm. Crystal radius 27.5 mm..... 188

Fig. 9.28 MRSS (MPa) contours for four crystal lengths. (a) 20.0 mm ; (b) 40.0 mm ; (c) 80.0 mm ; (d) 100.00 mm. Crystal Radius 40.0 mm..... 193

Fig. 9.29 (a) Axial along the crystal axis and (b) radial thermal gradients as a function of distance

from the interface for two crystal radius. Curve (1) for a radius of 27.5 mm ; and curves (2) and (3) for a radius of 40.0 mm. Crystal lengths are (1) 55.0 mm ; (2) 40.0 mm and (3) 80.0 mm..... 194

Fig. 9.30 MRSS-CRSS (Yield) (MPa) for four crystal lengths. (a) 20.0 mm ; (b) 40.0 mm ; (c) 80.0 mm ; (d) 100.00 mm. Crystal Radius 40.0 mm..... 196

Fig. 9.31 Temperature fields for three growth velocities (a) 0.0001 cm/s, (b) 0.001 cm/s and (c) 0.01 cm/s. Temperature given in 10^{3o}C. Little change is observed from (a) to (b). From (b) to (c) gradients have increased. Radius 27.5 mm, length 55 mm, encapsulant thickness 21 mm..... 201

Fig. 9.32 MRSS-CRSS (Yield) (MPa) for the three temperature fields shown in Figure 9.31(a-c) corresponding to three growth velocities. (a) 0.0001 cm/s, (b) 0.001 cm/s and (c) 0.01 cm/s. In (a) and (b) the stress fields are similar. In (c) the stress distribution and stress values change..... 204

Fig. 9.33 Temperature profiles along the crystal surface in the environment surrounding the crystal employed in the calculations. The profiles are derived from Figure 8.19, curve 4, reproduced as curve G. The values of gradient are averaged in the crystal length considered. Encapsulant thickness 21 mm..... 206

Fig. 9.34 MRSS-CRSS (Yield) (MPa) for four temperature profiles with average gradients (a) 33°C/cm, (b) 17°C/cm, (c) 11°C/cm and (d) 8°C/cm. Radius 27.5 mm, length 55 mm. Encapsulant thickness 21 mm..... 209

Fig. 9.35 Temperature profiles used in the calculations for two boron oxide thicknesses. (a) 40 mm, (b) 50 mm. The profiles are derived from curve G. The values of gradients given are averaged along the crystal length..... 211

Fig. 9.36 MRSS-CRSS (Yield) (MPa) for three average gradients. (a) 58°C/cm, (b) 29°C/cm, (c)

19°C/cm. Radius 27.5 mm, length 55 mm, boron oxide thickness 40 mm..... 213

Fig. 9.37 MRSS-CRSS (Yield) (MPa) for three average gradients. (a) 50°C/cm, (b) 25°C/cm, (c) 17°C/cm. Radius 27.5 mm, length 55 mm, boron oxide thickness 50 mm..... 215

Fig. 9.38 MRSS-CRSS (Yield) (MPa) for two average gradients. (a) 14°C/cm, (b) 7°C/cm. Radius 40 mm, length 80 mm, boron oxide thickness 21 mm..... 218

Fig. 9.39 MRSS-CRSS (Yield) (MPa) for four average gradients. (a) 46°C/cm, (b) 26°C/cm, (c) 15°C/cm, (d) 9°C/cm. Radius 40 mm, length 80 mm, boron oxide thickness 40 mm..... 220

Fig. 9.40 MRSS-CRSS (Yield) (MPa) for a crystal length of 52 mm comparable to the boron oxide thickness of 50 mm. Radius 40 mm. Average gradient 50°C/cm... 222

Fig. 9.41 MRSS-CRSS (Yield) (MPa) for three average gradients. (a) 43°C/cm, (b) 14°C/cm, (c) 7°C/cm. Radius 40 mm, length 80 mm, boron oxide thickness 50 mm..... 224

Fig. 9.42 MRSS-CRSS (Yield) (MPa) for four temperature profiles with average gradients. (a) 33°C/cm, (b) 17°C/cm, (c) 11°C/cm and (d) 8°C/cm. Radius 27.5 mm, length 55 mm. Encapsulant thickness 21 mm. Argon pressure 2 atm..... 229

Fig. 9.43 Correlation between the measured temperature gradients across the encapsulant and the heat transfer coefficient values as a function of gas pressure and gas nature. Curve A from Refs. 143-144 using convection from a vertical wall ; and curve B using convection from an horizontal surface..... 234

Fig. 9.44 Element and nodal configuration at the interface for crystals with curved interface. (a) Convex interface, (b) Concave interface..... 237

Fig. 9.45 Temperature (10^{3o}C) and Von Mises stress (MPa) fields for a crystal with a convex interface shape. Radius 27.5 mm. Length 27.5 mm. Encapsulant thickness 21 mm. Temperature profile as shown in Figure 8.19, curve 4..... 239

Fig. 9.46 MRSS (MPa) contours for a crystal with convex interface at three lengths. (a) 27.5 mm, (b) 55 mm, (c) 82.5 mm. The largest stresses at the interface edge are (a) 7.22 MPa, (b) 9.19 MPa, (c) 9.66 MPa. Radius 27.5 mm, Boron oxide thickness 21mm. Profile as in Figure 8.19, curve 4..... 240

Fig. 9.47 MRSS-CRSS (Yield) (MPa) contours for a crystal with convex interface at three lengths (a) 27.5 mm, (b) 55 mm, (c) 82.5 mm. Radius 27.5 mm, boron oxide thickness 21 mm. Profile as in Figure 8.19, curve 4..... 242

Fig. 9.48 MRSS-CRSS (Yield) (MPa) contours in a (001) plane at a distance of 11 mm from the cone in the crystal shown in Figure 9.47(a)..... 244

Fig. 9.49 MRSS-CRSS (Yield) (MPa) contours in (001) planes at three distances form the cone. (a) 79.75 mm, (b) 66.0 mm, (c) 52.25 mm. Section corresponds to the crystal shown in Figure 9.47(c)..... 248

Fig. 9.50 (a) MRSS (MP) and (b) MRSS-CRSS (Yield) (MPa) for a crystal with convex interface. Boron oxide thickness 50 mm. Radius 27.5 mm. Length 55 mm. Average gradient 50°C/cm..... 249

Fig. 9.51 (a) MRSS (MP) and (b) MRSS-CRSS (Yield) (MPa) for a crystal with convex interface. Boron oxide thickness 50 mm. Radius 27.5 mm. Length 55 mm. Average gradient 17°C/cm..... 250

Fig. 9.52 (a) MRSS (MP) and (b) MRSS-CRSS (Yield) (MPa) for a crystal with convex interface. Boron oxide thickness 21 mm. Radius 40 mm. Length 80 mm. Average gradient 55°C/cm..... 252

Fig. 9.53 (a) MRSS (MP) and (b) MRSS-CRSS (Yield) (MPa) for a crystal with convex interface. (a) Radius

27.5 mm, (b) 40 mm. Boron oxide thickness 21 mm..... 254

Fig. 9.54 MRSS-CRSS (Yield) (MPa) contours in a (001) plane at a distance of 2.75 mm from the interface in the crystal shown in Figure 9.53(a)..... 256

Fig. 10.1 Temperature (10^{3o}C) field during cooling at four times. (a) 5 s, (b) 10 s, (c) 20 s, (d) 60 s, Initial gradient close to interface 70°C/cm. Argon temperature 1000°C..... 260

Fig. 10.2 MRSS-CRSS (Yield) (MPa) during cooling for the four temperature fields shown in Figure 10.1(a-d). (a) 5 s, (b) 10 s, (c) 20 s, (d) 60 s. Initial gradient 70°C/cm. Argon temperature 1000°C..... 263

Fig. 10.3 MRSS-CRSS (Yield) (MPa) contours in (001) planes at four distances from the bottom (interface) in the crystal shown in Figure 10.2(b) 10 s, (a) 2.75 mm, (b) 8.25 mm, (c) 16.5 mm, (d) 27.5 mm 268

Fig. 10.4 MRSS-CRSS (Yield) (MPa) in (001) planes at two distances from the bottom in the crystal shown in Figure 10.2 (d) 60 s, (a) 2.75 mm (b) 8.25 mm..... 271

Fig. 10.5 (a) Temperature field (10^{3o}C) and (b) MRSS-CRSS (Yield) (MPa) field for a crystal cooling in argon at 1000°C after 10 s. Initial gradient 35°C/cm..... 272

Fig. 10.6 (a) Temperature field (10^{3o}C) and (b) MRSS-CRSS (Yield) (MPa) field for a crystal cooling in argon at 1000°C after 60 s. Initial gradient 35°C/cm..... 273

Fig. 10.7 MRSS-CRSS (Yield) (MPa) in (001) planes at two distances from the bottom in the crystal shown in Figure 10.5 (b) 10 s. (a) 8.25 mm (b) 27.5 mm..... 275

Fig. 10.8 (a) Temperature field (10^{3o}C) and (b) MRSS-CRSS

(Yield) (MPa) field for a crystal cooling in argon at 1000°C after 10 s. Initial gradient 17.5°C/cm..... 277

Fig. 10.9 MRSS-CRSS (Yield) (MPa) in (001) planes a distance of 27.5 mm from the bottom in the crystal shown in Figure 10.8 (d) 10 s..... 279

Fig. 10.10 (a) Temperature field (10^3°C) and (b) MRSS-CRSS (Yield) (MPa) field for a crystal cooling in boron oxide at 1000°C after 10 s. Initial gradient 70°C/cm..... 280

Fig. 10.11 (a) Temperature field (10^3°C) and (b) MRSS-CRSS (Yield) (MPa) field for a crystal cooling in boron oxide at 1000°C after 10 s. Initial gradient 35°C/cm..... 281

Fig. 10.12 (a) Temperature field (10^3°C) and (b) MRSS-CRSS (Yield) (MPa) field for a crystal cooling in boron oxide at 1000°C after 10 s. Initial gradient 17.5°C/cm..... 282

Fig. 10.13 (a) Temperature field (10^3°C) and (b) MRSS-CRSS (Yield) (MPa) field for a crystal cooling in argon at 800°C after 10 s. Initial gradient 70°C/cm..... 284

Fig. 10.14 (a) Temperature field (10^3°C) and (b) MRSS-CRSS (Yield) (MPa) field for a crystal cooling in argon at 800°C after 10 s. Initial gradient 35°C/cm..... 285

Fig. 10.15 (a) Temperature field (10^3°C) and (b) MRSS-CRSS (Yield) (MPa) field for a crystal cooling in argon at 800°C after 10 s. Initial gradient 17.5°C/cm..... 286

Fig. 10.16 Temperature profiles in the crystal cooling in argon at 800°C for two initial gradients in the crystal. (a) 70°C/cm (b) 35°C/cm. The right part corresponds to the radial profiles and the left part to the axial profile. Full and broken lines correspond to the axis and surface temperatures respectively..... 288

Fig. 10.17 Temperature profiles in the crystal cooling in boron oxide at 1000°C for two initial gradients in the crystal. (a) 70°C/cm (b) 35°C/cm. The right part corresponds to the radial profiles and the left part to the axial profile. Full and broken lines correspond to the axis and surface temperatures respectively..... 289

LIST OF TABLES

Table 5.1 Observed (N_{exp}) and Calculated (N_1 and N_2) Dislocation Densities for Gallium Arsenide Single Crystals 39

Table 7.1 Resolved Shear Stress Components in (001) Crystals 65

Table 7.2 Resolved Shear Stress Components in a (010) Plane for a [001] Crystal 67

Table 8.1 Values of physical parameters used in the calculations 92

Table 9.1 Effect of Cone Angle on Thermal and Stress Fields 124

Table 9.2 Effect of Ambient Temperature on Axial Temperature Gradient and Stress 150

Table 9.3 Effect of Non-linearity of the Ambient Temperature Profile on Stress 162

Table 9.4 Table of Symmetry Correlations 198

Table 9.5 Effect of Thermal Conditions on Stresses 226

Table VI.1 Rotation performed for the calculation of the RSS 357

Table VI.2 Resolved Shear Stress component in the $<1\bar{1}0>$ {111} slip 358

Table VI.3 Compact form of the RSS from Table VI.2 360

LIST OF SYMBOLS

$[B]_i^{(e)}$	Matrix of derivatives of the interpolation functions, 4 x 2
$[B']_i^{(e)}$	Non-dimensional $[B]_i^{(e)}$ matrix, 4 x 2.
$[C]$	Compliance matrix, 4 x 4.
$[C']$	Non-dimensional [C] matrix, 4 x 4.
$\{\tilde{d}\}^{(e)}$	Displacement vector in element e, 2 x 1.
$\{d\}^{(e)}$	Nodal displacement vector in element e, 2n x 1.
$\{d\}_i^{(e)}$	Nodal displacement vector at node i element e, 2 x 1.
$\{d\}_{red.}^{(e)}$	Reduced $\{d\}_i^{(e)}$ vector, 2 x 1.
$\{d'\}$	Global displacement vector in reduced form, 2n x 1.
dV	Elemental volume.
E	Young's Modulus, MPa.
$\{F\}^{(e)}$	Force vector for element e, 2n x 1.
$\{F\}_i^{(e)}$	Force vector at node i in element e, 2 x 1.
$\{F_o\}_i^{(e)}$	Initial force vector at node i in element e, 2 x 1.
$\{F_o'\}^{(e)}$	Non-dimensional $\{F_o\}_i^{(e)}$ vector, 2 x 1.
$F_{o_i}'^{\ i}$	Element of $\{F_o'\}^{(e)}$ vector.
$\{F_o'\}$	Non-dimensional global force vector, 2n x 1.
g	Number of nodes in element
h	Heat transfer coefficient (h.t.c.)
h_c	Convective h.t.c.
h_r	Radiative h.t.c.
$[k]^{(e)}$	Stiffness matrix for element e, 2n x 2n.
$[k]_{ij}^{(e)}$	Stiffness submatrix for nodes i and j in element e, 2 x 2.

$[k']_{ij}^{(e)}$	Non-dimensional $\{k\}_{ij}^{(e)}$ matrix, 2 x 2.
k'_{ij}	Element of $\{k\}_{ij}^{(e)}$ matrix.
$[K']$	Non-dimensional global stiffness matrix.
$\{K^A\}$	Force vector for temperature field calculations.
$[K_H]$	Stiffness matrix from boundary conditions in temperature field calcualtions.
$[K_T]$	Stiffness matrix for temperature field calculations
L	Differential operator.
L_i	Natural co-ordinate.
l_{ij}	Length of element at thne boundary.
m	Degree of freedom in element.
$\vec{n}$	Unit normal vector to a surface.
N	Total number of nodes in the crystal.
[N]	Interpolation functions vector.
r	Radial co-ordinate.
r_o	Cristal radius.
t	Time.
t^*	non-dimensional time.
T	Temperature, ^oC.
T_o	Reference temperature.
T_{MP}	Temperature at melting point.
u_i	Radial displacement of node i.
u(r,z)	Radial displacement at point r, z.
v	Growth velocity.
$V^{(e)}$	Volume of element e.
w_i	Axial displacement of node i.
$w_i(r,z)$	Axial displacement at point of r, z.
W_i	Weighting function.

z	Axial co-ordinate.
α	Coefficient of thermal expansion, $^{o}C^{-1}$.
β	Non-dimensional temperature.
β_a	Ambient non-dimensional temperature.
β_s	Surface non-dimensional temperature.
γ_i	Eigenvalues of Fourier type algebraic equation.
γ_{rz}	Shear strain component in $\{\varepsilon\}$ tensor.
Δ	Area of element (cross-section).
$\{\varepsilon\}$	Strain tensor.
$\{\varepsilon_o\}$	Initial strain tensor.
ε_r	Radial strain component.
ε_θ	Azimuthal strain component.
ε_z	Axial strain component.
ξ	Non-dimensional axial displacement.
λ_i	Eingenvalues of Bessel type algebraic equation.
κ	Thermal diffusivity.
ν	Poisson's ratio.
ρ	Non-dimensional radial displacement.
$\{\sigma\}$	Stress tensor.
σ_r	Radial stress component.
σ_θ	Azimuthal stress component.
σ_z	Axial stress component.
σ_{VM}	Von Mises stress, MPa.
$\sigma_1\ \sigma_2\ \sigma_3$	Principal stresses.
σ_ρ	Non-dimentional radial stress component.
σ_θ	Non-dimentional azimuthal stress component.
σ_ξ	Non-dimentional axial stress component.

$\{\sigma\}_i^{(e)}$	Stress tensor at node i, element e.
τ_{rz}	Shear stress component.
$\tau_{\rho\xi}$	Non-dimentional shear stress component.

ACKNOWLEDGEMENTS

I would like to thank Dr. Fred Weinberg and Indira V. Samarasekera for their assistance and valuable discussions during the course of this work.

Support form the NSERC (Canada), Cominco Ltd., (Canada) and Universidad Nacional de Misiones, (Argentina) is gratefully acknowledged.

CHAPTER 1

INTRODUCTION

Gallium Arsenide (GaAs) is a crystal semiconductor compound that is increasingly being used in the production of semiconductor devices particularly microwave and microelectronic devices[1-3].

The advantages of GaAs over silicon (Si) are due to the differences in physical properties between both materials. Electron mobilities in GaAs are about four times higher than in Si with a power consumption which is a tenth of that in silicon. These become particularly significant as the VLSI circuits become more complex and the operating speed increases. In 1974 the first operating GaAs gate was produced. Ten years later GaAs IC's have been produced with 10,000 gates or 4 SKRAM[3]. In addition IC's are becoming smaller. A 1.1 by 1.6 mm chip may contain more than 600 active components plus contact pads, and work at about 10 Gbit/sec[4]. These facts indicate that GaAs is the most promising material for the next generation of supercomputers[5].

In optoelectronic devices Si has fewer applications than GaAs. Si does not glow brightly enough and does not lase because of the band gap structure[6]. On the other hand GaAs LED's are bright, can be made of different colours by impurity additions, and GaAs lases well because of its direct band gap structure[1]. At

present only about 11 % of the GaAs chips have optoelectronic applications. By 1992 the percentage is expected to increase to 25 %[7]. The combination of micro and optoelectronic properties of GaAs has led to the development of monolithic optoelectronic integration of simple circuits[8-10]. Special emphasis has been placed on the development of the multiquantum well laser.

In the area of solar cells GaAs is an excellent photoconverter with an efficiency of 20-24 %, as compared to Si at 15-18 % . GaAs solar cells are expected to reach efficiencies of 30 % with monolithic or hybrid tandem cells which are presently fabricated[11].

GaAs devices have advantages in radiation fields and at higher temperatures. They can operate in radiation fields 10^4 times larger that Si devices without deterioration, and at higher temperatures than silicon.

One of the disadvantages of GaAs at present is its high cost compared to Si (5.6 cents/mm^2 for GaAs compared to 0.16 cents/mm^2 for Si[12]). However after all fabricating costs are considered for devices, the difference in wafer cost represents only a small fraction of the total and is therefore proportionately less significant[7].

One disadvantage of GaAs, at present is its high dislocation density, as compared to silicon which is dislocation free. Dislocation in many cases may affect both the yield of devices during fabrication and the performance of the devices.

This investigation focuses on the dislocations present in melt grown GaAs. The dislocations are believed to be generated during liquid encapsulated Czochralski growth (LEC) by thermal stresses in the crystal. A mathematical model will be developed to determine the thermal and stress fields in the growing crystal as a function of the many growth variables. The objective is then to use this model to control and modify the growth conditions and thus reduce the dislocation density in a controlled way.

CHAPTER 2

THE GROWTH OF BULK GaAs CRYSTALS

2.1 The Liquid Encapsulated Czochralski Technque (LEC)

In the LEC technique[13-15], shown schematically in Figure 2.1, a single crystal of controlled orientation is pulled from the melt, vertically upwards, starting from a seed crystal. Both the seed and the melt are rotated at different velocities and in directions counter to each other. In general high purity Ga and As are placed in the melt crucible and the intermetallic GaAs synthesized in the high pressure crystal puller. Ga melts at 20.8^{o}C. As melts at 817°C at 28 atmospheres. The melting temperature of GaAs is 1238°C. At this temperature the arsenic partial pressure is 0.98 atm. Pressures of 50 atm. are therefore required to synthesize GaAs. Once the GaAs has formed, a much lower pressure of several atmospheres may be used to keep the GaAs from decomposing. Commercial crystal growers, in particular the "Melbourn" grower from Cambridge Instruments Ltd. is used extensively to grow GaAs crystals. Pressures inside the chamber can be raised to 50-70 atm. as required. In addition to the pressure inside the growing chamber, it was found that liquid encapsulation of the melt and the solid at the highest temperature was necessary to maintain stoichiometry. This is done by encapsulating the liquid with B_2O_3 which also covers the lower end of the growing crystal. The melt and encapsulant are

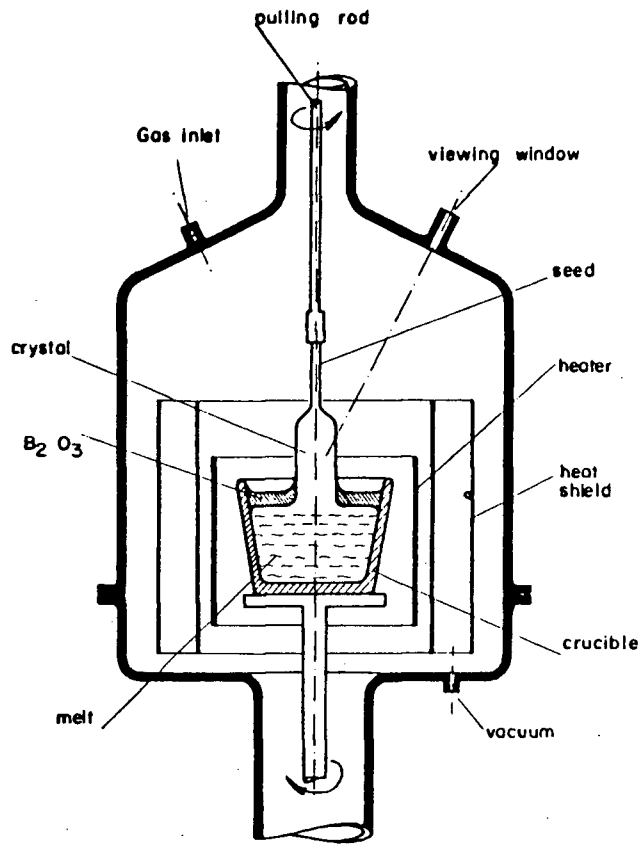

Figure 2.1. Schematic of a LEC pulling chamber

contained in a quartz or a pyrolitic boron nitride crucible[16]. Using the high pressure (HP) LEC process in the Melbourn puller, controlled orientation <100> crystals up to 75 mm in diameter and 8 kgm in weight can be grown with dislocation densities in the order of 10^4 / cm^2 .

As an alternative to the high pressure crystal growers, single crystals are being successfully grown at 1-2 atmospheres pressure using the LEC technique (LPLEC). In this case the starting material is polycrystalline GaAs which has been synthesized separately in a pressure vessel. A novel technique[4,17] permits in-situ synthesis in the LP growers by injection of As through the B_2O_3 layer into a Ga melt contained in the crucible. With the LPLEC growers, crystals of 100 mm diameter and 14 kgm weight have been produced[18-20].

The crystal growth process starts with a seed crystal, usually oriented for <100> or <111> growth, which is dipped into the melt. The crystal is then necked to reduce the propagation of dislocations from the seed to the crystal[21] and the diameter then slowly increased to the full diameter of the crystal.

The growth is monitored visually and with a TV camera. Once the diameter of the crystal is established by manual control of the power input, further control is done with an automatic weighing system which adjusts the power input with computer control[22-24]. Human errors, inabilities to see clearly through the encapsulant, and systematic errors in the weighing procedure due to capillary forces[25], result in variations in the crystal

diameter of the order of 5 mm. Attempts are being made to reduce these problems[6,19,26].

When crystal growth is completed, the crystal is removed from the B_2O_3 and slowly cooled in the chamber to minimize thermal stresses.

GaAs is normally semi-insulating. In some cases isoelectronic additions, such as In, are added to the melt to improve properties. Other solute additions are made to the melt to make the material n- or p-type semiconductors.

For n-type material dopants such as S, Se, Te, Sn, Si and Ge are added. For p-type material Zn and Mg[27] are added. The effect of solute additions and impurities on the electrical and mechanical properties of LEC-grown GaAs crystals and devices are discussed below.

2.2 Classification of Defects in LEC grown GaAs crystal

A defect is defined as any deviation from the crystal structure. Defects consist of :

i. Dislocations
ii. Chemical impurities
iii. Deviation from stoichiometry
iv. Lattice defects,
   1. vacancies and interstitials ;
   2. subgrains, grain boundaries,
      stacking faults, striations and others ;

3. inclusions and precipitates ;
4. microdefects, consisting of small dislocation loops, precipitates, helicoidal dislocations and others. These defects have characteristic lengths of 100 to 1 nm[28-30].

The origin and nature of many of these defects is not clearly understood[30,31]. Generally a number of defects are presented in the crystal, which interact with each other and multiply. An example is the presence of small precipitates on dislocation lines[32]. The precipitates are believed to be crystallites of As embedded in Ga matrices resulting from : 1) direct condensation of As point defects or 2) sweeping up of existing precipitates by moving dislocations.

2.3 Dislocations in LEC-GaAs

Large diameter GaAs <100> single crystals produced by a Melbourn puller have a dislocation density of approximately 5×10^4 /cm^2 [33]. Considerable effort is being directed toward producing low or zero density large diameter GaAs crystals. In 1982 the largest undoped GaAs crystal grown free of dislocation was 15 mm[34]. In 1985 a crystal 50mm in diameter was reported to have been grown dislocation and striation free[35,36]. In the latter case the crystal was grown using a modified LEC technique called VMFEC which includes a vertical magnetic field. The crystal in this case is fully encapsulated and the melt is doped. The

dislocation density can be reduced to 10^3 /cm^2 by doping the melt with n, p or isoelectronic impurities. Recent improvements of the thermal conditions during growth have resulted in undoped crystals with etch pit densities (EPD) of $5x10^3$ /cm^2 for 5 cm diameter crystal[37-39]. In one case 70 mm <100> undoped crystals were grown in low vertical temperature gradients having EPD of $5x10^3$ /cm^2 over 70 % of the wafer area and throughout 75 % of the ingot length[40].

Typical dislocation distributions on transverse sections of GaAs crystal are shown in Figure 2.2. In Figure 2.2a[41] the dislocation density (EDP) is shown along <100> and <110> directions on a (100) GaAs wafer surface showing maximum dislocations at the outside and minimum midway between the outside and the center, giving a W shape distribution across the entire wafer. Figure 2.2b shows EPD distribution in a (100) wafer surface taken near the tail end of a 5 cm diameter crystal. The etch pit distribution has the four-fold symmetry normally observed, with higher densities at the outside and centre of the wafer. Close to the end of the crystal, EPD maps on 5.0 cm diameter crystal show the four-fold symmetry degenerates to two-fold symmetry. This distortion is caused by the shift of the two minima in the [110] and [$\bar{1}\bar{1}$0] directions to positions closer to the edge of the wafer[33].

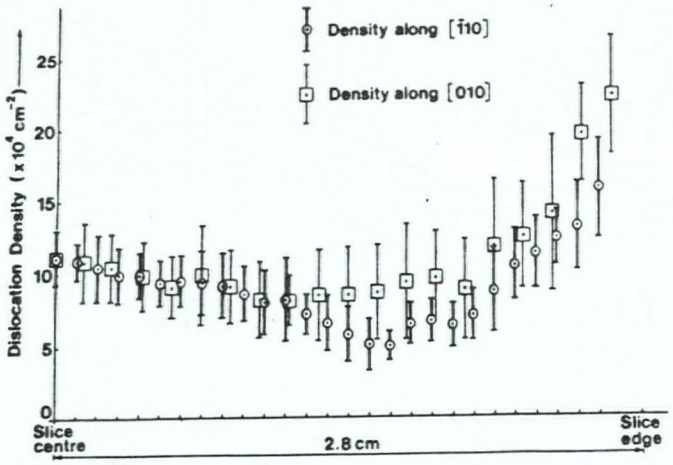

a

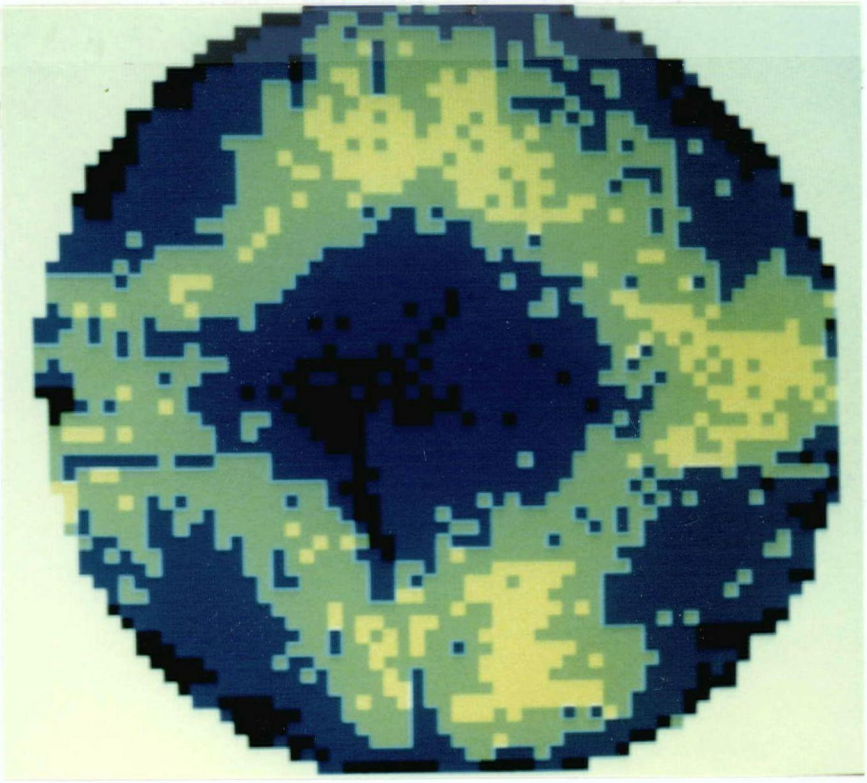

b

Fig. 2.2 a) Experimentally determined[41] dislocation density along [110] and [010].

b) EPD map[33] on a 5cm dia. wafer from the tail end . 10^4 Etch Pits/cm^2 . 1 < yellow < 12 < green < 15 < blue < 20 < black < 30 .

2.4 Effect of Dislocations on Properties of GaAs Devices

Dislocations are known to affect the electronic properties of GaAs in the following ways : 1) They are considered to be non-radiative recombination centers[42] ; 2) They absorb non radiative impurity atoms or point defects[43] ; 3) When dislocations are arrayed in cellular structures, carriers are not active at the cell walls[43].

The effect of dislocations on the properties of microelectronic and optoelectronic devices depends on the nature of the device and how it is fabricated. In optoelectronic devices, it has been reported that dislocations seriously reduce the lifetime of lasers[44], reduce the efficiency of LED's[42], and under an applied stress, increase the degradation of diodes by one order of magnitude[45,46]. The mechanism for these effects is unclear[47].

With microelectronic devices it was considered that dislocations did not significantly affect their properties[48]. However at the present time this has changed and dislocations are believed to affect the electrical properties of IC's of GaAs. These results are presented and discussed in Appendix I.

CHAPTER 3

THE ORIGIN OF DISLOCATIONS IN LEC GaAs CRYSTALS

Dislocations in GaAs are either seed related or growth related. The seed related dislocations result from the propagation and multiplication of dislocations from the seed into the main crystal. These dislocations can be reduced or eliminated by necking the seed crystal, as is commonly done, or by starting with a dislocation free seed crystal[35].

The growth related dislocations in the crystal are generally attributed to the thermal stresses generated in the crystal during growth. The dislocations nucleate in regions of maximum stress near the crystal surface, then propagate along slip planes and multiply. The dislocations can also be generated by thermal stresses at precipitates or foreign particles, and by the condensation of vacancies into dislocation loops which glide.

Examination of a <100> melt grown GaAs crystal wafer by transmission X-ray topography of etch pits (EPD) shows that the dislocations are not uniformly distributed throughout the wafer as shown in Figures 3.1 a at C . As described previously the dislocation density along a crystal diameter follows a W pattern with higher concentrations at the outside and center. In addition the dislocations form cells by concentrating along cell walls. Cell diameters have been observed of 0.1 mm in areas of

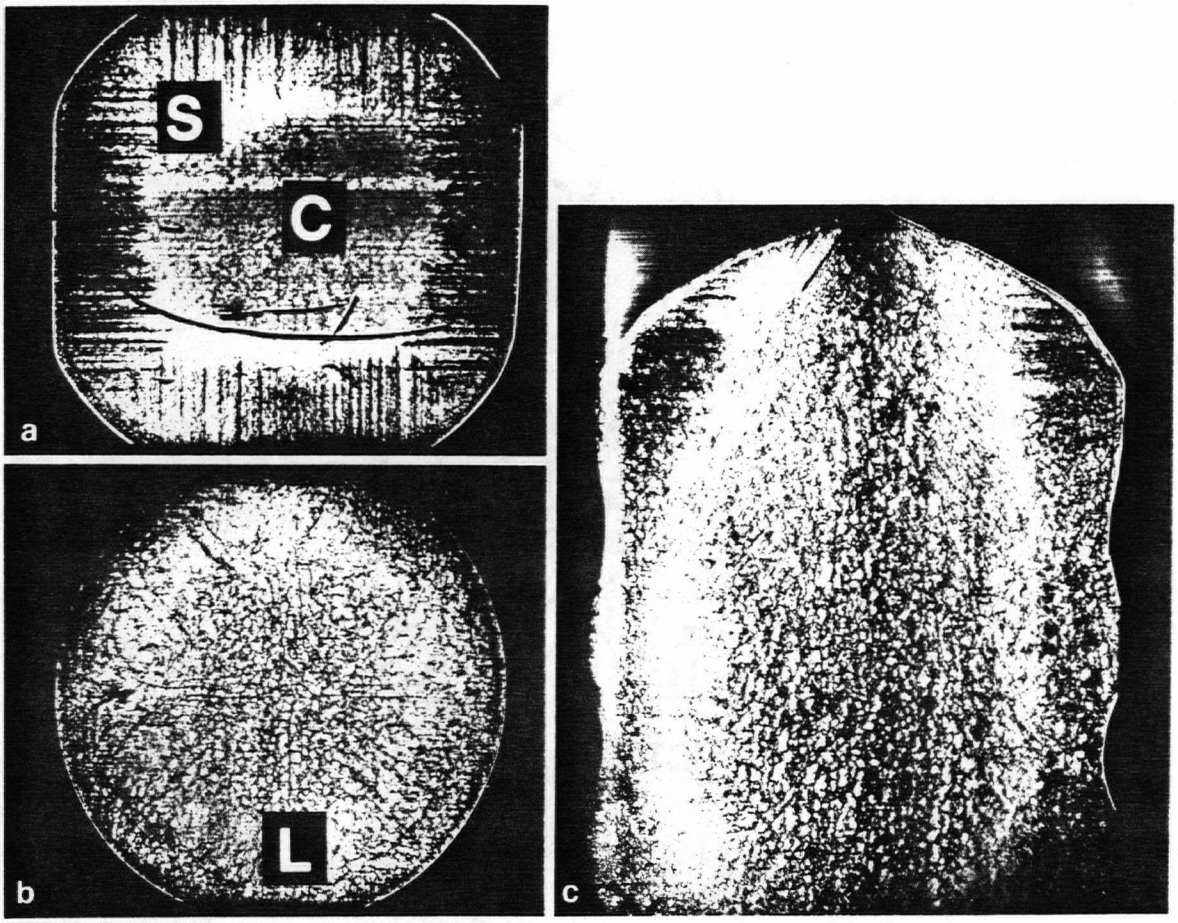

Figure 3.1 Transmission X-ray topography in GaAs - (a) and (b) undoped ; (c) Te-doped, (110) axial section[113]

dislocation densities of 10^5 /cm^2 (based on EPD). At lower densities the cells can increase in size up to 3 mm[30,110]. The cell wall directions on a (100) crystal face are randomly oriented.

The formation of cells in the GaAs wafers is not clearly understood. The most favoured mechanism is that dislocations generated near the crystal walls and in the centre glide and climb after solidification eventually forming the cell structure to minimize their energy. An alternative mechanism has been proposed by Holmes[111] in which the cell structure is attributed to constitutional supercooling at the surface, similar to cell formation in metal alloys. This mechanism appears unlikely[112] because of the low impurity levels in the GaAs, high stoichiometry at the interface and slow growth velocities.

In addition to cell structures on GaAs crystals, long linear arrays of dislocations are also observed as shown in Figure 3.1b at L. The linear arrays are observed in areas having a dislocation density of less than $2x10^4$ /cm^2 and produce a small tilt orientation difference of about 0.01^o in the crystal across the line. These arrays are roughly similar to lineage sub-boundaries in melt grown metal crystals attributed to the condensation of vacancies immediately behind the interface, forming dislocation loops which climb to form lineage boundaries.

Slip lines are sometimes observed on etched GaAs wafers as shown in Figure 3.1a at S, generally in areas of lower dislocation density (10^3 /cm^2)[113].

Specific observations and discussions of dislocation generation and multiplication in GaAs are given below :

1. The generation of dislocations by thermal stresses has been reported by Milvidskii and co-workers[114] and others[115,116]. Thermal stresses in the growing crystal result from radial and axial temperature gradients. When the local stress is greater than the critical resolved shear stress, glide occurs on the (111) slip planes in $\langle 1\bar{1}0 \rangle$ directions[117,118]. This mechanism was proposed for Si by Billig[119] and was applied to Ge by Penning[120].

2. The most probable mechanism for the generation of dislocations is stress concentration at heterogeneous sources at the crystal surface or in the bulk material. Small precipitates of As have been found at dislocations[32]. Amorphous precipitates of Ga or As have been observed on the cell walls in undoped GaAs[30]. Insular polycrystalline GaAs having diameters of 1000°A have been observed in Si doped GaAs which are associated with dislocation generation[30]. Steinemann and Zimmerly[121] associate dislocation generation with precipitates of excess Ge or impurity atoms. Excess Ga vacancies[115,122] in particular and native point defects in general[123125] which precipitate into dislocation loops have been considered as a source of dislocations. Lagowski et al.[126,127] have proposed a theory in which

the Ga vacancy is the critical native defect in the formation of the dislocation loops. This theory is presented in part b of Appendix I.

3. The stress distribution in growing crystals has been considered in several ways. Nikitenko and Indenbom[128] used photoelastic methods to observe the stress distribution in crystals. They also used mathematical models to establish the stress field in a growing crystal and derived the dislocation distribution based on local stress levels above the critical resolved shear stress. The distribution they predicted agreed reasonably well with observations. The correlation of thermal stress fields to dislocations has also been observed using X-ray diffraction to measure lattice strains in GaAs[129-131], photoelastic methods[132,133] and photoluminescent scanning[134].

In summary, several causes for the origin of dislocations in GaAs have been proposed in the literature. In crystals grown from melts far from stoichiometry the Ga vacancy may control the formation of dislocations. Under normal growth conditions, however stresses play a fundamental role in controlling dislocation densities by a glide mechanism. More experimental evidence supporting the stress related mechanism is presented in the next chapter.

CHAPTER 4

DISLOCATION DENSITY AND CRYSTAL GROWTH

The density and distribution of dislocations in LEC grown GaAs crystals is strongly dependent on a number of growth parameters. The dislocation density may be reduced, improving the crystal quality, by changing the growth conditions :

1) Reducing the radial and axial thermal gradients during growth
2) Adding impurities to solution harden the crystal increasing the CRSS
3) Reducing variations in the crystal radius during growth
4) Maintaining stoichiometry of the Ga and As in the melt.

More uniform dopant and impurity distribution in the crystal may be obtained by stopping fluid flow in the melt due to convection.

4.1 Stresses in the Crystal Due to Thermal Gradients

Thermal stresses in the crystal in LEC GaAs growth depend primarily on 1) the crystal dimensions and 2) the ambient variables affecting the temperature distribution in the crystal.

4.1.1 Crystal Dimensions

In this category the variables are crystal diameter, crystal length, cone angle and neck and seed dimensions.

Increasing the diameter of the crystal generally increases the dislocation density. At very large diameters this may not be the case. Increasing the diameter of crystals from 5.0 - 7.5 cm diameter to 12.7 - 15.2 cm diameter did not change the dislocation density [18].

The increase in dislocation density with increasing diameter can be due to an increase in axial and/or radial thermal gradients. Experimental observations are contradictory[135,136]. Results of calculations are also contradictory. According to Jordan et al.[137] both axial and radial gradients increase with radius. On the other hand, Brice[135] and Buckley-Golden and Humphreys[138] report that axial temperature gradients and axial temperature curvatures decrease with increasing radii.

The EPD indicating dislocation density, increases with distance from the seed end of the crystal. The dislocation distribution across the crystal has a W shape, as shown in Figure 4.1., which is maintained throughout the crystal. In low dislocation density crystals Elliot et al.[113] have reported high EPD values at both the seed and tail ends of the crystal.

The effect of cone angle on EPD has been evaluated experimentally by Chen and Holmes[110]. They found that the EPD decreases with increasing cone angle up to a value of about

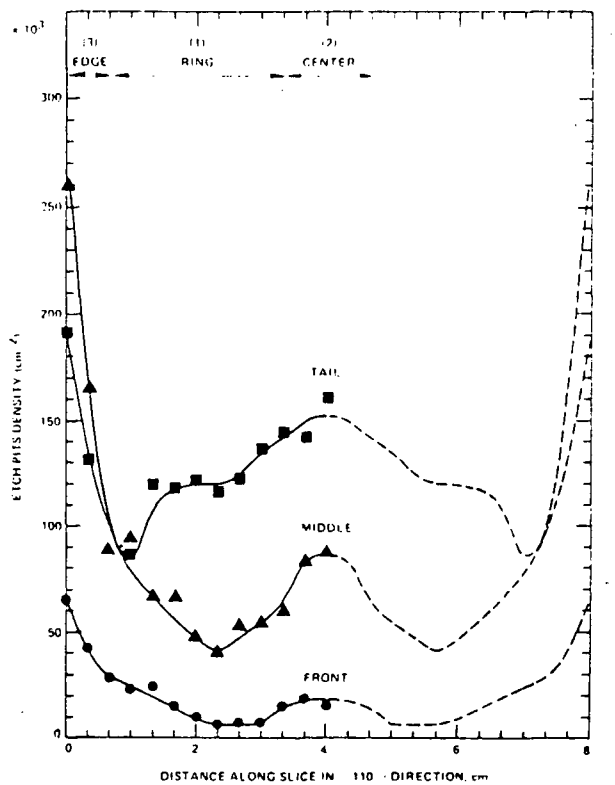

Figure 4.1 Radial dislocation density profiles across wafers obtained from the front, middle, and tail of a crystal. The radial profiles are "W" shaped, and the average EPD increases from the front to the tail.

25 degrees. Above this value they found no correlation between the EPD and cone angle. This agrees with Watanabe et al.[39].

Thermal stresses depend on the elastic constants of GaAs. Accordingly the crystal orientation should affect the dislocation density. For horizontal Bridgman growth of GaAs Plasket et al.[116] have found that the lowest dislocation density was obtained for crystals grown in the <013> direction. This cannot be taken advantage of because circular GaAs crystal wafers having (100) surfaces are required for production of IC's.

4.1.2 Thermal Conditions During Crystal Growth

Thermal gradients in the crystal depend directly on the thermal conditions in the surrounding environment through heat transfer at the boundary of the crystal. The heat transfer process can be characterized in a simple way by heat transfer coefficients and the ambient temperature around the crystal. The main factors affecting the heat transfer are : gas pressure, boron oxide layer thickness, and the geometry and position of the heater and shielding system.

Increasing gas pressure increases the EPD[39,110,115]. This effect is explained in terms of the variation of the heat transfer coefficient[110], which according to calculations increases as the square root of the pressure[137,139]. The change in heat transfer coefficient between the crystal and gas cannot explain the variation in the EPD observed.

The gas pressure during crystal growth cannot be reduced to reduce dislocation density. Without sufficient pressure at high temperatures As atoms leave the crystal. Excess Ga on the surface will result in pitted surfaces, twins and polycrystalinity [110,140,141]. In addition, changing the gas pressure changes the atomic fraction of As in the melt. This can influence the electrical resistivity of the material[142].

The dislocation density is also affected by the type of inert gas used. A nitrogen atmosphere gives an EPD one order of magnitude higher than argon[39]. With other inert atmospheres the EPD counts were found to increase in the order Kr, Ar, N_2 and He[143,144]. The effect is attributed to the different heat transfer efficiencies of the gases which change the thermal gradient in the boron oxide encapsulant.

In a conventional Melbourn grower increasing the B_2O_3 layer decreases the dislocation density in the crystal. Doubling the encapsulant thickness from 15 to 30 mm reduces by half the axial gradient[145-147]. At present 50 mm thick layers are used[35,148]. Enhanced heating of the B_2O_3 layer through windows in the susceptor cylinder results in lower axial gradients and therefore lower EPD. The addition of baffles above the crucible to reduce convection of the gas reduces the axial and radial gradients to $15^{o}C/cm$ and $3^{o}C/cm$ respectively for a B_2O_3 thickness of 30 mm. With this technique 5 cm diameter crystals can be produced with dislocation densities of $10^3/cm^2$ in large areas.

4.2 Alloy Addition to the GaAs

The reduction or elimination of dislocations in GaAs by alloy additions to the melt was reported as early as 1972[149]. The effectiveness of specific additions in reducing the as grown dislocation density in GaAs (20-25 mm diameter) is shown in Figure 4.2[150]. It can be seen that Te is the most effective in reducing the dislocation density followed by In, Sn and Zn. Seki and coworkers[151] determined that Zn, S, Te, Al and N are effective in reducing the dislocation density. Silicon[152,153] and Boron[154] have also been shown to have the same effect.

Dislocation free GaAs has been obtained doping the melt with N (20 mm in diameter)[155], Te (22 mm in diameter, <111> crystal)[156], Si (40-50 mm diameter)[157], In (50 mm in diameter)[35,36,158].

One important aspect of doping is that the addition produces n- or p-type material. If semi-insulating (Si) GaAs is required, only isoelectronic impurities can be added. Indium is the promising impurity to decrease dislocation density and obtain semi-insulating material[159-162].

The primary effect of doping is to increase the critical stress for dislocation generation. For undoped GaAs the CRSS is 7 g/mm while for Te-doped GaAs ($2x10^{18}$ atoms/cm^3) the CRSS is 40 g/mm[163]. This effect, as explained by Milvidskii et al.[163], appears because high temperature and low stresses create

favourable conditions for the formation of a stable impurity atmosphere (Cottrell atmospheres) surrounding moving

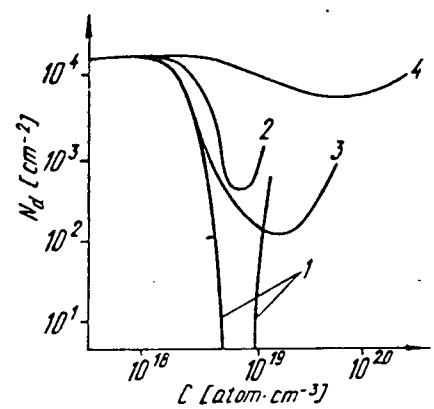

Figure 4.2 Mean density of "grown-in" dislocations in GaAs single crystals (20-25 mm in diameter) grown by the Czochralski LEC Technique, as a function of dopant concentration : (1) Te, (2) Sn, (3) In, (4) Zn.

dislocations. This reduces the dislocation velocity. The effectiveness of an element in stopping dislocation movement is given by a factor U^2/D where U is the elastic interaction of atoms with dislocations and D is the impurity diffusion coefficient.

A number of specific mechanisms have been proposed to account for the effect of solute atoms on dislocation mobility. Seki et al.[151] associated dislocation movement with breaking of bonds between solute elements and the matrix, with limited success. Sher et al.[164] related the bond length (d) to dislocation energies and hardness in semiconductors. They showed that dislocation energies per unit length are proportional to d^{-3} - d^{-9} and hardness to d^{-5} - d^{-11} . This analysis could be used to account for the reduction in dislocation density in GaAs by adding BAs[165] and GaN[151,155] and predicts GaP additions will reduce the density.

The reduction in dislocation density by In can be accounted for by solution hardening[166]. In this case the solute entity is not the In atom alone but consists of a cluster of five atoms. The cluster is formed by one In atom bounded by four As atoms, $InAs_4$, in a tetrahedral configuration which is embedded in a GaAs matrix. These results are supported by the experimental observations that the fcc (Ga,In) sublattice parameter increases linearly with In concentration and that the Ga-As and In-As bond length remains roughly constant as x is varied in $Ga^{(1-x)}In^{x}As$[167]. The dilation of an $InAs_4$ tetrahedra as compared to a $GaAs_4$ tetrahedra is 21 % . This is semiquantitatively calculated to have a stronger effect than solution hardening in metals.

Solute additions to the GaAs melt can markedly influence the behaviour of devices fabricated on the crystal wafer.

1) If sufficient solute is added constitutional supercooling could develop at the interface producing solute microsegregation in the crystal

2) Lineage structure can be developed in the crystal producing orientation variations.

3) Microdefects, including precipitates can be present in the crystal due to the solute present. As an example, Te additions at low levels produce stacking faults in the crystal[168-173]. Te additions at high levels produce prismatic dislocations in addition to stacking faults[172,173]. S additions have the same effect[168]. Helicoidal dislocations were observed in GaAs with small addition of Te ($2x10^{18}$ atoms/cm^3) and with Sn, S and Zn additions[168,174].

Controlled additions of elements to GaAs are made to produce p- or n-type crystals. The elements selected should result in the desired type of crystal with minimal other defects produced, as well as the reduction in dislocation density. It has been shown that Si is the best dopant for GaAs to produce n-type behaviour, at levels of near 10^{18} atoms/cm^3, as compared to Te and S[175,176]. In this case dislocations densities of $3x10^3$ /cm^2 are obtained with no microdefects. At higher dopant levels, above $3x10^{18}$ atoms/cm^3, straight and helicoidal dislocations become pronounced. Similar results are obtained with In dopant for levels greater than $2x10^{19}$ atoms/cm^3. At high In levels

(10^{20} atoms/cm^3) three different regimes of dislocations have been reported by Pichaud et al.[177] as shown in Figure 4.3 . In the figure the In concentration is shown to increase with distance along the growth direction (pulling axis) which changes the dislocation density.

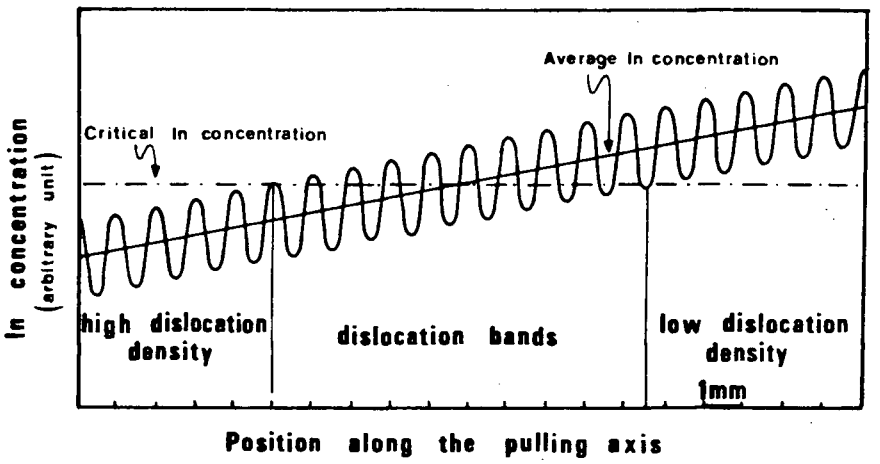

Figure 4.3 Hypothetical distribution of the dopant (In) along the pulling axis of the ingot. The indium concentration oscillates around a mean value which is proportional to the distance from the top of the ingot.

At the seed end and middle of the crystal, dislocations are tangled with a banded periodical distribution normal to the growth direction. In the final third of the crystal the bands disappear and the dislocation density is reduced. The oscillations in the In levels shown schematically in the figure are associated with convective flow in the melt.

Striation or linear boundaries are observed in undoped GaAs crystals[178]. The striation density can be reduced by applying a magnetic field at kilogauss levels to undoped GaAs[179], Se doped[179,180] and In doped[137]material. With a vertical magnetic field thermal oscillations in the melt due to convection can be reduced to less than $0.3^{o}C$ [181] but not eliminated[180]. However, at this time it is not clear how the magnetic field and convective flow quantitatively change the crystal characteristic. Numerical simulations[182] and modelling[183] indicate magnetic fields at kilogauss levels do not suppress convective flow. Recent results show a 2 KGauss field can stabilize flow and thermal fields[184]. The influence of a magnetic field on the impurity distribution in grown crystals is complex. Carbon concentrations are decreased and Chromium levels are increased[181]. Residual impurities are changed, as evidenced by a reduction in electrical resistivity of undoped crystals[185] .

The addition of In to GaAs to reduce dislocation densities without changing the electrical properties presents difficulties. Macrosegregation of the In along the crystal axis will occur as in Figure 4.3 . In addition the lattice spacing in GaAs changes with the In concentration which affects the quality of epitaxial layers deposited on the surface in device fabrication.

Specifically, misfit dislocations are produced at the SI GaAs substrate and MBE deposited GaAs above a critical deposited layer thickness. The critical layer thickness decreases exponentially with increasing In concentration. For a significant

reduction of dislocations, In concentrations greater than 10^{19} atoms/cm^3 are required. At concentrations of 10^{20} atoms/cm^3 the critical thickness of deposited material is about 1 micron which is small.

The effect of In alloying in FET characteristic has been examined by Hunter et al.[187]. Using direct ion implantation on In alloyed crystal wafer the FET's showed uniform properties along the wafer. Inhomogeneous FET's characteristic are expected from arrays fabricated on wafers with inhomogeneity in the resistivity. Non uniform resistivities along radial and axial directions are characteristic of In doped GaAs crystals with dislocation or dislocation free material[188]. The uniformity in the FET properties obtained by Hunter et al. could be a result of a post solidification annealing process as a result of the low growth velocities and low thermal gradients during crystal growth. Bulk annealing has produced uniformity improvements in undoped GaAs[188] and In doped GaAs[103].

CHAPTER 5

MODELS OF DISLOCATION GENERATION IN GaAs

Mathematical models for dislocation generation by glide due to thermal stresses have been developed using different approaches for the calculation of the thermal field in the crystal as well as the thermoelastic stress field.

5.1 Stress Fields

1. The temperature field in the growing crystal has been calculated numerically[189] assuming the interface is a paraboloid of revolution. The boundary conditions were determined experimentally by measuring the near surface temperatures at a number of positions along the crystal. The thermoelastic stresses were calculated assuming a cylindrical crystal with flat faces and using a plain strain approximation. The results are shown in Figure 5.1 for a <111> grown crystal. The calculated isotherms and RSS are shown as a function of position in the crystal in (a) and (b) for two crystals of different dimensions. The number to the right of the temperatures gives the CRSS. It is apparent that there are a few areas where the RSS is less than the CRSS (shown by the dashed lines). The isotherms in parts of the figure are first concave following the interface shape and change to convex after the 1200°C isotherm. Growth conditions and crystal characteristics are not given. In parts (c) and (d) of the figure

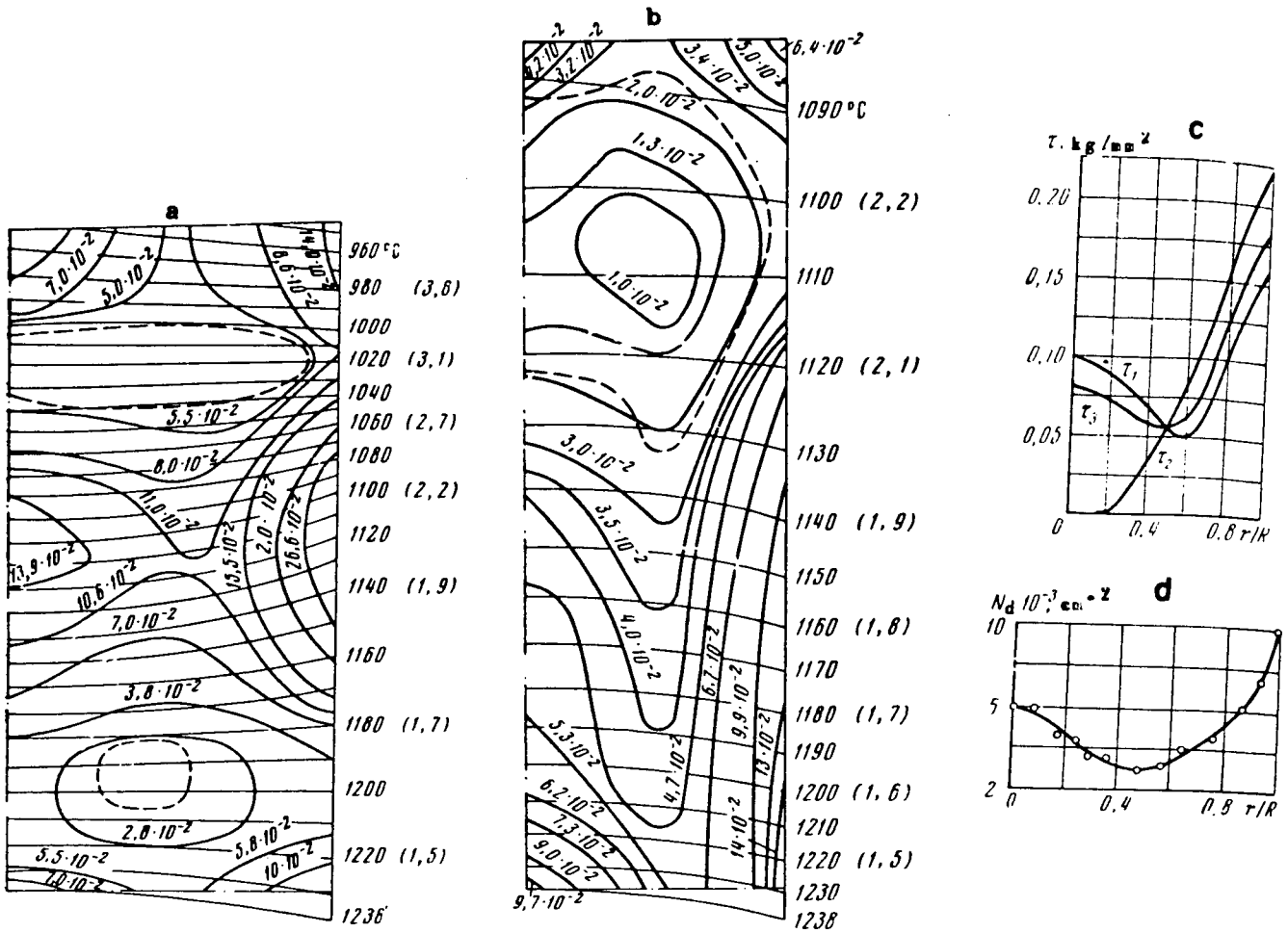

Fig. 5.1 (a) and (b) - Isotherms and shear stress topography in two gallium arsenide single crystal grown under different conditions. The figures next to the curves are τ_3 values (kg/mm^2) corresponding to the constant-stress lines. The dashed curves outline regions in which the effective stresses τ_3 are lower than the reduced yield stress. The figures in parentheses along the ordinate axis are the experimental critical stresses in 10^{-2} kg/mm^2.
(c) and (d) - Distribution of shear stresses τ_1, τ_2 and τ_3 (c) and dislocation density (d) over the cross-section of a gallium arsenide single crystal.

the mean RSS shows the typical W- shaped distribution of the dislocations along the wafer diameter ; the stress symmetry is not obtained. The effect of growth conditions is not analysed.

2. The temperature field in growing GaAs has been determined analytically by Jordan et al.[137,148,190]. They used a quasi-steady state approximation of the heat conduction equation in cylindrical coordinates. For the boundary conditions they assumed a constant temperature at a flat solid/liquid interface and convection/radiation heat loss at the surface of the crystal following Newton's Law of cooling. The heat transfer coefficients used were evaluated separately as a function of temperature[139,191]. Using the calculated thermal fields, the stresses in the crystal were calculated using a plain strain approximation, and the RSS was determined for a <100> oriented crystal. The local dislocation density was assumed to be proportional to the total RSS. This was defined as the sum of the absolute values of RSS acting on {111} $\langle 1\bar{1}0 \rangle$ slip system. The results are shown in Figure 5.2 in which the total RSS (TRSS) is plotted on a transverse plane of a cylindrical crystal. Typical four-fold symmetry is observed with stress minima midway between the outside and centre of the crystal along the <110> directions. The principal conclusions derived from the model follow :

1) Doubling the radius of the cylindrical crystal from 2 to 4 cm more than doubles the TRSS.

2) The dislocation density increases with increasing heat transfer coefficients.

3) The dislocation density can be reduced to zero if the heat transfer coefficient is small enough, estimated as one order of magnitude smaller than the values used in the calculations.

3. The temperature field is calculated numerically and the thermal stresses determined. However, in this case stress relaxation during growth is included in the analysis (Vakhrameev et al.[192]). The thermal field is determined by solving the steady state thermal conduction equation for the entire growth system including crystal, melt, gas and crucible. The encapsulant B_2O_3 is neglected[193]. The thermoelastic stress field is obtained by solving the displacement thermoelastic equation by a finite difference method[194]. Results are shown in Figure 5.3(a-c). In Figure 5.3(a) and (b) the dislocation density is shown as a function of temperature for a Burger vector perpendicular to and inclined to the growth direction <111>. A considerable fraction of the dislocations is observed to be on the periphery of the crystal at temperatures well below the melting temperature. Figure 5.3(c) shows dislocation densities, thermoelastic stresses, relaxed stresses and CRSS for undoped GaAs along the axis of the crystal. Two well defined regions are observed where dislocations are formed, one near the crystallization front at 1238°C and the other near 1140°C. Thermoelastic stresses in this case are relaxed about 80 % . The growth conditions are not given and the effect of growth parameters is not discussed.

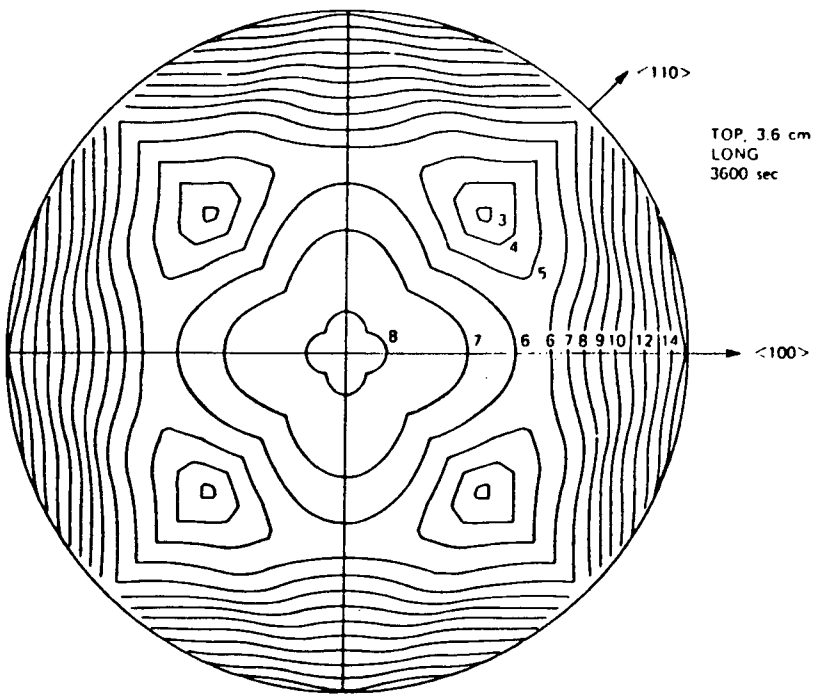

Figure 5.2 T R S S contours for the top wafer of a <001> GaAs boule.

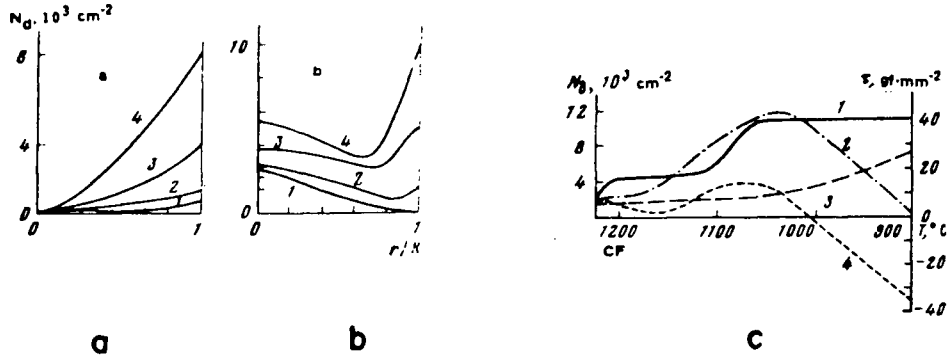

Figure 5.3 Distribution of the calculated dislocation density in a gallium arsenide single crystal being grown in the <111> direction for slip systems with Burgers dislocation vectors perpendicular
(a) and inclined
(b) to the growth axis at the following temperatures: 1) 1234, 2) 1200, 3) 1140, 4) 1050°C - T.
(c) Distribution of calculated dislocation density 1) thermoelastic stress, 2) relaxed thermal stress, 4) and critical stress for the formation of dislocation in undoped GaAs at the corresponding temperature, 3) along the axis of a single crystal during its growth ; CF) crystallization front.

4. Dussaux[195] has employed a finite element method to obtain both thermal and stress fields. The thermal field was calculated by solving the steady heat conduction equation in the crystal subject to Newton's Law of Cooling at the crystal surface as done by Jordan et al.[137,148,190] .

The numerical scheme chosen permits more realistic boundary conditions to be used such as temperature gradients outside the crystal and temperature dependent heat transfer coefficients. In addition different geometries can be considered. The stress field is calculated using the minimum energy principle method and an axisymmetric field is assumed. From the stress components the Von Mises stress is derived. Stresses are not resolved in the slip system. The Von Mises stress contours in the crystal for a fixed boron oxide layer, and thermal gradients are presented for two crystal diameters and different crystal lengths. The model is employed to compare the LEC and LEK (liquid encapsulated Kryopoulos) methods and not to an extensive analysis of dislocation generation in LEC growth.

5. Thermal stresses have been calculated using analytical approaches in which the plain strain approximation is not assumed. Instead of plain strain an axisymmetric approximation is used. Qualitative good agreement with plain strain and FEM calculations is obtained[196]. Using the same axisymmetric approximation[197,198], it was shown that the plain solutions are not always valid in determining the thermal streesses in the

crystal. These conclusions are obtained for semi-infinite geometries.

6. Galaktionov and Tropp[199] have considered a non standard approach to introduce the effect of axial gradients. They assume that the axial gradient of the total stresses (transient and residual) are numerically equal to the thermoelastic stresses produced by a hypothetical temperature field given by the axial gradient of the real field. In equation form this is expressed as

$$\frac{\partial}{\partial z}\,\sigma_{ij}\,[T(x,y,z)] \;=\; \sigma_{ij}\,[\frac{\partial}{\partial z}\,T(x,y,z)]$$

The method is used to calculate the residual stresses in infinite cylinders.

5.2 Calculation of Dislocation Densities

The dislocation density at a point in a growing crystal is a function of the local stresses generated by the thermal strains. The density may be assumed to be proportional to the maximum RSS (MRSS) or to a lesser value if the stress is considered to be relieved by plastic flow. This has been considered in a number of different ways :

1. Jordan et al. (model 2) assumed that the thermoelastic stresses were partially relieved by plastic flow but made no estimate of the amount relieved. The flow was assumed to be proportional to the TRSS.

2. Vakhrameev et al. (model 3) calculated that 80 % of the thermoelastic stress is relaxed by plastic flow.

3. Billig in 1956 and Indenbom in 1957 proposed that stresses are completely relaxed.

Billig[129] estimated the dislocation density using the following simple analysis. Consider a thin slab of thickness δr and length z. The application of a temperature gradient $\delta T/\delta r$ will expand the heated surface by $\delta r = \alpha z\, \delta T$. This expansion will bend the slab giving a curvature radius $1/R = (1/z)x(\delta z/\delta r)$. If stresses are relaxed by plastic deformation a number of edge dislocations are formed. The density n is given by the curvature and Burger's vector, $n = 1/Rb$, therefore

$$n = (\alpha/b)\ (\delta T/\delta r)$$

Using this relation Billig estimated dislocation densities in Ge of the order of $3.2x10^4$ $/cm^2$ for given growth conditions.

Indenbom proposed a similar expression in which the axial temperature gradient is considered. This is given by

$$n = (1/b)\ [d(\alpha T)\ /dt]$$

The above expression is part of a more complex equation that involves a tensorial dislocation density $\hat{n}$, given by

$$\hat{n} = -\vec{grad}\ T\ X\ \hat{\alpha}$$

where $\hat{\alpha}$ is the tensor of the coefficients of linear thermal expansion[202,203]. The contribution of the radial and axial temperature gradients to the total dislocation density is not clear[119,204].

Indenbom also proposed another expression to estimate the total dislocation density from plastic deformation ε

$$n = \varepsilon / bL$$

where L is the dislocation length which, for Ge and Si, is of the order of 0.25 mm. The Indenbom equations were extented[106,207] by introducing the CRSS in the glide plane to obtain the following expression for the dislocation density

$$n = (\alpha/b)\vec{\nabla}Tn - 2(\bar{\tau}_{cr}/Gb)(1/D)$$

which reduces to the equation given by Indenbom when the CRSS is zero. In the equation $\vec{\nabla}Tn$ is the mean axial temperature gradient, D is the crystal diameter and G is the shear modulus. The dislocation densities calculated with this equation are compared to measurements on GaAs in Table 5.1. The columns headed N1 and N2 are calculated values for the first and second terms of the above equation. This equation is not used in the present investigation because it is inconsistent with the evaluation of dislocation densities from stresses in the crystal. This is because a constant axial thermal gradient does not produce stresses.

In summary from the reported results it is not clear to what extent the thermoelastic stresses are relieved. In deriving dislocation densities adjustable parameters are introduced in pseudo-empirical equations which are not tested under controlled laboratory conditions. In addition, in the equations in which dislocation densities are directly proportional to thermal gradients, the role of stresses in generating dislocations is not clear.

Table 5.1 Observed (N_{exp}) and Calculated (N_1 and N_2) Dislocation Densities for Gallium Arsenide Single Crystals.

D, cm	∇T_a, deg/cm	N_{exp}, cm^{-2}	N_1, cm^{-2}	N_2, cm^{-2}	Growth method
1,0	142	$5\ 10^3$	$1,7\ 10^4$	$2,2\ 10^4$	
2,4	140	$\sim 3\text{-}5\ 10^4$	$2,0\ 10^4$	$2,2\ 10^4$	
2,4	120	$\sim 1\text{-}2\ 10^4$	$1,7\ 10^4$	$1,9\ 10^4$	The Czochralski
2,4	120	$\sim 0,9\ 10^3$	$1,7\ 10^5$	$1,9\ 10^5$	method
2,4	50	$\sim 5\text{-}6\ 10^3$	$5,7\ 10^5$	$7,8\ 10^5$	
2,7	190	$5\ 10^4$	$2,7\ 10^4$	$2,9\ 10^4$	
0,8	450	$\sim 1\ 10^5$	$0,6\ 10^5$	$0,7\ 10^5$	
0,8	380	$7\text{-}9\ 10^4$	$5,3\ 10^4$	$5,9\ 10^4$	Free zonal
0,8	290	$4\text{-}6\ 10^4$	$3,9\ 10^4$	$4,5\ 10^4$	melting
0,8	210	$2\text{-}3\ 10^4$	$2,6\ 10^4$	$3,2\ 10^4$	

Note : N_1 and N_2 were calculated with Eq.(2) and Indenbom's equation, respectively ; b=4,10 cm [21], $\alpha = 6,2\ 10^6\ deg^{-1}$, and it was assumed that $\tau_{er}/G \simeq 1\ 10^{-4}$.

CHAPTER 6

OBJECTIVES

In the previous chapters it has been pointed out that dislocation densities at the levels usually present in LEC GaAs are detrimental to the preformance of fabricated devices. New technological advances in the GaAs micro and optoelectronic industry require GaAs wafers of low dislocation density or free of dislocations.

Dislocations in LEC GaAs are generated during growth mainly due to thermal stresses. On the basis of a glide mechanism thermoelastic models have been developed to describe the dislocation distribution in as grown crystals. These models employ analytical and numerical methods. The models can qualitatively derive the W-shape and four-fold symmetry of the dislocation distribution. However they cannot determine the axial distribution in the growing crystal, nor can they be used to develop changes in growth conditions to reduce or eliminate dislocations in GaAs. This results from the analytical solution limitations, both plain strain and axisymmetric approximations, and the limited scope of the Dusseaux numerical model.

The models do not adequately take into account the primary growth parameters during crystal growth producing the thermal fields on which the models are based. Experimental measurements

of the thermal fields, as a function of the growth parameters, to incorporate into the model are very difficult to make in high pressure growers.

The main objective of this investigation is to further develop the mathematical model for dislocation generation and multiplication taking into account all of the variables related to crystal growth. Experimental observations reported in the literature of thermal fields and physical quantities of the GaAs and B_2O_3, and made in a high pressure grower will be used to establish the boundary conditions in the model. The model will be able to determine the axial dislocation distribution and will have the flexibility to incorporate any change in the growth conditions.

The model will be used to assess the dislocation density in crystals with the introduction of modifications of the thermal fields in the crystal growers. The objective would be to develop procedures for lowering or eliminating dislocation densities in the crystal without introducing other defects which affect the electrical behaviour of the crystals.

The investigation was carried out in the following sequence :

1. Based on a glide mechanism due to thermal stresses, mathematical models for dislocation generation in LEC GaAs during growth and subsequent cooling, were formulated, developed and validated.

2. Using the models, most important factors affecting dislocation generation in GaAs crystals during and after growth, were determined.

3. Based on the above results and the thermal history the role of thermal stresses in the generation of dislocations in LEC crystals, were clarified.

CHAPTER 7

FORMULATION OF THE MODELS

The production of crystals can be divided into two parts : crystal growth, which includes the solidification process, and the subsequent crystal cooling to ambient temperature. Both parts of the process are modelled separately. In the two models the basic assumption is made that the temperature fields and stress fields are decoupled[208].

A simplified flow chart of the models which derive the stress fields from the thermal fields is shown in Figure 7.1 . The flow chart for both parts of the process are identical ; the difference between both models is the way the thermal fields are calculated. At a specific time during growth, the stress fields are derived from the calculated thermal fields. The stress components are then used to calculate the Von Mises Stress or the Resolved Shear Stress (RSS) at a given point in the crystal. The RSS are the projections of the stress tensor in specific planes and directions. In our case those planes and directions are given by the glide system of GaAs {111} $\langle\bar{1}10\rangle$. For a crystal grown in the [001] direction, from the twelve combinations of planes and directions there are ten different RSS components. It is assumed in the model that when the maximum component of RSS is greater than a critical value, dislocations are generated and multiply during glide. The particular planes and directions in which the

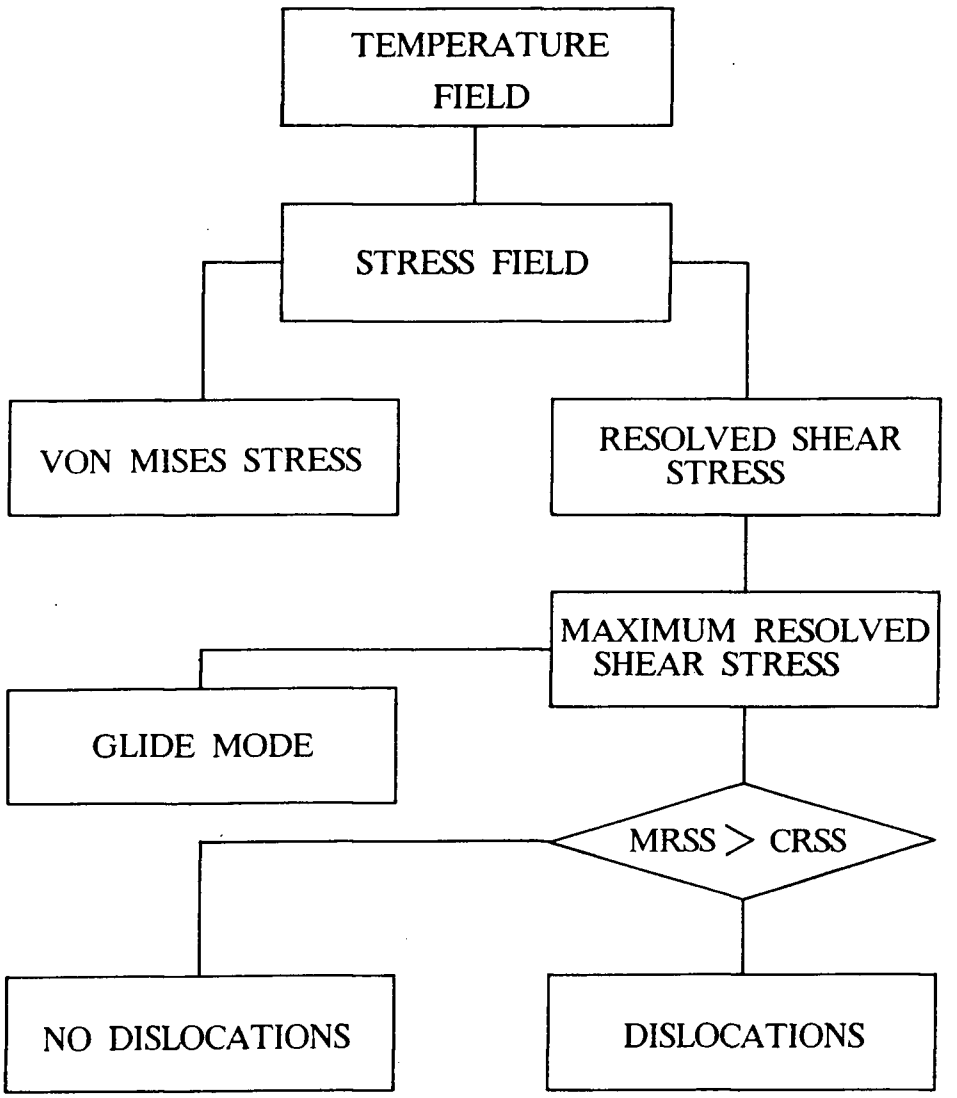

Figure 7.1 Flow chart of the model used to derive the stress fields.

RSS are maxima will determine the glide mode and crystallography of the dislocations being generated. It is also assumed that when one mode operates, the stress is relaxed and there is no further glide in other directions.

7.1 Model of crystal growth

7.1.1 Temperature Field

7.1.1.1 Governing Equations

A complete analysis of the temperature field in a LEC-GaAs crystal during growth requires the solution of a Stefan's problem with complex boundary conditions. The exact solution of this problem is time dependent and includes the four phases, crystal, gas, encapsulant and melt as well as the mold and the heat input/output to the mold. The heat transfer mechanisms include conduction, radiation and convection. To treat this problem mathematically the following assumptions are made :

1. The temperature field in the crystal is axially symmetric, i.e. $T = T(r,z,t)$

2. The interface shape is unaltered by dissipation of latent heat and remains at the melting point, T_{MP}

3. Heat transfer at the interface of the crystal (excluding the solidifying interface) follows Newton's Law of Cooling

4. The heat transfer coefficient and ambient temperature are allowed to vary along the lateral surface of the crystal, i.e. in contact with the encapsulant or the gaseous atmosphere

5. The temperature field is changed by a change in crystal length with time, i.e. a quasi-steady state approximation.

With the above assumptions the non- dimensional equation of heat conduction, with respect to a coordinate system fixed to the solidifying interface, as shown in Figure 7.2 , takes the form :

$$L(\beta) = \frac{\partial^2\beta}{\partial\rho^2} + \frac{1}{\rho}\frac{\partial\beta}{\partial\rho} + \frac{\partial^2\beta}{\partial\xi^2} - 2V\frac{\partial\beta}{\partial\xi} = 0 \quad \text{(a)} \tag{7.1}$$

$$\beta = \frac{T - T_0}{T_{MP} - T_0} \quad , \quad \rho = r/r_0 \quad , \quad \xi = z/r_0 \quad \text{(b)}$$

where $2V = v\, r_0/\kappa$, T_0 is the reference temperature, r_0 is the crystal radius, v the growth velocity and κ the thermal conductivity.

Solutions must also satisfy the following general boundary conditions :

i. Dirichlet condition

At the solid-liquid interface given by the suface of revolution $f(r,z) = 0$, $r < r_0$

$$\beta = 1 \tag{7.2}$$

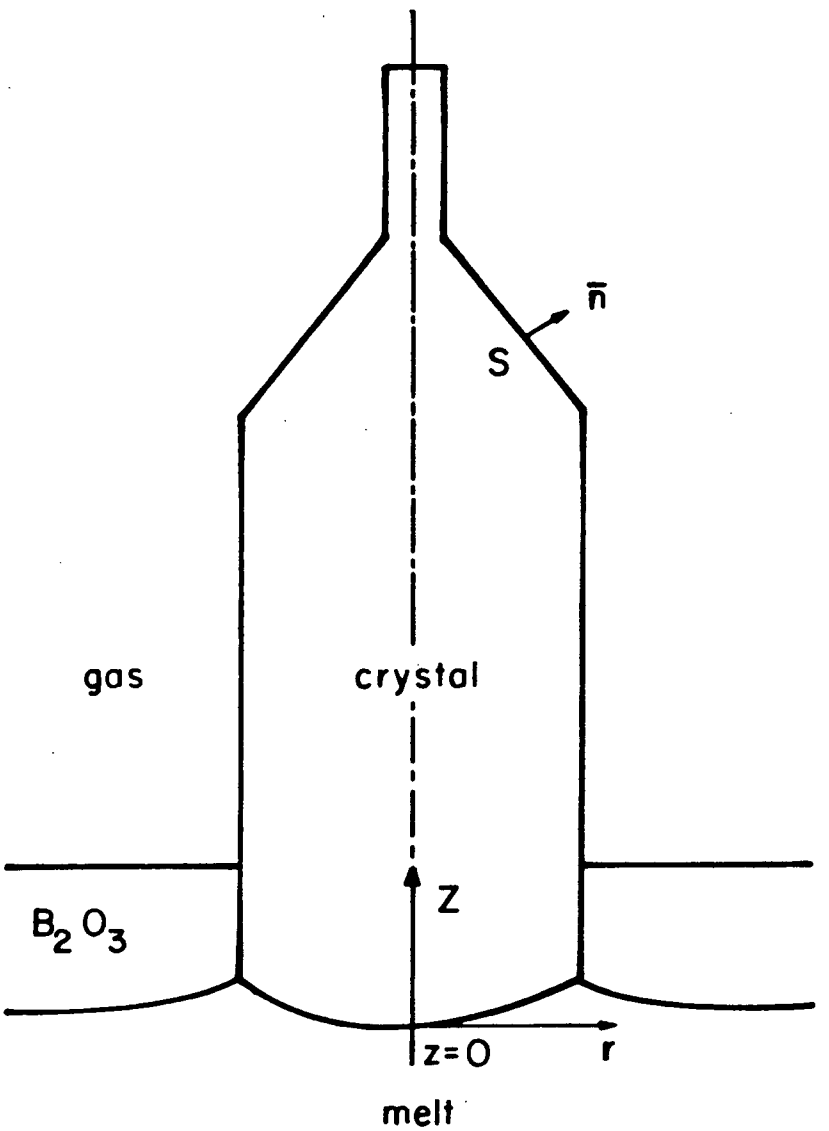

Figure 7.2 Crystal configuration and coordinate system used in the mathematical model.

ii. Neumann condition

At any point S on the cylindrical surface of the crystal,

$$\left(\frac{\partial \beta}{\partial \rho}\ \vec{n}_\rho + \frac{\partial \beta}{\partial \xi}\ \vec{n}_\xi\right)_S\ \vec{n} = -h(z)\ r_0[\beta_S - \beta_a(z)] \qquad (7.3)$$

where $\beta_a(z)$ is the normalized temperature of the ambient adjacent to the crystal surface at a distance z from the interface and β_S is the normalized temperature of the crystal at that point ; h(z) is the heat transfer coefficient between crystal surface and ambient at the same point.

The numerical scheme employed to solve this is given below.

7.1.1.2 Finite Element Equations

Among the different approaches for obtaining the element equations in a finite element method, the Galerkin's method was selected. In this method, after the whole domain in which a solution for the field variable β is required is discretized in small elements, the element equation is obtained by performing the following integration over each element,

$$\int_{D^{(e)}} L(\beta^{(e)})\ N_i^{(e)}\ d\ D^{(e)} = 0$$

with (7.4)

$$\beta^{(e)} = [N]\ \{\beta\}^{(e)} = [N_1\ N_2\ \ldots\ N_g] \begin{Bmatrix} \beta_1 \\ \beta_2 \\ \vdots \\ \beta_g \end{Bmatrix}$$

where the N's are the interpolation functions, the β_i are the nodal field values in element (e) and g is the degree of freedom of the element.

The interpolation functions must be such that there is continuity of the field variable and of its partial derivatives up to one order less than the highest order derivative in the operator. This means that interpolation functions for a C^1 problem are at first apparently required. However integration by parts and the use of the boundary conditions transform the problem in such a way as to show that less strict interpolation functions can be used. These calculations are presented in Appendix II where it is shown that the initial problem given by Equation (7.4) is transformed into the following equivalent equation

$$\int_{D^{(e)}} \left(\frac{\partial N_i}{\partial \rho} \frac{\partial \beta^{(e)}}{\partial \rho} + \frac{\partial N_i}{\partial \xi} \frac{\partial \beta^{(e)}}{\partial \xi} + 2V N_i \frac{\partial \beta^{(e)}}{\partial \xi} \right) dD^{(e)} +$$

$$+ r_0 h(z) \int_{S^{(e)}} N_i \beta^{(e)} dS^{(e)} =$$

$$= r_0 h(z) \beta_a(z) \int_{S^{(e)}} N_i dS^{(e)} \qquad (7.5)$$

where $S^{(e)}$ is the surface area of element (e) and $dS^{(e)}$ is the elemental surface. It is now clear from the above equation that interpolation functions for $C^{(0)}$ problems are required.

A suitable element shape chosen here for subdivision of axisymmetric bodies is the axisymmetric ring element with triangular cross-section.

The field variable is assumed to vary linearly inside the element and a three node element is chosen. For these linear triangular toroidal elements, interpolation functions for $C^{(0)}$ problems are the natural or area coodinates function L_i. The L_i's are defined as

$$L_i(\rho, \xi) = \frac{1}{2\Delta}(a_i + b_i \rho + c_i \xi) \tag{7.6}$$

where

$$a_i = \rho_j \xi_k - \rho_k \xi_j \; ; \; c_i = \rho_k - \rho_j \quad \text{and} \quad b_i = \xi_j - \xi_k \tag{7.7}$$

where (i, j, k) have module 3 and permute cyclically, (ρ_i, ξ_i) are the coordinates of the nodal points (vertices) of a triangle numbered counter-clockwise

$$2\Delta = \begin{vmatrix} 1 & \rho_1 & \xi_1 \\ 1 & \rho_2 & \xi_2 \\ 1 & \rho_3 & \xi_3 \end{vmatrix} \tag{7.8}$$

Δ is the area of the triangle.

The temperature within this element is expressed by the equation

$$\beta^{(e)} = [L_i]\{\beta\}^{(e)} = [L_1 \; L_2 \; L_3] \begin{Bmatrix} \beta_1 \\ \beta_2 \\ \beta_3 \end{Bmatrix}^{(e)} \tag{7.9}$$

where the β_i's are the nodal values of the temperature in element (e) in the local numeration.

Substituting $\beta^{(e)}$ given by Equation (7.9) into Equation (7.8) and considering that the integral should be performed for i from 1 to 3 we may write Equation (7.8) in matrix form as

$$\{[K_T]_{3x3} + [K_H]_{3x3}\}\ \{\beta\}^{(e)}_{1x3} = \{K_A\}_{1x3} \qquad (a)$$

where

$$K_{T_{ij}} = \int_{D(e)} \left\{\frac{\partial L_i}{\partial \rho}\frac{\partial L_j}{\partial \rho} + \left(\frac{\partial L_i}{\partial \xi} + 2VL_i\right)\frac{\partial L_j}{\partial \xi}\right\} dD^{(e)} \qquad (b)$$

$$K_{H_{ij}} = r_0 h(z) \int_{S(e)} L_i L_j \, dS^{(e)} \qquad (c) \qquad (7.10)$$

$$K_{A_{ij}} = r_0 h(z)\ \beta_a(z) \int_{S(e)} L_i \, dS^{(e)} \qquad (d)$$

The evaluation of $[K_T]$, $[K_H]$ and $[K_A]$ is given in Appendix III. $[K_T]$ is calculated exactly, $[K_H]$ and $[K_A]$ are calculated approximately for three different peripherial elements according to their orientation on the external surface with respect to the axis of the crystal ; i) vertical, ii) tilted and iii) horizontal peripherial elements.

$$K_{T_{ij}} = \frac{\pi \bar{\rho}^{(e)}}{2\Delta}(b_i b_j + c_i c_j) + \frac{\pi V b_j}{6}[3\ \bar{\rho}^{(e)} + \rho_j]$$

where $i,j = 1,2,3$

$$\bar{\rho}^{(e)} = \frac{\rho_1 + \rho_2 + \rho_3}{3}$$

(i) Vertical boundary

$$[K_H] = 2\pi h(z) r_0 \rho l_{ij} \begin{bmatrix} 1/3 & 1/6 & 0 \\ 1/6 & 1/3 & 0 \\ 0 & 0 & 0 \end{bmatrix}$$

$$\{K_A\} = \pi h(z) r_0 \beta_a(z) \rho l_{ij} \begin{Bmatrix} 1 \\ 1 \\ 0 \end{Bmatrix} \qquad (7.11)$$

(ii) Tilted Boundary

$$[K_H] = 2\pi h(z) r_0 \frac{l_{ij}}{12} \begin{bmatrix} 3\rho_i + \rho_j & \rho_i + \rho_j & 0 \\ \rho_i + \rho_j & \rho_i + 3\rho_j & 0 \\ 0 & 0 & 0 \end{bmatrix}$$

$$\{K_A\} = \pi h(z) r_0 \beta_a(z) (\rho_i + 2\rho_j) \frac{l_{ij}}{6} \begin{Bmatrix} 1 \\ 1 \\ 0 \end{Bmatrix}$$

(iii) Horizontal boundary

The same as in (i) but replacing ρ by $\bar{\rho}^{(e)}$. l_{ij} is the length of the element at the boundary.

Details of the numerical calculations including computer coding, type of mesh, mesh refinement, matrix assembly and matrix calculations are given later.

7.1.2 Stress Field Model

To calculate the thermal stresses in the crystal the following assumptions are made :

i. the body is linearly elastic and isotropic

ii. the thermoelastic field is axisymmetric

iii. the crystal is free from traction at the surface, i.e. at the surface $\hat{\sigma} \times \vec{n} = 0$, $\vec{n}$ is a vector perpendicular to the surface of the crystal.

7.1.2.1 Governing and Element Equations

To obtain the element equation, the minimum potential energy principle was used. The strain energy for a linear elastic solid is defined as

$$U_p(u,w) = \frac{1}{2} \int_V [\varepsilon] \{\sigma\} \, dV \qquad (7.12)$$

where $\{\sigma\}$ is the stress tensor and $[\varepsilon]$ is the strain tensor which for the present case have the following components

$$[\varepsilon] = [\varepsilon_r \quad \varepsilon_\theta \quad \varepsilon_z \quad \gamma_{rz}] \qquad \{\sigma\} = \begin{Bmatrix} \sigma_r \\ \sigma_\theta \\ \sigma_z \\ \tau_{rz} \end{Bmatrix} \tag{7.13}$$

The stress, according to Hook's Law and the Duhamel-Newman constitutive equation that accounts for the thermal strain, is

$$\{\sigma\} = [C]\,(\{\varepsilon\} - \{\varepsilon_0\}) \tag{7.14}$$

where $[\varepsilon_0]$ is the strain corresponding to a free expansion of the solid due to temperature differences with respect to reference temperature T_0 . This strain for an isotropic material with a coefficient of thermal expansion α is

$$\{\varepsilon_0\} = \alpha(T - T_0) \begin{Bmatrix} 1 \\ 1 \\ 1 \\ 0 \end{Bmatrix} \tag{7.15}$$

[C] is the compliance matrix which for this case is

$$[C] = \frac{E}{(1+\nu)\,(1-2\nu)} \begin{bmatrix} 1-\nu & \nu & \nu & 0 \\ \nu & 1-\nu & \nu & 0 \\ \nu & \nu & 1-\nu & 0 \\ 0 & 0 & 0 & \frac{1-2\nu}{2} \end{bmatrix} \tag{7.16}$$

with E the Young modulus and ν the Poisson's ratio. The $\{\varepsilon\}$ strain can be derived from the displacement $\{\tilde{d}\}$ as

$$\{\varepsilon\} = [B]\{\tilde{d}\} \qquad \{\tilde{d}\} = \begin{Bmatrix} u(r,z) \\ w(r,z) \end{Bmatrix} \tag{7.17}$$

where [B] is the following matrix of derivatives

$$[B] = \begin{bmatrix} \frac{\partial}{\partial r} & 0 \\ \frac{1}{r} & 0 \\ 0 & \frac{\partial}{\partial z} \\ \frac{\partial}{\partial z} & \frac{\partial}{\partial r} \end{bmatrix} \tag{7.18}$$

Taking into account the relation among stress, strain and displacement, the potential energy can be written as

$$\Pi(u,w) = U(u,w) = \int_V [\tilde{d}]\,[B]^T\,[C]\,[B]\,\{\tilde{d}\} - 2[\tilde{d}]\,[B]^T\,[C]\,\{\varepsilon_0\}\,dV \tag{7.19}$$

When the body is subdivided into small elements, it is assumed that within each element with g nodes the displacement field is approximated by

$$\{\tilde{d}\}^{(e)} = \begin{Bmatrix} u(r,z) \\ w(r,z) \end{Bmatrix}^{(e)} = \begin{Bmatrix} [N]\{u\}^{(e)} \\ [N]\{w\}_{(e)} \end{Bmatrix} = [N]\{d\}^{(e)} \tag{7.20}$$

where [N] are the interpolation functions matrix of order g and $\{d\}^{(e)}$ are the element nodal displacements. In this case the minimization process may be carried out element by element. As a result the force-displacement equation for the element is obtained as

$$\underset{2gx2g}{[k]^{(e)}}\ \underset{2gxl}{\{d\}^{(e)}} = \underset{2gxl}{\{F\}^{(e)}}$$

$$\{d\}^{(e)} = \begin{Bmatrix} \{d\}_1^{(e)} \\ \{d\}_2^{(e)} \\ \\ \{d\}_g^{(e)} \end{Bmatrix} = \begin{Bmatrix} u_1 \\ w_1 \\ u_2 \\ w_2 \\ : \\ u_g \\ w_g \end{Bmatrix} \qquad (7.21)$$

$$\underset{2gx2g}{[k]}^{(e)} = \begin{bmatrix} [k]_{11}^{(e)} & [k]_{12}^{(e)} \ldots\ldots\ldots & [k]_{1n}^{(e)} \\ [k]_{i1}^{(e)} & [k]_{i2}^{(e)} \ldots\ldots\ldots & [k]_{ig}^{(e)} \\ \\ [k]_{g1}^{(e)} & [k]_{g2}^{(e)} \ldots\ldots\ldots & [k]_{gg}^{(e)} \end{bmatrix} \qquad (7.22)$$

$$\underset{2gx1}{\{F\}}^{(e)} = \begin{Bmatrix} \{F\}_1^{(e)} \\ \{F\}_2^{(e)} \\ \\ \{F\}_g^{(e)} \end{Bmatrix}$$

In the stiffness matrix [K], the submatrices $[k]_{ij}$ are the stiffness matrices at node i and have the form

$$[k]_{ij}^{(e)} = \int_{V^{(e)}} {}^{2x4}[B]_i^{T(e)}\ {}^{4x4}[C]^{(e)}\ {}^{4x2}[B]_j^{(e)}\ dV$$

$$[B]_i^{(e)} = \begin{bmatrix} \dfrac{\partial N_i}{\partial r} & 0 \\ \dfrac{N_i}{r} & 0 \\ 0 & \dfrac{\partial N_i}{\partial z} \\ \dfrac{\partial N_i}{\partial z} & \dfrac{\partial N_i}{\partial r} \end{bmatrix} \qquad (7.23)$$

The initial force matrix $\{F_0\}_i^{(e)}$ is

$$[F_0\}_i^{(e)} = \int_{V^{(e)}} {}^{2x4}[B]_i^{T(e)}\ {}^{4x4}[C]\ {}^{4x1}[\varepsilon_0]_i^{(e)}\ dV \qquad (7.24)$$

7.1.2.2 Requirements for the interpolation functions.

Since only first order derivatives of displacement appear in the integrand for the potential energy, compatibility requires an interpolation function with continuity of displacement at the

element boundary only. However, for completeness, the interpolation functions must be able to represent rigid body displacements and constant strain states within an element; that is uniform states of displacement and first derivatives of displacements respectively. This $C^{(1)}$ continuity is satisfied with interpolation functions containing linear terms such as the natural coordinates used for the temperature field. This means that elements which are linear or of higher order are suitable.

For convenience, before obtaining the specific form of element matrices, the node equation is written in terms of non-dimensional quantities as

$$\overset{2x2}{[k']}^{(e)}_{ij} \; \overset{2x1}{\{d'\}}^{(e)}_{i} = \overset{2x1}{\{F_0'\}}^{(e)}_{i} \qquad \text{(a)} \qquad (7.25)$$

where

$$\{d'\}^{(e)}_{i} = \frac{E}{\alpha(T_{MP} - T_0)\, r_0} \{d\}^{(e)}_{i} \qquad \text{(b)}$$

$$\{k'\}^{(e)}_{ij} = \int [B']^{T(e)}_{i} [C'] [B']^{(e)}_{j} \rho \, d\rho \, d\xi \qquad \text{(c)}$$

where

$$[B']^{(e)}_{i} = r_0 [B]^{(e)}_{i} \qquad \text{(a)}$$

$$[C'] = \frac{(1+\nu)(1-2\nu)}{E} [C] \qquad \text{(b)}$$

$$\{F'_0\}_i^{(e)} = \beta_i \int [B']_i^{T(e)} \; [C'] \begin{Bmatrix} 1 \\ 1 \\ 1 \\ 0 \end{Bmatrix} \rho d\rho d\xi \qquad (c) \tag{7.26}$$

7.1.2.3 Formulas for Stress Calculations

The stress tensor is calculated at each node i in element e using the following equation

$$\{\sigma'\}_i^{(e)} = \begin{Bmatrix} \sigma_{\rho_i} \\ \sigma_{\theta_i} \\ \sigma_{\xi_i} \\ \tau_{\rho\xi_i} \end{Bmatrix}^{(e)} = \begin{bmatrix} 1-\nu & \nu & \nu & 0 \\ \nu & 1-\nu & \nu & 0 \\ \nu & \nu & 1-\nu & 0 \\ 0 & 0 & 0 & \frac{1-2\nu}{2} \end{bmatrix} \begin{Bmatrix} \varepsilon_{\rho_i} \\ \varepsilon_{\theta_i} \\ \varepsilon_{\xi_i} \\ \gamma_{\rho\xi_i} \end{Bmatrix} - \begin{Bmatrix} \beta_i \\ \beta_i \\ \beta_i \\ 0 \end{Bmatrix} \tag{7.27}$$

The strain components at each node are calculated from the nodal displacements as

$$\{\varepsilon'\}_i^{(e)} = [B^i]_i^{(e)} \{d'\}_i^{(e)} \tag{7.28}$$

For nodes at the axis of the body ε_θ is substituted for ε_ρ.

The stress calculated in this way is non-dimensional. To obtain the stress in absolute units the following relation is employed

$$\{\sigma\}_i^{(e)} = \frac{E\alpha\,(T_{MP} - T_0)}{(1-2\nu)}\,\{\sigma'_i\}^{(e)} \qquad (7.29)$$

7.1.2.4 Linear Elements

The linear elements are triangular toroids with nodes at the vertices of the triangle. The interpolation functions for these elements are the natural coordinates L_1, L_2 and L_3 and the displacement is written as

$$\{d\}^{(e)} = \begin{Bmatrix} L_1u_1 + L_2u_2 + L_3u_3 \\ L_1w_1 + L_2w_2 + L_3w_3 \end{Bmatrix} \qquad (7.30)$$

Making the corresponding calculations and substitutions, the terms of the stiffness and initial force matrices are

$$[k']_{ij}^{(e)} = \begin{bmatrix} k'_{11} & k'_{12} \\ k'_{21} & k'_{22} \end{bmatrix} \qquad (a)$$

$$k'_{11} = [(1-\nu)\,b_ib_j + \frac{(1-2\nu)}{2}\,c_ic_j]\,\frac{\bar{\rho}}{4\Delta} + \frac{\nu}{6}\,[b_i+b_j] +$$

$$+ (1-\nu)\,\Delta \int\!\!\int \frac{L_iL_j}{\rho}\,d\rho d\xi \qquad (b)$$

$$k'_{12} = [\nu b_ic_j + \frac{(1-2\nu)}{2}\,c_ib_j]\,\frac{\bar{\rho}}{4\Delta} + \frac{\nu}{6}\,c_j \qquad (c)$$

$$k'_{21} = \left[\nu b_j c_i + \frac{(1-2\nu)}{2} c_j b_i\right] \frac{\bar{\rho}}{4\Delta} + \frac{\nu}{6} c_i \qquad (d)$$

$$k'_{22} = \left[(1-\nu)\, c_i c_j + \frac{(1-2\nu)}{2} b_i b_j\right] \frac{\bar{\rho}}{4\Delta} \qquad (e)$$

(7.31)

$$F'_{0_1} = \frac{\beta_i}{2} \left(b_i \bar{\rho} + \frac{2\Delta}{3}\right) \qquad (f)$$

$$F'_{0_2} = \beta_i \frac{c_j \bar{\rho}}{2} \qquad (g)$$

An inspection of the above relations shows that all the terms can be evaluated exactly except the term containing $1/\rho$ which should be integrated numerically. One intermediate approximation consists of taking average values of ρ and L_i ($\bar{\rho}$ and $\bar{L} = 1/3$) for that term only. Once the displacement field is calculated the nodal strain and stresses at each element can be derived by back substitution in the corresponding equations. The stresses at the centroid of the element are the average stresses. The stress associated with each node is the average value of stresses from all elements sharing the node.

7.1.2.5 Quadratic Element

The quadratic element has six nodes, three nodes at the vertices and three nodes at midsides. Interpolation functions are

built from the natural coordinates. A detailed calculation of stiffness and force matrix elements is given in Appendix V. It is important to note that the nodal [B] matrix of these elements includes only derivatives of the non-zero terms of displacement at that node instead of the derivative of all the terms in the interpolated displacement in the element. More specifically, in the element the displacement components are interpolated as usual as

$$u^{(e)} = \sum_{j=i}^{6} N_j u_j \qquad w^{(e)} = \sum_{j=1}^{6} N_j w_j \tag{7.32}$$

where u_j and w_j are the nodal displacements and N the interpolation functions. For instance, by definition

$$\varepsilon^{(e)} = \frac{\partial u^{(e)}}{\partial r} = \sum_{j=1}^{6} \frac{\partial N_j}{\partial r} u_j \tag{7.33}$$

and a true quadratic element will have a B element at node i which is

$$B_{11_i} = \left(\sum_{j=1}^{6} \frac{\partial N_j}{\partial r} N_j \right)_{\substack{N_j = 0 \\ N_i = 1}} \qquad j \neq i \tag{7.34}$$

However in the pseudo-quadratic elements employed here, only the term $N_i . u_i$ is considered, i.e.

$$B_{11_i} = u_i \frac{\partial N_i}{\partial r} \tag{7.35}$$

It is also important to note that for the calculation of stresses the full [B] matrix is used in order to obtain representative and consistent values of stresses.

7.1.3 Von Mises and Resolved Shear Stresses

The stress tensor in cylindrical coordinates obtained with the finite element method gives a quantitative description of the thermally induced stresses. For a dislocation generation analysis, these stress components should be transformed into quantities that can be associated with the plastic deformation of the material. This stress field can be described in terms of the Von Mises and Resolved Shear Stresses (RSS) and these values must be compared to the yield stress and Critical Resolved Shear Stress for GaAs to determine if dislocations are generated.

The Von Mises Stress is related to the principal stresses by

$$\sigma_{VM} = \sqrt{1/2\,[(\sigma_1 - \sigma_2)^2 + (\sigma_1 - \sigma_3)^2 + (\sigma_2 - \sigma_3)^2]} \qquad (7.36)$$

The principal stresses, by definition, are the values of the stresses that diagonalize the stress tensor.

The RSS's are obtained by resolving the local stress tensor on the slip planes and slip directions. In GaAs the glide system is formed by the {111} planes and $\langle 1\bar{1}0 \rangle$ directions giving 12 slip combinations. The procedure as well as the detailed calculation to obtain the twelve RSS components is given in Appendix VI.

The twelve RSS for a crystal grown in the [001] direction are given in Table 7.2 . It can be seen that independent of the stress level, at every point in space there are three combinations of planes and directions that have the same resolved shear stress, these are

$$(111) \quad [\bar{1}10]$$

$$(\bar{1}11) \quad [110]$$

$$(\bar{1}\bar{1}1) \quad [1\bar{1}0]$$

This leaves only ten different stress levels which will be called "glide modes". The difference between modes labelled a and b is the sign of the term involving the shear stress. The ten modes are listed in Table 7.1 .

Three dimensional stress contours are difficult to produce, therefore for the analysis of stress distribution two sections of the crystal are used, sections normal and parallel to the axis or growth direction. For normal sections stresses as given in Table 7.1 are used. For parallel sections the (010) plane is chosen in view of the experimental evidence that higher dislocation densities occur in that plane. For these planes $\theta = 0$. Substituting in the given equations for the ten modes gives the results shown in Table 7.2 . It can be seen that in this plane there are only five different stress levels with the corresponding multiplicity.

The RSS are compared with different critical stresses given in the literature for yield, dislocation generation and

multiplication for doped and undoped GaAs as described in section 8.1 .

Table 7.1 Resolved Shear Stress Components in (001) Crystals

Plane	Direction	Resolved Shear Stress	Mode
	$[\bar{1}10]$	$\frac{\sqrt{6}}{6}\{-(\sigma_\rho-\sigma_\theta)\cos2\theta+\sqrt{2}\tau_{\rho\xi}\cos(\theta+\pi/4)\}$	I a
(111)	$[0\bar{1}1]$	$\frac{\sqrt{6}}{6}\{-(\sigma_\rho-\sigma_\theta)\sqrt{2}\sin\theta\sin(\theta+\pi/4)+(\sigma_\xi-\sigma_\theta)+$ $+\sigma_{\rho\xi}\cos\theta\}$	II a
	$[10\bar{1}]$	$\frac{\sqrt{6}}{6}\{\sigma_\rho-\sigma_\theta)\sqrt{2}\cos\theta\sin(\theta+\pi/4)-(\sigma_\xi-\sigma_\theta)-$ $-\tau_{\rho\xi}\sin\theta\}$	III a
	$[\bar{1}0\bar{1}]$	$\frac{\sqrt{6}}{6}\{(\sigma_\rho-\sigma_\theta)\sqrt{2}\cos\theta\cos(\theta+\pi/4)-(\sigma_\xi-\sigma_\theta)-$ $-\tau_{\rho\xi}\sin\theta\}$	IV a
$[\bar{1}11]$	$[0\bar{1}1]$	$\frac{\sqrt{6}}{6}\{(\sigma_\rho-\sigma_\theta)\sqrt{2}\sin\theta\cos(\theta+\pi/4)+(\sigma_\xi-\sigma_\theta)-$ $-\tau_{\rho\xi}\cos\theta\}$	V b
	$[110]$	$\frac{\sqrt{6}}{6}\{-(\sigma_\rho-\sigma_\theta)\cos2\theta+\sqrt{2}\tau_{\rho\xi}\cos(\theta+\pi/4)\}$	I a
	$[011]$	$\frac{\sqrt{6}}{6}\{-(\sigma_\rho-\sigma_\theta)\sqrt{2}\sin\theta\sin(\theta+\pi/4)+(\sigma_\xi-\sigma_\theta)-$ $-\tau_{\rho\xi}\cos\theta\}$	II b
$(\bar{1}\bar{1}1)$	$[\bar{1}0\bar{1}]$	$\frac{\sqrt{6}}{6}\{(\sigma_\rho-\sigma_\theta)\sqrt{2}\cos\theta\sin(\theta+\pi/4)-(\sigma_\xi-\sigma_\theta)+$ $+\tau_{\rho\xi}\sin\theta\}$	III a
	$[1\bar{1}0]$	$\frac{\sqrt{6}}{6}\{-(\sigma_\rho-\sigma_\theta)\cos2\theta+\sqrt{2}\tau_{\rho\xi}\cos(\theta+\pi/4)\}$	I a

Cont./

Cont./

	[011]	$\frac{\sqrt{6}}{6}\{(\sigma_\rho-\sigma_\theta)\sqrt{2}\sin\theta\cos(\theta+\pi/4)+(\sigma_\xi-\sigma_\theta)+\tau_{\rho\xi}\cos\theta\}$	V	a
$(1\bar{1}1)$	$[\bar{1}0\bar{1}]$	$\frac{\sqrt{6}}{6}\{(\sigma_\rho-\sigma_\theta)\sqrt{2}\cos\theta\cos(\theta+\pi/4)-(\sigma_\xi-\sigma_\theta)+\tau_{\rho\xi}\sin\theta\}$	IV	b
	$[\bar{1}\bar{1}0]$	$\frac{\sqrt{6}}{6}\{-(\sigma_\rho-\sigma_\theta)\cos 2\theta-\sqrt{2}\tau_{\rho\xi}\cos(\theta+\pi/4)\}$	I	b

Table 7.2 Resolved Shear Stress Components in a (010) Plane for a [001] Crystal.

Mode	RSS	Previous Modes	Plane	Direction
1	$\frac{\sqrt{6}}{6}[(\sigma_\xi - \sigma_\theta) + \tau_{\rho\xi}]$		(111)	$[\bar{1}10]$
		I a	(111)	$[110]$
			$(\bar{1}\bar{1}1)$	$[1\bar{1}0]$
2	$\frac{\sqrt{6}}{6}[-(\sigma_\rho - \sigma_\theta) - \tau_{\rho\xi}]$	I b	$(1\bar{1}1)$	$[\bar{1}\bar{1}0]$
3	$\frac{\sqrt{6}}{6}[(\sigma_\xi - \sigma_\theta) - \tau_{\rho\xi}]$	II a	(111)	$[0\bar{1}\bar{1}]$
		V a	$(1\bar{1}1)$	$[011]$
4	$\frac{\sqrt{6}}{6}[(\sigma_\xi - \sigma_\theta) - \tau_{\rho\xi}]$	II b	$(\bar{1}\bar{1}1)$	$[011]$
		V b	$(\bar{1}11)$	$[0\bar{1}1]$
5	$\frac{\sqrt{6}}{6}[\sigma_\rho - \sigma_\xi]$	III a	(111)	$[10\bar{1}]$
		III b	$(\bar{1}\bar{1}1)$	$[\bar{1}0\bar{1}]$
		IV a	$(\bar{1}11)$	$[\bar{1}0\bar{1}]$
		IV b	$(1\bar{1}1)$	$[10\bar{1}]$

7.2 Modelling for Cooling After growth

Once the crystal has reached its final length, it is pulled up to separate it from the melt and initiate cooling to room temperature. The effect of cooling in generating dislocations has not been established in the literature. However, the cooling

practice may induce thermal stresses that will generate more dislocations, particularly in the hot tail end region.

In order to study the effects of cooling in generating dislocations the following mathematical approach has been developed. To obtain the time dependent temperature field an analytical solution was chosen. The selection of this method was based on two factors. a) Solutions are easy to obtain and numerical evaluations are cheap compared to numerical methods. b) The importance of cooling has not been sufficiently established to justify the use of expensive and time consuming numerical methods.

The analytical temperature fields were calculated making the following assumptions :

1. The temperature field is time dependent and axisymmetric.

2. The crystal is a finite cylinder with constant cross-section.

3. The crystal is immersed in a medium (gas or liquid) at a constant temperature.

4. Newton's Law of Cooling applies at the crystal surface ; the heat transfer coefficient is constant and its value is determined by the temperature and nature of the surrounding medium.

5. The initial temperature of the crystal is axially dependent (radial temperature gradients during growth are

small) ; and it is given by a parabolic function that fits the temperature field at the axis of the crystal at the moment it is pulled from the melt.

With these assumptions, the temperature fields satisfies the following partial differential equation and conditions using non-dimensional quantities as before :

$$\frac{1}{\rho}\ \frac{\partial}{\partial \rho}\left(\rho \frac{\partial \beta}{\partial \rho}\right) + \frac{\partial^2 \beta}{\partial \xi^2} = \frac{\partial \beta}{\partial t^*} \qquad (7.37)$$

where $t^* = (\kappa / r_0^{\,2})\ t$

Initial Condition

at $t^* = 0$

$$\beta_0 = f(\rho) = p_0 + p_1 \xi + p_2 \xi^2 \qquad (7.38)$$

Boundary Conditions, with $h' = h r_0$

at $t^* > 0$

$$\left.\frac{\partial \beta}{\partial \rho}\right|_{\rho = 1} = -h' \beta \qquad (a)$$

$$\left.\frac{\partial \beta}{\partial \xi}\right|_{\xi = \xi_t} = -h' \beta \qquad (b) \qquad (7.39)$$

$$\left.\frac{\partial \beta}{\partial \xi}\right|_{\xi = 0} = h' \beta \qquad (c)$$

The solution to this problem as shown in Appendix V is given by

$$\beta(\rho, \xi, t^*) = 2h' \left[\sum_{\lambda} C_1(\lambda)\, e^{-\lambda^2 t^*}\, J_0(\lambda\rho)\right]$$

$$\left\{\sum_{\gamma} C_2(\gamma)\, e^{-\gamma^2 t^*}\, [\gamma \cos\gamma\xi + h' \sin\gamma\xi]\right. \qquad (7.40)$$

where the λ- values and γ- values are the solutions of the following algebraic equations

$$\lambda J_1(\lambda) = h'\, J_0(\lambda) \qquad (a)$$

$$\tan\gamma\xi_t = \frac{2\gamma h'}{\gamma^2 - h'^2} \qquad (b) \qquad (7.41)$$

with

$$C_1(\lambda) = \frac{1}{(h'^2 + \lambda^2)\, J_0(\lambda)} \qquad (a)$$

and

$$C_2(\gamma) = \frac{II}{I} \qquad (b)$$

$$II = \sin\gamma\xi_t \left\{p_0 + p_1(\xi_t + h'/\gamma^2) + p_2(\xi_t^2 - 2/\gamma^2) + \right.$$

$$\left. + 2\xi_t h'/\gamma^2\right\} + \frac{\cos\gamma\xi_t}{\gamma}\{-p_0 h' + p_1(1 - h'\xi_t) +$$

$$+ p_2(2\xi_t - h'\xi_t^2 + 2h'/\gamma^2\} + \frac{p_0 h'}{\gamma} - \frac{p_1}{\gamma} - \frac{2p_2 h'}{\gamma^3} \qquad (c)$$

(7.42)

$$I = \frac{\xi t}{2} (\gamma^2 + h'^2) + h' \qquad (d)$$

The temperature field calculated at a given time is employed to calculate the thermally induced stress field, with the aid of the finite element method described in section 7.1 . From these stresses the Von Mises and RSS are derived and compared to temperature dependent critical values for yield or dislocation generation.

7.3 Analytical Solutions

Analytical solutions for the temperature and stress fields were obtained and numerical evaluations of these solutions were compared with those obtained with finite element methods. The analytical solutions developed were obtained for simplified boundary conditions.

7.3.1 Analytical QSS Temperature Field

The quasi - steady state differential equation (7.1) is solved analytically for a simplified problem in which the following conditions are adopted :

1. Planar solid - liquid interface

2. Cylindrical crystal with constant cross-section

3. Uniform heat transfer coefficient h and constant ambient temperature T_a

4. Constant temperature at the ends of the crystal .

From these, the boundary conditions are written as

$$\left.\frac{\partial \beta}{\partial \rho}\right|_{\rho=1} = -h' \beta_s \qquad (a)$$

$$\beta|_{\xi=0} = 1 \qquad (b) \qquad (7.43)$$

$$\beta|_{\xi=\xi_t} = 0 \quad ; \quad \xi_t = \frac{Z_t}{r_0} \qquad (c)$$

where Z_t is the total length of the crystal.

The solution to the heat conduction equation (7.1), subject to the specified boundary conditions, is given by the following equation in term of the Bessel function of zero and first order J_0 and J_1

$$\beta(\rho, \xi) = 2hr_0 \, e^{v\xi} \sum_{\lambda} \frac{J_0(\lambda\rho)}{(\lambda^2+h^2r_0^2)J_0(\lambda)} \frac{[e^{-k_\lambda \xi} - e^{-2k_\lambda \xi_T} e^{k_\lambda \xi}]}{(1 - e^{-2k_\lambda \xi_T})} \qquad (7.44)$$

0

where the values are the solutions of the algebraic equation

$$\lambda J_1(\lambda) = hr_0 J_0(\lambda) \qquad (7.45)$$

and

$$k_\lambda^2 = v^2 + \lambda^2 \qquad (7.46)$$

Details of the calcuations are given in Appendix VII.

7.3.2 Analytical solutions for the Stress Field

Analytical solutions for the stress field were obtained using two different approximations : plane strain and axisymmetric. Two types of temperature fields were employed, temperature fields that depend on radius only (no axial temperature gradient) and general axisymmetric temperature fields.

7.3.2.1 Plane Strain Approximation

In this approximation it is assumed that the displacement field consists of primarily a radial component, with the axial component constrained to maintain zero axial traction at the two ends of a cylinder. For the two dimensional axisymmetric temperature field calculated in section 7.3.1, the three components of non-dimensional stress from Appendix IX are

$$\sigma_\rho = 2hr_0\, e^{v\xi} \sum_\lambda K_\lambda(\xi) \left[\frac{hr_0}{\lambda^2} - \frac{J_1(\lambda\rho)}{\lambda\rho} \frac{1}{J_0(\lambda)}\right] \qquad (a)$$

$$\sigma_\theta = 2hr_0\, e^{v\xi} \sum_\lambda K_\lambda(\xi) \left[\frac{hr_0}{\lambda^2} + \frac{1}{J_0(\lambda)} \left(\frac{J_1(\lambda\rho)}{\lambda\rho} - J_0(\lambda\rho)\right)\right] \qquad (b)$$

$$\sigma_\xi = 2hr_0\, e^{v\xi} \sum_\lambda K_\lambda(\xi) \left[\frac{2hr_0}{\lambda^2} - \frac{J_0(\lambda\rho)}{J_0(\lambda)}\right. \qquad (c)$$

where (7.47)

$$K_\lambda(\xi) = \frac{e^{-k_\lambda \xi} - e^{-2k_\lambda \xi_t} e^{k_\lambda \xi}}{(1 - e^{-2k_\lambda \xi_t})(\lambda^2 + h^2 r_0^2)} \quad \text{(d)}$$

For a radial temperature field given by

$$\beta = -\rho^2 \quad (7.48)$$

the stresses are given by the following relationships

$$\sigma_\rho = 1/4\,(\rho^2 - 1) \quad \text{(a)}$$

$$\sigma_\theta = 1/4\,(3\rho^2 - 1) \quad \text{(b)} \quad (7.49)$$

$$\sigma_\xi = \rho^2 - 1/2 \quad \text{(c)}$$

Details of the calculations are given in Appendix VII.

7.3.2.2 Axisymmetric Solutions

Analytical solutions using the axisymmetric approximation were obtained using Love's and Goodier's potentials. Goodier's potential gives a particular solution for the thermoelastic stresses while Love's potential gives a general solution for the isothermal elastic stresses. A combination of both potentials is necessary to satisfy the boundary conditions. In this case the body is a cylinder with constant cross-section and finite length. Solutions are obtained using finite Fourier transforms for

axisymmetric and radial temperature fields as in the plain strain case.

Details of the calculations and solutions are given in Appendix IX.

For purposes of comparison with the finite element method, non-dimensional stress component were obtained by multiplying the non-dimensional stresses by, a) $1 - 2\nu$ for the axisymmetric approximation and b) $(1 - 2\nu) / (1 - \nu)$ for the plane strain approximation with $\nu = 0.29$.

CHAPTER 8

EVALUATION OF THE MODELS

In this chapter the results of the models are compared with the analytical solutions presented in the last chapter. In addition the temperature fields obtained with the finite element method are compared with temperature measurements in a high pressure Melbourn puller during growth. The model is evaluated on the basis of these results.

8.1 Programming and Input Parameters

Based on the numerical scheme presented in the last chapter, programs in FORTRAN language were written for the calculation of temperatures and stresses in the GaAs crystal during growth. Flow charts are shown in Figures 8.1 and 8.2 . The flow charts corresponding to the computer programs employed for calculating the stresses with linear and quadratic elements are essentially the same. The mesh was automatically generated using a computer program with a flow chart as shown in Figure 8.3. Several different meshes using triangular elements were tested in order to select the one which gave the best results.

A Choleski method was selected for solving the linear system of equations that resulted from the finite element method. In the case of the temperature field calculations, the test employed for the selection of the solution method and optimum mesh

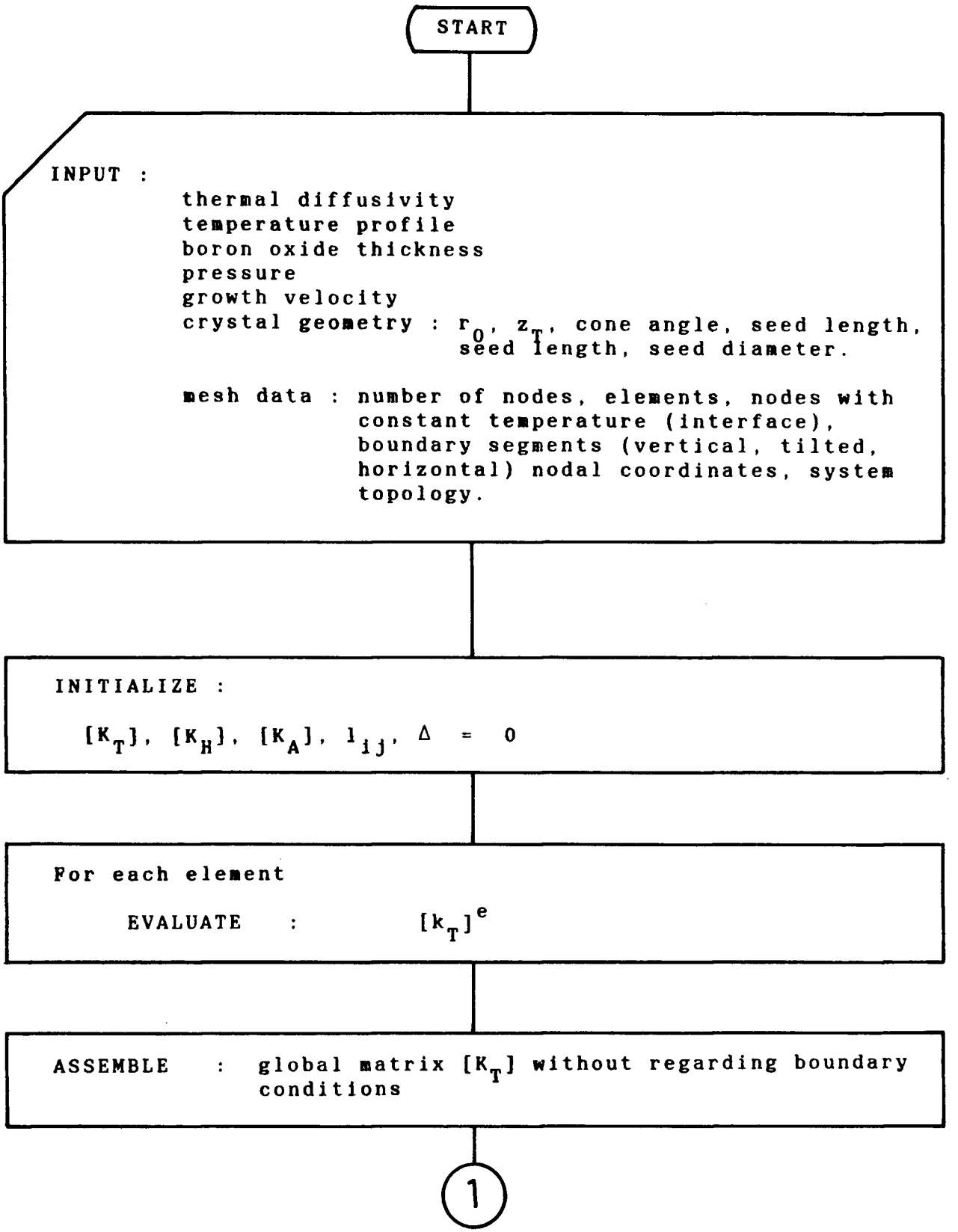
START
INPUT :
thermal diffusivity
temperature profile
boron oxide thickness
pressure
growth velocity
crystal geometry : r_0, z_T, cone angle, seed length, seed length, seed diameter.
mesh data : number of nodes, elements, nodes with constant temperature (interface), boundary segments (vertical, tilted, horizontal) nodal coordinates, system topology.
INITIALIZE :
$[K_T]$, $[K_H]$, $[K_A]$, l_{ij}, $\Delta = 0$
For each element
EVALUATE : $[k_T]^e$
ASSEMBLE : global matrix $[K_T]$ without regarding boundary conditions
1

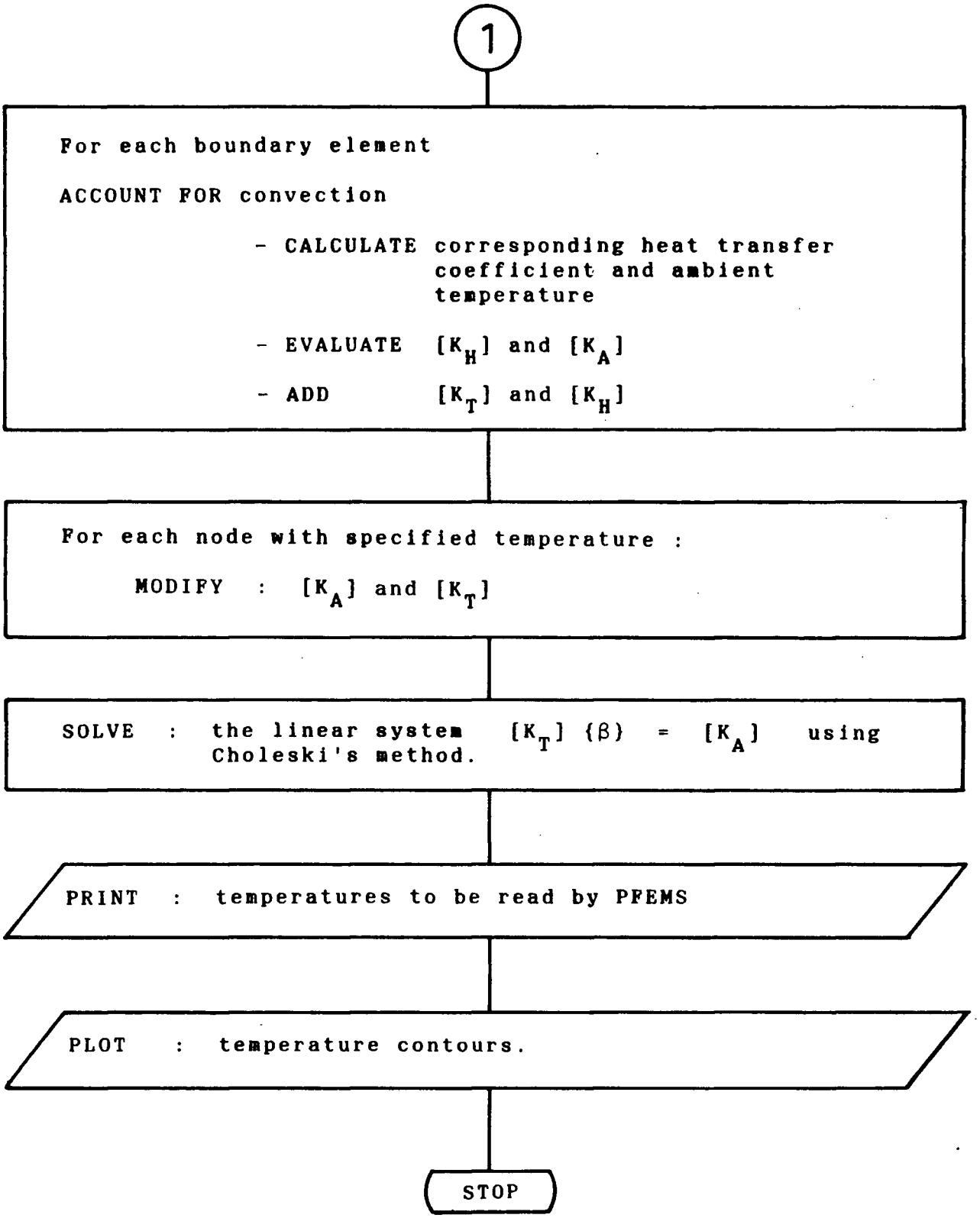

Figure 8.1 Flow chart of the computer program to calculate the temperature field in the crystal using a finite element method.

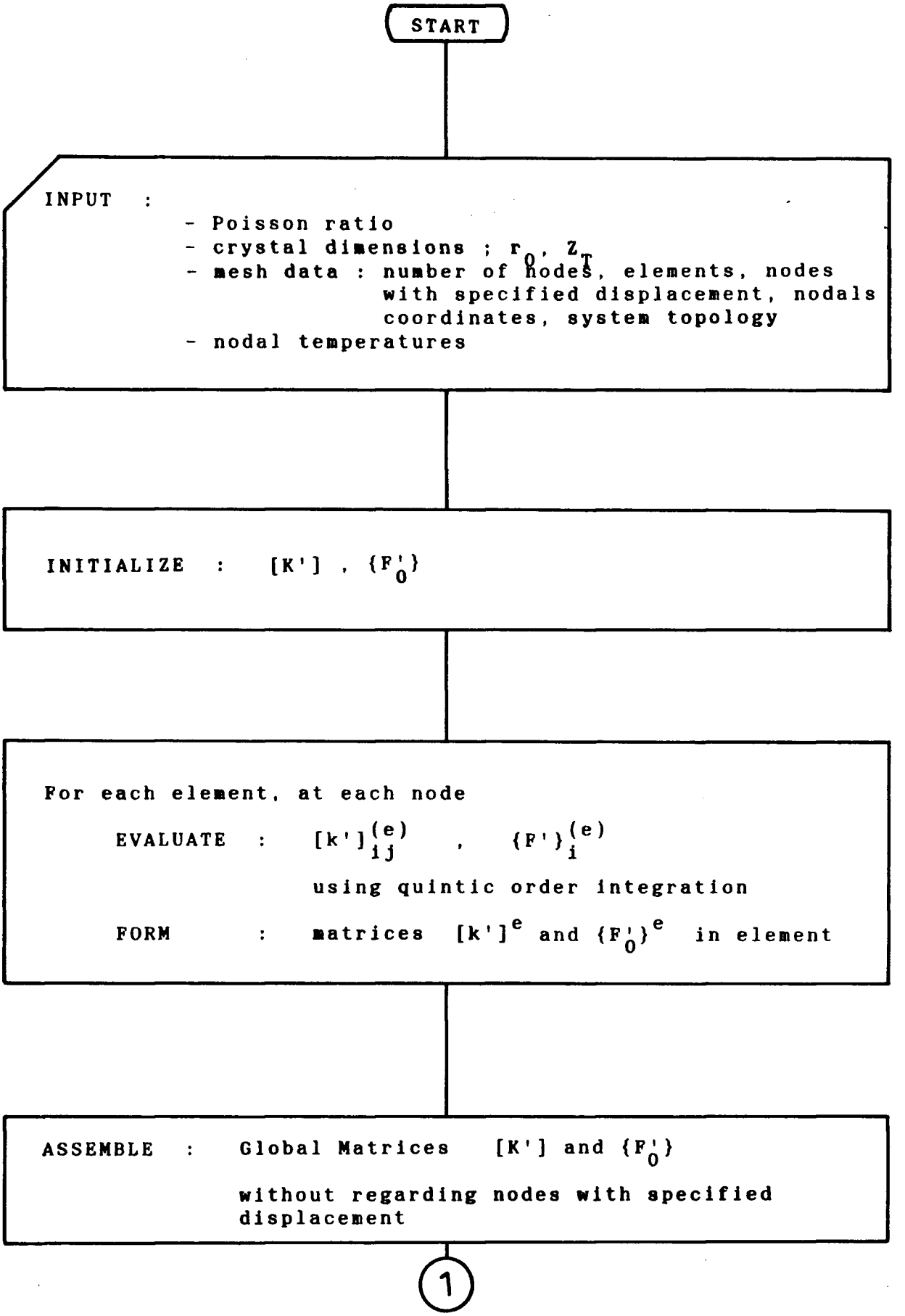
START
INPUT :
- Poisson ratio
- crystal dimensions ; r_0, Z_T
- mesh data : number of nodes, elements, nodes with specified displacement, nodals coordinates, system topology
- nodal temperatures
INITIALIZE : [K'] , $\{F'_0\}$
For each element, at each node
EVALUATE : $[k']^{(e)}_{ij}$, $\{F'\}^{(e)}_{i}$
using quintic order integration
FORM : matrices $[k']^e$ and $\{F'_0\}^e$ in element
ASSEMBLE : Global Matrices [K'] and $\{F'_0\}$
without regarding nodes with specified displacement
1

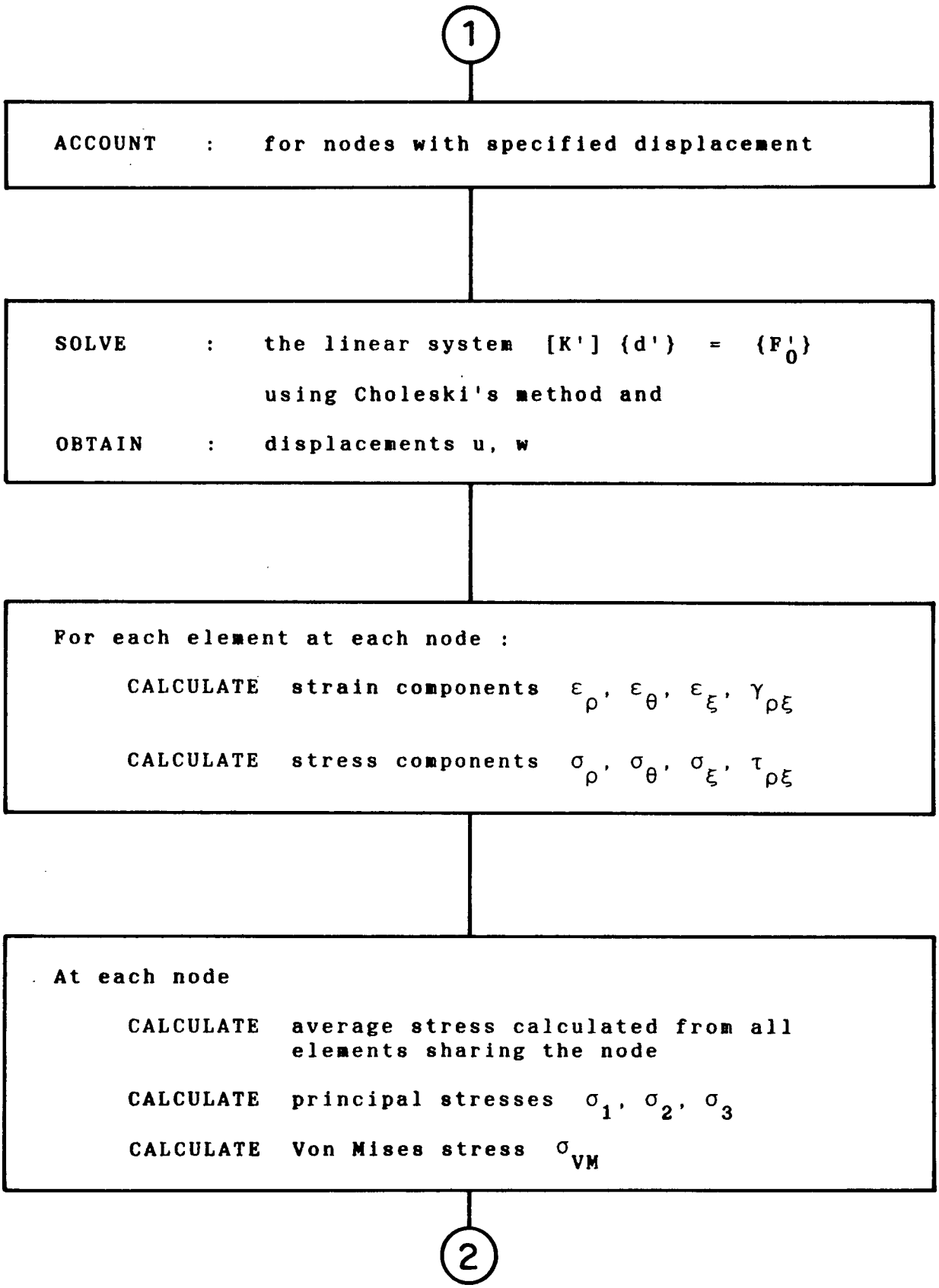
1
ACCOUNT : for nodes with specified displacement
SOLVE : the linear system [K'] {d'} = {F'0}
using Choleski's method and
OBTAIN : displacements u, w
For each element at each node :
CALCULATE strain components ερ, εθ, εξ, γρξ
CALCULATE stress components σρ, σθ, σξ, τρξ
At each node
CALCULATE average stress calculated from all elements sharing the node
CALCULATE principal stresses σ1, σ2, σ3
CALCULATE Von Mises stress σVM
2

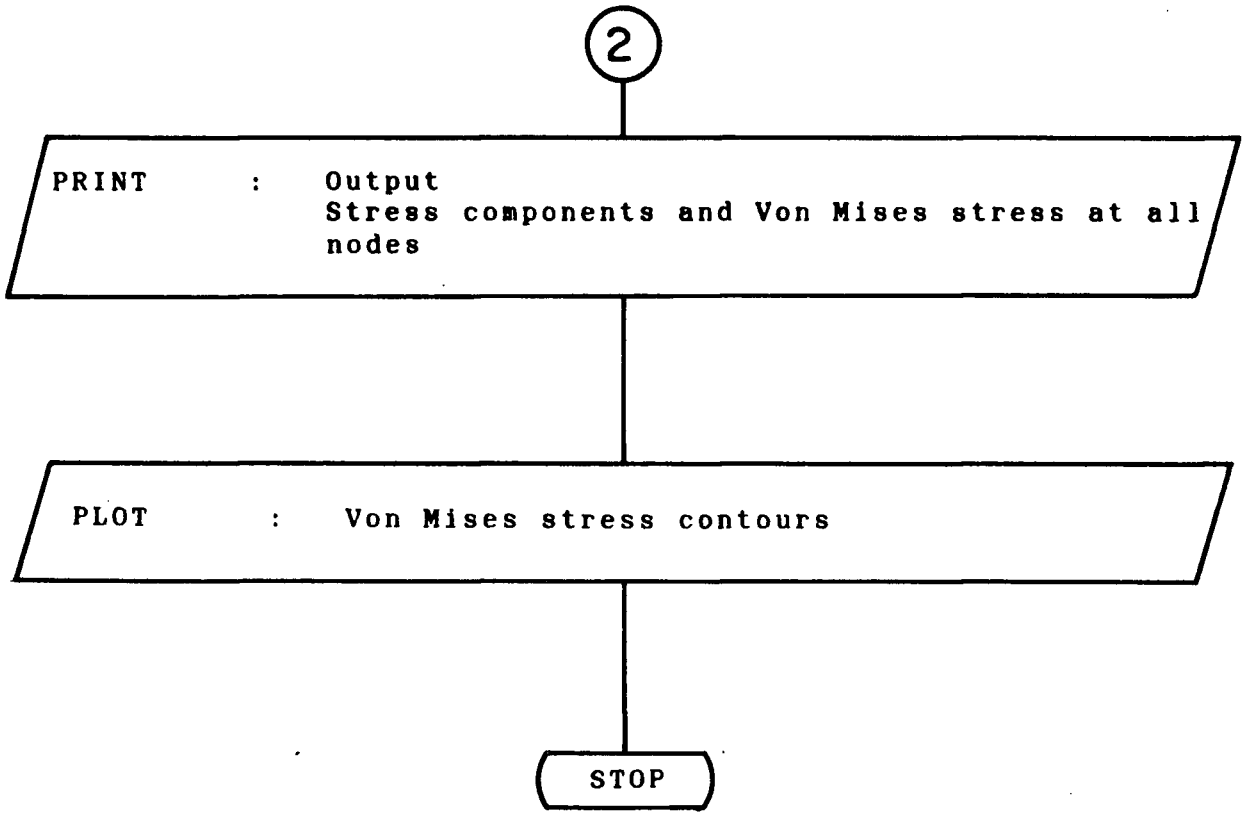

Figure 8.2 Flow chart of the computer program for the stress calculations using finite linear and quadratic elements.

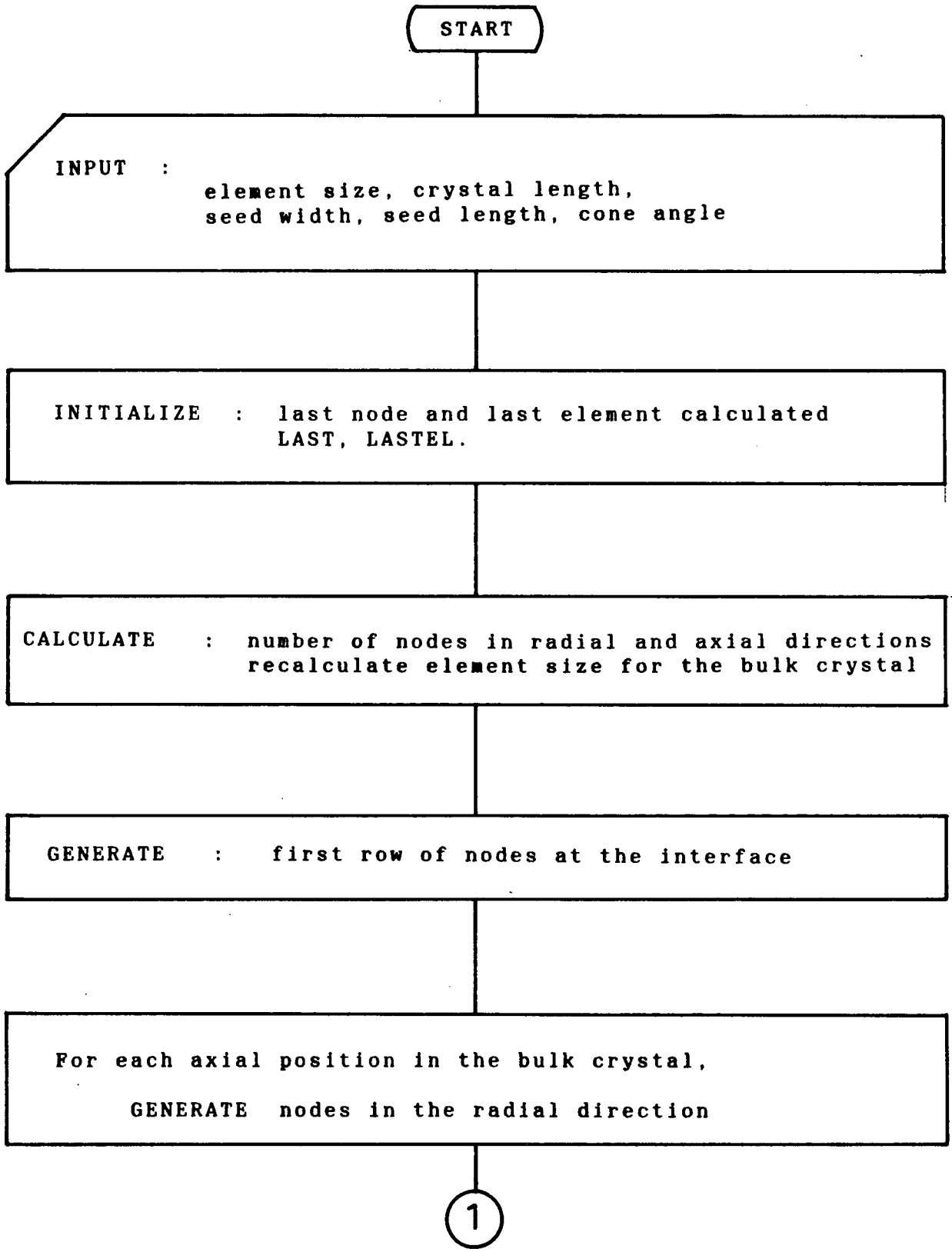
START
INPUT :
element size, crystal length,
seed width, seed length, cone angle
INITIALIZE : last node and last element calculated
LAST, LASTEL.
CALCULATE : number of nodes in radial and axial directions
recalculate element size for the bulk crystal
GENERATE : first row of nodes at the interface
For each axial position in the bulk crystal,
GENERATE nodes in the radial direction
1

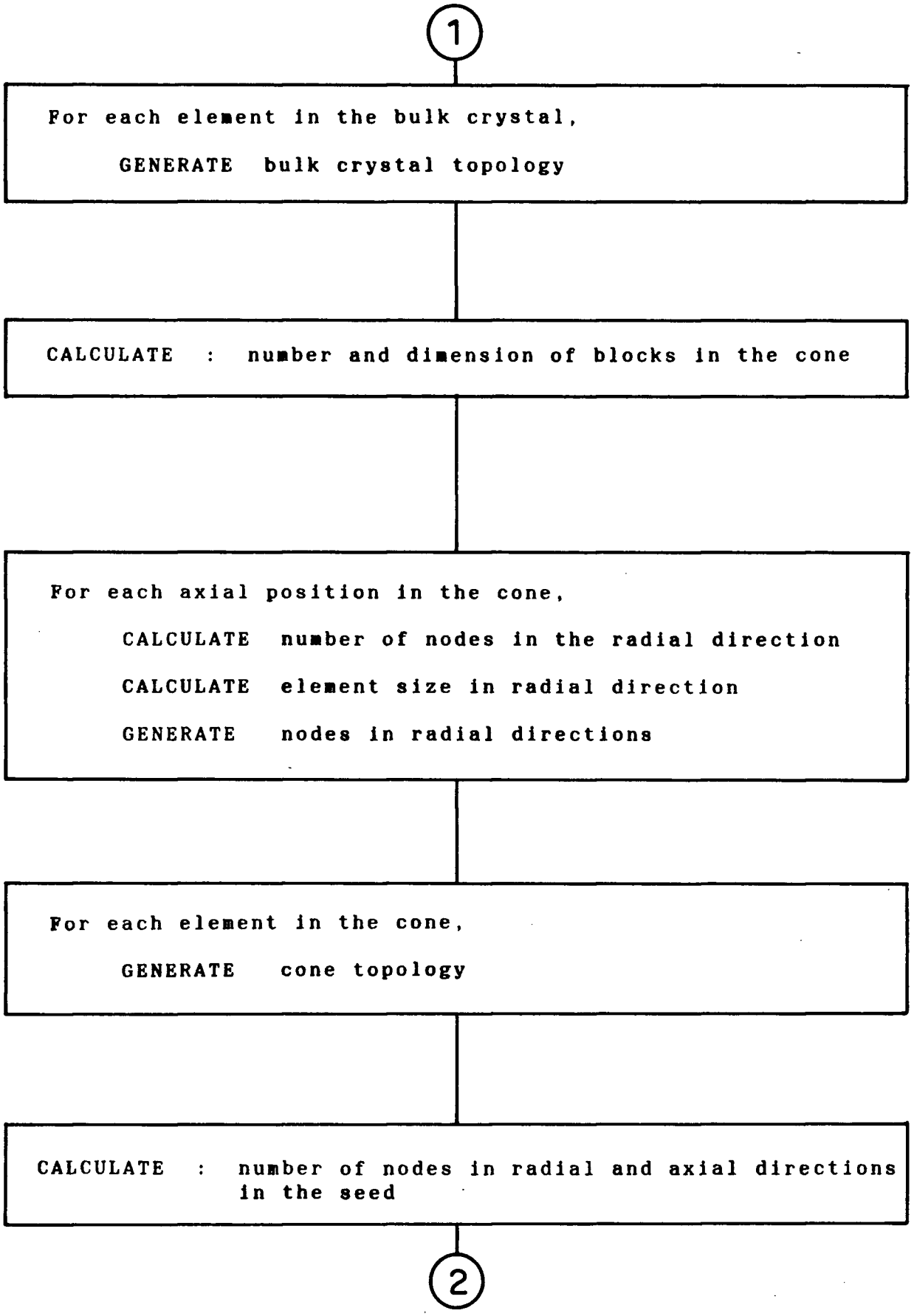
1
For each element in the bulk crystal,
GENERATE bulk crystal topology
CALCULATE : number and dimension of blocks in the cone
For each axial position in the cone,
CALCULATE number of nodes in the radial direction
CALCULATE element size in radial direction
GENERATE nodes in radial directions
For each element in the cone,
GENERATE cone topology
CALCULATE : number of nodes in radial and axial directions in the seed
2

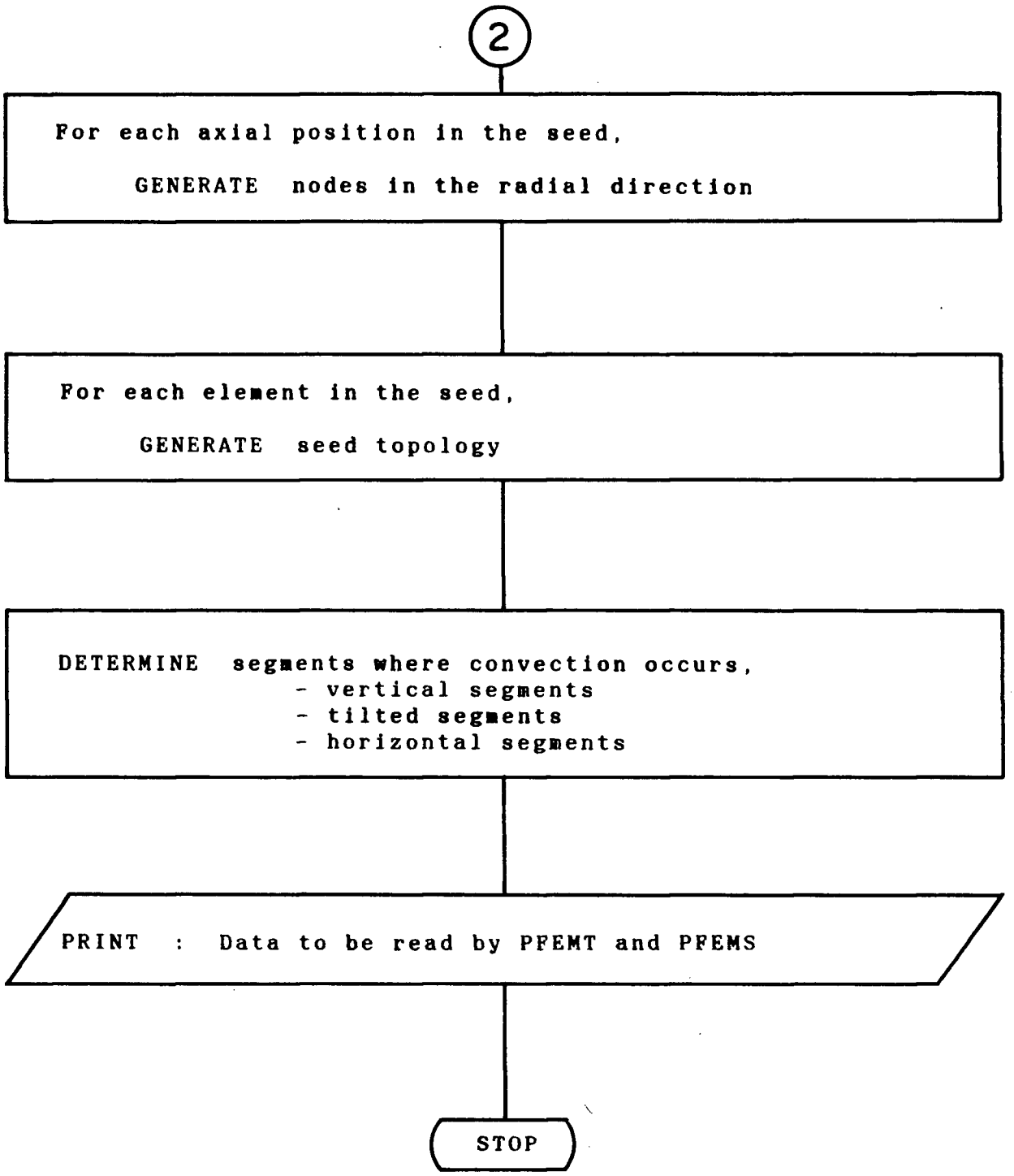

Figure 8.3 Flow chart of the mesh generator computer program.

consisted of applying uniform boundary conditions on the surface of the crystal. These conditions were : unit ambient temperature in the medium surrounding the crystal, constant heat transfer coefficient and unit temperature at the solid liquid interface. The temperature field in the crystal in such conditions should be uniform and have unit value.

The combination of mesh type and solution method selected gave temperature fields for a coarse mesh, which were 99 % of the theoretical value.

In the case of the thermoelastic stress calculations with the FEM, application of a unit temperature field throughout the crystal gave nondimensional stress values less that 10^{-4}. In such conditions the theoretical stress should be zero.

In addition, manual tests were carried out using simple meshes to ensure that the stiffness element matrices were symmetric and positively defined (eigenvalues should be positive). To minimize the computer memory requirements, which is critical for large systems, the stiffness matrix for the whole system was assembled directly in a linear array.

The output of the computational effort of the temperature calculations consisted of nodal temperatures and isotherm plots in the crystal. The output in the stress program consisted of nodal displacements, nodal stress components in cylindrical coordinates, nodal Von Mises stresses and Von Mises isostress contours in the crystal.

Two other programs were written for calculating the maximum component of resolved shear stress in planes perpendicular and parallel to the crystal axis. These planes correspond to a (001) plane and (010) plane respectively. Similar plots are obtained of the difference between the MRSS and experimental values of critical resolved shear stresses for dislocation generation (CRSS) or yield (YS). Values of CRSS for doped and Te-doped [CRSS(Te)] GaAs have been employed for the comparison. These values are temperature dependent. The flow charts of the programs are shown in Figures 8.4 and 8.5. In all cases the output also consists of nodal values of the corresponding stress and the mode (specific plane and direction) which gives the maximum component of stress.

The computer programs for the four calculations are listed in Appendix XI.

8.1.1 Input Parameters

The input parameters for the calculations in the different computer programs depend on the stage being modelled. For the mesh generation, only geometric parameters are given, they are :

1) crystal dimensions :
   - radius
   - length
   - cone angle
   - seed length
   - seed radius
   - interface shape

2) element size given by the distance between nodes.

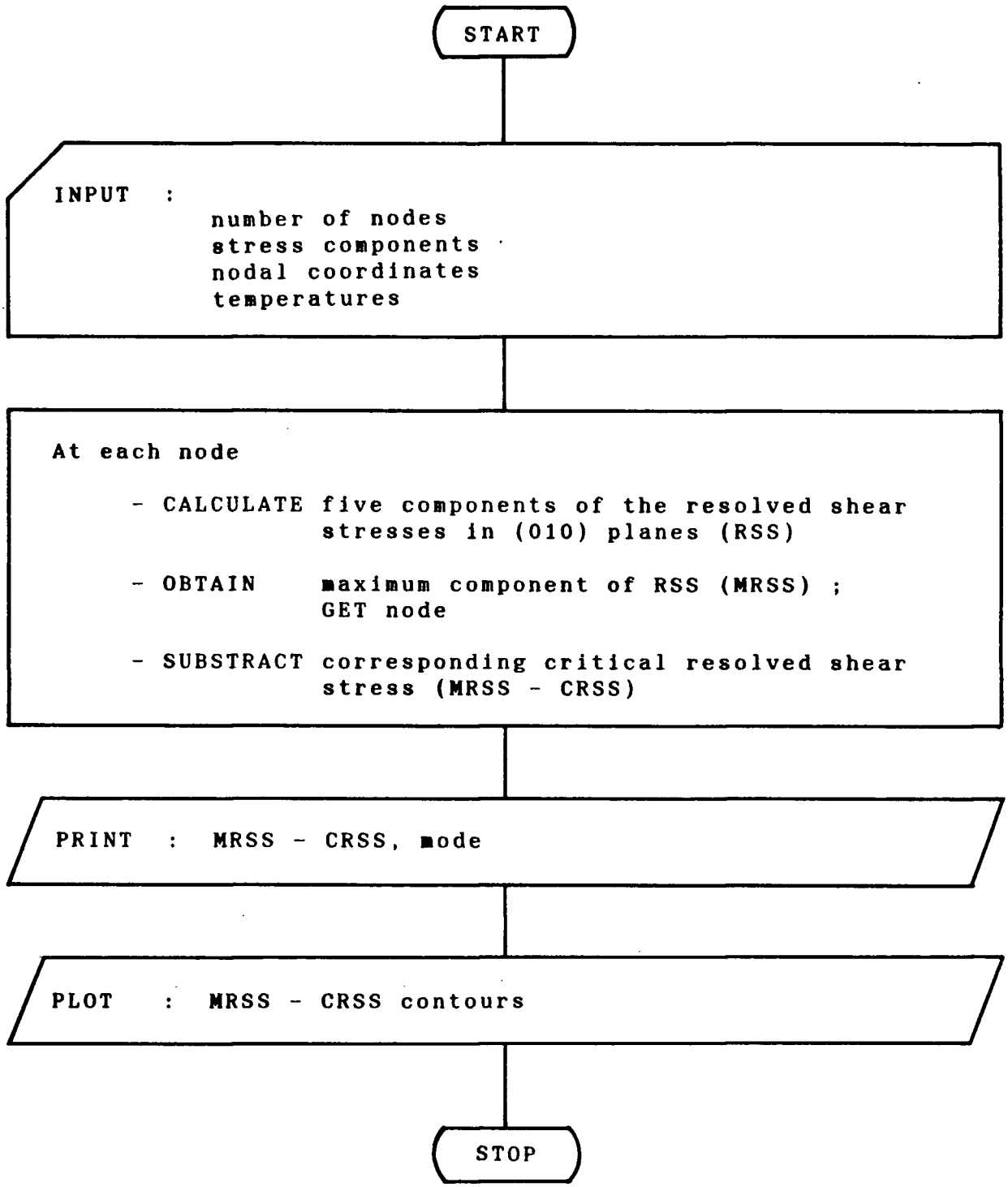

Figure 8.4 Flow chart of the computer program to calculate and plot RSS in a vertical (010) plane

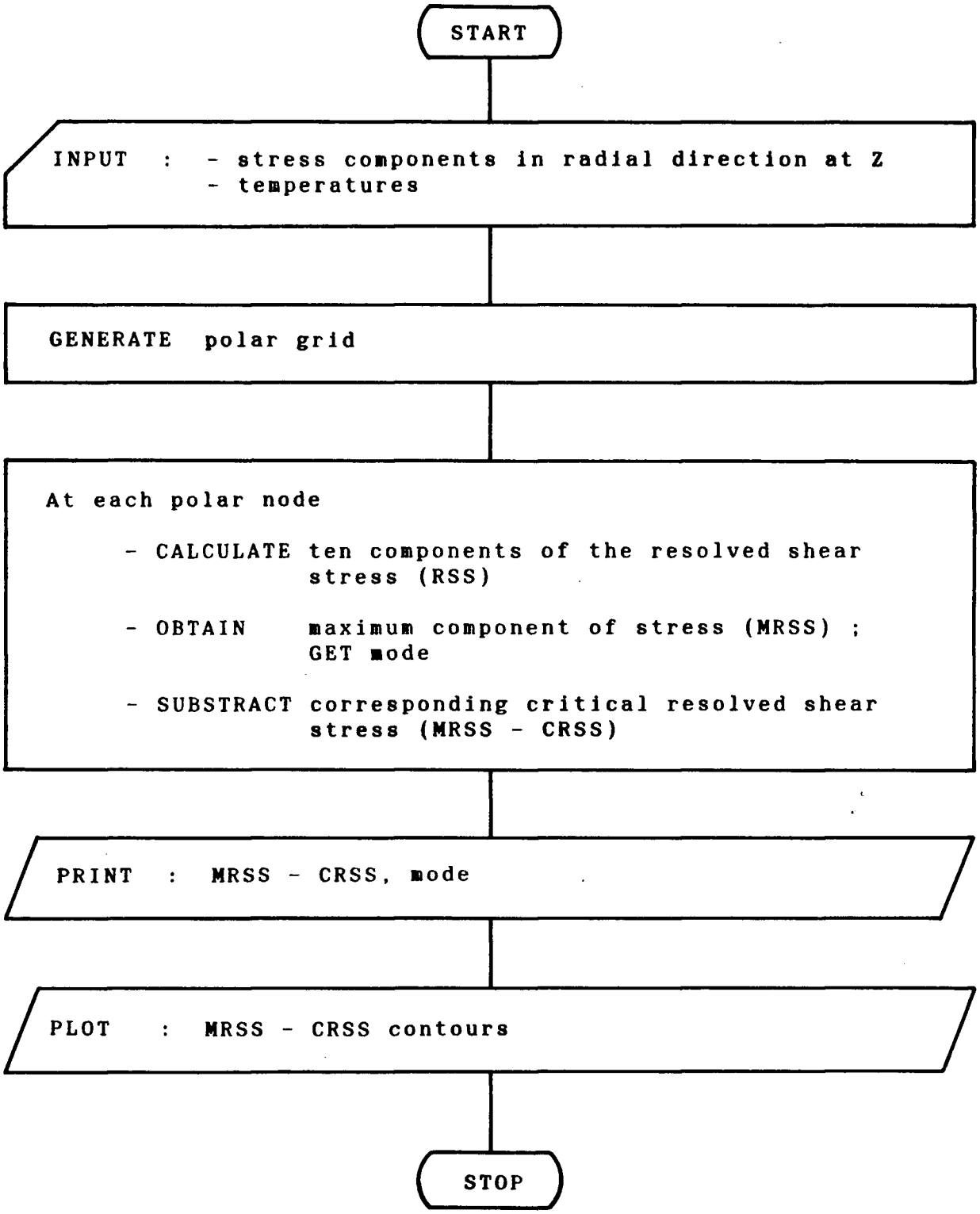

Figure 8.4 Flow chart of the computer program to calculate and plot RSS in a (001) plane

The input for the temperature program is the nodal and element configuration, the nodes at the interface and the segments where heat is transferred to the surrounding atmosphere. The physical data includes gas pressure, boric oxide height and temperature profiles in both media. From these the heat transfer coefficient at the corresponding temperature is calculated in the program. The heat transfer coefficient relative to the thermal conductivity includes heat transfer by radiation and convection

$$h = h_r + h_c$$

The heat transfer coefficient for radiation was derived by Jordan[190,191] from the Stefan-Boltzman equation leading to the following equation :

$$h_r = (2.27 \times 10^{11} / \kappa)\ \varepsilon_t T_a^3$$

where ε_t is the total emittance of GaAs and is a function of temperature and doping level.

The convective heat transfer coefficient to the gas and B_2O_3 layer was calculated assuming heat is transferred by free convection from a vertical wall into a fluid and is given by[191]

$$h_c[cm^{-1}] = \left(\frac{T - T_a}{l}\right)^{1/4} h'' p^{1/2}$$

where

$$h'' = .548 \frac{\kappa_a}{\kappa} [\rho_a^2 \ g \ \alpha_a \ C_{p_a} / \kappa_a \mu_a]^{1/2}$$

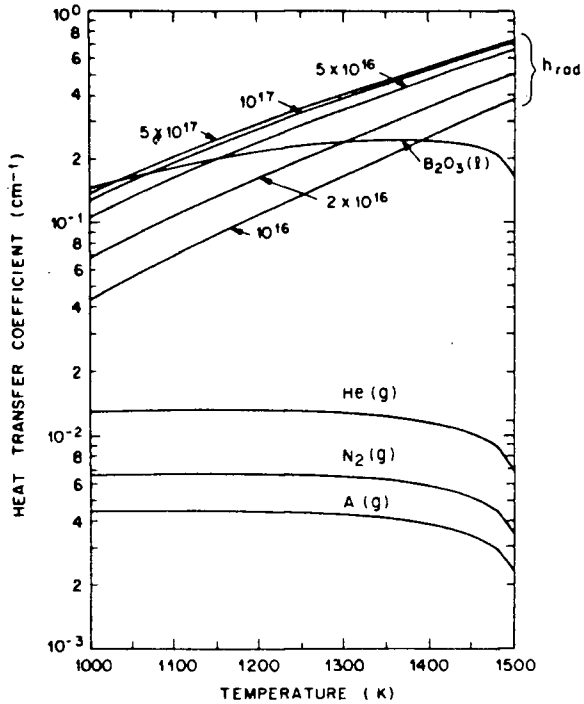

Figure 8.6 Estimated radiative and convection heat transfer coefficients for GaAs/B_2O_3 (l), He (g), N_2 (g) and A (g) as a function of ambient temperature. The numerical labels are the product of the carrier concentration X crystal diameter in units of cm^{-2}.

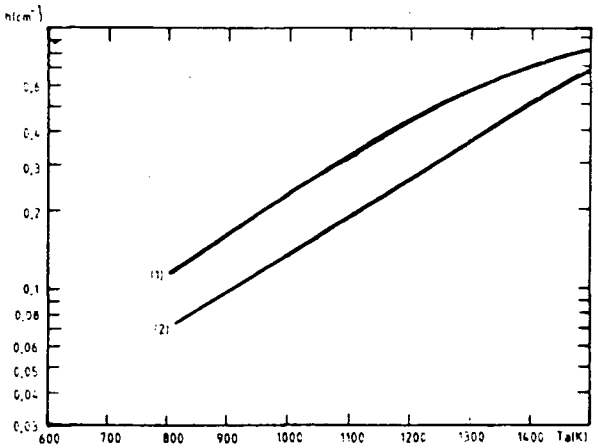

Figure 8.7 Total heat transfer coefficient h, in B_2O_3 and argon as a function of the ambient temperature T_a^3 (1) Total heat transfer coefficient in B_2O_3. (2) Total heat transfer coefficient in argon pressurized at 30 atm.

κ_a = ambient thermal diffusivity

ρ_a = ambient density

α_a = coefficient of thermal volume expansion

C_p = heat capacity

μ_a = viscosity

p = pressure

l = height of the fluid column

for a liquid medium p is taken as p = 1.

The numerical evaluation of the heat transfer coefficients was done by Jordan et al.[191] using temperature dependent values of the physical quantities involved. The results for a gas pressure of 1 atmosphere are shown in Figure 8.6 for the different media. The total heat transfer coefficients for boron oxide and argon at 30 atmospheres are shown in Figure 8.7 . In the program the heat transfer coefficients are evaluated by functions which fit the data and include the effect of temperature and pressure. Other physical parameters are the thermal diffusivity which is assumed to be temperature independent, and growth velocity.

The same nodal configuration employed in the calculation of temperatures must be used for the thermal stress calculations. The nodal temperatures are the input for this program. In addition the Poisson ratio and Young modulus are given. The values of the most important parameters are listed in Table 8.1.

Table 8.1 Values of physical parameters used in the calculations[191].

Melting point	1238 ^{o}C
Thermal conductivity	0.08 Watts/cm ^{o}K
Thermal diffusivity	0.04 ± 0.01 (800 ^{o}C - 1238 ^{o}C) (cm^2/sec)
Thermal expansion coefficient	1.0 X 10^{-5} ($^{o}K^{-1}$)
Young modulus	1.2 X 10^{11} Pa
Poisson ratio	0.29
α E / (1-2ν)	2.86 ± 0.1 (800 ^{o}C - 1238 ^{o}C) MPa $^{o}K^{-1}$

The yield and critical stresses employed for comparison with the MRSS were measured by Swaminathan and Copley[211] and Mildviskii et al.[163] respectively. The yield stress measured at temperatures well below the melting point are extrapolated to this point ; an inverse exponential temperature dependence was assumed as the experimental results suggest. The CRSS for undoped

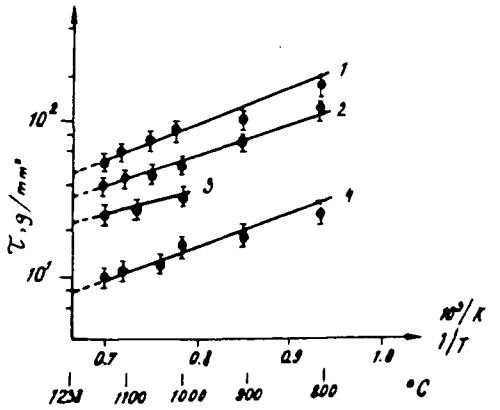

Figure 8.8 Temperature dependence of the critical stress for dislocation generation in GaAs : (1) Te-doped material, $n = 2 \times 10^{18}$ cm^{-3} ; (2) Te-doped material, $n = 7 \times 10^{17}$ cm^{-3} ; (3) Zn-doped material, $p = 9 \times 10^{18}$ cm^{-3} ; (4) undoped material.

and doped GaAs close to the melting point are shown in Figure 8.8. It can be noted that the CRSS for doped material is about one order of magnitude larger than for undoped material.

8.1.2 Numerical Evaluation of the Analytical Solutions

For the numerical evaluation of the analytical solutions for the different fields and conditions, programs in BASIC language were written. Programs were run in a VIC-20 microcomputer with expanded memory to 8 KRam. The λ value, solutions of Equation (7.45) were obtained using graphic methods[212]. The first five roots were used. The Bessel function J_0, J_1, I_0 and I_1 were evaluated using polynomial interpolations for the functions[213].

The summation of the Fourier series was carried out using between 20 to 40 terms. This was necessary because of the typical slow convergency of this series.

8.2 Comparison of Model Predictions with Analytical Solutions

8.2.1 Temperature Field

Numerical solutions obtained using the finite element method were compared with analytical solutions for the problem described in Section 7.3. Calculations were performed for two values of the heat transfer coefficient h. The values selected, 0.3 cm^{-1} and 0.6 cm^{-1}, are in the range applicable to a crystal being grown in a pressurized argon atmosphere of 3.04MPa. The crystal radius was 20 mm and the height 40 mm. The results are shown in Figures 8.9

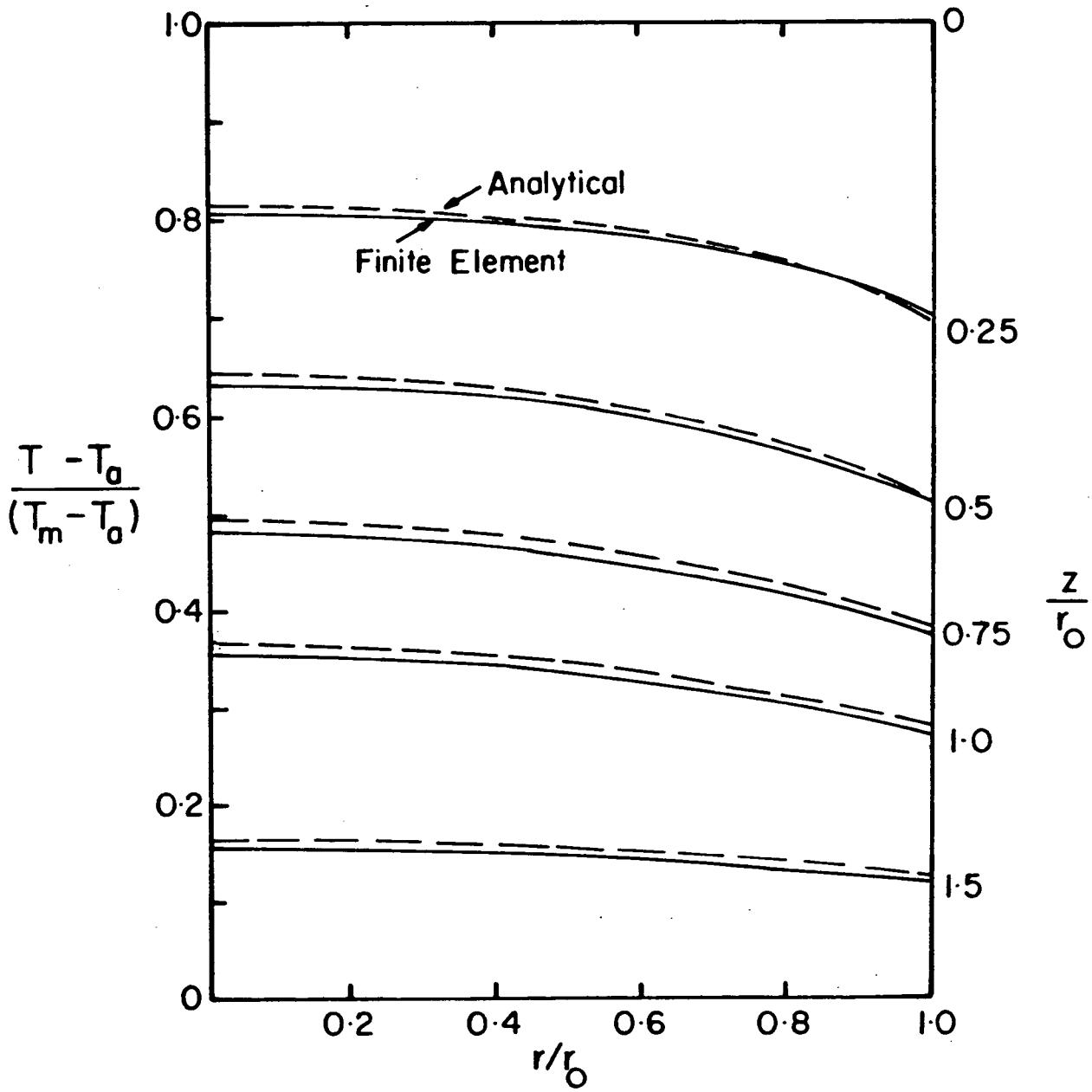

Figure 8.9 A comparison of finite element and analytical calculated temperature curves for h = 0.3 cm^{-1}.

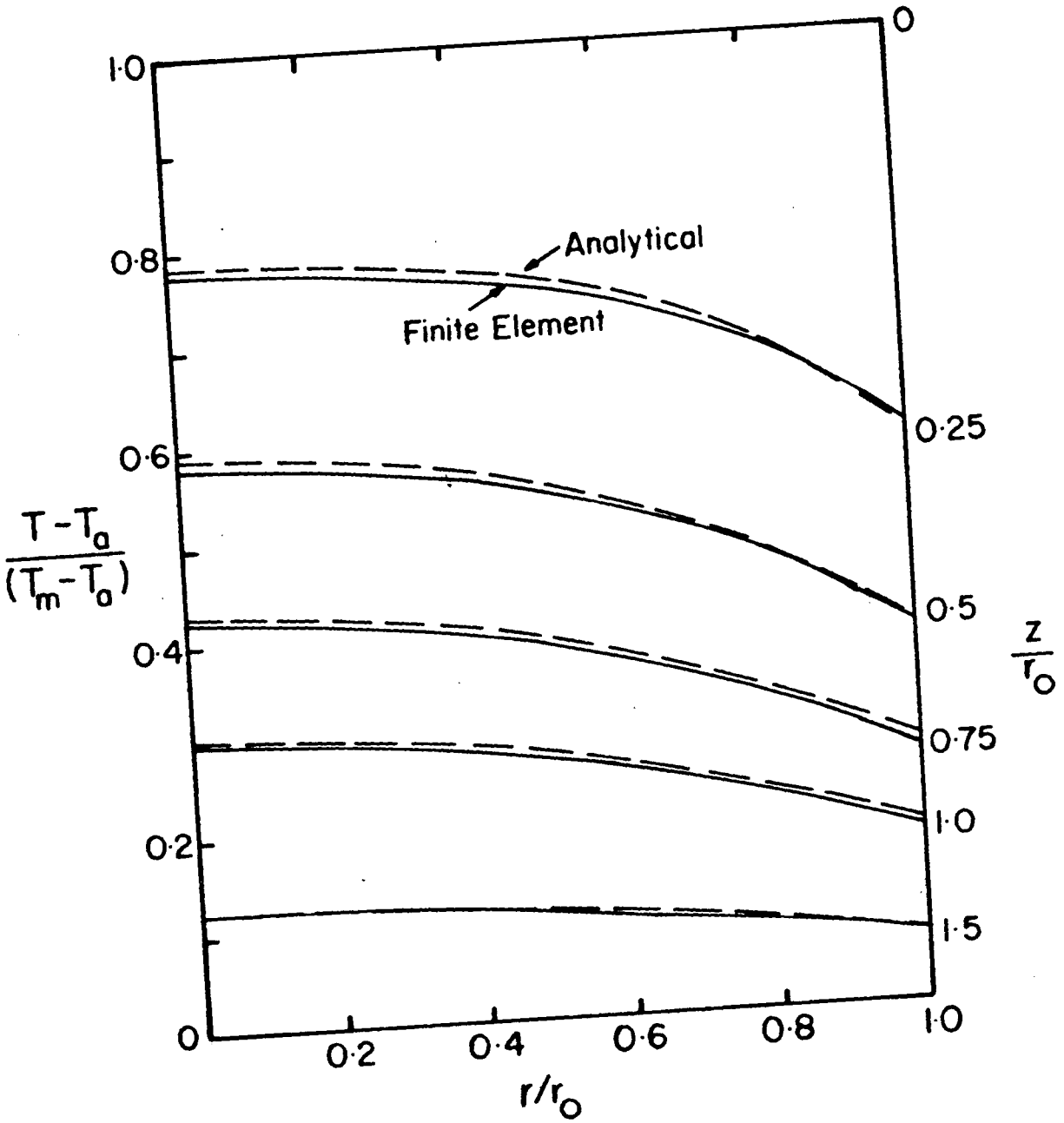

Figure 8.10 A comparison of finite element and analytical calculated temperature curves for h = 0.6 cm^{-1}.

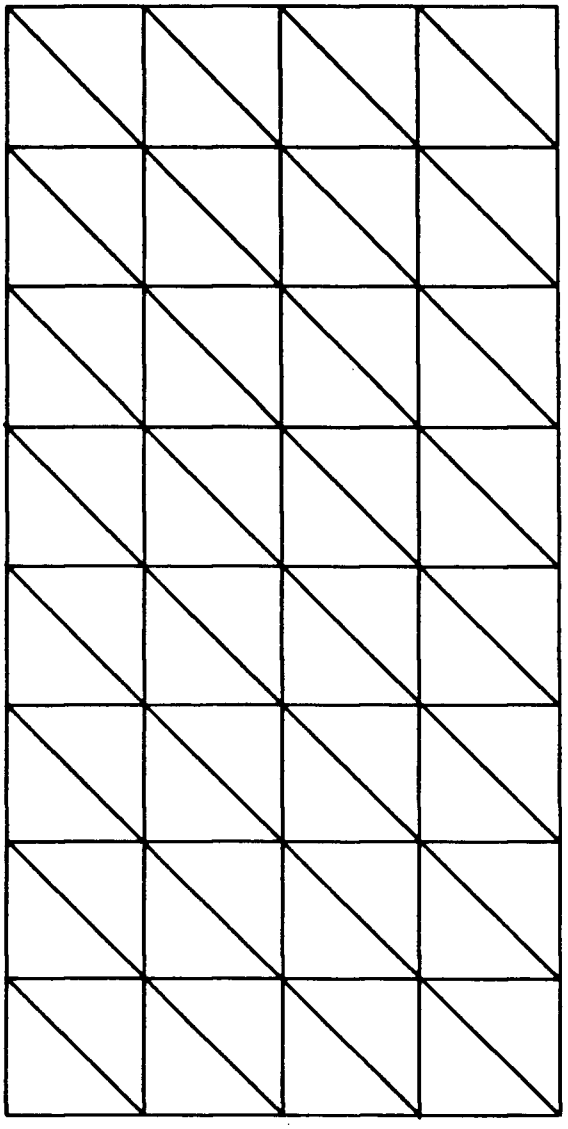

Figure 8.11 Mesh employed in the calculations of the temperature fields shown in Fig. 8.9 and 8.10. Number of nodes = 45. Number of elements = 64.

and 8.10 from which it is evident that the agreement is good. The finite element method gives temperatures which are slightly lower than the temperatures calculated analytically. A total of 64 elements were employed in the calculation and the corresponding number of nodes was 45. The mesh used is shown in Figure 8.11. Further refinement of the mesh did not appreciably change the results.

8.2.2 Stress Fields

Finite element solutions were obtained for a cylindrical crystal for radial and axisymmetric temperature fields using linear elements. A crystal of radius 20 mm, and length 40 mm was discretized into a mesh of 256 elements which consists of 153 nodes. The stresses were calculated on the basis of a) the computed nodal temperatures and b) a uniform temperature in the element derived by averaging the nodal temperatures.

For radial temperature fields, the radial stresses calculated by the finite element method for nodal and average element temperatures are plotted as a function of r/r_0 in Figure 8.12. For comparison the corresponding stresses determined analytically are also shown for both plane strain and axisymmetric displacements. The radial stresses effectively coincide for the two analytical solutions and the finite element solutions using the average element temperature. The results for the finite element method using computed nodal temperatures is well below the other three. This large difference is attributed

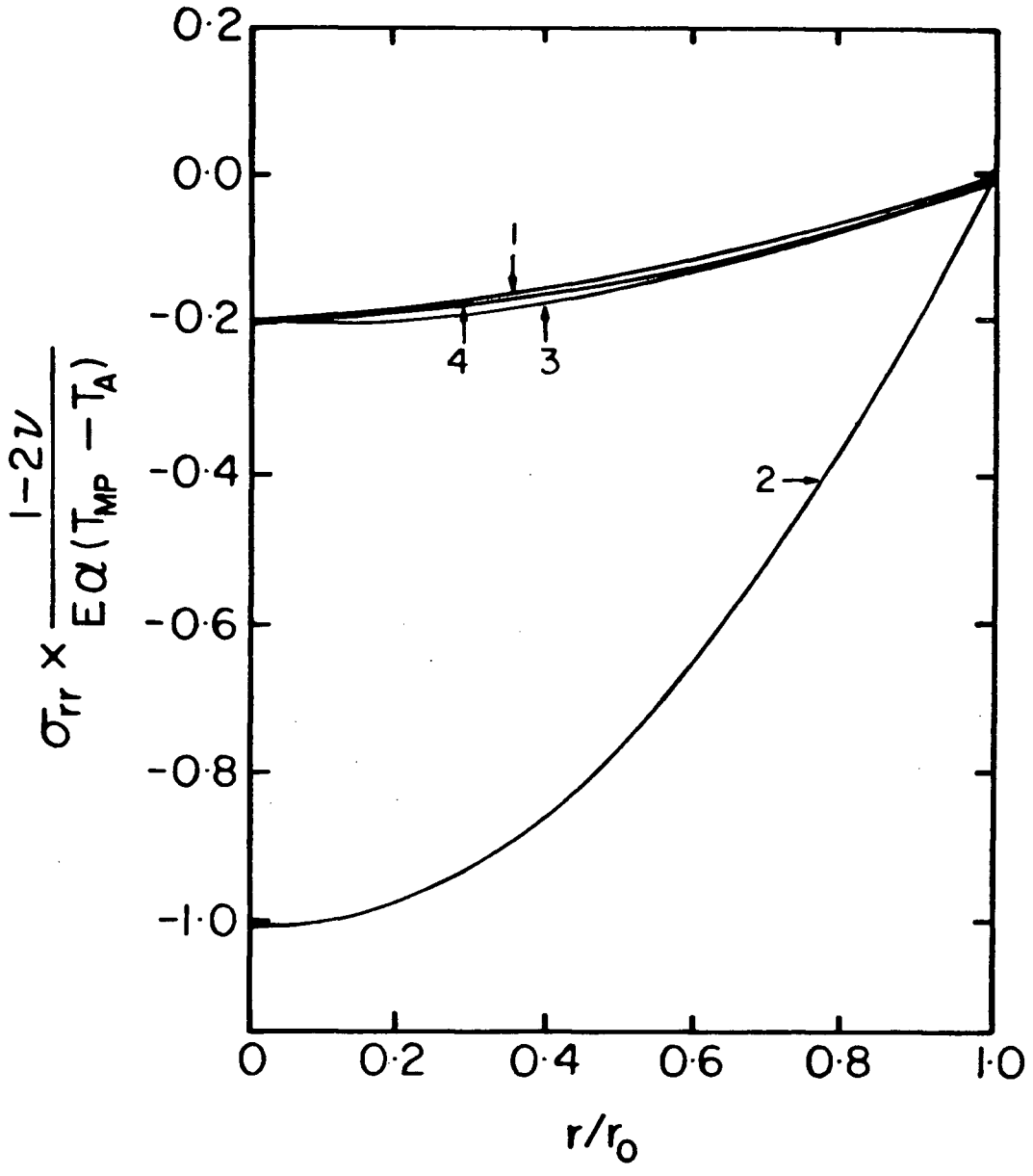

Figure 8.12 Calculated radial stresses as a function of r/r_o for radial temperature fields (1) Finite element with averaged element (2) Finite element with nodal temperatures (3) Analytical-plane strain (4) Analytical-axisymmetric.

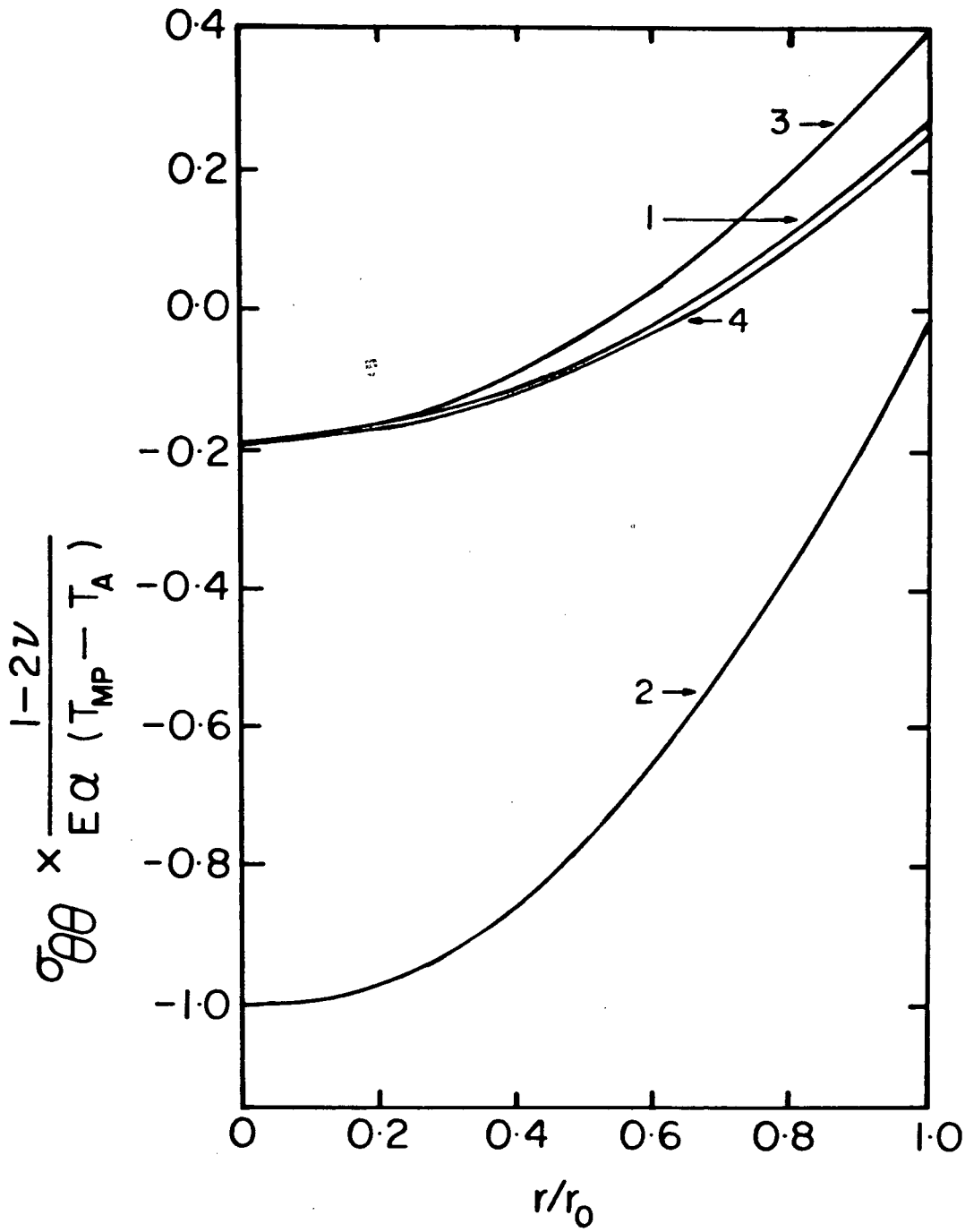

Figure 8.13 Calculated azimuthal stresses as a function of r/r_0 for radial temperature fields (1) Finite element with averaged element temperatures (2) Finite element with nodal temperatures (3) Analytical-plane strain (4) Analytical-axisymmetric.

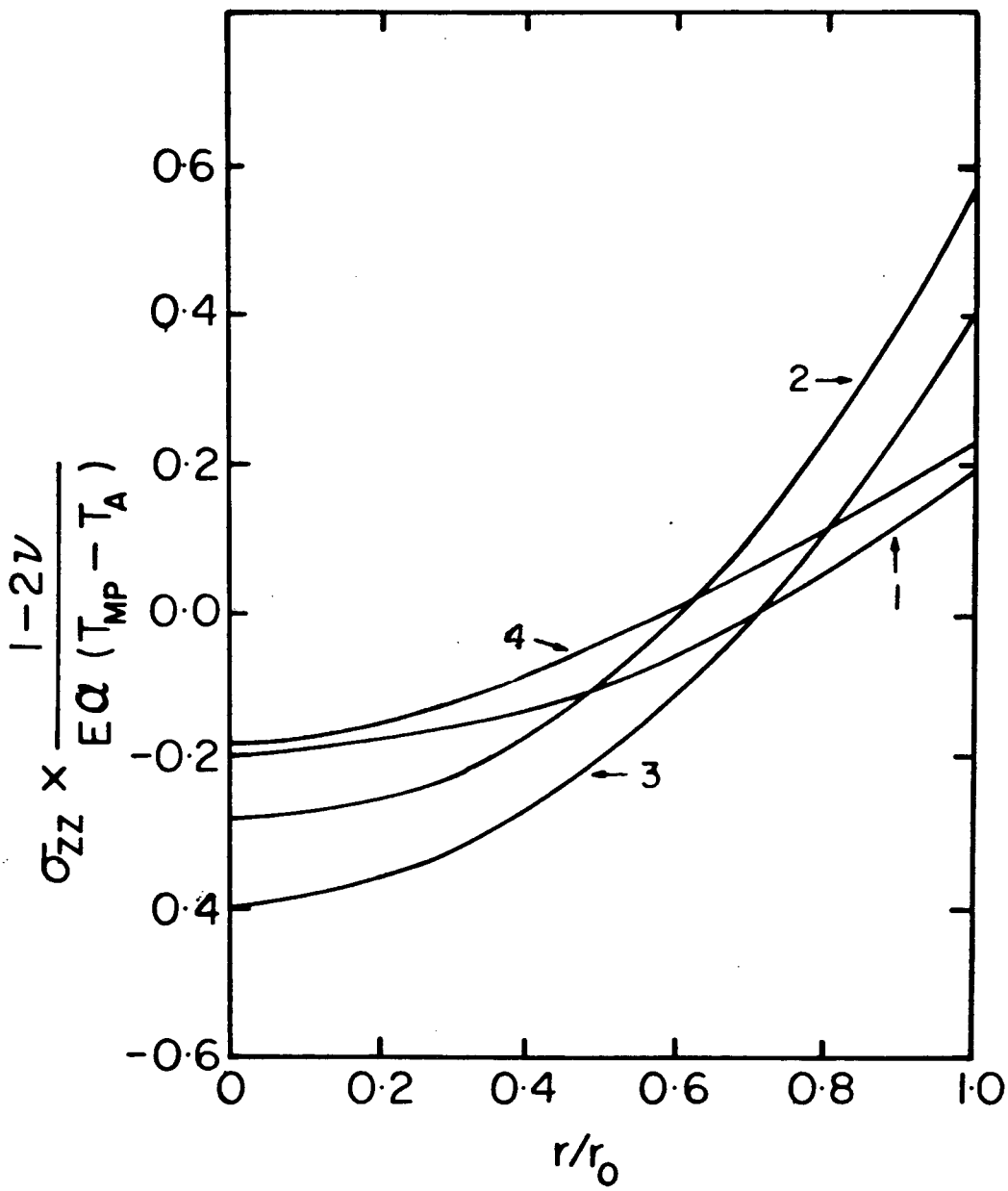

Figure 8.14 Calculated axial stresses as a function of r/r_o for radial temperature fields (1) Finite element with averaged element temperatures (2) Finite element with nodal temperatures (3) Analytical-plane strain (4) Analytical-axisymmetric.

to the incompatibility in the approximation of initial strain in comparison with the strain field in the linear element. If the nodal temperatures are used, without averaging, both the temperature and initial strain vary linearly within the element while the linear displacement formulation gives a constant strain within the element, which is inconsistent. When the nodal temperatures are averaged and assumed constant within the element, the initial strain is also constant and is consistent with the strain associated with the displacement field.

The azimuthal and axial stresses, as a function of r/r_0 for the same solution are shown in Figures 8.13 and 8.14 respectively. The results in Figure 8.13 are generally similar to the radial stresses in Figure 8.10 with the finite element nodal temperature method of introducing thermal strain giving a curve falling well below the other three. The plane strain analytical solution deviates from the other two a small amount with increasing r/r_0. The axial stress curves in Figure 8.14 have a different configuration than the radial and azimuthal solutions. The best agreement is between the finite element average temperature curve and the axisymmetric curve as before. The finite element nodal temperature curve is not valid for the reasons given previously. The analytical plane strain values deviates from the other two giving maximum tensile and compressive stresses.

To test the convergence of the finite element procedure, stress calculations were made with refined meshes for a radial

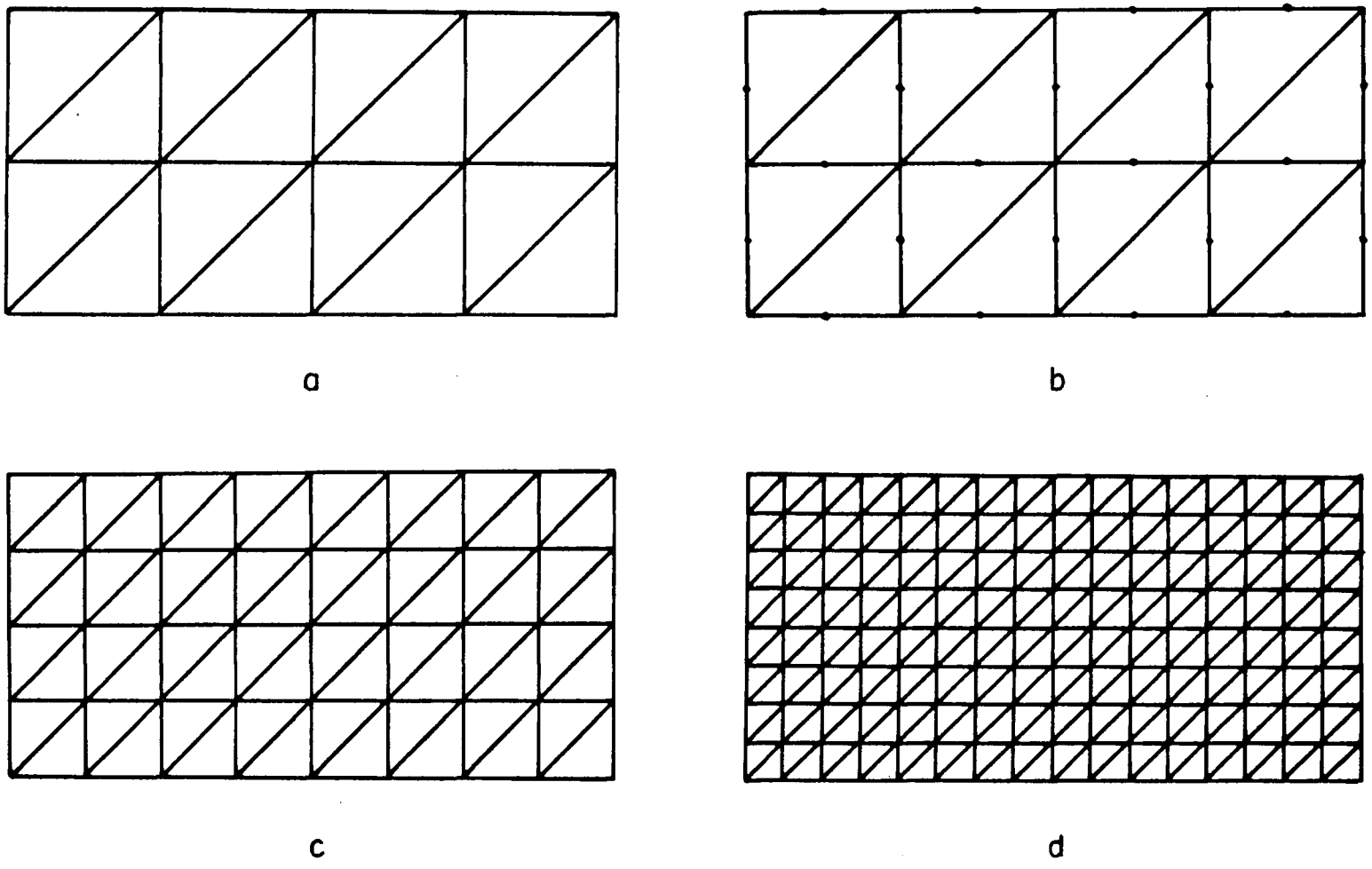

Figure 8.15 Four steps in the mesh refinement used to analyse the convergency of the finite element stress calculations. (a) NN = 15 NE = 16 (b) NN = 45, NE = 16 (c) NN = 45, NE = 64. (d) NN 153, NE = 256 (b) Quadratic elements. (a), (c) and (d linear elements.

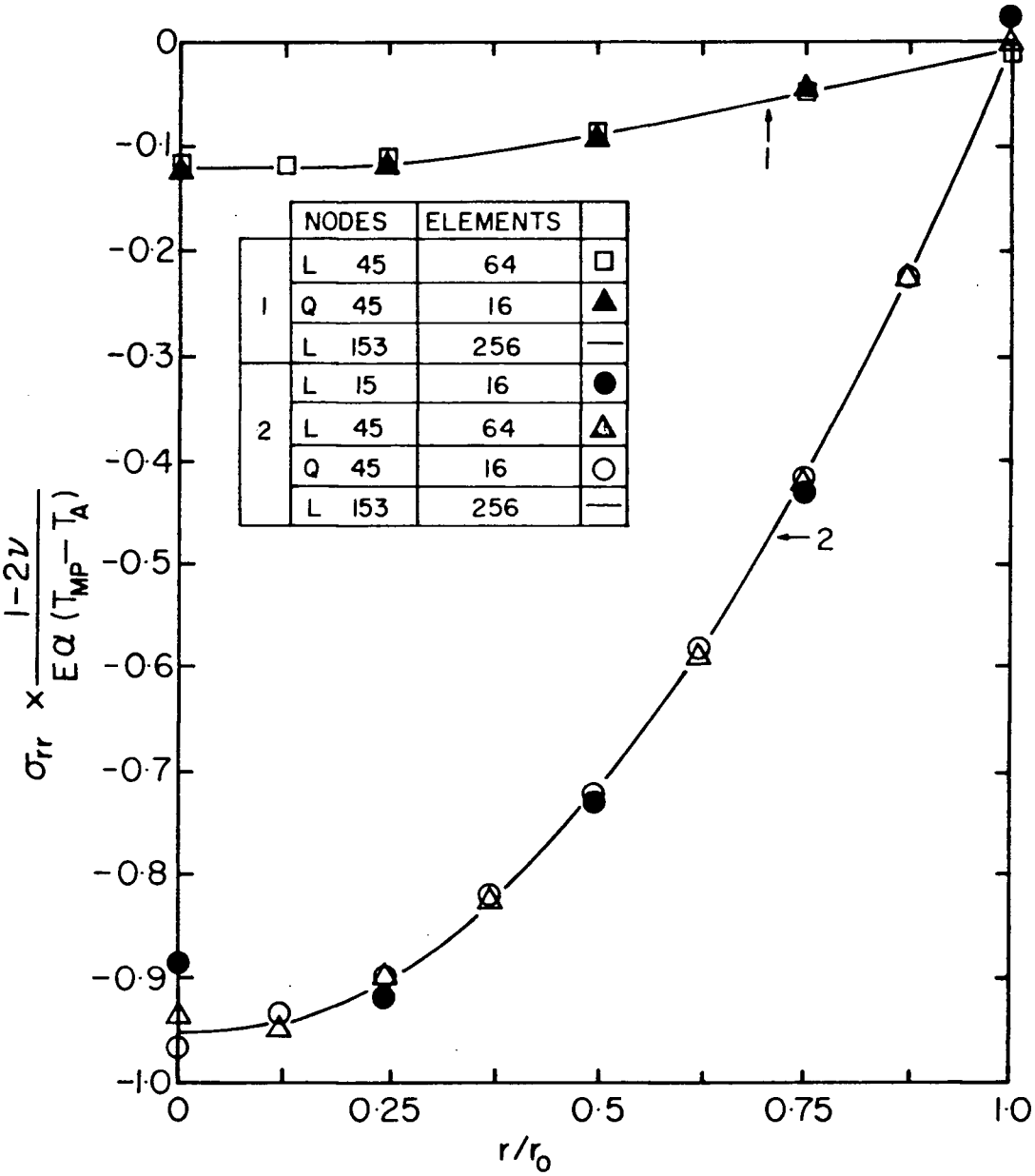

Figure 8.16 Calculated radial stresses as a function of r/r_o for different numbers of nodes and sizes of element (1) Finite element with averaged element temperature (2) Finite element with nodal temperatures. L = Linear element, Q = Quadratic element.

temperature field. Calculations were made as a function of r/r_0 for a cylinder of half a radius in length. The different steps in the mesh refinement are shown in Figure 8.15. The results of the stress calculations are shown in Figure 8.16 using individual node temperatures and average element temperatures. The results indicate that large changes in the number of nodes and elements have no significant effect on the calculated stresses in both cases. The results also show that the large difference between the nodal and averaged element temperature is not associated with element size but with the incompatibility between strains as described above. It is also evident that the quadratic element formulation does not lead to a significant difference in the computed stresses. For the same number of nodes fewer and larger elements are involved in the quadratic element formulation, as seen in Figure 8.16, and hence the improved accuracy of the quadratic interpolation of displacement is compromised by the coarser grid.

The finite element and analytical radial stress fields for an axisymmetric thermal field are shown in Figure 8.17. The temperature field corresponds to an h value of 0.3 cm^{-1} for a crystal of radius 20 mm and length 40 mm. The number of nodes and elements were 256 and 153 respectively. The finite element average temperature curve nearly coincides with the analytical axisymmetric curve for r/r_0 above 0.5, deviating below this value. As before, the finite element nodal temperature curve differs markedly from the others. The analytical plane strain curve has a higher compressive stress than the others.

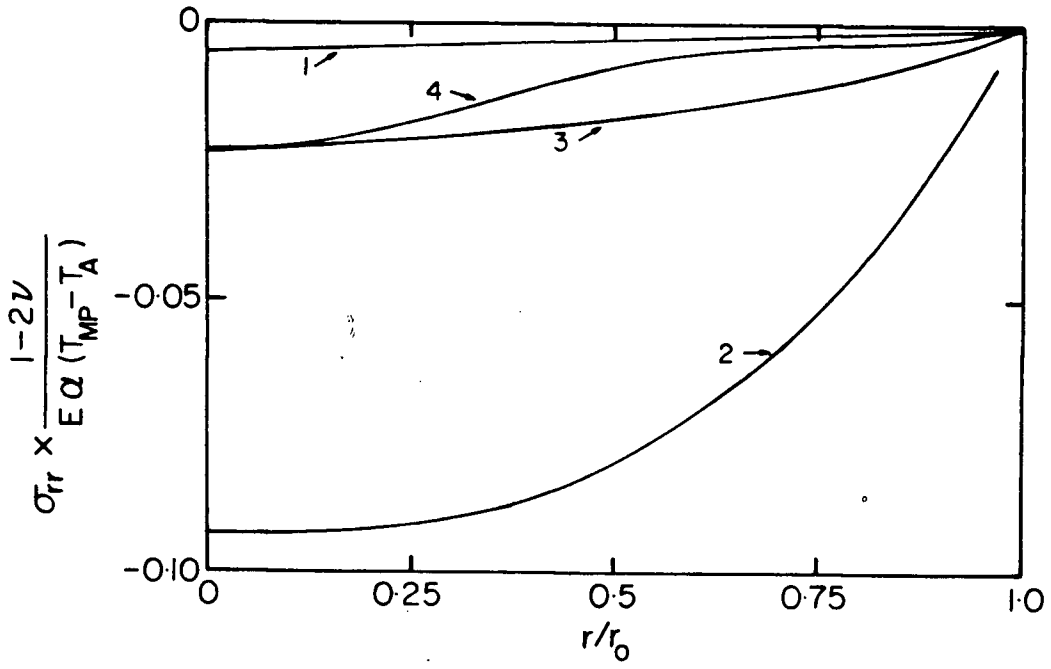

Figure 8.17 Calculated radial stresses as a function of r/r_o for axisymmetric thermal fields (1) Finite element with averaged element temperatures (2) Finite element with nodal temperatures (3) Analytical-plane strain (4) Analytical-axisymmetric.

The difference between the analytical axisymmetric curve and finite element average temperature curve is attributed to the slow convergence of the Fourier series combined with the use of the first order Bessel function I_1 in the analytical solution of the stress field which results in less precise values. Convergence in this series is oscillatory and values were calculated by averaging the last two terms in summations involving about 40 terms. The argument increases linearly with the number of terms and the I_1 Bessel functions diverge very rapidly with these arguments. This effect is not serious when radial temperature fields are used because of the simplicity of the function which is expanded (the unit function), as opposed to a complex z-dependent function which is expanded in the case of an axisymmetric two dimensional temperature field. The inclusion of the I functions was done in order to obtain a more general solution to the isothermal displacement differential equation. Recently solutions for similar equations have been obtained in semi-infinite cylinders including only the J Bessel functions in a less general but better behaved solution[168].

The results in Figure 8.17 also show that for axisymmetric temperature fields the plane strain approximation gives stresses which are more than double the stresses obtained with the finite element method using the axisymmetric approximations. Larger differences were usually observed close to the ends of longer crystal where conditions deviate markedly from plane strain. This result shows that the plane strain approximation is not always good for the analysis of thermally induced stresses. It should be

noted that this result has not been reported in the literature[214-217].

In summary, it has been shown that there is good agreement between the finite element analysis using average element temperatures and the analytical solution with the axisymmetric assumption. The analytical solution with the plane strain assumption does not fit as well due to the restriction of axial movement in this case. It may thus be concluded that the linear finite element analysis gives stresses that are comparable to the axisymmetric approximation and with the plane strain approximation when that condition applies.

8.3 Comparison of Model Predictions with Temperature Measurements

The temperature distribution in a growing crystal calculated from the model is compared to the results of temperature measurements[218] made in a LEC GaAs Melbourn crystal grower. The temperature measurements were made with the array of four thermocouples shown in Figure 8.18. The thermocouples were attached to the seed holder and moved up with the seed as the crystal was grown. Temperatures were recorded for the entire growth period of the crystal, giving the results shown in Figure 8.19.

To calculate the temperature distribution with the model, the thermal diffusivity was taken as 0.04 cm^2/s. The heat transfer coefficients between the crystal and the argon and B_2O_3 were determined from the values given in section 8.1.

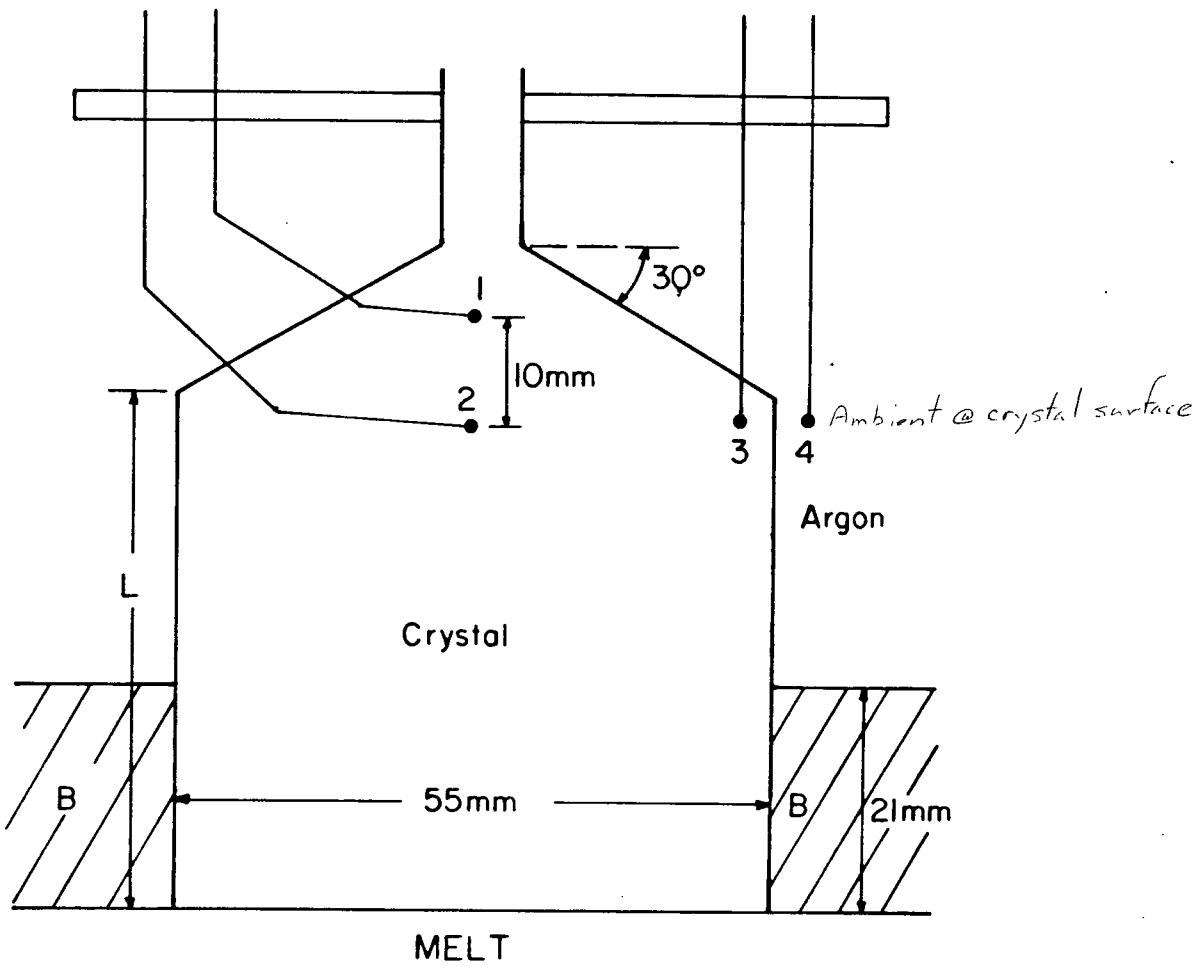

Figure 8.18 Position of thermocouples in GaAs crystal. B = Boric oxide layer, argon pressure 3.04 MPa. Reference 218.

The ambient temperature distribution along the crystal, shown in Figure 8.19 (curve 4), is based on temperature measurements adjacent to a fixed point on the crystal at different times during growth, converting time to distance with the growth velocity. It is assumed that this temperature distribution is time independent.

On the basis of this assumption, the measured ambient temperature is used to determine the heat transfer coefficient at each segment along the surface of the growing crystal. The temperature distribution within the crystal will change with time as the crystal is pulled from the melt.

The calculated and measured temperatures along the crystal axis at four different crystal lengths are shown in Figure 8.20. A comparison of the calculated and measured temperatures is only valid at the point where the calculated temperature coincides with the measured temperature, at points marked A, B, C and D in Figure 8.20 for the four crystal lengths. Agreement between the calculated and measured temperatures at these points is close ; within 15°C. For the short crystal (55.0 mm), the measured and calculated curves effectively coincide, indicating that the measured curve is time independent. For the longer crystals the measured curves are below the calculated curve indicating temperature dependence, i.e. that the temperature at a given point decreases after being measured by the thermocouple as the crystal grows. The difference increases with increasing crystal length.

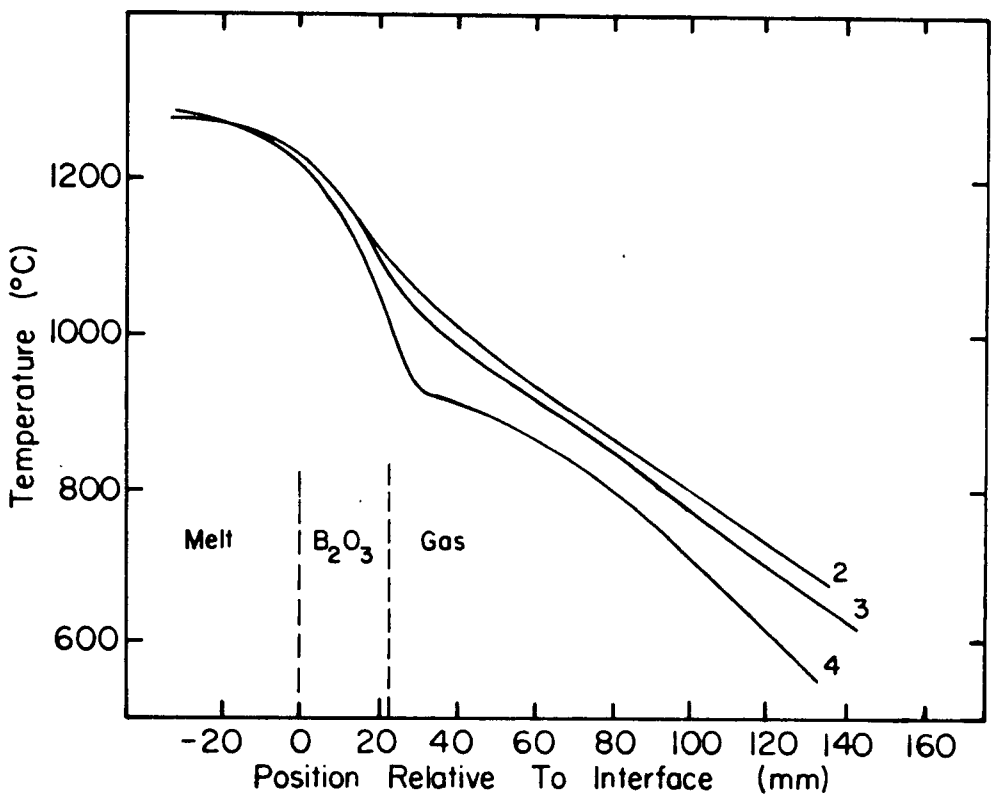

Figure 8.19 Temperatures measured with thermocouples 2, 3 and 4 in Figure 8.18 as a function of the relative position of the thermocouples with the interface. Reference 218.

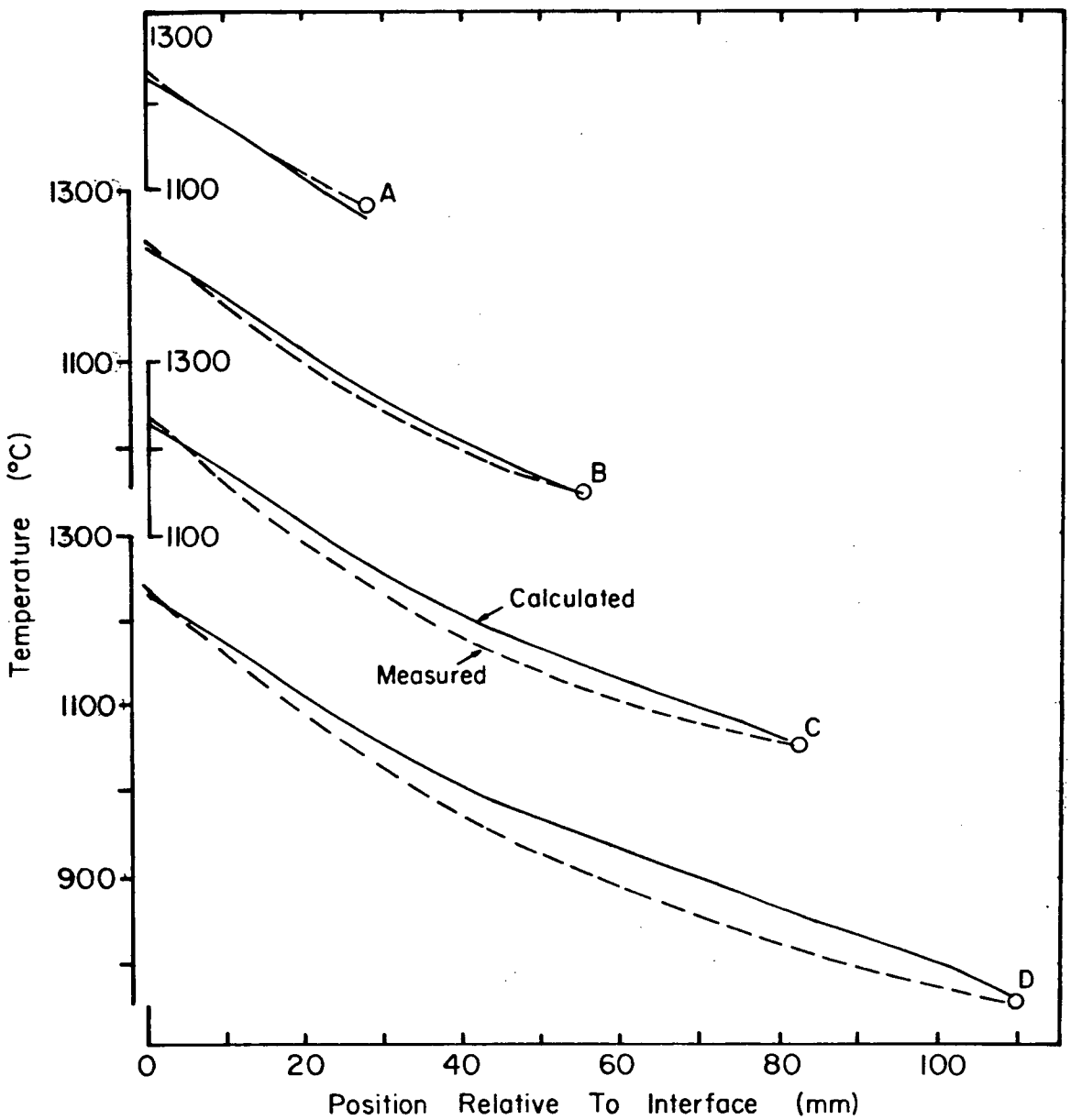

Figure 8.20 Measured and calculated temperatures along the crystal axis at four crystal lengths.

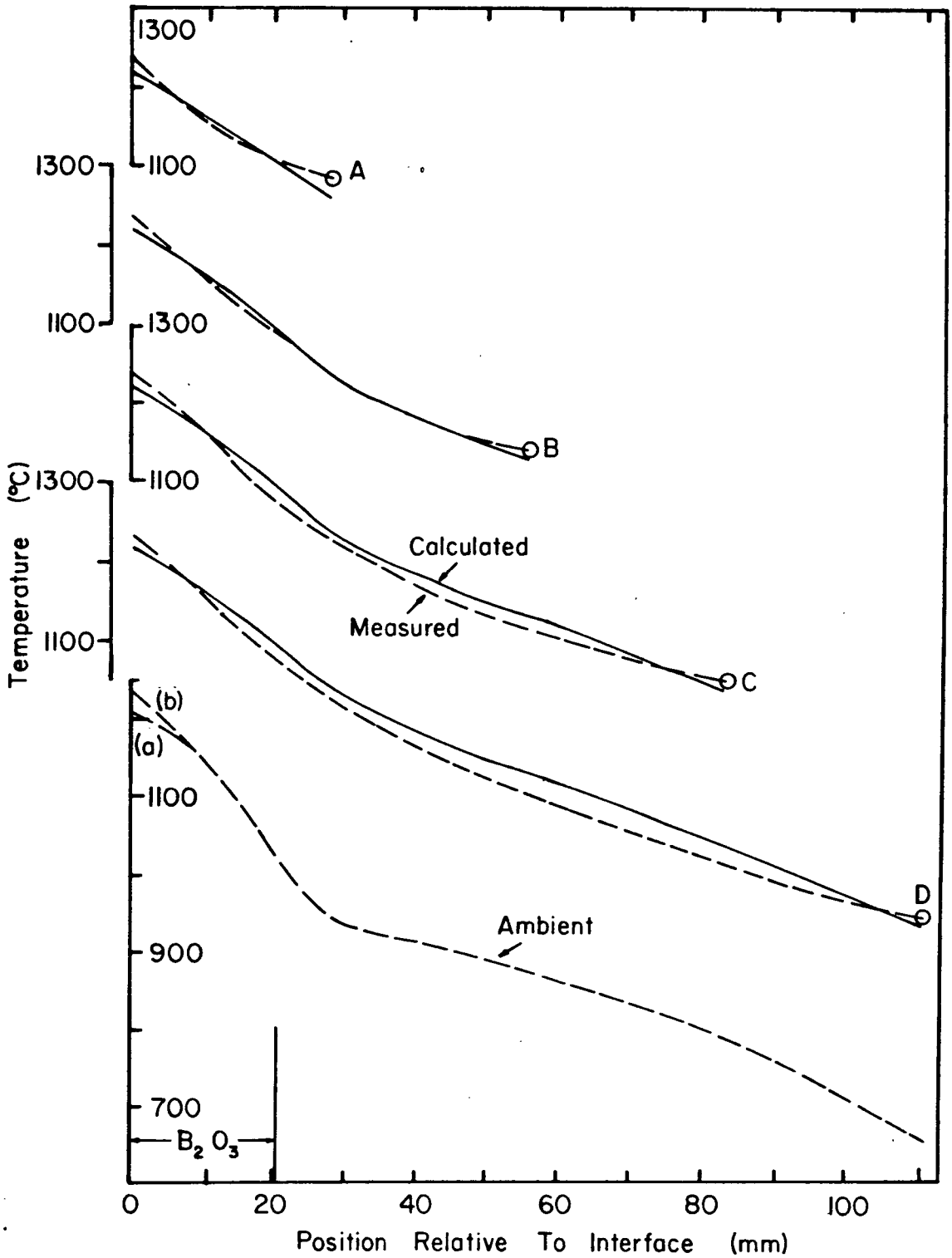

Figure 8.21 Measured and calculated temperatures adjacent to the outside surface of the crystal at four crystal lengths. The measured ambient temperature is also shown.

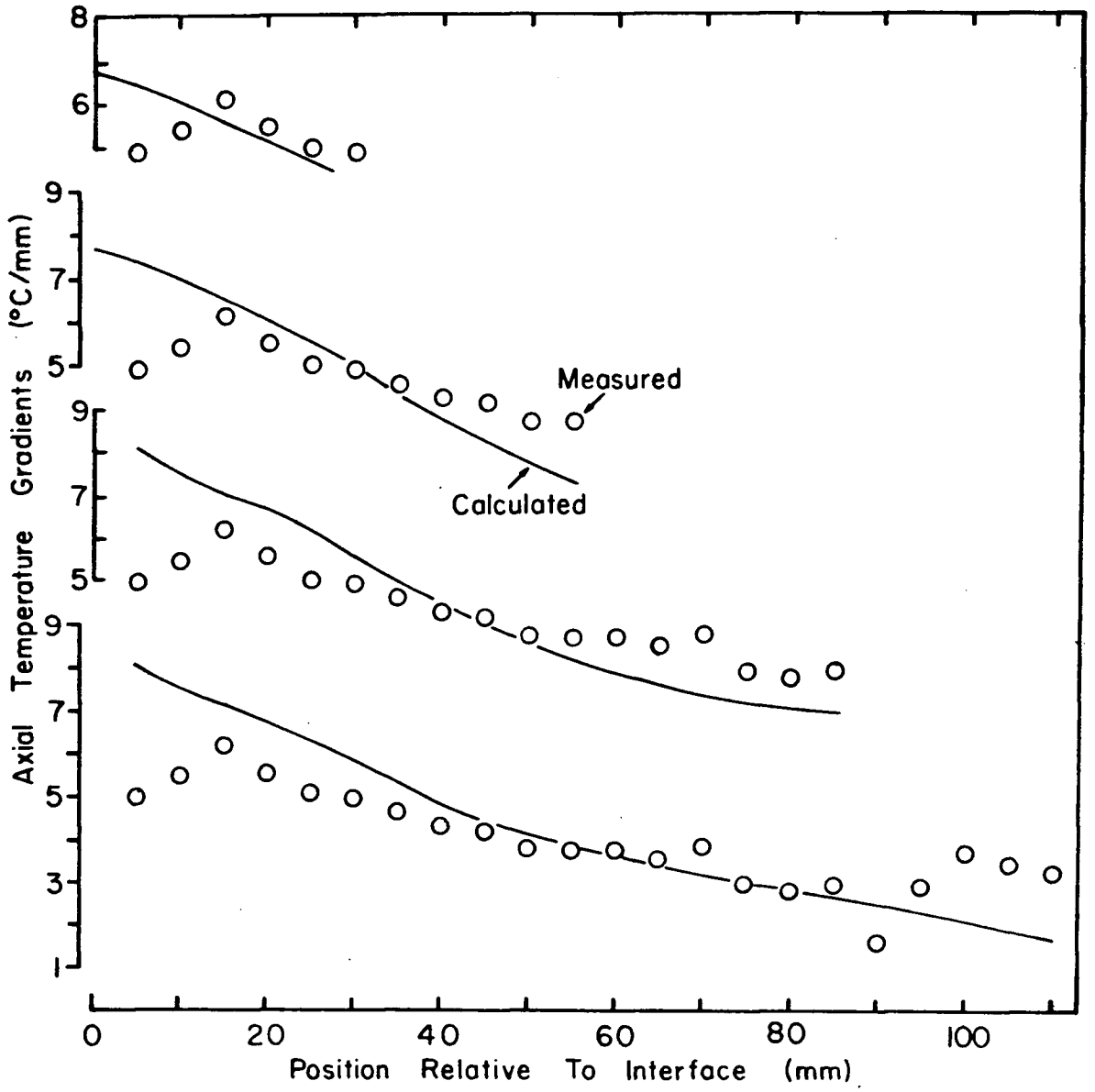

Figure 8.22 Measured and calculated axial temperature gradients along the crystal axis at four crystal lengths.

The temperature distribution near the edge of the crystal, both calculated and measured, for four crystal lengths is shown in Figure 8.21. The ambient temperature distribution is also included in the figure. Note that adjacent to the interface, curve (a) was measured and curve (b) was used as the ambient temperature in the model since the interface is assumed flat and at the freezing temperature. Comparing the calculated and measured values at points A, B, C and D shows there is reasonable agreement between the two values.

The calculated values are lower than the measured values by less than 25°C. As with the axial temperatures the measured values are below the calculated values over most of the crystal, the difference increasing with increasing crystal length.

The axial gradient was also measured during growth by thermocouples 1 and 2 in Figure 8.18. The results are compared to the calculated gradients in Figure 8.22. The measured gradients are significantly below the calculated gradients near the interface. At these points the measured gradients may correspond partly to the melt and partly to the crystal. In addition, the presence of a convex interface, as is shown later in this work, gives lower axial gradients than a flat interface in this region. For longer crystals the measured gradients are about 10 % below the calculated values, the difference increasing with crystal length. At the points where the comparison is valid the measured values are above the calculated values but within the range of the scatter of experimental measurements.

In summary, the valid points of comparison of the calculated and measured temperatures are in good agreement. Accordingly, the temperatures predicted by the model are indicative of the real temperatures in the crystal.

8.4 The Temperature Model for Cooling - Programming and Convergency

To calculate the temperature fields based on the analytical time dependent solutions, a FORTRAN program was written. This program is shown in Appendix XI. The flow chart of this program is shown in Figure 8.23. The value of λ were calculated using cubic interpolation from tables[219], the first six roots were used. The γ-values were obtained from Equation (7.41b) using a Newton - Raphson method to find the roots. The first 30 values were used.

With these six λ values, the radial part of the temperature converged to 98 % of its final value. With 30 γ values the axial part of the temperature converged to 98 % of its final value. The non-dimensional temperature was therefore calculated as 96 % of the exact solution.

A typical temperature field calculated during cooling is shown in Figure 8.24 a. The radius of the crystal is 27.5 mm and the length is 110.0 mm. Due to symmetry, only the right half of the crystal is shown. Close to the interface or tail end the axial temperature gradient changes from positive to negative. Also a high radial gradient is usually observed as opposed to what is observed during growth. In view of this and the fact that

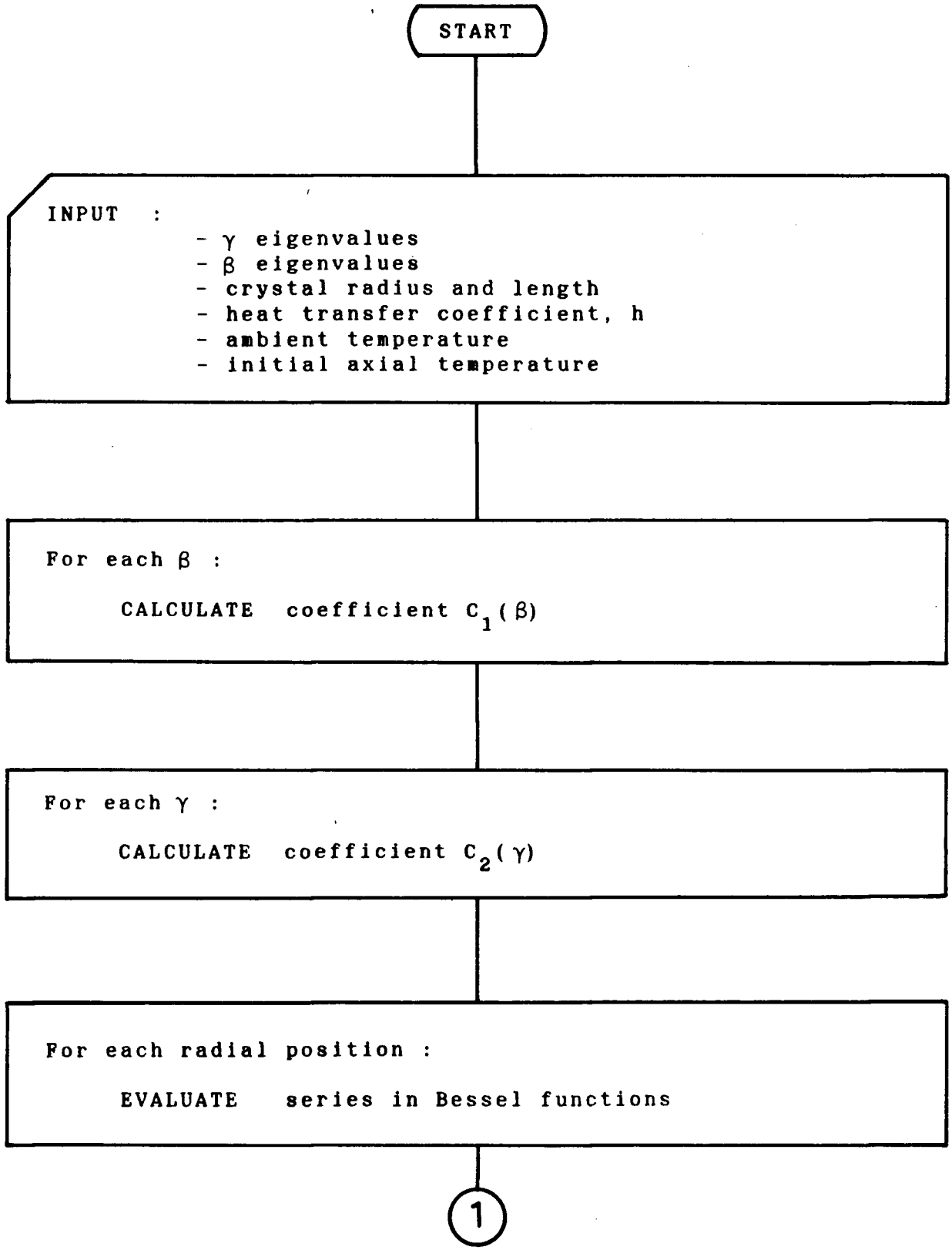
START
INPUT :
- γ eigenvalues
- β eigenvalues
- crystal radius and length
- heat transfer coefficient, h
- ambient temperature
- initial axial temperature
For each β :
CALCULATE coefficient $C_1(\beta)$
For each γ :
CALCULATE coefficient $C_2(\gamma)$
For each radial position :
EVALUATE series in Bessel functions
1

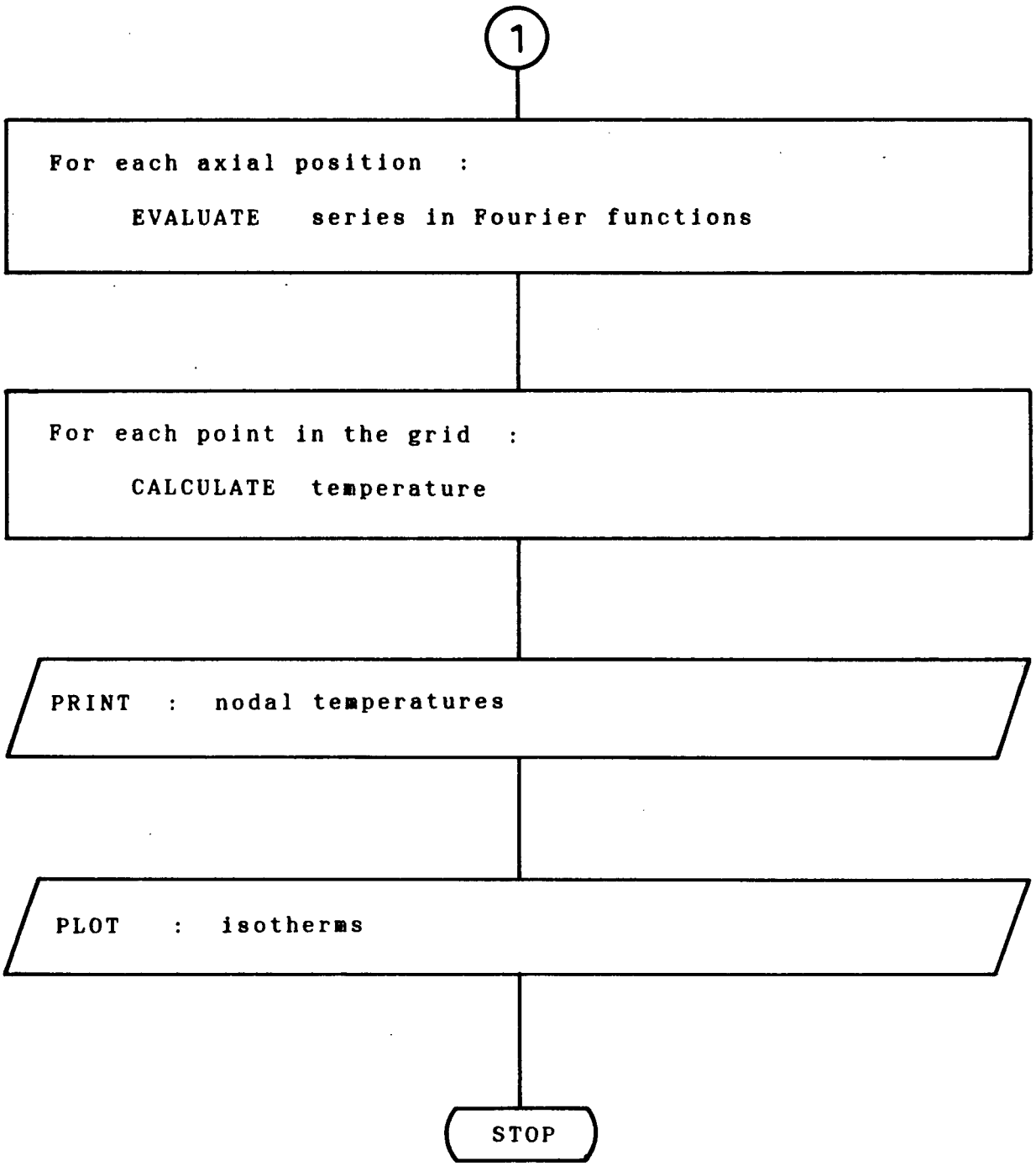

Figure 8.23 Flow chart of the computer program for the numerical evaluation of the analytical temperature fields during cooling of the crystal.

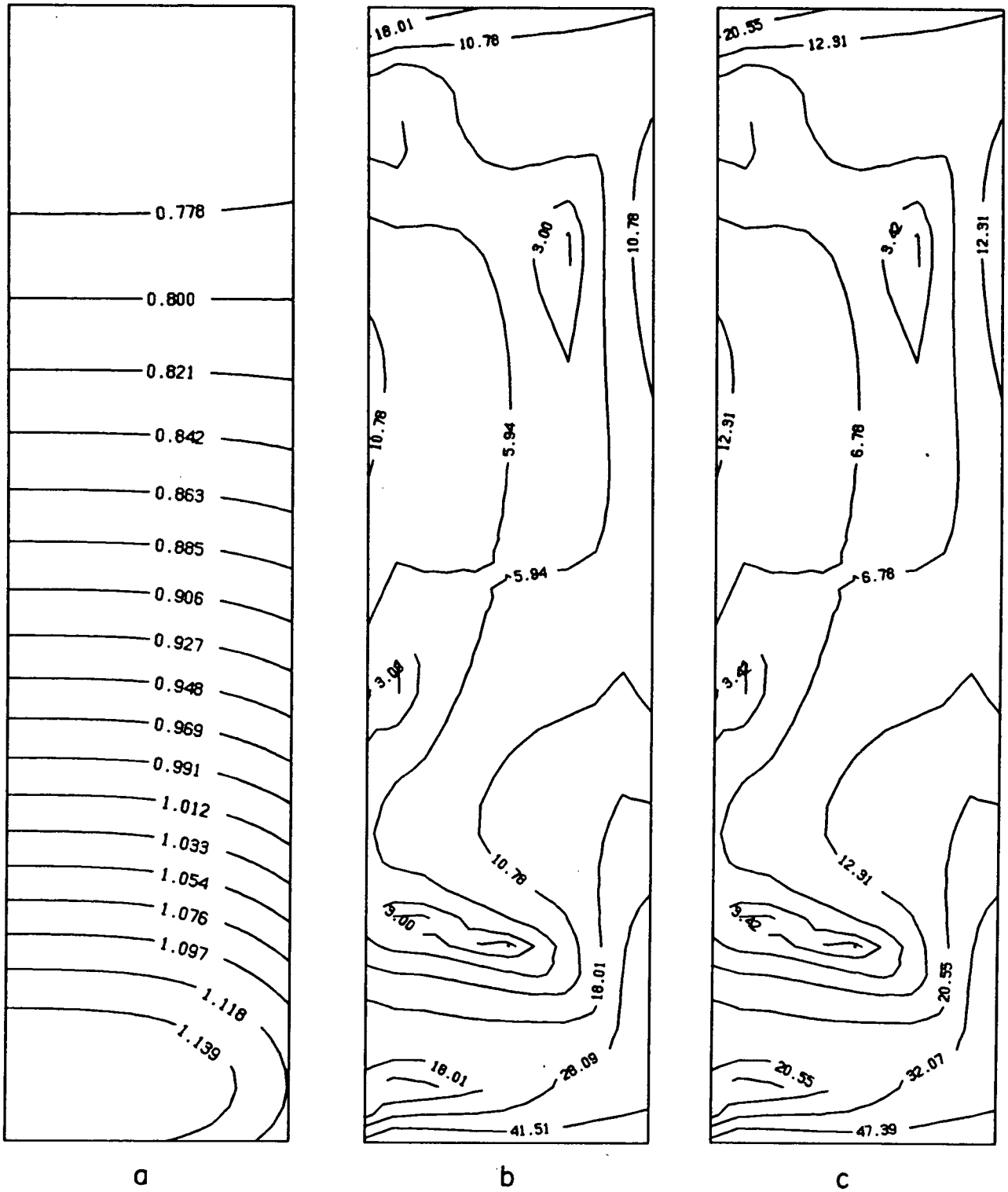

Figure 8.24 (a) Typical temperature field obtained during cooling units are 10^3 °C. (b) and (c) Von Mises stress contours (MPa) for the temperature field given in (a). (b) NN = 451, NE = 800. (c) NN = 1105, NE = 2048.

for the stress calculation average temperatures are used another mesh refinement was performed. This was done to determine if for a given mesh size the calculated stresses were representative. The results are shown in Figure 8.24 b and c. Figure 8.24 b shows the Von Mises stress field induced by the temperature field in part (a) of the figure, calculated using a mesh containing 451 nodes and 800 elements. Figure 8.24 c shows the same stress field obtained employing a mesh of 1105 nodes and 2048 elements. It is seen that exactly the same stress pattern is obtained with stress values which are about 10 % less in the coarse mesh following an expected tendency. The computing effort involved, however increased quadratically with the number of nodes. Accordingly the coarser mesh was selected.

CHAPTER 9

RESULTS AND ANALYSIS

The mathematical model presented in the previous chapters is used to study the effect of the different variables in generating dislocations during growth and cooling to ambient temperature. The variables related to crystal geometry during growth include the following :

1. Cone angle (CA), given by the angle between the cone surface and the horizontal
2. Crystal length (CL), given by the distance between the solid-liquid interface and the start of the cone
3. Crystal radius (R),
4. Interface shape

The variables associated with the growth process include the following :

5. Growth velocity (V)
6. Boron oxide thickness (B)
7. Thermal gradients (argon, AG and boron oxide, BG)
8. Gas pressure (GP)
9. Gas composition

The variables associated with the cooling process include the following :

10. The nature of the media in which the crystal is immersed. This may be boron oxide or argon gas
11. Temperature of the cooling media
12. Thermal conditions in the crystal at the start of cooling.

The effect of the above variables on the calculated stress fields and dislocation density are now considered.

9.1 Cone Angle

Crystal and Growth Parameters Assumed
R, 20 mm ; CL, 10 mm ; B, 10 mm ; BG, 100 ^{o}C/cm ;
AP, 30 atm ; AG, 50°C/cm.

The cone angles considered are 7.1, 30, 45, 54.7 and 65 degrees. The angle 54.7^{o} corresponds to the cone surface coincident with the (111) plane.

The calculated Von Mises stress distribution on a vertical plane for the five cone angles considered is shown in Figure 9.1(a-e). The maximum Von Mises Stress (MVMS) levels occur at the shoulder where the cone reaches the full radius of the crystal. High stress levels occur along both the cone surface and the crystal axis. The lowest Von Mises stresses (LVMS) are below the seed.

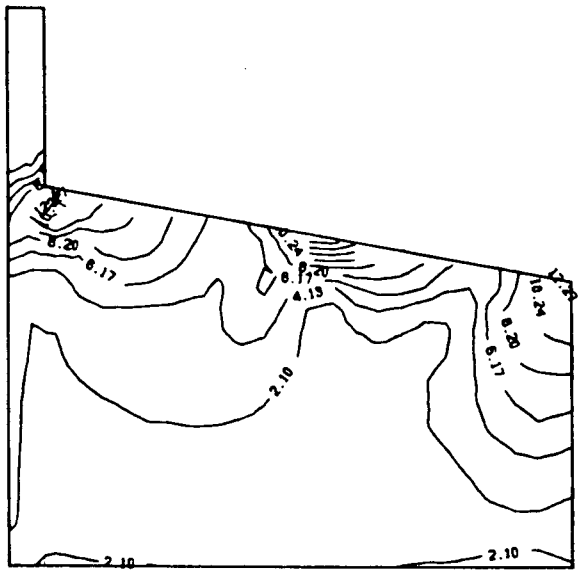
8.20
8.17
4.13
10.24
8.20
6.17
2.10
2.10
2.10

a

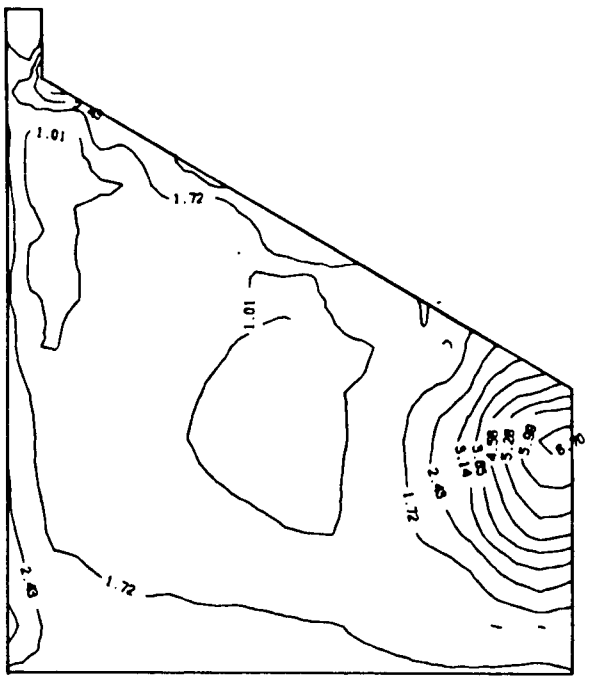
1.01
1.72
1.01
2.49
1.72
1.72

b

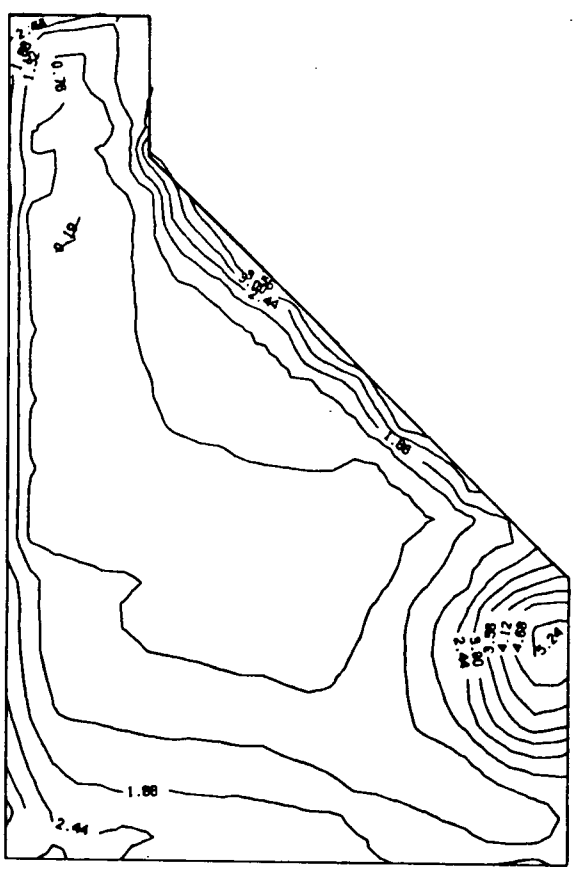
1.88
2.44
1.88
2.44

c

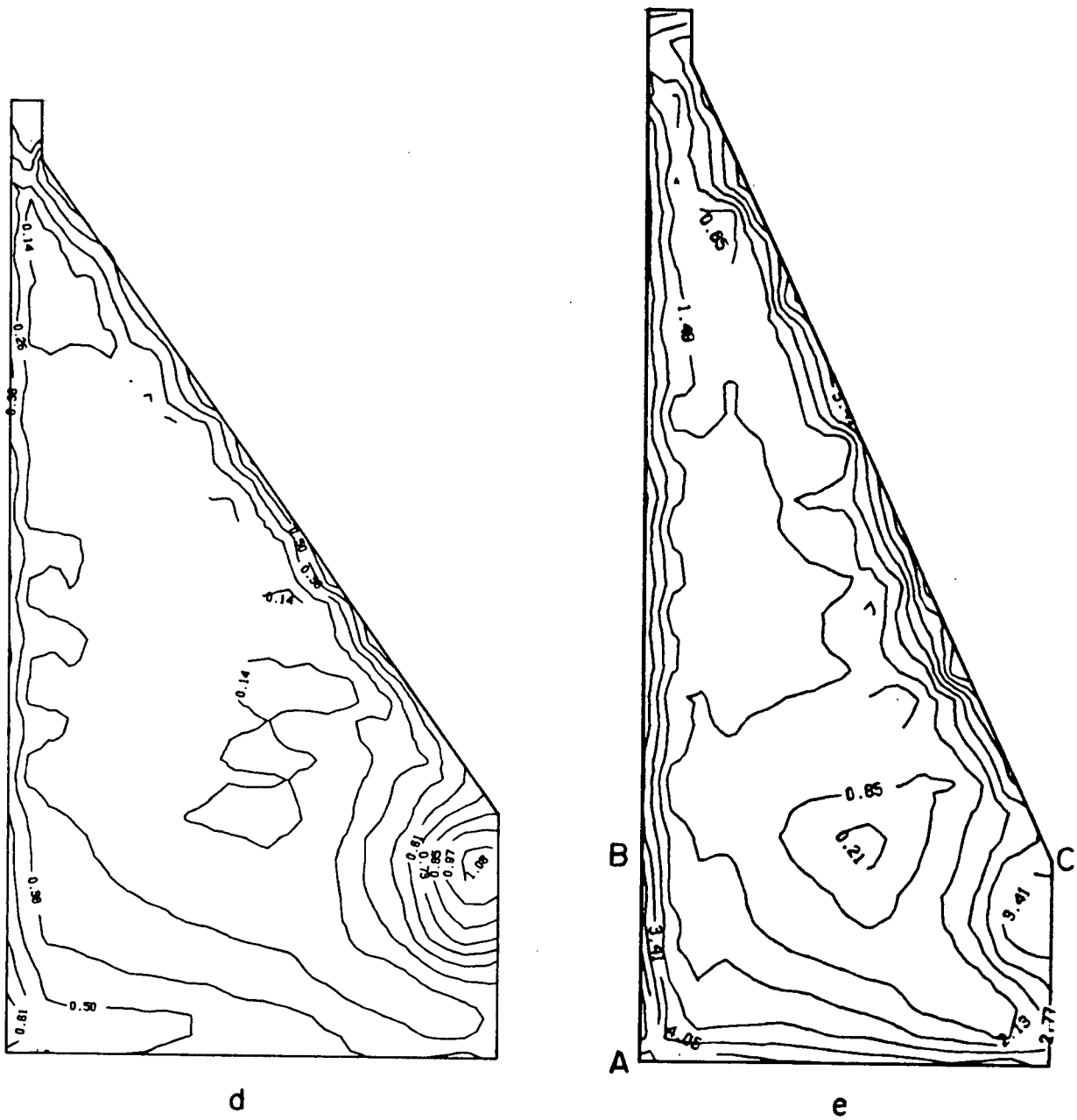

Figure 9.1 Von Mises Stress contours (MPa) in vertical planes for five cone angles. (a) 7.1^{o}, (b) 30°, (c) 45°, (d) 54.7^{o}, (e) 65°. Cone surface in (d) coincides with a (111) plane. Crystal radius, 20 mm ; crystal length, 10 mm ; B_2O_3 thickness, 10 mm ; B_2O_3 gradient, $100^{o}C/cm$; argon pressure, 30 atm. ; argon gradient, $50^{o}C/cm$.

Table 9.1 Effect of Cone Angle on Thermal and Stress Fields

Cone Angle (^{o})	Thermal Gradients, ^{o}C/cm		MVMS MPa	AMRSS MPa *	AMRSS/MVMS
	Radial	Axial			
7.1	6.7	55	18.4	8.7	0.47
30.	4.1	50	6.7	3.1	0.46
45.	2.7	54	5.2	2.5	0.48
54.7	3.2	56	1.1	2.6	2.4
65.	2.5	55	5.0	2.3	0.45

The largest MVMS, as shown in Table 9.1, occurs in the crystal with the sharpest cone angle of 7.1^o. The MVMS drops appreciably when the cone angle is increased from 7.1^o to 30°, and decreases further by a smaller amount between 30° and 45°. The MVMS reaches a minimum for a cone angle of 57.4^o then increases between 52.4^o and 65°. Similar behaviour is observed when the LVMS is considered as a function of cone angle.

In order to account for the effect of the cone angle on the VMS two sources of thermal stress are considered namely the temperature fields and the geometrical constraints. The temperature field is the origin of thermal stresses. The stress level is roughly determined by the thermal gradients. Generally, large radial thermal gradients combined with large axial gradients produce large stresses in cylinders. If the axisymmetric body does not have constant cross-section, additional stresses may develop due to geometrical constraints.

For the crystal geometry considered here temperature gradients are calculated as follows. The axial gradients are calculated from the temperature differences between the interface and a point in the crystal axis 10 mm above, labelled A and B respectively in Figure 9.1(e) . The radial gradients are calculated from the temperature differences between point B and C which are also shown in Figure 9.1(e). The results are given in Table 9.1.

From Table 9.1 the axial gradients are observed to be relatively insensitive to the cone angle, varying by about 3 % about the mean gradient of 53°C/cm. On the other hand the radial gradients vary appreciably about the mean gradient of 4.2^{o}C/cm. The gradient drops sharply from 6.7^{o}C/cm between 7.1^{o} and 30°, drops further at 45°, rises at 54.7^{o} and then drops again at 65°.

Considering the MVMS values in Table 9.1, the drop in MVMS between 7.1^{o} and 30° can be accounted for by the change in radial gradient. The minimum MVMS for 54.7^{o} is attributed to the geometrical constraints arising from the variations in radius of the crystal at the cone, as well as the radial gradient. For a zero cone angle, conditions similar to plain stress will prevail at the cone surface, with zero axial and shear components of the axisymmetric stress tensor. Under such conditions the VMS will have maximum values because there are only two large non-zero diagonal stress components. For the same thermal conditions, when the cone is not zero a similar stress level will have a different distribution of stress components giving a third non-zero

principal stress. The difference between the principal stress components decreases as the cone angle increases, giving the observed VMS dependence with cone angle. For cone angles larger than 54.7^{o} another factor should be included in the analysis. Under these conditions the crystals are effectively larger than the low cone angle crystals. Therefore the constraints are such that conditions closer to those of plane strain apply. In such cases it was shown in the last chapter that stresses are larger than under the more general axisymmetric conditions.

From the above discussion, at low cone angles the VMS is expected to decrease with increasing cone angle. At high cone angles, however, the VMS is expected to increase with increasing cone angle. Therefore a minimum in the VMS should exist at intermediate cone angles. In this case that minimum is observed for a cone angle of 54.7^{o}.

The maximum component of the resolved shear stress (MRSS) in vertical (010) planes for the five cone angles considered is shown in Figure 9.2(a-e). The MRSS stress distributions are similar to the VMS distributions. The dependence of the MRSS on the cone angle is determined by considering the absolute maximum MRSS (AMRSS) developed in the crystal which is representative of the stress level in the whole crystal. The AMRSS occurs at the shoulder as is shown in the VMS distributions. The AMRSS for the angles considered is listed in Table 9.1 column 5. For low cone angles the AMRSS decreases rapidly similar to that shown for the VMS. For cone angles of 45° and larger the AMRSS remains

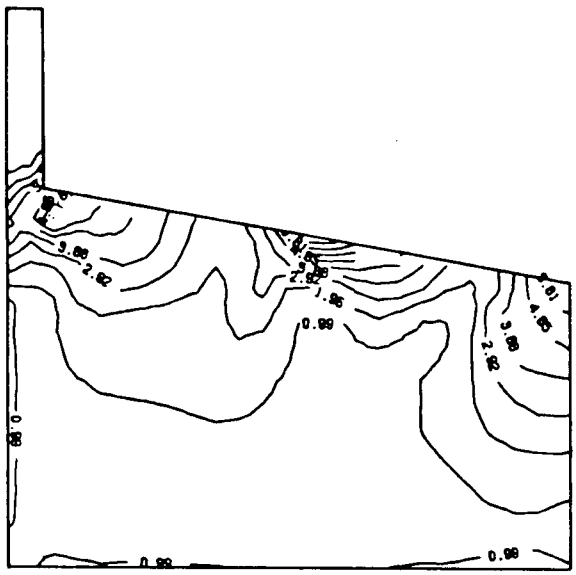

a

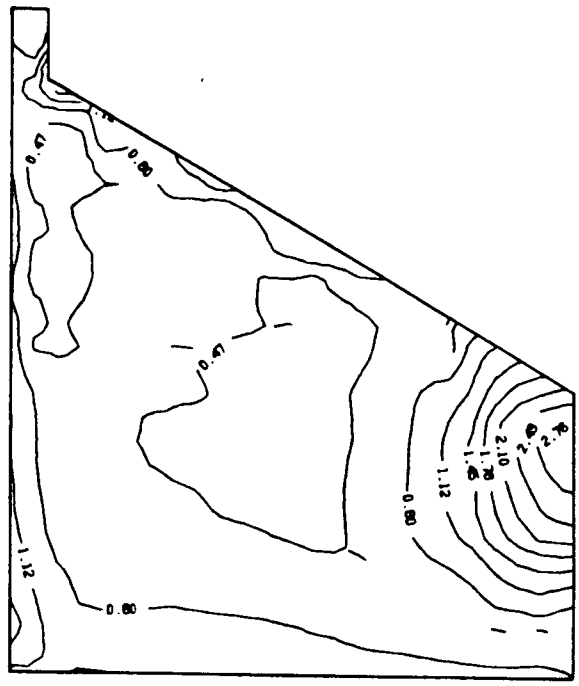

b

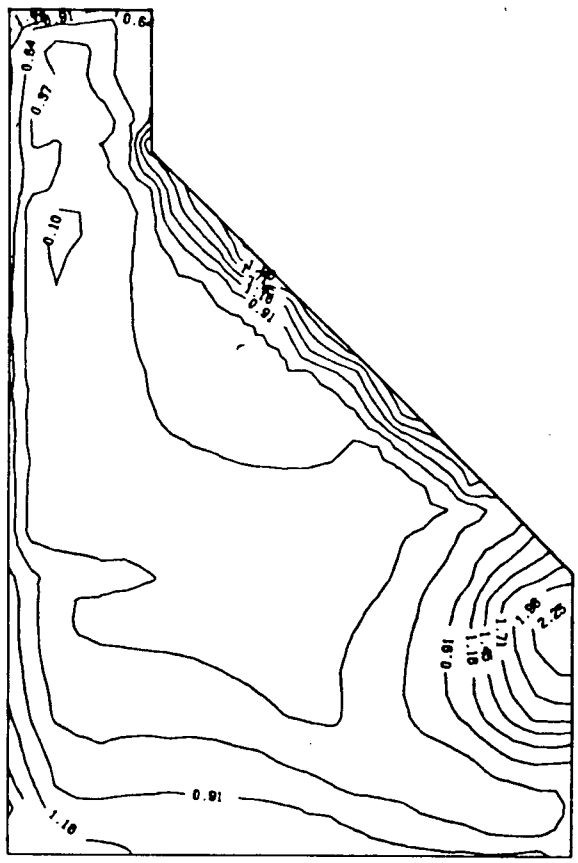

c

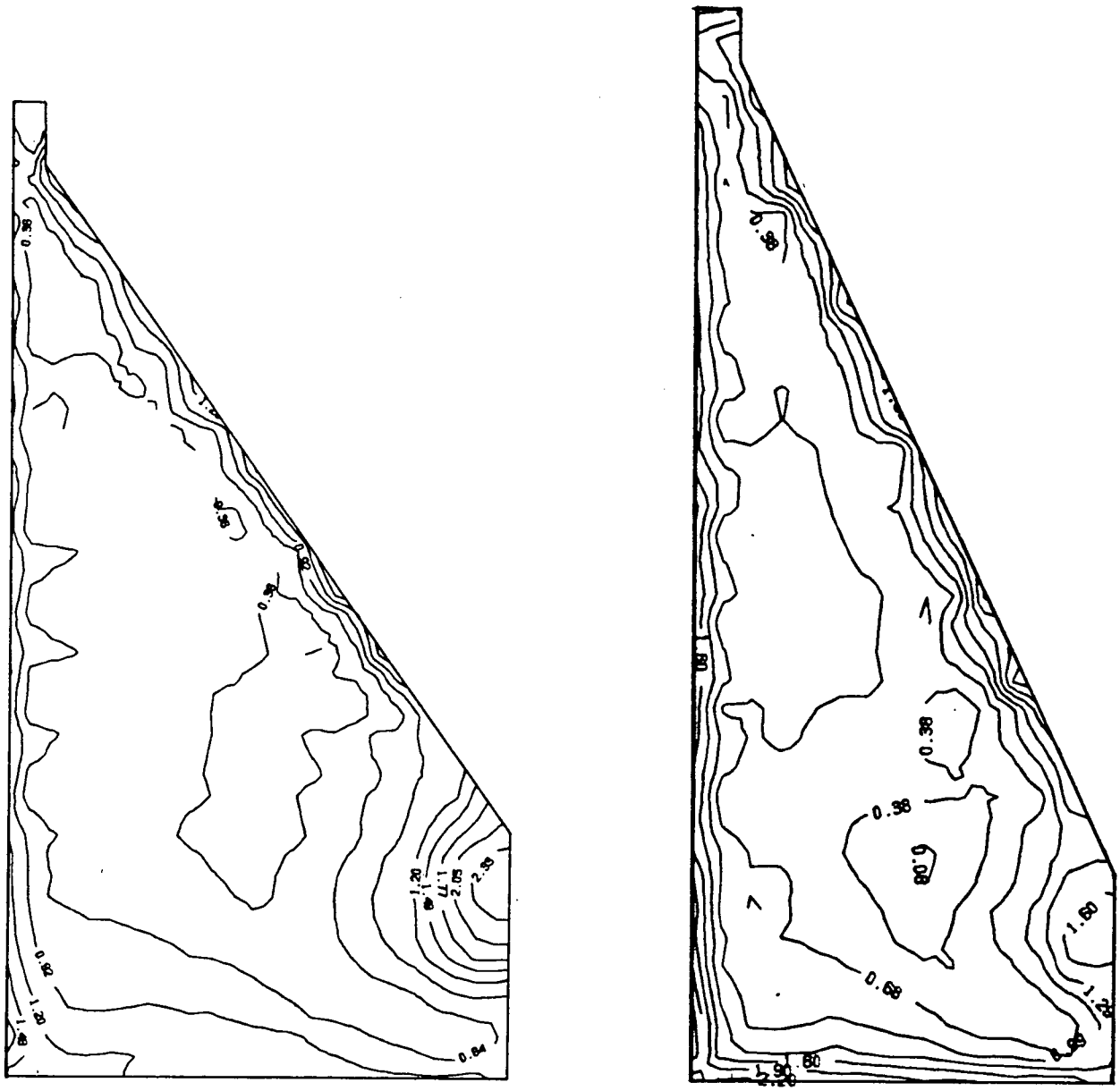

Figure 9.2 Maximum resolved shear stress (MRSS) contours in MPa, in vertical (010) planes for five cone angles. (a) 7.1^{o}, (b) 30°, (c) 45°, (d) 54.7^{o}, (e) 65°. Cone surface in (d) coincides with a (111) plane. Conditions are the same as in Figure 9.1 .

essentially constant. The large drop in the AMRSS at low cone angles supports the conclusion that the stresses are dependent entirely on the thermal field changes rather than on geometrical constraints. At large cone angles, the MRSS differs from the VMS. The difference can be seen in Table 9.1 column 6 where the AMRSS/MVMS is listed. For all cone angles except 54.7^{o} the AMRSS is less than half the MVMS. At 54.7^{o} a singularity occurs such that the AMRSS is more than double the MVMS. The singularity at $54:7^{o}$ cone angle is attributed to the model assumption of no traction at the crystal surface and the difference in the definition of the VMS and RSS components.

The condition of no traction requires the projection of the stress tensor on a direction normal to the crystal surface to be zero. In this case, for a given stress level, the stress components must accommodate in a direction parallel to the crystal surface. For a cone angle presenting a surface parallel to a (111) plane, the stress components lie on the (111) plane. In this case the RSS components are expected to be at maxima since by definition they are projections onto these planes in the $<1\bar{1}0>$ directions. The VMS, on the other hand, is an indication of the shear stress in isotropic materials and therefore does not include the crystallographic properties of the material.

These results show the advantage of using the MRSS over the VMS for the analysis of stresses generating dislocations. From the VMS results it may be mistakenly concluded that a 54.7^{o} cone angle is beneficial in order to reduce dislocation generation. A

different conclusion can be obtained using the RSS which is the stress generating dislocations by glide. The results using the MRSS show that there is no such beneficial effect using a 54.7^{o} cone angle. On the contrary, if growth conditions are such that stress levels given by the VMS are changed, the effect on dislocation densities is double at this angle.

The present calculations differ significantly from the calculations reported by Jordan et al.[137]. In the present case the MRSS is used, whereas Jordan et al. use the total resolved shear stress (TRSS) which is the sum of the twelve RSS values. For the 45° cone angle the TRSS distribution shown in Figure 9.3 is similar to the MRSS distribution shown in Figure 9.2(c), but the stress levels of the TRSS are seven times larger than the MRSS and three times larger than the VMS levels. Adding the components to make the TRSS is inconsistent with the concept of a vectorial or tensorial quantity since the magnitude cannot be calculated by a linear addition of components. Moreover the TRSS can be indefinitely increased by considering an unlimited number of secondary slip systems which is also inconsistent.

The effective stress associated with dislocation generation and movement can be determined by substracting from the MRSS the critical resolved shear stress for yield or the value reported for dislocation generation. This is done in Figure 9.4 in which (a) the yield stress is substracted from the MRSS [CRSS (yield)], (b) the CRSS for dislocation generation given by Milvidskii and Bochkareev[150,163] is substracted [CRSS (MB)] and (c) the CRSS

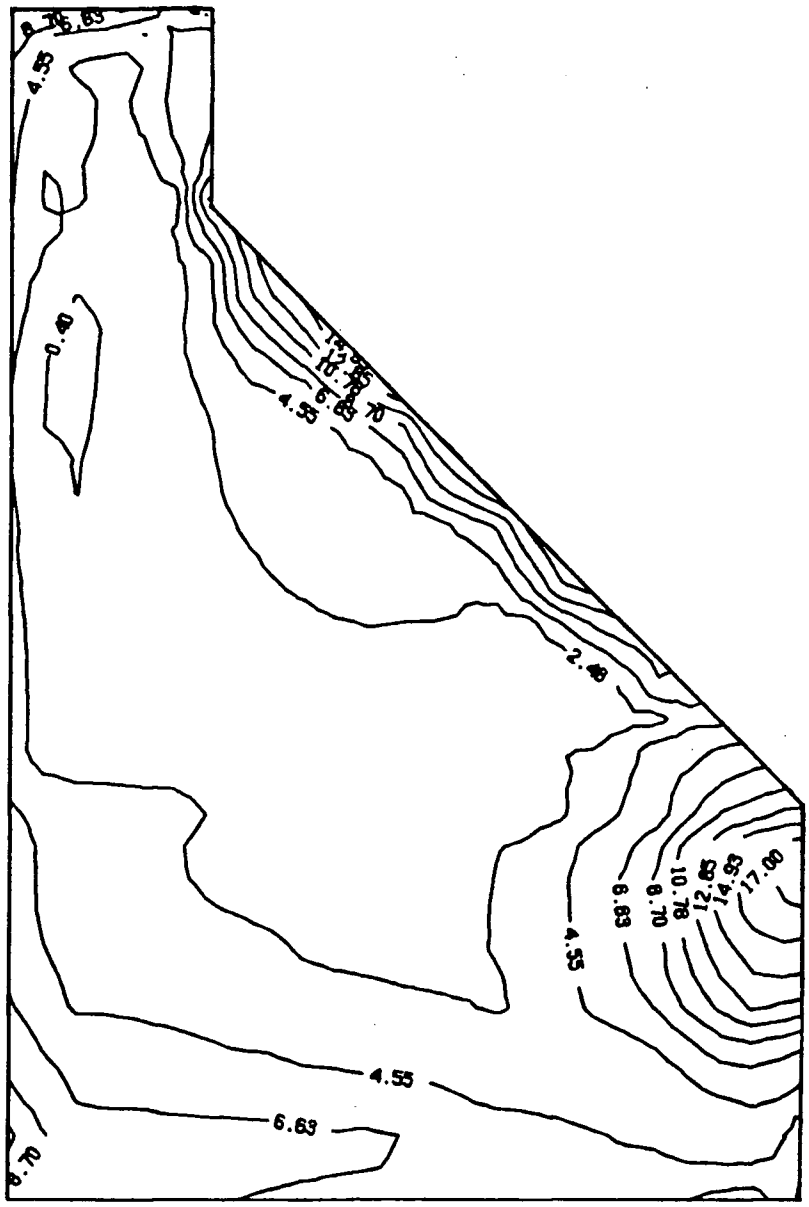

Figure 9.3 Total resolved shear stress (TRSS) contours in MPa for the 45° cone angle crystal. Compare the large stress levels of the TRSS with the stress levels for same crystal shown in Figure 9.1(c) for the VMS and Figure 9.2(c) for the MRSS.

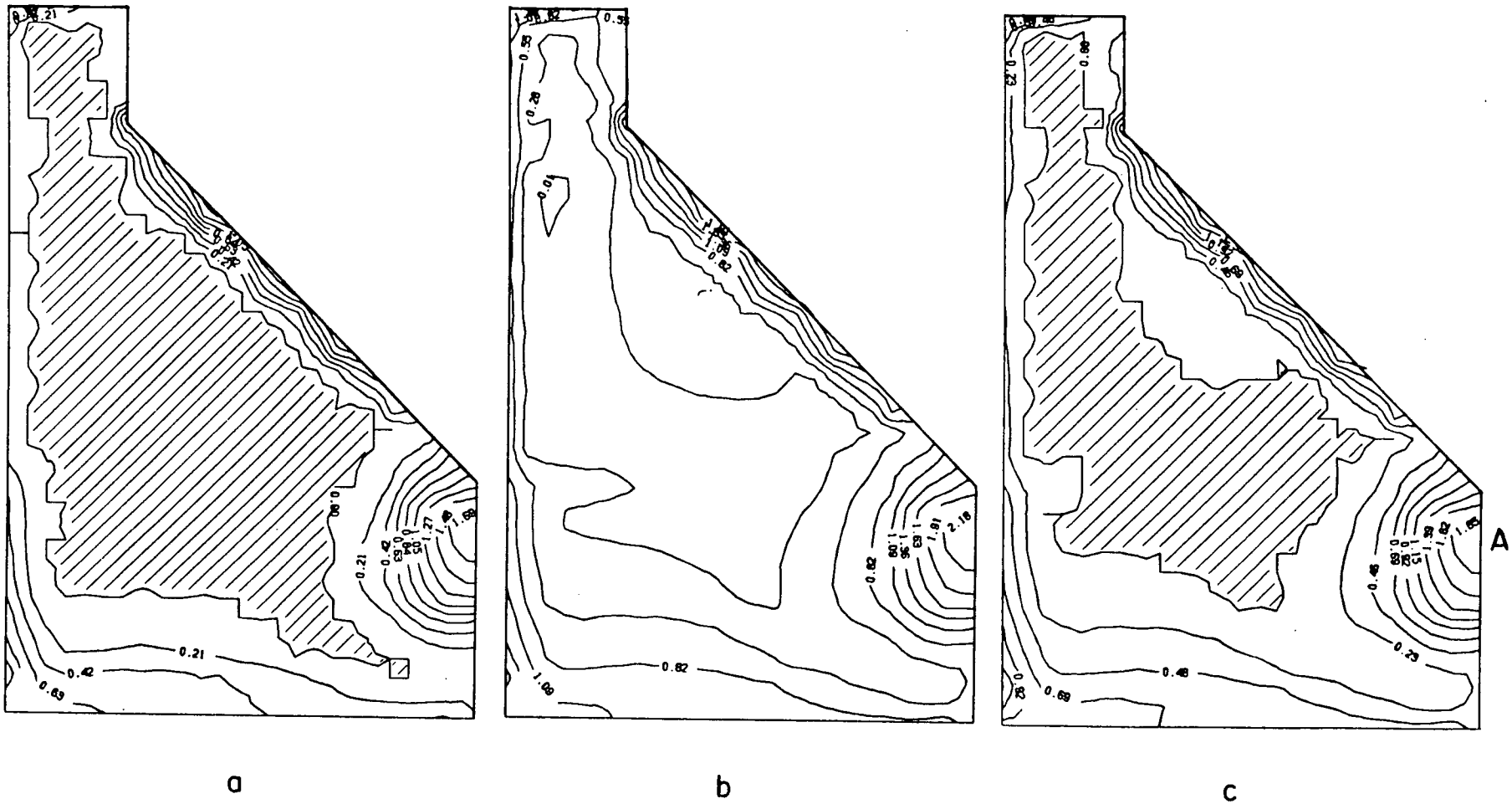

Figure 9.4 Contours of the MRSS (MPa) in excess of : (a) CRSS (yield) ; (b) CRSS (MB) ; (c) CRSS (MBTe). Shaded regions indicate areas in which the MRSS is less than the CRSS.

for Te-doped crystals is substracted [CRSS (MBTe)]. The shaded areas in the figures indicate where the effective stress is zero. It can be seen that the MRSS is less than the yield stress in most of the crystal except in the centre and near the surface. The largest stresses occur in a region below the shoulder at A. The MRSS is always greater than the CRSS (MB) as shown in (b). Doping with Te in (c) gives regions in the crystal where the MRSS does not exceed the CRSS (MBTe) comparable to (a).

The specific directions and planes associated with the maximum resolved shear stresses in the crystal are shown in Figure 9.5.

Plots of stress distribution for other cone angles are given in Appendix XIII. These plots show similar patterns to that shown in Figure 9.4 with the exception of the crystal with a cone angle of 7.1^{o} (Figure 9.6(a-c)).

9.1.1 Effect of Cone Angle on Stress Symmetry

The effect of cone angle on the MRSS distribution on planes perpendicular to the growth direction is shown in Figure 9.7(a-e). The planes in (a-d) are 7.5 mm from the interface, and the plane in (e) is 8 mm from the interface. The vertical direction in the figures is [010] and the horizontal direction [100]. In Figure 9.7(a), for the smallest cone angle (7.1^{o}), the stress distribution is complex with low stresses at the centre followed by a ring with higher stresses which exhibits four-fold symmetry.

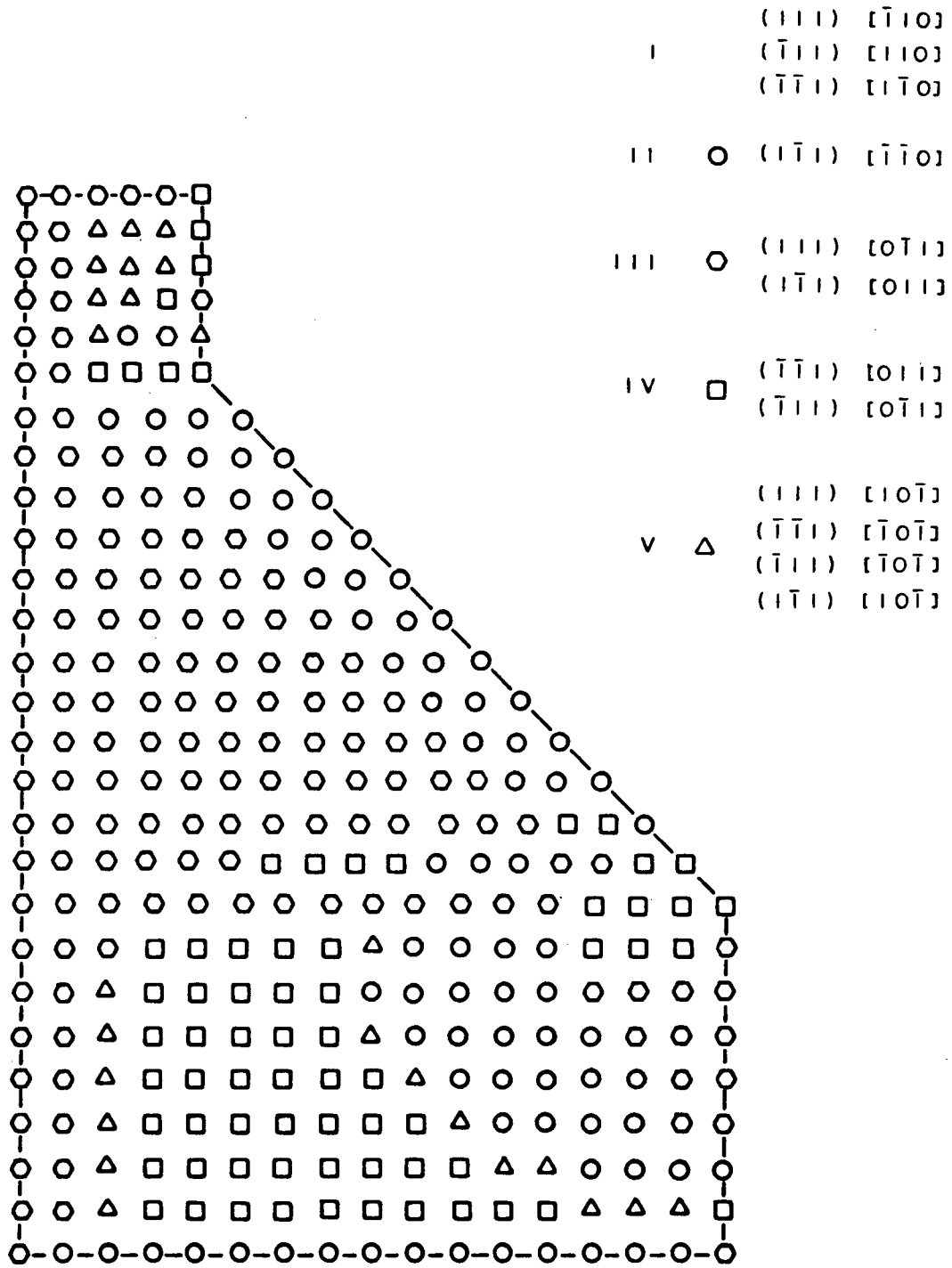

Figure 9.5 Slip mode distribution in the (010) plane for the 45° cone angle crystal corresponding to the MRSS distribution shown in Figure 9.2(c).

Midway between the centre and the edge of the wafer there is a ring with minimum stresses which exhibits circular symmetry. At the edge of the wafer the stresses increase to a maximum value. The stress at the edge is five times larger than the stress at the centre. This complex pattern is consistent with what is observed in Figure 9.6(a) at 7.5 mm from the interface. The ring at the center with higher stresses is due to the irregular contours in the upper half of the crystal, at A in Figure 9.6(a).

For higher cone angles the stress distribution is simpler. The crystals with 30° and 45° cones shown in Figure 9.7(b) and (c), exhibit almost circular symmetry with low stresses in the central area which includes half the total surface area. Outside this region the stress rapidly increases towards the edge of the wafer. For both cone angles the stresses at the edge are about five times larger than at the centre.

For larger cone angles a region of higher stresses starts to build up at the central region, as shown in Figure 9.7(d) and (e), producing the characteristic W-shaped stress distribution across the diameter. For the largest cone angle (65°) the stresses at the centre are three times larger than the minimal stresses at the mid radius position. At the edge the stresses are about eight times larger than the minimum values. It is shown later that the qualitative characteristics of symmetry presented here are general. This is because the symmetry patterns of the stress fields are independent of the thermal gradients, providing

the temperature profile remains linear and the growth conditions (radius, boron oxide thickness, etc.) remain unchanged.

The density and distribution of dislocations in the crystal is related to the local excess stress above the critical resolved shear stress (MRSS-CRSS). When the CRSS (Yield) is taken as the CRSS, the residual stress depends on the cone angle. For the smallest cone angle the MRSS is always larger than the CRSS (Yield) and the symmetry is very similar to the symmetry of the MRSS as shown in Figure 9.6(a). For larger cone angles the MRSS in excess of the CRSS (Yield) is greater than zero in the central and peripheral regions in the wafer. This is shown in Figure 9.8 for the 65° cone angle. Similar results are obtained for the other cone angles.

The stress distributions on cross-sections 2.5 mm from the interface are shown for cone angles 7.1^{o} (Figure 9.9(a-b) and 45° (Figure 9.9(c)). In Figure 9.9(a) the MRSS distribution exhibits a W shape across the diameter and has eight-fold symmetry in the centre. The MRSS-CRSS (Yield) (Figure 9.9(b)) in the central region is below zero so that no dislocations or symmetry patterns will be evident. As the cone angle increases the eight-fold symmetry in the centre is replaced by four-fold symmetry as shown in Figure 9.9(c) for a 45° cone angle. In this case the dislocation symmetry will be evident. It can also be observed in this figure that the centre has stress levels three times larger than the edge. The stress distribution along the radius depends on the direction. In the [110] directions the stress starts to

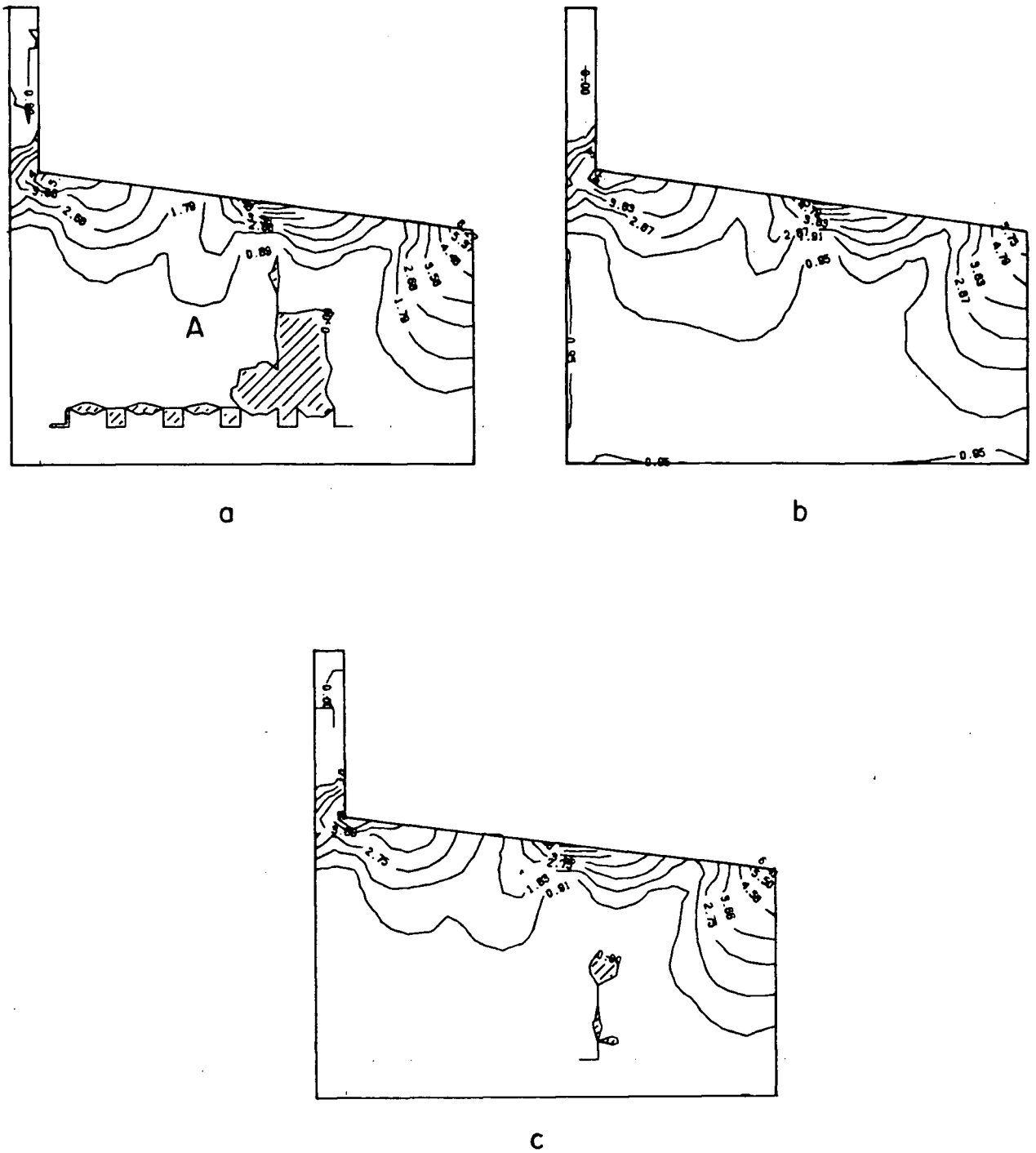

Figure 9.6 Contours in MPa of the MRSS in excess of (a) CRSS (Yield) ; (b) CRSS (MB) and (c) CRSS (MBTe). In most of the crystal the MRSS is larger than the critical values. The bump shaped contours (A) give complex stress distributions in perpendicular cross-sections.

[010]

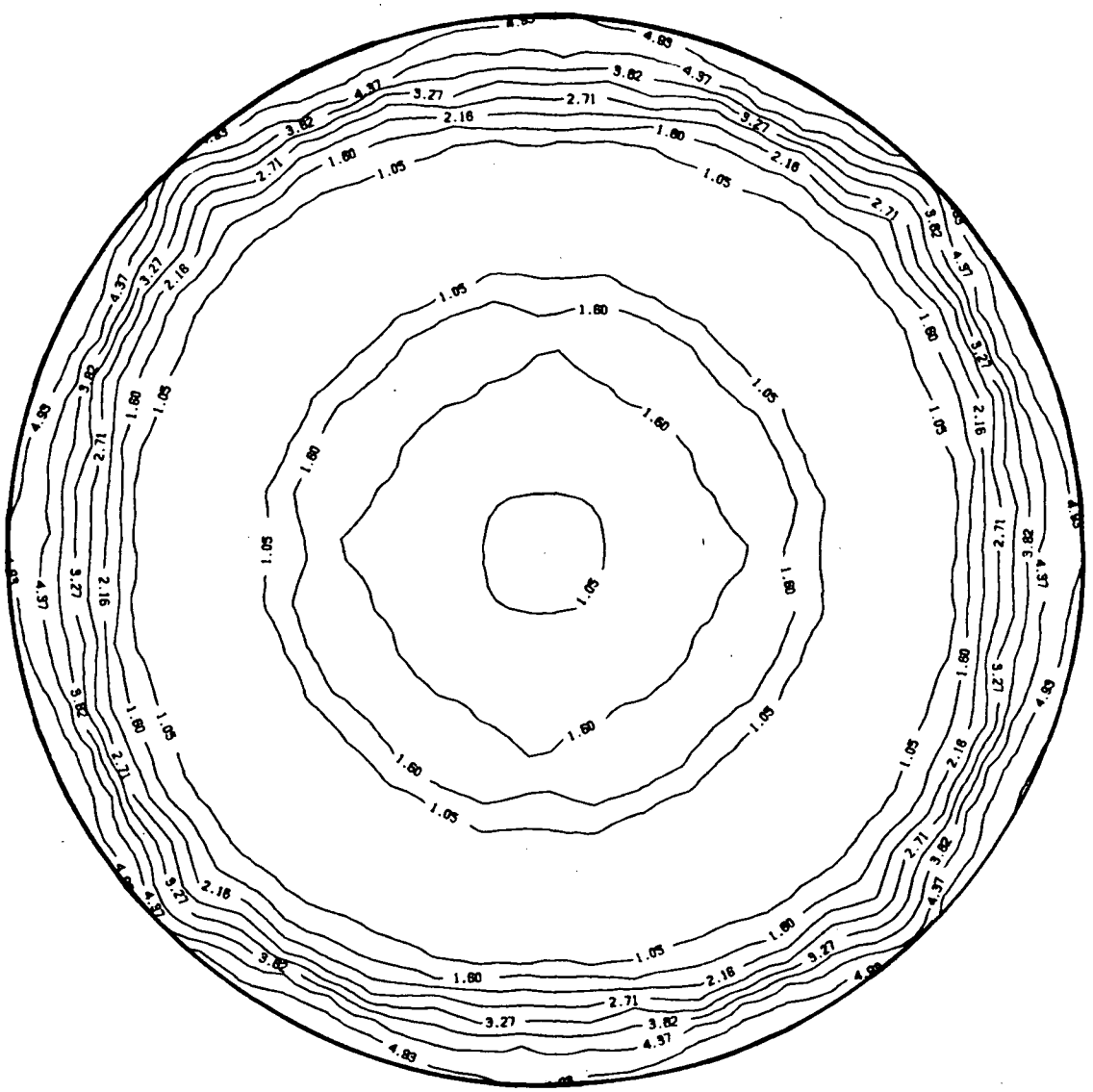

[100]

a

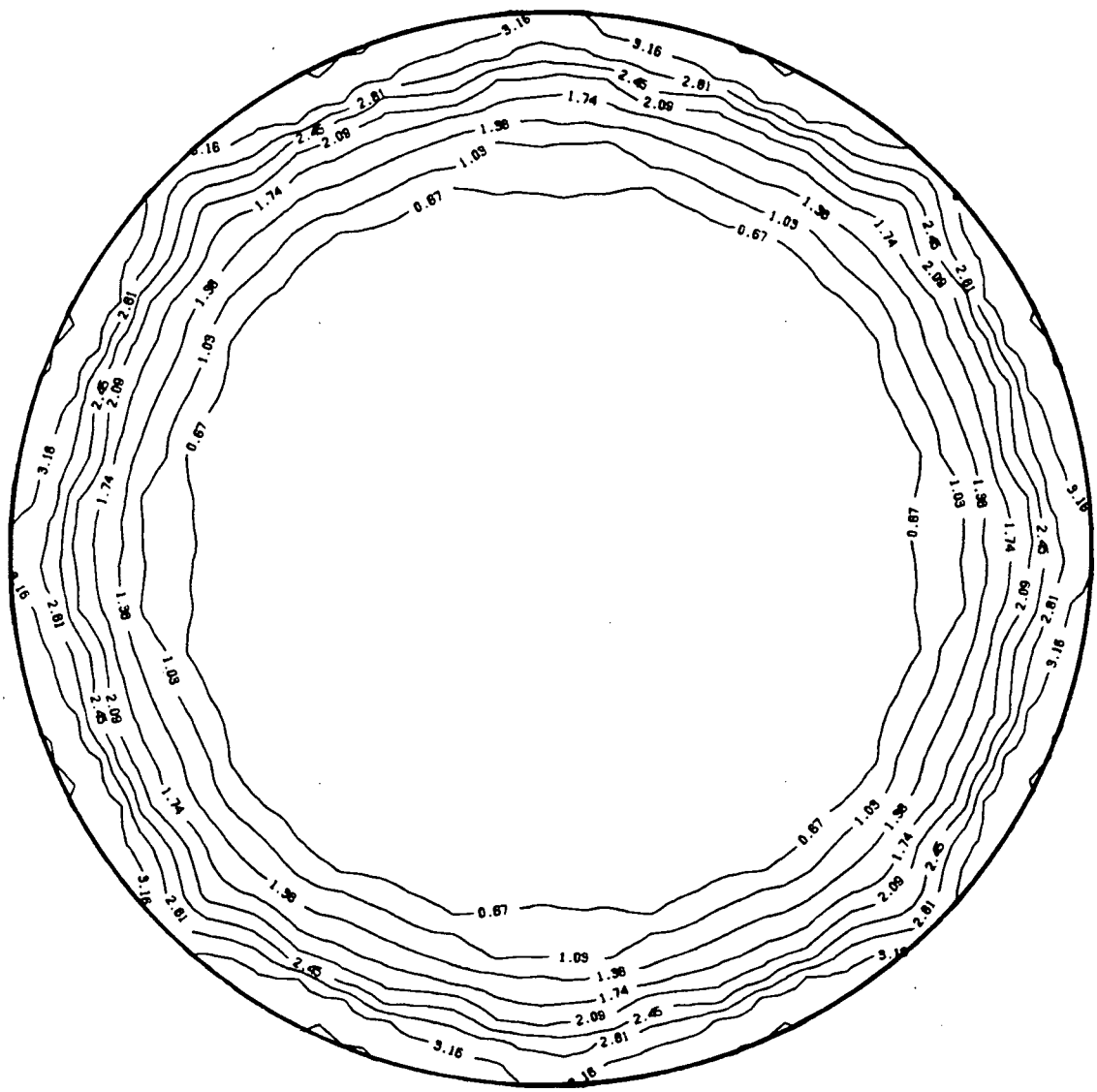

b

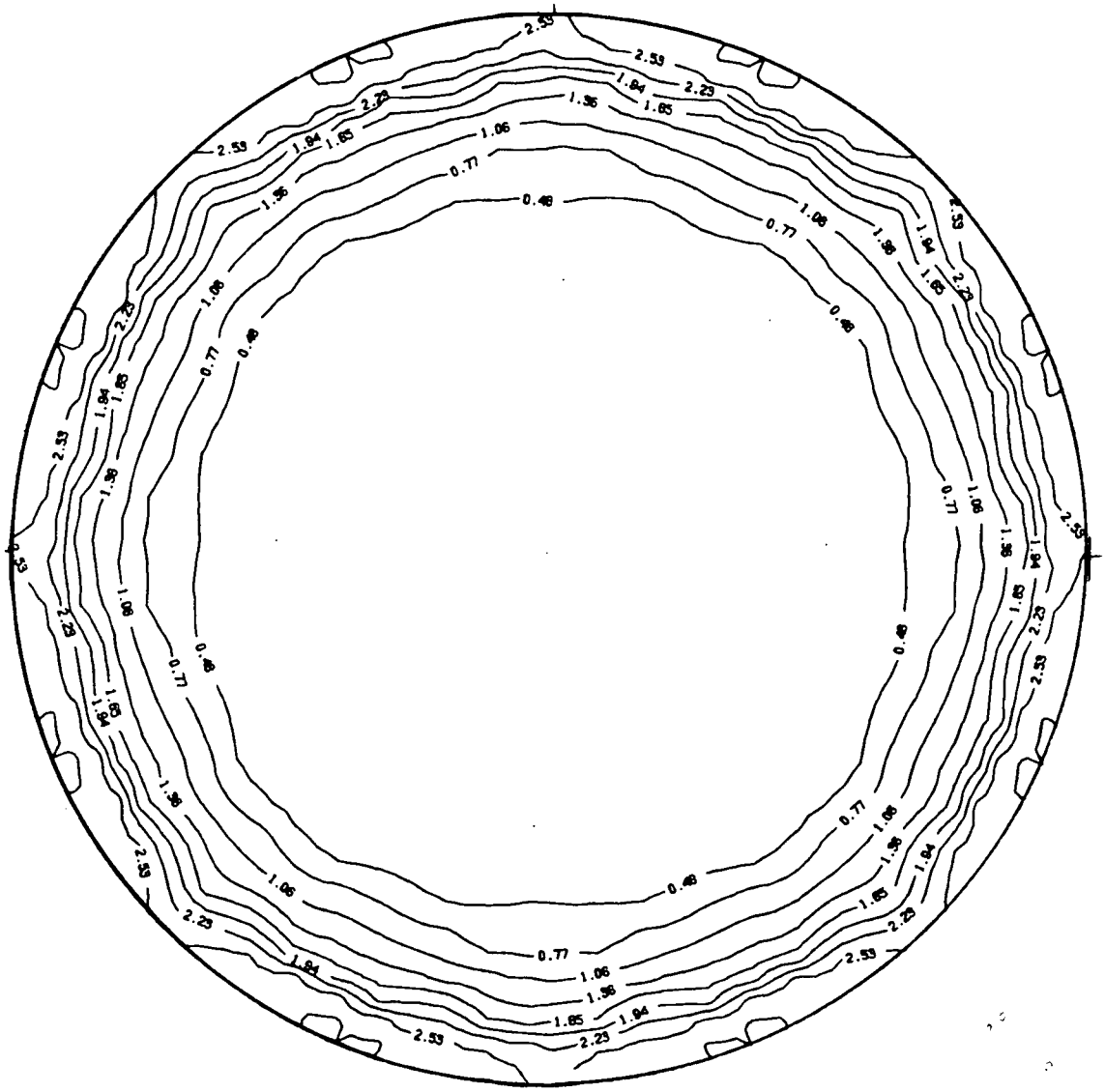

C

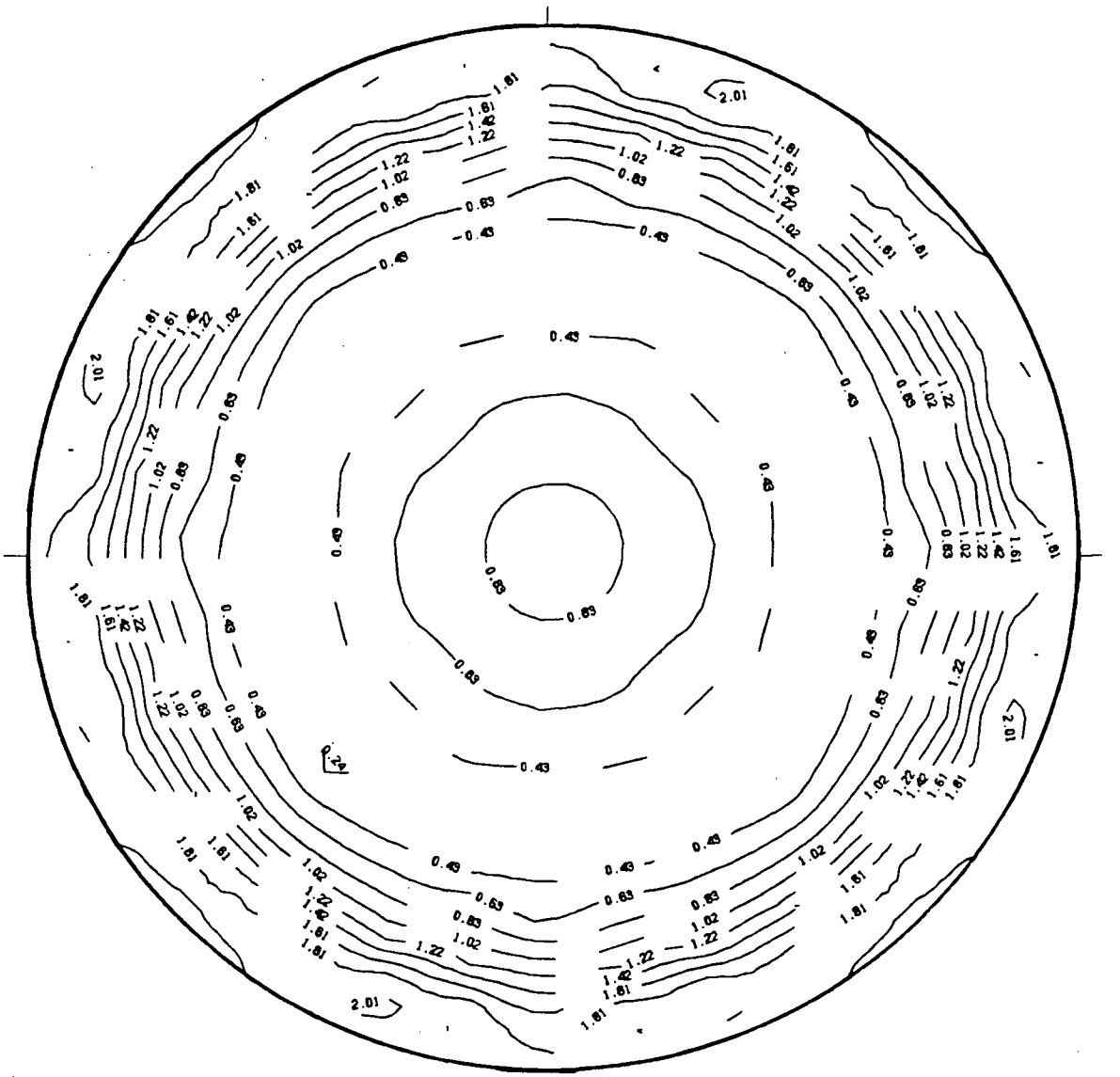

Figure 9.7 MRSS contours (MPa) in cross-sections perpendicular to the crystal axis for five cone angles. (a) 7.1^{o}, (b) 30°, (c) 45°, (d) 54.7^{o}, (e) 65°. Section (a-d) are 7.5 mm from the interface and section (e) is 8.0 mm from the interface. The horizontal direction corresponds to the [100] direction and the vertical direction corresponds to the [010] direction.

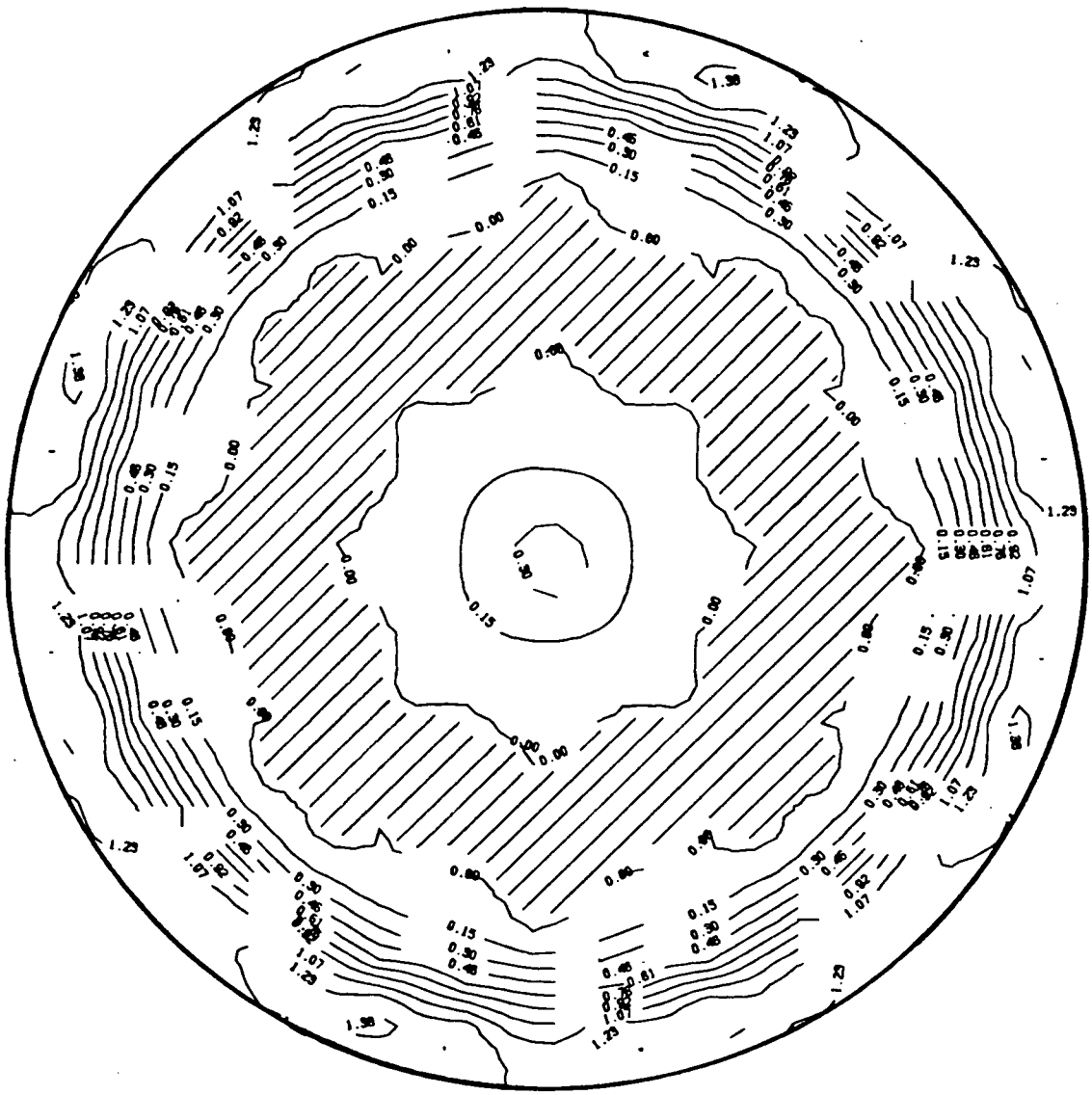

Figure 9.8 Contours of the MRSS-CRSS (Yield) (MPa) for the 65° cone angle crystal. MRSS contours are shown in Figure 9.7(e). At high cone angles MRSS levels are larger than CRSS at the centre and outside part of the wafer.

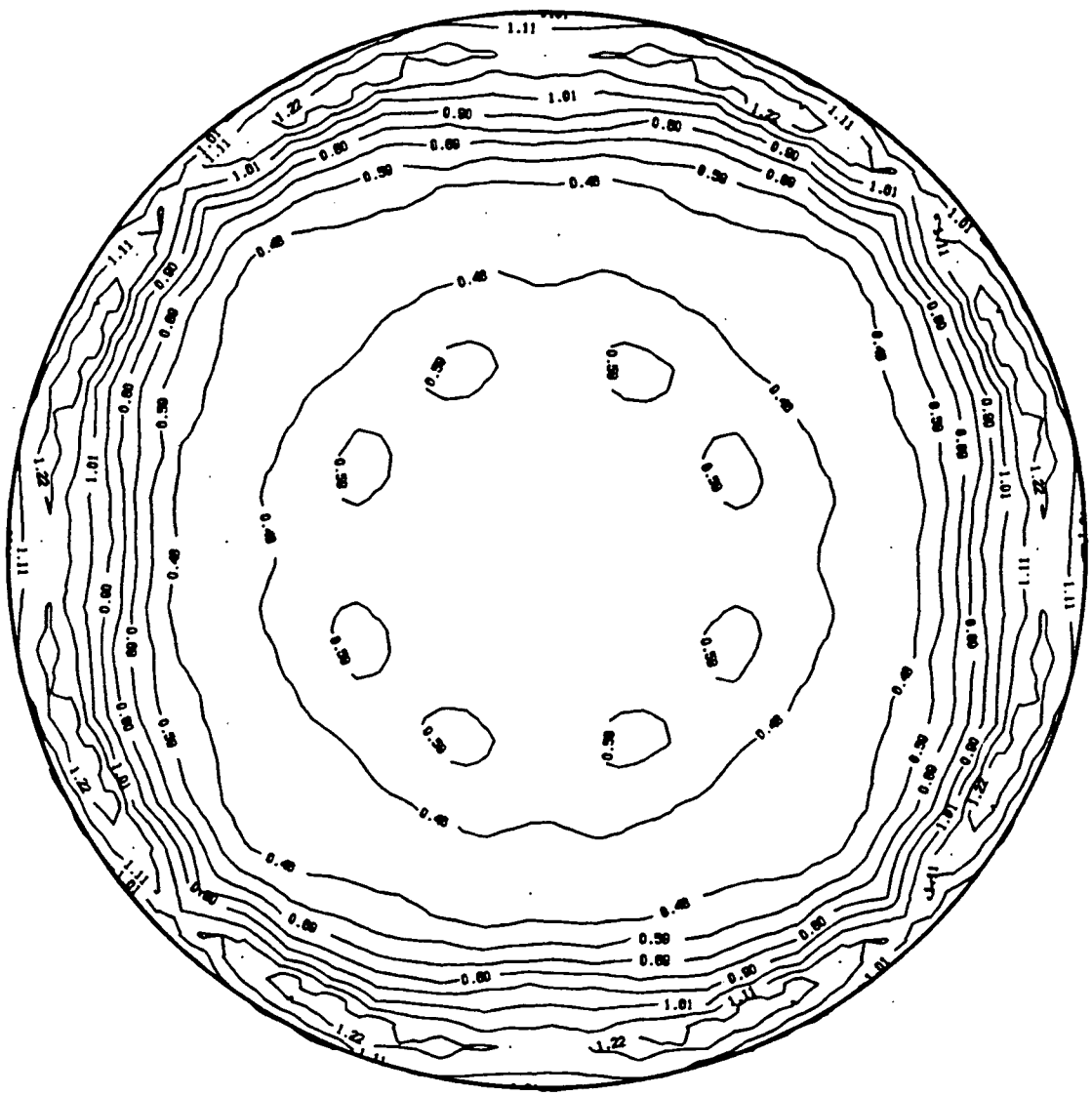

a

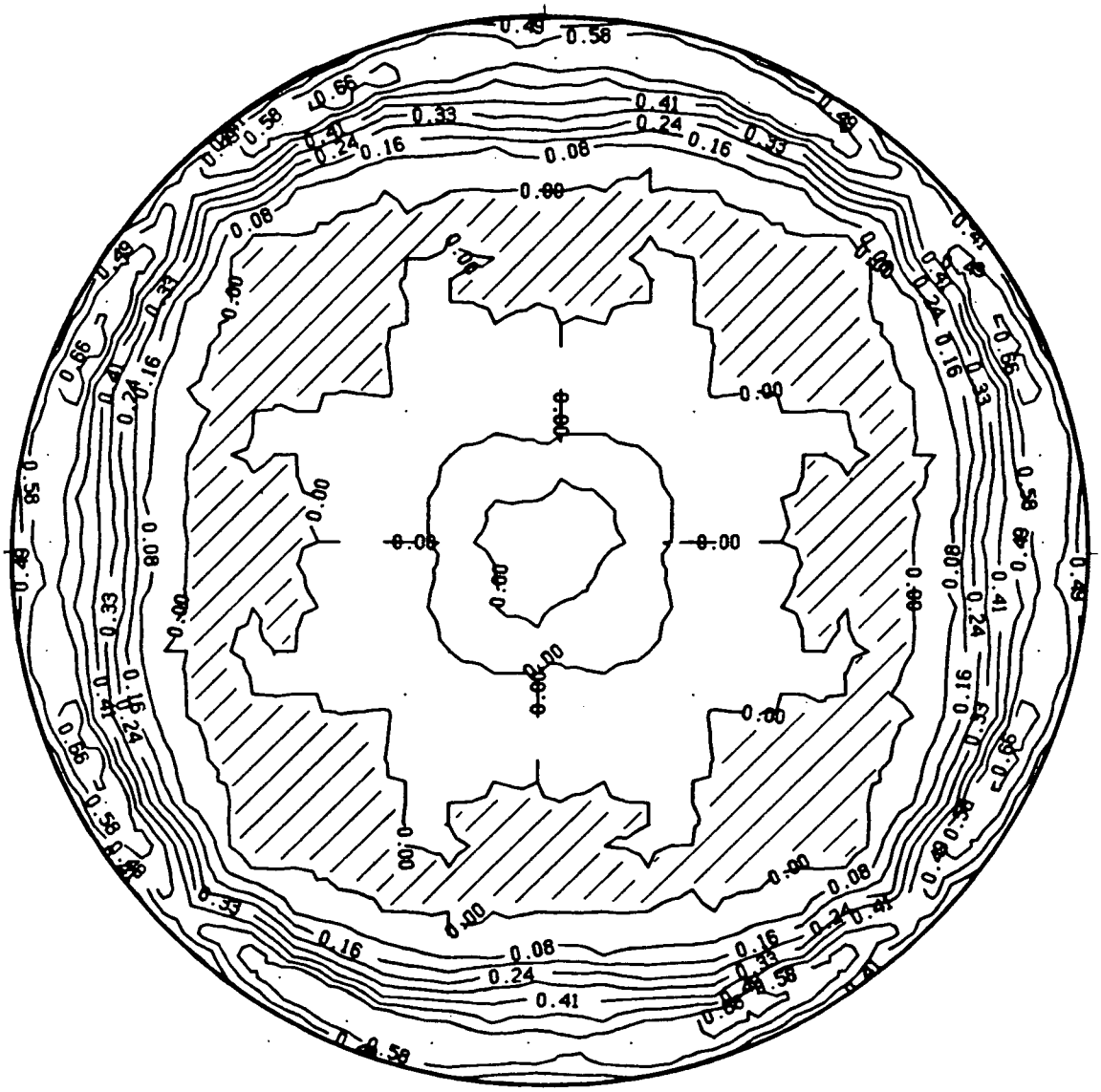

b

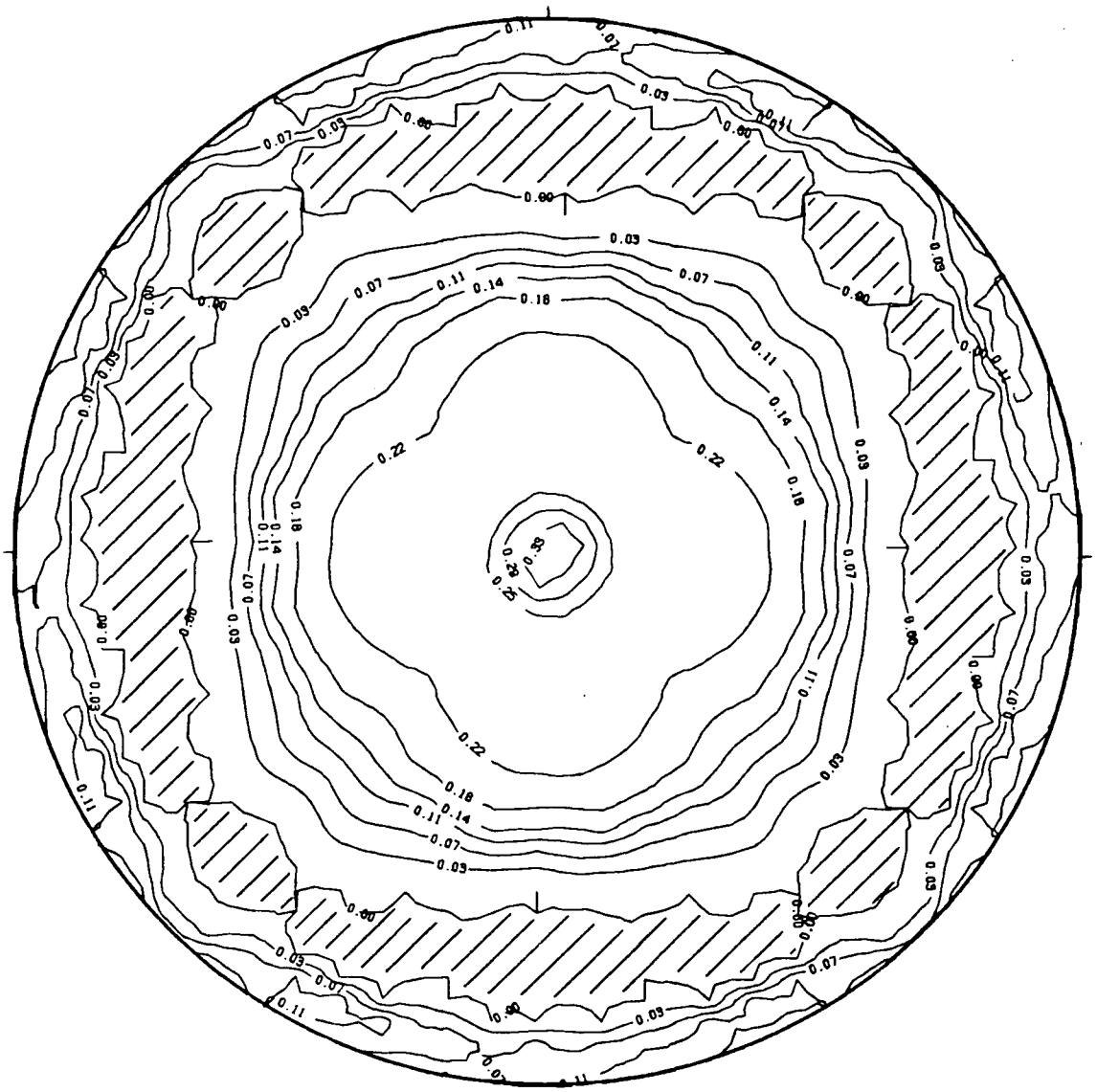

C

Figure 9.9 Stress contours (MPa) in cross-section 2.5 mm from the interface. (a) and (b) in a 7.1^{o} cone angle crystal. (c) in a 45° cone angle crystal. (a) MRSS contours. (b) and (c) MRSS-CRSS (Yield). For the 7.1^{o} cone angle there is eight-fold symmetry at the centre in (a) which is not seen in (b) because stress levels are less than CRSS. For the 45° cone angle there is four-fold symmetry.

drop closer to the center than in any other direction ; in addition the stress remains low even close to the edge. As a result larger areas of low stresses are present in the <110> directions. Similar conclusions were obtained with the higher cone angles.

In all the cases considered there is one common characteristic present. At the edge of the wafer eight-fold symmetry is always present with minima in the <100> and <110> directions. This is more apparent in Figure 9.7(d), where the maxima are symmetrically distributed. The eight-fold symmetry at the edge is associated with an eight-fold distribution of the slip mode. This is shown in Figure 9.10. It is also observed that the local minima at the edge in the <100> and <110> directions are associated with a change in the slip mode.

9.1.2 Effect of Thermal Conditions

In order to assess the effect of the thermal conditions on the stress distribution during growth, stress fields are determined in crystals having a 45° cone angle for different thermal gradients in the boron oxide and argon gas, as listed in Table 9.2 .

The calculated temperature distribution in the growing crystal for a range of thermal gradients is shown in Figure 9.11(a-d). The isotherms are observed to be very flat for low thermal gradients with a small curvature at the shoulder of the crystal.

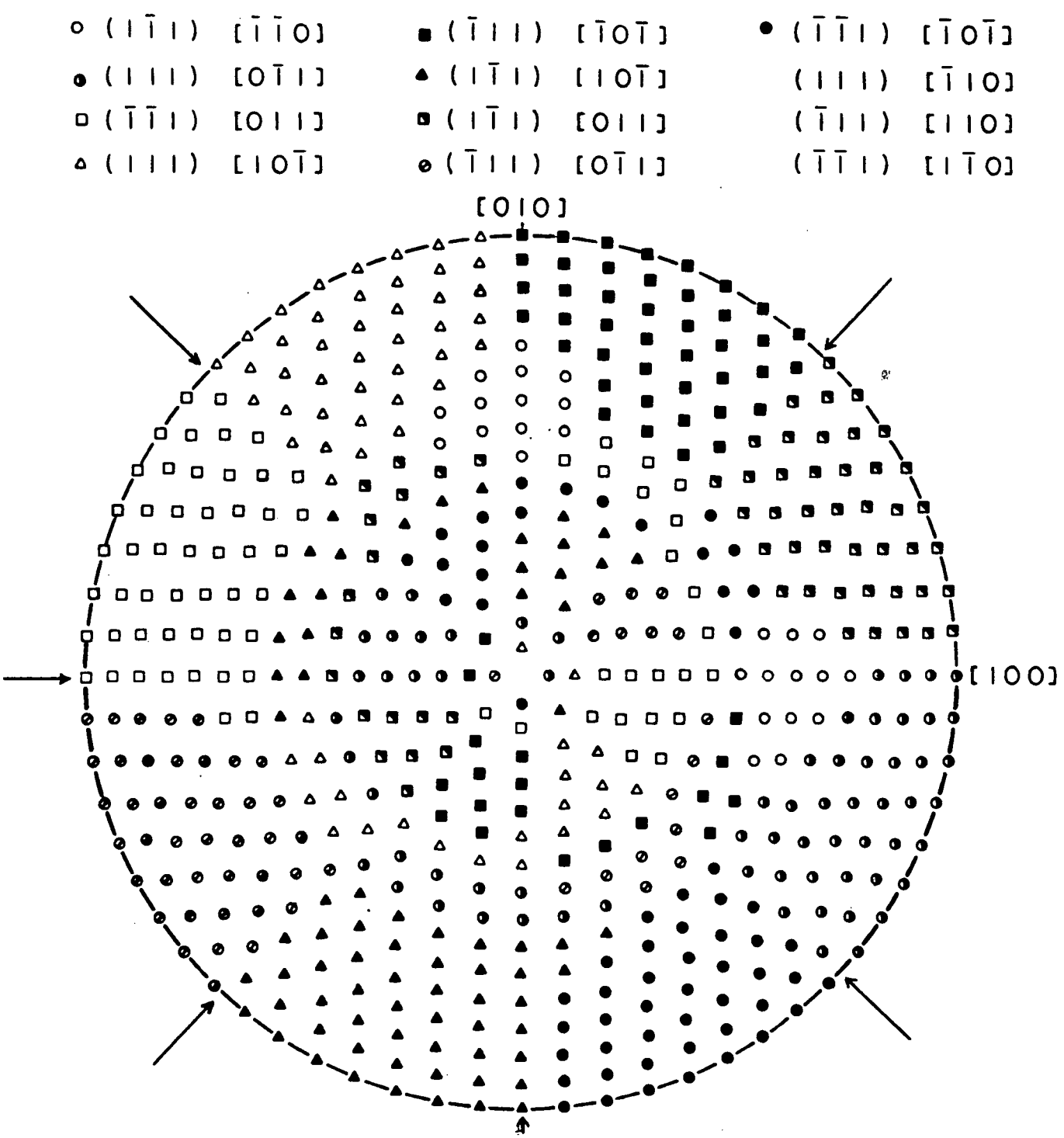

Figure 9.10 Slip mode distribution in a (001) plane corresponding to the MRSS distribution shown in Figure 9.7(c) for the 45° cone angle crystal at 7.5 mm from the interface. The eight-fold distribution of the mode at the edge of the section is associated with the eight-fold symmetry of the MRSS.

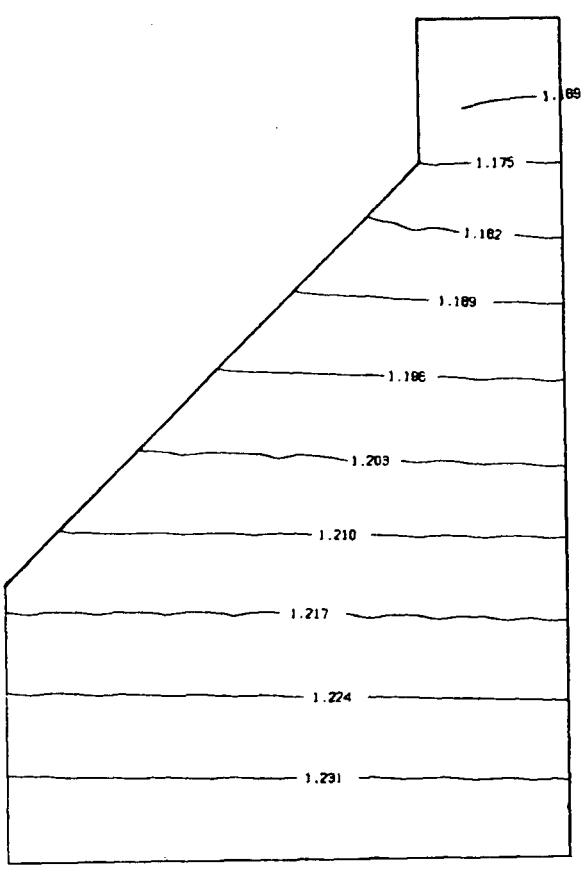
1.169
1.175
1.182
1.189
1.196
1.203
1.210
1.217
1.224
1.231

a

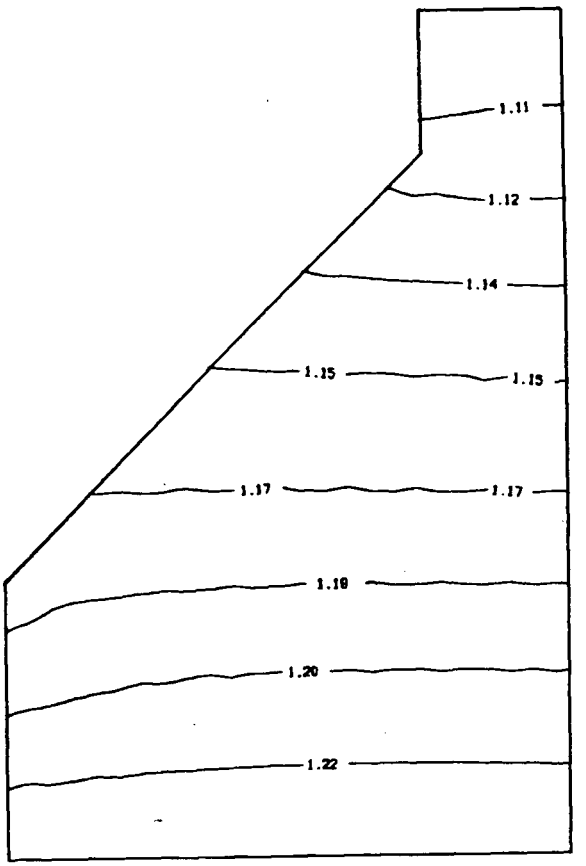
1.11
1.12
1.14
1.15
1.15
1.17
1.17
1.19
1.20
1.22

b

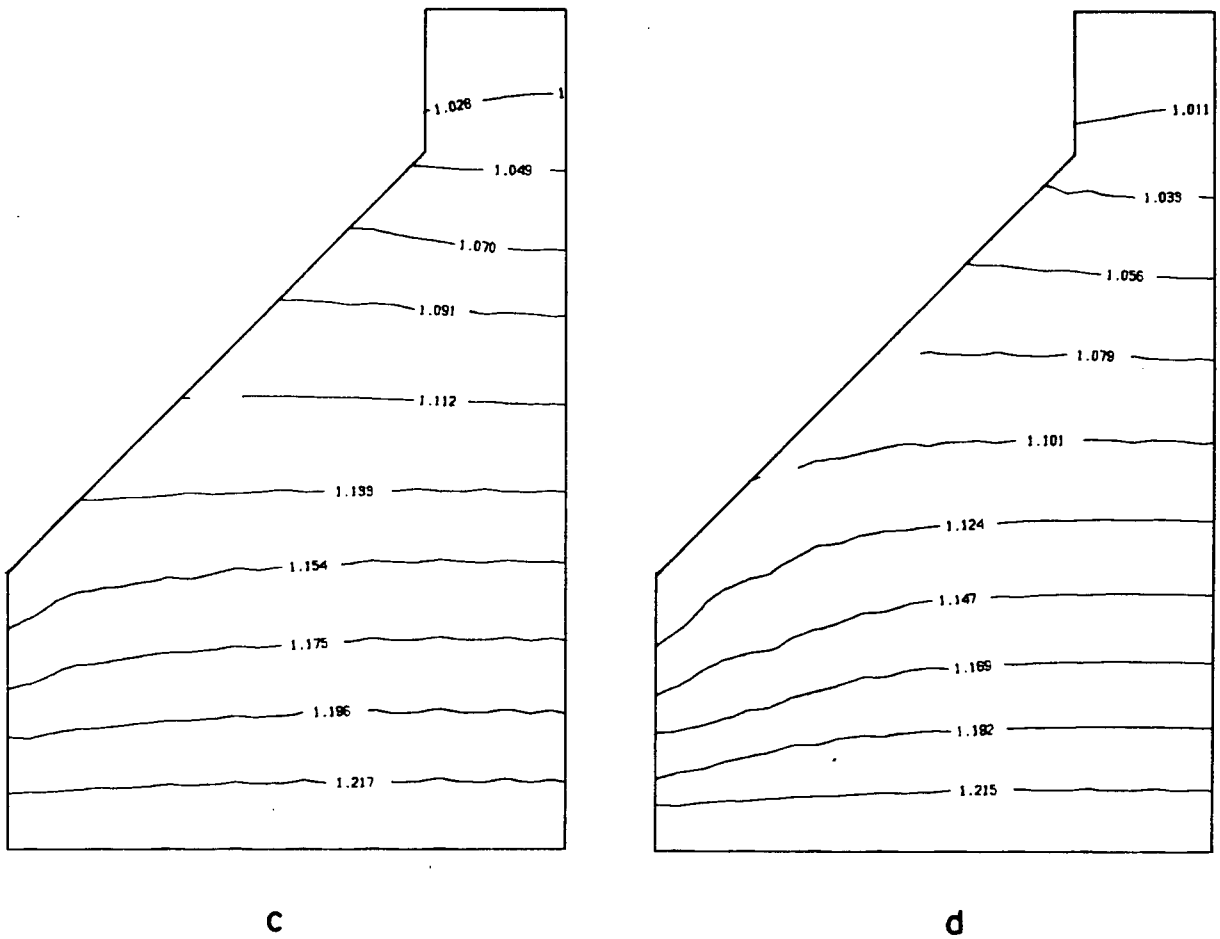

Figure 9.11 Temperature distribution as a function of external temperature gradient for a 45° cone angle crystal. Thermal gradients in the boron oxide are : (a) $50^{o}C/cm$, (b) $100^{o}C/cm$, (c) $200^{o}C/cm$ and (d) $400^{o}C/cm$. Temperatures are given in $10^{3o}C$. For low gradients isotherms are nearly flat and slightly convex. For larger gradients isotherms are curved and concave.

Table 9.2 Effect of Ambient Temperature on Axial Temperature Gradient and Stress

Temperature Gradients, ^{o}C/cm			AMRSS, MPa
Boron oxide	Argon	Axial	
50	25	25	0.59
100	50	48	2.55
200	100	84	5.12
400	100	98	11.91

For a temperature gradient of 400°C/cm (Figure 9.11(d)), the isotherms are clearly curved with the curvature increasing near the shoulder. The figure also shows that the axial temperature gradient is higher than the radial gradient. The axial gradients in the crystal for the different imposed gradients are listed in Table 9.2. It can be seen that these gradients are not linearly related. In the same table the largest MRSS (AMRSS), which occurs below the shoulder, is also listed. The relation between the axial gradient and the AMRSS is not linear.

The stress distribution in the crystal growing under a thermal gradient of 50°C/cm is shown in Figure 9.12(a) and (b), for a 200°C/cm gradient in Figure 9.13(a) and (b) and for a 400°C/cm gradient in Figure 9.14(a) and (b). Part (a) gives the MRSS, part (b) the MRSS-CRSS (Yield). At 50°C/cm (Figure 9.12(a)) the MRSS has a different stress distribution than at higher gradients specifically the high stress below the shoulder

Figure 9.12 Stress contours (MPa) in a (010) plane for a 45° cone angle crystal grown with a 50°C/cm gradient in the boron oxide. (a) MRSS contours does not show the bump shaped stress distribution below the shoulder in (a). The MRSS-CRSS (Yield) is positive only in a few regions in (b).

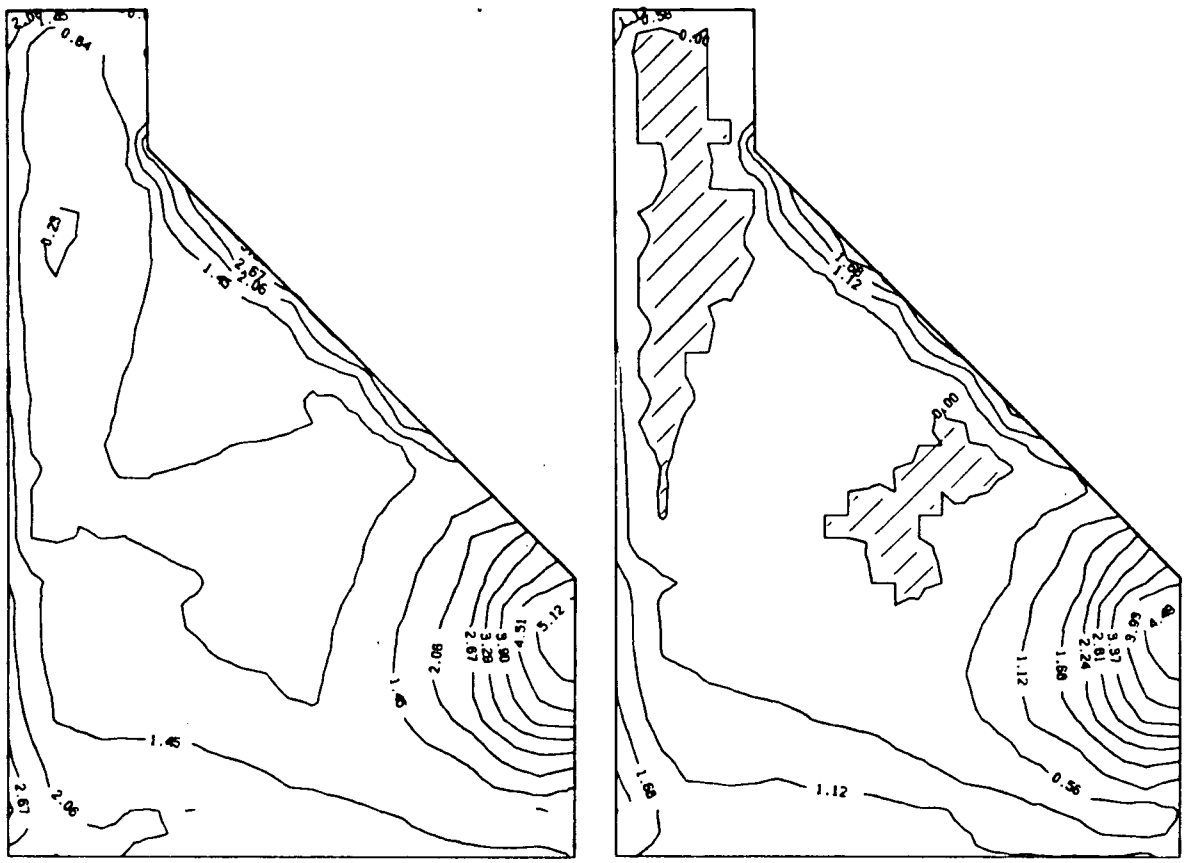

Figure 9.13 (a) MRSS contours and (b) MRSS-CRSS (Yield) contours for a 200°C/cm gradient in the boron oxide. Units are in MPa. MRSS stress are large below the shoulder in (a). The MRSS-CRSS is greater than zero in most of the crystal in (b).

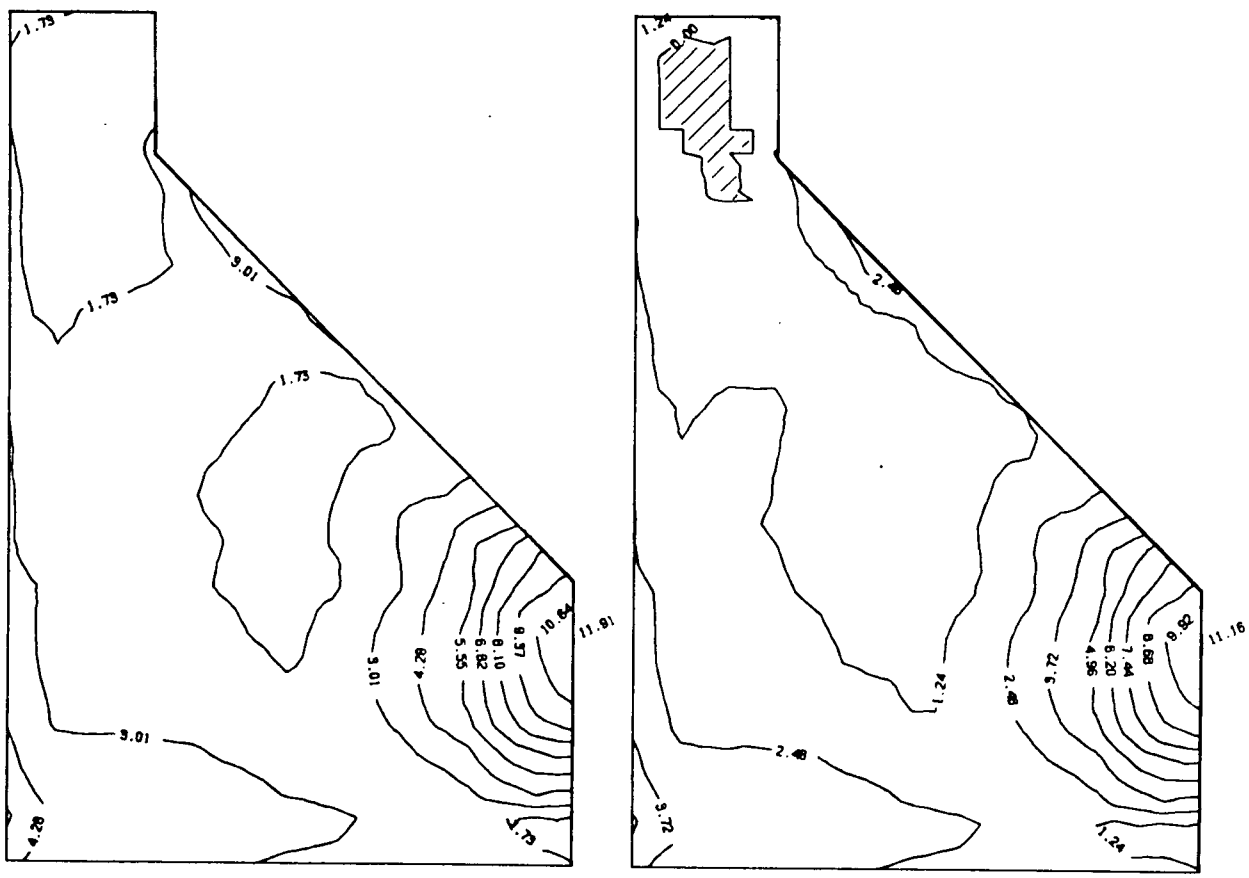
1.73
9.01
1.73
1.73
5.01
4.29
5.55
6.82
8.10
9.57
10.64
11.91
9.01
4.29
1.24
2.48
1.24
2.48
3.72
4.96
6.20
7.44
8.68
9.92
11.16
2.48
3.72
1.24

a

b

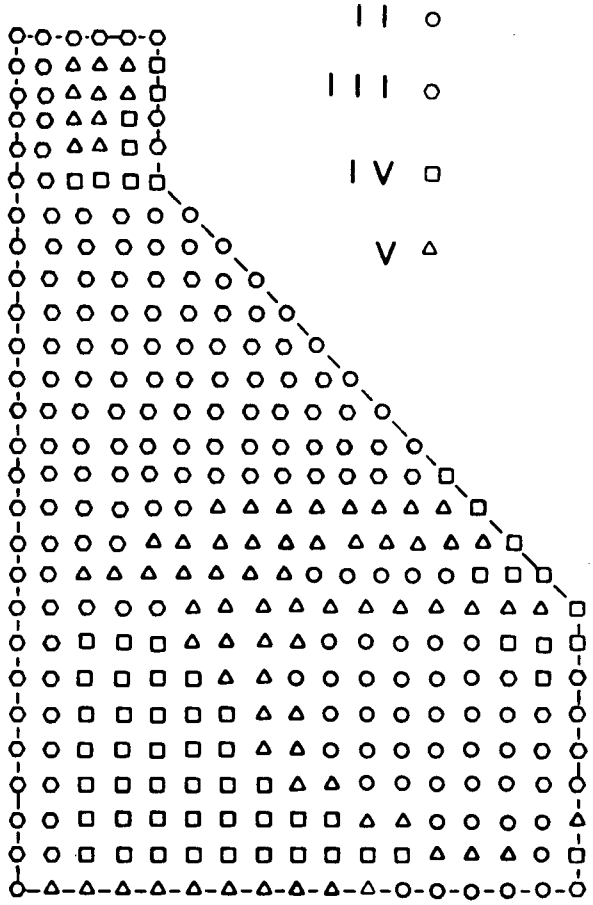

Figure 9.14 (a) MRSS contours. (b) MRSS-CRSS (Yield) contours. (c) Slip mode distribution. Gradient in the boron oxide is 400°C/cm. In (a) contours are similar to those obtained for a 200°C/cm gradient. Stress levels have doubled. In (b) only a small area in the seed developed stresses less than the CRSS. In (c) the mode distribution is similar to that shown in Figure 9.5 for a 100°C/cm gradient.

disappears. At the higher gradients, Figures 9.13(a) and 9.14(a) the MRSS configuration is similar. The MRSS level increases as the thermal gradient increases. This is shown in part (b) of Figures 9.12 to 9.14. For a gradient $50^{o}C/cm$ almost the whole crystal section has MRSS-CRSS (Yield) levels below zero.

The slip mode which is operative at $400^{o}C/cm$ is the same to the mode which operates at $100^{o}C/cm$ as seen by comparing Figures 9.14(c) and 9.5. From this it can be concluded that similar slip modes come from similar stress configurations and this is independent of the value of the constant temperature gradient. Similar slip modes are expected for stress distributions with similar relation among stress components. In addition the symmetry of the MRSS does not change when the thermal gradient is increased from $100^{o}C/cm$ to $400^{o}C/cm$ as shown by Figures 9.7(c) and 9.15.

9.1.3 Effect of the Heat Transfer Coefficient

Conditions : BG, $100^{o}C/cm$; AG, $50^{o}C/cm$

In order to determine how sensitive the calculations are to the magnitude of the heat transfer coefficients, the calculations were repeated with values of the heat transfer coefficient increased and decreased by a factor of 1.3 respectively. The results are shown in Figure 9.16 for the temperature profiles at the surface of the crystal. Four profiles are presented ; three correspond to the three different heat transfer coefficients and the fourth corresponds to the ambient temperature. The

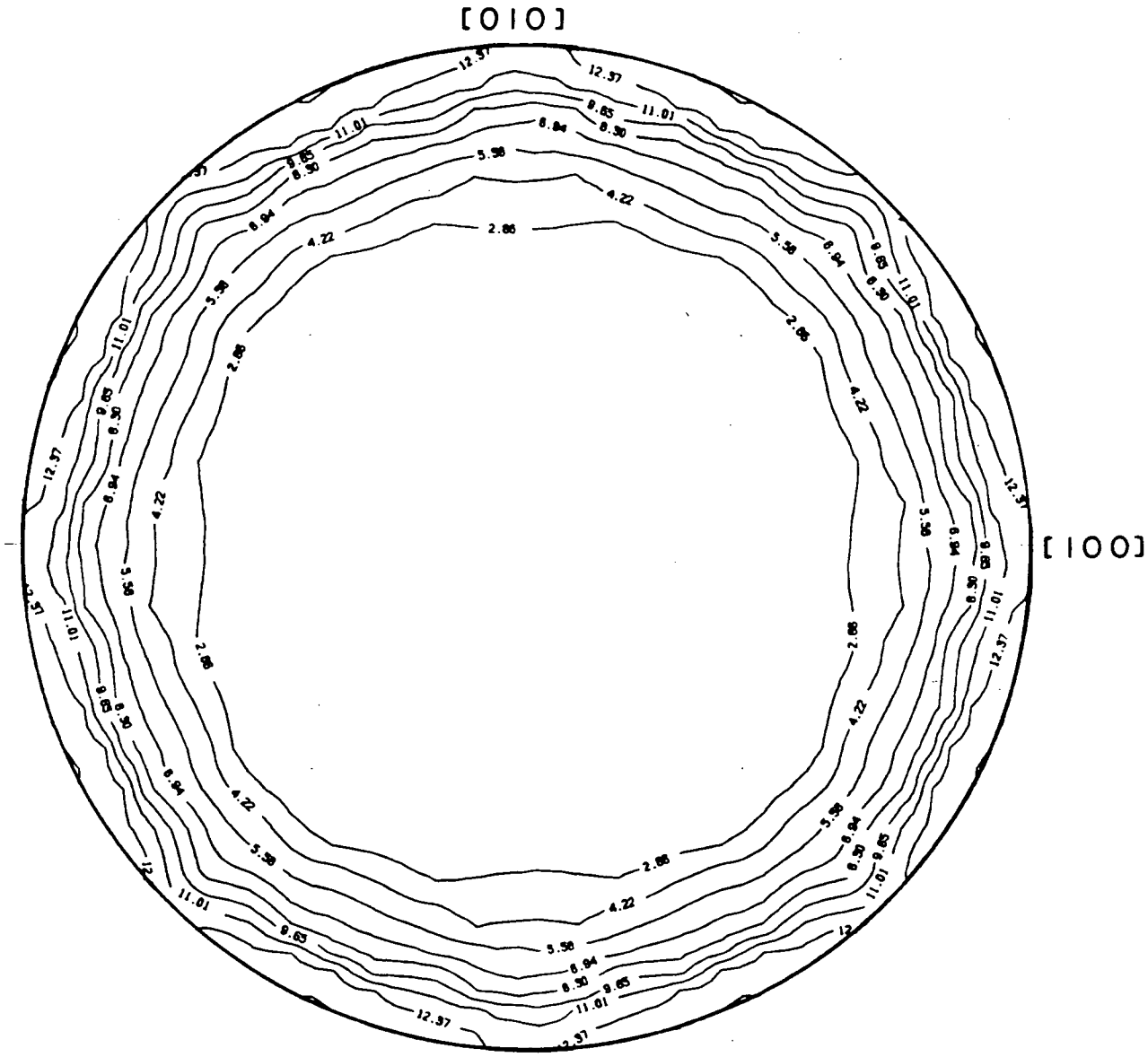

Figure 9.15 MRSS contours in MPa in a cross-section at 7.5 mm from the interface for the crystal shown in Figure 9.14(a). The symmetry is similar to that shown in Figure 9.7(c) for a 100°C/cm gradient.

temperature profiles at the surface and centreline, which are not shown, are very similar to those in Figure 9.16.

The largest effect of the change in heat transfer coefficient is observed at the seed end. The change in temperature follows the change in the heat transfer coefficient. At the crystal/cone junction the temperature change is small, approximately $5^{o}C$. At the seed the effect is more pronounced because the seed radius is small and heat transfer is controlled at the seed surface. In the bulk crystal there is mixed control at the surface and in the bulk material. As a result, a change in heat transfer coefficient does not substantially modify the temperature field.

The stress fields are shown in Figure 9.17 and 9.18 for the two heat transfer coefficients h / 1.3 and h X 1.3 respectively. (a) corresponds to the MRSS distribution and (b) corresponds to the MRSS-CRSS (Yield). Comparing the maximum values of MRSS occurring below the shoulder, it can be seen that the stress varies only about 20 % in the whole span of heat transfer coefficient values. The span represents 53 % of the original values at the corresponding temperature.

Inside the crystal, changing the heat transfer coefficient has a strong effect on the stress field. Note that the minimum value of MRSS increases from 0.05 MPa to 0.16 MPa. Increasing the heat transfer coefficient does not change the dislocation distribution (Figure 9.17(b) and Figure 9.18(b)). This can be

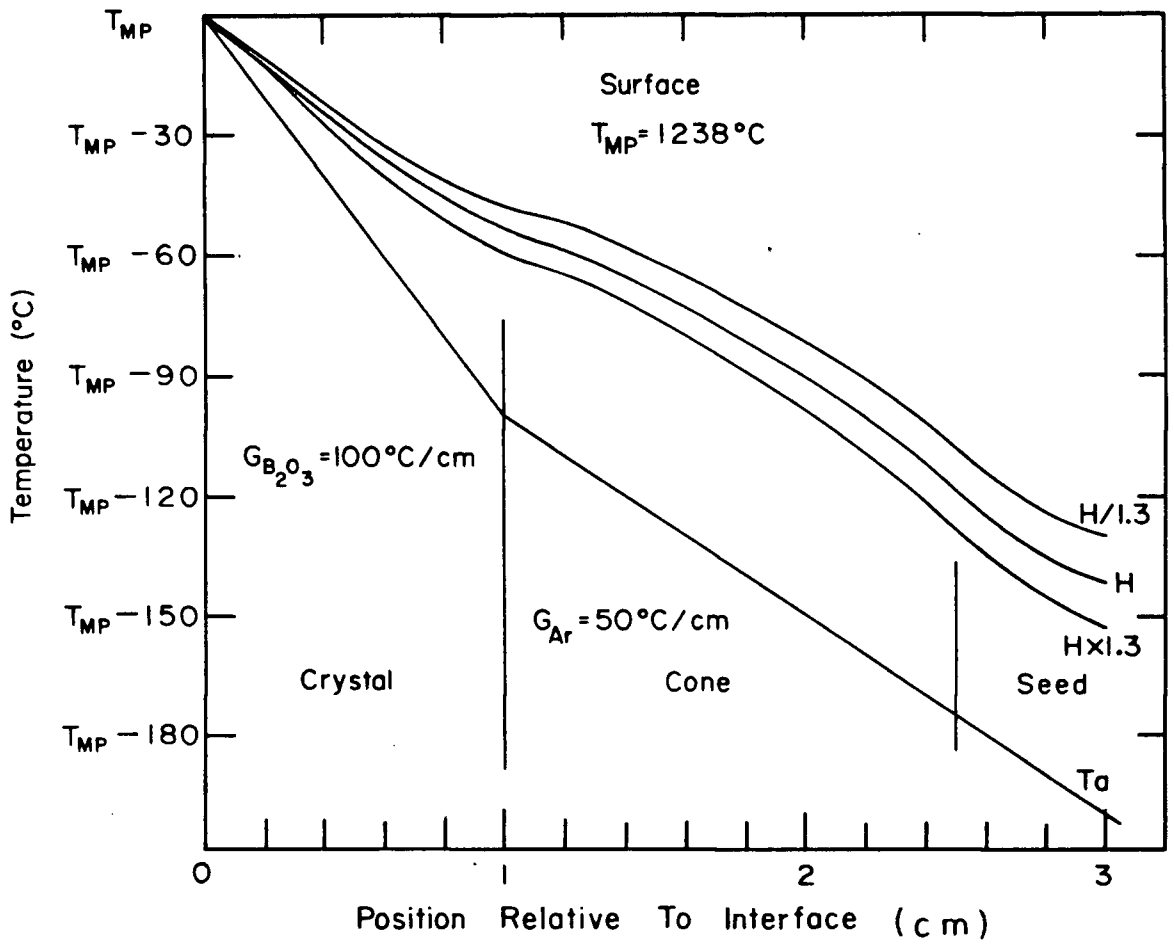

Figure 9.16 Temperature profiles at the surface of 45° cone angle crystals for three diferent conditions. Curve H corresponds to the temperatures calculated using the original heat transfer coefficient values. In curves H / 1.3 and H x 1.3 the original heat transfer coefficient values were divided and multiplied by 1.3 respectively.

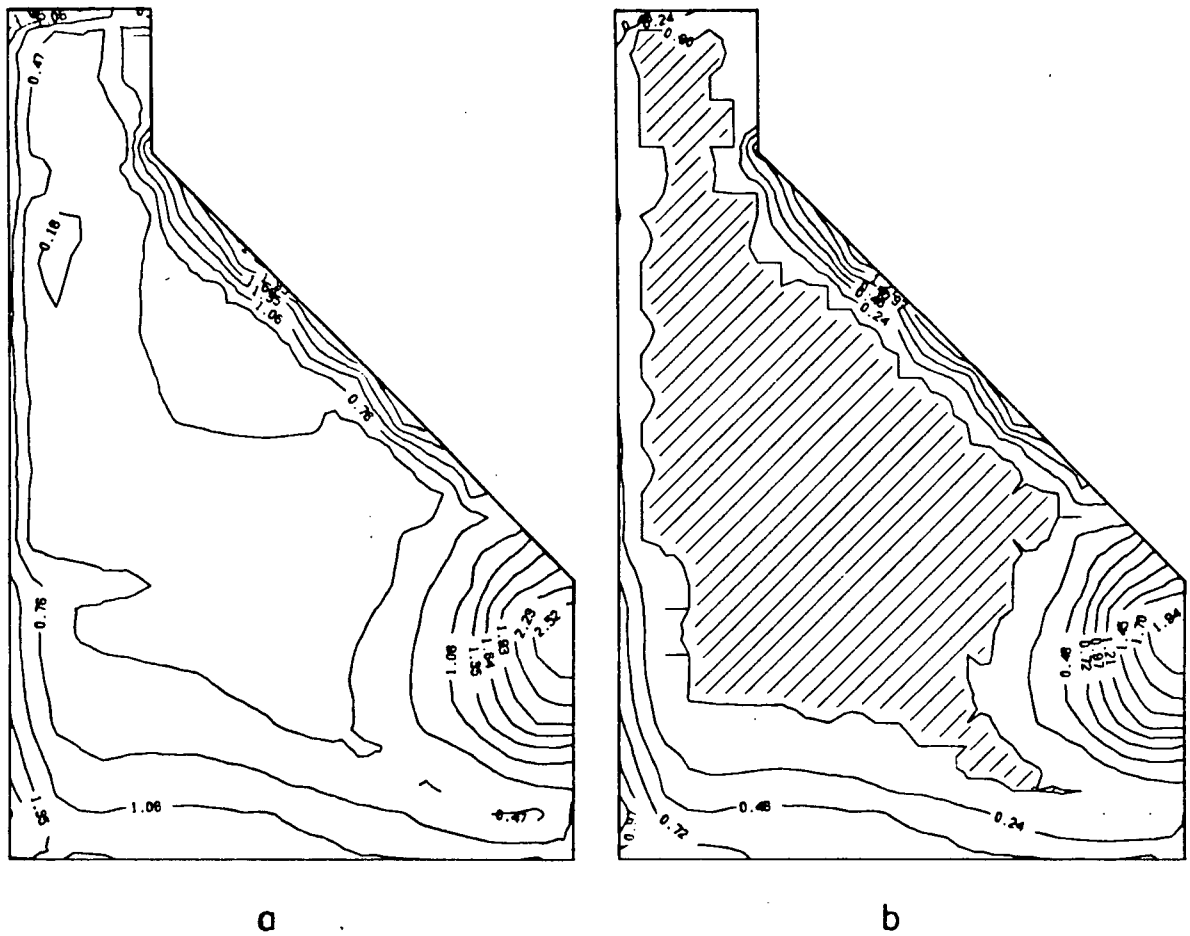

Figure 9.17 Stress contours in MPa derived from the temperature field obtained using heat transfer coefficient values 1.3 larger than original values. (a) MRSS contours. (b) MRSS-CRSS (Yield).

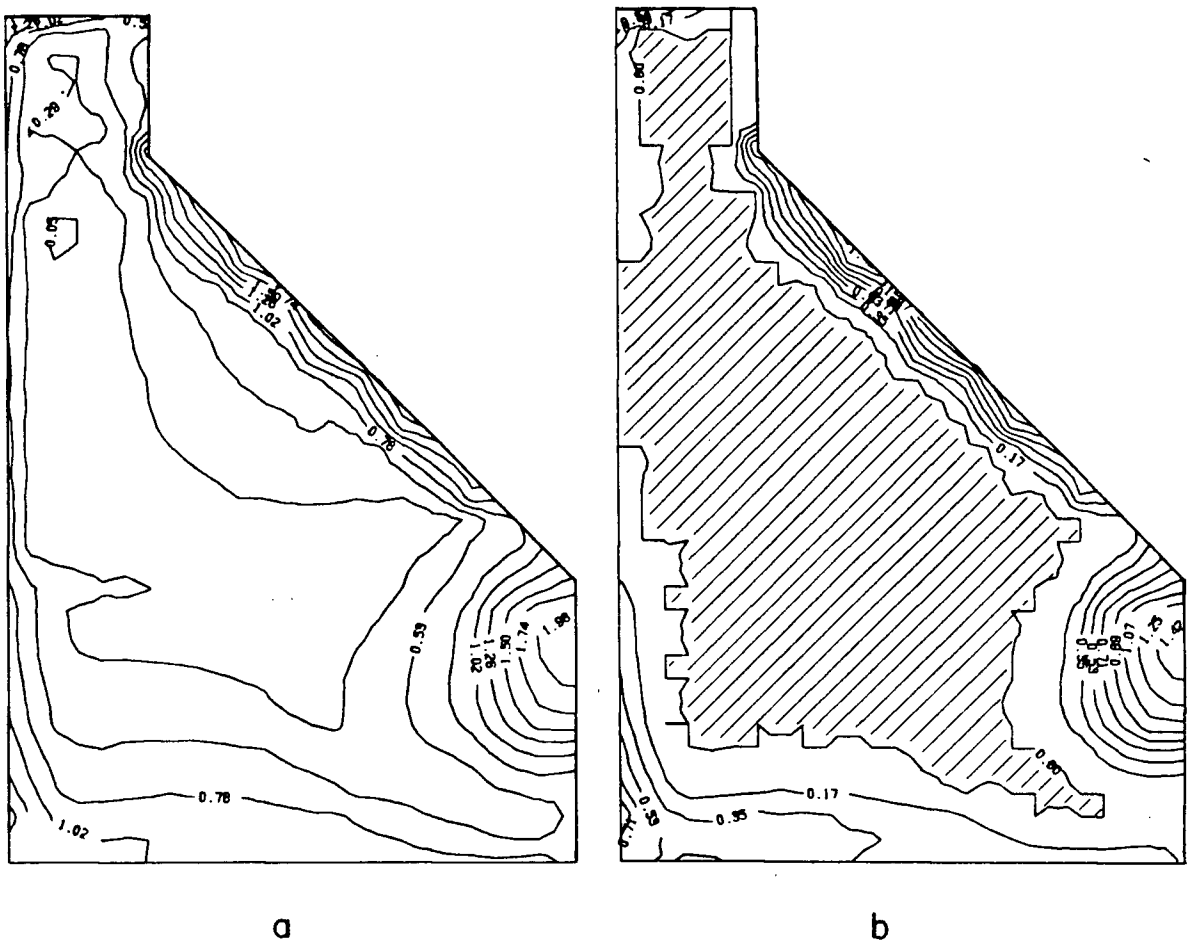

Figure 9.18 Stress contours in MPa derived from the temperature field obtained using heat transfer coefficient values 1.3 times smaller than original values. (a) MRSS contours. (b) MRSS-CRSS (Yield). Variations of only 20 % are observed in the maximum MRSS values between (a) and Figure 9.17(a).

accounted for by the increase in the thermal gradients in the crystal resulting from the increase in heat transfer coefficient, which leads to two opposite effects. These are the higher thermal stresses and the higher CRSS in the crystal resulting from the lower temperatures. When both effects are considered the net result of the increase in heat transfer coefficient on the dislocation distribution is negligible

9.1.4 Effect of Non-linearity in the Temperature Profile

The temperature field in the crystal depends almost entirely on two parameters, the heat transfer coefficient at the crystal surface and the temperature profile in the media surrounding the crystal. These two variables are interrelated and may depend on many factors like heat input into the mold, crystal diameter and gas pressure. However when the temperature profile, the height of the boron oxide layer, the gas composition and the pressure are known, the heat transfer is determined at each point on the crystal surface. This heat transfer coefficient, together with the temperature profile, crystals dimensions, and growth velocity, determine the temperature field inside the crystal. In the previous section it was shown that a 30 % variation in the heat transfer coefficient does not substantially affect the stress field. However it was shown that changing the temperature profile in the surrounding media has an important effect. Increasing or decreasing the thermal gradient markedly changes the thermal stresses. In those calculations the temperature profile in both the boron oxide and the argon gas was assumed to

vary linearly with distance from the solid/liquid interface. This may not be the case, as shown by the temperature profiles measured along the crystal surface.

In order to determine the importance of non-linearity of the imposed temperature profile, temperatures and stresses are calculated for the four growth conditions listed in Table 9.3 .

Table 9.3 Effect of Non-linearity of the Ambient Temperature Profile on Stress

Run	Temperature Gradients, $^{o}C/cm$		ΔT in B_2O_3 ^{o}C
	B_2O_3	Argon	
1	140	100	350
2	200, z < 1.0 100, z > 1.0	100	350
3	100, z < 1.0 50, z > 1.0	50	200
4	45, z < 1.0 90, z > 1.0	0	180

Note : Boron oxide thickness = 25 mm ; argon pressure = 30 atm. ; radius = 20 mm ; length = 10 mm ; cone angle = 30° . z is the distance from the solid/liquid interface.

The calculations are divided in two sets 1, 2 and 3, 4 taking into account the difference in temperature across the boron oxide layer. Each pair of conditions gives similar average temperature gradients across the encapsulant. The difference is in the temperature profile. In 1 the gradient is constant, in 2 and 3 the gradient is larger close to the melt, and in 4 the gradient is larger close to the encapsulant/gas interface.

The MRSS for the four cases are given in Figure 9.19(a-d). Comparing (a) and (b) it is seen that the relative stress distribution in both cases are similar. The AMRSS below the shoulder for case 2 in (b) is twice as large as the equivalent stress for 1 in (a). The minimum MRSS inside the crystal in (b) is about 20 times larger than in (a). Comparing 3 and 4 in Figure 9.19 the MRSS distributions differ. In (d) the stress concentration occurs along the cone surface rather than below the shoulder as in cases 1 to 3. The AMRSS on the cone surface in (d) is about 1.6 times larger than in (c) for 3. The lowest stress in (c) occurs at two positions, in the cone and below the cone. In Figure 9.19(d) the lowest stress occurs only below the cone. The value of the minimum MRSS in (c) and (d) is the same.

The symmetry of the stresses in (001) planes perpendicular to the growth direction is similar for 1, 2 and 3 of Table 9.3 and similar to the symmetry obtained for crystals grown with a 1 cm deep encapsulant and a gradient of 100°C/cm. These symmetry patterns are shown in Figure 9.7(c) and 9.9(c). The symmetry of the stresses for 4, however, is four-fold at sections 5.0 and

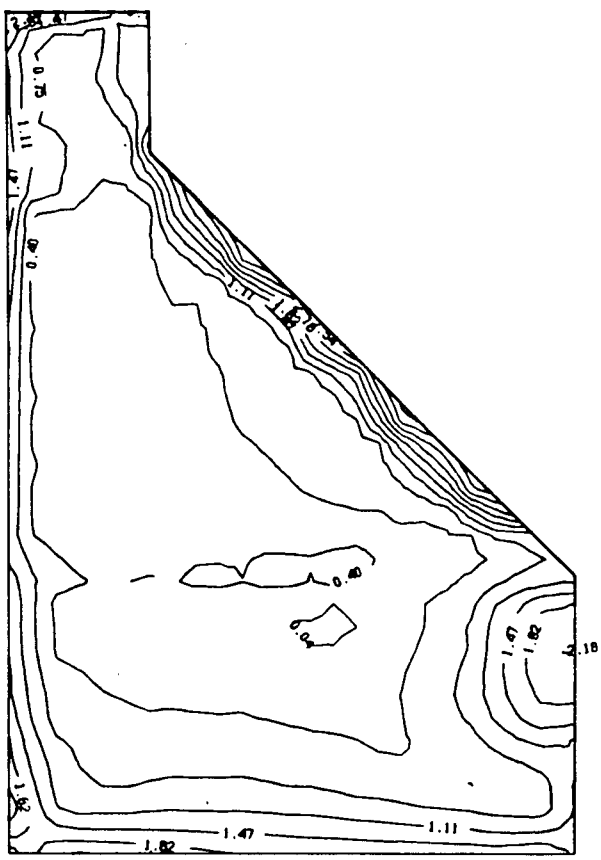
0.75
1.11
1.47
0.40
0.40
0.04
1.47
1.82
2.18
1.62
1.47
1.11
1.82

a

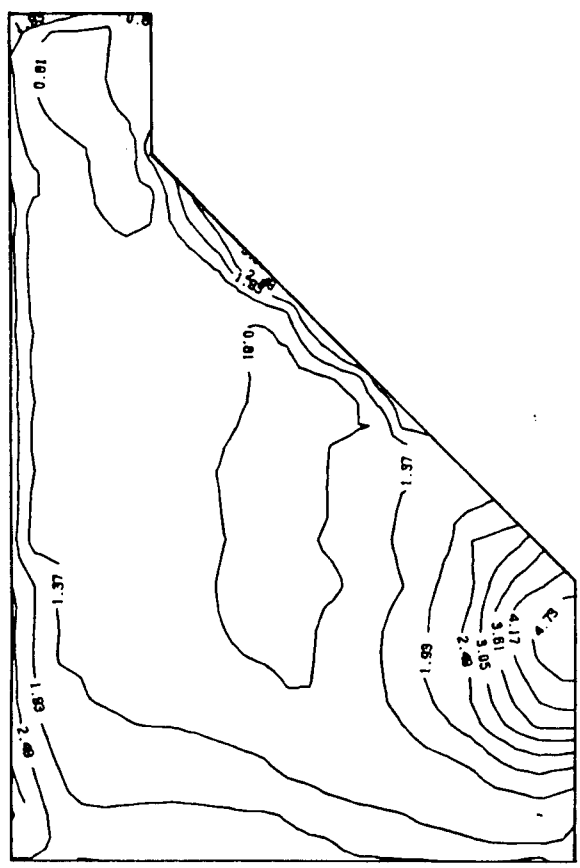
0.81
0.81
1.37
1.37
1.93
2.49
3.05
3.61
4.17
4.73

b

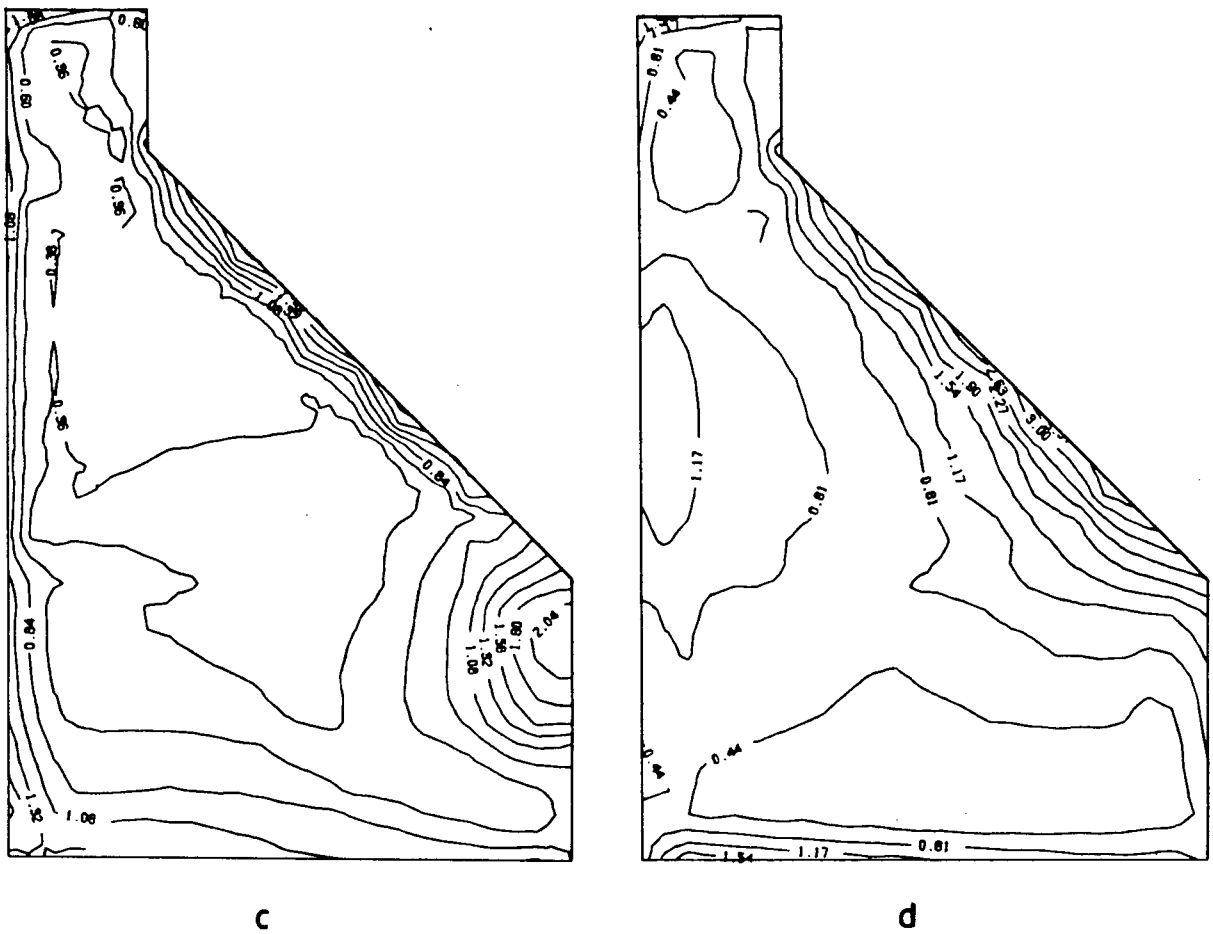

Figure 9.19 MRSS (MPa) contours for a crystal growing under four different conditions given in Table 9.3. (a) Run #1 ; (b) Run #2 ; (c) Run #3 ; (d) Run #4. From (a) to (b) the AMRSS doubles. In (d) the bump shape below the shoulder does not appear.

7.5 mm from the interface. At 5.0 mm evidence of two-fold symmetry is observed as shown in Figure 9.20.

The MRSS-CRSS (Yield) for conditions 1 to 4 are shown in Figure 9.21(a-d). For 1 the stress over large areas of the crystal is less than the CRSS, for 2 only small areas have stresses below the CRSS. Similar results are obtained for 3 and 4. In 4, however, the region with zero stress at the cone has moved to a position below the cone.

When comparing the stresses obtained for a boron oxide layer 2.5 cm thick (Table 9.3) with stresses generated with a 1 cm layer, the MRSS-CRSS (Yield) for 1 is comparable to the distribution obtained using a gradient of $100^{o}C/cm$ across the encapsulant (Figure 9.4(a)). It is noted that in 1 larger gradients are present, 40 % larger in the crystal and 300 % larger in the cone when compared to the gradients in a 1 cm thick layer. This result shows the importance of suppressing the thermal discontinuity occuring with the 1 cm thick encapsulant.

The stress distribution of Figure 9.21(b) for case 2 is comparable to the distribution in Figure 9.13(b) for a 1 cm thick layer. Comparable distributions are also obtained in Figure 9.21(c) for case 3 and Figure 9.4(a) for a 1 cm layer. This shows that for this crystal length, increasing the depth of the boron oxide from 1 to 2.5 cm with the same temperature profile in the ambient does not decrease the dislocation density. In addition it can be observed that the areas with stresses less than the CRSS (Yield) in Figure 9.21(c) are similar to those in Figure 9.21(a).

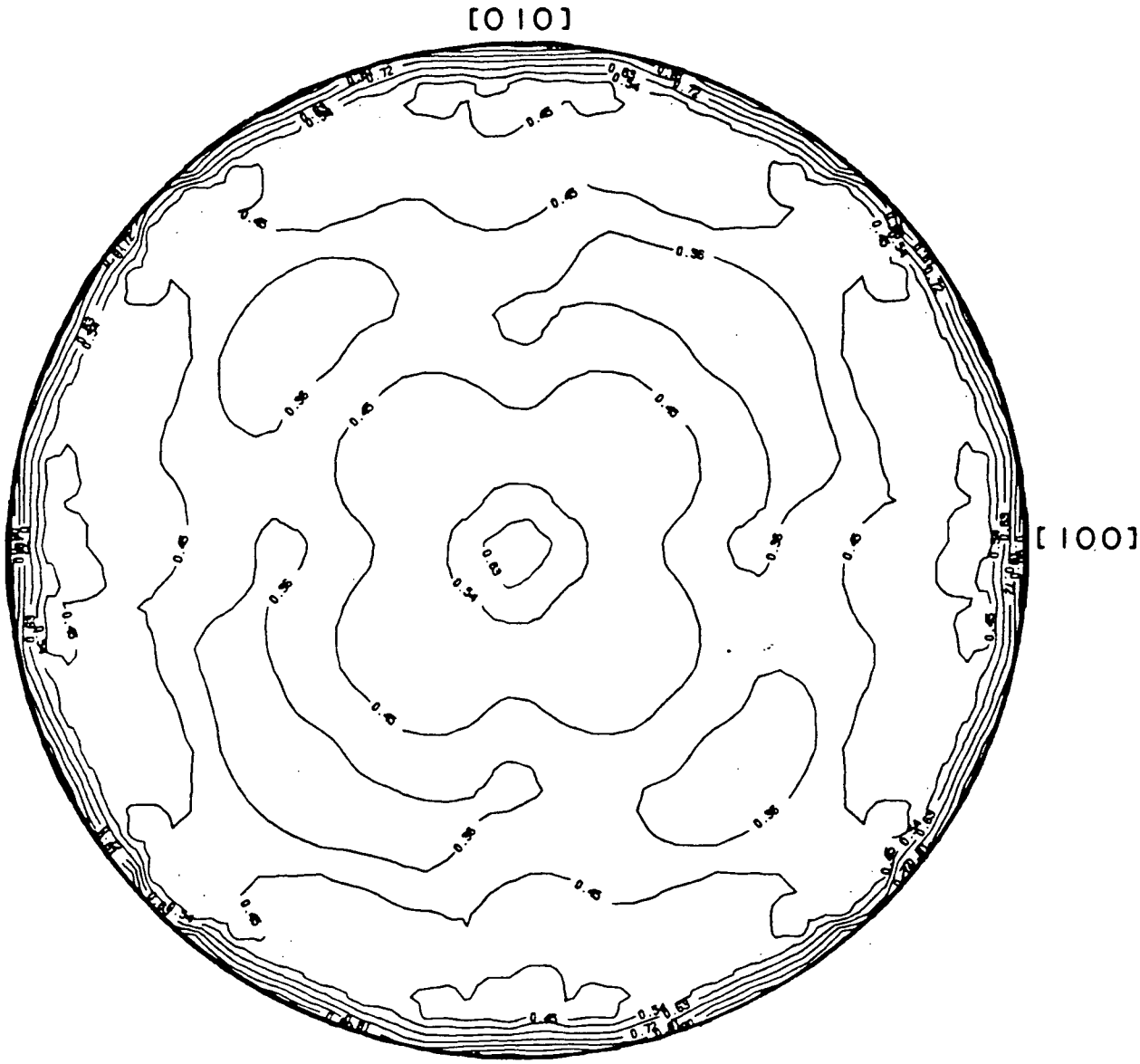

Figure 9.20 MRSS (MPa) contours in a (001) plane at a distance of 5.0 mm from the interface in the crystal shown in Figure 9.19(d) (run #4). The four-fold symmetry with a slight two-fold symmetry is observed.

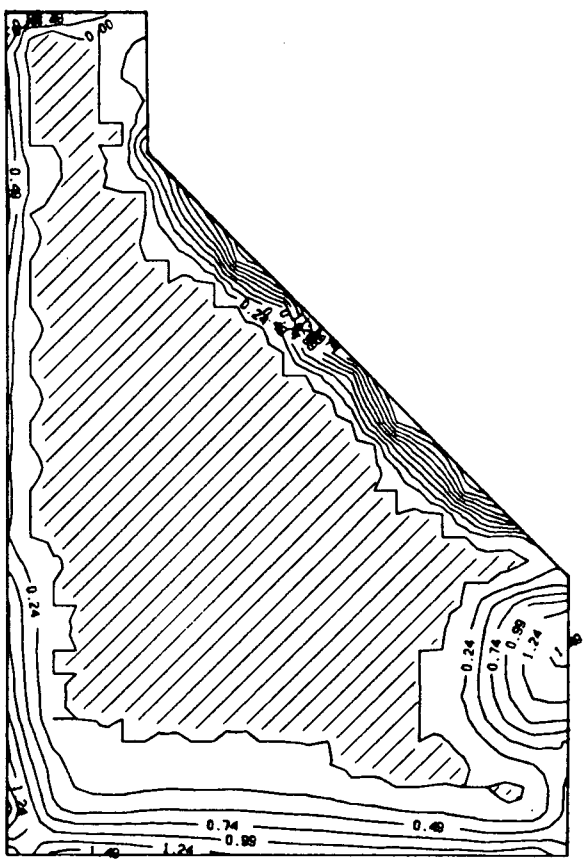
0.00
0.24
0.24
0.74
0.99
1.24
0.74
0.49
0.99
1.24

a

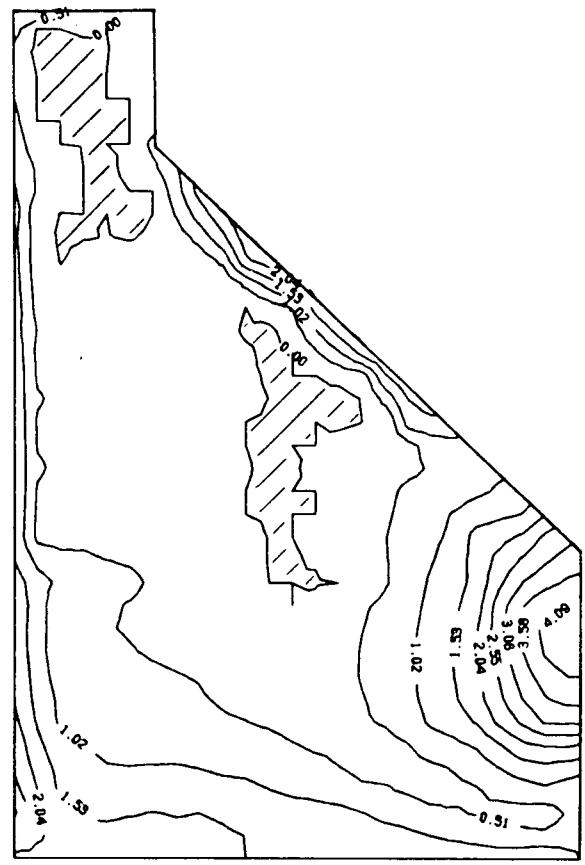
0.00
0.00
1.02
1.53
2.04
2.55
3.06
3.58
4.09
1.02
1.53
2.04
0.51

b

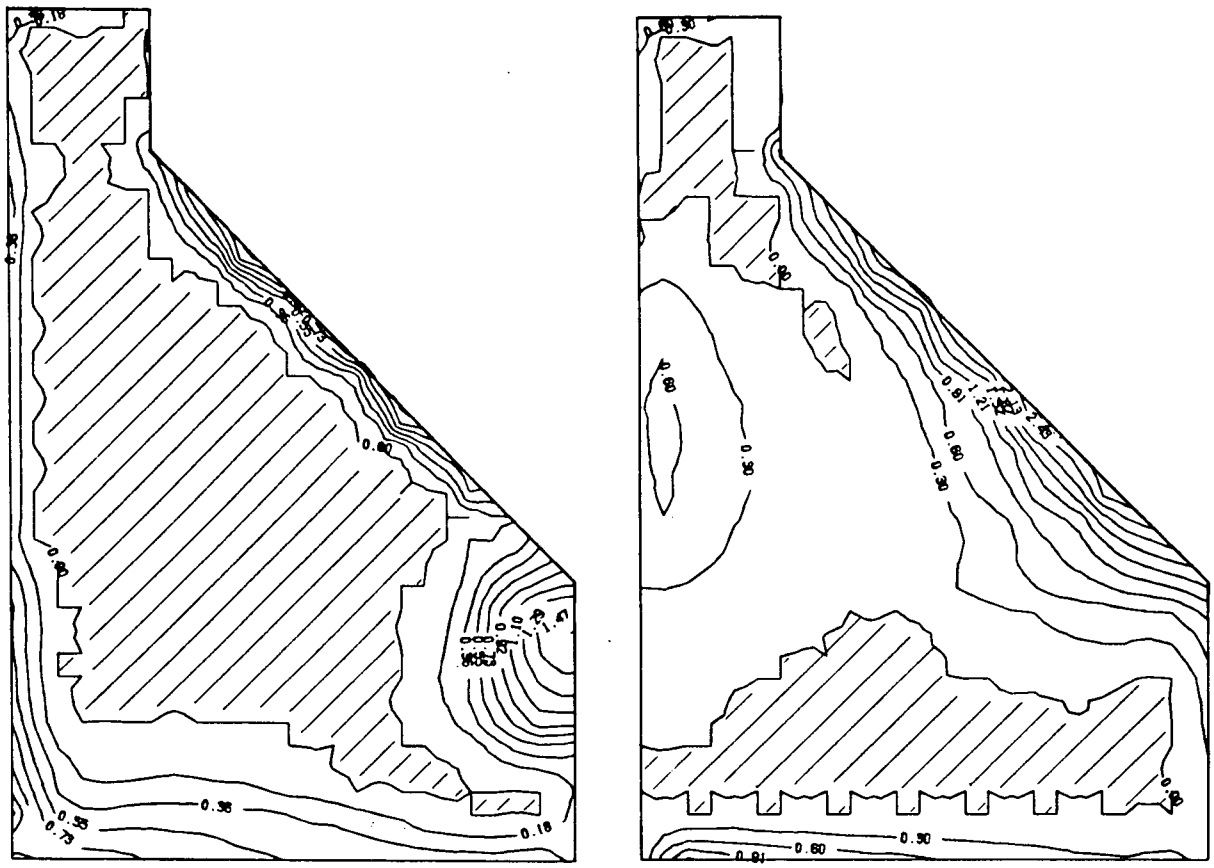

Figure 9.21 MRSS-CRSS (Yield) contours (MPa) for the four growth conditions shown in Table 9.3 and MRSS contours shown in Figure 9.19 (a) Run #1 ; (b) Run #2 ; (c) Run #3 ; (d) Run #4 .

In 1, however, the gradient is almost twice as large as the average gradient in 3. This shows the detrimental effect on stress of gradients which are not constant.

From the results presented in this section it has been shown that the effect of the shape of the imposed temperature profile is very important and that the approximation of a constant gradient in the temperature profile in the boron oxide, as done by Dusseaux[195], gives stresses which are different than the stresses obtained using variable gradients. In addition it has been shown that increasing the boron oxide thickness alone, without considering the changes in the thermal profiles in the surrounding media, does not contribute to a substantial decrease in the stress levels.

9.2 Crystal Length

Conditions : R, 27.5 mm ; B, 21.0 mm

CL : a) 13.75 mm ; b) 27.5 mm ;

c) 55.0 mm ; d) 82.5 mm ;

e) 110 mm .

In the previous section it was shown that the ambient temperature profile is a very important variable in determining the stress level in a growing crystal. This is for both the axial temperature gradient and the curvature of the temperature profile. As a result it is very important to use, as input in the model, temperature profiles which are as close as possible to real conditions inside the crystal growth chamber. Measurements

of temperature profiles during growth have been reported using the thermocouple arrangement shown in Figure 8.18. The results are shown in Figure 8.19 in which curve 4 gives the ambient temperature adjacent to the crystal surface.

The MRSS distribution for the five crystal lengths considered are shown in Figure 9.22(a-e). Comparing distributions shows the following.

1) In all cases high stress levels occur at the centre and the outside part of the crystal. For the shortest crystal, (a) high stresses are also present close to the solid-liquid interface.

2) The location of the maximum (AMRSS) is always at the crystal surface and its position in the axial direction changes with crystal length. For crystal lengths less than the thickness of the encapsulant the position of the AMRSS is below the shoulder. For longer crystals the AMRSS is above the encapsulant-gas surface.

3) The minimum stresses occur at both ends of the crystal and also in a narrow axial band along the crystal, usually half way between the centre and outside part of the crystal. The position of the minimum moves to the crystal surface at both ends. The stress distribution in the radial direction always exhibits a W shape . Close to the ends the valleys in the W are closer to the outside part of the crystal.

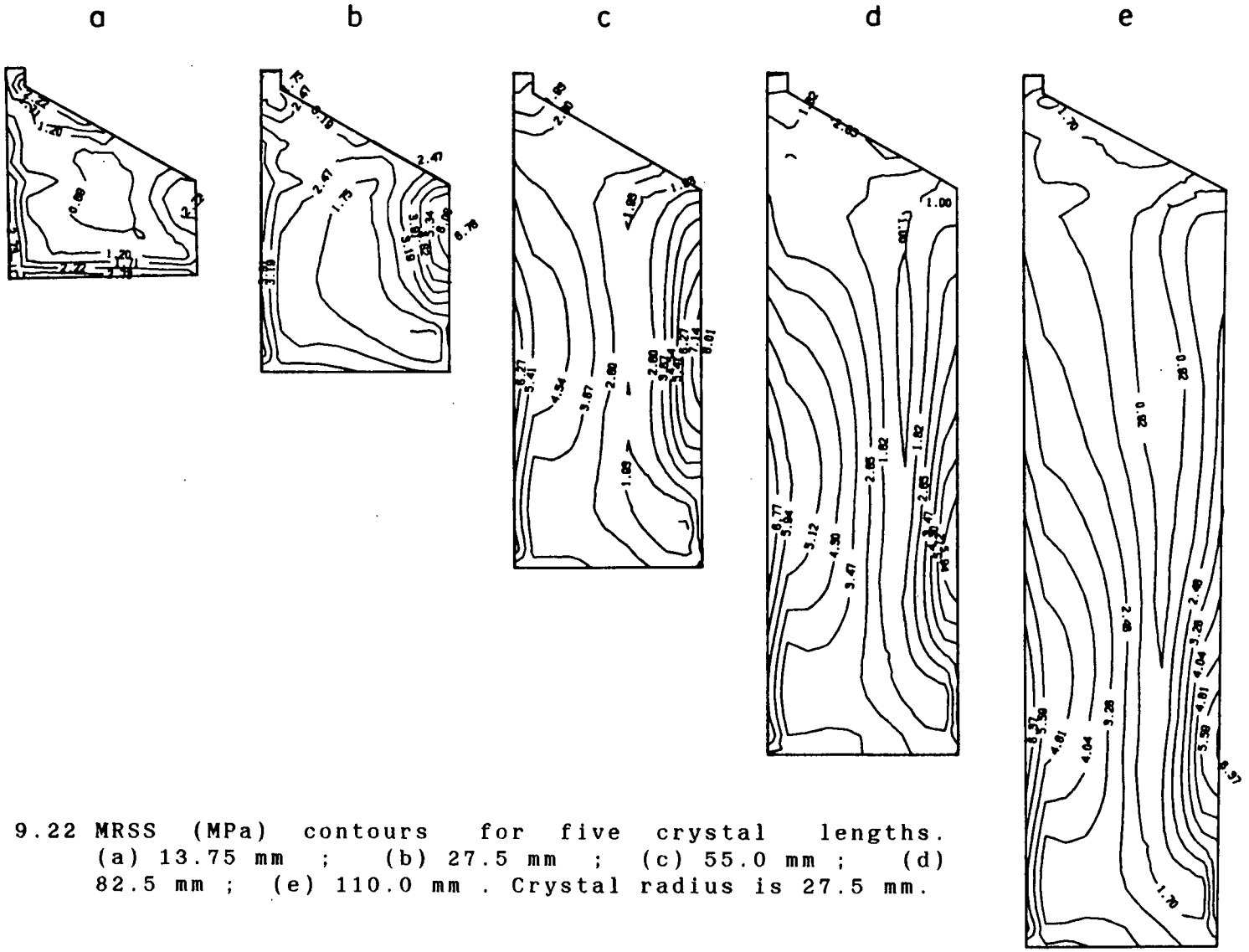

Figure 9.22 MRSS (MPa) contours for five crystal lengths. (a) 13.75 mm ; (b) 27.5 mm ; (c) 55.0 mm ; (d) 82.5 mm ; (e) 110.0 mm . Crystal radius is 27.5 mm.

4) The value of the AMRSS which is representative of the stress level in the whole crystal, increases with crystal length, reaching a maximum value for (c), and slightly decreases for longer crystals. The maximum AMRSS for (c), for a crystal length of 55.0 mm (aspect ratio = diameter/length = 1) is the result of two main factors. First, higher stresses are expected above the encapsulant surface because of the discontinuity in the media surrounding the crystal. This produces a sudden change in heat transfer coefficient and gives a maximum curvature in the temperature profile in the surrounding media. In Figure 8.19 curve 4, this is observed at 30 mm from the interface. As a result of these changes in the temperature field the stresses are high. The second factor contributing to the largest AMRSS for (c) is related to the geometry of the deformation. For the 55 mm crystal length the effect of the thermal transition occurs at the midlength of the crystal. The material in this region is more restrained to deform than the regions close to the ends. This quasi-plane strain deformation gives higher stresses.

The contours of the MRSS-CRSS (Yield) for the five crystal of increasing lengths are shown in Figure 9.23(a-e). The results are similar to the MRSS considered previously. In addition it can be observed that at the shortest length for (a) there is a small area in the cone as well as below the cone where the MRSS is less than the CRSS (Yield). For the two largest crystals ((d) and (e))

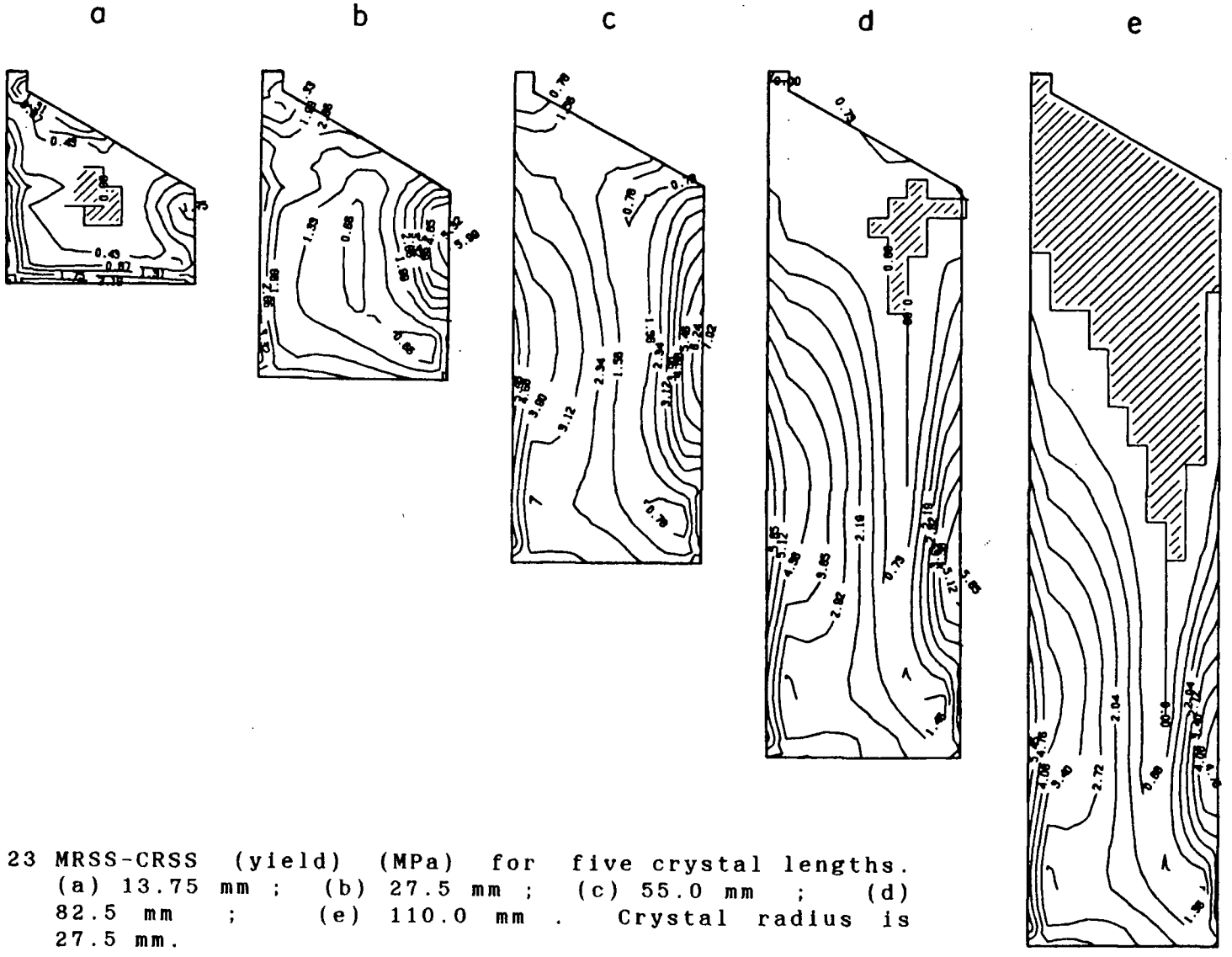

Figure 9.23 MRSS-CRSS (yield) (MPa) for five crystal lengths. (a) 13.75 mm ; (b) 27.5 mm ; (c) 55.0 mm ; (d) 82.5 mm ; (e) 110.0 mm . Crystal radius is 27.5 mm.

the top of the crystal does not develop stresses higher than the CRSS (Yield). When the CRSS (MB) stresses for dislocation generation in undoped GaAs is considered, the contours and stress values are very similar to those obtained for the MRSS (Figure 9.22). The contours of the MRSS-CRSS (MBTe) in Te-doped material are similar to those obtained when the yield stress is considered and shown in Figure 9.23.

The operative slip mode of the MRSS as a function of position in the crystal is shown in Figure 9.24(a-e). The distribution indicates that the slip mode operating may not be associated with the stress level. The slip mode alternatively may be related to specific regions in the crystal. The most frequent modes are III and IV. Mode III appears in the area of maximum stress above the encapsulant surface and at the centre of the crystal. It also appears in the cone and in the central region at a distance from the interface greater than 27.5 mm. Mode IV preferentially appears in the following regions (a) close to the interface (b) above the region of maximum stresses and (c) below the shoulder. The other slip modes are less frequent.

9.2.1 Effect of crystal Length on Stress Symmetry

The effect of crystal length on stress symmetry is presented in two ways. First, different cross-sections are followed during growth and the symmetry changes are described. Following this the symmetry at each crystal length is considered and the changes with length are reported.

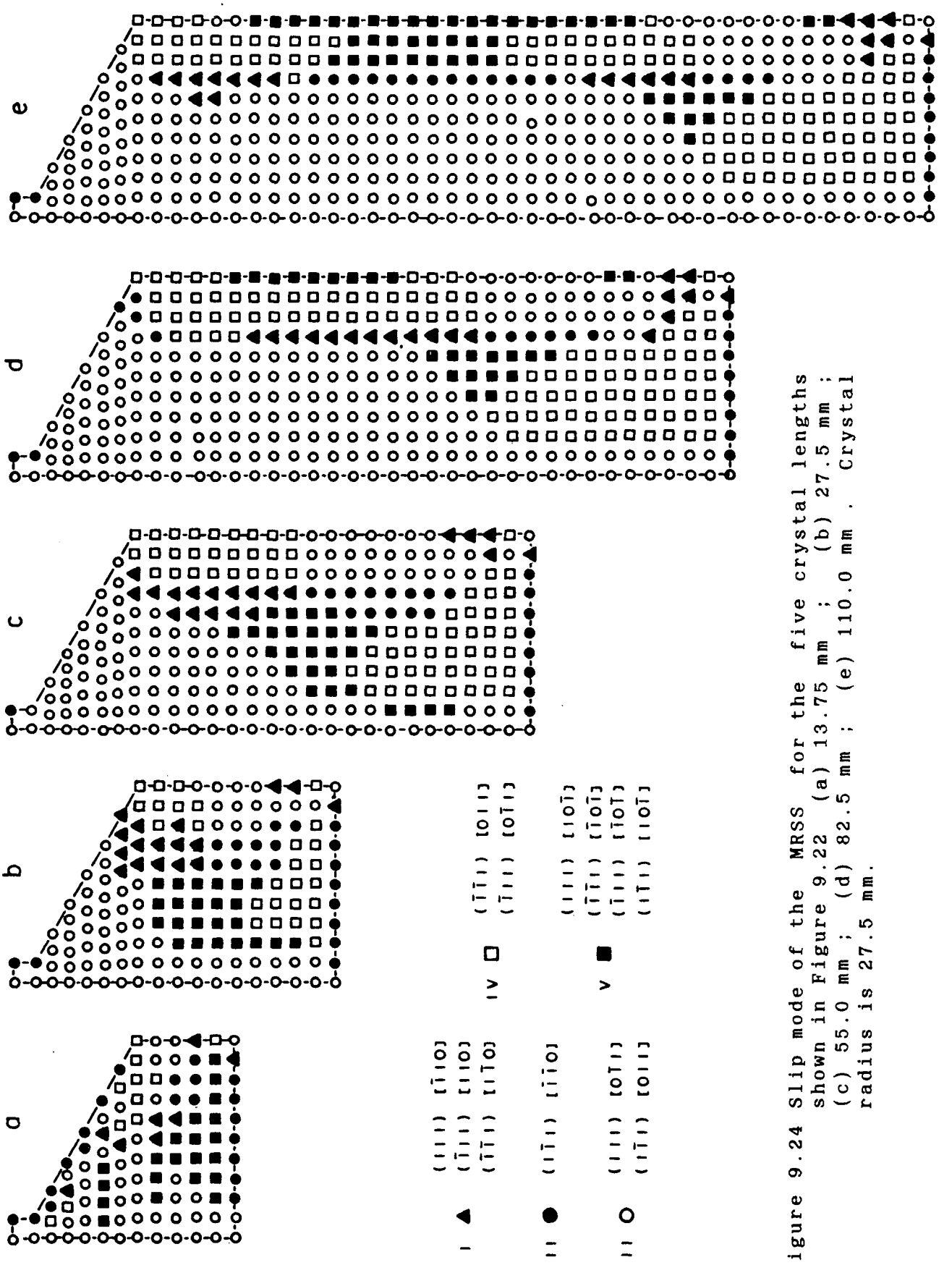

Figure 9.24 Slip mode of the MRSS for the five crystal lengths shown in Figure 9.22 (a) 13.75 mm ; (b) 27.5 mm ; (c) 55.0 mm ; (d) 82.5 mm ; (e) 110.0 mm . Crystal radius is 27.5 mm.

Considering the stress symmetry during growth four sections fixed in the crystal are examined at 8.25 mm, 49.5 mm, 77.0 mm and 104.5 mm from the cone. The symmetry and stress levels in these cross-sections are considered in relation to dislocation formation. In the model the dislocation density formed at any given time and position is assumed to be proportional to the MRSS-CRSS (Yield). However, the stress level changes during growth. It is therefore important to introduce two new considerations. The first is related to hardening. The effect of hardening is to decrease the effective stress in the crystal due to dislocation interactions. The decrease in stress is proportional to the square root of the dislocation density, i.e. $A \times \sqrt{n}$, where A is the interaction constant and n is the dislocation density. According to Vakhrameev et al.[192] A varies from 2 to 4 x 10^{-2}MPa x m. The magnitude of stress involved in the interaction varies between 4 x 10^{-3}MPa and 4 x 10^{-2}MPa for dislocation densities of 10^{2} to $10^{4}/cm^{2}$. These stresses are negligible with respect to the thermoelastic stresses developed during growth. Therefore it may be concluded that the hardening effect is minimal for normal dislocation densities.

The second consideration is partially a consequence of the first and is related to the increase in dislocations after each step during growth. Because there is no hardening effect it is assumed that the dislocation density in a given section increases proportionally to the difference in MRSS-CRSS (Yield) values between two steps. The final density is given by the maximum stress reached at each point.

The specific observations in the four sections follow. In all cases the MRSS-CRSS (Yield) is considered.

1) Section at 8.25 mm from the cone.

CL : (a) 13.75 mm ; (b) 27.5 mm ;

(c) 55.0 mm ; (d) 82.5 mm .

The stress distibutions at the four steps are shown in Figure 9.25(a-d). The distribution shown in (a) corresponds to an early stage of growth when the crystal is contained by the encapsulant. The stress level in most of the crystal section is less than 1 MPa. The symmetry changes depending on the position in the section. Circular symmetry is obtained in the centre which changes to four-fold, eight-fold, circular and finally eight-fold on moving from the centre to the edge of the crystal. In Figure 9.25(a) the dislocation density is low and has the same symmetry. In (b) the stress level at the edge is about 6 times higher than in (a). The changes are not as important at the centre where the stress has not quite doubled. In a ring midway between the centre and the edge the stress has substantially increased. The symmetry is almost circular except at the edge where the eight-fold symmetry is stronger than in (a). In (c) the stress at the periphery has decreased 30 % with respect to (b). At the centre the stress has doubled. In the central area the symmetry has taken a more definite four-fold pattern which appears again in the ring midway between the centre and the edge. In this case there is a slight two-fold symmetry which can be seen as an elongation of the minimum stress area in the [110] direction with

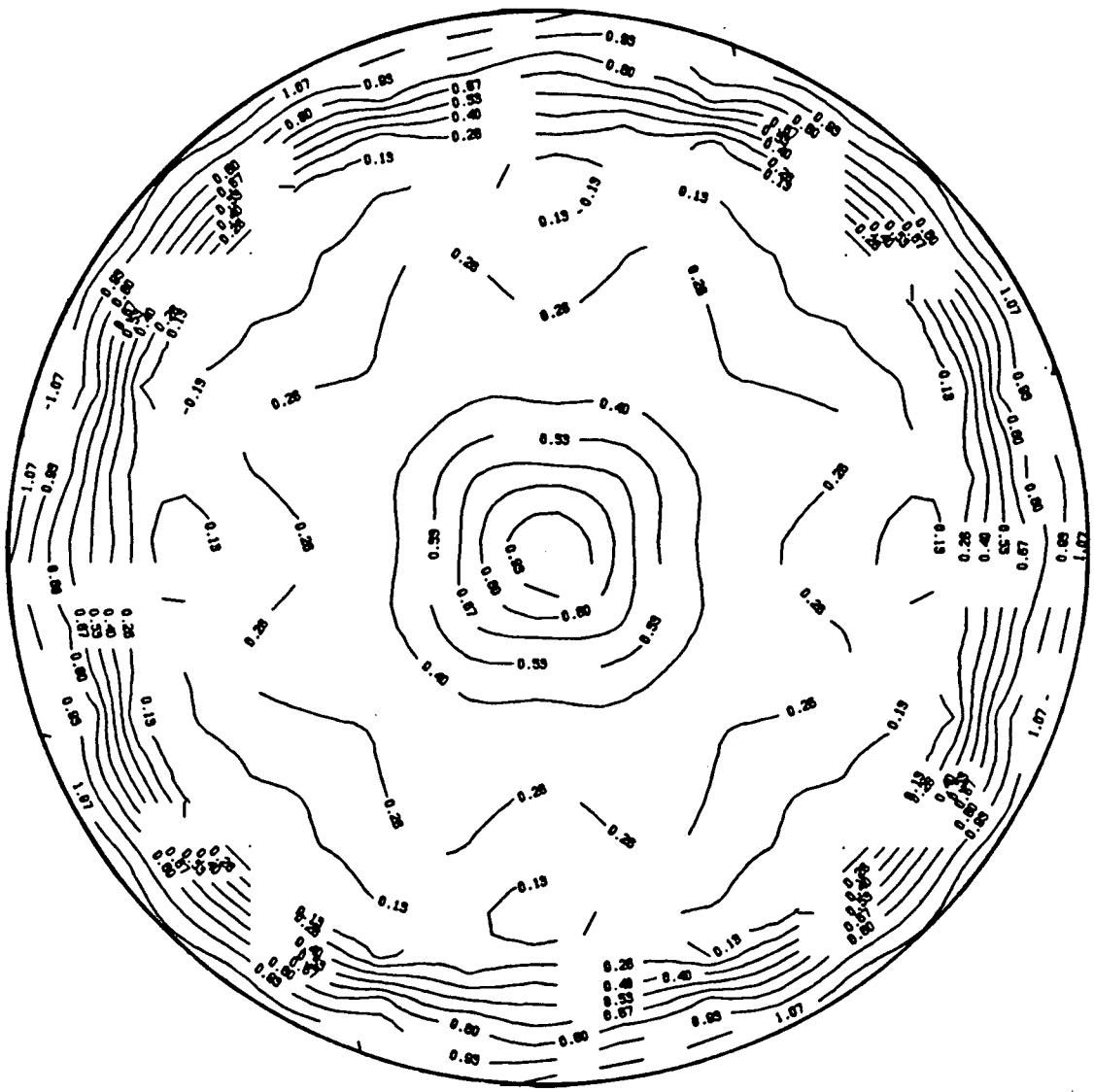

a

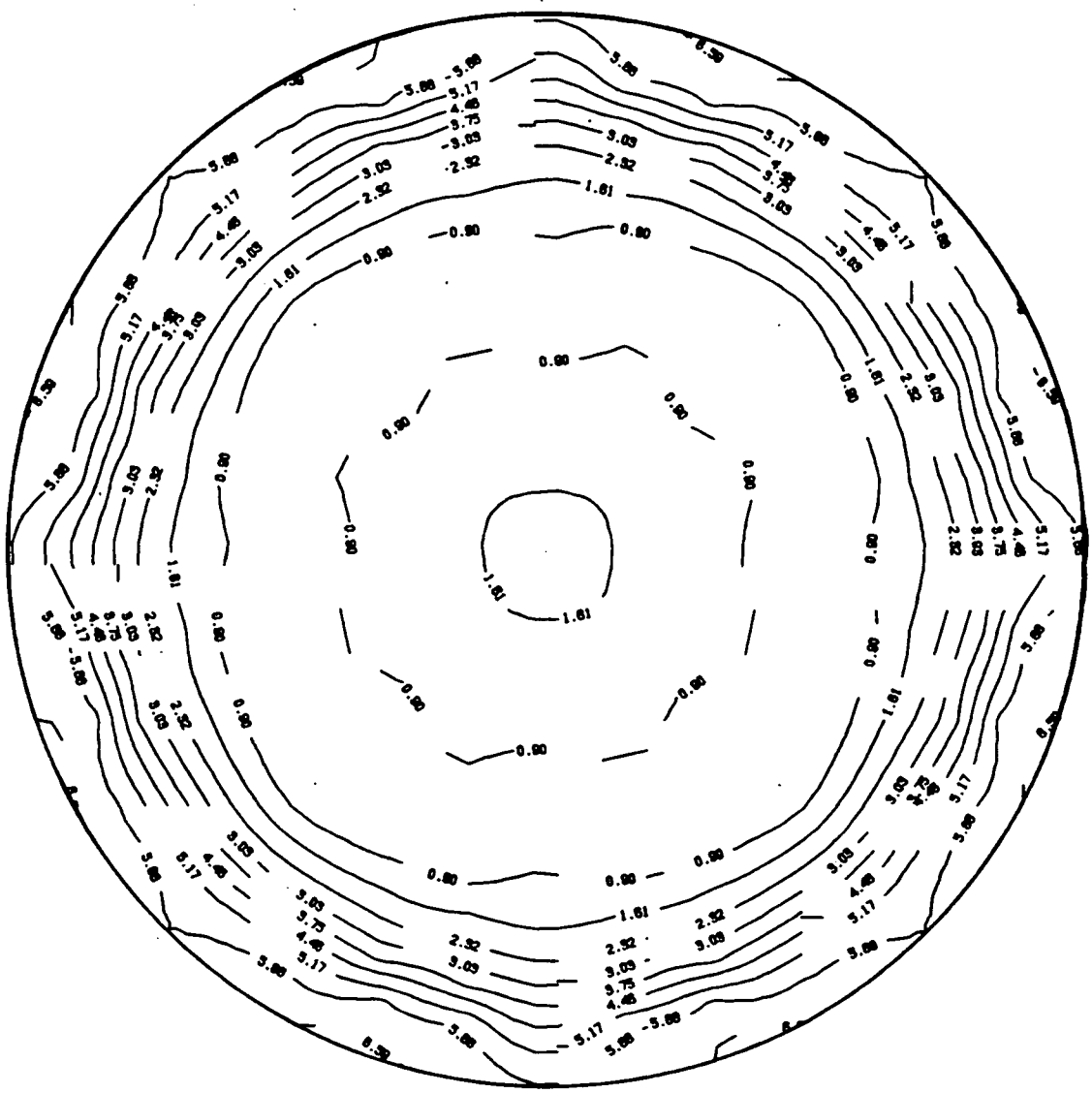

b

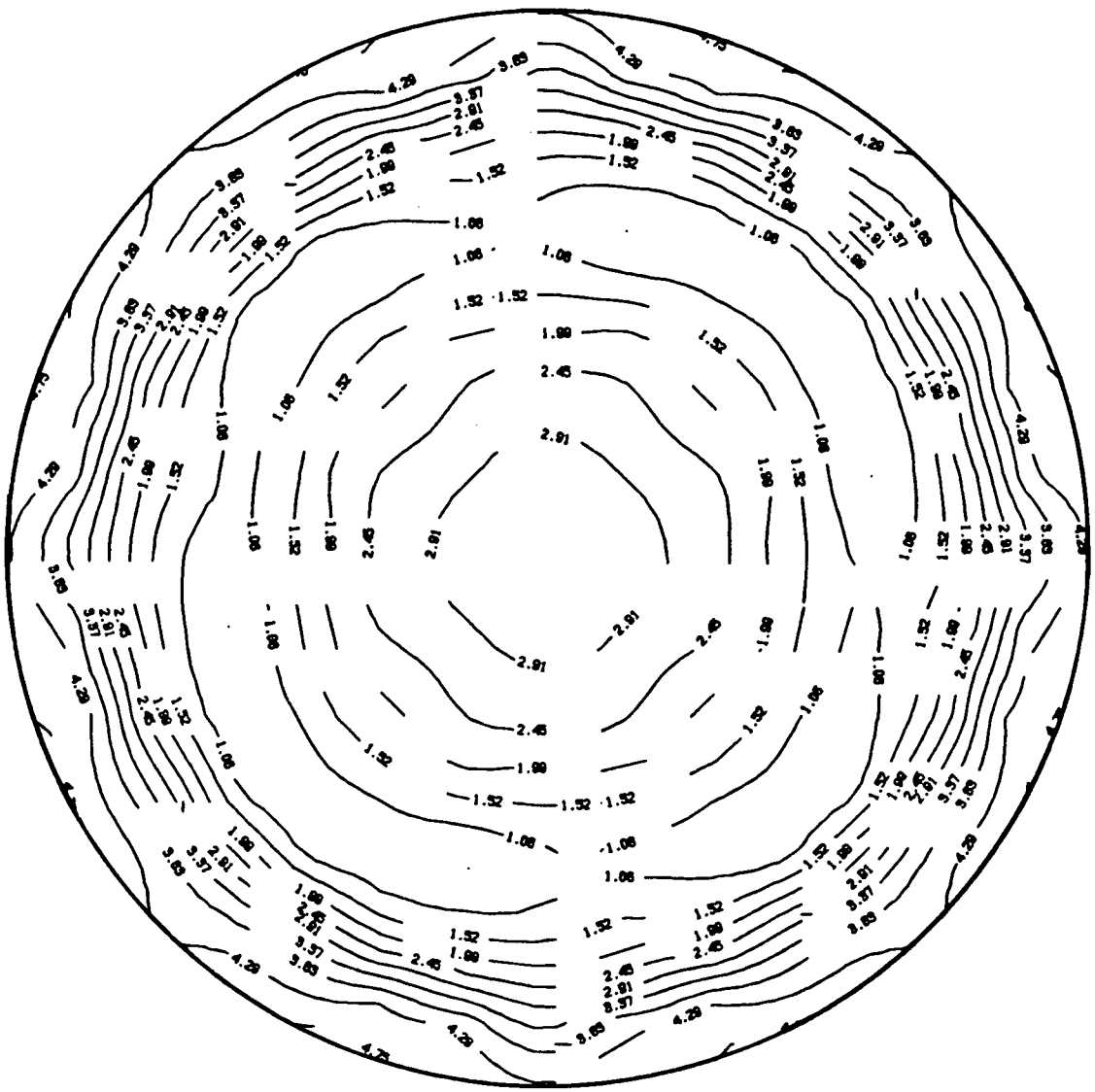

C

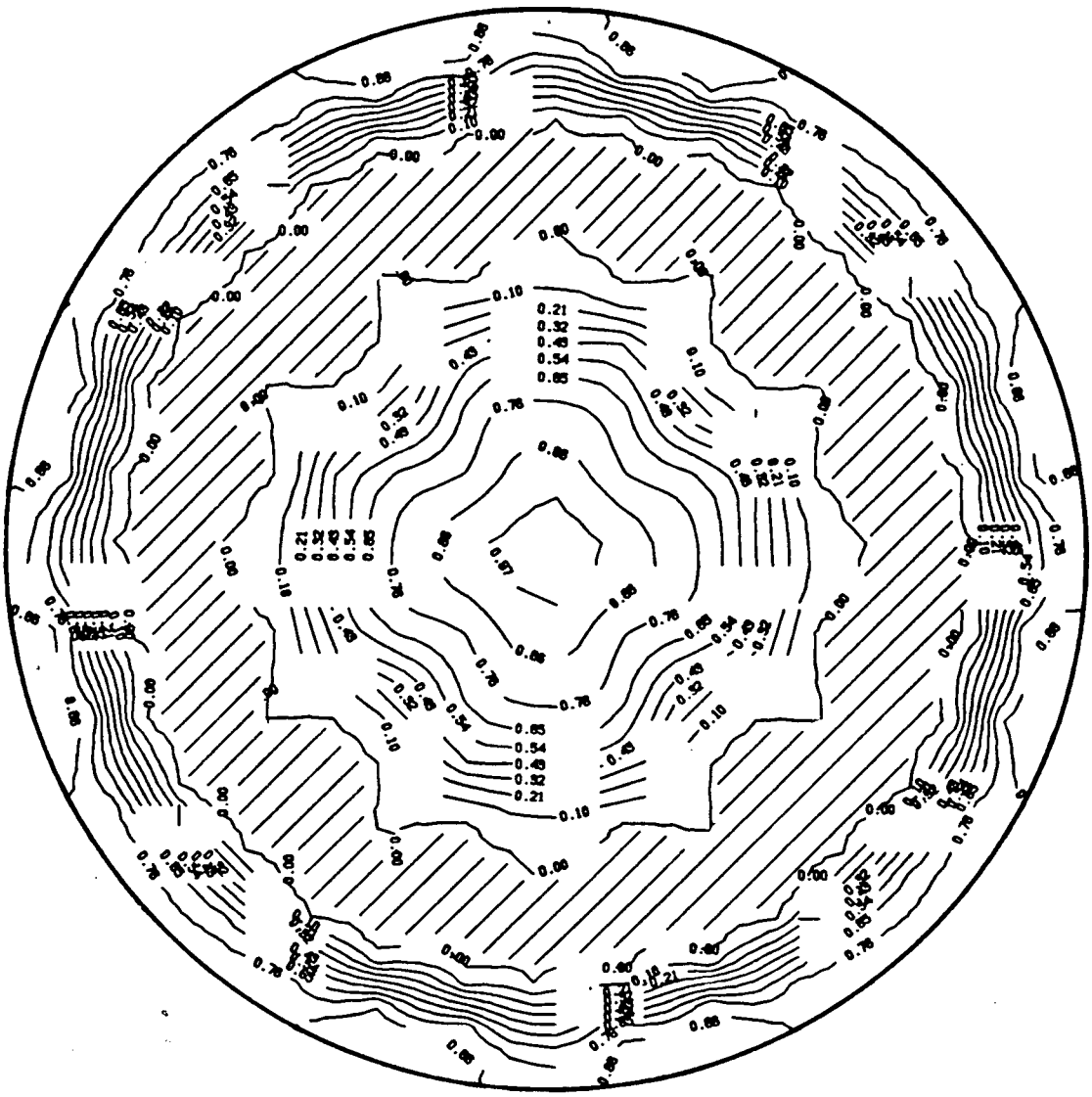

d

Figure 9.25 MRSS-CRSS (Yield) (MPa) in a (001) plane at a distance of 8.25 mm from the cone at four crystal lengths. (a) 13.75 mm ; (b) 27.5 mm ; (c) 55.0 mm ; (d) 82.5 mm. Crystal radius 27.5 mm.

respect to the [110] direction. In (d) the stress level has decreased in the whole wafer and therefore no more dislocations are generated with further growth. At the end of growth the final dislocation density distribution in this wafer will be determined by the maximum stress reached during growth. At the edge this stress is reached in (b). At the centre and midway region the largest stress is reached in (c). From these maximum values it may be predicted that the wafer will show a W-shaped dislocation distribution along a diameter. The branches of the W will be more than twice as high as the centre. The eight-fold symmetry at the edge will be hardly noticed since it occurs in a narrow ring with dislocation variations of the order of 10 % . The four-fold symmetry will be also very weak.

2) Section at 49.5 mm from the the cone.

CL : (a) 55.0 mm ;

(b) 82.5 mm .

The stress distributions for cross-sections at 49.5 mm from the cone is shown in Figure 9.26(a) and (b). Figure 9.26(a) corresponds to a stress distribution close to the interface. The following characteristics can be distinguished. The central part has four-fold symmetry and the rest of the surface has almost circular symmetry. The stress level is the same at the centre and the edge, and the minimum occurs close to the edge.

In (b) the stress level in the central region has increased by 50 % and at the edge the stress has doubled with respect to (a). The symmetry in (b) is almost circular throughout the

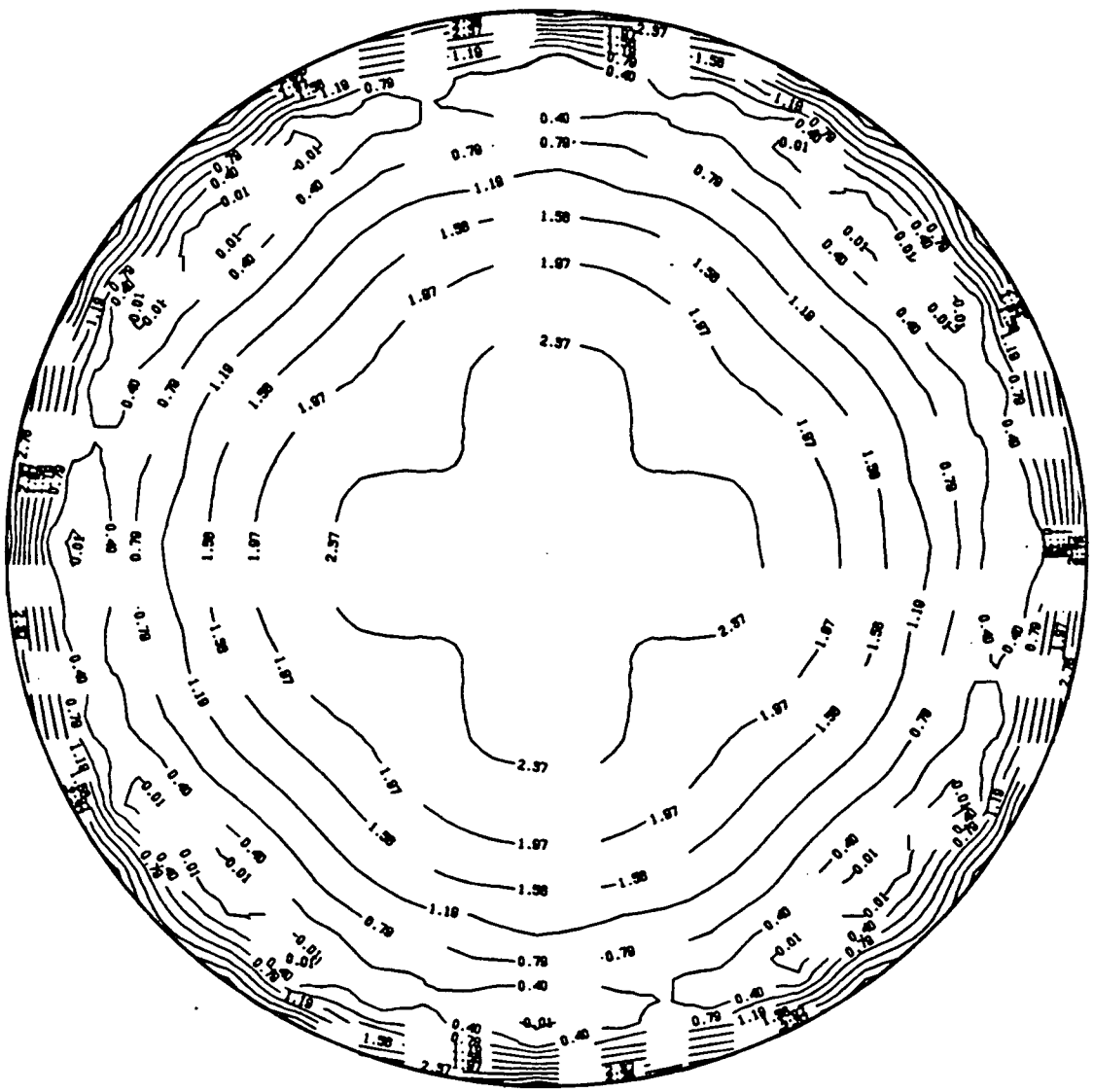

a

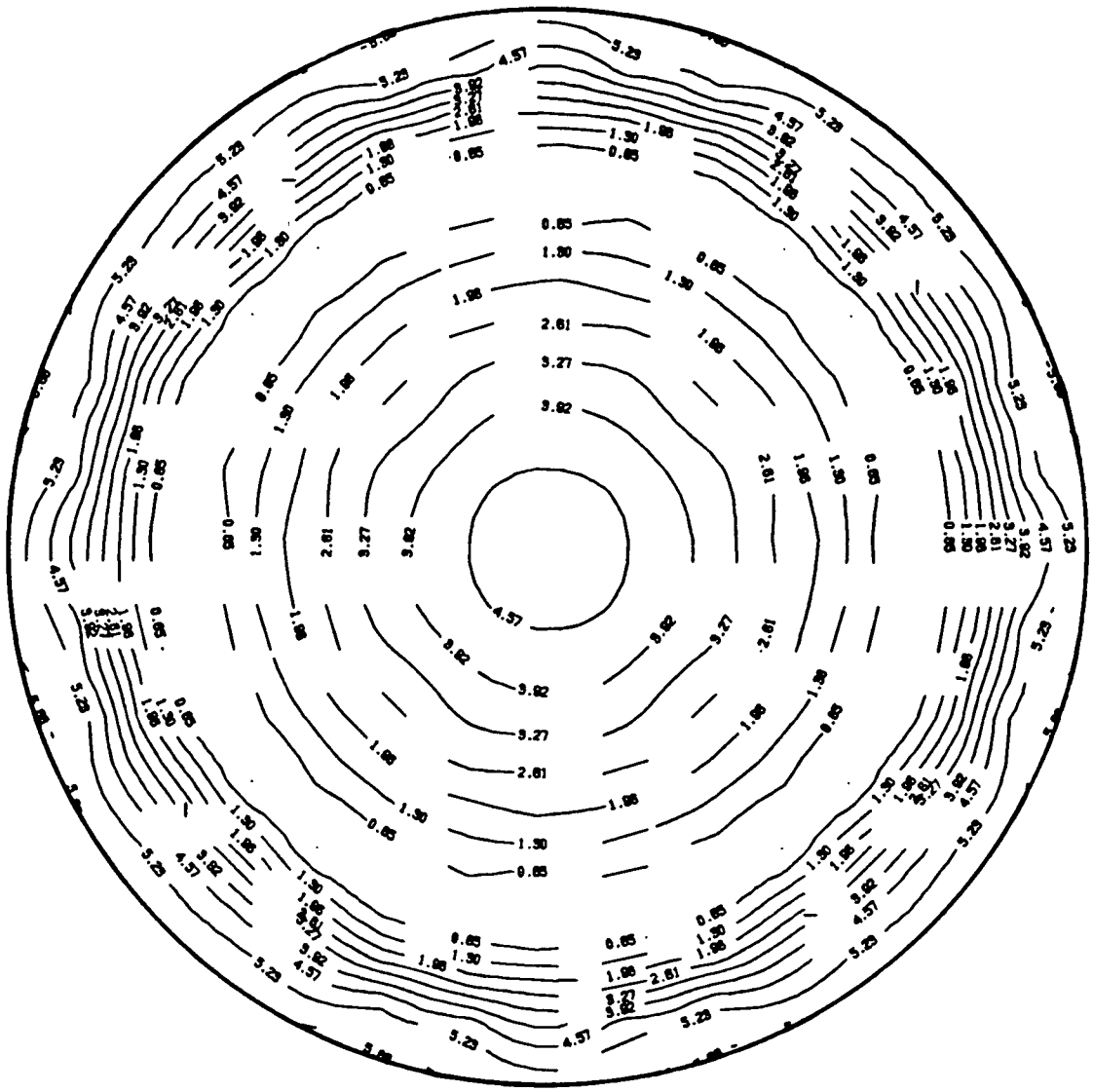

Figure 9.26 MRSS-CRSS (Yield) (MPa) in a (001) plane at a distance of 49.5 mm from the cone at two crystal lengths. (a) 55.0 mm ; (b) 82.5 mm. Crystal radius 27.5 mm.

section. The final maximum dislocation density in this wafer may be determined by the stresses developed in (b). In this case a W-shaped distribution is predicted with the center of the W of the same height as the branches. Since a considerable number of dislocations are generated in (a) with four-fold symmetry, this will be present in the final distribution. When the dislocation density distribution predicted in this section is compared with the final dislocation distribution given in (1) for a section close to the cone, the predicted dislocations far from the cone will be 10 % lower in the outer region and 50 % higher in the centre.

3) Section at 77.0 mm from the cone.

CL : (a) 82.5 mm ;

(b) 110.0 mm .

The stress distributions for a wafer 77 mm from the cone are shown in Figure 9.27(a) and (b). Similar patterns as in 2) are observed in this case. The differences are that in (a) the four-fold symmetry is expanded and in (b) there are four minimum stress regions midway between the centre and the edge in the <100> directions.

4) Section at 104.5 mm from the cone.

CL : 110.0 mm.

The only cross-section available at this distance from the cone corresponds to the longest crystal shown in Figure 9.21(e) and it is close to the solid/liquid interface. The stress

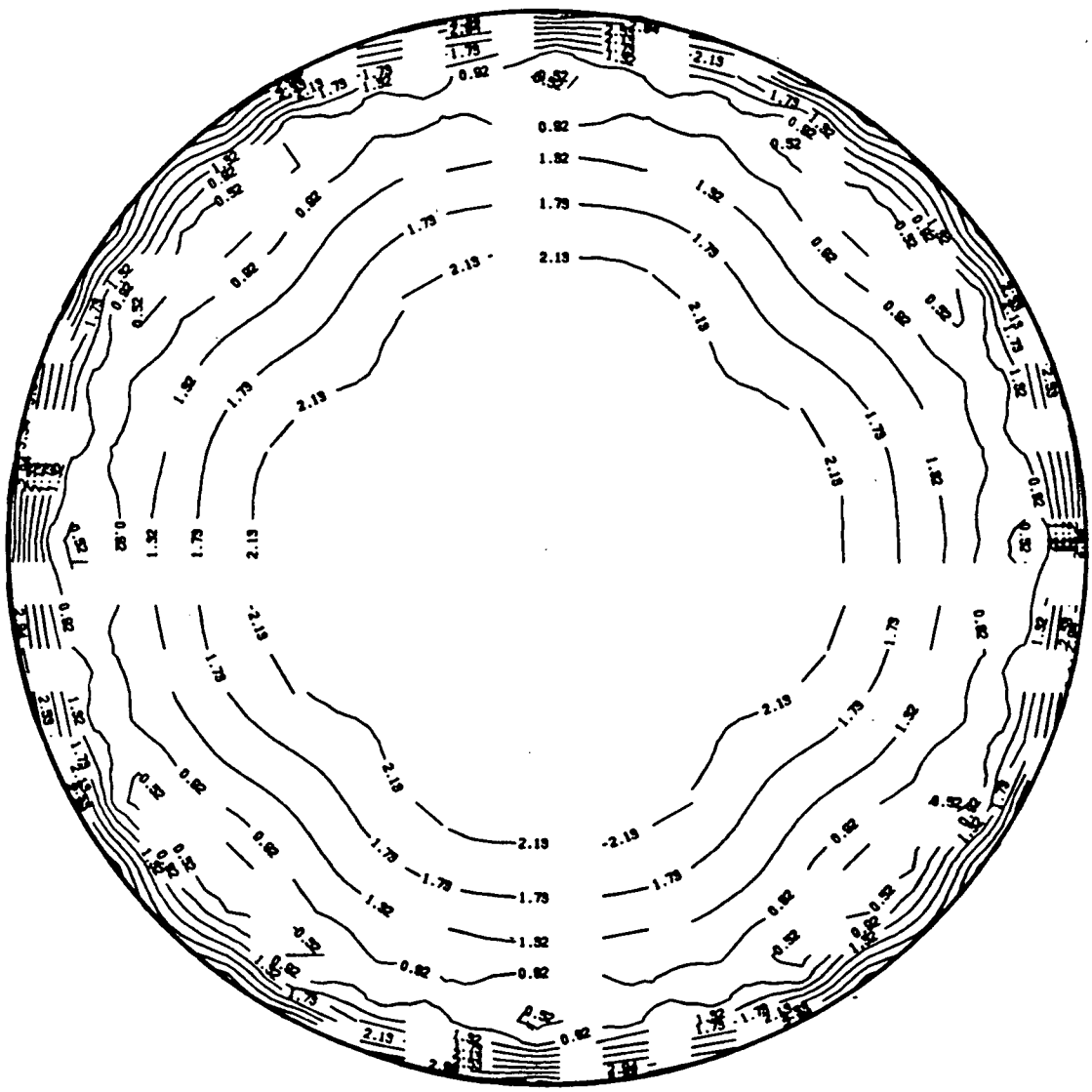

D

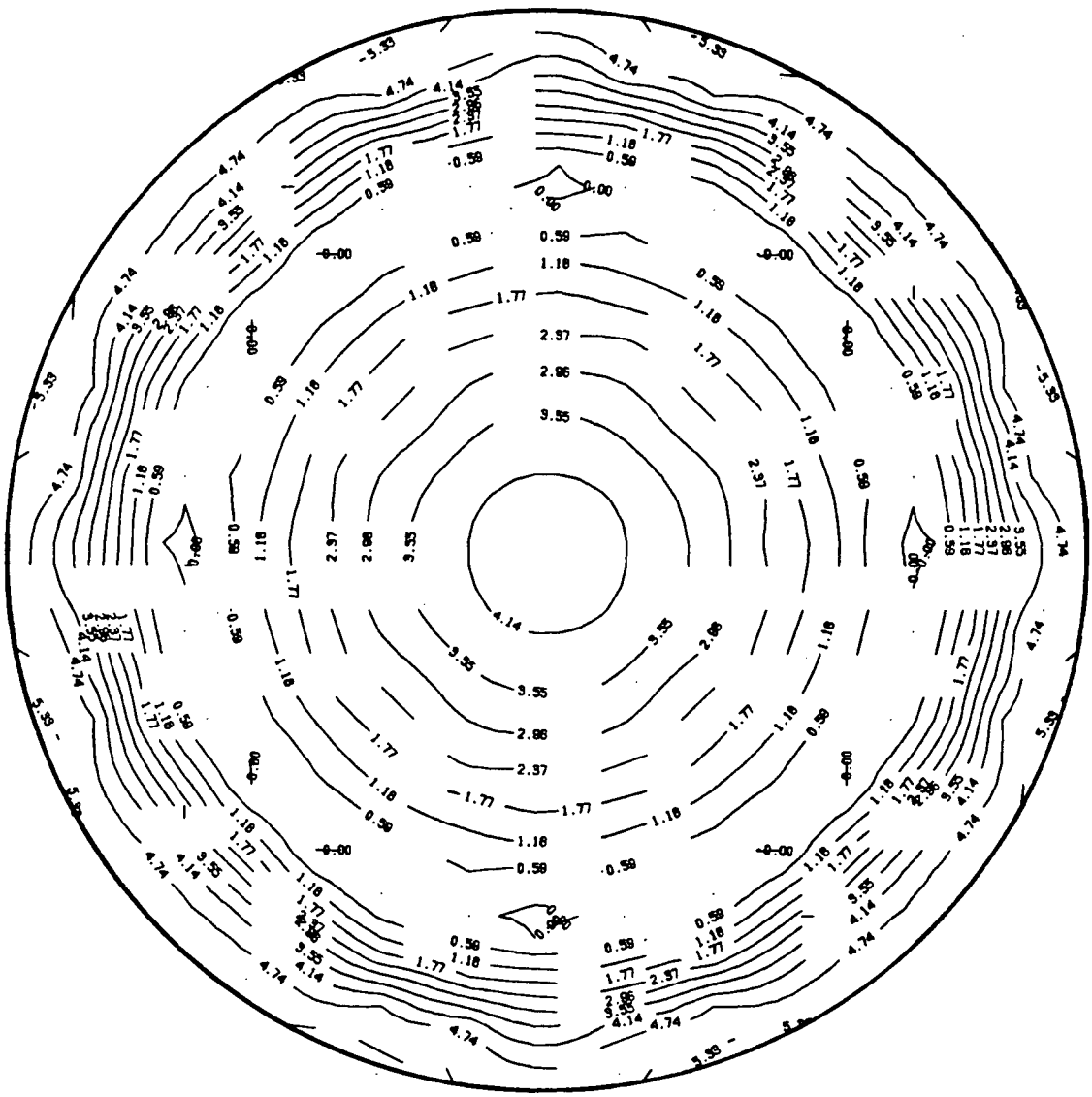

Figure 9.27 MRSS-CRSS (Yield) (MPa) in a (001) plane at a distance of 77.0 mm from the cone at two crystal lengths. (a) 82.5 mm ; (b) 110.0 mm. Crystal radius 27.5 mm.

distribution in this section is very similar to the distribution shown in Figure 9.27(a). If growth is completed when this length is reached the dislocation distribution at the tail end will have the features observed in Figure 9.27(a). These are

1) an expanded four-fold symmetry,

2) a dislocation distribution in the radial direction with a W shape across the diameter having a minimum very close to the edge, a wide peak in the centre, and branches equally high. The average dislocation density in this wafer will be half of the dislocation density for a wafer considered in 3) at 27.5 mm.

If instead of following the stress distributions during growth in specific sections, the distributions of stresses are observed along the crystal at each of the five lengths considered, the following patterns can be observed.

1) The eight-fold symmetry at the edge of the sections is always present. This symmetry is associated with an eight-fold distribution of the slip mode of the MRSS.

2) In the radial direction, the stress distribution always shows a W shape.

3) The four-fold symmetry is stronger close to the interface between 5.5 mm and 11.0 mm. It also appears at the top of the crystal near the cone.

4) A slight tendency to a two-fold symmetry when present is always accompanied by a four-fold symmetry.

5) Far from the ends, at least 13.75 mm, the stress symmetry is almost axisymmetric with slight four-fold symmetry at the center and eight-fold symmetry at the edge.

6) For crystal lengths larger than 55.0 mm, cross-sections far from the interface have the minimum stress levels in the <100> directions rather than in the <110> directions. The area where this minimum occurs is very small.

9.3 Crystal Radius

Conditions : R, 40.0 mm ; CA, 30° ; B, 21.0 mm ;
AP, 30 atm ;
CL : (a) 10.0 mm ; (b) 40.0 mm ;
(c) 80.0 mm ; (d) 100.0 mm .

The effect of increasing the crystal radius from 27.5 mm to 40 mm on internal crystal stresses and dislocation distributions is determined assuming that the temperature profile in the medium surrounding the crystal has not changed when the radius is increased. In this case the temperature profile is given in Figure 8.19 (curve 4).

Values for the MRSS at the four crystal lengths considered are shown in Figure 9.28(a-d). The MRSS distributions follow the

same general patterns as those observed with the smaller crystal radius, with two main differences. The first is that the maximum stress, considering the whole growth process, occurs when the crystal is 40.0 mm long in (b), with an aspect ratio of 1 rather than 2 as in the smaller crystal. This difference is consistent with the explanation given in the last section. The maximum stress usually occurs above the encapsulant surface. If this position coincides with the midlength position in the crystal there is an extra contribution to the stress due to the quasi-plane strain conditions prevailing there. The second difference is the higher stress level for the larger crystal. In this case increasing the radius 45 % increases the stresses by 40 % indicating that the MRSS increases proportionally with the radius.

The effect of increasing the radius on stress levels has been explained in the literature by considering the effect of increasing the radius on the thermal field. As pointed out previously, the results for the effect of radius on temperature fields are contradictory. This could result from the limitations of the solutions employed to study this effect. In the present investigation the effect of radius on thermal gradients is first considered as a possible cause for the observed effect on stresses. The comparison can be made using two criteria. It can be made for two crystals of same aspect ratio, or between two crystals with the same length. In this investigation the second method is chosen. (The conclusions obtained with both methods are similar). For the comparison crystal lengths for which the

maximum stresses occur are chosen. For the 27.5 mm radius crystal the length is 55 mm. For the 40.0 mm radius crystal the length is 40 mm. Because the lengths are different, another length for the 40 mm radius crystal is also considered, specifically 80 mm length. For the three crystals, gradients in two directions are considered ; axial gradients along the crystal axis and average radial gradient. The calculated gradients are shown in Figure 9.29(a) for the axial gradients and (b) for the radial gradients as a function of distance from the interface. Curve (1) corresponds to the 27.5 mm crystal and curves (2) and (3) for the 40 mm crystal. It can be observed in the figures that the curve (3) is below curve (1) in (a) and curve (1) is between (2) and (3) in (b). From these observations it can be concluded that the thermal field is not influenced by changes in radius and that the large change in stress observed cannot be accounted for by the change in thermal field.

An alternative explanation for the effect of radius on stress is related to the specific geometry of the crystal. In the case of cylindrical bodies the radial gradient has a different effect on stresses than in cubic geometries. In cylinders a constant radial gradient can develop stresses ; in cubes it cannot. A radial gradient in a cylinder generates incompatibilities in the strain components for free expansion. From the present results it is concluded that the same radial gradient in two cylinders of different radius creates larger incompatibilities in a crystal with larger radius. This is more clearly seen when it is considered that the effect of thermal

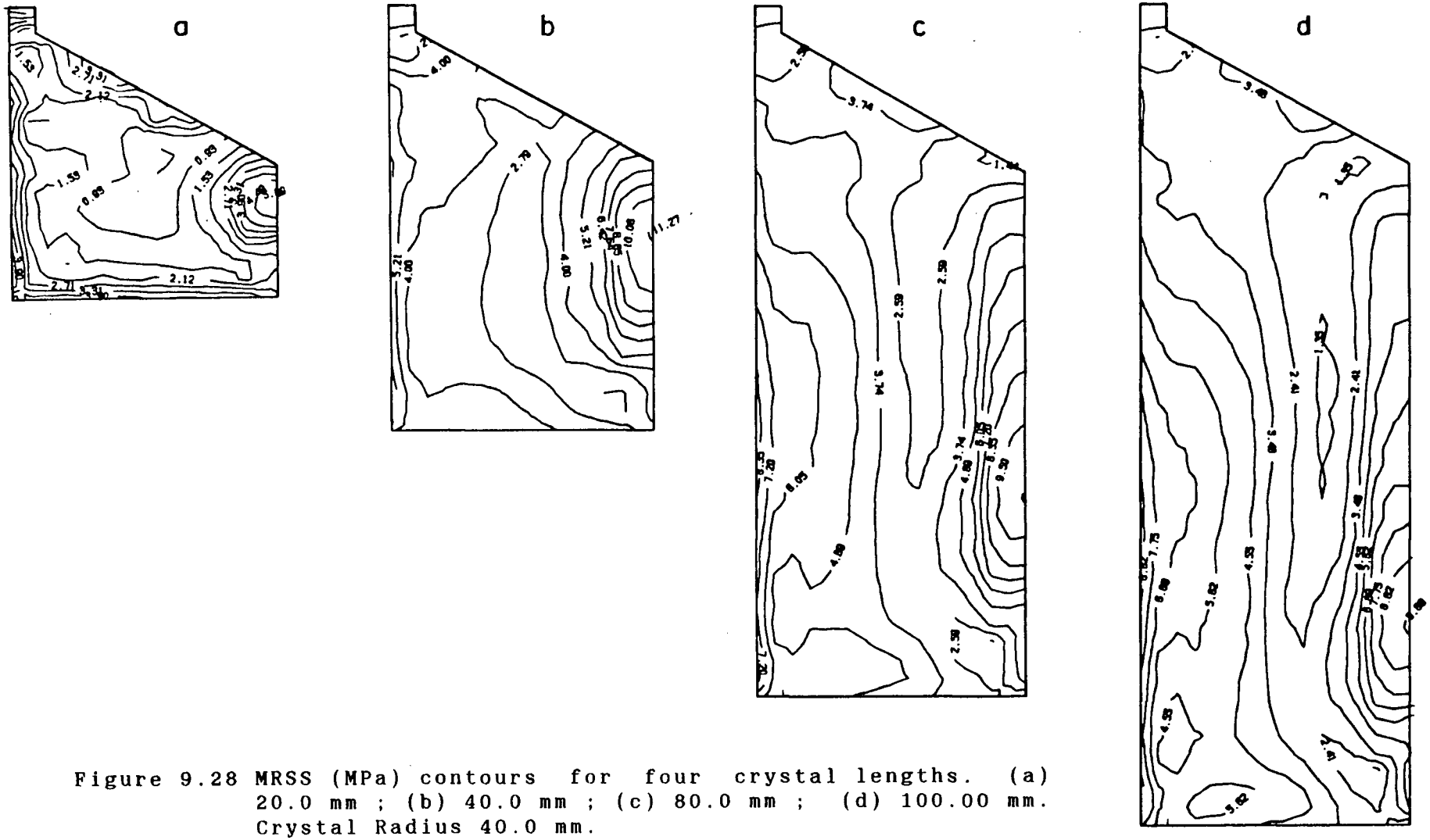

Figure 9.28 MRSS (MPa) contours for four crystal lengths. (a) 20.0 mm ; (b) 40.0 mm ; (c) 80.0 mm ; (d) 100.00 mm. Crystal Radius 40.0 mm.

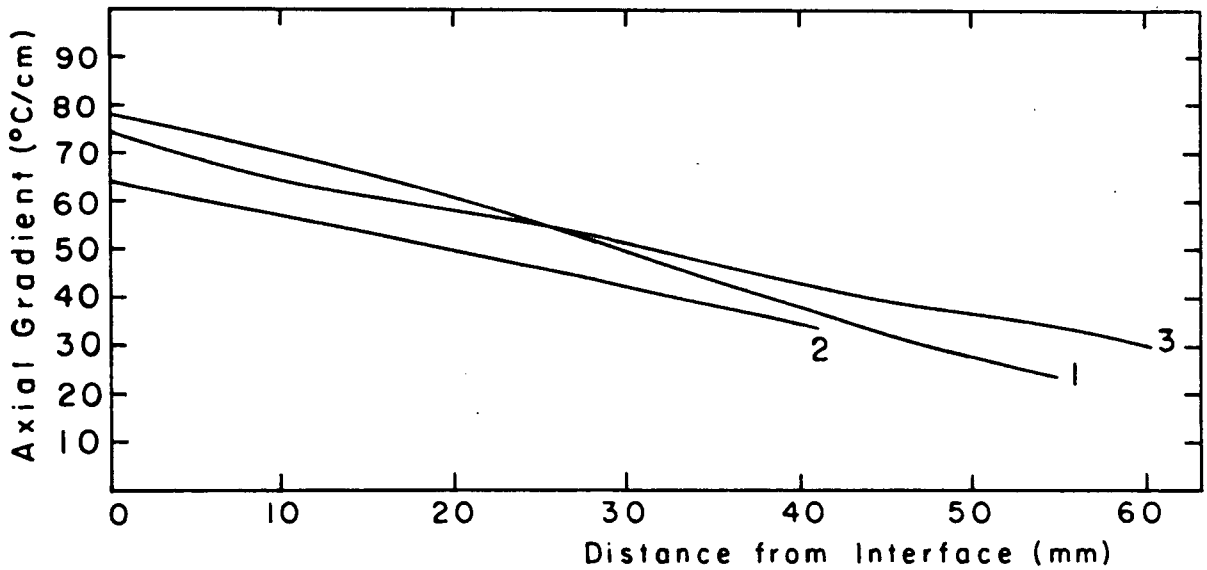

a

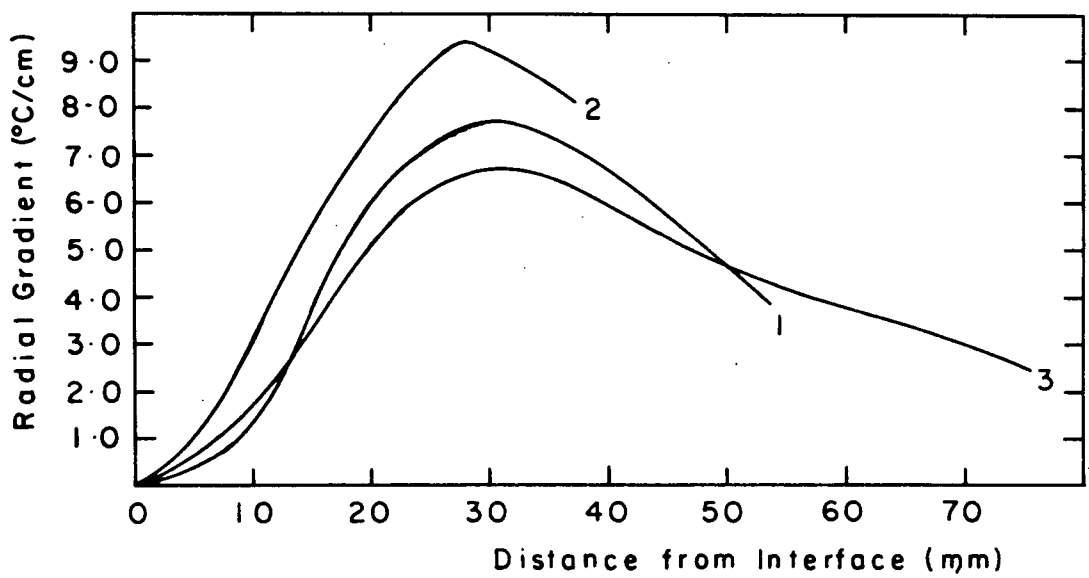

b

Figure 9.29 (a) Axial along the crystal axis and (b) radial thermal gradients as a function of distance from the interface for two crystal radius. Curve (1) for a radius of 27.5 mm ; and curves (2) and (3) for a radius of 40.0 mm. Crystal lengths are (1) 55.0 mm ; (2) 40.0 mm and (3) 80.0 mm.

strain is included as an initial strain calculated as a free expansion from a reference temperature. This free expansion (contraction in this case) increases with increasing distance from the centre. The degree of incompatibility is expected to follow the expansion, which in turn will generate larger stresses.

The effect of a constant radial gradient G on the stress in cylinders of different radii can be quantitatively evaluated using the plane strain approximation. The stress components for a temperature field T = -Gr

$$\sigma_r = \frac{G}{3}(r - r_0)\frac{\alpha E}{1 - \nu}$$

$$\sigma_\theta = \frac{G}{3}(2r - r_0)\frac{\alpha E}{1 - \nu}$$

$$\sigma_z = G(r - 2/3r_0)\frac{\alpha E}{1 - \nu}$$

It can be seen that the stress components increases linearly with the radius r_0.

The MRSS-CRSS (Yield) contours for the four lengths considered are shown in Figure 9.30(a-d). The results shown are similar to those obtained with the smaller crystal, with areas having stress levels below the CRSS in (a) and (d). The distribution of the MRSS-CRSS (Yield) for the four crystal

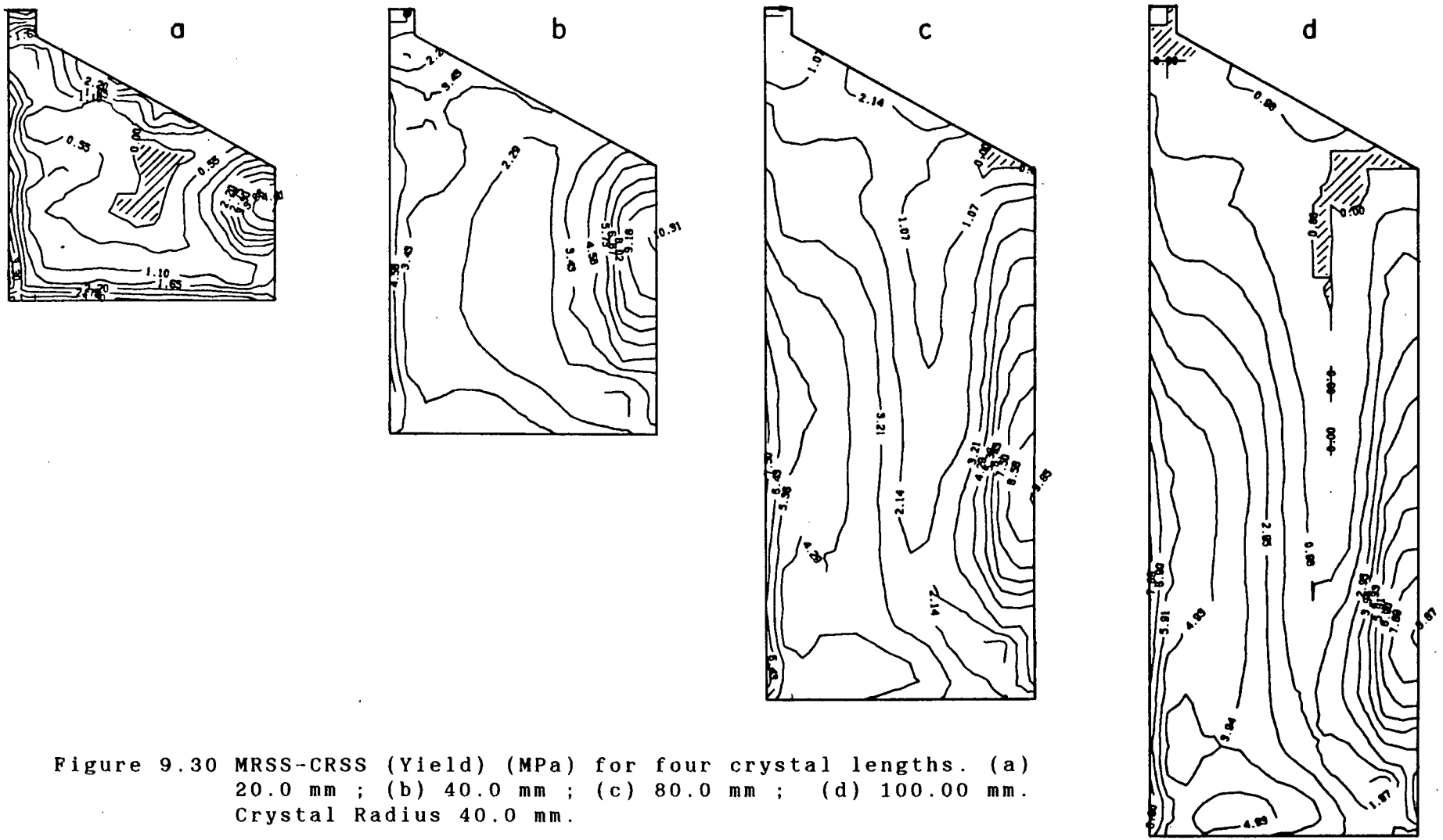

Figure 9.30 MRSS-CRSS (Yield) (MPa) for four crystal lengths. (a) 20.0 mm ; (b) 40.0 mm ; (c) 80.0 mm ; (d) 100.00 mm. Crystal Radius 40.0 mm.

lengths show contours and levels which are very similar to the MRSS contours. The distribution of MRSS-CRSS (MBTe) are similar to those in Figure 9.30(a-d).

9.3.1 Effect of Radius on Stress Symmetry

The stress symmetry in crystals with four different lengths has been examined. The cross-sections studied correspond to the same relative positions considered in the crystals with smaller radius. As before, the analysis was done in two ways namely following a fixed cross-section in the crystal during growth and analysing the symmetry distribution in the crystal for each crystal length. From the second analysis, the conclusions are similar to those obtained for the smaller radius. From the first analysis by following a cross-section and comparing the results with those obtained for the smaller radius crystal, the following conclusions were reached.

There is a correlation of symmetry with distance from the cone between the two crystal radii. This correlation is given in Table 9.4 which was obtained in the following way. Consider the sections at 77 mm (2.8 x R) for the 27.5 mm crystal and 72 mm (1.8 x R) for the 40 mm crystal. Both sections have very similar stress symmetries during growth. In this case the stress symmetries shown in Figure 9.27(a) and (b) corresponding to a relative distance from the cone of 2.8 times the radius is reproduced in the larger crystal but at a relative distance of 1.8 times the radius. Similar correlations are obtained following other section at the same distances from the cones for the two radius.

Table 9.4 Table of Symmetry Correlations

Radius [mm]	Distance from Shoulder [mm]	Relative Distance from shoulder	Figure
27.5	8.25	0.3	9.25
40.0	12.0	0.3	
27.5	77.0	2.8	9.26
40.0	72.0	1.8	
27.5	104.5	3.8	9.27
40.0	112.0	2.8	

Because this correlation is with actual distance, the effect of the thermal field is expected to predominate over the effect of the boundary conditions. If the symmetry is determined by the thermal field alone, there should also be a strong correlation between the symmetries and the actual distance from the interface. This correlation is not observed. On the contrary, for long crystals there is correlation of symmetries but with the relative distance from the interface for same crystal lengths. The correlation with actual distance from the cone, however, suggests that the thermal history of the wafer is important in determining the stress symmetry. This would results in sections passing through the same thermal fields having the same symmetry history regardless of the crystal radius.

9.4 Growth Velocity

Conditions : R, 27.5 mm ; CL, 55.0 mm ; B, 21 mm ;
Temperature profile as in Figure 8.19, curve 4,
Velocity (a) 0.0001 cm/s, (b) 0.001 cm/s,
(c) 0.01 cm/s .

To determine the effect of changes in the growth velocity on the thermal and stress fields, the calculations were repeated with growth velocities of 0.0001 and 0.01 cm/s. The temperature fields for the three velocities considered are shown in Figure 9.31(a-c). Comparing Figure 9.31(b) and (a), it is noted that decreasing the velocity has little effect on the temperature distribution. Increasing the velocity (Figure 9.31(b) and (c)) significantly increases the axial and radial temperature gradients in the crystal.

The results indicate that at velocities of 0.001 cm/s and lower the thermal system is at steady state, and effectively independent of velocity. Above 0.001 cm/s this is not the case, primarily due to the value of thermal diffusivity used (0.04 cm/s) which is comparable to the velocity. The specific effect of growth velocity on the thermal fields is complex. In the quasi steady state approximation, the temperature field changes only as a result of the movement of the solidifying interface ; the initial transient is neglected. In the present calculations, and independent of the heat transfer at the crystal

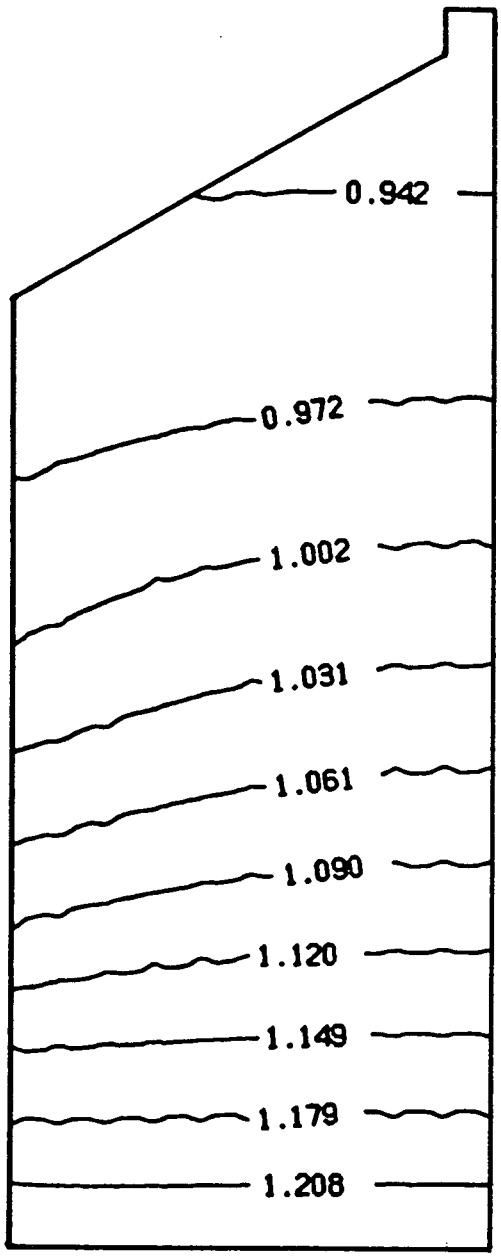
0.942
0.972
1.002
1.031
1.061
1.090
1.120
1.149
1.179
1.208

a

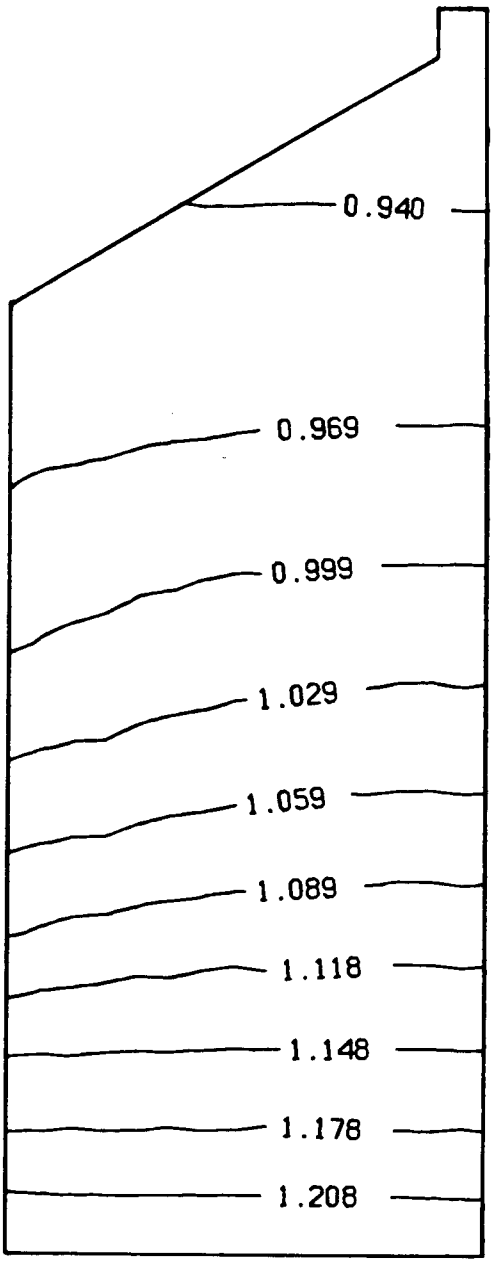
0.940
0.969
0.999
1.029
1.059
1.089
1.118
1.148
1.178
1.208

b

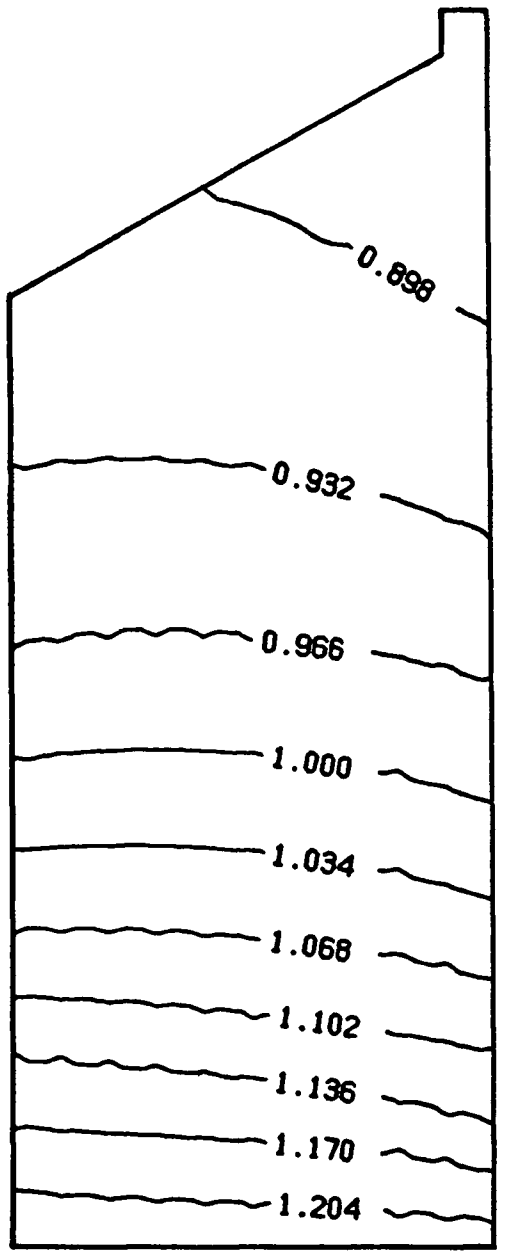

Figure 9.31 Temperature fields for three growth velocities (a) 0.0001 cm/s, (b) 0.001 cm/s and (c) 0.01 cm/s. Temperature given in 10^{30}C. Little change is observed from (a) to (b). From (b) to (c) gradients have increased. Radius 27.5 mm, length 55 mm, encapsulant thickness 21 mm.

36/3.6/36 cm/h.

surface, there are two limiting cases. At low velocities steady state fields are expected ; at high velocities uniform temperature fields are expected with the temperature the same as the moving boundary.

For comparable values of velocity and diffusivity any qualitative analysis must include the fact that the external surface is cooling following Newton's law of cooling. In this case the situation is complicated by the fact that there is mixed control in the bulk and the surface of the crystal with a Biot number which has values close to one.

The MRSS contours corresponding to the three thermal fields shown in Figure 9.31(a-c) are given in Figure 9.32(a-c). Comparing the MRSS values at 0.0001 cm/s with those at 0.001 cm/s, the differences are small ; approximately 2 % for the highest values of the MRSS and 4 % for the lowest. Comparing 0.01 cm/s with 0.001 cm/s, the highest values of MRSS have approximately doubled and the lowest values more than doubled. In addition, the area close to the interface with minimum MRSS disappears as the velocity increases.

9.5 Thermal Conditions

The temperature distribution in the growing crystal is dependent on the thermal environment surrounding the crystal and the crystal geometry. The effect of the thermal environment is modelled using the temperature measurements reported by Grant et al.[218] as shown in Figure 8.19, curve 4.

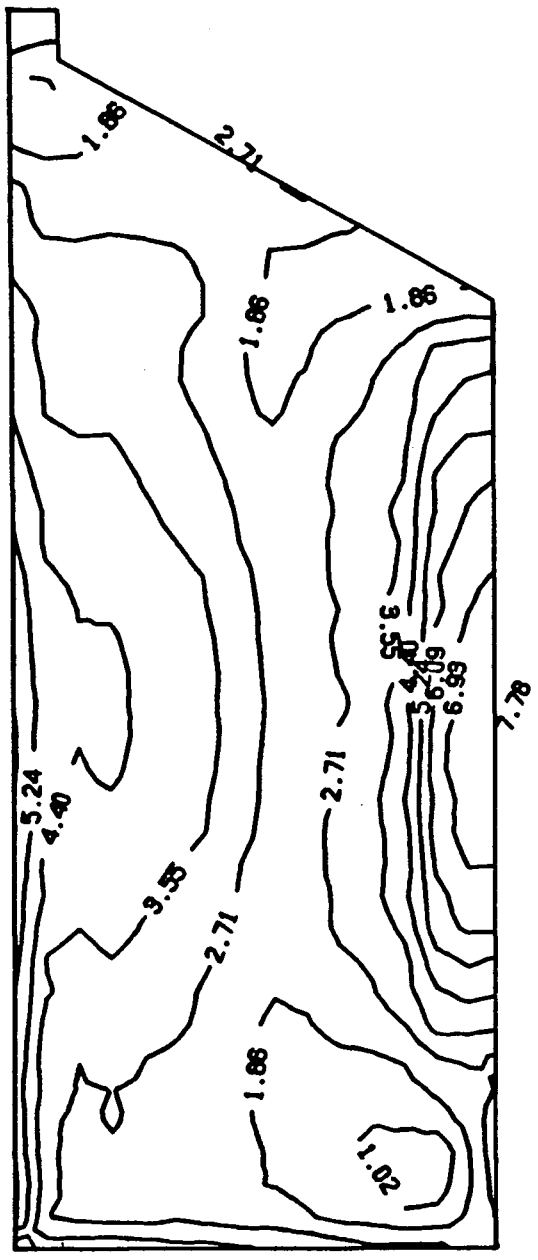
1.86
2.71
1.86
1.86
5.24
4.40
3.55
2.71
2.71
1.86
1.02
6.99
7.78

a

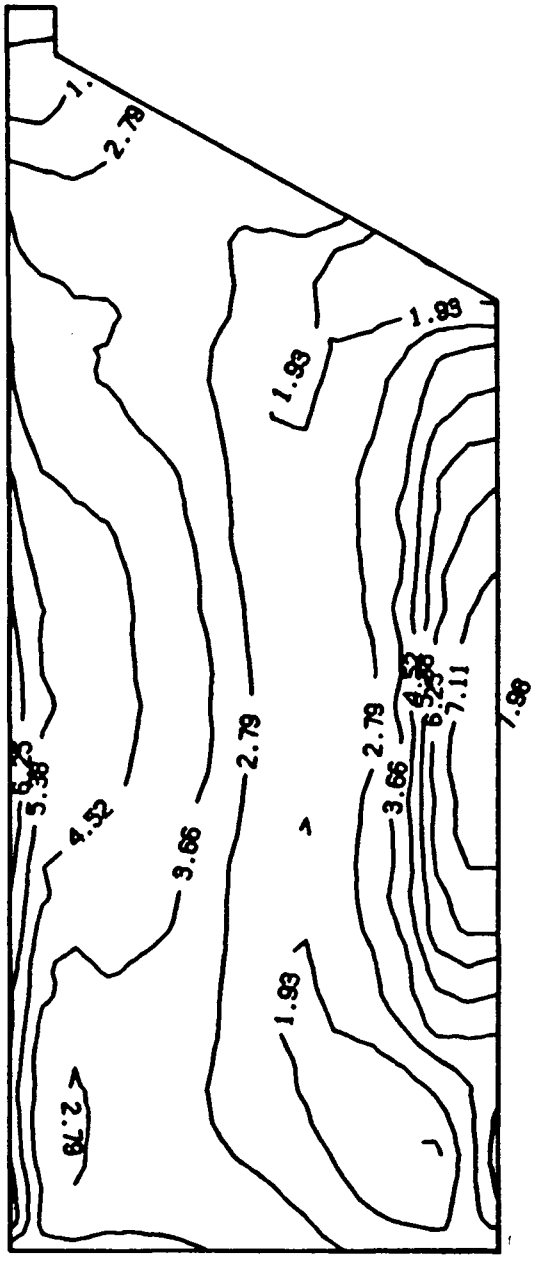
1.93
1.93
4.52
3.66
2.79
2.79
1.93
7.11
7.98

b

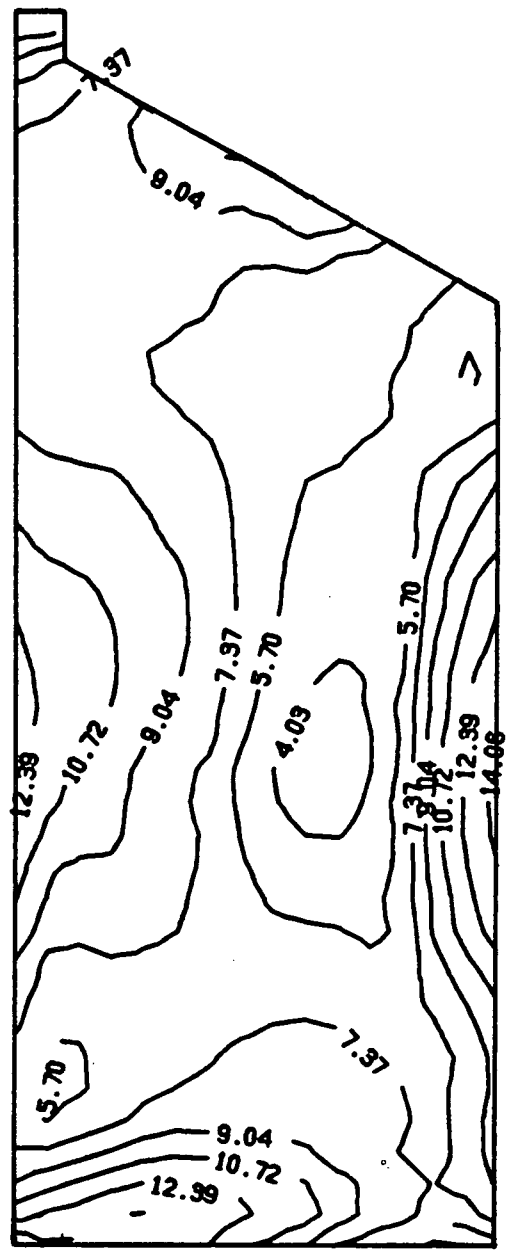

Figure 9.32 MRSS-CRSS (Yield) (MPa) for the three temperature fields shown in Figure 9.31(a-c) corresponding to three growth velocities. (a) 0.0001 cm/s, (b) 0.001 cm/s and (c) 0.01 cm/s. In (a) and (b) the stress fields are similar. In (c) the stress distribution and stress values change.

The thermal profile for the different thicknesses of boron oxide is modelled assuming that the temperature at the top and bottom of the oxide is independent of thickness for constant power input. This makes the temperature gradient across the oxide linearly proportional to the thickness, as demonstrated experimentally[146-148].

It is also assumed that reducing the axial gradients in the chamber by increasing the power input or increasing the boron oxide thickness changes the magnitude of the local temperature but does not change the shape of the temperature profile. This means that only the coefficients in the polynomials fitting the original profile are proportionally reduced by a given factor for the new growth conditions.

The boron oxide thicknesses considered are 21, 40 and 50 mm the latter being the maximum thickness currently used experimentally. For each thickness, several temperature gradients are considered. The crystal radii examined are 27.5 mm and 40.0 mm.

9.5.1 Radius 27.5 mm

9.5.1.1 Boron oxide thickness 21.0 mm

Average gradients (a) 66°C/cm, (b) 33°C/cm,
(c) 17°C/cm, (d) 8°C/cm

The temperature profiles considered are given in Figure 9.33. Five profiles are shown. The profile labelled G with the

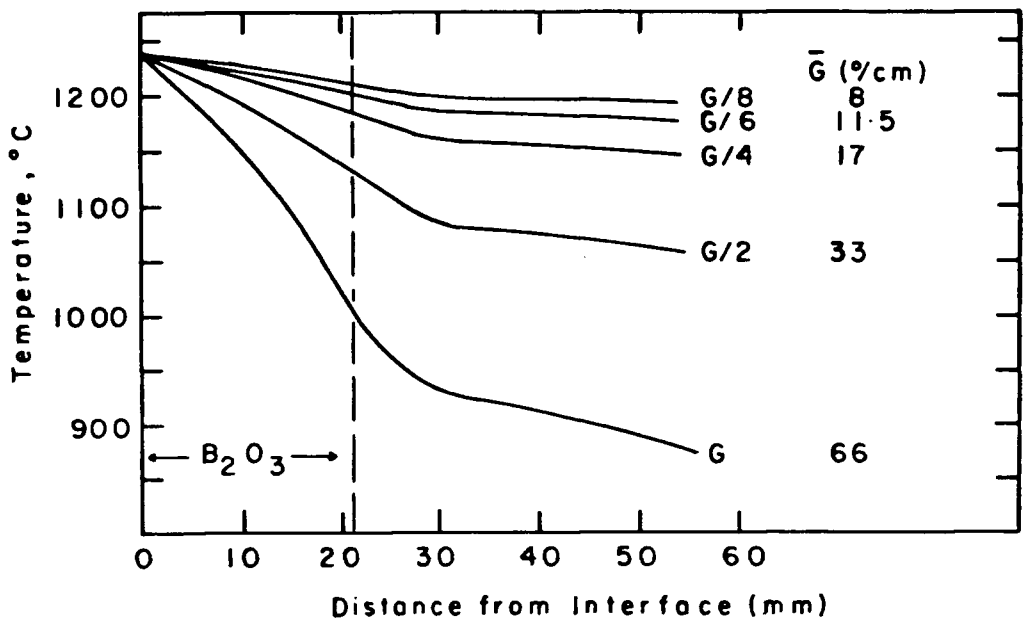

Figure 9.33 Temperature profiles along the crystal surface in the environment surrounding the crystal employed in the calculations. The profiles are derived from Figure 8.19, curve 4, reproduced as curve G. The values of gradient are averaged in the crystal length considered. Encapsulant thickness 21 mm.

steepest gradient, is the same as shown in Figure 8.19, curve 4, which was determined experimentally.

The results for the MRSS-CRSS (Yield) for four temperature profiles are shown in Figure 9.34(a-d). The stress contours for the temperature profile G were shown in Figure 9.33(c). Comparing Figure 9.34(a-d) it can be noted that the stress distribution patterns are similar in the four cases. The stress levels, however, decreases considerably with the average gradient. As a result of the lower stress levels the area with zero stress gradually increases from (a) to (d). The regions with zero stress start to grow from the regions with lower stresses. These regions are in the seed, shoulder and above the interface edge. At the lowest gradient in (d) most of the crystal has stresses which are less than the CRSS (Yield). The two remaining regions with non zero stresses are located where the highest stresses usually appear ; in the crystal surface above the encapsulant and in the crystal axis.

9.5.1.2 Boron oxide thickness 40.0 mm

AVG (a) 58 cm/s, (b) 29 cm/s,
(c) 19 cm/s

B 50.0 mm

AVG (a) 50°C/cm, (b) 25°C/cm,
(c) 12.5^{o}C/cm.

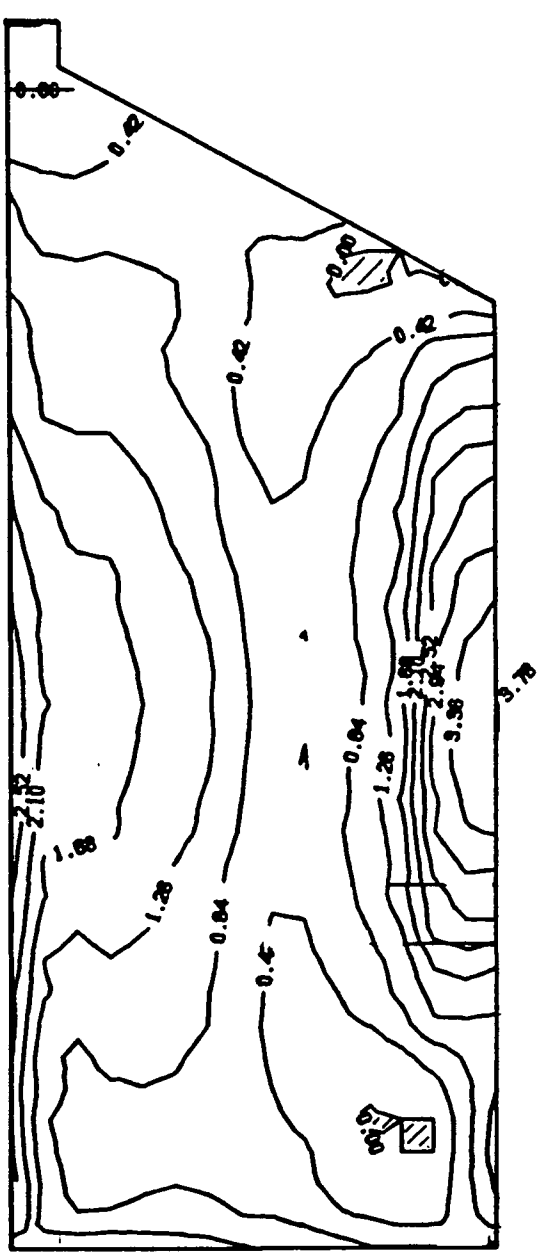
0.00
0.42
0.42
0.42
0.84
1.26
1.68
2.10
2.52
3.78

a

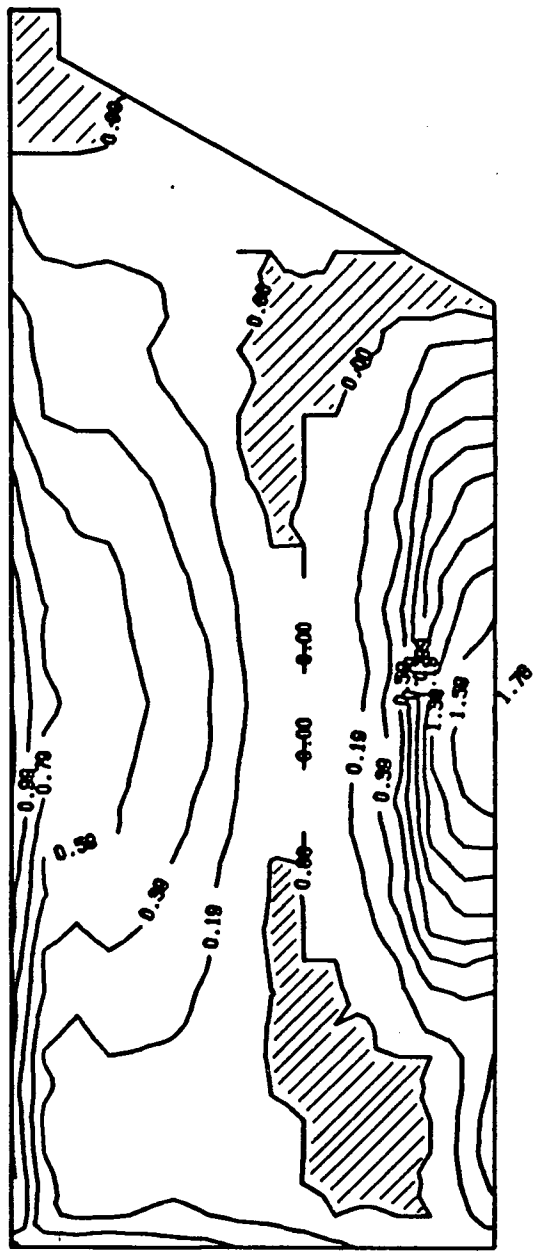
0.00
0.00
0.00
0.19
0.39
0.59
0.79
0.99
1.19
1.39
1.78

b

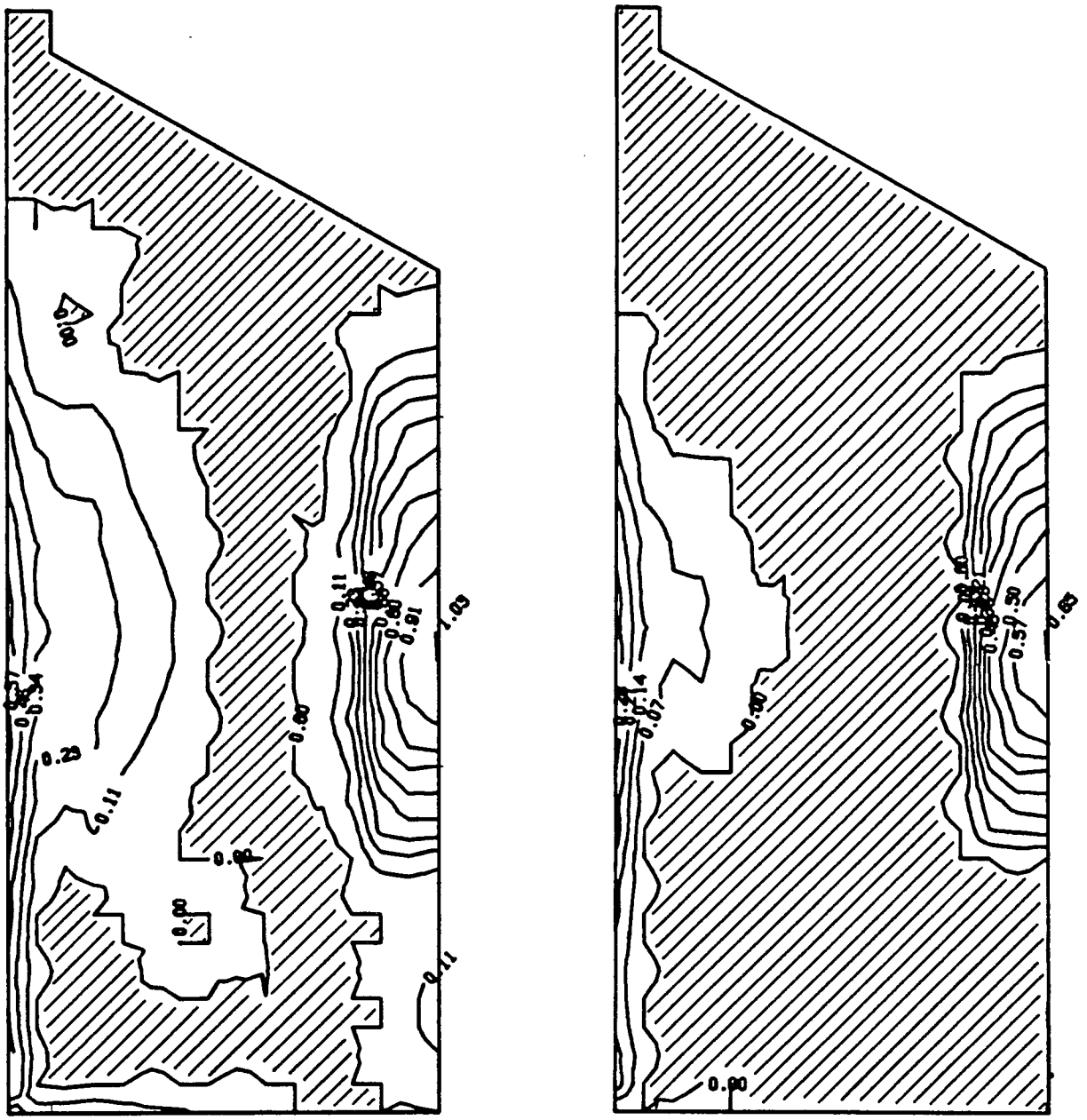

Figure 9.34 MRSS-CRSS (Yield) (MPa) for four temperature profiles with average gradients (a) 33°C/cm, (b) 17°C/cm, (c) 11°C/cm and (d) 8°C/cm. Radius 27.5 mm, length 55 mm. Encapsulant thickness 21 mm.

The temperature profiles for both encapsulant thicknesses are shown in Figures 9.35(a) and (b). In (a) for the 40 mm encapsulant and in (b) for the 50 mm. In each case three temperature profiles are considered, the average gradient for each profile is also given. For comparison the original profile for the 21.0 mm encapsulant is also shown.

The results for the MRSS-CRSS (Yield) for the two encapsulant thicknesses are shown in Figures 9.36(a-c) for the 40 mm thickness and Figure 9.37(a-c) for the 50 mm thickness. Parts (a) to (c) corresponds to the three different thermal profiles shown in Figure 9.35(a) and (b).

To observe the effect of increasing the encapsulant thickness only the three figures to be compared are : 9.23(c) for the 21 mm, 9.36(a) for the 40 mm and 9.37(a) for the 50 mm thickness. It can be noted that increasing the boron oxide thickness changes the relative stress distribution. The changes are the extended low stress region close to the interface and the shift of the stress concentration to a position above the encapsulant surface.

For thick encapsulants, the large and uniform low stress region in the low part of the crystal has a stress distribution in a radial direction which maintains the W shape with extended valleys and sharp peaks in the centre and edge of the crystal. In the case of the 50 mm thickness in Figure 9.37(a) the stress concentration region below the shoulder is small because the encapsulant is only 5 mm shorter than the crystal length.

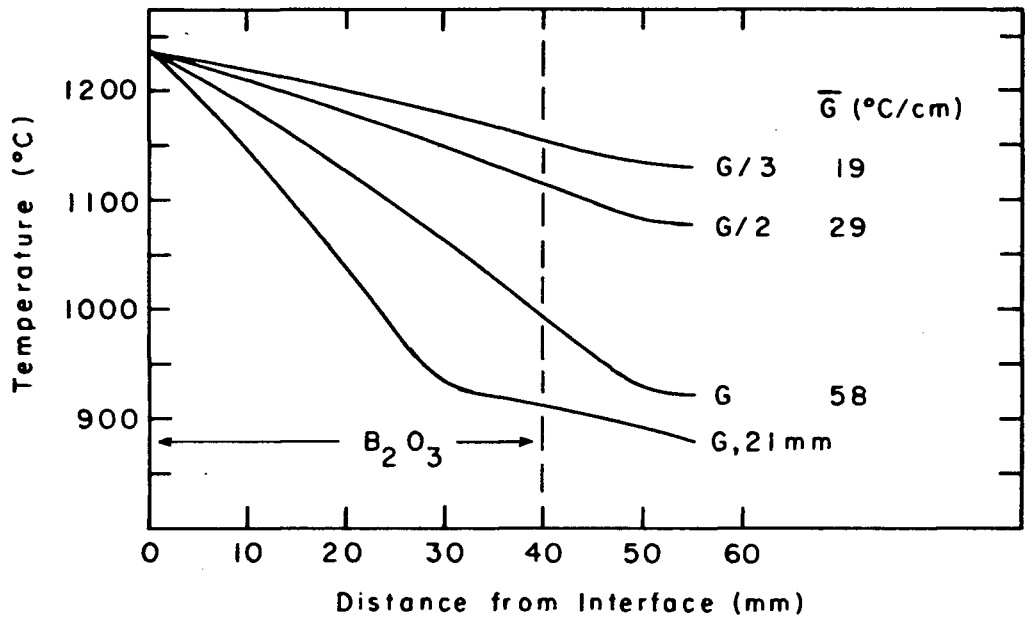

a

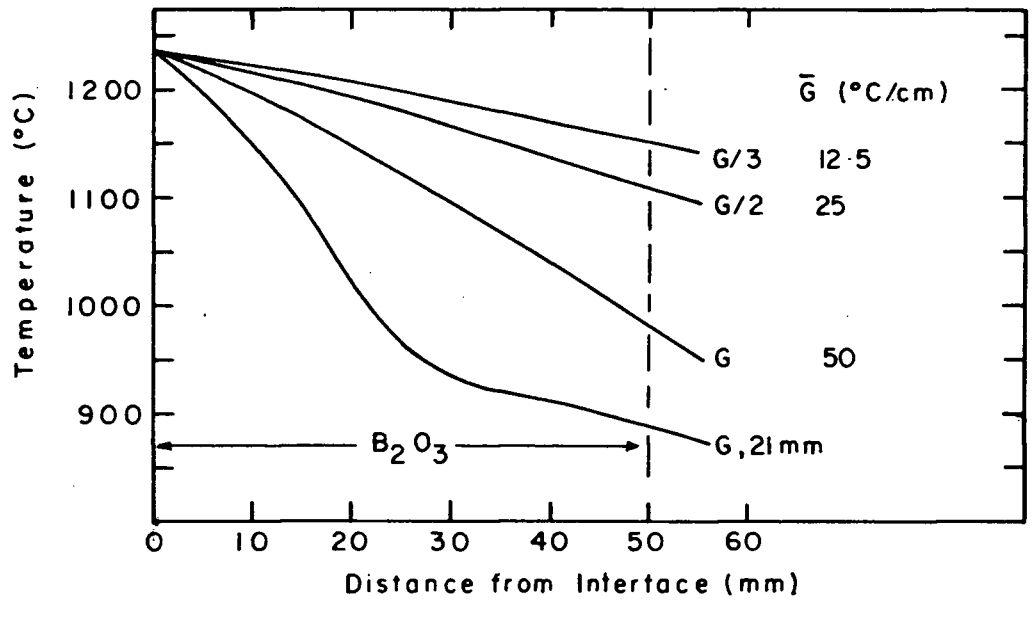

b

Figure 9.35 Temperature profiles used in the calculations for two boron oxide thicknesses. (a) 40 mm, (b) 50 mm. The profiles are derived from curve G. The values of gradients given are averaged along the crystal length.

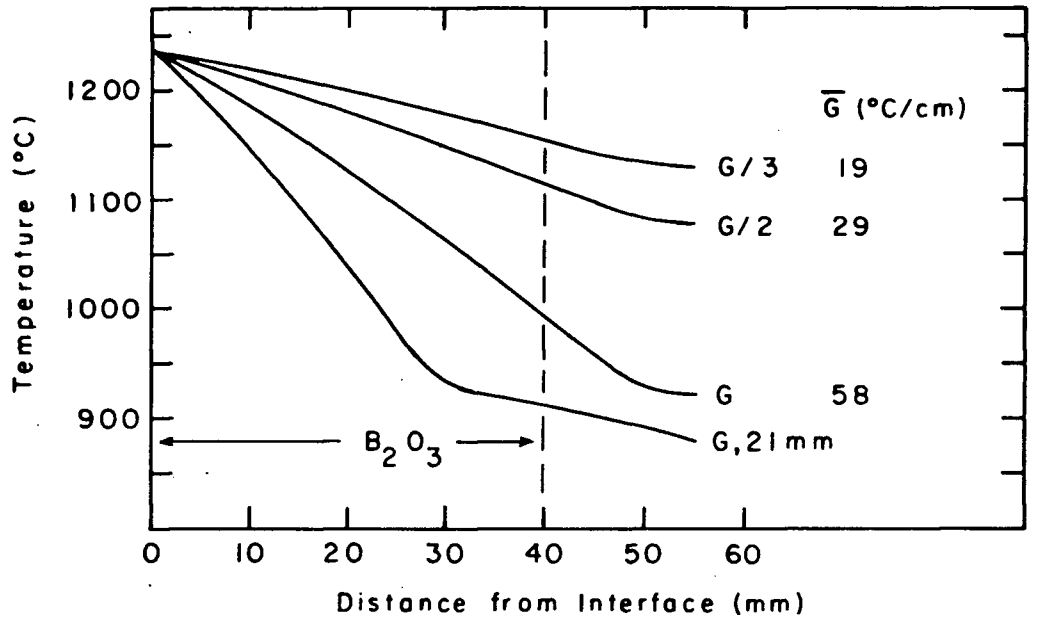

a

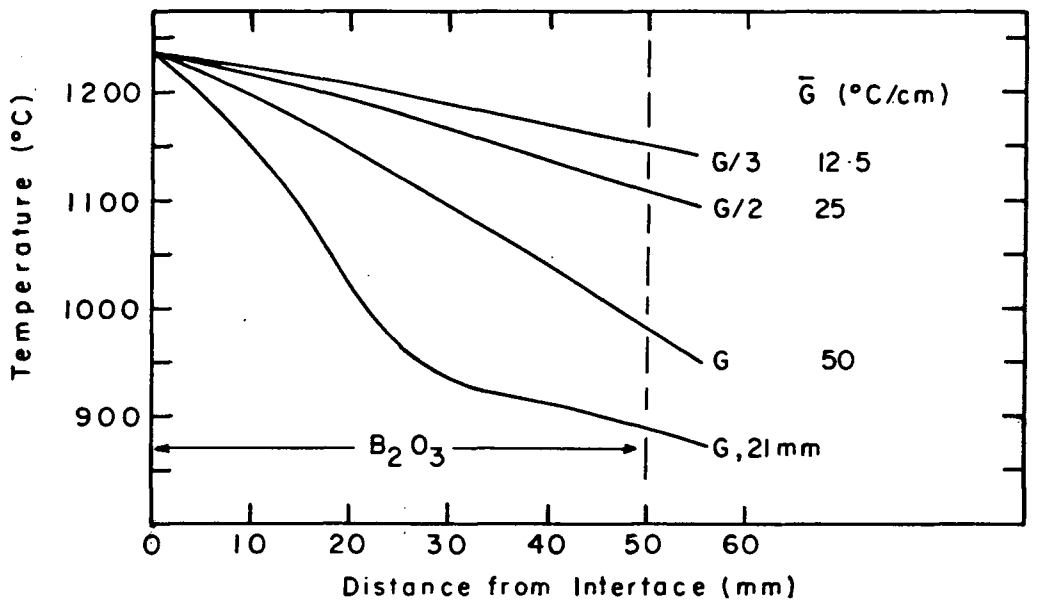

b

Figure 9.35 Temperature profiles used in the calculations for two boron oxide thicknesses. (a) 40 mm, (b) 50 mm. The profiles are derived from curve G. The values of gradients given are averaged along the crystal length.

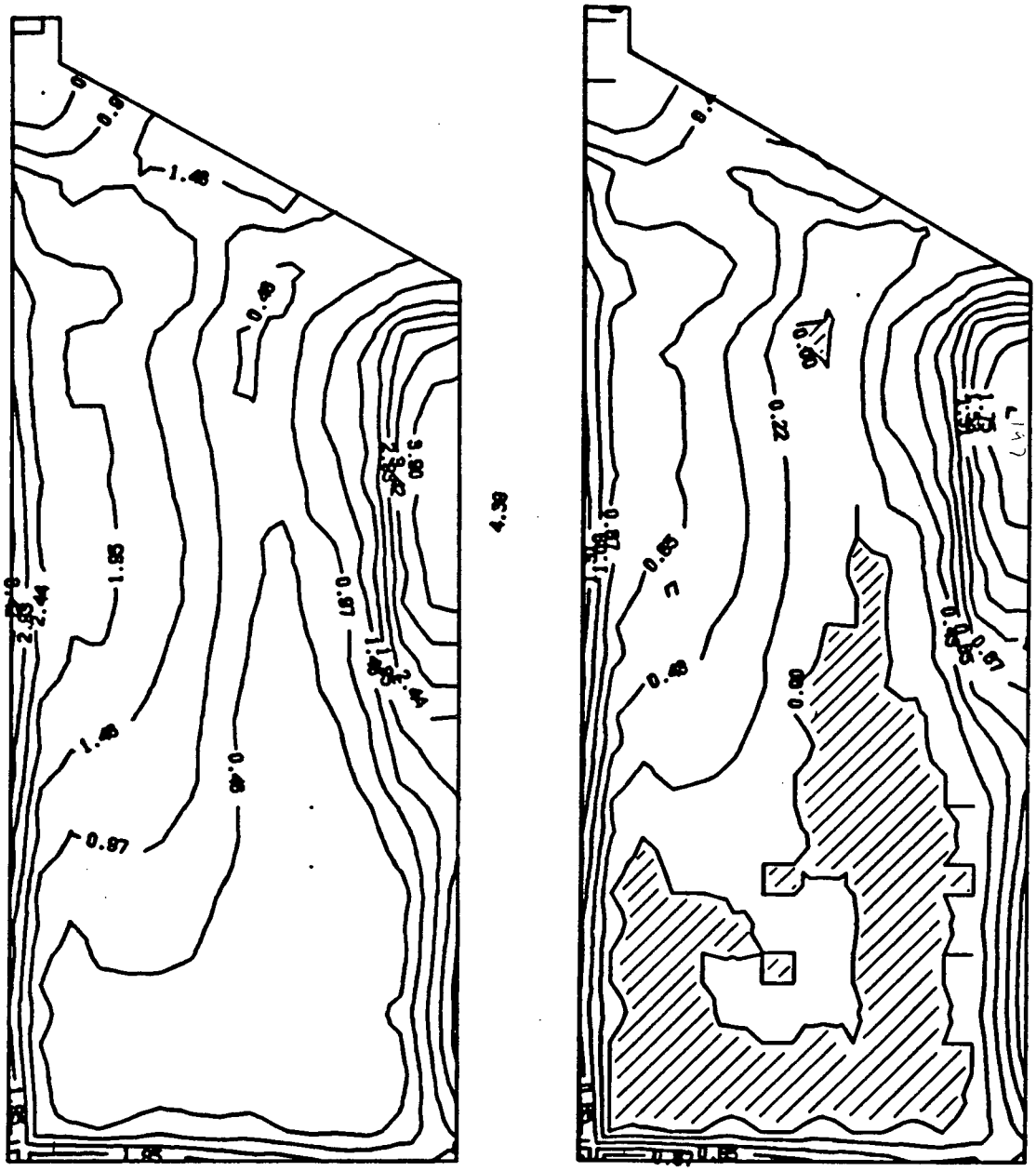

a

b

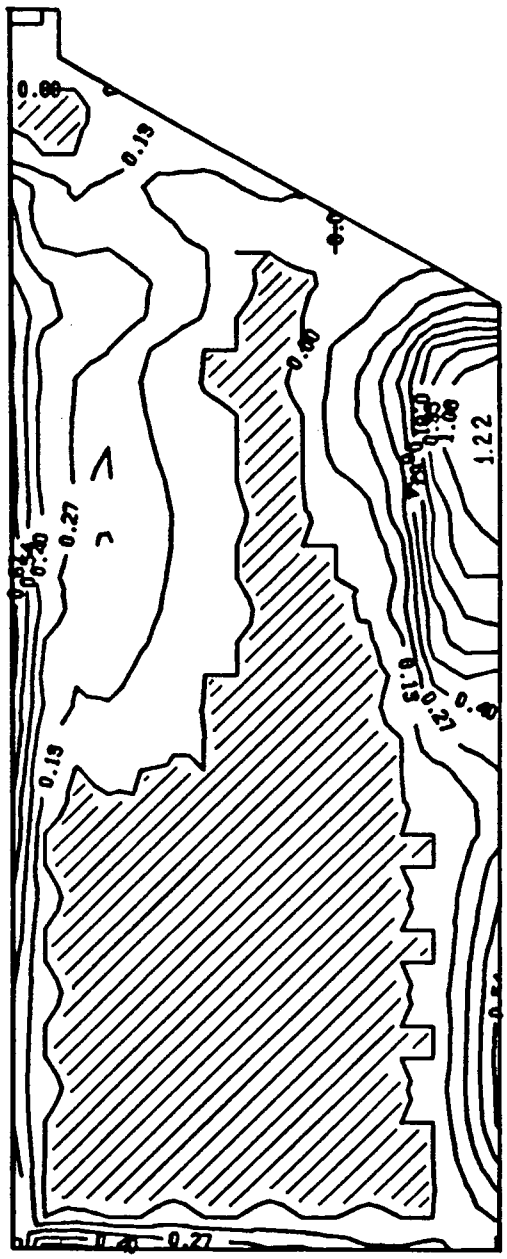

c

Figure 9.36 MRSS-CRSS (Yield) (MPa) for three average gradients. (a) 58°C/cm, (b) 29°C/cm, (c) 19°C/cm. Radius 27.5 mm, length 55 mm, boron oxide thickness 40 mm.

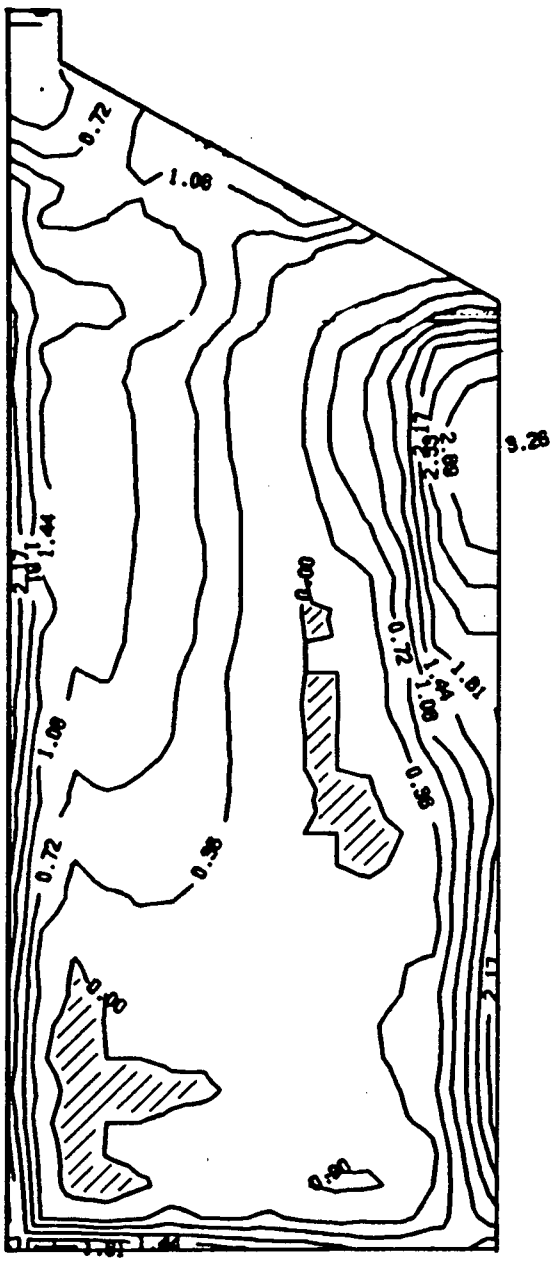

a

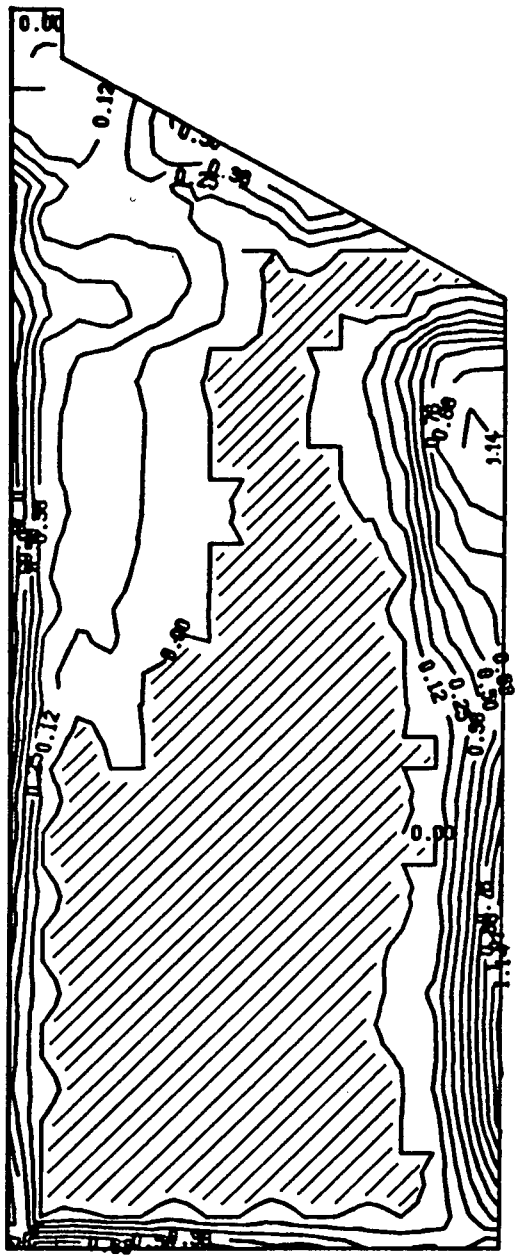

b

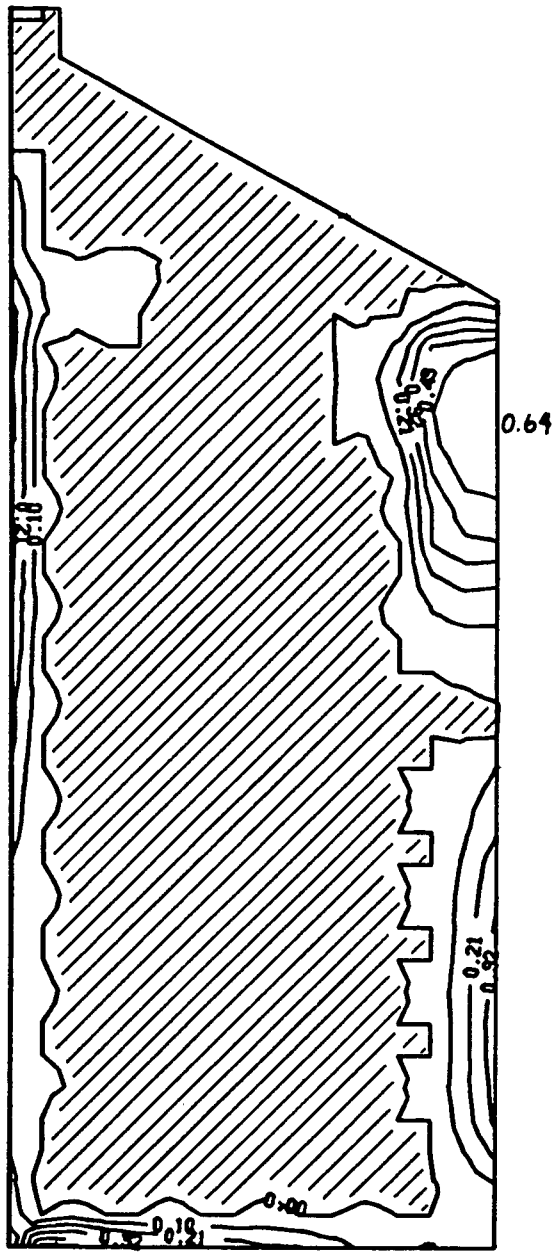

C

Figure 9.37 MRSS-CRSS (Yield) (MPa) for three average gradients. (a) 50°C/cm, (b) 25°C/cm, (c) 17°C/cm. Radius 27.5 mm, length 55 mm, boron oxide thickness 50 mm.

The absolute stress also changes with an increase in the encapsulant thickness. Doubling the thickness reduces by half the maximum stress.

When thermal profiles with lower gradients are considered for both encapsulant thicknesses, the region in the crystal with zero MRSS-CRSS (Yield) expands from the low stress regions close to the interface as the gradient decreases. The largest zero stress region is obtained in Figure 9.37(c) for an encapsulant thickness of 50 mm and a gradient of 12.5^{o}C/cm. It is noted that similar surface areas were obtained with a 21 mm thickness for a gradient of 8°C/cm. This shows that independent of encapsulant thickness, a critical gradient of about 10°C/cm should be achieved in order to obtain large areas with stresses less than the CRSS (Yield). From the practical point of view, a thicker encapsulant is preferred for the following reasons. To get the desired 10°C/cm level, the thermal gradient should be reduced eight times with the 21 mm thickness and only three times with the 50 mm thickness. This is because of the reduction of gradients when increasing the thickness. In addition in low gradient environments large areas of crystal are exposed to high temperatures. Without proper encapsulation there is decomposition of GaAs, resulting in the formation of liquid Ga drops which damages the crystal and leads to non-stoichiometric melts which is also detrimental.

9.5.2 Radius 40.0 mm

9.5.2.1 Boron oxide thickness 21 mm

AVG : a) 14°C/cm, (b) 7°C/cm

The results for the MRSS-CRSS (Yield) with a boron oxide layer thickness of 21 mm are shown in Figure 9.38(a) and (b). Part (a) corresponds to the profile labelled G/4 (14°C/cm) and (b) to the profile G/8 (7°C/cm) in Figure 9.33. It is noted that the average gradients in these profiles are lower because of the longer crystal considered. Comparing Figure 9.38(a) and (b) with Figure 9.34(c) and (d) for the 27.5 mm crystal, it can be noted that in the case of the 40 mm crystal, the relative zero MRSS-CRSS (Yield) area for the same profile is not as large as in the case of the 27.5 mm crystal. In the 40 mm crystal, however, the top of the crystal in Figure 9.38(b) shows zero stress. This is due to the difference in length between the two crystals.

9.5.2.2 Boron oxide thickness 40 mm

AVG : (a) 46°C/cm, (b) 26°C/cm,
(c) 15°C/cm, (d) 9°C/cm.

The MRSS-CRSS (Yield) contours for the four gradients are shown in Figure 9.39(a-d). Note that the profile with an average gradient of 9°C/cm is not shown in Figure 9.35(a). The 9°C/cm average gradient in the encapsulant and gas is five times smaller than the original temperature profile labelled G in Figure 9.33. Comparing the results of Figures 9.39(a-d) with those in Figure 9.36(a-d) for the 27.5 mm crystal it can be observed

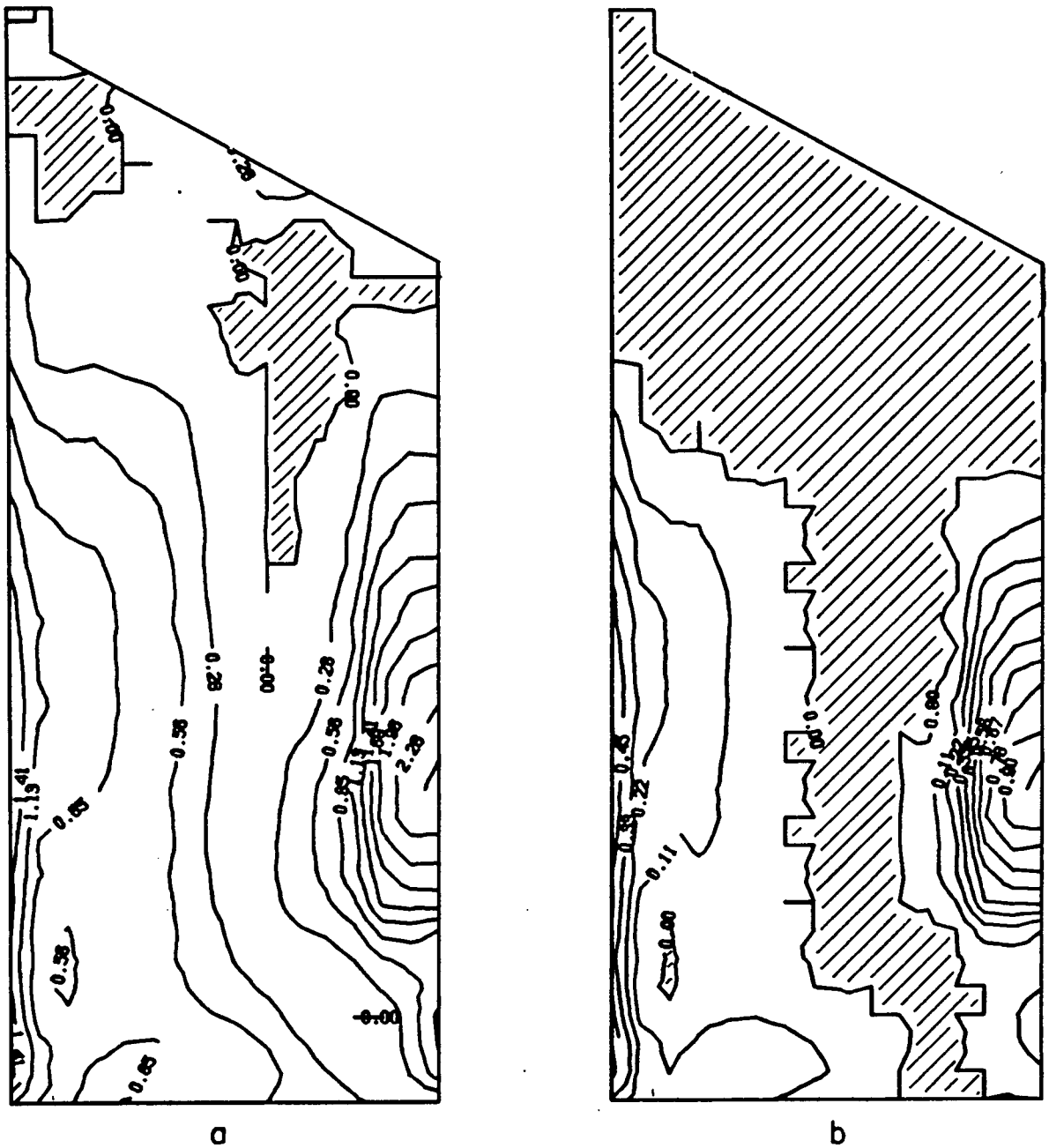

Figure 9.38 MRSS-CRSS (Yield) (MPa) for two average gradients. (a) 14°C/cm, (b) 7°C/cm. Radius 40 mm, length 80 mm, boron oxide thickness 21 mm.

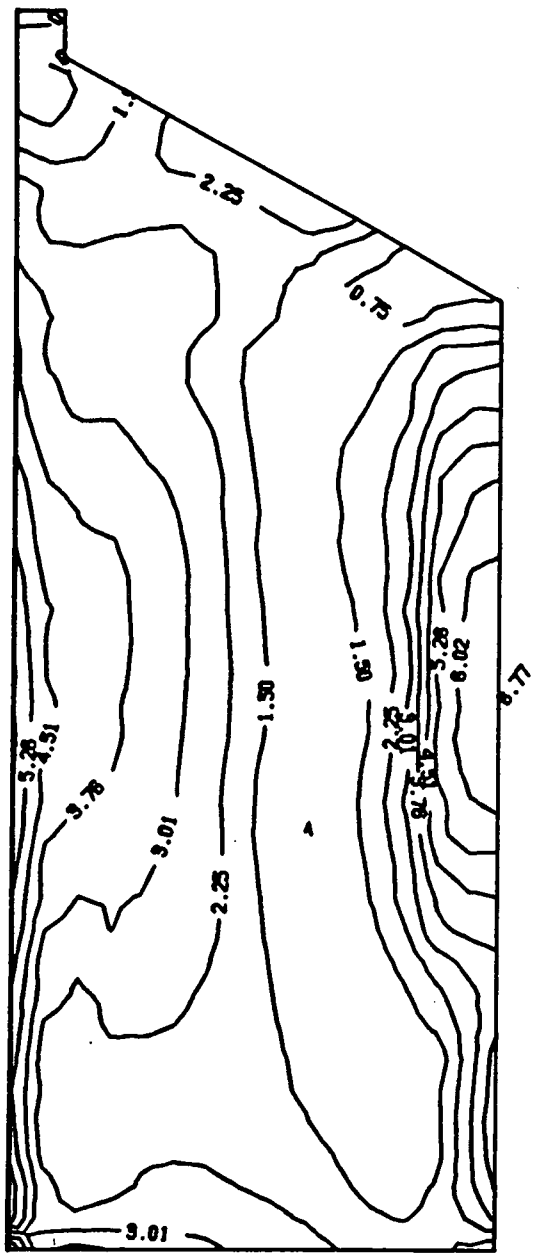

a

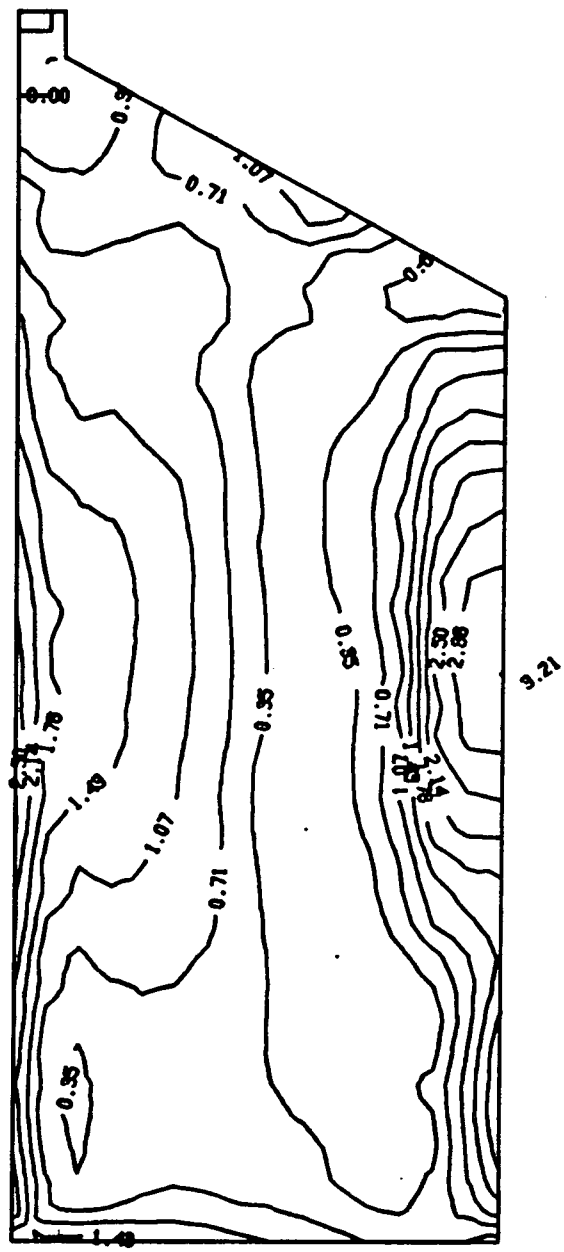

b

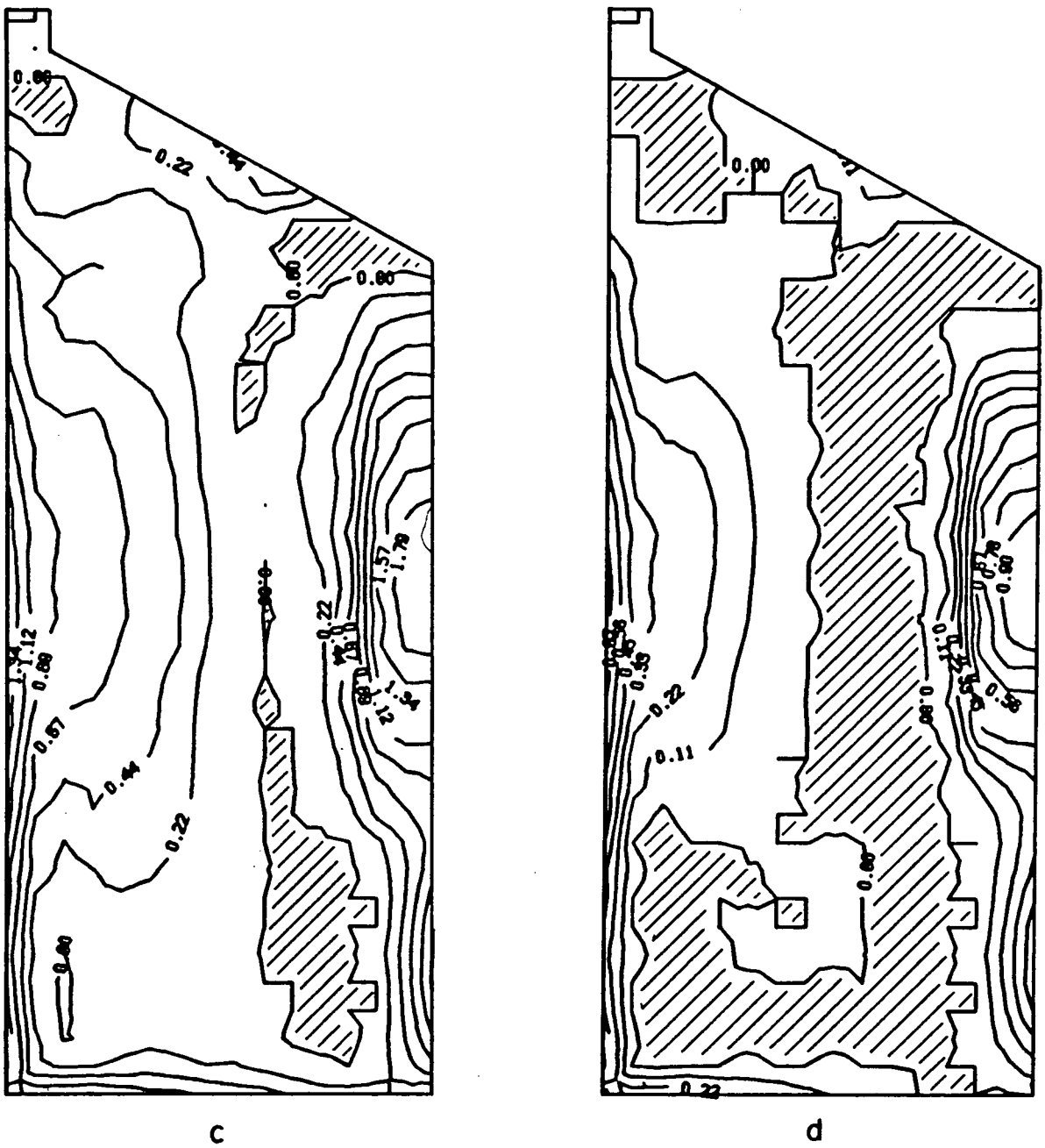

Figure 9.39 MRSS-CRSS (Yield) (MPa) for four average gradients. (a) 46°C/cm, (b) 26°C/cm, (c) 15°C/cm, (d) 9°C/cm. Radius 40 mm, length 80 mm, boron oxide thickness 40 mm.

that the concentration of stresses in the larger crystal occurs at the midlength instead of the top of the crystal as in the 27.5 mm crystal.

In addition it is observed that to obtain similar relative areas with zero MRSS-CRSS (Yield), the gradients in the environment surrounding the 40 mm crystal should be further reduced.

9.5.2.3 Boron Oxide thickness 50 mm,

AVG : (a) $43^{o}C/cm$, (b) $14^{o}C/cm$,

(c) $7^{o}C/cm$.

In order to determine if the stress level has reached a maximum value considering the whole growth period, stress calculations are made for a 40 mm crystal with a length comparable to the encapsulant thickness. The crystal length is 52 mm and the average gradient is $50^{o}C/cm$. The results for MRSS-CRSS (Yield) are shown in Figure 9.40. It is observed that the stress concentration occurs below the shoulder. In Figure 9.41(a) the distribution for the same stress for a crystal length of 80 mm is shown. In this case the stress concentration occurs above the encapsulant surface. The stress value in the longer crystal is higher than the largest stress value in the shorter crystal. From these results and those obtained with the 27.5 mm crystal radius it is possible to generalize the finding to most of the situations in LEC growth. The largest stress at a given crystal length occurs above the encapsulant surface. If this

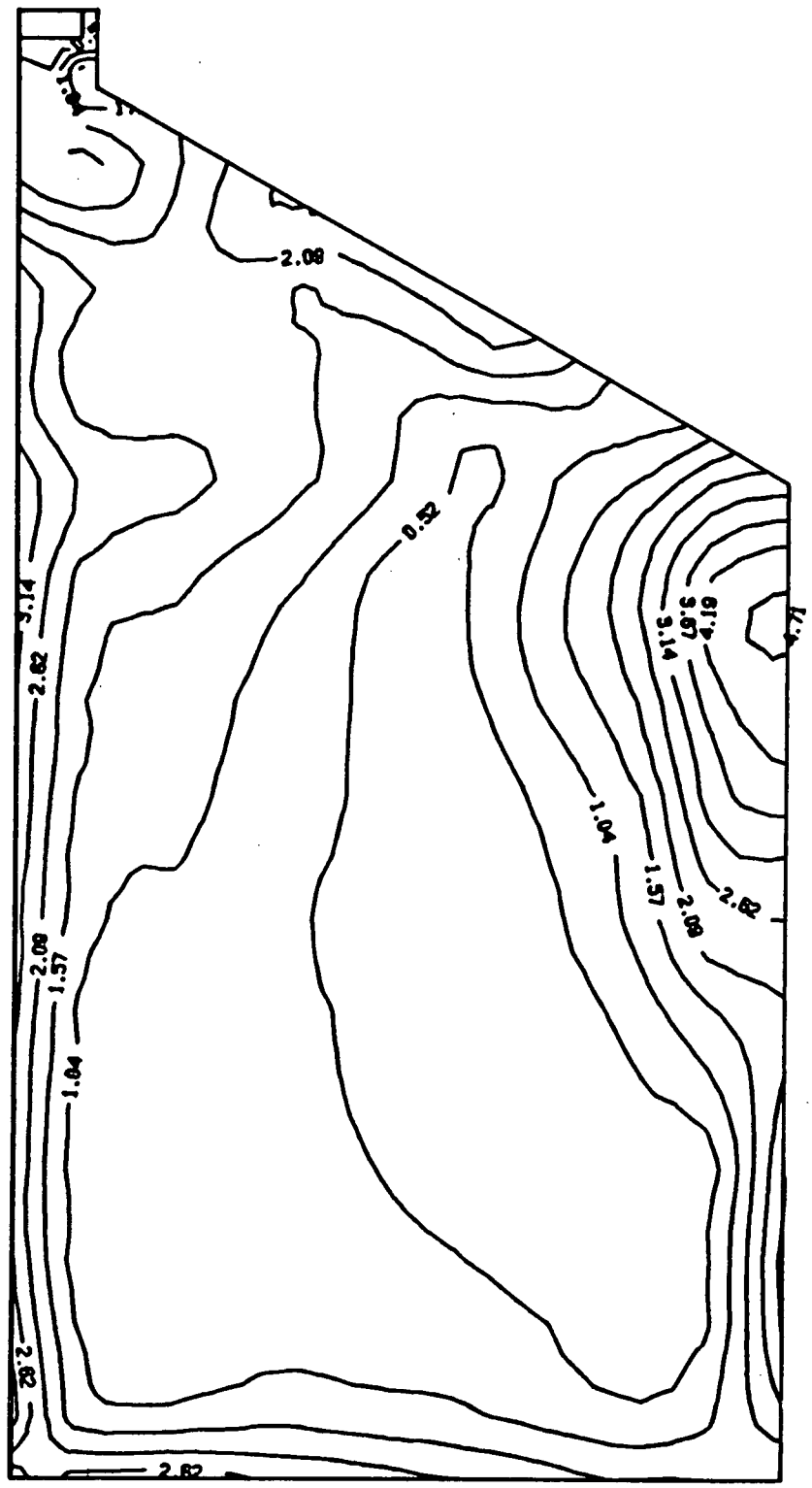

Figure 9.40 MRSS-CRSS (Yield) (MPa) for a crystal length of 52 mm comparable to the boron oxide thickness of 50 mm. Radius 40 mm. Average gradient 50°C/cm.

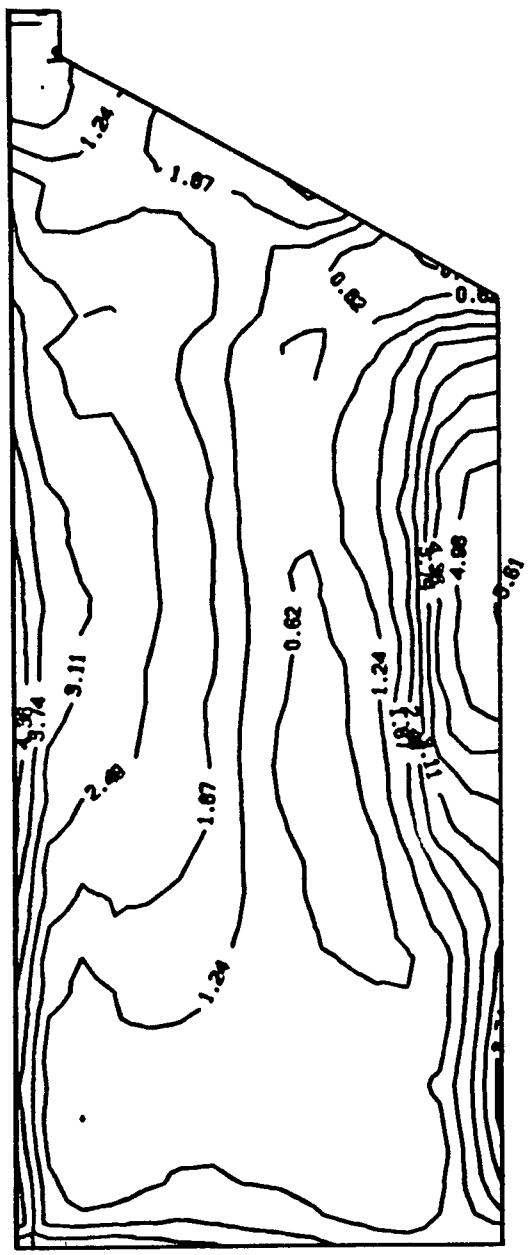
1.24
1.87
0.62
0.62
1.24
1.87
1.24
3.11
2.48
4.98
5.61

a

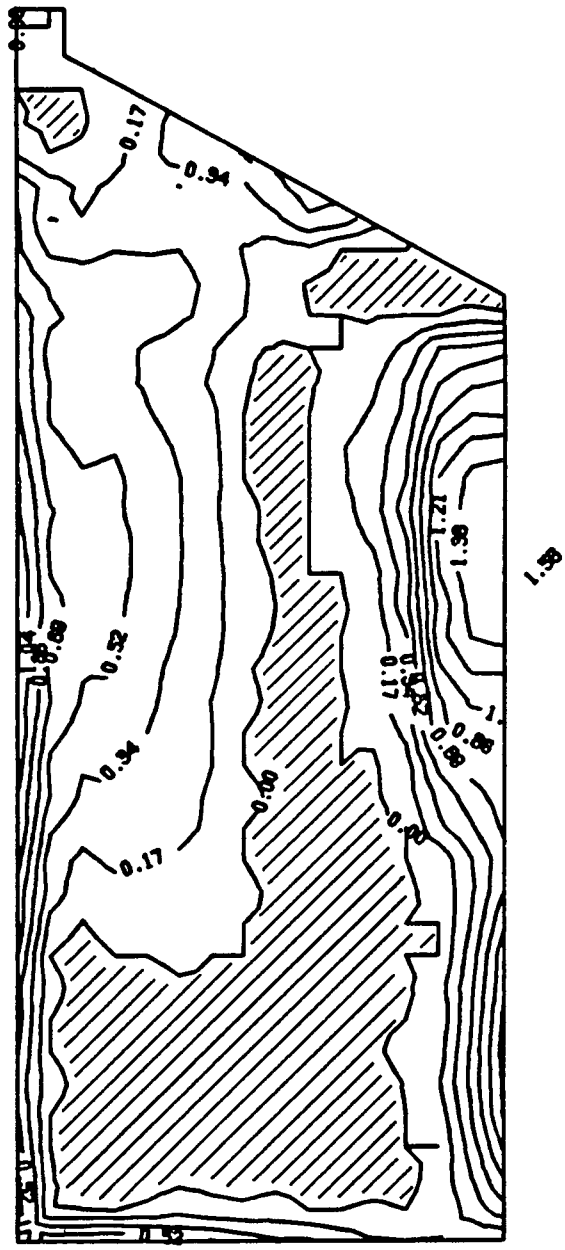
0.17
0.94
0.52
0.94
0.17
0.00
0.00
1.21
1.38
1.58

b

Figure 9.41 MRSS-CRSS (Yield) (MPa) for three average gradients. (a) 43°C/cm, (b) 14°C/cm, (c) 7°C/cm. Radius 40 mm, length 80 mm, boron oxide thickness 50 mm.

position is half-way along the crystal length, the stress is the largest in the whole growth period.

The stress distributions for the three gradients considered are shown in Figure 9.41(a-c). As in the case of the 40 mm encapsulant, the gradient should be further reduced to obtain similar relative areas with zero stress when comparing with the 27.5 mm crystals distributions.

The evaluation of the results presented in this section are summarized in Table 9.4. In this table the largest value of MRSS-CRSS (Yield) is given as a function of boron oxide thickness, gradient of the thermal profile and crystal radius. The stress values correspond to crystals with an aspect ratio of 2. For each condition the relative stress increment due to an increase in radius is also reported. It is clear from the tabulated values that the stress decreases as more favourable growth conditions apply, i.e. thicker encapsulant and lower gradient. It is also observed that the relative stress change due to an increase in radius increases as the stress level decreases (or more favourable conditions are present). In the case of the thickest encapsulant and the lowest gradient used in the calculations, the stress increases 143.7 % when increasing the radius from 27.5 mm to 40 mm. This shows that the effect on stresses with increasing the radius is not linear.

A comparison of the stress contours for all conditions listed in the table shows that similar stress distributions are

Table 9.4 Effect of Thermal Conditions on Stresses

Boron Oxide Thickness [mm]	G	AMRSS - CRSS (Yield) MPa		% change
		R = 2.75 cm	R = 4.0 cm	
21.0	G	7.02	9.65	37.46
	G/2	3.76		
	G/4	1.78	2.76	55.0
	G/6	1.03		
	G/8	0.65	1.02	56.0
40.0	G	4.39	6.77	54.2
	G/2	1.97	3.21	62.9
	G/3	1.22	2.01	64.7
	G/5		1.02	
50.0	G	3.26	5.61	72.08
	G/2	1.14		
	G/3	0.64	1.56	143.7
	G/5		0.47	

obtained for similar values of stress. For instance, similar areas with zero stress are given in the crystals with the following conditions

1) B = 21 mm, G/6, r = 2.75 mm ;

2) B = 21 mm, G/8, r = 40 mm ;

3) B = 40 mm, G/5, r = 40 mm.

9.6 Gas Pressure and Composition

Conditions : AP, 2 atm ; R, 27.5 mm ; CL, 55 mm ;
B, 21 mm ;
Temperature profiles as in Figure 9.33 ;
AVG : (a) 66°C/cm, (b) 33°C/cm,
(c) 17°C/cm, (d) 11°C/cm.

The effect of gas pressure is considered in the model through the effect of pressure on the convective part of the heat transfer coefficient between crystal and gas. In the equations used for the numerical evaluation, the convective heat transfer coefficient changes with the square root of pressure.

The results for the MRSS-CRSS (Yield) are shown in Figures 9.42(a-d) for four gradients. The effect of pressure on the four gradients can be analysed by comparing the stress values with the results obtained for a pressure of 30 atmospheres. For this Figure 9.42(b-c) should be compared with Figures 9.34(a-c). It is observed that the stress configuration for the four gradients at 2 atmospheres is similar to the stress configuration for the same

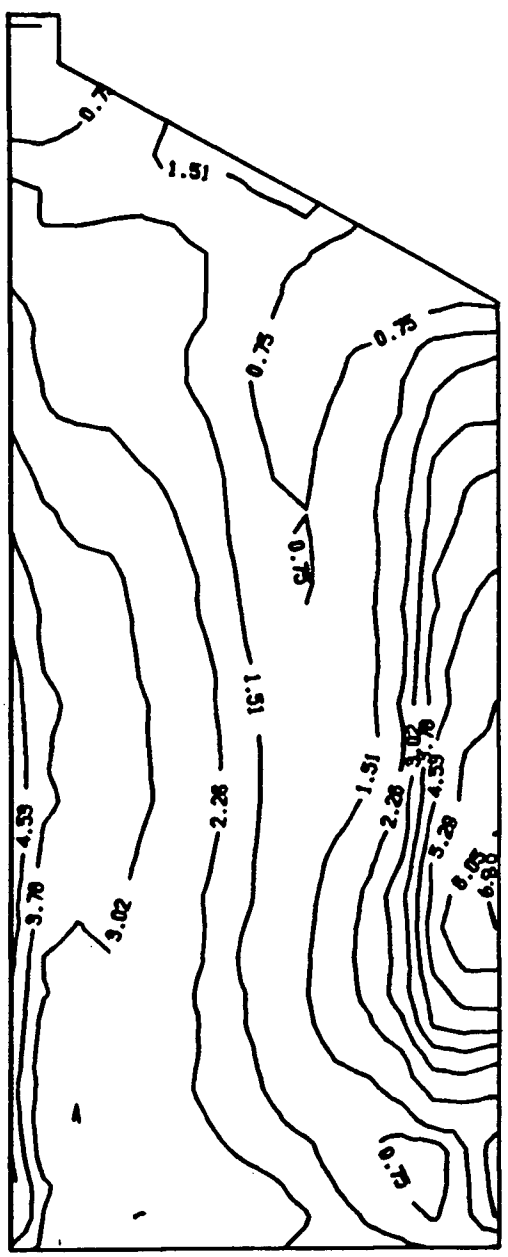
1.51
0.75
0.75
0.75
1.51
2.28
1.51
2.28
4.53
3.78
3.02
5.28
0.75

a

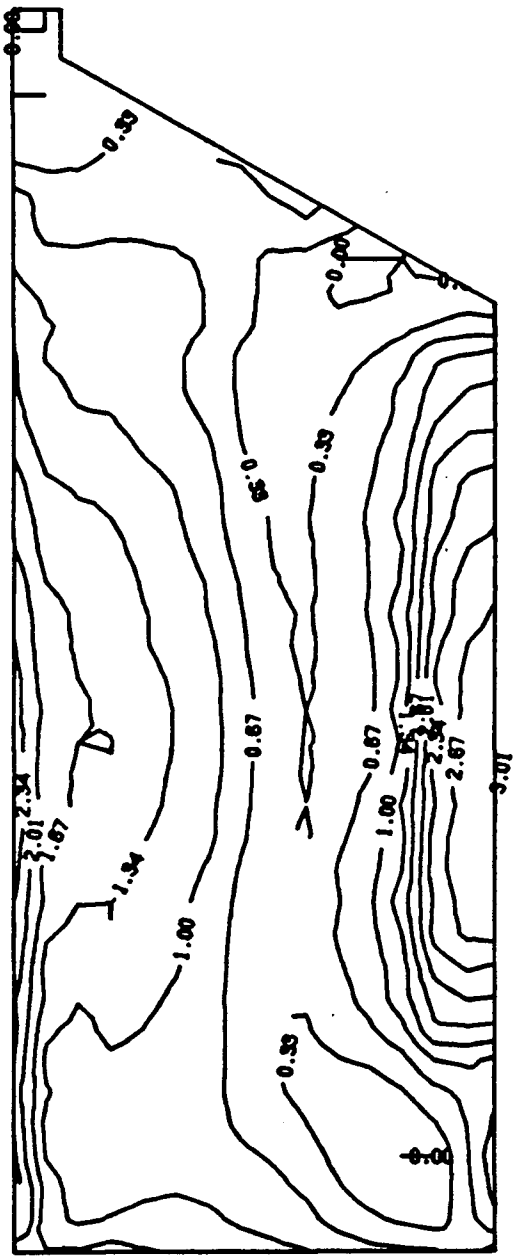
0.33
0.33
0.67
0.67
1.00
1.34
1.00
0.33
2.67
3.01

b

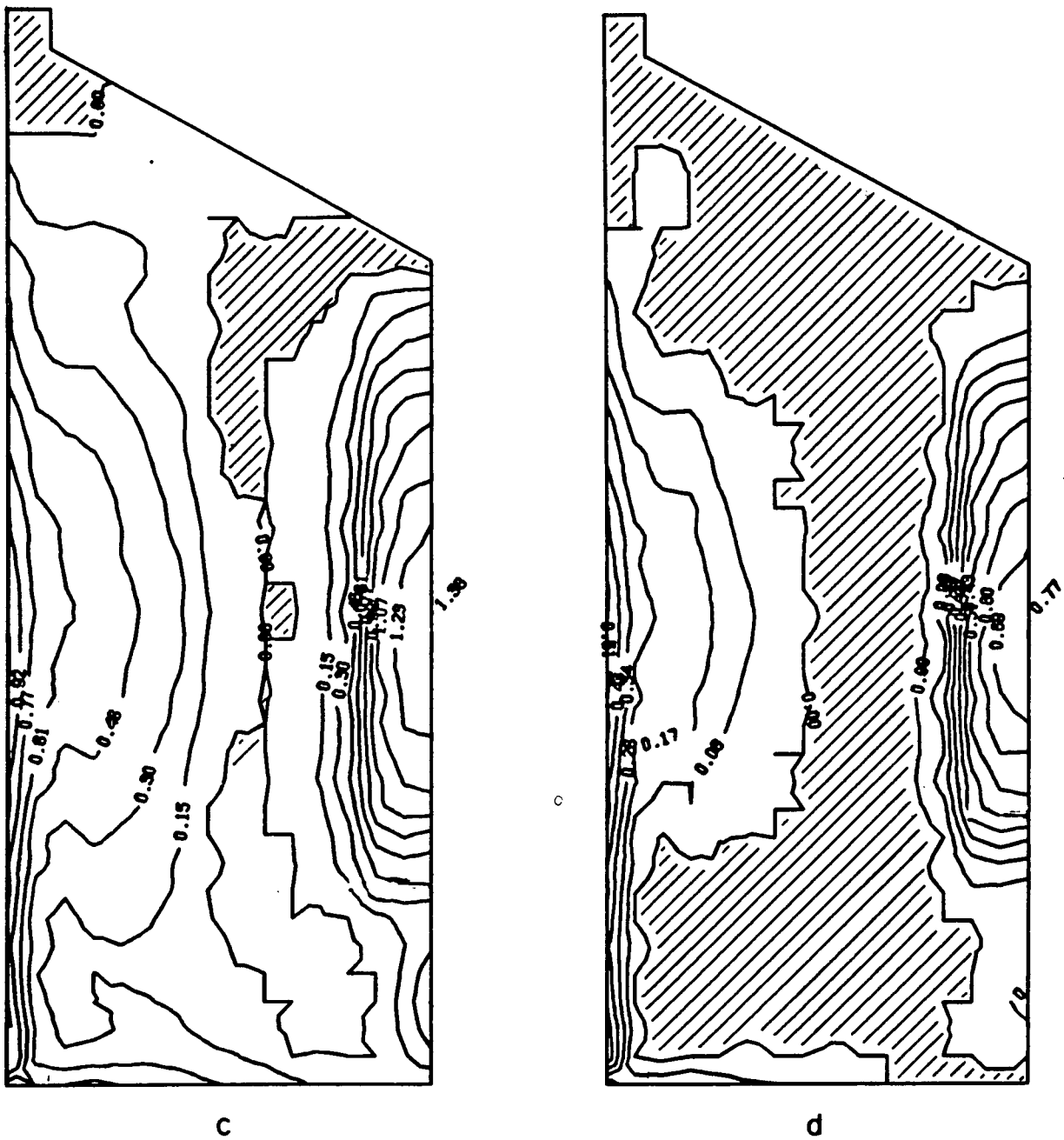

Figure 9.42 MRSS-CRSS (Yield) (MPa) for four temperature profiles with average gradients. (a) 33°C/cm, (b) 17°C/cm, (c) 11°C/cm and (d) 8°C/cm. Radius 27.5 mm, length 55 mm. Encapsulant thickness 21 mm. Argon pressure 2 atm.

imposed temperature profiles at a pressure of 30 atmospheres. At the largest gradient considered, the stress decreases only 3 % from 30 to 2 atmospheres. For the lower gradients the decrease is in the order of 20 %. For the lowest gradient considered the area with zero MRSS-CRSS (Yield) in Figure 9.42(d) increased about 25 % following the decrease in the largest stress value.

The results presented here show that the effect of pressure is not as important as might be expected. The weak effect of pressure observed in the present calculations when a stronger effect is expected, can be accounted for in the following way.

In the model the effect of pressure is included as affecting the convective component of the heat transfer coefficient as the square root of pressure. Reducing the pressure from 30 to 2 atmospheres reduces the value of convective heat transfer coefficient by 74 % . At low pressures the convective part is less than 10 % of the total value of the heat transfer coefficient. In this case the maximum variation in the total coefficient associated with the reduction in pressure will be less than 30 % . It was shown in Section 9.1 above, that a 30 % change in heat transfer coefficient does not substantially affect the stress level in the crystal. This explains why the effect of pressure in the present calculations is not significant.

A stronger effect of pressure is expected because pressure may markedly affect the temperature profile of the media surrounding the crystal. In the present calculations, it was assumed that changing the pressure does not alter the temperature

of the environment. This may not be the actual situation. When the pressure changes, not only the heat transfer coefficient at the crystal-gas interface changes but also the efficiency in heat transfer in the gas is altered. This higher efficiency will be manifested by a larger heat transfer coefficient at the boron oxide-gas interface. The net effect will be to decrease the temperature of the boron oxide surface increasing the gradient across the encapsulant and probably in the gas.

The change in heat transfer coefficient at the boron oxide-gas surface can be qualitatively described, assuming a free convection mechanism applies at this surface. In this case the heat transfer coefficient associated with this process can be written as

$$h_c = Nu\ k/l = 0.14\ (Gr\ Pr)^{1/3}\ (k/l) \qquad (9.1)$$

where Nu, Gr and Pr are the Nusselt, Grashof and Prandl numbers respectively. "k" is the thermal conductivity. "l" is the characteristic length of the horizontal heated surface from which heat is extracted. If it is assumed that the gas behaves like an ideal gas, the pressure dependence is introduced in the Grashof number through the density. In this case the heat transfer coefficient will depend on pressure with an exponent 2/3. For this pressure dependence the heat transfer coefficient is reduced by 83 % when depressurizing the chamber from 30 to 2 atmospheres. At the encapsulant-gas surface this change is more important than similar changes of the convective heat transfer coefficient at

the crystal-gas surface since in the first case convection is the main heat transfer mechanism. This is because boron oxide is transparent to radiation. Consequently the thermal gradient across the encapsulant will be more directly affected by pressure changes. On the other hand, increasing the pressure increases the heat transfer coefficient at the crystal-gas surface. In this case heat extraction from the crystal is improved reducing thermal gradients in the gas. The net effect of increasing the convective heat transfer coefficient at the crystal surface and increasing the gradients across the encapsulant could result in a stronger effect in the stress distribution in the crystal than any changes in the convective heat transfer coefficient.

The experimental results of Emori et al.[143-144] are in agreement with the effect of pressure on the thermal gradient across the encapsulant discussed above. For argon gas, reducing the pressure from 20 to 5 kg/cm^2 reduces the thermal gradient in the encapsulant from approximately $160^oC/cm$ to $140^oC/cm$; the thickness of encapsulant is not given. For neon and helium gases larger gradients were measured, with neon having the largest gradient. Changing gas pressure in neon has a stronger effect on gradients than in helium. They have explained the results by calculating the heat transfer coefficients for the different gases and pressures. For the calculation heat transfer from a vertical wall was assumed. In this case the heat transfer coefficient equation is written as

$$h = 0.53\ (k/l)\ (Gr\ Pr)^{1/4} \qquad (9.2)$$

This equation involves the same quantities as in Equation (9.1). The differences are the values of the numerical coefficients, the exponents affecting the quantities and the meaning of the characteristic length "l". In this case "l" is the length of the crystal which acts as a vertical wall. The calculations show a very good correlation between the gradient in the boron oxide for the different gases and pressures with the heat transfer coefficient values. This correlation is reproduced in Figure 9.43, curve A. The correlation, however, is basically inconsistent since the measurements were made without a crystal being present. Moreover, introducing the crystal and using a larger heat transfer coefficient will tend to reduce the temperature gradient across the encapsulant as explained above.

Fortuitously, the correlation in Figure 9.43 (curve A) gives the correct tendency but through a different mechanism. The gas pressure affects the temperature gradient across the encapsulant through changes in the heat transfer coefficient at the encapsulant-gas surface. A correlation between heat transfer coefficient values for heat transfer from an horizontal wall (Equation (9.1)) and measured gradients from Emori et al.[143,144] gives the results shown in Figure 9.43, curve B. In this case a deviation from linearity is observed. The correlation, however, is consistent with the physical process analysed.

From the model results and the above discussion it is possible to conclude that the gas pressure and gas composition

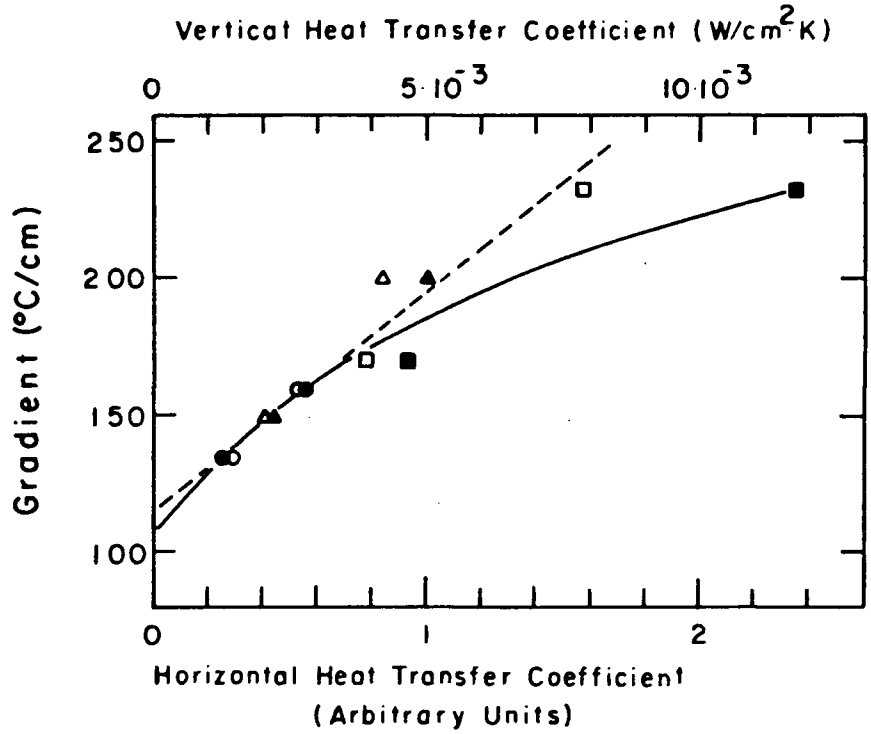

Gas	Pressure kg/cm²	Vertical	Horizontal
Ar	20 , 5	○	●
N_2	20 , 5	△	▲
He	20 , 5	□	■

Figure 9.43 Correlation between the measured temperature gradients across the encapsulant and the heat transfer coefficient values as a function of gas pressure and gas nature. Curve A from Refs. 143-144 using convection from a vertical wall ; and curve B using convection from an horizontal surface.

may affect the stress distribution in the crystal. A change in the heat transfer coefficient between the crystal and the gas is not enough to explain the large effect on dislocation density changes associated with gas pressure and composition. A full description of the effect of these variables requires the inclusion of the heat transfer mechanisms at the encapsulant-gas interface. A decrease in gas pressure decreases the heat flux to the gas at this surface which results in smaller thermal gradients across the encapsulant. Such an environment will give lower stresses in the crystal. Since the temperature profile in the environment is input in the model and reliable data on the effect of gas pressure and compositon is not available, precise calculations on this matter were not done.

9.7 Curvature of the Solid-Liquid Interface

The effect of a non-planar solid-liquid interface on the stresses is studied considering convex and concave interface shapes with respect to the melt. In both cases the interface is assumed to be a paraboloid of revolution which is represented by the following analytical functions

$$\xi = \pm 0.3 \rho^2$$

ρ and ξ are the nondimensional radial and axial position respectively with the origin situated at the axis of the crystal ; the + and - signs correspond to the convex and concave interfaces respectively. The value of the constant 0.3 gives the

relative displacement between the center and edge of the interface. The mesh used in this case is shown in Figure 9.44(a) for a convex and (b) for a concave interface. They are generated manually. The effect of a number of growth conditions combined with the interface shape is considered. The most important observations follow.

9.7.1 Convex interface

The effect of a convex interface combined with the effect of crystal length, thermal conditions and crystal radius is considered.

9.7.1.1 Crystal Length

Conditions : R, 27.5 mm ; CA, 30° ; AP, 30 atm. ;
B, 21 mm ;
Temperature profile as in Figure 8.19, curve 4,
CL : (a) 27.5 mm = R, (b) 55.0 mm = 2 R,
(c) 82.5 mm = 3 R .

The temperature and Von Mises stress fields for a crystal length of 55 mm are shown in Figure 9.45. In the right part of the figure the temperature field is different than that for a crystal with a flat interface. In the lower half of the crystal the isotherms present a large curvature following the interface shape and giving negative radial gradients. In this part of the crystal the axial gradients are larger at the crystal edge than

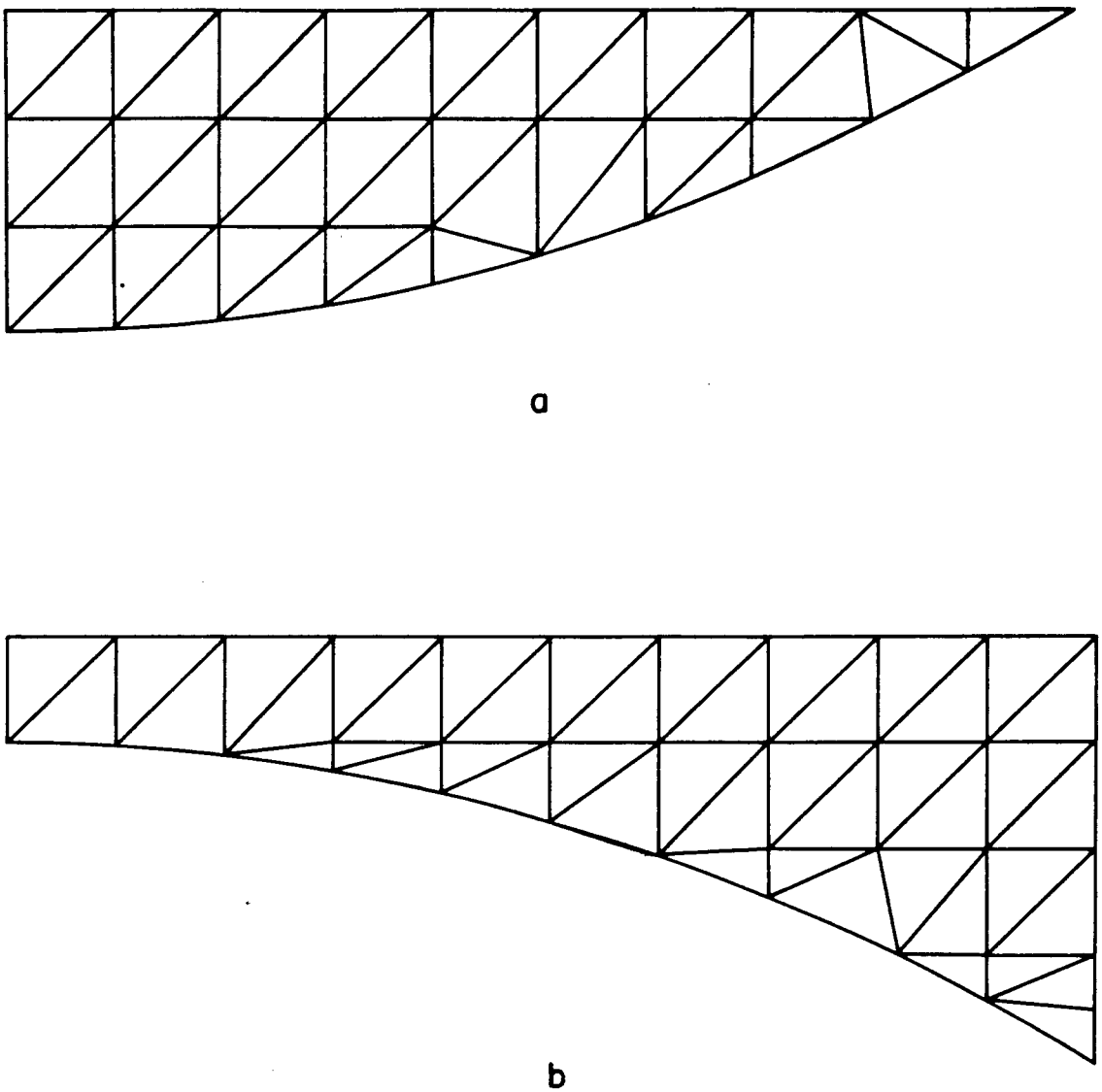

Figure 9.44 Element and nodal configuration at the interface for crystals with curved interface. (a) Convex interface, (b) Concave interface.

at the axis. The axial gradients at the axis do not change with distance from the interface.

The Von Mises stress field which is shown in the right part of Figure 9.45 is different than the distribution obtained with a planar interface. The largest VMS is observed to be in two regions in the crystal, below the crystal shoulder and at the edge of the solid-liquid interface. The origin and nature of the first stress concentration was discussed previously for the case of a planar interface. The magnitude of the VMS in this region is about 14 % less than for a planar interface. The stress concentration at the interface edge, which is unique for a curved interface, shows stress values which are 30 to 40 % larger than the stress below the shoulder. On the other hand the region with low stresses, which for a planar interface is at the interface edge, has moved to the center and lower part of the crystal near the axis. The lowest stresses are three times smaller than for a planar interface.

The largest stress at the interface edge is associated with the large radial and axial gradients in that region. The lowest stress close to the crystal axis and about 2 cm from the interface is associated with the nearly constant gradient in this region.

The MRSS contours for the three crystal lengths are shown in Figure 9.46(a-c). Comparing the right part of Figure 9.45 and Figure 9.46(a), it is observed that the VMS and MRSS relative

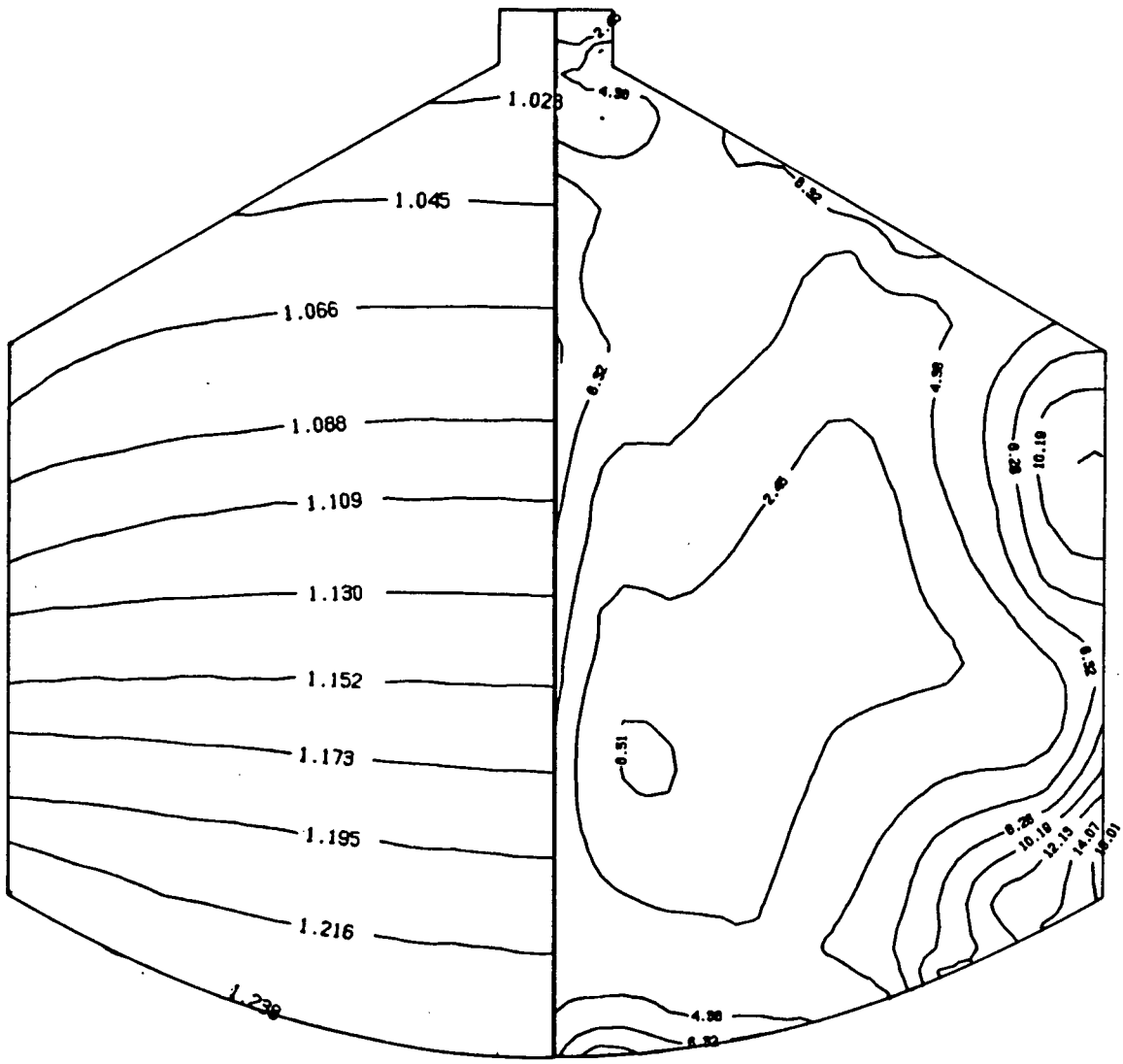

Figure 9.45 Temperature (10^{3o}C) and Von Mises stress (MPa) fields for a crystal with a convex interface shape. Radius 27.5 mm. Length 27.5 mm. Encapsulant thickness 21 mm. Temperature profile as shown in Figure 8.19, curve 4.

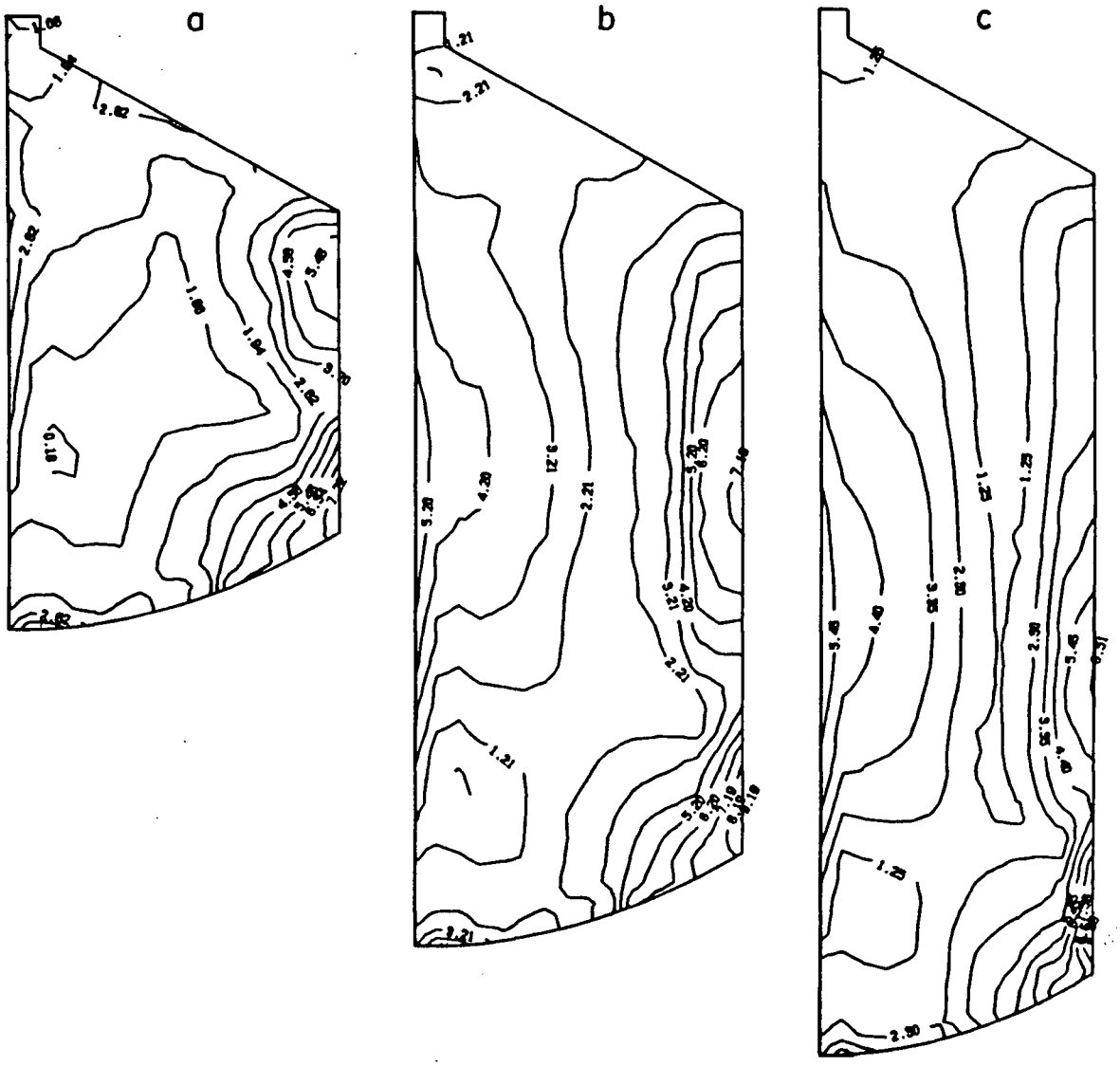

Figure 9.46 MRSS (MPa) contours for a crystal with convex interface at three lengths. (a) 27.5 mm, (b) 55 mm, (c) 82.5 mm. The largest stresses at the interface edge are (a) 7.22 MPa, (b) 9.19 MPa, (c) 9.66 MPa. Radius 27.5 mm, Boron oxide thickness 21mm. Profile as in Figure 8.19, curve 4.

distributions are similar. The absolute levels for the MRSS are approximately half of the corresponding VMS at any point.

The effect of crystal length in the MRSS distribution is shown in Figure 9.46(a-c). Comparing the three distributions it is possible to distinguish two regions with specific and reproducible characteristics. One is the region close to the interface which extends to a distance of approximately a radius from the interface at the axis. The second is the crystal above this region. The stress distribution, in the lower part of the crystal, experiences little change with crystal length and is characteristic of the convex interface shape. The region above this has a stress distribution similar to the distribution in a crystal with flat interface. From this it is concluded that the effect of this convex interface does not extends further than a length comparable to the crystal radius.

The largest stress value at the interface edge increases with crystal length from (a) to (b) and slightly increases from (b) to (c). This last effect is attributed to a slight increase in axial temperature gradient.

The stress distributions of the MRSS-CRSS (Yield) is shown in Figure 9.47(a-c) for the three crystal lengths. In (a) there are two regions with zero stress which are associated with the regions with the lowest stresses from Figure 9.46(a). This zero stress region also appears in (b) and (c). In (c) the upper part of the crystal shows a large area with zero stress.

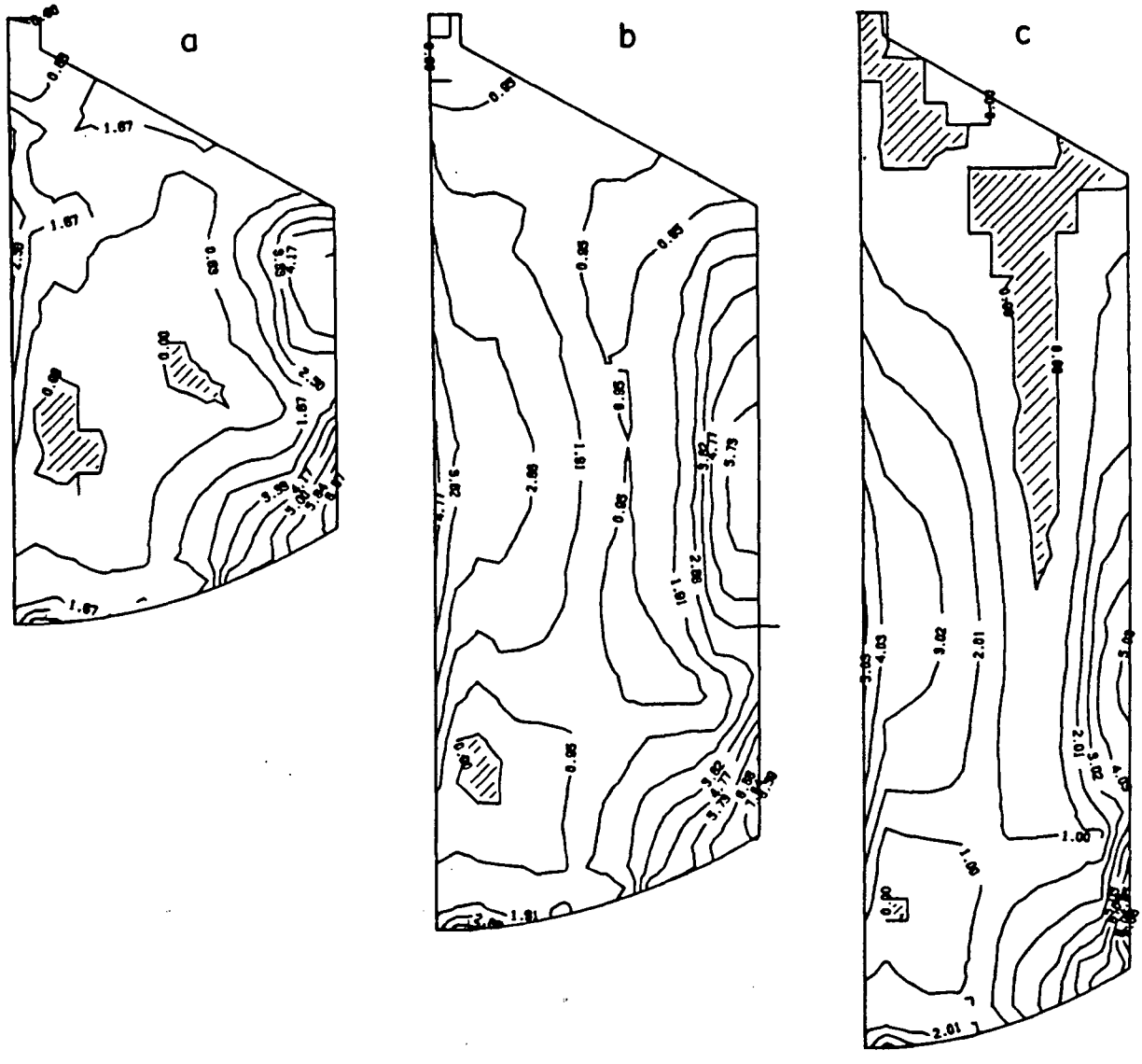

Figure 9.47 MRSS-CRSS (Yield) (MPa) contours for a crystal with convex interface at three lengths (a) 27.5 mm, (b) 55 mm, (c) 82.5 mm. Radius 27.5 mm, boron oxide thickness 21 mm. Profile as in Figure 8.19, curve 4.

The dislocation density in the crystal at the end of growth depends on the position in the crystal. The large MRSS-CRSS (Yield) in Figure 9.47(a-c) at the interface edge suggests that the dislocations at the crystal surface are formed right after solidification and not above the encapsulant surface as with the plane interface. The axial MRSS-CRSS (Yield) near the crystal surface is lowest close to the cone, gradually increasing with distance from the cone. At a distance of 50 mm from the cone the MRSS-CRSS (Yield) is double that close to the cone. At the centre, the largest stresses at a distance of a radius from the interface is half the stress at the edge. At the seed and bottom ends of the crystal the stresses are low and never reach the maximum stresses. At the seed end, the maximum stress is always less than 3.0 MPa that is, half the value at the edge. Similar results are obtained at the tail end where the maximum stress at the centre occurs very close to the interface. Thus cross-sections at any distance from the cone will have a W-shaped MRSS-CRSS (Yield) distribution along a diameter except at the tail end where the MRSS-CRSS (Yield) distribution is U-shaped. The edge of the U is three times higher than the centre.

The symmetry of the MRSS-CRSS (Yield) in (001) planes depends on the position of the plane with respect to the cone. Close to the cone the MRSS-CRSS (Yield) has the symmetry shown in Figure 9.48. This cross-section is at a distance of 11.0 mm from the cone when the crystal is 27.5 mm long (Figure 9.47(a)). The maximum stress is reached at this point.

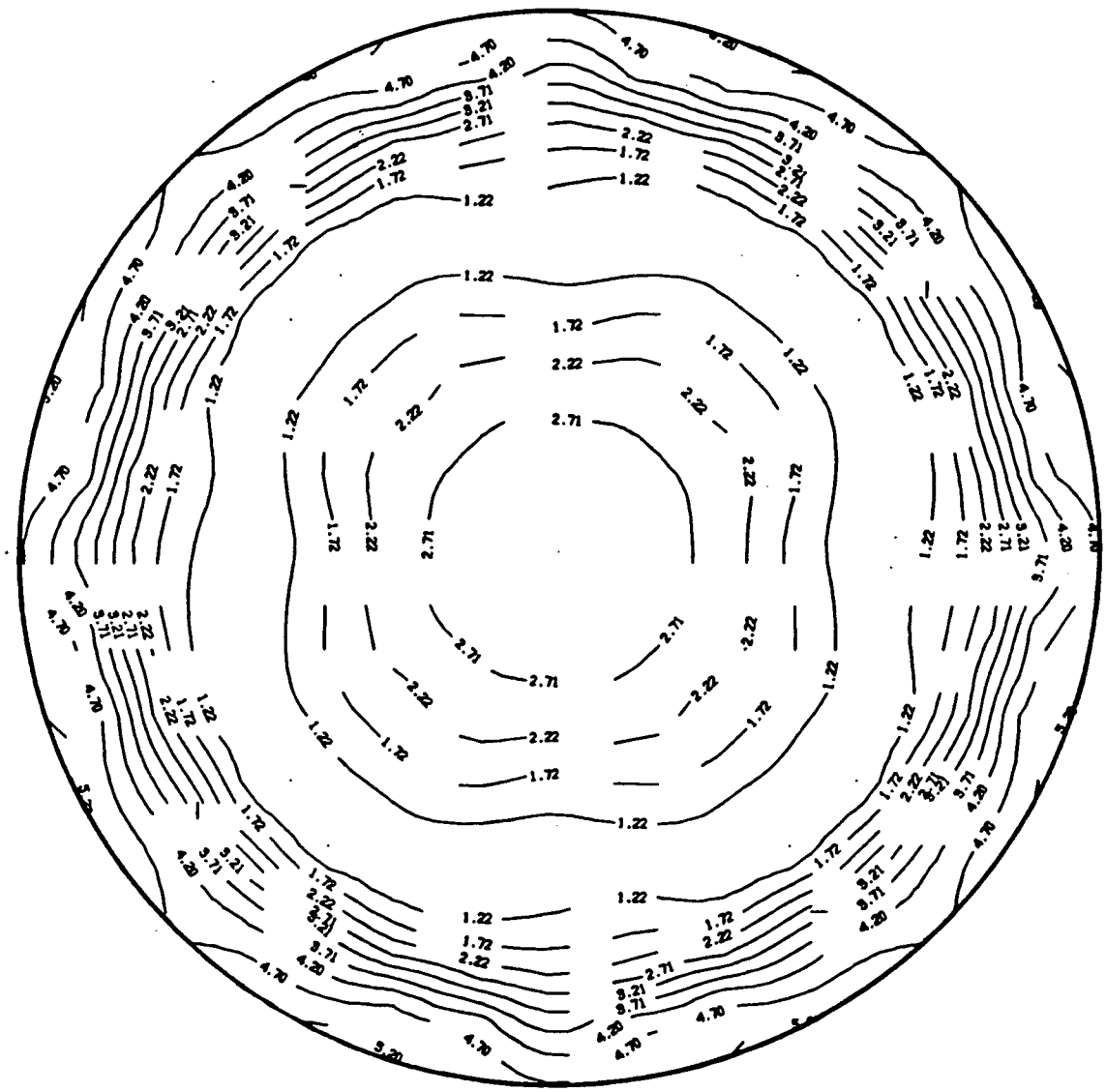

Figure 9.48 MRSS-CRSS (Yield) (MPa) contours in a (001) plane at a distance of 11 mm from the cone in the crystal shown in Figure 9.47(a).

The symmetry of the MRSS-CRSS (Yield) in sections which are more than 55 mm far from the ends of the crystal at the end of growth will be determined by the sequence of symmetry changes shown in Figure 9.49(a-c). Despite the fact that these sections were taken from only one crystal (Figure 9.47(c)), it was observed that all the sections far from the ends pass through the same symmetry patterns and stress levels. Close to the interface (part (a)) there is four-fold symmetry with an U-distribution along a diameter. At the edge eight-fold symmetry is present. In this region the dislocations are expected to have the same symmetry. Sections from the tail end show a symmetry of the dislocations as shown in Figure 9.49(a).

9.7.1.2 Effect of Encapsulant Thickness and Gradient

Conditions : B, 50 mm ;

Temperature profiles as in Figure 9.35(b),

The results for the stress distributions for two gradients are shown in Figure 9.50(a-b) for a $50^{o}C/cm$ gradient and Figure 9.51(a-b) for a $12.5^{o}C/cm$ gradient. Part (a) in each figure corresponds to the MRSS distribution and part (b) to the MRSS-CRSS (Yield) distribution.

The MRSS distributions for the two gradients show a concentration of stress at the interface edge and below the shoulder. The stress at the interface edge is about 80 % larger than below the shoulder. The lowest stress level occurs at the

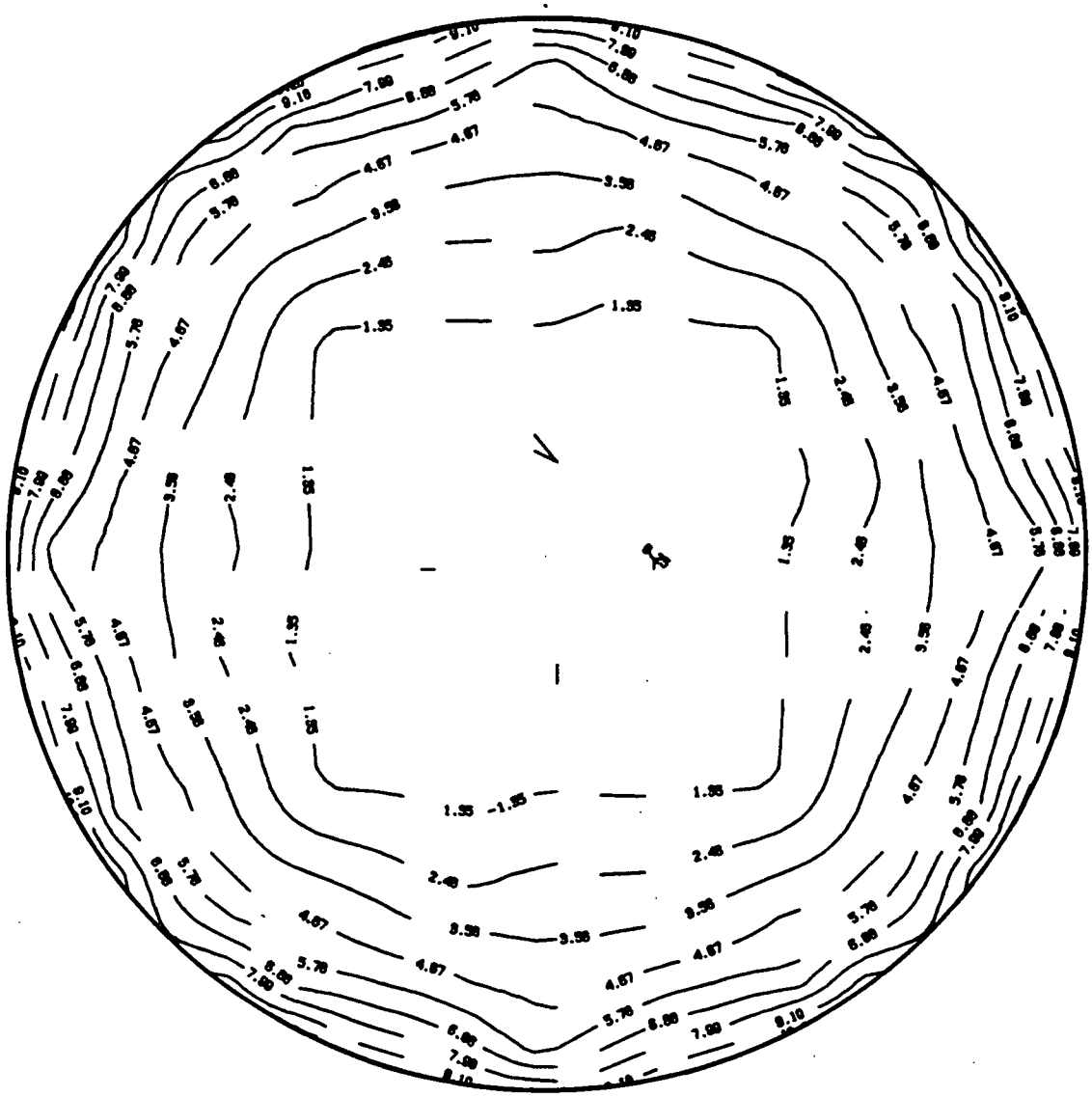

a

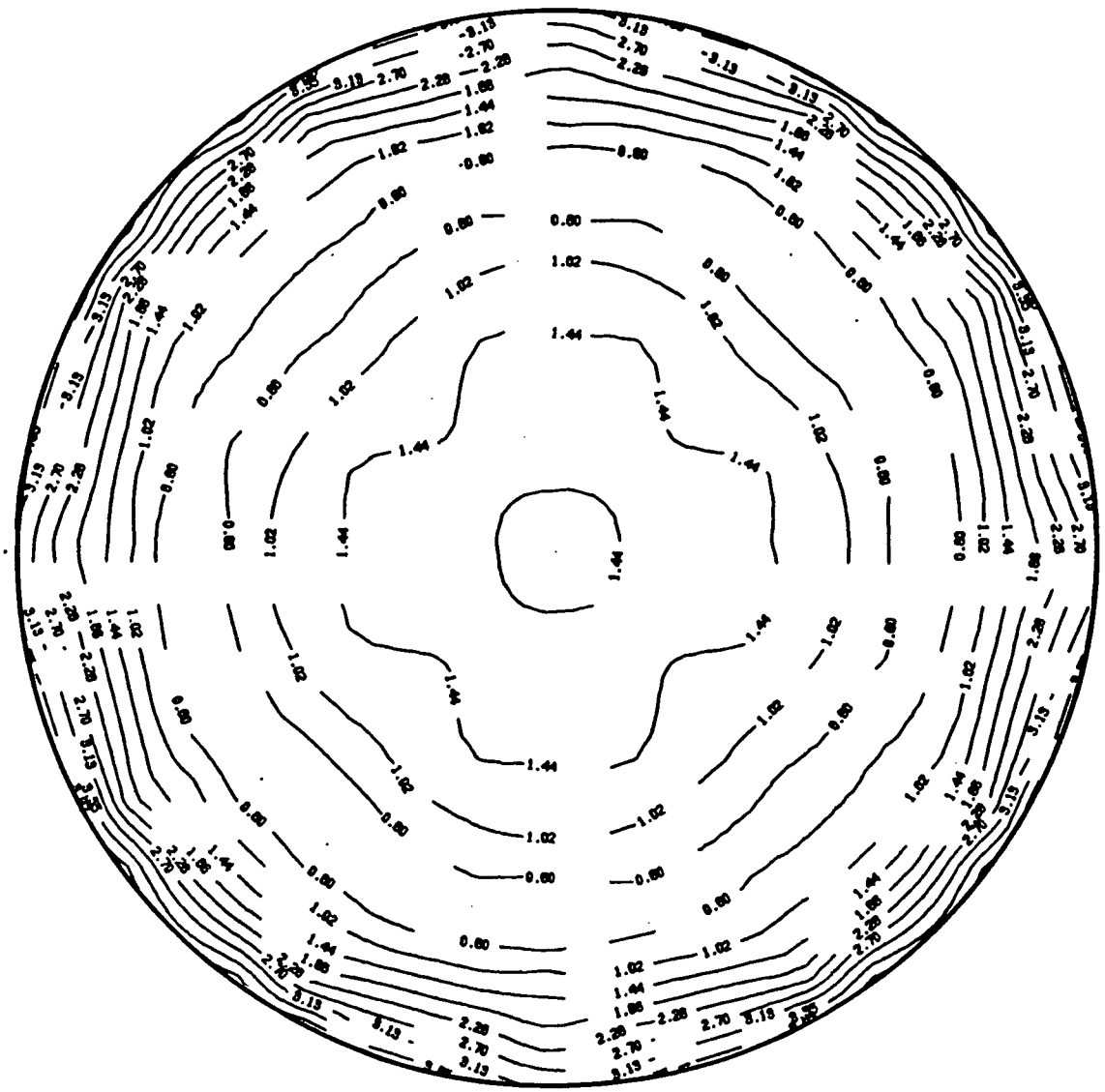

b

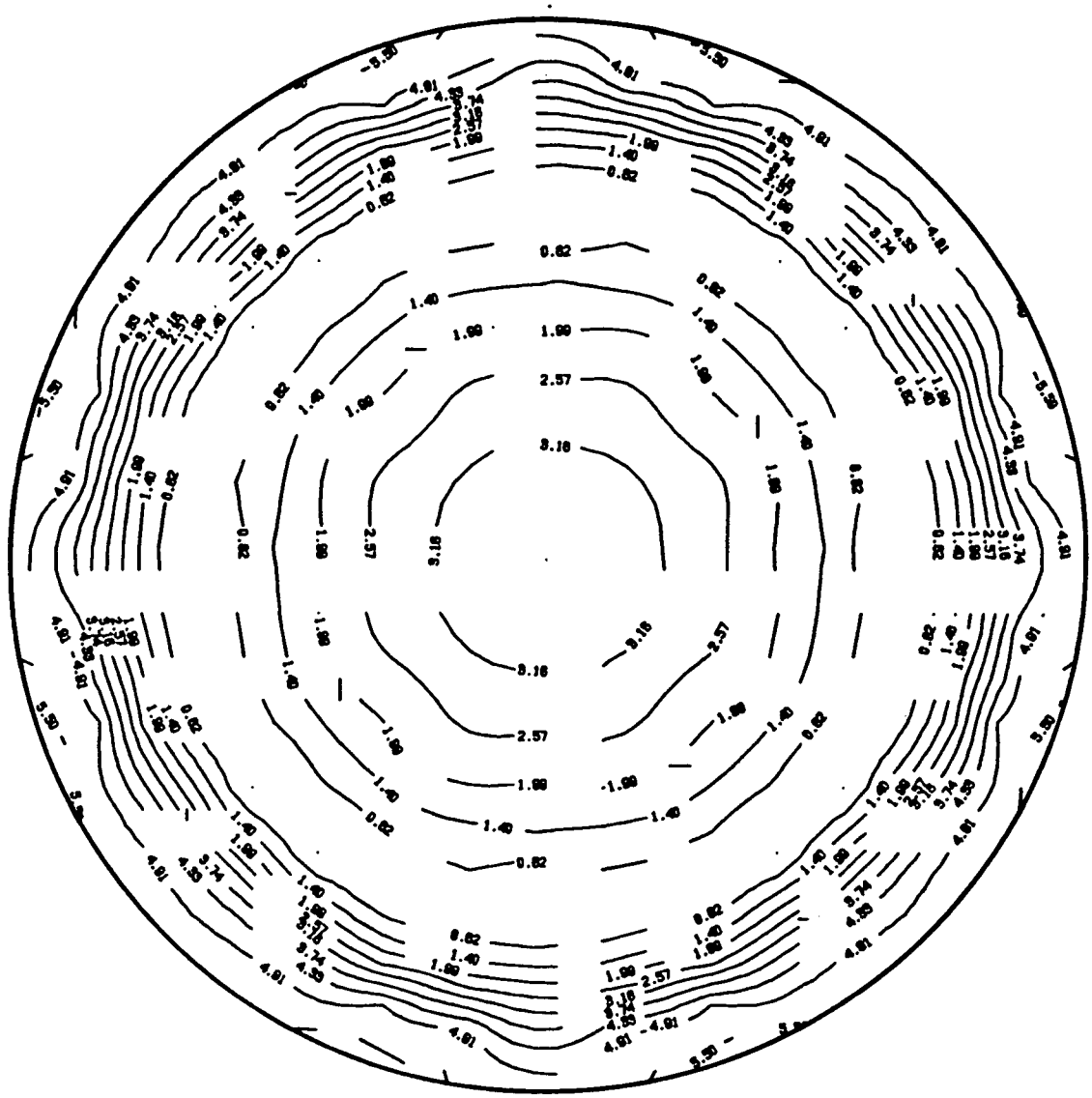

Figure 9.49 MRSS-CRSS (Yield) (MPa) contours in (001) planes at three distances form the cone. (a) 79.75 mm, (b) 66.0 mm, (c) 52.25 mm. Section corresponds to the crystal shown in Figure 9.47(c).

Figure 9.50 (a) MRSS (MP) and (b) MRSS-CRSS (Yield) (MPa) for a crystal with convex interface. Boron oxide thickness 50 mm. Radius 27.5 mm. Length 55 mm. Average gradient 50°C/cm.

Figure 9.51 (a) MRSS (MP) and (b) MRSS-CRSS (Yield) (MPa) for a crystal with convex interface. Boron oxide thickness 50 mm. Radius 27.5 mm. Length 55 mm. Average gradient 17°C/cm.

centre of the crystal. The largest stress value at the interface edge decreases proportionally with a reduction in gradient.

The MRSS-CRSS (Yield) in part (b) of the figures for the two gradients shows zero stress regions. The area of this region substantially increases with the gradient. For both conditions large areas close to the interface edge show stresses which are larger than the CRSS (Yield).

9.7.1.3 Effect of crystal Radius

Conditions : R, 40 mm ; CL, 80 mm ; B, 21 mm ;
Temperature profile a in Figure 8.19, curve 4.

The MRSS and the MRSS-CRSS (Yield) for this crystal are shown in Figure 9.52(a) and (b) respectively. The stress distributions are similar to those obtained with the 27.5 mm crystal with two common characteristics. Large stress levels exist at the interface edge and above the encapsulant surface. The largest stress occurs at the interface edge. It is important to note that while the stress level above the encapsulant surface increases as the radius increases (45 %), the stress level at the interface edge only increases about 10 %. On the other hand the symmetry of stresses in (001) planes show the same features as described for the 27.5 mm crystal.

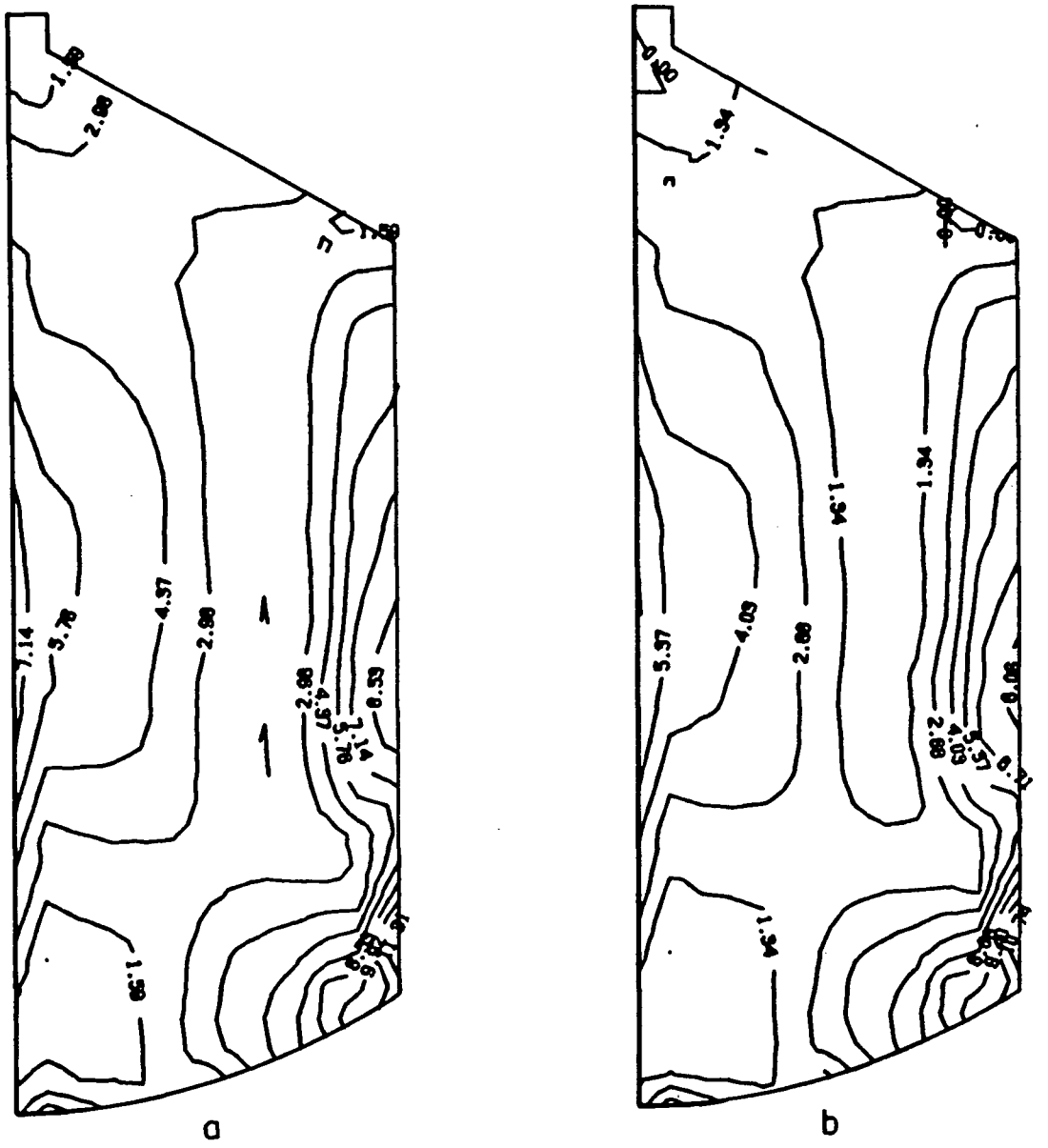

Figure 9.52 (a) MRSS (MP) and (b) MRSS-CRSS (Yield) (MPa) for a crystal with convex interface. Boron oxide thickness 21 mm. Radius 40 mm. Length 80 mm. Average gradient 55°C/cm.

9.7.2 Concave Interface

Conditions : B, 21 mm ;

Temperature profile as in Figure 8.19, curve 4,

a) R, 27.5 mm ; CL, 55 mm ;

b) R, 40 mm ; CL, 80 mm.

The results for the MRSS-CRSS (Yield) for the two crystal radii are shown in Figure 9.53(a) and (b). Part (a) for the 27.5 mm radius and part (b) for the 40 mm radius.

As in the case of the convex interface, the stress distribution may be divided in two regions. One close to the interface and extending a distance from the interface comparable to the radius and another formed by the region above this section. The low region has stress distributions which are similar for both crystal radii and are characteristic of the concave interface shape. Very large stresses are present at the interface with largest stress at the centre of the crystal.

In the second region, well above the interface, the stress distribution is similar to that obtained with a planar interface. The largest stresses occur at the interface and therefore the dislocation density is controlled by the stress distribution at the concave interface. For this interface shape, the stress distribution in the radial direction follows the W shape with the centre about 15 % higher than the edges.

The effect of increasing the radius for a concave interface is different than that obtained for a convex interface. For

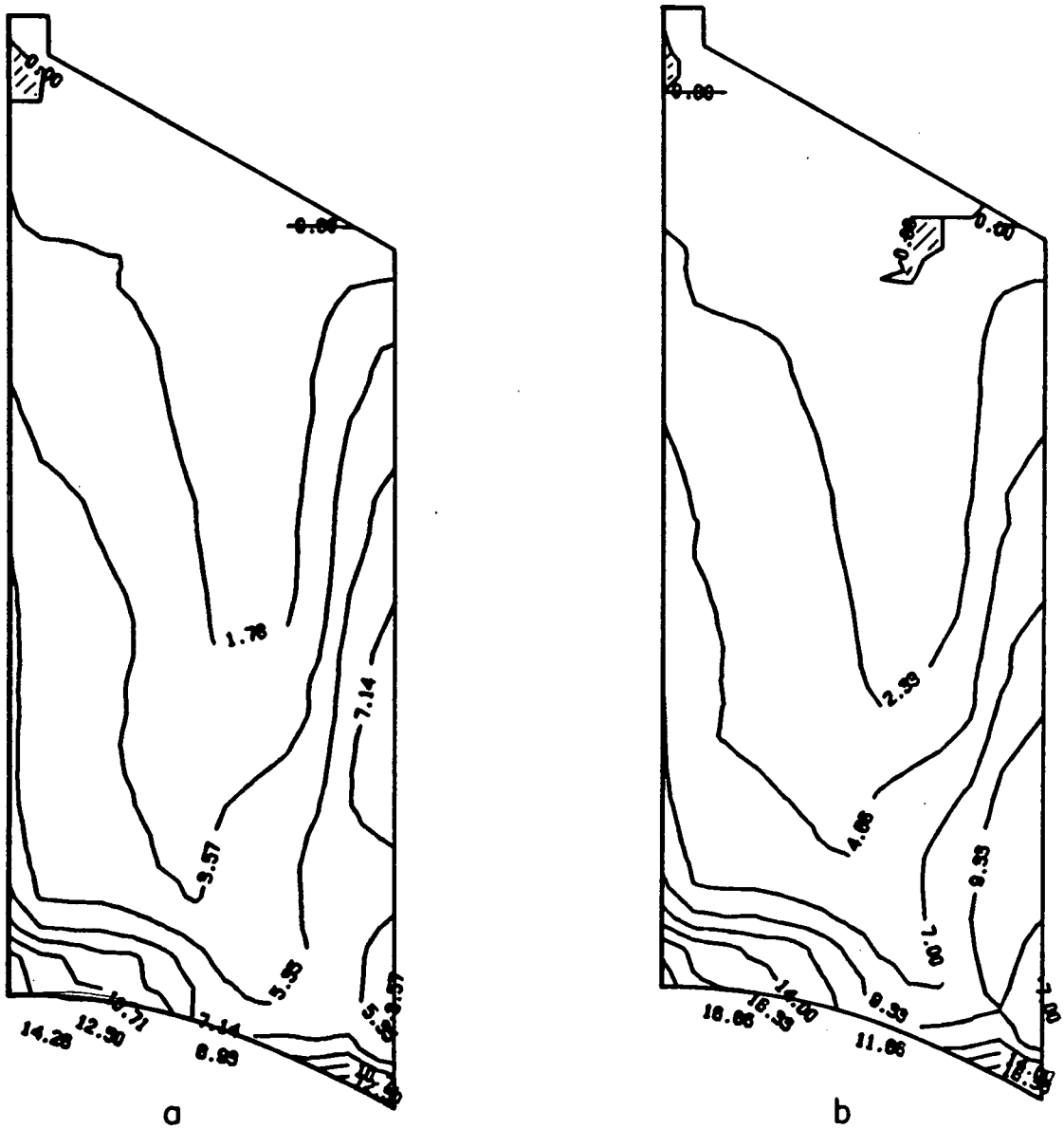

Figure 9.53 (a) MRSS (MP) and (b) MRSS-CRSS (Yield) (MPa) for a crystal with concave interface. (a) Radius 27.5 mm, (b) 40 mm. Boron oxide thickness 21 mm.

the concave interface increasing the radius about 45 % increases the largest stress value from 14.26 MPa to 18.86 MPa (30 %).

The symmetry of the dislocations formed close to the interface is shown in Figure 9.54. This (001) plane corresponds to a section at 2.75 mm from the interface for the 27.5 mm crystal. Similar symmetry is observed for the 40 mm crystal. In the central region eight-fold symmetry is observed. Four-fold symmetry is also observed in a ring close to the edge. In this case typical eight-fold at the edge is not observed.

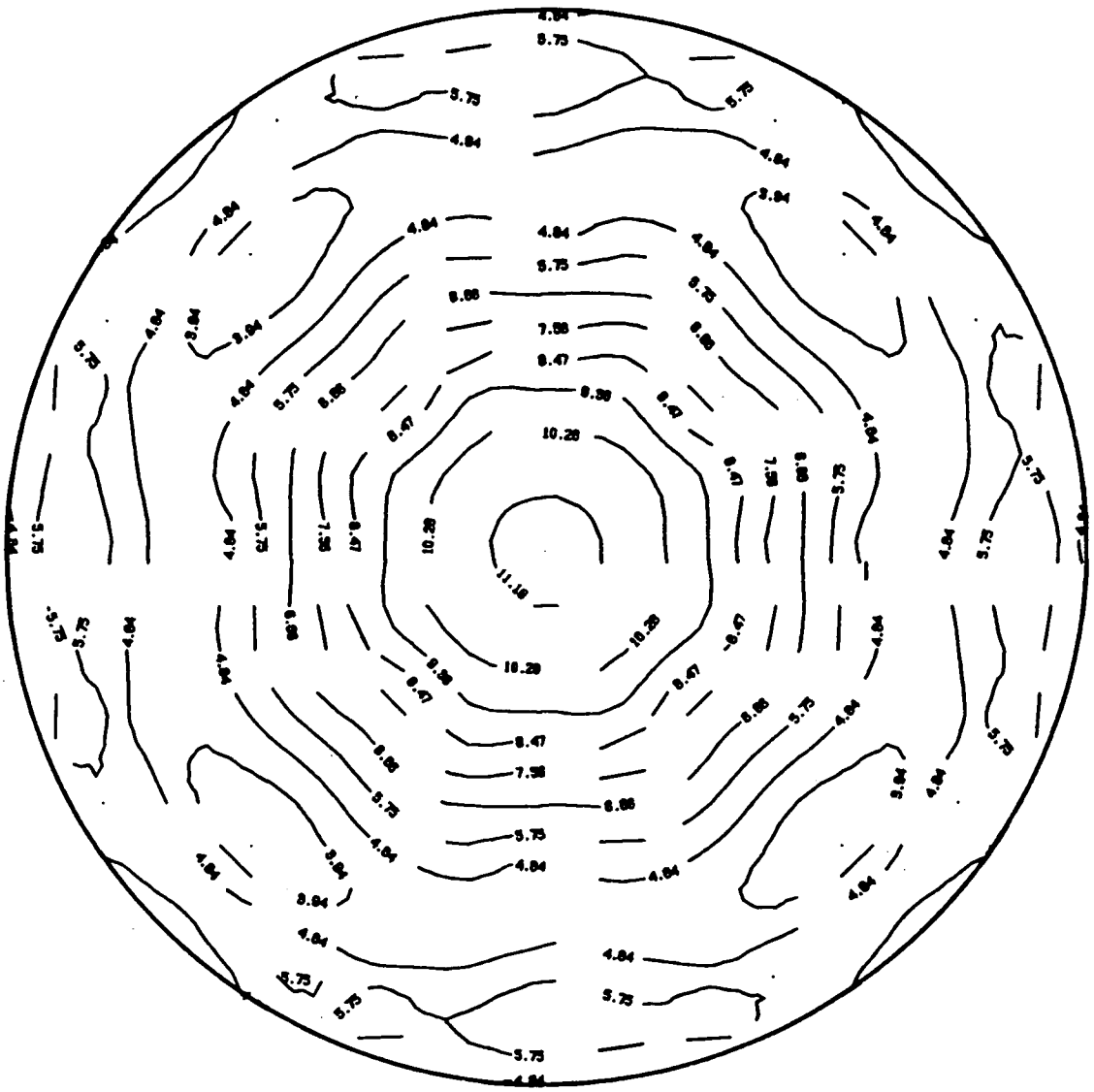

Figure 9.54 MRSS-CRSS (Yield) (MPa) contours in a (001) plane at a distance of 2.75 mm from the interface in the crystal shown in Figure 9.53(a).

CHAPTER 10

RESULTS FOR COOLING AFTER GROWTH

Using the combined analytical and numerical scheme described in Chapter 7 and evaluated in Chapter 8 the temperature and stress fields during cooling after growth are calculated. Results are obtained for a crystal with a radius 27.5 mm and a length of 110.0 mm. This length corresponds to the largest length for which stress and temperature calculations are made during growth. The axial temperature at the end of growth is the initial temperature field for the cooling model with the radial gradient neglected.

In the calculation of the thermal and stress fields in the crystal after solidification, the initial temperature profile in the crystal, and the thermal characteristics of the media surrounding the crystal are of major significance. In the calculations, three temperature gradients in the region of length R above the interface are considered, 70, 35 and 17.5^{o}C/cm designated as GC, GC/2 and GC/4. These gradients are about half the gradients in the growing chamber during solidification.

The crystal as it cools, is surrounded by either argon at 30 atmospheres or boron oxide. The argon temperatures considered are 800 and 1000°C and the boron oxide temperature is taken as 1000°C.

10.1 Ambient Temperature 1000°C

10.1.1. Argon

10.1.1.1. Initial Gradient GC = 70°C/cm

The temperature distribution over the right half of a vertical section of a crystal after 5 seconds from solidification is shown in Figure 10.1(a). The results show that in a region of about 1 cm adjacent to the interface, the temperature has dropped rapidly. The axial gradient in this region changes from positive to negative. The radial gradients are high, and the temperature drop at the edge is large, about 80°C. The radial gradient is negative between the interface and the 1000°C isotherm, and then becomes positive at lower temperature. With a changing ambient temperature, which is normally the case, ambient temperatures will be lower than the crystal surface temperatures resulting in negative radial gradients throughout the crystal. The assumption of constant ambient temperature in the model will likely give calculated stress levels which are too low. This error will become less significant as the ambient temperature gradients become smaller.

The temperature distribution 10 seconds after solidification is shown in Figure 10.1(b). Comparing (a) and (b) the curvature of the isotherms near the interface has increased giving higher radial gradients. In (b) the axial gradient at the interface is less than in (a) and the distance above the interface where the axial gradient changes sign has increased.

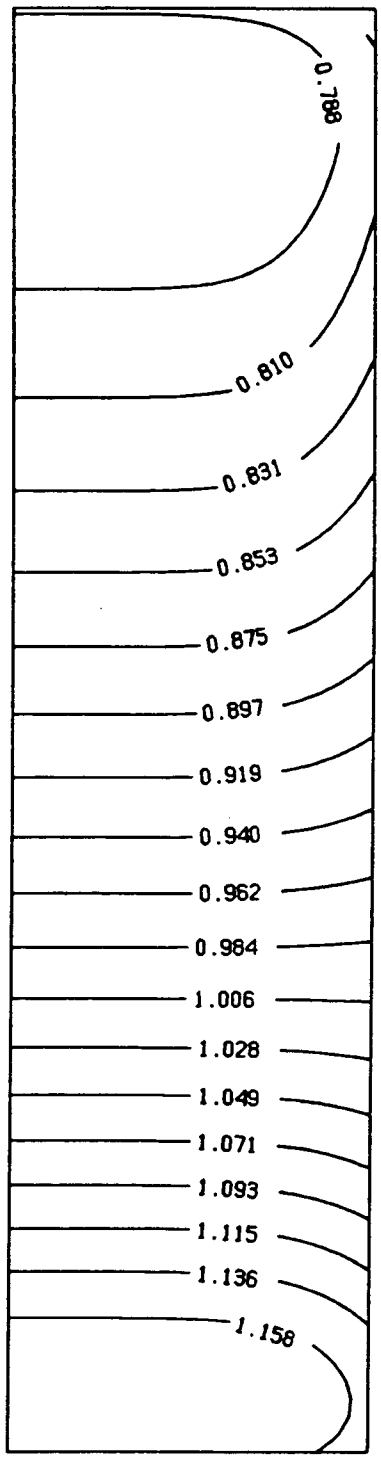
0.788
0.810
0.831
0.853
0.875
0.897
0.919
0.940
0.962
0.984
1.006
1.028
1.049
1.071
1.093
1.115
1.136
1.158

a

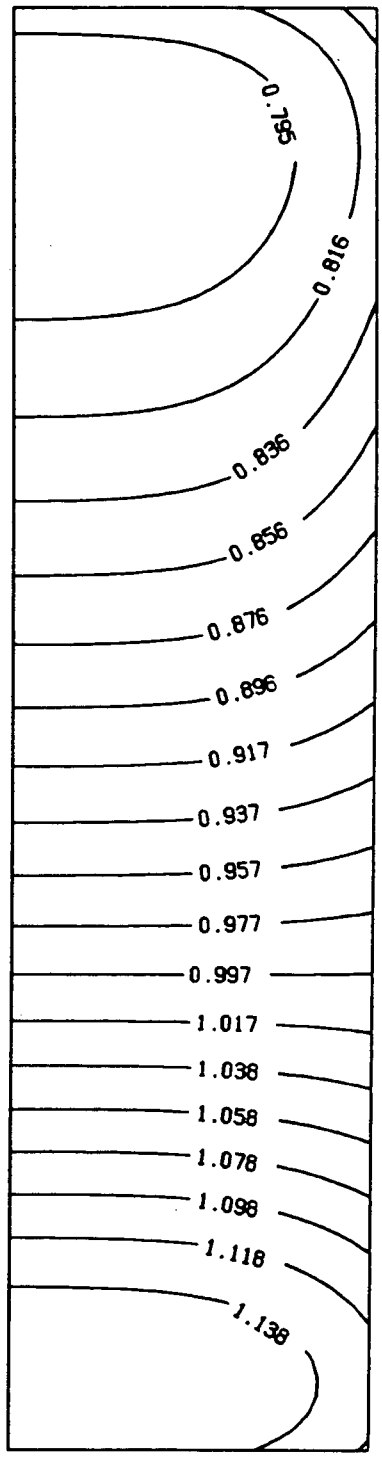
0.795
0.816
0.836
0.856
0.876
0.896
0.917
0.937
0.957
0.977
0.997
1.017
1.038
1.058
1.078
1.098
1.118
1.138

b

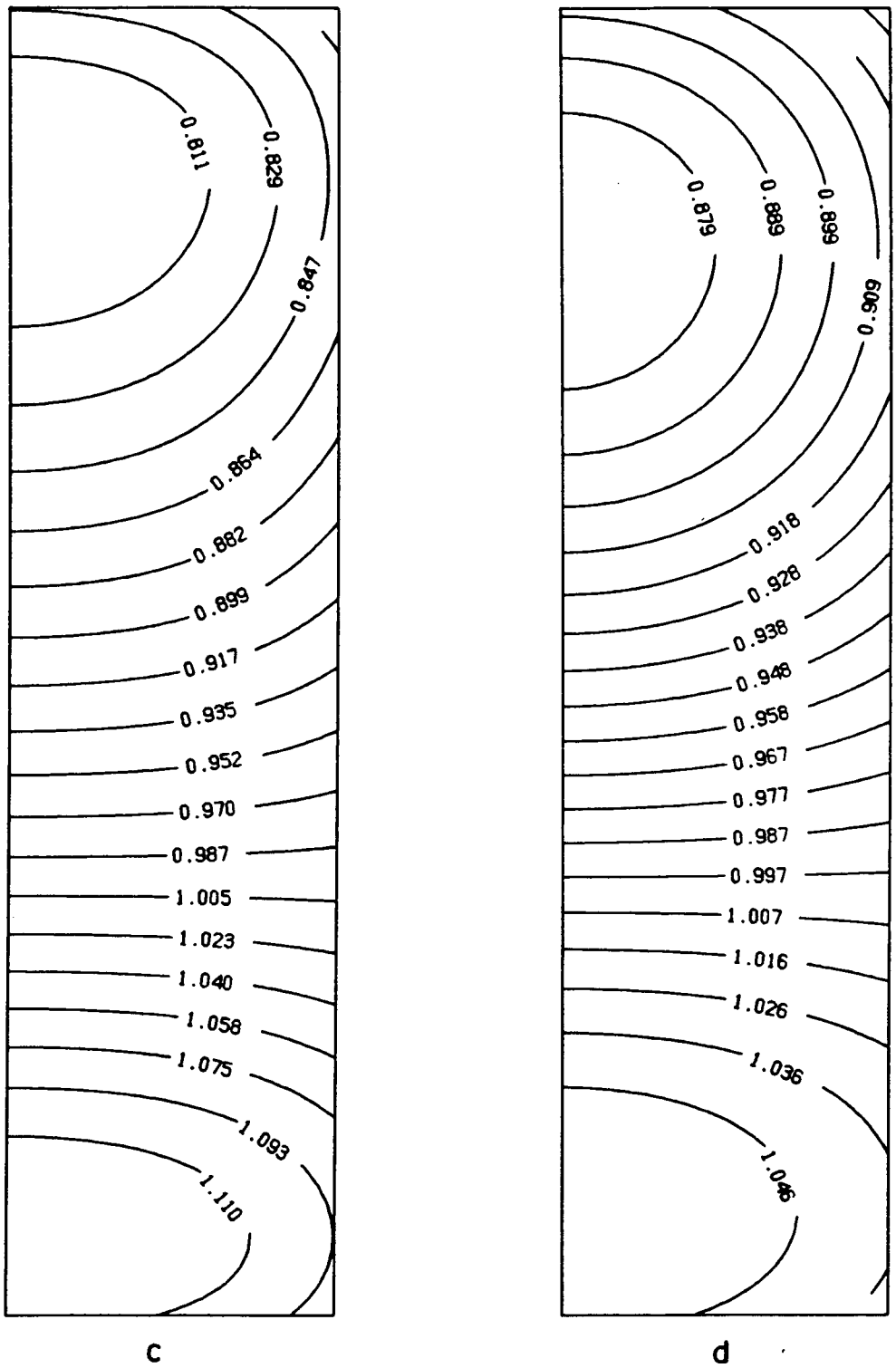

Figure 10.1 Temperature (10^{3o}C) field during cooling at four times. (a) 5 s, (b) 10 s, (c) 20 s, (d) 60 s, Initial gradient close to interface 70°C/cm. Argon temperature 1000°C

The temperature distribution after 20 seconds (Figure 10.1(c)) shows continuing high radial gradients close to the interface and a considerably decreasing axial gradient. After 60 seconds (Figure 10.1(d)) the temperature distribution has become much more uniform. By 300 seconds, the calculations show the temperature distribution is almost uniform throughout the crystal.

The very rapid cooling in the first five minutes after solidification supports the quasi-steady state approximation assumed in the calculations of the temperature distribution during crystal growth.

Further examination of the isotherms in Figure 10.1(a-d) shows that mixed control of the heat transfer process occurs during cooling. This can be concluded from the observation that the 1000°C isotherm does not move considerably from a to d in Figure 10.1. Heat transfer control at the surface would considerably move such isotherm upwards in the crystal. On the other hand, heat transfer control in the bulk crystal would give larger than the observed radial gradient.

The MRSS-CRSS (Yield) determined from the temperature distributions shown in Figure 10.1(a-d) are shown in Figure 10.2(a-d). The largest stresses are observed to occur at the interface. A low stress region is present about 1 cm above the interface midway between the outside surface and the vertical axis which moves towards the axis with time. As a result of the

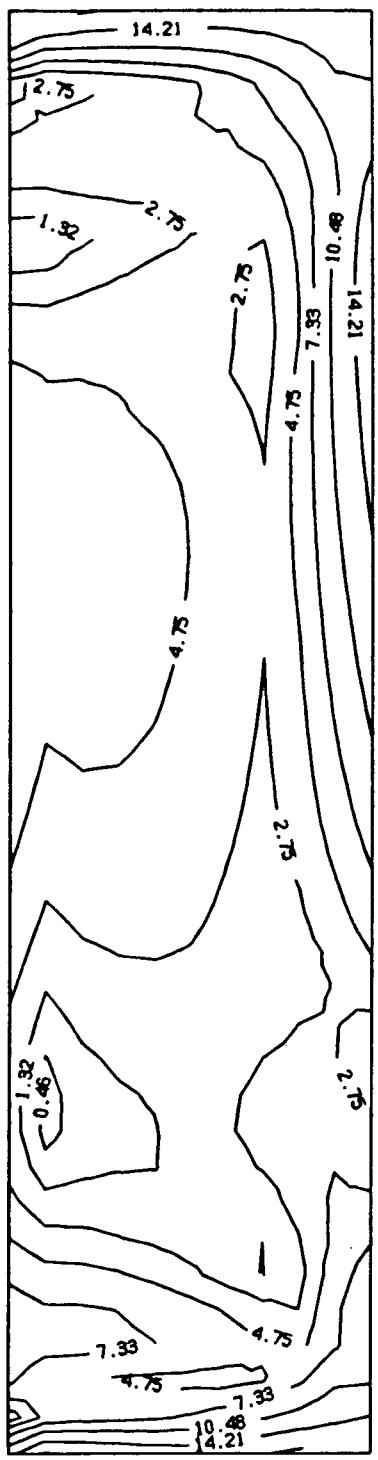
14.21
2.75
1.32
2.75
2.75
10.48
14.21
7.33
4.75
4.75
4.75
2.75
1.32
0.48
2.75
7.33
4.75
7.33
10.48
14.21

a

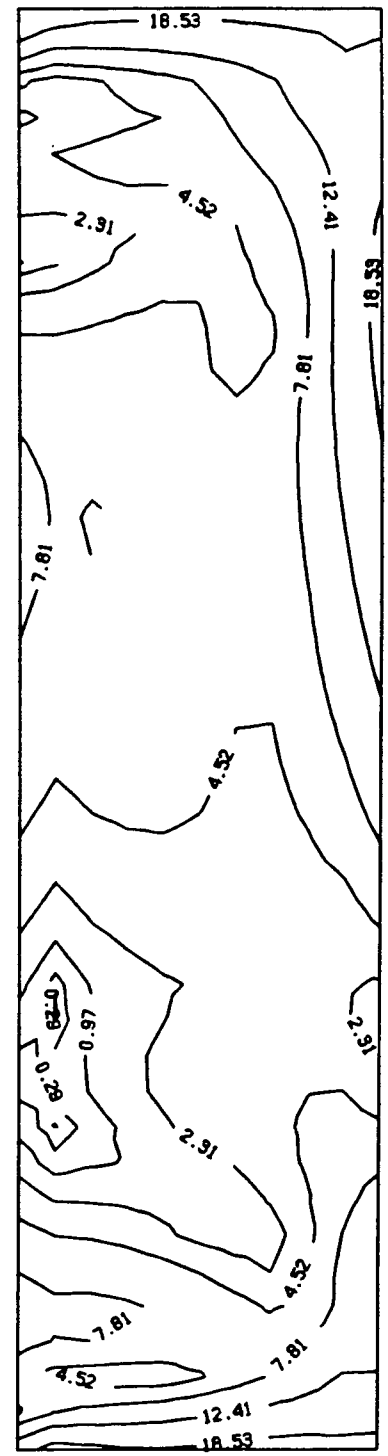
18.53
4.52
2.91
12.41
18.53
7.81
7.81
4.52
0.28
0.97
2.91
2.91
4.52
7.81
4.52
7.81
12.41
18.53

b

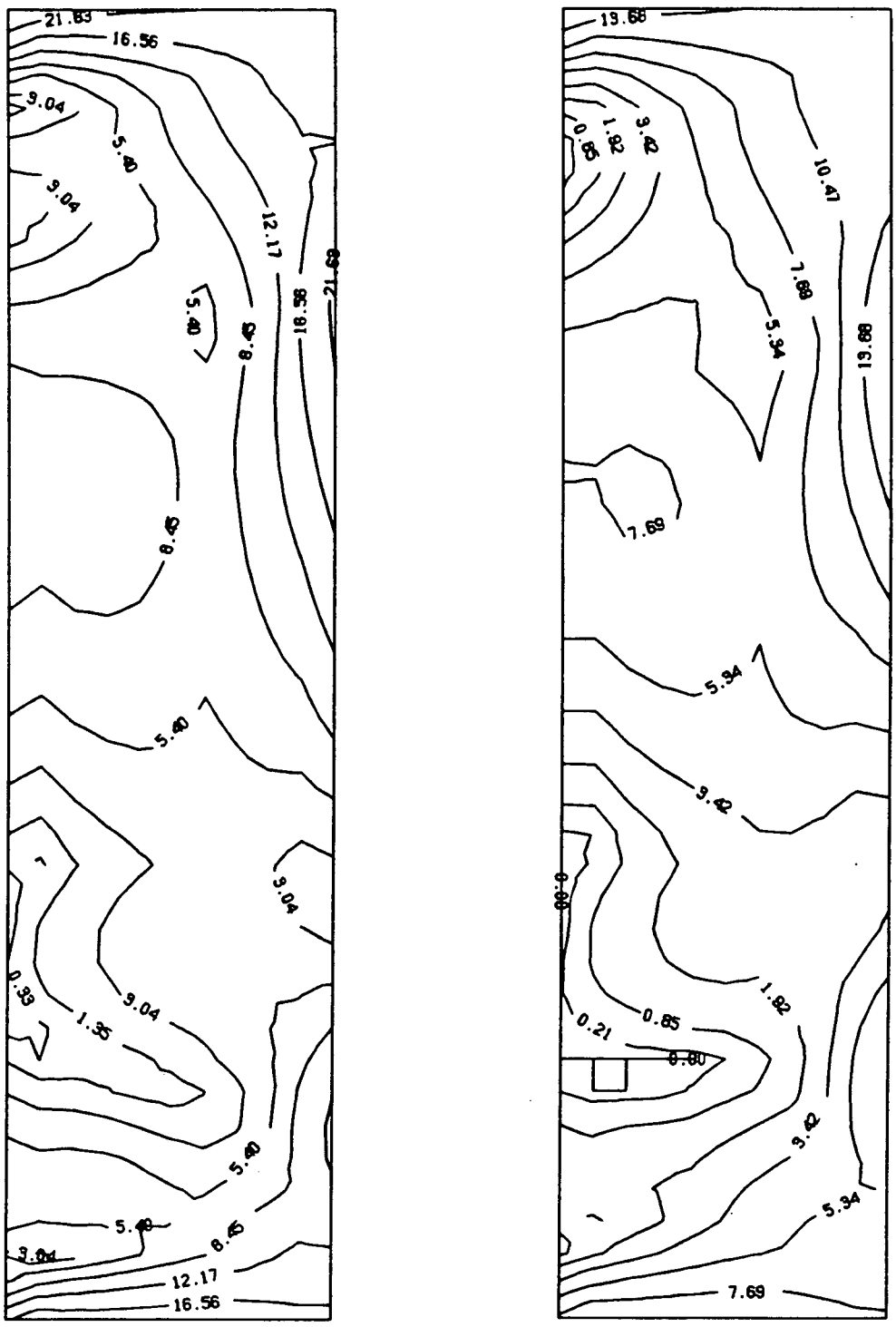

Figure 10.2 MRSS-CRSS (Yield) (MPa) during cooling for the four temperature fields shown in Figure 10.1(a-d). (a) 5 s, (b) 10 s, (c) 20 s, (d) 60 s. Initial gradient 70°C/cm. Argon temperature 1000°C.

movement the stress distribution along the crystal diameter changes from a W to a U shape with time.

The largest MRSS-CRSS (Yield) near the interface occurs about 10 seconds after growth stops, and ranges between 18 and 4.5 MPa. These stress values are appreciably larger than the values at the same position in the crystal during growth and are about 3 times the stress in the crystal above the boron oxide when growth is stopped. This would result in a three-fold increase in dislocation density in the vicinity of the end of the crystal generated during cooling.

The MRSS-CRSS (Yield) for crystal cross-sections at 2.75, 8.25, 16.5 and 27.5 mm from the interface are shown in Figure 10.3(a-d), the main characteristics of the stress symmetries observed are :

1) At 2.75 mm from the interface the outer ring has an eight-fold symmetry and the stress distribution across a diameter is U shaped.

2) At 8.25 mm from the interface the centre has four-fold symmetry and two-fold symmetry..

3) At 16.5 mm from the interface there is circular symmetry. There are four minimum stress regions in the <100> directions.

4) At 27.5 mm from the interface there is two-fold symmetry.

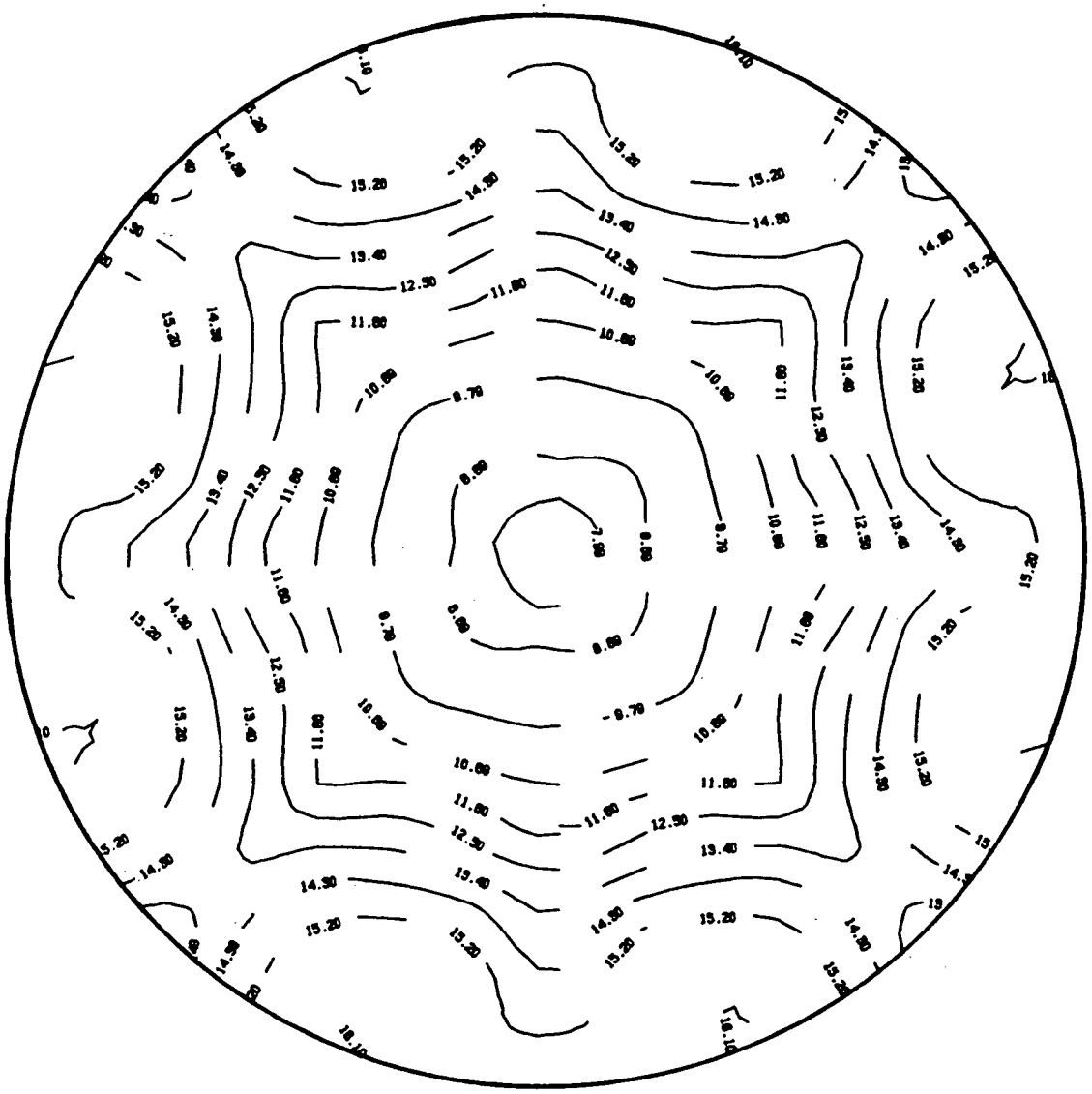

a

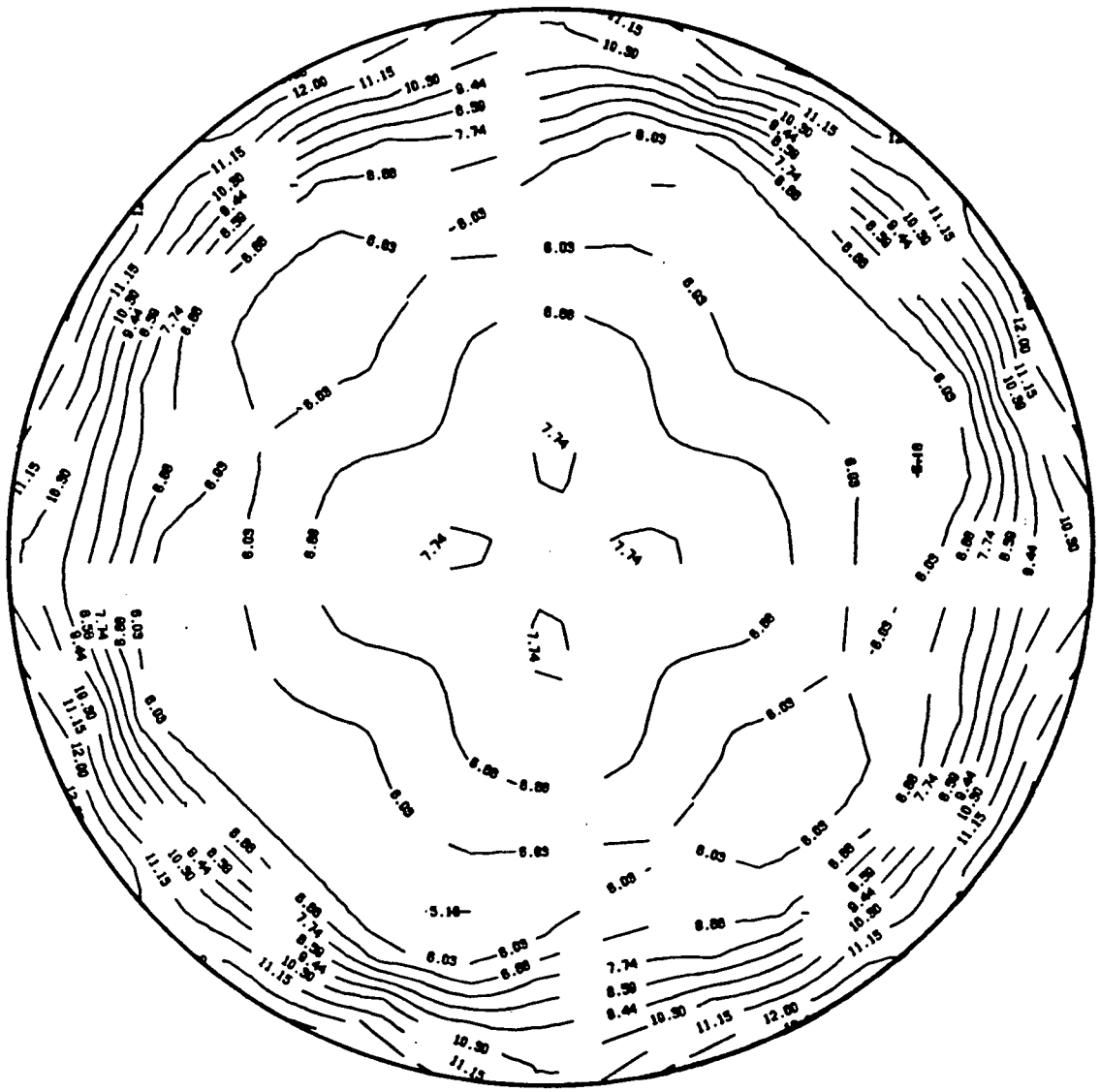

b

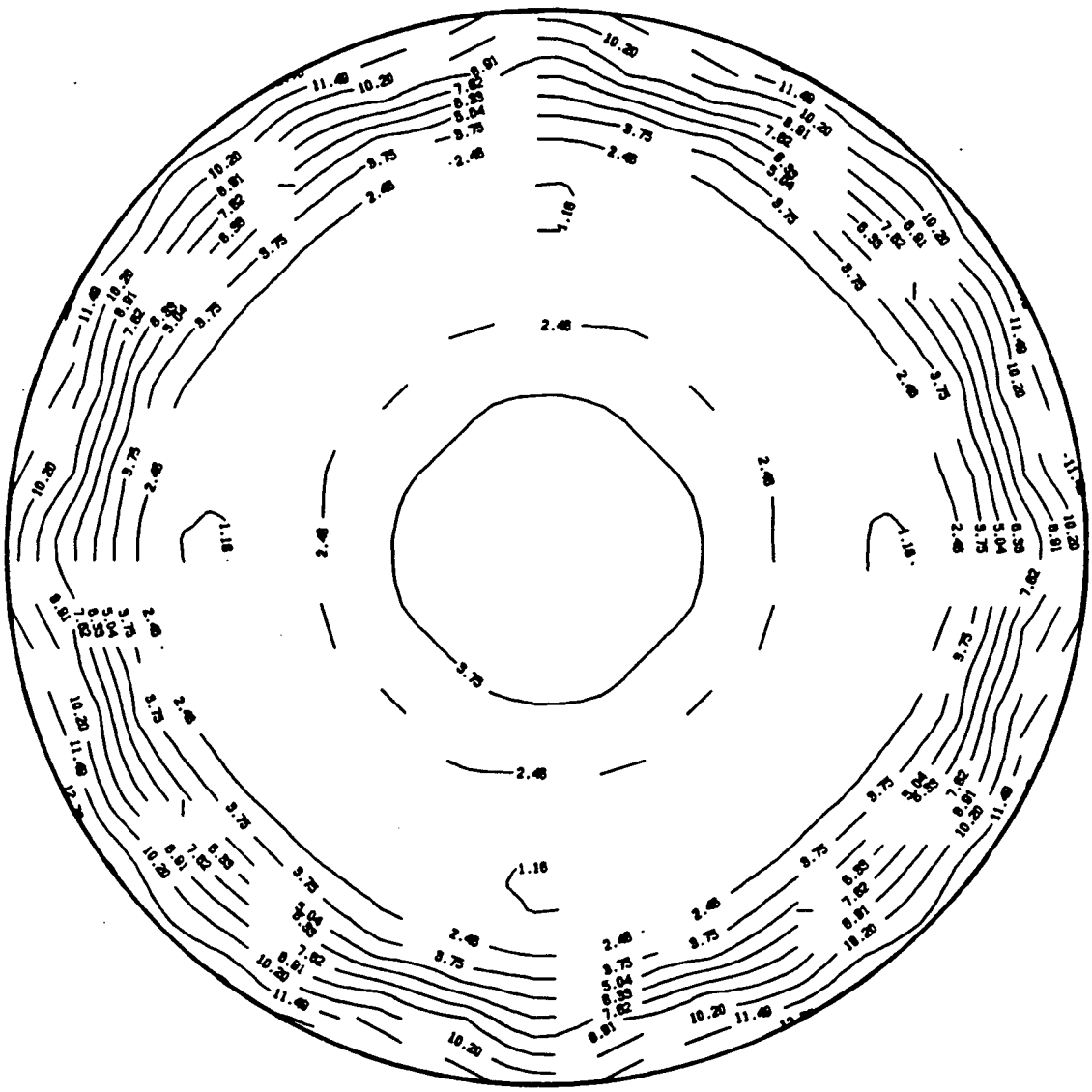

C

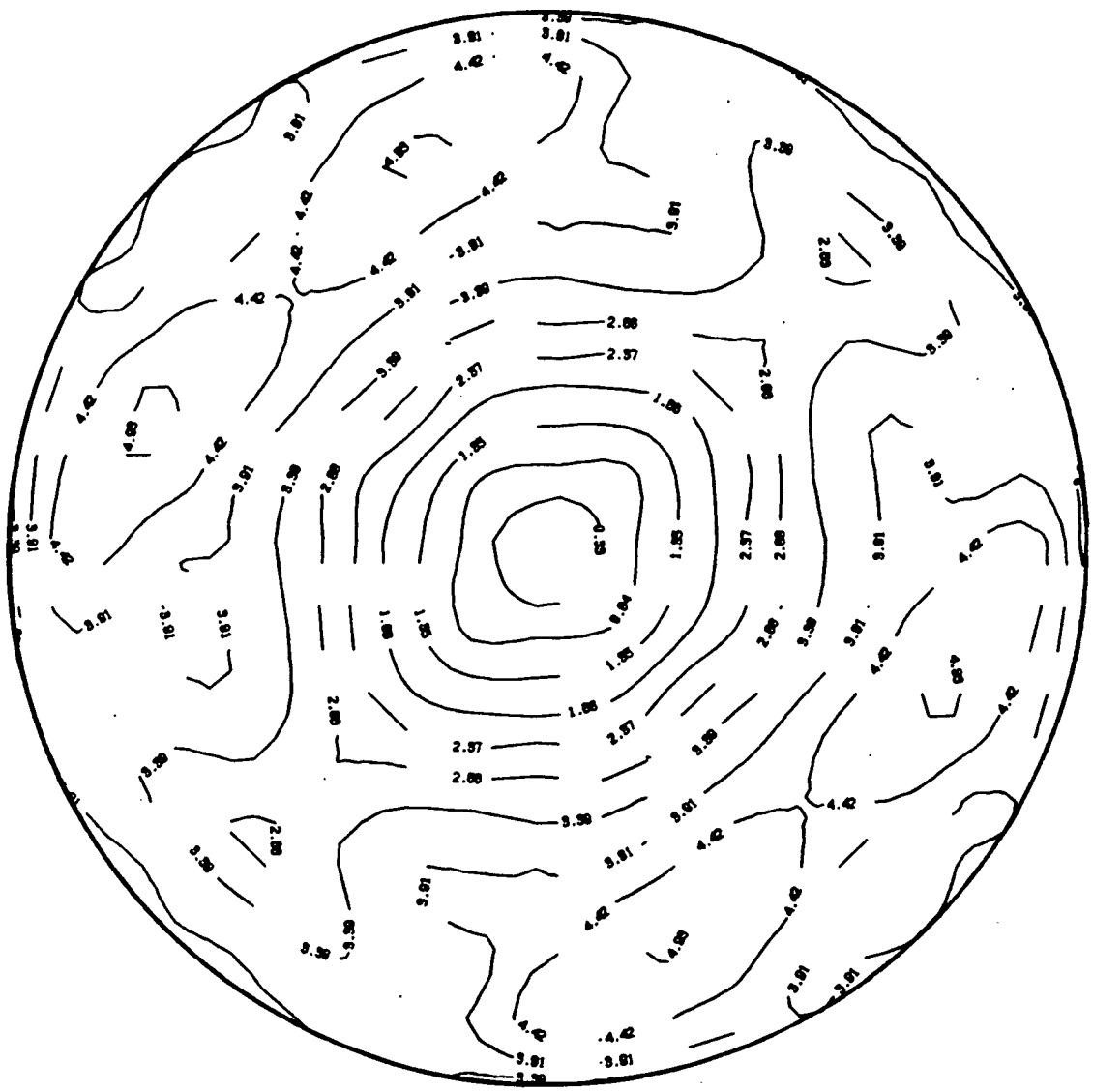

Figure 10.3 MRSS-CRSS (Yield) (MPa) contours in (001) planes at four distances from the bottom (interface) in the crystal shown in Figure 10.2(b) 10 s, (a) 2.75 mm. (b) 8.25 mm (c) 16.5 mm (d) 27.5 mm .

The stress distribution and symmetry are time dependent. At 2.75 mm from the interface the eight-fold symmetry in Figure 10.3(a) at 10 seconds changes at 60 seconds to the eight-fold symmetry shown in Figure 10.4(a). At 8.25 mm from the interface, the two and four-fold symmetries in Figure 10.3(b) at 10 seconds change at 60 seconds to the two-fold symmetry shown in Figure 10.4(b).

10.1.1.2 Initial Gradient GC/2 = 35°C/cm

In this case the stresses reach a maximum at 10 seconds. The temperature field is shown in Figure 10.5(a) and the corresponding MRSS-CRSS (Yield) field in Figure 10.5(b). Comparing Figure 10.5(a) with Figure 10.4(a) for a 70°C/cm gradient it is noted that the isotherms for the 35°C/cm gradient have larger curvature than for the 70°C/cm gradient. The MRSS-CRSS (Yield) distribution in Figure 10.5(b) is similar to the distribution in Figure 10.4(b) for the 70°C/cm gradient. Large curvature in the isotherms and large stresses are still present at 60 seconds as shown in Figure 10.6(a-b).

The MRSS-CRSS (Yield) in a cross-section at 2.75 mm from the interface has eight-fold symmetry. At 8.25 mm the stress has a strong two-fold symmetry (Figure 10.7(b)). The two-fold symmetry gradually changes to a near circular symmetry with small traces of four-fold symmetry given by weak local minima in the <110> directions as shown in Figure 10.7(b). The U-shaped stress distributions along a diameter is present in all cross-sections.

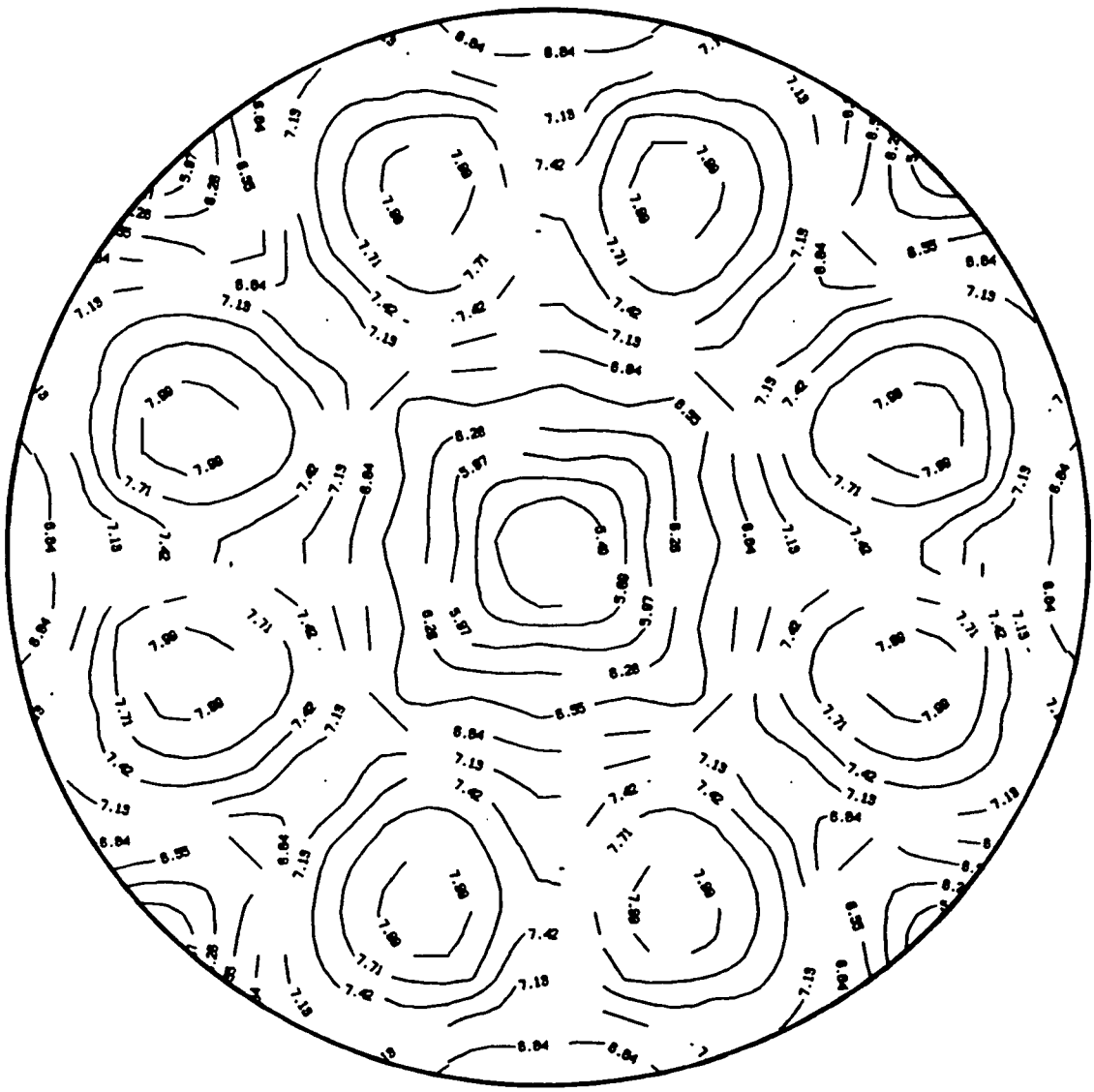

0

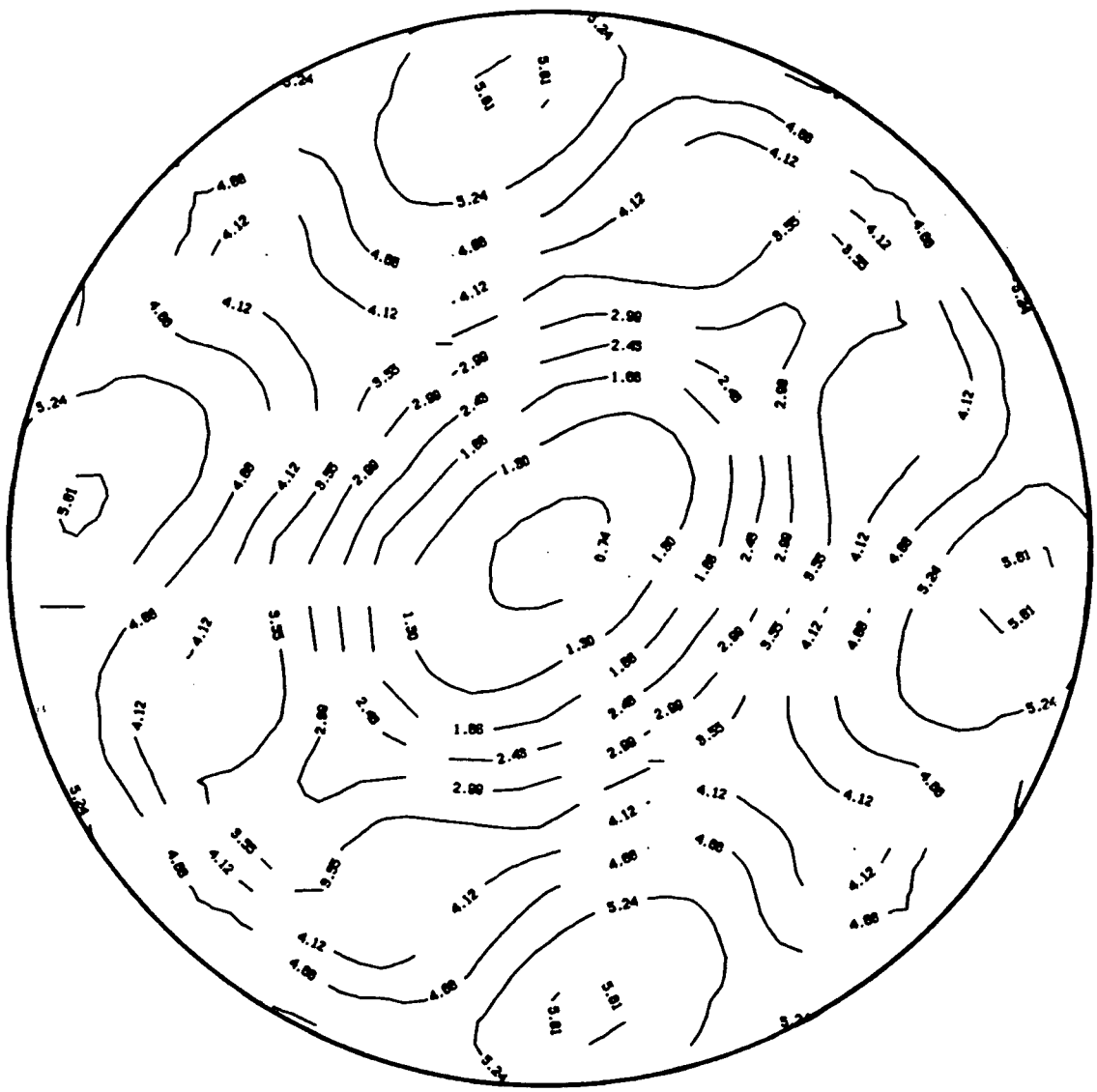

Figure 10.4 MRSS-CRSS (Yield) (MPa) in (001) planes at two distances from the bottom in the crystal shown in Figure 10.2 (d) 60 s, (a) 2.75 mm (b) 8.25 mm.

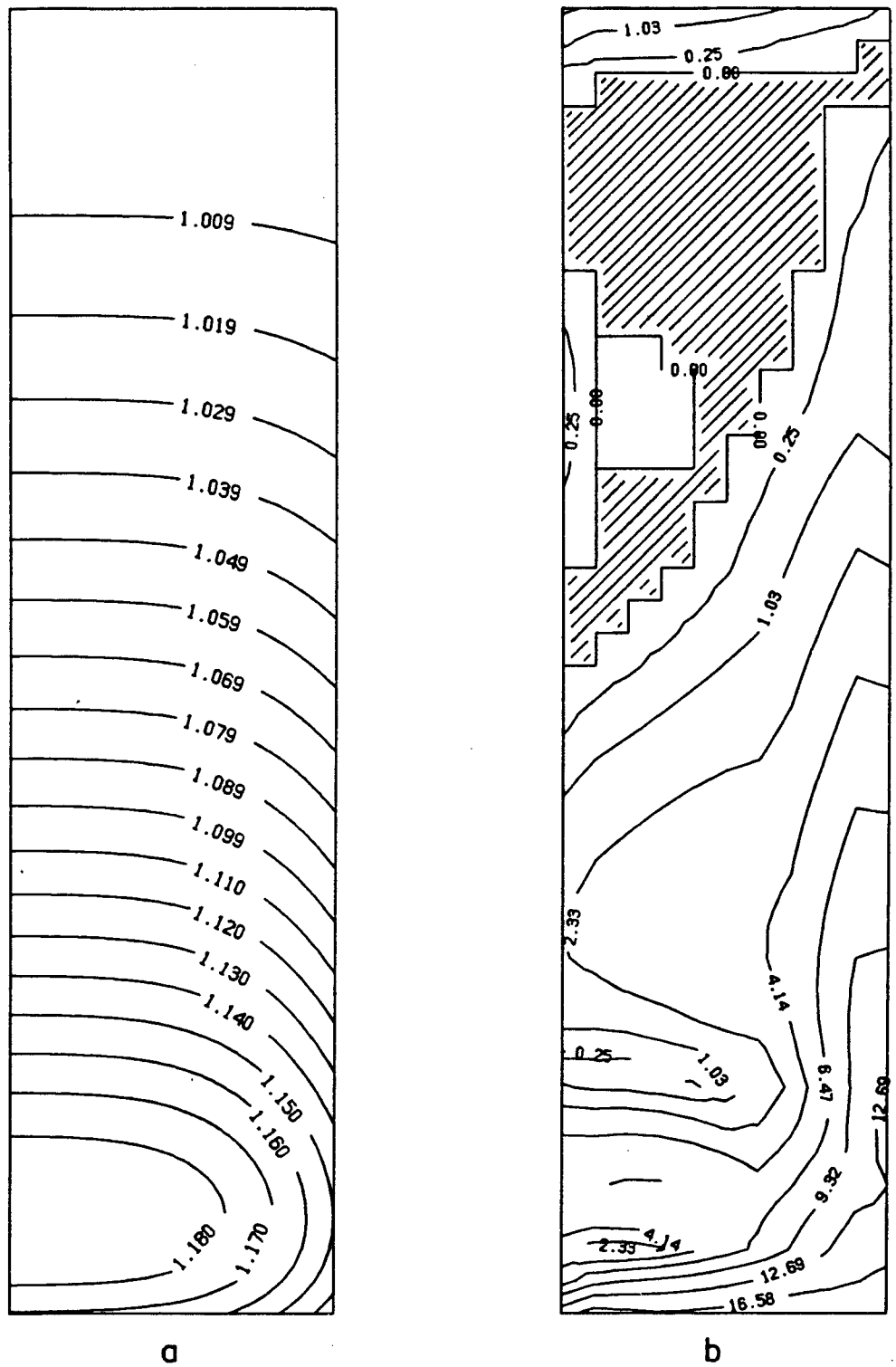

Figure 10.5 (a) Temperature field (10^{30}C) and (b) MRSS-CRSS (Yield) (MPa) field for a crystal cooling in argon at 1000°C after 10 s. Initial gradient 35°C/cm.

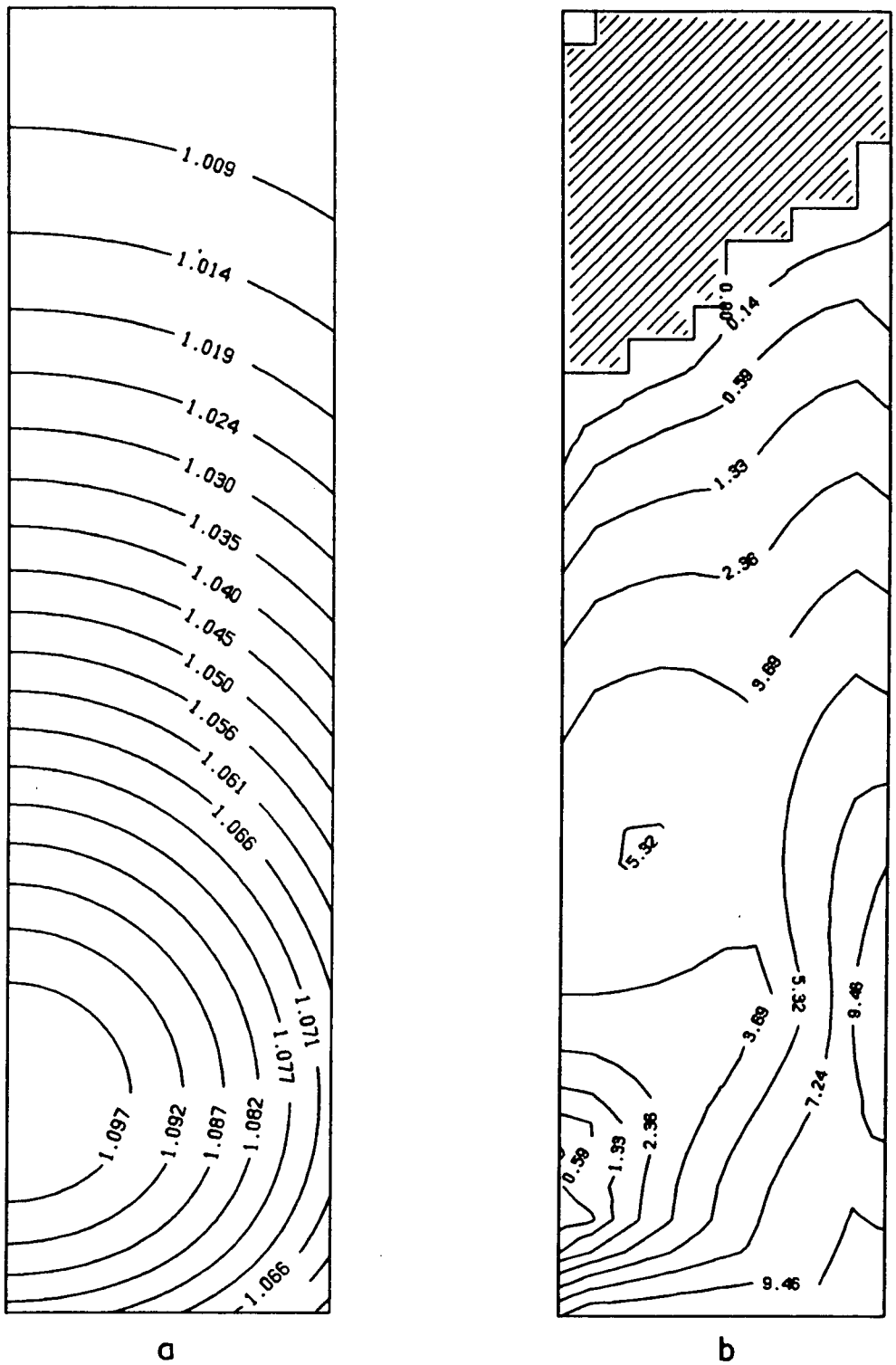

Figure 10.6 (a) Temperature field (10^{3o}C) and (b) MRSS-CRSS (Yield) (MPa) field for a crystal cooling in argon at 1000°C after 60 s. Initial gradient 35°C/cm.

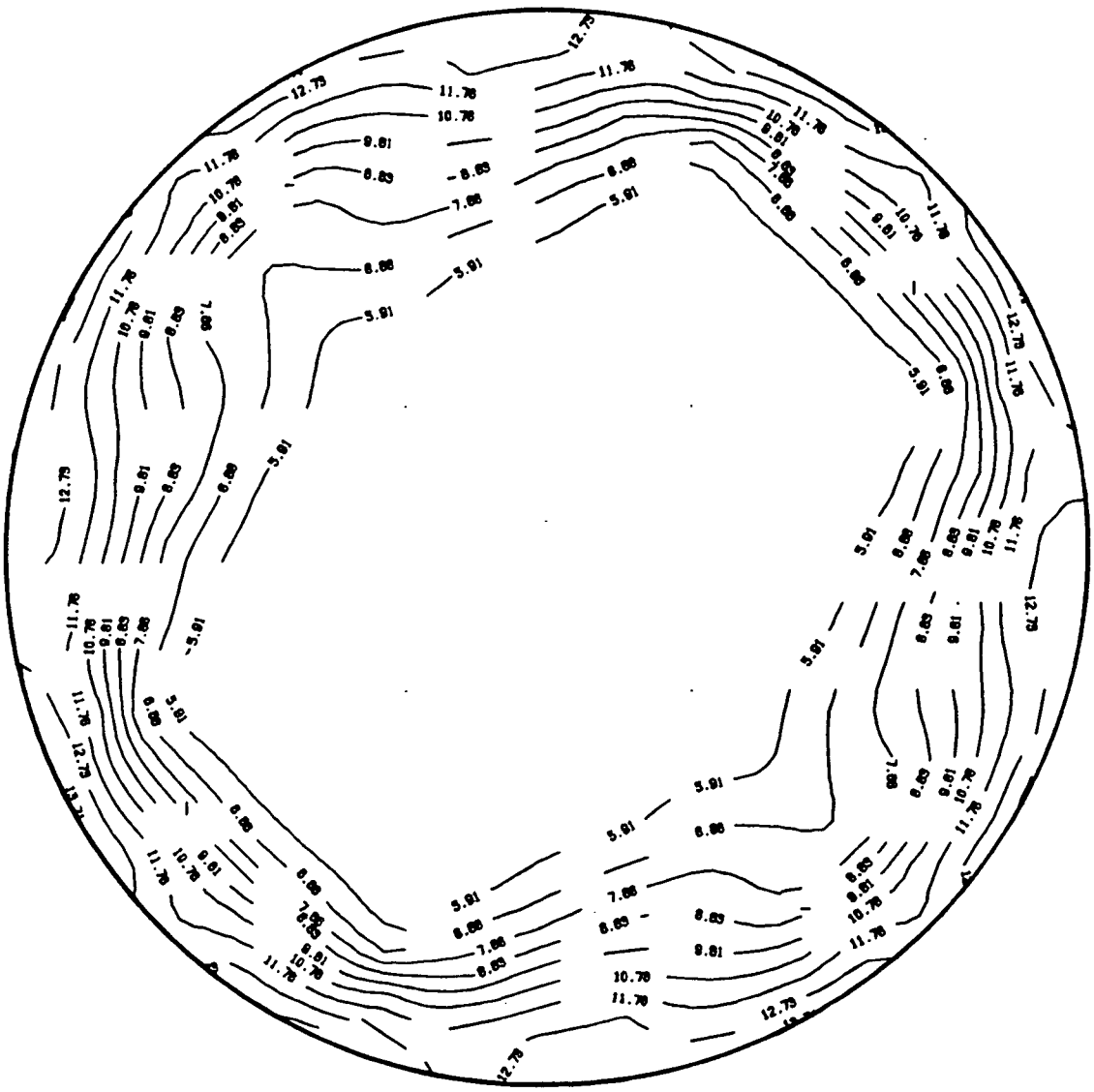

a

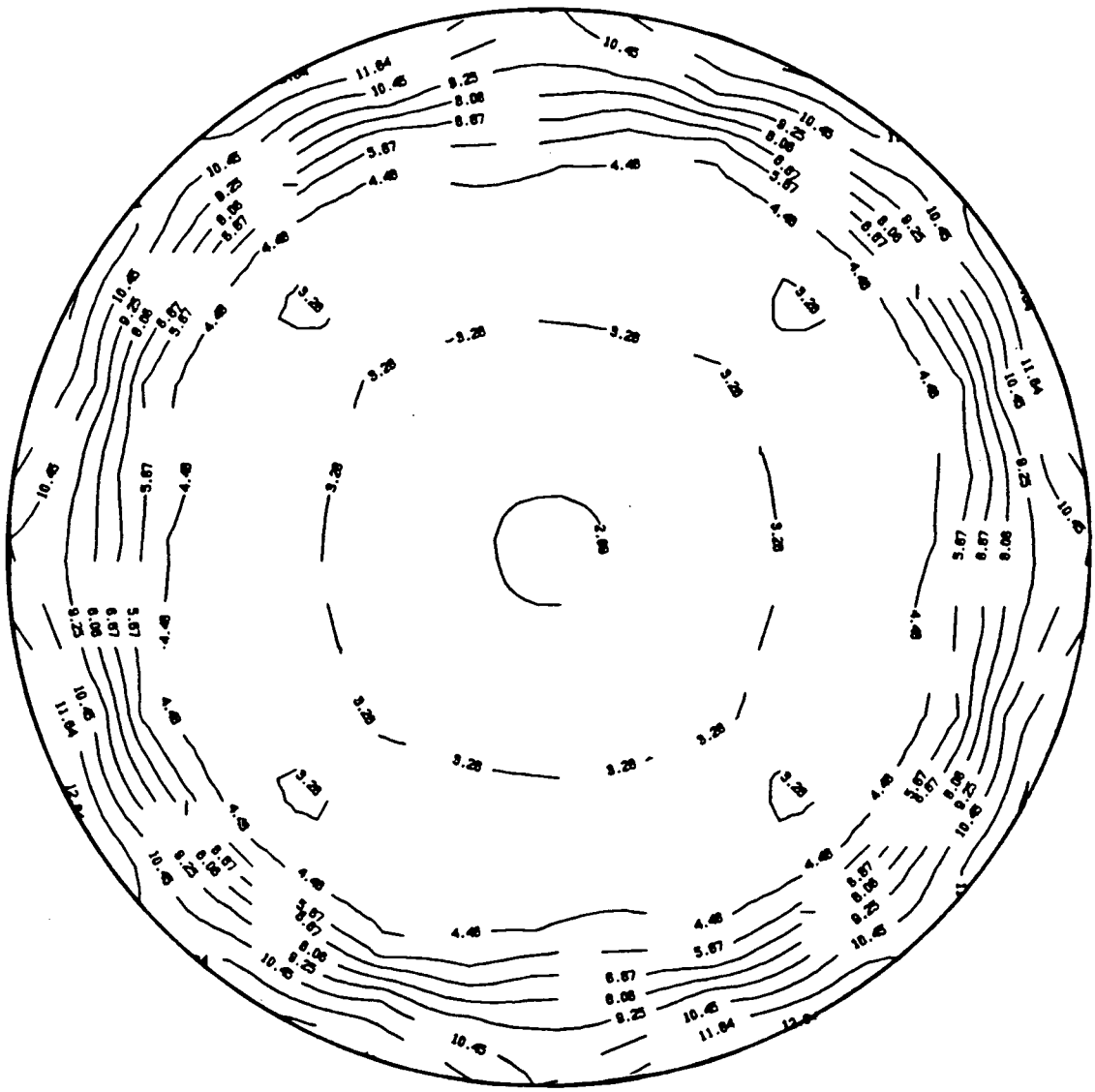

Figure 10.7 MRSS-CRSS (Yield) (MPa) in (001) planes at two distances from the bottom in the crystal shown in Figure 10.5 (b) 10 s. (a) 8.25 mm (b) 27.5 mm.

10.1.1.3 Initial Gradient GC/4 = 17.5^{o}C/cm

The temperature field (Figure 10.8(a)) gives isotherms which have the highest curvature among the initial gradients considered. The MRSS-CRSS (Yield) (Figure 10.8(b) field in the region close to the interface is similar to the previous cases. The region with large stress near the crystal surface and adjacent to the interface is expanded to encompass nearly all of the crystal. The stress distribution along the diameter is U-shaped.

The MRSS-CRSS (Yield) in cross-sections shows

1) eight-fold symmetry close to the interface

2) two-fold symmetry above the interface and up to a distance from the interface of 16.5 mm

3) Near circular symmetry at 27.5 mm from the interface with low stresses in the centre covering more than half the section surface area and large stress gradients at the edge. These give a U-shaped stress distribution with a broad base.

The large stresses persist after 60 seconds but they are not larger than the ones observed at 10 seconds. The stress distribution in cross-sections at 60 seconds is similar to the distribution at 10 seconds. Along a diameter the stress distribution tends to take a V shape rather than U shape. At a distance of 27.5 mm from the interface the central region in the

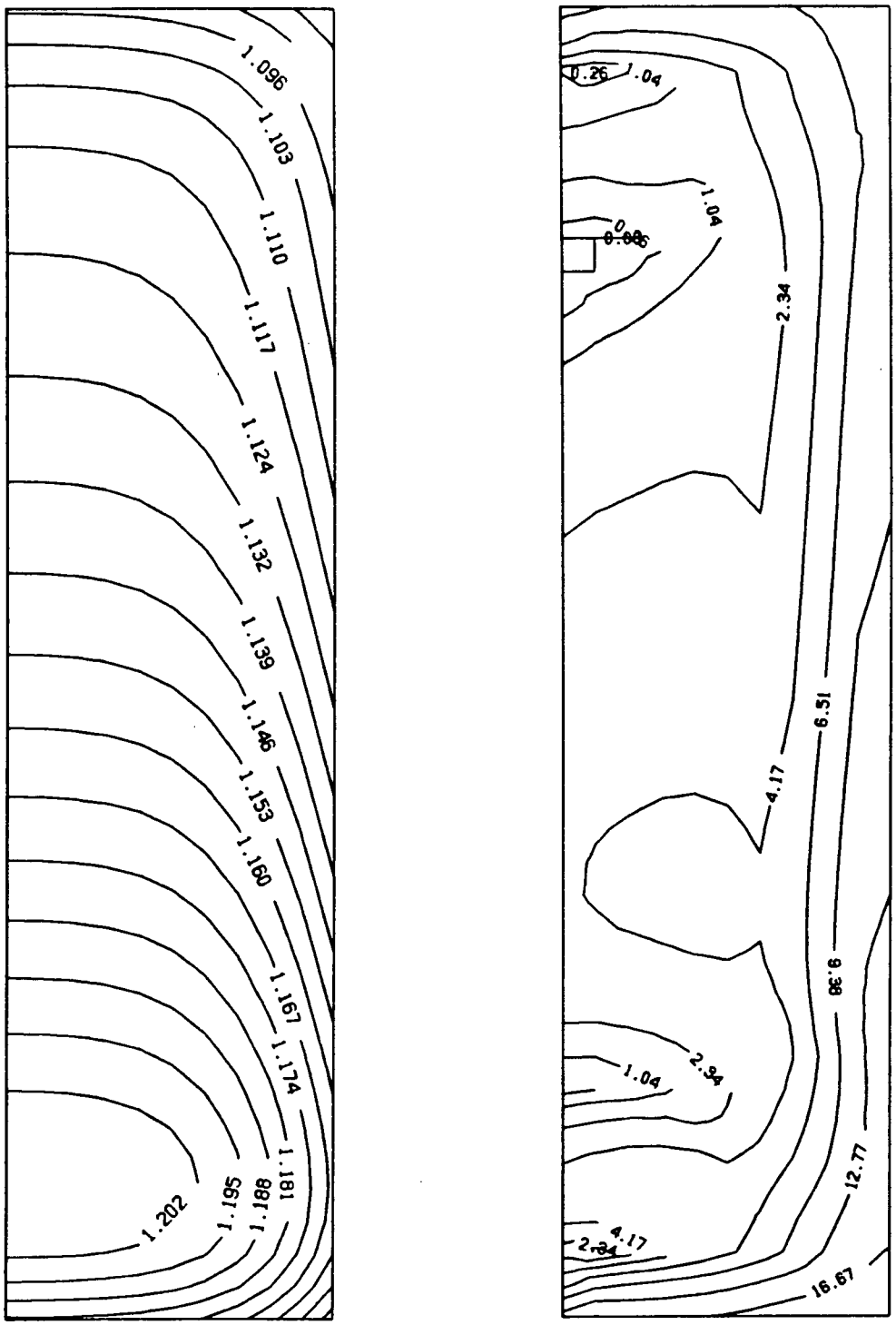

Figure 10.8 (a) Temperature field (10^{30}C) and (b) MRSS-CRSS (Yield) (MPa) field for a crystal cooling in argon at 1000^{0}C after 10 s. Initial gradient 17.5^{0}C/cm.

wafer shows a well distinguished eight-fold symmetry (Figure 10.9). The stress level in this section is higher than at 10 seconds and therefore the symmetry may be evident in the dislocation density distribution.

10.1.2. Boron Oxide

The calculations are repeated for the same initial thermal fields in the crystal used above $70^{o}C/cm$ and $17.5^{o}C/cm$ and assuming the surrounding medium is boron oxide.

The temperature and stress fields for the three thermal gradients GC, GC/2 and GC/4 are shown in Figure 10.10 to 10.12. Parts a and b show the two fields in that order. Results at 10 seconds are shown which exhibits the highest cooling stresses.

The MRSS-CRSS (Yield) distributions in Figure 10.10(b) to 10.12(b) are similar in shape to the distributions obtained with an argon atmosphere, but stresses are 20 % higher in magnitude.

The MRSS-CRSS (Yield) in cross-sections present some distinctive characteristics. At 10 seconds and 27.5 mm from the interface the two-fold symmetry is replaced by a near circular symmetry which is also present at 16.5 mm. In addition cross-sections at 5 seconds show that the eight-fold symmetry close to the interface and the two-fold symmetry above do not form instantly but evolve from a close to circular symmetry and a four-fold symmetry respectively.

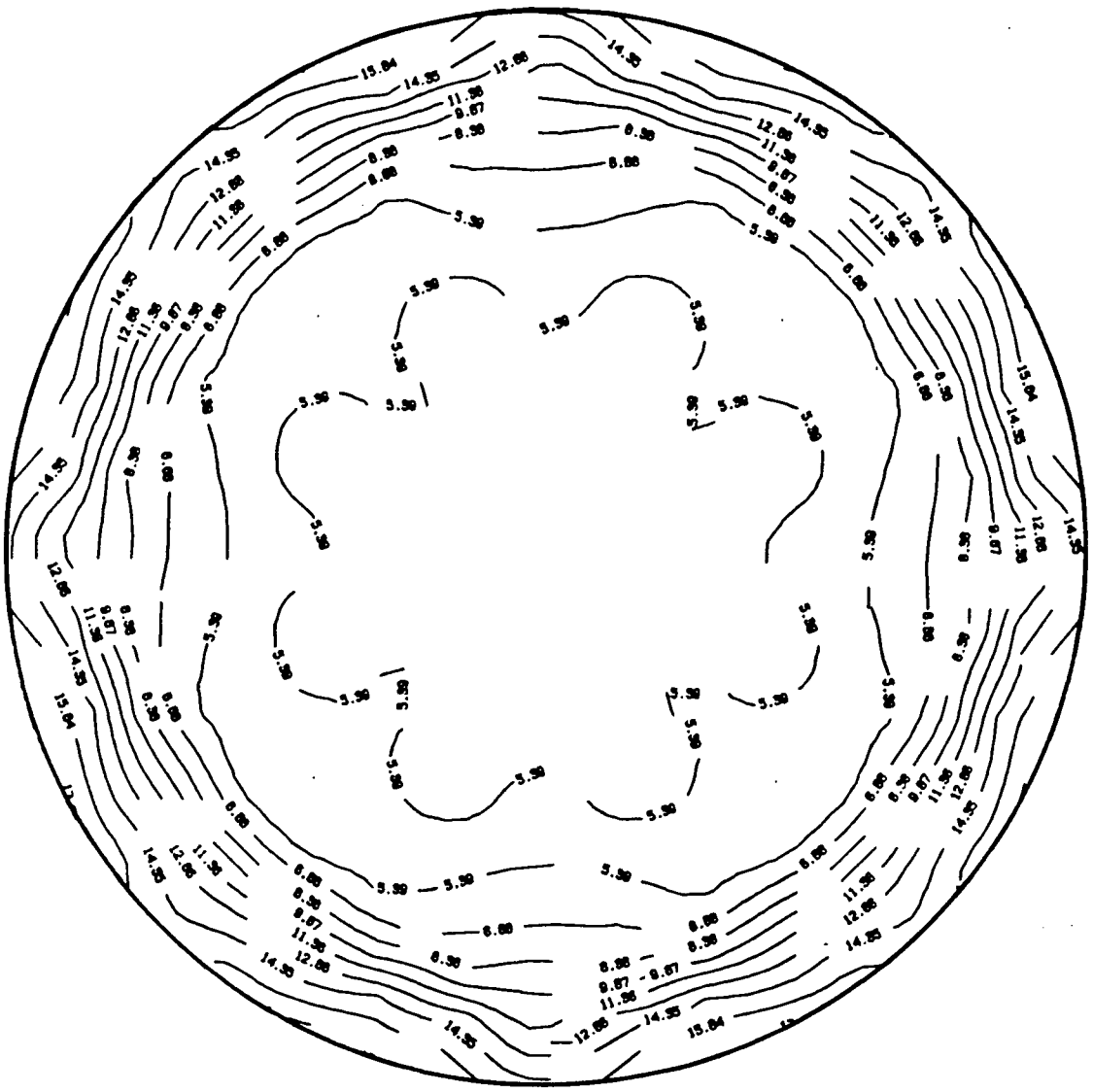

Figure 10.9 MRSS-CRSS (Yield) (MPa) in (001) planes a distance of 27.5 mm from the bottom in the crystal shown in Figure 10.8 (d) 10 s.

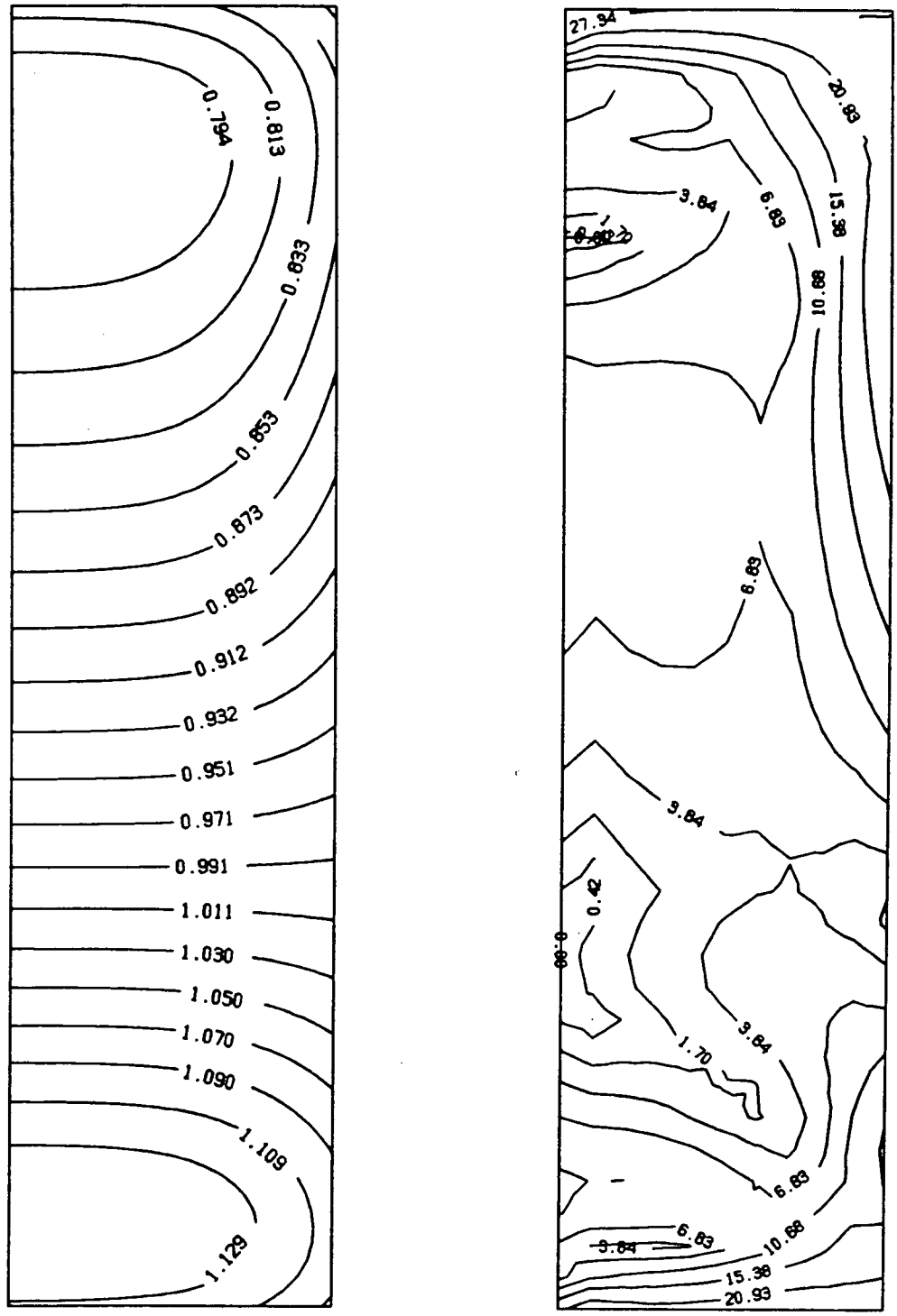

Figure 10.10 (a) Temperature field (10^{3o}C) and (b) MRSS-CRSS (Yield) (MPa) field for a crystal cooling in boron oxide at 1000°C after 10 s. Initial gradient 70°C/cm.

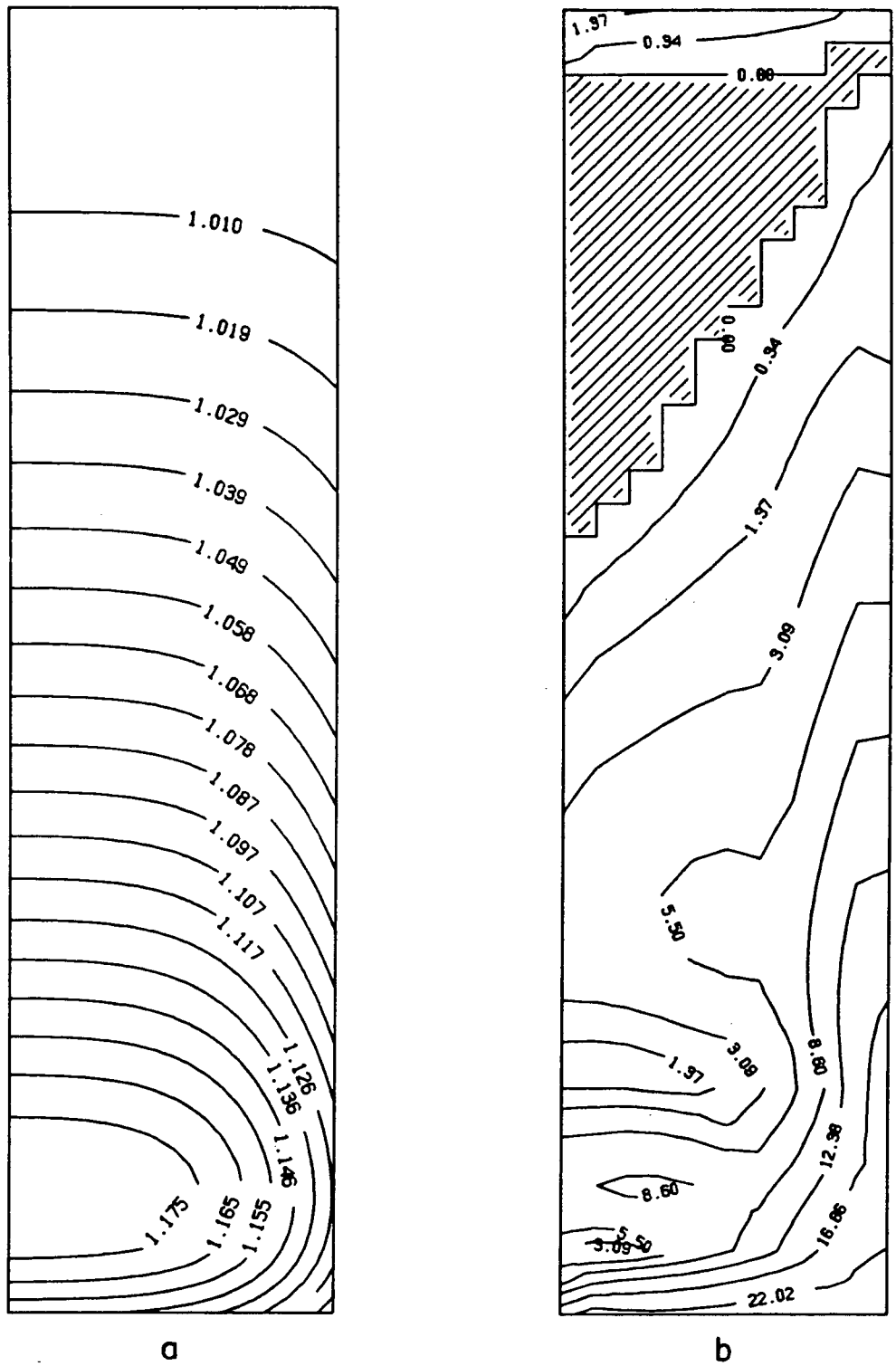

Figure 10.11 (a) Temperature field (10^{3o}C) and (b) MRSS-CRSS (Yield) (MPa) field for a crystal cooling in boron oxide at 1000°C after 10 s. Initial gradient 35°C/cm.

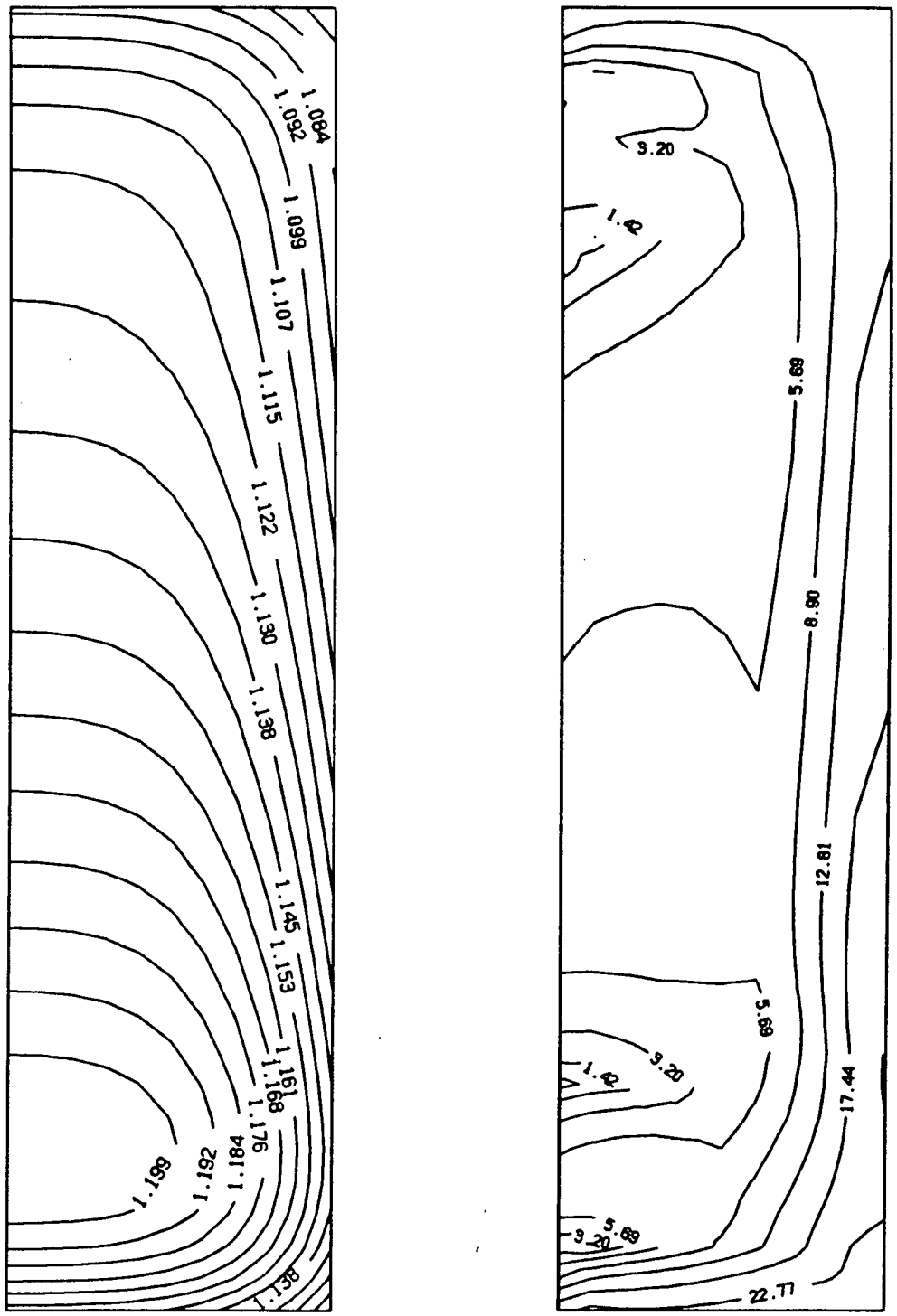

Figure 10.12 (a) Temperature field (10^{3o}C) and (b) MRSS-CRSS (Yield) (MPa) field for a crystal cooling in boron oxide at 1000°C after 10 s. Initial gradient 17.5^{o}C/cm.

10.2 Ambient Temperature 800°C/cm

In this case only an argon atmosphere is considered since the boron oxide layer is generally well above 800°C.

The temperature and stress fields after 10 seconds for three initial temperature gradients are shown in Figures 10.13 to 10.15. The stress distributions are seen to be similar to that obtained for 1000°C, and the stress levels between those obtained when the surrounding media was argon and boron oxide. The stress fields in the cross-sections exhibit a few different features, the most prominent difference being the lack of local minima in the <100> directions.

10.3 Analysis of the Results for Cooling

The most significant result from the results described in the last section is that all conditions examined gave much larger stresses than the stress levels developed during growth. This clearly indicates the importance of proper cooling to minimize dislocation density in the tail end of the crystal and in some cases in the entire crystal. Cooling in argon is shown to produce smaller stresses than cooling in boron oxide. This result, in a very broad sense, can be directly correlated with the heat transfer coefficient, since larger heat transfer coefficients produce larger stresses. The effect of the heat transfer coefficient is such that a larger value will cool the surface more efficiently, leading to larger thermal gradients in both radial and axial directions.

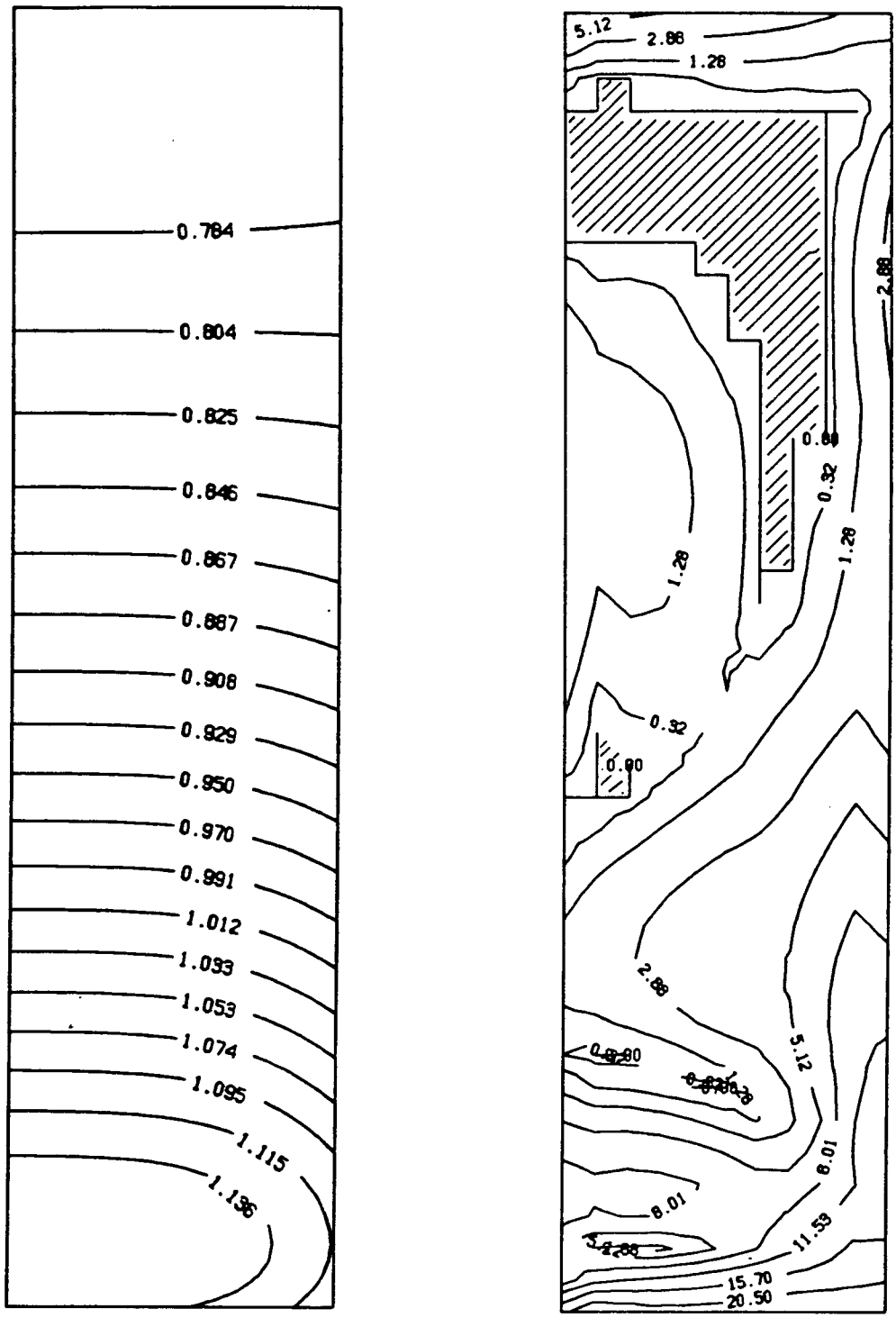

Figure 10.13 (a) Temperature field (10^{3o}C) and (b) MRSS-CRSS (Yield$_o$) (MPa) field for a crystal cooling in argon at 800°C after 10 s. Initial gradient 70°C/cm.

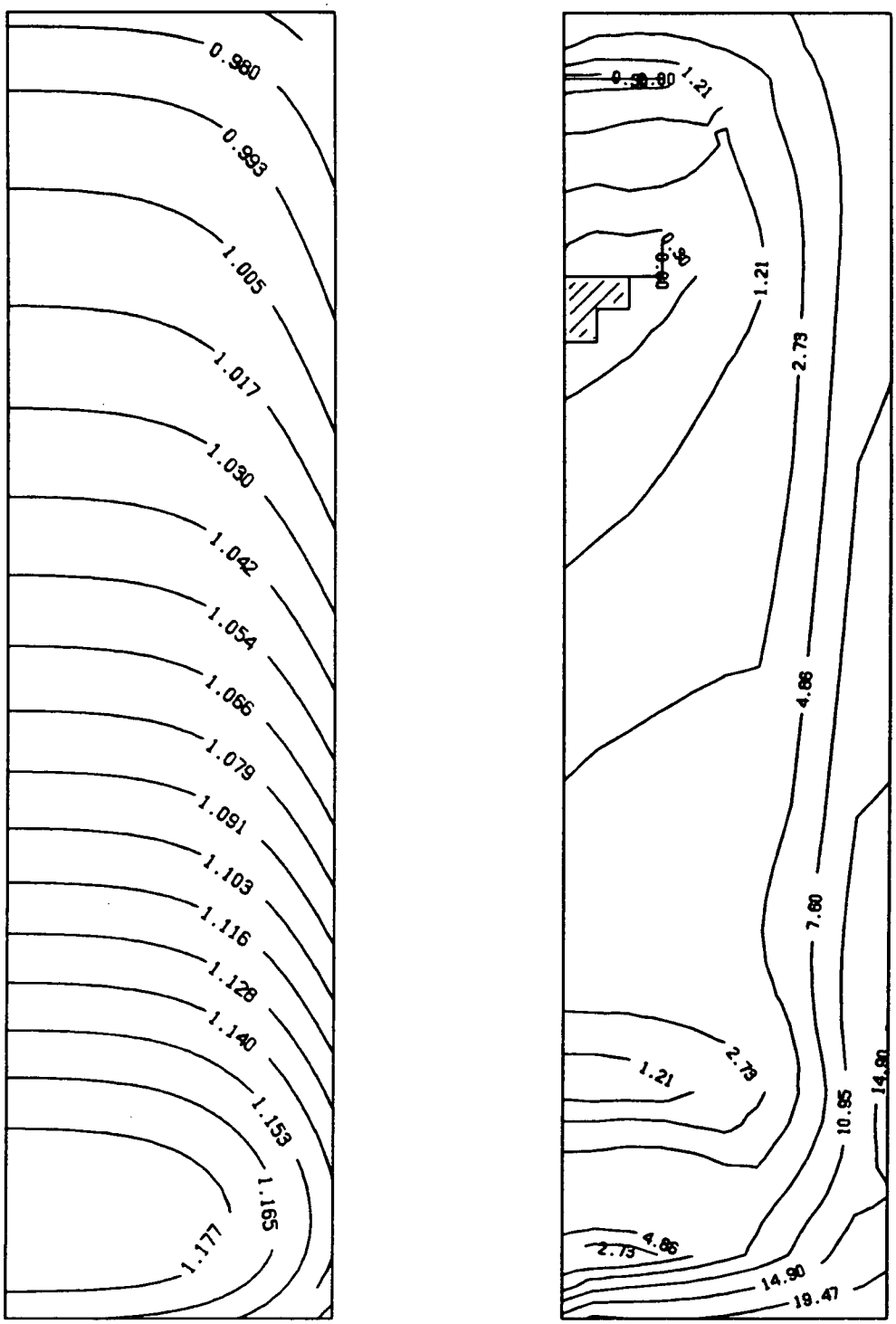

Figure 10.14 (a) Temperature field (10^{3o}C) and (b) MRSS-CRSS ($Yield_o$) (MPa) field for a crystal cooling in argon at 800°C after 10 s. Initial gradient 35°C/cm.

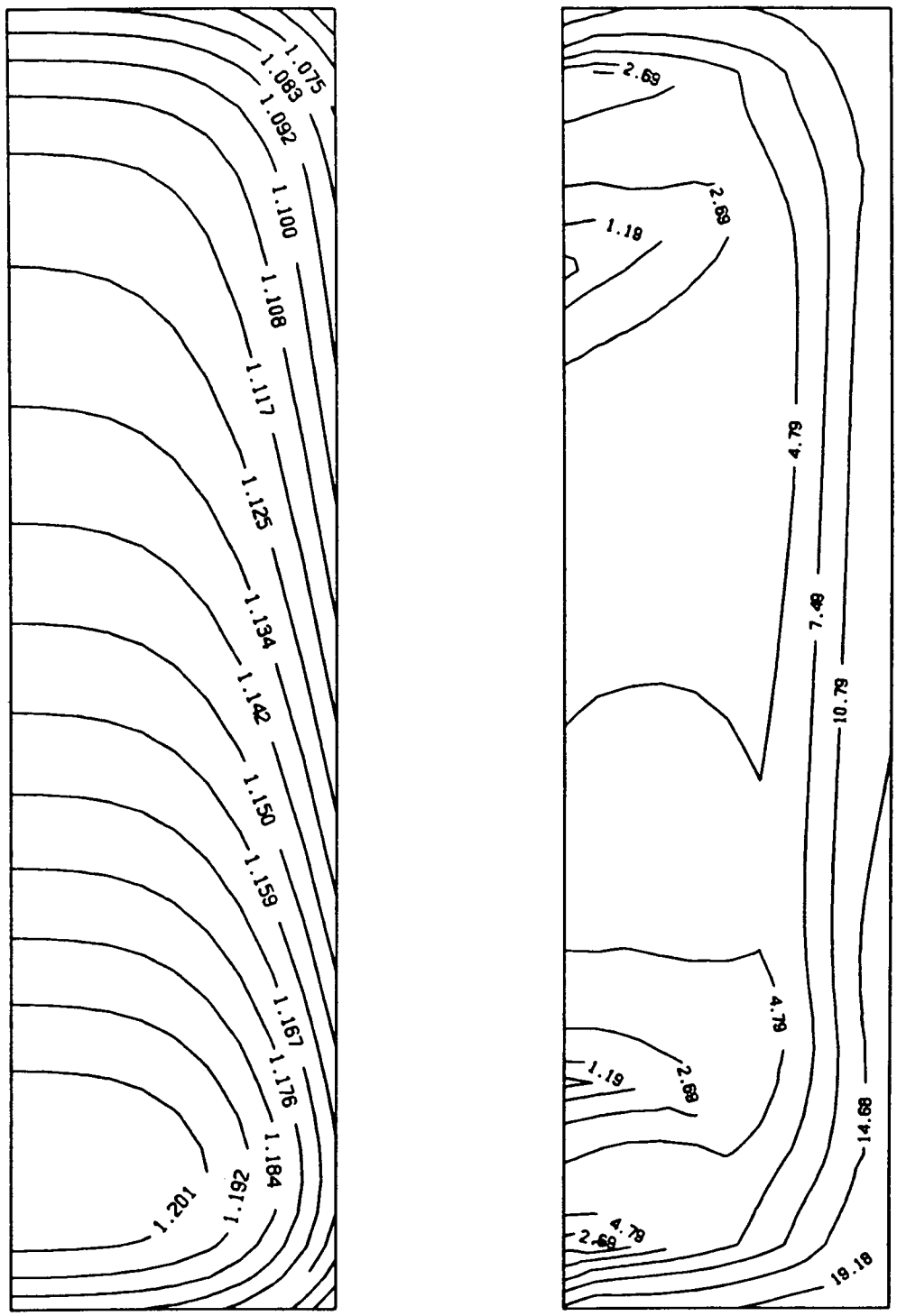

Figure 10.15 (a) Temperature field (10^{3o}C) and (b) MRSS-CRSS (Yield$_o$) (MPa) field for a crystal cooling in argon at 800°C after 10 s. Initial gradient 17.5^{o}C/cm.

In addition to the external conditions, the conditions in the crystal at the start of cooling must also be considered. Low thermal gradients in the crystal gives stresses along the surface of the crystal as a result of the large radial gradients. However, the magnitude of the stresses near the interface cannot be explained in terms of radial and axial gradients separately. This is shown in Figure 10.16 for a 800°C argon temperature and Figure 10.17 for a 1000°C boron oxide temperature. In each case two initial gradients are considered, (a) GC and (b) GC/2. In Figure 10.16 the comparable stresses in both cases is attributed to the larger radial gradient in curve (a) and larger axial gradient in curve (b). In Figure 10.17 the larger radial gradient in curve (b) than in Figure 10.16 can account for the larger stresses. The largest stress for initial condition GC (a) in Figure 10.17 cannot be accounted for by a difference in axial or radial gradient. In this case the largest stress is attributed to the rapid change in radial gradient (curvature) with distance from the interface observed. The changes in radial gradient create more constrains for a free thermal expansion which leads to higher stresses.

The above analysis shows the advantage of calculating thermal stresses using the axisymmetric approximation over the plane strain approximation which cannot account for axial temperature variations.

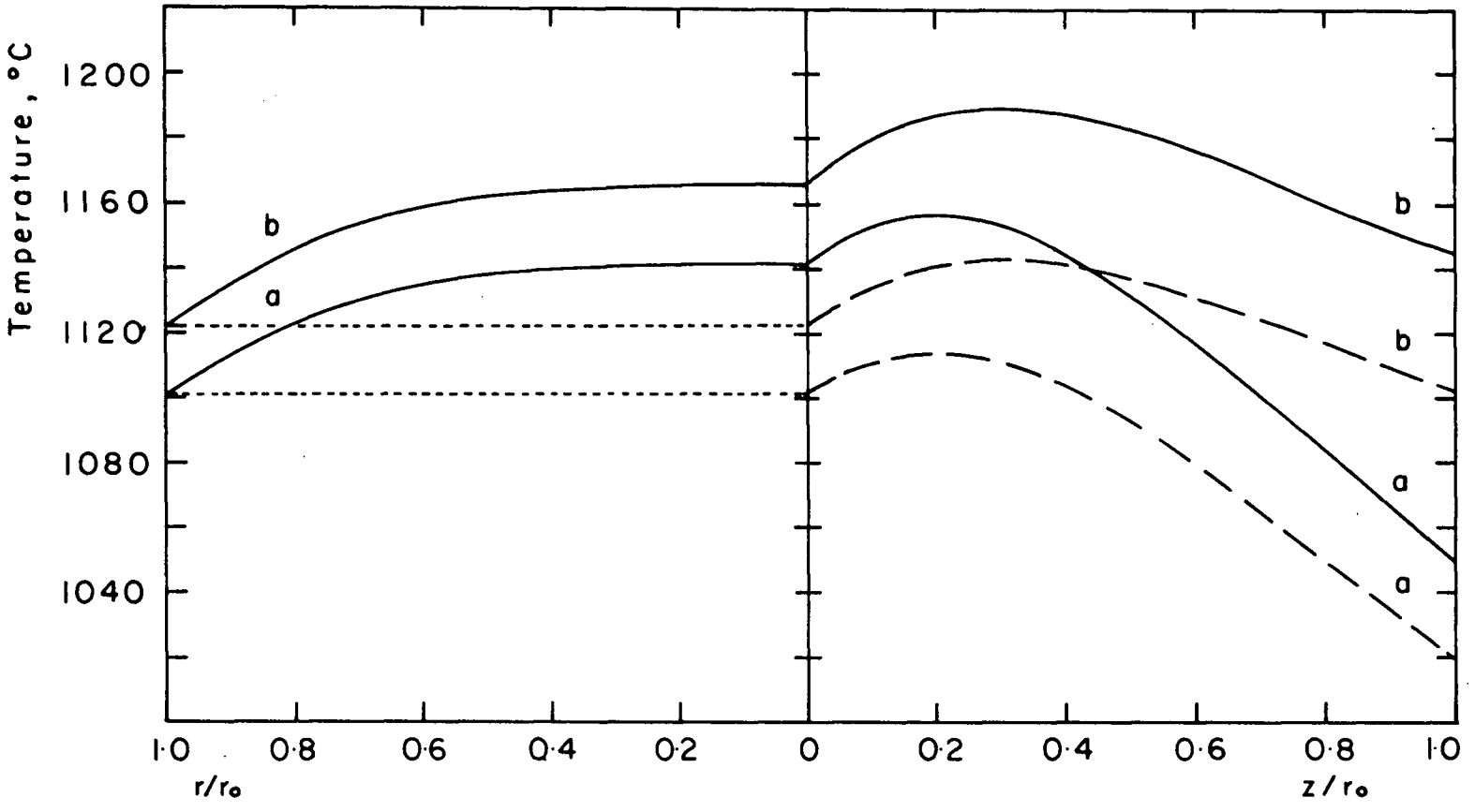

Figure 10.16 Temperature profiles in the crystal cooling in argon at 800°C for two initial gradients in the crystal. (a) 70°C/cm (b) 35°C/cm. The right part corresponds to the radial profiles and the left part to the axial profile. Full and broken lines correspond to the axis and surface temperatures respectively.

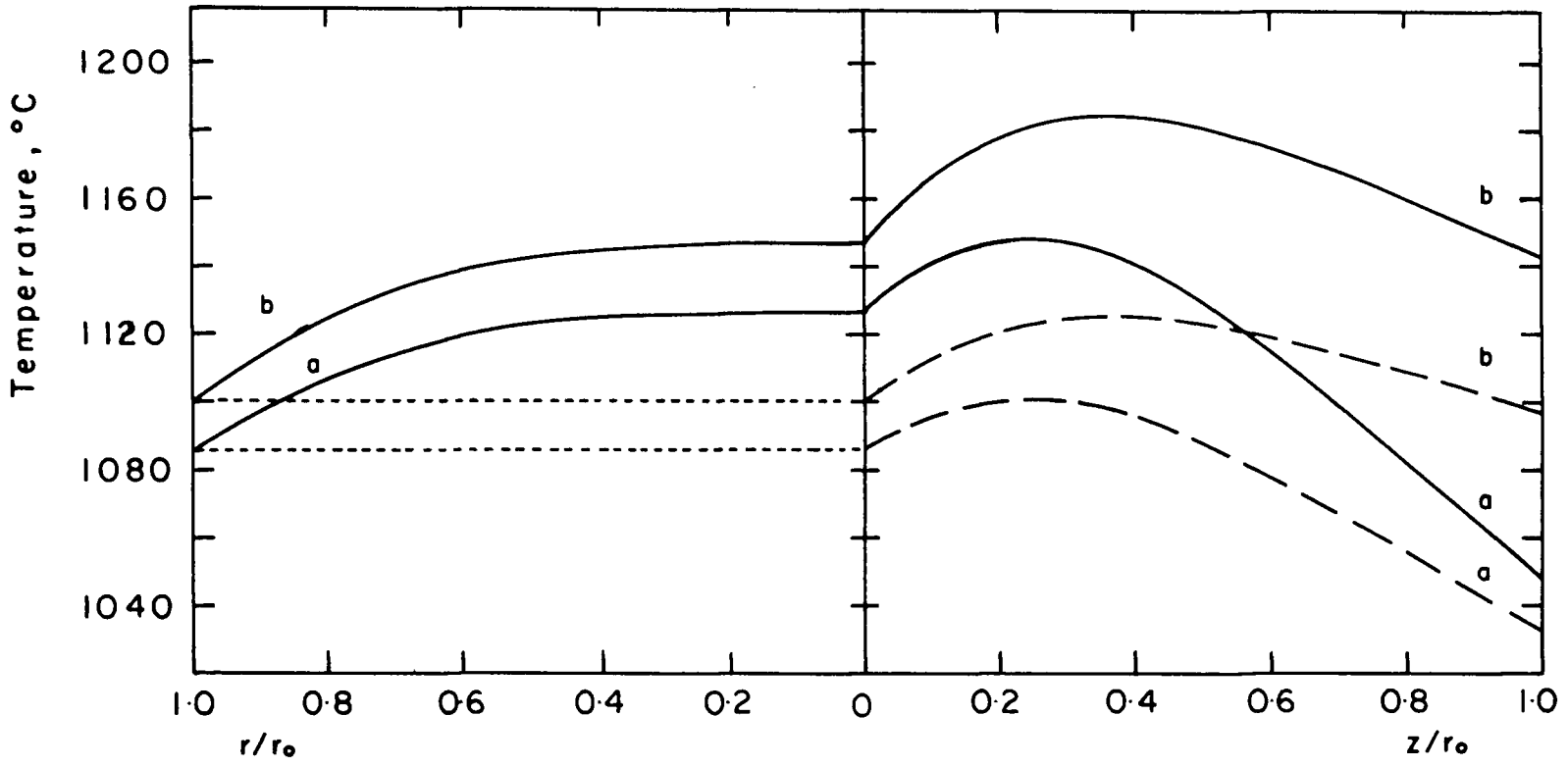

Figure 10.17 Temperature profiles in the crystal cooling in boron oxide at 1000°C for two initial gradients in the crystal. (a) 70°C/cm (b) 35°C/cm. The right part corresponds to the radial profiles and the left part to the axial profile. Full and broken lines correspond to the axis and surface temperatures respectively.

CHAPTER 11

SUMMARY AND CONCLUSIONS

In the present investigation the stress distribution in GaAs crystals has been calculated, analysed and related to dislocation formation during solidification and cooling. The calculations were made assuming that the material is thermoelastic, and that axisymmetric conditions apply. The numerical solutions of the differential equations were obtained employing finite element techniques. For the temperature calculations the quasi-steady state heat conduction equation was employed and the element equations were obtained using the Galerkin's method. The boundary conditions assumed constant temperature at the solid/liquid interface and Newton's law of cooling at the crystal surface. Linear triangular toroidal elements were used to discretize the crystal. The element equations for the stress calculations were obtained using the minimum energy principle. Linear and quasi-quadratic elements were used to discretize the crystal domain. Numerical values of the finite element solutions satisfying simplified boundary conditions were compared with numerical values of analytical solutions. In the stress calculations, numerical solutions were obtained for radial and axisymmetric temperature fields and compared with plane strain and axisymmetric analytical solutions. In addition, the temperatures calculated with the numerical method were compared with

temperatures measured in a high pressure grower. The mathematical model for the temperature and stress fields were evaluated on the basis of these results. The most important results and conclusions obtained from the evaluation are given below.

Temperature Field

1. The finite element solutions of the temperature equation gave results in good agreement with the numerical values of the analytical solutions, obtained for the same problem. For the analytical solutions simplified boundary conditions were used consisting of constant temperatures at the end of the crystal and constant heat transfer coefficient at the crystal-gas interface. The heat transfer coefficients used were 0.3 and 0.6 cm^{-1}. The crystal was taken as a cylinder of aspect ratio two.

2. Refinement of the mesh in the finite element solutions did not change the numerical values of the calculated temperatures.

3. The calculated temperatures are in good agreement with reported temperature measurements in GaAs crystals in a Melbourn crystal grower at 3.04 MPa pressure.

Stress Field

4. The stress components calculated by the finite element method converge to different values depending on the initial strain values (nodal temperatures) used in the calculations.

5. For linear and quasi-quadratic displacements inside the element, a linear initial strain in the element gives stress components close to one order of magnitude higher than a constant initial strain.

6. For a given nodal configuration, the linear element formulation with a constant initial strain gives stress components that converge faster than with the pseudo-quadratic element. This is attributed to the use of an incomplete B matrix in the pseudo-quadratic element.

7. For radial temperature fields, the stresses calculated by finite element using average temperatures are in good agreement with analytical axisymmetric solutions. They agree less well with analytical plane strain solutions. The finite element solutions using linear initial strains differ markedly from the anlytical solutions.

8. For axisymmetric temperature fields the stresses calculated with the finite element method are three times smaller than the stresses calculated using the plane strain approximation. The analytical axisymmetric stress values agree less well with the finite element solutions due to the divergency of

the Bessel function of first order for large numbers of terms in the Fourier series employed in the solutions.

Specific results on the model formulation were obtained. Calculations were made for a crystal length of 10 mm, radius 20 mm, cone angle 45°, encapsulant thickness 10 mm. The results consist of the following.

9. Calculated stress values have been reported in which the 12 RSS values are added to give a local RSS. Adding the 12 RSS gives stress distributions with stress levels which are 7 times larger than the MRSS and 3 times larger than the VMS distributions. Adding the RSS components is inconsistent with the concept of a tensorial quantity.

10. Changing the heat transfer coefficient in a span representing 53 % of the original values does not substantially change the temperature and stress distribution in the crystal. The stress levels change only 20 % .

11. Changing the temperature gradient in the environment surrounding the crystal has a strong effect on temperature and stress distributions in the crystal. The axial temperature gradient in the crystal is usually half the gradient of the environment, except at the highest gradient of $400^{o}C/cm$ used which gives axial gradients one quarter of the environment gradient. The maximum stress in the crystal decreases proportionally to the decrease in gradient of the environment except at the lowest gradients near $50^{o}C/cm$.

12. A stress concentration usually occurs below the crystal shoulder for crystal lengths comparable to the encapsulant thickness. The concentration disappears at low gradients ($50^{o}C/cm$).

13. Increasing the gradient from $100^{o}C/cm$ to $400^{o}C/cm$ has little effect on the operative slip system. The changes on stress distribution symmetries in transverse planes are minimal.

14. The stress field on transverse sections of the crystal usually exhibits eight-fold symmetry at the edge. The symmetry is associated with the slip mode of the MRSS which has an eight-fold distribution.

15. Increasing the encapsulant thickness from 10 mm to 25 mm without changing the temperature profile in the environment surrounding the crystal has little effect on the temperature and stress distribution.

16. The temperature profile shape in the boron oxide significantly influences the stress level and stress distribution in the crystal.

    a) A constant gradient across the encapsulant gives the lowest stress values.

    b) A non-constant gradient in the boron oxide changes the stress symmetry, resulting in stronger four-fold symmetry on transverse planes.

The model was used to study the effect of the growth condition. The main results and conclusions are given below.

Cone Angle

The cone angles considered were 7°, 30°, 45°, 54.7^{o} and 65°. Encapsulant thickness and crystal length were 10 mm crystal radius 20 mm. The results indicate that :

17. The VMS and MRSS distributions are similar for each cone angle.

18. The VMS exhibits a minimum stress level for the cone angle 54.7^{o} which corresponds to a cone parallel to the (111) plane. At low cone angles the stress behaviour can be accounted for by the decrease in radial temperature gradients. At large cone angles the stress increases possibly due to constraints in the strain field.

19. The MRSS levels are independent of the cone angle.

20. The MRSS gives levels generally half the VMS levels. At 54.7^{o} cone angle the MRSS is two times larger than the VMS. The singularity is due to the condition of no traction at the cone surface. For a cone surface coinciding with a (111) plane the RSS components are at a maximum.

21. The stress symmetry in transverse planes changes with cone angle. At 2.5 mm from the interface the symmetry in the central area changes from eight-fold for 7° cone angle to

four-fold for larger angles. At transverse sections 50 mm from the interface the symmetry changes from four-fold for the 7° cone angle to axisymmetric for the larger angles. At the edge of the sections there is always eight-fold symmetry. For the given growth conditions these symmetries may not be apparent in dislocations distributions because the stress levels are lower than the critical yield stresses.

Crystal Length

The crystal lengths considered were up to 110 mm long. Two crystal radii were studied 27.5 mm and 40.0 mm. The conclusions are valid for a 21 mm encapsulant unless it is specified that the same conclusion is valid for other conditions.

22. For any crystal length the radial stress distribution is W-shaped with higher stresses at the crystal centre and near the vertical surfaces. The valleys in the W tend to be closer to the outside surfaces near the top and bottom ends of the crystal.

23. Lower stresses are observed at both ends of the crystal for crystal lengths larger than the encapsulant thickness.

24. For a crystal shorter than the encapsulant thickness, there is a stress concentration below the shoulder. For longer crystals there is a stress concentration above the encapsulant surface. These are valid for any encapsulant thickness and temperature gradients in the environment

surrounding the crystal. It should be noted that this may not be the case for short crystals and linear temperature profiles in the encapsulant as described in paragraph 12 above.

25. The stress level increases with crystal length reaching a maximum for a crystal length twice the encapsulant thickness. The stress slightly decreases for longer crystals. This result is valid for all encapsulant thicknesses and thermal gradients studied. The maximum stress above the encapsulant is due to the thermal discontinuity at the encapsulant surface. When this coincides with the mid-length position in the crystal quasi-plane strain conditions contribute to give the largest stress level during growth.

26. The slip mode corresponding to the MRSS cannot be associated with a stress level. In longitudinal (010) planes the most common modes are III, IV and V.

27. The stress symmetry in transversal (001) planes shows the following patterns :

    a) There is always eight-fold symmetry at the edge of the sections.

    b) The four-fold symmetry is stronger closer to the solid/liquid interface. It also appears at the seed end.

c) Two-fold symmetry results from a degeneration of the four-fold symmetry. It is manifested by an elongation of the minima in the <110> and <1$\bar{1}$0> directions.

d) Far from the ends, there is axisymmetry, except at the edge of the section where there is eight-fold symmetry.

e) For crystal lengths larger than two radii and sections far from the interface, the minimum stress levels are in the <100> directions rather than in the <110> directions.

28. The dislocation distribution predicted with the model for normal growth conditions shows that :

a) The dislocation density at the seed and tail ends are lower than far from the ends.

b) The four-fold symmetry always forms close to the interface.

c) There is a correlation of stress symmetry with distance from the cone between two crystals with radius 27.5 mm and 40.0 mm.

Growth Velocity

29. For growth velocities of 10^{-3}cm/sec and lower, the temperature field is at steady state, and the effect of growth velocity on the stress field is negligible. For larger velocities larger gradients and stresses are obtained.

Effect of Radius

30. Increasing the radius increases the stress levels. There is little change on the relative stress distribution. The effect of increasing the radius on stress levels depends on the thermal conditions in the environment. For thin encapsulants (21 mm) and normal gradients (100°C/cm) the relative stress level increment is similar to the relative radius increment. For thick encapsulants (40-50 mm) and/or low thermal gradients the relative effect of increasing the radius is 2 to 3 times larger than the relative radius increment.

Effect of Thermal Conditions

31. Increasing the encapsulant thickness and decreasing the thermal gradient in the environment surrounding the crystal decreases the stress level. The relation between stress level and gradient reduction is nearly linear.

32. The radial and axial temperature gradients in the crystal do not significantly change with a change in crystal radius from 27.5 mm to 40.0 mm. The stress level change cannot be accounted for by changes in the thermal gradients.

33. The higher stress level with the larger radius is due to an incompatibility of the strain field in a cylinder arising from radial temperature gradients. A given radial gradient creates larger stresses in a larger crystal.

34. To obtain large areas (80 % of the crystal) in which the stresses are lower than the yield stress, an average gradient in the surrounding environment should be less than $10^{o}C/cm$ for the 27.5 mm crystal and $7^{o}C/cm$ for the 40.0 mm crystal. This requires that the gradient during normal growth be reduced by a factor of 6 to 8 for encapsulant thickness of 21 mm.

Gas Pressure and Nature

35. The large effect of pressure on dislocation density observed experimentally cannot be accounted for by the corresponding pressure dependence of the heat transfer coefficient between the crystal and the surrounding gas. The effect of pressure is likely related to effects in the surrounding gas. The transfer efficiency of the gas will change which can significantly modify the thermal gradients across the encapsulant and in the gas. This is indicated by the larger heat transfer coefficients between the encapsulant surface and gas for higher gas pressure.

Solid/Liquid Interface Shape-Convex Curvature

36. A convex interface significantly modifies the stress distribution in a region approximately one radius from the interface. The modifications consist of the following

a) A stress concentration at the interface edge.

b) A U-shaped stress distribution close to the interface.

c) The above characteristics do not change with crystal length.

d) Highest stress values are obtained at the edge of the interface for all crystal lengths. This indicates that dislocations are generated immediately after solidification.

e) Stress levels are reduced by increasing the encapsulant thickness and decreasing the temperature gradients. The stress concentration is not eliminated by increasing the encapsulant thickness.

f) Increasing the crystal radius does not change the stress level or distribution close to the interface.

Concave Curvature

37. A concave interface shape substantially modifies the stress distribution in regions adjacent to and about one radius thickness from the interface. The modifications consist of the following

a) Stress concentrations are developed at the centre and edge of the crystal at the interface. The stress levels are the largest and about twice as large as stress levels observed above the encapsulant surface.

b) Increasing the crystal radius does not change the stress distribution. The stress level increases proportionally to the relative change in radius.

Cooling the Crystal to Ambient Temperature after Growth

The effect on temperature and stress distributions during cooling has been analysed. The temperature fields were obtained using analytical time dependent solutions of the heat conduction equation. Solutions were obtained assuming a parabolic initial temperature profile in the axial direction. It was also assumed that the crystal is immersed in a medium which is either argon or boron oxide and the medium is at a constant temperature. The temperatures were 800°C or 1000°C for the argon atmosphere and 1000°C for the boron oxide. The analytical series solutions were found to converge to 96 % of the theoretical limit value. The stress fields were calculated using the numerical finite element method employed for the stress calculations during growth. The analysis focused on a region adjacent to the interface and extending to a distance of a radius from the interface. The crystal radius and length were 27.5 mm and 110 mm respectively. Temperature profiles showing three gradients were considered. The main results and conclusions follow.

38. The temperature and stress fields during cooling differ markedly from the fields obtained during growth. In the region of interest close to the interface the differences are :

a) Larger radial gradients.

b) Larger stress levels of the order of two to four times higher than during growth.

The specific characteristics of the fields are :

a) The largest stress is reached between 10 and 20 seconds after cooling starts.

b) In most cases the equilibrium temperature is reached after 5 to 10 minutes.

c) The stress level is not strongly dependent on cooling and initial conditions. Larger stresses are obtained with larger radial and axial gradients. These combined with different axial gradients along the axis and at the crystal surface give the largest stresses.

d) The stress level decreases rapidly with distance from the interface ; the larger the initial axial gradient is, the shorter the distance. In actual cooling conditions this may not be the case because the temperature in the media is not constant, as assumed.

39. The symmetry of the stress in (001) transverse planes markedly differs from the symmetries obtained during growth. The most important characteristics are :

a) The radial stress distribution always shows a U or V shape instead of the usual W shape.

b) At 2.75 mm from the interface the eight-fold symmetry is stronger and appears in a larger ring at the edge which is about half the wafer area.

c) At 8.25 mm from the interface two-fold symmetry is observed which is formed by an elongation of the two minima in the <110> and <1$\bar{1}$0> directions and a displacement of these minima to a position closer to the edge of the wafer.

d) For distances larger than 8.25 mm the symmetry depends on cooling conditions and time. The differnt symmetries observed are two-fold, eight-fold or nearly axisymmetric with four minima either in the <100> or <110> directions.

e) The symmetry is time dependent. The two-fold symmetry evolves from a four-fold symmetry present at an early stage during cooling. The eight-fold symmetry close to the tail end evolves from a nearly circular symmetry.

40. The results suggest that a considerable number of dislocations may be generated during cooling giving dislocation densities two to four times larger than far from the tail. In this case the larger densities observed in LEC crystals may be accounted for by the stresses generated during the cooling process. The two-fold symmetries observed experimentally in wafers from the seed end support this conclusion.

41. The similarity between the EL2 distributions in wafer from the tail end showing the two-fold symmetry and sometimes

minima in the <100> directions supports the mechanism proposed by Holmes et al.[80,81] for the EL2 formation. This mechanism as described in Appendix I, involves dislocation climb during cooling.

Summary of the Conclusions

1) A mathematical model for temperature and stress calculations during growth and cooling of LEC GaAs has been developed and validated.

2) The model results describe the dislocation distribution in LEC GaAs with a mechanism for dislocation formation in which only thermal stresses are involved.

3) The effect on dislocation distribution of the different growth variables is presented and discussed.

4) The calculations show that large areas in the crystal can have local resolved shear stress below the critical resolved shear stresses and therefore be free of dislocations. This requires low temperature gradients, between 7 and 10°C/cm for 5.5 and 8.0 cm diameter crystals.

5) The importance of cooling on dislocation formation has been established.

REFERENCES

1. L. Hollan, J.P. Hallais and J.C. Brice ; Current Topics in Material Science. 5.E. Kaldis Ed. North Holland. Amsterdam, 1980, pp.1-218.

2. D.N. McQuiddy, J.W. Wassel, J.B. Lagrange and W. Wisseman ; IEEE Trans. on Microwave and Techniques, MTT-32(9), 1984, pp.997-1008.

3. P. Greiling, IBID, pp.1144-1156.

4. C.A. Solte, Semiconductors and Semimetals, Semiinsulating GaAs, 20, 1984, pp.89-158.

5. L.F. Eastman, IBID, pp.42-45.

6. T.E. Bell., IEEE Spectrum, Oct.1985, pp.46-52.

7. P. Robinson, BYTE. Nov.1984, pp.211-227.

8. J.P. Noblanc, Semi-insulating III-V Materials, Shiva Publ. Ltd., 1882, pp.380-393.

9. N. Bar-Chaim, K.Y. Lau, I. Ury and A. Yariv, Appl. Phys. Lett., 44(10), 1984, pp.941-943.

10. T. Sanada, S. Yamakoshi, O. Wada, T. Fujii, T. Sakurai, and M. Sasaki, Appl. Phys. Lett., 44(3), 1984, pp.325-327.

11. R.P. Gale, J.C.C. Fan, G.W. Turner, R.L. Chapman and J.V. Pantano, Appl. Phys. Lett., 44(6), 1984, pp.632-634.

12. R. Birenbaum, Canadian Research, Dec.1985, pp.14-19.

13. E,P.A. Metz, R.C. Miller and R. Mazelsky, J. Appl. Phys., 33, 1962, pp.2016.

14. J.B. Mullin, B.W. Staugham and W.S. Buckell, J. Phys. Chem. Solids, 26, 1965, pp.782.

15. J.B. Mullin, R.J. Heritage, C.H. Holliday and B.W. Straugham, J. Crystal Growth, 34, 1968, pp.281.

16. T.R. Aucoin, M.J. Wade, R.L. Ross, R.O. Savage, Solid State Techn., Jan.1979, pp.59-67.

17. R.C. Puttbach, G. Elliot and W.M. Ford, Int. Conf. Vapor Growth Epitaxy/Am. Conf. Crystal Growth, 5th, San Diego, Calif., 1981.

18. B.Ford, J.Galt, J. Barrera and N.Helgeland, ACCG-6, ICVGE-6, Atlantic City, New Jersey, July 1984, pp.1-20.

19. G.Elliot, AACG/West-8, Fallen Leaf Lake, CA., June 4-7, 1985.

20. R.K. Willardson in "3rd Inter. Conf. on Semi-Insulating III-V Compounds", Kah-nee-ta 1984, ed. by D.C. Look and J.S. Blakemore (Shiva, Nantwich, Cheshire, England 1984), pp.96-110.

21. W.C. Dash, J. Appl. Phys., 30(14), 1959, pp.355-358.

22. W. Bardsley, D.T.J. Hurle and B.C. Joyce, J. Crystal Growth, 40, 1977, pp.13-20.

23. IBID, pp. 21-28.

24. IBID, 42, 1977, pp.47-482.

25. A.S. Jordan, R. Caruso, A.R. Von Neida and J.W. Neilsen, J. Appl. Phys., 52, 1981, pp.3331.

26. D. Vandermater, A.G. Elliot and Chia-Li Wei, AACG/West-8, Fallen Leaf Lake, CA., June 4-7, 1985.

27. C.R. Lewis, C.W. Ford and J.G. Werthen, Appl. Phys. Lett., 45(8), 1984, pp.895-897.

28. A.J.R. de Kock, W.M. Van Wijgert, J.H.T. Hengst and J.M.P.L. Huybregts, J. Crystal Growth, 31, 1977, pp.13-28.

29. T. Kamejima, J.Matsui, Y. Seki and H. Watanabe, J. Appl. Phys., 50(5), 1979, pp.3312-3321.

30. F.A. Ponce, F.C. Wang and R.Hishes in "3rd Inter. Conf. on Semi-Insulating III-V Compounds", Kah-nee-ta 1984, ed. by D.C. Look and J.S. Blakemore (Shiva, Nantwich, Cheshire, England 1984), pp.68-75.

31. A. Authier, J. Crystal Growth, 42, 1977, pp.612-620.

32. A.G. Cullis, P.D. August and D.J. Stirland, J. Appl. Phys., 41(5), 1980, pp.2556-2560.

33. F.Weinberg, Private Communication.

34. G. Jacob, J.P. Farges, C. Shemali, M. Duseaux, J. Hallais, W.J. Bartels and P.J. Rosknoer, J. Crystal Growth, 57, 1982, pp.245-258.

35. H. Khoda, K. Yamada, H. Nakanishi, T. Kobayashi, J. Osaka and K. Hoshikawa, J. Crystal Growth, 71, 1985, pp.813-816.

36. F. Hyuga, H. Kohda, H. Nakanishi, T. Kobayashi and K. Hoshikawa, Appl. Phys. Lett., 47(6), 1985, pp.620-622.

37. T. Shimada, K. Terashima, H. Nakajima and T. Fukuda, Jap. J. Appl. Phys., 23(1), 1984, pp.L23-L25.

38. IBID, 23(7), 1984, pp.L441-L444.

39. M. Watanabe, T. Fujii, S. Washizuka, S. Yashiro, J. Ushizawa and S. Matsumura, ACCG-6, ICVGE-6, Atlantic City, N.J., July 15-20, 1984.

40. A.G. Elliot, C. Wei, R. Ferraro, G. Woolhouse, M. Scott and R. Hiskes, J. Crystal Growth, 70, 1984, pp. 169-178.

41. S. Clark and D.J. Stirland, Inst. Phys. Conf. Ser., 60(7), 1981, pp. 339-344.

42. R.J. Roedel, A.J. Von Neida, R. Caruso and L.R. Dawson, J. Electroch. Soc., 126, 1979, pp.637.

43. T. Kamejima, F. Shimura, Y. Matsumoto, H. Watanabe and J. Matsui, Jap. J. Appl. Phys., 23(11), 1982, pp.L721-L723.

44. P.M. Petroff and R.L. Hartman, Appl. Phys. Lett., 23, 1973, pp.469.

45. W.A. Brantley and D.A. Harrison, in "Proc. IEEE Reliability Physics Symp.", April 1973, pp.267.

46. G. Zaeschmar, in "AGARD Proc.", London, Ed. H. Hodara (Natl. Tech. Info. Service, Springfield, VA.) (219), 1977.

47. Y. Kadota, K. Chino, Jap. J. Appl. Phys., 22(10), 1983, pp.1563-1566.

48. G. Jacob, C. Venger, J.P. Farges, J. Hallais, G.M. Martin, M.G. Berth and G. Poibland, Int. Phys. Conf. Ser., (56), 1981, pp.455-464.

49. J.V. DiLorenzo, A.S. Jordan, A.R. Von Neida and P. O'Connor, in "3rd Inter. Conf. on Semi-Insulating III-V Compounds", Kah-nee-ta 1984, ed. by D.C. Look and J.S. Blakemore (Shiva, Nantwich, Cheshire, England 1984).

50. Y. Nanishi, S. Ishida, T. Honda, H. Yamazaki and S. Miyazawa, Jap. J. Appl. Phys., 21(6), 1982, pp.L335-L337,

51. Y. Nanishi, S. Ishida and S. Miyazawa, Jap. J. Appl. Phys., 22(1), 1983, pp.L54-L56.

52. S. Miyazawa, Y. Ishii, A. Ishida and Y. Nanishi, Appl. Phys. Lett., 43(9), 1983, pp.853-855.

53. T. Takebe, M. Shimazu, A. Kawasaki, T. Kotani, R. Nakai, K. Kikuchi, S. Murai, K. Tada, S. Akai and T. Suzuki, in "3rd Inter. Conf. on Semi-Insulating III-V Compounds", Kah-nee-ta 1984, ed. by D.C. Look and J.S. Blakemore (Shiva, Nantwich, Cheshire, England 1984), pp.335-346.

54. H.V. Winston, A.T. Hunter, H.M. Olsen, R.P. Bryan and R.E. Lee, Appl. Phys. Lett., 45(4), 1984, pp.447-449.

55. H. Yamazaki, T. Honda, S. Ishida and Y. Kawasaki, Appl. Phys. Lett., 45(10), 1984, pp.1109-1111.

56. S. Myazawa, T. Mizutani and H. Yamazaki, Jap. J. Appl. Phys., 21(9), 1982, pp.L542-L544.

57. M. Peigen, W. Ju, Z. Yuanxi, Y. Jinhua and L. Shouchum in "3rd Inter. Conf. on Semi-Insulating III-V Compounds", Kah-nee-ta 1984, ed. by D.C. Look and J.S. Blakemore (Shiva, Nantwich, Cheshire, England 1984), pp.134-140.

58. R.T. Blunt, S. Clark and D.J. Stirland, IEEE Trans. on Microwave and Techniques, MTT-30(7), 1982, pp.943-949.

59. R.T. Blunt, in "Semi-Insulating III-V Materials", Evian 1982, S. Makram-Ebeid and B. Tucks eds., (Shiva, Nantwich, England 1982), pp.107-112.

60. T. Matsumura, H. Emori, K. Terashima and T. Fukuda, Jap. J. Appl. Phys., 22, 1983, pp.L154.

61. A. Tamura and T. Onuma, Jap. J. Appl. Phys., 24(4), 1985, pp.510-511.

62. T. Honda, Y. Ishii, S. Miyazawa, H. Yamazaki and Y. Nanishi, Jap. J. Appl. Phys., 22, 1983, pp.L270-L272.

63. K. Watanabe, H. Nakanishi, K. Yamada, and K. Hoshikawa, Appl. Phys. Lett., 45(6), 1984, pp.643-645.

64. F. Hyuga, Jap. J. Appl. Phys., 24(2), 1985, pp.L160-L162.

65. M. Otsubo, M. Nakatani and K. Shirahata, Evian 1982, S. Makram-Ebeid and B. Tucks eds., (Shiva, Nantwich, England 1982), pp.130-133.

66. I. Grant, D. Rumsby, R.M. Ware, M.R. Brozel and B. Tuck, IBID, pp.98-106.

67. M.R. Brozel, L. Eaves and J.P.J. McCann, in "3rd Inter. Conf. on Semi-Insulating III-V Compounds", Kah-nee-ta 1984, ed. by D.C. Look and J.S. Blakemore (Shiva, Nantwich, Cheshire, England 1984), pp.287-301.

68. S. Makram-Ebeid, P. Langlade and G.M. Martin, IBID, pp.184-201.

69. P.F. Lindquist, J. Appl. Phys., 48, 1977, pp.1262.

70. E.M. Swiggard, S.H. Lee and F.W. Von Batchelder, Int. Phys. Conf. Ser., 45, 1979, pp.125.

71. R.G. Wilson and C.A. Evans, Jr. Int. Phys. Conf. Ser., 56, 1981, pp.563.

72. W. Kutt, D. Blimberg, M. Maier, H. Krautle, F. Kohl and E. Bauser, Appl. Phys. Lett., 44(11), 1984, pp.1078-1080.

73. C.D. Brandt, A.M. Hennel, L.M. Pawlowicz, F.P. Dabkowski, J. Lagowski and H.C. Gatos, Appl. Phys. Lett., 47(6), 1985, pp.607-609.

74. A.G. Milnes in "Deep Impurities in Semiconductors", Wiley, New York, 1973, pp.57.

75. A.M. Huber, N.T. Linh, M. Valladon, J.L. Debrun, G.M. Martin, A. Mitonneau and A. Mircea, J. Appl. Phys., 50, 1979, pp.4022.

76. G.M. Martin, G. Jacob, J. Poiblud, A. Goltzene and C. Schwab, Inst. Phys. Conf. Ser., (59), 1981, pp.281-286.

77. T. Ishida, M. Maeda and S. Takeuchi, Appl. Phys., 21, 1980, pp.257.

78. E.R. Weber, H. Ennen, U. Kaufmann, J. Windscheif and J. Schneider, J. Appl. Phys., 53, 1982, pp.6140.

79. J. Lagowski, H.C. Gatos, J.M. Parsey, K. Koda, M. Kaminska, and W. Walakiewicz, Appl. Phys. Lett., 40, 1982, pp.342.

80. D.E. Holmes, R.T. Chen, K.R. Elliott, C.G. Kirkpatrick and P.W. Yu, IEEE Trans. on Microwave Theory and Techniques, MTT-30(7), 1982, pp.949-955.

81. D.E. Holmes, R.T. Chen, K.R. Elliott and C.G. Kirkpatrick, Appl. Phys. Lett., 40(1), 1982, pp.46-51.

82. C.G. Kirkpatrick, R.T. Chen, D.E. Holmes, P.M. Asbeck, K.R. Elliott, R.D. Fairman and J.R. Oliver in "Semiconductors and Semimetals", Seminsulating GaAs, 20, 1984, pp.159-231.

83. L.B. Ta, H.M. Hobgood, A. Rohatgi and R.N. Thomas, J. Appl. Phys., 53(8), 1982, pp.5771-5775.

84. D.E. Holmes, R.T. Chen, K.R. Elliott and C.G. Kirkpatrick, Appl. Phys. Lett., 43(3), 1983, pp.305-307.

85. D.E. Holmes, H. Kuwamoto, C.G. Kirkpatrick and R.T. Chen, in "3rd Inter. Conf. on Semi-Insulating III-V Compounds", Kah-nee-ta 1984, ed. by D.C. Look and J.S. Blakemore (Shiva, Nantwich, Cheshire, England 1984), pp.204-213.

86. D.J. Stirland, I. Grant, M.R. Brozel and R.M. Ware, Inst. Phys. Conf. Proc., (67) Sec.1, 1983, pp.285-290.

87. M.S. Skolnick, D.A.O. Hope and B. Cockayne, in "3rd Inter. Conf. on Semi-Insulating III-V Compounds", Kah-nee-ta 1984, ed. by D.C. Look and J.S. Blakemore (Shiva, Nantwich, Cheshire, England 1984), pp.446.

88. D.J. Stirland, M.R. Brozel and I. Grant, Appl. Phys. Lett., 46(11), 1985, pp.1066-1068.

89. K. Wada and N. Inoue, Appl. Phys. Lett., 47(9), 1985, pp.945-947.

90. K.R. Elliott, R.T. Chen, S.G. Greenbaum and R.J. Wagner in "3rd Inter. Conf. on Semi-Insulating III-V Compounds", Kah-nee-ta 1984, ed. by D.C. Look and J.S. Blakemore (Shiva, Nantwich, Cheshire, England 1984), pp.239-245.

91. IBID, Appl. Phys. Lett., 44(9), 1984, pp.907-909.

92. U. Kaufmann, J. Windscheif, M. Beaumler, J. Schneider and F. Kohl, in "3rd Inter. Conf. on Semi-Insulating III-V Compounds", Kah-nee-ta 1984, ed. by D.C. Look and J.S. Blakemore (Shiva, Nantwich, Cheshire, England 1984), pp.246-253.

93. E.R. Weber in "3rd Inter. Conf. on Semi-Insulating III-V Compounds", Kah-nee-ta 1984, ed. by D.C. Look and J.S. Blakemore (Shiva, Nantwich, Cheshire, England 1984), pp.296-301.

94. N. Tsukada, T. Kikuta and K. Ishida, Jap. J. Appl. Phys., 24(9), 1985, pp.L689-L692.

95. J. Lagowski, D.G. Lin, T.P. Chen, M. Skowronski and H.C. Gatos, Appl. Phys. Lett., 47(9), 1985, pp.929-931.

96. M. Taniguchi, Y. Mochizuki and T. Ikoma, in "3rd Inter. Conf. on Semi-Insulating III-V Compounds", Kah-nee-ta 1984, ed. by D.C. Look and J.S. Blakemore (Shiva, Nantwich, Cheshire, England 1984), pp.231-245.

97. M. Taniguchi and T. Ikoma, Appl. Phys. Lett., 45(1), 1984, pp.69-71.

98. J. Lagowski, D.J. Lin, T. Aoyama and H.C. Gatos, Appl. Phys. Lett., 44(3), 1984, pp.336-338.

99. IBID, in "3rd Inter. Conf. on Semi-Insulating III-V Compounds", Kah-nee-ta 1984, ed. by D.C. Look and J.S. Blakemore (Shiva, Nantwich, Cheshire, England 1984), pp.223-230.

100. K. Ishida, A. Yahata and T. Kikuta, Jap. J. Appl. Phys., 24(4), 1985, pp.L250-L252.

101. A. Kadota and K. Chin, Jap. J. Appl. Phys., 22(10), 1983, pp.1563-1566.

102. F. Hasegawa, N. Yamamoto and Y. Nannichi, Appl. Phys. Lett., 45(4), 1984, pp.461-463.

103. J. Osaka, F. Hyuga and K. Watanabe, Appl. Phys. Lett., 47(12), Dec.1985, pp.1307-1309.

104. R.T. Chen, D.E. Holmes and P.M. Asbeck, Appl. Phys. Lett., 45(4), 1984, pp.549-561.

105. A.T. Hunter, H. Kimura, J.P. Baukus, H.V. Winston and O.J. Marsh, Appl. Phys. Lett., 44(1), 1984, pp.74-76.

106. B. Wakefield, P.A. Leigh, M.H. Lyons and C.R. Elliott, Appl. Phys. Lett., 45(1), 1984, pp.66-68.

107. C.P. Lee, in "Semi-Insulating III-V Materials", Evian 1982, S. Makram-Ebeid and B. Tucks eds., (Shiva, Nantwich, England 1982), pp.324-335.

108. S. Makram-Ebeid A. Mitonneau and G. Laurence, IBID, pp.336-343.

109. C. Kocot and C. Stolte, IEEE Trans. on Microwave and Techniques, MTT-30 (7), 1982, pp.963-968.

110. R.T. Chen and D.E. Holmes, J. Crystal Growth, 61, 1983, pp.111-124.

111. D.E. Holmes, K.R. Elliott, R.T. Chen and C.G. Kirkpatrick, in "Semi-Insulating III-V Compounds", Evian 1982, S. Makram-Ebeid and B. Tucks eds., (Shiva, Nantwich, England 1982), pp.10-27.

112. G. Shoeck and W.A. Tiller, Phil. Mag., 5, 1960, pp.43-63.

113. A.G. Elliot, C. Wei, R. Ferraro, G. Woolhouse, M. Scott and R. Hiskes, J. Crystal Growth, 70, 1984, pp.169-178.

114. Yu. A. Grigoriev, J.P. Grishin, G.F. Juznetsov, M.G. Milvidski, V.B. Osvenski, I.N. Shershakova and S.S. Shifrin, Izv. Ak. Nauk. SSSR. Ser. Fiz., 44(2), 1980, pp.300-303.

115. J.C. Brice, J. Crystal Growth, 7, 1970, pp.9-12.

116. T.S. Plasket, J.M. Woodall and A. Segmuller, J. Electroch. Soc., 118, 1971, pp.115-117.

117. E. Schmid and N. Boas, "Plasticity of Crystals", Chapman and Hall Ltd., London, 1968.

118. J.J. Gilman, "Micromechanics of Flow in Solids", McGraw Hill Book Co., N.Y., 1968.

119. E. Billig, Proc. Roy. Soc., A235, 1956, pp.37-55.

120. P. Penning, Philips Res. Repts., 13, 1958, pp.79-97.

121. A. Steinemann and U. Zimmerli, in "Crystal Growth", Boston, June 20-24, 1966, H.S. Peiser Ed. London, Pergamon Press, 1967, pp.81-87.

122. J.C. Brice and G.D. King, Nature, 209, 1966, pp.1364.

123. M. Duseaux and G. Jacob, Appl. Phys. Lett., 40(9), 1982, pp.790-792.

124. G. Jacob, in "Semi-Insulating III-V Materials", Evian 1982, S. Makram-Ebeid and B. Tucks eds., (Shiva, Nantwich, England 1982), pp.2-18.

125. G. Jacob, J.P. Farges, C.Shemali, M. Duseaux, J. Hallais, W.J. Bartels and P.J. Rosknoer, J. Crystal Growth, 57, 1982, pp.245-258.

126. J. Lagowski, H.C. Gatos, T. Aoyama and D.G. Lin, in "3rd Inter. Conf. on Semi-Insulating III-V Compounds", Kah-nee-ta 1984, ed. by D.C. Look and J.S. Blakemore (Shiva, Nantwich, Cheshire, England 1984), pp.60-67.

127. IBID, Appl. Phys. Lett., 45(6), 1984, pp.680-682.

128. V.I. Nitikenko and V.L. Indenbom, Sov. Phys. Cryst., 6(3), 1961, pp.341-346.

129. S. Yasuami, H. Mikami and A. Hojo, Jap. J. Appl. Phys., 22(10), 1983, pp.1567-1569.

130. G.T. Brown, M.S. Skolnick, G.R. Jones, B.K. Tannerr and S.J. Barnett, in "3rd Inter. Conf. on Semi-Insulating III-V Compounds", Kah-nee-ta 1984, ed. by D.C. Look and J.S. Blakemore (Shiva, Nantwich, Cheshire, England 1984), pp.77-82.

131. T. Kitano, T. Ishikawa, H. Ono and J. Matsui, in "4th Conf. on Semi-Insulating III-V Materials, May 18-21, 1986. Hakone, Japan.

132. M. Yamada, Phys. Lett., 47(4), 1985, pp.365-367.

133. P. Dobrilla and J.S. Blakemore, in "4th Conf. on Semi-Insulating III-V Materials, May 18-21, 1986. Hakone, Japan.

134. H.J. Horel, M. Albert, D. Guidotti and E. Farrel, in "4th Conf. on Semi-Insulating III-V Materials, May 18-21, 1986. Hakone, Japan.

135. J.C. Brice, J. Crystal Growth, 2, 1968, pp.395-401.

136. V.A. Borodin, V.N. Erofrev, J.A. Startsev and V.A. Tatarchenko, Izv. Ak. Nauk. SSSR. Ser. Fiz., 40(7), 1976, pp.103-105.

137. A.S. Jordan, R. Caruso and A.R. Von Neida, The Bell Sys. Techn. J., 59(4), 1980, pp.593-637.

138. I.M. Buckley-Golden and C.J. Humphreys, pma., 39(1), 1979, pp.41-57.

139. A.S. Jordan, J. Crystal Growth, 49(3), 1980, pp.631-642.

140. R. Thyagarajan, R.C. Narula and T.R. Parashar, Indian J. Pure and Appl. Phys., 17, 1979, pp.650-654.

141. B. Lent, M. Bonnet, N. Visentin and J.P. Duchemin, Microelectronics J., 13(1), 1982, pp.5-9.

142. Y. Kadota, M. Kakimoto, Y. Masa, A. Tanaka and T. Yokoyama, in "3rd Inter. Conf. on Semi-Insulating III-V Compounds", Kah-nee-ta 1984, ed. by D.C. Look and J.S. Blakemore (Shiva, Nantwich, Cheshire, England 1984), pp.157-159.

143. H. Emori, T. Matsumura, T. Kikuta and T. Fukuda, Jap. J. Appl. Phys., 22(11), 1983, pp.1652-1655.

144. H. Emori, K. Terashima, F. Orito, T. Kikuta and T. Fukuda, in "3rd Inter. Conf. on Semi-Insulating III-V Compounds", Kah-nee-ta 1984, ed. by D.C. Look and J.S. Blakemore (Shiva, Nantwich, Cheshire, England 1984), pp.111-117.

145. T. Fukuda, K. Terashima, T. Katsumata, F. Orito, S. Ozawa, T. Okobata and T. Sato, ACCG/6, OCVGE/6, Atlantic City (N.J.), July 1984.

146. T. Shimada, K. Terashima, H. Nakajima and T. Fukuda, Jap. J. Appl. Phys., 23(1), 1984, pp.L23-L25.

147. T. Shimada, T. Obokata and T. Fukuda, Jap. J. Appl. Phys., 23(7), 1984, pp.L441-L444.

148. A.S. Jordan, A.R. Von Neida and R. Caruso, J. Crystal Growth, 70, 1984, pp.555-573.

149. N.S. Belyatsukaya, S.P. Grishina, E.V. Lopatin, M.G. Milvidski, V.P. Osvenskii and V.G. Formin, Sov. Phys. Cryst., 17, 1972, pp.126.

150. M.G. Milvidskii, V.B. Osvenskii and S.S. Shifrin, J. Crystal Growth, 52, 1981, pp.396-403.

151. Y. Seki, H. Watanabe and J. Matsui, J. Appl. Phys., 49(2), 1978, pp.822-828.

152. T. Suzuki, S. Akai, K. Kohe, I. Nishida, K. Fujita and N. Kito, Sumitomo Elec. Tech. Rev., 18, 1978, pp.105.

153. P.D. Greene, J. Crystal Growth, 50, 1982, pp.612.

154. K. Tada, A. Kawasaki, T. Kotani, R. Nakai, T. Kabebe, S. Akai and T. Yamaguchi, in "3rd Inter. Conf. on Semi-Insulating III-V Compounds", Kah-nee-ta 1984, ed. by D.C. Look and J.S. Blakemore (Shiva, Nantwich, Cheshire, England 1984), pp.36-44.

155. G. Jacob, J. Crystal Growth, 59, 1982, pp.669-671.

156. Yu. A Grigoriev, S.P. Grishin, G.F. Kuznetsov, M.G. Milvidskii, V.B. Osvenskii, I.N. Shershakova and S.S. Shifrin, Izv. Ak. Nauk. SSSR. Ser. Fiz., 44(2), 1980, pp.300-303.

157. R. Fornari, C. Paorici, L. Zanotti and G. Zuccalli, J. Crystal Growth, 63, 1983, pp.415.

158. H. Miyairi, T. Inada, T. Obokata, M. Nakajima, T. Katsumata and T. Fukuda, Jap. J. Appl. Phys., 24(9), 1985, pp.L729-L732.

159. D.L. Barret, S. McGuigan, H.M. Hobgood, G.W. Elrisge and R.N. Thomas, J. Crystal Growth, 70, 1984, pp.179-184.

160. H.M. Hobgood, R.N. Thomas, D.L. Barret, G.W. Elridge, M.M. Sopira and M.C. Driver, in "3rd Inter. Conf. on Semi-Insulating III-V Compounds", Kah-nee-ta 1984, ed. by D.C. Look and J.S. Blakemore (Shiva, Nantwich, Cheshire, England 1984), pp.149-156.

161. E.J. Foulkes, M.R. Brozel, I. Grant, P. Singer, B. Waldock and R.M. Ware, IBID, pp.160-164.

162. H. Kimura, C.B. Afable, H. M. Olsen, A.T. Hunter and H.V. Winston, J. Crystal Growth, 70, 1984, pp.185-190.

163. M.G. Milvidskii and E.P. Bochkarev, J. Crystal Growth, 44, 1978, pp.61-74.

164. A. Sher, A.B. Chen and W.E. Spicer, Appl. Phys. Lett., 46(1), 1985, pp.54-56.

165. S. Miyazawa, 1983 European Patent Application 833021652. (From Ref. 164).

166. H. Ehrenreich and J.P. Hirth, Appl. Phys. Lett., 46(1), 1985, pp.668-670.

167. J.C. Mikkelsen Jr., and J.B. Boyce, Phys. Rev. B.28, 1983, pp.7130.

168. T. Kamejima, J. Matsui, Y. Seki and H. Watanabe, J. Appl. Phys., 50(5), 1979, pp. 3312-3321.

169. D. Laister and G.M. Jenkins, J. Mater. Science, 3, 1968, pp.584.

170. D. Laister and G.M. Jenkins, Phil. Mag., 20, 1971, pp.361 ; and IBID, 23, pp.1077.

171. L.M. Morgulis, M.G. Milvidskii and B.B. Osvenskii, Izv. Ak. Nauk. SSSR. Ser. Fiz., 38(7), 1974, pp.65-73.

172. P.M. Hutchinson and P.S. Robson, Phil. Mag., 30, 1974, pp.65-73.

173. S.S. Ruvimov, L.M. Sorokin, M. Paziman, I. Khaindenraikh, R. Sholts and R.O. Starobogatov, Sov. Phys. Solid State, 24(5), 1982, pp.869-870.

174. S.S. Shifrin and A.V. Markov, Sov. Phys. Cryst., 25(5), 1980, pp.625-627.

175. R. Fornari, P. Franzosi, G. Salviati, C. Ferrari and C. Ghezzi, J. Crystal Growth, 72, 1985, pp.717-125.

176. M.P. Scott, S.S. Laderman and A.G. Elliot, Appl. Phys. Lett., 45(12), 1985, pp.1280-1282.

177. B. Pichaud, N. Burle-Durbec, F. Minari and M. Duseaux, J. Crystal Growth, 71, 1985, pp.648-654.

178. M. Nakajima, T. Katsumata, K. Terashima and K. Ishida, Jap. J. Appl. Phys., 24(1), 1985, pp. L65-L68.

179. J. Osaka and K. Oshikawa, in "3rd Inter. Conf. on Semi-Insulating III-V Compounds", Kah-nee-ta 1984, ed. by D.C. Look and J.S. Blakemore (Shiva, Nantwich, Cheshire, England 1984), pp.126-133.

180. J. Osaka, T. Kobayashi and K. Hoshikawa, Jap. J. Appl. Phys., 23(4), 1984, pp.L195-L197.

181. K. Terashima, T. Katsumata, F. Orito and T. Fukuda, Jap. J. Appl. Phys., 23(4), 1984, pp.L302-L304.

182. W. Langlois and Ki Lun Li, J. Crystal Growth, 62, 1983, pp.481.

183. G.M. Oreper and J. Szekeley, J. Crystal Growth, 64, 1983, pp.505.

184. M. Mihelcic and K. Wingerath, J. Crystal Growth, 71, 1985, pp.163-168.

185. K. Terashima, T. Katsumata, F. Orito, T. Kikuta and T. Fukuda, Jap. J. Appl. Phys., 22(6), 1983, pp.L325-L327.

186. M. Shinohara, T. Ito, K. Yamada and Y. Imamura, Jap. J. Appl. Phys., 24(9), 1985, pp.L711-L713.

187. H.V. Winston, A.T. Hunter, H.M. Olsen, R.P. Bryan and R.E. Lee, in "3rd Inter. Conf. on Semi-Insulating III-V Compounds", Kah-nee-ta 1984, ed. by D.C. Look and J.S. Blakemore (Shiva, Nantwich, Cheshire, England 1984), pp.402-405.

188. S. Miyazawa, T. Honda, Y. Ishi and S. Ishida, Appl. Phys. Lett., 44(4), 1984, pp.410-412.

189. N.A. Avdonin, S.S. Vakhrameev, M.G. Milvidskii, V.B. Osnskii, B.A. Sakharov, V.A. Smirnov and Yu.F. Shchelkin, Izv. Ak. Nauk. SSSR. Ser. Fiz., 36(3), 1972, pp.502-507.

190. A.S. Jordan, R. Caruso, A.R. Von Neida and J.M. Nielsen, J. Appl. Phys., 52(5), 1981, pp.3331-3336.

191. A.S. Jordan, J. Crystal Growth, 49(3), 1980, pp.631-642.

192. S.A. Vakhrameev, V.B. Osvenskii and S.S. Shifrin, Izv. Ak. Nauk. SSSR. Ser. Fiz., 44(2), 1980, pp.54-58.

193. M.G. Milvidskii, V.A. Smirnov, I.V. Starshinova and Yu.F. Shchelkin, Izv. Ak. Nauk. SSSR. Ser. Fiz., 40(7), 1976, pp.97-102.

194. S.S. Vakhrameev, M.G. Milvidskii, V.B. Osvenskii, V.A. Smirnov and Yu.F. Shchelkin, Growth of Crystals, 12, 1977, ed. by A.A. Chernov, Consultants Bureau, N.Y., 1984, pp.296-301.

195. M. Duseaux, J. Crystal Growth, 61, 1983, pp.576-590.

196. G. Szabo, J. Crystal Growth, 73, 1985, pp.131-141.

197. T. Iwaki and N. Kobayashi, Trans. ASME, J. Appl. Mech., AM-48, 1981, pp.866.

198. N. Kobayashi and T. Iwaki, J. Crystal Growth, 73, 1985, pp.96-110.

199. E.V. Galaktionov and E.A. Tropp, Izv. Ak. Nauk. SSSR. Ser. Fiz., 40(7), 1976, pp.62-68.

200. D.I. Antonov, E.N. Kolesnikova, U.M. Krymov, S.P. Nikanorov, M.P. Proskura and V.S. Yuterev, Izv. Ak. Nauk. SSSR. Ser. Fiz., 40, 1970, pp.69-73.

201. D.I. Antonov, E.V. Galaktionov, V.M. Krymov and E.A. Tropp, IBID, pp.74-77.

202. V.L. Indenbom, Sov. Phys. Cryst., 2, 1958, pp.587.

203. F.R.N. Nabarro, "Theory of Crystal Dislocations" Oxford Univ. Press, London, 1967.

204. V.I. Nikitenko and V.L. Indenbom, Sov. Phys. Cryst., 6(3), 1961, pp.341-346.

205. V.L. Indenbom, Izv. Ak. Nauk. SSSR. Ser. Fiz., 37(11), 1973, pp.5-11.

206. S.V. Tsivinskii, Izv. Ak. Nauk. SSSR. Ser. Fiz., 37(11), 1973, pp.163-165.

207. S.V. Tsivinskii, Izv. Ak. Nauk. SSSR. Ser. Fiz., 40(7), 1976, pp.165-166.

208. J.L. Nowinski, "Theory of Thermoelasticity with Applications", Sijthoff and Noordhoof Int. Publ., Alphen Aan den Rijn, 1978.

209. K.H. Huebner and E.A. Thornton, "The Finite Element Method for Engineers", J. Wiley and Sons, N.Y., 1982.

210. R.D. Cook, "Concepts and Application of Finite Element Analysis", 2nd ed. J. Wiley and Sons, N.Y., 1981.

211. V. Swaminathan and S.M. Copley, J. Am. Ceram. Soc., 58, 1975, pp.482.

212. H.A. Nancarrow, Proc. Phys. Soc., 45, 1933, pp.462.

213. Handbook of Mathematical Functions, Ed. by M. Abramowitz and I.A. Stegun, Dover, N.Y., 1965.

214. R.H. Gallagher, J. Padlog and P.P. Bijlaard, ARS Journal, May 1962, pp.700-707.

215. E. Wilson, AIAA Journal, 3(12), Dec.1965, pp.2269-2274.

216. N.P. Dario and W.A. Bradley, Int. J. for Num. Methods in Eng., 5, 1973, pp.573-583.

217. R.W. Clough, and Y. Rashid, J. of the Eng. Mech. Div., ASME, EM1, 1965, pp.71-85.

218. I. Grant, B. Smith, D. Rumsby and R.W. Ware, Cambridge Instrument Co., Dustat Rd., Cambridge, Private Communication.

219. H.S. Carslaw and J.C. Jaeger, "Conduction of Heat in Solids" 2nd ed., Oxford Press, Oxford, 1958.

APPENDIX I

EFFECT OF DISLOCATIONS ON GaAs AND DEVICES

I.1 Effect of Dislocation on Properties

The semi-insulating property of GaAs makes it suitable for use as substrate for the fabrication of integrated circuits, simplifying device isolation and permitting low capacitance interconnections through the substrate[49]. The choice of ion implantation for device fabrication imposes rigorous conditions on substrate properties, especially homogeneity. The semi-insulating property is essential. Inhomogeneous FET performance has been correlated with dislocation distribution in Cr doped and undoped semi-insulating GaAs[50-53]. Moreover, on a micro-scale level, it is found that the FET threshold voltage is affected by dislocations located at less than 20-30 microns from the FET. There has been no consensus on how or how much, the threshold voltage is affected[54,55]. Recently, this correlation has been examined more carefully and related to the interaction of dislocations as sources of sinks or point defects and the EL2 level concentration distribution which is strongly correlated with FET characteristics.

In additions, a great amount of effort has been directed to evaluate the role of dislocations on semi-insulating properties. Dislocation distributions have been directly correlated with leakage current distribution[56,57], resistivity[58-61], and carrier

concentration in Si implanted LEC-growth, semi-insulating GaAs[62,64]. Leakage current and sheet resistance have M-shaped distribution, while resistivity and carrier concentration have the W-shape. In addition, it is found that dislocations affect the sheet carrier concentration within about a 75 micron radius area[64].

In Cr-doped LEC GaAs the reports are conflicting. On one hand, it is found that Cr follows a M-shaped distribution inverse of the W-shaped EPD distribution, suggesting that the dislocations can affect the Cr concentration and annealing behaviour of donor impurities[65]. On the other hand, no variation of Cr concentration associated with dislocation is found[66], and the resistivity variations follow the W-shaped distribution. Moreover resistivity does not correlate with Cr except at high concentrations. It was also reported that Cr concentration across a wafer follows a U-shaped distribution, while the Cr++ concentration follows a W-shaped distribution[67]. Cr is usually added to the melt to obtain semi-insulating GaAs.

At present, extensive studies are being carried out in order to understand the mechanisms that determine the semi-insulating properties of GaAs[68]. The production of high resistivity materials depends on a critical compensation among the different dopants present. In the four-level model an excess of shallow donors is compensated by an excess of deep acceptors over deep donors[69]. In the three-level model an excess of acceptor over donors is compensated by the deep donors[70]. The shallow donors

are believed to be due to S and Si or to the intentional doping of Te. Shallow acceptors are due mainly to C, Mn or other impurities. The energy levels of shallow donors and acceptors are ubicated close to the conduction and valence band respectively.

The deep acceptor is due to Cr and the deep donor is the so called EL2 or EL2 family. Both are mid-gap levels. For Cr-doped GaAs the four level compensation mechanism applies while for undoped GaAs the three level mechanism applies.

The most important commercially available SI substrate is Cr-doped. However, the large diffusion coefficient of Cr[71] has detrimental effects in the IC's technology. Attempts to substitute Cr for the one order of magnitude slower Vanadium[72] is unlikely because Vanadium plays no direct role in the compensation process in GaAs[73]. These two facts lead to concentrate the efforts on undoped SI GaAs and consequently on understanding the nature and role of EL2. In this review a short summary of the findings on EL2 is given below because of the interaction of the EL2 with dislocations.

Originally the EL2 level was associated with oxygen[73] until it was demonstrated that it was not due to this element[74,76]. In addition Martin et al[76] have shown that it is not related to Cr. Alternatively, a strong correlation with the dislocation distribution is found ; the EL2 concentration along the wafer showed the typical W-shaped distribution. It is proposed that the EL2 origin is due to a complex lattice defect growing in the presence of stress. This was supported by the finding that the

EL2 level is created in GaAs during mechanical deformation[77] and that antisite defects form during plastic deformation by dislocation climb[78]. It was then proposed that the EL2 is the As(Ga) antisite or a complex containing the antisite[79]. In addition, the stoichiometry of the melt in LEC GaAs is shown to correlate with the SI properties of the material with a transition from SI for As rich melts to p-type material at the critical As concentration of 0.475 atom fraction[80-82]. This transition is also observed during annealing of SI undoped Ga rich melts[83]. The proposed reaction leading to the antisite through dislocation climb is :

$$V(Ga) + As(As) \longrightarrow As(Ga) + V(As)$$

The most striking correlation of EL2 level distribution with EPD distribution[84,85] is shown in Figure I.1 (a,b) where the EL2 level distribution is shown for wafers from the seed end (a) and from the tail end (b). The typical four-fold symmetry of dislocation correlates perfectly at the seed end. It is interesting to note the two following aspects : first four local minima are observed in the <110> and second, at the seed end a two-fold symmetry appears with a mirror plane coincident with a (110) plane. Two-fold symmetry of dislocations at the seed end has been reported by Weinberg[33]. Nevertheless, the fact that the EL2 level is not directly proportional to dislocations has led to the proposal that the EL2 concentration is proportional to the dislocation density and to the amount of dislocation climb[86]. At present the antisite has been found[90,91,94,95] and shown to be

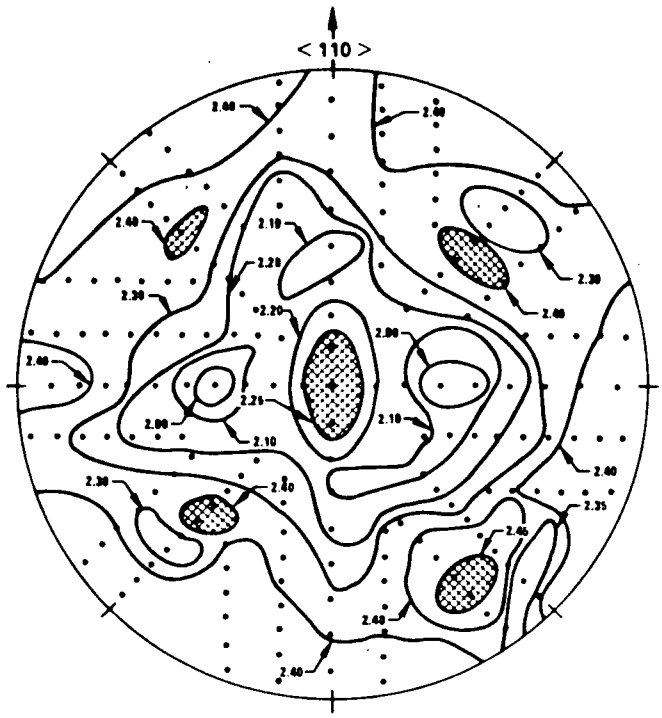

Figure I.1 EL2 contour plot taken at the seed of a(100) 3-in-diam LEC GaAs crystal. The solid dots indicate positions where absorption measurements were made, and the contour lines were drawn to be consistent with the measurements. The number assigned to each contour indicated the EL2 concentration in units of 10^{16} cm^{-3} (i.e., 2.05 means 2.05 X 10^{16} cm^{-3}). The cross-hatched areas indicate local maxima.

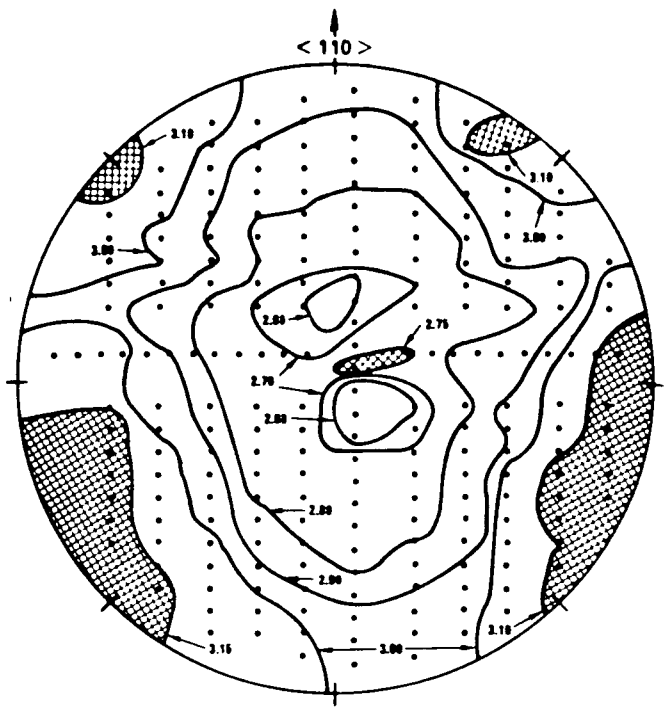

Figure I.1(a) EL2 contour plot at the tail end of the crystal depicted in Figure 1(a). This EL2 distribution has a mirror plane coincident with a (110) plane.

stable at high temperatures[97,93] and believed to be the origin of the EL2 level[89].

The enhanced concentration of EL2 level at dislocations has also been attributed to the aggregation of EL2 centers similar to a Cottrell atmosphere[87]. Whatever the mechanism for [EL2] enhancement is, it has been demonstrated that dislocations play a fundamental role. This is based on the direct observation of the EL2 concentration at single dislocations[88].

However, there is not complete understanding of the semi-insulating mechanism in GaAs.

1) There is more than one midgap trap (an EL2 "family")[96,97]

2) A midgap level related to oxygen with larger electron capture cross-section has been identified[98,99].

3) The characterization techniques of EL2 have been inconsistent[100,101], specifically, different response of the mid gap level have been obtained in heat treated horizontal Bridgeman grown and LEC grown GaAs[102].

4) There is a close correspondence between the increase in sheet and resistance and an increase in EL2 concentration (opposed to what is expected) in dislocation free GaAs[103].

The EL2 level has been associated with undesired backgating effects[108,110]. This reinforces the need for a complete understanding of the origin and properties of this level.

The presence of carbon in GaAs has been shown to affect directly the threshold voltage of implanted FET[104] (carbon concentration in LEC GaAs depends on the water content of the encapsulant[105]). Carbon is found segregated at the cell walls of the cellular arrays of dislocations[106]. Also it has been shown that oxygen, chromium and silicon impurities in undoped GaAs segregated to the dislocation clusters[43].

I.2 Dislocations and Fermi Level

Dislocations in GaAs have been correlated with a shift of Fermi level by Lagowski[126,127]. This is illustrated in Figure I.2(a-c). In Figure I.2(a) the effect of the melt composition on dislocation density is shown for lightly doped GaAs. Note that the minimum occurs above 0.500 atomic fraction. The shift is within the uncertainty of the measurements. In Figure I.2(b) and (c) the Fermi energy and dislocation density are shown as a function of carrier concentration. The concentration of dopant is below the impurity hardening regime. Note that n-type doping reduces the dislocation density. This effect is accounted for by a vacancy condensation mechanism in which the Ga vacancies may be the critical native defect. The As vacancy which can also be important in dislocation generation, can be created upon migration of the Ga vacancy to the neighbouring As site,

$$V(Ga) + As(As) \longrightarrow V(As) + As(Ga)$$

In this reaction the As antisite As(Ga) is also created. Both vacancies are midgap levels (V(Ga) in the lower half and V(As) in

a

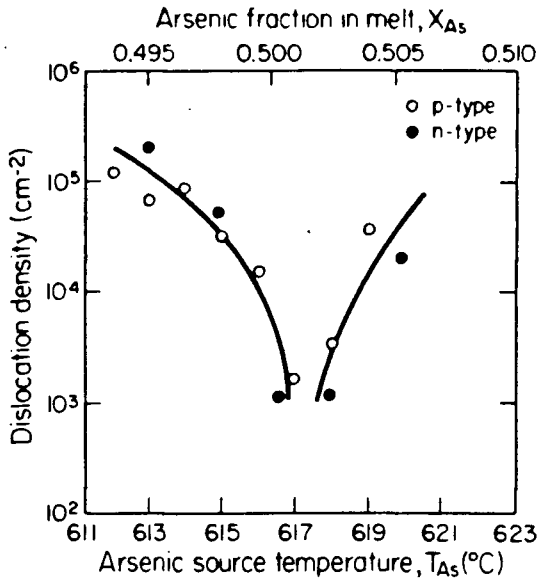

Fig. I.2 a Dislocation density vs arsenic source temperature (melt stoichiometry) for lightly doped n-type and p-type GaAs

b

c

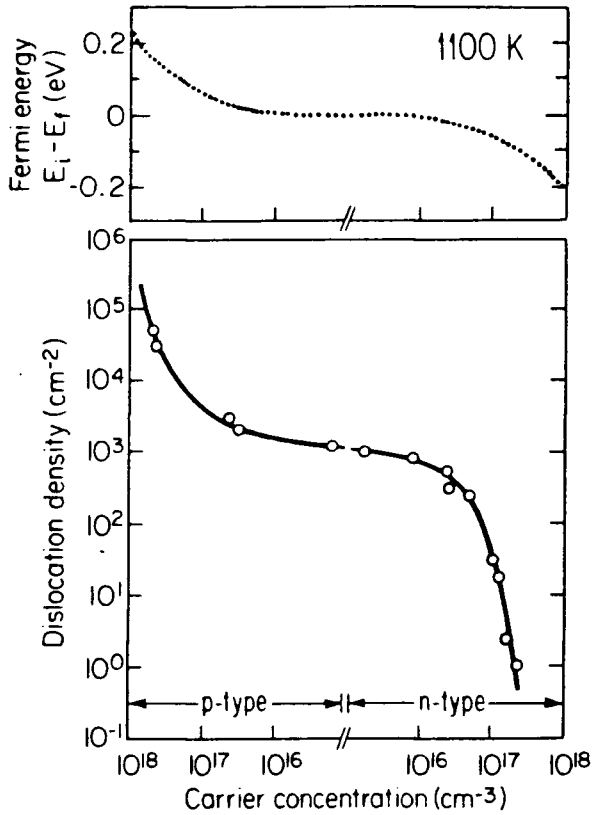

Fig. I.2 b,c Dislocation density vs 300-K free-carrier concentration for crystals grown from optimum melt stoichiometry and under optimal thermal stresses. Upper poition shows the corresponding values of the Fermi energy at 1100-K.

the upper half of the band). Their occupancies will depend on the Fermi level. The amount of neutral states would determine the migration of the vacancies and the ability to coalesce into dislocation loops. The downward shift of the Fermi level caused by the n- to p-type transition increases the fraction of neutral V(Ga) states. In lightly doped material the above reaction takes place between charged (occupied) states

$$V(Ga)^{++} + As(As) \text{ -----> } As(Ga) + V(As)^{+} + 3e-$$

The rate of reaction decreases with the third power of electron concentration. Since dislocation density increases upon transition to p-type it is assumed that the V(Ga) migrates rather than the V(As) since the reaction involving this type of defect would lead to the opposite behaviour with the transition from n- to p-type material. The exact mechanism for vacancy condensation, however, is not known.

APPENDIX II

Integration by Parts of the Element Equation for the Temperature Field

A useful formula for the integration by parts can be written as [210]

$$\int_{D^{(e)}} N\, P_{,\xi}\, dD^{(e)} = -\int_{D^{(e)}} N_{,\xi}\, P\, dD^{(e)} + \int_{S^{(e)}} N\, P\, n_{\xi}\, dS^{(e)} \qquad (II.1)$$

and

$$\int_{D^{(e)}} N\, \frac{1}{\rho}\, (P)_{,\rho}\, dD^{(e)} = -\int_{D^{(e)}} N_{,\rho}\, P\, dD^{(e)} + \int_{S^{(e)}} N\, P\, n_{\rho}\, dS^{(e)} \qquad (II.2)$$

Where N and P are given functions of ξ and ρ, and the comma indicates derivative, n_{ξ} and n_{ρ} are director cosines of the normal $\vec{n}$ to the elemental surface $dS^{(e)}$ in the ξ and ρ directions respectively.

The integral to integrate by parts is :

$$\int_{D^{(e)}} N_i \left(\frac{\partial^2 \beta}{\partial \rho^2} + \frac{1}{\rho} \frac{\partial \beta}{\partial \rho} + \frac{\partial^2 \beta}{\partial \xi^2} - 2V \frac{\partial \beta}{\partial \xi} \right) dD^{(e)} = 0 \qquad (II.3)$$

Using the above formulae for integration by parts, we get

$$\int_{D^{(e)}} N_i \left(\frac{1}{\rho} \frac{\partial}{\partial \rho} \rho \frac{\partial \beta}{\partial \rho} \right) dD^{(e)} = -\int_{D^{(e)}} \frac{\partial N_i}{\partial \rho} \cdot \frac{\partial \beta}{\partial \rho}\, dD^{(e)} + \int_{S^{(e)}} N_i \frac{\partial \beta}{\partial \rho}\, n\, dS^{(e)} \qquad (II.4)$$

and

$$\int_{D^{(e)}} N_i \frac{\partial}{\partial \xi} \frac{\partial \beta}{\partial \xi} dD^{(e)} = - \int_{D^{(e)}} \frac{\partial N_i}{\partial \xi} \frac{\partial \beta}{\partial \xi} dD^{(e)} + \int_{S^{(e)}} N_i \frac{\partial \beta}{\partial \xi} n_\xi dS^{(e)} \qquad (II.5)$$

Substituting in (II.3), it is obtained that

$$\int_{D^{(e)}} \frac{\partial N_i}{\partial \rho} \cdot \frac{\partial \beta}{\partial \rho} - \frac{\partial N_i}{\partial \xi} \frac{\partial \beta}{\partial \xi} - 2V N_i \frac{\partial \beta}{\partial \xi} dD^{(e)} + \int_{S^{(e)}} N_i \left(\frac{\partial \beta}{\partial \rho} \cdot n_\rho + \frac{\partial \beta}{\partial \xi} \cdot n_\xi \right) dS^{(e)} = 0$$

Using the boundary condition (7.3) we finally get that

$$\int_{D^{(e)}} \frac{\partial N_i}{\partial \rho} \cdot \frac{\partial \beta}{\partial \rho} + \frac{\partial N_i}{\partial \xi} \frac{\partial \beta}{\partial \xi} + 2V N_i \frac{\partial \beta}{\partial \xi} dD^{(e)} + r_0 \int_{S^{(e)}} N_i h(z) \beta^{(e)} dS^{(e)} = r_0 \int_{S^{(e)}} N_i h(z) \beta_a(z) dS^{(e)}$$

APPENDIX III

Evaluation of the Matrix Elements for the Temperature Field

a) Evaluation of $K_{T_{ij}}$

Making the following substitutions in Equations (7.10)

$$dD^{(e)} = 2\pi \rho d\rho d\xi$$

$$\frac{\partial L_i}{\partial \rho} = \frac{b_i}{2\Delta} \quad ; \quad \frac{\partial L_i}{\partial \xi} = \frac{c_i}{2\Delta}$$

we get

$$K_{T_{ij}} = \frac{2\pi}{(2\Delta)^2} (b_i b_j + c_i c_j) \int \rho \, d\rho d\xi + 2V b_j \frac{2\pi}{(2\Delta)} \int L_i \rho \, d\rho d\xi$$

Substituting $\rho = \sum_{k=1}^{3} \rho_k L_k$ and using tables for the integrals of the natural coordinates we get :

$$K_{T_{ij}} = \frac{\pi \bar{\rho}^{(e)}}{\Delta 2} (b_i b_j + c_i c_j) + \frac{\pi V b_j}{6} [3 \rho^{(e)} + \rho_j]$$

where $\rho^{(e)} = (\sum_{i=1}^{3} \rho_i) / 3$

b) Evaluation of $K_{H_{ij}}$

These elements are evaluated for three different orientation of the external surface of the peripherial elements : i) vertical surfaces (parallel to the crystal axis) ; ii) tilted surfaces (inclined with respect to the axis) and iii) horizontal surfaces (perpendicular to the axis).

i) Vertical surface

Consider an element like the one in the figure

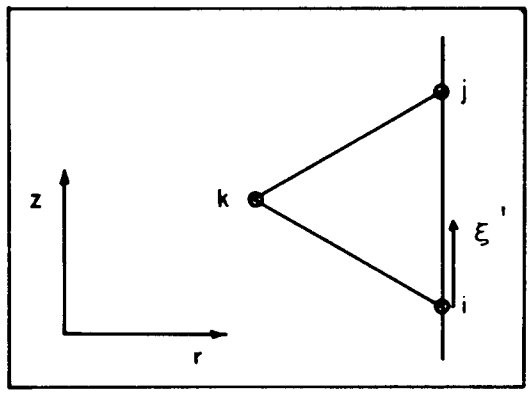

The only contribution to the integral (7.10c) comes from the surface i-j. The elemental surface area in terms of the local variable ξ' is $dS^{(e)} = 2\pi\rho d\xi'$ with ρ = constant. Therefore

$$K_{H_{ij}} = r_0 h(z) \int_{S^{(e)}_{(i\to j)}} L_i L_j \, dS^{(e)} = r_0 h(z)\, 2\pi\rho \int_0^{l_{ij}} L_i L_j \, d\xi'$$

where l_{ij} is the distance between nodes i and j. Between these two nodes the natural coordinates can be written as

$$L_i = 1 - \frac{\xi'}{l_{ij}} \quad \text{and} \quad L_j = \frac{\xi'}{l_{ij}}$$

Substituting and integrating we get :

$i \neq j$

$$K_{H_{ij}} = 2\pi h(z)\ r_0 \rho \frac{l_{ij}}{6}$$

$i = j$

$$K_{H_{ij}} = 2\pi h(z)\ r_0 \rho \frac{l_{ij}}{3}$$

ii) Tilted Surface

For an element with tilted external surface the elemental surface area can be written as

$$dS^{(e)} = 2\pi \rho\ d\xi'$$

where ξ' is the local coordinate as shown in the figure

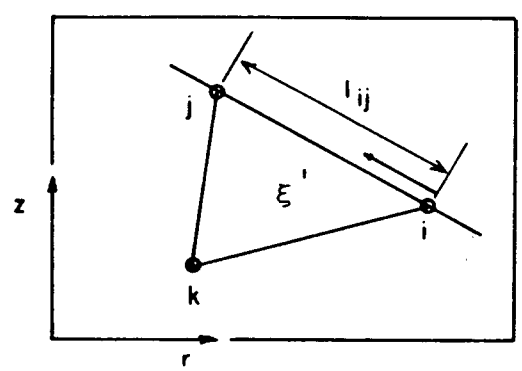

Then

$$K_{H_{ij}} = 2\pi r_0 h(z) \int_0^{l_{ij}} L_i L_j \rho\ d\xi'$$

ρ can be written as a function of ρ_i , ρ_j and the local coordinate ξ' as

$$\rho = \rho_i + (\rho_j - \rho_i) \frac{\xi'}{l_{ij}}$$

Substituting ρ , L_i and L_j for the above expression and integrating we get

$$[K_H] = 2\pi h(z)\, r_0 \frac{l_{ij}}{12} \begin{bmatrix} 3\rho_i + \rho_j & \rho_i + \rho_j \\ \rho_i + \rho_j & \rho_i + 3\rho_j \end{bmatrix}$$

iii) Horizontal Surface

For an element with horizontal external surface the elemental surface area can be written as

$$dS^{(e)} = 2\pi \rho \, d\rho$$

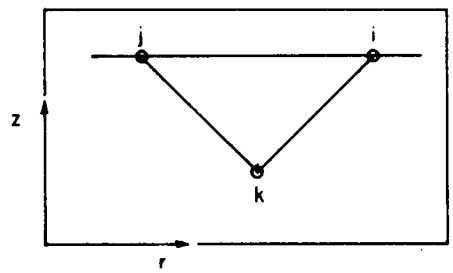

The natural coordinates are also written as

$$L_i = 1 - \frac{\rho'}{l_{ij}}$$

and

$$L_j = \frac{\rho'}{l_{ij}}$$

Approximating ρ by $\bar{\rho}^S = (\rho_i + \rho_j)/2$

$$K_{H_{ij}} = 2\pi r_0 h(z) \bar{\rho}(S) \int_0^{l_{ij}} L_i L_j \, d\rho'$$

Integrating, the elements are :

$i = j$

$$K_{H_{ij}} = 2\pi r_0 h(z) \bar{\rho}(S) \frac{l_{ij}}{3}$$

$i \neq j$

$$K_{H_{ij}} = 2\pi r_0 h(z) \bar{\rho}(S) \frac{l_{ij}}{6}$$

c) Evaluation of Elements K_{A_i}

Making the same substitutions as in b, for $dS^{(e)}$, L_i and L_j and ρ in (7.10d) for the three cases and interating we get

i) Vertical Boundary Element

$$\{K_A\} = \pi h(z) r_0 \beta_a(z) \rho l_{ij} \begin{Bmatrix} 1 \\ 1 \\ 0 \end{Bmatrix}$$

ii) Tilted Boundary Element

$$\{K_A\} = \pi h(z) r_0 \beta_a(z) (\rho_i + 2\rho_j) \frac{l_{ij}}{6} \begin{Bmatrix} 1 \\ 1 \\ 0 \end{Bmatrix}$$

iii) Horizontal Boundary Element

$$\{K_A\} = \pi h(z)\ r_0\ \beta_a(z)\ \bar{\rho}\ l_{ij} \begin{Bmatrix} 1 \\ 1 \\ 0 \end{Bmatrix}$$

APPENDIX IV

Evaluation of Stiffness Matrix Elements for Linear Elements

Substituting the expressions for [B'] and [C'] and multiplying the four elements of the stiffness matrix of element e are :

$$k'_{11} = \frac{1}{(2\Delta)^2} \left[(1-\nu)\, b_i b_j + \nu 2\Delta \frac{b_i L_i}{\rho} + \nu 2\Delta \frac{b_j L_j}{\rho} + \right.$$

$$\left. + (1-\nu)\,(2\Delta)^2 \frac{L_i L_j}{\rho^2} + \frac{1-2\nu}{2} c_i c_j \right] \rho\, d\rho\, d\xi$$

$$k'_{12} = \frac{1}{(2\Delta)^2} \left[\nu b_i b_j + \nu 2\Delta \frac{c_j L_i}{\rho} + \frac{1-2\nu}{2} c_i b_j \right] \rho\, d\rho\, d\xi$$

$$k'_{21} = \frac{1}{(2\Delta)^2} \left[\nu b_j c_i + \nu 2\Delta \frac{c_i L_i}{\rho} + \frac{1-2\nu}{2} c_j b_i \right] \rho\, d\rho\, d\xi$$

$$k'_{22} = \frac{1}{(2\Delta)^2} \left[(1-\nu)\, c_i c_j + \frac{1-2\nu}{2} b_i b_j \right] \rho\, d\rho\, d\xi$$

The force vector components are

$$F_{0_1} = \frac{\beta_i}{2} \left(b_i \bar{\rho} + \frac{2\Delta}{3} \right)$$

$$F_{0_2} = \beta_i c_i \frac{\bar{\rho}}{2}$$

Also the initial force vector is

$$\left\{ F_0' \right\}_i = \frac{\beta_i}{2\Delta} \int \begin{Bmatrix} b_i + 2\Delta \dfrac{L_i}{\rho} \\ \\ c_i \end{Bmatrix} \rho \, d\rho d\xi$$

Using tables for the integration of area coordinates we get

$$k'_{11} = [(1 - \nu) b_i b_j + \frac{1 - 2\nu}{2} c_i c_j] \frac{\bar{\rho}}{4\Delta} +$$

$$+ \frac{\nu}{6} (b_i + b_j) + (1 - \nu) \Delta \int \frac{L_i L_j}{\rho} \, d\rho d\xi$$

$$k'_{12} = [\nu b_i c_j + \frac{1 - 2\nu}{2} c_i b_j] \frac{\bar{\rho}}{4\Delta} + \frac{\nu}{6} c_j$$

$$k'_{21} = [\nu b_j c_i + \frac{1 - 2\nu}{2} c_j b_i] \frac{\bar{\rho}}{4\Delta} + \frac{\nu}{6} c_i$$

$$k'_{22} = [(1 - \nu) c_i c_j + \frac{1 - 2\nu}{2} b_i b_j] \frac{\bar{\rho}}{4\Delta}$$

APPENDIX V

Quadratic Element Calculations

The stiffness matrix for the quadratic element is a 12 x 12 matrix with three different regions

$$\begin{bmatrix} [k']^{11} & [k']^{12} & [k']^{13} & & & \\ [k']^{21} & [k']^{22} & [k']^{23} & & \text{Symmetric} & \\ [k']^{31} & [k']^{32} & [k']^{33} & & & \\ [k']^{41} & [k']^{42} & [k']^{43} & [k']^{44} & [k']^{45} & [k']^{46} \\ [k']^{51} & [k']^{52} & [k']^{53} & [k']^{54} & [k']^{55} & [k']^{56} \\ [k']^{61} & [k']^{62} & [k']^{63} & [k']^{64} & [k']^{65} & [k']^{66} \end{bmatrix}$$

III II

where the $[k']^{qp}$ are the 2 X 2 matrices relating nodes q and p. The displacement vector for any element is a 12 X 1 matrix as well as the force matrix $\{F_o^1\}^{(e)}$

$$\{d\}^{(e)} = \begin{Bmatrix} u_1 \\ w_1 \\ u_2 \\ w_2 \\ \vdots \\ u_6 \\ w_6 \end{Bmatrix} \qquad F_o' = \begin{Bmatrix} F_{o_{11}} \\ F_{o_{12}} \\ \vdots \\ F_{o_{61}} \\ F_{o_{62}} \end{Bmatrix}$$

The interpolation functions for the element are built from the area coordinates L_i as

$$N_i = L_i\,(2L_i - 1) \qquad i = 1, 2, 3 \text{ and}$$

$$N_{i+3} = 4L_iL_{i+1} \qquad i + 1 \text{ has module three ;}$$

i.e. $i = 3$ $\quad i + 1 = 1$

The form of the $[B']_q^{(e)}$ matrix for node q depends on the value of q :

for $q \leq 3$

$$[B']_q^{(e)} = \frac{4L_q - 1}{2\Delta} \begin{bmatrix} b_q & 0 \\ \dfrac{L_q\,(2L_q - 1)}{(4L_q - 1)} & 0 \\ 0 & c_q \\ c_q & b_q \end{bmatrix}$$

and for $q > 3$

$$[B']_{q=3+i}^{(e)} = \frac{4}{2\Delta} \begin{bmatrix} b_iL_{i+1} + L_ib_{i+1} & 0 \\ \dfrac{2\Delta L_iL_{i+1}}{\rho} & 0 \\ 0 & c_iL_{i+1} + L_ic_{i+1} \\ c_iL_{i+1} + L_ic_{i+1} & b_iL_{i+1} + L_ib_{i+1} \end{bmatrix}$$

again i + 1 has module 3 .

Using these [B'] matrices in Equation (7.25c) operating and performing the integrations we get the following values for the stiffness modal matrix elements in the three regions.

a) Region I, nodes 1 to 3

Case 1 q = p

$$k'^{qp}_{11} = [(1-\nu)\, b_q b_p + \frac{1-2\nu}{2}\, c_p c_q]\, \frac{\Sigma \rho_n + 2\rho_q}{10(2\Delta)} + \frac{\nu}{15}\,(b_q + b_p)$$

$$+ (1-\nu)\,|J| \int \frac{L_q(2L_q - 1)\, L_p(2L_p - 1)}{\rho_1 L_1 + \rho_2 L_2 + \rho_3 L_3}\, dL_1 dL_2$$

$$k'^{qp}_{12} = (\nu\, b_q c_p + \frac{1-2\nu}{2}\, c_q b_p)\, (\frac{\Sigma \rho_n + 2\rho_q}{10(2\Delta)}) + \frac{\nu\, c_p}{15}$$

$$k'^{qp}_{21} = [\nu\, c_q b_p + \frac{1-2\nu}{2}\, c_p b_q]\, \frac{\Sigma \rho_n + 2\rho_q}{10(2\Delta)} + \frac{\nu c_q}{15}$$

$$k'^{qp}_{22} = [(1-\nu)\, c_q c_p + \frac{1-2\nu}{2}\, b_q b_p]\, \frac{\Sigma \rho_n + 2\rho_q}{10(2\Delta)}$$

Case 2 $q \neq p$

$$k'^{qp}_{11} = -\left[(1-\nu)\, b_q b_p + \frac{1-2\nu}{2}\, c_p c_q\right]\left(\frac{\Sigma \rho_n + \rho_p + \rho_q}{30(2\Delta)}\right) - \frac{\nu}{30}(b_q + b_p) + (1-\nu)\,|J| \int \frac{L_q(2L_q - 1)\, L_p(2L_p - 1)}{\rho_1 L_1 + \rho_2 L_2 + \rho_3 L_3}\, dL_1 dL_2$$

$$k'^{qp}_{12} = -\left[\nu b_q c_p + \frac{1-2\nu}{2}\, c_q b_p\right]\left(\frac{\Sigma \rho_n + \rho_p + \rho_q}{30(2\Delta)}\right) - \frac{\nu\, c_p}{30}$$

$$k'^{qp}_{21} = -\left[\nu c_q b_p + \frac{1-2\nu}{2}\, c_p b_q\right]\left(\frac{\Sigma \rho_n + \rho_p + \rho_q}{30(2\Delta)}\right) - \frac{\nu\, c_q}{30}$$

$$k'^{qp}_{22} = -\left[(1-\nu)\, c_q c_p + \frac{1-2\nu}{2}\, b_q b_p\right]\left(\frac{\Sigma \rho_n + \rho_p + \rho_q}{30(2\Delta)}\right)$$

b) <u>Region II, Nodes q, p > 3</u>

$q = j + 3$

$p = i + 3$

Case 1 $i = j$

$$k'^{3+i,\ 3+j}_{11} = \frac{2}{15}\,\frac{1-\nu}{2\Delta}\, I'_1 + 2\nu(b_i + b_{i+1} + b_j + b_{j+1}) + \frac{1-2\nu}{2}\,\frac{I'_4}{2\Delta} + 16(1-\nu)\, I_5$$

$$k'^{3+i,\ 3+j}_{12} = \frac{2}{15}\ \frac{\nu I'_{14}}{2\Delta} + 2\nu\ (c_j + c_{j+1}) + \frac{1 - 2\nu}{2}\ \frac{I'_{41}}{2\Delta}$$

$$k'^{3+i,\ 3+j}_{21} = \frac{2}{15}\ \frac{\nu I'_{41}}{2\Delta} + 2\nu\ (c_i + c_{i+1}) + \frac{1 - 2\nu}{2}\ \frac{I'_{14}}{2\Delta}$$

$$k'^{3+i,\ 3+j}_{22} = \frac{2}{15}\ (1 - \nu)\ I'_4 + \frac{1 - 2\nu}{2}\ I'_1\ \ \frac{1}{2\Delta}$$

Where

$$I'_1 = 2b_ib_j\ (\Sigma\rho_n + 2\rho_{i+1}) + 2b_{i+1}b_{j+1}\ (\Sigma\rho_n + 2\rho_i) +$$

$$+ b_ib_{j+1}\ (\Sigma\rho_n + \rho_{i+1} + \rho_j) + b_{i+1}b_j\ (\Sigma\rho_n + \rho_i + \rho_{j+1})$$

$$I_5 = |J|\ \ \frac{L_iL_{i+1}\ L_jL_{j+1}}{\Sigma\rho_nL_n}\ \ dL_1dL_2$$

$$I'_{14} = 2b_ic_j\ (\Sigma\rho_n + 2\rho_{i+1}) + 2b_{i+1}c_{j+1}\ (\Sigma\rho_n + 2\rho_i) +$$

$$+ b_ic_{j+1}\ (\Sigma\rho_n + \rho_{i+1} + \rho_j) + b_{i+1}c_j\ (\Sigma\rho_n + \rho_i + \rho_{j+1})$$

$$I'_{41} = 2c_ib_j\ (\Sigma\rho_n + 2\rho_{i+1}) + 2c_{i+1}b_{j+1}\ (\Sigma\rho_n + 2\rho_i) +$$

$$+ c_ib_{j+1}\ (\Sigma\rho_n + \rho_{i+1} + \rho_j) + c_{i+1}b_j\ (\Sigma\rho_n + \rho_i + \rho_{j+1})$$

Case 2 $i \neq j \neq i+1$ $\quad j + 1 = i$

$$k'^{3+i,\ 3+j}_{11} = \frac{2}{15} \frac{1-\nu}{2\Delta} I''_1 + \nu(b_i + 2b_{i+1} + 2b_j + b_{j+1}) +$$

$$+ \frac{1-2\nu}{2} \frac{I'_4}{2\Delta} + 16(1-\nu) I_5$$

$$k'^{3+i,\ 3+j}_{12} = \frac{2}{15} \frac{\nu I''_{14}}{2\Delta} + \nu(2c_j + c_{j+1}) + \frac{1-2\nu}{2} \frac{I''_{41}}{2\Delta}$$

$$k'^{3+i,\ 3+j}_{21} = \frac{2}{15} \frac{\nu I''_{41}}{2\Delta} + \nu(c_i + 2c_{i+1}) + \frac{1-2\nu}{2} \frac{I''_{14}}{2\Delta}$$

$$k'^{3+i,\ 3+j}_{22} = \frac{2}{15(2\Delta)} (1-\nu) I''_4 + \frac{1-2\nu}{2} I''_1$$

Where

$$I''_1 = b_i b_j (\Sigma\rho_n + \rho_{i+1} + \rho_{j+1}) + b_{i+1} b_{j+1} (\Sigma\rho_n + \rho_i + \rho_j) +$$

$$+ b_i b_{j+1} (\Sigma\rho_n + \rho_{i+1} + \rho_j) + 2b_{i+1} b_j (\Sigma\rho_n + 2\rho_i)$$

$$I''_{14} = b_i c_j (\Sigma \rho_n + \rho_{i+1} + \rho_{j+1}) + b_{i+1} c_{j+1} (\Sigma \rho_n + \rho_i + \rho_j) +$$

$$+ b_i c_{j+1} (\Sigma \rho_n + \rho_{i+1} + \rho_j) + 2 b_{i+1} c_j (\Sigma \rho_n + 2\rho_i)$$

$$I''_{41} = c_i b_j (\Sigma \rho_n + \rho_{i+1} + \rho_{j+1}) + c_{i+1} b_{j+1} (\Sigma \rho_n + \rho_i + \rho_j) +$$

$$+ c_i b_{j+1} (\Sigma \rho_n + \rho_{i+1} + \rho_j) + 2 c_{i+1} b_j (\Sigma \rho_n + 2\rho_i)$$

Case 3 $j \neq i \neq j+1$ $\quad i + 1 = j$

$$k'^{3+i,\ 3+j}_{11} = \frac{2}{15} \frac{1 - \nu}{2\Delta} I''_1{}' + \nu (2b_i + b_{i+1} + b_j + 2b_{j+1}) +$$

$$+ \frac{1 - 2\nu}{2} \frac{I''_4{}'}{2\Delta} + 16 (1 - \nu) I_5$$

$$k'^{3+i,\ 3+j}_{12} = \frac{2}{15} \frac{\nu I''_{14}{}'}{2\Delta} + \nu (c_j + 2c_{j+1}) + \frac{1 - 2\nu}{2} \frac{I''_{41}{}'}{2\Delta}$$

$$k'^{3+i,\ 3+j}_{21} = \frac{2}{15} \frac{\nu I''_{41}{}'}{2\Delta} + \nu (2c_i + c_{i+1}) + \frac{1 - 2\nu}{2} \frac{I''_{14}{}'}{2\Delta}$$

$$k'^{3+i,\ 3+j}_{22} = \frac{2}{15(2\Delta)} (1 - \nu) I''_4{}' + \frac{1 - 2\nu}{2} I''_4{}'$$

Where

$$I''_{1}{}^{'} = b_i b_j (\Sigma\rho_n + \rho_{i+1} + \rho_{j+1}) + b_{i+1} b_{j+1} (\Sigma\rho_n + \rho_i + \rho_j) +$$

$$+ 2b_i b_{j+1} (\Sigma\rho_n + 2\rho_j) + b_{i+1} b_j (\Sigma\rho_n + \rho_i + \rho_{j+1})$$

$$I''_{14}{}^{'} = b_i c_j (\Sigma\rho_n + \rho_{i+1} + \rho_{j+1}) + b_{i+1} c_{j+1} (\Sigma\rho_n + \rho_i + \rho_j) +$$

$$+ 2b_i c_{j+1} (\Sigma\rho_n + 2\rho_j) + b_{i+1} c_j (\Sigma\rho_n + \rho_i + \rho_{j+1})$$

$$I''_{41}{}^{'} = c_i b_j (\Sigma\rho_n + \rho_{i+1} + \rho_{j+1}) + c_{i+1} b_j (\Sigma\rho_n + \rho_i + \rho_j) +$$

$$+ 2c_i b_{j+1} (\Sigma\rho_n + 2\rho_j) + c_{i+1} b_j (\Sigma\rho_n + \rho_i + \rho_{j+1})$$

c) <u>Region III, Mixed Nodes $q \leq 3$; $p = 3+i$; $i = 1,2,3$</u>

Case 1 $q = i$

$$k'^{q,i+3}_{11} = \frac{1}{30} \quad \frac{1-\nu}{2\Delta} b_q I'_1 + \nu(3b_q - b_i + 2b_{i+1}) +$$

$$+ \frac{1-2\nu}{2} \frac{c_q}{2\Delta} I'_4 + 4(1-\nu) I'_5$$

$$k'^{q,i+3}_{12} = \frac{1}{30} \quad \frac{\nu}{2\Delta} b_q I'_4 + \nu(2c_{i+1} - c_i) + \frac{1-2\nu}{2} \frac{c_q I_1'}{2\Delta}$$

$$k'^{q,i+3}_{21} = \frac{1}{30}\left[\frac{\nu}{2\Delta} c_q I'_1 + 3\nu c_q + \frac{1-2\nu}{2}\frac{b_q I'_4}{2\Delta}\right]$$

$$k'^{q,i+3}_{22} = \frac{1}{30(2\Delta)}\left[(1-\nu)\, c_q I'_4 + \frac{1-2\nu}{2} b_q I'_1\right]$$

where

$$I'_1 = (3b_{i+1} - b_i)\Sigma\rho_n + \rho_q (4b_i + 11b_{i+1}) - \rho_{i+1} b_i$$

$$I'_4 = (3c_{i+1} - c_i)\Sigma\rho_n + \rho_q (4c_i + 11c_{i+1}) - \rho_{i+1} c_i$$

$$I'_5 = |J| \int \frac{L_q (2L_q - 1) L_i L_{i+1}}{\Sigma \rho_n L_n}\, dL_1 dL_2$$

Case 2 $\quad q \neq i \qquad i+1 \neq q$

$$k'^{q,3+i}_{11} = \frac{1}{30}\left[\frac{(1-\nu)}{2\Delta} b_q I''_1 - \nu(b_i - b_{i+1} + b_q) + \right.$$

$$\left. + \frac{1-2\nu}{2}\frac{c_q I''_4}{2\Delta} + 4(1-\nu) I'_5\right]$$

$$k'^{q,3+i}_{12} = \frac{1}{30}\left[\frac{\nu b_q I''_4}{2\Delta} - \nu(c_i + c_{i+1}) + \frac{1-2\nu}{2}\frac{c_q I''_1}{2\Delta}\right]$$

$$k_{21}^{'q,3+i} = \frac{1}{30}\left[\frac{\nu c_q I_1^{"}}{2\Delta} - \nu c_q + \frac{1-2\nu}{2}\frac{b_q I_4^{"}}{2\Delta}\right]$$

$$k_{22}^{'q,3+i} = \frac{1}{30(2\Delta)}\left[(1-\nu)\, c_q I_4^{"} + \frac{1-2\nu}{2} b_q I_1^{"}\right]$$

where

$$I_1^{"} = (b_i - b_{i+1})(4\rho_q - \Sigma\rho_n) - (\rho_i b_{i+1} + \rho_{i+1} b_i)$$

$$I_4^{"} = (c_i - c_{i+1})(4_q - \Sigma\rho_n) - (\rho_i b_{i+1} + \rho_{i+1} b_i)$$

Case 3 $i \neq q$; $i + 1 = q$

$$k_{11}^{'q,3+i} = \frac{1}{30}\left[\frac{1-\nu}{2\Delta} b_q I_1^{"'} + \nu(3b_q + 2b_i - b_{i+1}) + \frac{1-2\nu}{2}\frac{c_q}{2\Delta} I_4^{"'} + 4(1-\nu) I_5^{'}\right]$$

$$k_{12}^{'q,3+i} = \frac{1}{30}\left[\frac{\nu}{2\Delta} b_q I_4^{"'} + \nu(2c_i - c_{i+1}) + \frac{1-2\nu}{2}\frac{c_q I_1^{"'}}{2\Delta}\right]$$

$$k_{21}^{'q,3+i} = \frac{1}{30}\left[\frac{\nu c_q I_1^{"'}}{2\Delta} + 3\nu c_q + \frac{1-2\nu}{2}\frac{b_q I_4^{"'}}{2\Delta}\right]$$

$$k_{22}^{'q,3+i} = \frac{1}{30(2\Delta)} \cdot (1 - \nu)\, c_q\, I_4^{"'} + \frac{1 - 2\nu}{2}\, b_q\, I_1^{"'}$$

where

$$I_1^{"'} = (3b_i - b_{i+1}) \Sigma \rho_n + \rho_q (11b_i + 4b_{i+1}) - \rho_i b_{i+1}$$

$$I_4^{"'} = (3c_i - c_{i+1}) \Sigma \rho_n + \rho_q (11c_i + 4c_{i+1}) - \rho_i c_{i+1}$$

d) Calculation of force matrix elements F_{o_q}'

Substituting [B'] and [C'] into (7.26c) and performing the multiplication and integration we get :

for $q \leq 3$

$$\{F_o'\}_q = \frac{1}{6} \beta_q \rho_q \begin{Bmatrix} b_q \\ \\ c_q \end{Bmatrix}$$

for $q > 3$

$$\{F_o'\}_{i+3} = \frac{\beta_q}{6} \begin{Bmatrix} b_i(\Sigma \rho_n + \rho_{i+1}) + b_{i+1}(\Sigma \rho_n + \quad_i) + 2\Delta \\ \\ c_i(\Sigma \rho_n + \rho_{i+1}) + c_{i+1}(\Sigma \rho_n + \rho_i) \end{Bmatrix}$$

e) Strain Components

The strain components as a function of the reduced displacement for the calculation of stresses at node q in element e are

Case 1 $q \leq 3$

$$\varepsilon_{\rho,q} = \frac{1}{2\Delta}[3b_q u_{red,q} - b_{q+1} u_{red,q+1} - b_{q+2} u_{red,q+2} + 4b_{q+1} u_{3+q} + 4b_{q-1} u_{3+q-1}]$$

$$\varepsilon_{\theta,q} = \frac{u_{red,q}}{\rho_q}$$

$$\varepsilon_{\xi,q} = \frac{1}{2\Delta}[3c_q w_{red,q} - c_{q+1} w_{red,q+1} - c_{q+2} w_{red,q+2} + 4c_{q+1} w_{red,3+q} + 4c_{q-1} w_{red,3+q-1}]$$

$$\gamma_{\rho\xi,q} = \frac{1}{2\Delta}[3(c_q u_{red,q} + b_q w_{red,q}) - (c_{i+1} u_{red,q+1} + b_{i+1} w_{red,q+1}) - (c_{q+2} u_{red,q+2} + b_{q+2} w_{red,q+2}) + 4(c_{q+1} u_{red,q+3} + b_{q+1} w_{red,q+3}) + 4(c_{q-1} u_{red,q-1+3} + b_{q-1} w_{q-1+3})]$$

Case 2 $\quad q > 3 \; ; \quad q = 3+1 \; ; \quad i = 1,2,3.$

$$\varepsilon_{\rho\,3+1} = \frac{1}{2\Delta}\,[b_i\,u_{red,i} + b_{i+1}\,u_{red,i+1} - b_{i+2}\,u_{red,i+2} +$$

$$+ 2(b_i + b_{i+1})\,u_{red,i+3} +$$

$$+ 2b_{i-1}\,(u_{red,i+1+3} + u_{red,i-1+3})]$$

$$\varepsilon_{\theta\,,3+i} = \frac{u_{i+3}}{\rho_{i+3}}$$

$$\varepsilon_{\xi\,,3+i} = \frac{1}{2\Delta}\,[c_i\,w_{red,i} + c_{i+1}\,w_{red,i+1} - c_{i+2}\,w_{red,i+2} +$$

$$+ 2(c_i + c_{i+1})\,w_{red,i+3} +$$

$$+ 2c_{i-1}\,(w_{red,3+(i+1)} + w_{red,3+(i-1)})]$$

$$\gamma_{\rho\,\xi,i+3} = \frac{1}{2\Delta}\,[\,c_i\,u_{red,i} + b_i\,w_{red,i} + c_{i+1}\,u_{red,i+1} +$$

$$+ b_{i+1}\,w_{red,i+1} - (c_{i+2}\,u_{red,i+2} + b_{i+2}\,w_{red,i+2}) +$$

$$+ 2[(c_i + c_{i+1})\,u_{red,i+3} + (b_i + b_{i+1})\,w_{red,i+3} +$$

$$+ c_{i-1}(u_{red,(i+1)+3} + u_{red,i-1+3}) +$$

$$+ b_{i-1}\,(w_{red,3+i+1} + w_{red,3+i-1})]\,]$$

APPENDIX VI

Calculation of Resolved Shear Stresses

The 12 slip plane and direction combinations for the {111} $\langle 0\bar{1}1 \rangle$ glide system are given in Table V.I.

For a crystal grown in the [001] direction vhich is coincident with the Z-axis, the three directions in the (111) plane, for instance, are shown in the Figure. Similar figures for the other three (111) planes can be drawn

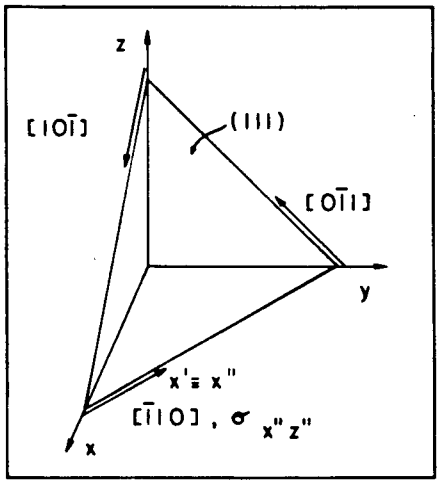

The first step, for operational reasons, is to project the stress tensor onto a cartesian coordinates system. The second step consists of rotating the cartesian system in order to make one of the axis coincident with the glide direction and any of the other axis perpendicular to the glide plane. The shear stress on that plane and direction is the corresponding resolved shear stress to be calculated. For the calculations the definition of the tensor is used. A set of quantities T, with respect to a

coordinate system is a tensor if under a rotation of the system the quantities T, transforms as

$$\tilde{T} = M.T.M^{-1}$$

where M is the operator performing the rotation of axis which is defined positive when is done in the clockwise direction.

a) Stress in Cartesian Coordinates

The transformation from a cylindrical system of coordinates (ρ, θ, z) to a cartesian (x, y, z) is identical to a rotation $-\theta$ over the z-axis as shown in Figure.

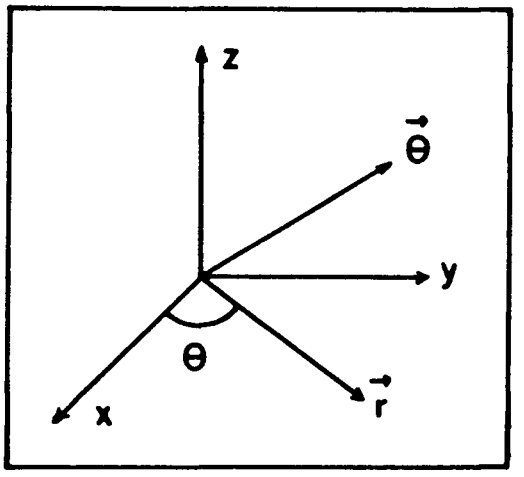

The matrix for this transformation is

$$M_z(-\theta) = \begin{bmatrix} \cos\theta & -\sin\theta & 0 \\ \sin\theta & \cos\theta & 0 \\ 0 & 0 & 1 \end{bmatrix}$$

for this type of transformations the inverse operation is

$$M_z^{-1}(-\theta) = M_z^T(-\theta) = M_z(\theta)$$

and therefore

$$\begin{bmatrix} \sigma xx & \sigma xy & \sigma xz \\ \sigma yx & \sigma yy & \sigma yz \\ \sigma xz & \sigma yz & \sigma zz \end{bmatrix} = \begin{bmatrix} \cos\theta & -\sin\theta & 0 \\ \sin\theta & \cos\theta & 0 \\ 0 & 0 & 1 \end{bmatrix} \times \begin{bmatrix} \sigma_\rho & 0 & \tau_{\rho z} \\ 0 & \sigma_\theta & 0 \\ \tau_{\rho z} & 0 & \sigma_z \end{bmatrix} \times$$

$$\times \begin{bmatrix} \cos\theta & \sin\theta & 0 \\ -\sin\theta & \cos\theta & 0 \\ 0 & 0 & 1 \end{bmatrix}$$

which gives

$$\begin{aligned} \sigma_{xx} &= \sigma_\rho \cos^2\theta + \sigma_\theta \sin^2\theta \\ \sigma_{yy} &= \sigma_\rho \sin^2\theta + \sigma\theta \cos^2\theta \\ \sigma_{zz} &= \sigma_z \\ \sigma_{xy} &= \sin\theta \cos\theta (\sigma_\rho - \sigma_\theta) \\ \sigma_{xz} &= \tau_{\rho z} \cos\theta \\ \sigma_{yz} &= \tau_{\rho z} \sin\theta \end{aligned}$$

b) Sample Calculation of the RSS in the (111) Plane and [110] Direction

Two rotations are performed : with the first rotation over the z-axis by an angle $\alpha = 3/4\pi$ the rotated system (x', y', z' = z) has the x'-axis coincident with the $[\bar{1}10]$ direction ; with the second rotation over the x'-axis by an angle β such that $\cos\beta = \sqrt{3}/3$, the new system (x" = x', y", z") has the z"-axis

perpendicular to the (111) plane. In this case the desired stress component is $\sigma_{x"z"}$.

The matrix for the combined rotation in the order the rotation is performed, is calculated as

$$M(\alpha, \beta) = M_{x'}(\beta)\, M_{z}(\alpha)$$

with

$$M_{x'}(\beta) = \begin{bmatrix} 1 & 0 & 0 \\ 0 & \cos\beta & \sin\beta \\ 0 & -\sin\beta & \cos\beta \end{bmatrix}$$

and

$$M_{z}(\alpha) = \begin{bmatrix} \cos\alpha & \sin\alpha & 0 \\ -\sin\alpha & \cos\alpha & 0 \\ 0 & 0 & 1 \end{bmatrix}$$

Multiplying both matrices to obtain $M(\alpha, \beta)$ and performing the rotation of the tensor the desired $\sigma_{x"\ z"}$ component is :

$$\sigma_{x"\ z"} = (\sigma_{xx} - \sigma_{yy}) \sin\alpha \cos\alpha \sin\beta + \sigma_{xy} (\sin^2\alpha \sin\beta - \cos^2\alpha \sin\beta) + \sigma_{xz} \cos\alpha \cos\beta + \sigma_{yz} \sin\alpha \cos\beta$$

Similar calculations are repeated for the other 11 projections. The performed rotations and corresponding calculated component for each case are listed in Table VI.1 .

Table VI.1 Rotation performed for the calculation of the RSS

Slip plane	Slip direction	ROTATIONS 1 axis	1 angle	2 axis	2 angle	Calculated Component
111	$\bar{1}10$	z	3/4 π	x'	β	x"z"
	$0\bar{1}1$	x	π/4	z'	β	z"x"
	$10\bar{1}$	y	π/4	x'	β	x"y"
$\bar{1}11$	$\bar{1}0\bar{1}$	y	3/4 π	x'	- β	x"y"
	$0\bar{1}1$	x	π/4	z'	π/2- β	y"z"
	110	z	π/4	x'	- β	x"z"
$\bar{1}\bar{1}1$	011	x	-π/4	z'	-(π-β)	x"z"
	$\bar{1}0\bar{1}$	y	-3/4 π	z'	-(π-β)	x"z"
	$1\bar{1}0$	z	-π/4	x'	β	x"z"
$1\bar{1}1$	011	x	-π/4	z'	- β	x"z"
	$10\bar{1}$	y	π/4	x'	π/2-β	x"z"
	$\bar{1}\bar{1}0$	z	-3/4 π	x'	- β	x"z"

When the values of the cartesian components of stress are replaced in terms of the cylindrical components the twelve RSS are :

Table VI.2 Resolved Shear Stress component in the $\langle 1\bar{1}0\rangle$ {111} slip

Plane	Direction	Resolved Shear Stress
	$[\bar{1}10]$	$\frac{\sqrt{6}}{6}\{-(\sigma_\rho-\sigma_\theta)(\cos^2\theta-\sin^2\theta)+\tau_{\rho z}(\cos\theta-\sin\theta)\}$
(111)	$[0\bar{1}1]$	$\frac{\sqrt{6}}{6}\{-(\sigma_\rho\sin^2\theta+\sigma_\theta\cos^2\theta)+$ $+\sigma_{zz}-(\sigma_\rho-\sigma_\theta)\sin\theta\cos\theta+\tau_{\rho z}\cos\theta\}$
	$[10\bar{1}]$	$\frac{\sqrt{6}}{6}\{\sigma_\rho co^2\theta+\sigma_\theta\sin^2\theta-\sigma_{zz}+(\sigma_\rho-\sigma_\theta)\sin\theta\cos\theta-\sigma_{\rho z}\sin\theta\}$
	$[\bar{1}0\bar{1}]$	$\frac{\sqrt{6}}{6}\{\sigma_\rho\cos^2\theta+\sigma_\theta\sin^2\theta-\sigma_{zz}-(\sigma_\rho-\sigma_\theta)\cos\theta\sin\theta-\tau_{\rho z}\sin\theta\}$
$[\bar{1}11]$	$[0\bar{1}1]$	$\frac{\sqrt{6}}{6}\{-(\sigma_\rho\sin^2\theta+\sigma_\theta\cos^2\theta)+$ $+\sigma_{zz}+(\sigma_\rho-\sigma_\theta)\cos\theta\sin\theta-\tau_{\rho z}\cos\theta\}$
	$[110]$	$\frac{\sqrt{6}}{6}\{-(\sigma_\rho-\sigma_\theta)\cos^2\theta-\sin^2\theta)+\tau_{\rho z}(\cos\theta-\sin\theta)\}$
	$[011]$	$\frac{\sqrt{6}}{6}\{-(\sigma_\rho\sin^2\theta+\sigma_\theta\cos^2\theta)+$ $+\sigma_{zz}-(\sigma_\rho-\sigma_\theta)\cos\theta\sin\theta-\tau_{\rho z}\cos\theta\}$
$(\bar{1}\bar{1}1)$	$[\bar{1}0\bar{1}]$	$\frac{\sqrt{6}}{6}\{\sigma_\rho\cos^2\theta+\sigma_\theta\sin^2\theta-$ $-\sigma_{zz}+(\sigma_\rho-\sigma_\theta)\cos\theta\sin\theta+\tau_{\rho z}\sin\theta\}$
	$[110]$	$\frac{\sqrt{6}}{6}\{-(\sigma_\rho-\sigma_\theta)(\cos^2\theta-\sin^2\theta)+\tau_{\rho z}(\cos\theta-\sin\theta)\}$

Cont./

Cont./

	[011]	$\frac{\sqrt{6}}{6}\{-(\sigma_\rho \sin^2\theta+\sigma_\theta \cos^2\theta)+$ $+\sigma_{zz}+(\sigma_\rho-\sigma_\theta)\cos\theta\sin\theta+\tau_{\rho z}\cos\theta\}$
$(1\bar{1}1)$	$[10\bar{1}]$	$\frac{\sqrt{6}}{6}\{\sigma_\rho \cos^2\theta+\sigma_\theta \sin^2\theta-$ $-\sigma_z-(\sigma_\rho-\sigma_\theta)\cos\theta\sin\theta+\tau_{\rho z}\sin\theta\}$
	$[\bar{1}\bar{1}0]$	$\frac{\sqrt{6}}{6}\{-(\sigma_\rho-\sigma_\theta)(\cos^2\theta-\sin^2\theta)-\tau_{\rho z}(\cos\theta+\sin\theta)\}$

Using trigonometric relations they can be put in a more elegant form as follows :

Table VI.3 Compact form of the RSS from Table VI.2

Plane	Direction	Resolved Shear Stress	Mode
	$[\bar{1}10]$	$\frac{\sqrt{6}}{6}\{-(\sigma_\rho-\sigma_\theta)\cos2\theta+\sqrt{2}\tau_{\rho\xi}\cos(\theta+\pi/4)\}$	I a
(111)	$[0\bar{1}1]$	$\frac{\sqrt{6}}{6}\{-(\sigma_\rho-\sigma_\theta)\sqrt{2}\sin\theta\sin(\theta+\pi/4)+(\sigma_\xi-\sigma_\theta)+\sigma_{\rho\xi}\cos\theta\}$	II a
	$[10\bar{1}]$	$\frac{\sqrt{6}}{6}\{\sigma_\rho-\sigma_\theta)\sqrt{2}\cos\theta\sin(\theta+\pi/4)-(\sigma_\xi-\sigma_\theta)-\tau_{\rho\xi}\sin\theta\}$	III a
	$[\bar{1}0\bar{1}]$	$\frac{\sqrt{6}}{6}\{(\sigma_\rho-\sigma_\theta)\sqrt{2}\cos\theta\cos(\theta+\pi/4)-(\sigma_\xi-\sigma_\theta)-\tau_{\rho\xi}\sin\theta\}$	IV a
$[\bar{1}11]$	$[0\bar{1}1]$	$\frac{\sqrt{6}}{6}\{(\sigma_\rho-\sigma_\theta)\sqrt{2}\sin\theta\cos(\theta+\pi/4)+(\sigma_\xi-\sigma_\theta)-\tau_{\rho\xi}\cos\theta\}$	V b
	$[110]$	$\frac{\sqrt{6}}{6}\{-(\sigma_\rho-\sigma_\theta)\cos2\theta+\sqrt{2}\tau_{\rho\xi}\cos(\theta+\pi/4)\}$	I a
	$[011]$	$\frac{\sqrt{6}}{6}\{-(\sigma_\rho-\sigma_\theta)\sqrt{2}\sin\theta\sin(\theta+\pi/4)+(\sigma_\xi-\sigma_\theta)-\tau_{\rho\xi}\cos\theta\}$	II b
$(\bar{1}\bar{1}1)$	$[\bar{1}0\bar{1}]$	$\frac{\sqrt{6}}{6}\{(\sigma_\rho-\sigma_\theta)\sqrt{2}\cos\theta\sin(\theta+\pi/4)-(\sigma_\xi-\sigma_\theta)+\tau_{\rho\xi}\sin\theta\}$	III a
	$[1\bar{1}0]$	$\frac{\sqrt{6}}{6}\{-(\sigma_\rho-\sigma_\theta)\cos2\theta+\sqrt{2}\tau_{\rho\xi}\cos(\theta+\pi/4)\}$	I a

Cont./

Cont./

	[011]	$\frac{\sqrt{6}}{6}\{(\sigma_\rho-\sigma_\theta)\sqrt{2}\sin\theta\cos(\theta+\pi/4)+(\sigma_\xi-\sigma_\theta)+$ $+\tau_{\rho\xi}\cos\theta\}$	V a
$(1\bar{1}1)$	$[\bar{1}0\bar{1}]$	$\frac{\sqrt{6}}{6}\{(\sigma_\rho-\sigma_\theta)\sqrt{2}\cos\theta\cos(\theta+\pi/4)-(\sigma_\xi-\sigma_\theta)+$ $+\tau_{\rho\xi}\sin\theta\}$	IV b
	$[\bar{1}\bar{1}0]$	$\frac{\sqrt{6}}{6}\{-(\sigma_\rho-\sigma_\theta)\cos2\theta-\sqrt{2}\tau_{\rho\xi}\cos(\theta+\pi/4)\}$	I b

APPENDIX VII

Temperature Field During Cooling

The problem to solve is given by the following equations.

$$\frac{1}{\rho}\frac{\partial}{\partial \rho}\left(\rho \frac{\partial \beta}{\partial \rho}\right) + \frac{\partial^2 \beta}{\partial \xi^2} = \frac{\partial \beta}{\partial t^*} \qquad \text{(VII.1)}$$

I.C.'s at $t^* = 0$

$$\beta_0 = p_0 + p_1 \xi + p_2 \xi^2 \qquad \text{(VII.2)}$$

B.C.'s at $t^* > 0$

$$\left.\frac{\partial \beta}{\partial \rho}\right|_{\rho=1} = -h'\beta \qquad \text{(VII.3)}$$

$$\left.\frac{\partial \beta}{\partial \xi}\right|_{\xi=\xi t} = -h'\beta \qquad \text{(VII.4)}$$

$$\left.\frac{\partial \beta}{\partial \xi}\right|_{\xi=0} = h'\beta \qquad \text{(VII.5)}$$

A solution is obtained by separation of variables i.e.

$$\beta(\rho, \xi, t^*) = R(\rho)\, Z(\xi)\, T^*(t^*) \qquad \text{(VII.6)}$$

Morever, we assume $T^*(t^*) \alpha e^{-\Psi t^*}$, Ψ is constant. Substituting β in (VII.1) and operating we get

$$\frac{1}{R(\rho)}\ \frac{1}{\rho}\ \frac{d}{d\rho}\left(\rho\frac{dR(\rho)}{d\rho}\right) + \frac{1}{Z(\xi)}\ \frac{d^2Z(\xi)}{d\xi^2} = -\Psi \qquad \text{(VII.7)}$$

which is satisfied if each term is constant, say $-\lambda^2$ and $-\gamma^2$ respectively. This gives the following ordinary differential equations and conditions

$$\frac{d^2R}{d(\lambda\rho)^2} + \frac{1}{(\lambda\rho)}\ \frac{dR}{d(\lambda\rho)} + R = 0 \qquad \text{(VII.8)}$$

with R such that

$$\left.\frac{dR}{d\rho}\right/_{\rho=1} = -h'R \qquad \text{(VII.9)}$$

and

$$\frac{d^2Z}{d\xi^2} + \gamma^2 Z = 0 \qquad \text{(VII.10)}$$

with Z subject to

$$\left.\frac{dZ}{d\xi}\right/_{\xi=\xi_t} = -h'Z \qquad \text{(VII.11)}$$

$$\left.\frac{dZ}{d\xi}\right/_{\xi=0} = h'Z \qquad \text{(VII.12)}$$

and also λ, γ and Ψ must satisfy

$$\lambda^2 + \gamma^2 = \Psi \qquad \text{(VII.13)}$$

The solutions of (VII.8) and (VII.9) are the Bessel functions of zero order, i.e. $R(\rho)$ $J_0(\lambda\rho)$ for all the λ values satisfying the algebraic equation (see Appendix VIII)

$$\lambda J_1(\alpha) = h' J_0(\lambda) \qquad \text{(VII.14)}$$

As shown in Appendix VIII, these functions constitute a complete and orthogonal set of vectors.

The solutions of (VII.10) are the harmonic functions, in order to satisfy the B.C.'s (VII.11) and (VII.12) we choose as solutions

$$Z_\gamma(\xi) = A \cos\gamma\xi + B \sin\gamma\xi \qquad \text{(VII.15)}$$

substituting in (VII.12) and (VII.13) we obtain respectively that

$$\frac{A}{B} = \frac{\gamma}{h'} \qquad \text{(VII.16)}$$

and

$$\tan \gamma \xi_t = \frac{2\gamma h'}{\gamma^2 - h'^2} \qquad \text{(VII.17)}$$

(VII.17) gives the condition to obtain the γ-values. Moreover, the functions (VII.15) subject to (VII.11) and (VII.12) are orthogonal (see Carslaw and Jaegger).

The general solution for β is therefore

$$\beta(\rho, \xi, t^*) = \sum_{\lambda,\gamma} C^*(\alpha,\gamma)\, e^{-(\lambda^2 + \gamma^2)t^*}\, J_0(\lambda\rho)\, [\gamma \cos\gamma\xi + hr_o \sin\gamma\xi] \qquad \text{(VII.18)}$$

where the summation extends to all the λ and γ-values which are roots of (VII.14) and (VII.17) respectively.

To obtain the coefficients $C^*(\lambda,\gamma)$ the initial condition (VII.2) is applied and the inner product in the space-function is performed, that is

$$\left[\int_0^{\xi t} (p_0 + p_1\xi + p_2\xi^2)(\gamma\cos\gamma\xi + h'\sin\gamma\xi)\, d\xi\right] \int_0^1 \rho\, J_0(\lambda\rho)\, d\rho =$$

$$= C^*(\lambda,\gamma) \int_0^{\xi t} (\gamma\cos\gamma\xi + h'\sin\gamma\xi)^2\, d\xi \int_0^1 \rho J_0^2(\lambda\rho)\, d\rho \qquad \text{(VII.19)}$$

It is observed that $C^*(\lambda,\gamma)$ can be written as

$$C^*(\lambda,\gamma) = C_1(\lambda)\; C_2(\gamma) \qquad \text{(VII.20)}$$

After performing the integration the coefficients are found to be

$$C_1(\lambda) = \frac{1}{(h'^2 + \lambda^2)\, J_0(\lambda)} \qquad \text{(VII.21)}$$

and

$$C_2(\gamma) = II \;/\; I \qquad \text{(VII.22)}$$

with

$$I = \frac{\xi_t}{2}(\gamma^2 + h'^2) + h' \qquad \text{(VII.23)}$$

and

$$II = \sin\gamma\xi_t \{p_0 + p_1(\xi_t + h'/\gamma^2) + p_2(\xi_t^2 - 2/\gamma^2 + 2\,{}_t h'/\gamma^2)\} +$$

$$+ \frac{\cos\gamma\xi_t}{\gamma} \{-p_0 h' + p_1(1 - h'\xi_t) + p_2(2\xi_t - h'\xi_t^2 + 2h'/\gamma^2)\} +$$

$$+ \frac{p_0 h'}{\gamma} - \frac{p_1}{\gamma} - \frac{2p_2 h'}{\gamma^3} \qquad \text{(VII.24)}$$

Also the solution for β can be written as a product of two independent series

$$\beta(\rho, \xi, t^*) = 2h'\Big[\sum_\lambda C_1(\lambda)\, e^{-\lambda^2 t^*} J_0(\lambda\rho)\Big]$$

$$\Big\{\sum_\gamma C_2(\gamma)\, e^{-\gamma^2 t^*} [\gamma\cos\gamma\xi + h'\sin\gamma\xi]\Big\} \qquad \text{(VII.25)}$$

APPENDIX VIII

Analytical Solution of the Temperature Field

The partial differential equation to be solved is :

$$\frac{\partial^2 \beta}{\partial \rho^2} + \frac{1}{\rho} \frac{\partial \beta}{\partial \rho} + \frac{\partial^2 \beta}{\partial \xi^2} - 2V \frac{\partial \beta}{\partial \xi} = 0 \qquad \text{(VIII.1)}$$

subject to the following Boundary Conditions :

$$\left.\frac{\partial \beta}{\partial \rho}\right|_{\rho = 1} = -hr_0 \beta \qquad \text{(a)}$$

$$\beta = 1 \quad \text{at} \quad \xi = 0 \qquad \text{(b)} \qquad \text{(VIII.2)}$$

$$\beta = 0 \quad \text{at} \quad \xi = \xi_t \qquad \text{(c)}$$

Equation (VII.1) can be solved by separating variables

$$\beta(\rho, \xi) = R(\rho)\, Z(\xi)$$

which leads to the following two ordinary differential equation

$$\frac{d^2 R}{d(\lambda\rho)^2} + \frac{1}{\lambda\rho} \frac{dR}{d(\lambda\rho)} + R = 0 \qquad \text{(VIII.3)}$$

$$\frac{d^2R}{d\xi^2} - 2V\frac{dZ}{d\xi} - \lambda^2 Z = 0 \qquad \text{(VIII.4)}$$

Solutions of (VIII.3) are the Bessel functions of zero order $R(\rho)\ J_o\ (\lambda\rho)$

Equation (VIII.4) is linear and homogeneous with constant coefficients with the general solution

$$Z(\xi) = (A_\lambda\ e^{\xi\sqrt{V^2+\ ^2}} + B_\lambda\ \bar{e}^{\ \xi\sqrt{V^2+\lambda^2}})\ e^{V\xi}$$

where A_λ and B_λ are constant to be determined. The general solution is therefore

$$\beta(\rho,\xi) = e^{V\xi} \sum_\lambda J_o(\lambda\rho)\ [A_\lambda\ e^{k\lambda\,\xi} + B_\lambda\ e^{-k\lambda\,\xi} \qquad \text{(VIII.5)}$$

where $K_\lambda = V^2 + \lambda^2$, and the summation is carried out over all the possible values of .

From (VIII.2a) we get that

$$\lambda J_{1'}(\lambda) = hr_0\ J_0(\lambda) \qquad \text{(VIII.6)}$$

from which the values of λ are obtained.

From (VIII.2b) and (c) it is obtained that

$$1 = \sum_{\lambda} J_0(\lambda \rho) \; [A_\lambda + B_\lambda] \qquad \text{(VIII.7)}$$

and

$$0 = e^{V\xi_t} \sum_{\lambda} J_0(\lambda\rho) \; [A_\lambda e^{k_\lambda \xi_t} + B_\lambda e^{-k_\lambda \xi_t}] \qquad \text{(VIII.8)}$$

In order to calculate A_λ and B_λ from the above equations it is necessary to show that the functions $J(\lambda\rho)$ from (VIII.6) form a complete sub-set of orthogonal functions.

To do this let us calculate the coefficients for the expansion of the unit function in terms of $J(k\rho)$, that is

$$\int_0^1 1 \; \rho \; J_0(k\rho) \; d = \sum_{\lambda} \int_0^1 J_0(\lambda\rho) \; \rho \; J_0(k\rho) \; d\rho (A_\lambda + B_\lambda)$$

where 1 was substituted by (VIII.7) and ρ is used as a weighing function.

Using properties of the Bessel Functions* the integral inside the summation in (VIII.9) can be written as

for $\lambda \neq k$

$$\int_0^1 J_0(\lambda\rho) J_0(k\rho) \; \rho d\rho = \frac{1}{\lambda^2 - k^2} \; [k\rho J_0(\lambda\rho) J_0'(k\rho) -$$

$$- \lambda\rho J_0(k\rho) J_0'(\lambda\rho)]_0^1 = \frac{1}{\lambda^2 - k^2} \; [-kJ_0(\lambda) J_1(k) + \lambda J_0(k) J_1(\lambda)] =$$

$$= \frac{1}{\lambda^2 - k^2} \left[-J_0(\lambda)\, hr_0 J_0(k) + J_0(k)\, hr_0 J_0(\lambda) \right] = 0$$

which shows the $J_0(\lambda\rho)$ are orthogonal. The last two equalities were obtained using the relation between derivatives $J_0'(\lambda\rho) = -J_1(\lambda\rho)$ and Equation (VIII.6).

For $\lambda = k$ and following the same procedure gives the norm as

$$\int_0^1 J_0^2(\lambda\rho)\rho\, d\rho = \frac{1}{2}\left[1 + \frac{h^2 r_o^2}{\lambda^2}\right] J_0^2(\lambda) \qquad \text{(VIII.10)}$$

Knowing the $J_0(\lambda\rho)$'s are orthogonal with a norm given by (VIII.10) from (VIII.9), we get after integration that

$$A_\lambda + B_\lambda = \frac{2hr_0}{(\lambda^2 + h^2 r_0^2)\, J_0(\lambda)} \qquad \text{VII.11}$$

Another equation for A_λ and B_λ is obtained from (VIII.8). This is valid for any ρ, which means each term should cancel, i.e.

$$A_\lambda\, e^{k_\lambda \xi t} + B_\lambda\, \bar{e}^{k_\lambda \xi t} = 0 \qquad \text{(VIII.12)}$$

* Mathematical Methods in Physics. J. Mathews and R.L. Walker. W.A. Benjamin Eds. N.Y.

From (VII.11) and (VII.12) we get

$$A_\lambda = -B_\lambda \bar{e}^{2k_\lambda \xi_t} \qquad \text{(VIII.13)}$$

and

$$B_\lambda = \frac{2hr_0}{(\lambda^2 + h^2 r_0^2)\, J_0(\lambda)} \quad \frac{1}{(1 - \bar{e}^{2k_\lambda \xi_t})} \qquad \text{(VIII.14)}$$

Finally the complete expression for the solution for the temperature field can be written as

$$\beta(\rho,\xi) = 2hr_0\, e^{V\xi} \sum_\lambda \frac{J_0(\lambda\rho)}{(\lambda^2 + h^2 r_0^2)\, J_0(\lambda)} \frac{e^{-k_\lambda \xi} - \bar{e}^{2k_\lambda \xi_t} e^{k_\lambda \xi}}{1 - \bar{e}^{2k_\lambda \xi_t}} \qquad \text{(VIII.15)}$$

with $k_\lambda^2 = V^2 + \lambda^2$ and the λ's satisfy

$$\lambda\, J_1(\lambda) = hr_0\, J_0(\lambda) \qquad \text{(VIII.16)}$$

APPENDIX IX

Plane Strain Analytical Stresses

The plane strain analytical solutions for stresses are derived assuming there is only radial displacement and allowing an axial displacement in order to satisfy the condition of no axial traction at the ends of the cylinder.

In non-dimensional variables these solutions are

$$\sigma_\rho = \int_0^1 \beta\,\rho\,d\rho - \frac{1}{\rho^2}\int_0^\rho \beta\rho\,d\rho \qquad (IX.1)$$

$$\sigma_\theta = \int_0^1 \beta\rho\,d\rho + \frac{1}{\rho^2}\int_0^\rho \beta\rho\,d\rho - \beta \qquad (IX.2)$$

$$\sigma_\xi = 2\int_0^1 \beta\,\rho\,d\rho - \beta \qquad (IX.3)$$

with a conversion factor given by

$$\{\sigma\}_{dim} = \frac{\alpha E(T_{MP} - T_a)}{1 - \nu}\{\sigma\} \qquad (IX.4)$$

A. Axisymmetric Thermal Field

For the general temperature field given by Equation (VIII.15) the stress components, after integrating by parts, are

$$\sigma\rho = 2hr_0\, e^{V\xi} \sum_{\lambda} K_{\lambda}(\xi) \left[\frac{hr_0}{\lambda^2} - \frac{J_1(\lambda\rho)}{\lambda\rho} \quad \frac{1}{J_0(\lambda)}\right] \tag{IX.5}$$

$$\sigma_{\theta} = 2hr_0\, e^{V\xi} \sum_{\lambda} K(\xi) \left\{\frac{hr_0}{\lambda^2} + \frac{1}{J_0(\lambda)} \left[\frac{J_1(\lambda\rho)}{\lambda\rho} - J_0(\lambda\rho)\right]\right\} \tag{IX.6}$$

$$\sigma_{\xi} = 2hr_0\, e^{V\xi} \sum_{\lambda} K(\xi) \left[\frac{2hr_0}{\lambda^2} - \frac{J_0(\lambda\rho)}{J_0(\lambda)}\right] \tag{IX.7}$$

where

$$K_{\lambda}(\xi) = \frac{e^{-k_{\lambda}\xi} - e^{-2k_{\lambda}\xi_t}\, e^{k_{\lambda}\xi}}{(1 - e^{-2k_{\lambda}\xi_t})(\lambda^2 + h^2 r_0^2)} \tag{IX.8}$$

To obtain these expressions the following integral was used

$$\int_0^Z J_0(Z)\, Z dZ = J_1(Z)\, Z \tag{IX.9}$$

The evaluation of stresses at the center to the cylinder is accomplished by using the following limiting values

$$J_0(0) = 1 \quad \text{and} \quad \left.\frac{J_1(\lambda\rho)}{\lambda\rho}\right/_{\rho \to 0} = 1/2 \tag{IX.10}$$

B. Radial Temperature Field

For a temperature field given by $\beta = -\rho^2$ the values of stress are immediately obtained as :

$$\sigma\rho = \frac{1}{4}(\rho^2 - 1) \qquad \text{(IX.11)}$$

$$\sigma_\theta = \frac{1}{4}(3\rho^2 - 1) \qquad \text{(IX.12)}$$

$$\sigma_\xi = \rho^2 - 1/2 \qquad \text{(IX.13)}$$

APPENDIX X

ANALYTICAL ASISYMMETRIC SOLUTIONS FOR STRESSES

X.1 Axisymmetric Temperature Field

A) Love's Potential

The reduced Love's potential $L^* = L/E\alpha\beta_f r_o^3$ satisfies the biharmonic differential equation :

$$\nabla^2 \nabla^2 L^* = 0 \qquad \text{where} \qquad \nabla^2 = \frac{\partial^2}{\partial \rho^2} + \frac{1}{\rho}\frac{\partial}{\partial \rho} + \frac{\partial^2}{\partial \xi^2}$$

with L^*, by symmetry, only a function of ρ and ξ .

Performing a cosine finite Fourier transform on the biharmonic equation we get

$$\left(\frac{d}{d\rho^2} + \frac{1}{\rho}\frac{d}{d\rho} - \frac{n^2\pi^2}{\xi_t^2}\right)\left(\frac{d^2}{d\rho^2} + \frac{1}{\rho}\frac{d}{d\rho} - \frac{n^2\pi^2}{\xi_t^2}\right) L_c^*(n,\rho) = 0$$

where by definition the following relations were used

$$F_{fc}\{L^*(\xi,\rho)\} \equiv L_c^*(n,\rho) = \int_0^{\xi t} L^*(\xi,\rho)\cos\frac{n\pi\xi}{\xi_t}\, d\xi$$

and

$$F_{fc}\left\{\frac{\partial^2 L^*(\xi,\rho)}{\partial\xi^2}\right\} \equiv \int_0^{\xi_t} \frac{\partial^2 L^*}{\partial\xi^2}\cos\frac{n\pi\xi}{\xi_t}\, d\xi =$$

$$= (-1)^n \left.\frac{\partial L^*}{\partial \xi}\right|_{\xi_t} - \left.\frac{\partial L^*}{\partial \xi}\right|_{0} - \frac{n^2\pi^2}{\xi_t^2} L^*_c(n,\rho)$$

with the assumption that

$$\left.\frac{\partial L^*}{\partial \xi}\right|_{\xi_t} = \left.\frac{\partial L^*}{\partial \xi}\right|_{0} = 0$$

The antitransform is performed by summation of the following series :

$$L^*(\xi,\rho) = \frac{1}{\xi_t} L^*_c(0) + \frac{2}{\xi_t} \sum_{n=1}^{\infty} L^*_c(n,\rho) \cos\frac{n\pi\xi}{\xi_t}$$

A fairly general solution of the biharmonic equation which is the modified bi-Bessel equation, is obtained as a combination of the modified Bessel functions of order zero and one as

$$L_c(n,\rho) = A(l_n)\, I_o(l_n) + B(l_n)\, (l_n\rho)\, I_1(l_n\rho)$$

with

$$l_n = n\pi/\xi_t$$

what can be verified using the following recurrent relations among derivatives of the modified Bessel functions

$$x\, I'_n(x) = x\, I_{n-1}(x) - x\, I_n(x) \;;$$

$$x\, I'_n(x) = x\, I_{n+1}(x) + x\, I_n(x) \;;$$

The functions K_ν are not included because they diverge for $\rho \to 0$.

The general form of the antitransformed Love's potential is therefore :

$$L^*(\xi,\rho) = \frac{2}{\xi_t} \sum_{n=1}^{\infty} [A(l_n)\, I_0(l_n\rho) + B(l_n)\,(l_n\rho)\, I_1(l_n\rho)$$

$$\cos l_n\xi$$

with A_{l_n} and B_{l_n} constants to be determined from the boundary conditions.

B) Goodier's Potential

In terms of a reduced potential $\phi^* = \phi(1-\nu)/(1+\nu)\alpha\beta_f r_0^2$ and the nondimensional quantities ρ, ξ, and β, the Goodier's potential can be accomplished by solving the differential equation

$\nabla^2 \phi^* = \beta(\rho,\xi)$ where ∇^2 is the harmonic operator in cylindrical coordinates and $\beta(\rho,\xi)$ is the temperature distribution in the body given by Equation (VIII.15). The form of this function, a series of a products of functions $J_0(\lambda,\rho)\, Z_\lambda(\xi)$ of one variable, suggests that we can propose a solution for ϕ^* as a series of functions ϕ_λ^* such that

$$\nabla^2 \phi_\lambda^* = J_0(\lambda\rho)\, Z_\lambda(\xi)$$

$Z(\xi)$ being the function

$$Z_\lambda(\xi) = e^{V\xi}\,[e^{-k_\lambda\xi} - e^{-2k_\lambda\xi_t}\, e^{k_\lambda\xi}]$$

Performing a sine finite Fourier transform on the differential equation such that

$$F_{fs}\left\{\frac{\partial^2 \phi_\lambda^*}{\partial \xi^2}\right\} \qquad \phi^*_{\lambda,n,n} = \int_0^{\xi_t} \frac{\partial^2 \phi_\lambda^*}{\partial \xi^2} \sin l_n \xi \, d\xi =$$

$$= l_n \left[(-1)^{n+1} \phi_\lambda^*(\xi_t) + \frac{\partial \phi_\lambda^*}{\partial \xi}\Big|_0\right] - l_n^2 \, \phi^*_{\lambda,n}(n)$$

where

$$\phi^*_{\lambda,n} = \int_0^{\xi_t} \phi^*_\lambda(\rho,\xi) \sin l_n \xi \, d\xi$$

with the antitransform given by

$$\phi^*_\lambda(\xi,\rho) = \frac{2}{\xi_t} \sum_{n=1}^{\infty} \phi^*_{\lambda,n} \sin l_n \xi$$

We get the transformed differential equation as

$$\left(\frac{\partial^2}{\partial \rho^2} + \frac{1}{\rho}\frac{\partial}{\partial \rho} - l_n^2\right) \phi^*_{\lambda,n}(n,\rho) = J_0(\lambda\rho) \, Z_{\lambda,n}(n)$$

Where it was assumed that

$$\frac{\partial \phi^*}{\partial \xi}\Big|_{=0} = \frac{\partial \phi^*}{\partial \xi}\Big|_{\xi=\xi_t} = 0$$

for a particular solution.

Also

$$Z_{\lambda,n}(n) = F_s\{Z_\lambda(\xi)\}$$

The differential equation for $\phi^*_{\lambda,n}$ can be modified to get

$$\left(\frac{d^2}{d(\lambda\rho)^2} + \frac{1}{\rho}\frac{d}{d(\lambda\rho)} - \frac{l_n^2}{\lambda^2}\right)\phi^*_{\lambda,n}(n,\rho) = \frac{J_0(\lambda\rho)}{\lambda^2} Z_{\lambda,n}(n)$$

A particular solution can be obtained as

$$\phi^*_{\lambda,n} = A\, J_0(\lambda\rho)$$

Substituting and using the following relations among derivatives of J_0 and J_1 :

$$J'_0(\lambda\rho) = -J_1(\lambda\rho)$$

and

$$J''_0(\lambda\rho) = -J_0(\lambda\rho) + \frac{J_1(\lambda\rho)}{\lambda\rho}$$

we get that

$$A = -\frac{Z_{\lambda,n}(n)}{\lambda^2 + l_n^2/\lambda^2}$$

and

$$\phi^*_{\lambda,n} = -\frac{Z_{\lambda,n}(n)}{\lambda^2 + l_n^2} J_0(\lambda\rho)$$

Applying the antitransform

$$\phi^*_\lambda(\xi,\rho) = - J_0(\lambda\rho)\ \frac{2}{\xi_t}\ \sum_{n=1}^{\infty}\ \frac{Z_{,n}(n)}{(\lambda^2 + l_n^{\,2})}\ \sin l_n\xi$$

The complete solution for ϕ^* is therefore

$$\phi^*(\rho,\xi) = -2hr_0\ \sum_{\lambda}\ \frac{J_0(\ \ )}{\lambda^2(\lambda^2 + h^2r_0^2)\ J_0(\lambda)}$$

$$\frac{2}{\xi_t}\ \sum_{n=1}^{\infty}\ \frac{Z^*_{\lambda,n}(n)\ \sin l_n\xi}{(1 + l_n^{\,2}/\lambda^2)\ (1 - e^{-2k_\lambda \xi_t})}$$

which can be put in a more suitable way as

$$\phi^*(\rho,\xi) = -\frac{4hr_0}{\xi_t}\ \sum_{n=0}^{\infty}\ \sin l_n\ \xi^*$$

$$\sum_{\lambda}\ \frac{J_0(\lambda\rho)}{J_0(\lambda)(\lambda^2 + h^2r_0^{\,2})(\lambda^2 + l_n^{\,2})(1 - e^{-2k_\lambda \xi_t})}\ Z_{\lambda,n}(n)$$

C. Calculation of Constants A_{l_n} and B_{l_n} and Stresses

The non-dimensional components of stress derived from Love's and Goodier's potentials are

$$\sigma_\rho(\xi,\rho) = \frac{\partial}{\partial\xi}\ [\nu\nabla^2 L^* - \frac{\partial^2 L^*}{\partial\rho^2}] + \frac{1}{1-\nu}(\frac{\partial^2\phi^*}{\partial\rho^2} - \beta\ )$$

$$\sigma_\theta(\xi,\rho) = \frac{\partial}{\partial\xi}\left[\nu\nabla^2 L^* - \frac{1}{\rho}\frac{\partial L^*}{\partial\rho}\right] + \frac{1}{1-\nu}\left(\frac{1}{\rho}\frac{\partial\phi^*}{\partial\rho} - \beta\right)$$

$$\sigma_\xi = \frac{\partial}{\partial\xi}\left[(2-\nu)\nabla^2 L^* + \frac{\partial^2 L^*}{\partial\xi^2}\right] + \frac{1}{1-\nu}\left(\frac{\partial^2\phi^*}{\partial\xi^2} - \beta\right)$$

$$\tau_{\rho\xi} = \frac{\partial}{\partial\rho}\left[(1-\nu)\nabla^2 L^* - \frac{\partial^2 L^*}{\partial\xi}\right] + \frac{1}{1-\nu}\frac{\partial^2\phi^*}{\partial\rho\partial\xi}$$

Subject to the following boundary conditions

$$\sigma_\rho = \tau_{\rho\xi} = 0 \Big|_{\rho=1} \quad \text{and} \quad \sigma_\xi = 0 \Big|_{\substack{\xi=\xi_t \\ \xi=0}}$$

After derivating, the stress components are

$$\sigma_\rho = \frac{2}{\xi_t}\sum_n \left\{\left\{I_0(l_n\rho)\left[A_{l_n} - B_{l_n}(2\nu-1)\right] + I_1(l_n\rho)\left[B_{l_n}(l_n\rho) - \frac{A_{l_n}}{l_n\rho}\right]\right\} l_n^3 - \frac{2hr_0}{1-\nu}\sum \frac{Z_{\lambda,n}(n)\left[J_0(\lambda\rho)\, l_n^2/\lambda^2 + J_1(\lambda\rho)/\lambda\rho\right]}{(1-e^{-2k_\lambda\xi_t})(\lambda^2+h^2r_0^2)\left[1+(l_n/\lambda)^2\right]J_0(\lambda)}\right\}$$

$$\sin l_n\xi$$

$$\sigma_\theta = \frac{2}{\xi_t} \sum_n \sin l_n\xi \left\{ \left[\frac{I_1(l_n\rho)}{l_n\rho} A_{l_n} - I_0(l_n\rho)(2\nu-1) B_{l_n} \right] l_n^3 \right.$$

$$\left. + \frac{2hr_0}{1-\nu} \sum_\lambda \frac{Z_{\lambda,n}(n) \left[J_1(\lambda\rho)/\lambda\rho - J_0(\lambda\rho)(1 + l_n^2/\lambda^2) \right]}{(\lambda^2 + h^2 r_0^2) J_0(\lambda) (1 - e^{-2k_\lambda \xi_t}) (1 + l_n^2/\lambda^2)} \right\}$$

$$\sigma_\xi = \frac{2}{\xi_t} \sum_n \sin l_n\xi \left\{ \left(I_0(l_n\rho) \left[A_{l_n} - 2(2-\nu) B_{l_n} \right] + \right. \right.$$

$$\left. + I_1(l_n\rho)(l_n\rho) B_{l_n} \right) l_n^3 +$$

$$\left. + \frac{2hr_0}{1-\nu} \sum_\lambda \frac{J_0(\lambda\rho) Z_{\lambda,n}(n)}{(\lambda^2 + h^2 r_0^2)(1 - e^{-2k_\lambda \xi_t})(1 + l_n^2/\lambda^2)} \right\}$$

$$\tau_{\rho\xi} = \frac{2}{\xi_t} \sum_n \cos l_n\xi \left\{ \left(I_0(l_n\rho) B_{l\rho_n} + I_1(l_n\rho) \right. \right.$$

$$\left. \left[A_{l_n} + 2(1-\nu) B_{l_n} \right] \right) l_n^3 +$$

$$\left. + \frac{2hr_0}{1-\nu} l_n \sum_\lambda \frac{J_1(\lambda\rho) Z_{\lambda,n}(n)}{\lambda(\lambda^2 + h^2 r_0^2) J_0(\lambda)(1 + l_n^2/\lambda^2)(1 - e^{-2k_\lambda \xi_t})} \right\}$$

These components of non-dimensional stress should be multiplied by $E\,\alpha\,\beta_f$ to obtain the stress in absolute units ; i.e. $|\sigma|_{dim} = F_\alpha \beta_f |\sigma|$. For the calculation of stresses at the axis, $\rho = 0$, the following limits are used :

$$\left.\frac{I_1(x)}{x}\right|_x = 1/2 \qquad J_1(0) = 0$$

$$J_0(0) = 1$$

$$\left. I_0(x) \right|_{x\,0} = 1 \qquad \left.\frac{J_1(x)}{x}\right|_{x\,0} = 1/2$$

The evaluation of the constants A_{l_n} and B_{l_n} is carried out by solving the system of linear algebraic equations resulting from the application of the boundary conditions $\sigma_\rho\big|_{\rho=1}=0$ and $\tau_{\rho\xi}\big|_{\rho=1}=0$

$$A_{l_n}\left[I_0(l_n) - \frac{I_1(l_n)}{l_n}\right] + B_{l_n}\left[I_1(l_n)\, l_n - (2\nu - 1)\, I_0(l_n)\right] =$$

$$= \frac{2hr_0}{1-\nu}\,\frac{1}{l_n^{\,3}}\,\sum K_{\lambda,n}(n)\,(l_n^{\,2} + hr_0)$$

$$A_{l_n} I_1(l_n) + B_{l_n}\left[I_0(l_n)\, l_n + 2(1-\nu)\, I_1(l_n)\right] =$$

$$= -\frac{2h^2 r_0^{\,2}}{1-\nu}\,\frac{1}{l_n^{\,2}}\,\sum_\lambda K_{\lambda,n}(n)$$

where

$$K_{\lambda,n}(n) = \frac{Z_{\lambda,n}(n)}{\lambda^2(\lambda^2 + h^2 r_0^2)\ (1 + l_n^2/\lambda^2)\ [1 - e^{-2k_\lambda \xi_t}]}$$

Solving for A_{l_n} and B_{l_n} we get

$$A_{l_n} = \frac{2hr_0}{\Delta(1-\nu)\ l_n^2} \left(\Sigma\ K_{\lambda,n}(n)\ \{I_0(l_n)\ [l_n^2 + 2hr_0\ (1-\nu)] + \right.$$

$$\left. + \frac{I_1(l_n)}{l_n}\ [l_n^2(hr_0 + 2(1-\nu)) + 2hr_0(1-\nu)]\ \}\right.$$

and

$$B_{l_n} = \frac{1}{\Delta}\ \{ - \frac{2h^2 r_0^2}{1 - \nu}\ \frac{\Sigma\ K_{\lambda,n}(n)}{l_n^2}\ [I_0(l_n) + \frac{l_n}{hr_0}\ I_1(l_n)]\ \}$$

where

$$\Delta = I_0^2(l_n)\ l_n - \frac{I_1^2(l_n)}{l_n}\ [2(1 - \nu) + l_n^2]$$

D. Calculation of $Z_{\lambda,n}$

$$Z_{\lambda,n}(n) = F_s\ \{Z_\lambda(\xi)\}$$

$$= \int_0^{\xi_t} e^{V\xi}\ [e^{-k_\lambda \xi} - e^{-2k_\lambda \xi_t}\ e^{k_\lambda \xi}]\ \sin \frac{n\pi}{\xi_t}\ \xi\ d\ \xi$$

$$= \frac{n\pi}{\xi_t} e^{-k_\lambda \xi_t} \left\{ \frac{e^{k_\lambda \xi_t} - (-1)^n e^{V\xi_t}}{(V-k_\lambda)^2 + \frac{n^2\pi^2}{\xi_t^2}} - \frac{e^{-k_\lambda \xi_t} - (-1)^n e^{V\xi_t}}{(V+k_\lambda)^2 + \frac{n^2\pi^2}{\xi_t^2}} \right\}$$

2. Analytical Axisymmetric Solution for $\beta = -\rho^2$

The same procedure form part 1 is followed applied to a temperature field that depends on radius only, i.e. $\beta = -\rho^2$.

A. Love's Potential

The differential equation for the Love's potential is the same as shown in Part A, as well as the solution i.e.

$$L^*(\xi,\rho) = \frac{2}{\xi_t} \sum_{n=1}^{\infty} [A_{l_n} I_0(l_n\rho) + B_{l_n} (l_n\rho) I_1(l_n\rho)] \cos l_n\xi$$

B. Goodier's Potential

The differential equation for the Goodier's Potential is

$$\frac{\partial^2 \phi^*}{\partial \rho^2} + \frac{1}{\rho} \frac{\partial \phi^*}{\partial \rho} + \frac{\partial^2 \phi^*}{\partial \xi^2} = -\rho^2$$

After a sine finite Fourier transform is performed, we get

$$\frac{\partial^2 \phi_n^*}{\partial \rho^2} + \frac{1}{\rho} \frac{\partial \phi_n^*}{\partial \rho} - l_n^2 \phi_n^* = -\rho^2 f_n$$

where

$$f_n = \int_0^{\xi_t} \sin \frac{n\pi}{\xi_t} \xi \, d\xi = \frac{1}{l_n} [1 - (-1)^n]$$

The particular solution proposed is $\phi_n^* = a\rho^2 + b\rho + c$, which gives, after solving for a, b and c

$$a = \frac{f_n}{l_n^2}, \qquad b = 0, \qquad c = \frac{4f_n}{l_n^4}$$

Finally, performing the antitransform

$$\phi^*(\rho, \xi) = \frac{2}{\xi_t} \Sigma \frac{1 - (1)^n}{l_n^3} \left(\rho^2 + \frac{4}{l_n^2}\right) \sin l_n \xi$$

C) Calculation of Stresses and Constants A_{l_n} and B_{l_n}

The stress components derived from both Love's and Goodier's potentials are :

$$\sigma_\rho = \frac{2}{\xi_t} \Sigma_n \left\{ \{ I_0(l_n\rho) [A_{l_n} - B_{l_n} (2\nu - 1)] + \right.$$

$$\left. + I_1(l_n\rho) \left[B_1(l_n\rho) - \frac{A_{l_n}}{l_n\rho}\right] \right\} l_n^3 + \frac{[1-(-1)^n}{(1-\nu) l_n} \left(\frac{2}{l_n^2} + \rho^2\right) \Big\} \sin l_n \xi$$

$$\sigma_\theta = \frac{2}{\xi_t} \Sigma \left\{ \left[\frac{I_1(l_n\rho)}{l_n\rho} A_{l_n} - I_0(l_n\rho) B_{l_n} (2\nu - 1)\right] l_n^3 + \right.$$

$$- \frac{[1 - (-1)^n]}{(1 - \nu)\ l_n} \left(\frac{2}{l_n^2} + \rho^2\right)\Big\} \sin l_n \xi$$

$$\sigma_\xi = \frac{2}{\xi_t} \Sigma \Big\{\{I_0(l_n\rho)\ [A_{l_n} - 2(2 - \nu)\ B_{l_n}] + I_1(l_n\rho)\ B_{l_n}\}\ l_n^3 -$$

$$- \frac{4\ [1 - (-1)^n]}{(1 - \nu)\ l_n^3} \Big\} \sin l_n \xi$$

and

$$\tau_{\rho\xi} = \frac{2}{\xi_t} \Sigma \Big\{\{I_0(l_n\rho)(l_n\rho)\ B_{l_n} + I_1(l_n\rho)[A_{l_n} + 2(1-\nu)\ B_{l_n}]\}\ l_n^3 +$$

$$+ \frac{2}{1 - \nu} \frac{[1 - (-1)^n]}{l_n^2} \rho \Big\} \cos l_n \xi$$

These non-dimensional components of stresses should be multiplied by $E\alpha\ \beta_f$ to obtain the stress level in absolute units ; i.e.

$$\{\sigma\}_{dim} = E\alpha\ \beta_f\ \{\sigma\}$$

The evaluation of the constants A_{l_n} and B_{l_n} is done as before, using the boundary conditions :

i) $\sigma_\rho = 0$ at $\rho = 1$

$$A_{l_n}\left[I_0(l_n) - \frac{I_1(l_n)}{l_n}\right] + B_{l_n}[I_1(l_n)\ l_n - (2\nu - 1)\ I_0(l_n)] =$$

$$= -\frac{[1 - (-1)^n]}{(1 - \quad) \, l_n^4} \left(\frac{2}{l_n^2} + 1\right)$$

$$= 0 \qquad \text{for} \quad n = 2n'$$

$$= -\frac{2}{(1 - \nu) \, l_n^{*2}} \left(\frac{2}{l_n^{*2}} + 1\right) \text{ with } l_n^* = \frac{(2n + 1)\pi}{\xi_t}$$

ii) from $\tau_{\rho\xi} = 0$ at $\rho = 1$

$$A_{l_n} \, I_1(l_n^*) + B_{l_n} \, [I_0(l_n^*) \, l_n^* + 2(1 - \nu) \, I_1(l_n^*) =$$

$$= -\frac{4}{(1-\nu)} \, \frac{1}{l_n^{*5}}$$

That is the only non-zero A_{l_n} and B_{l_n} come from odd values of the integer n

Solving for A_l^* and B_l^* and droping the asterisk

$$A_{l_n} = -\frac{2}{D(1-\nu) \, l_n^4} \{I_0(l_n) \left[\frac{4\nu}{l_n} + l_n\right] + 2 \, I_1(l_n)$$

and

$$B_{l_n} = -\frac{2}{D(1-\nu) \, l_n^4} \{I_0(l_n) \, \frac{2}{l_n} - I_1(l_n) \left[\frac{4}{l_n^2} + 1\right.$$

with

$$l_n = \frac{(2n + 1)\pi}{\xi_t}$$

and

$$D = I_0^2(l_n)\, l_n - \frac{I_1^2(l_n)}{l_n}\,[2(1 - \nu) + l_n^2]$$

The evaluation of stress components at the axis of the cylinder is done using the limit values given in part 1 of I_0/ρ and I_1/ρ

APPENDIX XI

COMPUTER PROGRAMS

XI.1 Mesh Generator

```
C
C     THIS PROGRAM GENERATES MESHES FOR FLEMT AND PFLEMS
C
C        FOR CRYSTAL , CONE AND SEED OF BOULE
C
C
      DIMENSION RC(4000),ZC(4000),NODE(10000,3)
      DIMENSION NV1(100),NV2(100),HV(100),TINFV(100)
      DIMENSION NT1(100),NT2(100),HT(100),TINFT(100)
      DIMENSION NH1(20),NH2(20),HH(20),TINFH(20)
      DIMENSION LASTN(100),M(100)
      INTEGER NN,NBC,NBCL,LAST,LASTEL,NELO,NELP,NODE
      INTEGER CBN,LL,M,LASTN,BNS,BNL,NNHCV
      INTEGER NV1,NV2,NT1,NT2,NH1,NH2
      REAL XL,HBC,WBC,RC,ZC,HEIGHT,BH,RAD,BLE,BHS,BWL
      REAL HV,HT,HH,TINFV,TINFH,TINFT
C
C
C       READ DIMENSIONS OF CRYSTAL AND CONE ANGLE
C
      READ(5,1010) SIZE,XL
      READ(5,1015) SEEDW,TAN,SH
C
C       CALCULATE NUMBER OF BLOCKS FOR CYLINDER
C
      NBC=XL/SIZE
      HBC=XL/NBC
C
C       CALCULATE BLOCK WIDTH
C
      NBCL=1./SIZE
      WBC=1./NBCL
C
C       INITIALIZE VARIABLES
C
      NNINT=0
      NEINT=0
      ZINT=0.0
      LASTEL=NEINT
      LAST=NNINT
C
C       GENERATE FIRST ROW OF NODES
C
      DO 50 I=1,NBCL
      NOD=LAST + I
      RC(NOD)=WBC*(I-1)
      ZC(NOD)=0.0
50    CONTINUE
C
      LAST=LAST+NBCL+1
      RC(LAST)=1.0
      ZC(LAST)=0.0
C
C       GENERATE REMAINING ROWS IN THE CRYSTAL
C
      DO 200 I=1,NBC
C
      DO 100 J=1,NBCL
```

```
      NOD=LAST+J
      RC(NOD)=WBC*(J-1)
      ZC(NOD)=HBC*I
100   CONTINUE
C
      LAST=LAST+NBCL+1
      RC(LAST)=1.0
      ZC(LAST)=HBC*I
C
C        GENERATE CRYSTAL TOPOLOGY
C
      DO 150 K=1,NBCL
      NELO=2*K-1+LASTEL
      NODE(NELO,1)=LAST-2*NBCL+K-2
      NODE(NELO,2)=LAST-NBCL+K
      NODE(NELO,3)=NODE(NELO,2)-1
C
      NELP=2*K+LASTEL
      NODE(NELP,1)=NODE(NELO,1)
      NODE(NELP,2)=NODE(NELP,1)+1
      NODE(NELP,3)=NODE(NELO,2)
C
150   CONTINUE
      LASTEL=LASTEL+2*NBCL
C
C        CYCLE FOR NEXT BLOCK
C
200   CONTINUE
C
C
C       GENERATE NODES AND TOPOLOGY FOR CONE
C
      M(1)=NBCL
       LASTN(1)=LAST
C
C        CALCULATE NUMBER AND DIMENSION OF BLOCKS
C
      HEIGHT=(1.-SEEDW)*TAN
      CBN=HEIGHT/SIZE+1
      BH=HEIGHT/CBN
C
      DO 600 I=1,CBN
      RAD=1.-BH*I/TAN
      L=I+1
      M(L)=RAD/SIZE+1
      BLE=RAD/M(L)
      LASTN(L)=LASTN(I)+M(L)+1
C
      NLINE=M(L)
      DO 500 J=1,NLINE
C
      NOD=LASTN(I)+J
      RC(NOD)=BLE*(J-1)
      ZC(NOD)=BH*I+XL
500   CONTINUE
C
      RC(LASTN(L))=RAD
      ZC(LASTN(L))=BH*I+XL
C
      DO 540 J=1,NLINE
C
      NELO=2*J-1+LASTEL
      NODE(NELO,1)=LASTN(I)-M(I)+J-1
      NODE(NELO,2)=LASTN(I)+J+1
      NODE(NELO,3)=NODE(NELO,2)-1
C
      NELP=2*J+LASTEL
      NODE(NELP,1)=NODE(NELO,1)
      NODE(NELP,2)=NODE(NELP,1)+1
      NODE(NELP,3)=NODE(NELO,2)
C
540   CONTINUE
```

```
      IF(M(L).LT.M(I))GO TO 549
C
      LASTEL=LASTEL+2*M(L)
      GO TO 600
C
549   LASTEL=LASTEL+2*M(L)+1
      NODE(LASTEL,1)=LASTN(I)-1
      NODE(LASTEL,2)=LASTN(I)
      NODE(LASTEL,3)=LASTN(L)
C
C
C        CYCLE FOR NEXT BLOCK IN THE CONE
C
600   CONTINUE
C
C        GENERATE NODES AND TOPOLOGY IN THE SEED
C
      BNS=SH/SIZE+1
      BHS=SH/BNS
      BNL=SEEDW/SIZE+1
      BWL=SEEDW/BNL
      LL=CBN+1
      LAST=LASTN(LL)
      PHT=XL+HEIGHT
C
      DO 700 I=1,BNS
C
      DO 650 J=1,BNL
C
      NOD=LAST+J
      RC(NOD)=BWL*(J-1)
      ZC(NOD)=BHS*I+PHT
650   CONTINUE
C
      LAST=LAST+BNL+1
      RC(LAST)=SEEDW
      ZC(LAST)=BHS*I+PHT
C
      DO 680 J=1,BNL
C
      NELO=2*J-1+LASTEL
      NODE(NELO,1)=LAST-2*BNL+J-2
      NODE(NELO,2)=LAST-BNL+J
      NODE(NELO,3)=NODE(NELO,2)-1
C
      NELP=2*J+LASTEL
      NODE(NELP,1)=NODE(NELO,1)
      NODE(NELP,2)=NODE(NELP,1)+1
      NODE(NELP,3)=NODE(NELO,2)
C
680   CONTINUE
C
      LASTEL=LASTEL+2*BNL
C
700   CONTINUE
C
      NN=LAST
      NE=LASTEL
C
C        DETERMINE SEGMENTS WHERE CONVECTION OCCURS
C
      DO 800 I=1,NBC
      HV(I)=0.6
      TINFV(I)=0.0
      NV1(I)=(NBCL+1)*I+NNINT
      NV2(I)=(NBCL+1)*(I+1)+NNINT
800   CONTINUE
```

```
C
      DO 810 I=1,BNS
      I$=I+NBC
      HV(I$)=0.3
      TINFV(I$)=0.0
      NV1(I$)=LASTN(LL)+(BNL+1)*(I-1)
      NV2(I$)=NV1(I$)+BNL+1
810   CONTINUE
C
      DO 820 I=1,CBN
      HT(I)=0.6
      TINFT(I)=0.0
      NT1(I)=LASTN(I)
      J=I+1
      NT2(I)=LASTN(J)
820   CONTINUE
C
      DO 830 I=1,BNL
      HH(I)=0.0
      TINFH(I)=0.0
      NH1(I)=NN-I+1
      NH2(I)=NN-I
830   CONTINUE
C
      NNHCV=NBC+BNS
      NNHCT=CBN
      NNHCH=BNL
C
C       PRINT THE DATA IN FORMAT TO BE READ BY FLEMT AND PFLEMS
C
      WRITE(6,1005) NN,NE
      WRITE(6,1006) NNHCV,NNHCH,NNHCT
1005  FORMAT(5X,'NN= ',I4,5X,'NE= ',I4,//)
1006  FORMAT(5X,'NNHCV=',I3,'NNHCH=',I3,'NNHCT=',I3,/)
      DO 900 I=1,NN
      ZC(I)=ZC(I)+ZINT
      WRITE(6,1020)I,RC(I),ZC(I)
900   CONTINUE
C
      DO 910 K=1,NE
      WRITE(6,1025)K,NODE(K,1),NODE(K,2),NODE(K,3)
910   CONTINUE
C
      NNCL=NBCL+1
      T=1.0
      DO 920 I=1,NNCL
      WRITE(6,1030)I,T
920   CONTINUE
C
      DO 930 I=1,NNHCV
      WRITE(6,1040)NV1(I),NV2(I),HV(I),TINFV(I)
930   CONTINUE
C
      DO 940 I=1,NNHCT
      WRITE(6,1040)NT1(I),NT2(I),HT(I),TINFT(I)
940   CONTINUE
C
      DO 950 I=1,NNHCH
      WRITE(6,1040)NH1(I),NH2(I),HH(I),TINFH(I)
950   CONTINUE
C
C       FORMAT STATEMENTS
C
1010  FORMAT(2(2X,F10.5))
1015  FORMAT(3(2X,F10.5))
1020  FORMAT(2X,I4,2(2X,F10.5))
1025  FORMAT(4(2X,I4))
1030  FORMAT(2X,I3,2X,F10.5)
1040  FORMAT(2(2X,I4),2(2X,F10.5))
      STOP
      END
```

XI.2 Finite Linear Element Program for the Temperature Calculations during Growth

```
CTHIS IS A PROGRAM TO CALCULATE THE TEMPERATURE DISTRIBUTION
C IN LEC-GAAS DURING GROWTH USING A FINITE LINEAR ELEMENT
C METHOD (SECOND VERSION).
C
C
      DIMENSION IP(375),RES(375)
      INTEGER*4 LLB,LUB,IP,ITER,NHRS
      REAL*4 RES,EPS
      REAL*8 TB,DRATIO
      INTEGER*4 LHB,NRHS,JEXP,NSCALE
      DIMENSION TB(2)
      INTEGER*4 NN,NDIMA,NSOL,NDIMBX,IPERM,NDIMT
      REAL*8 TM,RINF,T,TT,DET
      REAL*8 DTA,RBAR,A1,A2,A3,B1,B2,B3
      REAL*8 C1,C2,C3,VK,TM$,CONST,DEL2
      REAL*8 BLV,CONSTV,CINFV,BLT,CONSTT
      REAL*8 CINVT,BLH,CONSTH,CINFH,RBARH
      DIMENSION TM(111,111),T(111),RINF(111),IPERM(222),TT(111,111)
      DIMENSION RC(500),ZC(500),NODE(900,3)
      DIMENSION NTS(50),HV(60),TINFV(60),HH(60),TINFH(60)
      DIMENSION BLV(60),NV1(60),NV2(60)
      DIMENSION BLT(40),NT1(40),NT2(40),HT(40),TINFT(40)
      DIMENSION BLH(40),NH1(40),NH2(40),RBARH(40)
      DIMENSION TM$(3,3),N(3),RC$(3),ZC$(3)
      DIMENSION TG(50,50),TGR(111),CVAL(20),IOP(8),VOP(8)
      REAL TG,CVAL,VOP,TMIN,DTEM,DX,DY,C,XSIZE,YSIZE
      INTEGER NX,NY,NRNG,IDIMX,NC,IOP
      REAL BORAXH,HBORAX,HARGON
      REAL TINFAR,TINFBO,ZBAR,TMBOR
      REAL TBOR,CA2,CA3,CA4,CB2,CB3,CB4
C
C
C
C  READ THE NUMBER OF NODES AND ELEMENTS OF THE SYSTEM
C
C
      READ(5,1005)NN,NE
C
C  INITIALIZE PARAMETERS
C
C
      DO 10 I=1,NN
      RINF(I) = 0.0
      RC(I) = 0.0
      ZC(I) = 0.0
      T(I) = 0.0
      DO 10 J = 1,NN
      TM(I,J) = 0.0
10    CONTINUE
C
C  READ THE NUMBER OF NODES WITH SPECIFIED TEMPERATURES
C  AND THE NUMBER OF BOUNDARY SEGMENTS,VERTICAL AND NON
C  VERTICAL,WHERE HEAT CONVECTION OCCUR.
C
C
      READ(5,1010)NNST,NNHCV,NNHCH,NNHCT
C
C  READ GROWTH PARAMETERS:RADIUS,CONDUCTIVITY,VELOCITY
C  AND LENGTH.
C
      READ(5,1015)RO,TK,V,XL,DTA
C
```

```
      READ(5,1018) CA,SW,SH,BORAXH
      READ(5,1019) CB2,CB3,CB4,CA2,CA3,CA4
C
      WRITE(6,1019) CB2,CB3,CB4,CA2,CA3,CA4
C
C  READ NUMBER OF NODE VS. NODAL COORDINATES
C
      DO 100 J = 1,NN
      READ(5,1020)I,RC(I),ZC(I)
100   CONTINUE
C
C  READ ELEMENT NUMBER VS. NODE NUMBERS
C
      DO 105 I = 1,NE
      READ(5,1025)J,NODE(J,1),NODE(J,2),NODE(J,3)
105   CONTINUE
C
C  READ NODE NUMBER VS. SPECIFIED TEMPERATURE
C
      DO 110 I = 1,NNST
      READ(5,1030) NT,TNT
      NTS(I) = NT
      T(NTS(I)) = TNT
110   CONTINUE
C
C  READ PAIRS OF NODE NUMBERS DEFINING BOUNDARY SEGMENT
C  WHERE CONVECTION OCCURS,CALCULATE THE CORRESPONDING
C  CHTC AND AMBIENT TEMPERATURE.
C
C
      TMBOR=1238.0
      TMBOR=1.-(1238.-TMBOR)/DTA
      TBOR=TINFBO(DTA,TMBOR,CB2,CB3,CB4,3.000)
      DO 140 I = 1,NNHCV
      READ(5,1040) NV1(I),NV2(I)
      ZBAR=(ZC(NV1(I))+ZC(NV2(I)))*RO/2.
      IF(ZBAR.LT.3.000) TINFV(I)=TINFBO(DTA,TMBOR,CB2,CB3,CB4,ZBAR)
      IF(ZBAR.GT.3.000.OR.ZBAR.EQ.3.000) TINFV(I)=TINFAR(DTA,TBOR,CA2,
     1CA3,CA4,ZBAR)
C
      IF(ZBAR.LT.BORAXH.OR.ZBAR.EQ.BORAXH) HV(I)=HBORAX(DTA,TINFV(I))
      IF(ZBAR.GT.BORAXH) HV(I)=HARGON(DTA,TINFV(I))
C
140   CONTINUE
C
C
      DO 145 J=1,NNHCT
      READ(5,1040)NT1(J),NT2(J)
      ZBAR=(ZC(NT1(J))+ZC(NT2(J)))*RO/2.
C
      IF(ZBAR.LT.3.000) TINFT(J)=TINFBO(DTA,TMBOR,CB2,CB3,CB4,ZBAR)
      IF(ZBAR.GT.3.000.OR.ZBAR.EQ.3.000) TINFT(J)=TINFAR(DTA,
     1TBOR,CA2,CA3,CA4,ZBAR)
C
      IF(ZBAR.LT.BORAXH) HT(J)=HBORAX(DTA,TINFT(J))
      IF(ZBAR.GT.BORAXH) HT(J)=HARGON(DTA,TINFT(J))
C
145   CONTINUE
      DO 150 J = 1,NNHCH
      READ(5,1040) NH1(J),NH2(J)
      ZBAR=ZC(NH1(J))*RO
      TINFH(J)=TINFAR(DTA,TBOR,CA2,CA3,CA4,ZBAR)
      HH(J)=HARGON(DTA,TINFH(J))
C
150   CONTINUE
C
C  WRITE HEADLINES
C
155   WRITE(6,2010)
      WRITE(6,2020) RO,V,XL
      WRITE(6,2030) NN,NE
```

```
C
      WRITE(6,2035) CA,SW,SH
      WRITE(6,2038) DTA,BORAXH
C
C
C
C  PRINT SPECIFIED TEMPERATURES
C
175   WRITE(6,2080)
      DO 180 I = 1,NNST
      TSP=1238.
      WRITE(6,2090) I,NTS(I),TSP
180   CONTINUE
C
C  PRINT BOUNDARY SEGMENT NODES,HTCH AND HTCV,AND
C  AMBIENT TEMPERATURE.
C
      WRITE(6,2100)
      DO 190 I = 1,NNHCV
      TINF=1238-(1.-TINFV(I))*DTA
      WRITE(6,2110) I,NV1(I),NV2(I),HV(I),TINF
190   CONTINUE
C
      IF(NNHCT.EQ.1) GO TO 196
      WRITE(6,2105)
      DO 195 I=1,NNHCT
      TINF=1238-(1.-TINFT(I))*DTA
      WRITE(6,2110)I,NT1(I),NT2(I),HT(I),TINF
195   CONTINUE
C
C
196   IF(NNHCV.EQ.1) GO TO 250
      WRITE(6,2120)
      DO 200 I = 1,NNHCH
      TINF=1238-(1.-TINFH(I))*DTA
      WRITE(6,2110) I,NH1(I),NH2(I),HH(I),TINF
200   CONTINUE
C
C  CYCLE FOR EACH ELEMENT, K , AND FORM THE INFLUENCE
C  MATRIX OF THE SYSTEM
C
C
250   DO 400 K = 1,NE
      N1 = NODE(K,1)
      N2 = NODE(K,2)
      N3 = NODE(K,3)
      RC$(1) = RC(NODE(K,1))
      RC$(2) = RC(NODE(K,2))
      RC$(3) = RC(NODE(K,3))
      ZC$(1) = ZC(NODE(K,1))
      ZC$(2) = ZC(NODE(K,2))
      ZC$(3) = ZC(NODE(K,3))
      RBAR = (RC$(1) + RC$(2) + RC$(3))/3.
      A1 = RC$(2)*ZC$(3) - RC$(3)*ZC$(2)
      A2 = RC$(3)*ZC$(1) - RC$(1)*ZC$(3)
      A3 = RC$(1)*ZC$(2) - RC$(2)*ZC$(1)
      B1 = ZC$(2) - ZC$(3)
      B2 = ZC$(3) - ZC$(1)
      B3 = ZC$(1) - ZC$(2)
      C1 = RC$(3) - RC$(2)
      C2 = RC$(1) - RC$(3)
      C3 = RC$(2) - RC$(1)
      DEL2= ABS(RC$(1)*(ZC$(2)-ZC$(3)) + RC$(2)*(ZC$(3)-ZC$(1)) + RC$(3)
     1*(ZC$(1)-ZC$(2)))
C
C  CALCULATE THE ELEMENTS OF THE MATRIX FOR EACH ELEMENT
C
      VK = (3.1415927*V*RO)/(12.0*TK)
      CONST = (3.1415927*RBAR)/DEL2
```

```
C
      TM$(1,1) = (B1**2 + C1**2)*CONST + (2.*RC$(1) + RC$(2) + RC$(3))*B
     11*VK
      TM$(1,2) = (B1*B2 + C1*C2)*CONST + (RC$(1) + 2.*RC$(2) + RC$(3))*B
     12*VK
      TM$(2,1) = (B1*B2 + C1*C2)*CONST + (2.*RC$(1) + RC$(2) + RC$(3))*B
     11*VK
      TM$(2,2) = (B2**2 + C2**2)*CONST + (RC$(1) + 2.*RC$(2) + RC$(3))*B
     12*VK
      TM$(1,3) = (B1*B3 + C1*C3)*CONST + (RC$(1) + RC$(2) + 2.*RC$(3))*B
     13*VK
      TM$(3,1) = (B1*B3 + C1*C3)*CONST + (2.*RC$(1) + RC$(2) + RC$(3))*B
     11*VK
      TM$(2,3) = (B2*B3 + C2*C3)*CONST + (RC$(1) + RC$(2) + 2.*RC$(3))*B
     13*VK
      TM$(3,2) = (B2*B3 + C2*C3)*CONST + (RC$(1) + 2.*RC$(2) + RC$(3))*B
     12*VK
      TM$(3,3) = (B3**2 + C3**2)*CONST + (RC$(1) + RC$(2) + 2.*RC$(3))*B
     13*VK
C
C  ASSEMBLE SYSTEM MATRIX WITHOUT REGARDING BOUNDARY CONDITIONS
C
      N(1) = N1
      N(2) = N2
      N(3) = N3
      DO 300 I$ = 1,3
      I = N(I$)
      DO 300 J$ = 1,3
      J = N(J$)
      TM(I,J) = TM(I,J) + TM$(I$,J$)
300   CONTINUE
C
CCYCLE FOR NEXT ELEMENT
C
400   CONTINUE
C
C  ACCOUNT FOR CONVECTION AT BOUNDARY,FORM RINF MATRIX
C
      DO 420 I = 1,NNHCV
      BLV(I) = ABS(ZC(NV1(I)) - ZC(NV2(I)))
      CONSTV = 6.1853832*BLV(I)*HV(I)*RO*RC(NV1(I))
      TM(NV1(I),NV1(I)) = TM(NV1(I),NV1(I)) + CONSTV/3.
      TM(NV1(I),NV2(I)) = TM(NV1(I),NV2(I)) + CONSTV/6.
      TM(NV2(I),NV1(I)) = TM(NV2(I),NV1(I)) + CONSTV/6.
      TM(NV2(I),NV2(I)) = TM(NV2(I),NV2(I)) + CONSTV/3.
C
      CINFV = 3.1416*HV(I)*TINFV(I)*RO*RC(NV1(I))*BLV(I)
      RINF(NV1(I)) = RINF(NV1(I)) + CINFV
      RINF(NV2(I)) = RINF(NV2(I)) + CINFV
420   CONTINUE
C
      IF(NNHCT.EQ.1) GO TO 435
      DO 430 I=1,NNHCT
      BLT(I)=ABS(SQRT((RC(NT1(I))-RC(NT2(I)))**2+(ZC(NT1(I))-ZC(NT2(I))
     1)**2))
      RBAR=(RC(NT1(I))+RC(NT2(I)))/2.
      CONSTT=3.1416*HT(I)*RO*BLT(I)/6.
C
      TM(NT1(I),NT1(I))=TM(NT1(I),NT1(I))+CONSTT*(3.*RC(NT1(I))+
     1RC(NT2(I)))
C
      TM(NT1(I),NT2(I))=TM(NT1(I),NT2(I))+CONSTT*2.*RBAR
C
      TM(NT2(I),NT1(I))=TM(NT2(I),NT1(I))+CONSTT*2.*RBAR
```

```
C
      TM(NT2(I),NT2(I))=TM(NT2(I),NT2(I))+CONSTT*(RC(NT1(I))+
     13.*RC(NT2(I)))
C
      CINFT=3.1416*HT(I)*RO*BLT(I)*TINFT(I)/3.
C
      RINF(NT1(I))=RINF(NT1(I))+CINFT*(RC(NT1(I))+2.*RC(NT2(I)))
C
      RINF(NT2(I))=RINF(NT2(I))+CINFT*(2.*RC(NT2(I))+RC(NT1(I)))
C
430   CONTINUE
435   IF(NNHCH.EQ.1) GO TO 445
      DO 440 J = 1,NNHCH
      BLH(J) = SQRT((RC(NH1(J)) - RC(NH2(J)))**2 + (ZC(NH1(J)) - ZC(NH2(
     1J)))**2)
      RBARH(J) = (RC(NH1(J)) + RC(NH2(J)))/2.
      CONSTH = 6.2832*RO*HH(J)*BLH(J)*RBARH(J)
      TM(NH1(J),NH1(J)) = TM(NH1(J),NH1(J)) + CONSTH/3.
      TM(NH1(J),NH2(J)) = TM(NH1(J),NH2(J)) + CONSTH/6.
      TM(NH2(J),NH1(J)) = TM(NH2(J),NH1(J)) + CONSTH/6.
      TM(NH2(J),NH2(J)) = TM(NH2(J),NH2(J)) + CONSTH/3.
      CINF = 3.1416*HH(J)*TINFH(J)*RO*RBARH(J)*BLH(J)
      RINF(NH1(J)) = RINF(NH1(J)) + CINF
      RINF(NH2(J)) = RINF(NH2(J)) + CINF
440   CONTINUE
C
C  MODIFY TM AND RINF TO ACCOUNT FOR NODES WITH SPECIFIED
C        TEMPERATURE
C
445   DO 450 I = 1,NNST
      DO 448 J=1,NN
       RINF(J)=RINF(J)-TM(J,NTS(I))
       TM(NTS(I),J)=0.0
       TM(J,NTS(I))=0.0
448   CONTINUE
      RINF(NTS(I))=1.
      TM(NTS(I),NTS(I))=1.
450   CONTINUE
C
C
C  CALL SOUBROUTINE FSLE TO SOLVE THE LINEAR SYSTEM
C  OF EQUATIONS
C
458   NDIMA = NN
      NSOL = 1
      NDIMBX = NN
      NDIMT = NN
      CALL SLE(NN,NDIMA,TM,NSOL,NDIMBX,RINF,T,IPERM,NDIMT,TT,DET,JEXP)
      GO TO 475
C
C
460   LHB=21
      IJMAX=(LHB-1)*NN+NN-(LHB-1)
      DO 465 I=1,IJMAX
       TB(I)=0.0
465   CONTINUE
      DRATIO=1.E-5
      NRHS=1
      NSCALE=0
      DO 470 J=1,NN
       DO 470 I$=1,LHB
         I=J+I$-1
         IF(I.GT.NN) GO TO 470
         IJ=(LHB-1)*(J-1)+I
         TB(IJ)=TM(I,J)
470   CONTINUE
C
C    CALL DFBAND
C
      CALL DFBAND(TB,RINF,NN,LHB,NRHS,DRATIO,
     1            DET,JEXP,NSCALE)
```

```
C
475   WRITE(6,2500) DET,JEXP
C
C
CPRINT OUTPUT
C
      WRITE(6,2200)
      DO 500 I = 1,NN
       TGR(I)=1.238-(1.-T(I))*DTA/1000.
       WRITE(6,2300) I,T(I),TGR(I)
500   CONTINUE
C
C     CALCULATE NEW GRID
C
      NX=50
      NY=50
      IDIMX=NX
C
      TMIN=TGR(1)
C
      DO 550 I=1,NN
550    IF(TMIN.GT.TGR(I)) TMIN=TGR(I)
C
      WRITE(6,2400) TMIN
C
      XMIN=0.0
      YMIN=0.0
      XMAX=10.
      YMAX=10.
C
      DX=(XMAX-XMIN)/(NX-1)
      DY=(YMAX-YMIN)/(NY-1)
C
      NRNG=2
      C=10.
      OPT=0.0
C
      DO 600 I=1,NN
       RC(I)=(1.-RC(I))*5.0
       ZC(I)=ZC(I)*5.0
600   CONTINUE
C
       CALL CGRID1(TG,IDIMX,NX,NY,XMIN,YMIN,
     1             DX,DY,RC,ZC,TGR,NN,C,NRNG,OPT)
C
C    PLOT GRID
C
      XSIZE=10.
      YSIZE=10.
      NC=12
      IOP(1)=1
      IOP(2)=1
      IOP(3)=0
      IOP(4)=1
      IOP(5)=1
      VOP(5)=3.
      IOP(6)=1
      IOP(7)=0
      IOP(8)=1
      VOP(8)=.12
C
      DTEM=(1.238-TMIN)/(NC-1)
C
      DO 700 I=1,NC
700    CVAL(I)=1.238-DTEM*(I-1)
C
      CALL CONTUR(XSIZE,YSIZE,TG,IDIMX,NX,NY,
     1            CVAL,NC,IOP,VOP)
C
```

```
      CALL PLOTND
C
C
C  FORMAT STATEMENTS
C
1005  FORMAT(2(2X,I3))
1010  FORMAT(4(2X,I3))
1015  FORMAT(2X,F5.2,2X,F7.4,2X,F7.5,2(2X,F7.3))
1018  FORMAT(4F12.5)
1019  FORMAT(6(2X,F10.5))
1020  FORMAT(2X,I4,2(2X,F10.5))
1025  FORMAT(4(2X,I4))
1030  FORMAT(2X,I3,2X,F10.5)
1040  FORMAT(2(2X,I4))
2010  FORMAT(1H1,2X,' A FLEM SOLUTION FOR THE TEMPERATURE FIELD IN LEC-G
     1AAS CRYSTALS',//)
2020  FORMAT(5X,'RADIUS (CM) = ',F7.5,//,5X,'VELOCITY (CM/SEC) = ',F7.5,
     1//5X,'LENGTH (CM) = ',F7.3,//)
2030  FORMAT(5X,'NO. OF NODES = ',I3,//,5X,'NO. OF ELEMENTS = ',I3,//)
2035  FORMAT(5X,'CONE ANGLE =',F12.5,'DEG.',/,
     1       5X,'SEED WIDTH =',F12.5,'CM',/,
     2       5X,'SEED HEIGHT =',F12.5,'CM',/)
2038  FORMAT(5X,'TMP-TINF =',F12.5,'DEG. C',/,
     1       5X,'BORAX HEIGHT =',F12.5,'CM',/)
2040  FORMAT(10X,'NODES VS. NODAL COORDINATES',//,6X,'I',13X,'R(I)',13X,
     1'Z(I)',//)
2050  FORMAT(5X,I3,2(7X,F10.5))
2060  FORMAT(' ',///,15X,'SYSTEM TOPOLOGY',//,'ELEMENT NUMBER',11X,'NODE
     1 NUMBERS',//)
2070  FORMAT(5X,I3,10X,3(5X,I3))
2080  FORMAT(' ',///,5X,'NODES WITH SPECIFIED TEMPERATURES',//,7X,'I',4X
     1,'NODE',6X,'TEMPERATURE',//)
2090  FORMAT(2X,2(4X,I3),5X,F15.7)
2100  FORMAT(' ',//,'BOUNDARY SEGMENTS WHERE CONVECTIVE HEAT FLUX OCCUR'
     1,//,5X,'I',6X,'NODE NUMBER PAIR',4X,'H',8X,'TINF',//,20X,'VERTICAL
     2 BOUNDARY',/)
2105  FORMAT(' ',//,2X,'TILTED BOUNDARY',//)
2110  FORMAT(2X,3(3X,I3),2(8X,F10.5))
2120  FORMAT(' ',/,20X,'NON-VERTICAL BOUNDARY',/)
2200   FORMAT(' ',//,5X,'NODE NUMBER',10X,'T(I)',//)
2300  FORMAT(10X,I3,6X,2(F15.4))
2400  FORMAT(//,10X,'TMIN= ',F15.6)
2500  FORMAT('DETERMINANT IS',G16.7,'10**',I20,//)
      STOP
      END
C
C
C     FUNCTIONS TO CALCULATE TINF
C
C
      REAL FUNCTION TINFBO(DTA,TMBOR,CB2,CB3,CB4,ZZ)
      REAL DTA,CB2,CB3,CB4,ZZ,TMBOR
C
      TINFBO=TMBOR+(CB2*(ZZ-0.000)+CB3*(ZZ-0.000)**2+
     1CB4*(ZZ-0.000)**3)/DTA
C
      RETURN
      END
```

```
C
C
      REAL FUNCTION TINFAR(DTA,TBOR,CA2,CA3,CA4,ZZ)
      REAL DTA,TBOR,CA2,CA3,CA4,ZZ
C
      TINFAR=TBOR+(CA2*(ZZ-3.000)+CA3*(ZZ-3.000)**2+
     1CA4*(ZZ-3.000)**3)/DTA
C
      RETURN
      END
C
C
C     FUNCTIONS TO CALCULATE HTC
C
C
      REAL FUNCTION HBORAX(DTA,TE)
      REAL DTA,TE
C
      HBORAX=0.8*EXP(1.041E-3*(11.-DTA*(1.-TE))-
     13.2671E-6*(11.-DTA*(1.-TE))**2)
C
      RETURN
      END
C
C
      REAL FUNCTION HARGON(DTA,TE)
      REAL DTA,TE
C
      HARGON=0.66*EXP(3.2319E-3*(11.-DTA*(1.-TE)))
C
      RETURN
      END
```

XI.3 Finite Linear Element Program for the Stress Calculations

```
C
C
C THIS PROGRAM CALCULATES THE DISPLACEMENTS AND STRESSES
C  IN LEC_GAAS CRYSTALS DURING GROWTH USING A FLEM METHOD
C
C
      REAL DVMS,XIM,XI,XCN
      REAL*4 STR,E$
      DIMENSION STR(6),E$(3)
      INTEGER*4 IERROR,NVEC
      REAL*8 E,AB
      DIMENSION AB(21),E(6)
      INTEGER*4 NN,NEQ,LH,IJ
      INTEGER*4 JS,JSJS,IJS,JSJ
      INTEGER*4 NSOL,IPERM,NSCALE,LHB
      INTEGER*4 LLB,LUB,IP,JEXP,ITER
      INTEGER*4 NHRS
      REAL*8 EPS,RES
      REAL*8 DAA,DRATIO
      DIMENSION DAA(40000)
      REAL*8 DSS,DDET
      DIMENSION DSS(992)
      DIMENSION SIGRB$(3),SIGTB$(3),SIGZB$(3),TAUB$(3),SSP$(6)
      DIMENSION DSK$(6,6),A(3),B(3),C(3),DSS$(6)
      DIMENSION T$(3),N(3),RC$(3),ZC$(3)
      DIMENSION RC(600),ZC(600),NODE(1000,3),T(600),NSRD(100),NSAD(100)
      DIMENSION U(600),V(600),NSAS(100)
      DIMENSION U$(3),V$(3),SIGR$(3),SIGTH$(3),SIGZ$(3),TAURZ$(3),XBAR(3
     1)
      DIMENSION SIGRP(600),SIGTHP(600),SIGZP(600),TAURZP(600),NEPN(600)
      DIMENSION DEL2P(1000)
      DIMENSION NSS(300)
      DIMENSION W(7),XL(3,7)
      REAL*8 DSK$1,DSK$,DSS$
      REAL*8 FUNC,CONS,ALPHA1,ALPHA2,BETA1,BETA2
      REAL*8 EPR,EPZ,GRZ,TBAR,U,V
      REAL*8 XL,W,RBAR,DEL2,DEL2P,A,B,C
C
      DIMENSION VMS(166),VONMS(50,50),TEMP(50,50)
      DIMENSION CVAL(10),IOP(8),VOP(8)
      REAL VONMS,TEMP,XMIN,XMAX,YMIN,YMAX
      REAL DX,DY,VOP,CVAL,XSIZE,YSIZE,S
      INTEGER IDIMX,IOP,NX,NY,NC,NRNG
C
C  READ THE NUMBER OF NODES AND NODES WITH SPECIFIED DISPLACEMENT
C
      READ(5,1005)NN,NE,NNSRD,NNSAD
C
C  INITIALIZE VARIABLES
C
      NEQ = 2*NN
C
C
      LHB=26
      LH=LHB-1
C
      IJMAX=LH*(NEQ-1)+NEQ
C
      DO 8 I=1,IJMAX
      DAA(I)=0.0
8     CONTINUE
C
```

```
      DO 10 I=1,NEQ
      DSS(I) = 0.0
C
10    CONTINUE
      DO 20 I=1,NN
      U(I) = 0.0
      V(I) = 0.0
      RC(I) = 0.0
      ZC(I) = 0.0
      T(I) = 0.0
      SIGRP(I) = 0.0
      SIGTHP(I) = 0.0
      SIGZP(I) = 0.0
      TAURZP(I) = 0.0
      DEL2P(I)=0.0
20    CONTINUE
C
C  READ CONSTANT AND COEFFICIENTS
C
      READ(5,1010) XNU
      READ(5,1015) RO,VEL,XLE,DTA
C
      DO 100 J = 1,NN
      READ(5,1020) I,RC(I),ZC(I)
100   CONTINUE
C
C  READ SYSTEM TOPOLOGY
C
      DO 105 I = 1,NE
      READ(5,1025)J,NODE(J,1),NODE(J,2),NODE(J,3)
105   CONTINUE
C
C
C  READ NODE NUMBERS WITH SPECIFIED DISPLACEMENT
C
      NNSRD=0
      DO 110 I = 1,NN
       IF(RC(I).GT.0.0) GO TO 110
       NNSRD=NNSRD+1
       NSRD(NNSRD)=I
      WRITE(6,1030) NSRD(NNSRD)
110   CONTINUE
C
C
C  READ TEMPERATURES
C
      DO 120 J = 1,NN
      READ(5,1040)I,T(I)
120   CONTINUE
C
C  PRINT DATA AND HEADLINES
C
      WRITE(6,2010)
      WRITE(6,2020)RO,VEL,XLE
      WRITE(6,2030)XNU
      WRITE(6,2035)NN,NE,NNSRD
C
C
C  PRINT HEADLINES FOR DISPLACEMENTS
C
      WRITE(6,2100)
C
C  FORM MATRIX FOR INITIAL STRAIN AND STIFFNESS MATRIX
C
C
C    GIVE VALUES TO WEIGHT FUNCTIONS AND NATURAL
C
C      COORDINATES FOR NUMERICAL INTEGRATION OF
C
C             QUINTIC ORDER
C
```

```
      ALPHA1=.059715871789770
      BETA1=.470142064105115
      ALPHA2=.797426985353087
      BETA2=.101286507323456
C
      W(1)=.225
      W(2)=.132394152788506
      W(3)=W(2)
      W(4)=W(3)
      W(5)=.125939180544827
      W(6)=W(5)
      W(7)=W(6)
C
      XL(1,1)=1./3.
      XL(1,2)=ALPHA1
      XL(1,3)=BETA1
      XL(1,4)=BETA1
      XL(1,5)=ALPHA2
      XL(1,6)=BETA2
      XL(1,7)=BETA2
C
      XL(2,1)=1./3.
      XL(2,2)=BETA1
      XL(2,3)=ALPHA1
      XL(2,4)=BETA1
      XL(2,5)=BETA2
      XL(2,6)=ALPHA2
      XL(2,7)=BETA2
C
      DO 140 I=1,7
      XL(3,I)=1.-(XL(1,I)+XL(2,I))
140   CONTINUE
      DO 400 K=1,NE
C
      N(1) = NODE(K,1)
      N(2) = NODE(K,2)
      N(3) = NODE(K,3)
C
      TBAR=(T(NODE(K,1))+T(NODE(K,2))+T(NODE(K,3)))/3.
      T$(1) = TBAR
      T$(2) = TBAR
      T$(3) = TBAR
C
      RC$(1) = RC(NODE(K,1))
      RC$(2) = RC(NODE(K,2))
      RC$(3) = RC(NODE(K,3))
C
      ZC$(1) = ZC(NODE(K,1))
      ZC$(2) = ZC(NODE(K,2))
      ZC$(3) = ZC(NODE(K,3))
C
      A(1) = RC$(2)*ZC$(3) - RC$(3)*ZC$(2)
      A(2) = RC$(3)*ZC$(1) - RC$(1)*ZC$(3)
      A(3) = RC$(1)*ZC$(2) - RC$(2)*ZC$(1)
C
      B(1) = ZC$(2) - ZC$(3)
      B(2) = ZC$(3) - ZC$(1)
      B(3) = ZC$(1) - ZC$(2)
C
      C(1) = RC$(3)- RC$(2)
      C(2) = RC$(1) - RC$(3)
      C(3) = RC$(2) - RC$(1)
C
      RBAR = (RC$(1) + RC$(2) + RC$(3))/3.
      ZBAR = (ZC$(1) + ZC$(2) + ZC$(3))/3.
      DEL2 = ABS(RC$(1)*(ZC$(2) - ZC$(3)) + RC$(2)*(ZC$(3) - ZC$(1))+
     1RC$(3)*(ZC$(1) - ZC$(2)))
C
C
C
```

```
C
      DO 200 I$=1,3
C
C  FORM MATRIX FOR INITIAL STRAIN IN ELEMENT K
C
      K$ = 2*I$ - 1
      DSS$(K$)=T$(I$)*(B(I$)*RBAR+DEL2/3.)/2.
C
      K$ = 2*I$
      DSS$(K$) = T$(I$)*RBAR*C(I$)/2.
C
C FORM STIFFNESS MATRIX FOR ELEMENT K
C
      DO 200 J$ = 1,3
C
C     INTEGRATE NUMERICALLY TERM IN L(I$)*L(J$)/RO
C
      FUNC=0.0
C
      DO 195 I=1,7
      FUNC=FUNC+W(I)*XL(I$,I)*XL(J$,I)/
     1(RC$(1)*XL(1,I)+RC$(2)*XL(2,I)+RC$(3)*XL(3,I))
195   CONTINUE
C
      IF(I$.EQ.J$) GO TO 198
      PIN=(1.-XNU)*DEL2/(24.*RBAR)
      GO TO 199
198   PIN=(1.-XNU)*DEL2/(12.*RBAR)
C
C
199   DSK$1=((1.-XNU)*B(I$)*B(J$)+(.5-XNU)*C(I$)*C(J$))*RBAR/(2.*DEL2)
C
      K$=2*I$-1
      L$=2*J$-1
C
      DSK$(K$,L$)=DSK$1+XNU*(B(I$)+B(J$))/6.+FUNC*DEL2*(1-XNU)/2.
C
      K$=2*I$
C
      DSK$(K$,L$)=(XNU*B(J$)*C(I$)+(.5-XNU)*B(I$)*C(J$))*
     1RBAR/(2.*DEL2)+XNU*C(I$)/6.
C
      L$=2*J$
C
      DSK$(K$,L$)=((1.-XNU)*C(I$)*C(J$)+(.5-XNU)*B(I$)*B(J$))*
     1RBAR/(2.*DEL2)
C
      K$=2*I$-1
C
      DSK$(K$,L$)=(XNU*B(I$)*C(J$)+(.5-XNU)*B(J$)*C(I$))*
     1RBAR/(2.*DEL2)+XNU*C(J$)/6.
C
C
C  CYCLE FOR NEXT NODE
C
200   CONTINUE
C
      GO TO 262
C
C
C     CALCULATE EINGENVALUES OF THE
C     STIFFNESS ELEMENT MATRIX
C
C
      WRITE(6,2510)K
C
      DO 250 I$=1,6
      DO 250 J$=1,I$
      I$J$=I$*(I$-1)/2+J$
      AB(I$J$)=DSK$(I$,J$)
250   CONTINUE
C
```

```
      NVEC=0
      NEQ$=6
      CALL DSYMAL(AB,NEQ$,E,IERROR,NVEC)
C
      DO 260 I$=1,6
      WRITE(6,261) I$,E(I$)
260   CONTINUE
C
261   FORMAT(I3,F12.8)
      WRITE(6,2510) IERROR
C
C
C
C  ASSEMBLE MATRICES WITHOUT REGARDING B.C.
C
262   DO 300 I$=1,3
C
      I = N(I$)
C
      M$ = 2*I$ - 1
      M = 2*I - 1
      DSS(M) = DSS(M) + DSS$(M$)
C
      M$ = 2*I$
      M = 2*I
      DSS(M) = DSS(M) + DSS$(M$)
C
C
      DO 300 J$ = 1,3
C
      J = N(J$)
C
      M$ = 2*I$ - 1
      M = 2*I - 1
      N$ = 2*J$ - 1
      N1 = 2*J - 1
      IF(N1.GT.M) GO TO 280
C
      IJ=LH*(N1-1)+M
C
      DAA(IJ)=DAA(IJ)+DSK$(M$,N$)
C
C
280   N$ = 2*J$
      N1 = 2*J
      IF(N1.GT.M) GO TO 285
C
      IJ=LH*(N1-1)+M
C
      DAA(IJ)=DAA(IJ)+DSK$(M$,N$)
C
C
285   M$ = 2*I$
      M = 2*I
      IF(N1.GT.M) GO TO 290
C
      IJ=LH*(N1-1)+M
C
      DAA(IJ)=DAA(IJ)+DSK$(M$,N$)
C
C
290   N$ = 2*J$ - 1
      N1 = 2*J - 1
      IF(N1.GT.M) GO TO 300
C
      IJ=LH*(N1-1)+M
C
      DAA(IJ)=DAA(IJ)+DSK$(M$,N$)
C
C
C  ASSEMBLE ELEMENTS OF THE NEXT NODE IN ELEMENT K
C
300   CONTINUE
```

```
C
C  CYCLE FOR NEXT ELEMENT
C
400   CONTINUE
C
C  MODIFY SK AND SS TO ACCOUNT FOR
C
C  NODES WITH SPECIFIED DISPLACEMENT
C
C
C       FOR AXIAL NODES NO RADIAL
C            DISPLACEMENT
C
      DO 500 J$=1,NNSRD
       JS=2*NSRD(J$)-1
       JSJS=LH*(JS-1)+JS
       DAA(JSJS)=1.0
       DSS(JS)=0.0
       DO 490 I$=1,LH
        I=JS+I$
        IJS=LH*(JS-1)+I
        DAA(IJS)=0.0
C
485     IF(I$.GT.JS.OR.I$.EQ.JS) GO TO 490
        J=JS-I$
        JSJ=LH*(J-1)+JS
        DAA(JSJ)=0.0
490    CONTINUE
500   CONTINUE
C
C
C       FOR NODE 1,NO AXIAL
C         DISPLACEMENT
C
      JS=2
      JSJS=LH*(JS-1)+JS
      DAA(JSJS)=1.0
      DSS(JS)=0.0
C
      DO 505 I$=1,LH
       I=JS+I$
       IJS=LH*(JS-1)+I
       DAA(IJS)=0.0
       IF(I$.GT.JS.OR.I$.EQ.JS) GO TO 505
       J=JS-I$
       JSJ=LH*(J-1)+JS
       DAA(JSJ)=0.0
505   CONTINUE
C
C
      DRATIO=1.E-5
      NRHS=1
      NSCALE=0
C
C  SOLVE THE LINEAR SYSTEM
C
C  CALLING DFBAND
C
C
C
      CALL DFBAND(DAA,DSS,NEQ,LHB,NRHS,DRATIO,DDET,JEXP,NSCALE)
C
      WRITE(6,2005) DDET,JEXP
C
C
C  PRINT DISPLACEMENTS
C
C
      WRITE(6,2115)
      DO 600 I = 1,NN
      J = 2*I - 1
      U(I) = DSS(J)
      K = 2*I
      V(I)=DSS(K)
```

```
C
      WRITE(6,2110)I,U(I),V(I)
600   CONTINUE
C
C
C  CALCULATE STRESSES AT ALL NODES IN EACH ELEMENT
C
C
      DO 700 I = 1,NE
C
      N(1)=NODE(I,1)
      N(2)=NODE(I,2)
      N(3)=NODE(I,3)
C
      RC$(1) = RC(NODE(I,1))
      RC$(2) = RC(NODE(I,2))
      RC$(3) = RC(NODE(I,3))
C
      ZC$(1) = ZC(NODE(I,1))
      ZC$(2) = ZC(NODE(I,2))
      ZC$(3) = ZC(NODE(I,3))
C
C
      TBAR=(T(NODE(I,1))+T(NODE(I,2))+T(NODE(I,3)))/3.
C
C
      T$(1) = TBAR
      T$(2) = TBAR
      T$(3) = TBAR
C
      U$(1) = U(NODE(I,1))
      U$(2) = U(NODE(I,2))
      U$(3) = U(NODE(I,3))
C
      V$(1) = V(NODE(I,1))
      V$(2) = V(NODE(I,2))
      V$(3) = V(NODE(I,3))
C
      A(1)=RC$(2)*ZC$(3)-RC$(3)*ZC$(2)
      A(2)=RC$(3)*ZC$(1)-RC$(1)*ZC$(3)
      A(3)=RC$(1)*ZC$(2)-RC$(2)*ZC$(1)
C
      B(1) = ZC$(2) - ZC$(3)
      B(2) = ZC$(3) - ZC$(1)
      B(3) = ZC$(1) - ZC$(2)
C
      C(1) = RC$(3) - RC$(2)
      C(2) = RC$(1) - RC$(3)
      C(3) = RC$(2) - RC$(1)
C
      DEL2=ABS(RC$(1)*(ZC$(2)-ZC$(3))+RC$(2)*(ZC$(3)-ZC$(1))+RC$(3)*(ZC$
     1(1)-ZC$(2)))
C
      RBAR=(RC$(1)+RC$(2)+RC$(3))/3.
      ZBAR=(ZC$(1)+ZC$(2)+ZC$(3))/3.
C
C
      EPR=(B(1)*U$(1)+B(2)*U$(2)+B(3)*U$(3))/DEL2
C
      EPZ=(C(1)*V$(1)+C(2)*V$(2)+C(3)*V$(3))/DEL2
C
      GRZ=(C(1)*U$(1)+C(2)*U$(2)+C(3)*U$(3)+
     1B(1)*V$(1)+B(2)*V$(2)+B(3)*V$(3))/DEL2
C
C  CALCULATE STRESSES AT EACH NODE IN ELEMENT I
C
      DO 900 I$=1,3
C
      IF(RC$(I$).EQ.0.0)GO TO 895
C
      SIGR$(I$)=(1.-XNU)*EPR+XNU*EPZ+XNU*U$(I$)/RC$(I$)-T$(I$)
```

```
C
      SIGTH$(I$)=XNU*(EPR+EPZ)+(1.-XNU)*U$(I$)/RC$(I$)-T$(I$)
C
      SIGZ$(I$)=XNU*EPR+(1.-XNU)*EPZ+XNU*U$(I$)/RC$(I$)-T$(I$)
C
      TAURZ$(I$)=(1.-2.*XNU)*GRZ/2.
C
      GO TO 899
C
895   SIGR$(I$)=EPR+XNU*EPZ-T$(I$)
C
      SIGTH$(I$)=SIGR$(I$)
C
      SIGZ$(I$)=2.*XNU*EPR+(1.-XNU)*EPZ-T$(I$)
C
      TAURZ$(I$)=(1.-2.*XNU)*GRZ/2.
C
899   SIGRP(N(I$))=SIGRP(N(I$))+SIGR$(I$)*DEL2
      SIGTHP(N(I$))=SIGTHP(N(I$))+SIGTH$(I$)*DEL2
      SIGZP(N(I$))=SIGZP(N(I$))+SIGZ$(I$)*DEL2
      TAURZP(N(I$))=TAURZP(N(I$))+TAURZ$(I$)*DEL2
      DEL2P(N(I$))=DEL2P(N(I$))+DEL2
C
C   CYCLE FOR NEXT NODE IN ELEMENT I
C
900   CONTINUE
C
C
C
C  CYCLE FOR NEXT ELEMENT
C
700   CONTINUE
C
C  CALCULATION OF AVERAGE STRESSES AT ALL NODES
C
      WRITE(6,2550)
      WRITE(6,2555)
C
C
      DO 960 I=1,NN
C
      SIGRAV=SIGRP(I)/DEL2P(I)
      SIGTHA=SIGTHP(I)/DEL2P(I)
      SIGZAV=SIGZP(I)/DEL2P(I)
      TAURZA=TAURZP(I)/DEL2P(I)
C
C    CALCULATE PRINCIPAL STRESSES AND VON MISES STRESSES
C
      DO 950 I$=1,6
      STR(I$)=0.0
950   CONTINUE
C
      STR(1)=SIGRAV
      STR(3)=SIGTHA
      STR(4)=TAURZA
      STR(6)=SIGZAV
C
      N$=3
      NVEC=0
C
      CALL SYMAL(STR,N$,E$,IERROR,NVEC)
C
      VMS(I)=SQRT(((E$(3)-E$(2))**2+(E$(3)-E$(1))**2+
     1(E$(2)-E$(1))**2)/2.)
C
      VMS(I)=VMS(I)*2.91*DTA
      WRITE(6,2560)I,SIGRAV,SIGTHA,SIGZAV,TAURZA,VMS(I)
C
960   CONTINUE
C
C   PLOT CONTOURS OF VONMS AND TEMP
C
```

```
      NC=10
      NX=50
      NY=50
      IDIMX=NX
      XMIN=0.0
      YMIN=0.0
      XMAX=10.
      YMAX=10.
      DX=(XMAX-XMIN)/(NX-1)
      DY=(YMAX-YMIN)/(NY-1)
C
      DO 970 I=1,NN
      RC(I)=RC(I)*5.0
      ZC(I)=ZC(I)*5.0

970   CONTINUE
C
C
      VMSMIN=VMS(1)
C
      DO 975 I=1,NN
975   IF(VMSMIN.GT.VMS(I)) VMSMIN=VMS(I)
C
      VMSMAX=VMS(1)
C
      DO 978 I=1,NN
978   IF(VMSMAX.LT.VMS(I)) VMSMAX=VMS(I)
C
      DVMS=(VMSMAX-VMSMIN)
C
      NRNG=2
      S=10.
      OPT=0.0
C
      CALL CGRID1(VONMS,IDIMX,NX,NY,XMIN,YMIN,DX,DY,
     1RC,ZC,VMS,NN,S,NRNG,OPT)
C
C
      XSIZE=10.
      YSIZE=10.
      IOP(1)=1
      IOP(2)=1
      IOP(3)=0
      IOP(4)=1
      IOP(5)=0
      IOP(6)=1
      IOP(7)=0
      IOP(8)=1
      VOP(8)=.08
      IDIMX=NX
C
      M=1
      XNC=NC
C
      DO 985 I=1,NC
       XI=I
       XIM=(XI-1.)/(XNC-1.)
       CVAL(I)=VMSMIN+DVMS*XIM**M
985   CONTINUE
      CALL CONTUR(XSIZE,YSIZE,VONMS,IDIMX,NX,NY,
     1CVAL,NC,IOP,VOP)
C
C
      CALL PLOTND
990   WRITE(6,2001)
C
C
C  READEING FORMATS
C
1005  FORMAT(4(2X,I3))
1015  FORMAT(2X,F5.2,2X,F7.5,2(2X,F7.3))
1010  FORMAT(2X,F5.3,2(2X,E12.5),2X,F10.2)
1020  FORMAT(2X,I4,2(2X,F10.5))
```

```
1025  FORMAT(4(2X,I4))
1030  FORMAT(2X,I3)
1040  FORMAT(10X,I3,6X,F15.4)
C
C  WRITING FORMATS
C
2001  FORMAT('SOLUTION FAILED')
2005  FORMAT('DETERMINANT IS',G16.7,'*10**',I20)
2010  FORMAT(2X,'A FLEM SOLUTION FOR THERMAL DISPLACEMENTS',//,5X,'AND S
     1TRESSES IN LEC-GAAS CRYSTALS',//)
2020  FORMAT(5X,'RADIUS (CM) = ',F7.5,/,5X,'VELOCITY (CM/SEC) =',F7.5,/,
     15X,'LENGTH (CM) =',F7.3,//)
2030  FORMAT(5X,'NU =',F5.3,/)
2035  FORMAT(5X,'NUMBER OF NODES = ',I3,/,5X,'NUMBER OF ELEMENTS = ',I3
     1,/,5X,'NO.OF NODES WITH NO RADIAL DISPLACEMENT = ',I3,/,5X,'NO.OF
     2NODES WITH NO AXIAL DISPLACEMNT = ',I3,/)
2040  FORMAT(10X,'NODES VS NODAL COORDINATES AND VS TEMPERATURE',//,6X,'
     1I',13X,'R(I)',9X,'Z(I)',4X,'TEMEPERATURE',//)
2050  FORMAT(5X,I3,4X,2(3X,F10.5),2X,F15.4)
2060  FORMAT(' ',//,15X,'SYSTEM TOPOLOGY',//,'ELEMENT NUMBER',11X,'NODE
     1NUMBERS',//)
2070  FORMAT(5X,I3,10X,3(5X,I3))
2080  FORMAT(' ',//,5X,'NODES ON THE AXIS WITH NO RADIAL DISPLACEMENT',/
     1)
2085  FORMAT(' ',/,5X,'NODES WITH NO AXIAL DISPLACEMENT',/)
2090  FORMAT(20X,I3)
2099  FORMAT(/,5X,'ITERATION NUMBER = ',I3,//)
2100  FORMAT(' ',//,10X,'DISPLACEMENT FIELD: RADIAL AND AXIAL',/,5X,'NOD
     1E NUMBER',4X,'RADIAL',11X,'AXIAL',/)
2110  FORMAT(9X,I3,2(5X,E15.6))
2115  FORMAT(5X,'CALCULATED DISPLACEMENT FIELD',/)
2120  FORMAT(/,5X,'NODES AND DISPLACEMENTS AT THE FREE BOUNDARY',/)
2500  FORMAT(' ',//,2X,'STRESSES CALCULATED AT ALL NODES IN EACH ELEMENT
     1',//,2X,'ELEMENT',1X,'NODE',4X,'SIGMAR',4X,'SIGMATH',4X,'SIGMAZZ',
     25X,'TAURZ',//)
2510  FORMAT(5X,I3)
2520  FORMAT(10X,I3,5X,4(E14.5))
2550  FORMAT(' ',/,5X,'AVERAGE STRESSES AT EACH NODE',/)
2555  FORMAT(2X,'NODE',2X,'NEPN',7X,'SIGRAV',7X,'SIGTHAV',6X,'SIGZAV',8X
     1,'TAURZAV',/)
2560  FORMAT(1X,I3,3X,5(E14.5))
C
C
      STOP
      END
```

XI.4 Finite Quadratic Element Program for the Stress Calculations

```
C
C
C THIS PROGRAM CALCULATES THE DISPLACEMENTS AND STRESSES
C  IN LEC_GAAS CRYSTALS DURING GROWTH USING A FQEM METHOD
C
C
C  ELEMENTS ARE CALCULATED EXACTLY AND USING
C
C  A QUINTIC NUMERICAL INTEGRATION FORMULA
C
C
      REAL*4 STR,E$,VMS
      DIMENSION STR(6),E$(3)
      INTEGER*4 IERROR,NVEC,NEQ$
      REAL*4 E
      DIMENSION AB(78),E(12)
      INTEGER*4 NN,NEQ
      INTEGER*4 NSOL,IPERM
      INTEGER*4 LLB,LUB,NHRS,IP,JEXP,ITER
      REAL*4 A,B,EPS,RES
      DIMENSION AA(11160),BB(90),IP(90),RES(90)
      DIMENSION IJ(90,90)
      REAL*4 SK,SS,DES,DESDD,DET,SSN,DDES,DELDES
      DIMENSION SK(90,90),DES(90),SS(90),IPERM(180),DESDD(90,90)
      DIMENSION SK$(12,12),SS$(12),T$(6),N(6),RC$(6),ZC$(6)
      DIMENSION A(3),B(3),C(3)
      DIMENSION RC(300),ZC(300),NODE(600,6),T(300),NSRD(100),NSAD(100)
      DIMENSION U(300),V(300),NSAS(300)
      DIMENSION U$(6),V$(6)
      DIMENSION SIGRP(300),SIGTHP(300),SIGZP(300),TAURZP(300),NEPN(300)
      DIMENSION DEL2P(300)
      DIMENSION NSS(300)
C
      DIMENSION W(7),XL(3,7)
      REAL*4 ALPHA1,ALPHA2,BETA1,BETA2,W,XL
C
C
C
C   READ NUMBER OF NODES AND NODES
C
C   WITH SPECIFIED DISPLACEMENTS
C
C
      READ(5,1005)NN,NE,NNSRD,NNSAD
C
C  INITIALIZE VARIABLES
C
      NEQ = 2*NN
C
      DO 10 I=1,NEQ
      SS(I) = 0.0
      DES(I) = 0.0
C
      DO 10 J=1,NEQ
      SK(I,J) = 0.0
10    CONTINUE
      DO 20 I=1,NN
      U(I) = 0.0
      V(I) = 0.0
      RC(I) = 0.0
      ZC(I) = 0.0
      T(I) = 0.0
      SIGRP(I) = 0.0
      SIGTHP(I) = 0.0
```

```
      SIGZP(I) = 0.0
      TAURZP(I) = 0.0
      DEL2P(I)=0.0
20    CONTINUE
C
C  READ CONSTANT AND COEFFICIENTS
C
      READ(5,1010) XNU
      READ(5,1015) RO,VEL,XLE
C
      DO 100 J = 1,NN
      READ(5,1020) I,RC(I),ZC(I)
      WRITE(6,1020) I,RC(I),ZC(I)
100   CONTINUE
C
C  READ SYSTEM TOPOLOGY
C
      DO 105 I = 1,NE
      READ(5,1025)J,(NODE(J,I$),I$=1,6)
      WRITE(6,1025)J,(NODE(J,I$),I$=1,6)
105   CONTINUE
C
C
C  READ NODE NUMBERS WITH SPECIFIED DISPLACEMENT
C
      DO 110 I = 1,NNSRD
      READ(5,1030) NSRD(I)
      WRITE(6,1030) NSRD(I)
110   CONTINUE
C
C
C  READ TEMPERATURES
C
      DO 120 J = 1,NN
      READ(5,1040) I,T(I)
120   CONTINUE
C
C  PRINT DATA AND HEADLINES
C
      WRITE(6,2010)
      WRITE(6,2020)RO,VEL,XLE
      WRITE(6,2030)XNU
      WRITE(6,2035)NN,NE,NNSRD
C
C
C  PRINT HEADLINES FOR DISPLACEMENTS
C
      WRITE(6,2100)
C
C  FORM MATRIX FOR INITIAL STRAIN AND STIFFNESS MATRIX
C
C     GIVE VALUES TO WEIGHT FUNCTIONS AND
C
C     NATURAL COORDINATES FOR NUMERICAL
C
C     INTEGRARTION OF QUINTIC ORDER
C
      ALPHA1=.05971587178977
      BETA1 =.47014206410511 5
      ALPHA2=.797426985353087
      BETA2 =.101286507323456
C
      W(1)=.225
      W(2)=.132394152788506
      W(3)=W(2)
      W(4)=W(2)
      W(5)=.125939180544827
      W(6)=W(5)
      W(7)=W(5)
C
```

```
      XL(1,1)=1./3.
      XL(1,2)=ALPHA1
      XL(1,3)=BETA1
      XL(1,4)=BETA1
      XL(1,5)=ALPHA2
      XL(1,6)=BETA2
      XL(1,7)=BETA2
C
      XL(2,1)=1./3.
      XL(2,2)=BETA1
      XL(2,3)=ALPHA1
      XL(2,4)=BETA1
      XL(2,5)=BETA2
      XL(2,6)=ALPHA2
      XL(2,7)=BETA2
C
      DO 140 I=1,7
      XL(3,I)=1.-(XL(1,I)+XL(2,I))
140   CONTINUE
C
C
      DO 600 K=1,NE
C
C
      DO 180 I$=1,6
      N(I$)=NODE(K,I$)
      RC$(I$)=RC(NODE(K,I$))
      ZC$(I$)=ZC(NODE(K,I$))
180   CONTINUE
C
C
      DO 185 I$=1,3
      T$(I$)=T(NODE(K,I$))
      I$R=I$+3
      I$1=I$+1
      IF(I$1.GT.3) I$1=I$1-3
      T$(I$R)=(T(NODE(K,I$))+T(NODE(K,I$1)))/2.
C
185   CONTINUE
C
      GO TO 189
      TBAR=0.0
      DO 187 I$=1,6
      TBAR=TBAR + T(NODE(K,I$))
187   CONTINUE
      DO 188 I$=1,6
      T$(I$)=TBAR/6.
188   CONTINUE
189    DO 190 I$=1,3
       J$=I$+1
       K$=J$+1
       IF(J$.GT.3) J$=J$-3
       IF(K$.GT.3) K$=K$-3
C
       A(I$)=RC$(J$)*ZC$(K$)-RC$(K$)*ZC$(J$)
       B(I$)=ZC$(J$)-ZC$(K$)
       C(I$)=RC$(K$)-RC$(J$)
C
190    CONTINUE
C
      SR = RC$(1) + RC$(2) + RC$(3)
      RBAR=SR/3.
      ZBAR = (ZC$(1) + ZC$(2) + ZC$(3))/3.
      DEL2 = ABS(RC$(1)*(ZC$(2) - ZC$(3)) + RC$(2)*(ZC$(3) - ZC$(1))+
     1RC$(3)*(ZC$(1) - ZC$(2)))
C
C
C  FORM MATRIX FOR INITIAL STRAIN IN ELEMENT K
C
C    FORM MATRIX FOR INITIAL STRAIN
C    IN ELEMENT K NODES 1 TO 3
C
```

```
      DO 230 I$=1,3
C
       K$=2*I$-1
      SS$(K$)=T$(I$)*B(I$)*RC$(I$)/6.
C
       K$=2*I$
      SS$(K$)=T$(I$)*C(I$)*RC$(I$)/6.
C
C   FORM STIFFNESS MATRIX FOR ELEMENT K
C         NODES 1 TO 3
C
      DO 230 J$=1,3
      XNT=0.0
C
C
C     INTEGRATE NUMERICALLY TERM IN LI'S
C
      DO 195 I=1,7
C
      XNT=XNT+W(I)*XL(I$,I)*(2.*XL(I$,I)-1.)*
     1XL(J$,I)*(2.*XL(J$,I)-1.)/
     2(RC$(1)*XL(1,I)+RC$(2)*XL(2,I)+RC$(3)*XL(3,I))
C
195   CONTINUE
C
      IF(I$.EQ.J$)GO TO 210
C
      X1=-(SR+RC$(I$)+RC$(J$))/(30.*DEL2)
      X2=-.5
      GO TO 215
C
210   X1=(SR+2.*RC$(I$))/(10.*DEL2)
      X2=1.
 215   K$=2*I$-1
       L$=2*J$-1
C
       SK1=((1.-XNU)*B(I$)*B(J$)+(.5-XNU)*C(I$)*C(J$))*X1
C
       SK$(K$,L$)=SK1+X2*(B(I$)+B(J$))*XNU/15.+(1.-XNU)*
     1DEL2*XNT/2.
C
       K$=2*I$
C
       SK$(K$,L$)=(XNU*C(I$)*B(J$)+(.5-XNU)*C(J$)*B(I$))*
     1X1+X2*XNU*C(I$)/15.
C
       L$=2*J$
C
       SK$(K$,L$)=((1.-XNU)*C(I$)*C(J$)+(.5-XNU)*B(I$)*B(J$))*X1
C
       K$=2*I$-1
C
       SK$(K$,L$)=(XNU*B(I$)*C(J$)+(.5-XNU)*C(I$)*B(J$))*
     1X1+X2*XNU*C(J$)/15.
C
230   CONTINUE
C
C  FORM INITIAL STRAIN MATRIX FOR
C     NODES 4 TO 6
C
      DO 250 I$=1,3
C
       I$1=I$+1
       IF(I$1.GT.3) I$1=I$1-3
C
       I$R=I$+3
C
       K$=2*I$R-1
C
      SS$(K$)=T$(I$R)*(B(I$)*(SR+RC$(I$1))+
     1B(I$1)*(SR+RC$(I$))+DEL2)/6.
C
```

```
        K$=2*I$R
C
        SS$(K$)=T$(I$R)*(C(I$)*(SR+RC$(I$1))+
       1C(I$1)*(SR+RC$(I$)))/6.
C
C    FORM MATRIX FOR NODES 4 TO 6
C
        DO 250 J$=1,3
C
         J$1=J$+1
         IF(J$1.GT.3) J$1=J$1-3

C
C
C     INTEGRATION OF TERM IN LI'S AND LJ'S
C
        YNT=0.0
C
        DO 235 I=1,7
C
        YNT=YNT+W(I)*XL(I$,I)*XL(I$1,I)*XL(J$,I)*XL(J$1,I)/
       1(RC$(1)*XL(1,I)+RC$(2)*XL(2,I)+RC$(3)*XL(3,I))
C
235     CONTINUE
C
        SR1=SR+RC$(I$1)+RC$(J$1)
        SR2=SR+RC$(I$)+RC$(J$)
        SR3=SR+RC$(I$1)+RC$(J$)
        SR4=SR+RC$(I$)+RC$(J$1)
C
        Y11=B(I$)*B(J$)*SR1+B(I$1)*B(J$1)*SR2+
       1B(I$)*B(J$1)*SR3+B(I$1)*B(J$)*SR4
C
        Y44=C(I$)*C(J$)*SR1+C(I$1)*C(J$1)*SR2+
       1C(I$)*C(J$1)*SR3+C(I$1)*C(J$)*SR4
C
        Y14=B(I$)*C(J$)*SR1+B(I$1)*C(J$1)*SR2+
       1B(I$)*C(J$1)*SR3+B(I$1)*C(J$)*SR4
C
        Y41=C(I$)*B(J$)*SR1+C(I$1)*B(J$1)*SR2+
       1C(I$)*B(J$1)*SR3+C(I$1)*B(J$)*SR4
C
        IF(I$.EQ.J$) GO TO 240
C
        IF(I$1.EQ.J$) GO TO 238
C
C   OTHERWISE J$+1=I$, NEXT
C
        Y11=Y11+B(I$1)*B(J$)*SR4
C
        Y44=Y44+C(I$1)*C(J$)*SR4
C
        Y14=Y14+B(I$1)*C(J$)*SR4
C
        Y41=Y41+C(I$1)*B(J$)*SR4
C
        YI11=B(I$)+2.*B(I$1)+2.*B(J$)+B(J$1)
        YI12=2.*C(J$)+C(J$1)
        YI21=C(I$)+2.*C(I$1)
C
        GO TO 245
C
238     Y11=Y11+B(I$)*B(J$1)*SR3
C
        Y44=Y44+C(I$)*C(J$1)*SR3
C
        Y14=Y14+B(I$)*C(J$1)*SR3
C
        Y41=Y41+C(I$)*B(J$1)*SR3
C
```

```
      YI11=2.*B(I$)+B(I$1)+B(J$)+2.*B(J$1)
      YI12=C(J$)+2.*C(J$1)
      YI21=2.*C(I$)+C(I$1)
C
      GO TO 245
C
240   Y11=Y11+B(I$)*B(J$)*SR1+B(I$1)*B(J$1)*SR2
C
      Y44=Y44+C(I$)*C(J$)*SR1+C(I$1)*C(J$1)*SR2
C
      Y14=Y14+B(I$)*C(J$)*SR1+B(I$1)*C(J$1)*SR2
C
      Y41=Y41+C(I$)*B(J$)*SR1+C(I$1)*B(J$1)*SR2
C
      YI11=2.*(B(I$)+B(I$1)+B(J$)+B(J$1))
      YI12=2.*(C(J$)+C(J$1))
      YI21=2.*(C(I$)+C(I$1))
C
C
 245   J$R=J$+3
C
       K$=2*I$R-1
       L$=2*J$R-1
C
      SK$(K$,L$)=(((1.-XNU)*Y11+(.5-XNU)*Y44)/
     1DEL2+XNU*YI11)/7.5+8.*(1.-XNU)*DEL2*YNT
C
       K$=2*I$R
C
      SK$(K$,L$)=((XNU*Y41+(.5-XNU)*Y14)/DEL2+
     1XNU*YI21)/7.5
C
       L$=2*J$R
C
      SK$(K$,L$)=((1.-XNU)*Y44+(.5-XNU)*Y11)/(DEL2*7.5)
C
       K$=2*I$R-1
C
      SK$(K$,L$)=((XNU*Y14+(.5-XNU)*Y41)/DEL2+
     1XNU*YI12)/7.5
C
250   CONTINUE
C
C   STIFFNESS MATRIX FOR MIXED NODES
C
      DO 290 I$=1,3
      DO 290 J$=1,3
C
       J$R=J$+3
C
       J$1=J$+1
       IF(J$1.GT.3) J$1=J$1-3
C
C
C     INTEGRATE TERM IN LJ'S AND LQ'S
C
      ZNT=0.0
C
      DO 255 I=1,7
C
      ZNT=ZNT+W(I)*XL(I$,I)*(2.*XL(I$,I)-1.)*
     1XL(J$,I)*XL(J$1,I)/
     2(RC$(1)*XL(1,I)+RC$(2)*XL(2,I)+RC$(3)*XL(3,I))
C
255   CONTINUE
C
      IF(I$.EQ.J$) GO TO 270
C
      IF(I$.EQ.J$1) GO TO 260
C
C   OTHERWISE Q NOT = I AND I+1 NOT =Q,NEXT
C
```

```
      Z11=(B(J$)+B(J$1))*(4.*RC$(I$)-SR)-
     1(RC$(J$)*B(J$1)+RC$(J$1)*B(J$))
C
      Z44=(C(J$)+C(J$1))*(4.*RC$(I$)-SR)-
     1(RC$(J$)*C(J$1)+RC$(J$1)*C(J$))
C
      ZI11=-(B(J$)+B(J$1)+B(I$))
      ZI12=-(C(J$)+C(J$1))
      ZI21=-C(I$)
C
      GO TO 280
C
260   Z11=(3.*B(J$)-B(J$1))*SR+(11.*B(J$)+
     14.*B(J$1))*RC$(I$)-B(J$1)*RC$(J$)
C
      Z44=(3.*C(J$)-C(J$1))*SR+(11.*C(J$)+
     14.*C(J$1))*RC$(I$)-C(J$1)*RC$(J$)
C
      ZI11=2.*B(I$)+2.*B(J$)
      ZI12=2.*C(J$)-C(J$1)
      ZI21=3.*C(I$)
C
      GO TO 280
C
270   Z11=(3.*B(J$1)-B(J$))*SR+(4.*B(J$)+
     111.*B(J$1))*RC$(I$)-B(J$)*RC$(J$1)
C
      Z44=(3.*C(J$1)-C(J$))*SR+(4.*C(J$)+
     111.*C(J$1))*RC$(I$)-C(J$)*RC$(J$1)
C
      ZI11=2.*B(I$)+2.*B(J$1)
      ZI12=-C(J$)+2.*C(J$1)
      ZI21=3.*C(I$)
 280   K$=2*I$-1
       L$=2*J$R-1
C
      SK$(K$,L$)=(((1.-XNU)*B(I$)*Z11+(.5-XNU)*C(I$)*Z44)/
     1DEL2+XNU*ZI11)/30.+2.*(1.-XNU)*DEL2*ZNT
C
       SK$(L$,K$)=SK$(K$,L$)
C
       K$=2*I$
C
      SK$(K$,L$)=((XNU*C(I$)*Z11+(.5-XNU)*B(I$)*Z44)/
     1DEL2+XNU*ZI21)/30.
C
C
       SK$(L$,K$)=SK$(K$,L$)
C
       L$=2*J$R
C
      SK$(K$,L$)=((1.-XNU)*C(I$)*Z44+(.5-XNU)*B(I$)*Z11)/
     1(30.*DEL2)
C
       SK$(L$,K$)=SK$(K$,L$)
C
       K$=2*I$-1
C
      SK$(K$,L$)=((XNU*B(I$)*Z44+(.5-XNU)*C(I$)*Z11)/
     1DEL2+XNU*ZI12)/30.
C
C
       SK$(L$,K$)=SK$(K$,L$)
C
C
290   CONTINUE
C
      GO TO 355
      WRITE(6,2510)K
      DO 300 I$=1,12
      WRITE(6,301) (SK$(I$,J$),J$=1,12)
```

```
      DO 300 J$=1,I$
      I$J$=I$*(I$-1)/2+J$
      AB(I$J$)=SK$(I$,J$)
300   CONTINUE
301   FORMAT(12F8.5)
C
      NVEC=0
      NEQ$=12
      CALL SYMAL(AB,NEQ$,E,IERROR,NVEC)
      DO 350 I$=1,12
      WRITE(6,351) I$,E(I$)
350   CONTINUE
C
351   FORMAT(I3,F12.6)
      WRITE(6,2560) IERROR
C  ASSEMBLE MATRICES WITHOUT REGARDING B.C.
C
355   DO 500 I$=1,6
C
      I = N(I$)
C
      M$ = 2*I$ - 1
      M = 2*I - 1
      SS(M) = SS(M) + SS$(M$)
C
      M$ = 2*I$
      M = 2*I
      SS(M) = SS(M) + SS$(M$)
C
C
      DO 500 J$ = 1,6
C
      J = N(J$)
C
      M$ = 2*I$ - 1
      M = 2*I - 1
      N$ = 2*J$ - 1
      N1 = 2*J - 1
      SK(M,N1) = SK(M,N1) + SK$(M$,N$)
C
      N$ = 2*J$
      N1 = 2*J
      SK(M,N1) = SK(M,N1) + SK$(M$,N$)
C
      M$ = 2*I$
      M = 2*I
      SK(M,N1) = SK(M,N1) + SK$(M$,N$)
C
      N$ = 2*J$ - 1
      N1 = 2*J - 1
      SK(M,N1) = SK(M,N1) + SK$(M$,N$)
C
C  ASSEMPLE ELEMENTS OF THE NEXT NODE IN ELEMENT K
C
500   CONTINUE
C
C  CYCLE FOR NEXT ELEMENT
C
600   CONTINUE
C
C  MODIFY SK AND SS TO ACCOUNT FOR NODES WITH SPECIFIED DIS¢LACEMENT
C
      DO 700 I=1,NNSRD
      J = 2*NSRD(I) - 1
      DO 690 L=1,NEQ
      SK(J,L)=0.0
      SK(L,J)=0.0
690   CONTINUE
      SS(J) = 0.0
      SK(J,J)=1.
700   CONTINUE
C
```

```
C
      DO 706 I=1,1
      L=2*I
      DO 705 J=1,NEQ
      SK(J,L)=0.0
      SK(L,J)=0.0
705   CONTINUE
      SS(L)=0.0
      SK(L,L)=1.
706   CONTINUE
C
      GO TO 708
      NSOL=1
      CALL FSLE(NEQ,NEQ,SK,NSOL,NEQ,SS,DES,IPERM,NEQ,DESDD,DET,JEXP)
      WRITE (6,2005) DET,JEXP
      GO TO 720
C
708   LUB=41
      LLB=41
      LK=2*LLB+LUB
      LIN=NEQ*(LK+1)
      DO 710 I=1,NEQ
      BB(I)=SS(I)
      DO 710 J=1,NEQ
      IJ(I,J)=LK*J+I-LLB
      IF (IJ(I,J).GT.LIN) GO TO 710
      AA(IJ(I,J))=SK(I,J)
710   CONTINUE
C
C       CALL FOR GBAND
C
      NHRS=+1
      ITER=0
      CALL GBAND(AA,BB,NEQ,LLB,LUB,NHRS,IP,DET,JEXP,BB,RES,ITER,EPS)
      WRITE(6,2005) DET,JEXP
C
C  PRINT DISPLACEMENTS
C
C
720   WRITE(6,2115)
      DO 790 I = 1,NN
      J = 2*I - 1
      U(I) = BB(J)
      K = 2*I
      V(I) = BB(K)
C
      WRITE(6,2110)I,U(I),V(I)
790   CONTINUE
C
C
C  CALCULATE STRESSES AT ALL NODES IN EACH ELEMENT
C
C
      DO 950 I = 1,NE
C
       DO 810 I$=1,6
        N(I$)=NODE(I,I$)
        RC$(I$)=RC(NODE(I,I$))
        ZC$(I$)=ZC(NODE(I,I$))
        U$(I$)=U(NODE(I,I$))
        V$(I$)=V(NODE(I,I$))
810    CONTINUE
C
      DO 815 I$=1,3
      T$(I$)=T(NODE(I,I$))
C
      I$R=I$+3
      I$1=I$+1
      IF(I$1.GT.3) I$1=I$1-3
      T$(I$R)=(T(NODE(I,I$))+T(NODE(I,I$1)))/2.
C
815   CONTINUE
C
      GO TO 819
```

```
      TBAR=0.0
      DO 817 I$=1,6
      TBAR=TBAR+T(NODE(I,I$))
817   CONTINUE
      DO 818 I$=1,6
      T$(I$)=TBAR/6.
818   CONTINUE
C
819    DO 820 I$=1,3
        J$=I$+1
        K$=J$+1
C
        IF(J$.GT.3) J$=J$-3
        IF(K$.GT.3) K$=K$-3
C
        A(I$)=RC$(J$)*ZC$(K$)-RC$(K$)*ZC$(J$)
        B(I$)=ZC$(J$)-ZC$(K$)
        C(I$)=RC$(K$)-RC$(J$)
C
820    CONTINUE
C
      DEL2=ABS(RC$(1)*(ZC$(2)-ZC$(3))+RC$(2)*(ZC$(3)-ZC$(1))+RC$(3)*(ZC$
     1(1)-ZC$(2)))
C
      RBAR=(RC$(1)+RC$(2)+RC$(3))/3.
      ZBAR=(ZC$(1)+ZC$(2)+ZC$(3))/3.
C
C
C       CALCULATION OF STRESSES AT
C
C         NODES 1 TO 3 IN ELEMENT
C
       DO 850 I$=1,3
C
      I$M1=I$-1
      IF(I$M1.EQ.0) I$M1=3
C
      I$1=I$+1
      IF(I$1.GT.3) I$1=I$1-3
C
      I$2=I$+2
      IF(I$2.GT.3) I$2=I$2-3
C
      I$R=I$+3
      I$RM1=I$M1+3
C
C
      EPR=(3.*B(I$)*U$(I$)-B(I$1)*U$(I$1)-B(I$2)*U$(I$2)
     1+4.*(B(I$1)*U$(I$R)+B(I$M1)*U$(I$RM1)))/DEL2
C
      EPZ=(3.*C(I$)*V$(I$)-C(I$1)*V$(I$1)-C(I$2)*V$(I$2)
     1+4.*(C(I$1)*V$(I$R)+C(I$M1)*V$(I$RM1)))/DEL2
C
      GRZ1=C(I$)*U$(I$)+B(I$)*V$(I$)
      GRZ2=C(I$1)*U$(I$R)+B(I$1)*V$(I$R)
      GRZ3=C(I$M1)*U$(I$RM1)+B(I$M1)*V$(I$RM1)
      GRZ4=C(I$1)*U$(I$1)+C(I$2)*U$(I$2)
      GRZ5=B(I$1)*V$(I$1)+B(I$2)*V$(I$2)

C
      GRZ=(3.*GRZ1+4.*(GRZ2+GRZ3)-GRZ4-GRZ5)/DEL2
C
C
      IF(RC$(I$).EQ.0.0) GO TO 830
C
      EPT=U$(I$)/RC$(I$)
      GO TO 840
C
830   EPT=EPR
C
840   SIGR$=(1.-XNU)*EPR+XNU*(EPT+EPZ)-T$(I$)
C
```

```
      SIGTH$=XNU*(EPR+EPZ)+(1.-XNU)*EPT-T$(I$)
C
      SIGZ$=XNU*(EPR+EPT)+(1.-XNU)*EPZ-T$(I$)
C
      TAURZ$=(.5-XNU)*GRZ
C
C
C
C
869   SIGRP(N(I$))=SIGRP(N(I$))+SIGR$*DEL2
      SIGTHP(N(I$))=SIGTHP(N(I$))+SIGTH$*DEL2
      SIGZP(N(I$))=SIGZP(N(I$))+SIGZ$*DEL2
      TAURZP(N(I$))=TAURZP(N(I$))+TAURZ$*DEL2
      DEL2P(N(I$))=DEL2P(N(I$))+DEL2
C
C   CYCLE FOR NEXT NODE IN ELEMENT I
C
850    CONTINUE
C
C       CALCULATION OF STRESSES AT
C
C       NODES 4 TO 6 IN ELEMENT
C
       DO 900 I$=1,3
C
        I$R=I$+3
C
        I$1=I$+1
        IF(I$1.GT.3) I$1=I$1-3
C
      I$2=I$+2
      IF(I$2.GT.3) I$2=I$2-3
C
      I$R1=I$1+3
C
      I$M1=I$-1
      IF(I$M1.EQ.0) I$M1=3
C
      I$RM1=I$M1+3
C
      EPR=(B(I$)*U$(I$)+B(I$1)*U$(I$1)-B(I$2)*U$(I$2)+
     12.*(B(I$)+B(I$1))*U$(I$R))/DEL2+
     22.*B(I$M1)*(U$(I$R1)+U$(I$RM1))/DEL2
C
      EPZ=(C(I$)*V$(I$)+C(I$1)*V$(I$1)-C(I$2)*V$(I$2)+
     12.*(C(I$)+C(I$1))*V$(I$R))/DEL2+
     22.*C(I$M1)*(V$(I$R1)+V$(I$RM1))/DEL2
C
      GRZ1=C(I$)*U$(I$)+C(I$1)*U$(I$1)-C(I$2)*U$(I$2)
      GRZ2=B(I$)*V$(I$)+B(I$1)*V$(I$1)-B(I$2)*V$(I$2)
      GRZ3=(C(I$)+C(I$1))*U$(I$R)+(B(I$)+B(I$1))*V$(I$R)
      GRZ4=B(I$M1)*(V$(I$R1)+V$(I$RM1))
      GRZ5=C(I$M1)*(U$(I$R1)+U$(I$RM1))
C
      GRZ=(GRZ1+GRZ2+2.*(GRZ3+GRZ4+GRZ5))/DEL2
C
C
      IF(RC$(I$R).EQ.0.0) GO TO 880
      EPT=U$(I$R)/RC$(I$R)
C
      GO TO 890
C
880   EPT=EPR
C
890   SIGR$=(1.-XNU)*EPR+XNU*(EPT+EPZ)-T$(I$R)
C
      SIGTH$=XNU*(EPR+EPZ)+(1.-XNU)*EPT-T$(I$R)
C
      SIGZ$=XNU*(EPR+EPT)+(1.-XNU)*EPZ-T$(I$R)
C
      TAURZ$=(.5-XNU)*GRZ
C
```

```
C
899      SIGRP(N(I$R))=SIGRP(N(I$R))+SIGR$*DEL2
         SIGTHP(N(I$R))=SIGTHP(N(I$R))+SIGTH$*DEL2
         SIGZP(N(I$R))=SIGZP(N(I$R))+SIGZ$*DEL2
         TAURZP(N(I$R))=TAURZP(N(I$R))+TAURZ$*DEL2
         DEL2P(N(I$R))=DEL2P(N(I$R))+DEL2
C
900    CONTINUE
C
C
950    CONTINUE
C
C  CALCULATION OF AVERAGE STRESSES AT ALL NODES
C
       WRITE(6,2550)
       WRITE(6,2555)
C
C
       DO 960 I=1,NN
C
       SIGRAV=SIGRP(I)/DEL2P(I)
       SIGTHA=SIGTHP(I)/DEL2P(I)
       SIGZAV=SIGZP(I)/DEL2P(I)
       TAURZA=TAURZP(I)/DEL2P(I)
C
C    CALCULATE PRINCIPAL AND VON MISES STRESSES
C
       DO 955 I$=1,6
       STR(I$)=0.0
955    CONTINUE
C
       STR(1)=SIGRAV
       STR(3)=SIGTHA
       STR(4)=TAURZA
       STR(6)=SIGZAV
C
       N$=3
       NVEC=0
C
       CALL SYMAL(STR,N$,E$,IERROR,NVEC)
C
       VMS=SQRT(((E$(3)-E$(1))**2+(E$(2)-E$(1))**2+(E$(3)-E$(2))**2)/2.)
C
       WRITE(6,2560)I,SIGRAV,SIGTHA,SIGZAV,TAURZA,VMS
C
960    CONTINUE
C
C
C  READEING FORMATS
C
1005   FORMAT(4(2X,I3))
1015   FORMAT(2X,F5.2,2X,F7.5,2X,F7.3)
1010   FORMAT(2X,F5.3,2(2X,E12.5),2X,F10.2)
1020   FORMAT(2X,I3,2(2X,F10.5))
1025   FORMAT(7(2X,I3))
1030   FORMAT(2X,I3)
1040   FORMAT(10X,I3,6X,F15.4)
C
C  WRITING FORMATS
C
2001   FORMAT('SOLUTION FAILED')
2005   FORMAT('DETERMINANT IS',G16.7,'*10**',I20)
2010   FORMAT(2X,'A FLEM SOLUTION FOR THERMAL DISPLACEMENTS',//,5X,'AND S
      1TRESSES IN LEC-GAAS CRYSTALS',//)
2020   FORMAT(5X,'RADIUS (CM) = ',F7.5,/,5X,'VELOCITY (CM/SEC) =',F7.5,/,
      15X,'LENGTH (CM) =',F7.3,//)
2030   FORMAT(5X,'NU =',F5.3,/)
2035   FORMAT(5X,'NUMBER OF NODES = ',I3,/,5X,'NUMBER OF ELEMENTS = ',I3
      1,/,5X,'NO.OF NODES WITH NO RADIAL DISPLACEMENT = ',I3,/,5X,'NO.OF
      2NODES WITH NO AXIAL DISPLACEMNT = ',I3,/)
```

```
2040  FORMAT(10X,'NODES VS NODAL COORDINATES AND VS TEMPERATURE',//,6X,'
     1I',13X,'R(I)',9X,'Z(I)',4X,'TEMEPERATURE',//)
2050  FORMAT(5X,I3,4X,2(3X,F10.5),2X,F15.4)
2060  FORMAT(' ',//,15X,'SYSTEM TOPOLOGY',//,'ELEMENT NUMBER',11X,'NODE
     1NUMBERS',//)
2070  FORMAT(5X,I3,10X,3(5X,I3))
2080  FORMAT(' ',//,5X,'NODES ON THE AXIS WITH NO RADIAL DISPLACEMENT',/
     1)
2085  FORMAT(' ',/,5X,'NODES WITH NO AXIAL DISPLACEMENT',/)
2090  FORMAT(20X,I3)
2099  FORMAT(/,5X,'ITERATION NUMBER = ',I3,//)
2100  FORMAT(' ',//,10X,'DISPLACEMENT FIELD: RADIAL AND AXIAL',/,5X,'NOD
     1E NUMBER',4X,'RADIAL',11X,'AXIAL',/)
2110  FORMAT(9X,I3,2(5X,E15.6))
2115  FORMAT(5X,'CALCULATED DISPLACEMENT FIELD',/)
2120  FORMAT(/,5X,'NODES AND DISPLACEMENTS AT THE FREE BOUNDARY',/)
2500  FORMAT(' ',//,2X,'STRESSES CALCULATED AT ALL NODES IN EACH ELEMENT
     1',//,2X,'ELEMENT',1X,'NODE',4X,'SIGMAR',4X,'SIGMATH',4X,'SIGMAZZ',
     25X,'TAURZ',//)
2510  FORMAT(5X,I3)
2520  FORMAT(10X,I3,5X,4(E14.5))
2550  FORMAT(' ',/,5X,'AVERAGE STRESSES AT EACH NODE',/)
2555  FORMAT(2X,'NODE',7X,'SIGRAV',7X,'SIGTHAV',6X,
     1'SIGZAV',8X,'TAURZAV',/)
2560  FORMAT(1X,I3,3X,5(E14.5))
C
C
      STOP
      END
```

XI.5 Program for the Calculations of the MRSS-CRSS in (010) Sections

```
C
C
C       THIS PROGRAM CALCULATE AND PLOT
C
C
C       MAXIMUN RESOLVED SHEAR STRESSES
C
C
      DIMENSION T(600),RSSM$(5)
      DIMENSION SIGR(500),SIGZ(500),SIGT(500),TARZ(500)
      DIMENSION RC(500),ZC(500),RSSM(500),RSMG(50,50)
      DIMENSION CVAL(20),IOP(8),VOP(8)
      REAL TAUCR,T,DTA
      REAL SIGR,SIGT,SIGZ,TARZ,RC,ZC,RSSM,RSMG,CVAL,VOP
      REAL C,XMIN,YMIN,DX,DY,DRSM,XSIZE,YSIZE
      INTEGER NN,IDIMX,NX,NY,NRNG,NC,IOP,IMAX$
      REAL TAUCRM,TAUCTE,TAUCRJ,RSSM$
      REAL XIN,XI,XCN
C
      DTA=200.
C
      NN=111
C
      WRITE(6,11)
11    FORMAT(9X,'NODE',10X,'MAX.SHEAR STRESS(MPA)',/)
      DO 20 I=1,NN
20     READ(5,21) SIGR(I),SIGT(I),SIGZ(I),TARZ(I)
21    FORMAT(7X,4(E14.5))
C
      DO 30 J=1,NN
       READ(5,31) I,RC(I),ZC(I)
       RC(I)=RC(I)*5.0
       ZC(I)=ZC(I)*5.0
30    CONTINUE
31    FORMAT(2X,I4,2(2X,F10.5))
C
39    DO 40 I=1,NN
40     READ(5,41)J,T(J)
C
41    FORMAT(10X,I3,6X,F15.4)
C
C
      DO 50 I=1,NN
C
      TAUCR=TAUCRJ(DTA,T(I))
C
       RSSM(I)=0.0
       SRT=(SIGR(I)-SIGT(I))*2.91*DTA/SQRT(6.)
       SZT=(SIGZ(I)-SIGT(I))*2.91*DTA/SQRT(6.)
       SRZ=(SIGR(I)-SIGZ(I))*2.91*DTA/SQRT(6.)
       TARZ(I)=TARZ(I)*2.91*DTA/SQRT(6.)
C
C
       RSSM$(1)=ABS(-SRT+TARZ(I))-TAUCR
C
       RSSM$(2)=ABS(-SRT-TARZ(I))-TAUCR
C
       RSSM$(3)=ABS(SZT+TARZ(I))-TAUCR
C
       RSSM$(4)=ABS(SZT-TARZ(I))-TAUCR
C
       RSSM$(5)=ABS(SRZ)-TAUCR
C
```

```
        RSMAX$=RSSM$(1)
        IMAX$=1
C
        DO 45 I$=1,5
         IF(RSMAX$.LT.RSSM$(I$)) GO TO 43
         GO TO 45
43       RSMAX$=RSSM$(I$)
         IMAX$=I$
45      CONTINUE
C
        RSSM(I)=RSMAX$
C
        IF(RSSM(I).LT.0.0) RSSM(I)=0.0
C
C
         WRITE(6,51) I,RSSM(I),IMAX$
C
50     CONTINUE
C
C
51     FORMAT(10X,I3,12X,F15.6,4X,I3)
C
C     CALCULATE RSMMAX AND RSMMIN
C
       RSMMAX=RSSM(1)
       DO 70 I=1,NN
70     IF(RSMMAX.LT.RSSM(I)) RSMMAX=RSSM(I)
C
       RSMMIN=RSSM(1)
       DO 80 I=1,NN
80     IF(RSMMIN.GT.RSSM(I)) RSMMIN=RSSM(I)
       WRITE(6,82) RSMMAX
82     FORMAT(/,5X,'RSMMAX=',F15.7,/)
C
C    CALCULATE REGULAR GRID
C
       NX=50
       NY=50
       IDIMX=NX
C
C
       XMIN=0.0
       YMIN=0.0
       XMAX=10.
       YMAX=10.
       DX=(XMAX-XMIN)/(NX-1)
       DY=(YMAX-YMIN)/(NY-1)
       NRNG=2
       C=10.
       OPT=0.0
C
       CALL CGRID1(RSMG,IDIMX,NX,NY,XMIN,YMIN,
      1             DX,DY,RC,ZC,RSSM,NN,C,NRNG,OPT)
C
C     PLOT GRID
C
88     XSIZE=10.
       YSIZE=10.
       NC=10
       IOP(1)=1
       IOP(2)=1
       IOP(3)=0
       IOP(4)=1
       IOP(5)=0
       IOP(6)=1
       IOP(7)=0
       IOP(8)=1
       VOP(8)=.10
C
       DRSM=(RSMMAX-RSMMIN)
       M=1
       XNC=NC
```

```
C
      DO 90 I=1,NC
      XI=I
      XIN=(XI-1.)/(XNC-1.)
      CVAL(I)=RSMMIN+DRSM*XIN**M
90    CONTINUE
C
      CALL CONTUR(XSIZE,YSIZE,RSMG,IDIMX,NX,NY,
     1            CVAL,NC,IOP,VOP)
C
      CALL PLOTND
      RETURN
      END
C
C  FUNCTION TO CALCULATE
C
C  CRITICAL STRESS AT T(I)
C
      REAL FUNCTION TAUCRM(DTA,TT)
      REAL DTA,TT
      TAUCRM=6.8647E-2*EXP(5.1989E3/(1511-DTA*(1.-TT))-3.4407)
      RETURN
      END
C
C     CRITICAL STRESSES FOR
C
C     TE-DOPED GAAS (M AND B)
C
      REAL FUNCTION TAUCTE(DTA,TT)
      REAL DTA,TT
C
      TAUCTE=.39227*EXP(5.9205E3/(1511-DTA*(1.-TT))-3.9183)
C
      RETURN
      END
C
C    CRITICAL STRESSES FOR YIELD
C

      REAL FUNCTION TAUCRJ(DTA,TT)
      REAL DTA,TT
C
      TAUCRJ=.5625*EXP(5.0596E3/(1511-DTA*(1.-TT))-3.3485)
C
      RETURN
      END
```

XI.6 Program for the Calculations of MRSS-CRSS in (001) Sections

```
C
C
C       THIS PROGRAM PLOT RESOLVED SHEAR
C
C       STRESSES IN POLAR COORDINATES
C
C
      DIMENSION T(11),RSS$(10)
      DIMENSION RSSG(50,50),RSS(700),XP(700),YP(700)
      DIMENSION VOP(8),IOP(8),CVAL(10)
      DIMENSION RS(11),TS(11),ZS(11),RZS(11),RO(11)
      REAL RS,TS,ZS,RZS,RO,RSSG,RSS,XP,YP
      REAL THETA,DTHETA,VOP,CVAL,C
      INTEGER IOP,NC,IDIMX,NN,NV,NX,NY,IMAX$
      REAL TAUCR,TAUCTE,TAUCRM,TAUCRJ,RSS$
      REAL XI,XNC,XIN
C
C
C
      DTA=200.
C
      WRITE(6,2)
2     FORMAT(//,5X,'RESOLVED SHEAR STRESS',/'MAXIMUN COMPONENT',/)
C
      READ(5,6) ZC
6     FORMAT(20X,F10.5)
C
      WRITE(6,7) ZC
7      FORMAT(10X,'HEIGHT = ',F10.5,/)
C
      WRITE(6,8)
8     FORMAT(//,5X,'NV',8X,'RSS(MPA)',6X,'MODE',/)
C
C
C       READ STRESSES FROM RO=0 TO 1. AT Z
C
      DO 10 I=1,11
10    READ(5,11) RS(I),TS(I),ZS(I),RZS(I)
11    FORMAT(7X,4(E14.5))
C
      DO 15 I=1,11
      READ(5,16) T(I)
       WRITE(6,16) T(I)
15    CONTINUE
16    FORMAT(19X,F15.4)
C
C
C       CALCULATE NUMBER OF POINTS OVER CIRCLE
C
C       OF RADIUS RO WHERE STRESSES WILL BE
C
C              CALCULATED
C
      NV=1
C
      DO 40 I=1,10
       I$1=I+1
C
      TAUCR=TAUCRJ(DTA,T(I$1))
C
       RO(I)=5.*I/10
       NN=4*I
       DTHETA=6.2831853/NN
       RSB=(RS(I$1)-TS(I$1))*2.91*DTA/SQRT(6.)
```

```
      ZSB=(ZS(I$1)-TS(I$1))*2.91*DTA/SQRT(6.)
      RZS(I$1)=RZS(I$1)*2.91*DTA/SQRT(6.)
C
C
      DO 40 J=1,NN
       THETA=DTHETA*(J-1)
       XP(NV)=RO(I)*COS(THETA)+5.
       YP(NV)=RO(I)*SIN(THETA)+5.
       PI4=.7853982
C
       TERM1=-RSB*COS(2.*THETA)
       TERM2=SQRT(2.)*RZS(I$1)*COS(THETA+PI4)
       RSS$(1)=ABS(TERM1+TERM2)-TAUCR
C
C
       RSS$(2)=ABS(TERM1-TERM2)-TAUCR
C
C
       TERM3=-SQRT(2.)*RSB*SIN(THETA)*SIN(THETA+PI4)+ZSB
C
       TERM4=RZS(I$1)*COS(THETA)
C
       RSS$(3)=ABS(TERM3+TERM4)-TAUCR
C
C
       RSS$(4)=ABS(TERM3-TERM4)-TAUCR
C
C
       TERM5=SQRT(2.)*RSB*COS(THETA)*SIN(THETA+PI4)-ZSB
C
       TERM6=RZS(I$1)*SIN(THETA)
C
       RSS$(5)=ABS(TERM5-TERM6)-TAUCR
C
C
       RSS$(6)=ABS(TERM5+TERM6)-TAUCR
C
C
       TERM7=SQRT(2.)*RSB*COS(THETA)*COS(THETA+PI4)-ZSB
C
       RSS$(7)=ABS(TERM7-TERM6)-TAUCR
C
C
       RSS$(8)=ABS(TERM7+TERM6)-TAUCR
C
C
       TERM8=SQRT(2.)*RSB*SIN(THETA)*COS(THETA+PI4)+ZSB
C
       RSS$(9)=ABS(TERM8+TERM4)-TAUCR
C
C
       RSS$(10)=ABS(TERM8-TERM4)-TAUCR
C
C     CALCULATE MAXIMUN COMPONENT OF RSS
C
        RSMAX$=RSS$(1)
      IMAX$=1
C
       DO 30 I$=1,10
        IF(RSMAX$.LT.RSS$(I$)) GO TO 20
        GO TO 30
20      RSMAX$=RSS$(I$)
        IMAX$=I$
30     CONTINUE
C
       RSS(NV)=RSMAX$
       IF(RSS(NV).LT.0.0) RSS(NV)=0.0
C
       WRITE(6,41) NV,RSS(NV),IMAX$
C
       NV=NV+1
C
40    CONTINUE
```

```
C
41     FORMAT(5X,I3,3X,F15.7,4X,I3)
C
C      CALCULATE RSSMAX AND RSSMIN
C
       RSSMAX=RSS(1)
C
      NV=NV-1
C
C
      DO 50 I=1,NV
50     IF(RSSMAX.LT.RSS(I)) RSSMAX=RSS(I)
C
      RSSMIN=RSS(1)
C
      DO 60 I=1,NV
60    IF(RSSMIN.GT.RSS(I)) RSSMIN=RSS(I)
C
C
C     CALCULATE NEW REGULAR GRID USING CGRID1
C
      NX=50
      NY=50
      IDIMX=NX
      XMIN=0.0
      YMIN=0.0
      XMAX=10.
      YMAX=10.
      DX=(XMAX-XMIN)/(NX-1)
      DY=(YMAX-YMIN)/(NY-1)
      NRNG=2
      C=10.
      OPT=0.0
C
      CALL CGRID1(RSSG,IDIMX,NX,NY,XMIN,YMIN,
     1            DX,DY,XP,YP,RSS,NV,C,NRNG,OPT)
C
C     PLOT GRID
C
C
      XSIZE=10.
      YSIZE=10.
      NC=10
      IOP(1)=1
      IOP(2)=1
      IOP(3)=0
      IOP(4)=2
      IOP(5)=0
      IOP(6)=1
      IOP(7)=0
      IOP(8)=1
      VOP(8)=.08
C
      DRSS=(RSSMAX-RSSMIN)
      K=1
      XNC=NC
C
C
      WRITE(6,70)
70    FORMAT(//,3X,'I',11X,'CVAL(I)',/)
      DO 80 I=1,NC
       XI=I
       XIN=(XI-1.)/(XNC-1.)
       CVAL(I)=RSSMIN+DRSS*XIN**K
       WRITE(6,81) I,CVAL(I)
80    CONTINUE
81    FORMAT(2X,I3,10X,F10.5)
C
      CALL CONTUR(XSIZE,YSIZE,RSSG,IDIMX,NX,NY,
     1            CVAL,NC,IOP,VOP)
C
```

```
      CALL PLOTND
      RETURN
      END
C
C      FUNCTION TO CALCULATE
C
C      CRITICAL STRESSES AT T(I)
C
C      FOR UNDOPED GAAS (M AND B)
C
      REAL FUNCTION TAUCRM(DTA,TT)
      REAL DTA,TT
C
      TAUCRM=6.8647E-2*EXP(5.1989E3/(1511-DTA*(1.-TT))-3.4407)
C
      RETURN
      END
C
C      CRITICAL STRESSES FOR
C
C      TE-DOPED GAAS (M AND B)
C
      REAL FUNCTION TAUCTE(DTA,TT)
      REAL DTA,TT
C
      TAUCTE=.39227*EXP(5.9205E3/(1511-DTA*(1.-TT))-3.9183)
C
      RETURN
      END
C
C     CRITICAL STRESSES
C
C     FOR YIELD (S AND C)
C
C     USED BY JORDAN
C
      REAL FUNCTION TAUCRJ(DTA,TT)
      REAL DTA,TT
C
      TAUCRJ=.5625*EXP(5.0596E3/(1511-DTA*(1.-TT))-3.3485)
C
      RETURN
      END
```

XI.7 Program for the Numerical Evaluation of Temperatures During Cooling

```
C
C
C         THIS PROGRAM CALCULATES THE
C
C       TEMPERATURE FIELD DURING COOLING
C
C         OF LEC-GROWN GAAS USING AN
C
C        ANALYTICAL AXISYMMETRIC TIME
C
C          DEPENDENT SOLUTION
C
C
      INTEGER NB,NG,NN,NR,NZ,IG
      REAL*8 TIME,RO,ZT,DTA,H,HP
      REAL*8 B,C,BETA,GAMMA
      REAL*8 FAC1,FAC2,FAC3,FAC4,FAC5
      REAL*8 BF,C1,C2
      REAL*8 TTIME,Z,RO,BARG,BFR
      REAL*8 TGAMMA,TBETA,TEM
      REAL*4 ARG,ARX
      REAL*4 TGR,CVAL,VOP,TMIN,TMAX
      REAL*4 RSIZE,ZSIZE
      REAL*8 DR,DZ,DTEM
      INTEGER IDIMR,NC,IOP
C
      DIMENSION BETA(30),GAMMA(30),C1(30),C2(30)
      DIMENSION TEM(5000),TGR(11,41),IOP(8),VOP(8),CVAL(20)
      DIMENSION TBETA(50)
C
C       READ CONSTANT AND PARAMETERS
C
C       AND PRINT HEADLINES AND PARAMETERS
C
C
      READ(5,5) TIME
5     FORMAT(F15.7)
      WRITE(6,6)
6     FORMAT(//,5X,'ANALYTICAL SOLUTION FOR THE',/,
     15X,'TRANSIENT TEMPERATURE FIELD DURING',/,
     25X,'COOLING OF LEC-GROWN GAAS CRYSTALS',/)
C
      READ(5,10) NB,NG
      READ(5,10) NR,NZ
10    FORMAT(2I3)
C
      READ(5,20) RO,ZT
      XL=ZT*RO
20    FORMAT(2F15.7)
      READ(5,20) DTA,H
      READ(5,20) B,C
      WRITE(6,30) TIME
30    FORMAT(5X,'TIME(NDIM)=',F15.7,/)
C
      WRITE(6,40) RO,XL
40    FORMAT(5X,'RADIUS(CM)=',F10.5,5X,
     1'LENGTH(CM)=',F10.5,/)
      WRITE(6,50) H,DTA
50    FORMAT(5X,'HEAT TRANSFER COEFFICIENT(1/CM)=',
     1F10.5,/,5X,'DTA(DC)=',F10.5,/)
      WRITE(6,60)B,C
60    FORMAT(5X,'T(TIME=0)-TMP=',F9.3,'*Z+',F7.3,'*Z**2',/)
```

```
C
      B=B/DTA
      C=C/DTA
      HP=H*RO
C
      DO 80 I=1,NB
       READ(5,85) BETA(I)
80    CONTINUE
C
85    FORMAT(F15.7)
C
      DO 90 J=1,NG
       READ(5,85) GAMMA(J)
2      GAMMA(J)=GAMMA(J)/4.
90    CONTINUE
C
C
C      CALCULATION OF COEFFICIENTS
C
C       C1(BETA) AND C2(GAMMA)
C
C
      WRITE(6,110)
110   FORMAT(5X,'BETA(I)',6X,'C1(BETA)',//)
C
C
      DO 150 I=1,NB
C
       IF(BETA(I).LT.3.0) BF=BOFL3(BETA(I))
       IF(BETA(I).GT.3.0.OR.BETA(I).EQ.3.0) BF=BOFG3(BETA(I))
C
       C1(I)=(HP**2+BETA(I)**2)*BF
       C1(I)=1./C1(I)
C
       WRITE(6,20) BETA(I),C1(I)
C
150   CONTINUE
C
      DO 200 J=1,NG
C
       ARG=GAMMA(J)*ZT
C
       FAC1=1.+B*(ZT+HP/GAMMA(J)**2)+
     1 C*(ZT**2+2.*(ZT*HP-1.)/GAMMA(J)**2)
       FAC1=FAC1*SIN(ARG)
C
       FAC2=-HP+B*(1.-HP*ZT)+
     1 C*(2.*ZT-HP*ZT**2+2.*HP/GAMMA(J)**2)
       FAC2=FAC2*COS(ARG)/GAMMA(J)
C
       FAC3=(HP-B-2.*C*HP/GAMMA(J)**2)/GAMMA(J)
C
       FAC4=ZT*(GAMMA(J)**2+HP**2)/2.+HP
C
       C2(J)=(FAC1+FAC2+FAC3)/FAC4
C
       WRITE(6,20) GAMMA(J),C2(J)
C
200   CONTINUE
C
C
C     SUMMATION OF SERIES IN
C
C       BESSEL FUNCTIONS
C
      WRITE(6,300)
300   FORMAT(10X,'NN',6X,'TEMP(ND)',6X,'TEMP(*10**3 DC)',//)
C
      DR=1./(NR-1.)
C
      DO 400 I=1,NR
       RO=DR*(I-1)
C
```

```
          TBETA(I)=0.0
C
          DO 350 I$=1,NB
C
           ARX=-TIME*BETA(I$)**2
           BARG=BETA(I$)*RO
C
           IF(BARG.LT.3.0) BFR=BOFL3(BARG)
           IF(BARG.GT.3.0.OR.BARG.EQ.3.0) BFR=BOFG3(BARG)
C
           TBETA(I)=TBETA(I)+C1(I$)*EXP(ARX)*BFR
C
350       CONTINUE
400      CONTINUE
C
C
C      SUMMATION OF SERIES IN
C
C       FOURIER FUNCTIONS
C
C     AND TEMPERATURE CALCULATION
C
C
2          NN=1
           DZ=ZT/(NZ-1.)
C
           DO 500 J=1,NZ
C
            Z=DZ*(J-1)
C
            TGAMMA=0.0
C
            DO 450 J$=1,NG
C
             ARG=GAMMA(J$)*Z
C
             ARX=-TIME*GAMMA(J$)**2
C
             TGAMMA=TGAMMA+C2(J$)*EXP(ARX)*
         1   (GAMMA(J$)*COS(ARG)+HP*SIN(ARG))
C
450         CONTINUE
C
            DO 480 I=1,NR
C
             TTIME=2.*HP*TBETA(I)*TGAMMA
C
             TGR(I,J)=1.238-(1.-TTIME)*DTA/1000.0
C
             WRITE(6,510) NN,TTIME,TGR(I,J)
C
             NN=NN+1
C
480         CONTINUE
C
500      CONTINUE
C
510      FORMAT(10X,I5,6X,2F15.4)
C
C
C          PLOT ISOTHERMS
C
C
         IDIMR=NR
C
         TMIN=TGR(1,1)
C
         DO 550 I=1,NR
          DO 550 J=1,NZ
           IF(TMIN.GT.TGR(I,J)) TMIN=TGR(I,J)
550      CONTINUE
```

```
C
      WRITE(6,560) TMIN
560   FORMAT(//,'TMIN=',F10.6,/)
C
      TMAX=TGR(1,1)
C
      DO 600 I=1,NR
       DO 600 J=1,NZ
        IF(TMAX.LT.TGR(I,J)) TMAX=TGR(I,J)
600   CONTINUE
C
      WRITE(6,610) TMAX
610   FORMAT(/,'TMAX=',F10.6,/)
C
      RSIZE=3.0
      ZSIZE=12.0
      NC=20
C
      IOP(1)=1
      IOP(2)=1
      IOP(3)=0
      IOP(4)=1
      IOP(5)=1
      VOP(5)=3.
      IOP(6)=0
      IOP(7)=0
      IOP(8)=1
      VOP(8)=.12
C
      DTEM=(TMAX-TMIN)/(NC-1.)
C
      DO 700 I=1,NC
       CVAL(I)=TMAX-DTEM*(I-1.)
       WRITE(6,710) CVAL(I)
700   CONTINUE
710   FORMAT(5X,F15.7)
C
C
      CALL CONTUR(RSIZE,ZSIZE,TGR,IDIMR,NR,NZ,
     1CVAL,NC,IOP,VOP)
C
      CALL PLOTND
C
      STOP
      END
C
C
C
C     POLYNOMIAL APPROXIMATION OF
C
C     BESSEL FUNCTION FOR ARGUMENT
C
C         LESS THAN 3.0
C
C
      REAL FUNCTION BOFL3(DB)
      REAL*8 DB
      REAL BB
      BB=DB/3.
C
      BOFL3=1.-2.2499997*BB**2+1.2656208*BB**4-
     10.3163866*BB**6+0.0444479*BB**8-
     20.0039444*BB**10+0.00021*BB**12
C
      RETURN
      END
```

```
C
C
C     POLYNOMIAL APPROXIMATION OF
C
C     BESSEL FUNCTION FOR ARGUMENT
C
C       GREATER THAN 3.0
C
C
      REAL FUNCTION BOFG3(DB)
      REAL*8 DB
      REAL CARG,BB
C
      BB=3./DB
C
      BOFG3=.79788456-0.00000077*BB-0.0055274*BB**2-
     10.00009512*BB**3+0.00137237*BB**4-0.00072805*BB**5
     2+0.00014476*BB**6
C
      CARG=3./BB-0.78539816-0.04166397*BB-
     10.00003954*BB**2+0.00262573*BB**3-0.00054125*BB**4
     2-0.00029333*BB**5+0.00013558*BB**6
C
      BOFG3=BOFG3*COS(CARG)*SQRT(BB/3.0)
C
      RETURN
      END
```

APPENDIX XII

XII.1 Program for the Numerical Evaluation of Analytical Axisymmetric Temperature Fields

```
1 OPEN4,4:CMD4
2 DIM AL(5)
3 FOR M=1 TO 5
4 READ AL(M)
5 PRINT AL(M)
6 NEXT M
7 READ V,RO,K,ZT
8 PRINT "V=";V;"RO=";RO;"K=";K;"LENGTH=";ZT
9 FOR M=1 TO 7
10 :LET Z=.25*M:PRINT CHR$(10);"HEIGHT=";Z;CHR$(10)
11 :FOR L=1 TO 11
12 :LET RO=(L-1)*.1
13 LET TP=0
14 LET K1=(V*RO)/(2*K)
15 REM LOOP TO SUM BESSEL SERIES
16 FOR N=1 TO 5
17 :LET KA=SQR(K1^2+AL(N)^2)
18 :LET EZ=EXP(KA*Z)
19 :LET ET=EXP(-2*KA*ZT)
20 :LET C1=(EZ^(-1)-ET*EZ)/(1.-ET)
21 :LET X=AL(N)*RO
22 :IF X<=3. THEN GOSUB 100
23 :IF X>3. THEN GOSUB 150
24 :LET JR=JX
25 :LET X=AL(N)
26 :IF X<=3. THEN GOSUB 100
27 :IF X>3. THEN GOSUB 150
28 :LET JA=JX
29 :LET TP=TP+(JR/JA)*(C1/(AL(N)^2+1.44))
31 NEXT N
32 LET T=2.4*EXP(K1*Z)*TP
33 PRINT "RAD. POSITION=",RO;"TEMPERATURE=",T
36 :NEXT L
38 NEXT M
40 PRINT#4:CLOSE4
50 END
100 REM SUB BESSEL A
101 LET J1=1.-2.245*(X/3)^2+1.26562*(X/3)^4-.31638*(X/3)^6+.
04444*(X/3)^8
102 LET J2=-.00394*(X/3)^10+.00024*(X/3)^12
103 LET JX=J1+J2
105 RETURN
```

```
150 REM SUB BESSEL B
151 LET F1=.79788-.00552*(3/X)^2-.00009*(3/X)^3+.00137*(3/X)
^4
152 LET F2=-.00072*(3/X)^5+.00014*(3/X)^6
153 LET FX=F1+F2
154 LET A1=X-.78539-.04166*(3/X)-.00004*(3/X)^2+.00262*(3/X)
^3
155 LET A2=-.00054*(3/X)^4-.00029*(3/X)^5+.00013*(3/X)^6
156 LET AX=A1+A2
157 LET JX=(FX*COS(AX))/SQR(X)
159 RETURN
160 DATA 1.345,4.1225,7.1825,10.29,13.4125
161 DATA .001,2.,.04
162 DATA 2.
```

XII.2 Program for the Numerical Evaluation of Analytical Analytical Axisymmetric Stresses for Radial Temperature Fields

```
1 REM CALCULATION OF STRESSES FOR T=-R^2
2 DIM AN(50),BN(50)
4 READ NU,ZT
6 OPEN4,4:CMD4:PRINT CHR$(27);CHR$(37);CHR$(67);"110"
7 PRINT CHR$(31);"CALCULATION OF STRESSES"
8 PRINT CHR$(30);CHR$(27);CHR$(48);"ANALYTICALLY"
13 PRINT "NU=";NU;"ZT=";ZT
14 PRINT "TEMPERATURE FIELD=-R^2"
20 REM CALCULATION OF AN AND BN
21 FOR N=1 TO 10
22 :LET LN=(2*N-1)*3.1416/ZT
23 :LET T=LN/3.75
25 :IF T<=1. THEN GOSUB 180
26 :IF T>1. THEN GOSUB 190
27 :LET D=IO^2*LN-I1^2*(2*(1-NU)+LN^2)/LN
41 REM CAL ALN
42 : LET CA=D*(1-NU)*LN^5
43 : LET A1=IO*(4*NU+LN^2)
44 : LET A2=2*I1*(2*(1-NU)-NU*LN^2)/LN
46 : LET AN(N)=-2*(A1+A2)/CA
49 REM CALC OF BLN
51 : LET BN(N)=-2*(2*IO-I1*(4+LN^2)/LN)/CA
52 :PRINT "N=";N;"AN(N)=";AN(N);"BN(N)=";BN(N)
53 NEXT N
55 REM CALCULATION OF STRESSES
58 FOR L=3 TO 5
59 :LET Z=(L-2)*.5
60 :PRINT CHR$(10);"HEIGHT=";Z;CHR$(10)
62 :FOR I=1 TO 11
63 PRINT CHR$(10)
64 : LET PR=0.0
65 : LET PT=0.0
66 : LET PZ=0.0
67 : LET PU=0.0
69 : LET RO=(I-1)*.1
72 : FOR N=1 TO 10
73 :  LET LN=(2*N-1)*3.1416/ZT
78 :  IF RO=0.0 THEN GOTO 120
79 :  LET T=LN*RO/3.75
80 :  IF T<=1. THEN GOSUB 180
81 :  IF T>1. THEN GOSUB 190
84 :  LET S1=(AN(N)*(IO-I1/(LN*RO))+BN(N)*(I1*LN*RO-(2*NU-1)
*IO))*LN^3
85 :  LET S3=(I1*AN(N)/(LN*RO)-IO*(2*NU-1)*BN(N))*LN^3
86 :  LET S5=(-AN(N)*IO+BN(N)*((1-NU)*I1*LN*RO-2*(2-NU)*IO))
*LN^3
```

```
87 :  LET S7=(AN(N)*I1+BN(N)*(IO*LN*RO+2*(1-NU)*I1))*LN^3
119 :  GOTO 131
120 REM STRESSES AT THE CENTER
121 :  LET S1=(AN(N)/2-BN(N)*(2*NU-1))*LN^3
122 :  LET S3=S1
123 :  LET S5=(-AN(N)-2*(2-NU)*BN(N))*LN^3
124 :  LET S7=0.0
131 : LET S2=2*(2/LN^2+RO^2)/((1-NU)*LN)
132 : LET S4=S2
133 : LET S6=-8/(LN^3*(1-NU))
134 : LET S8=4*RO/((1-NU)*LN^2)
138 : LET PR=PR+(S1+S2)*SIN(LN*Z)
139 : LET PT=PT+(S3+S4)*SIN(LN*Z)
140 : LET PZ=PZ+(S5+S6)*SIN(LN*Z)
141 : LET PU=PU+(S7+S8)*COS(LN*Z)
144 :  PRINT "N=";N;"PR=";PR;"PT=";PT;"PZ=";PZ;"PU=";PU
146 : NEXT N
147 : LET SR=2*PR/ZT
148 : LET SH=2*PT/ZT
149 : LET SZ=2*PZ/ZT
150 : LET TR=2*PU/ZT
151 : PRINT "RO=";RO;"SR=";SR;"ST=";SH;"SZ=";SZ;"TR=";TR
155 : NEXT I
156 :NEXT L
159 PRINT#4:CLOSE4
160 END
165 RETURN
180 REM CALCULATE IO AND I1 FOR T<=1
181 LET PO=1+3.51562*T^2+3.08994*T^4+1.20674*T^6
182 LET QO=.26597*T^8+.03607*T^10+.00458*T^12
183 LET IO=PO+QO
185 LET P1=.5+.8789*T^2+.51499*T^4+.15084*T^6
186 LET Q1=.02658*T^8+.00301*T^10+.00032*T^12
188 LET I1=(P1+Q1)*T*3.75
189 RETURN
190 REM CALCULATE IO AND I1 FOR T>1
191 LET T=1/T
195 LET PO=.39894+.01328*T+.00225*T^2-.00157*T^3
198 LET QO=.00916*T^4-.02057*T^5+.02635*T^6-.01647*T^7+.0039
2*T^8
199 LET IO=EXP(3.75/T)*(PO+QO)*SQR(T/3.75)
200 LET P1=.39894-.03988*T-.00362*T^2+.00163*T^3-.01031*T^4
201 LET Q1=.02282*T^5-.02895*T^6+.01787*T^7-.0042*T^8
202 LET I1=EXP(3.75/T)*(P1+Q1)*SQR(T/3.75)
205 RETURN
220 DATA .29,2
```

XII.3 Program for the Numerical Evaluation of Analytical Axisymmetric Stresses for Axisymmetric Temperature Fields

```
1 REM CALCULATION OF SIGR
2 DIM AL(5)
4 READ H,RO,K,V,NU,ZT
5 LET CT=(V*RO)/(2*K)
6 OPEN4,4:CMD4:PRINT CHR$(27);CHR$(37);CHR$(67);"120"
7 PRINT CHR$(31);"CALCULATION OF RADIAL STRESSES"
8 PRINT CHR$(30);CHR$(27);CHR$(48);"ANALYTICALLY"
9 FOR M=1 TO 5
10 :READ AL(M)
11 :PRINT AL(M)
12 NEXT M
13 PRINT "H=";H;"RO=";RO;"V=";V;"K=";K;"NU=";NU;"ZT=";ZT
15 FOR L=3 TO 5
16 LET Z=(ZT*.1)^2*2^(L-1)
17 PRINT CHR$(10);"HEIGHT=";Z;CHR$(10)
18 FOR I=1 TO 11
19 LET SP=0.0
20 LET RO=(I-1)*.1
21 FOR N=1 TO 5
22 :LET LN=N*3.1416/ZT
23 :LET T=LN/3.75
25 :IF T<=1. THEN GOSUB 100
26 :IF T>1. THEN GOSUB 150
27 :LET D=IO^2*LN-I1^2*(2*(1-NU)+LN^2)/LN
31 REM CALC OF KT
32 :LET KT=0
33 :FOR M=1 TO 5
35 :GOSUB 180
37 :LET KT=KT+ZA/(CZ*AL(M)^2)
39 :NEXT M
41 REM CAL ALN
43 :LET A1=IO*(LN^2+2*H*RO*(1-NU))
44 :LET A2=I1*(LN^2*(H*RO+2*(1-NU))+2*H*RO*(1-NU))/LN
46 :LET AN=2*H*RO*(A1+A2)*KT/(D*(1-NU)*LN^2)
49 REM CALC OF BLN
50 :LET CB=-2*(H*RO)^2/(D*(1-NU)*LN^2)
51 :LET B=IO+I1*LN/(H*RO)
52 :LET BN=CB*B*KT
55 REM CALC SRR
58 :IF RO=0 THEN GO TO 83
59 :LET T=LN*RO/3.75
60 :IF T<=1. THEN GOSUB 100
61 :IF T>1. THEN GOSUB 150
63 :LET S1=(IO*(AN-BN*(2*NU-1))+I1*(BN*LN*RO-AN/(LN*RO)))*LN
^3
65 REM CALC OF KTJ
66 :LET S2=0
67 :FOR M=1 TO 5
68 : GOSUB 180
```

```
69 : LET X=AL(M)*RO
70 : IF X<=3. THEN GOSUB 200
71 : IF X>3. THEN GOSUB 250
72 : LET J2=JO*(LN/AL(M))^2
73 : LET J3=J1/X
74 : LET X=AL(M)
75 : IF X<=3. THEN GOSUB 200
76 : IF X>3. THEN GOSUB 250
77 : LET J4=ZA/(JO*CZ)
78 : LET S2=S2+J4*(J3+J2)
79 :NEXT M
81 :LET SP=SP+(S1-2*H*RO*S2/(1-NU))*SIN(LN*Z)
82 :GOTO 93
83 :LET S1=(AN/2-BN*(2*NU-1))*LN^3
84 :LET KJ=0
85 :FOR M=1 TO 5
86 : GOSUB 180
87 : LET X=AL(M)
88 : IF X<=3. THEN GOSUB 200
89 : IF X>3. THEN GOSUB 250
90 : LET KJ=KJ+ZA*((LN/KA)^2+.5)/(JO*CZ)
91 :NEXT M
92 :LET SP=SP+(S1-2*H*RO*KJ/(1-NU))*SIN(LN*Z)
93 :PRINT "N=";N;"SP=";SP
94 NEXT N
95 LET SR=2*SP/ZT
96 PRINT"RO=";RO;"SR=";SR
97 NEXT I
98 NEXT L
99 PRINT#4:CLOSE4:END
100 REM CALCULATE IO AND I1 FOR T<=1
101 LET PO=1+3.51562*T^2+3.08994*T^4+1.20674*T^6
102 LET QO=.26597*T^8+.03607*T^10+.00458*T^12
103 LET IO=PO+QO
105 LET P1=.5+.8789*T^2+.51499*T^4+.15084*T^6
106 LET Q1=.02658*T^8+.00301*T^10+.00032*T^12
108 LET I1=(P1+Q1)*T*3.75
110 RETURN
150 REM CALCULATE IO AND I1 FOR T>1
151 LET T=1/T
155 LET PO=.39894+.01328*T+.00225*T^2-.00157*T^3
158 LET QO=.00916*T^4-.02057*T^5+.02635*T^6-.01647*T^7+.0039
2*T^8
159 LET IO=EXP(3.75/T)*(PO+QO)*SQR(T/3.75)
160 LET P1=.39894-.03988*T-.00362*T^2+.00163*T^3-.01031*T^4
161 LET Q1=.02282*T^5-.02895*T^6+.01787*T^7-.0042*T^8
162 LET I1=EXP(3.75/T)*(P1+Q1)*SQR(T/3.75)
165 RETURN
180 REM CALCULATION OF ZA AND CZ
181 LET KA=SQR(AL(M)^2+CT^2)
182 LET ET=EXP(-KA*ZT)
183 LET EV=EXP(CT*ZT)
184 LET CZ=(AL(M)^2+(H*RO)^2)*(1+(LN/AL(M))^2)*(1-ET^2)
187 LET Z1=(1/ET-(-1)^N*EV)/((CT-KA)^2+LN^2)
188 LET Z2=(ET-(-1)^N*EV)/((CT+KA)^2+LN^2)
```

```
189 LET ZA=LN*ET*(Z1-Z2)
193 RETURN
200 REM CALCULATION OF JO AND J1 FOR X<=3
201 LET Y=X/3
202 LET G1=1-2.245*Y^2+1.26562*Y^4-.31638*Y^6
203 LET G2=.04445*Y^8-.00394*Y^10+.00021*Y^12
204 LET JO=G1+G2
206 LET G3=.5-.56249*Y^2+.21093*Y^4
207 LET G4=.03954*Y^6+.00443*Y^8-.00031*Y^10
208 LET J1=(G3+G4)*X
210 RETURN
250 REM CALCULATION OF JO AND J1 FOR X>3
251 LET Y=3/X
252 LET F1=.79788-.00552*Y^2-.00009*Y^3+.00137*Y^4
253 LET F2=-.00072*Y^5+.00014*Y^6
254 LET T1=X-.78539-.04166*Y-.00004*Y^2+.00262*Y^3
255 LET T2=-.00054*Y^4-.00029*Y^5+.00013*Y^6
256 LET JO=(F1+F2)*COS(T1+T2)/SQR(X)
258 LET F3=.79788+.01659*Y^2+.00017*Y^3-.00249*Y^4
259 LET F4=.00113*Y^5-.0002*Y^6
260 LET T3=X-2.35619+.12499*Y+.00005*Y^2-.00638*Y^3
261 LET T4=.00074*Y^4+.00079*Y^5-.00029*Y^6
264 LET J1=(F3+F4)*COS(T3+T4)/SQR(X)
266 RETURN
270 DATA .6,2.,.04,.001,.29
271 DATA 5
272 DATA 1.345,4.1225,7.1825,10.29,13.4125
```

APPENDIX XIII

TEMPERATURE AND STRESS PLOTS FROM THE COMPUTER PROGRAMS OUTPUT (GROWTH)

Units are : 10^{3o}C for the temperatures and MPa for the stresses.

XIII.1 Cone Angle
CL, 10 mm ; R, 20 mm ; B, 10 mm ; AP, 30 atm. ;
BG, 100°C/cm ; AG, 50°C/cm.

XIII.1.1 Cone Angle 7.1°

XIII.1.1.1 (a) Temperature and Von Mises Stress
(b) MRSS ; (c) MRSS-CRSS (Yield) ;
(d) MRSS-CRSS (MB) ; (e) MRSS-CRSS (MBTe)

XIII.1.1.2 Cross-sections at 2.5 mm from the interface
(a) MRSS ; (b) MRSS-CRSS (Yield) ;
(c) MRSS-CRSS (MB) ; (d) MRSS-CRSS (MBTe)

XIII.1.1.3 Cross-sections at 7.5 mm from the interface
(a) MRSS ; (b) MRSS-CRSS (Yield) ;
(c) MRSS-CRSS (MB) ; (d) MRSS-CRSS (MBTe)

XIII.1.2 Cone Angle 30°

XIII.1.2.1 (a) Temperature and Von Mises Stress
(b) MRSS ; (c) MRSS-CRSS (Yield) ;
(d) MRSS-CRSS (MB) ; (e) MRSS-CRSS (MBTe)

XIII.1.2.2 Cross-sections at 7.5 mm from the interface
(a) MRSS ; (b) MRSS-CRSS (Yield) ;
(c) MRSS-CRSS (MB) ;

XIII.1.3 Cone Angle 45°

XIII.1.3.1 (a) Temperature and Von Mises Stress
(b) MRSS ; (c) MRSS-CRSS (Yield) ;
(d) MRSS-CRSS (MB) ; (e) MRSS-CRSS (MBTe) ;
(f) Slip Mode.

XIII.1.3.2 Cross-sections at 2.5 mm from the interface
(a) MRSS-CRSS (Yield) ; (b) MRSS-CRSS (MBTe) ;

XIII.1.3.3 Cross-sections at 7.5 mm from the interface
(a) MRSS ; (b) MRSS-CRSS (Yield) ;
(c) MRSS-CRSS (MBTe)

XIII.1.4 Cone Angle 54.7^{o}

XIII.1.4.1 (a) Temperature ; (b) Von Mises Stress
(c) MRSS ; (d) MRSS-CRSS (Yield) ;
(e) MRSS-CRSS (MB) ; (f) MRSS-CRSS (MBTe).

XIII.1.4.2 Cross-sections at 2.5 mm from the interface
(a) MRSS ; (b) MRSS-CRSS (Yield) ;

XIII.1.4.3 Cross-sections at 7.5 mm from the interface
(a) MRSS ; (b) MRSS-CRSS (Yield) ;

XIII.1.5 Cone Angle 65°

XIII.1.5.1 (a) Temperature and Von Mises Stress
(b) MRSS ; (c) MRSS-CRSS (Yield) ;
(d) MRSS-CRSS (MB) ; (e) MRSS-CRSS (MBTe).

XIII.1.5.2 Cross-sections at 8.0 mm from the interface
(a) MRSS ; (b) MRSS-CRSS (Yield) ;

XIII.1.6 Effect of Thermal Conditions

XIII.1.6.1 BG, 50°C/cm ; AG, 25°C/cm ; CA, 45° .

XIII.1.6.1.1 (a) Temperature and Von Mises Stress
(b) MRSS ; (c) MRSS-CRSS (Yield) ;
(d) MRSS-CRSS (MB) ; (e) MRSS-CRSS (MBTe).

XIII.1.6.1.2 Cross-sections at 5 mm from the interface
(a) MRSS ; (b) MRSS-CRSS (Yield) ;
(c) MRSS-CRSS (MB) ; (d) MRSS-CRSS (MBTe)

XIII.1.6.1.3 Cross-sections at 7.5 mm from the interface
(a) MRSS ; (b) MRSS-CRSS (Yield) ;
(c) MRSS-CRSS (MB) ; (d) MRSS-CRSS (MBTe)

XIII.1.6.2 BG, 200°C/cm ; AG, 100°C/cm

XIII.1.6.2.1 (a) Temperature and Von Mises Stress
(b) MRSS ; (c) MRSS-CRSS (Yield) ;
(d) MRSS-CRSS (MBTe) .

XIII.1.6.2.2 Cross-section at 2.5 mm from the interface, MRSS .

XIII.1.6.2.3 Cross-sections at 7.5 mm from the interface
(a) MRSS ; (b) MRSS-CRSS (Yield) ;

XIII.1.6.3 BG, 400°C/cm ; AG, 100°C/cm

XIII.1.6.3.1 (a) Temperature and Von Mises Stress
(b) MRSS ; (c) MRSS-CRSS (Yield) ;
(d) Slip Mode.

XIII.1.6.3.2 Cross-sections at 7.5 mm from the interface
(a) MRSS-CRSS (Yield) ; (b) Slip Mode.

XIII.1.7 Heat Transfer Coefficient
BG, 100°C/cm ; AG, 50°C/cm

XIII.1.7.1 H/1.3

XIII.1.7.1.1 (a) Temperature and Von Mises Stress
(b) MRSS ; (c) MRSS-CRSS (Yield) ;
(d) MRSS-CRSS (MB) ; (e) MRSS-CRSS (MBTe) .

XIII.1.7.1.2 MRSS-CRSS (Yield) in cross-sections at distance from the interface (a) 2.5 mm ; (b) 7.5 mm.

XIII.1.7.2 Hx1.3

XIII.1.7.2.1 (a) Temperature and Von Mises Stress
(b) MRSS ; (c) MRSS-CRSS (Yield) ;
(d) MRSS-CRSS (MB) ; (e) MRSS-CRSS (MBTe) .

XIII.1.7.2.2 MRSS-CRSS (Yield) in cross-sections at 2.5 mm from the interface

XIII.1.7.2.3 Cross-sections at 7.5 mm from the interface
(a) MRSS ; (b) MRSS-CRSS (Yield) ;

a

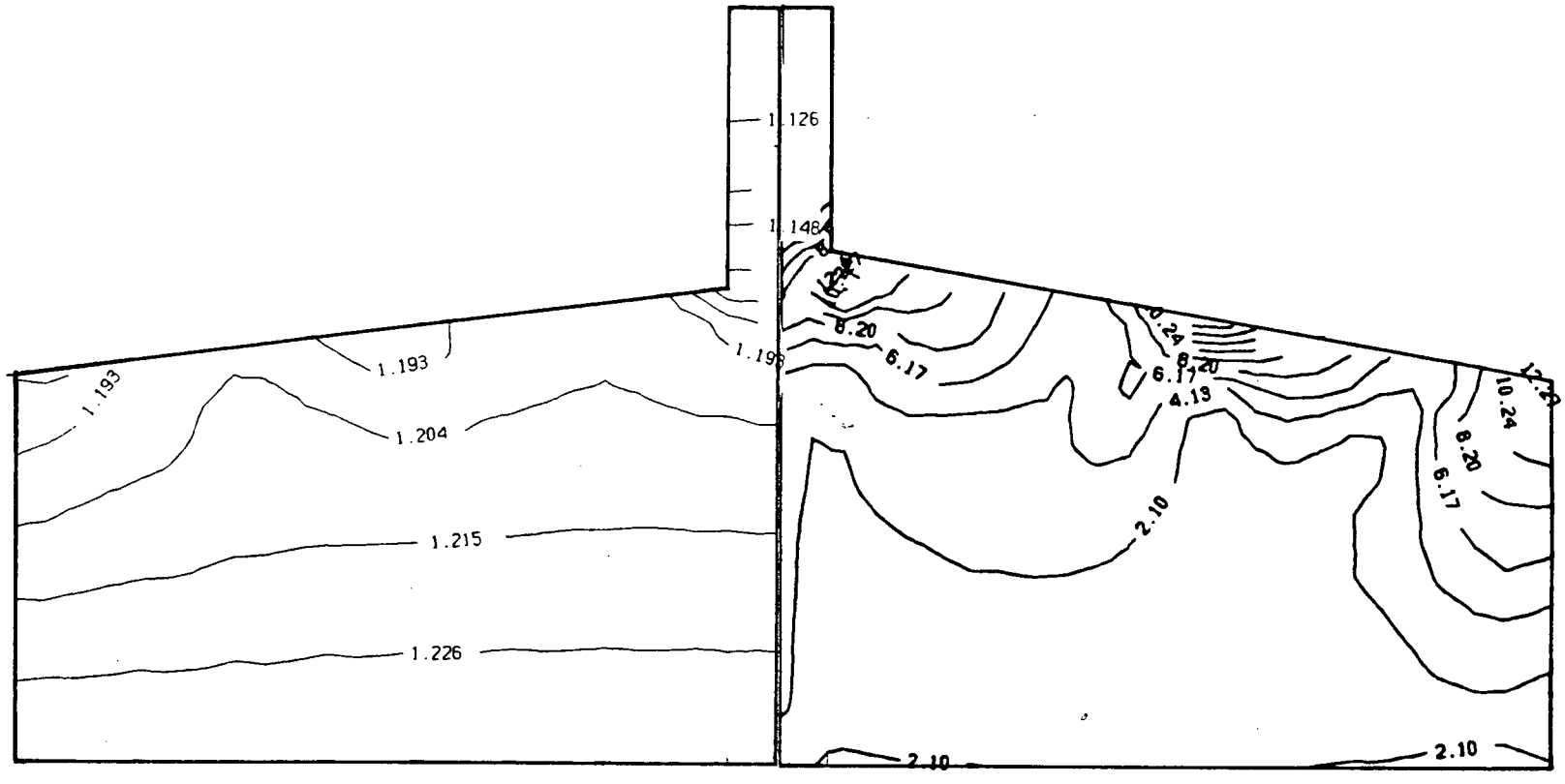
1.126
1.148
1.193
1.193
1.204
1.215
1.226
8.20
6.17
0.24
8.20
6.17
4.13
2.10
10.24
8.20
6.17
2.10
2.10

b

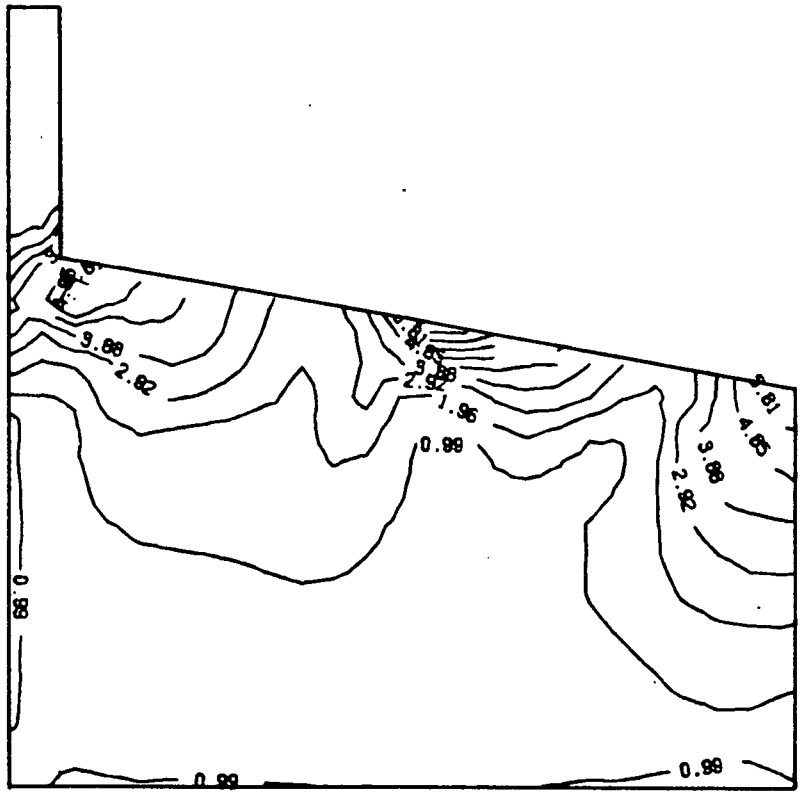
3.88
2.92
1.96
0.99
4.85
3.88
2.92
0.99
0.99
0.99

c

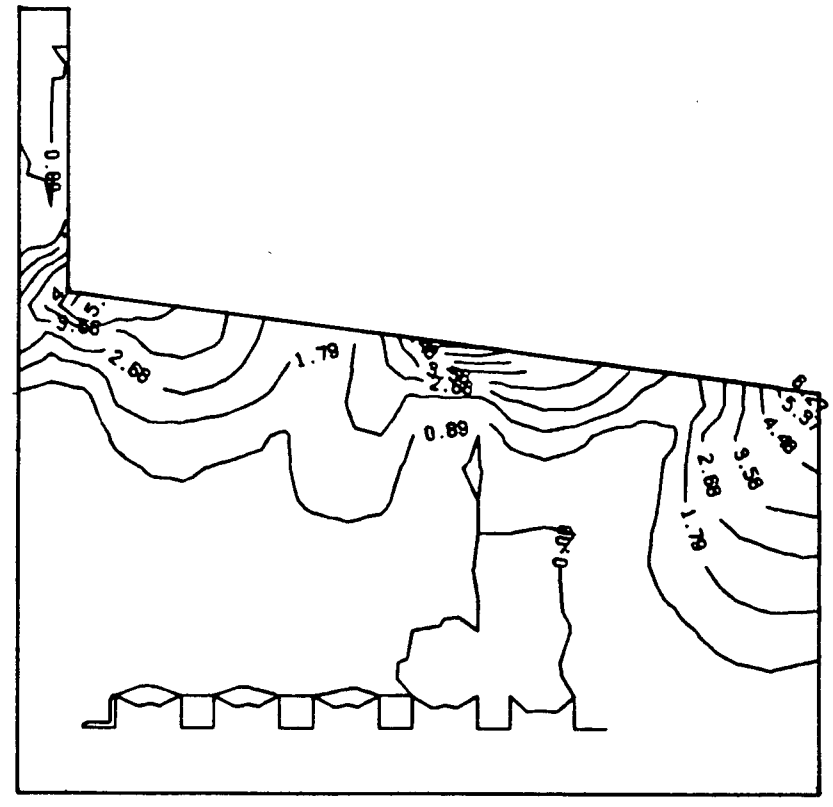
2.68
1.79
0.89
4.48
3.58
2.68
1.79

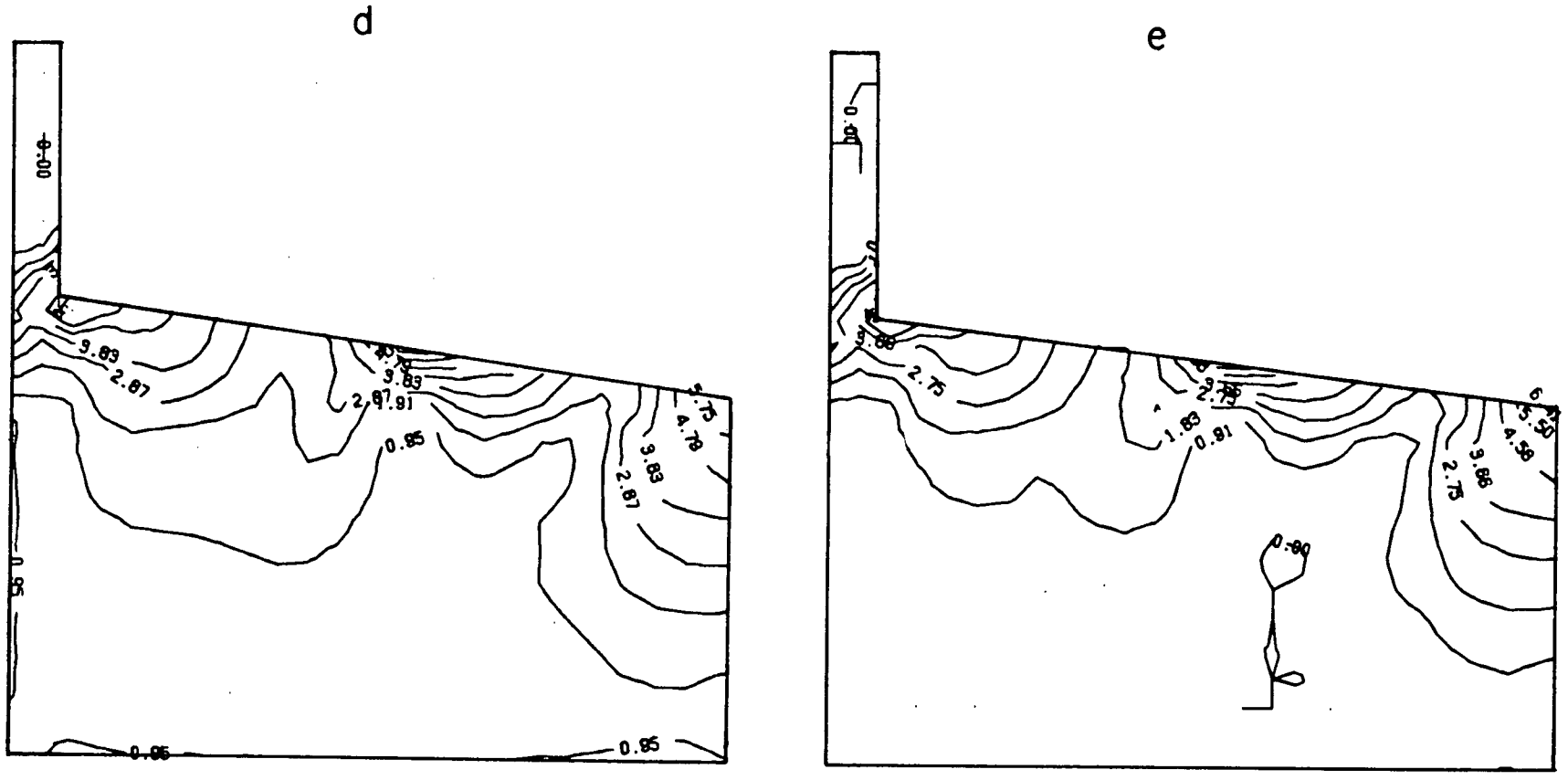

XIII.1.1.1 (a) Temperature and Von Mises Stress
(b) MRSS ; (c) MRSS-CRSS (Yield) ;
(d) MRSS-CRSS (MB) ; (e) MRSS-CRSS (MBTe)

a

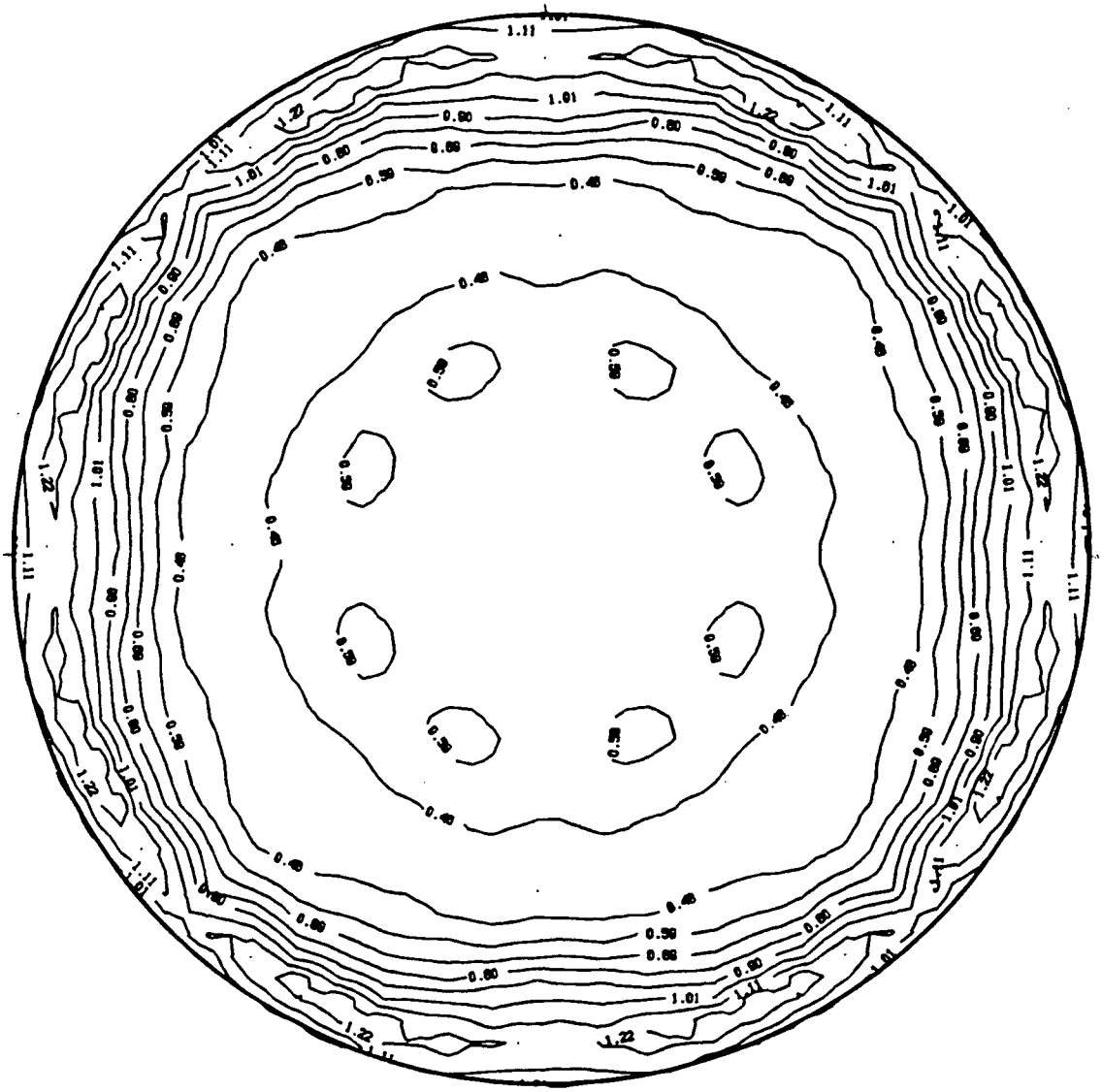

b

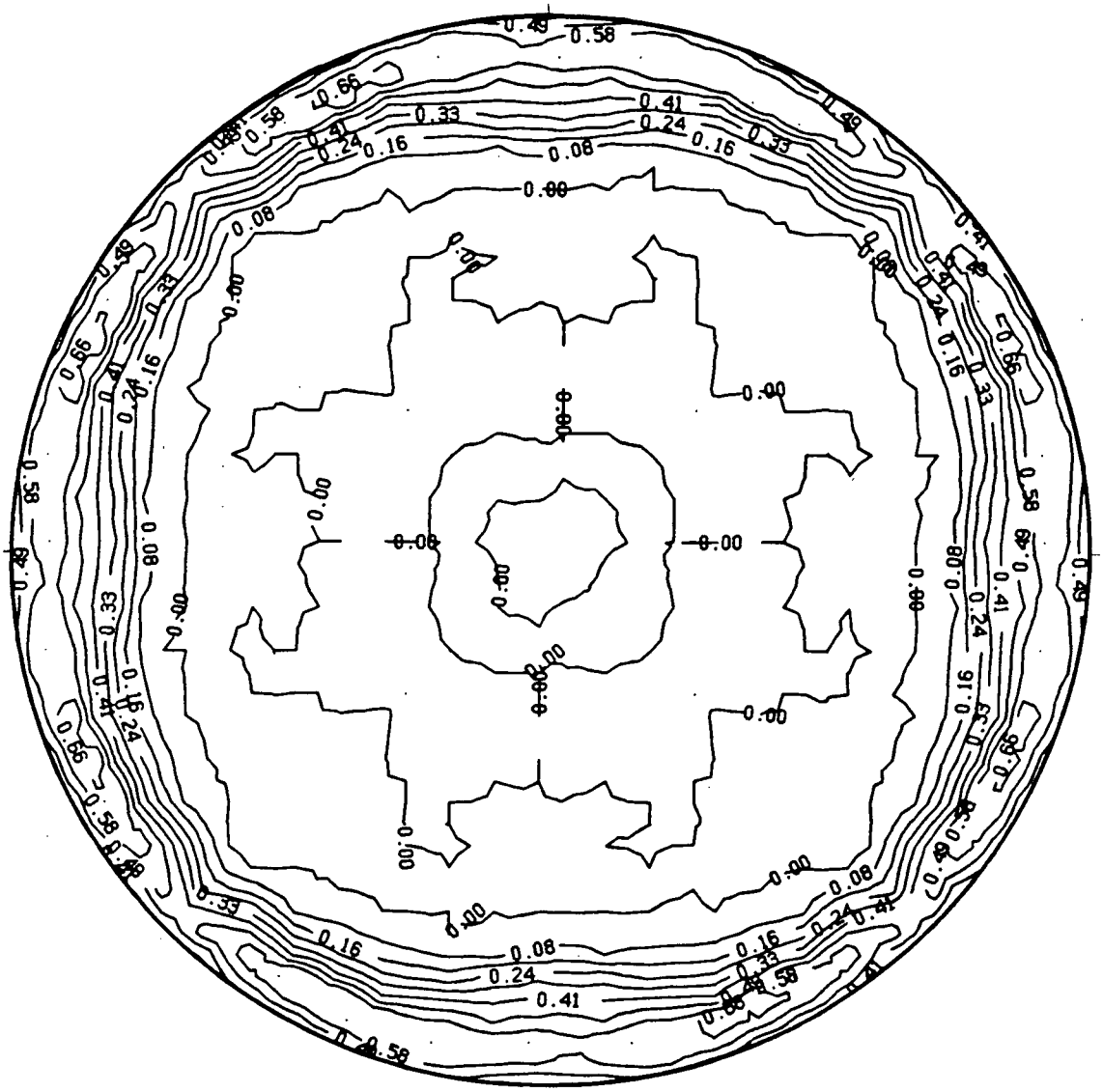

C

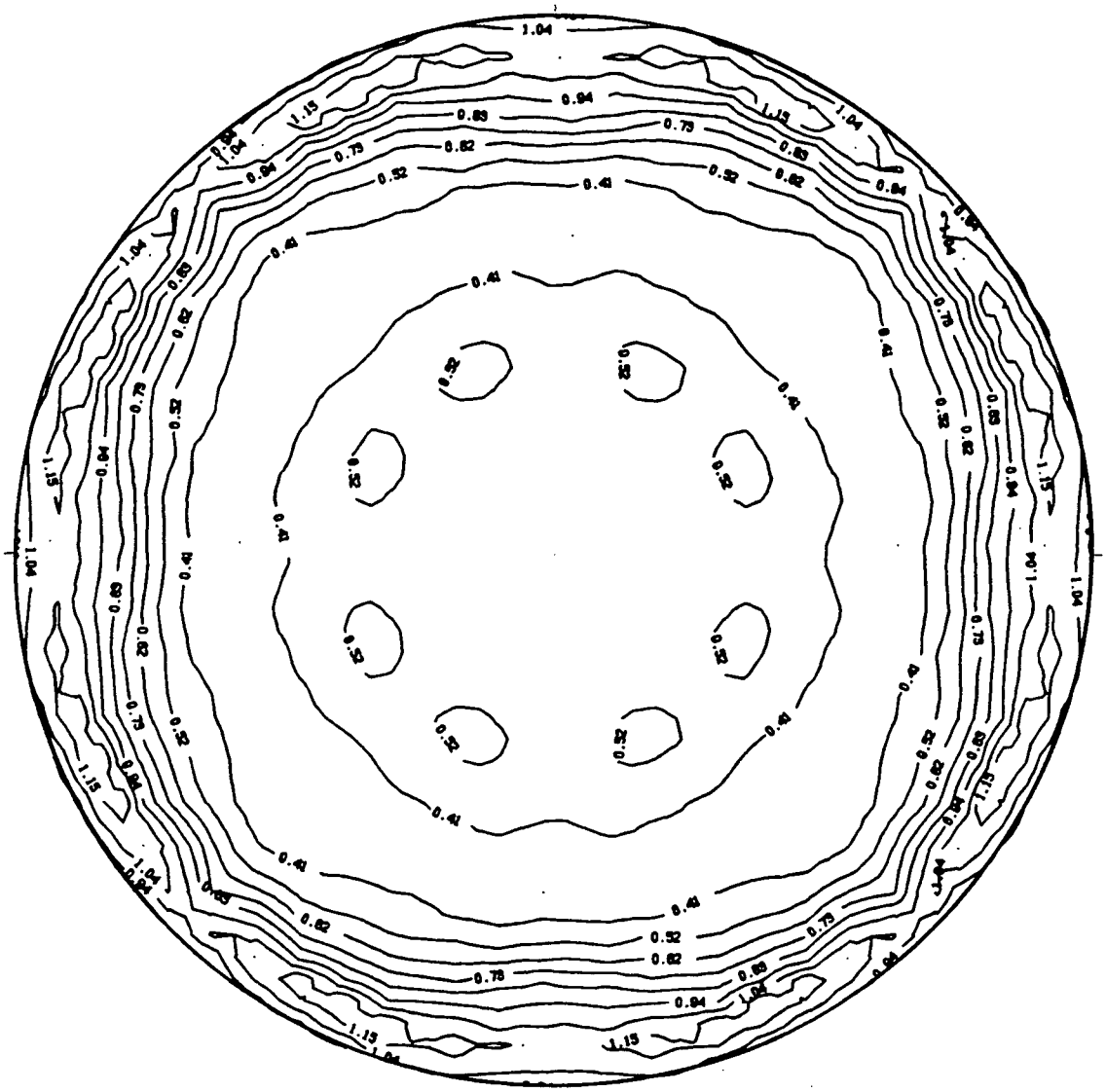

d

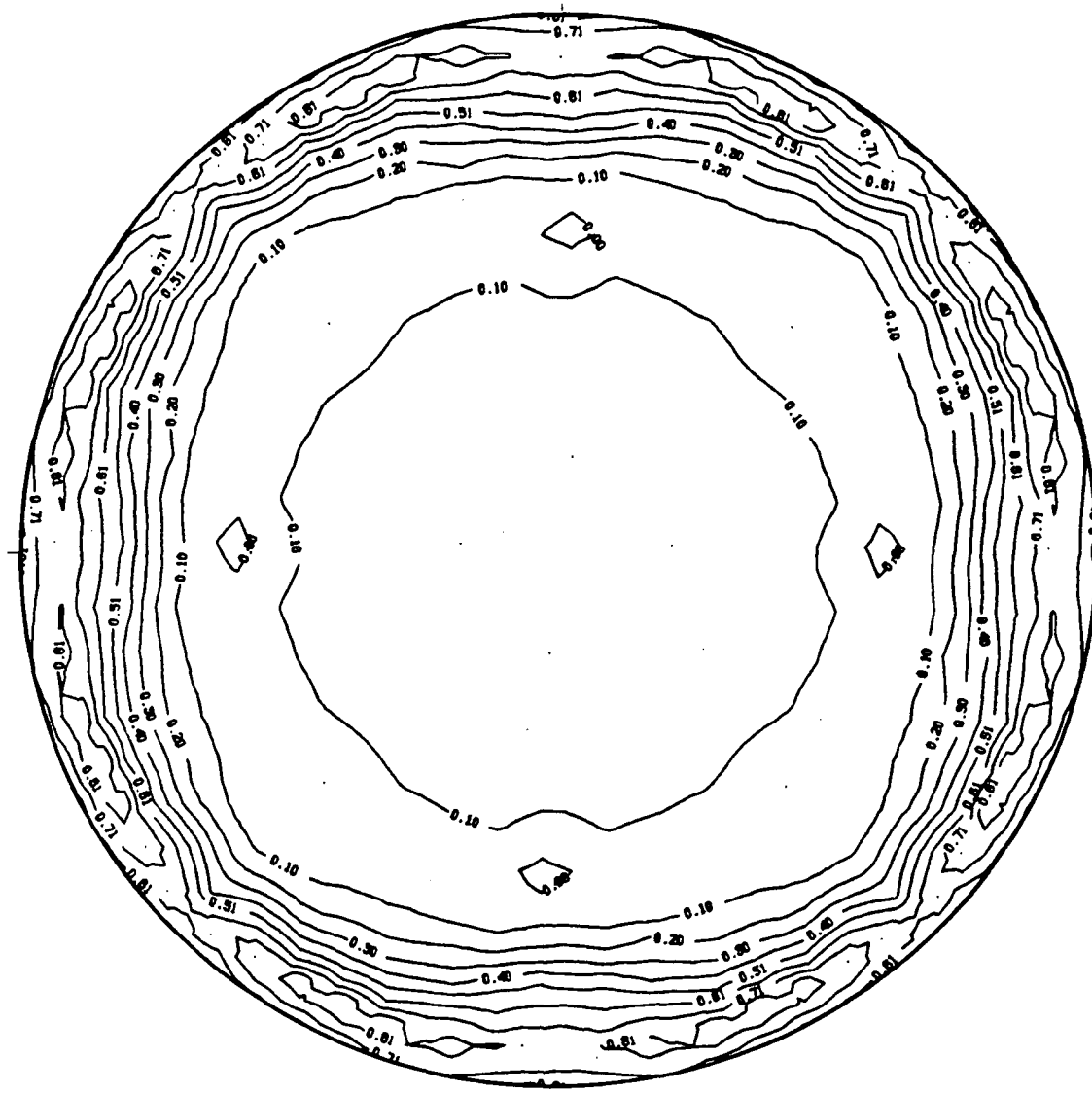

XIII.1.1.2 Cross-sections at 2.5 mm from the interface
(a) MRSS ; (b) MRSS-CRSS (Yield) ;
(c) MRSS-CRSS (MB) ; (d) MRSS-CRSS (MBTe)

a

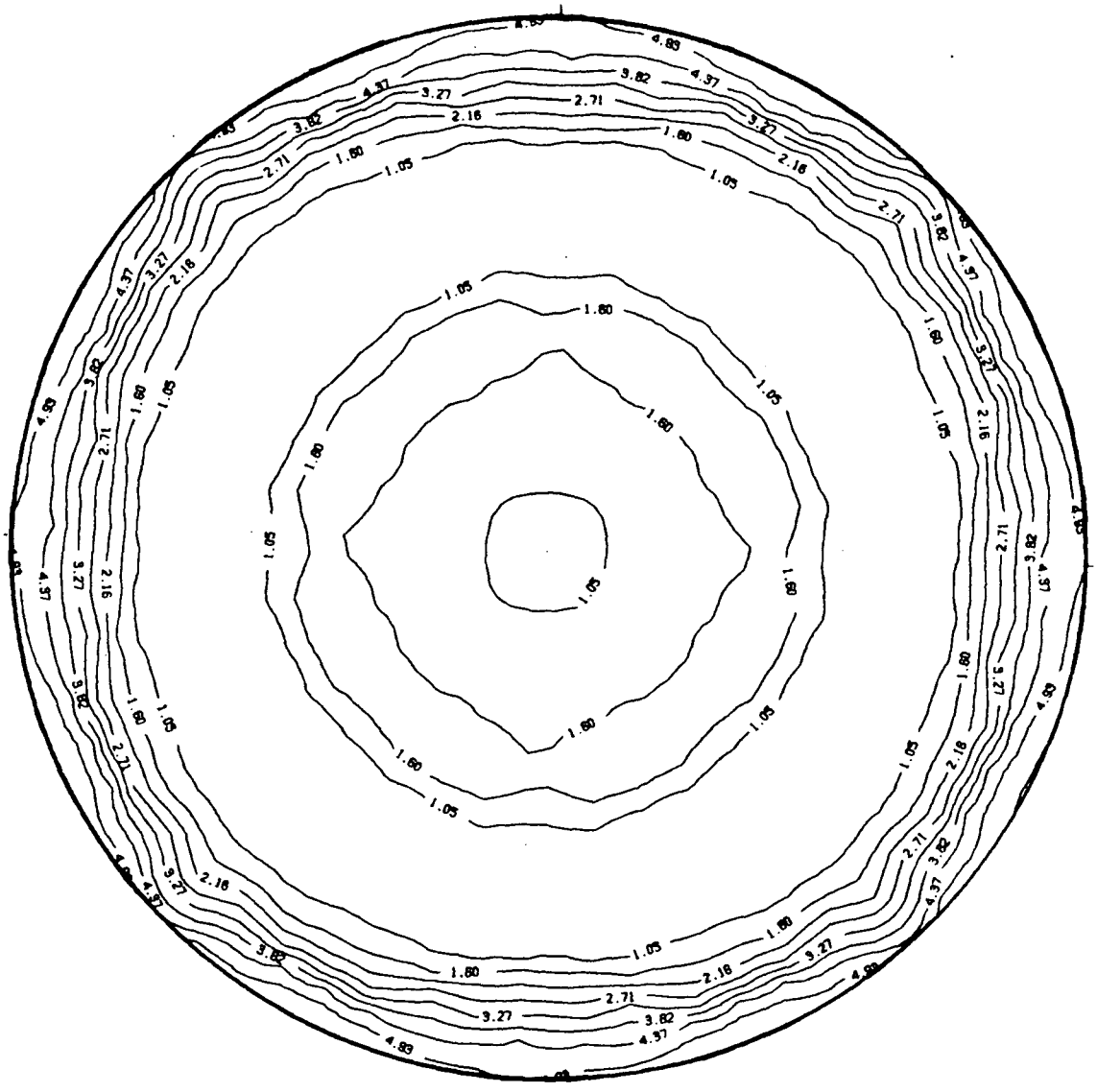

b

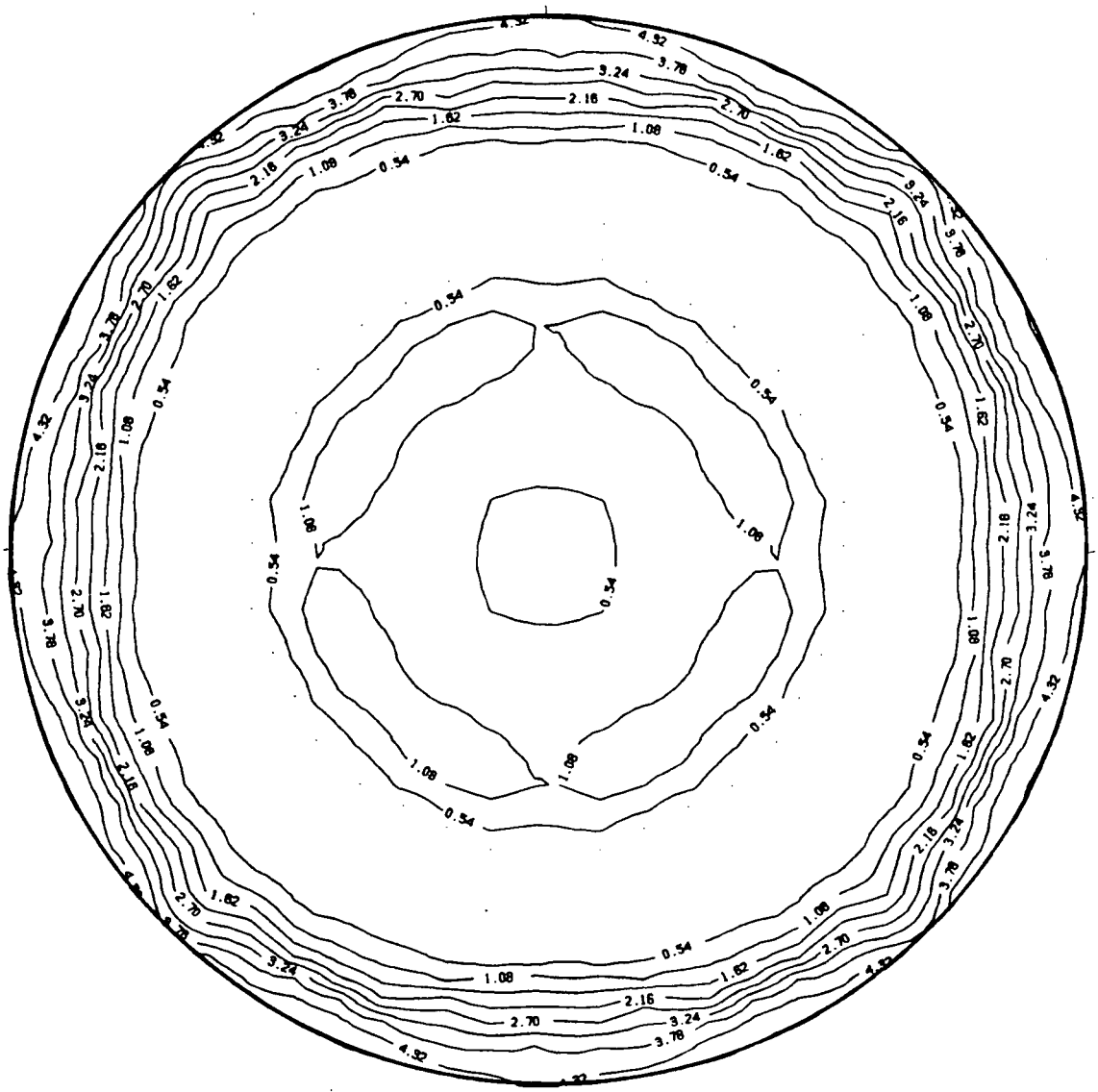

C

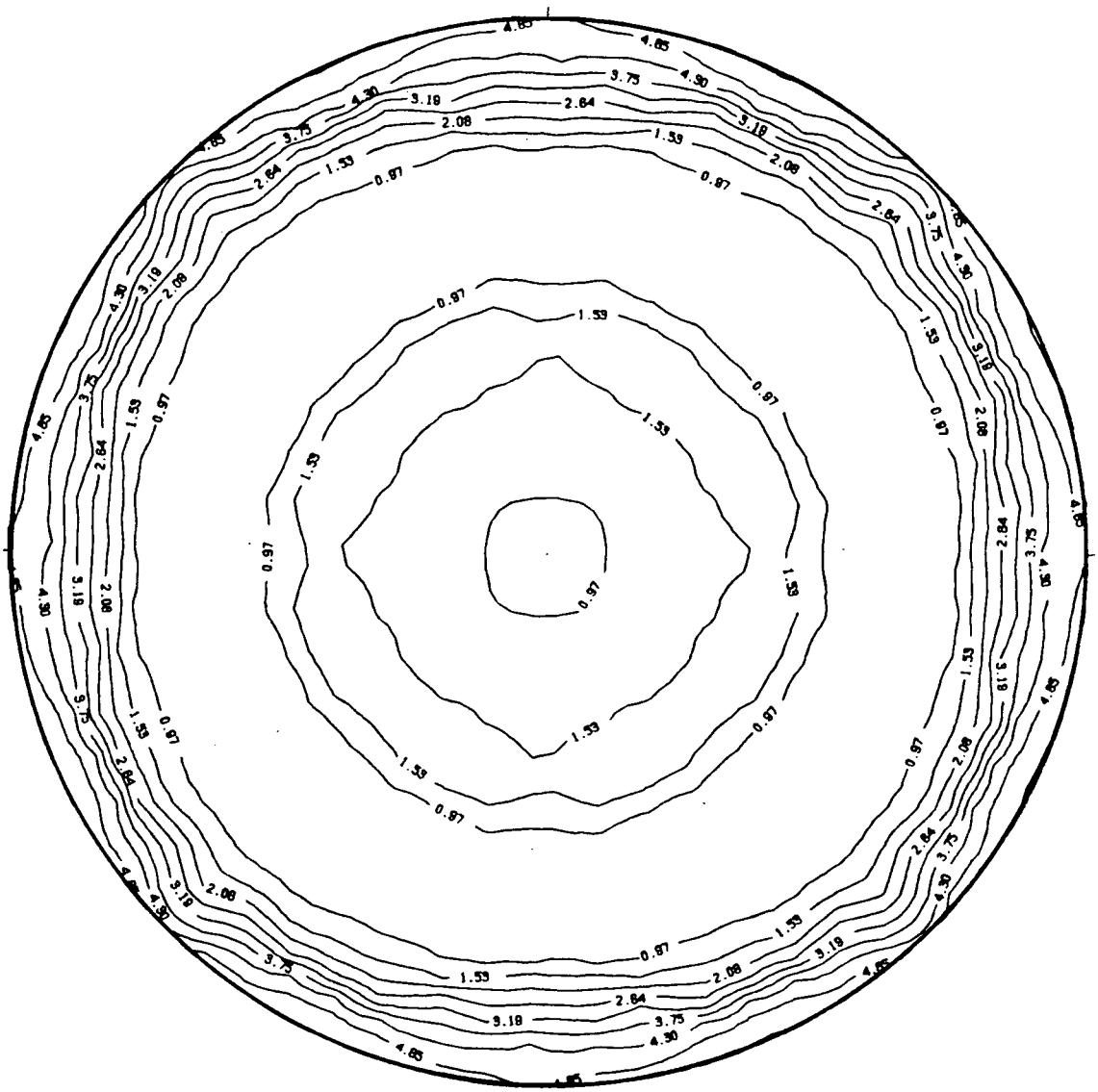

d

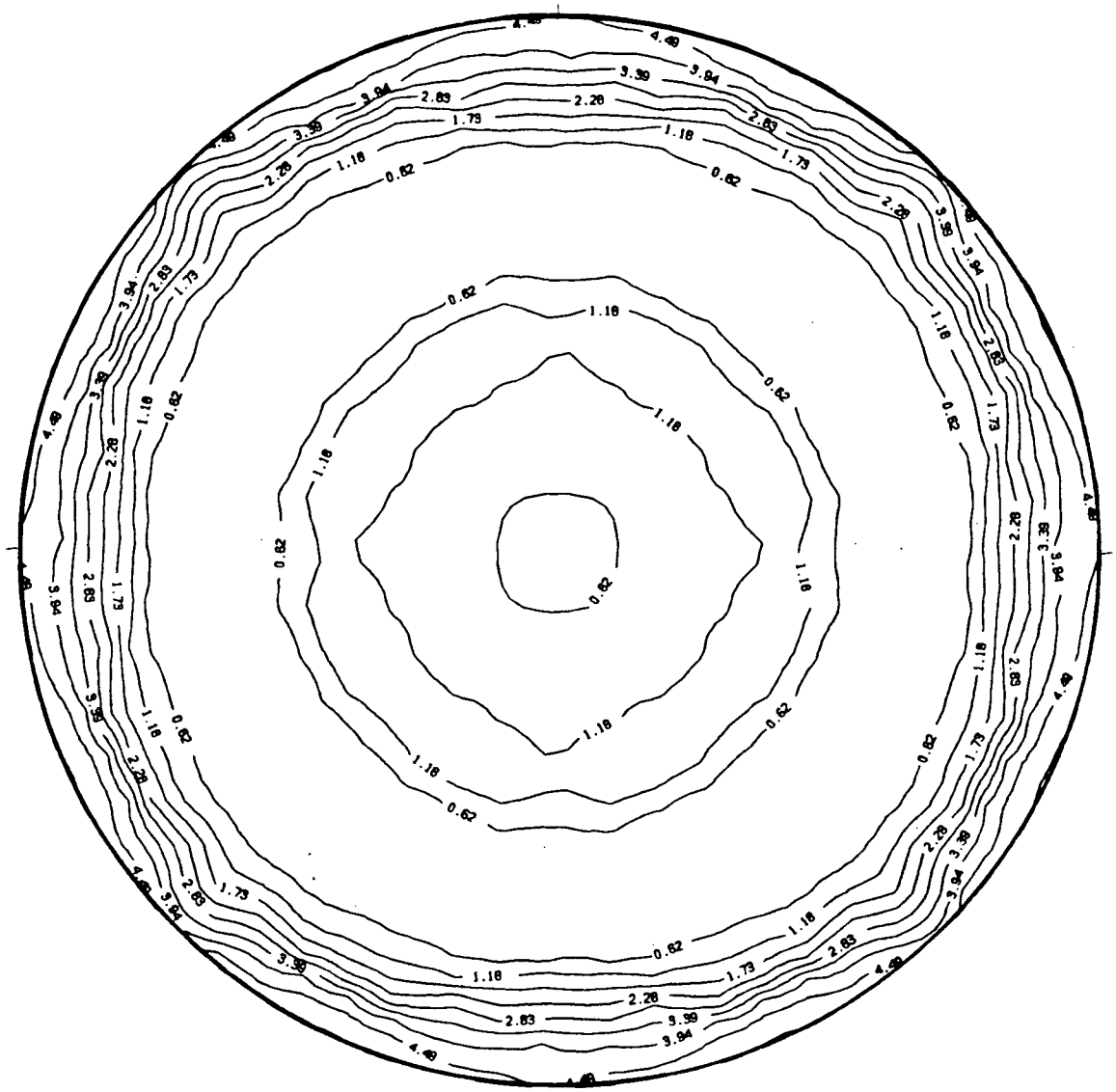

XIII.1.1.3 Cross-sections at 7.5 mm from the interface
(a) MRSS ; (b) MRSS-CRSS (Yield) ;
(c) MRSS-CRSS (MB) ; (d) MRSS-CRSS (MBTe)

a

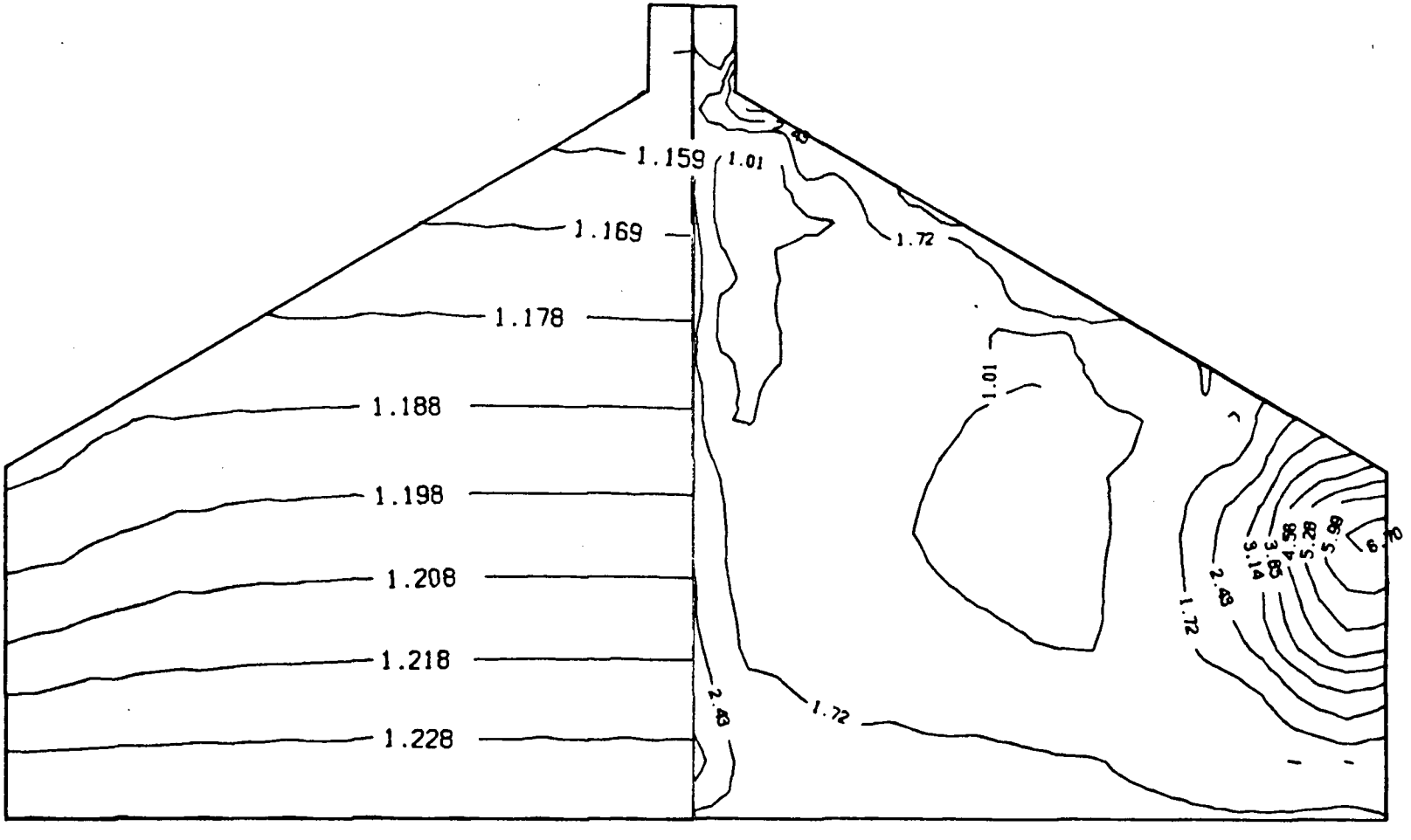
1.159
1.169
1.178
1.188
1.198
1.208
1.218
1.228
1.01
1.72
2.43
1.01
1.72
2.43
1.72
2.43
3.14
3.85
4.58
5.28
5.99
6.70

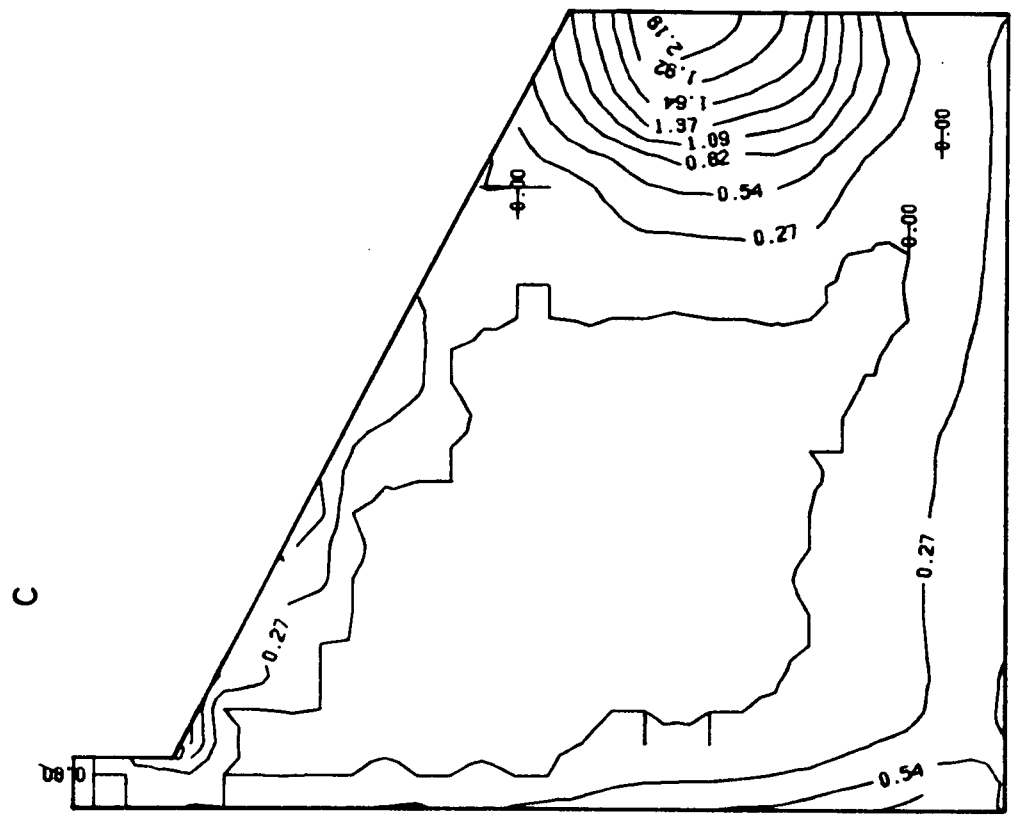
c
2.19
1.92
1.64
1.37
1.09
0.82
0.54
0.27
0.27
0.27
0.54
0.80

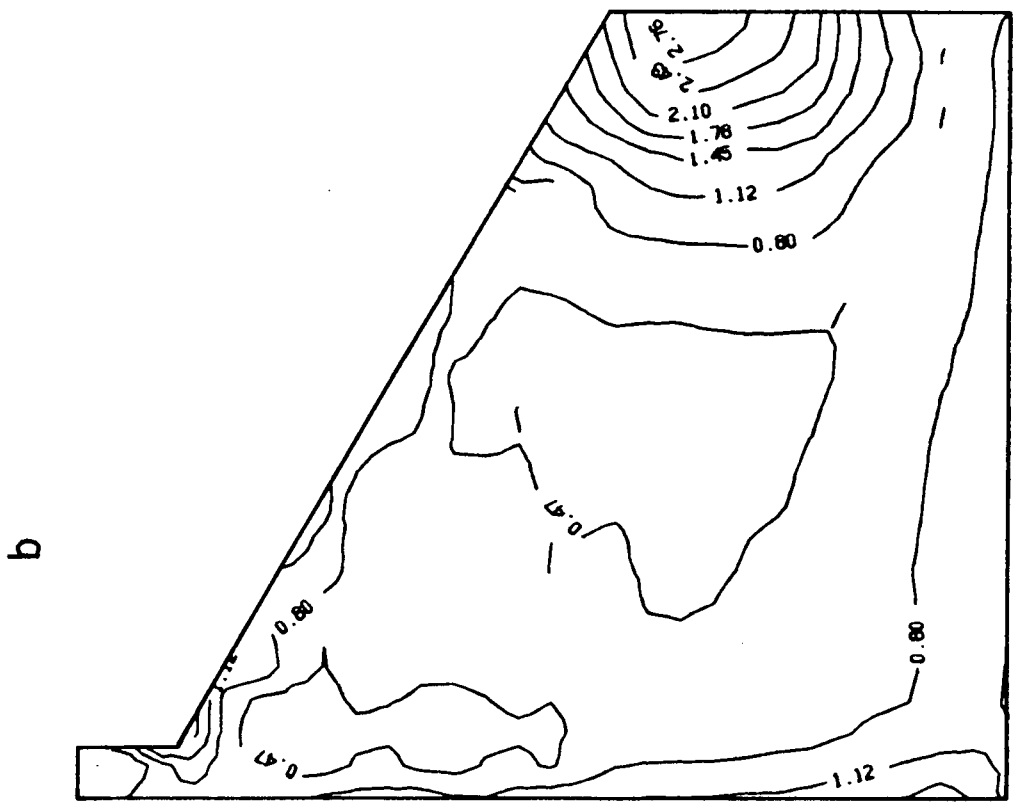
b
2.45
2.10
1.78
1.45
1.12
0.80
0.47
0.80
0.80
0.47
1.12

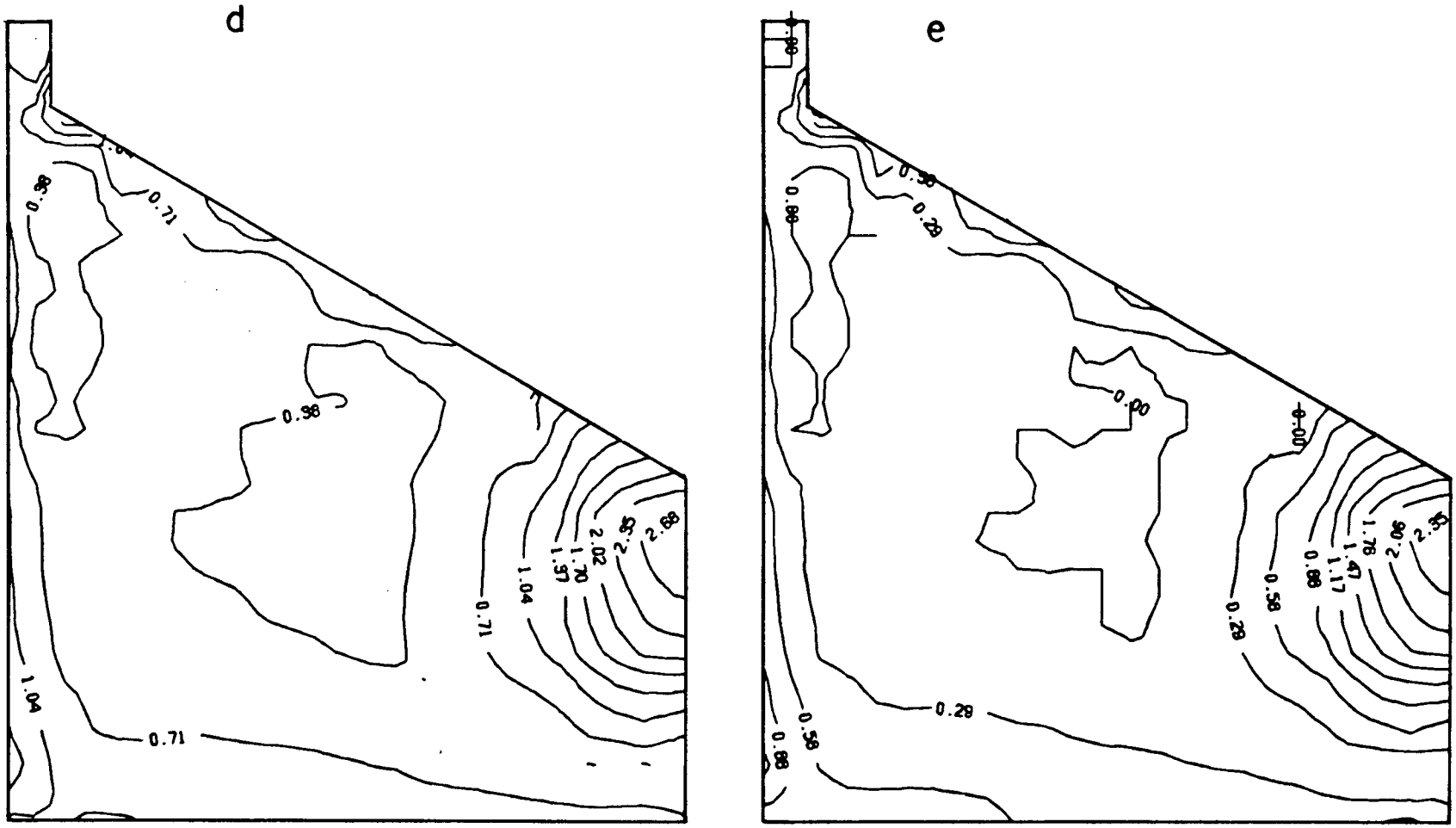

XIII.1.2.1 (a) Temperature and Von Mises Stress
(b) MRSS ; (c) MRSS-CRSS (Yield) ;
(d) MRSS-CRSS (MB) ; (e) MRSS-CRSS (MBTe)

a

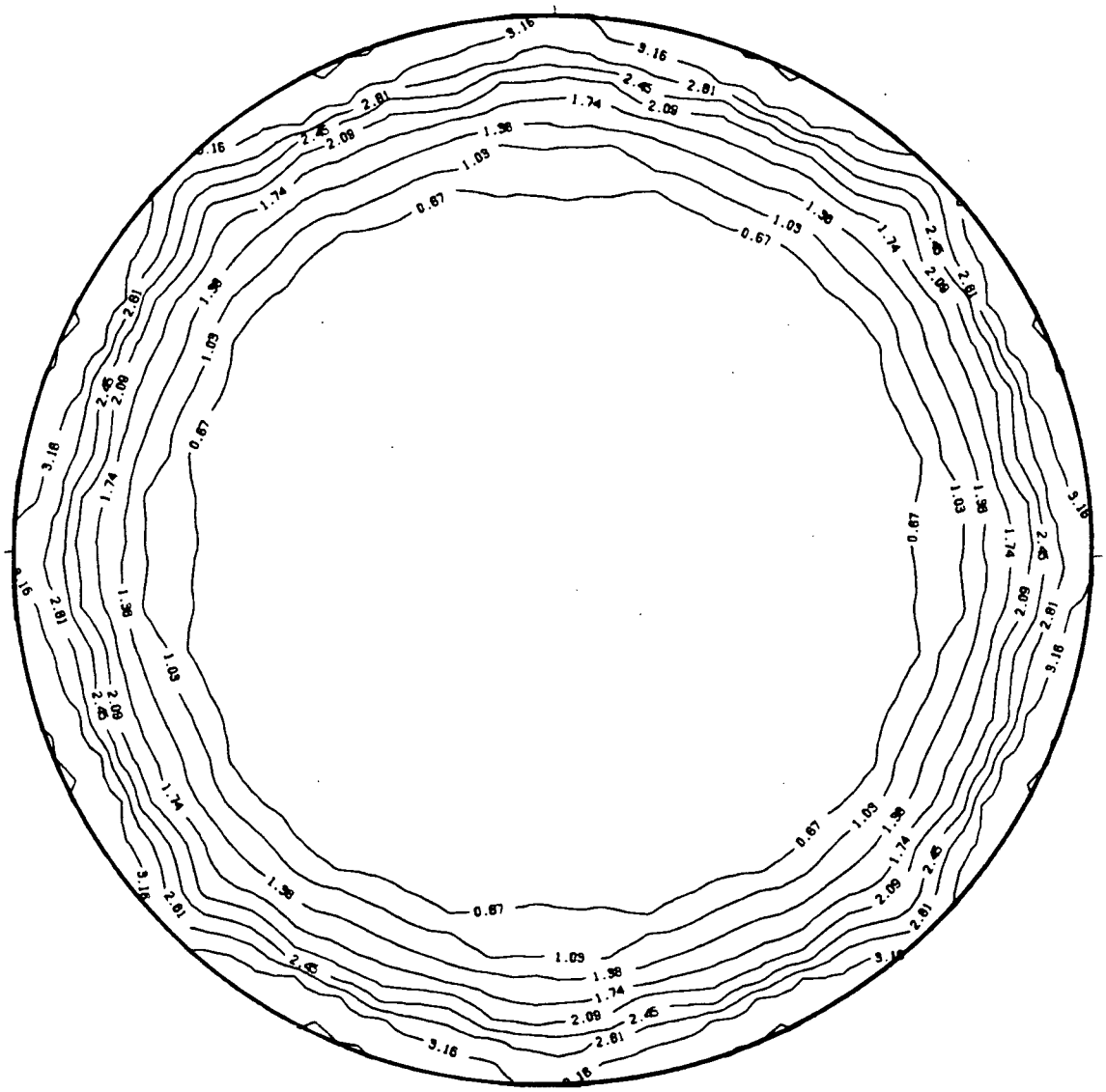

b

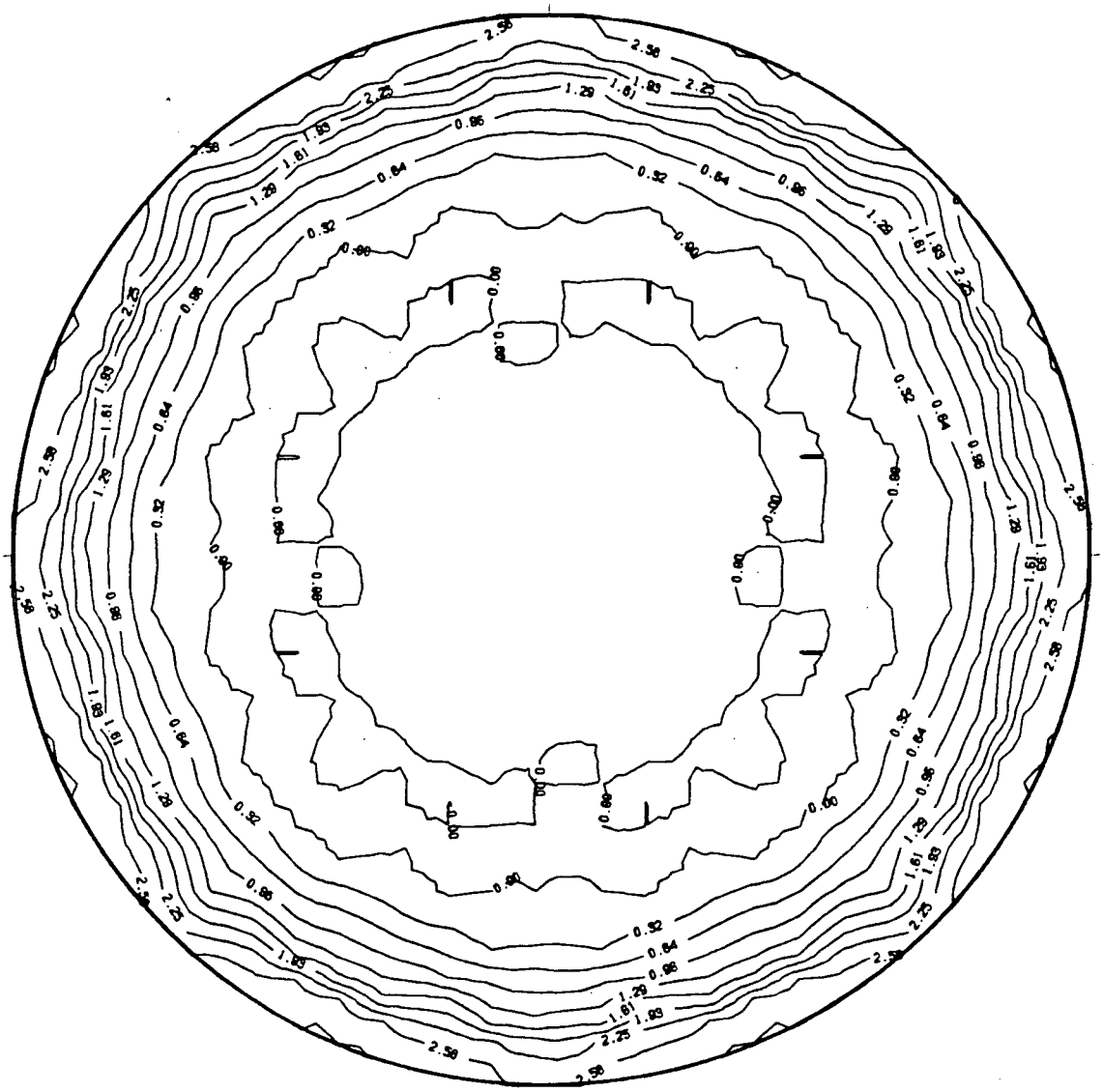

C

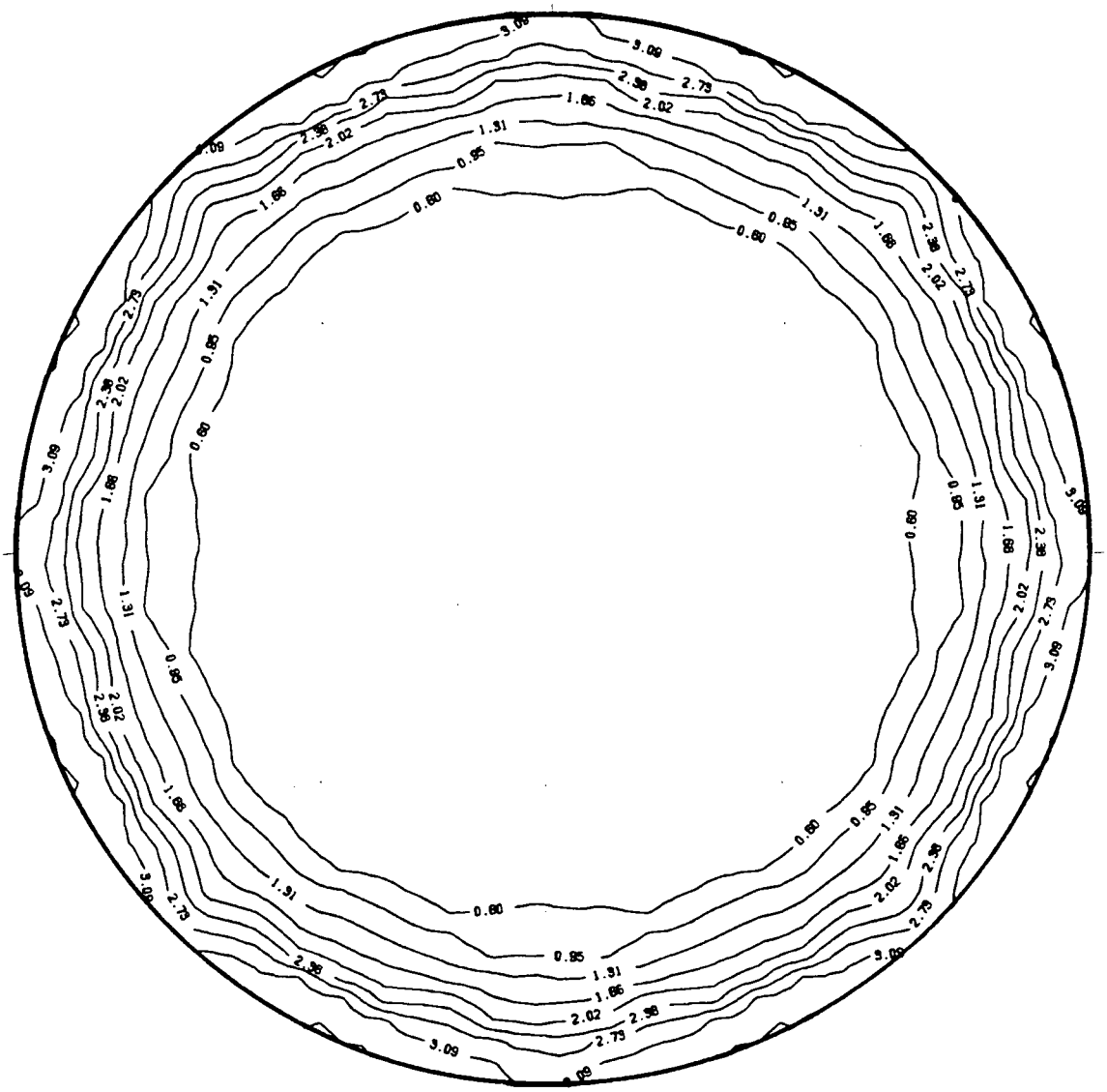

XIII.1.2.2 Cross-sections at 7.5 mm from the interface
(a) MRSS ; (b) MRSS-CRSS (Yield) ;
(c) MRSS-CRSS (MB) ;

a

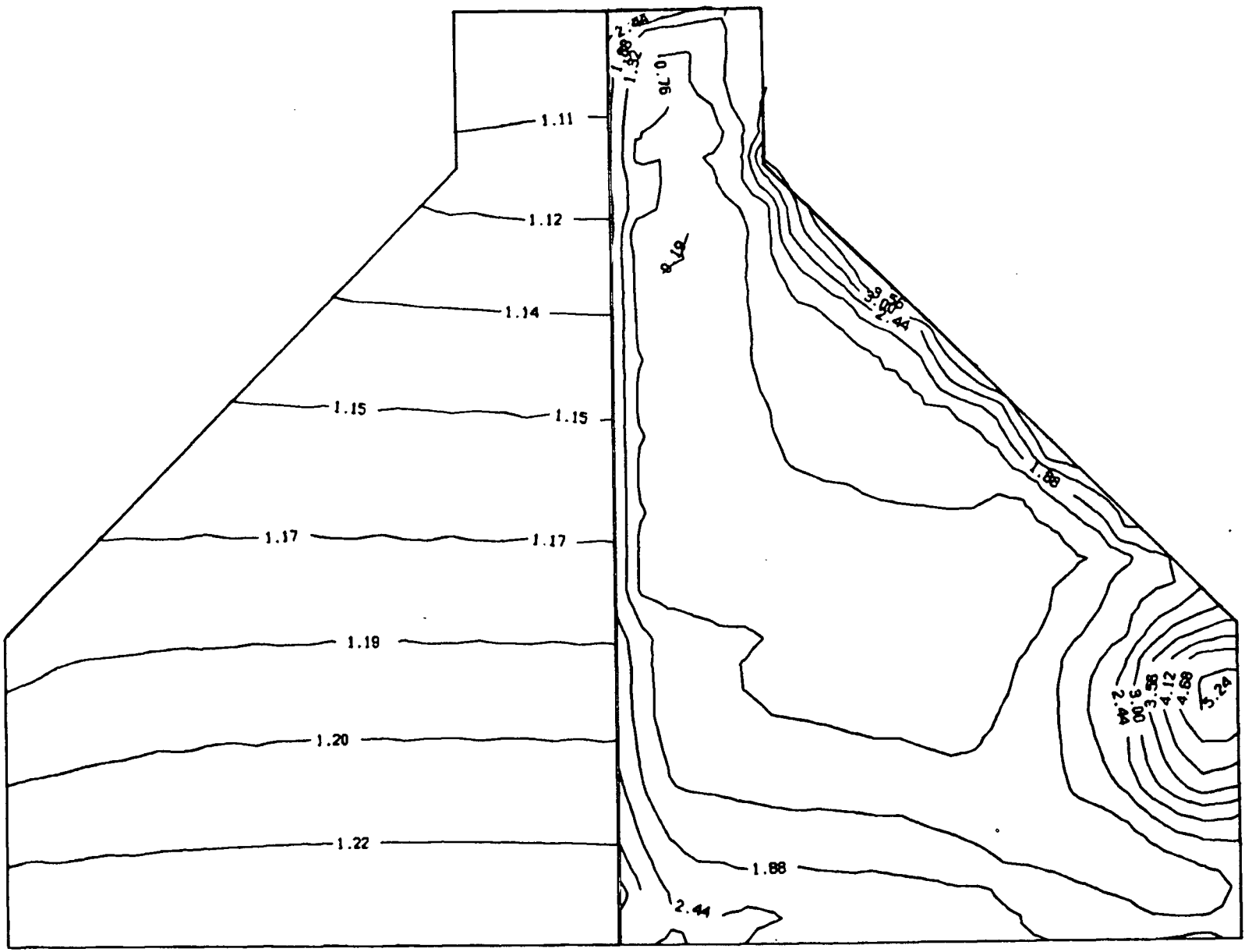
1.11
1.12
1.14
1.15
1.15
1.17
1.17
1.19
1.20
1.22
1.88
2.44
0.76
1.88
2.44
3.00
3.58
4.12
4.68
5.24

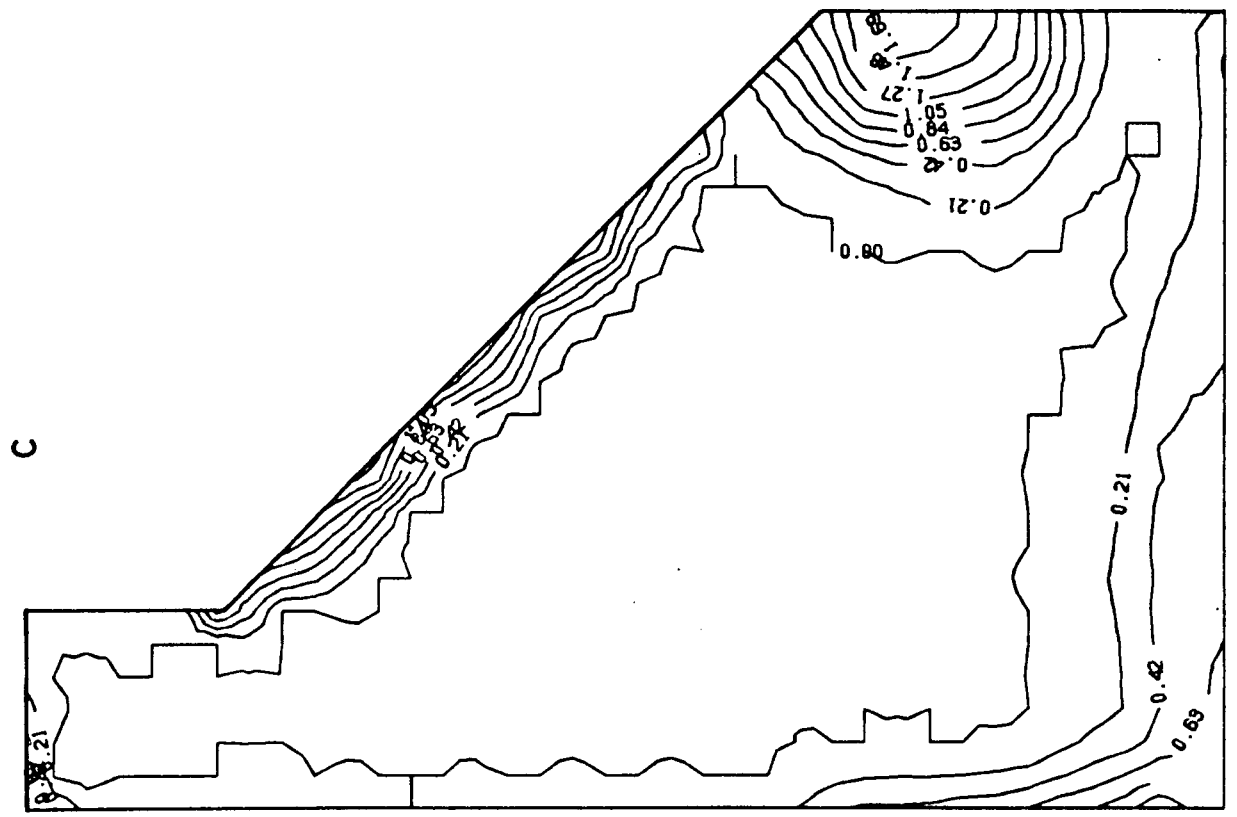
c
0.21
0.42
0.63
0.90
1.27
1.05
0.84
0.63
0.42
0.21

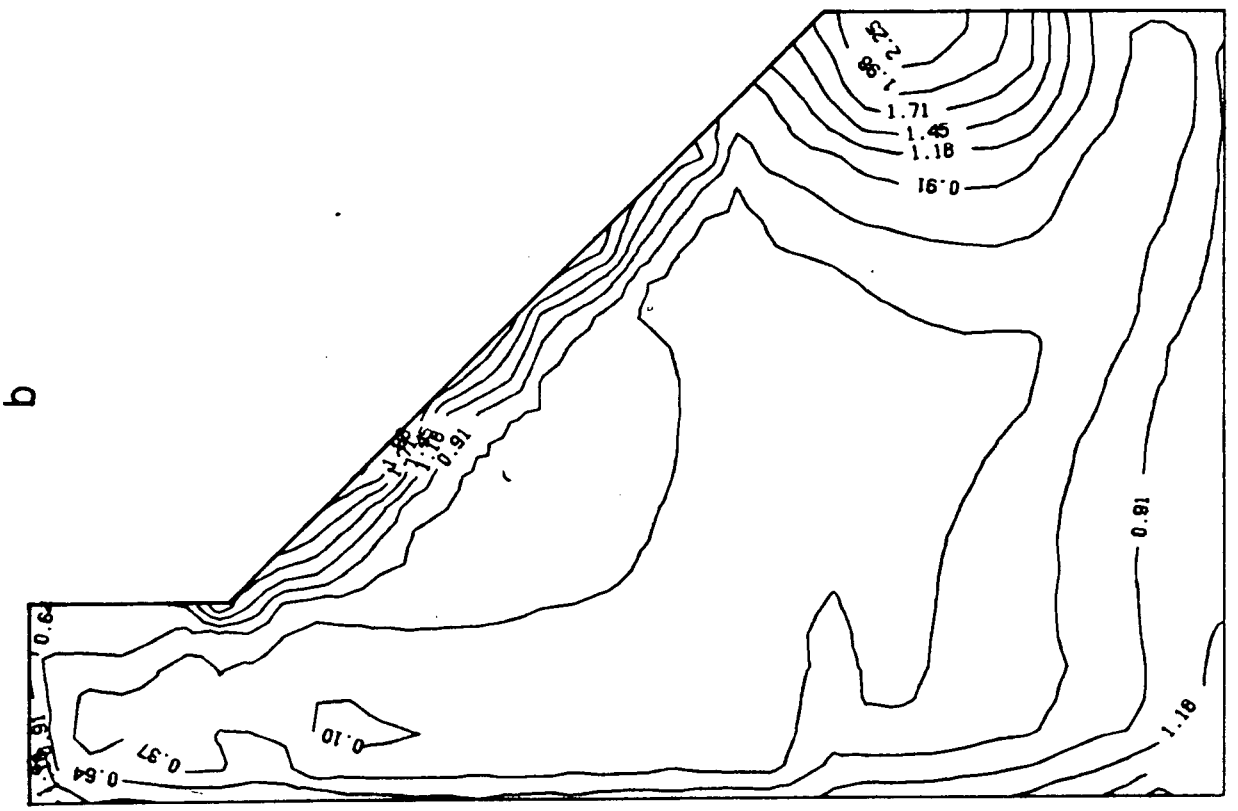
b
0.81
1.18
0.91
1.18
1.45
1.71
1.98
2.25
0.10
0.37
0.64

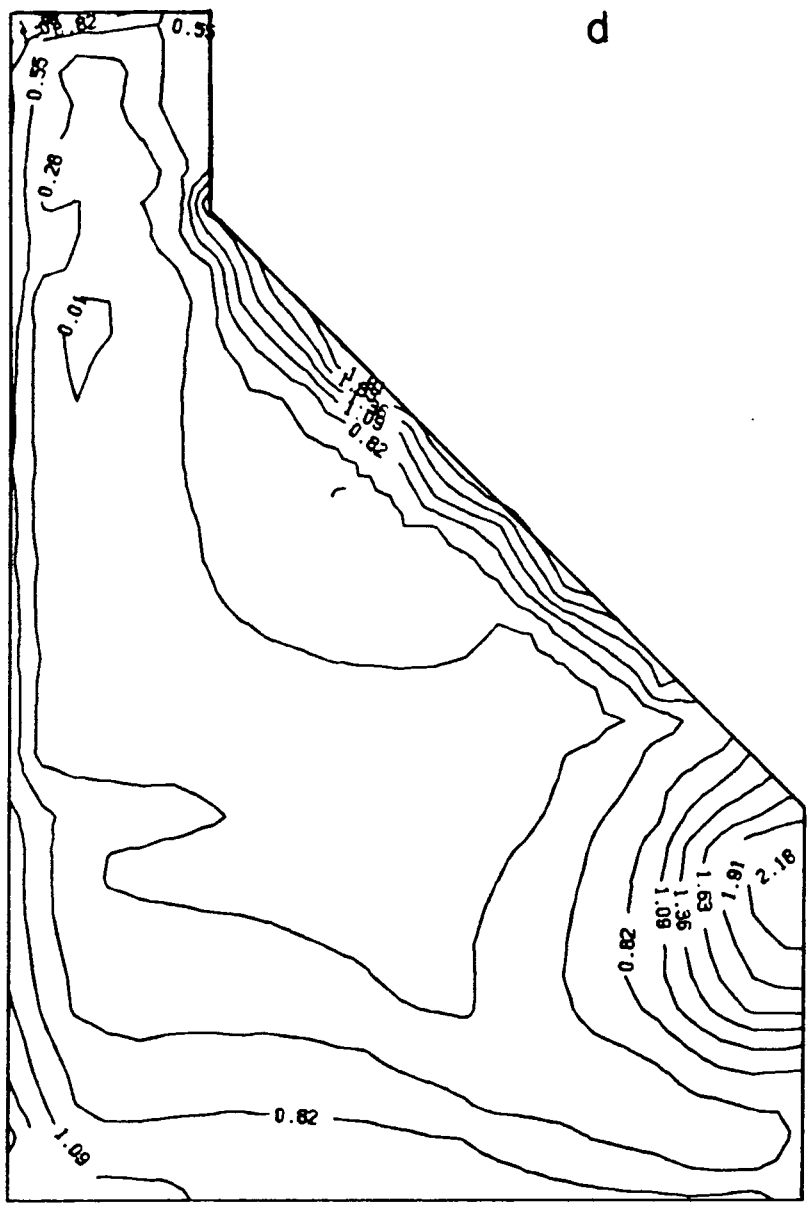
d
0.55
0.55
0.28
0.01
0.82
0.82
1.09
1.36
1.63
1.91
2.18
0.82
0.82
1.09

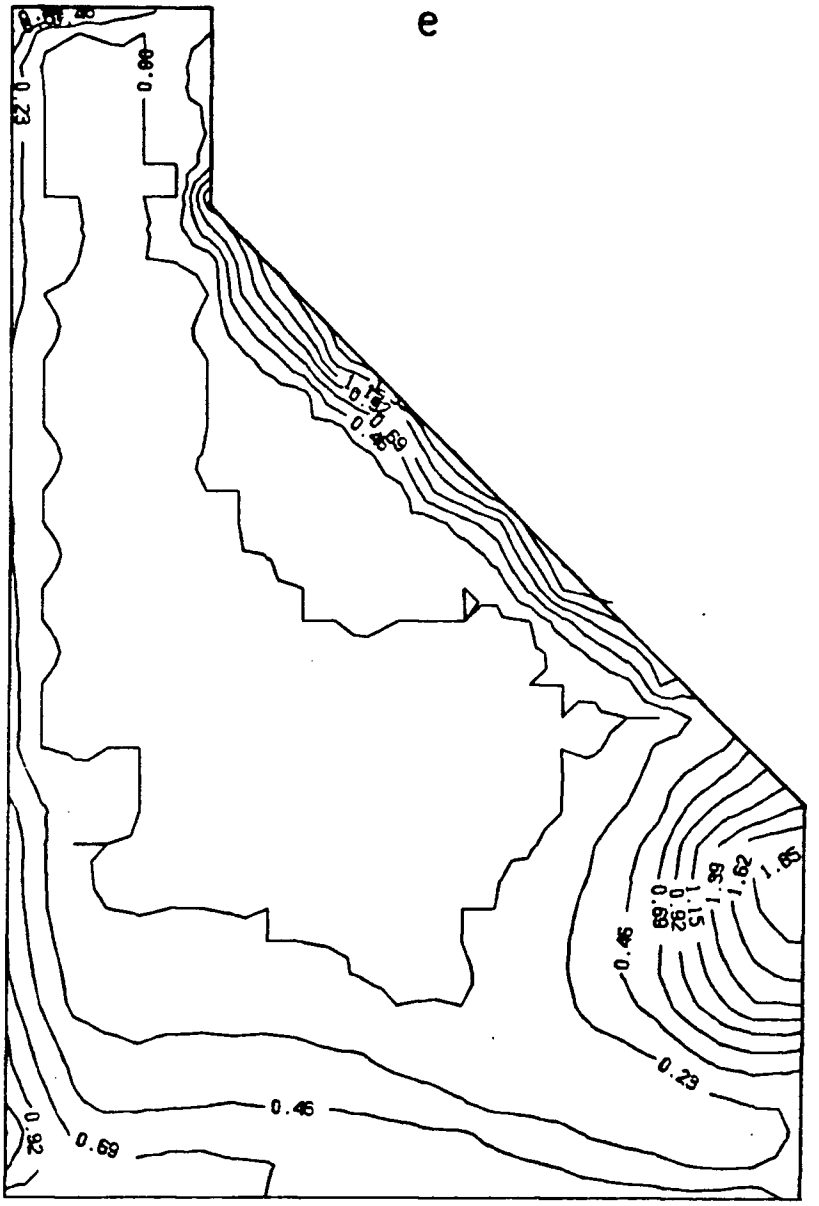

XIII.1.3.1 (a) Temperature and Von Mises Stress
(b) MRSS ; (c) MRSS-CRSS (Yield) ;
(d) MRSS-CRSS (MB) ; (e) MRSS-CRSS (MBTe)

a

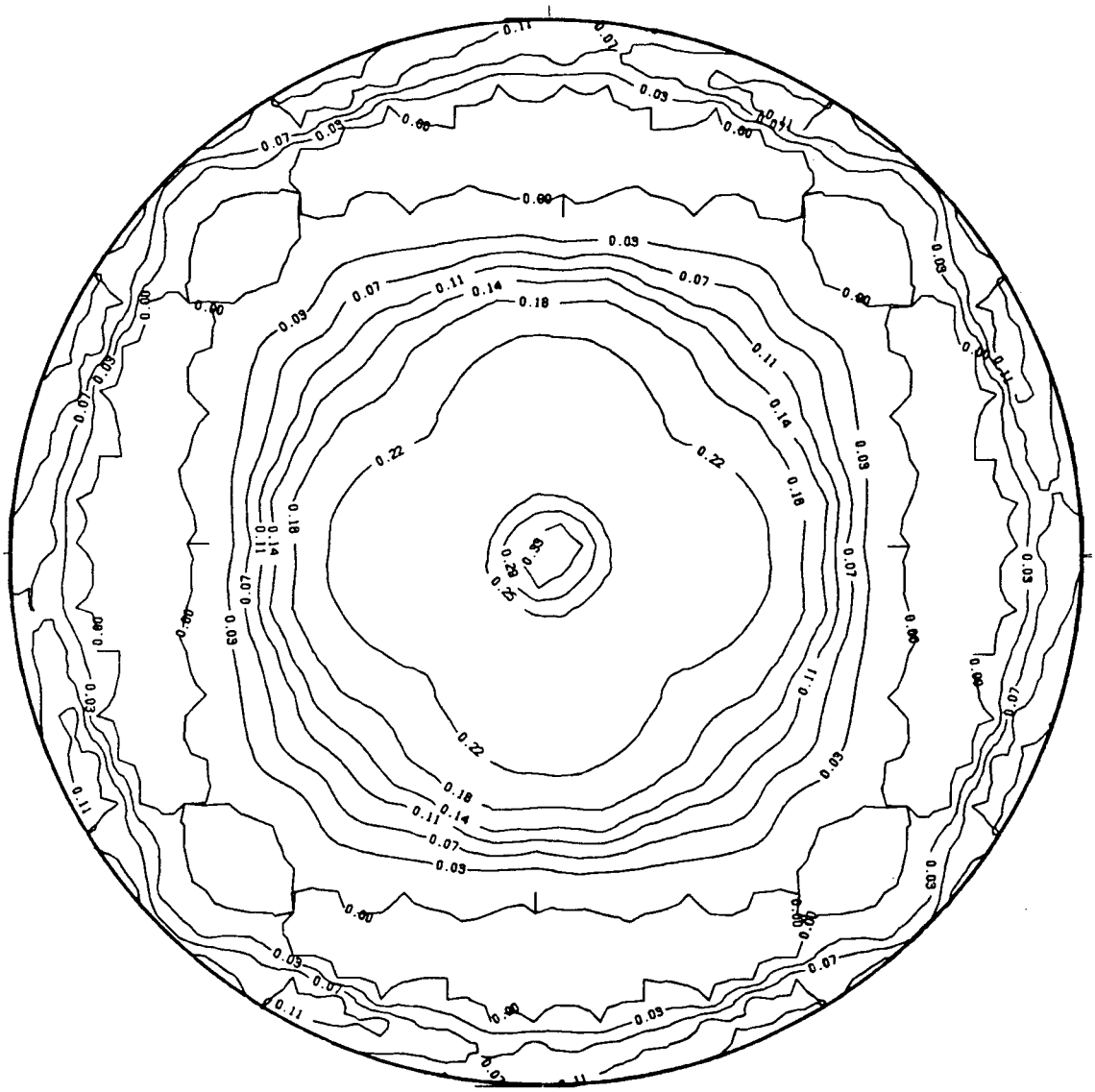

b

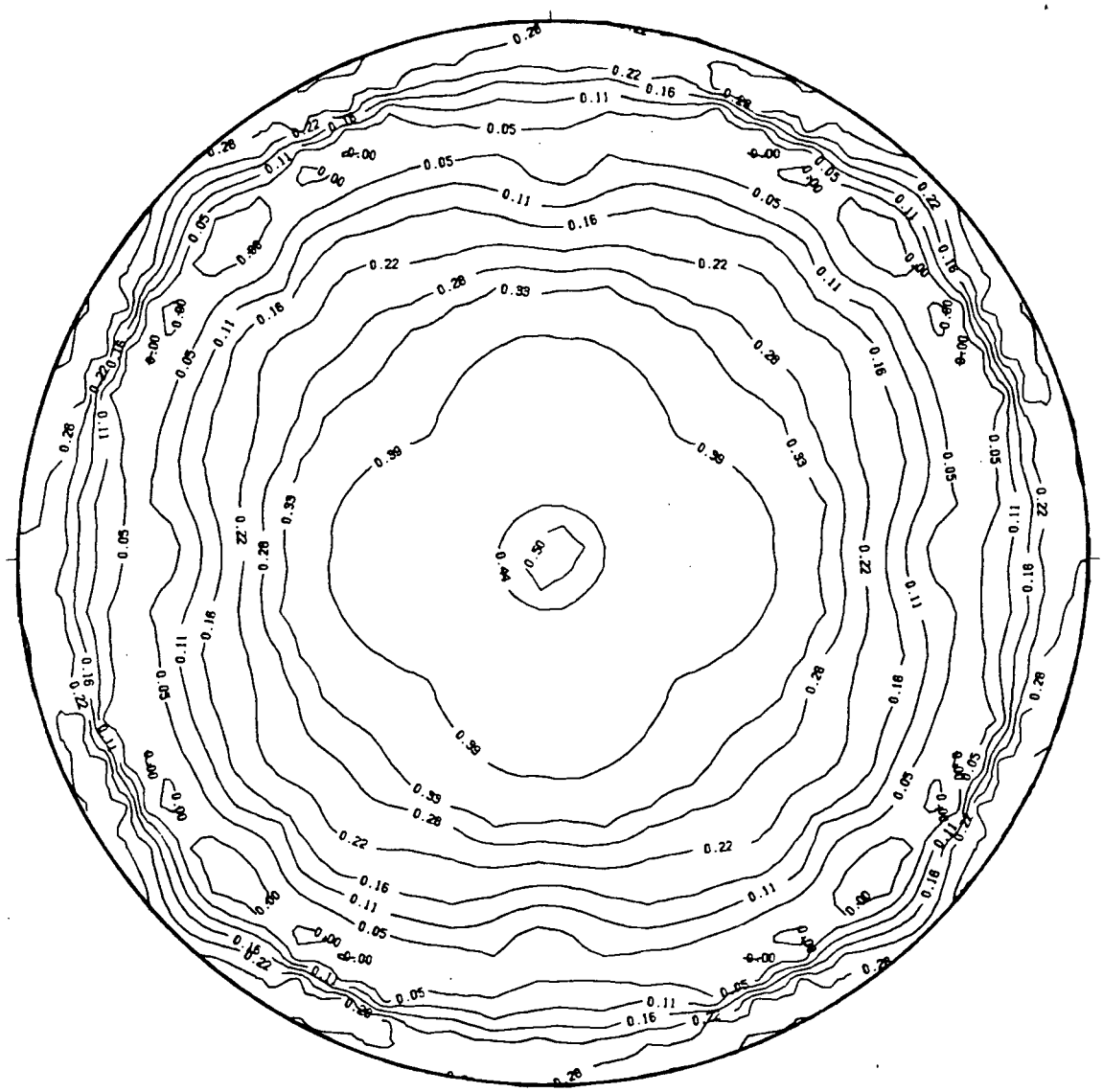

XIII.1.3.2 Cross-sections at 2.5 mm from the interface
(a) MRSS-CRSS (Yield) ; (b) MRSS-CRSS (MBTe) ;

a

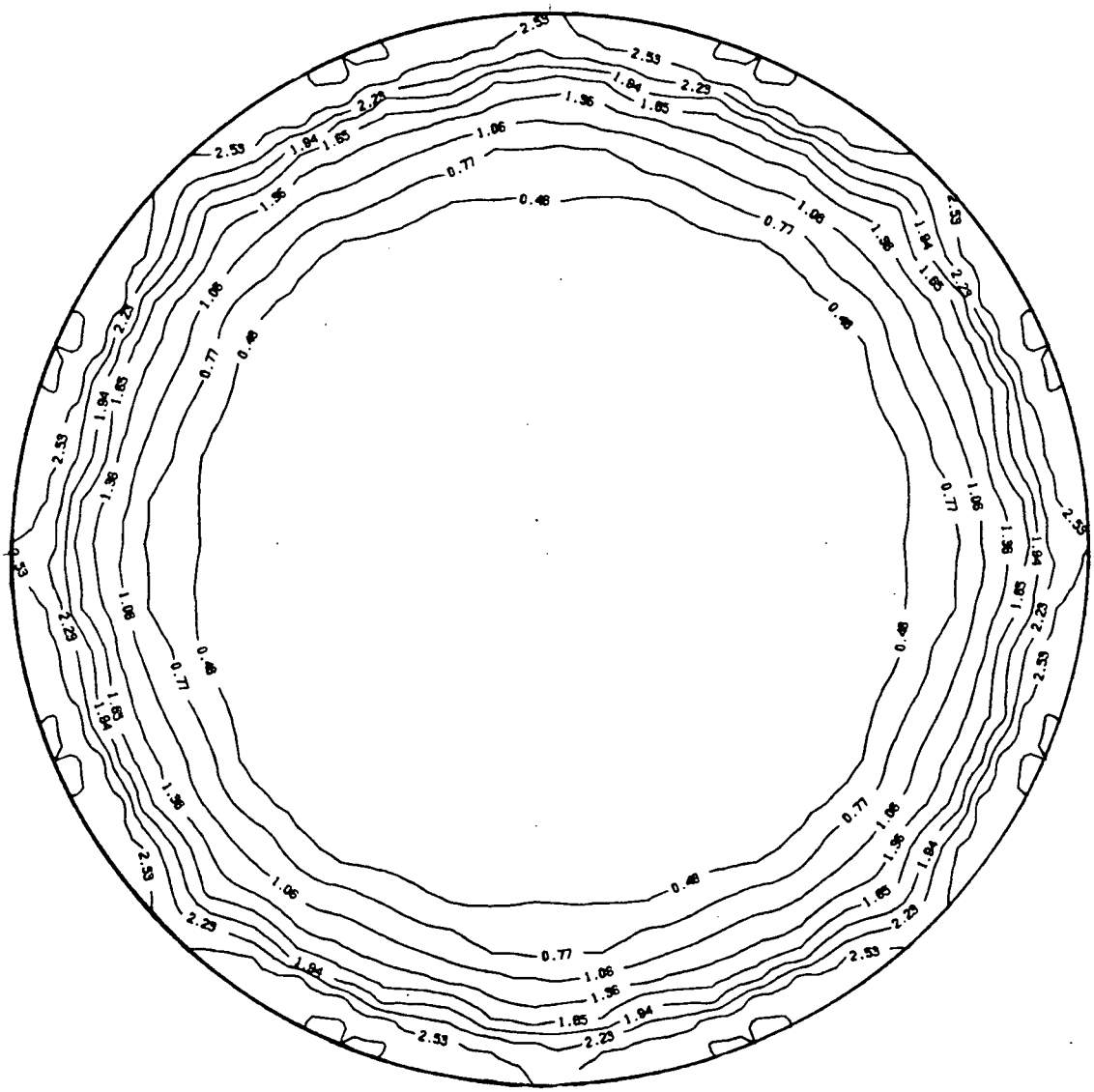

b

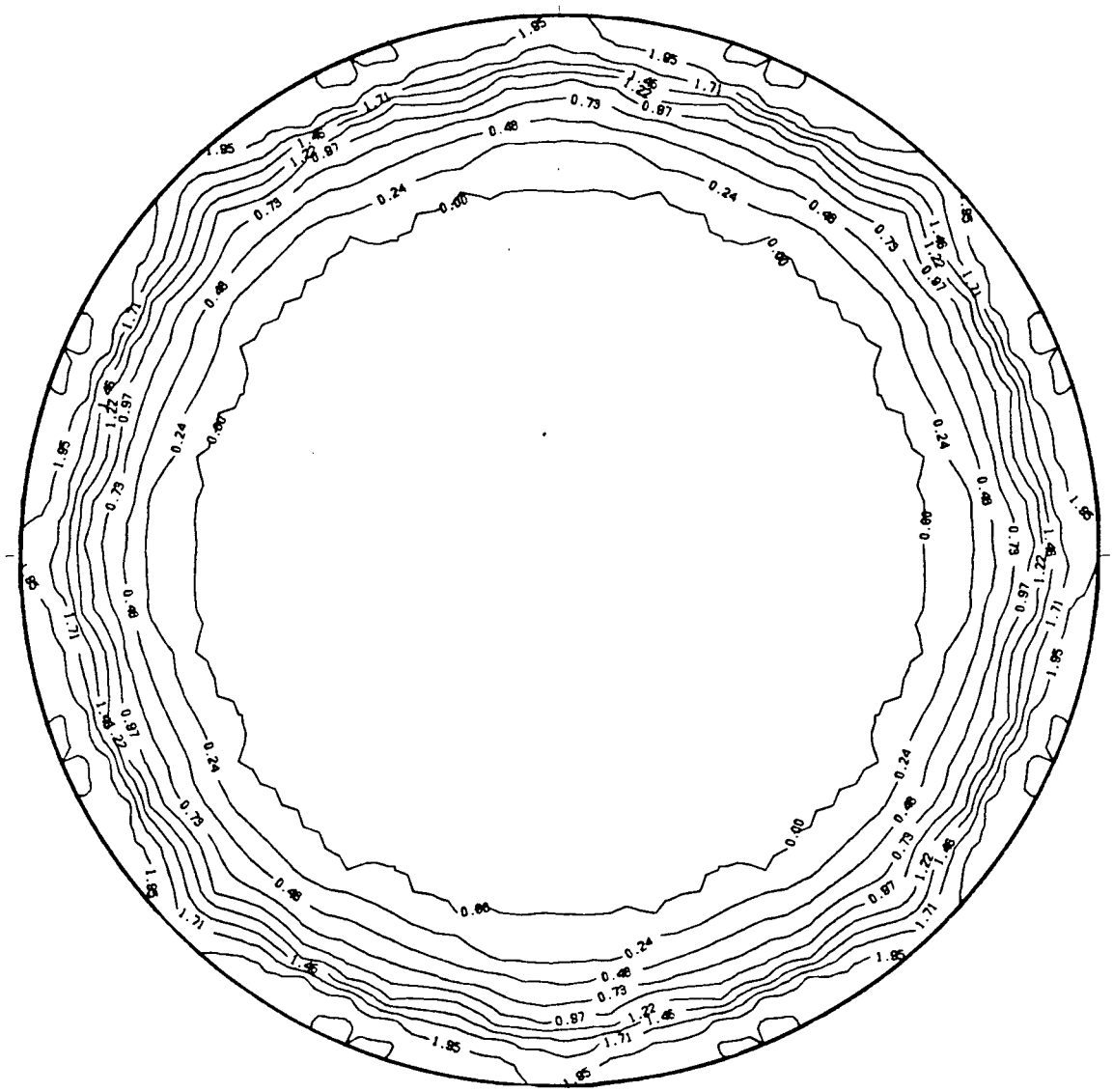

C

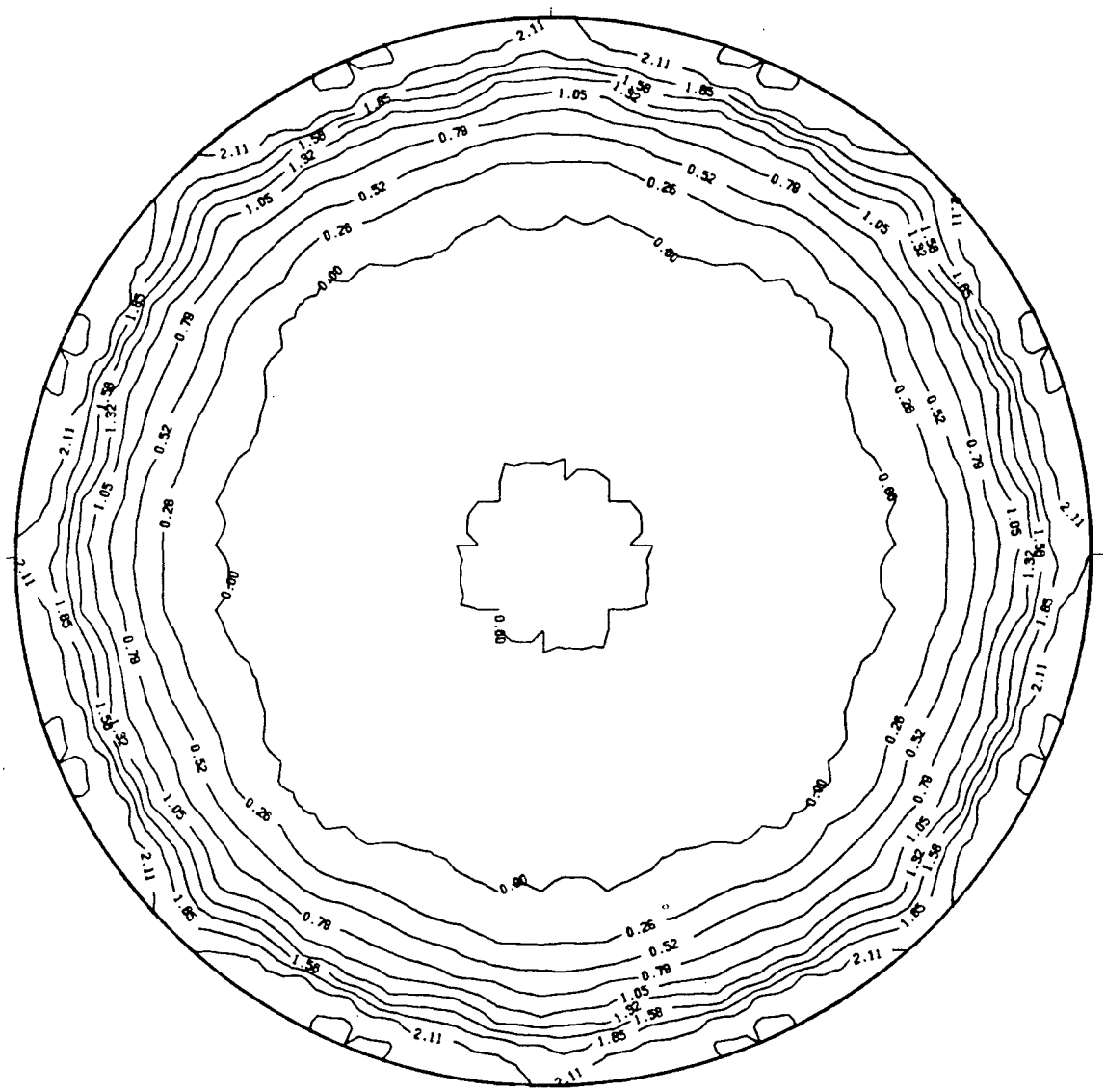

XIII.1.3.3 Cross-sections at 7.5 mm from the interface
(a) MRSS ; (b) MRSS-CRSS (Yield) ;
(c) MRSS-CRSS (MBTe)

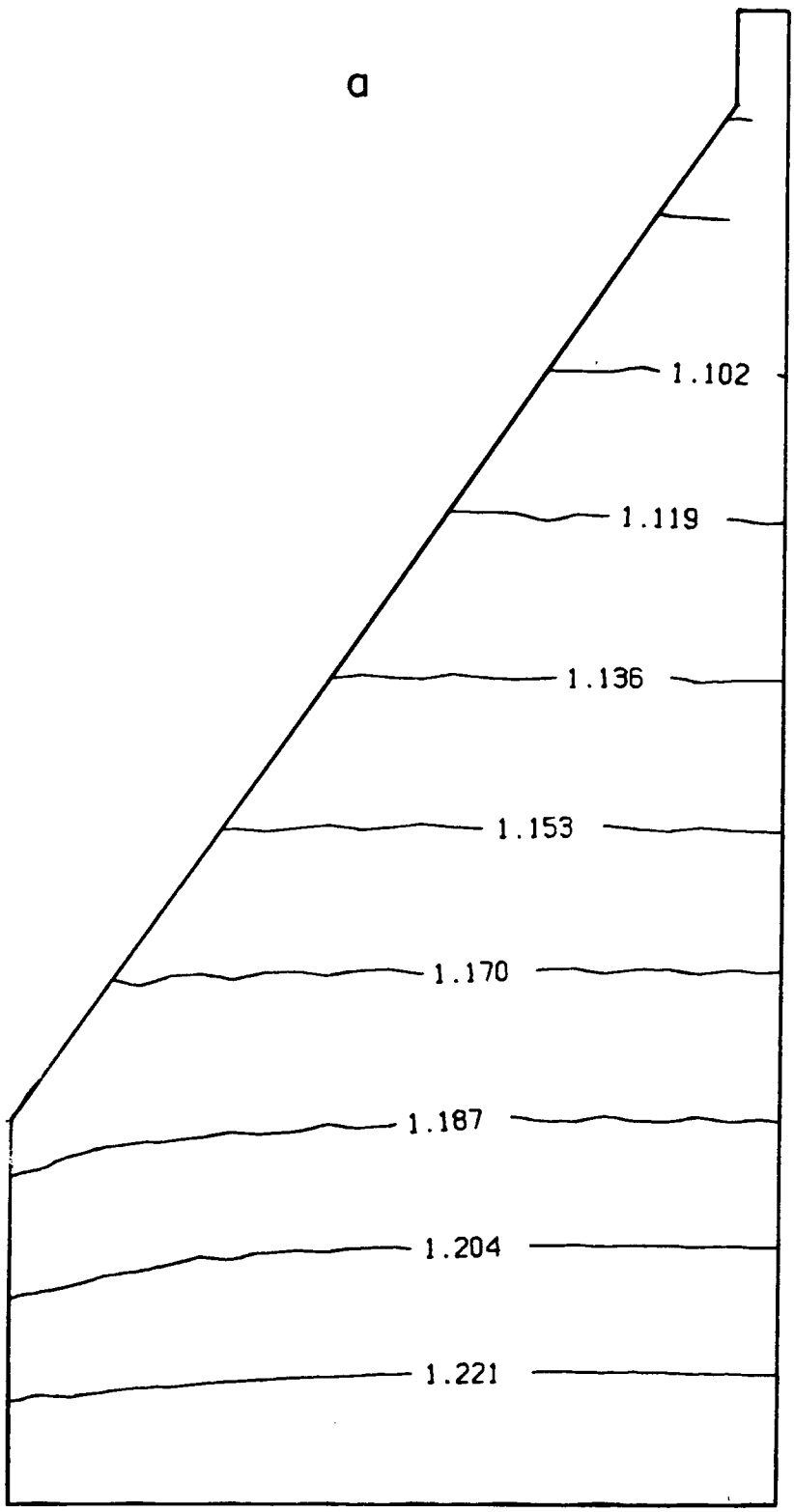
a
1.102
1.119
1.136
1.153
1.170
1.187
1.204
1.221

b
0.14
0.26
0.38
0.50
0.38
0.14
0.14
0.38
0.50
0.61
0.73
0.85
0.97
1.08
0.61

C

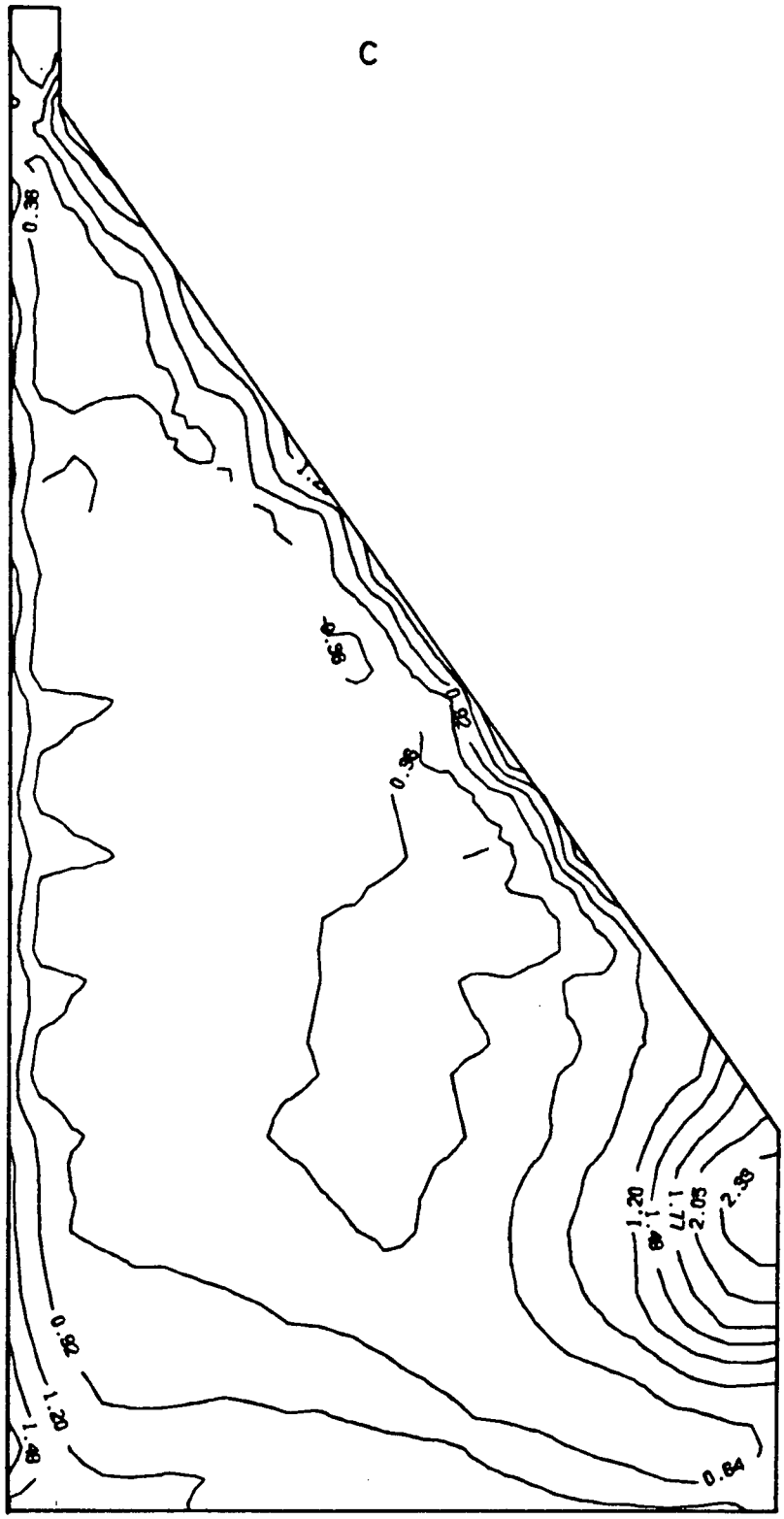

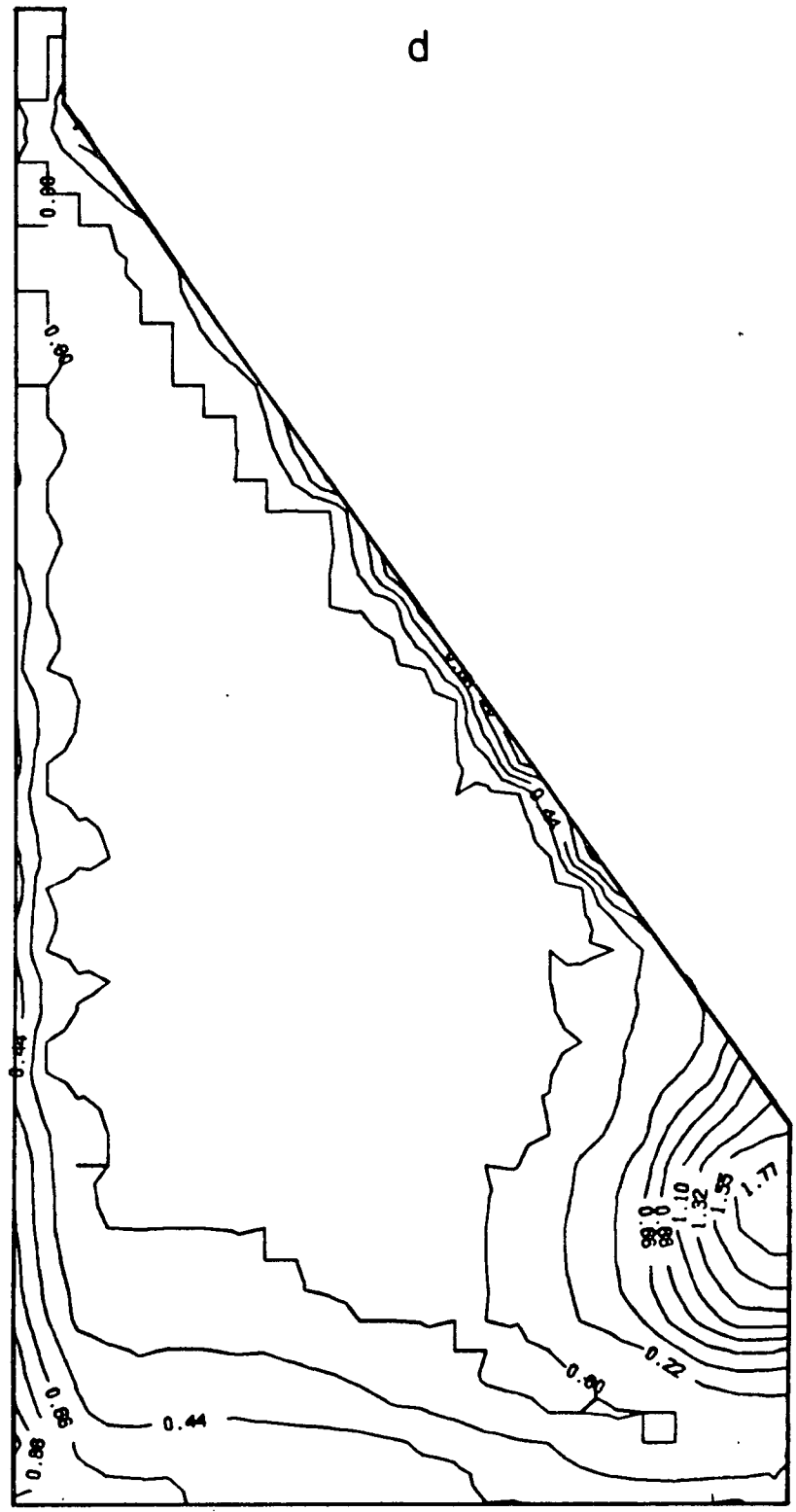
d
0.44
0.22
0.44
1.77

e

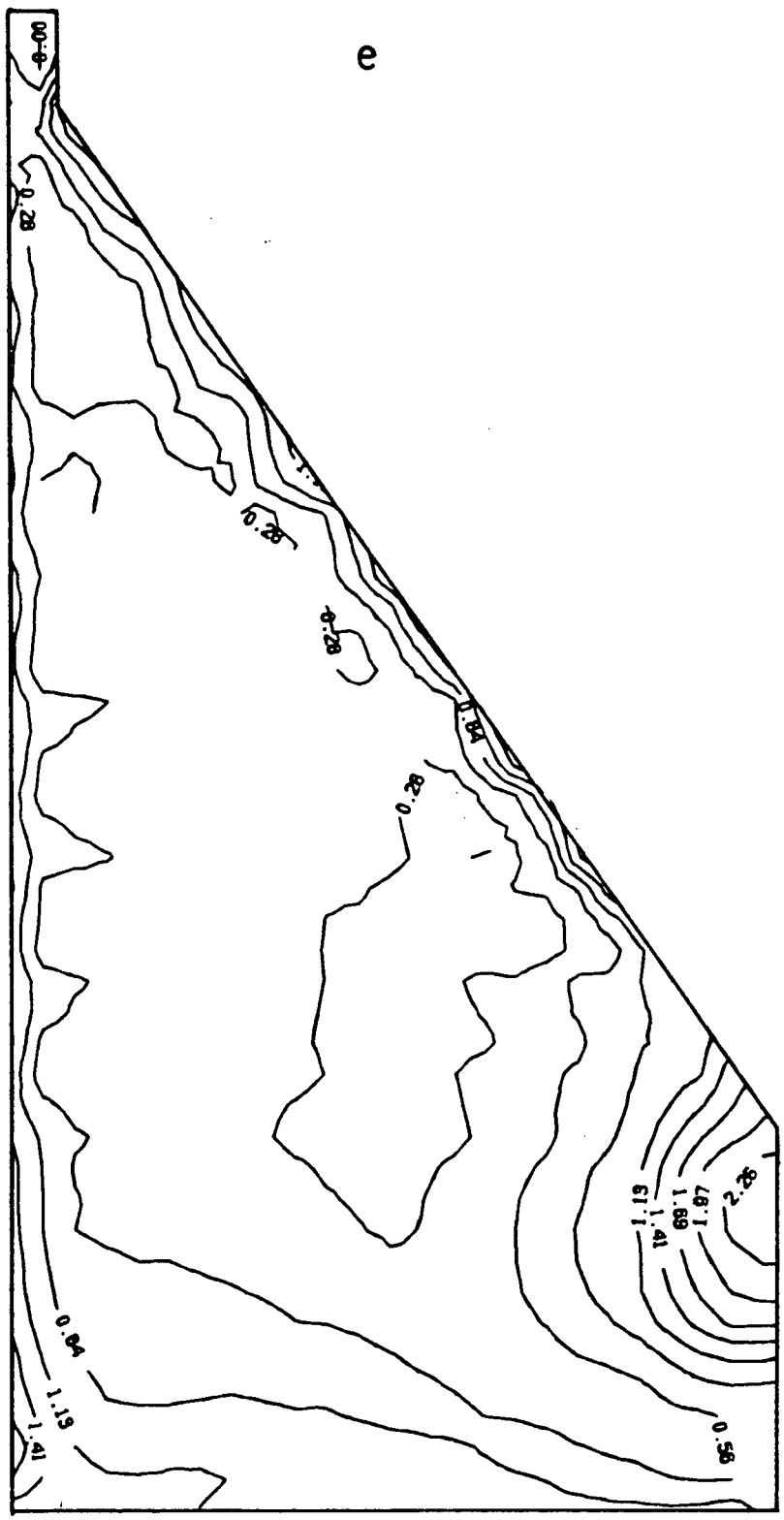
0.00
0.28
0.28
0.28
0.28
0.84
0.56
0.56
1.13
1.41
1.69
1.97
2.25
0.56
0.84
1.13
1.41

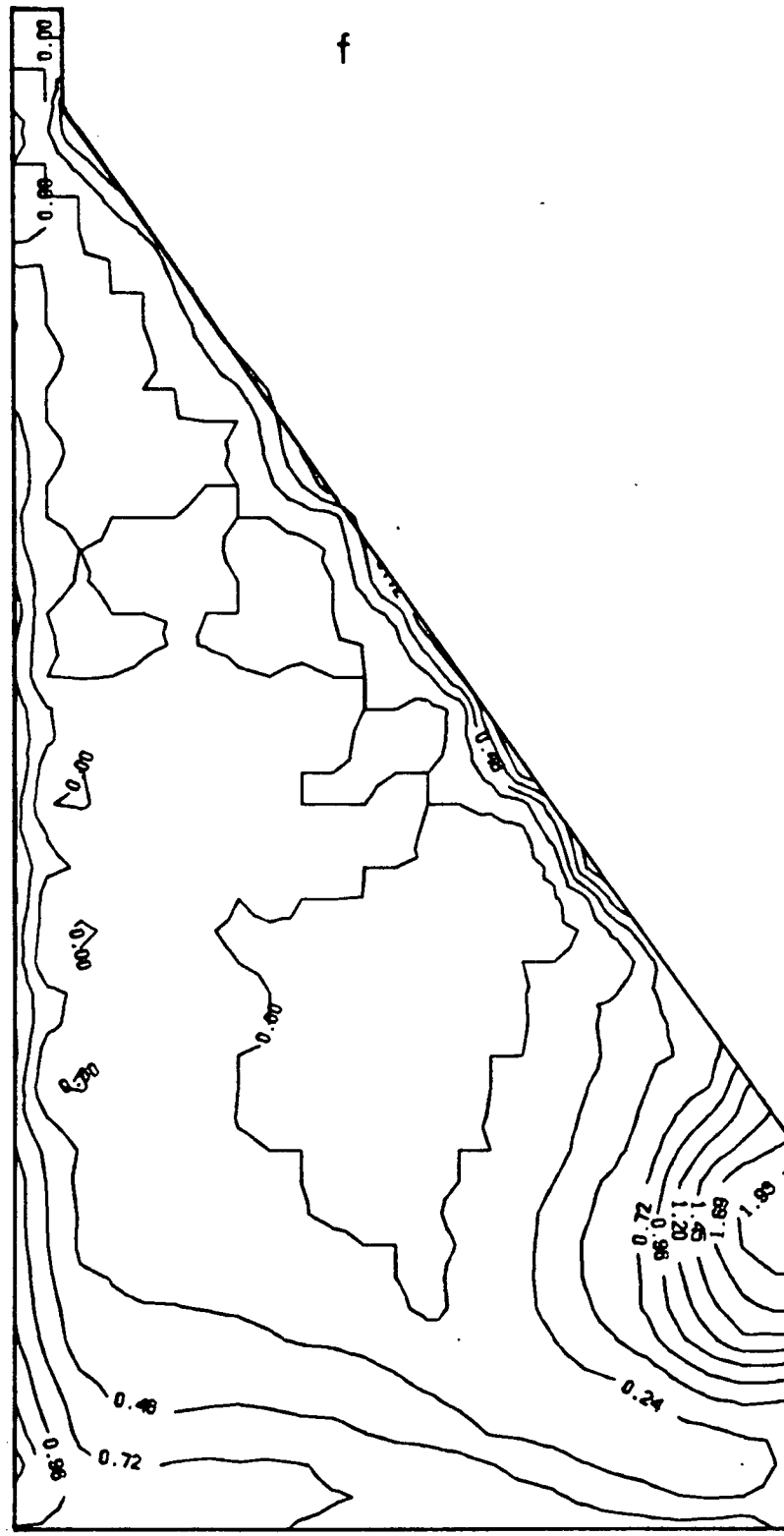

XIII.1.4.1 (a) Temperature ; (b) Von Mises Stress
(c) MRSS ; (d) MRSS-CRSS (Yield) ;
(e) MRSS-CRSS (MB) ; (f) MRSS-CRSS (MBTe).

a

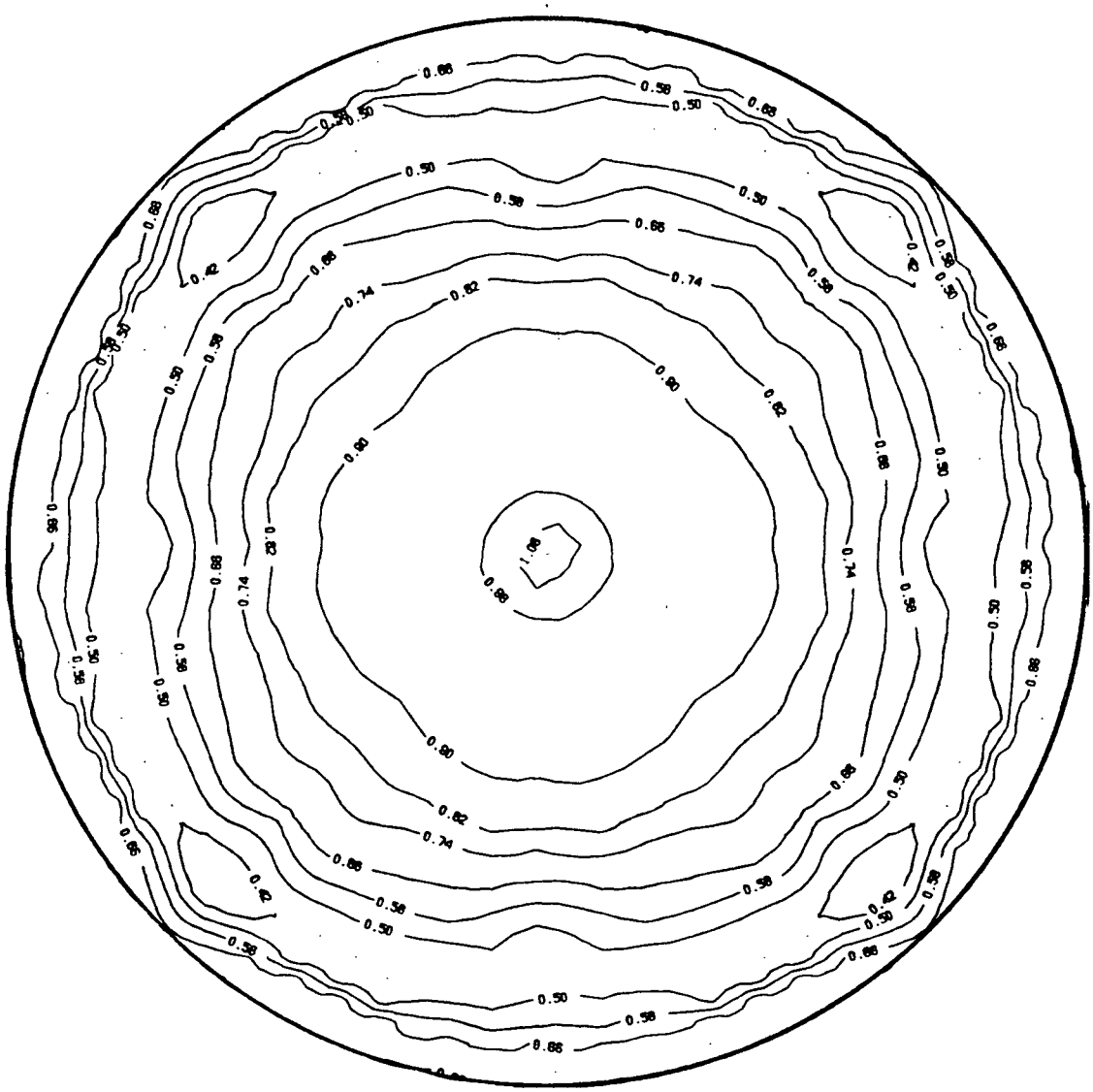

b

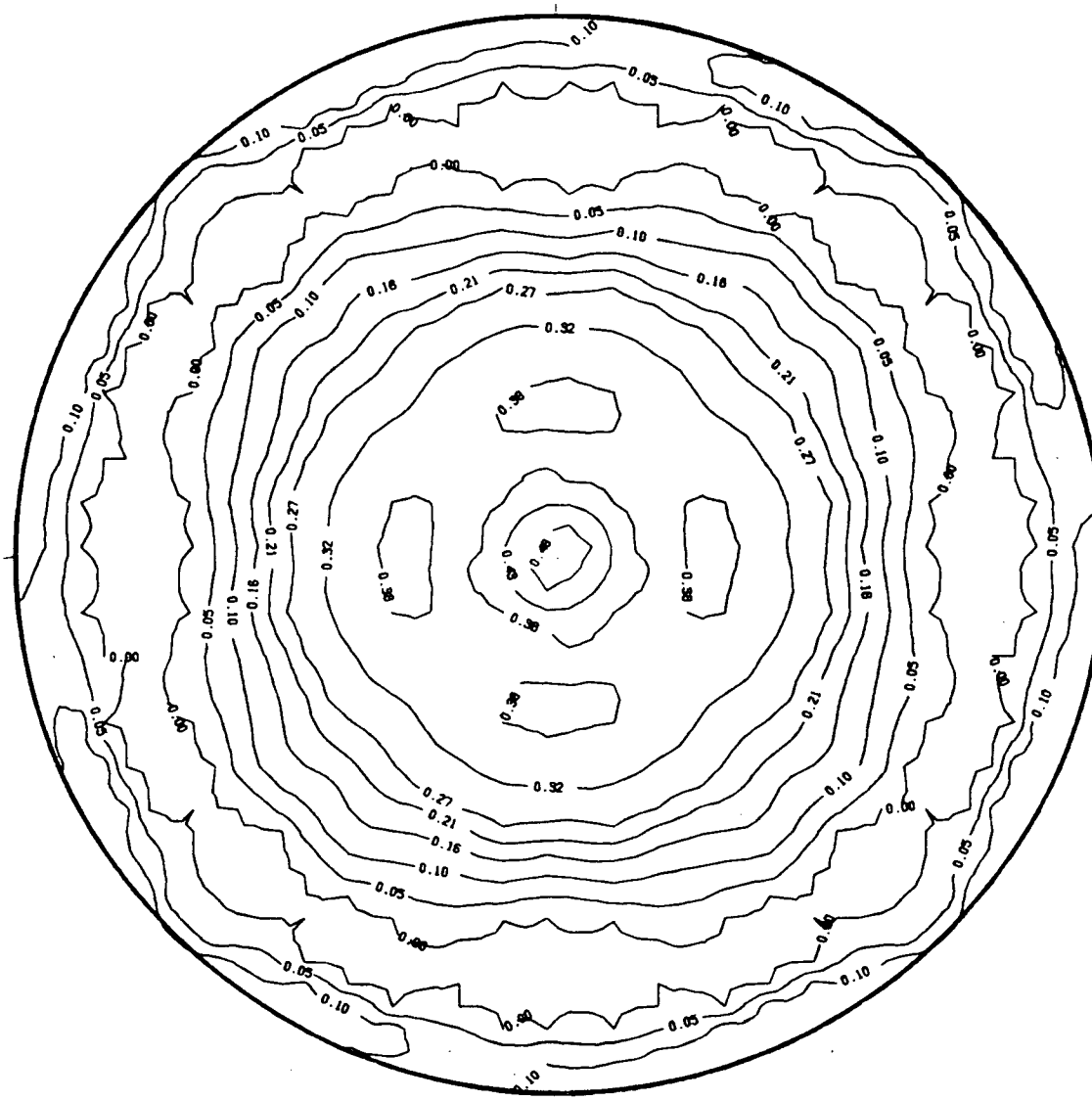

XIII.1.4.2 Cross-sections at 2.5 mm from the interface
(a) MRSS ; (b) MRSS-CRSS (Yield) ;

a

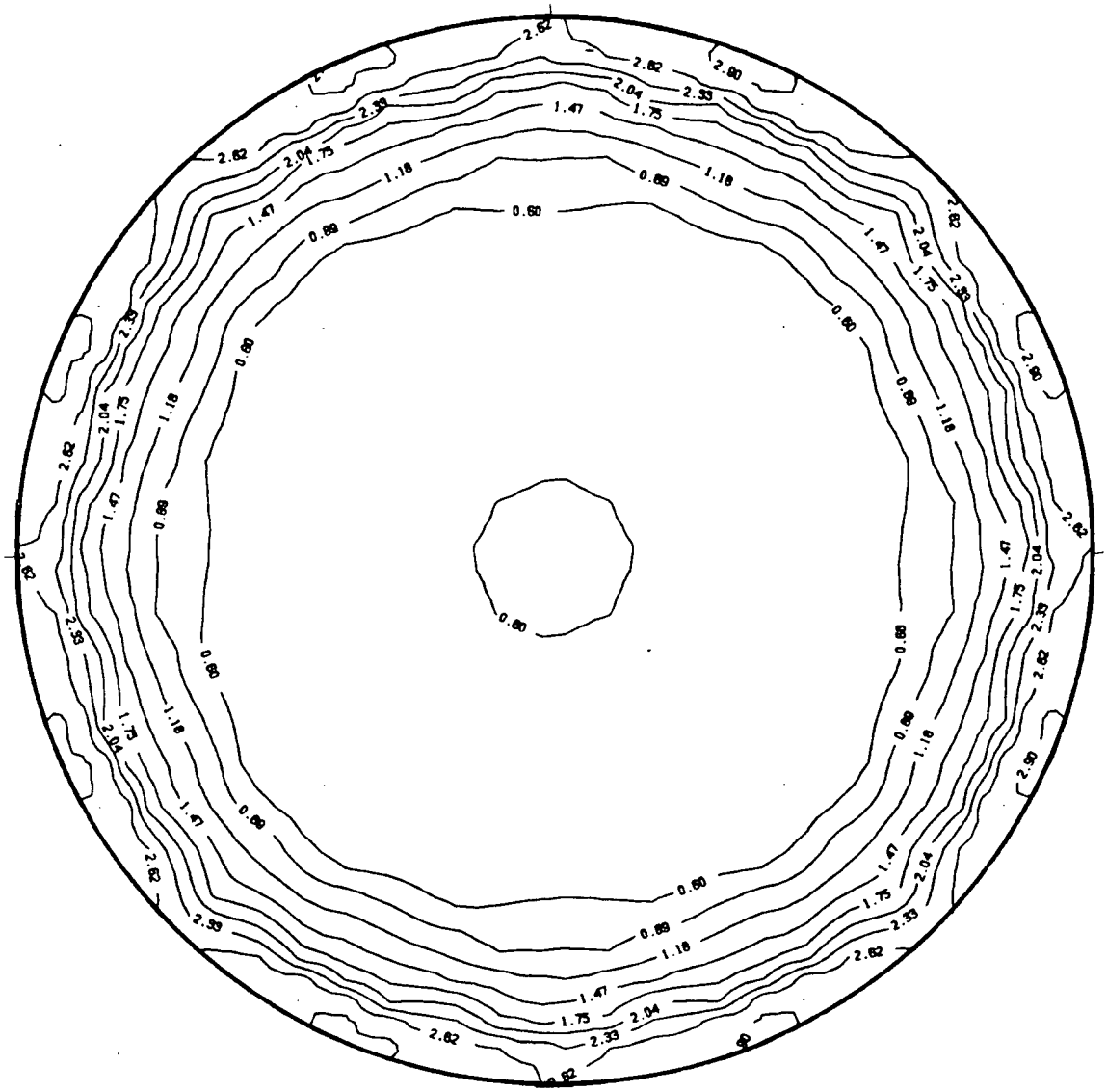

b

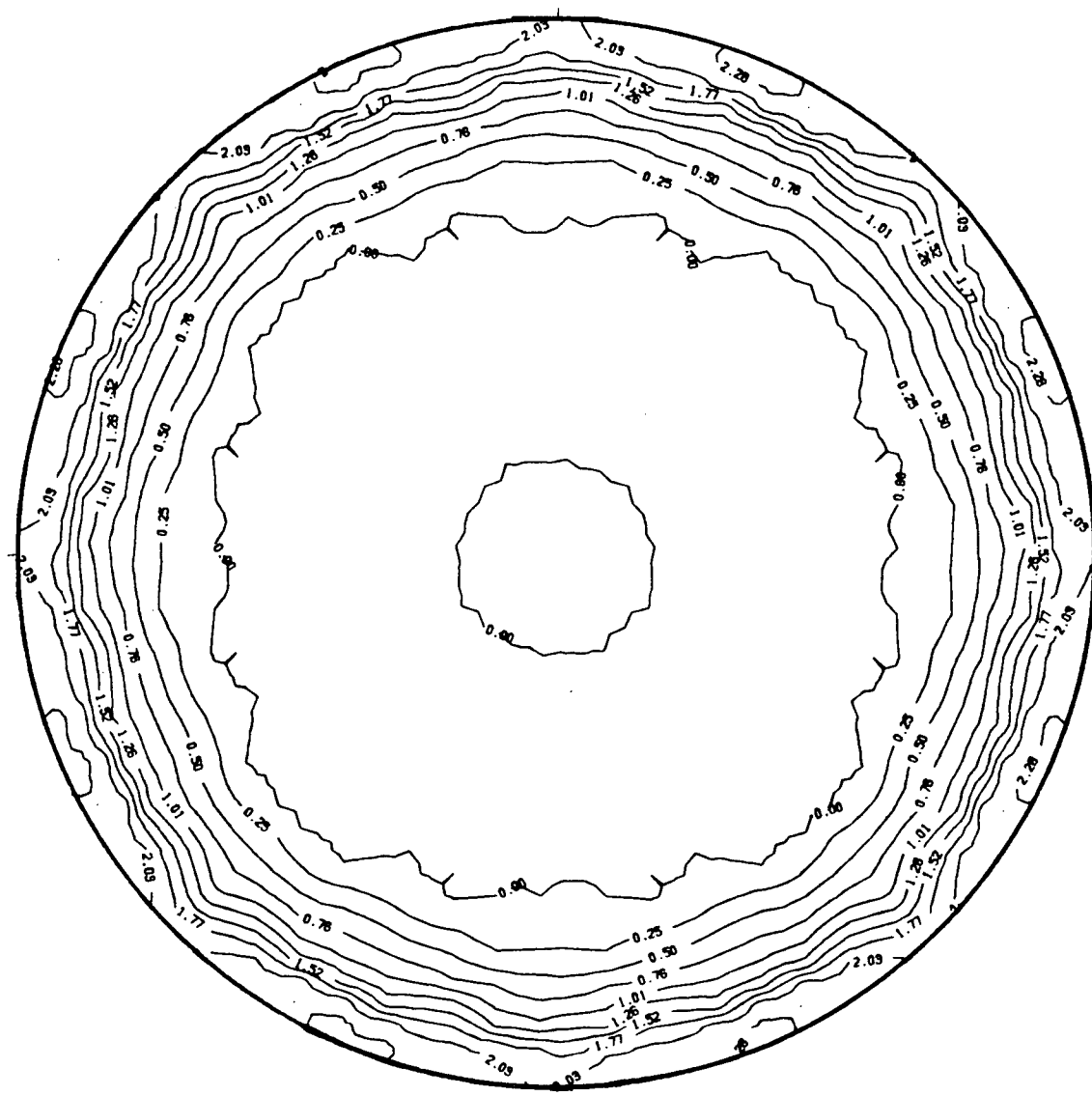

XIII.1.4.3 Cross-sections at 7.5 mm from the interface
(a) MRSS ; (b) MRSS-CRSS (Yield) ;

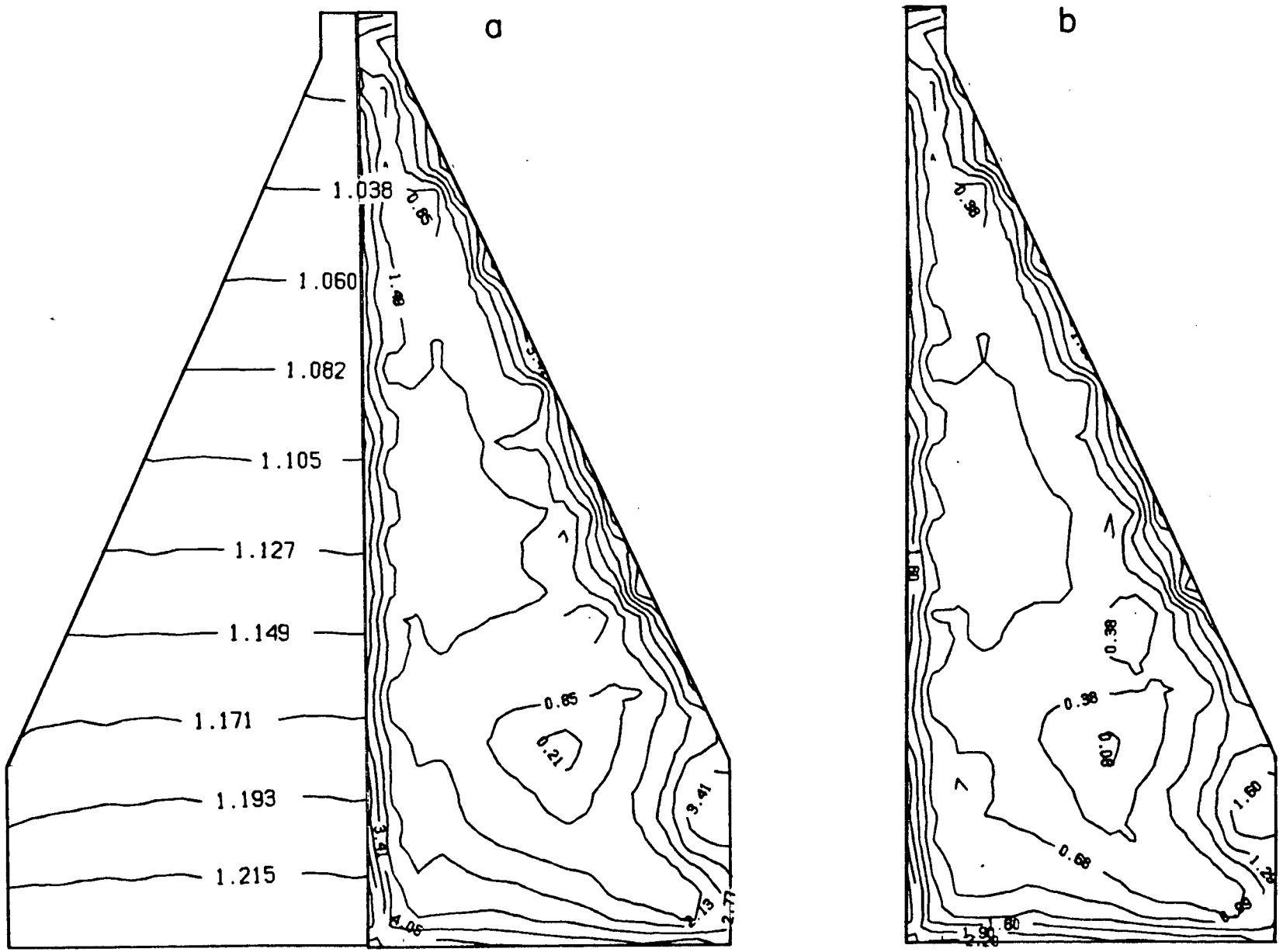
a
1.038
1.060
1.082
1.105
1.127
1.149
1.171
1.193
1.215
0.85
3.41
b

c
d
0.30
0.30
0.30
0.61
1.52
1.21

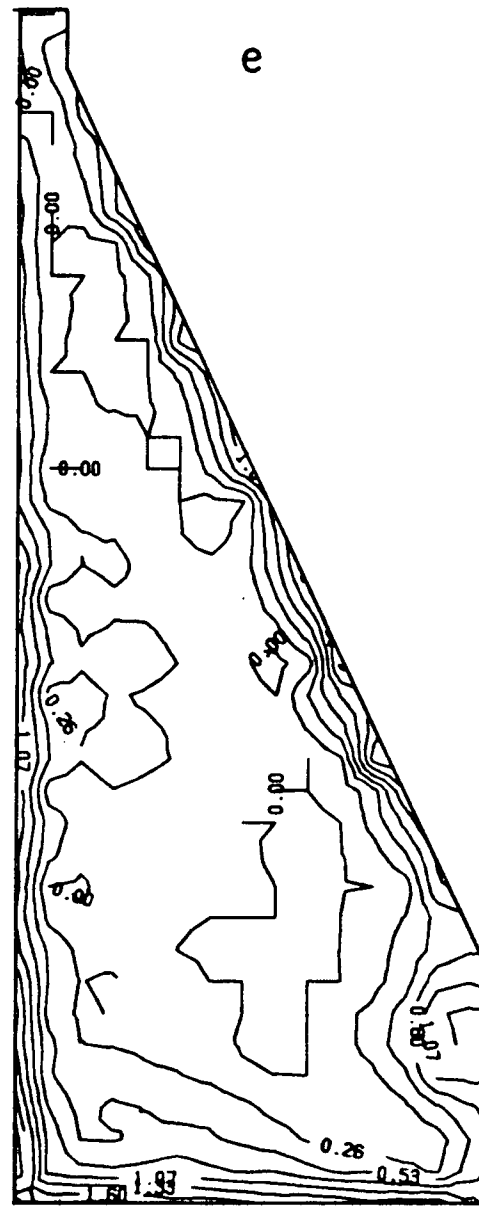

XIII.1.5.1 (a) Temperature and Von Mises Stress
(b) MRSS ; (c) MRSS-CRSS (Yield) ;
(d) MRSS-CRSS (MB) ; (e) MRSS-CRSS (MBTe).

a

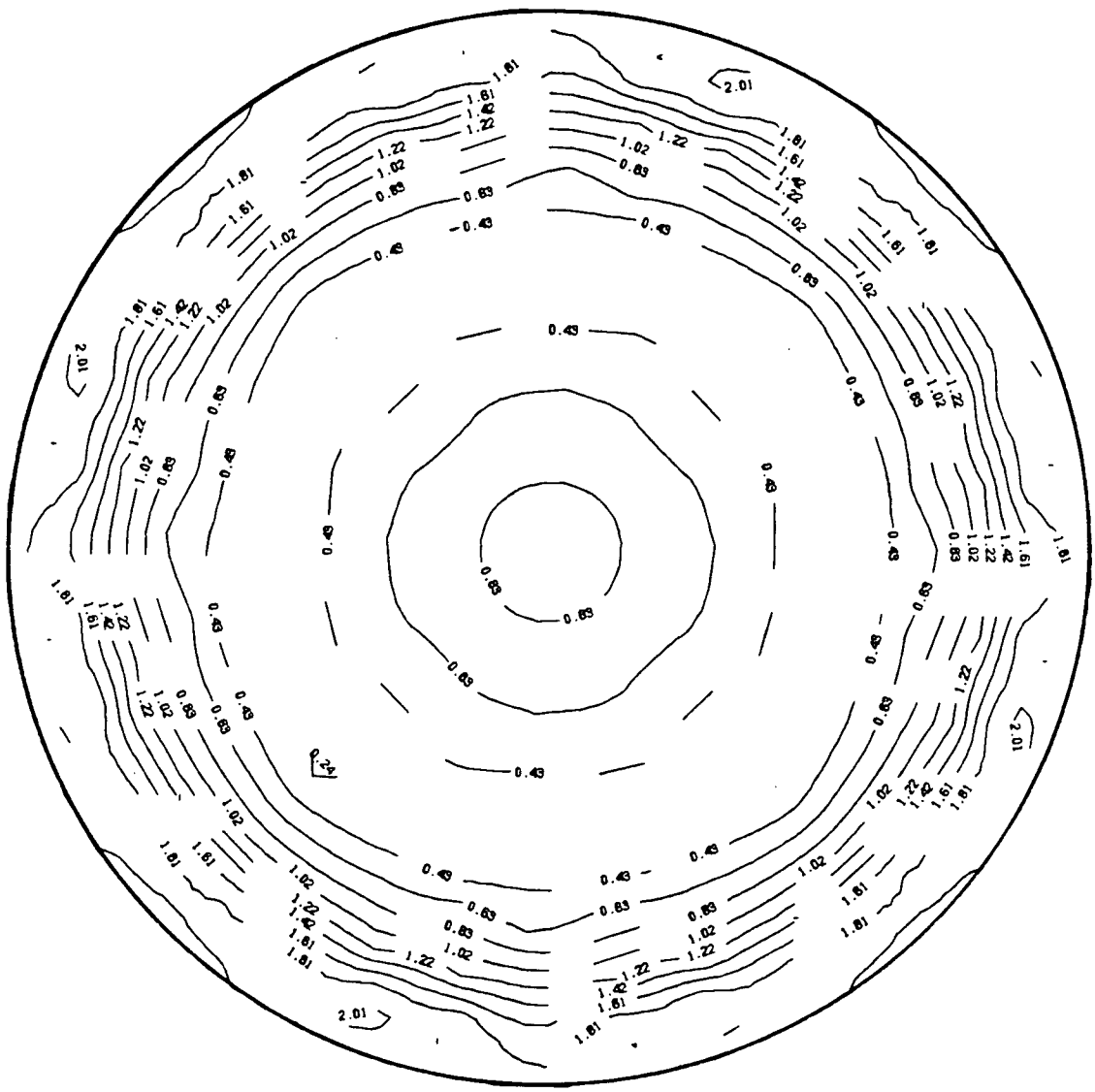

b

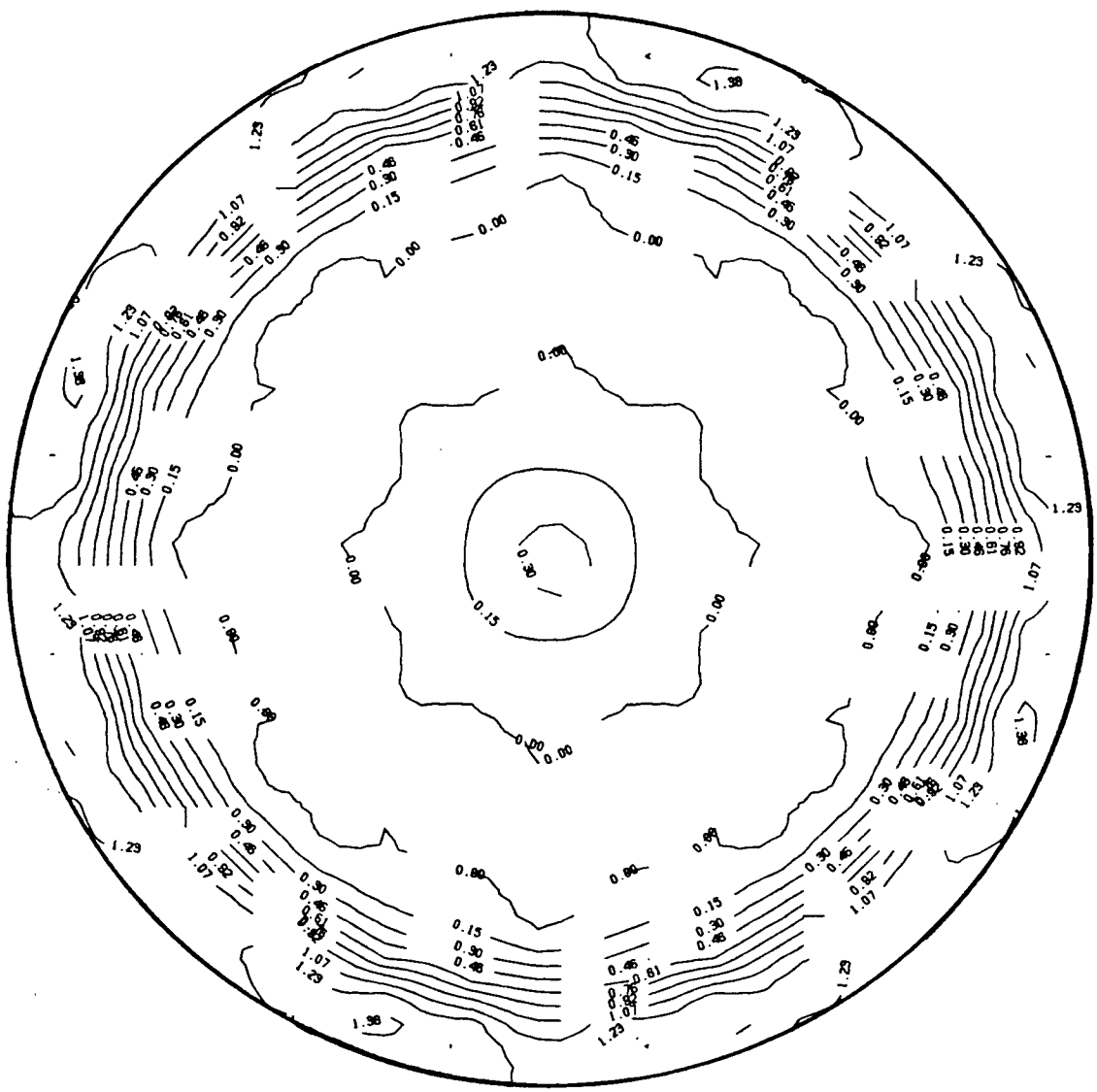

XIII.1.5.2 Cross-sections at 8.0 mm from the interface
(a) MRSS ; (b) MRSS-CRSS (Yield) ;

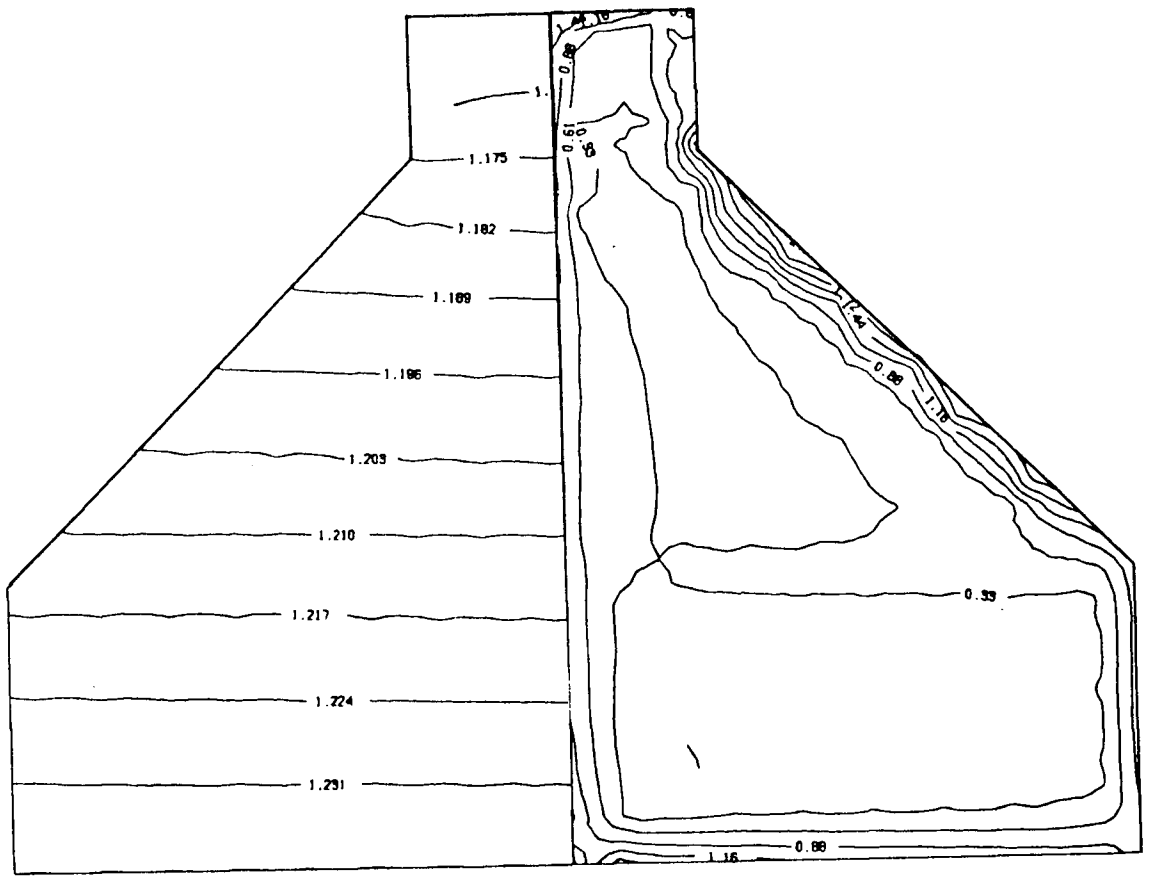
Temperature, 10^3 °C
Von Mises Stress, MPa
1.175
1.182
1.189
1.196
1.203
1.210
1.217
1.224
1.231
0.88
0.61
1.44
0.88
1.10
0.39
1.16
0.88

a

MRSS, MPa

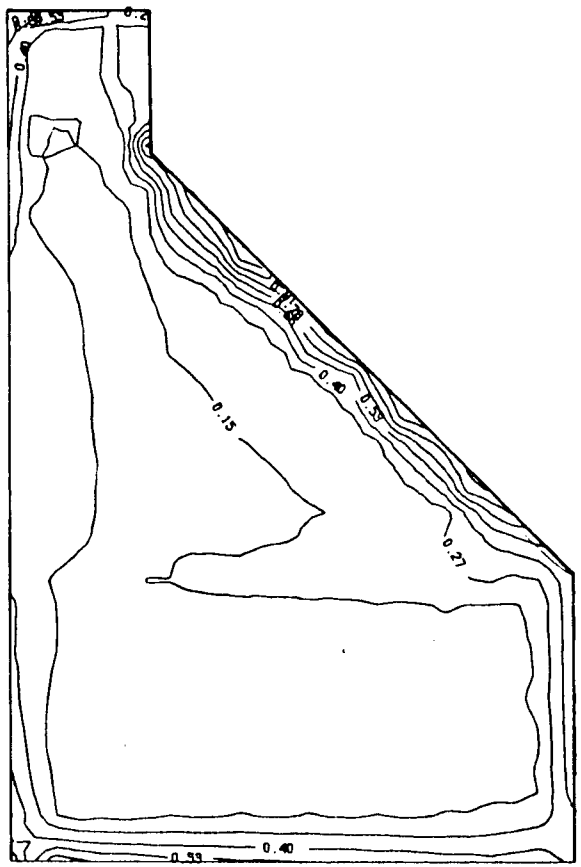

b

MRSS − CRSS (Y), MPa

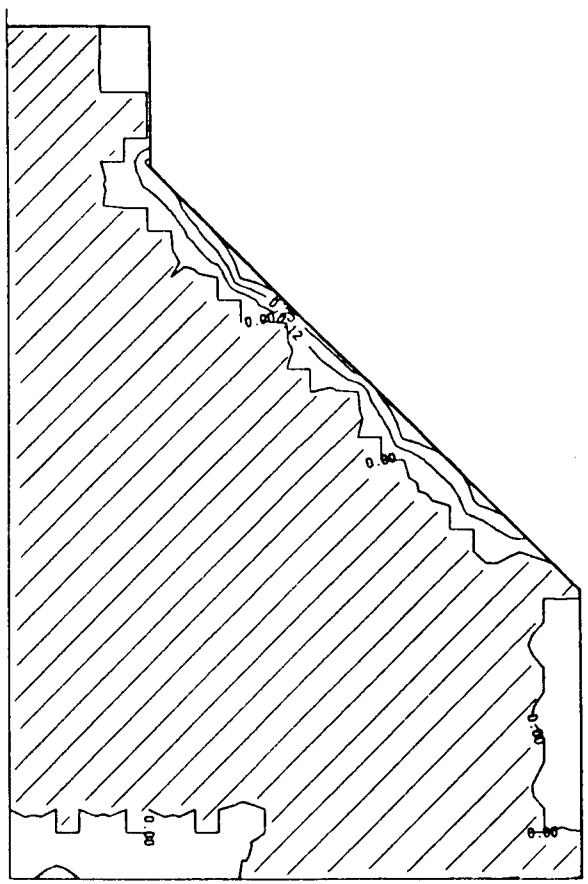

c

MRSS - CRSS (MB), MPa

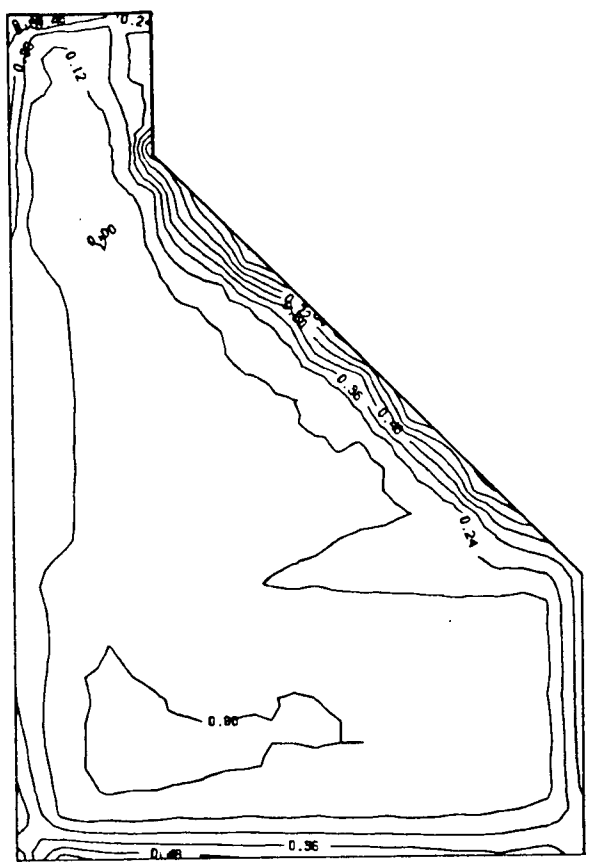

d

MRSS - CRSS (Te), MPa

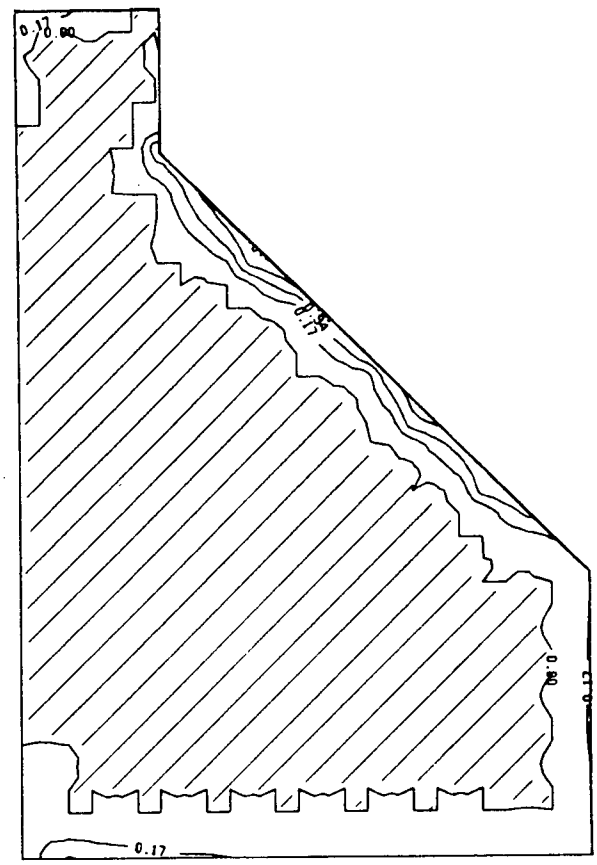

e

XIII.1.6.1.1 (a) Temperature and Von Mises Stress
(b) MRSS ; (c) MRSS-CRSS (Yield) ;
(d) MRSS-CRSS (MB) ; (e) MRSS-CRSS (MBTe).

MRSS, MPa

HEIGHT = 0.5 cm

a

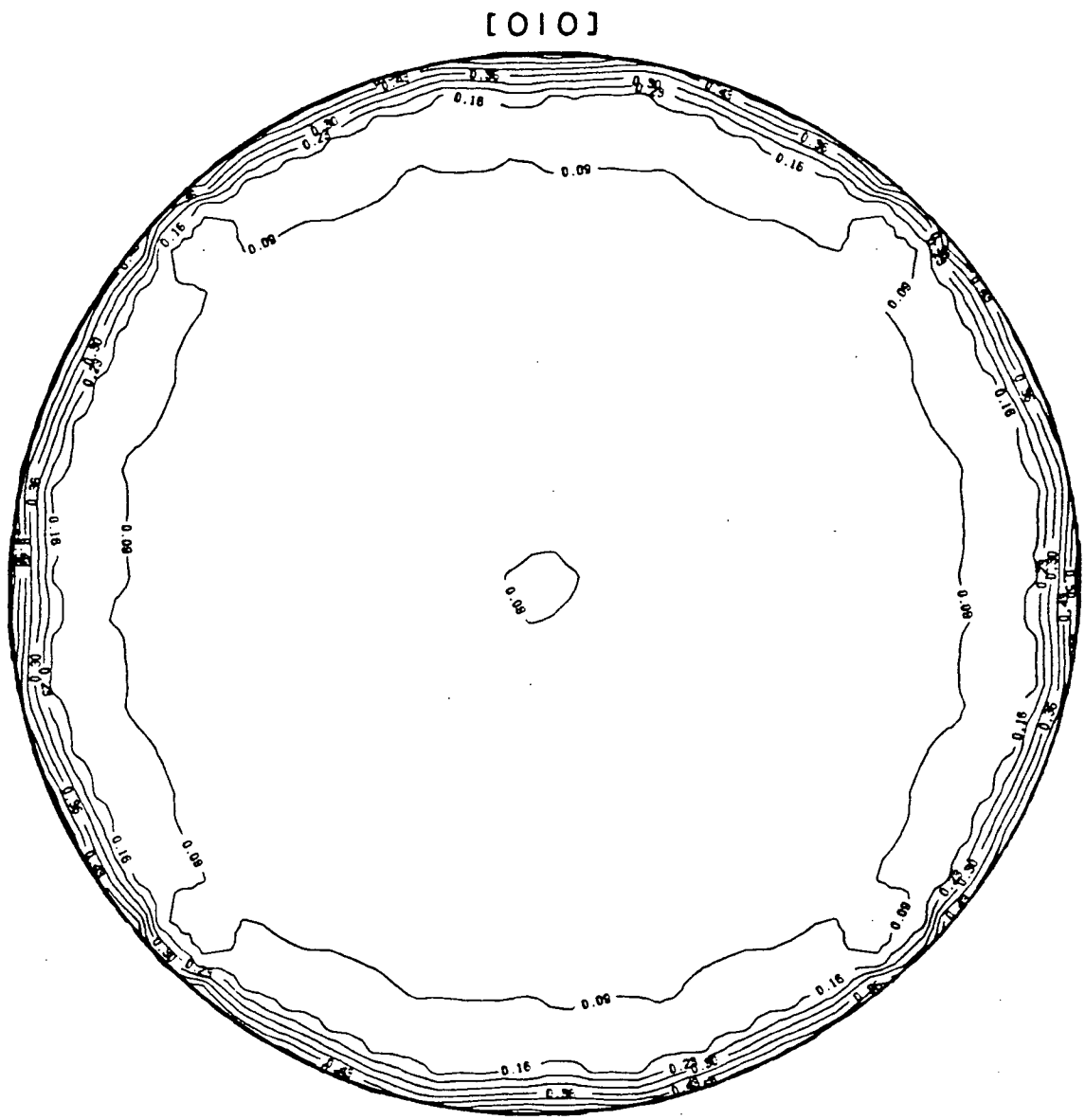

MRSS - CRSS(Y), MPa

HEIGHT = 0.50 cm

b

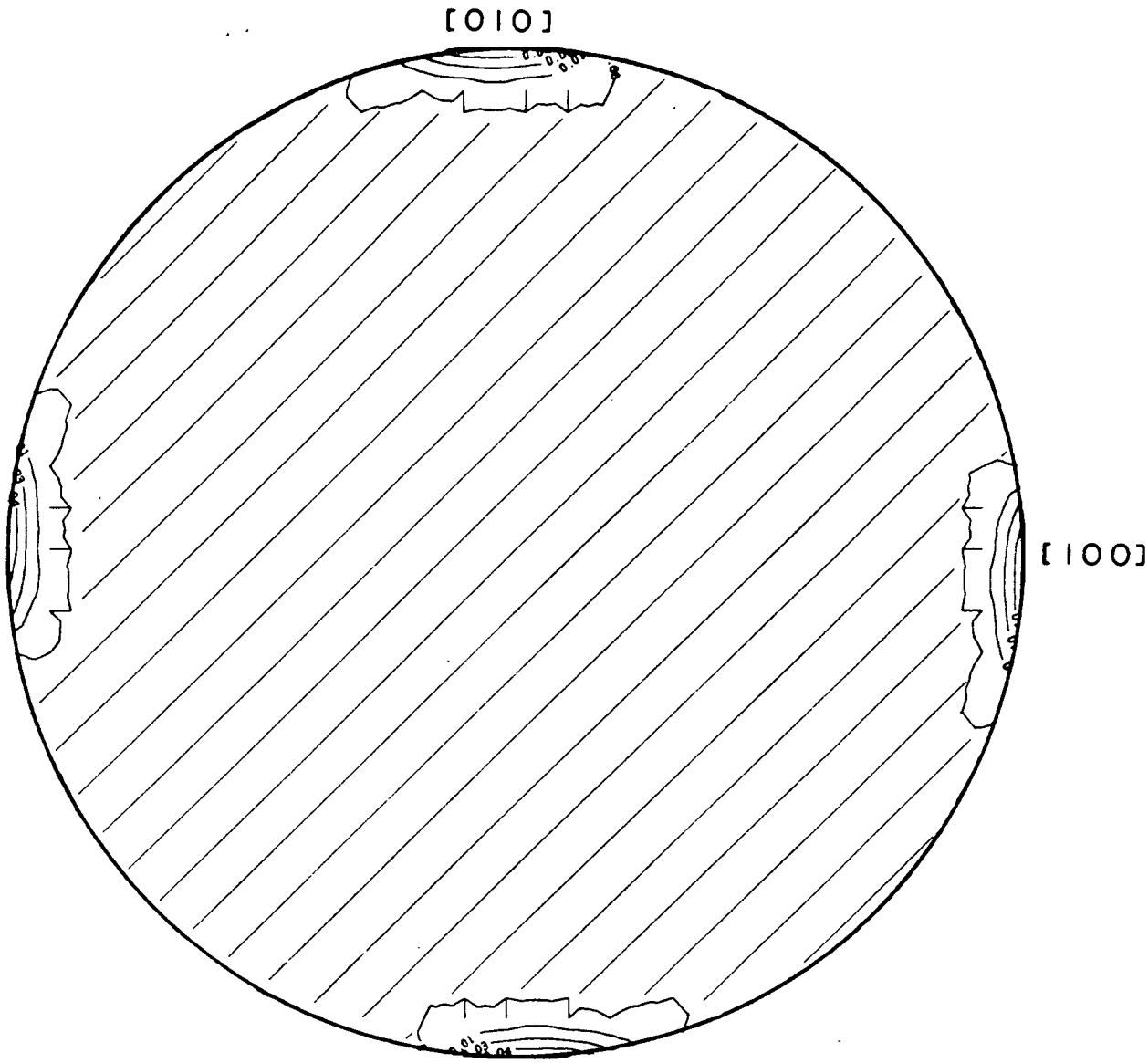

MRSS - CRSS(MB) - MPa HEIGHT = 0.50 cm

C

[010]

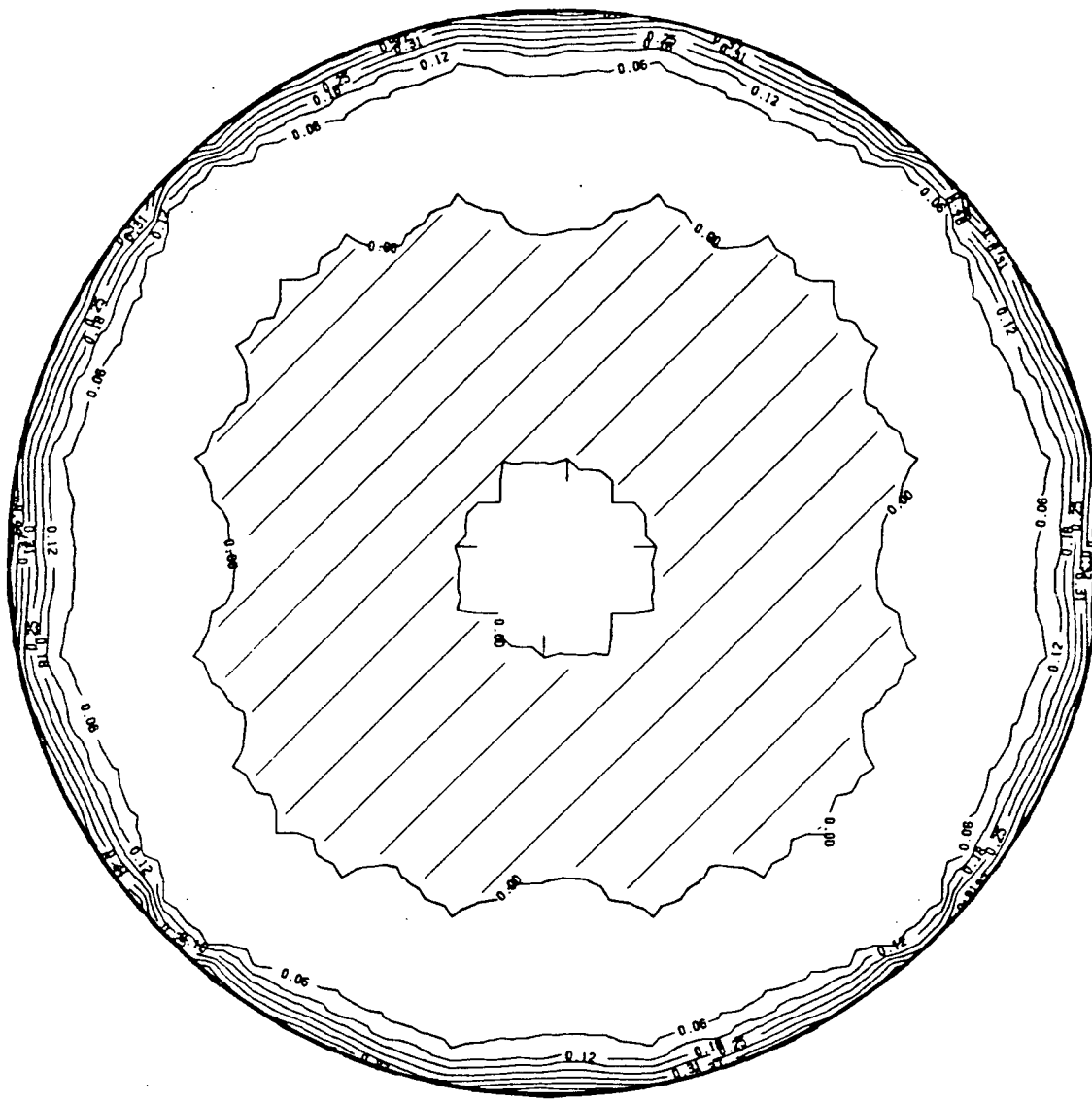

[100]

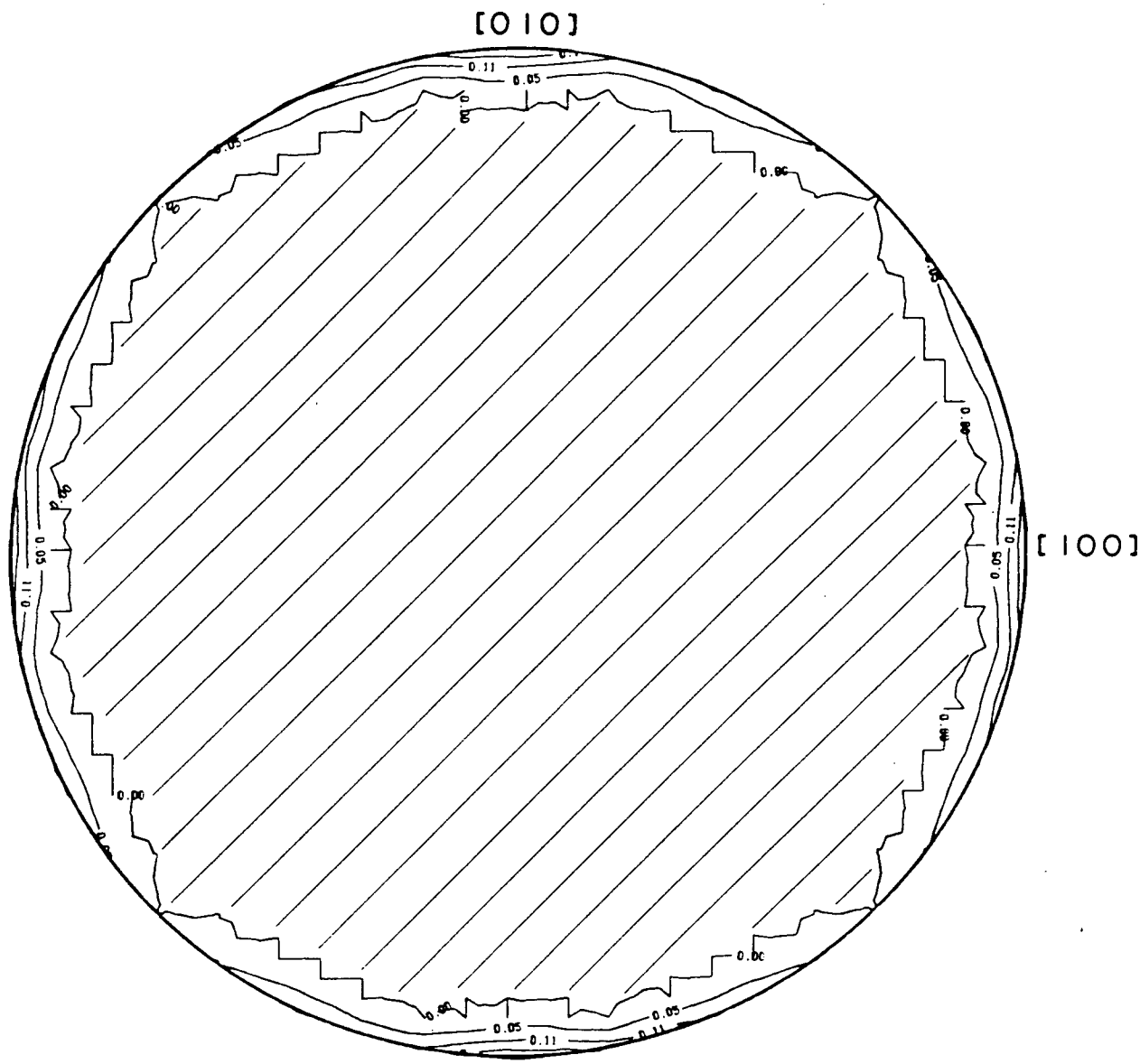

XIII.1.6.1.2 Cross-sections at 5 mm from the interface
(a) MRSS ; (b) MRSS-CRSS (Yield) ;
(c) MRSS-CRSS (MB) ; (d) MRSS-CRSS (MBTe)

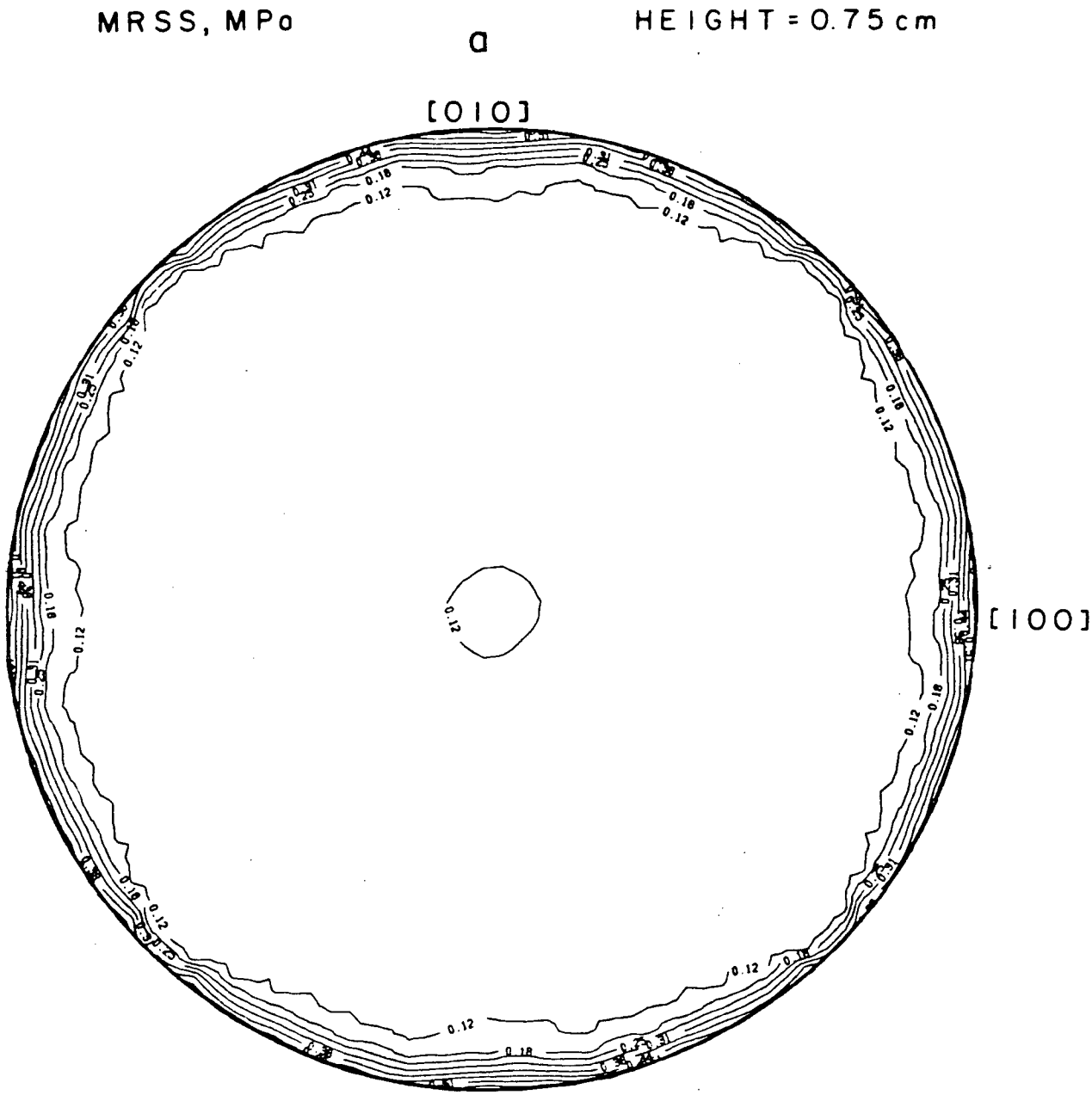
MRSS, MPa
a
HEIGHT = 0.75 cm
[010]
[100]
0.18
0.12

MRSS - CRSS (Y), MPa

HEIGHT = 0.75 cm

b

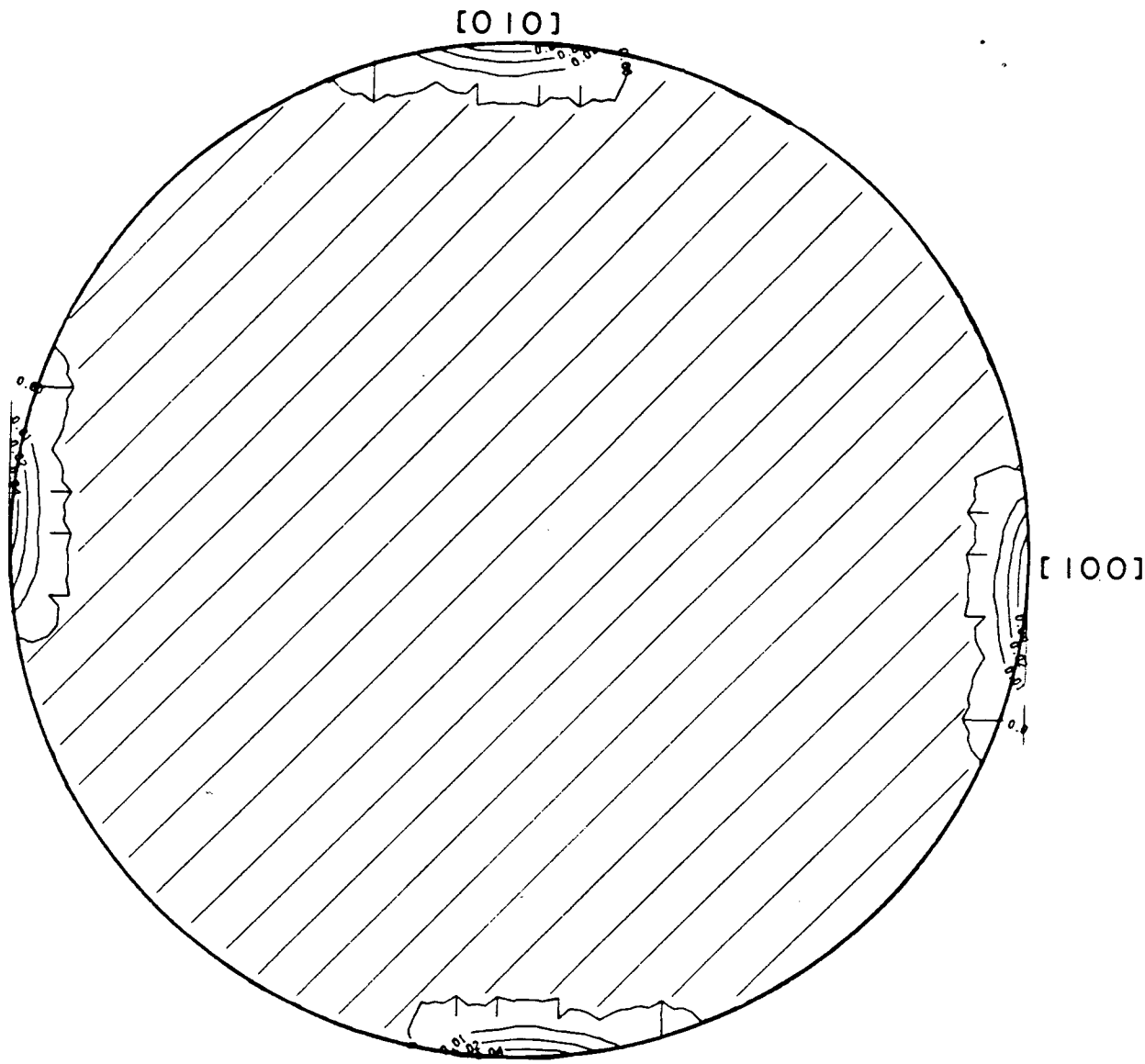

MRSS - CRSS(MB), MPa HEIGHT = 0.75 cm

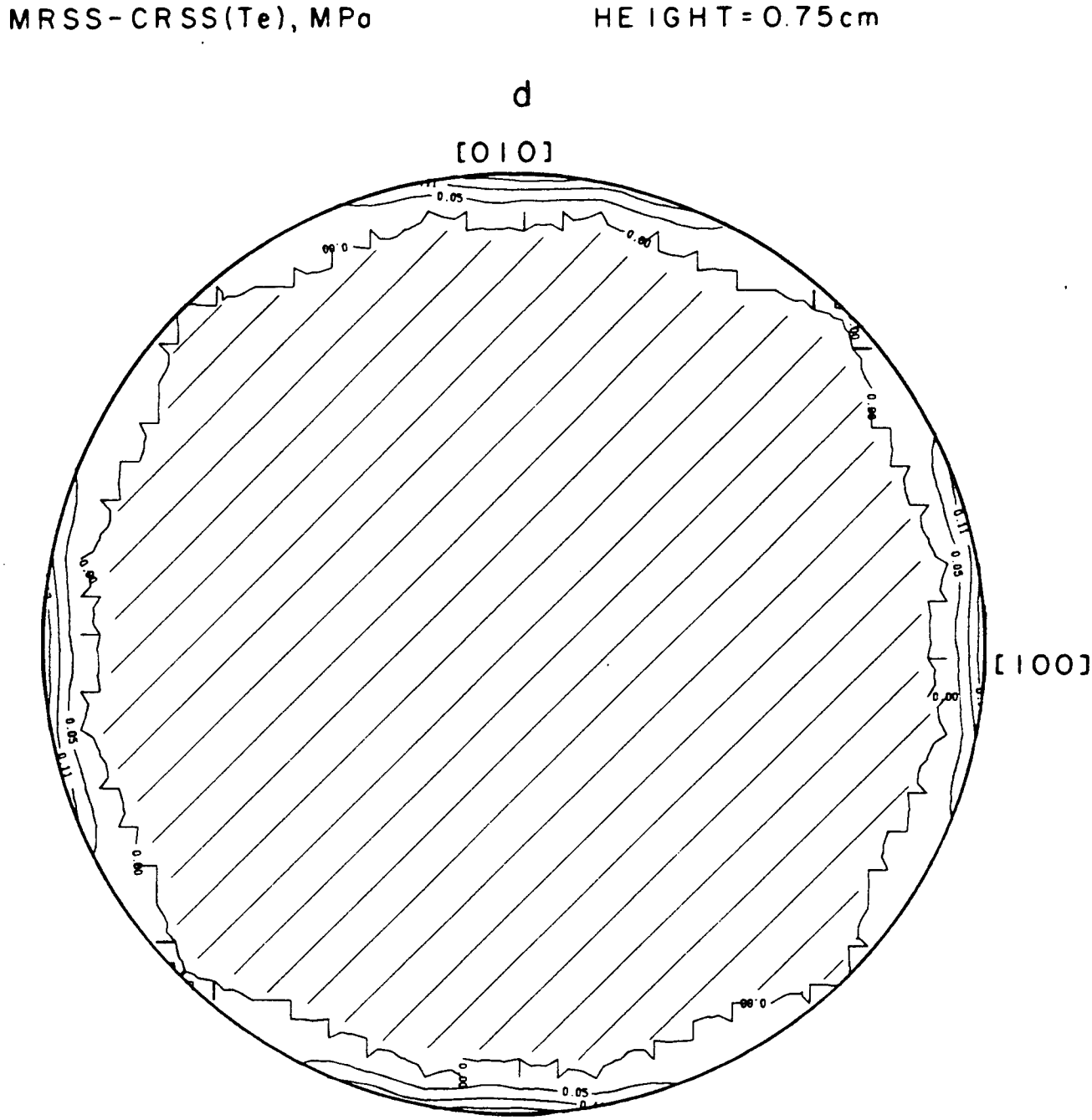

XIII.1.6.1.3 Cross-sections at 7.5 mm from the interface
(a) MRSS ; (b) MRSS-CRSS (Yield) ;
(c) MRSS-CRSS (MB) ; (d) MRSS-CRSS (MBTe)

Temperature, 10^3 °C

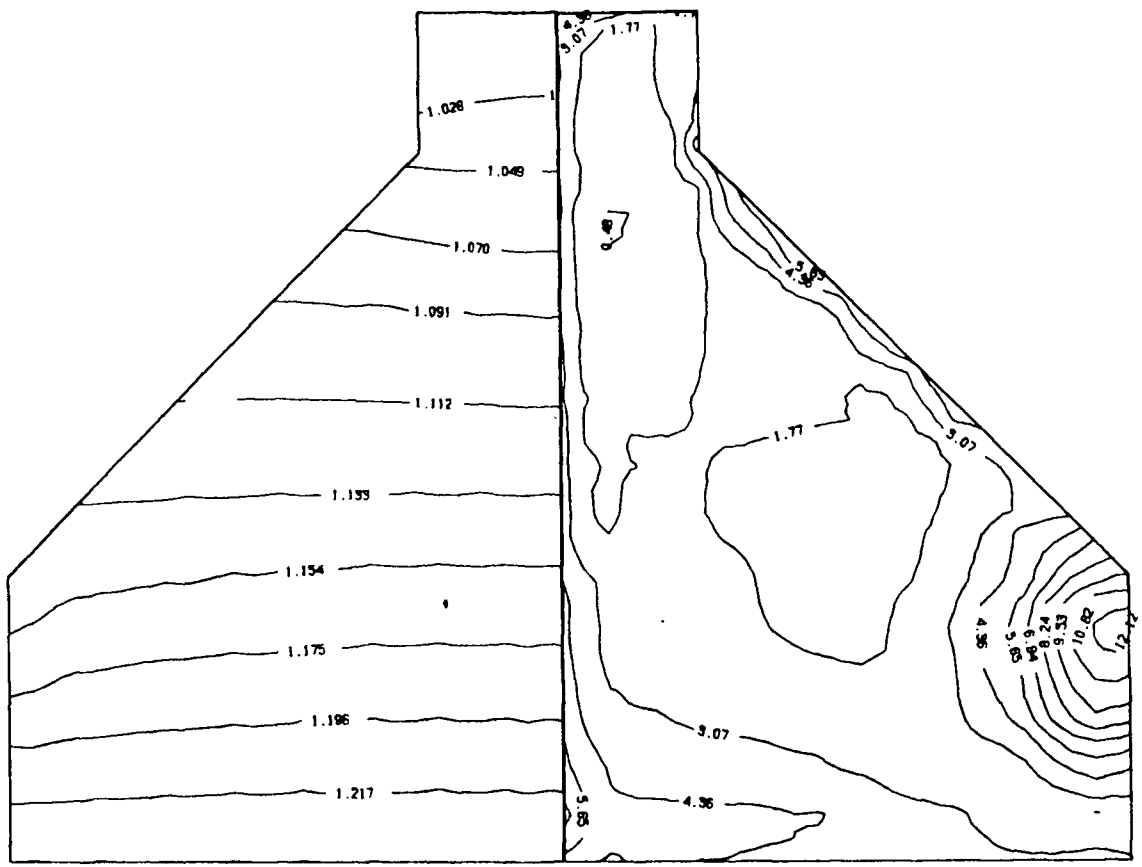

Von Mises Stress, MPa

a

MRSS, MPa

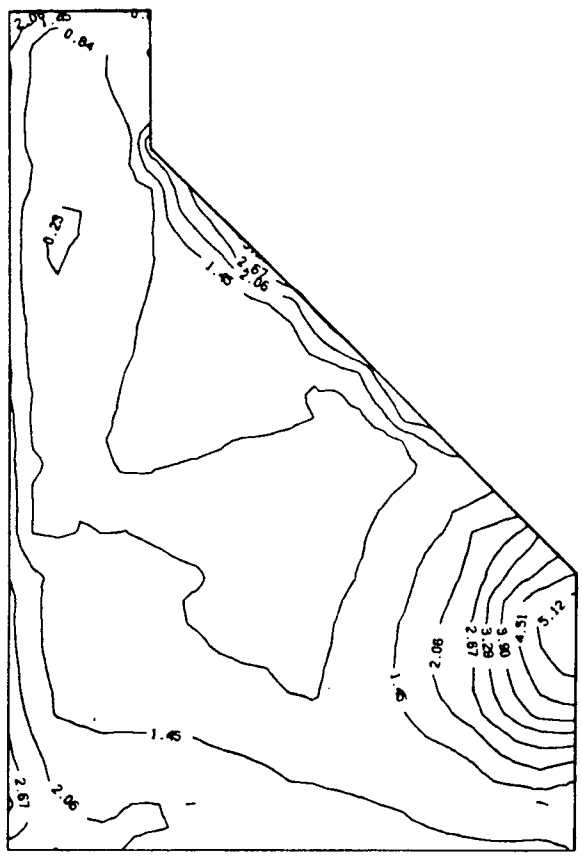

b

MRSS − CRSS (Y), MPa

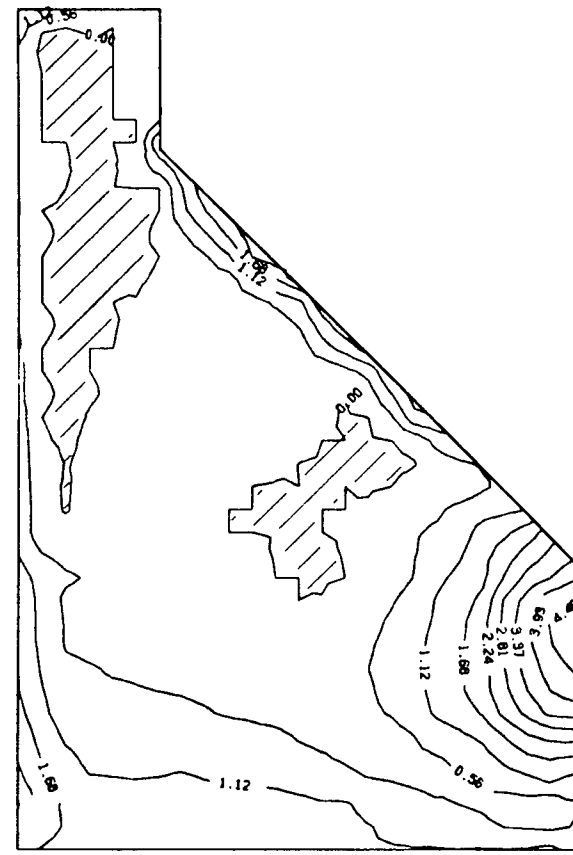

c

MRSS – CRSS(Te), MPa

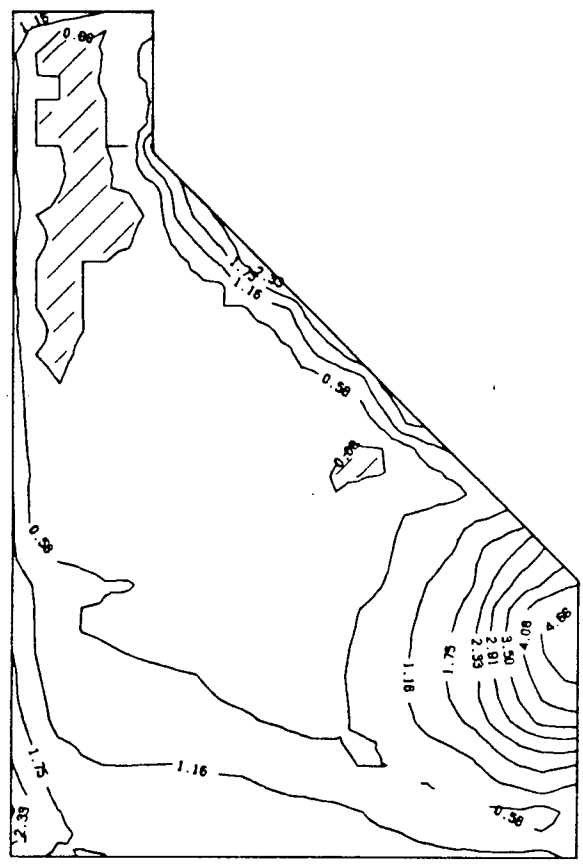

d

XIII.1.6.2.1 (a) Temperature and Von Mises Stress
(b) MRSS ; (c) MRSS-CRSS (Yield) ;
(d) MRSS-CRSS (MBTe) .

MRSS, MPa HEIGHT = 0.25 cm

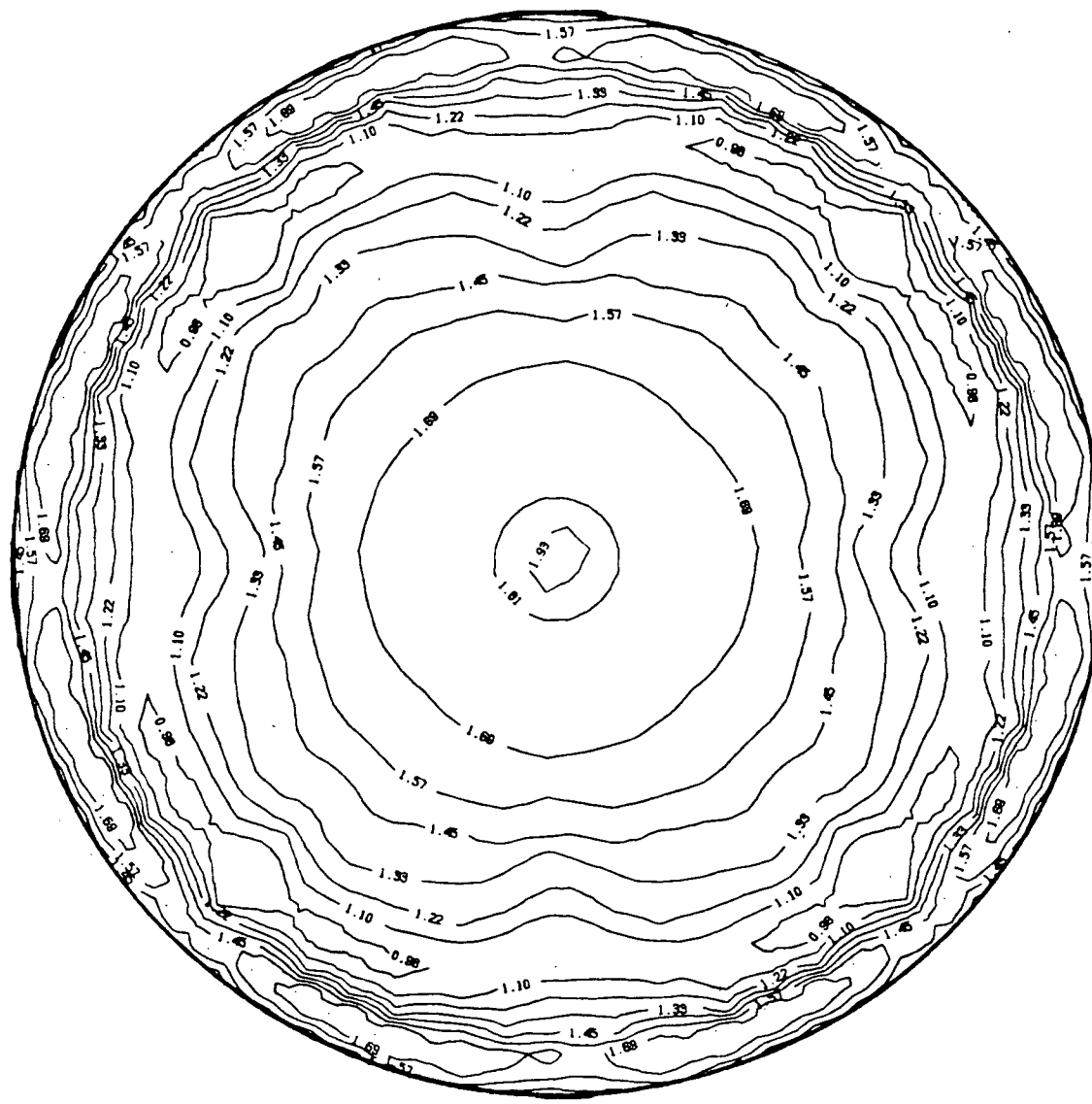

XIII.1.6.2.2 Cross-section at 2.5 mm from the interface, MRSS .

MRSS, MPa

a

HEIGHT = 0.75 cm

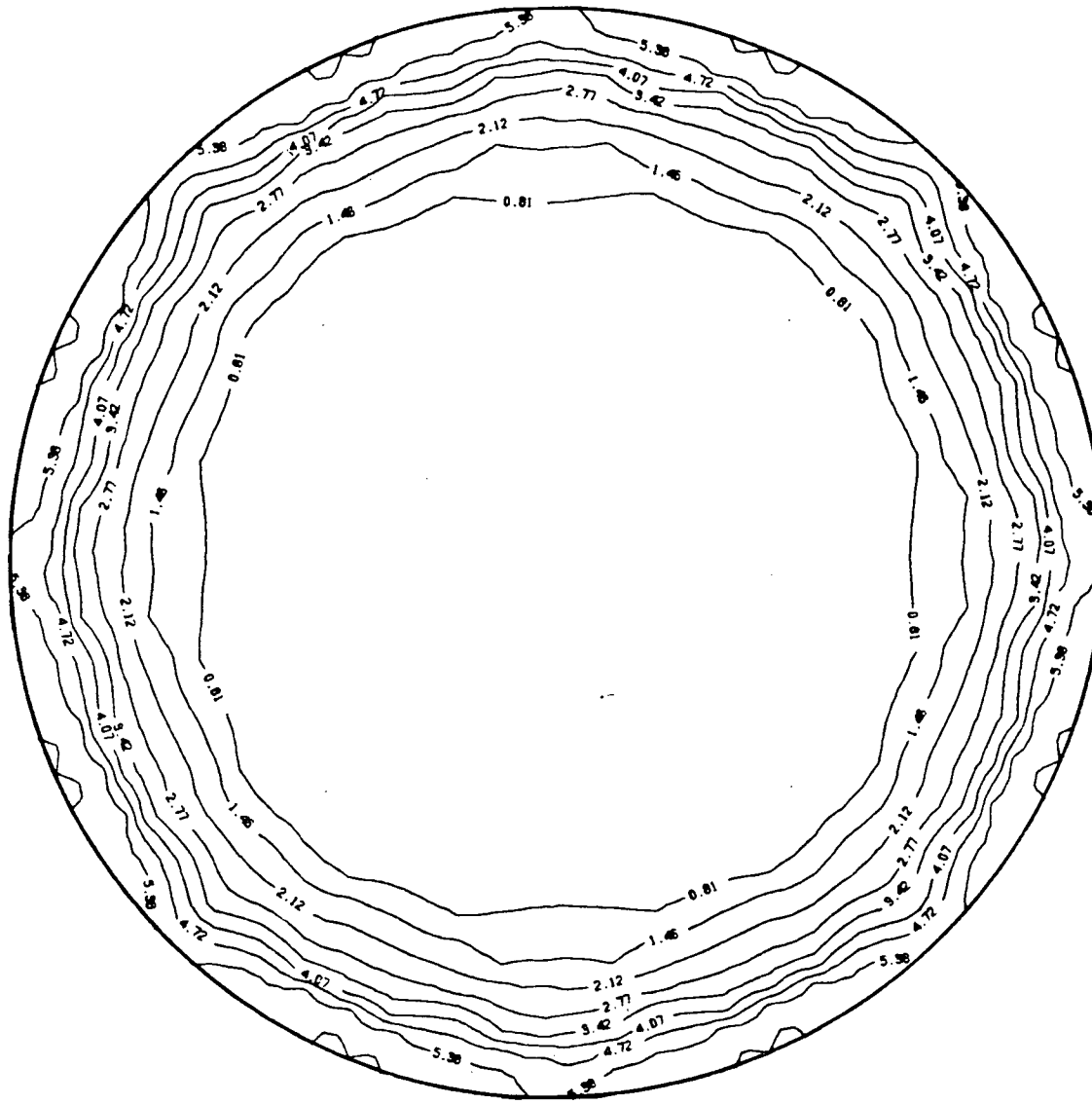

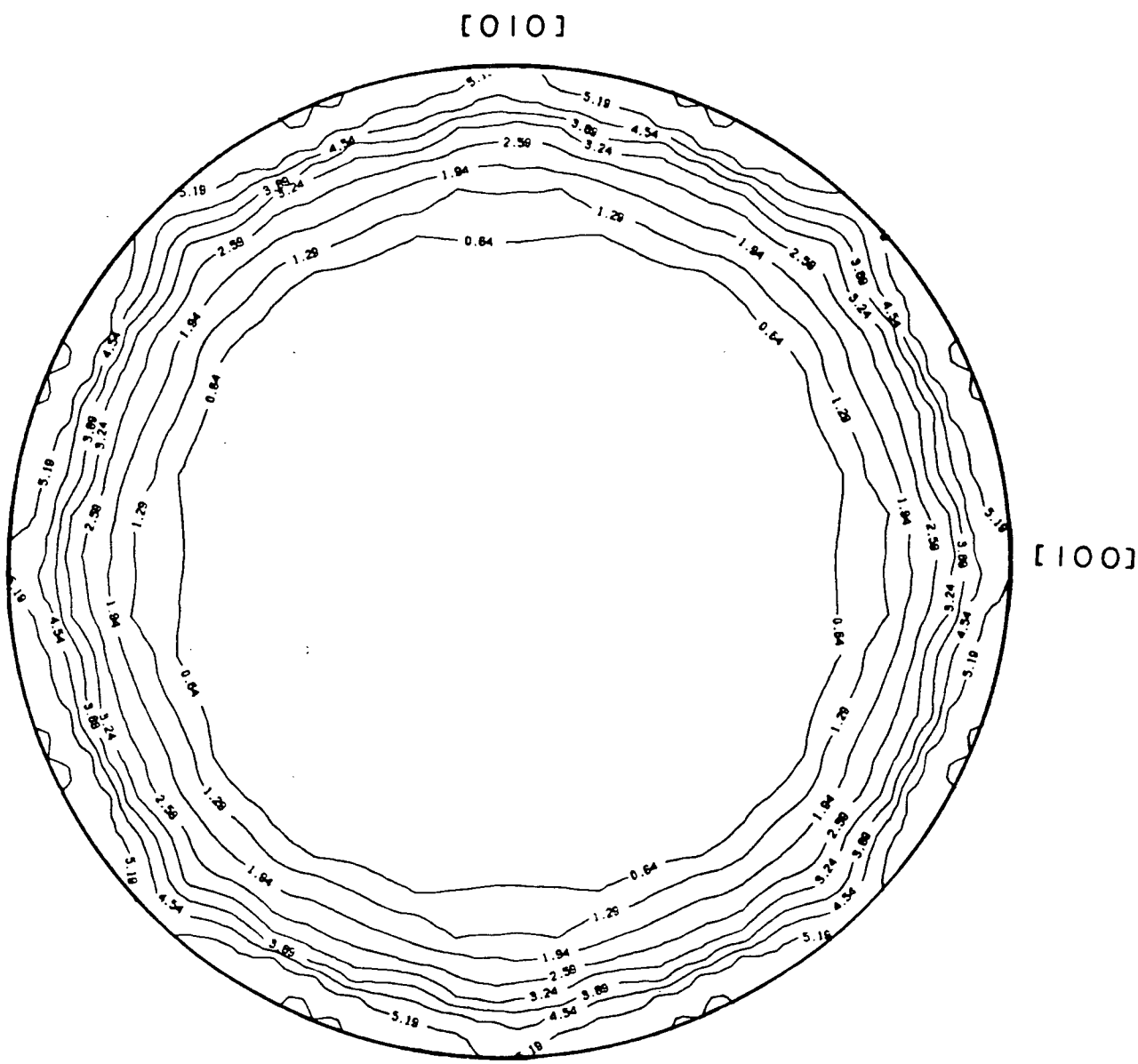

XIII.1.6.2.3 Cross-sections at 7.5 mm from the interface
(a) MRSS ; (b) MRSS-CRSS (Yield) ;

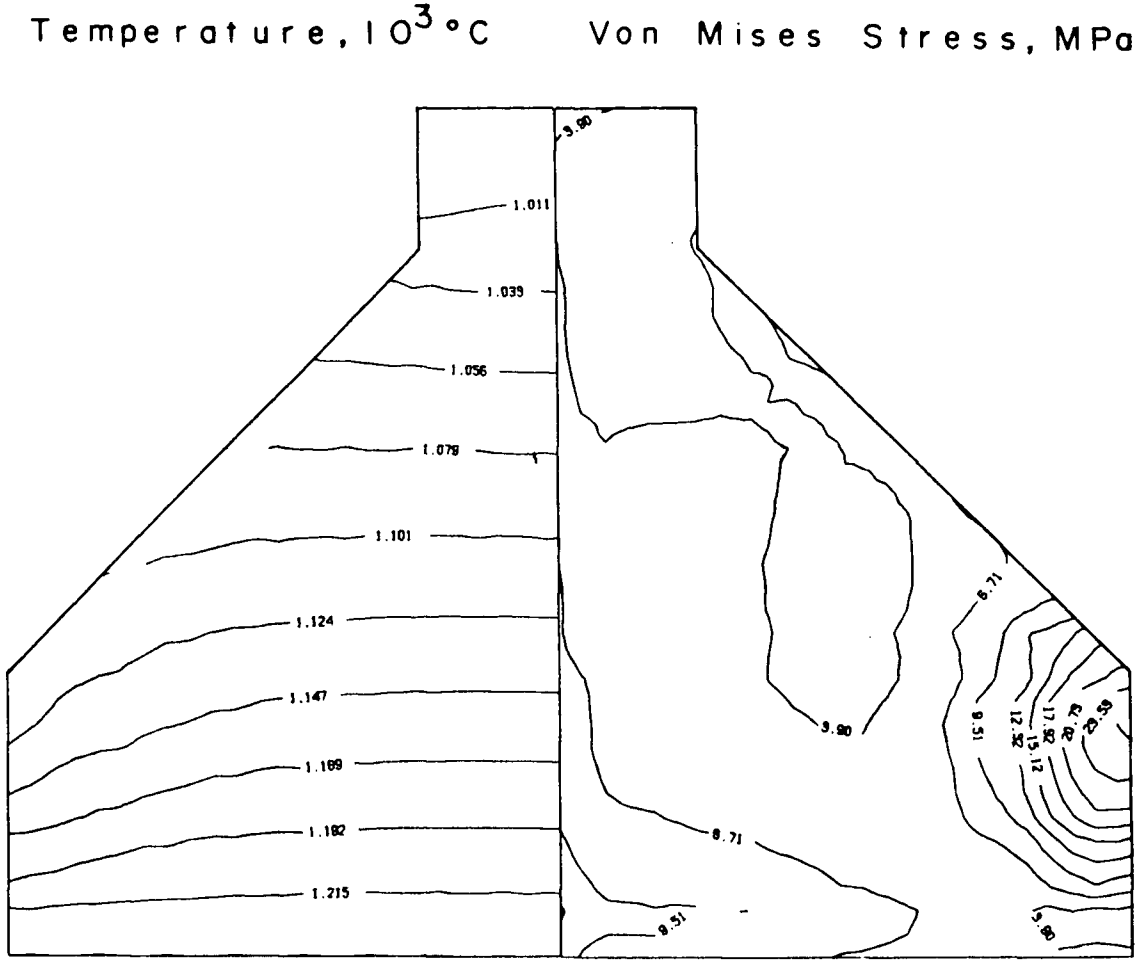
Temperature, 10^3 °C
Von Mises Stress, MPa
1.011
1.033
1.056
1.079
1.101
1.124
1.147
1.169
1.192
1.215
3.90
8.71
9.51
12.32
15.12
17.92
20.73
23.53

a

MRSS, MPa

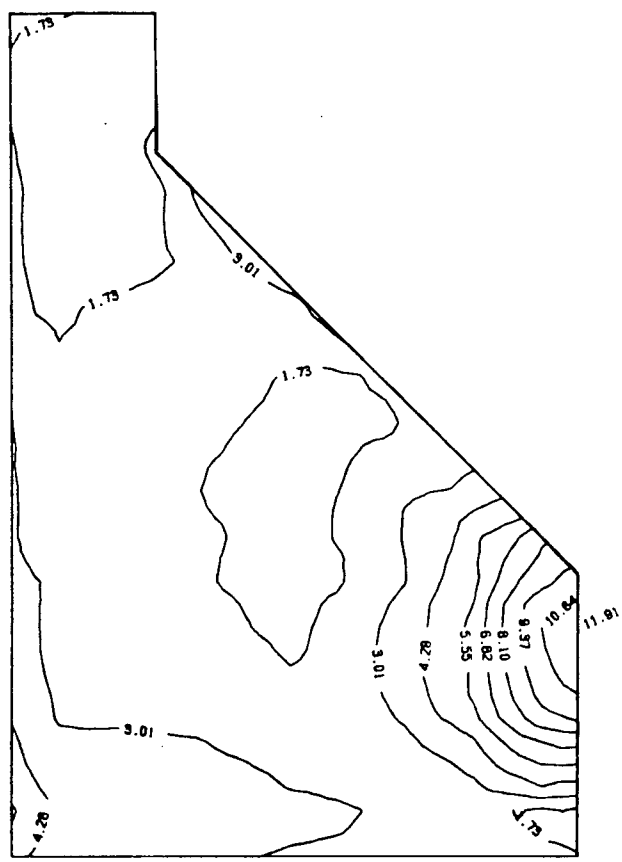

b

MRSS − CRSS (Y), MPa

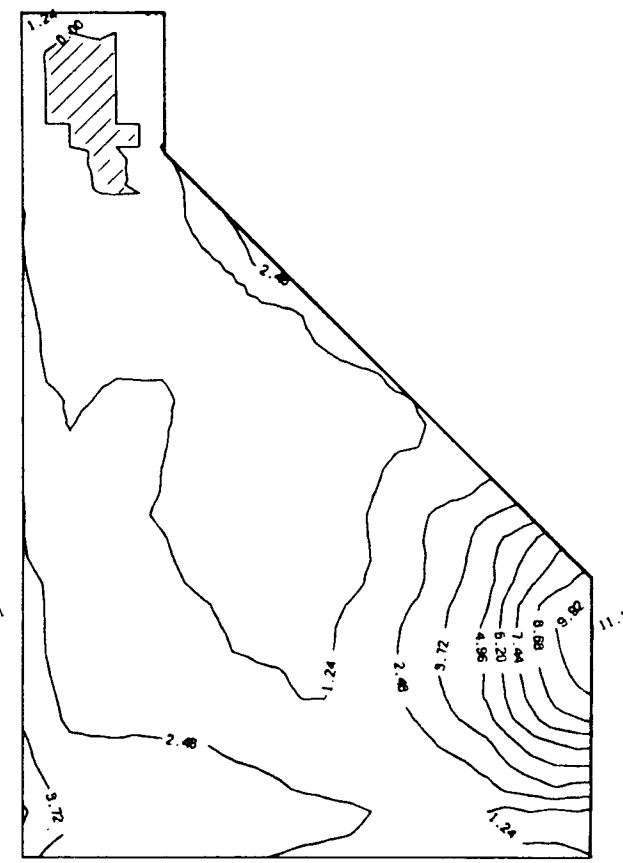

c

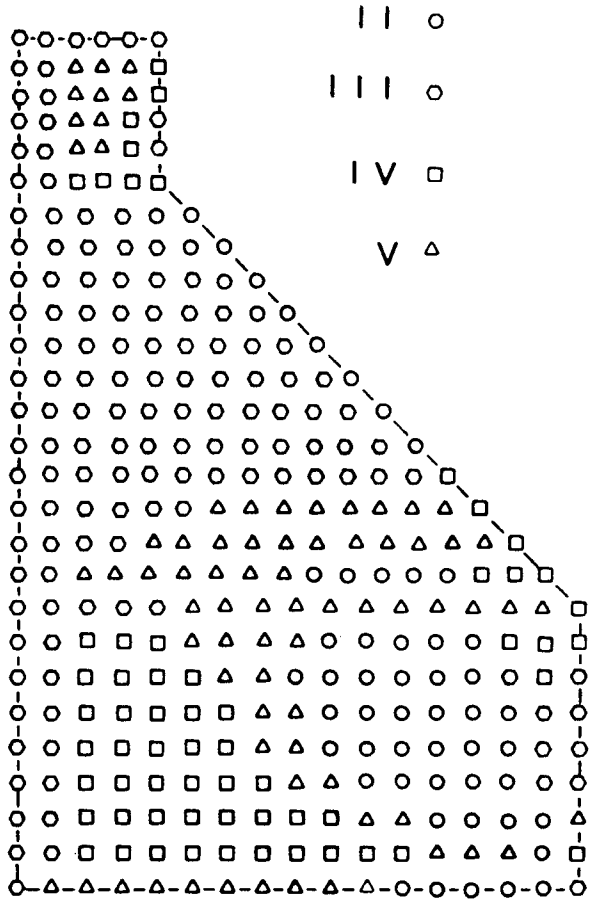

d

XIII.1.6.3.1 (a) Temperature and Von Mises Stress
(b) MRSS ; (c) MRSS-CRSS (Yield) ;
(d) Slip Mode.

MRSS - CRSS (Y), MPa HEIGHT = 0.75 cm

a

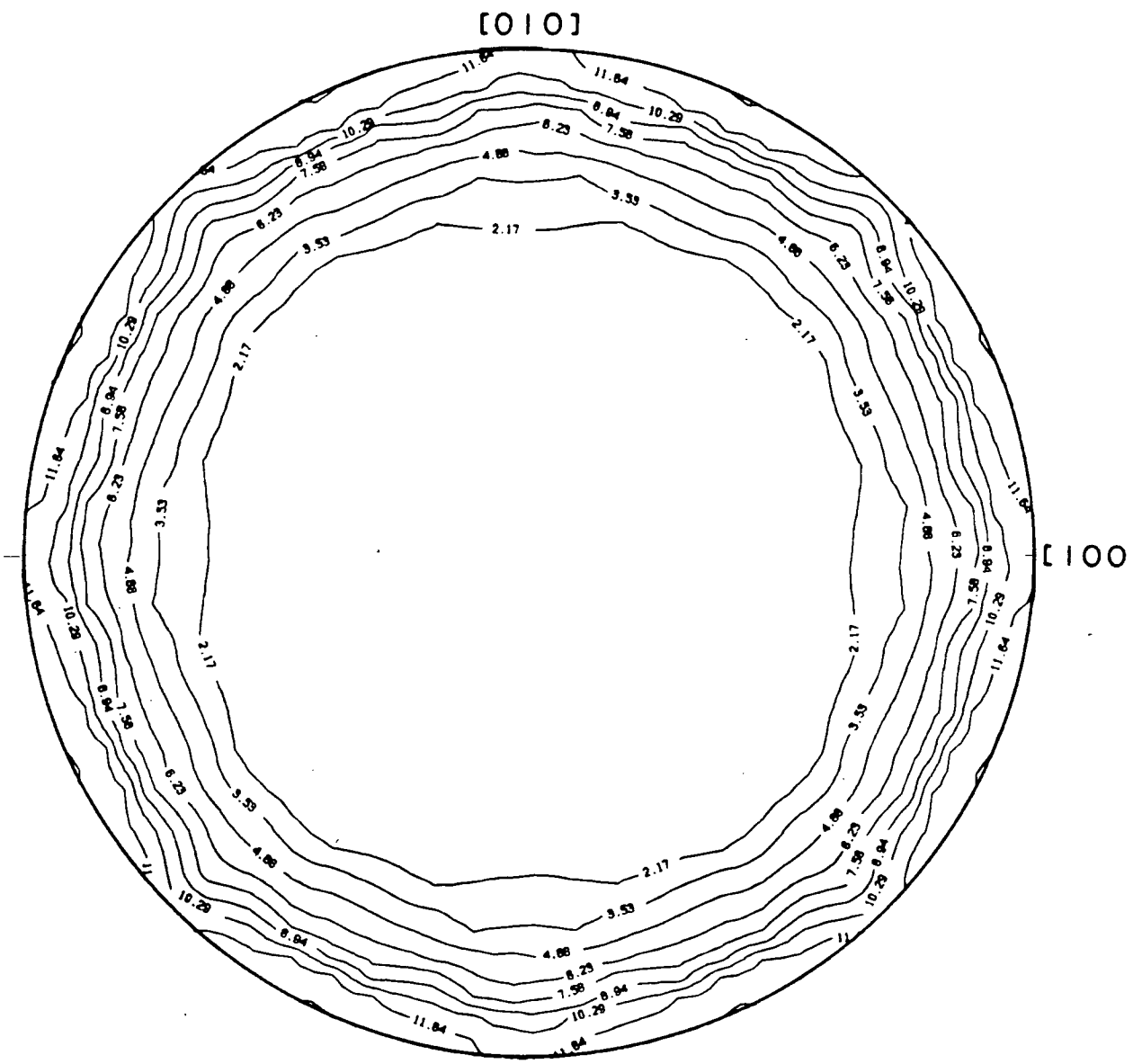

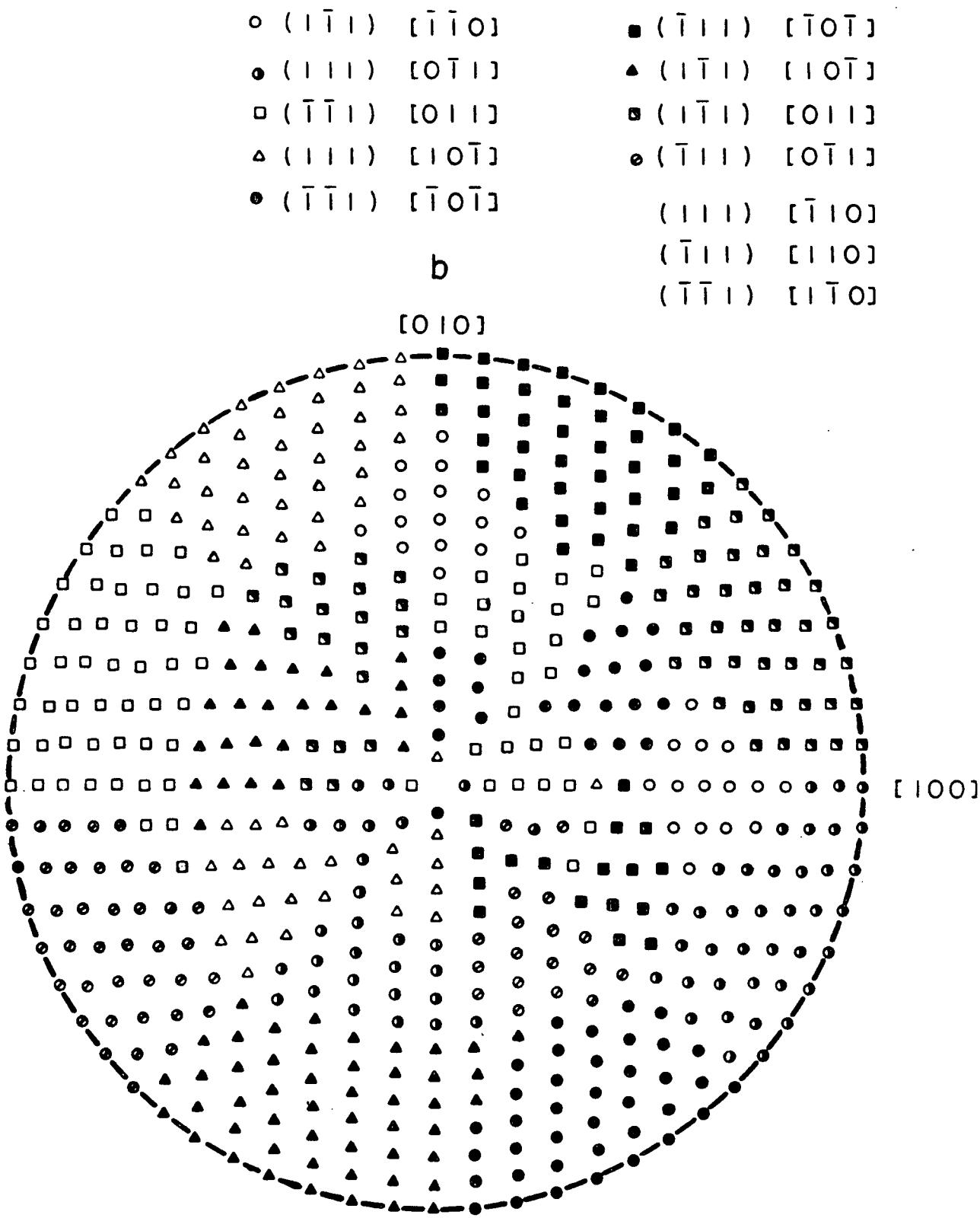

XIII.1.6.3.2 Cross-sections at 7.5 mm from the interface
(a) MRSS-CRSS (Yield) ; (b) Slip Mode.

Temperature, 10^3 °C Von Mises Stress, MPa

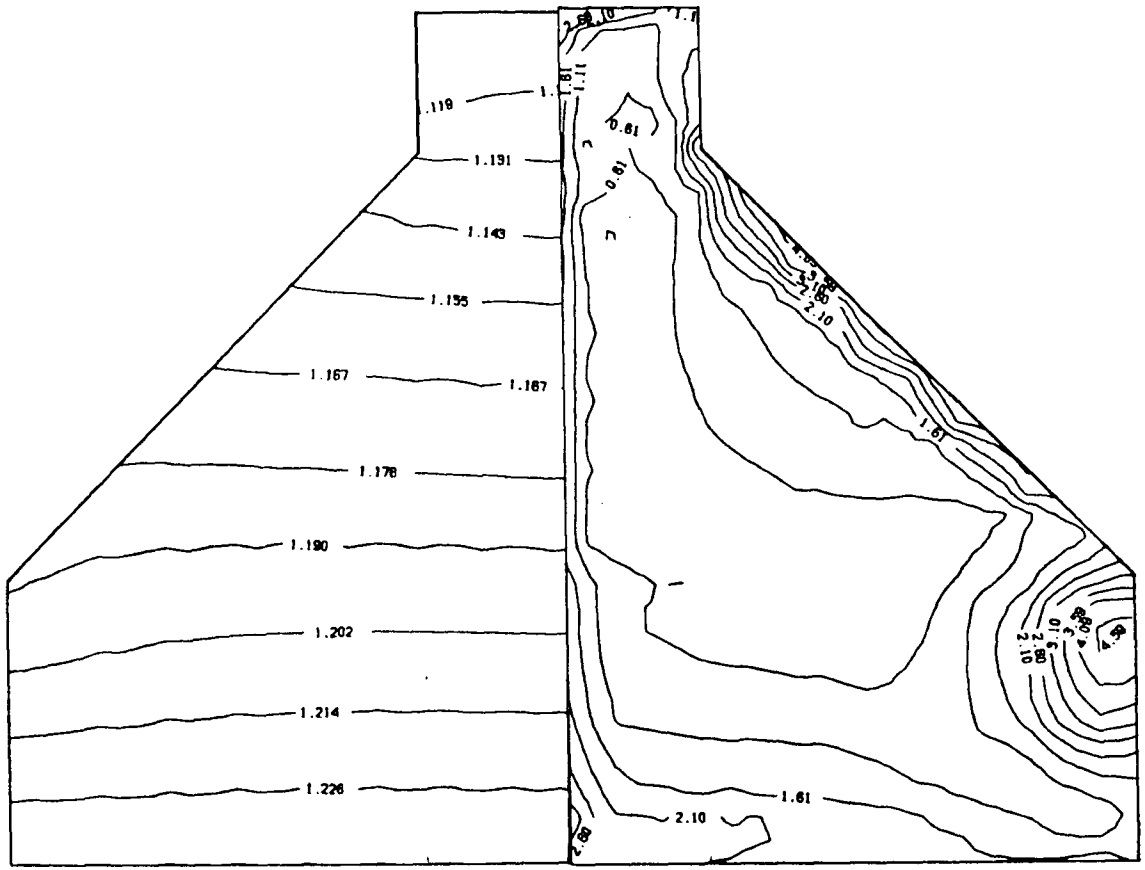

a

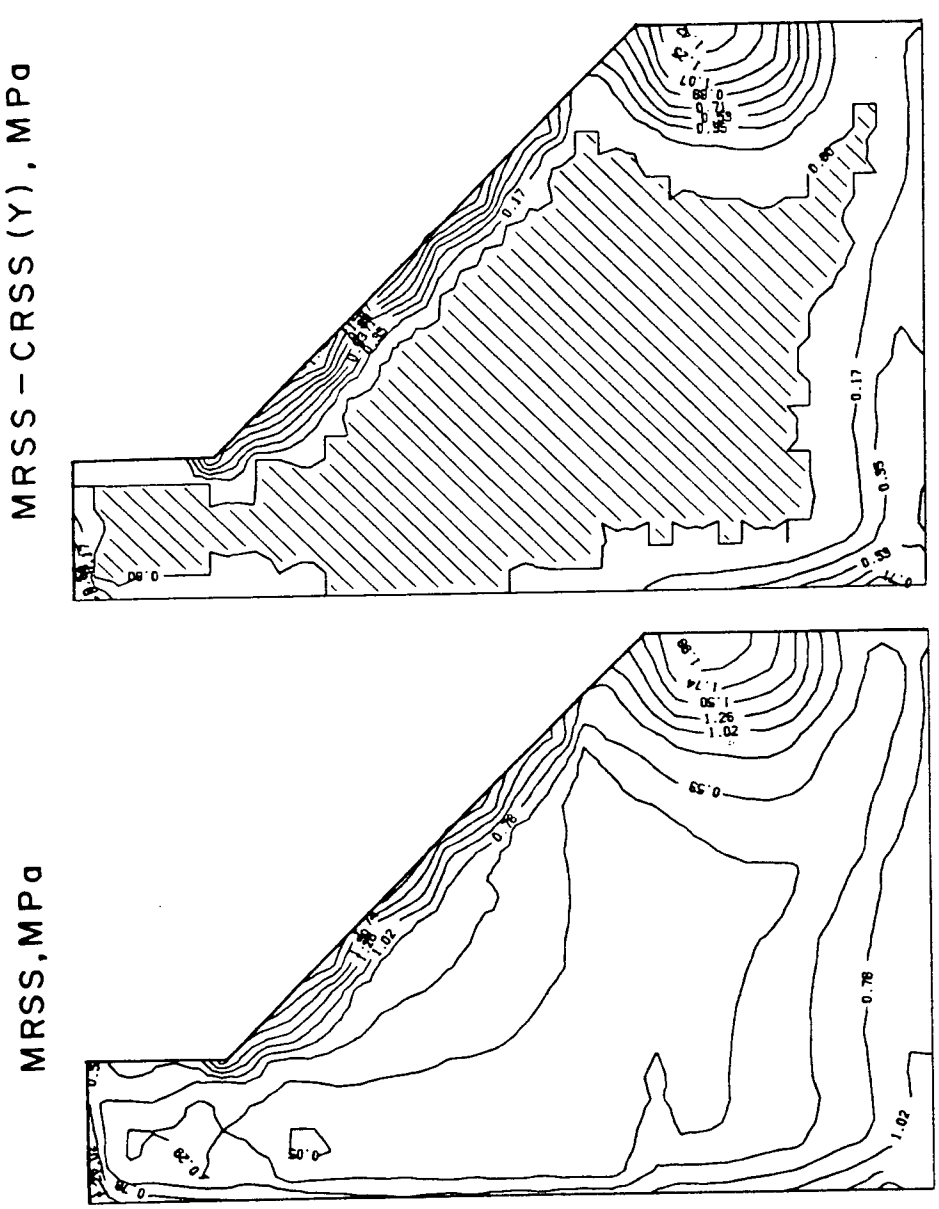
MRSS-CRSS(Y), MPa
MRSS,MPa
b
c

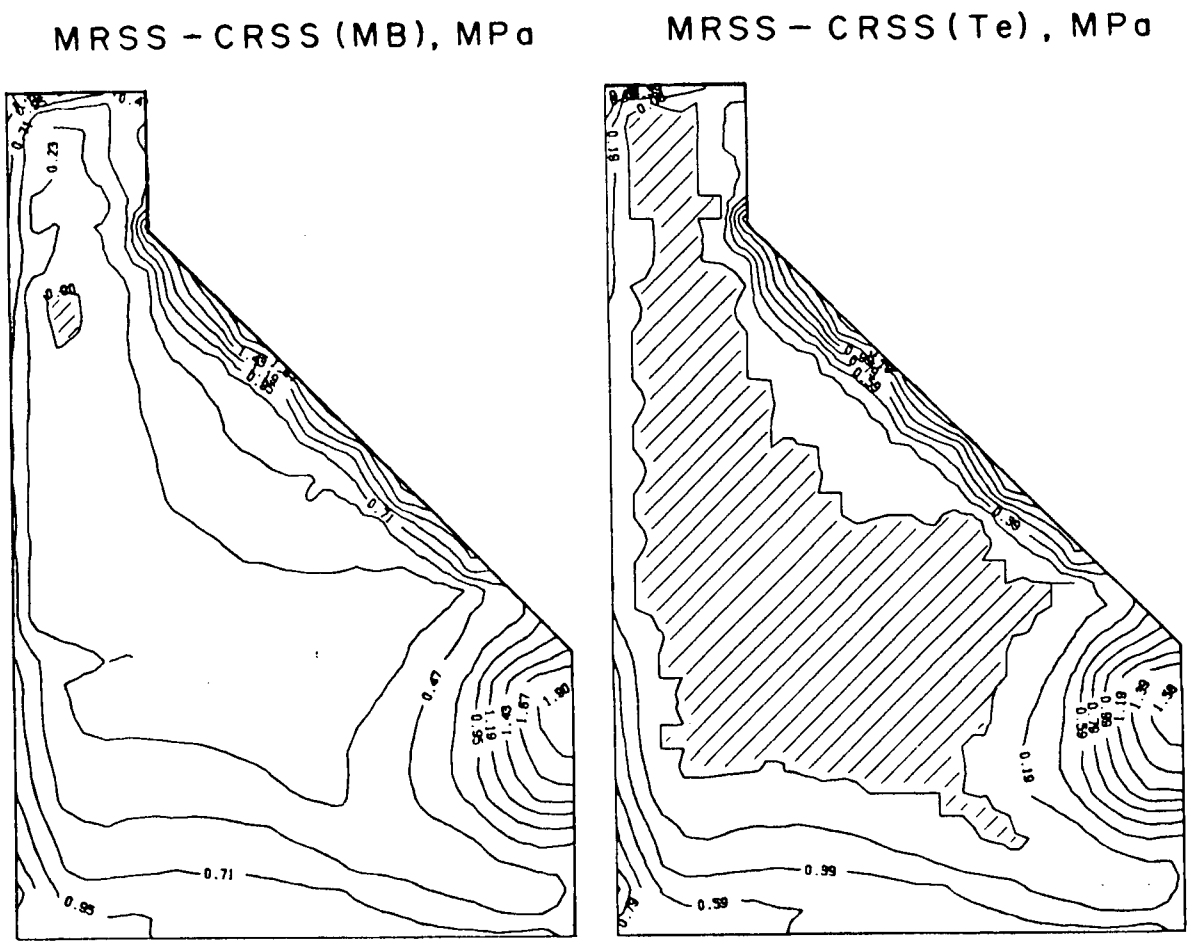

d e

XIII.1.7.1.1 (a) Temperature and Von Mises Stress
(b) MRSS ; (c) MRSS-CRSS (Yield) ;
(d) MRSS-CRSS (MB) ; (e) MRSS-CRSS (MBTe) .

MRSS-CRSS(Y), MPa

HEIGHT = 0.25 cm

a

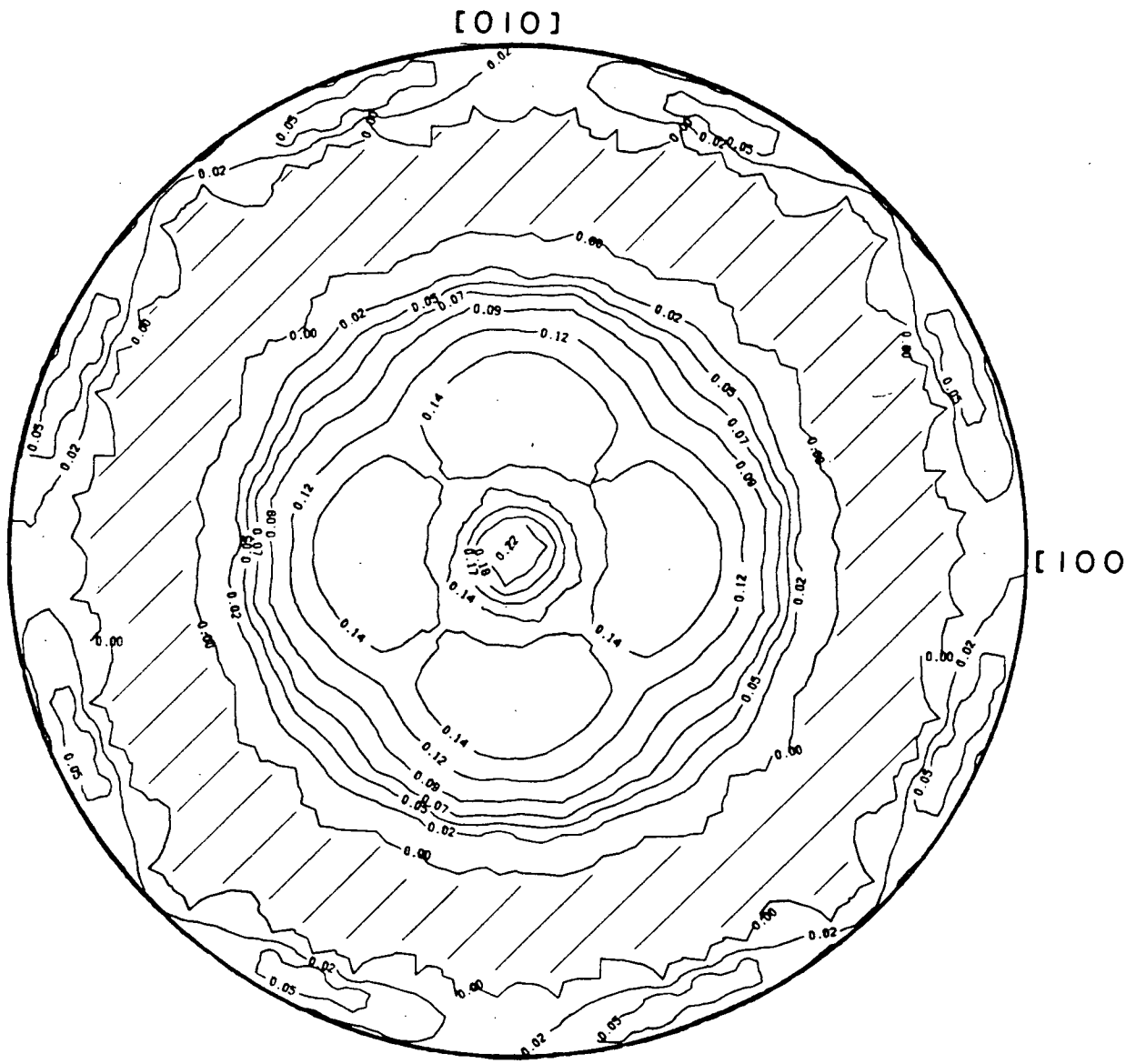

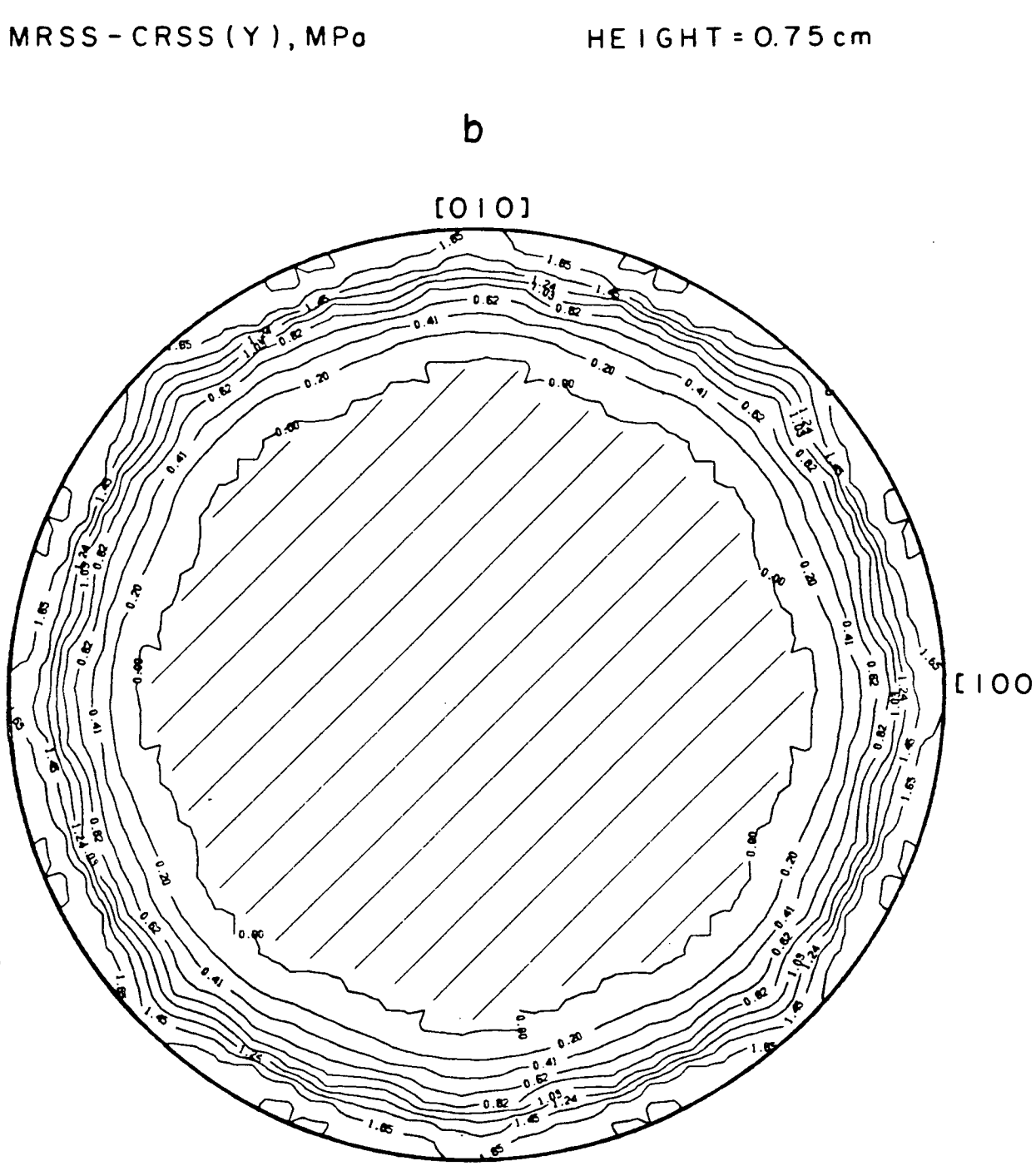

XIII.1.7.1.2 MRSS-CRSS (Yield) in cross-sections at distance from the interface (a) 2.5 mm ; (b) 7.5 mm.

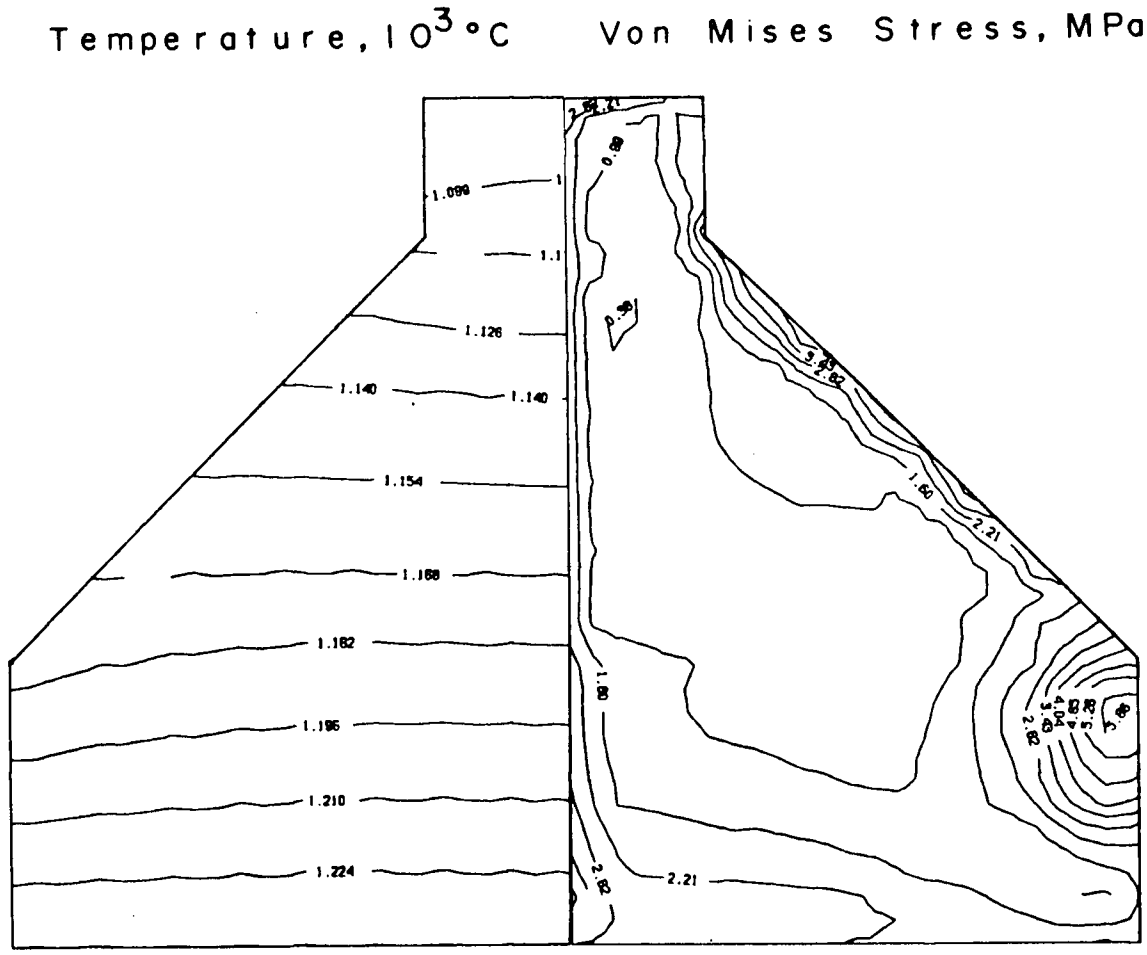
Temperature, 10^3 °C
Von Mises Stress, MPa
1.099
1.126
1.140
1.140
1.154
1.168
1.182
1.196
1.210
1.224
2.82
2.21
1.60
2.21
2.82
1.60
2.82
3.43
4.04

a

MRSS, MPa

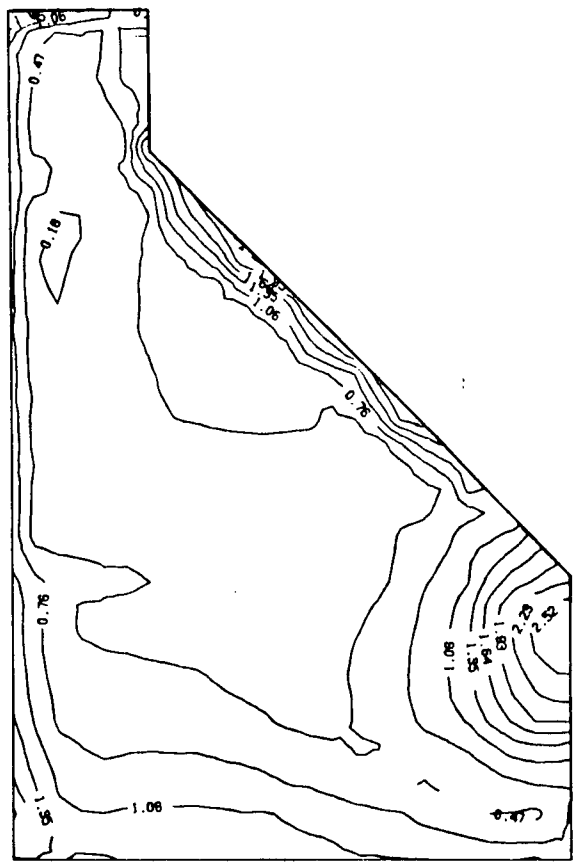

b

MRSS - CRSS (Y), MPa

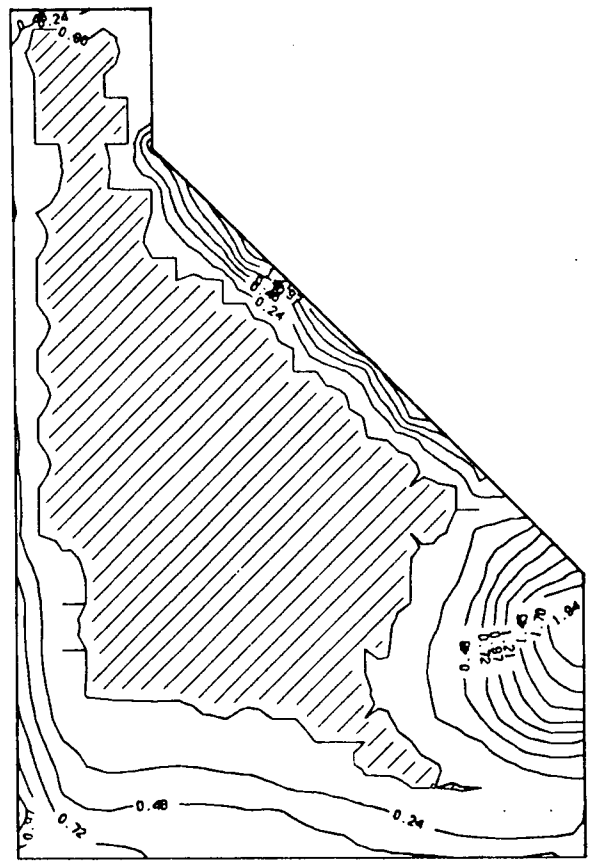

c

MRSS - CRSS (MB), MPa

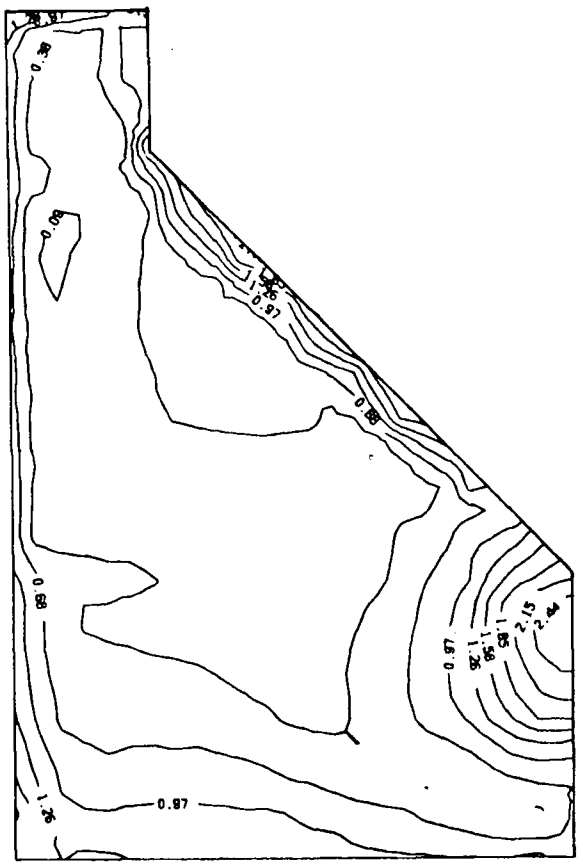

d

MRSS - CRSS (Te), MPa

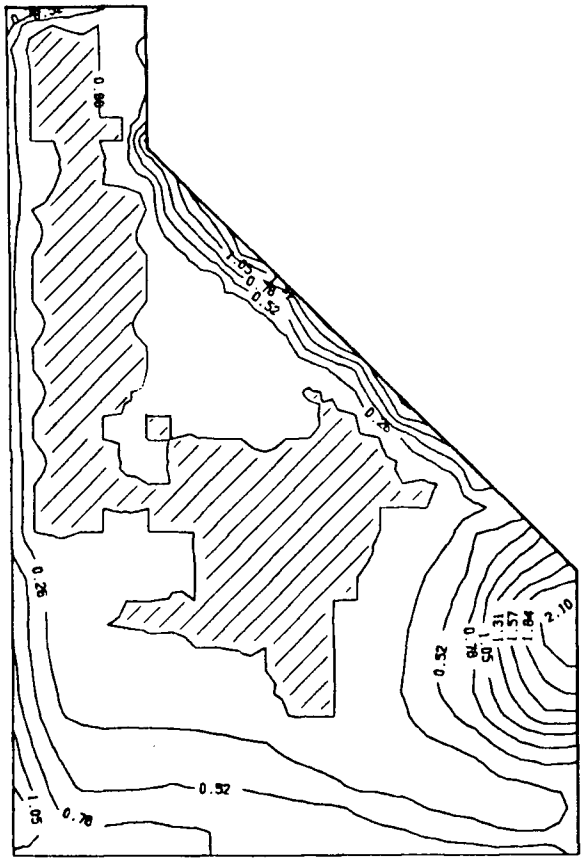

e

XIII.1.7.2.1 (a) Temperature and Von Mises Stress
(b) MRSS ; (c) MRSS-CRSS (Yield) ;
(d) MRSS-CRSS (MB) ; (e) MRSS-CRSS (MBTe) .

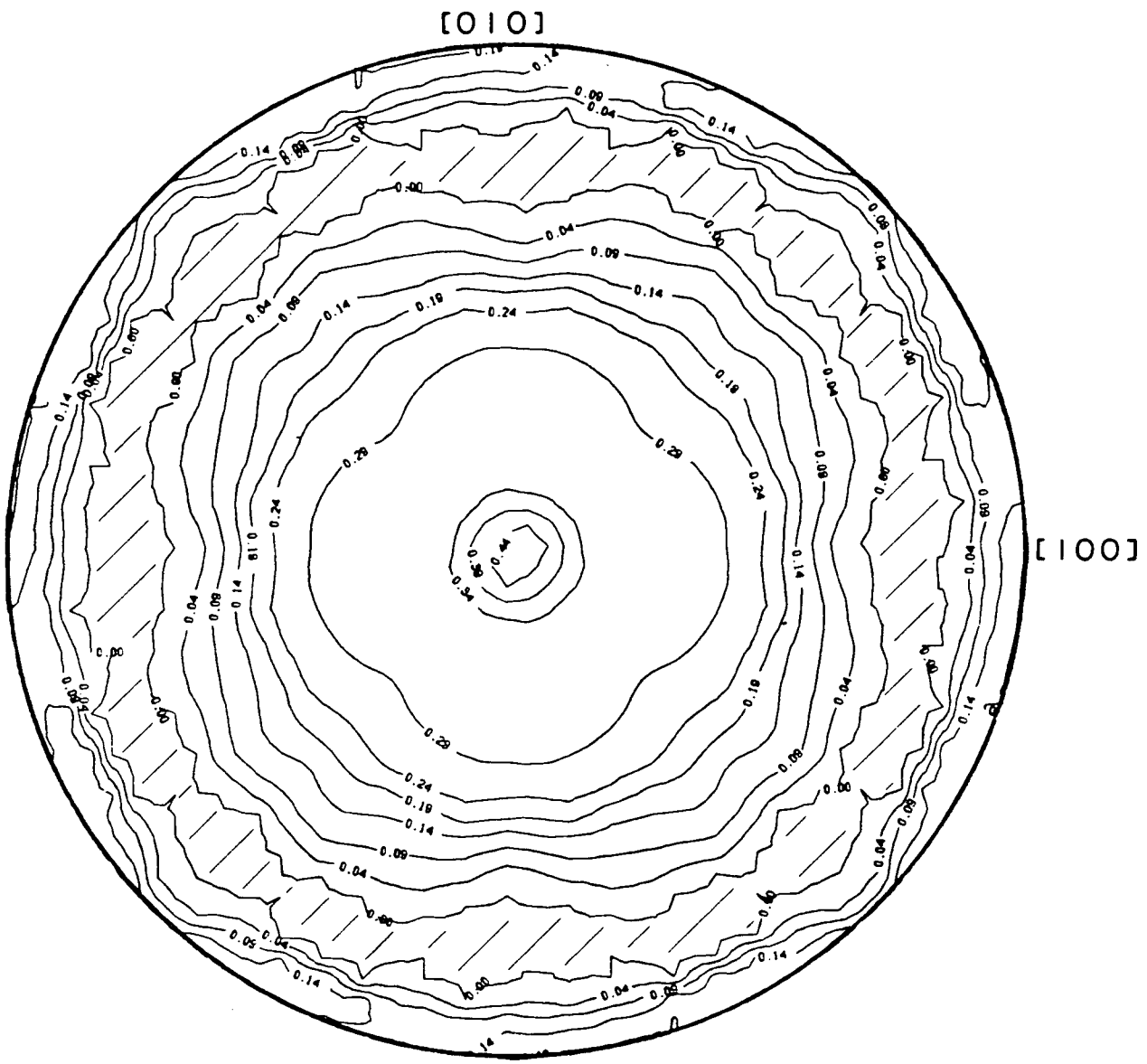

XIII.1.7.2.2 MRSS-CRSS (Yield) in cross-sections at 2.5 mm from the interface

MRSS, MPa

HEIGHT = 0.75 cm

a

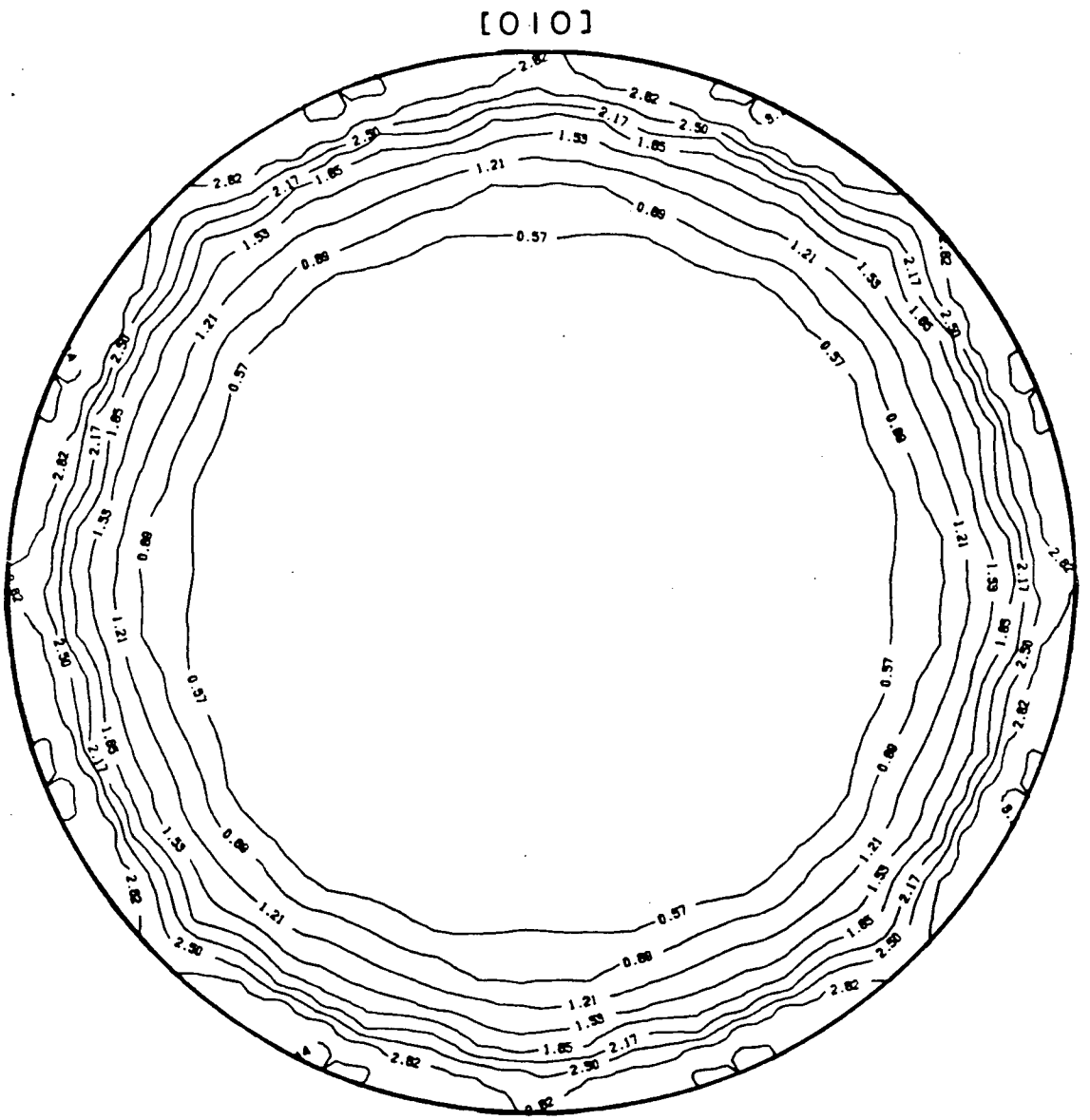

MRSS-CRSS(Y), MPa HEIGHT = 0.75 cm

b

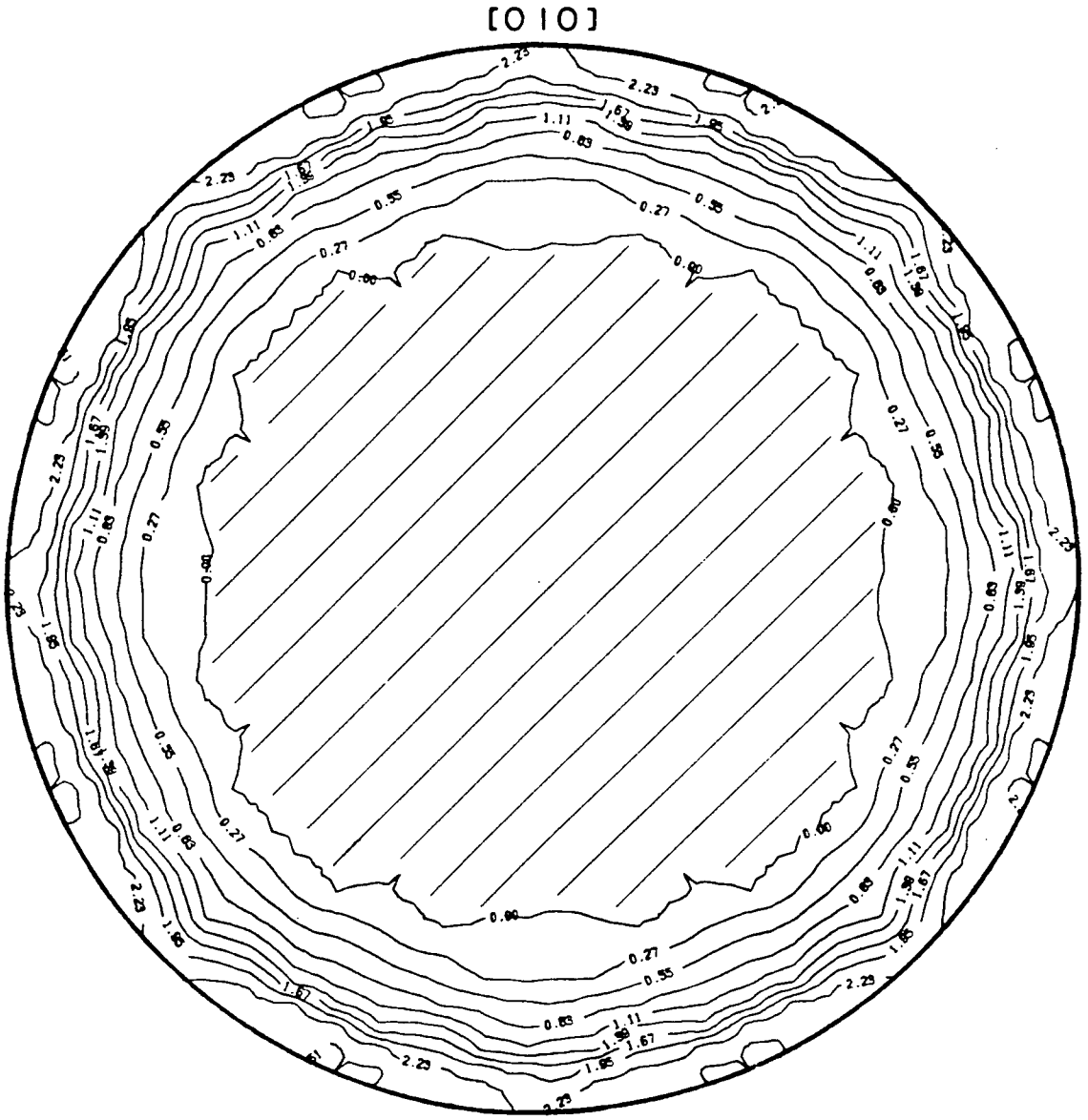

XIII.1.7.2.3 Cross-sections at 7.5 mm from the interface
(a) MRSS ; (b) MRSS-CRSS (Yield) ;

XIII.2 Crystal Length
R, 27.5 mm ; B,21 mm ; AP, 30 atm. ; CA, 30° .

XIII.2.1 CL, 13.75 mm

XIII.2.1.1 (a) Temperature and Von Mises Stress
(b) MRSS ; (c) MRSS-CRSS (Yield) ;
(d) MRSS-CRSS (MB) ; (e) MRSS-CRSS (MBTe) .

XIII.2.1.2 Cross-sections
(a) MRSS-CRSS (Yield) at 5.5 from the interface ;
(b) MRSS at 11.0 mm from the interface ;
(c) MRSS-CRSS (Yield) at 11.0 mm from the interface.

XIII.2.2 CL, 27.5 mm

XIII.2.2.1 (a) Temperature and Von Mises Stress
(b) MRSS ; (c) MRSS-CRSS (Yield) ;
(d) MRSS-CRSS (MB) ; (e) MRSS-CRSS (MBTe) .

XIII.2.2.2 MRSS-CRSS (Yield) in cross-sections at a distance of the interface of :
(a) 5.5 mm ; (b) 11.0 mm ; (c) 19.25 mm ;
(d) 24.75 mm ; (e) 27.5 mm .

XIII.2.3 CL, 55.0 mm

XIII.2.3.1 (a) Temperature and Von Mises Stress
(b) MRSS ; (c) MRSS-CRSS (Yield) ;
(d) MRSS-CRSS (MB) ; (e) MRSS-CRSS (MBTe) .

XIII.2.3.2 MRSS-CRSS (Yield) at 5.5 mm from the interface.

XIII.2.3.3 Cross-section at 11.0 mm from the interface
(a) MRSS ; (B) MRSS-CRSS (Yield) ;
(c) MRSS-CRSS (MB) ; (d) MRSS-CRSS (MBTe).

XIII.2.3.4 MRSS-CRSS (Yield) at a distance from the interface of
(a) 19.25 mm ; (b) 24.75 mm

XIII.2.3.5 Cross-section at 33 mm from the interface
(a) MRSS ; (B) MRSS-CRSS (Yield) ;
(c) MRSS-CRSS (MB) ; (d) MRSS-CRSS (MBTe).

XIII.2.3.6 MRSS-CRSS (Yield) at a distance from the interface of
(a) 38.5 mm ; (b) 46.75 mm ; (c) 52.25 mm.

XIII.2.4 CL, 82.5 mm

XIII.2.4.1 (a) Temperature and Von Mises Stress
(b) MRSS ; (c) MRSS-CRSS (Yield) ;
(d) MRSS-CRSS (MB) ; (e) MRSS-CRSS (MBTe) .

XIII.2.4.2 MRSS-CRSS (Yield) in cross-sections at a distance of the interface of
(a) 5.5 mm ; (b) 11.0 mm ; (c) 19.25 mm ;
(d) 24.75 mm ; (e) 33.0 mm ; (f) 38 .5 mm ;
(g) 46.75 mm ; (h) 52.25 mm ; (i) 60.5 mm ;
(j) 66 mm ; (k) 74.25 mm ; (l) 79.75 mm .

XIII.2.5 CL, 110 mm

XIII.2.5.1 (a) Temperature and Von Mises Stress
(b) MRSS ; (c) MRSS-CRSS (Yield) ;
(d) MRSS-CRSS (MB) ; (e) MRSS-CRSS (MBTe) .

XIII.2.5.2 MRSS-CRSS (Yield) in cross-sections at a distance from the interface of
(a) 5.5 mm ; (b) 11.0 mm ; (c) 24.75 mm ;
(d) 33.0 mm ; (e) 96.25 mm .

a

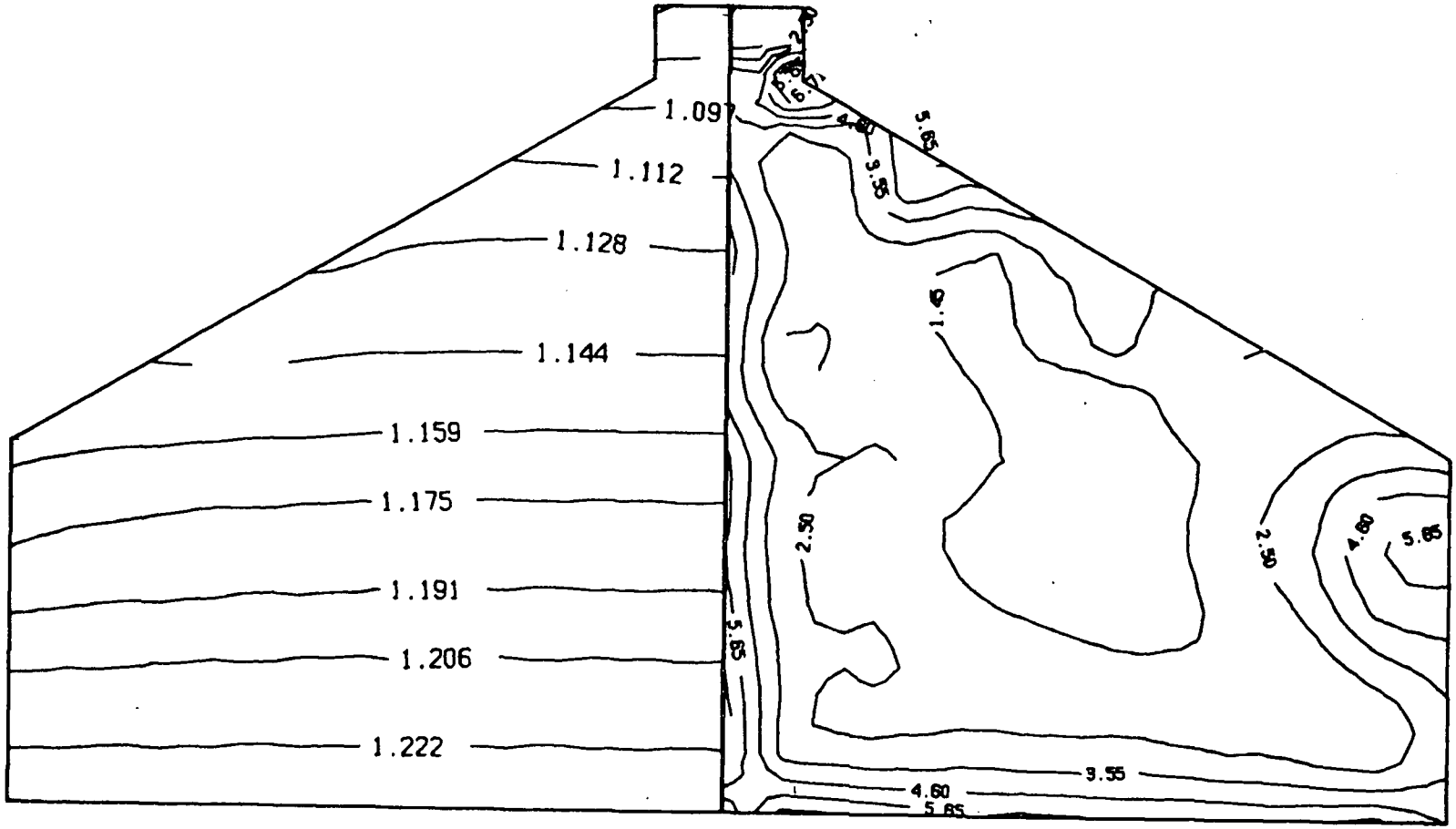

b

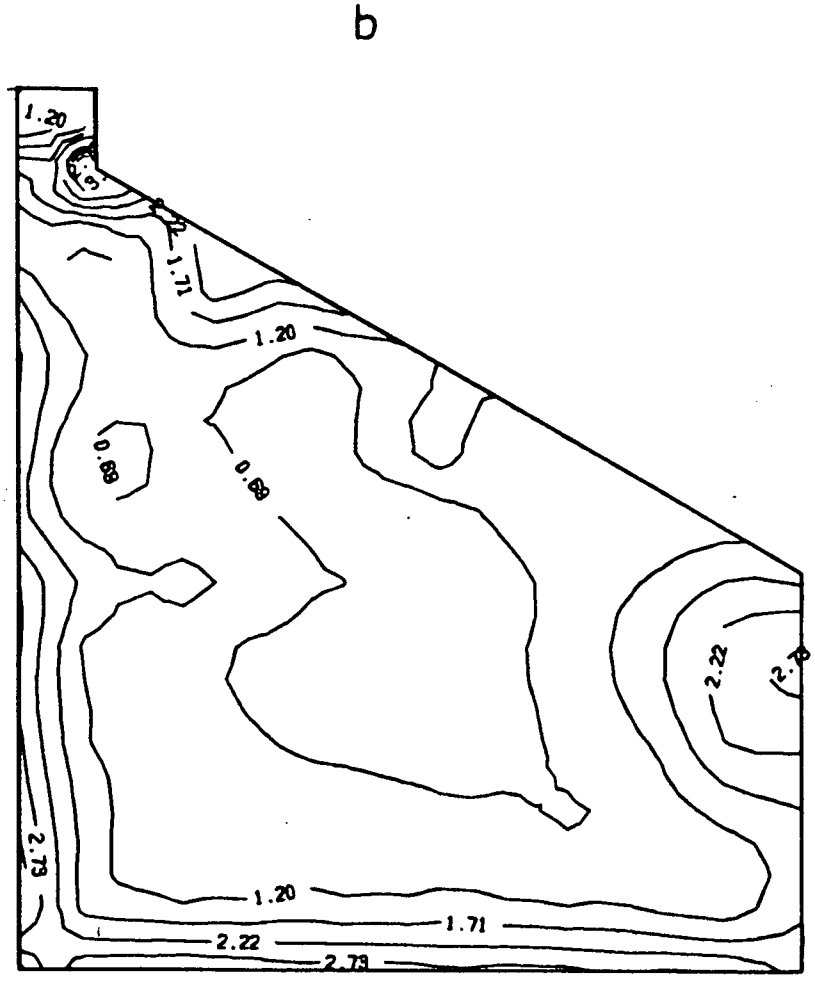
1.20
1.71
1.20
0.69
0.69
2.22
2.73
2.73
1.20
1.71
2.22
2.73

c

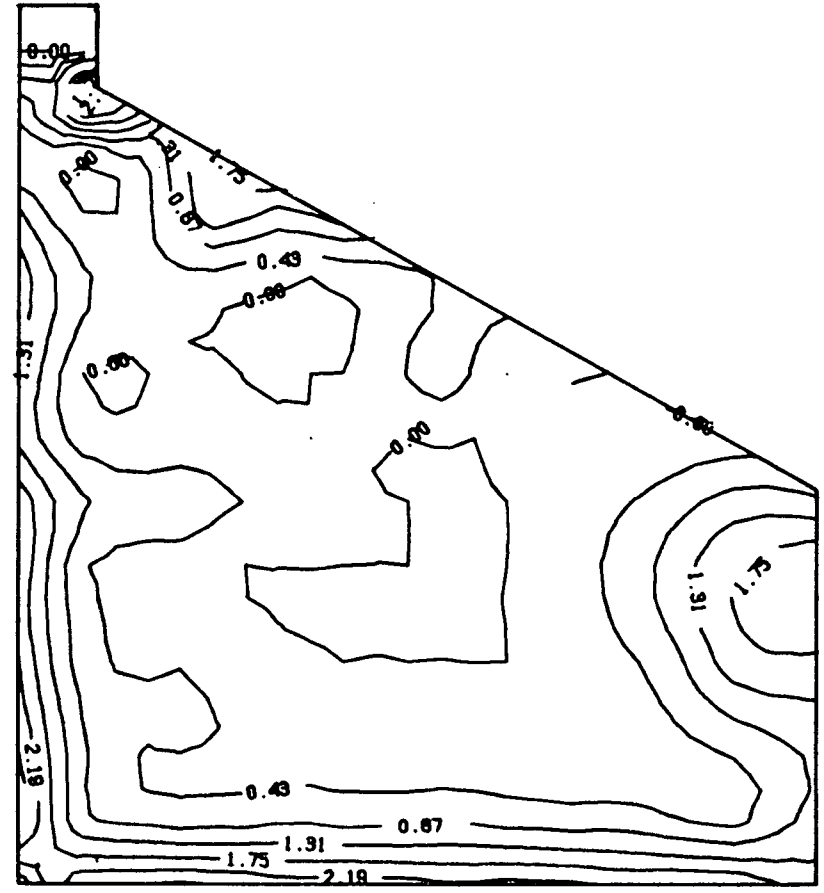
0.00
1.75
0.87
0.43
0.00
0.00
0.00
1.31
1.75
2.19
0.43
0.87
1.31
1.75
2.19

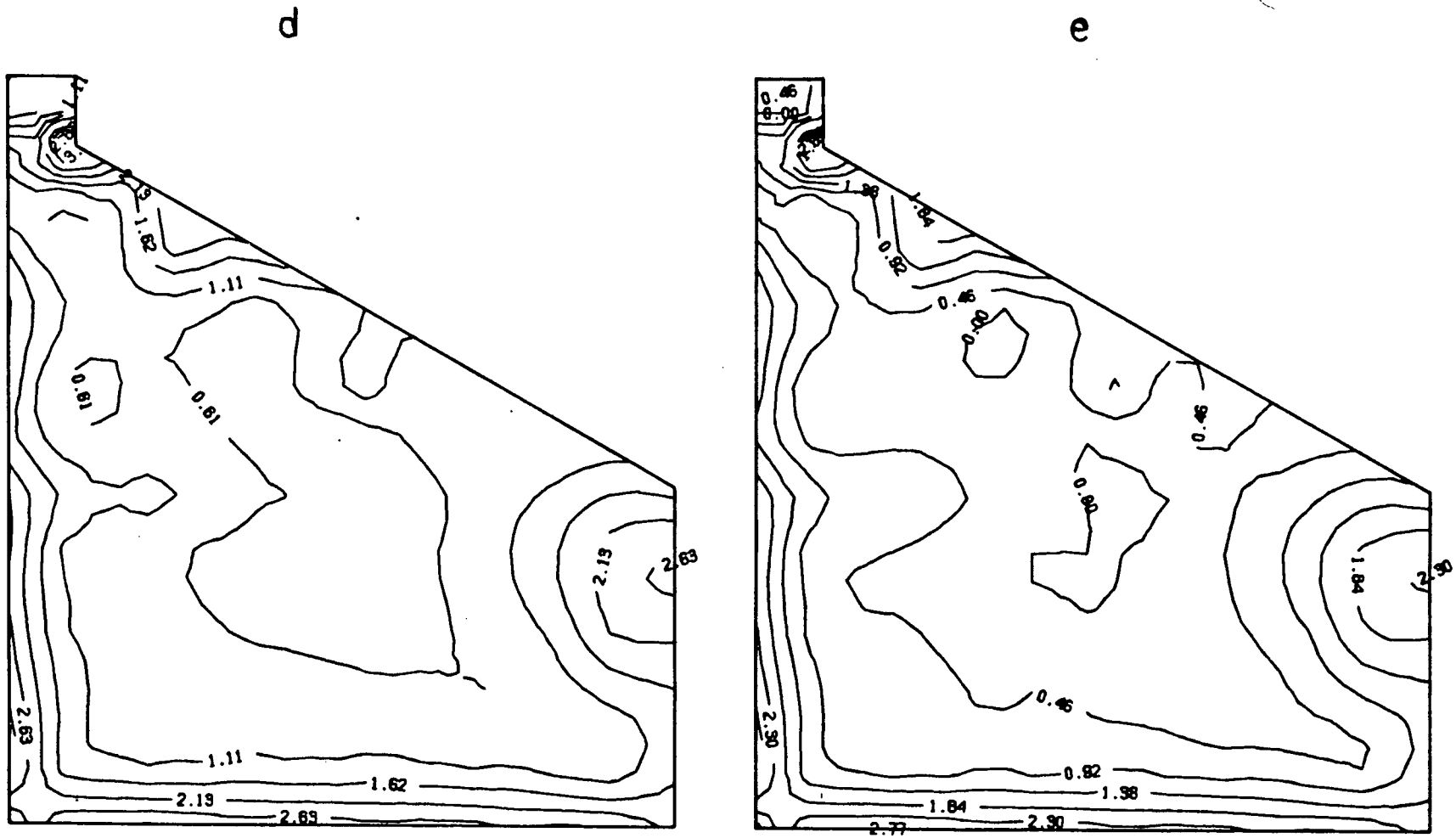

XIII.2.1.1 (a) Temperature and Von Mises Stress
(b) MRSS ; (c) MRSS-CRSS (Yield) ;
(d) MRSS-CRSS (MB) ; (e) MRSS-CRSS (MBTe) .

a

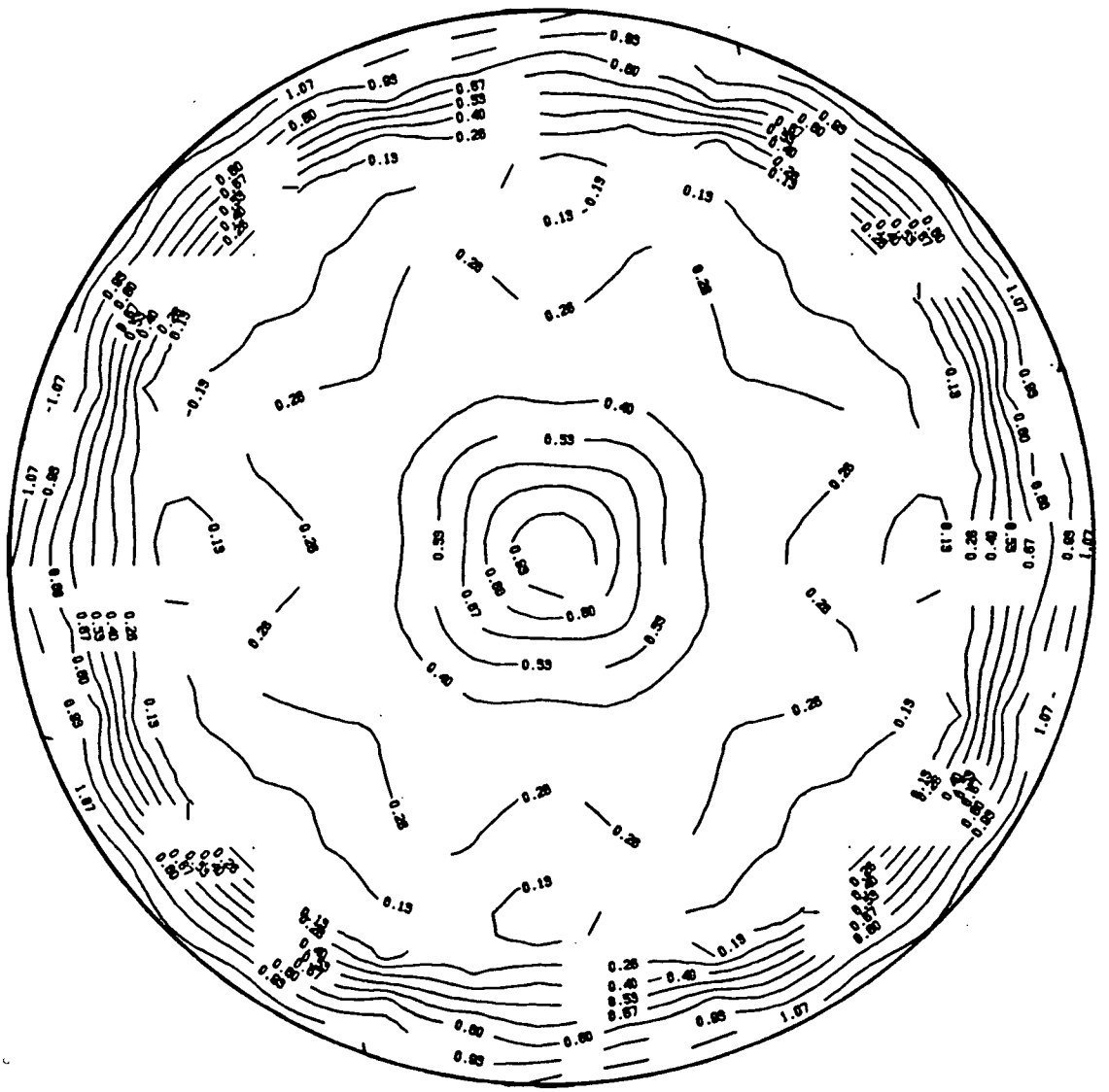

b

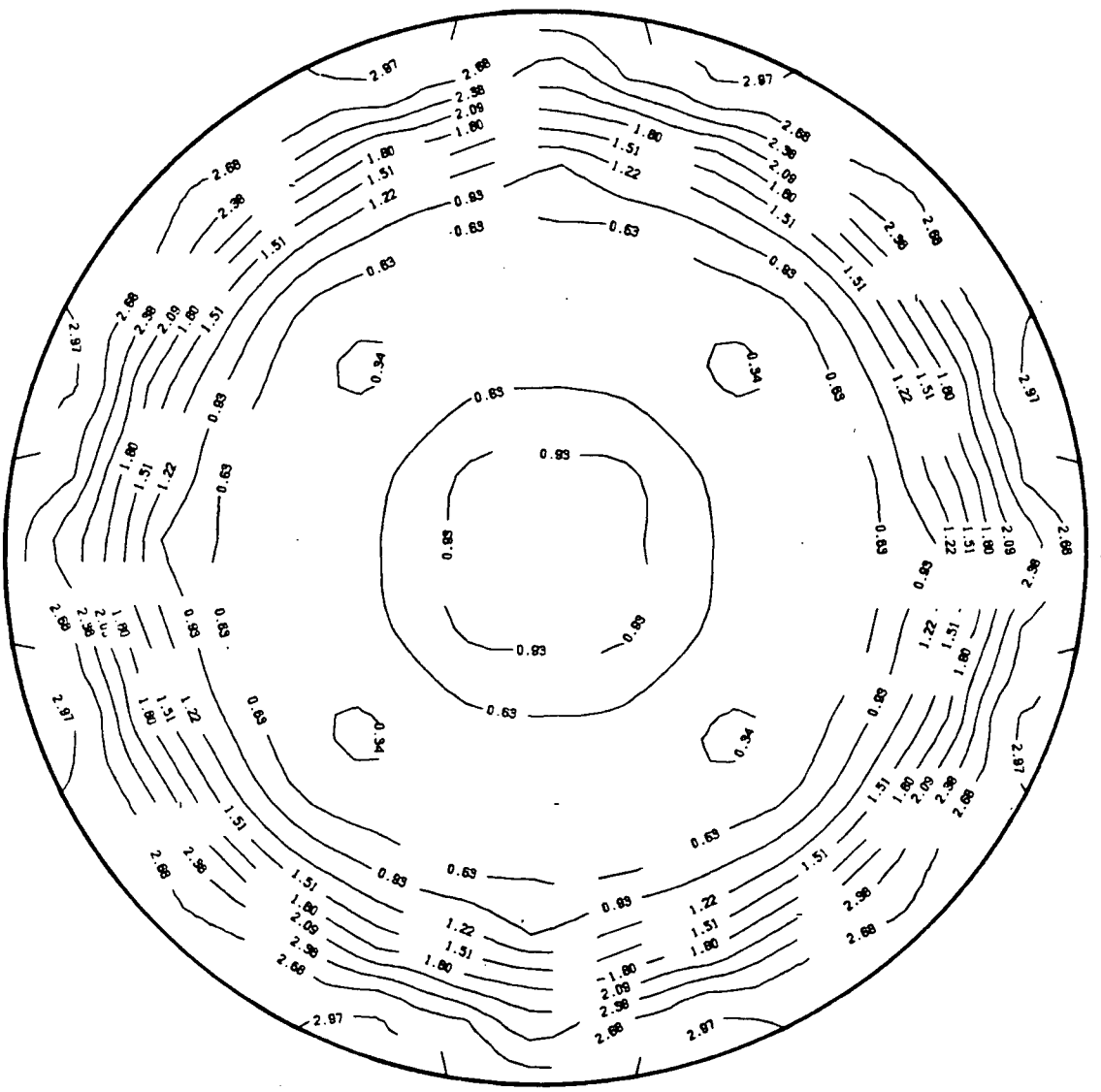

C

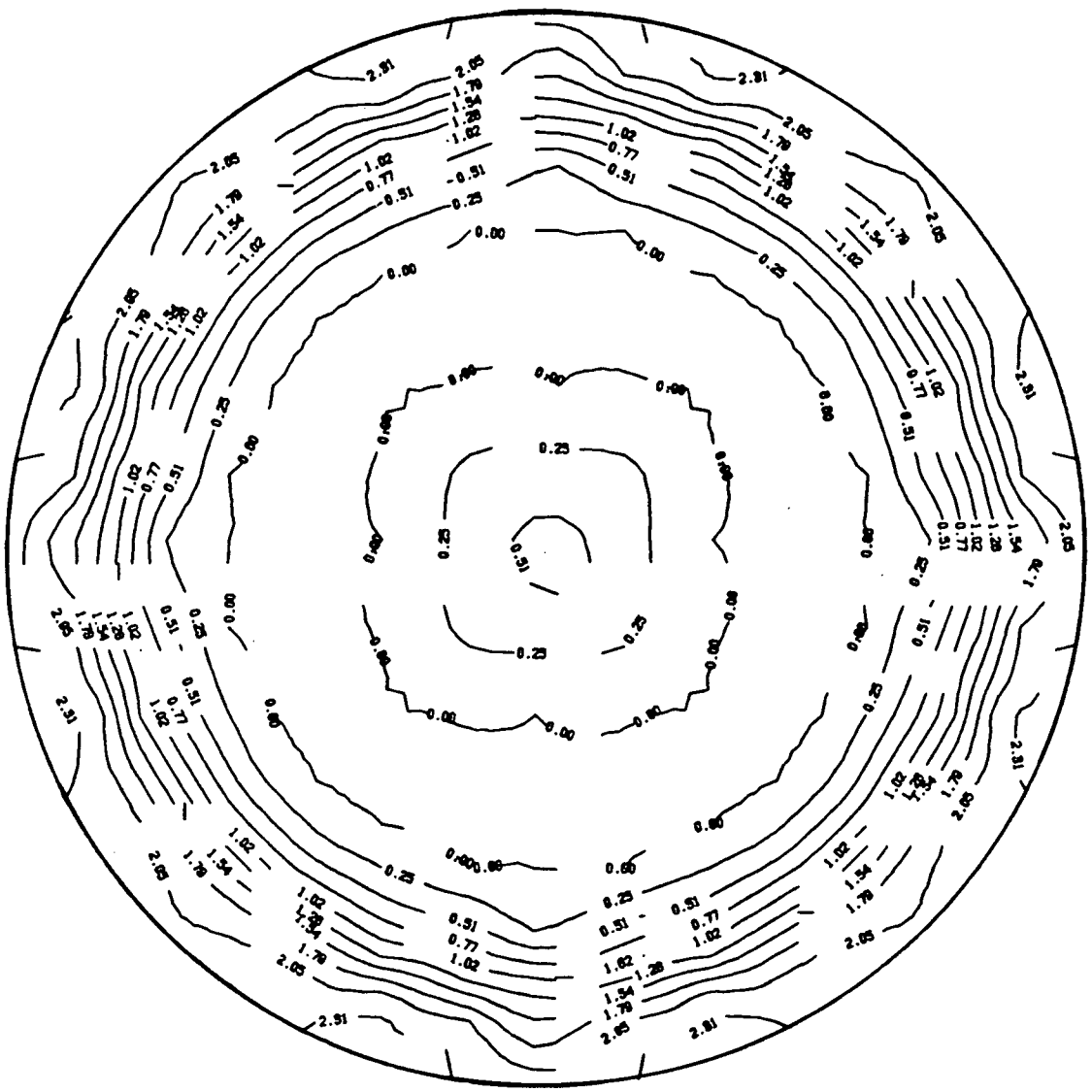

XIII.2.1.2 Cross-sections
(a) MRSS-CRSS (Yield) at 5.5 from the interface ;
(b) MRSS at 11.0 mm from the interface ;
(c) MRSS-CRSS (Yield) at 11.0 mm from the interface.

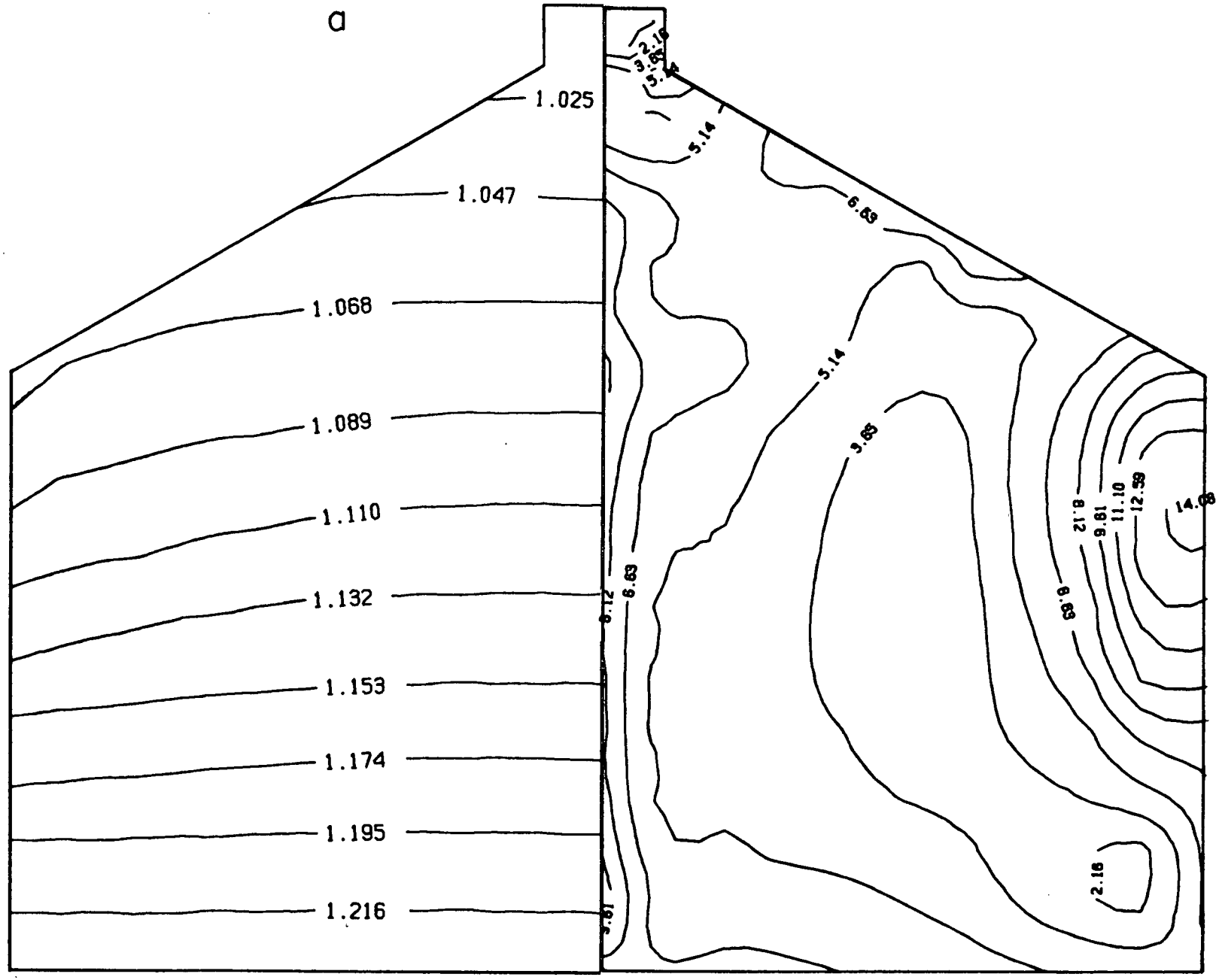
a
1.025
1.047
1.068
1.089
1.110
1.132
1.153
1.174
1.195
1.216
2.16
3.65
5.14
6.63
8.12
9.61
11.10
12.59
14.08

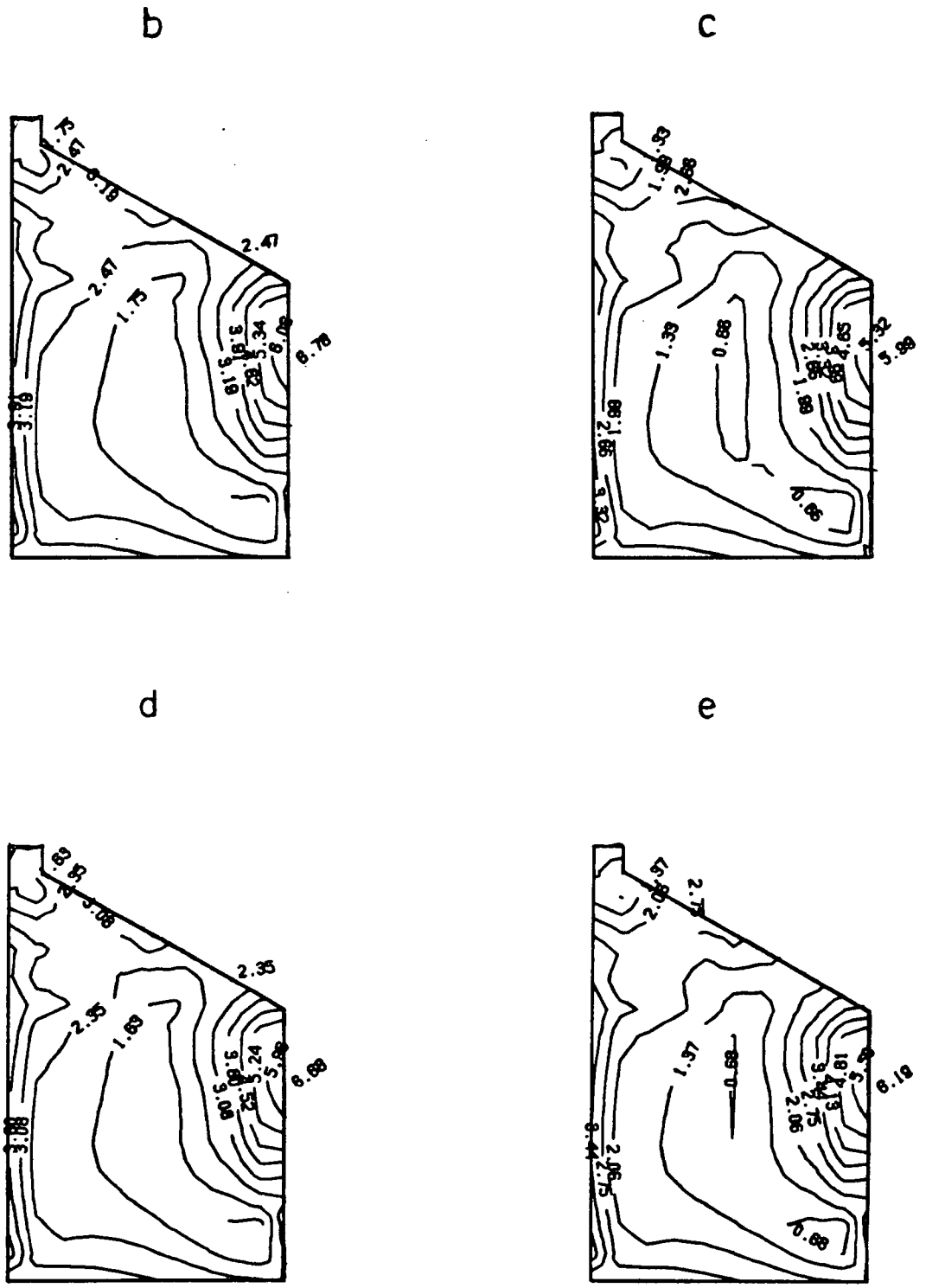

XIII.2.2.1 (a) Temperature and Von Mises Stress
(b) MRSS ; (c) MRSS-CRSS (Yield) ;
(d) MRSS-CRSS (MB) ; (e) MRSS-CRSS (MBTe) .

a

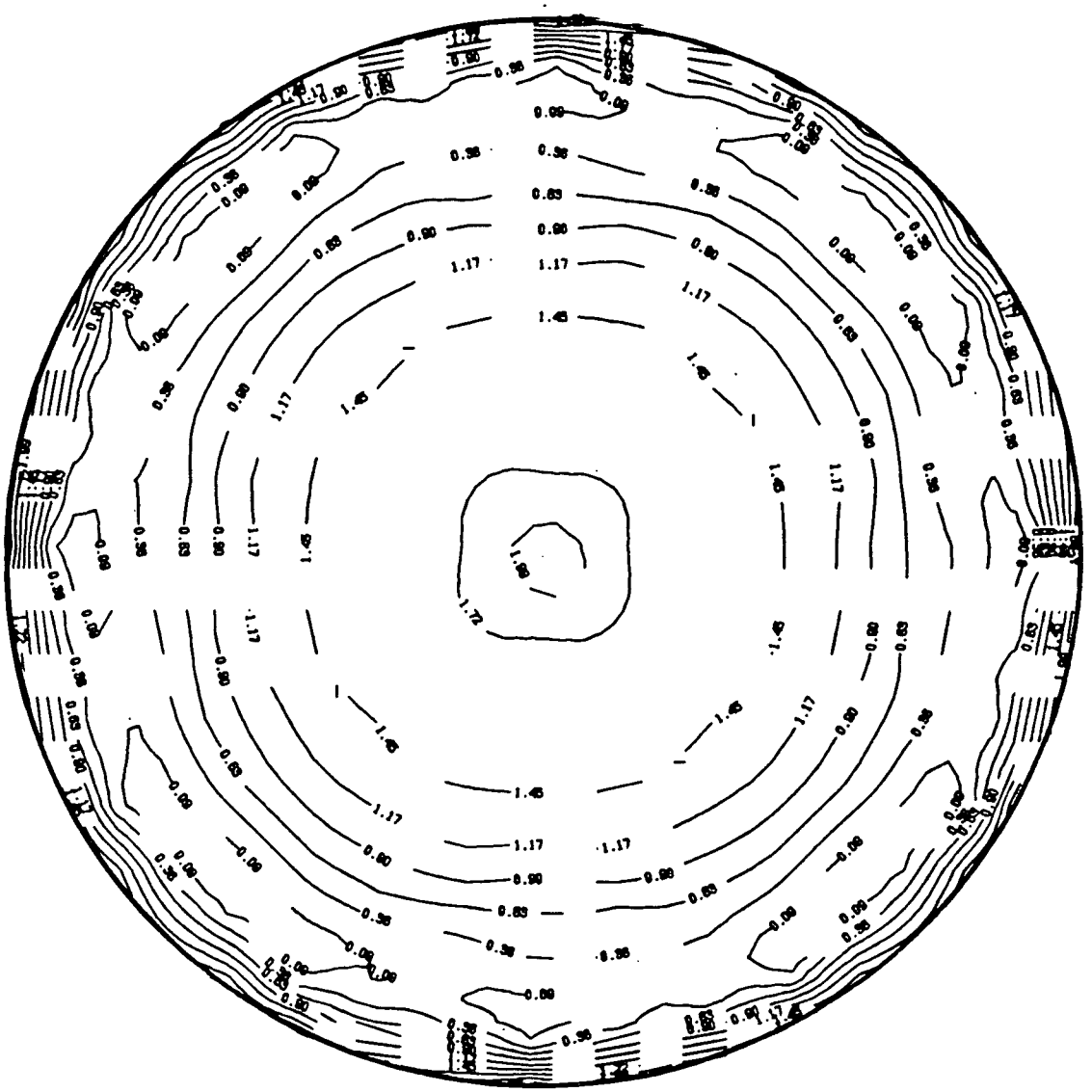

b

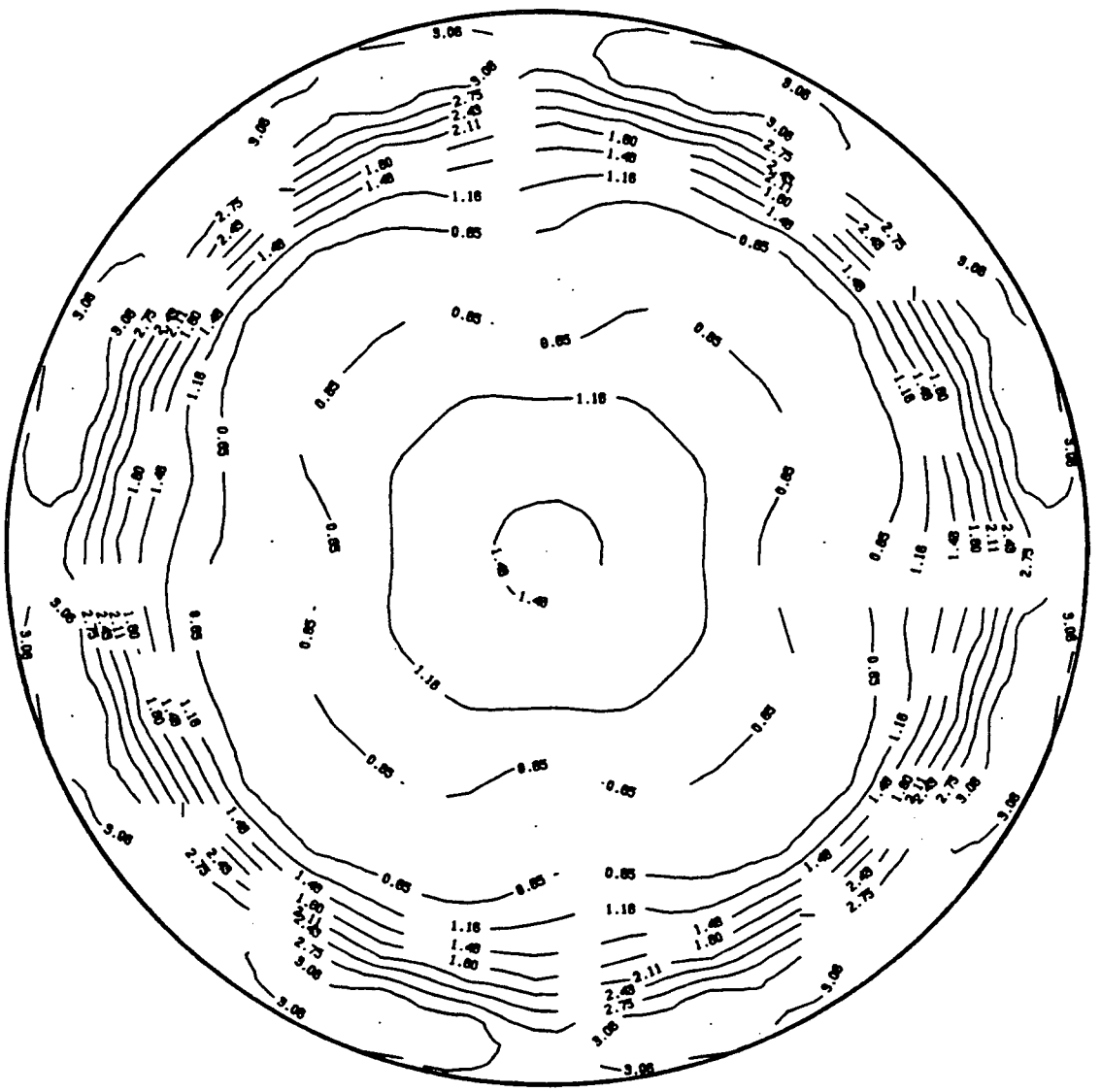

C

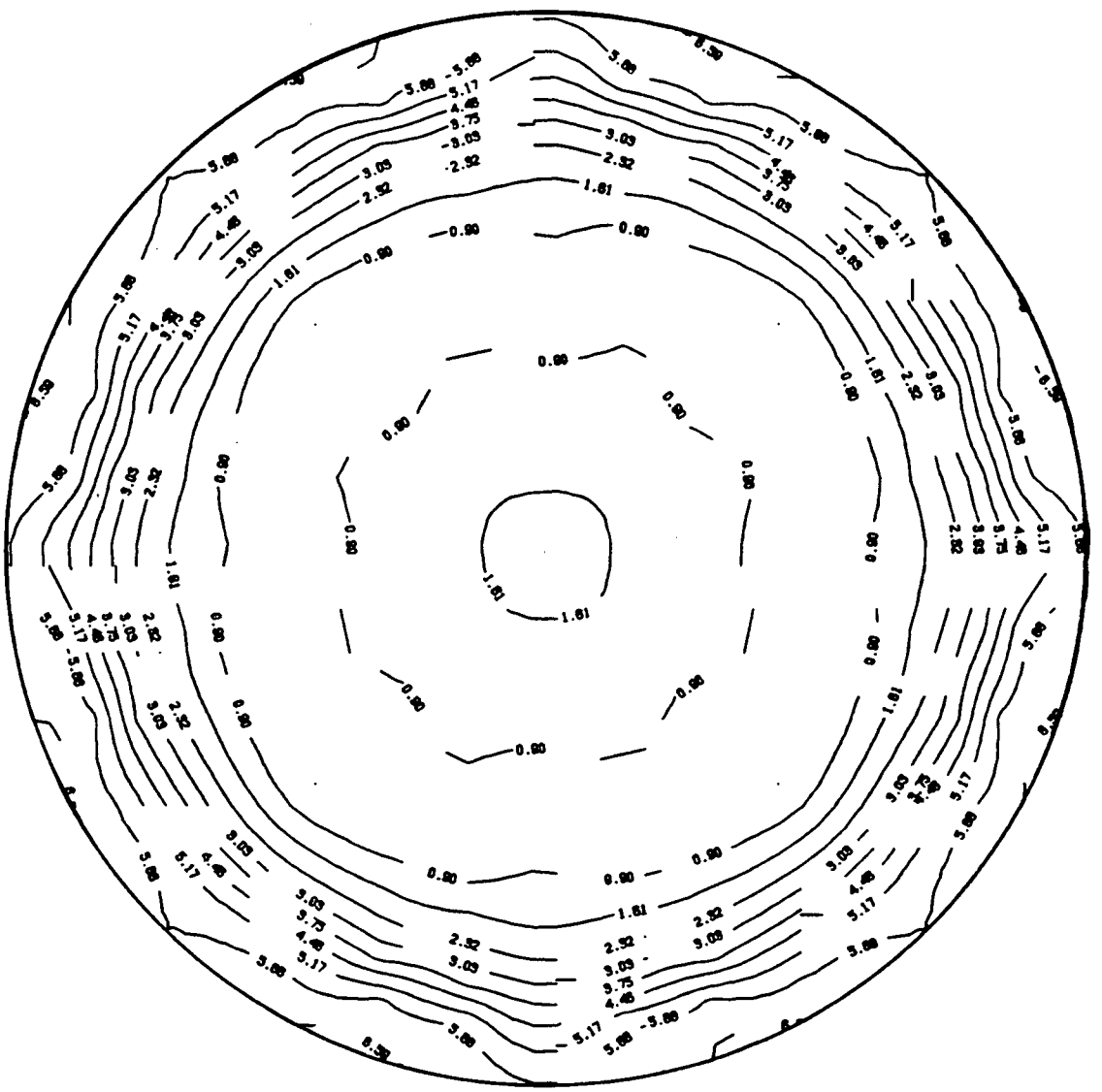

d

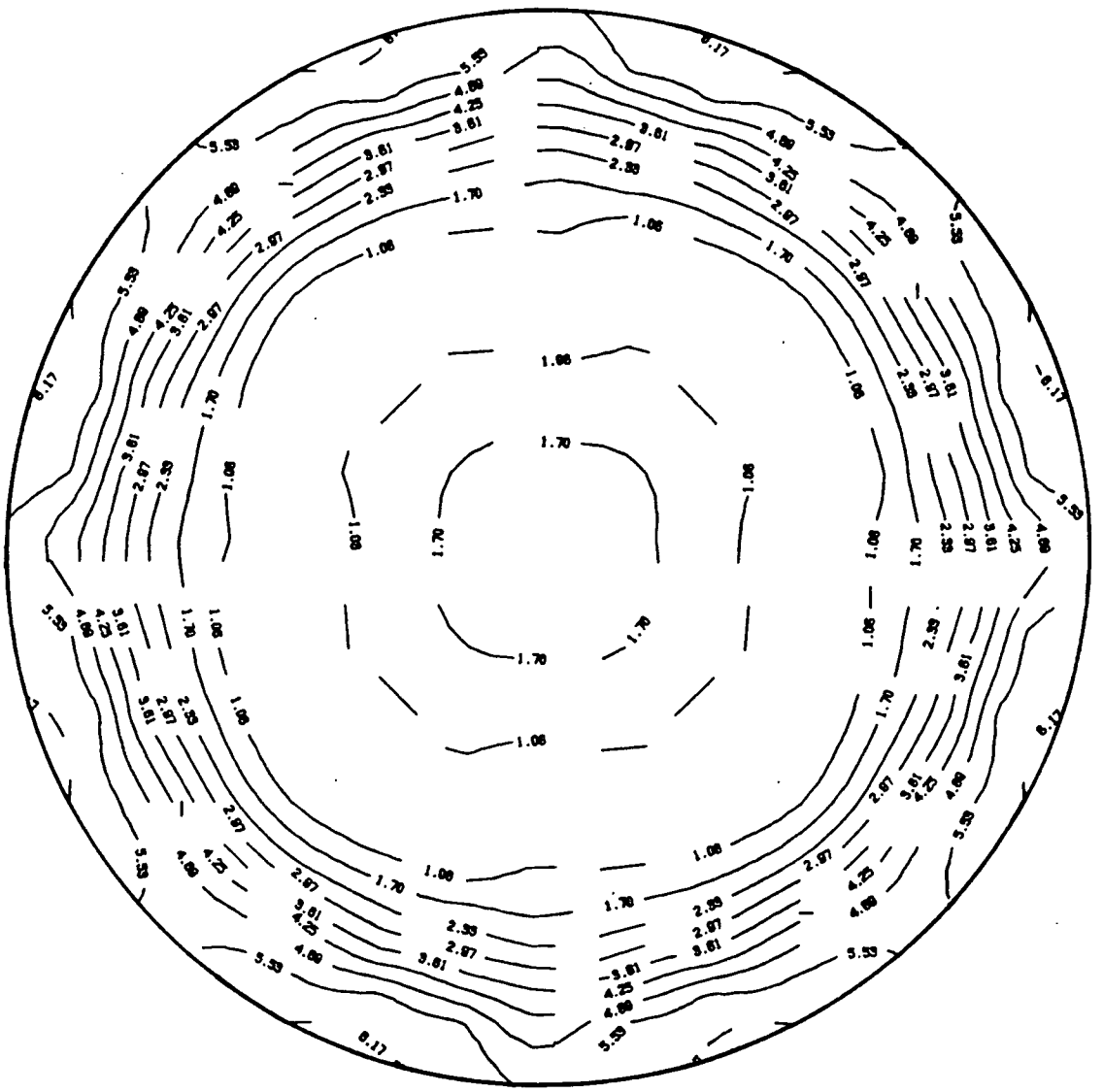

e

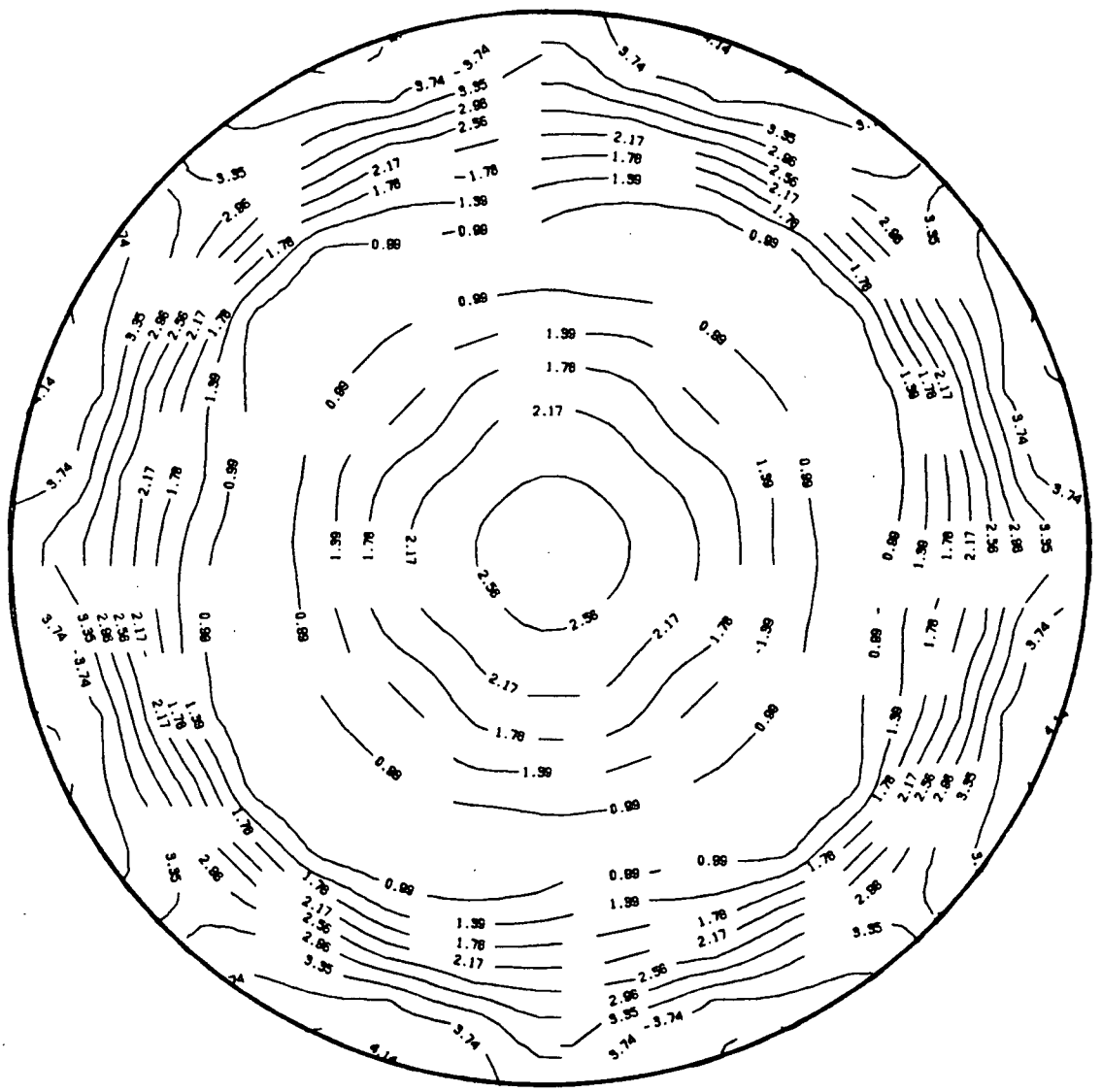

XIII.2.2.2 MRSS-CRSS (Yield) in cross-sections at a distance of the interface of :
(a) 5.5 mm ; (b) 11.0 mm ; (c) 19.25 mm ;
(d) 24.75 mm ; (e) 27.5 mm .

a

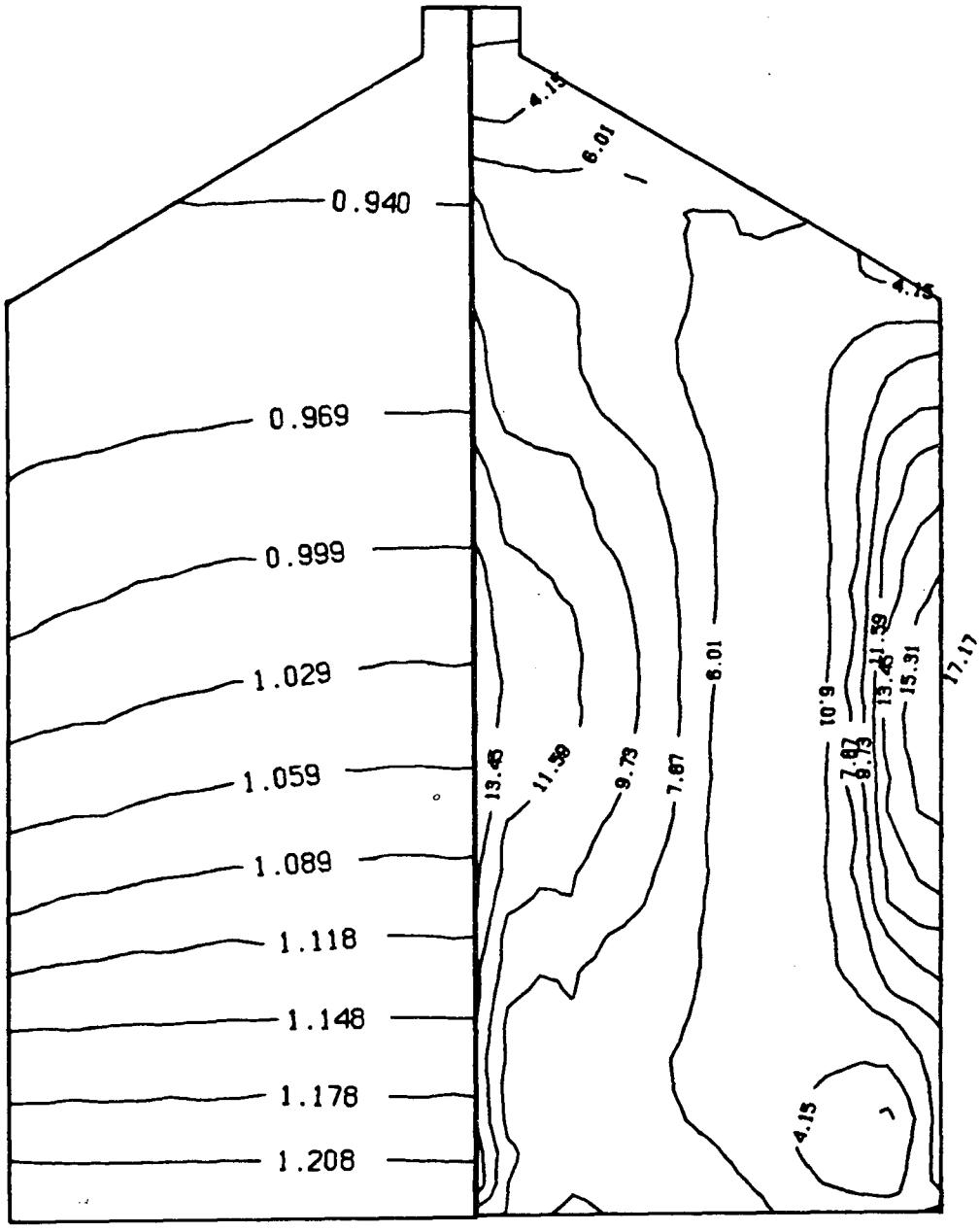
0.940
0.969
0.999
1.029
1.059
1.089
1.118
1.148
1.178
1.208
4.15
6.01
13.45
11.59
9.73
7.87
6.01
10.9
15.31
17.17
4.15

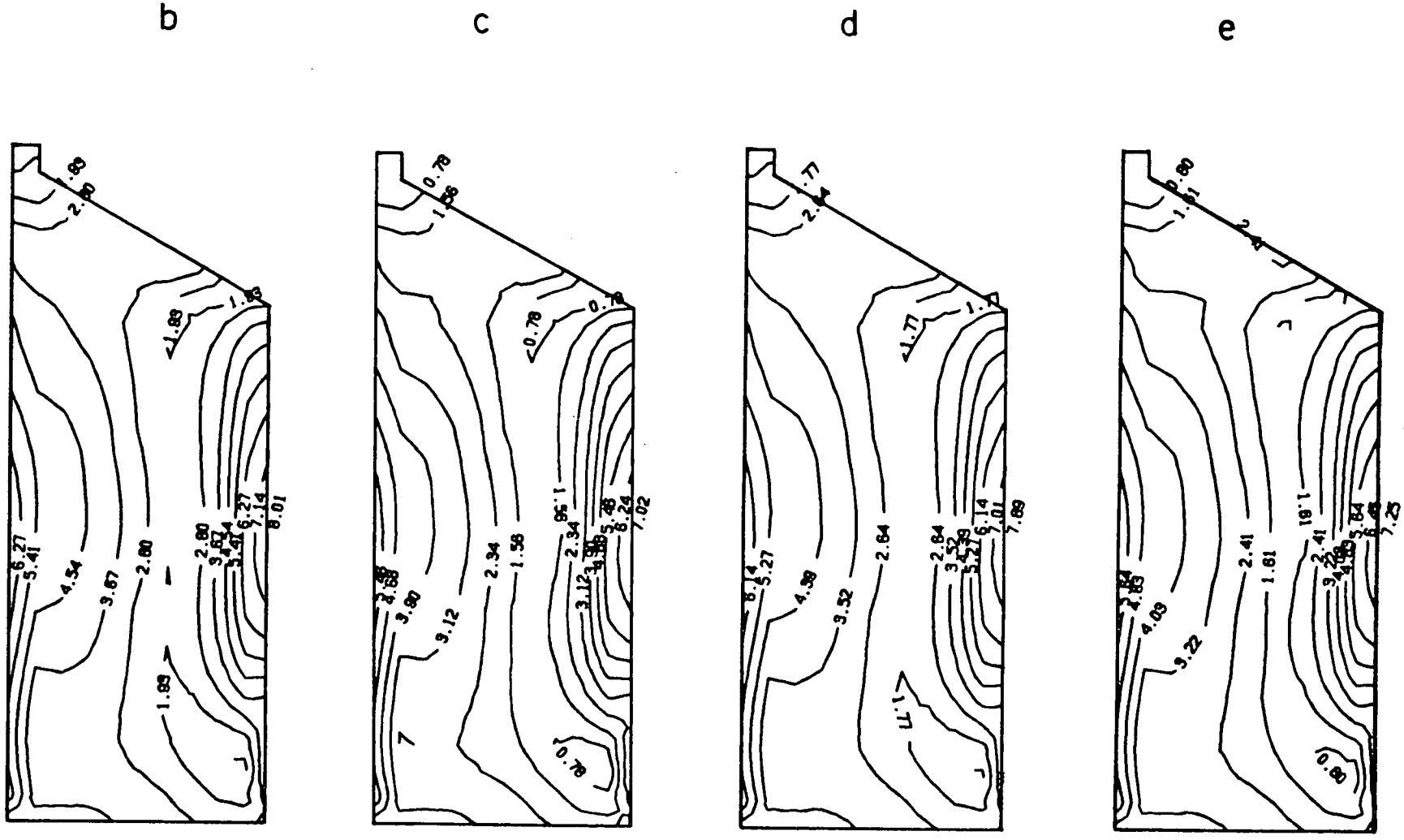

XIII.2.3.1 (a) Temperature and Von Mises Stress
(b) MRSS ; (c) MRSS-CRSS (Yield) ;
(d) MRSS-CRSS (MB) ; (e) MRSS-CRSS (MBTe) .

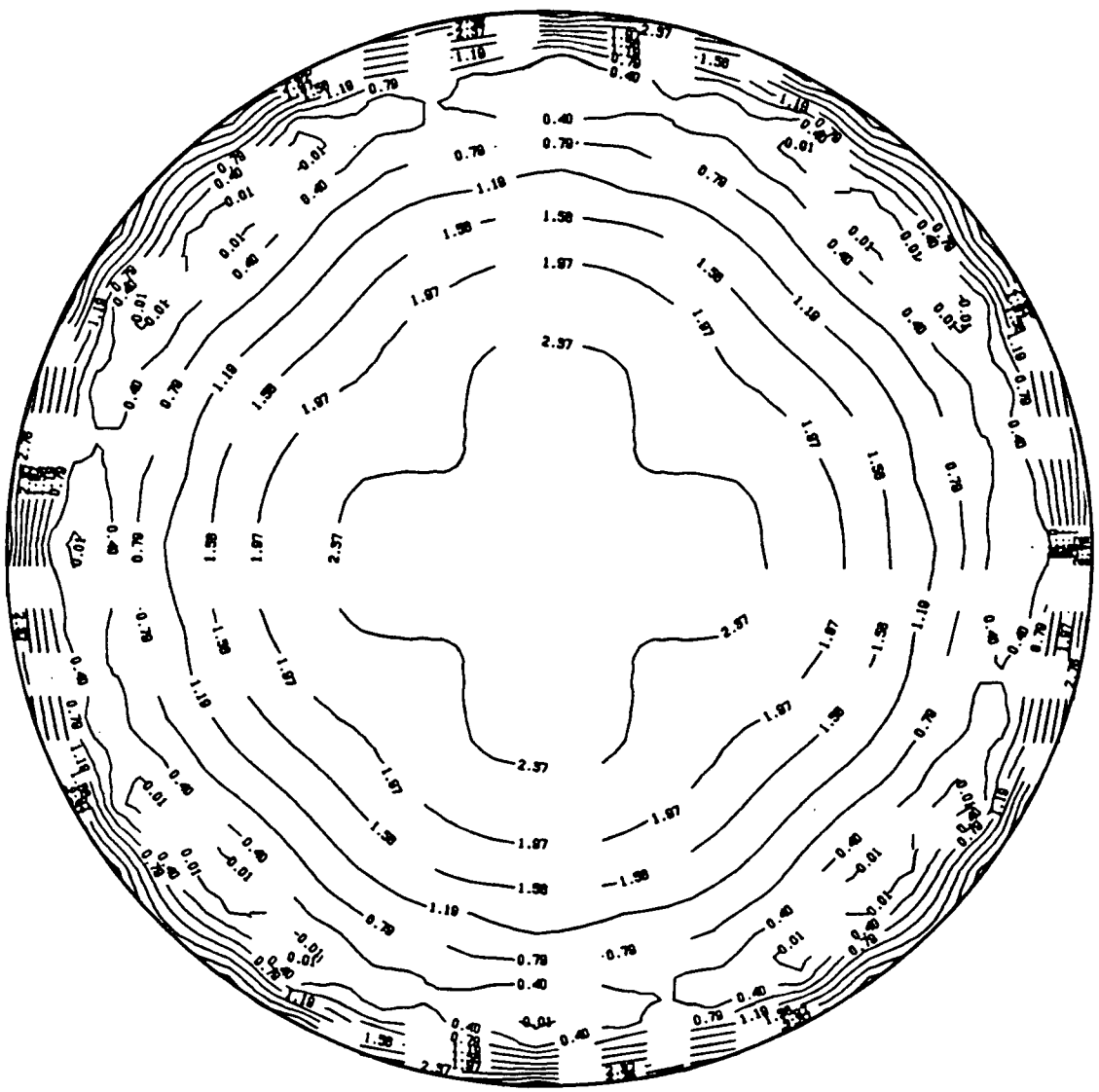

XIII.2.3.2 MRSS-CRSS (Yield) at 5.5 mm from the interface.

a

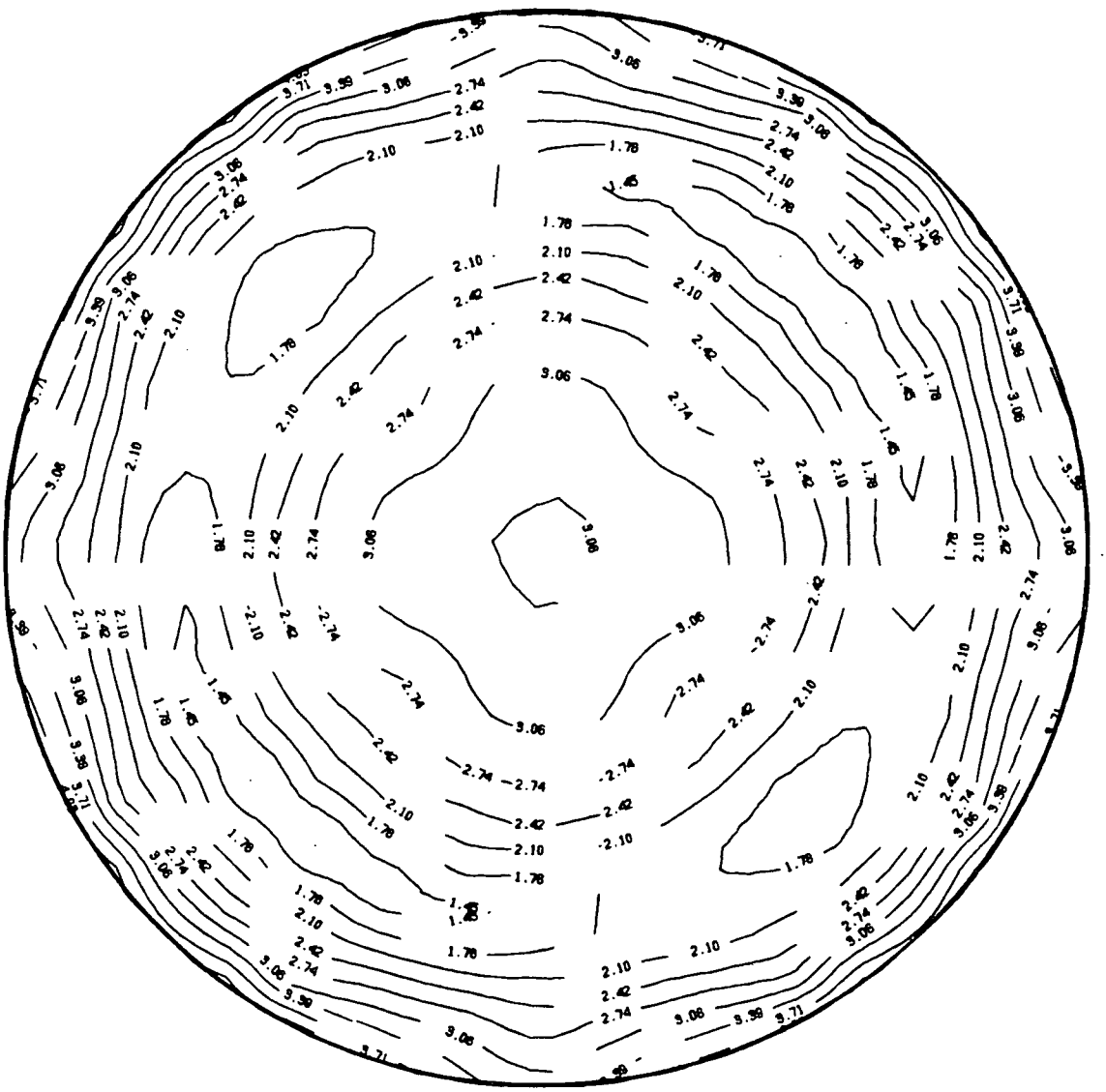

b

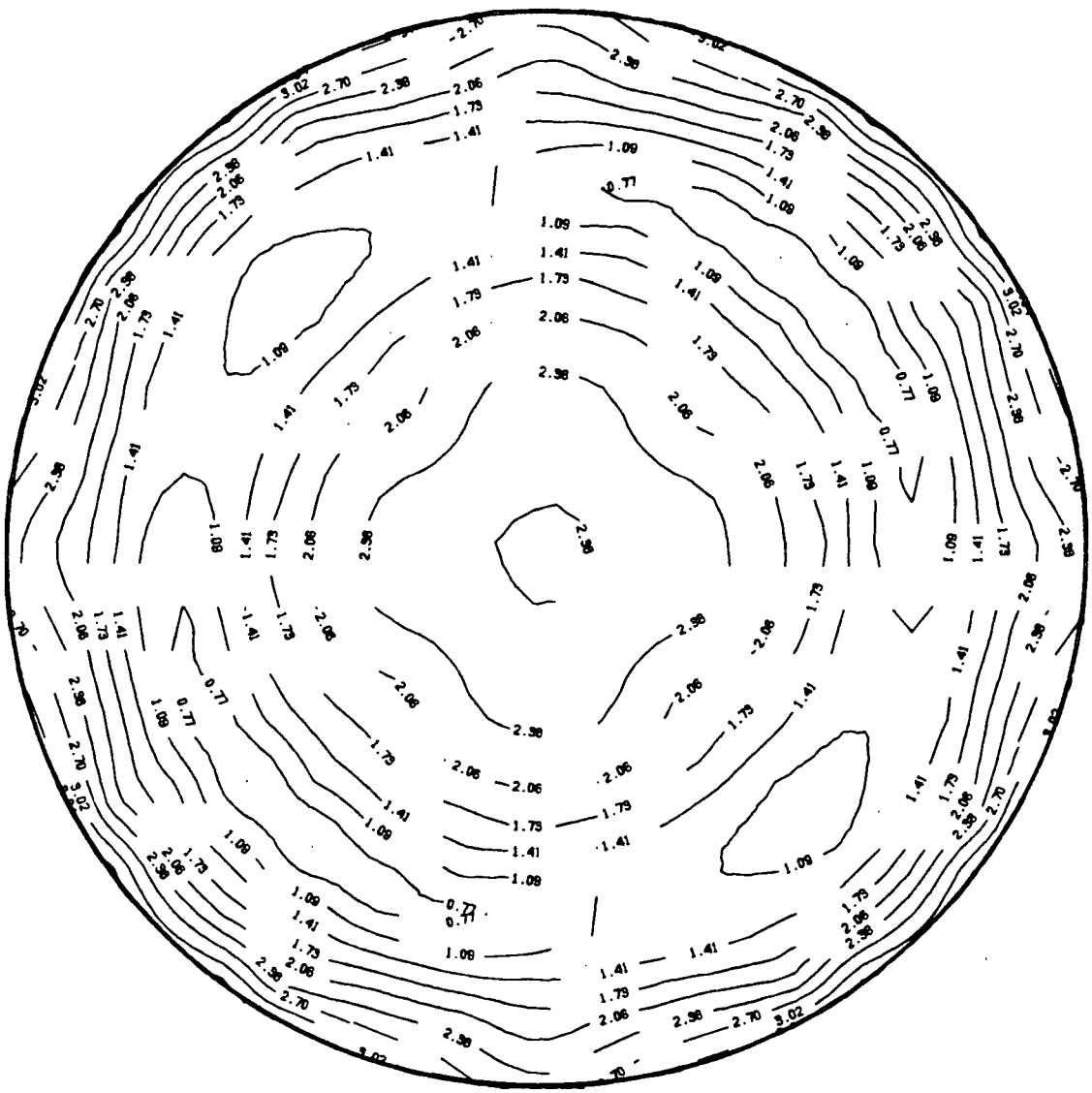

C

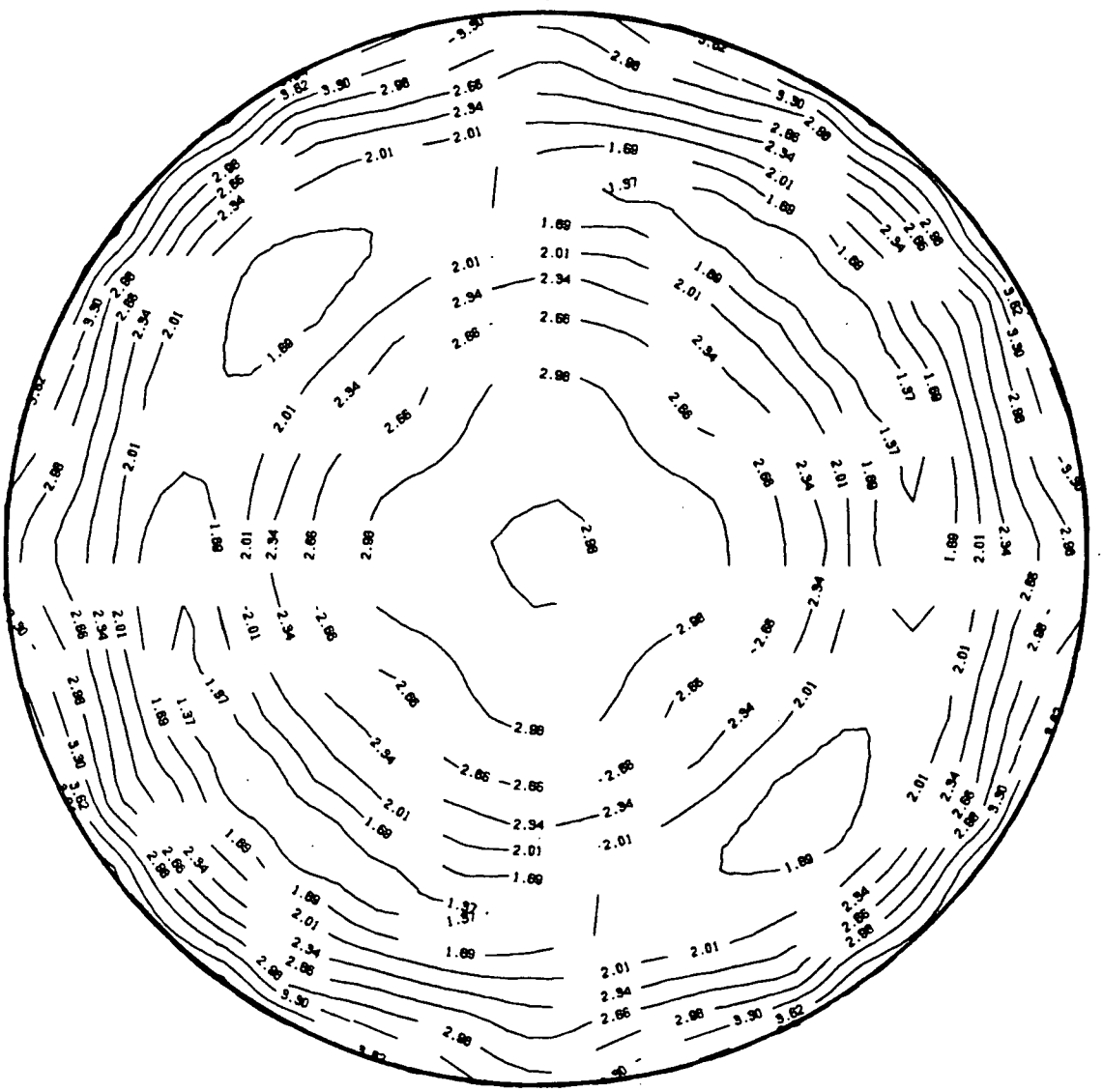

d

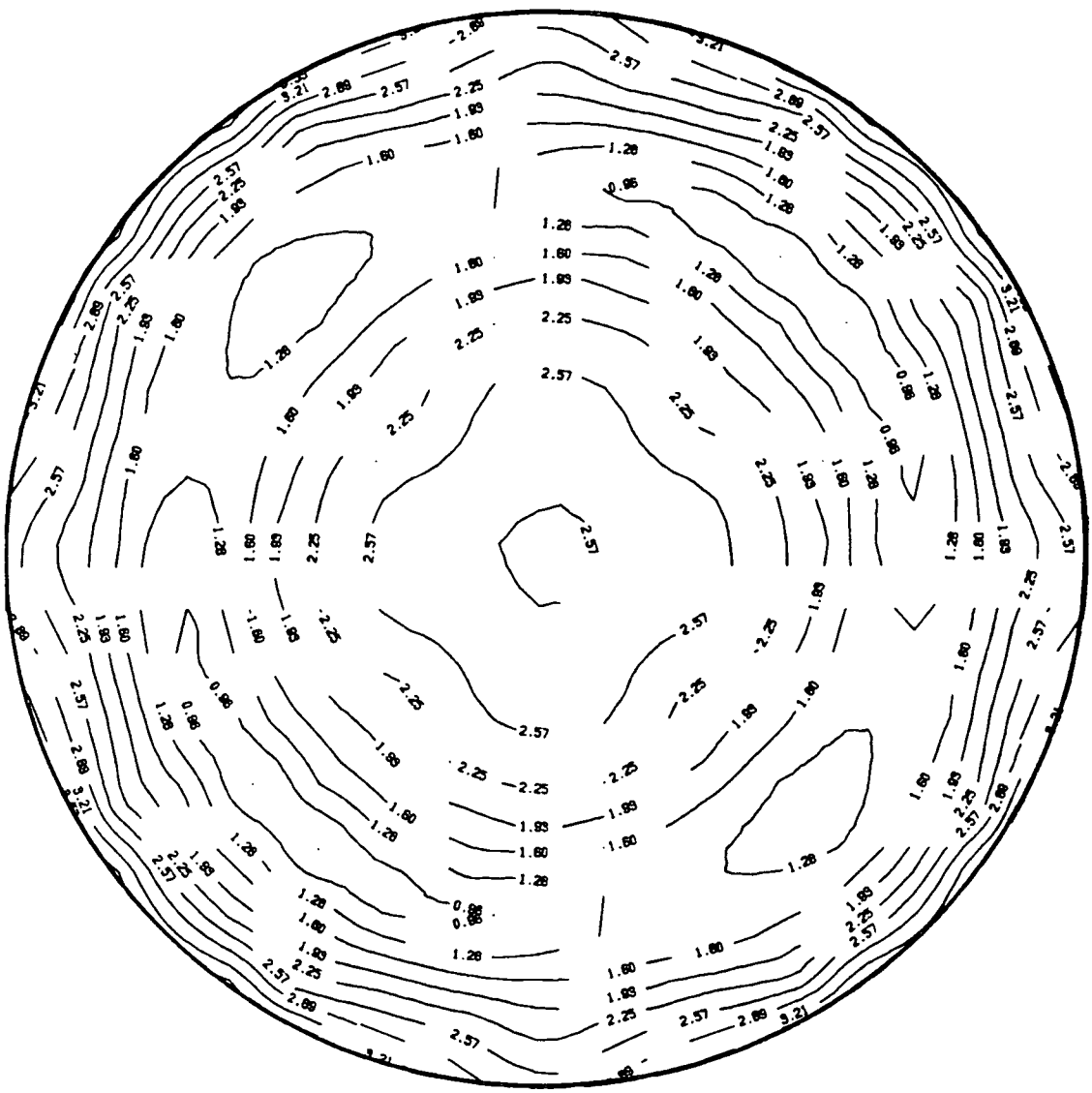

XIII.2.3.3 Cross-section at 11.0 mm from the interface
(a) MRSS ; (B) MRSS-CRSS (Yield) ;
(c) MRSS-CRSS (MB) ; (d) MRSS-CRSS (MBTe).

a

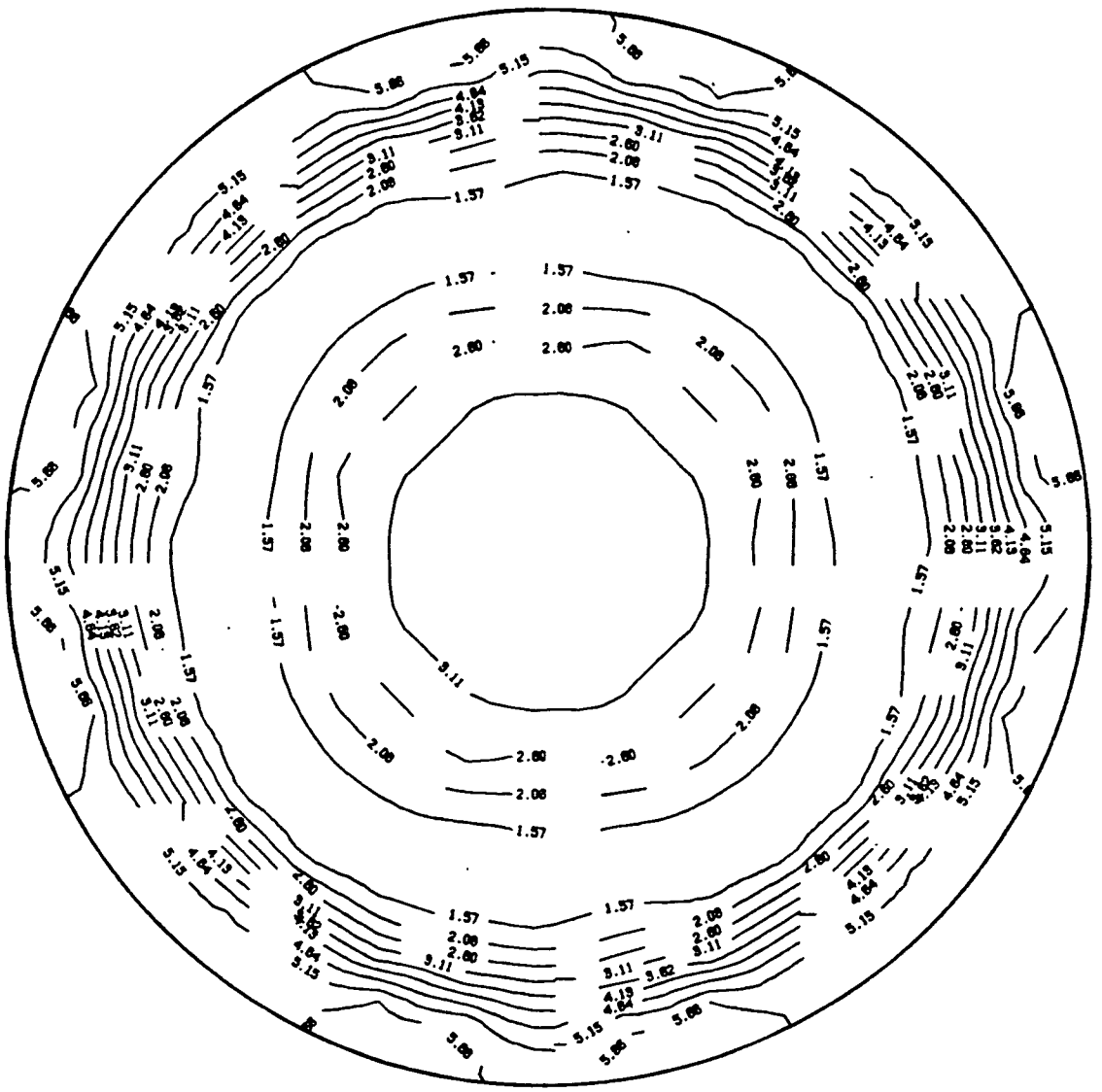

b

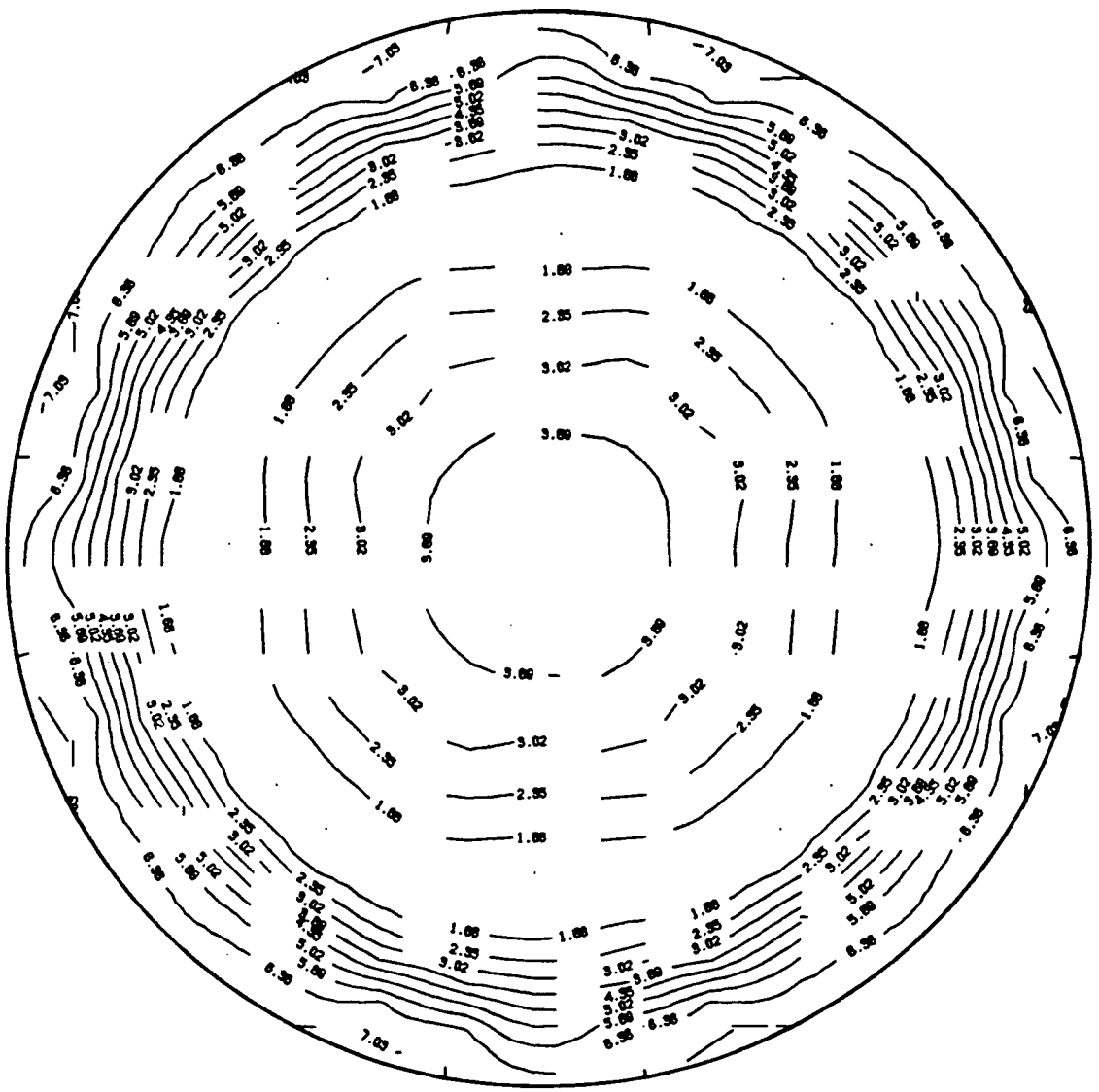

XIII.2.3.4 MRSS-CRSS (Yield) at a distance from the interface of (a) 19.25 mm ; (b) 24.75 mm

a

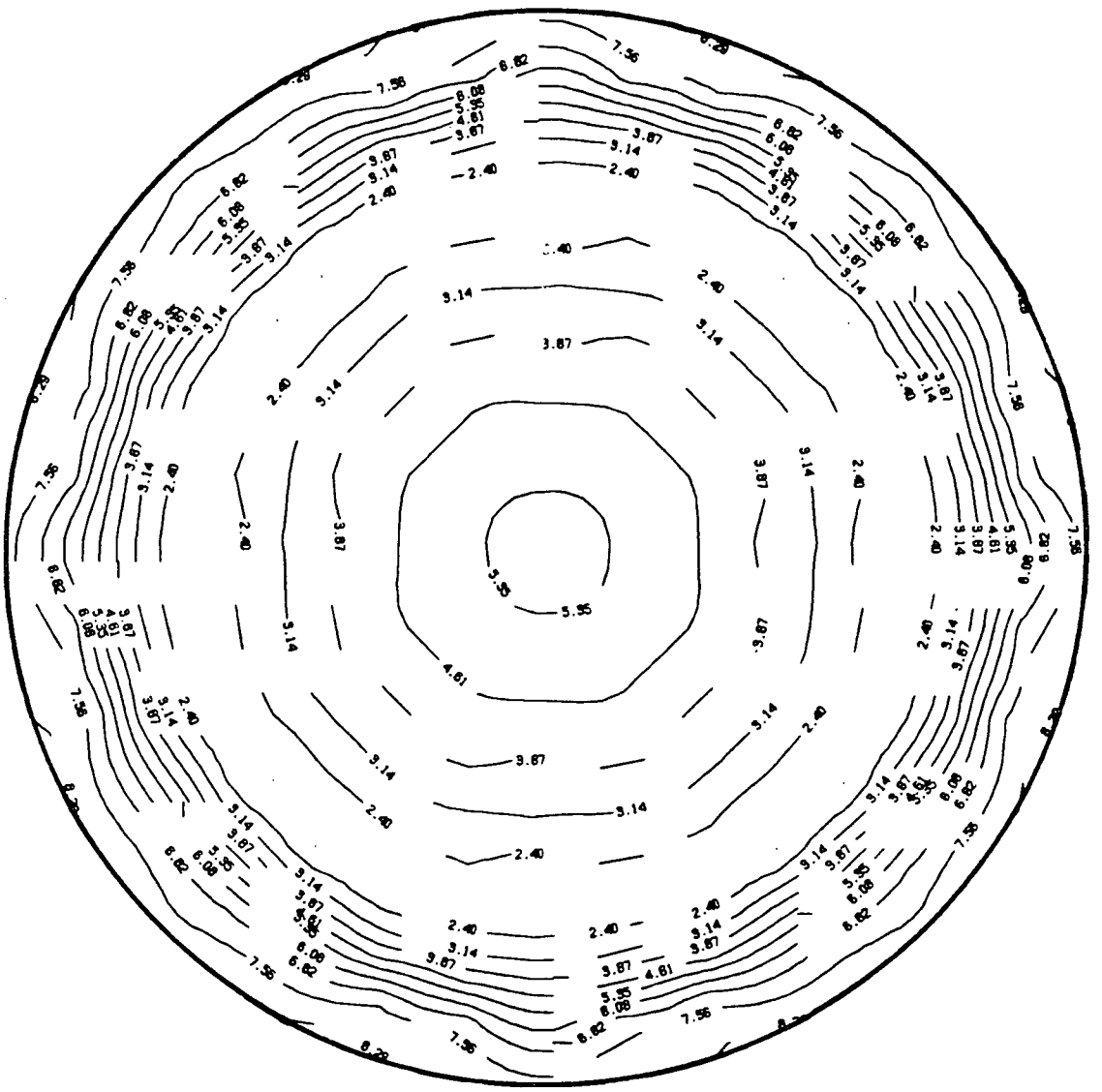

b

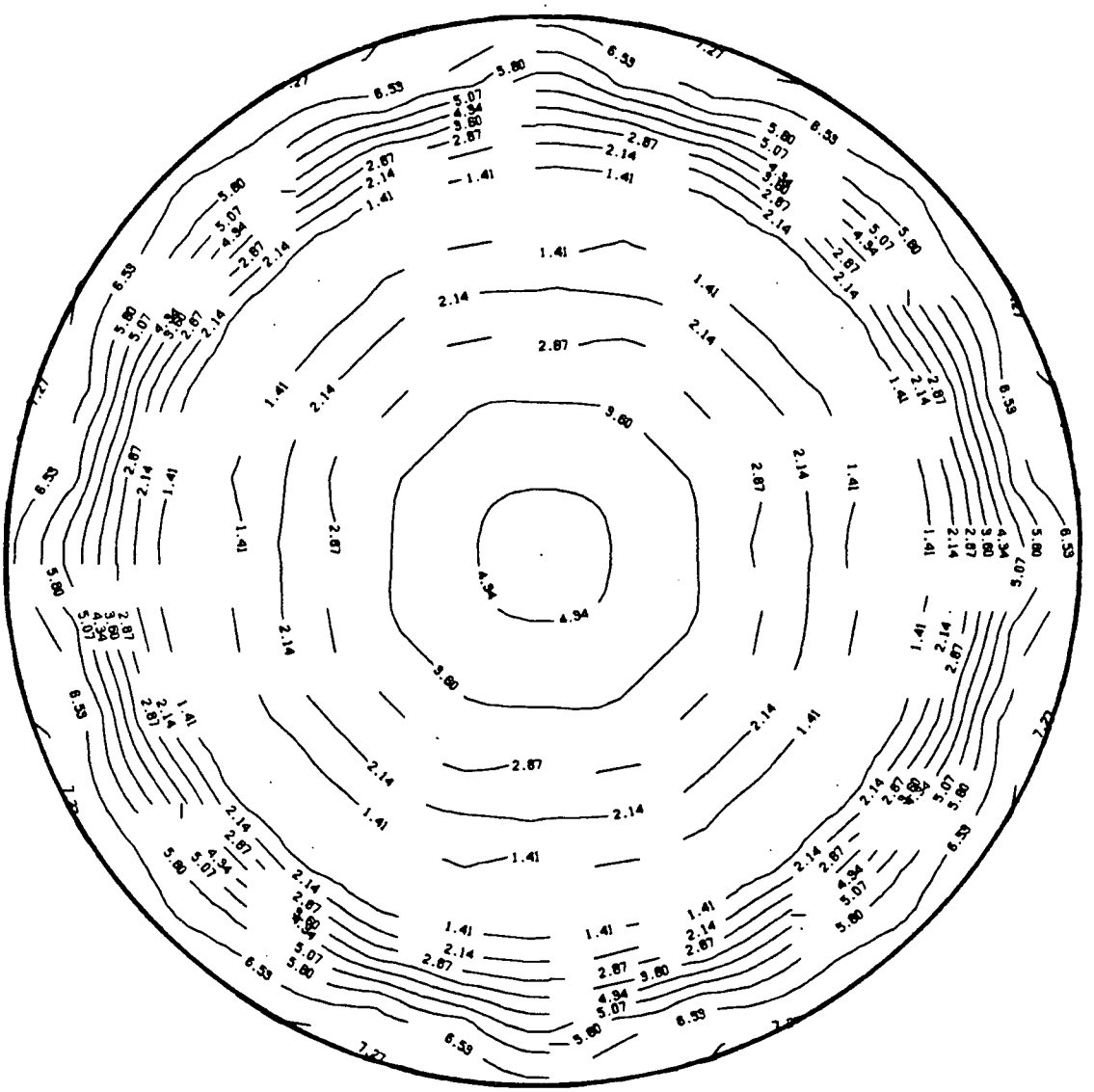

C

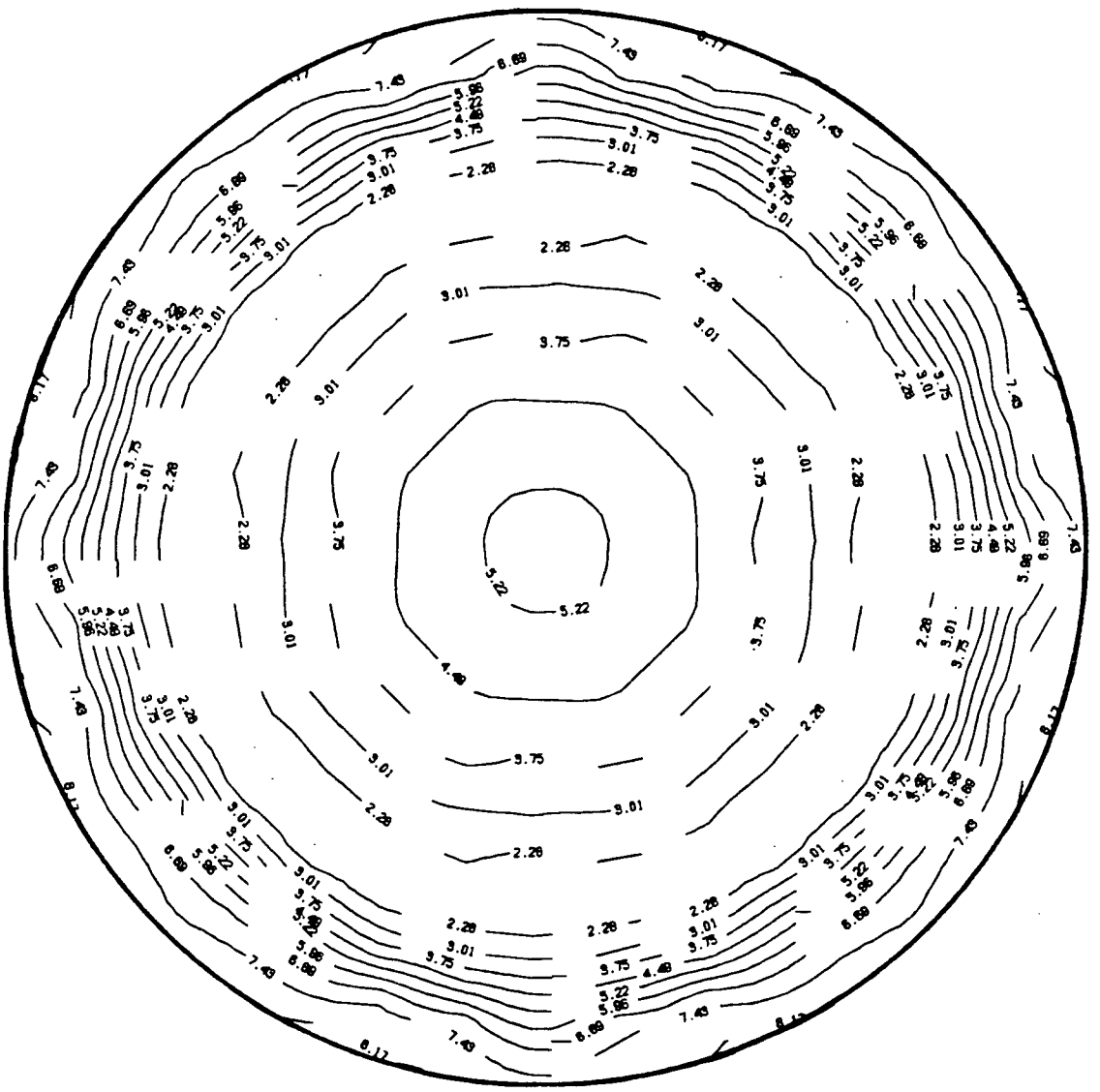

d

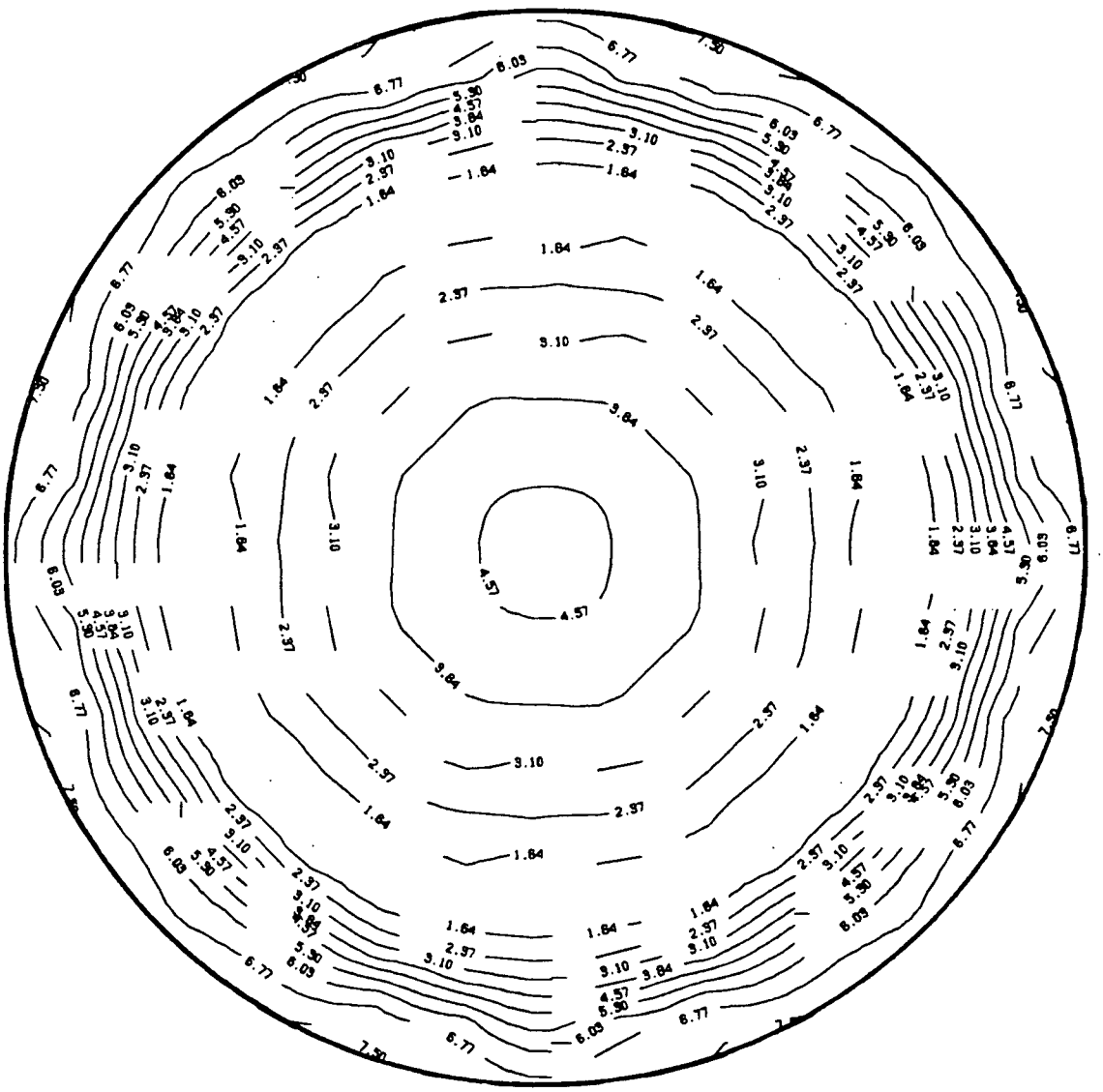

XIII.2.3.5 Cross-section at 33 mm from the interface
(a) MRSS ; (B) MRSS-CRSS (Yield) ;
(c) MRSS-CRSS (MB) ; (d) MRSS-CRSS (MBTe).

a

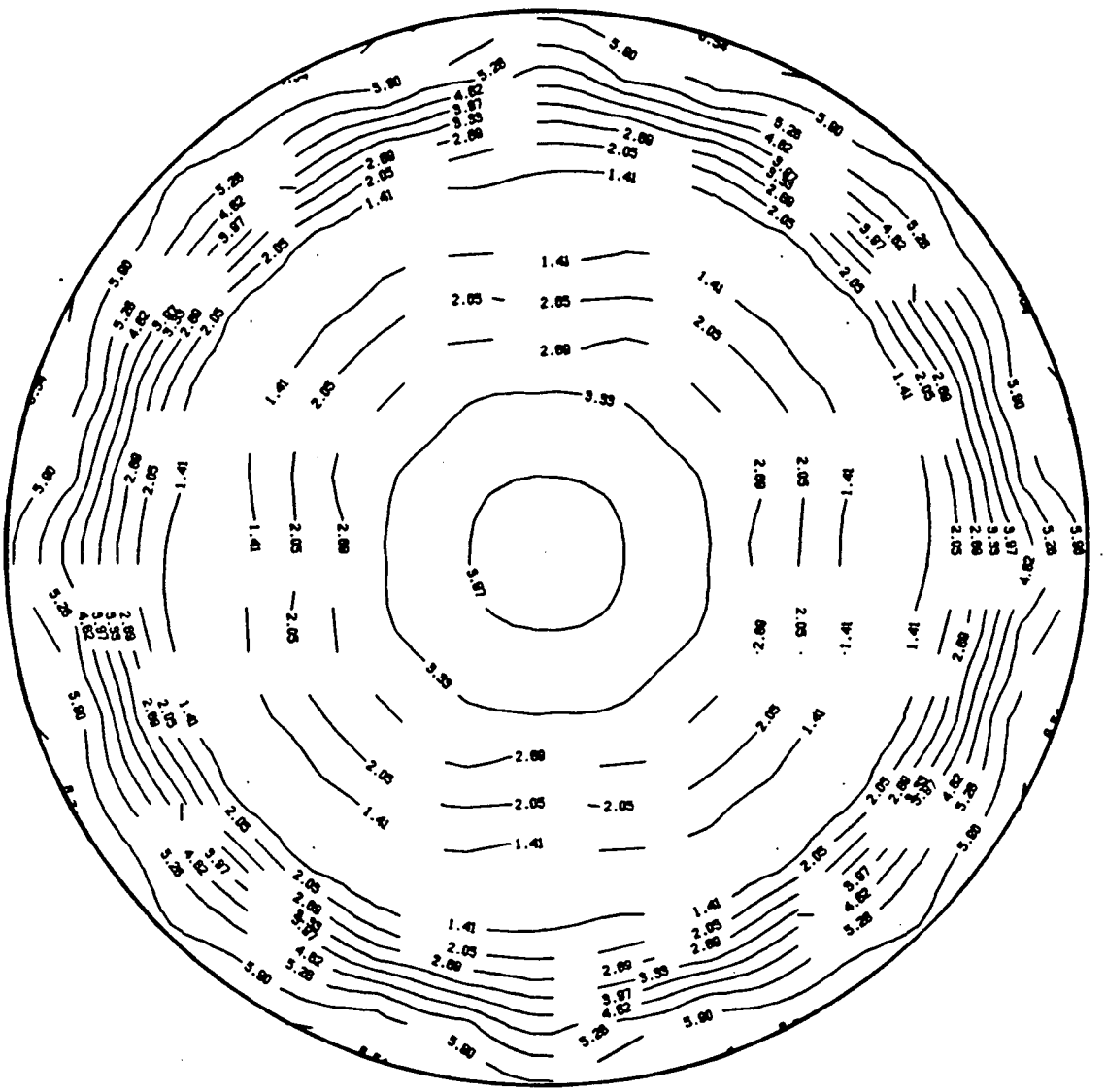

b

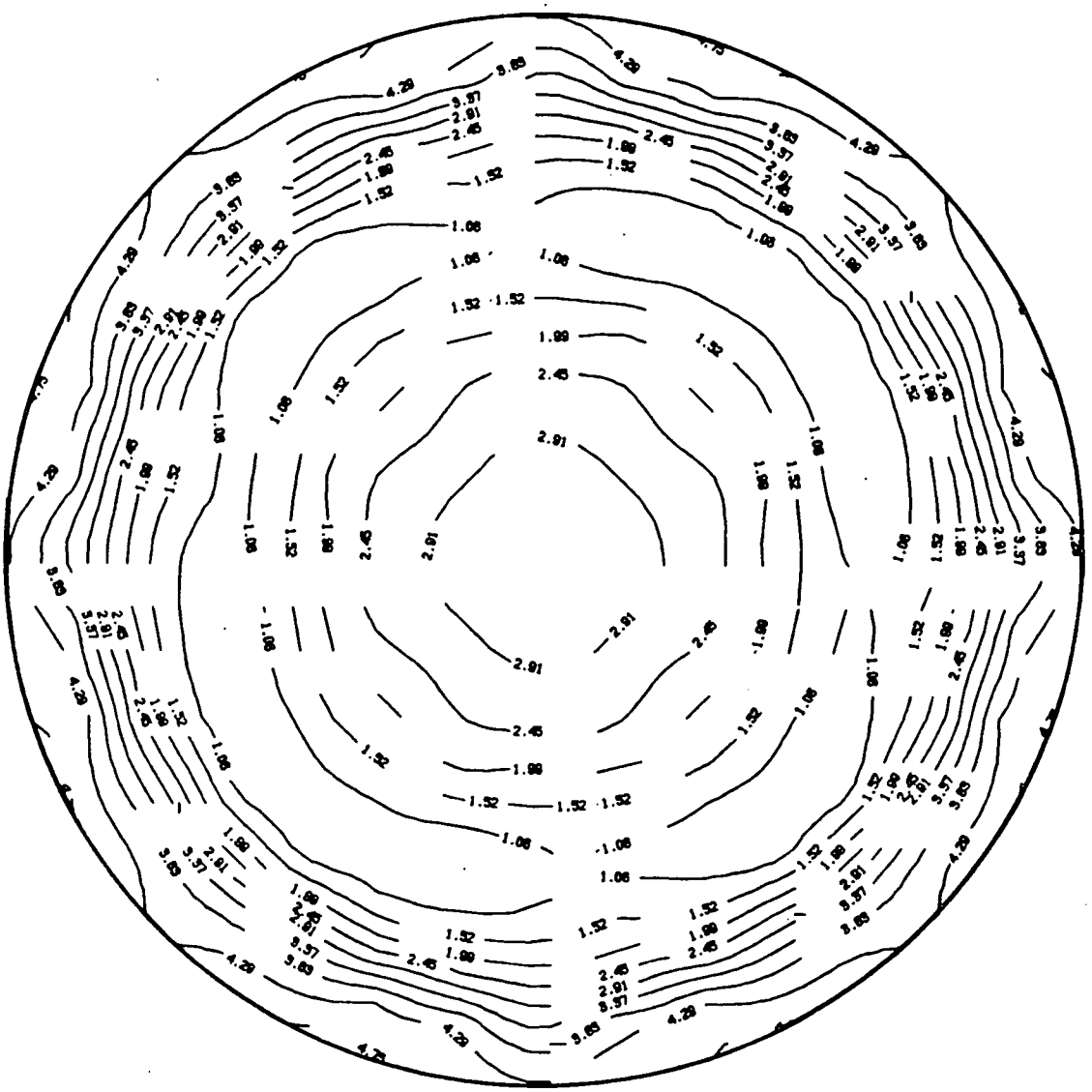

C

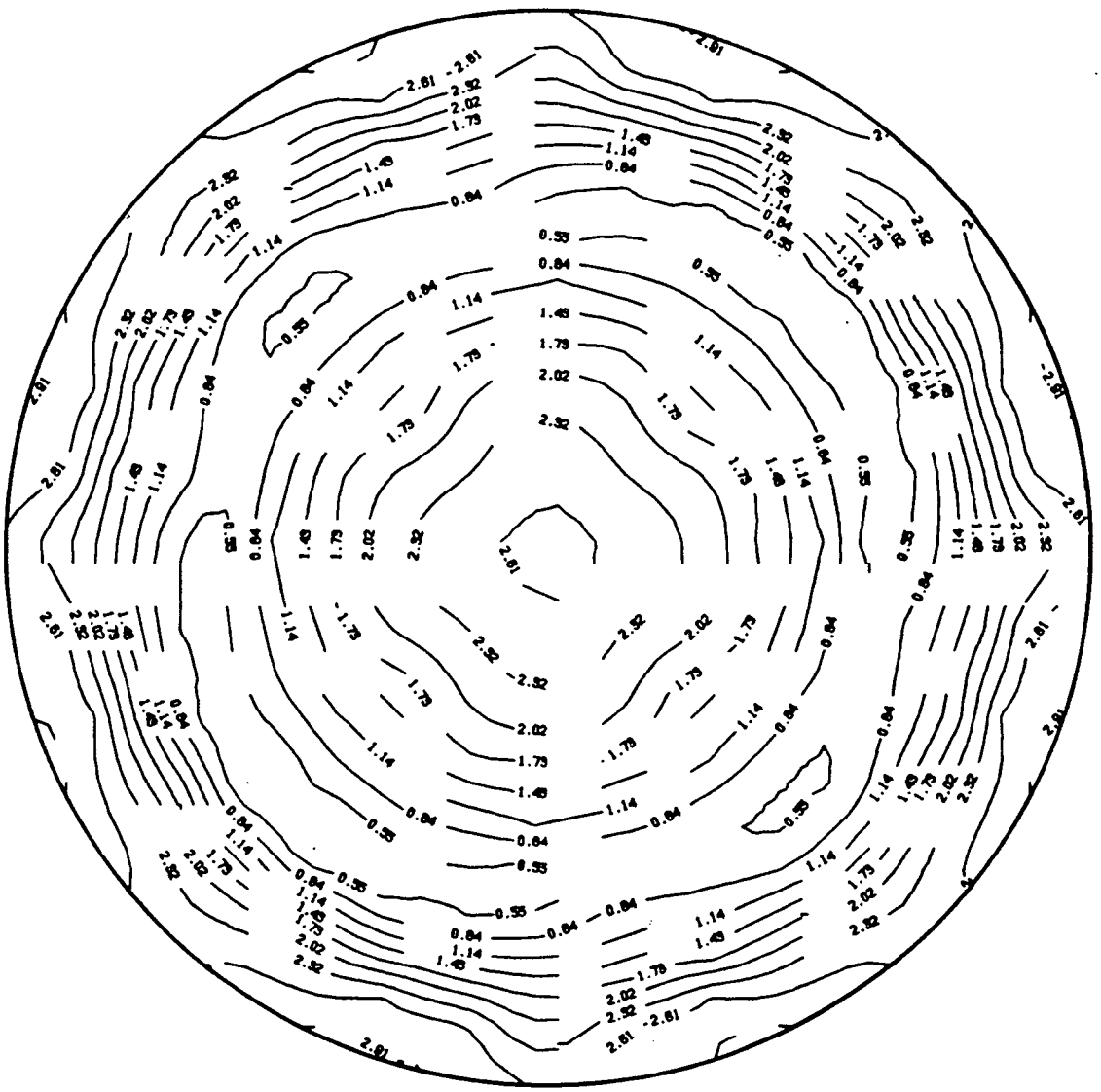

XIII.2.3.6 MRSS-CRSS (Yield) at a distance from the interface of (a) 38.5 mm ; (b) 46.75 mm ; (c) 52.25 mm.

a

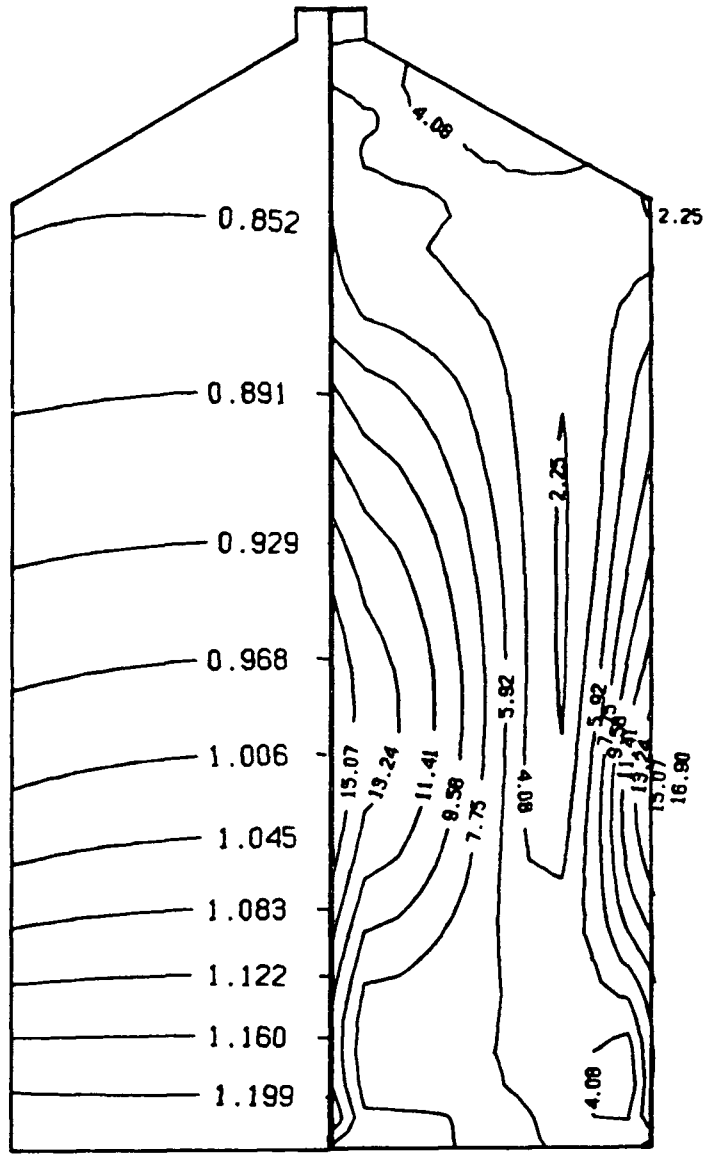
0.852
0.891
0.929
0.968
1.006
1.045
1.083
1.122
1.160
1.199
4.08
2.25
2.25
5.92
4.08
7.75
8.58
11.41
13.24
15.07
16.90
4.08

b

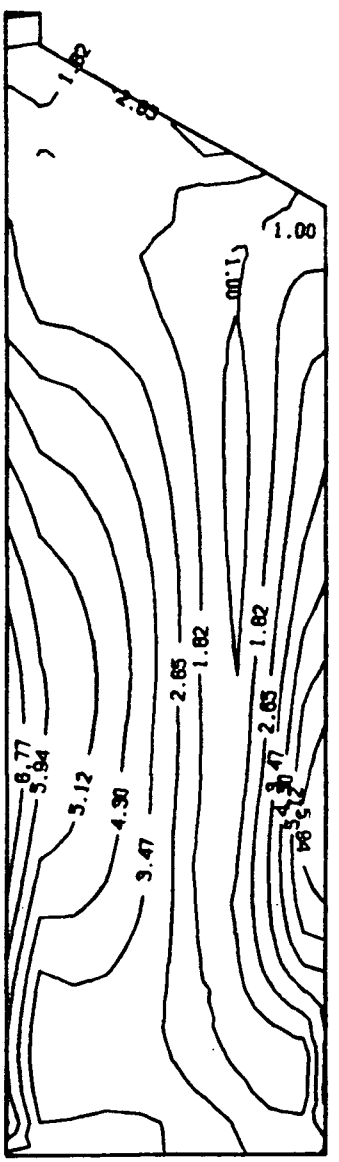
1.82
2.65
1.00
1.00
1.82
2.65
1.82
2.65
6.77
5.94
5.12
4.30
3.47

c

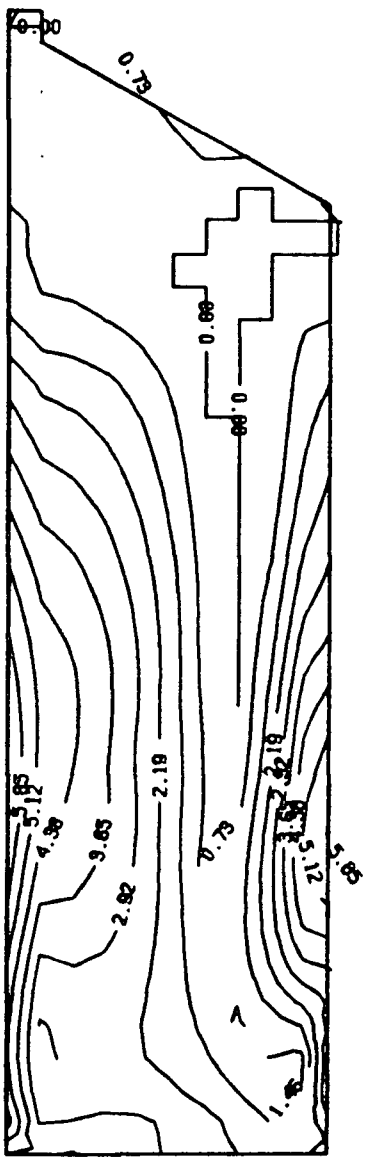
0.00
0.73
0.00
0.00
2.19
0.73
2.92
3.65
4.38
5.12
5.85

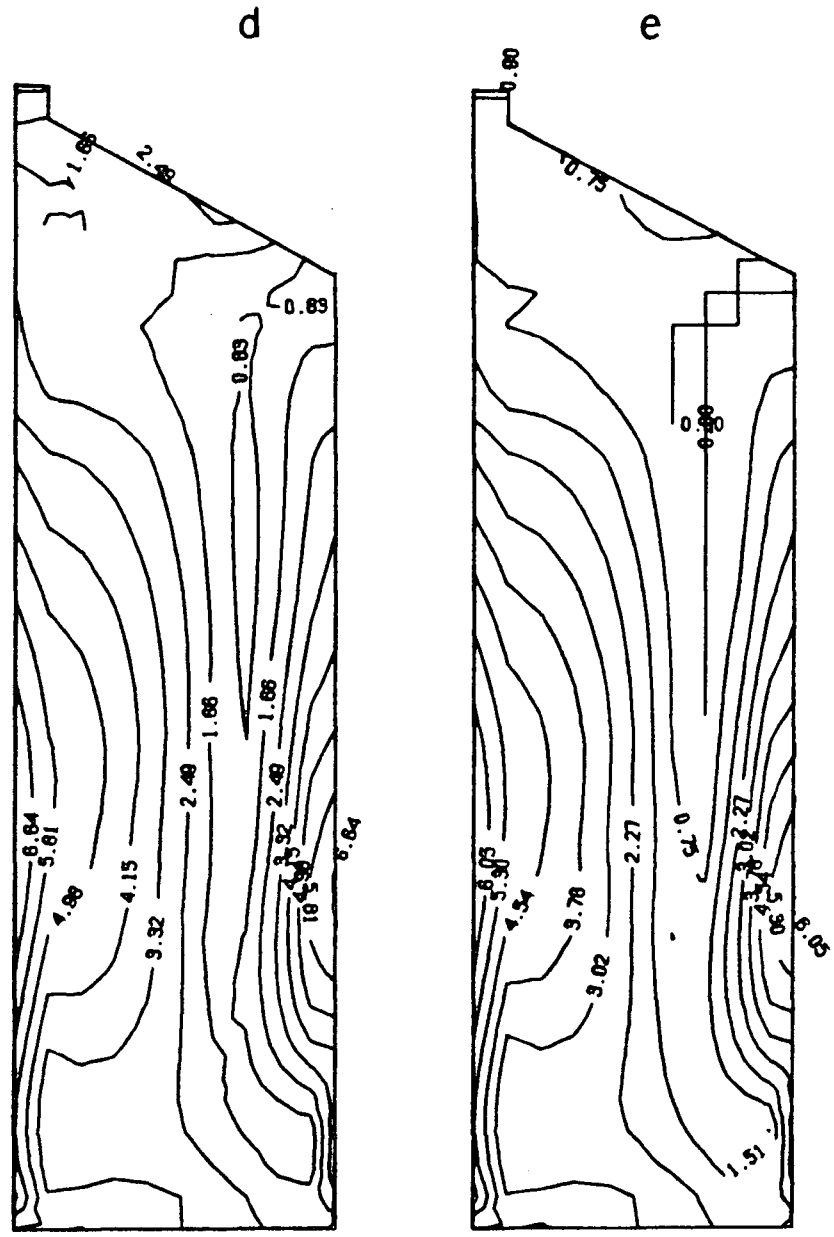

XIII.2.4.1 (a) Temperature and Von Mises Stress
(b) MRSS ; (c) MRSS-CRSS (Yield) ;
(d) MRSS-CRSS (MB) ; (e) MRSS-CRSS (MBTe) .

a

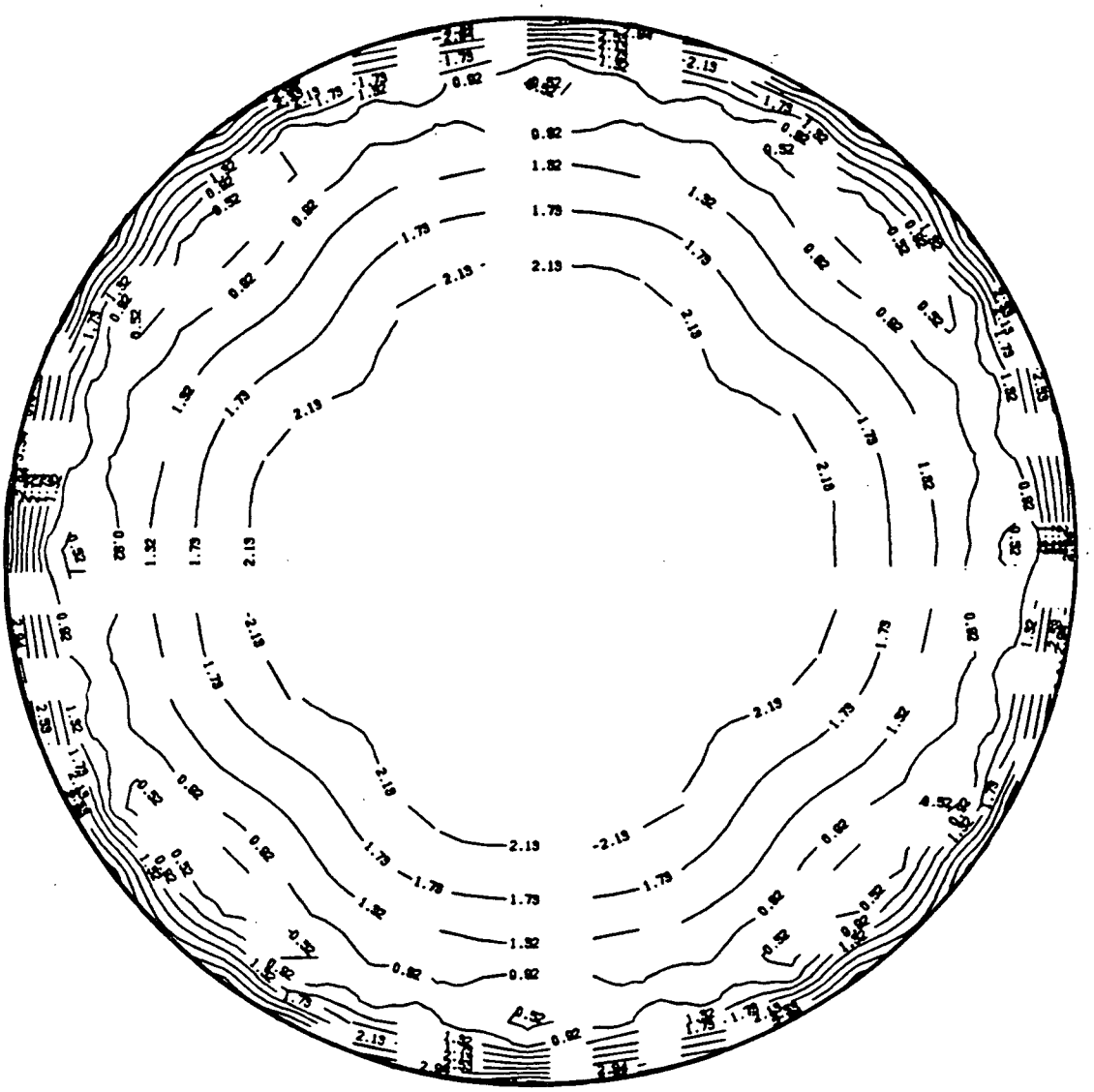

b

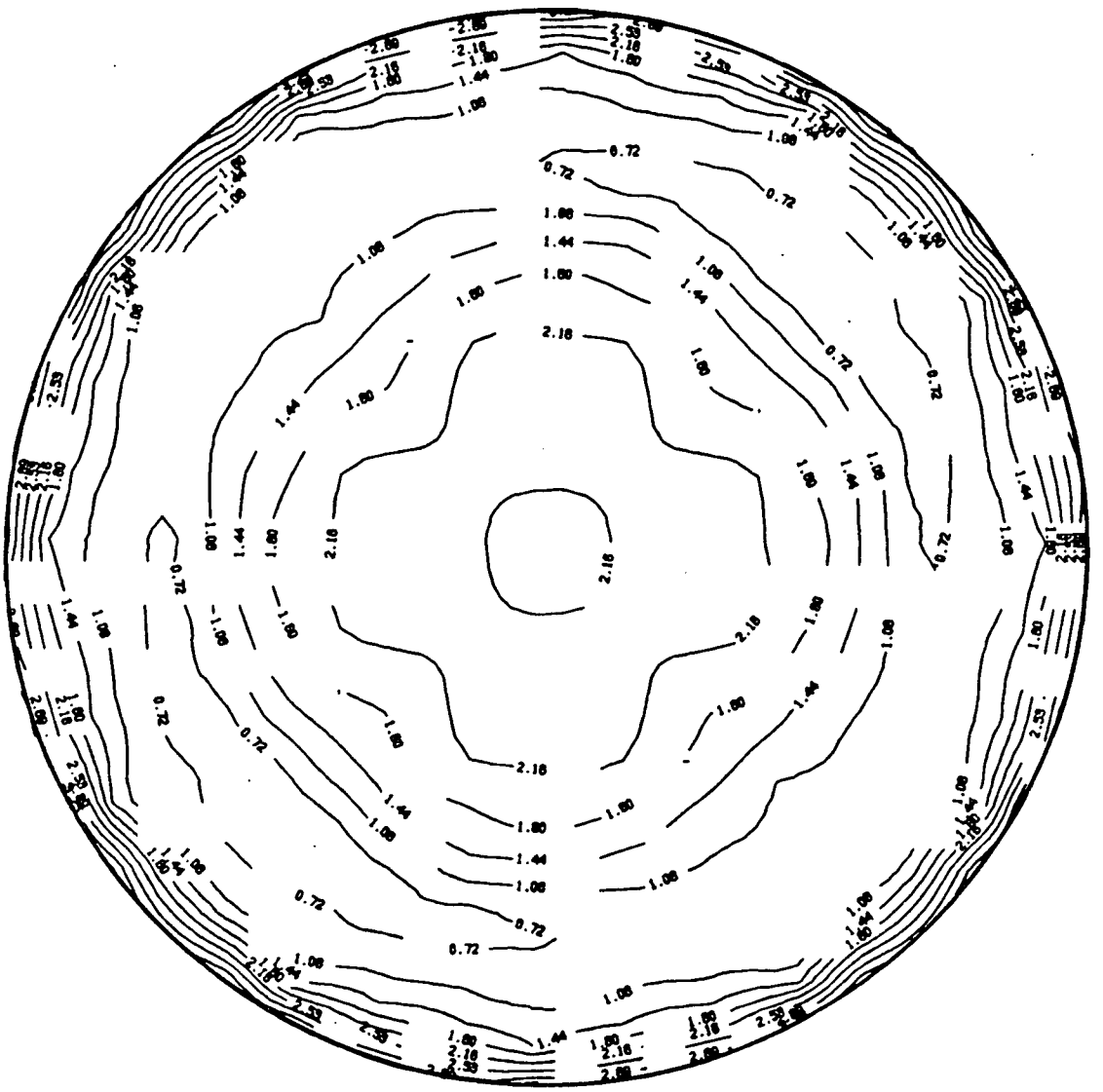

C

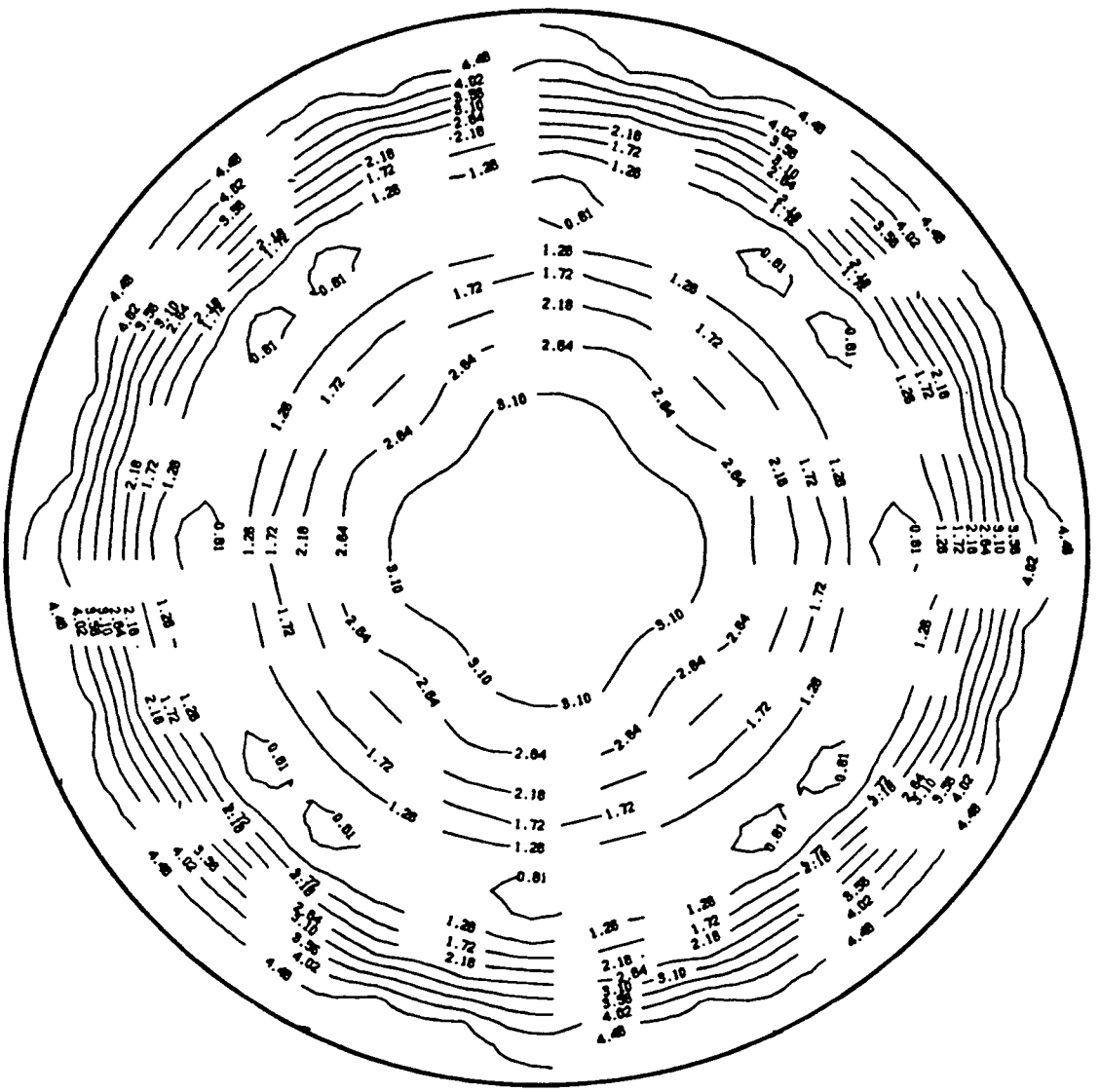

d

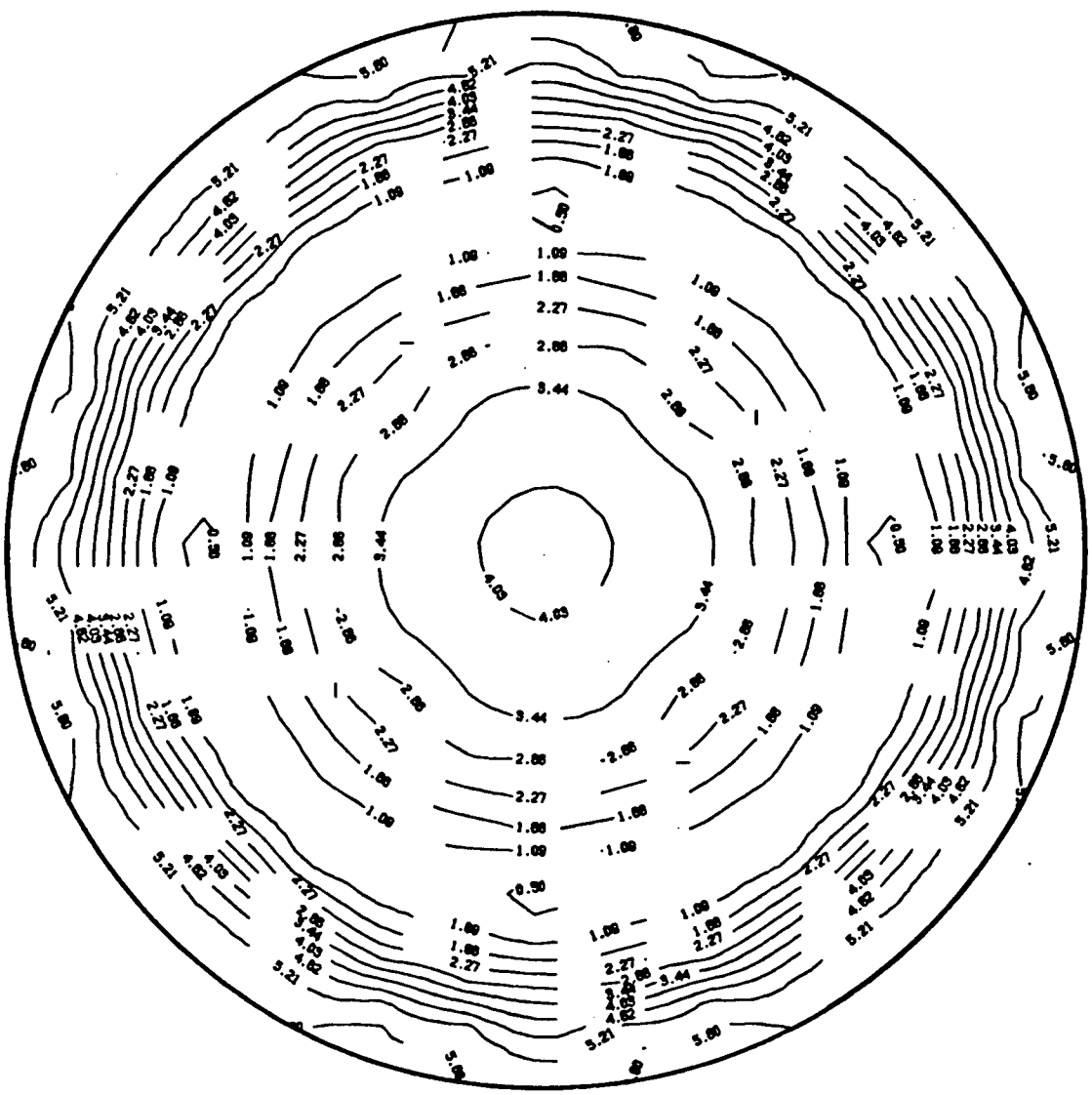

e

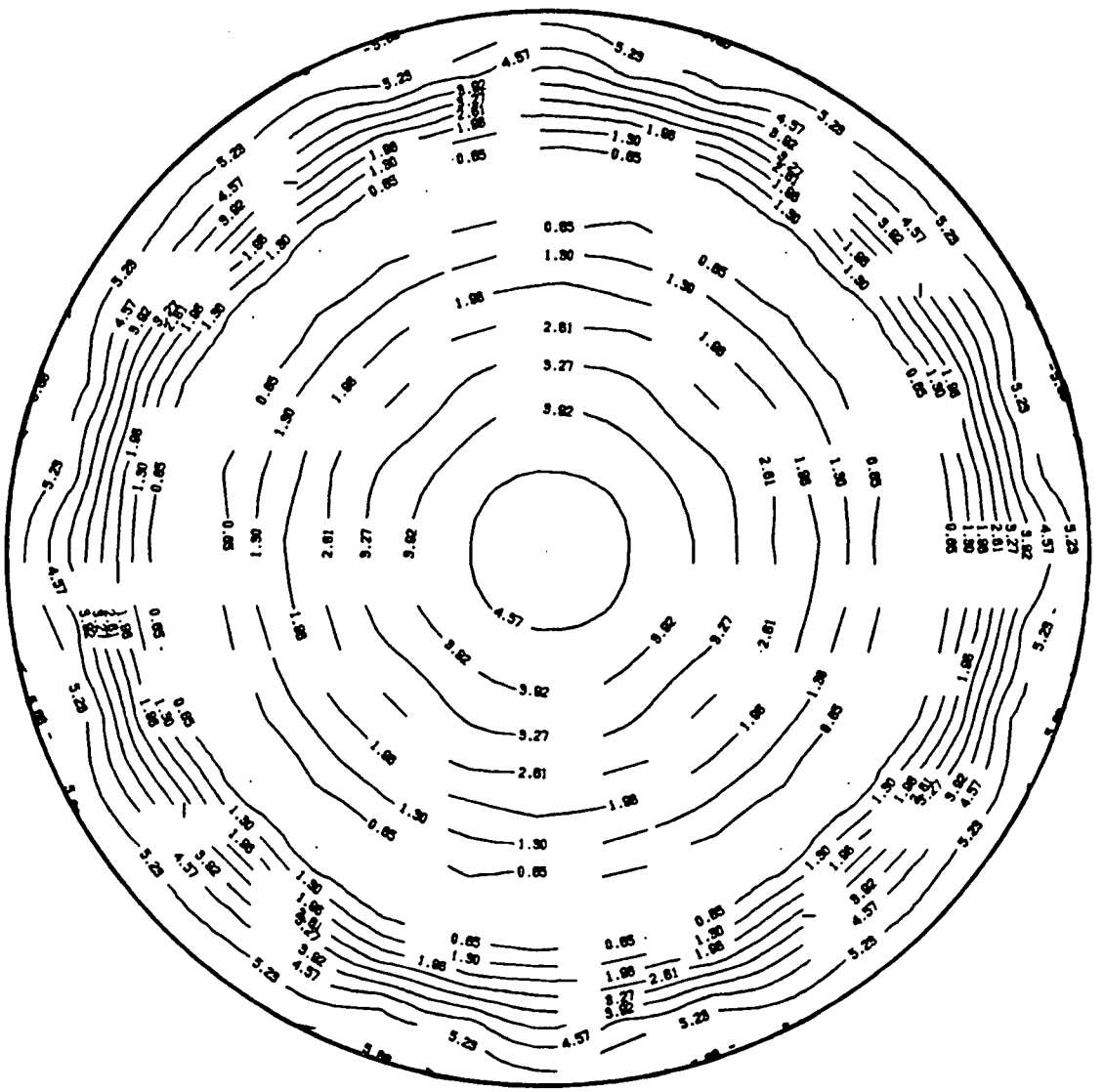

f

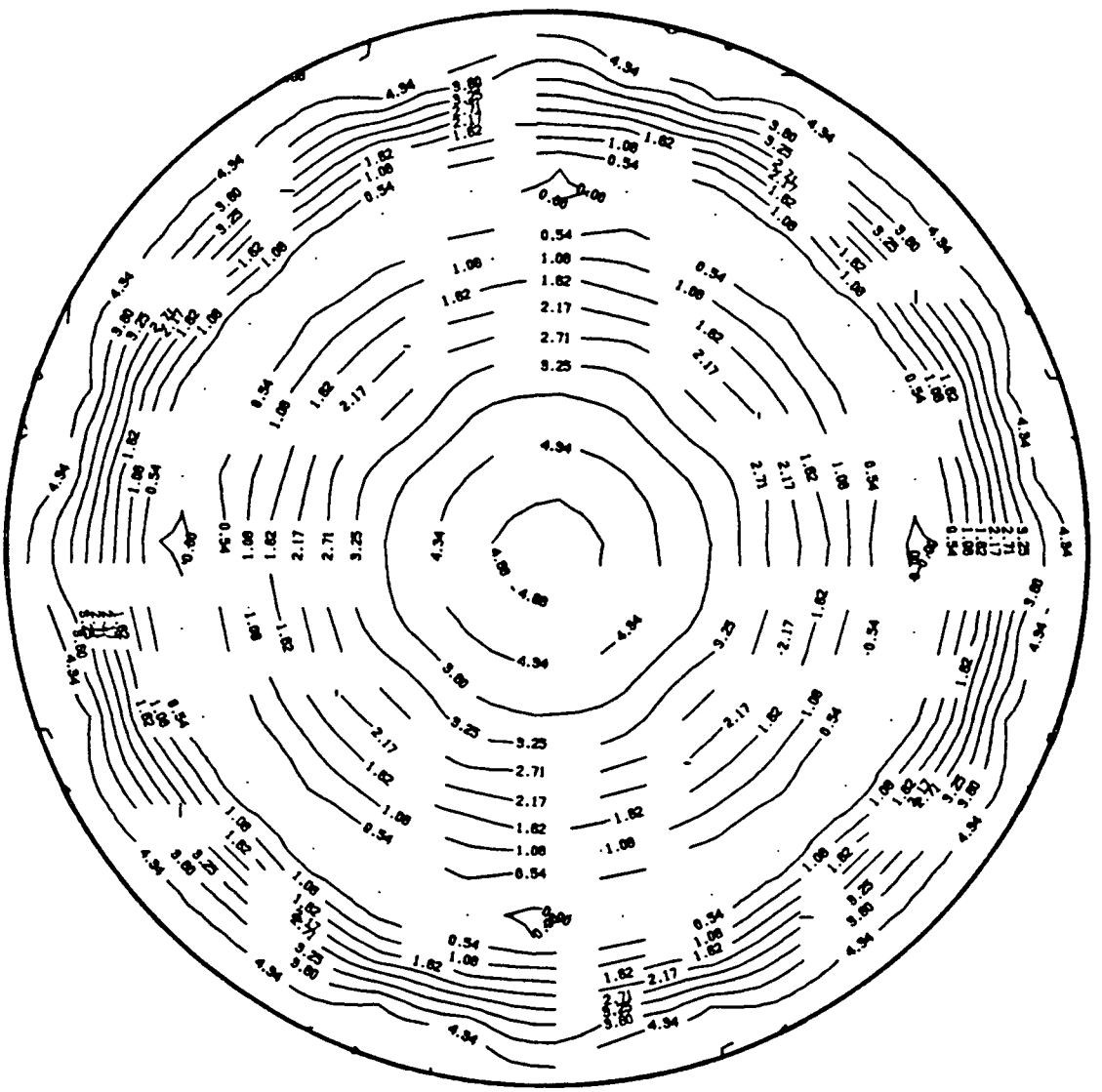

g

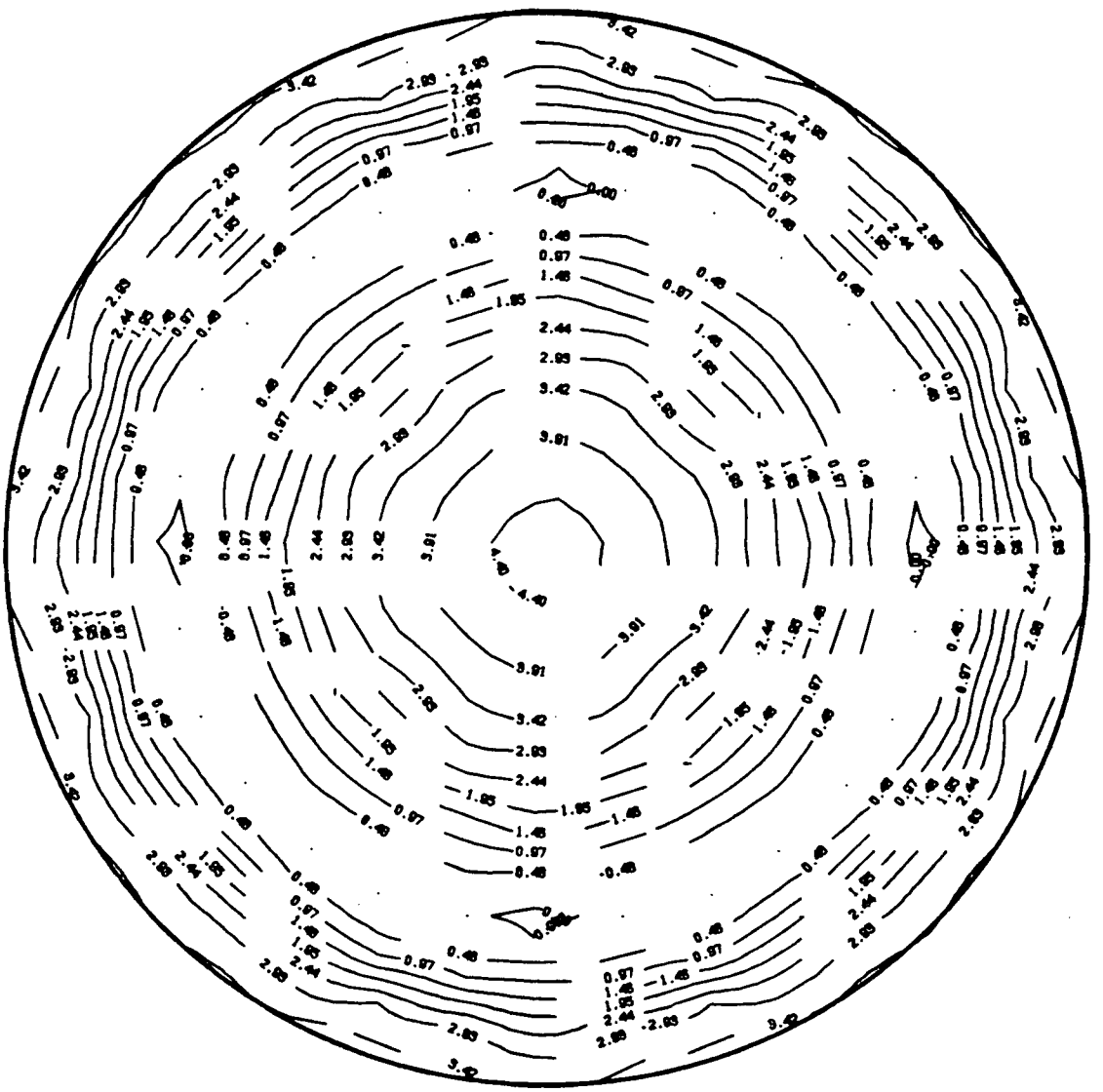

h

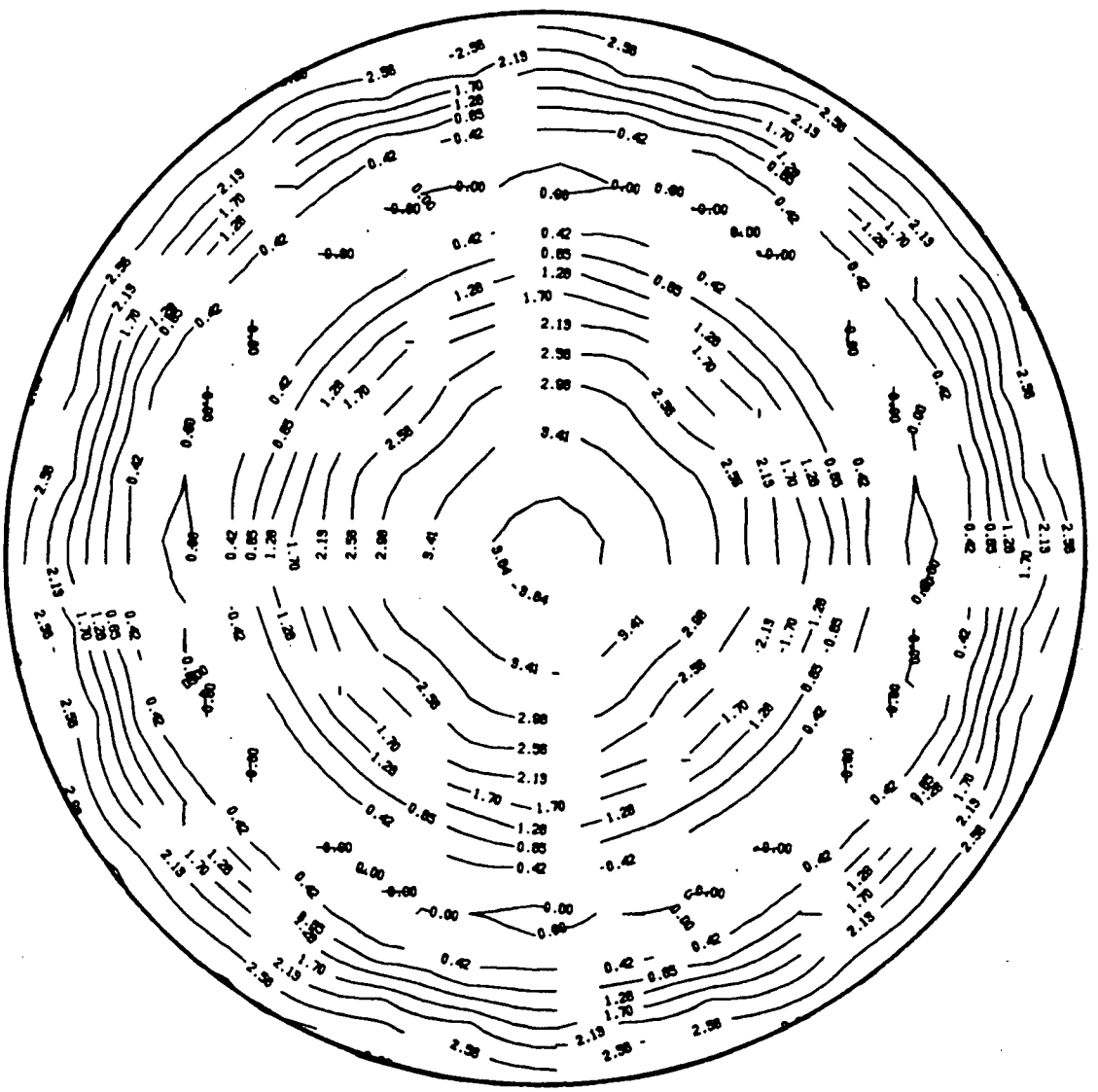

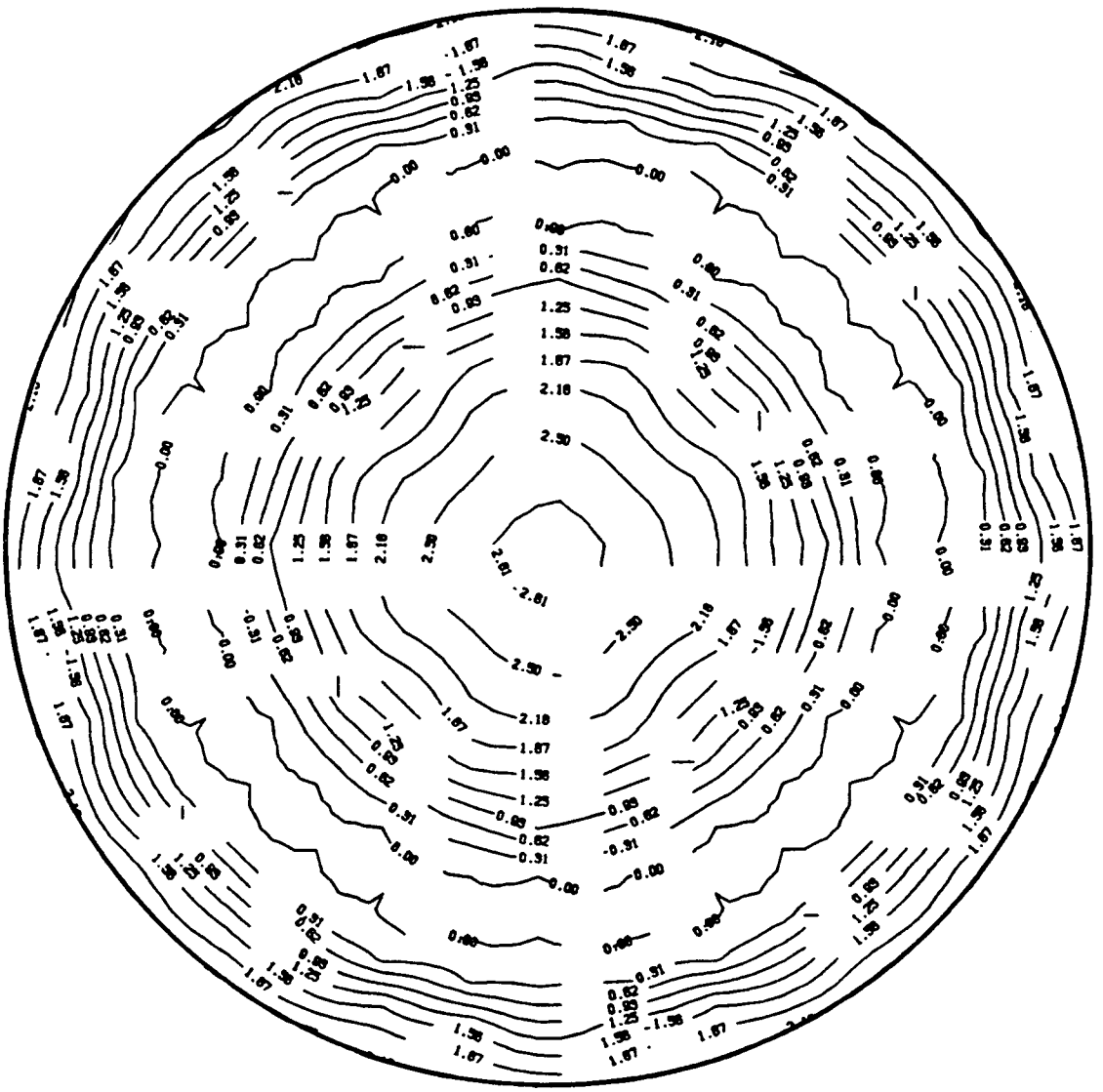

j

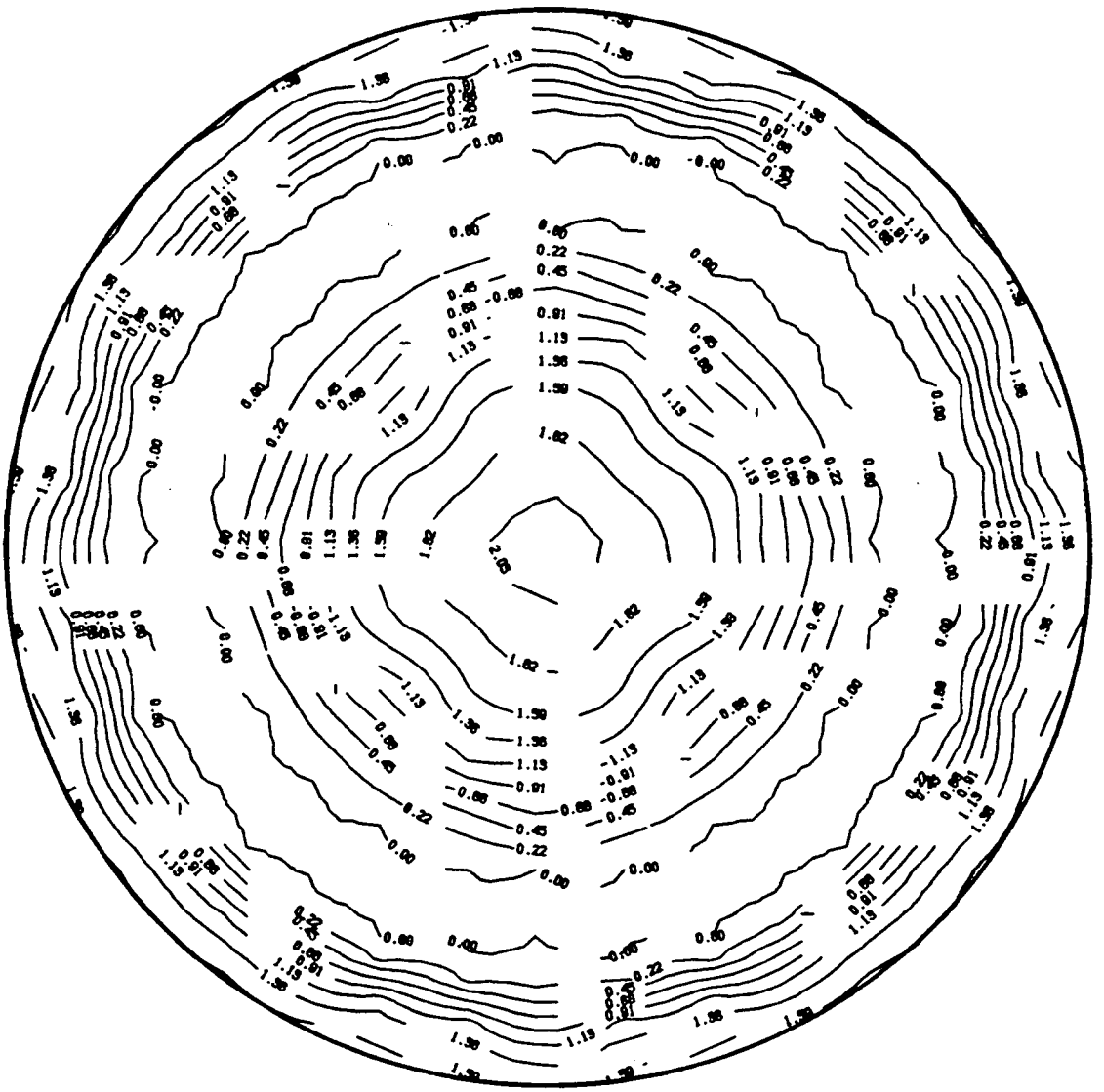

k

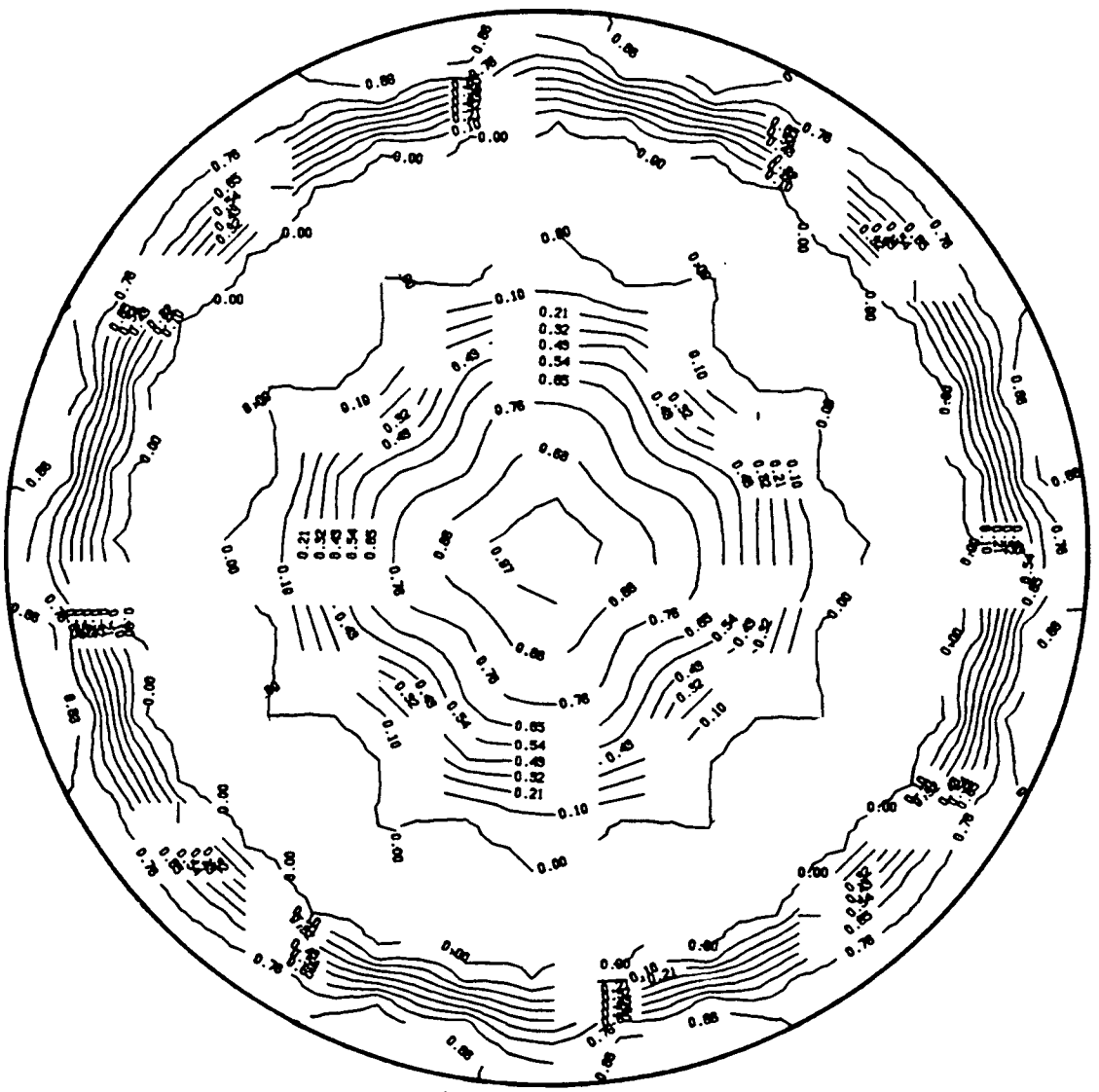

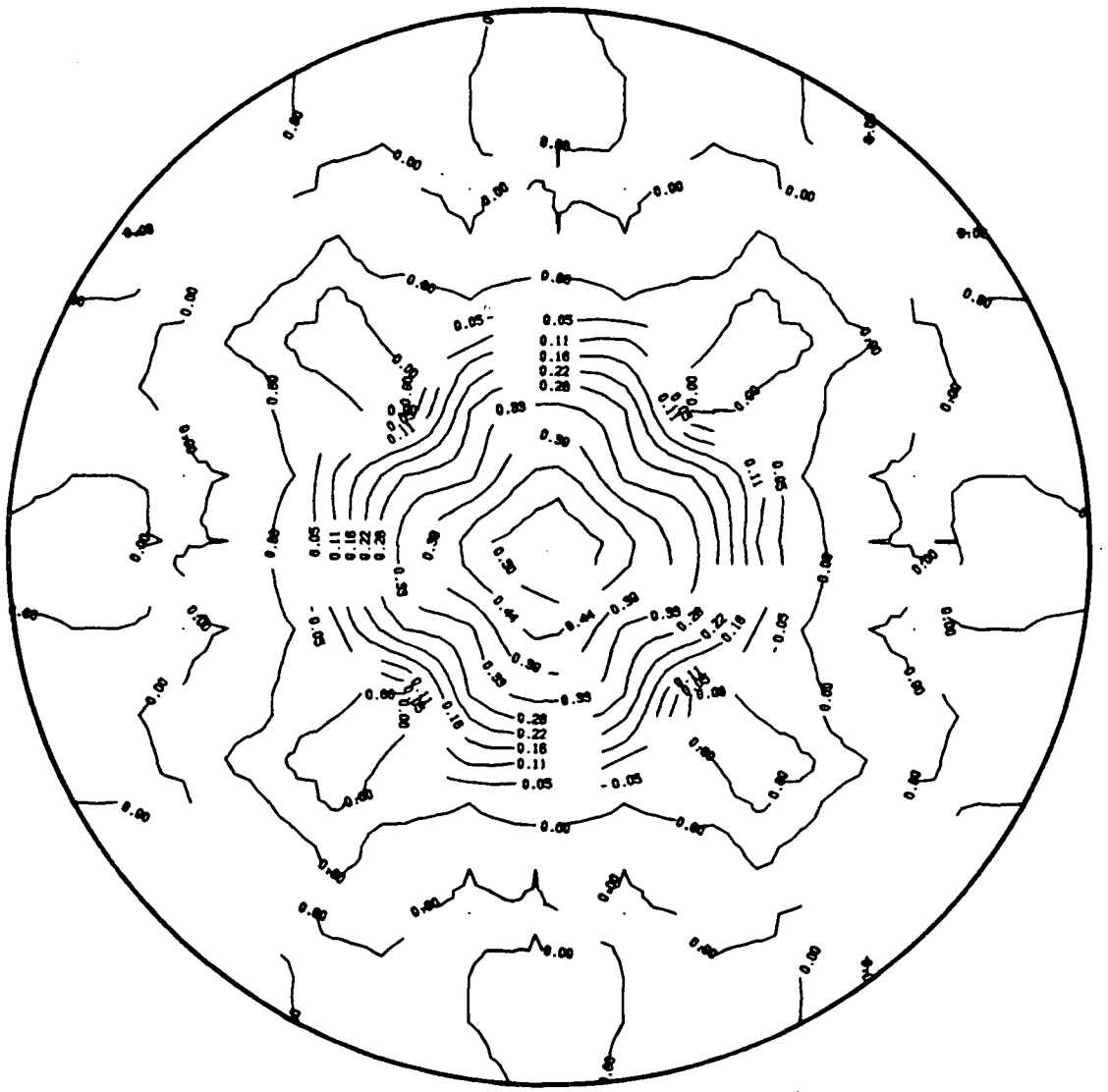

XIII.2.4.2 MRSS-CRSS (Yield) in cross-sections at a distance of the interface of
(a) 5.5 mm ; (b) 11.0 mm ; (c) 19.25 mm ;
(d) 24.75 mm ; (e) 33.0 mm ; (f) 38 .5 mm ;
(g) 46.75 mm ; (h) 52.25 mm ; (i) 60.5 mm ;
(j) 66 mm ; (k) 74.25 mm ; (l) 79.75 mm .

a

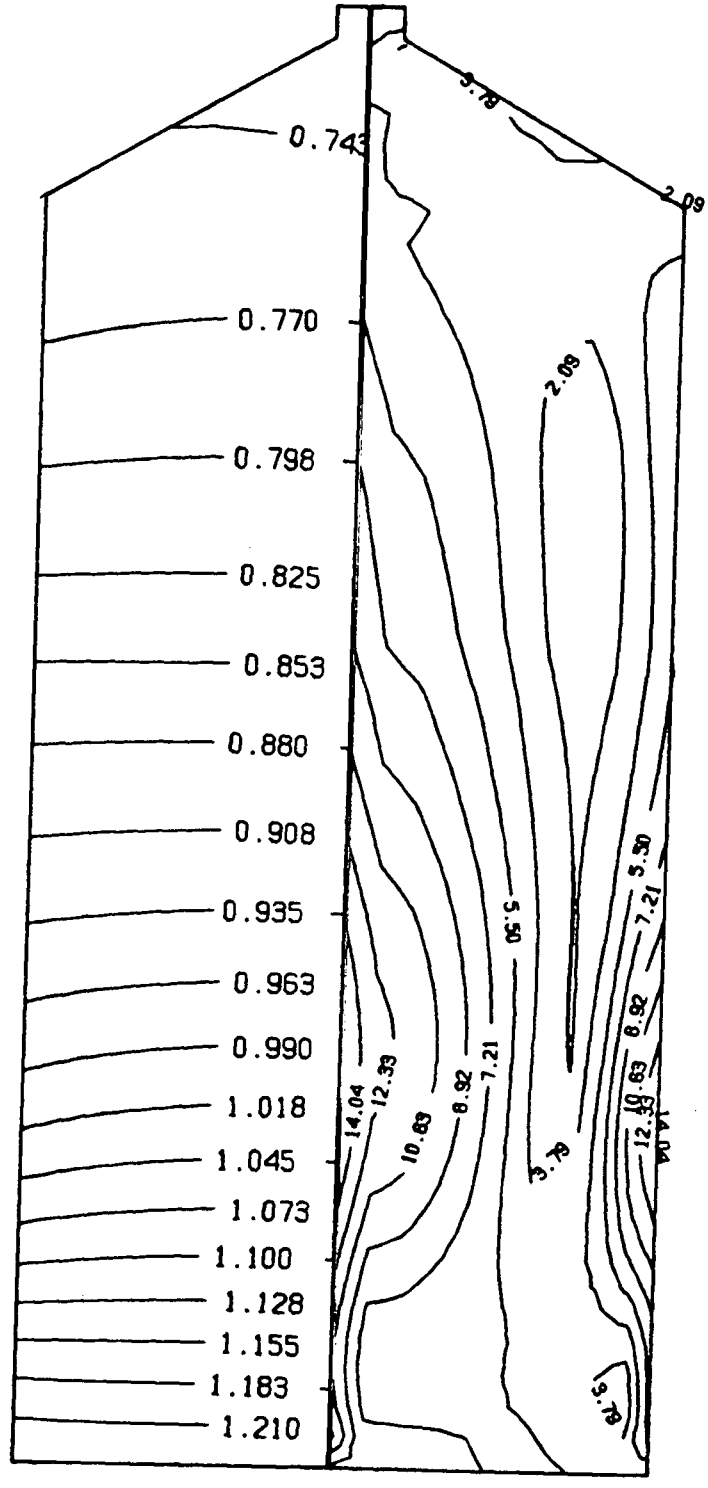
0.743
0.770
0.798
0.825
0.853
0.880
0.908
0.935
0.963
0.990
1.018
1.045
1.073
1.100
1.128
1.155
1.183
1.210
2.09
5.50
7.21
8.92
10.63
12.33
14.04

b

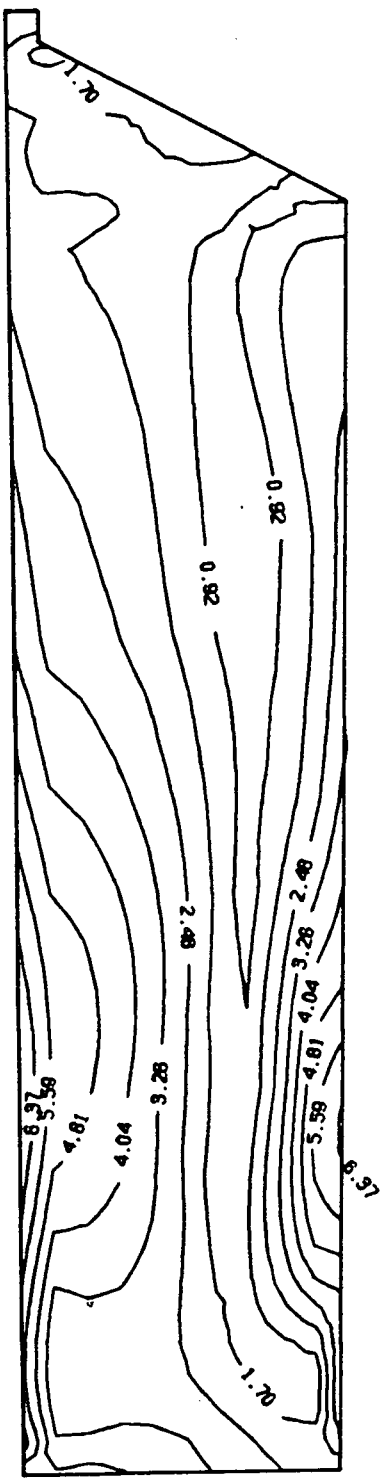

c

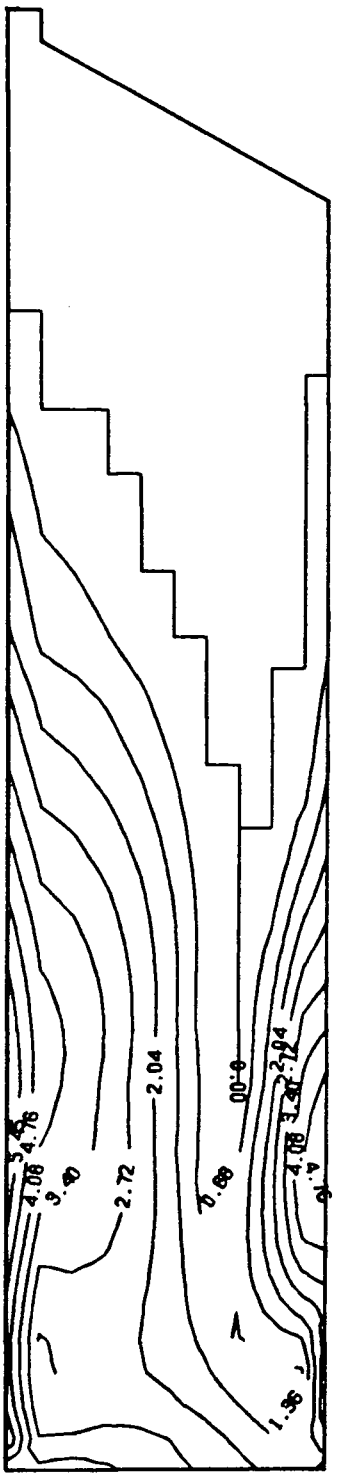

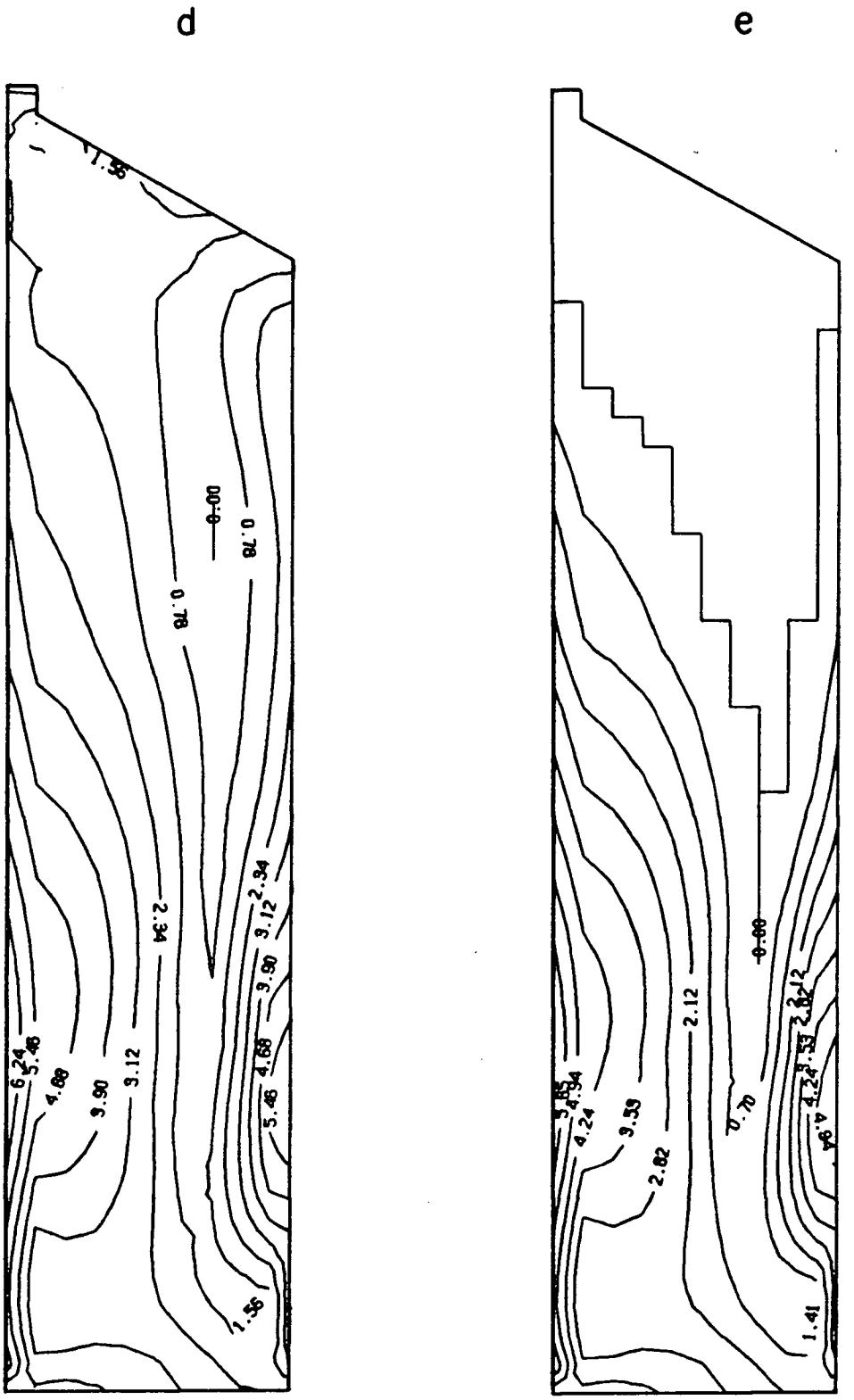

XIII.2.5.1 (a) Temperature and Von Mises Stress
(b) MRSS ; (c) MRSS-CRSS (Yield) ;
(d) MRSS-CRSS (MB) ; (e) MRSS-CRSS (MBTe) .

a

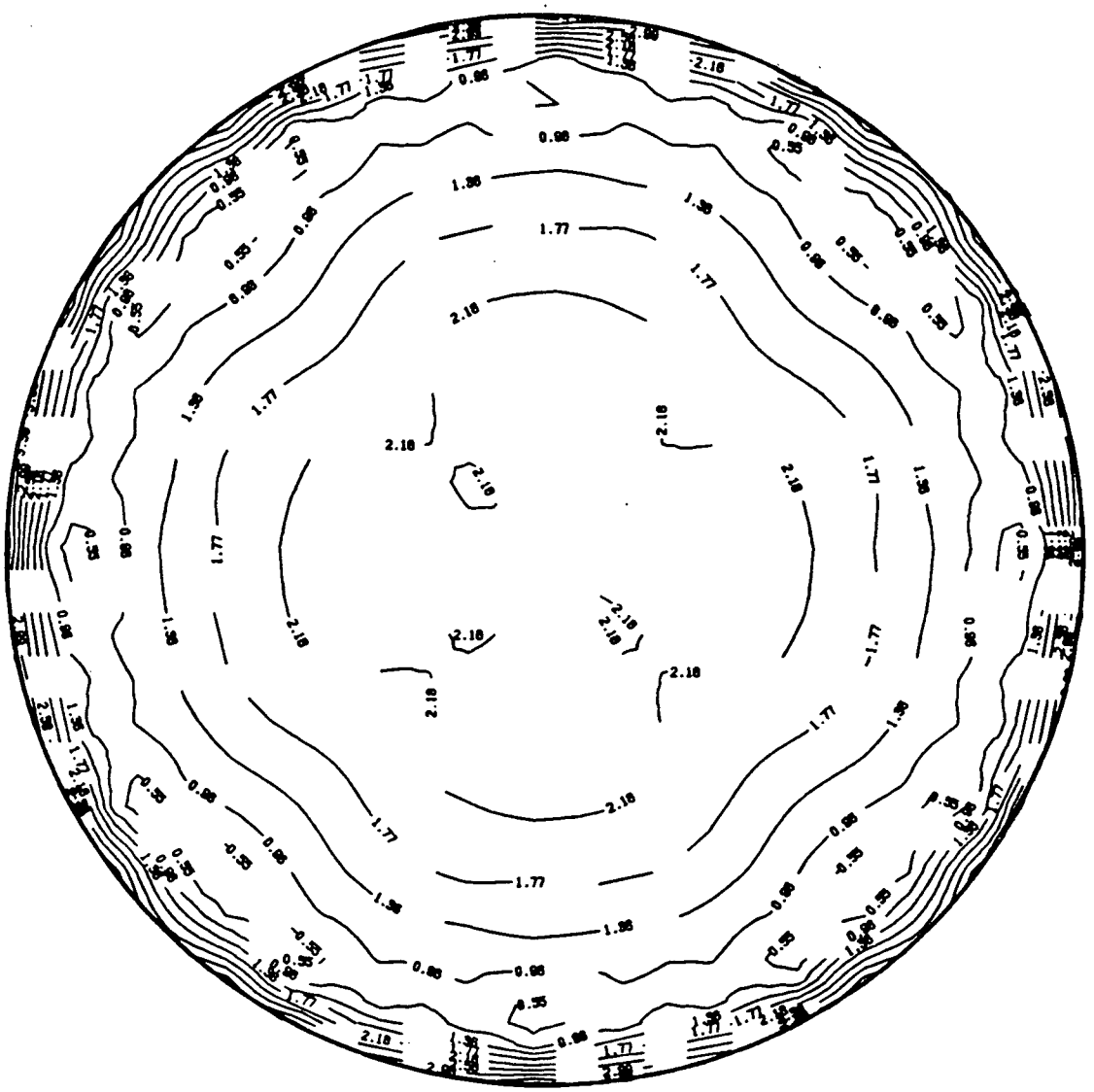

b

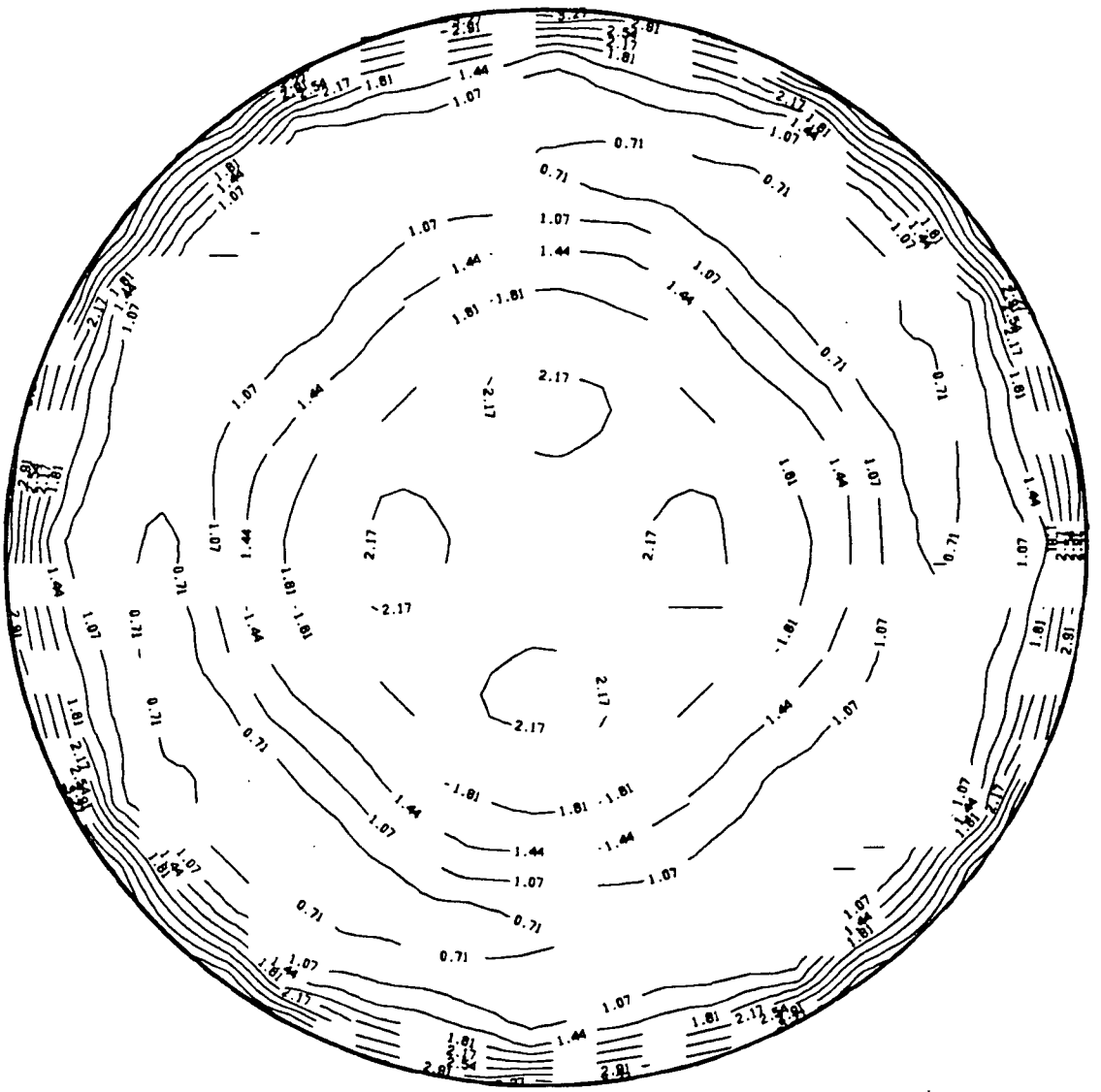

C

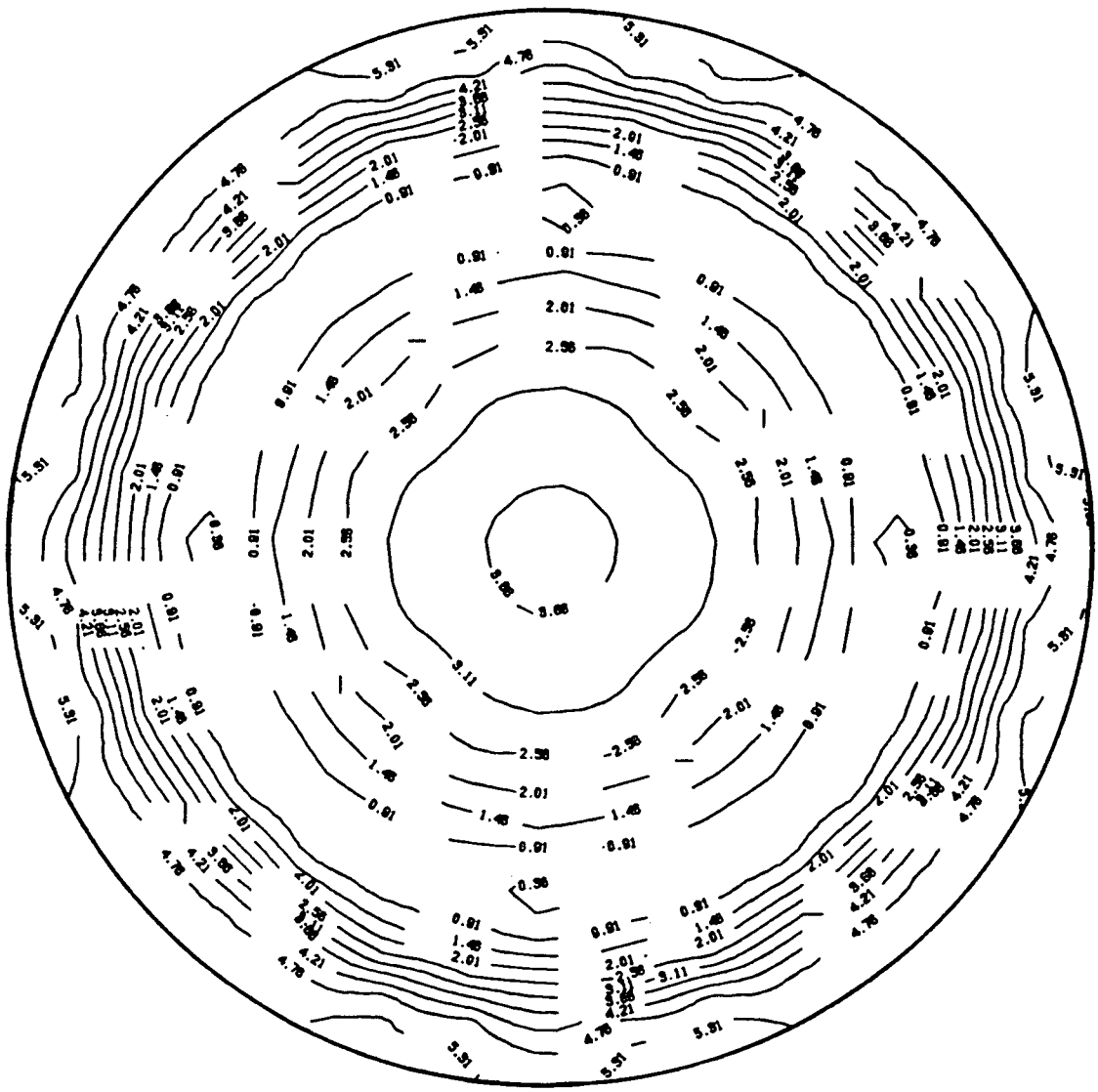

d

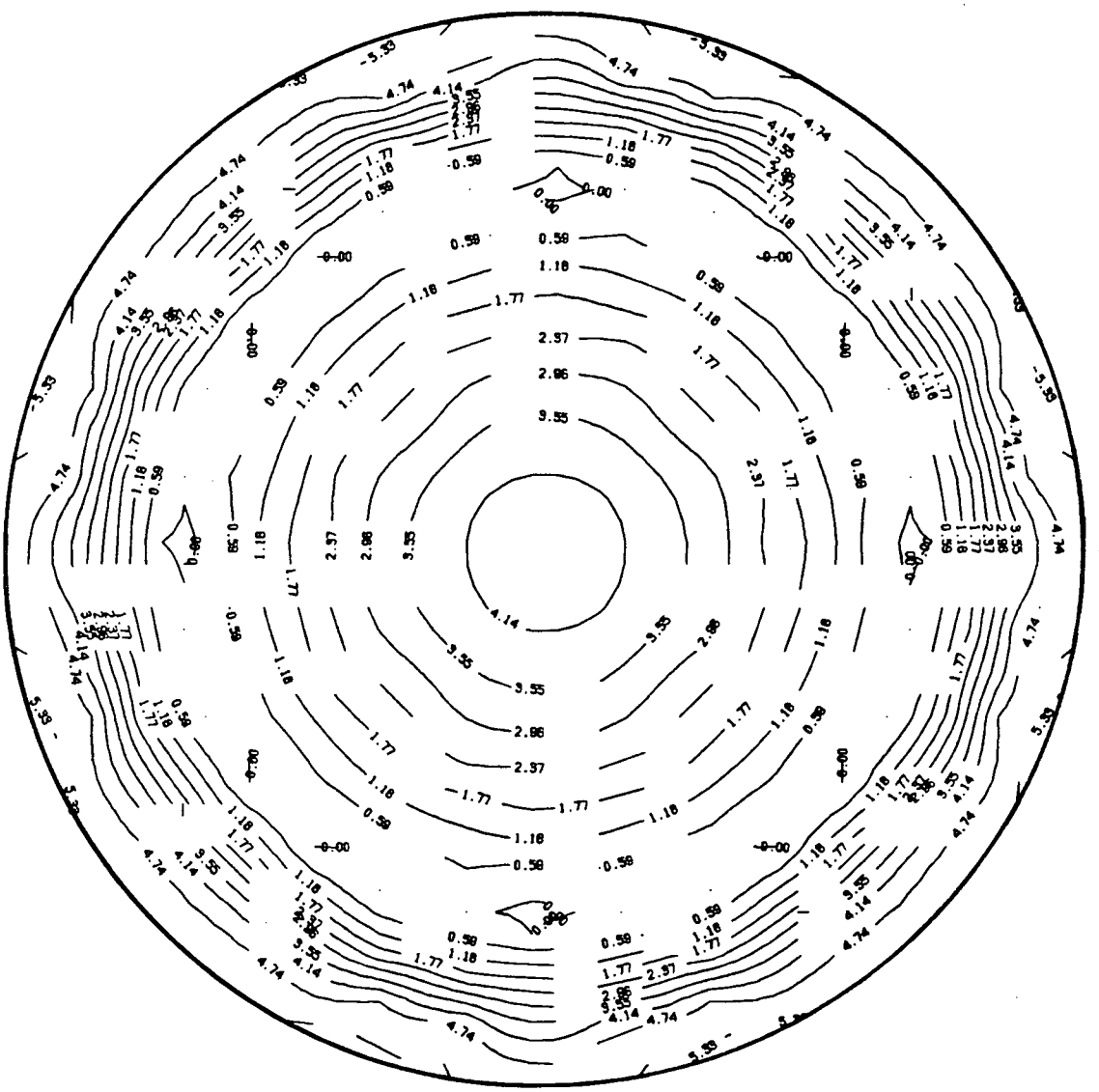

e

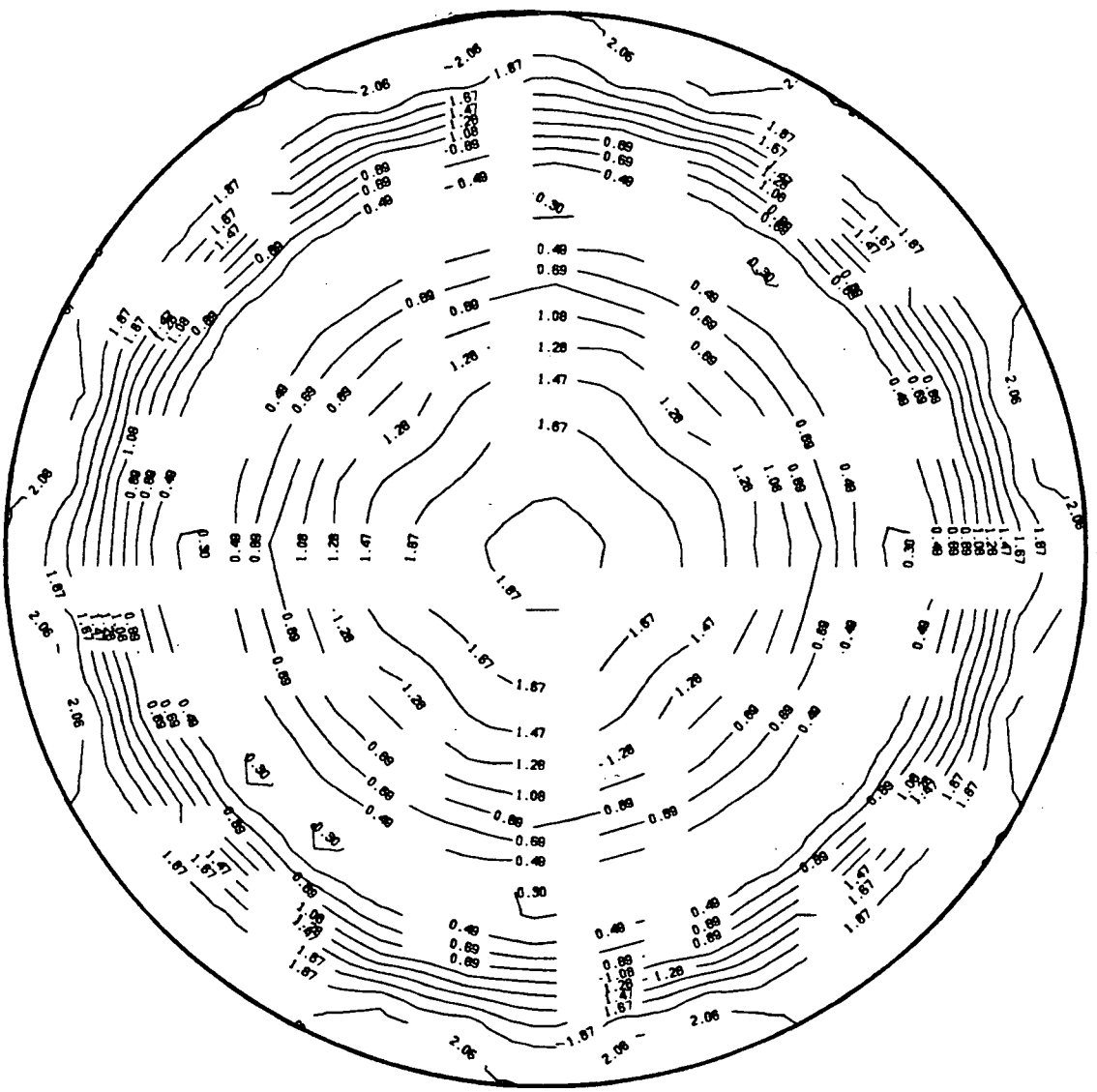

XIII.2.5.2 MRSS-CRSS (Yield) in cross-sections at a distance from the interface of
(a) 5.5 mm ; (b) 11.0 mm ; (c) 24.75 mm ;
(d) 33.0 mm ; (e) 96.25 mm .

XIII.3 Crystal Radius
R, 40 mm ; B, 21 mm ; CA, 30° ; AP, 30 atm. .

XIII.3.1 CL, 20 mm

XIII.3.1.1 (a) Temperature and Von Mises Stress
(b) MRSS ; (c) MRSS-CRSS (Yield) ;
(d) MRSS-CRSS (MB) ; (e) MRSS-CRSS (MBTe) .

XIII.3.1.2 Cross-sections at 8 mm from the interface
(a) MRSS ; (b) MRSS-CRSS (Yield)

XIII.3.1.3 Cross-sections at 16 mm from the interface
(a) MRSS ; (B) MRSS-CRSS (Yield)

XIII.3.2 CL, 40 mm

XIII.3.2.1 (a) Temperature and Von Mises Stress
(b) MRSS ; (c) MRSS-CRSS (Yield) .

XIII.3.2.2 MRSS-CRSS (Yield) in cross-sections at a distance of the interface of
(a) 8 mm ; (b) 16 mm ; (c) 28 mm ; (d) 36 mm .

XIII.3.3 CL, 80 mm

XIII.3.3.1 (a) Temperature and Von Mises Stress
(b) MRSS ; (c) MRSS-CRSS (Yield) ;
(d) MRSS-CRSS (MB) ; (e) MRSS-CRSS (MBTe) .

XIII.3.3.2 MRSS-CRSS (Yield) in cross-sections at a distance of the interface of
(a) 8 mm ; (b) 16 mm ; (c) 28 mm ; (d) 36 mm ;
(e) 48 mm ; (f) 56 mm ; (g) 68 mm ; (h) 76 mm .

XIII.3.4 CL, 100 mm
(a) Temperature and Von Mises Stress
(b) MRSS ; (c) MRSS-CRSS (Yield) ;
(d) MRSS-CRSS (MB) ; (e) MRSS-CRSS (MBTe) .

XIII.3.5 CL, 120 mm

XIII.3.5.1 (a) Temperature and Von Mises Stress
(b) MRSS ; (c) MRSS-CRSS (Yield) ;
(d) MRSS-CRSS (MB) ; (e) MRSS-CRSS (MBTe) .

XIII.3.5.2 MRSS-CRSS (Yield) in cross-sections at a distance of the interface of
(a) 8 mm ; (b) 16 mm ; (c) 28 mm ; (d) 36 mm ;
(e) 48 mm ; (f) 56 mm ; (g) 68 mm ; (h) 76 mm ;
(i) 88 mm ; (j) 96 mm ; (k) 108 mm ; (l) 116 mm .

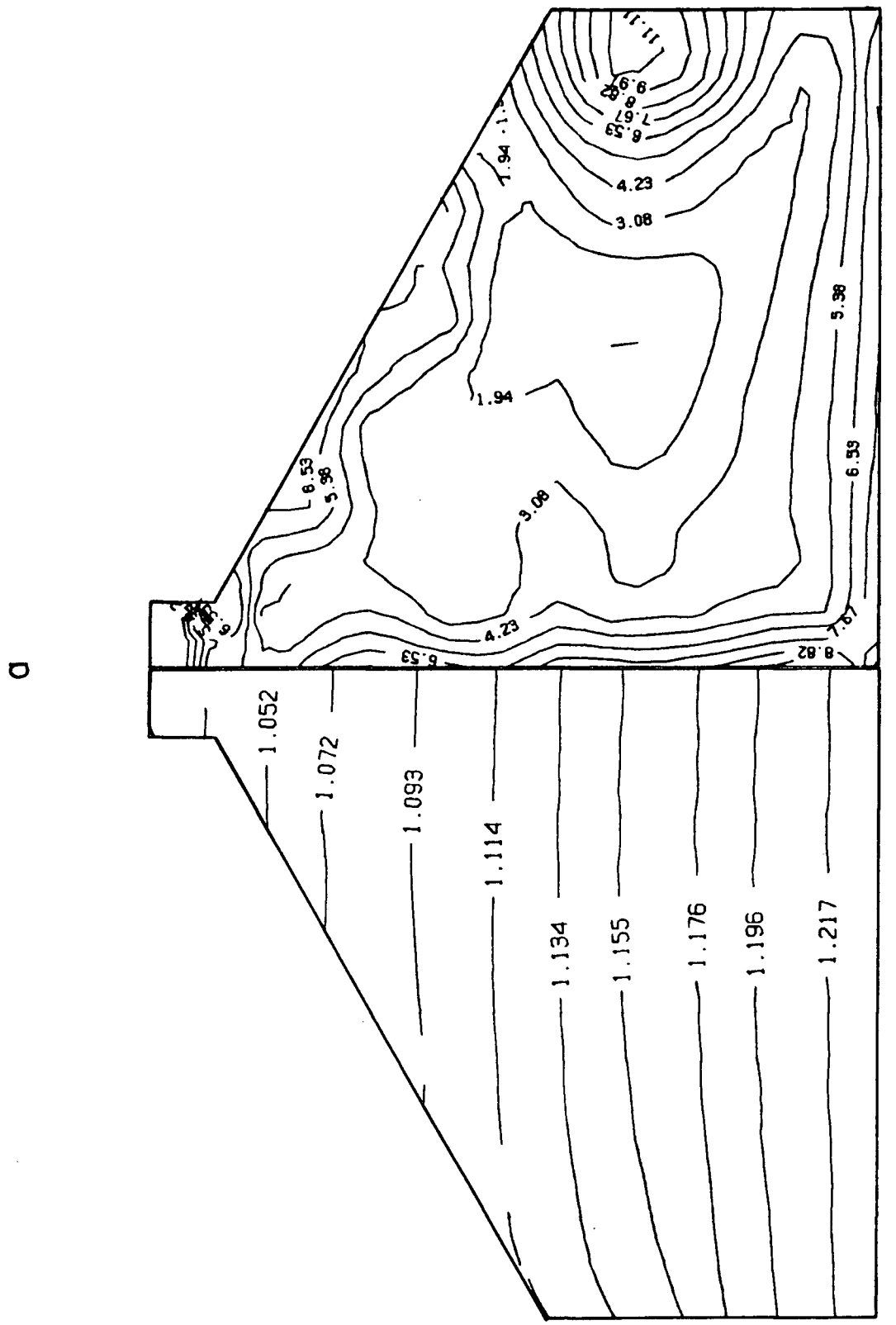
1.94
3.08
4.23
5.38
6.53
6.59
7.67
8.82
1.052
1.072
1.093
1.114
1.134
1.155
1.176
1.196
1.217

a

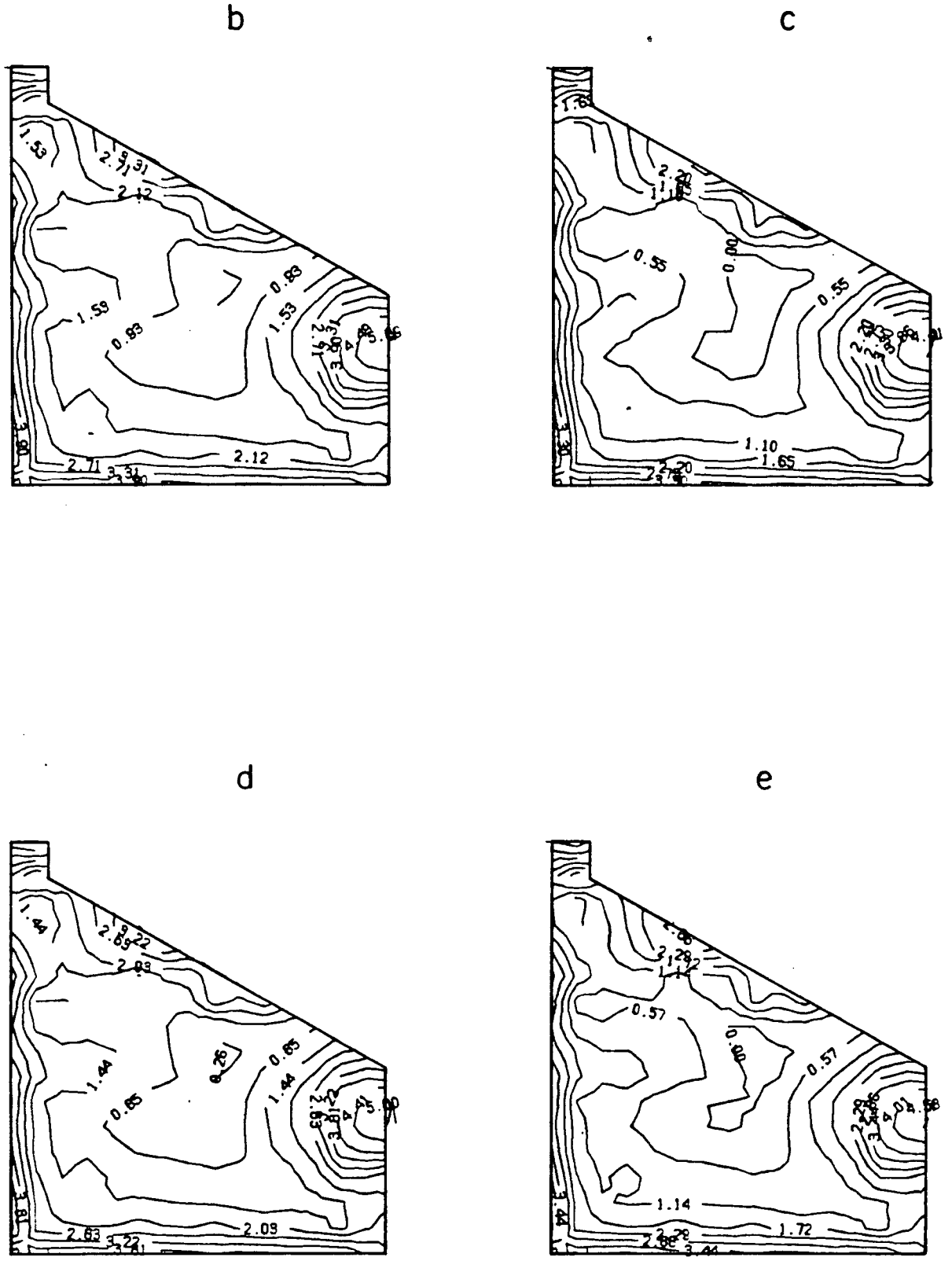

XIII.3.1.1 (a) Temperature and Von Mises Stress
(b) MRSS ; (c) MRSS-CRSS (Yield) ;
(d) MRSS-CRSS (MB) ; (e) MRSS-CRSS (MBTe) .

a

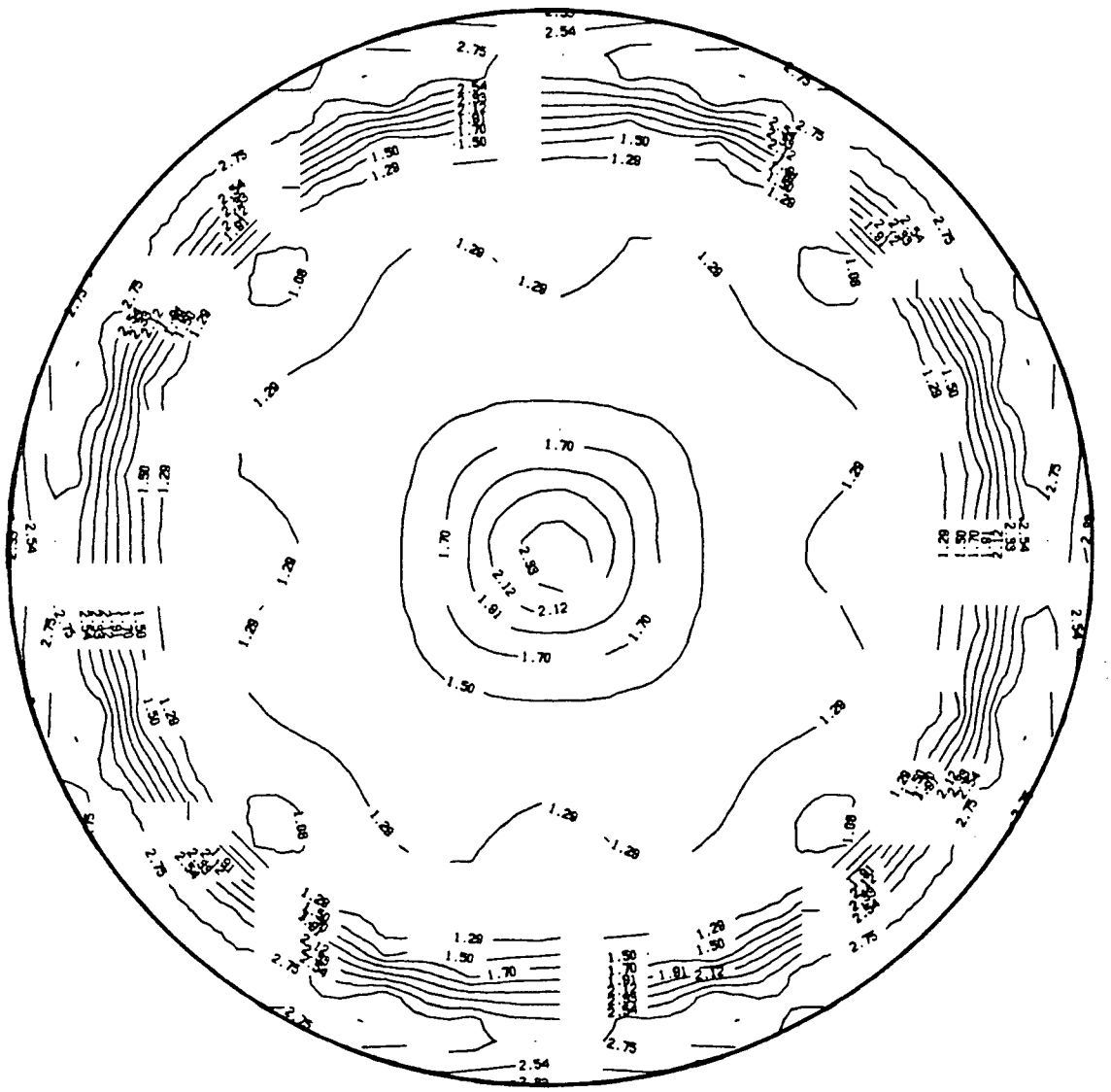

b

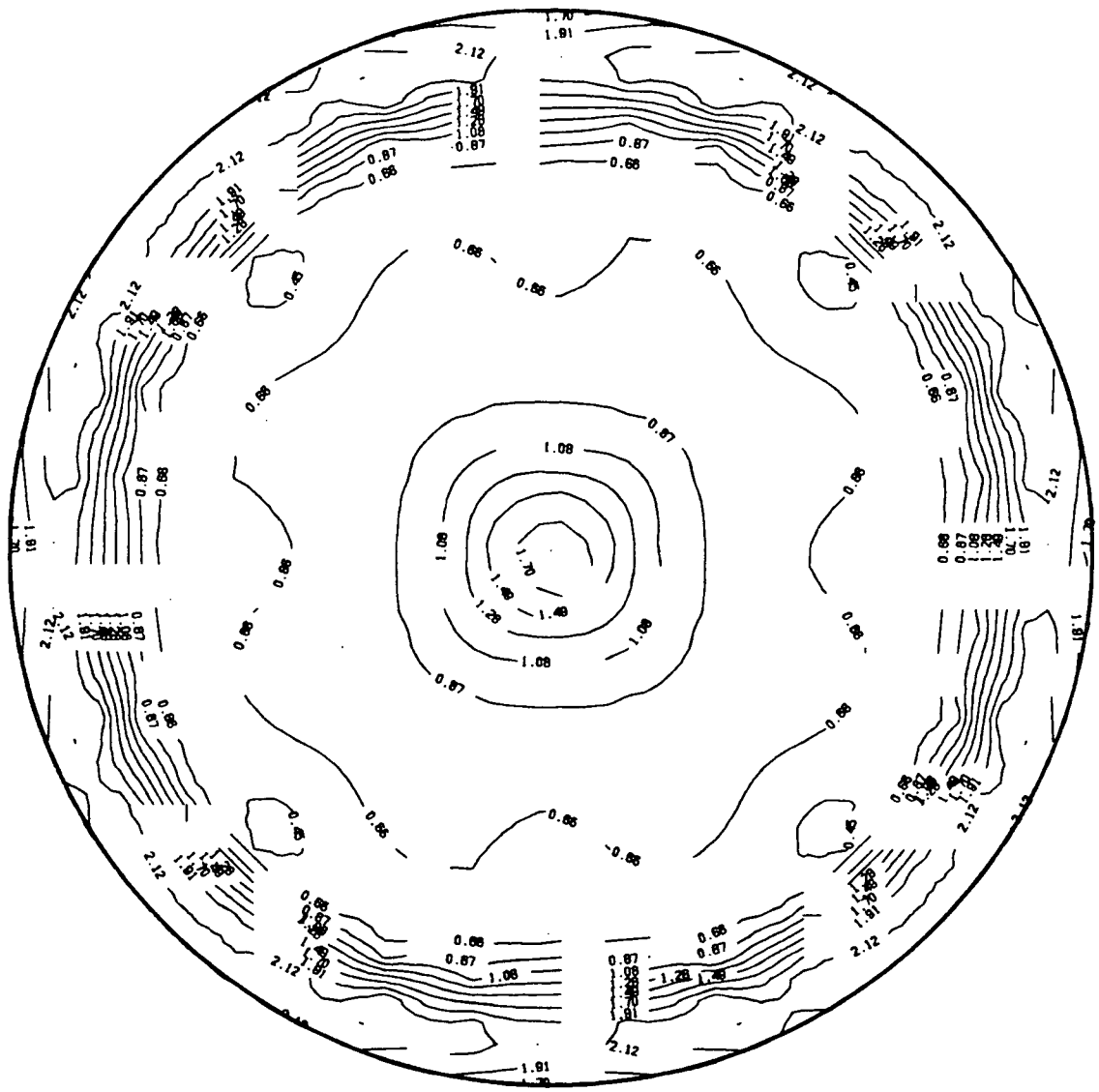

XIII.3.1.2 Cross-sections at 8 mm from the interface
(a) MRSS ; (b) MRSS-CRSS (Yield)

a

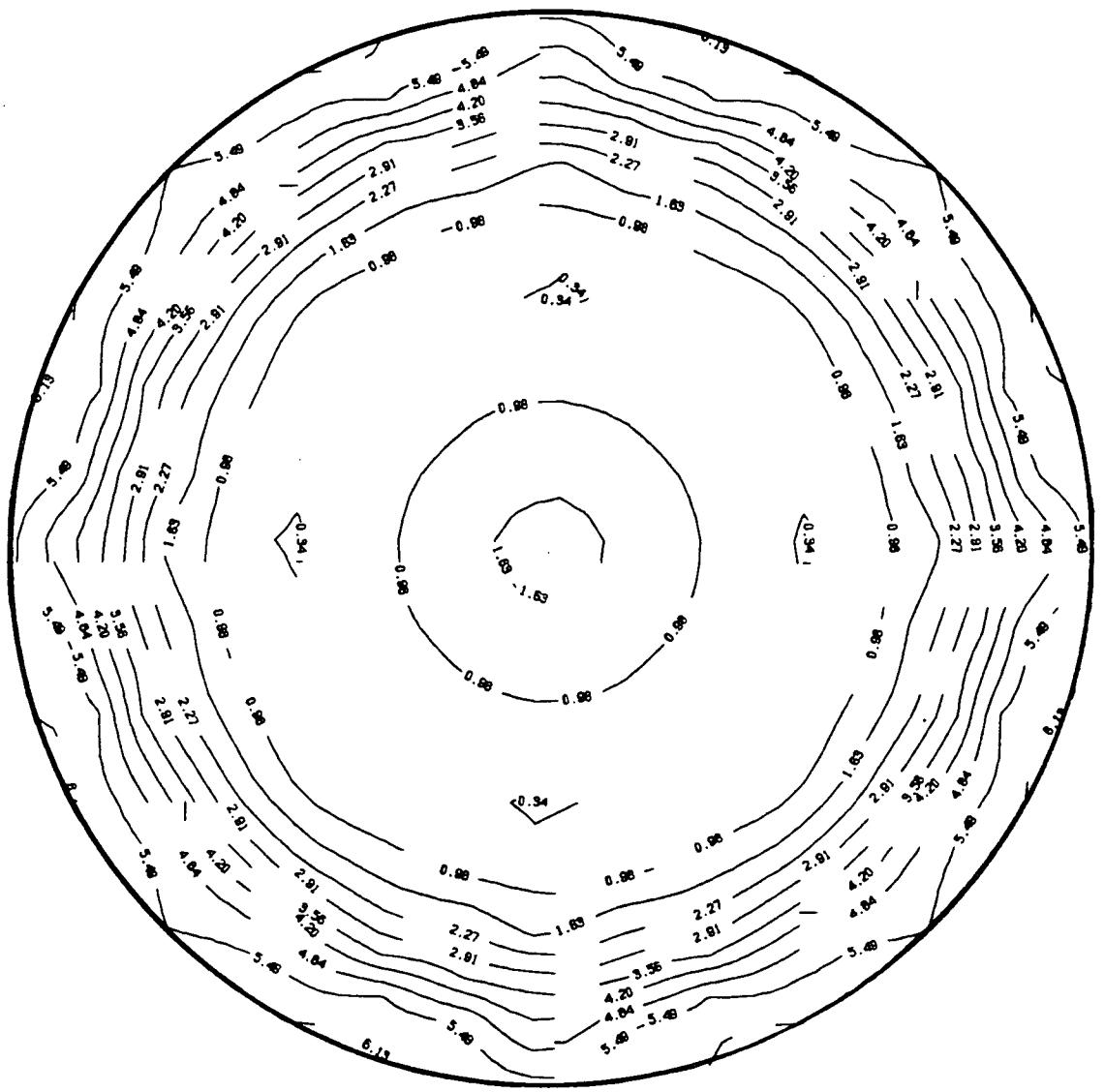

b

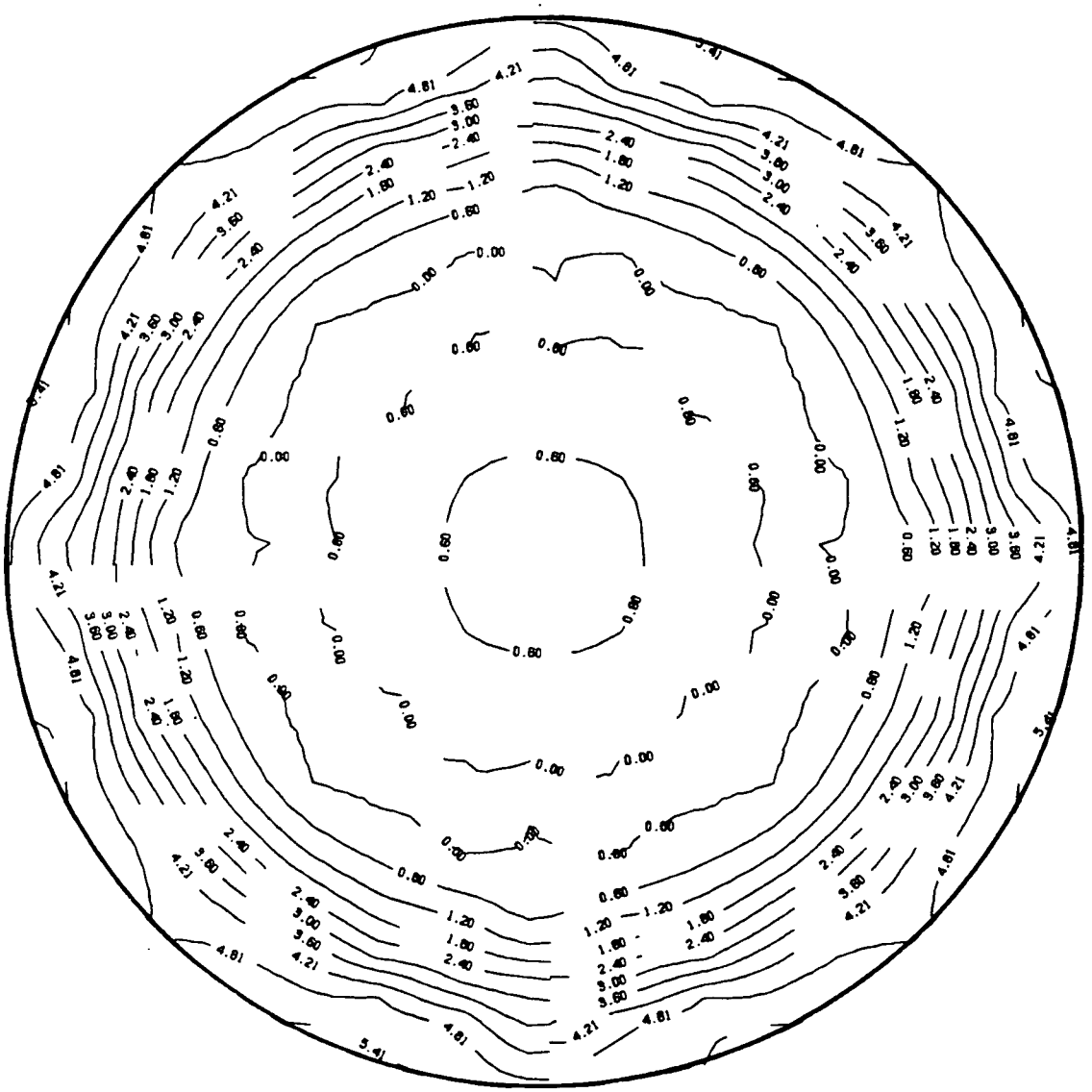

XIII.3.1.3 Cross-sections at 16 mm from the interface
(a) MRSS ; (B) MRSS-CRSS (Yield)

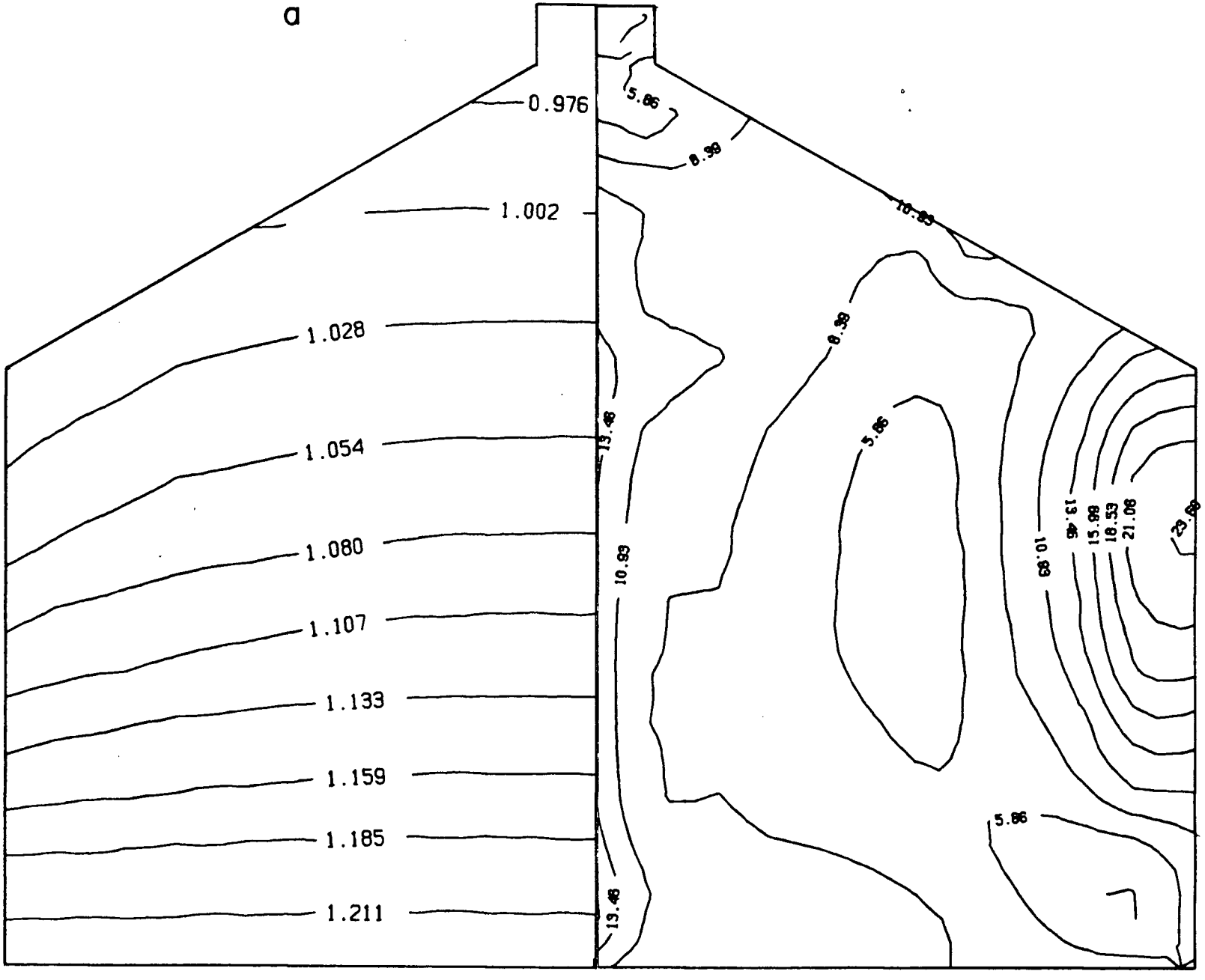
a
0.976
1.002
1.028
1.054
1.080
1.107
1.133
1.159
1.185
1.211
5.86
8.39
10.93
13.46
10.93
13.46
15.99
18.53
21.06
23.60
5.86

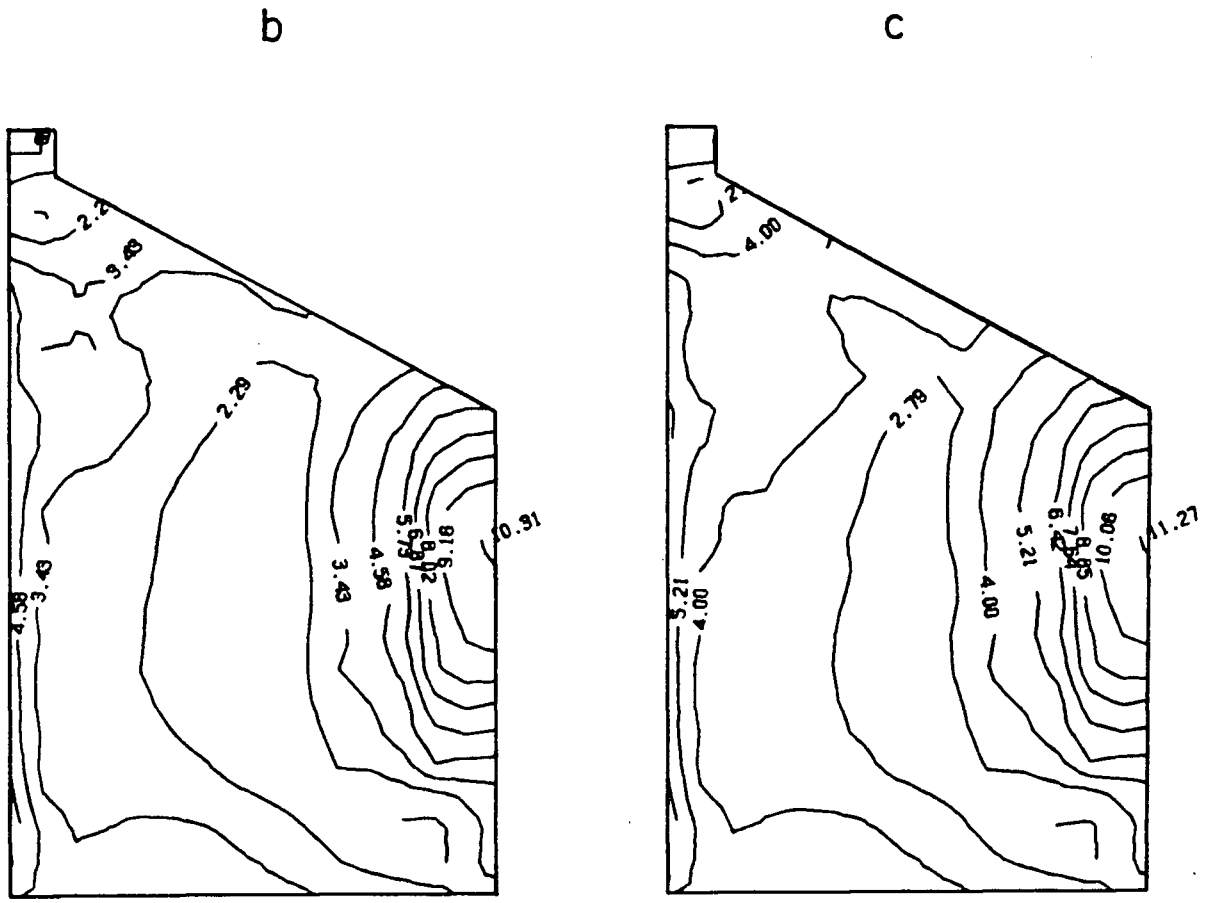

XIII.3.2.1 (a) Temperature and Von Mises Stress
(b) MRSS ; (c) MRSS-CRSS (Yield) .

a

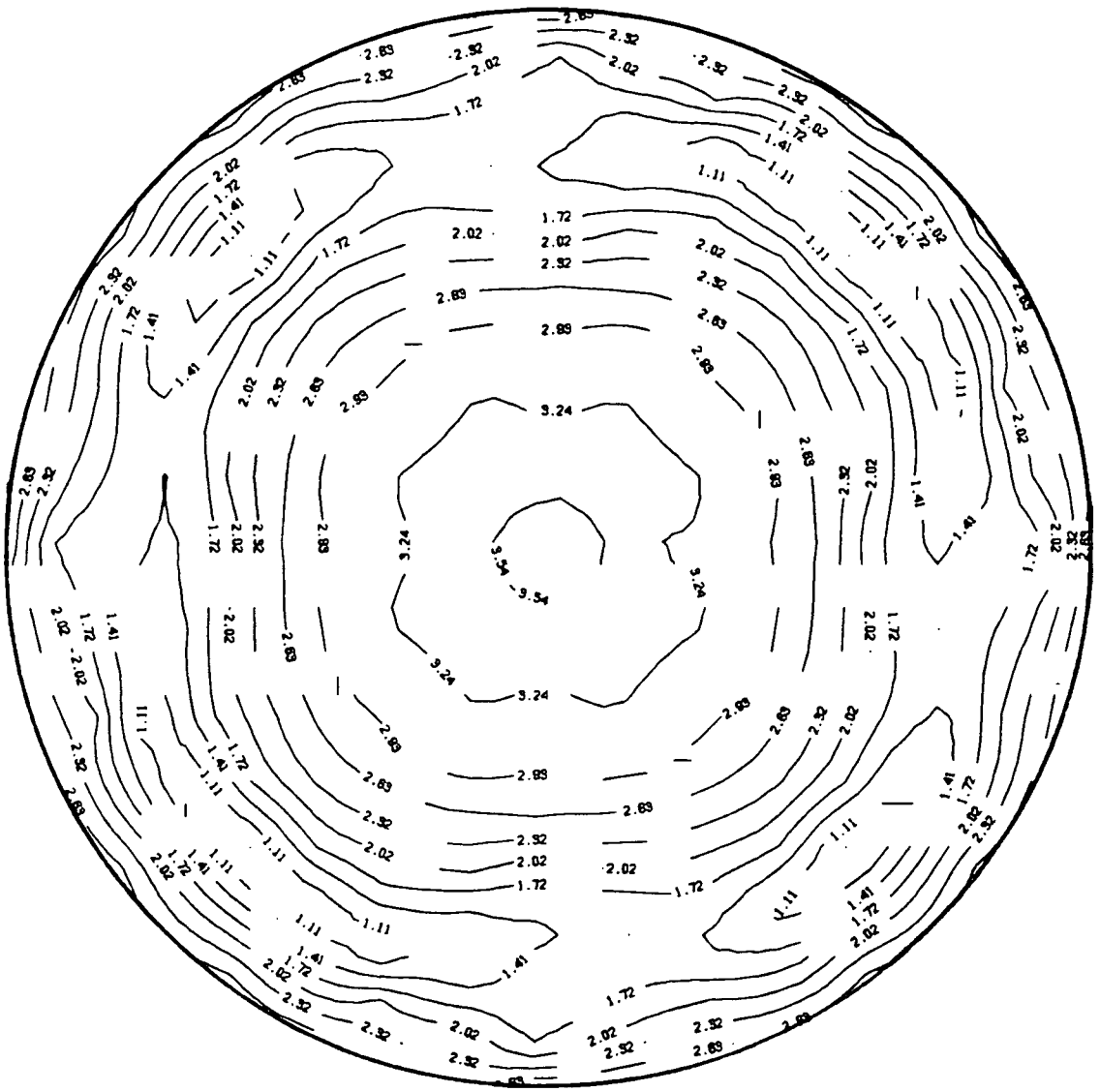

b

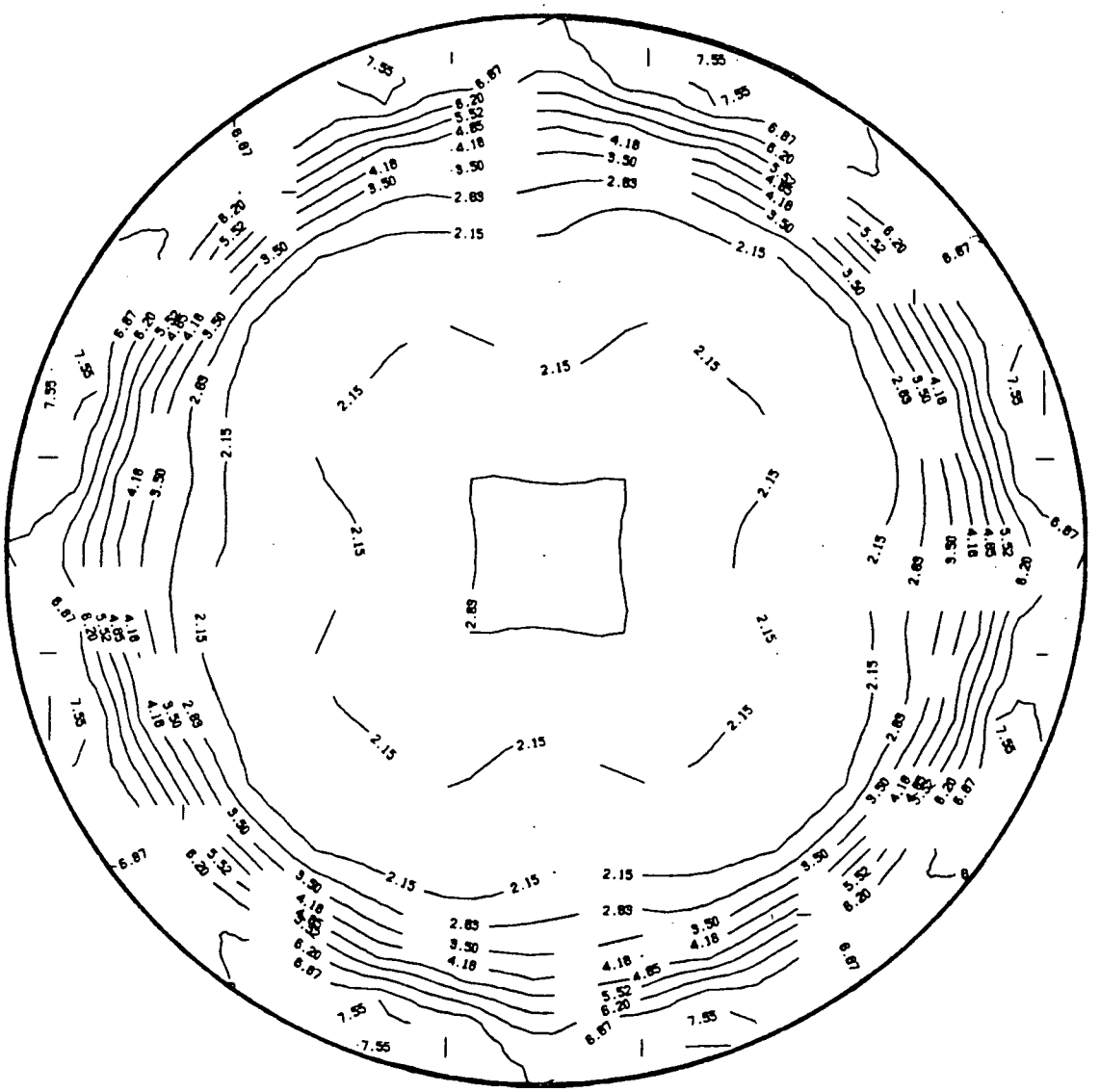

C

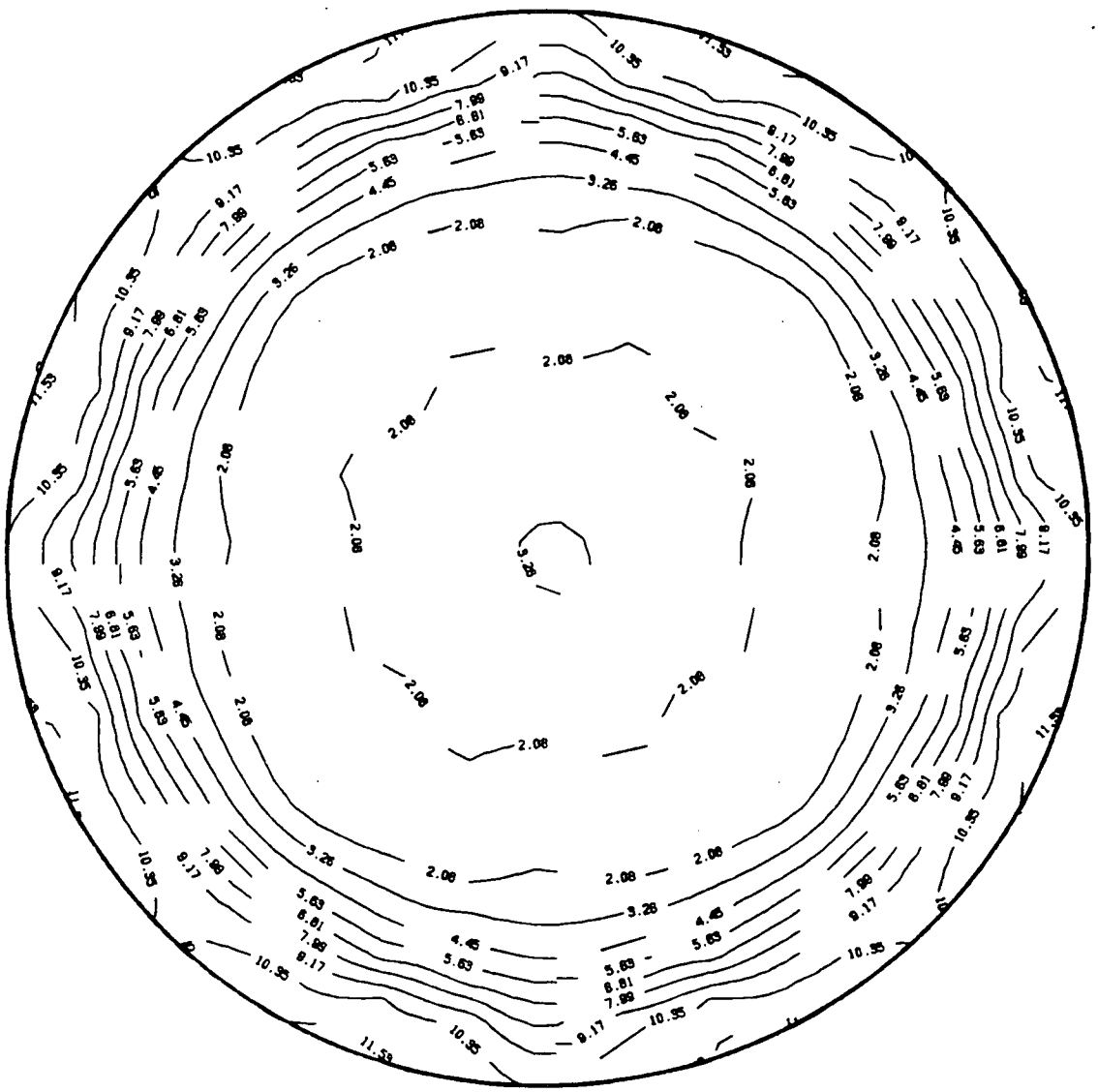

d

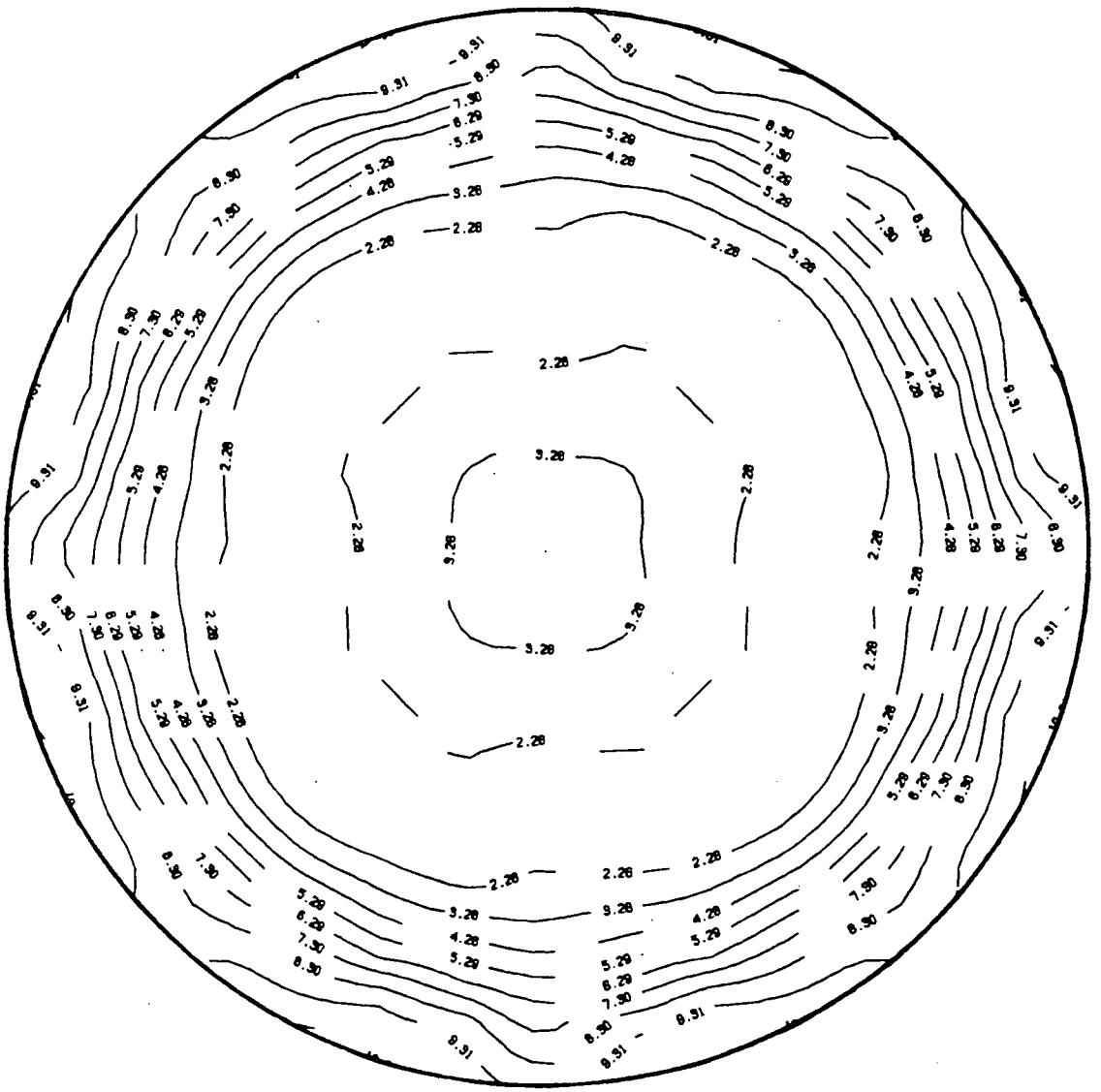

XIII.3.2.2 MRSS-CRSS (Yield) in cross-sections at a distance of the interface of
(a) 8 mm ; (b) 16 mm ; (c) 28 mm ; (d) 36 mm .

a

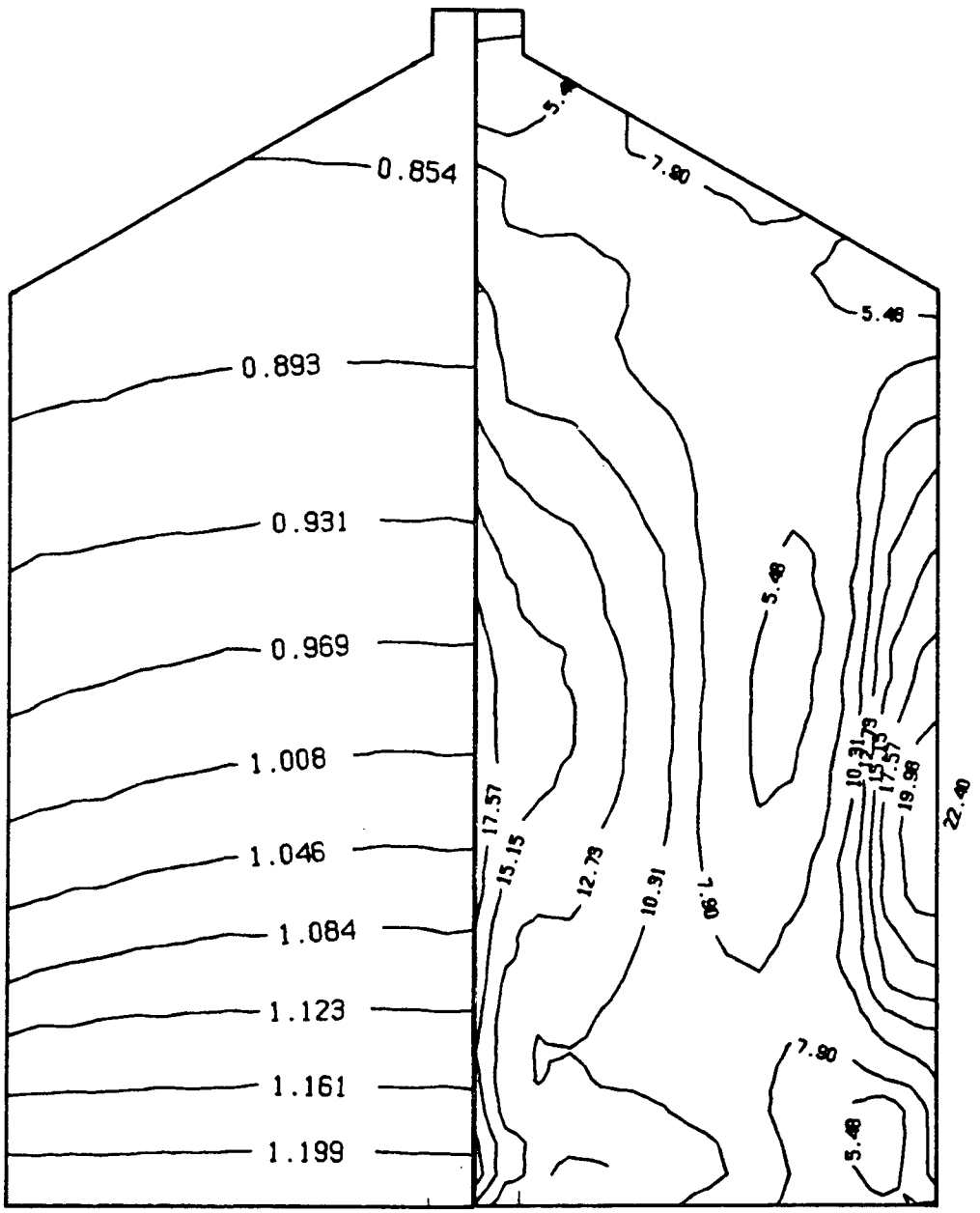
0.854
0.893
0.931
0.969
1.008
1.046
1.084
1.123
1.161
1.199
5.48
7.90
5.48
5.48
17.57
15.15
12.79
10.91
7.90
7.90
5.48
22.40

b

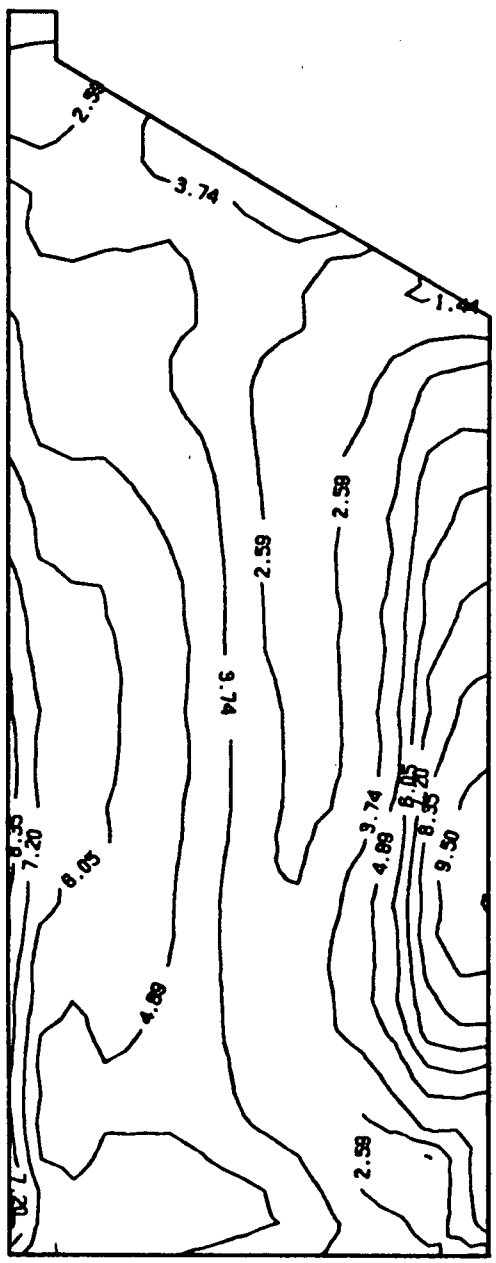
2.59
3.74
1.44
2.59
2.59
3.74
7.20
8.05
4.89
3.74
4.89
8.50
9.50
2.59
7.20

c

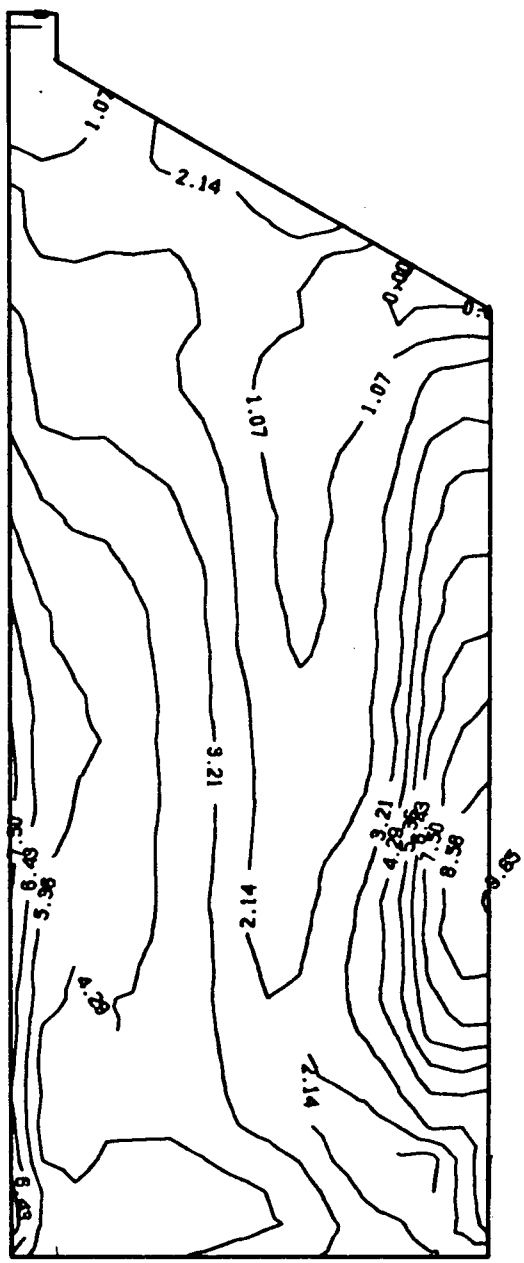
1.07
2.14
0.00
1.07
1.07
3.21
2.14
5.36
4.29
3.21
8.58
2.14

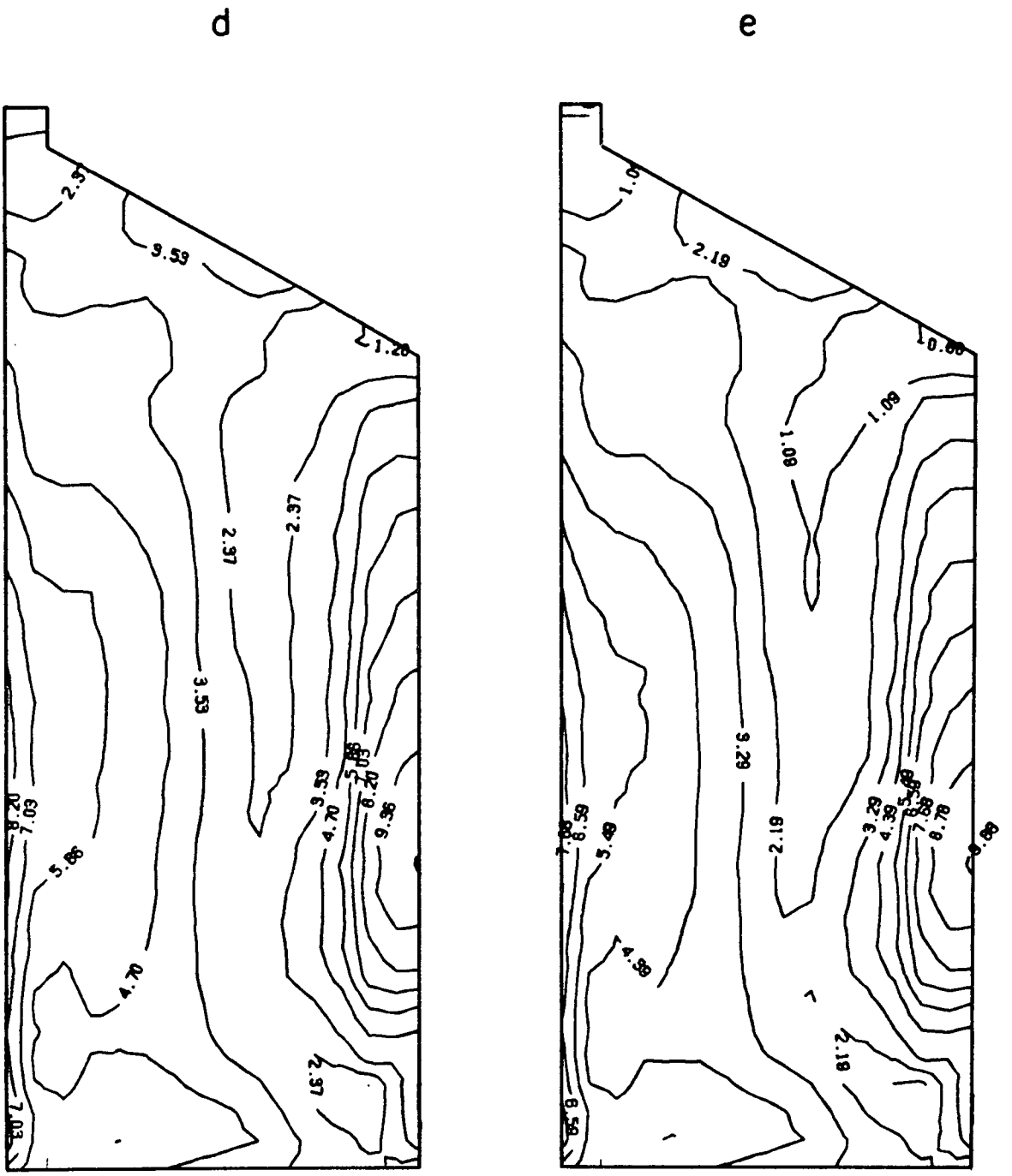

XIII.3.3.1 (a) Temperature and Von Mises Stress
(b) MRSS ; (c) MRSS-CRSS (Yield) ;
(d) MRSS-CRSS (MB) ; (e) MRSS-CRSS (MBTe) .

a

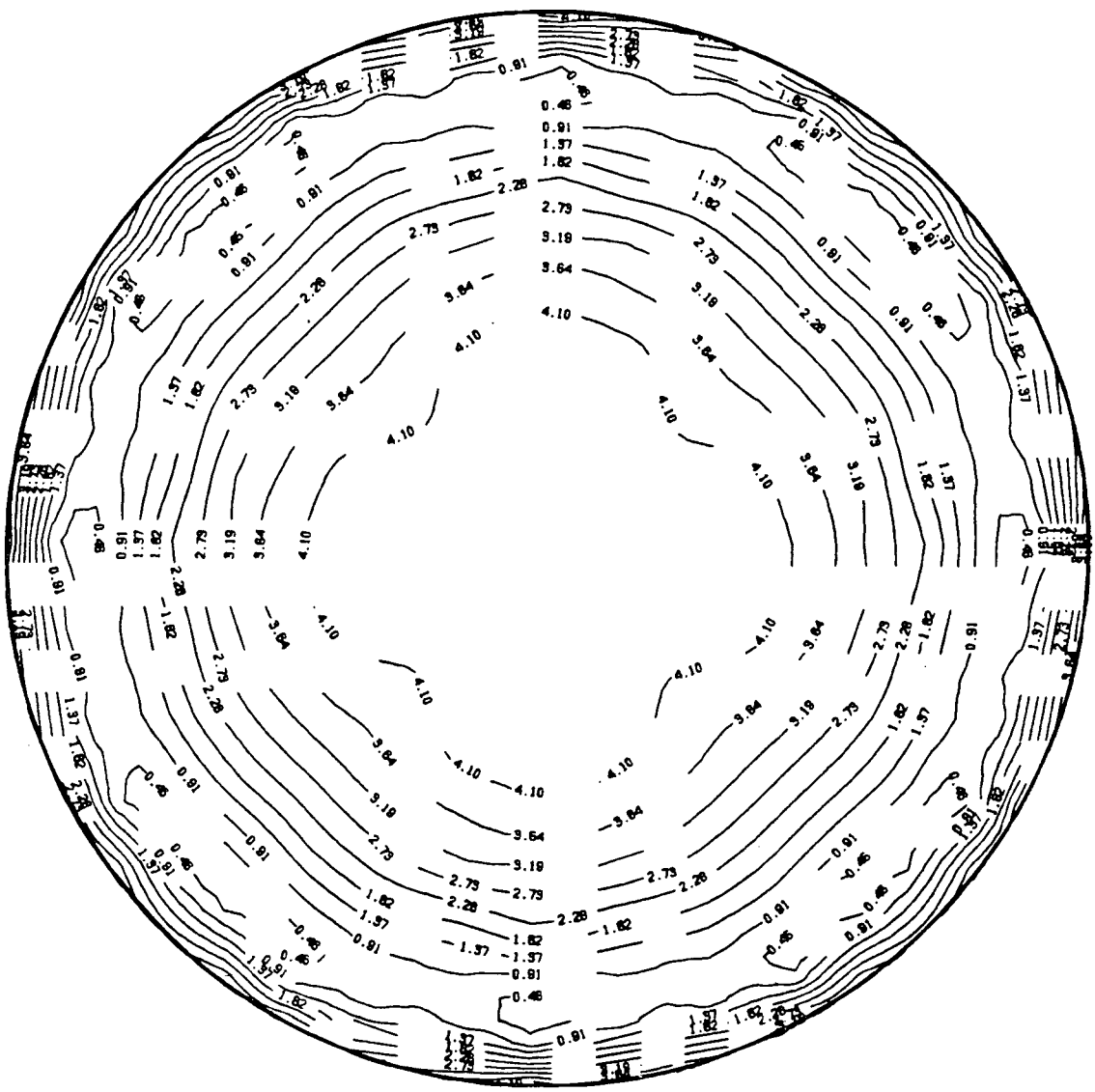

b

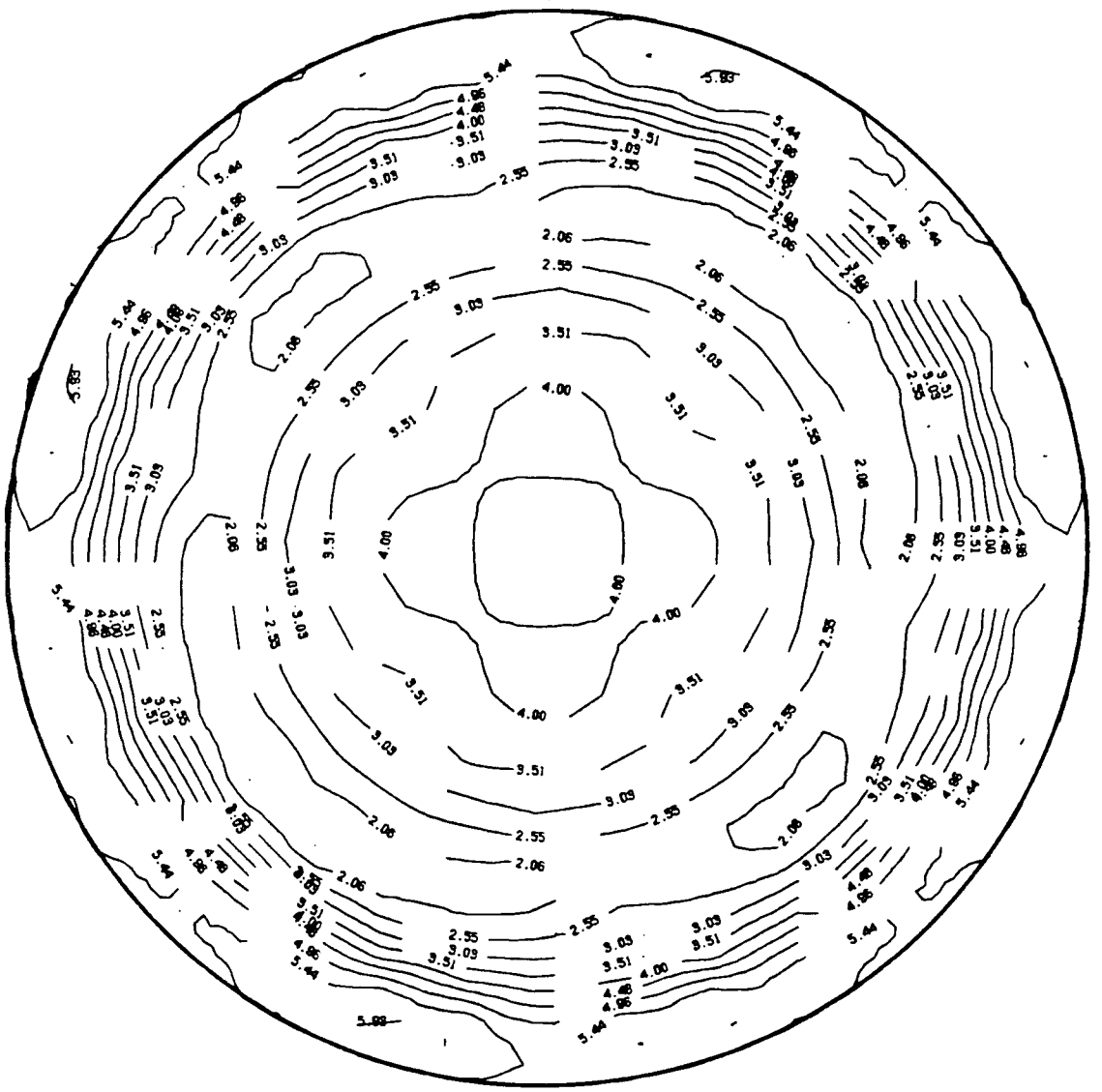

C

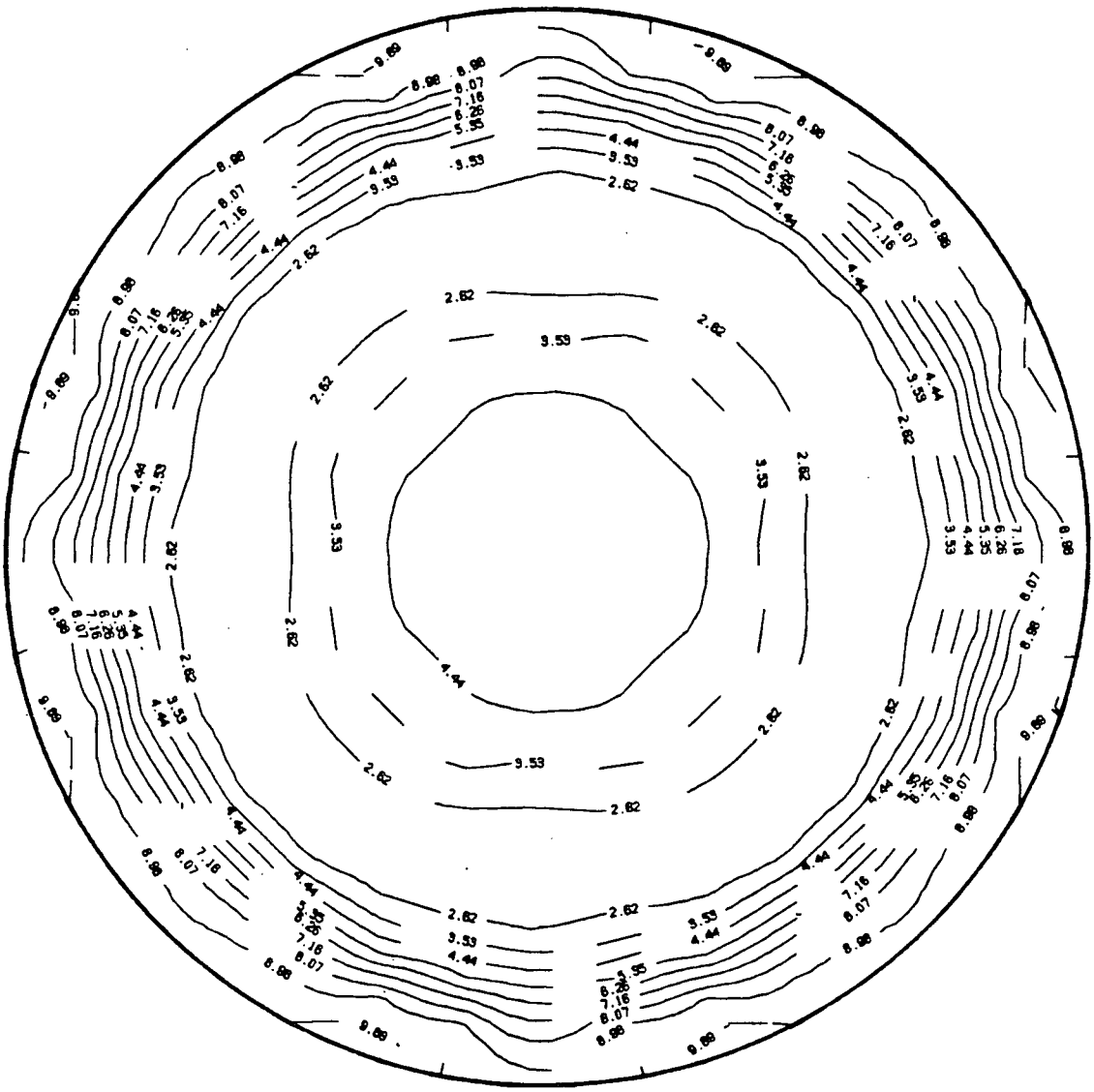

d

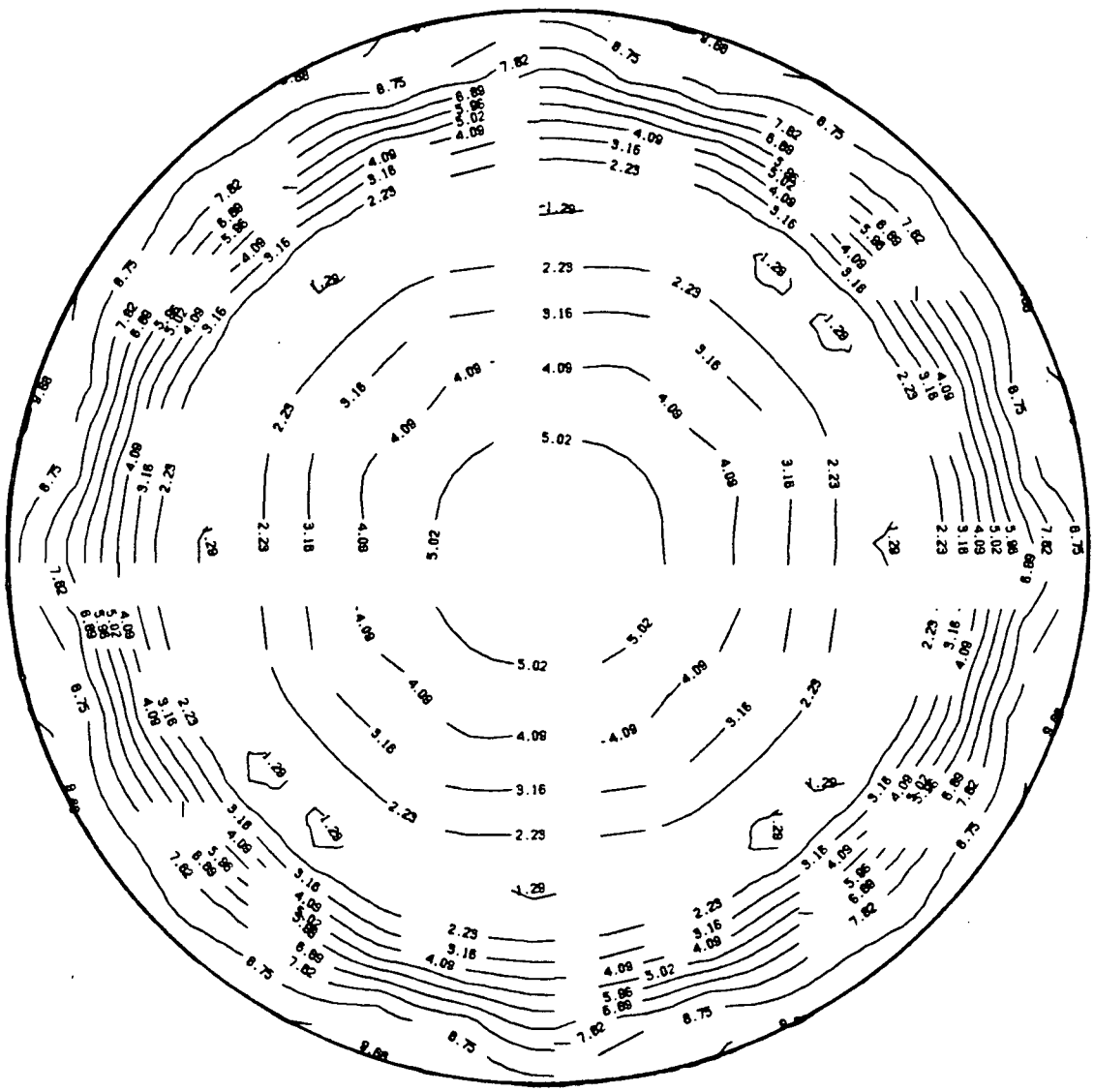

e

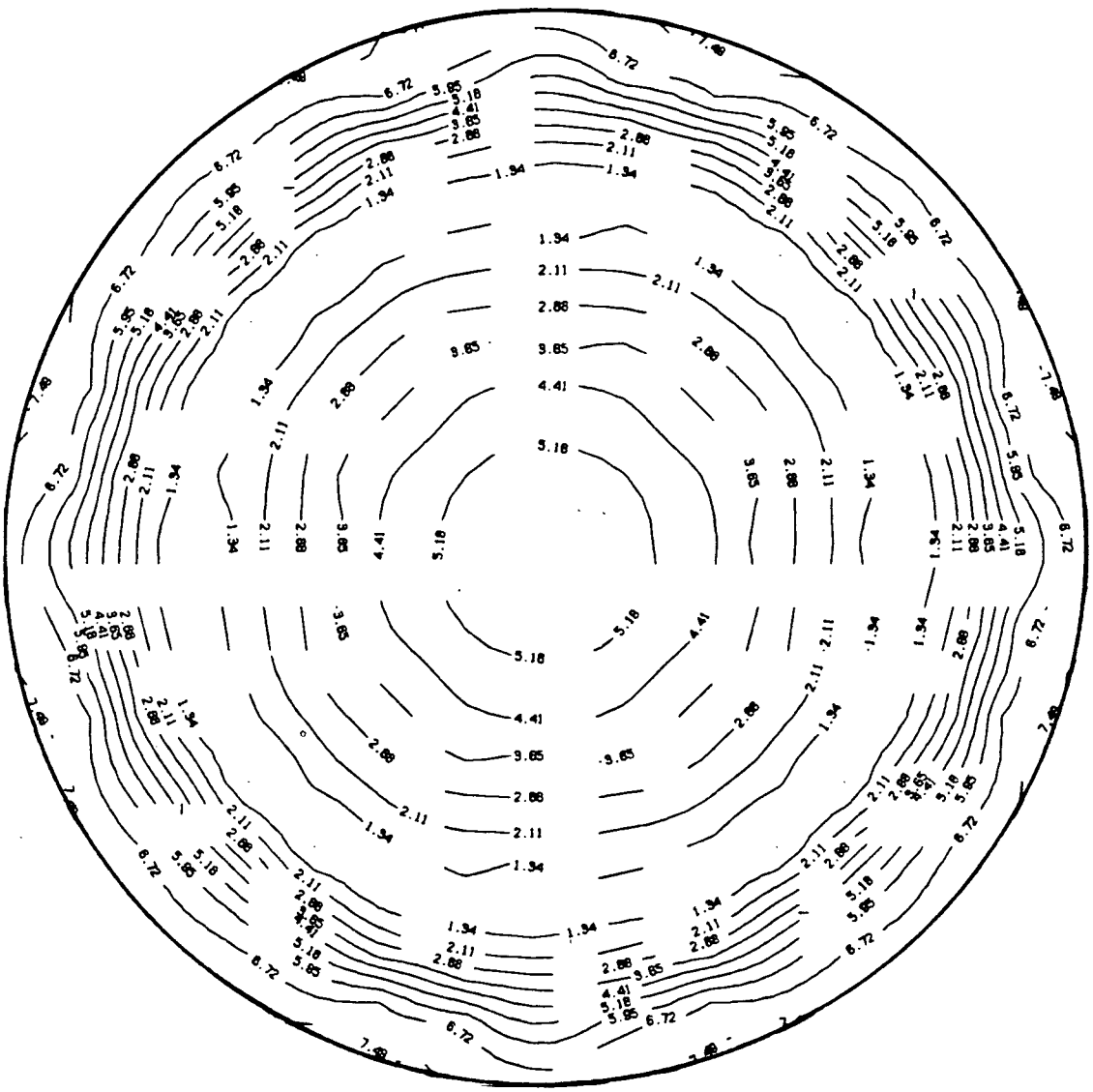

f

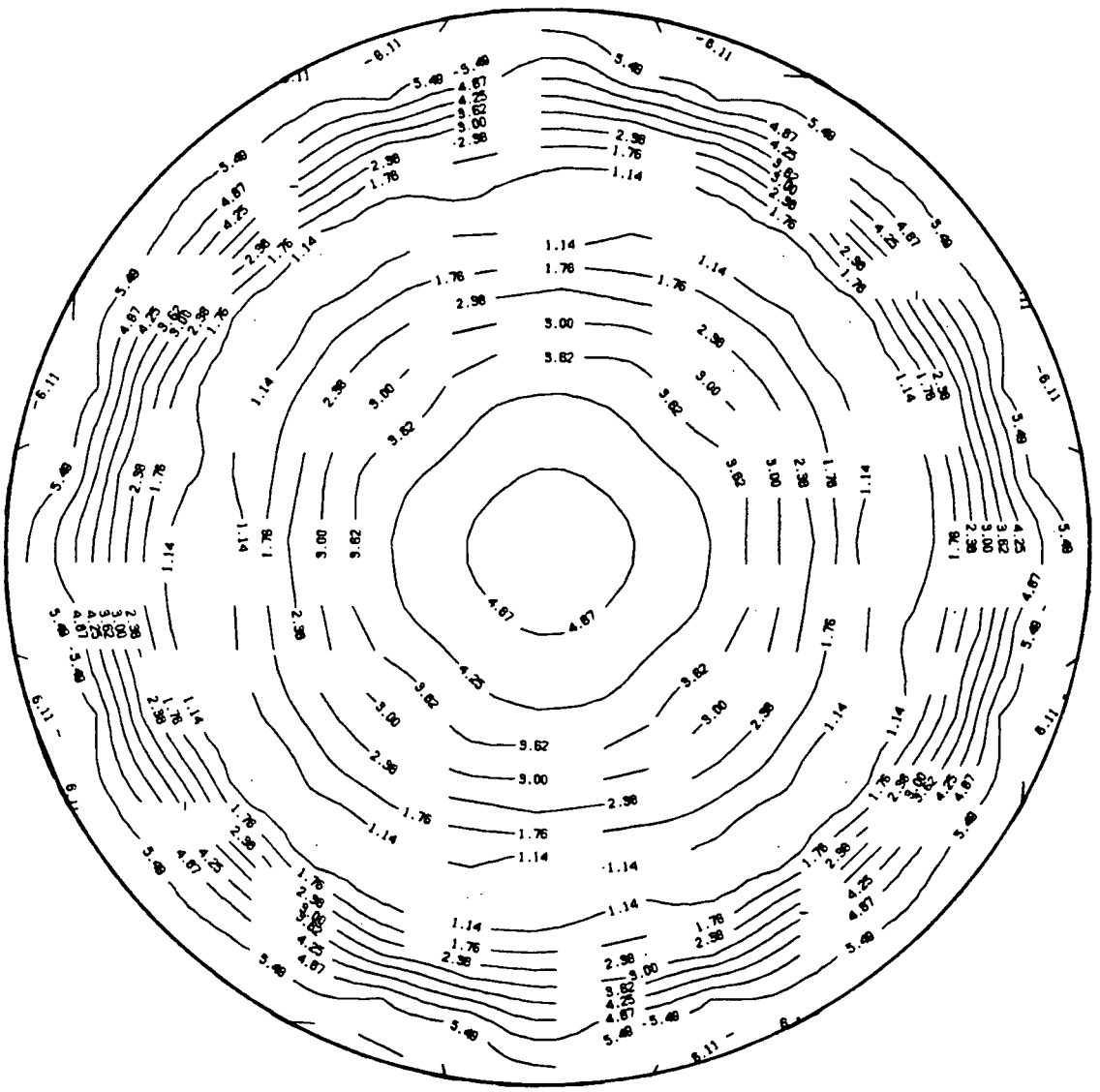

g

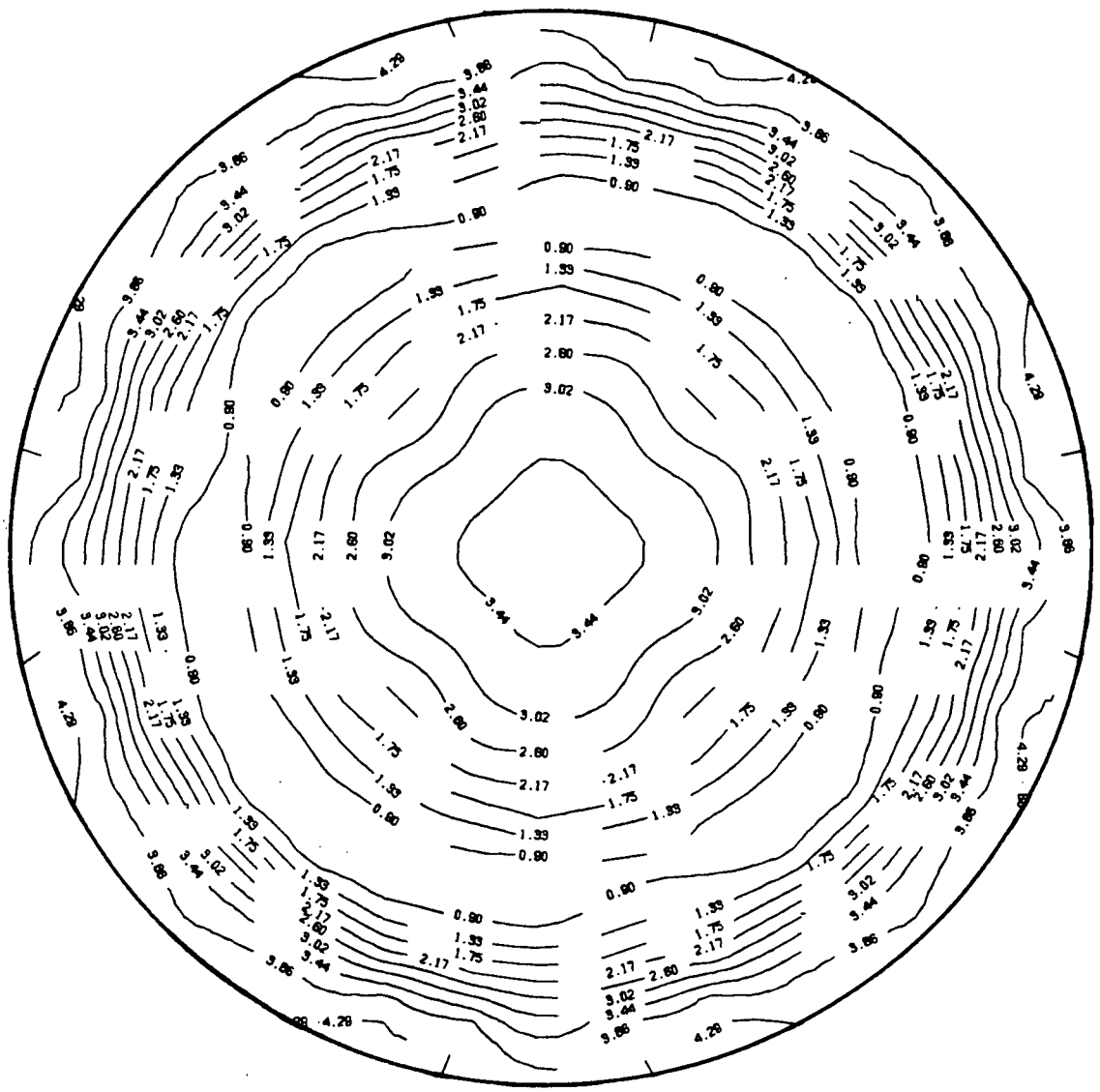

h

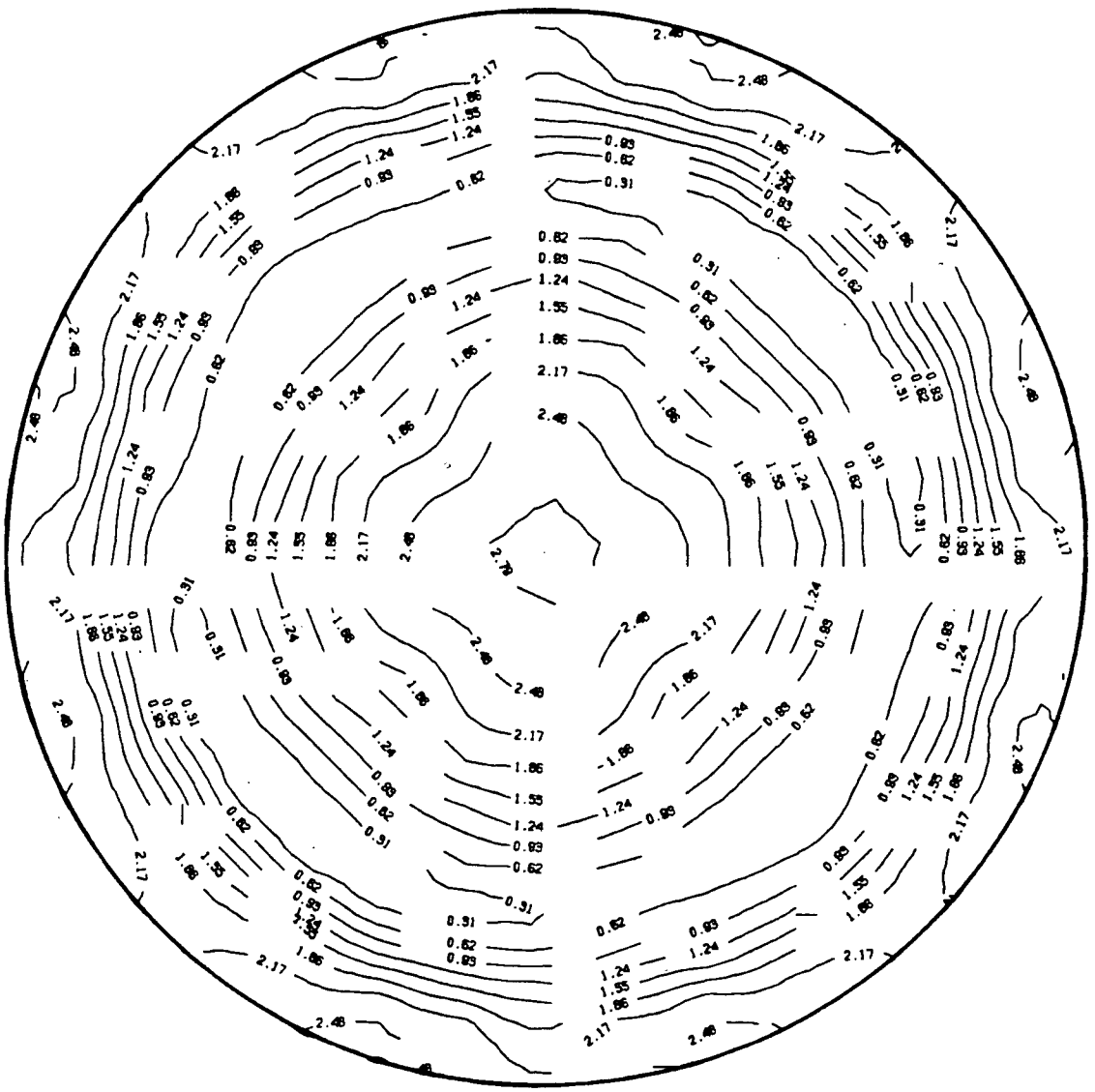

XIII.3.3.2 MRSS-CRSS (Yield) in cross-sections at a distance of the interface of
(a) 8 mm ; (b) 16 mm ; (c) 28 mm ; (d) 36 mm ;
(e) 48 mm ; (f) 56 mm ; (g) 68 mm ; (h) 76 mm .

a

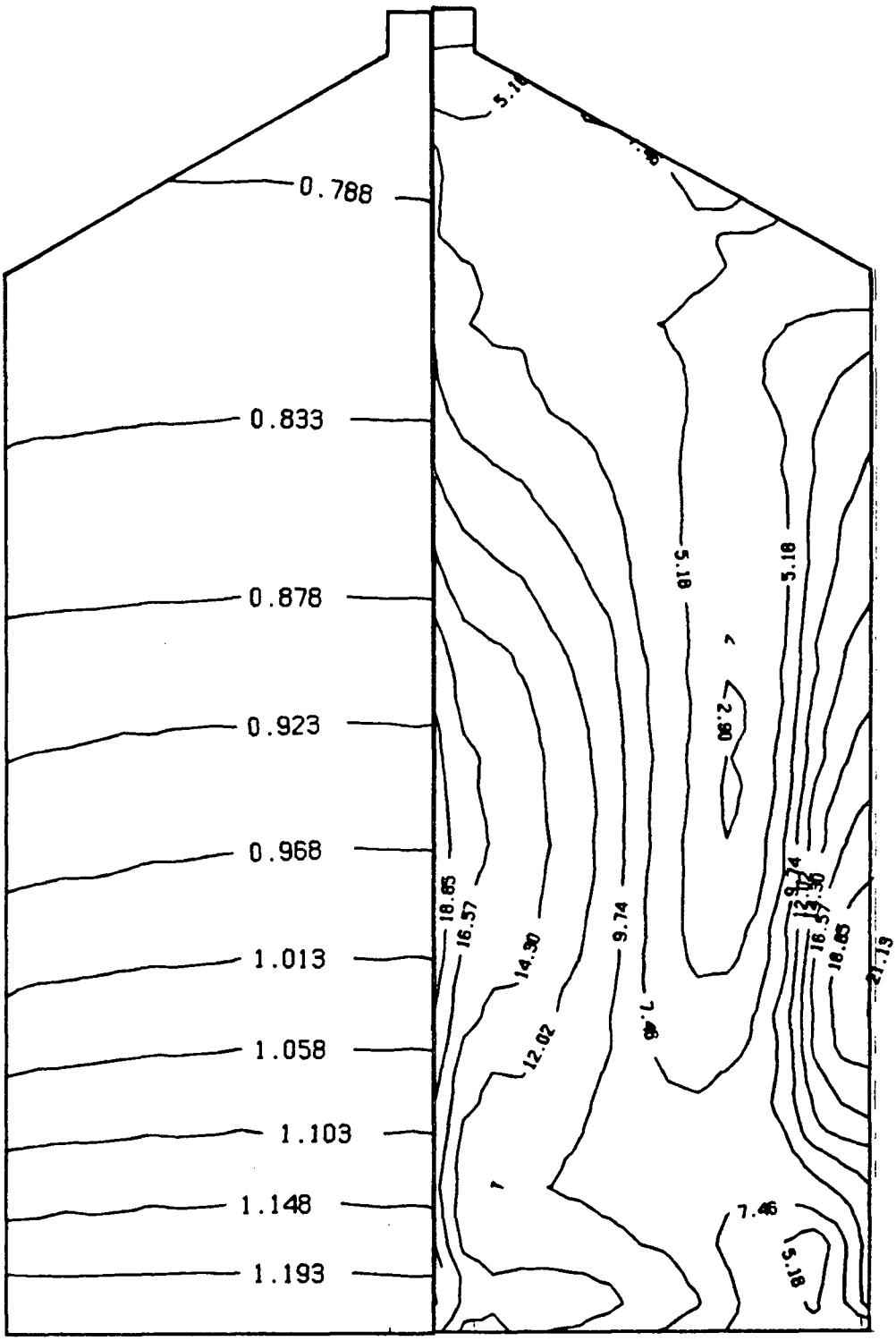
0.788
0.833
0.878
0.923
0.968
1.013
1.058
1.103
1.148
1.193
5.18
2.80
9.74
12.02
14.30
16.57
18.85
21.13
7.46

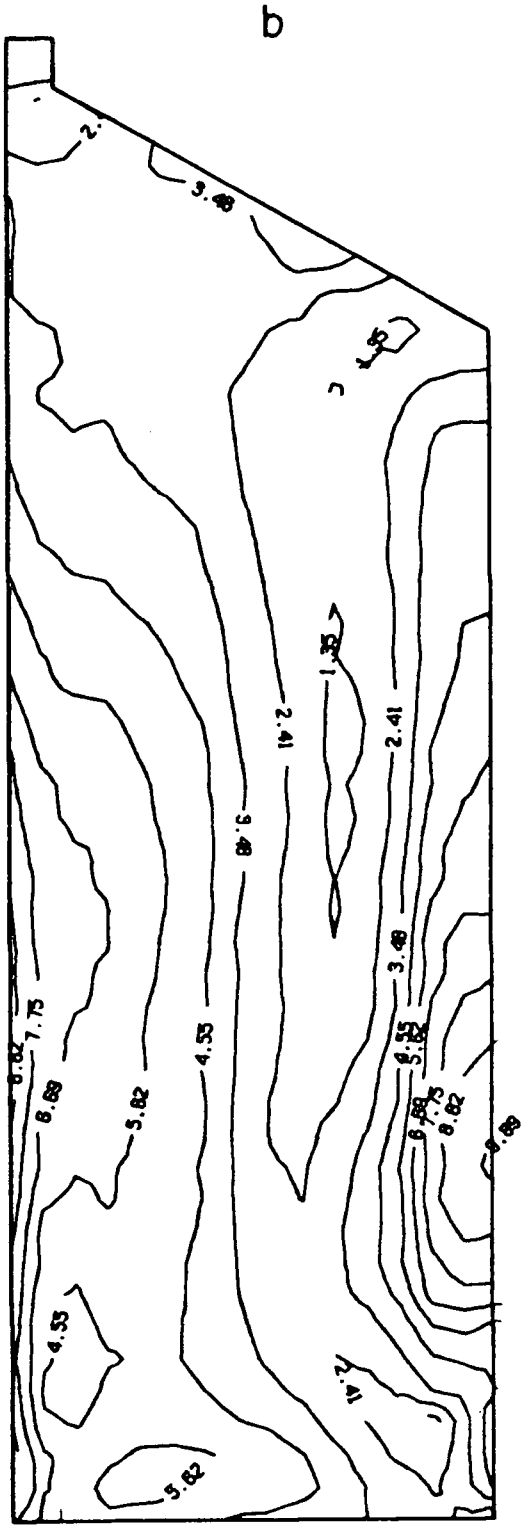
b
3.48
1.35
2.41
3.48
4.55
5.62
6.69
7.75
8.82
8.89
2.41
4.55
5.62

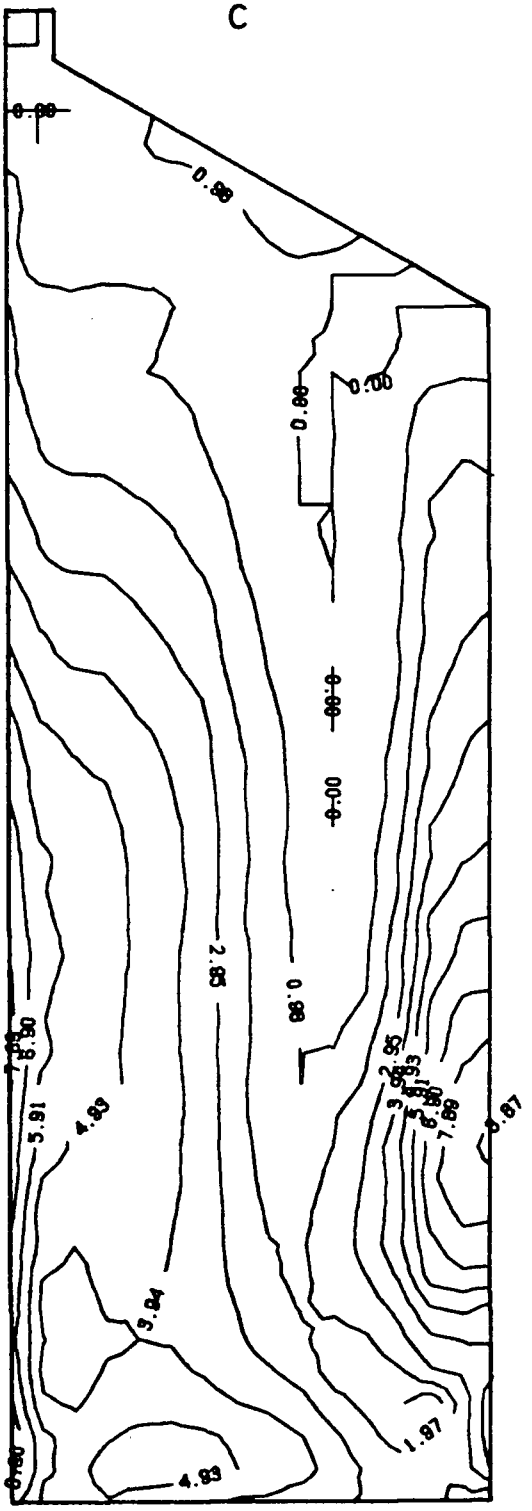
c
0.00
0.00
0.00
0.00
0.00
2.95
4.93
5.91
3.94
4.93
1.97
7.89
8.87

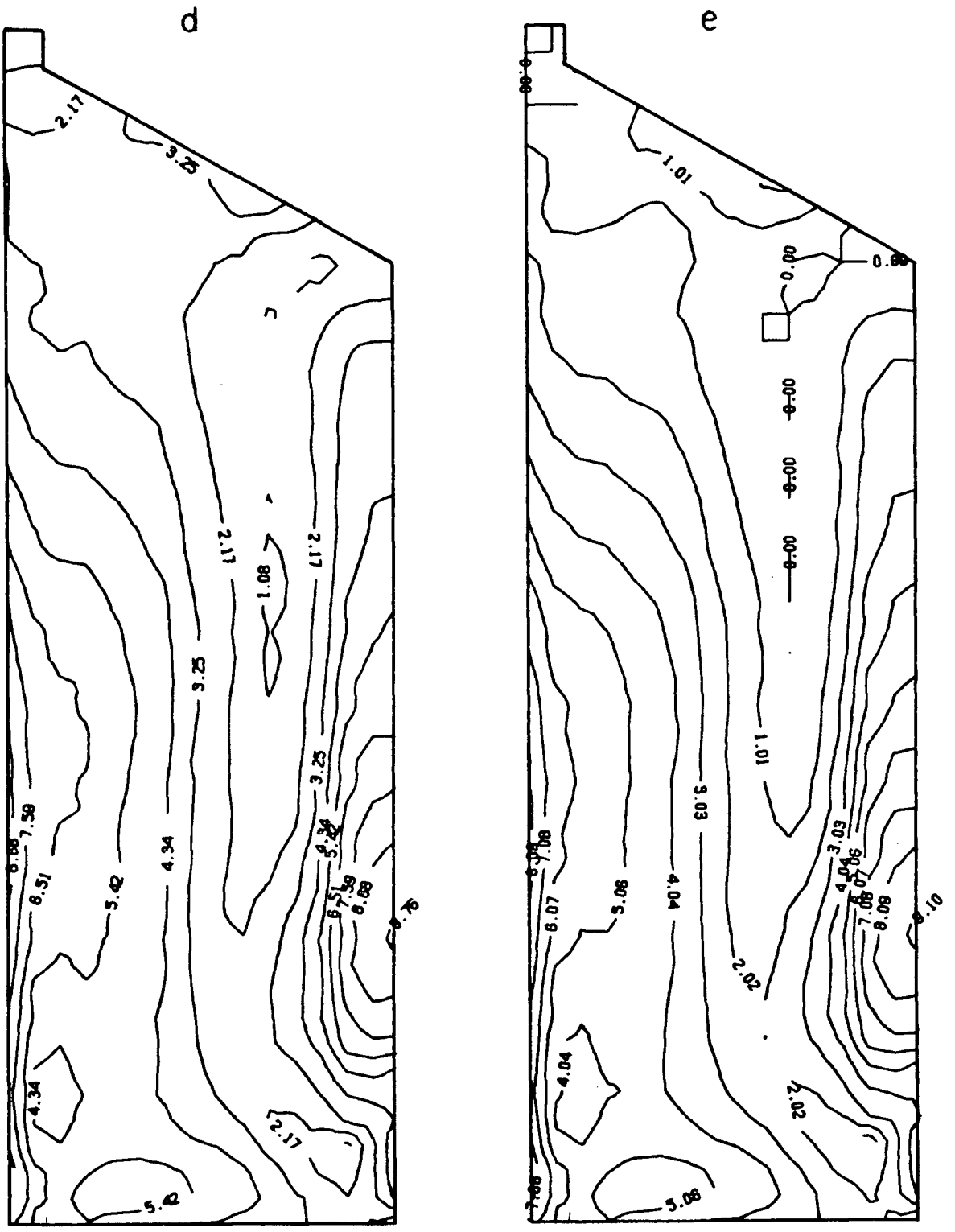

XIII.3.4 CL, 100 mm
(a) Temperature and Von Mises Stress
(b) MRSS ; (c) MRSS-CRSS (Yield) ;
(d) MRSS-CRSS (MB) ; (e) MRSS-CRSS (MBTe) .

a

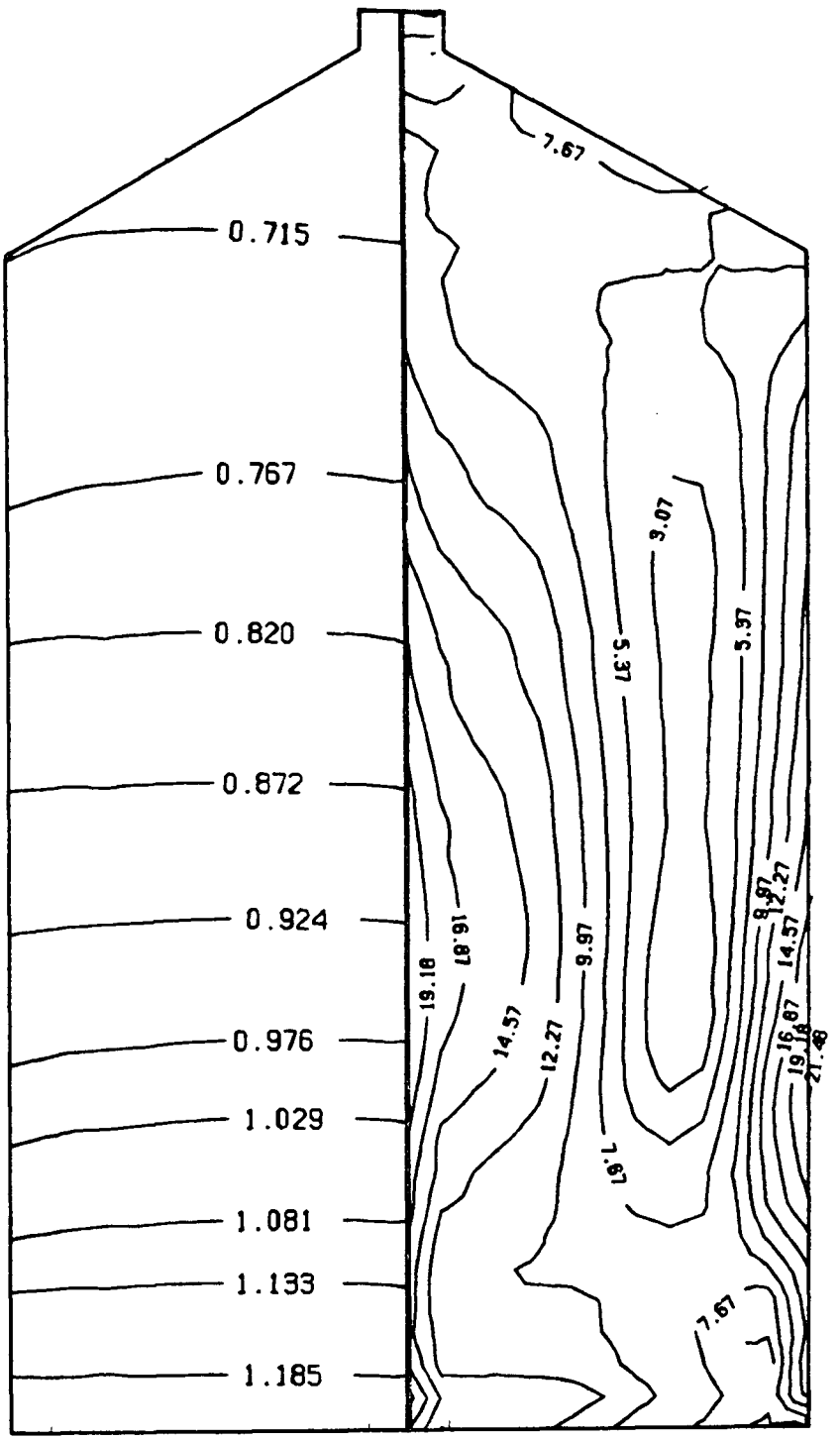
0.715
0.767
0.820
0.872
0.924
0.976
1.029
1.081
1.133
1.185
7.67
3.07
5.37
5.97
19.18
16.87
14.57
12.27
9.97
7.67
12.27
14.57
16.87
21.48
7.67

b

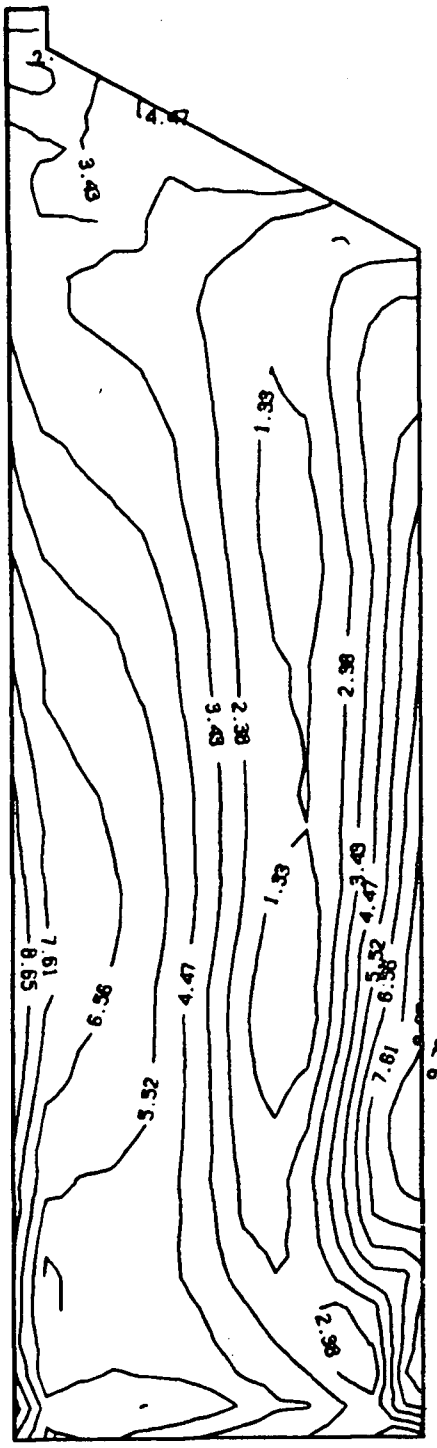
4.47
3.43
1.33
2.38
3.43
2.38
1.33
3.43
4.47
5.52
6.56
7.61
9.70
8.65
7.61
6.56
5.52
4.47
2.38

c

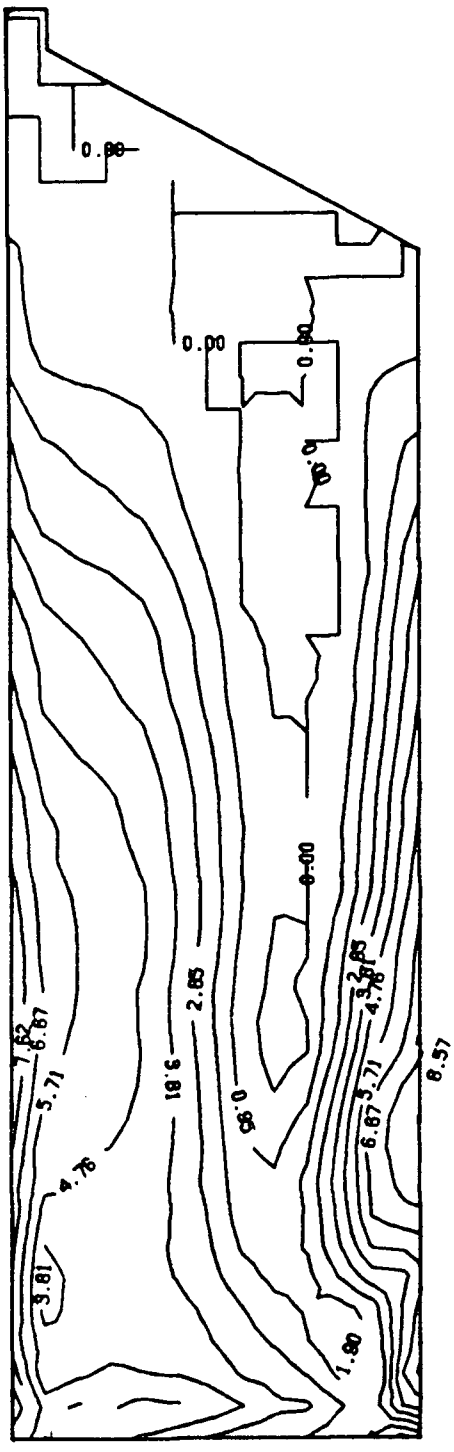
0.00
0.00
0.00
0.00
0.00
2.85
3.81
0.95
7.62
6.67
5.71
4.76
3.81
1.90
2.85
3.81
4.76
5.71
6.67
8.57

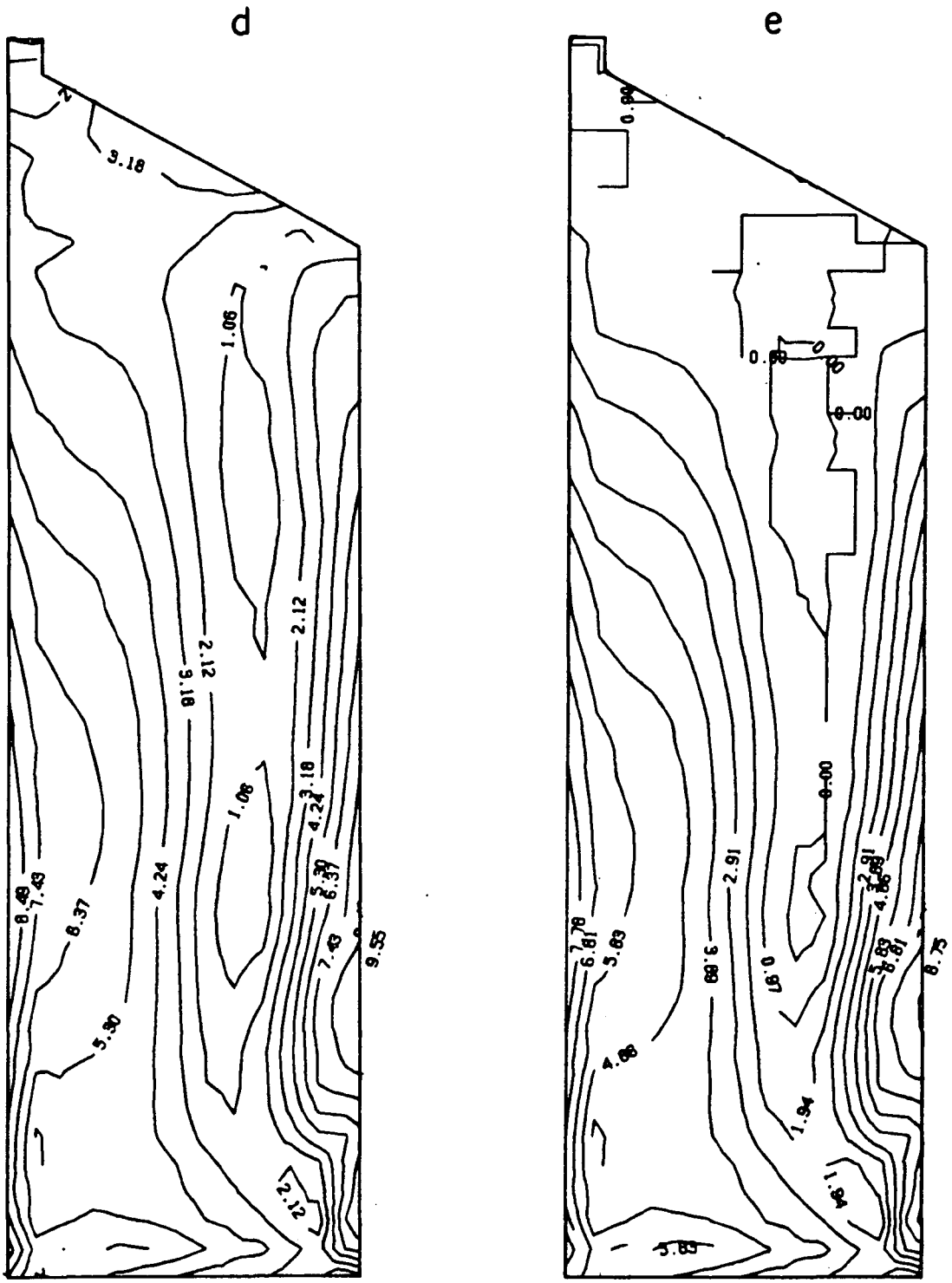

XIII.3.5.1 (a) Temperature and Von Mises Stress
(b) MRSS ; (c) MRSS-CRSS (Yield) ;
(d) MRSS-CRSS (MB) ; (e) MRSS-CRSS (MBTe) .

a

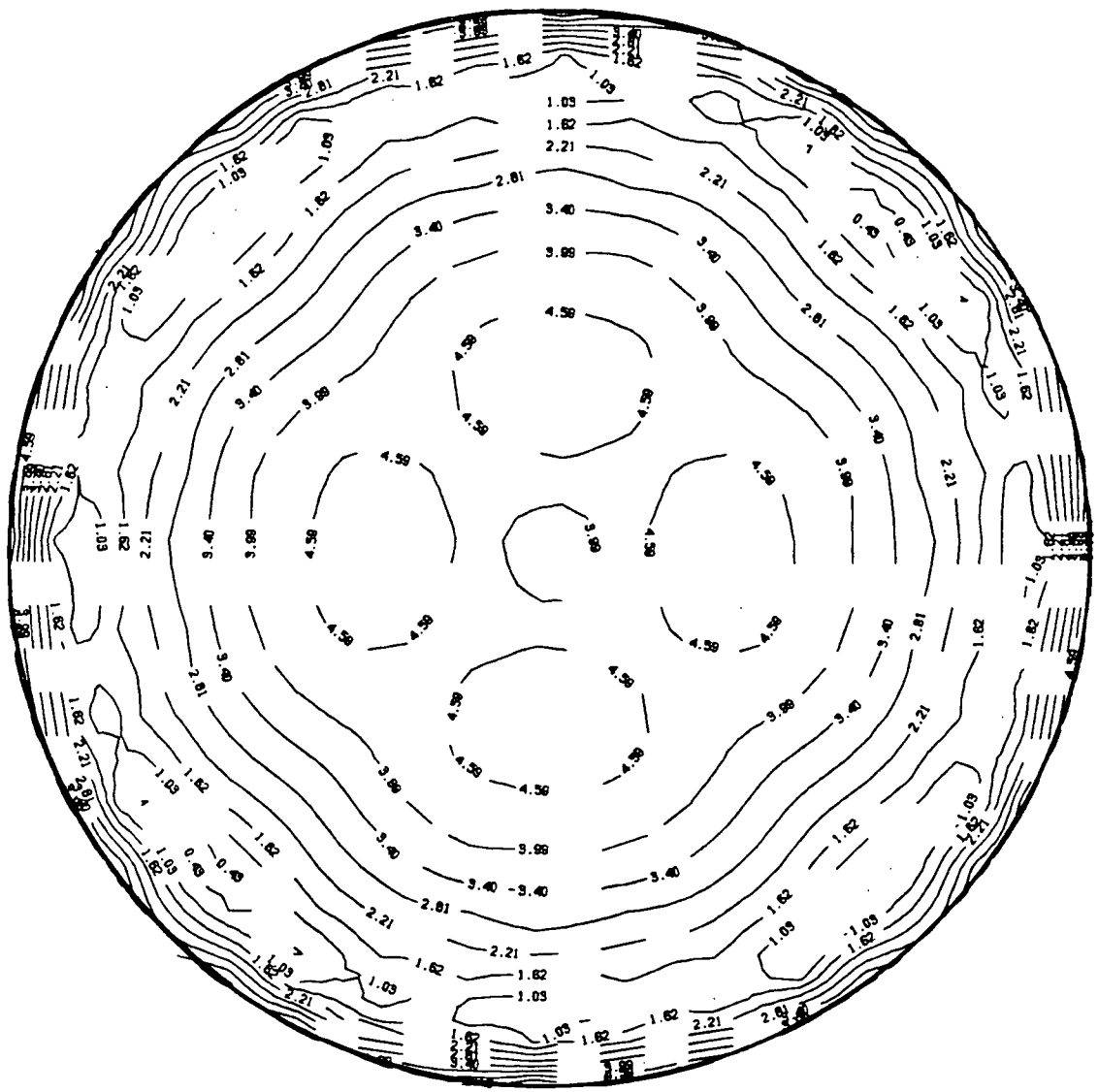

b

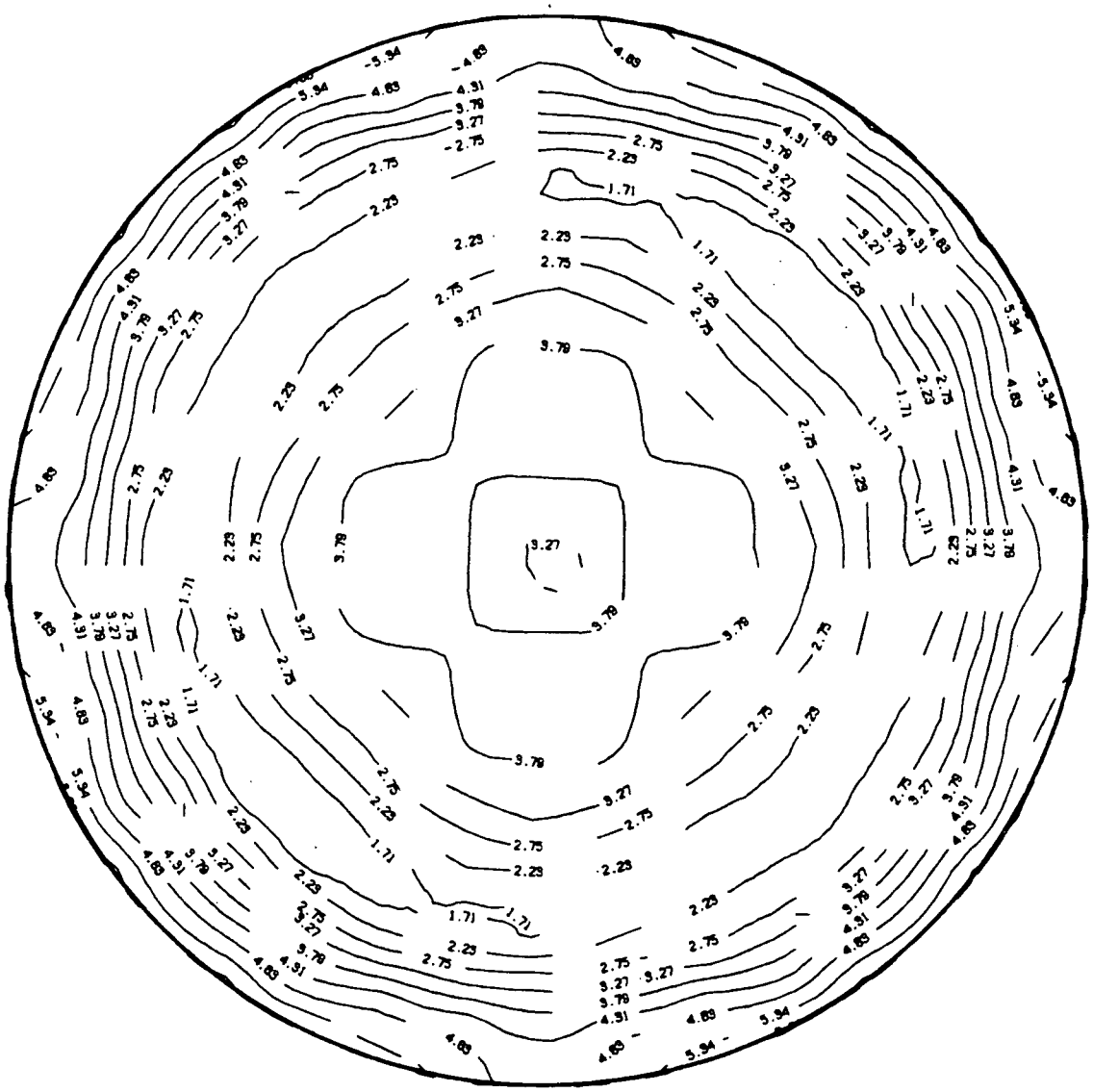

C

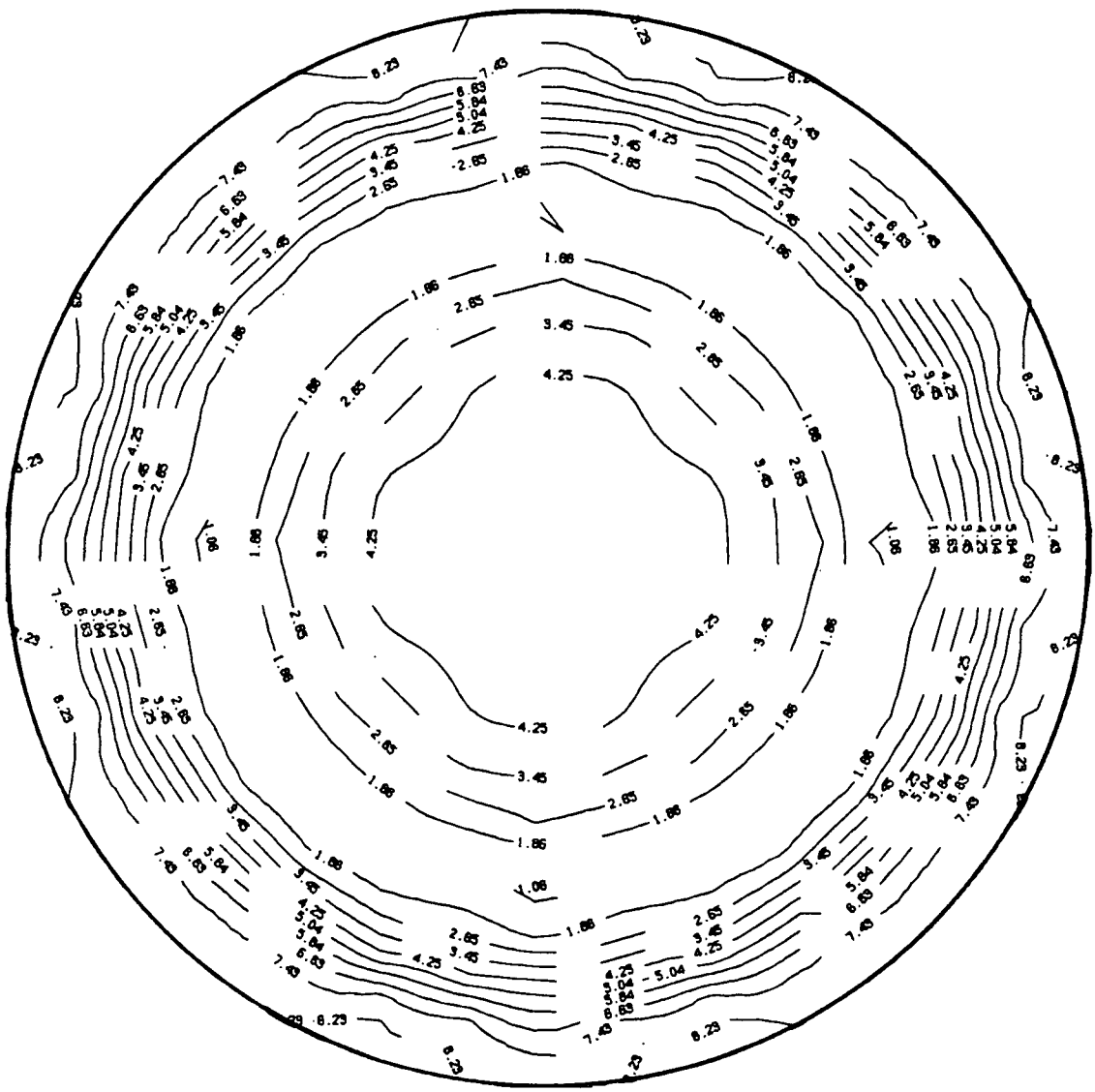

d

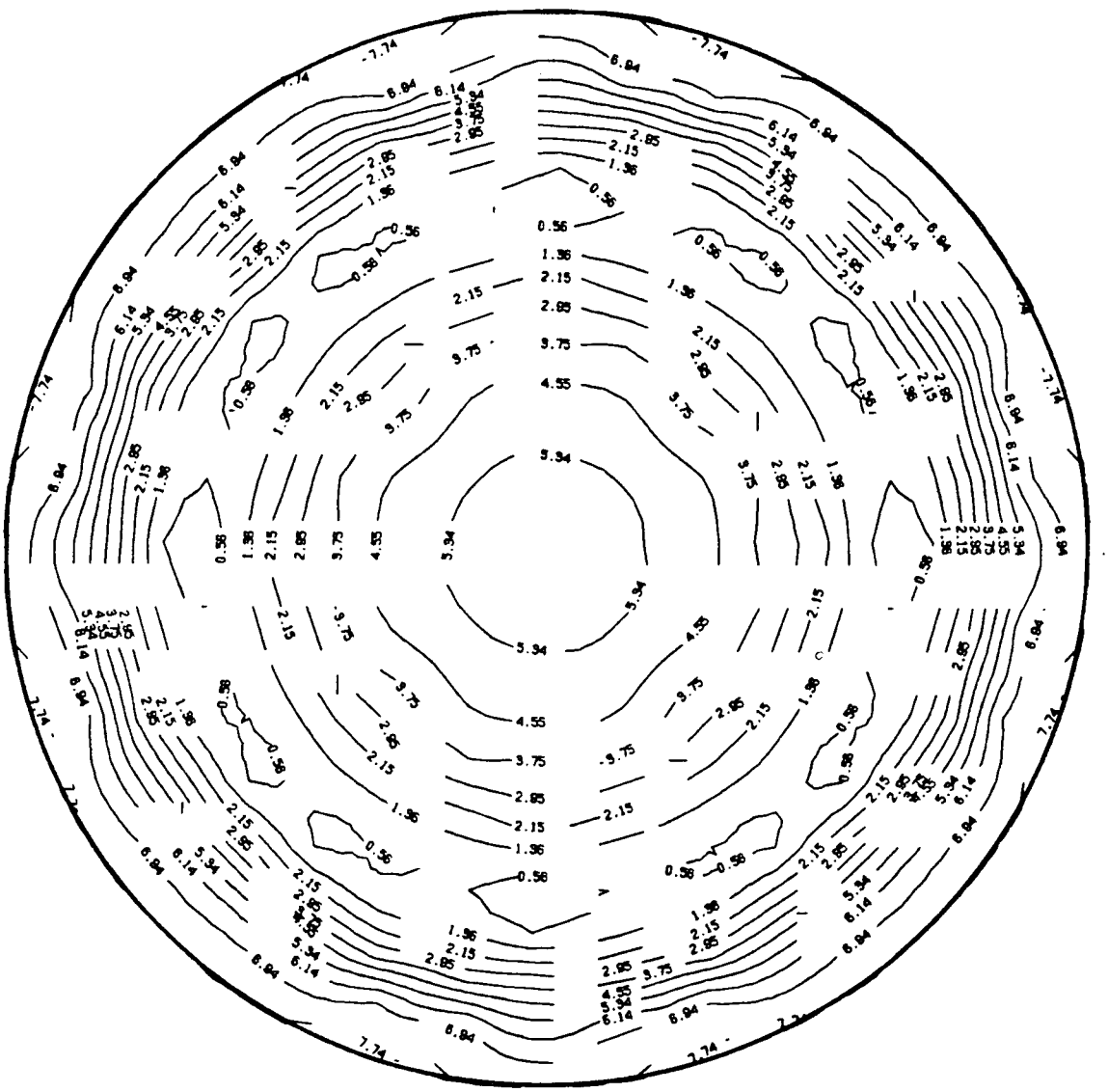

e

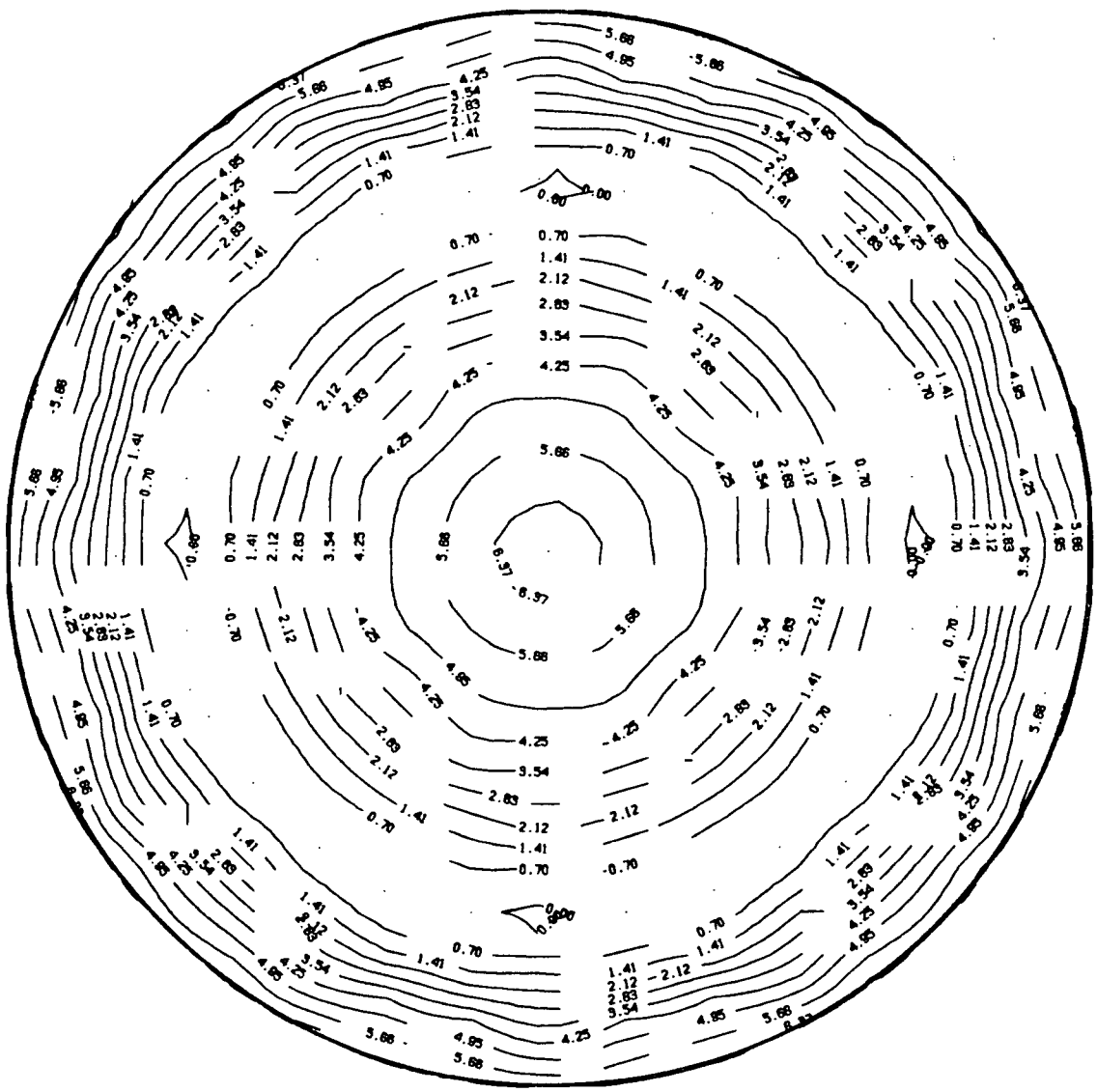
5.66
4.95
4.25
3.54
2.83
2.12
1.41
0.70
0.00
-0.70
-1.41
-2.12
-2.83
-3.54
-4.25
-4.95
-5.66
-6.37

f

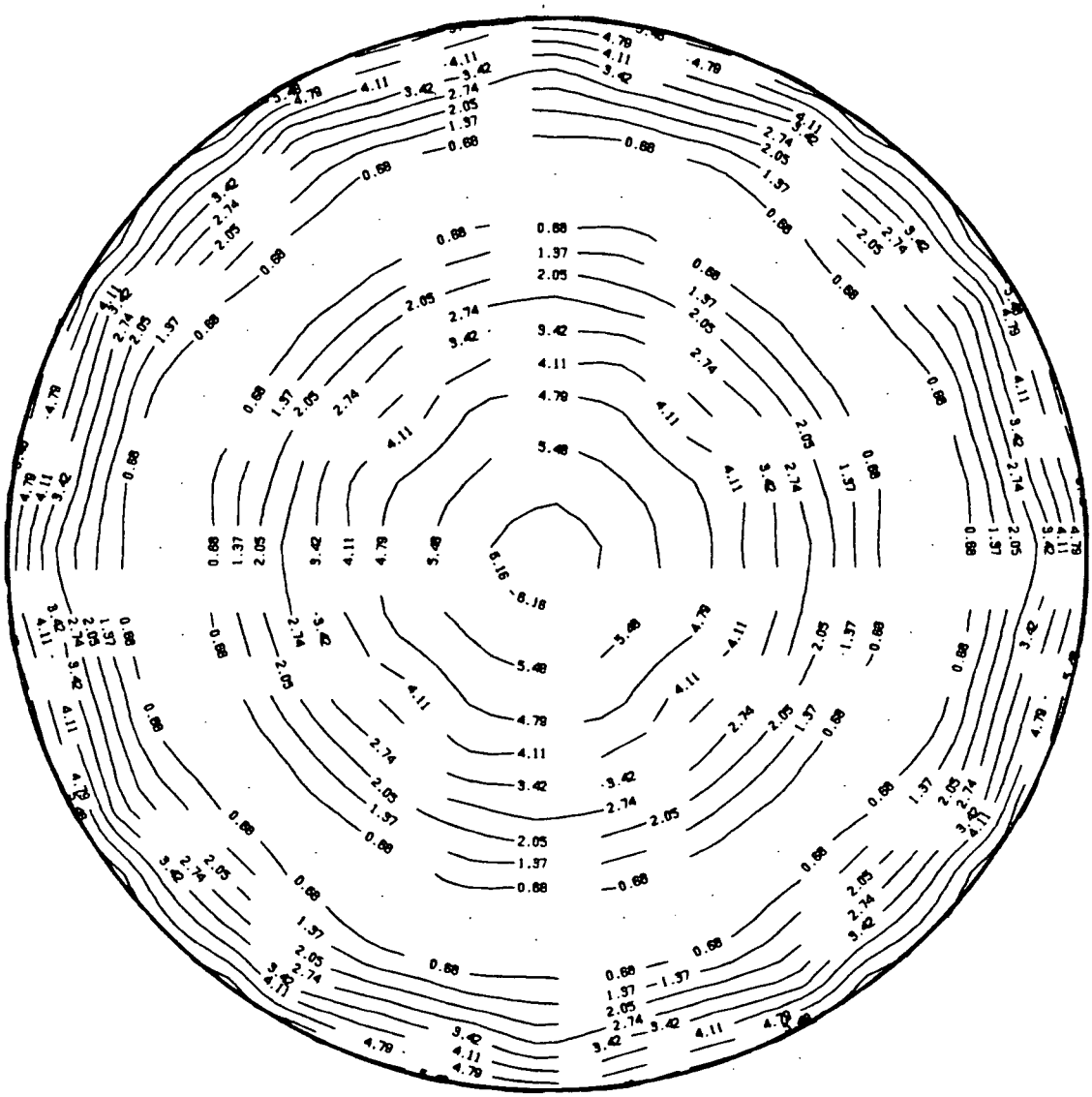

g

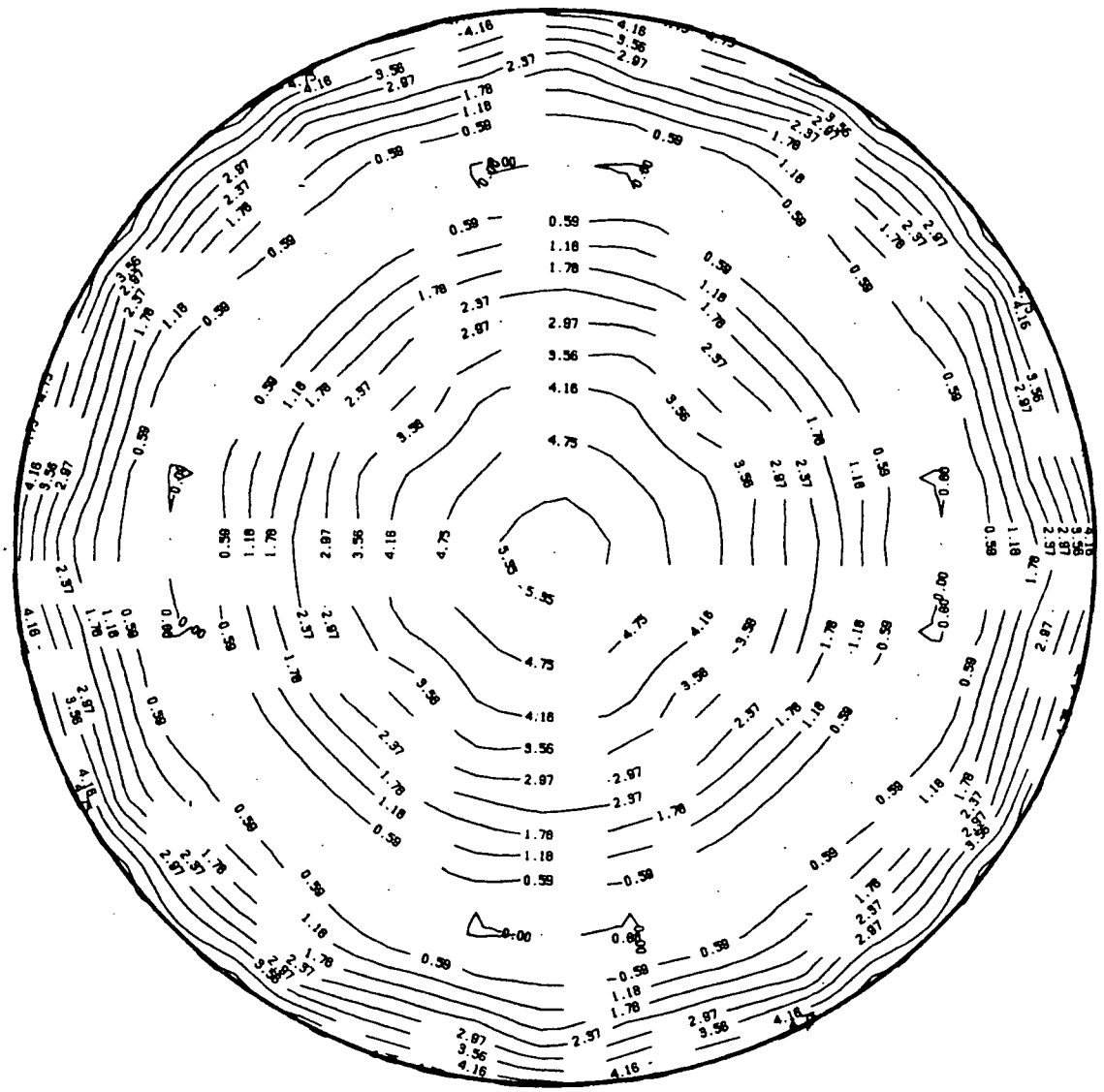

h

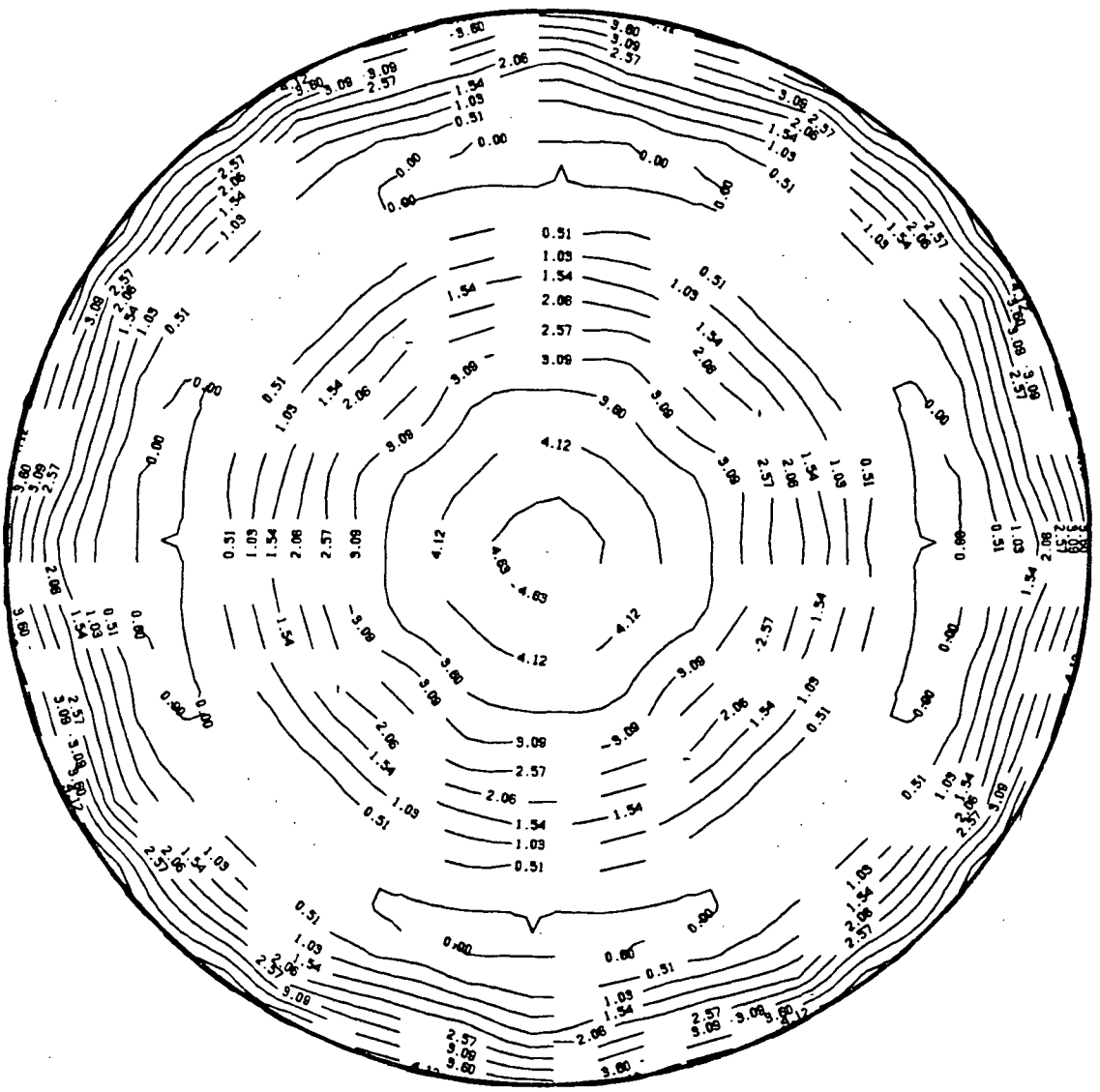

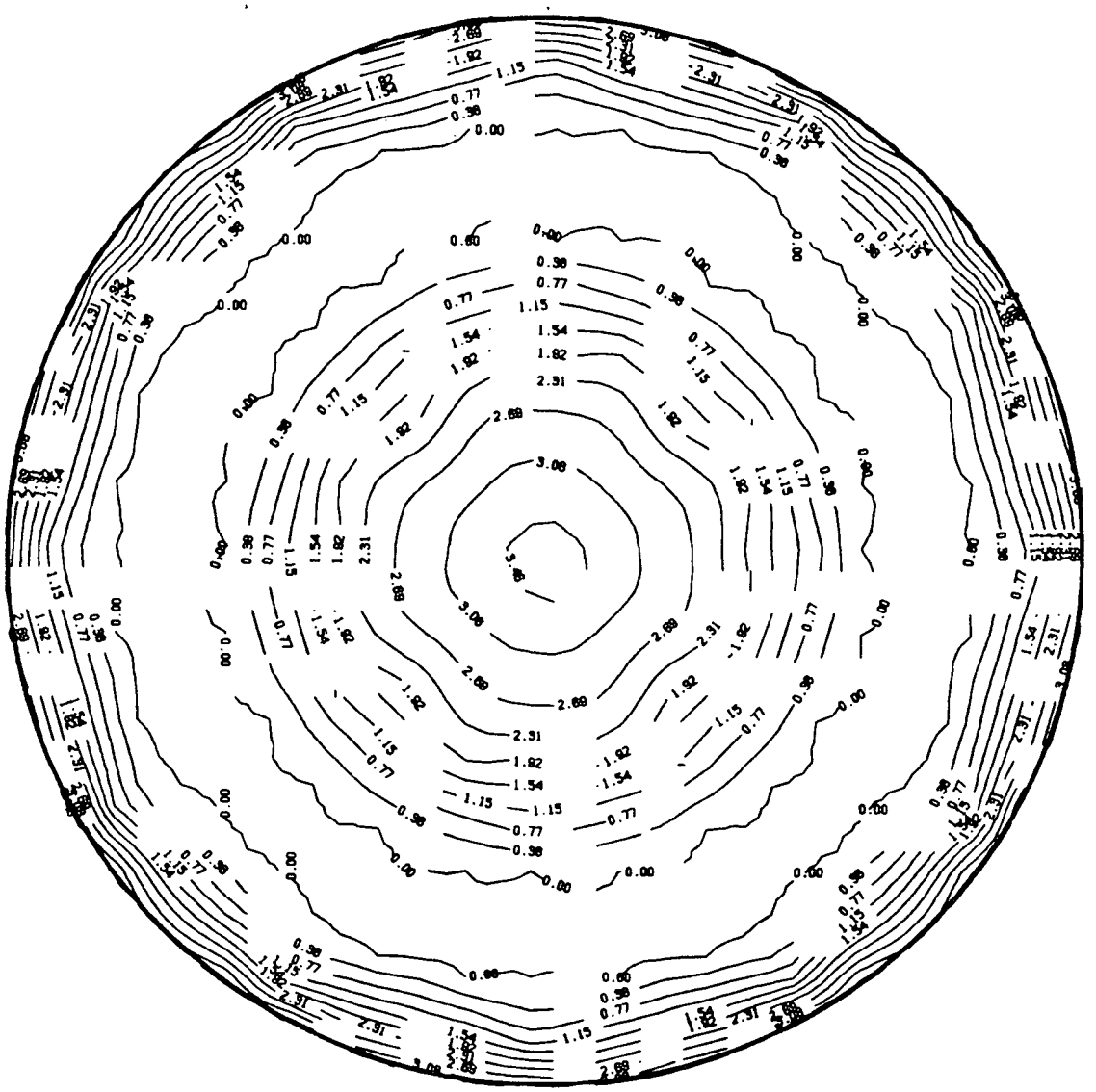
0.00
0.38
0.77
1.15
1.54
1.92
2.31
2.69
3.08

j

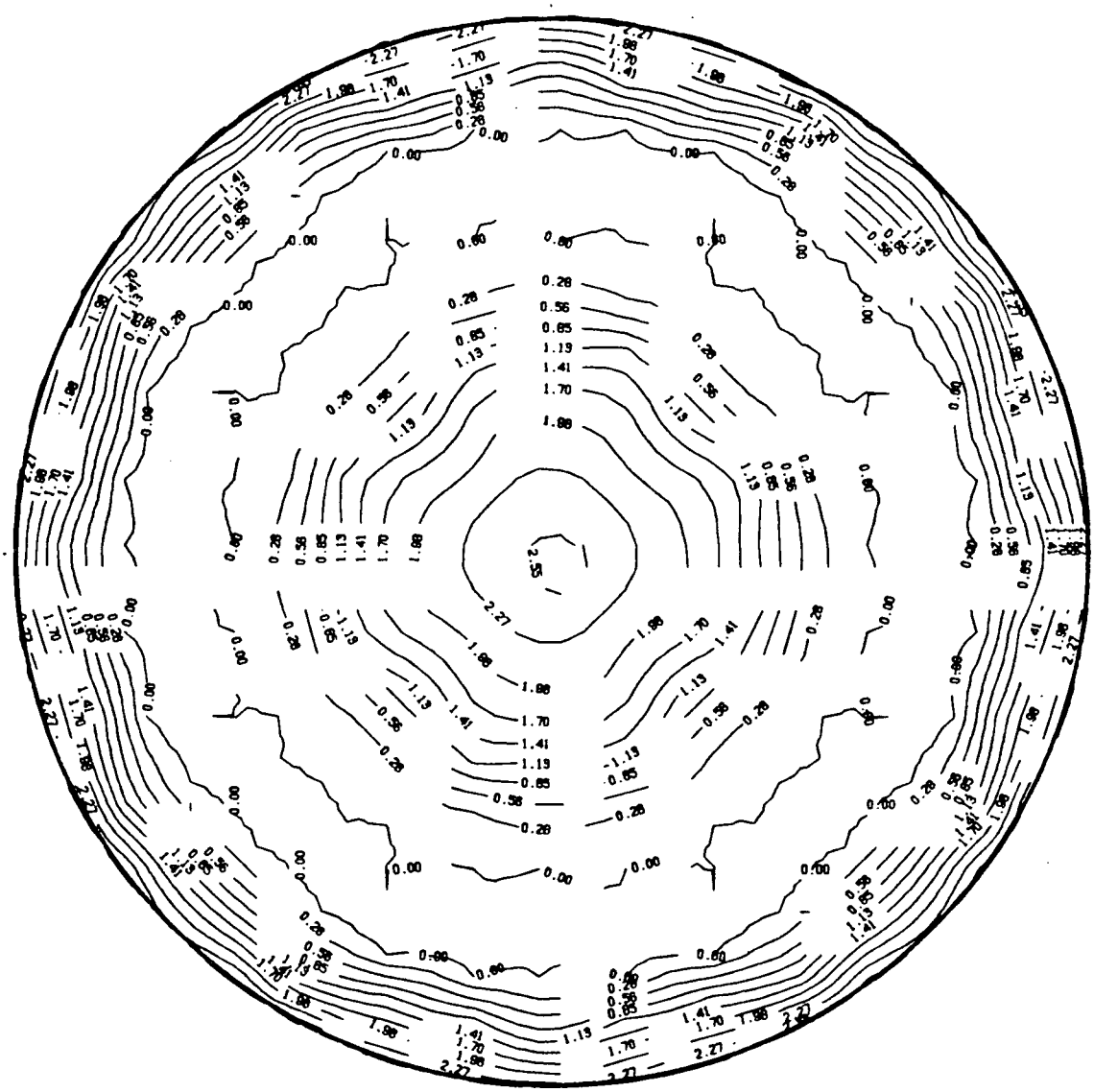

k

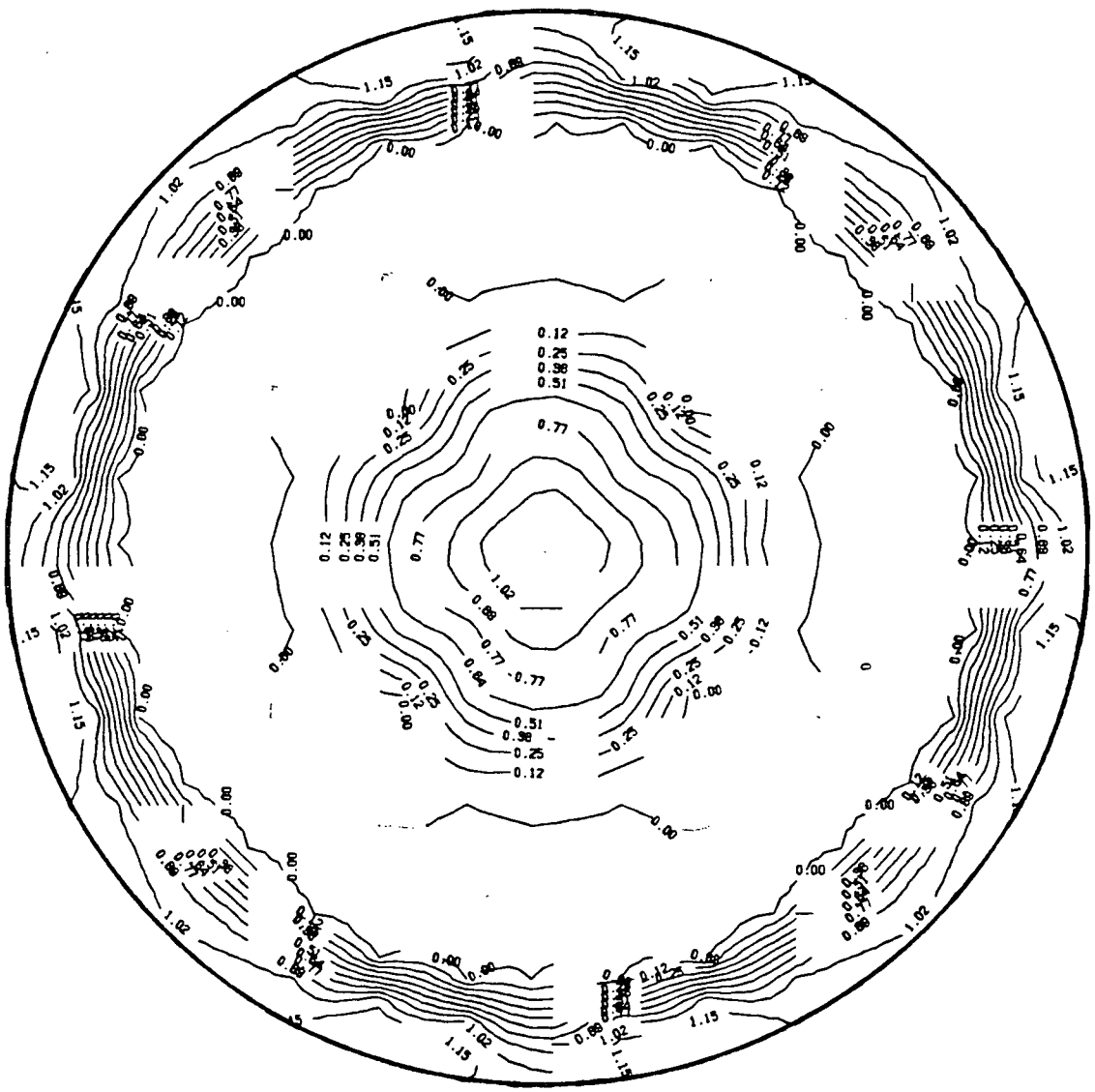

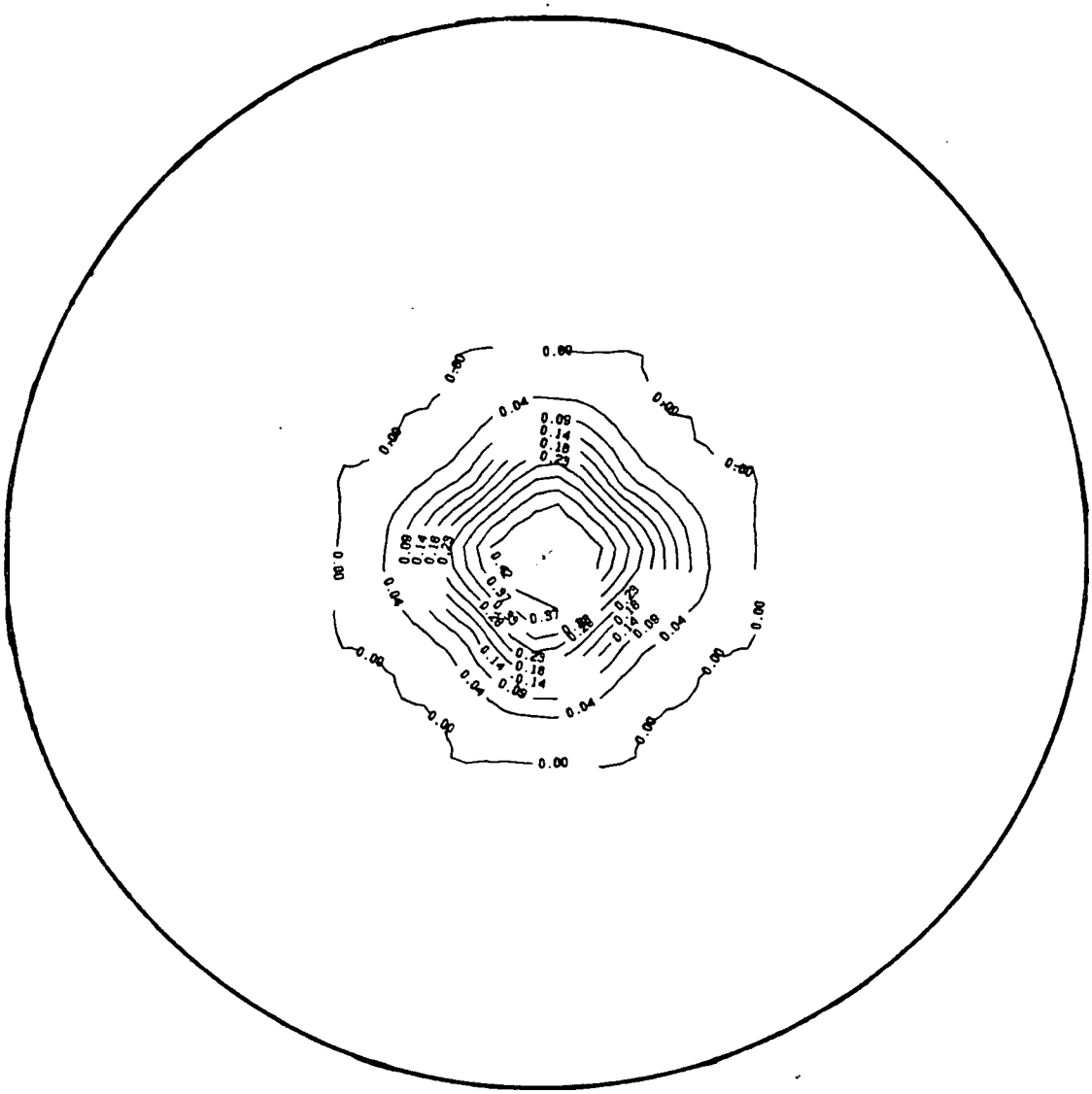

XIII.3.5.2 MRSS-CRSS (Yield) in cross-sections at a distance of the interface of
(a) 8 mm ; (b) 16 mm ; (c) 28 mm ; (d) 36 mm ;
(e) 48 mm ; (f) 56 mm ; (g) 68 mm ; (h) 76 mm ;
(i) 88 mm ; (j) 96 mm ; (k) 108 mm ; (l) 116 mm .

XIII.4 Growth Velocity
R 27.5 mm ; CL, 55 mm ; CA, 30° ; B, 21 mm .

XIII.4.1 V, 0.0001 cm/s
(a) Temperature and Von Mises Stress
(b) MRSS ; (c) MRSS-CRSS (Yield) ;
(d) MRSS-CRSS (MB) ; (e) MRSS-CRSS (MBTe) .

XIII.4.2 V, 0.01 cm/s
(a) Temperature and Von Mises Stress
(b) MRSS ; (c) MRSS-CRSS (Yield) ;
(d) MRSS-CRSS (MB) ; (e) MRSS-CRSS (MBTe) .

a

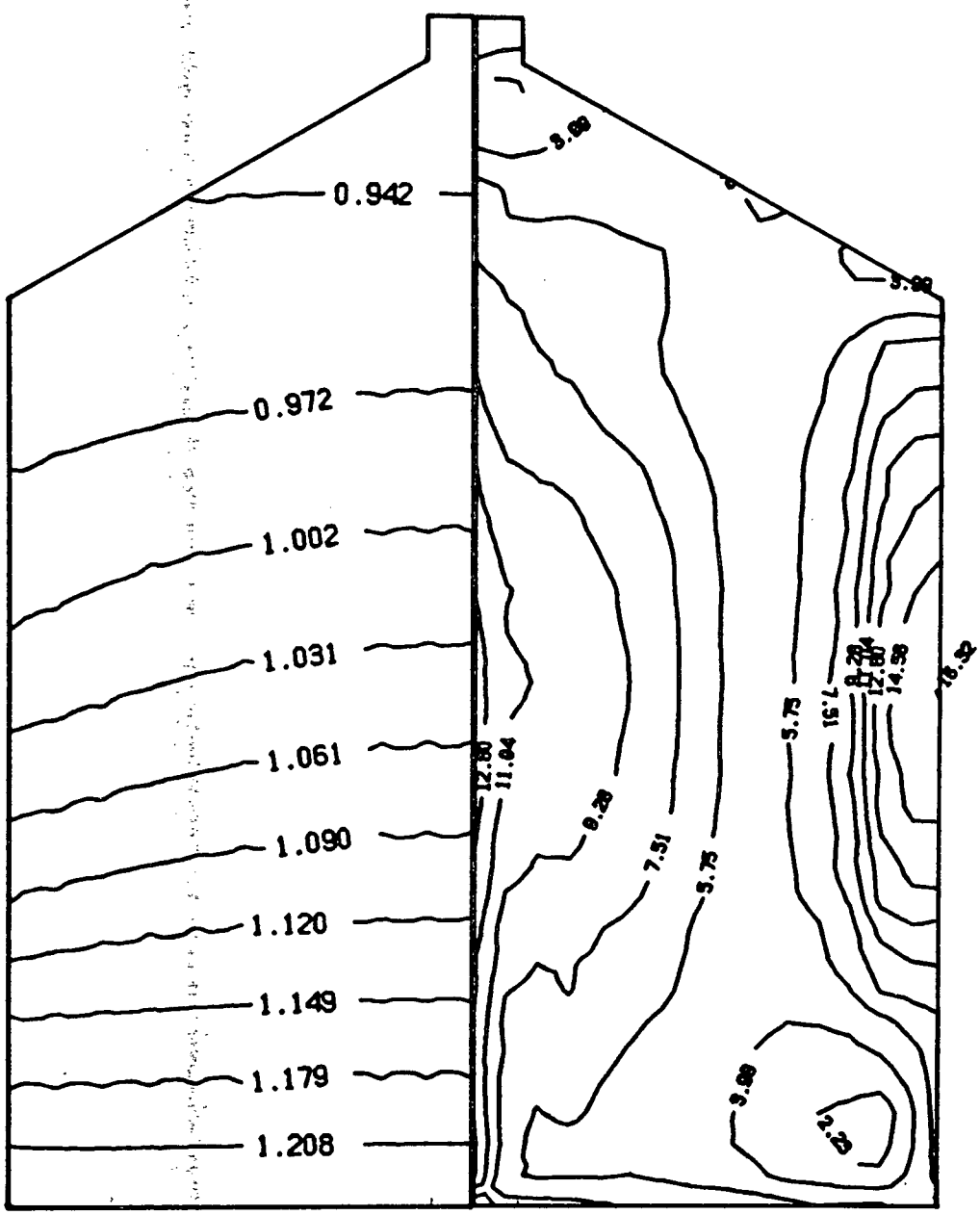
0.942
0.972
1.002
1.031
1.061
1.090
1.120
1.149
1.179
1.208
12.80
11.04
9.28
7.51
5.75
5.75
7.51
9.28
11.04
12.80
14.58
16.32
3.98
2.23

b

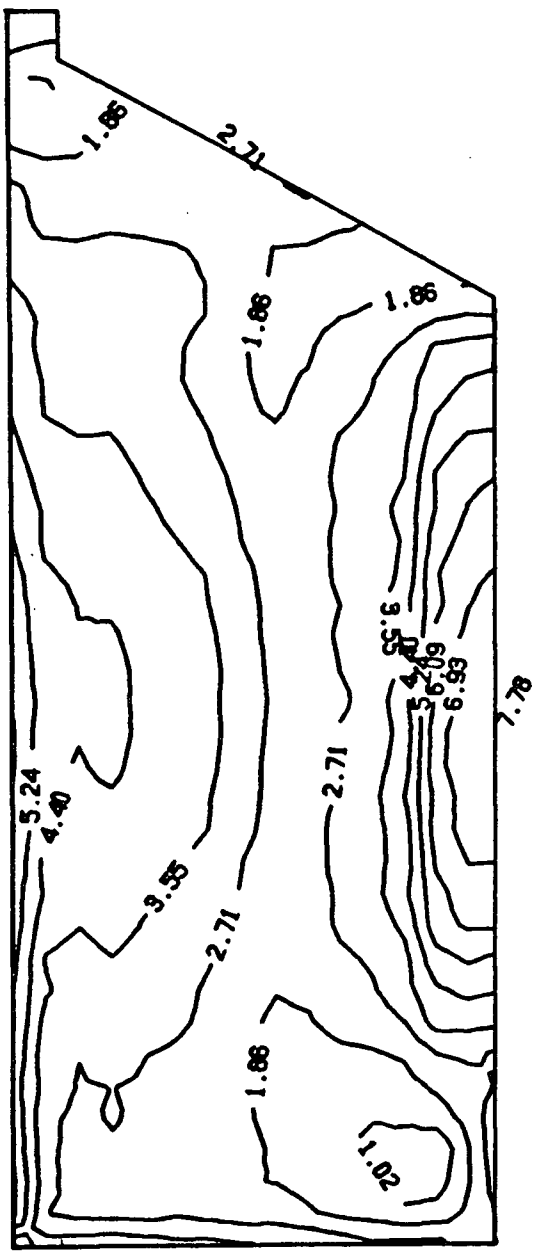
1.86
2.71
1.86
1.86
5.24
4.40
3.55
2.71
2.71
1.88
1.02
6.93
7.78

c

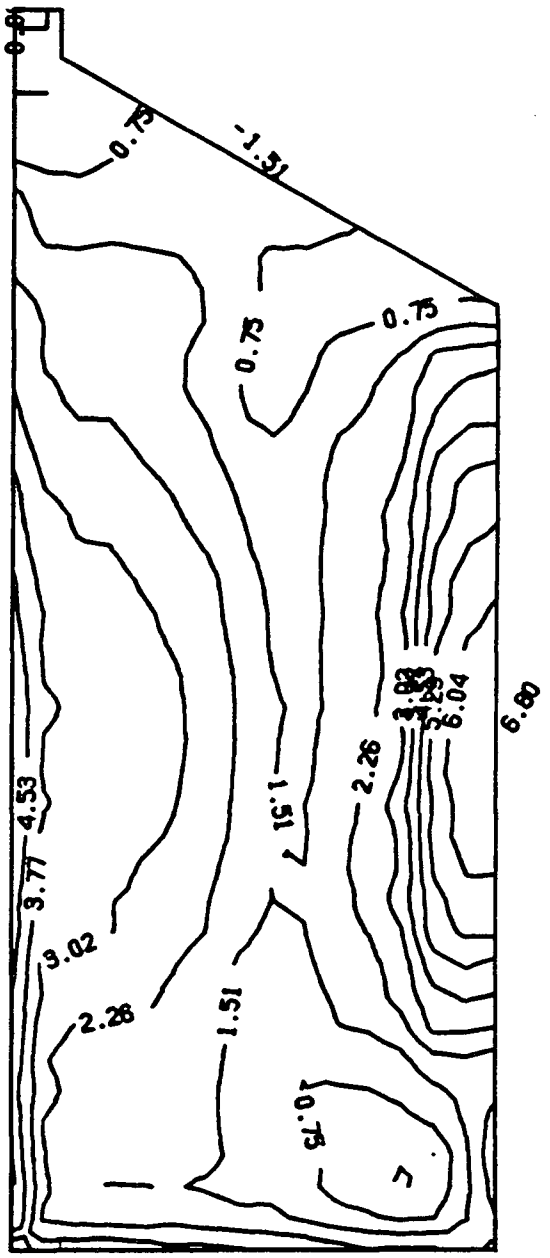
0.75
-1.51
0.75
0.75
4.53
3.77
3.02
2.26
1.51
2.26
6.04
6.80

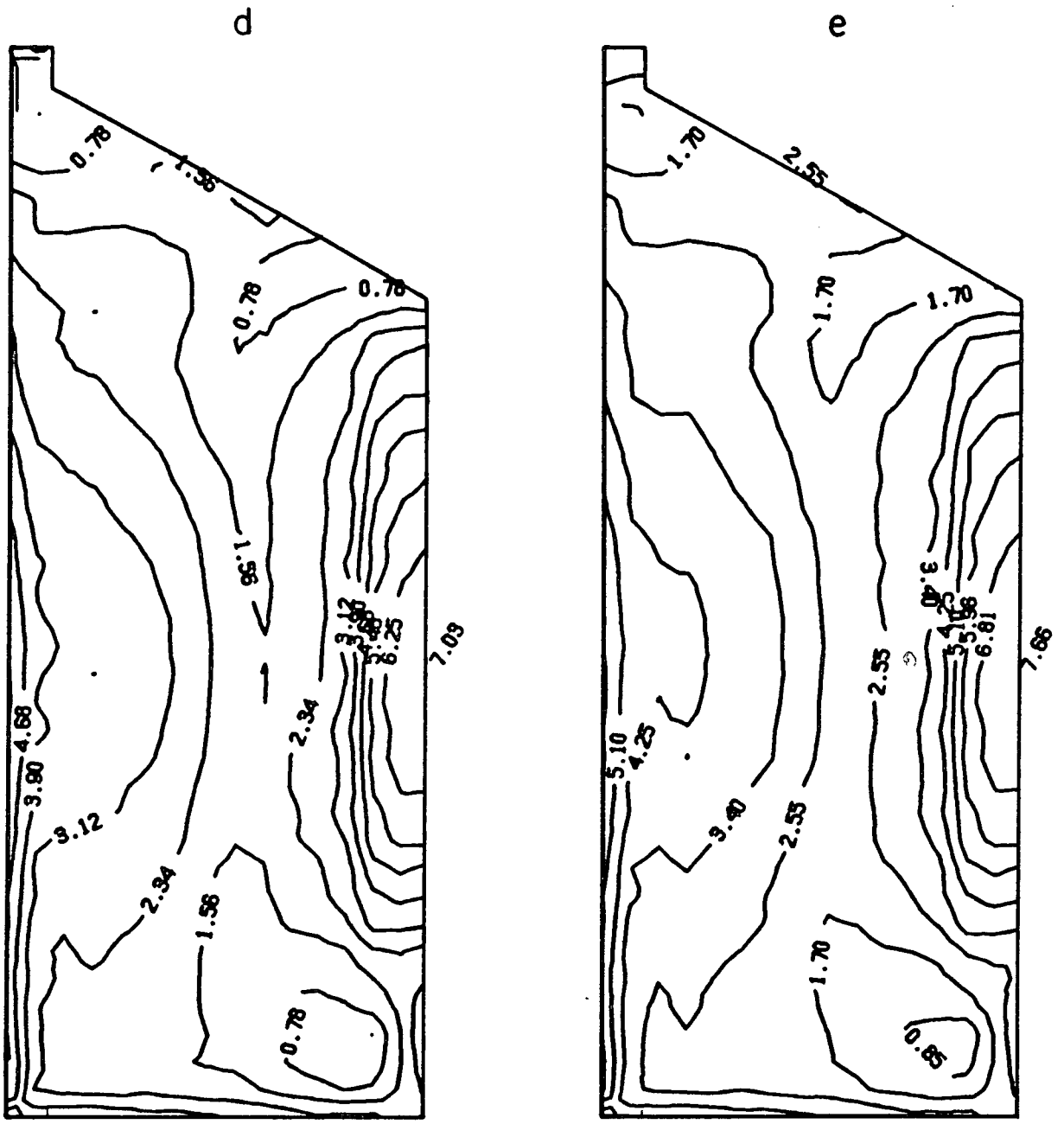

XIII.4.1 V, 0.0001 cm/s
(a) Temperature and Von Mises Stress
(b) MRSS ; (c) MRSS-CRSS (Yield) ;
(d) MRSS-CRSS (MB) ; (e) MRSS-CRSS (MBTe) .

a

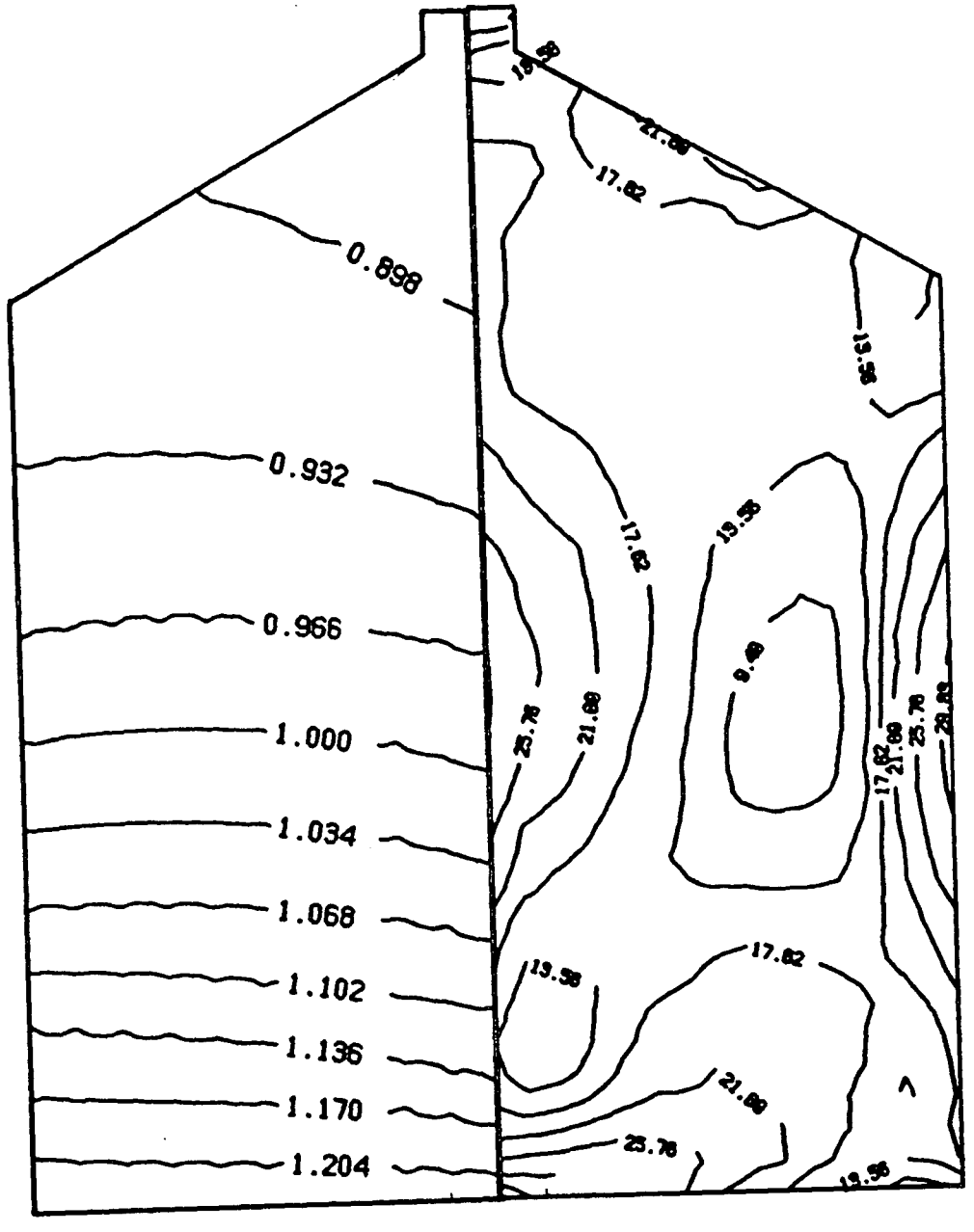
0.898
0.932
0.966
1.000
1.034
1.068
1.102
1.136
1.170
1.204
17.62
13.56
21.69
25.76
9.49

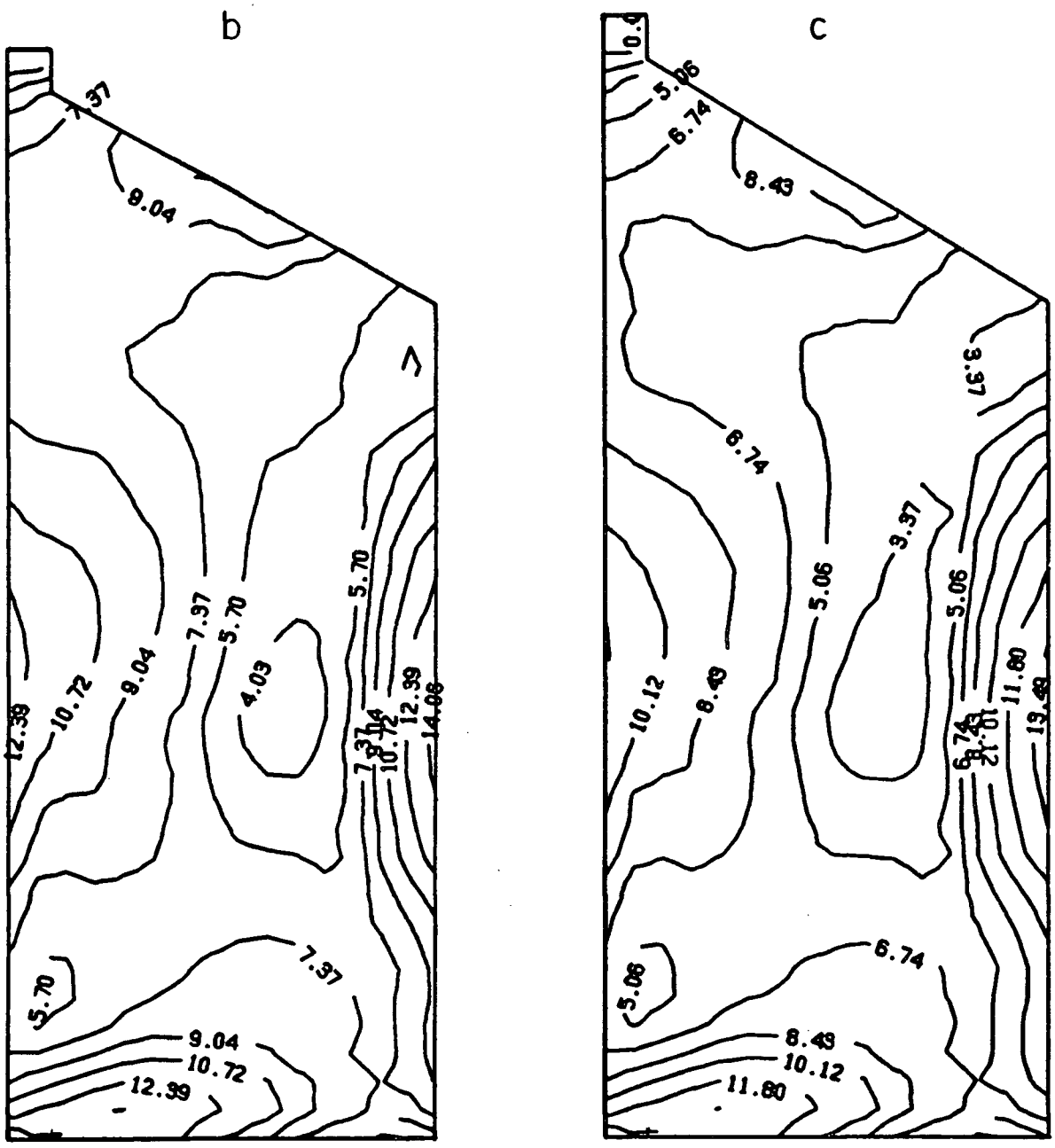
b
7.37
9.04
7.37
5.70
5.70
4.03
12.39
10.72
9.04
7.37
10.72
12.39
14.06
7.37
5.70
9.04
10.72
12.39
c
5.06
6.74
8.43
3.37
6.74
3.37
5.06
5.06
10.12
8.43
11.80
6.74
5.06
6.74
8.43
10.12
11.80

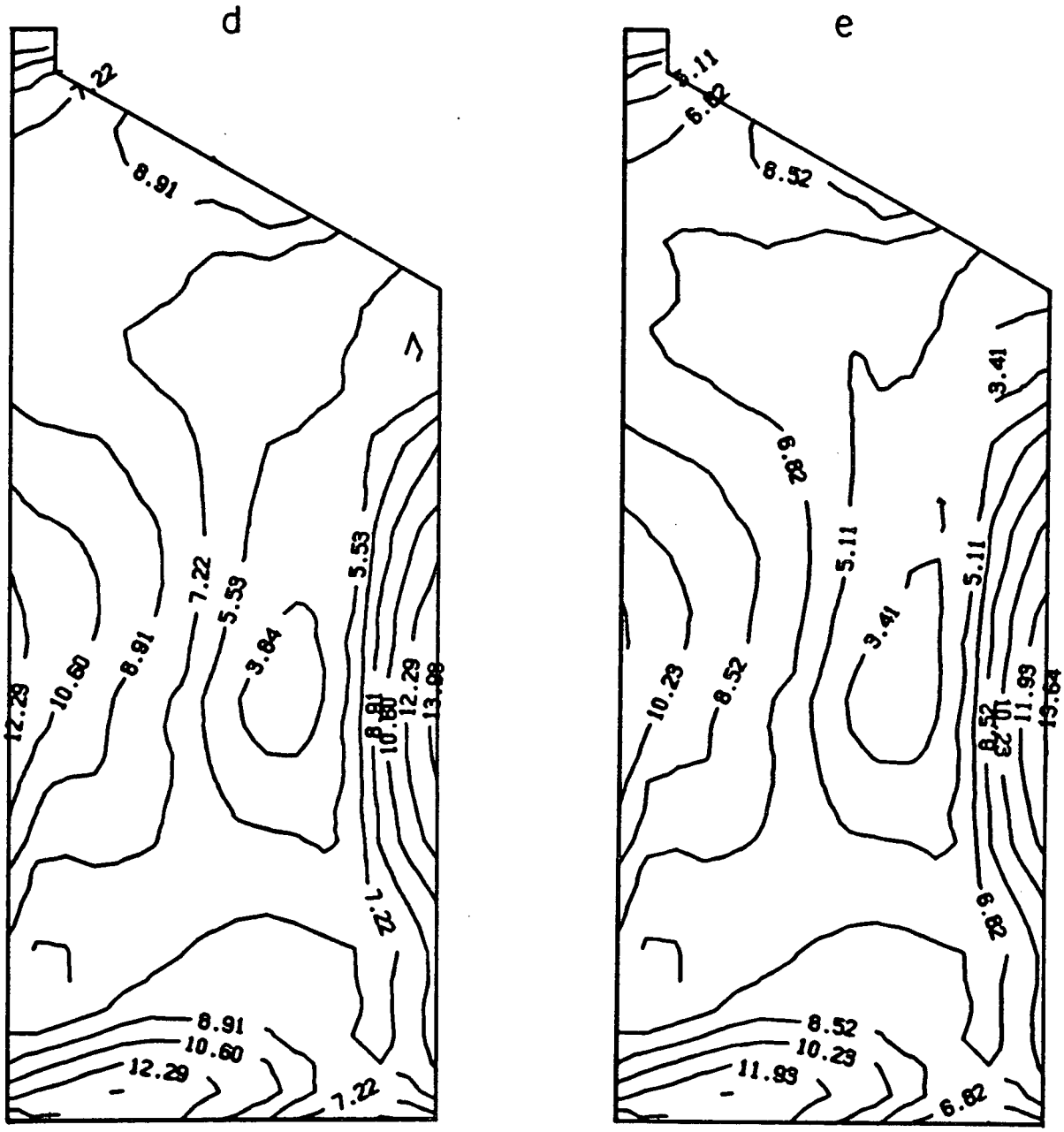

XIII.4.2 V, 0.01 cm/s
(a) Temperature and Von Mises Stress
(b) MRSS ; (c) MRSS-CRSS (Yield) ;
(d) MRSS-CRSS (MB) ; (e) MRSS-CRSS (MBTe) .

XIII.5 Thermal Condition R_{δ} 27.5 mm
CL, 55 mm ; CA, 30° ; AP, 30 atm.

XIII.5.1 B, 21 mm

XIII.5.1.1 G/2
(a) Temperature and Von Mises Stress
(b) MRSS ; (c) MRSS-CRSS (Yield) ;
(d) MRSS-CRSS (MB) ; (e) MRSS-CRSS (MBTe) .

XIII.5.1.2 G/4
(a) Temperature and Von Mises Stress
(b) MRSS ; (c) MRSS-CRSS (Yield) ;
(d) MRSS-CRSS (MB) ; (e) MRSS-CRSS (MBTe) .

XIII.5.1.3 G/6
(a) Temperature and Von Mises Stress
(b) MRSS ; (c) MRSS-CRSS (Yield) ;
(d) MRSS-CRSS (MB) ; (e) MRSS-CRSS (MBTe) .

XIII.5.1.4 G/8
(a) Temperature and Von Mises Stress
(b) MRSS ; (c) MRSS-CRSS (Yield) ;
(d) MRSS-CRSS (MB) ; (e) MRSS-CRSS (MBTe) .

XIII.5.2 B, 40 mm

XIII.5.2.1 G
(a) Temperature and Von Mises Stress
(b) MRSS ; (c) MRSS-CRSS (Yield) ;
(d) MRSS-CRSS (MB) ; (e) MRSS-CRSS (MBTe) .

XIII.5.2.2 G/2
(a) Temperature and Von Mises Stress
(b) MRSS ; (c) MRSS-CRSS (Yield) ;
(d) MRSS-CRSS (MB) ; (e) MRSS-CRSS (MBTe) .

XIII.5.2.3 G/3
(a) Temperature and Von Mises Stress
(b) MRSS ; (c) MRSS-CRSS (Yield) ;
(d) MRSS-CRSS (MB) ; (e) MRSS-CRSS (MBTe) .

XIII.5.3 B, 50 mm

XIII.5.3.1 G
(a) Temperature and Von Mises Stress
(b) MRSS ; (c) MRSS-CRSS (Yield) ;
(d) MRSS-CRSS (MB) ; (e) MRSS-CRSS (MBTe) .

XIII.5.3.2 G/2

(a) Temperature and Von Mises Stress
(b) MRSS ; (c) MRSS-CRSS (Yield) ;
(d) MRSS-CRSS (MB) ; (e) MRSS-CRSS (MBTe) .

XIII.5.3.3 G/3

(a) Temperature and Von Mises Stress
(b) MRSS ; (c) MRSS-CRSS (Yield) ;
(d) MRSS-CRSS (MB) ; (e) MRSS-CRSS (MBTe) .

a

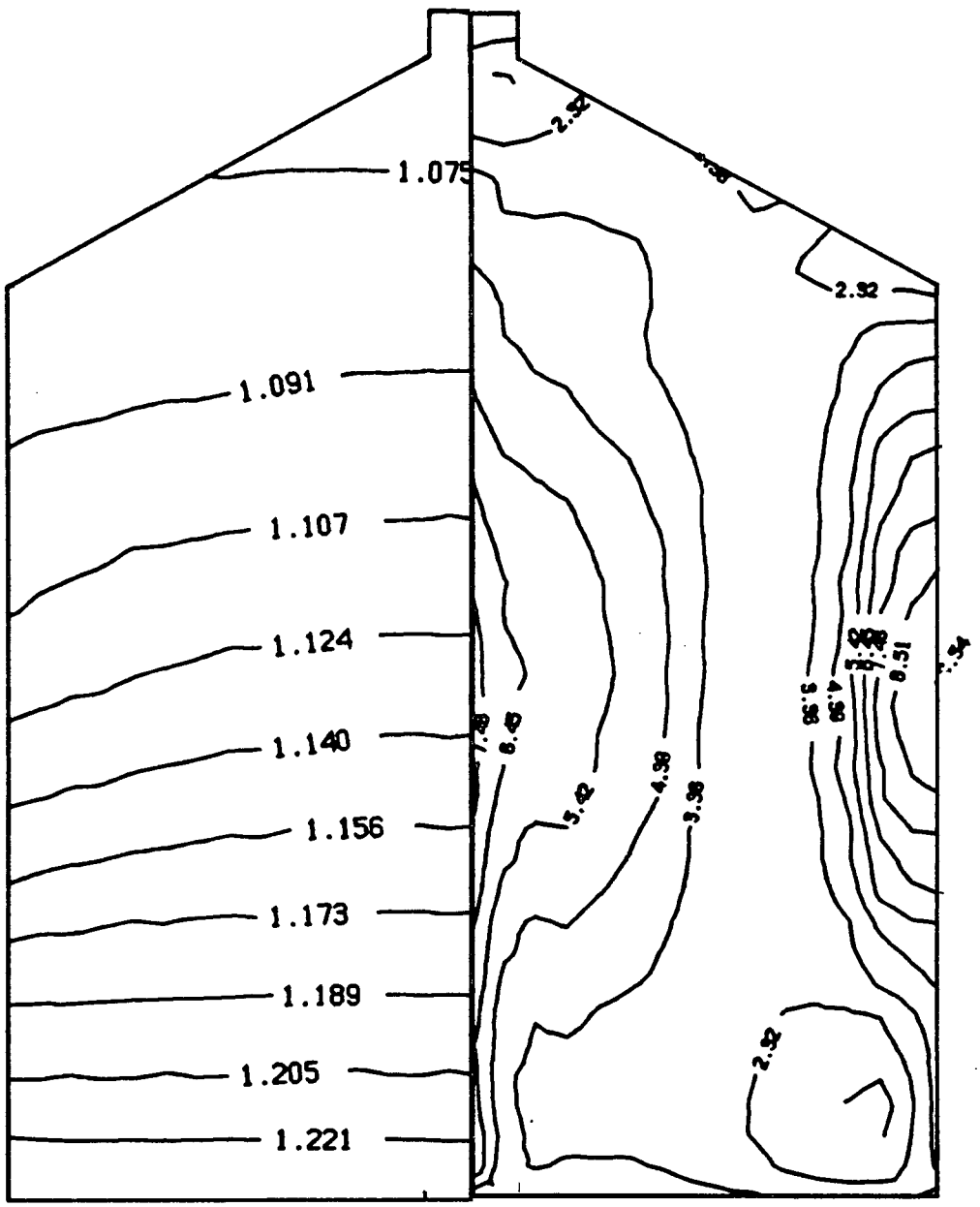
1.075
1.091
1.107
1.124
1.140
1.156
1.173
1.189
1.205
1.221
2.32
2.32
2.32
3.38
4.38
5.42
6.45
8.51

b

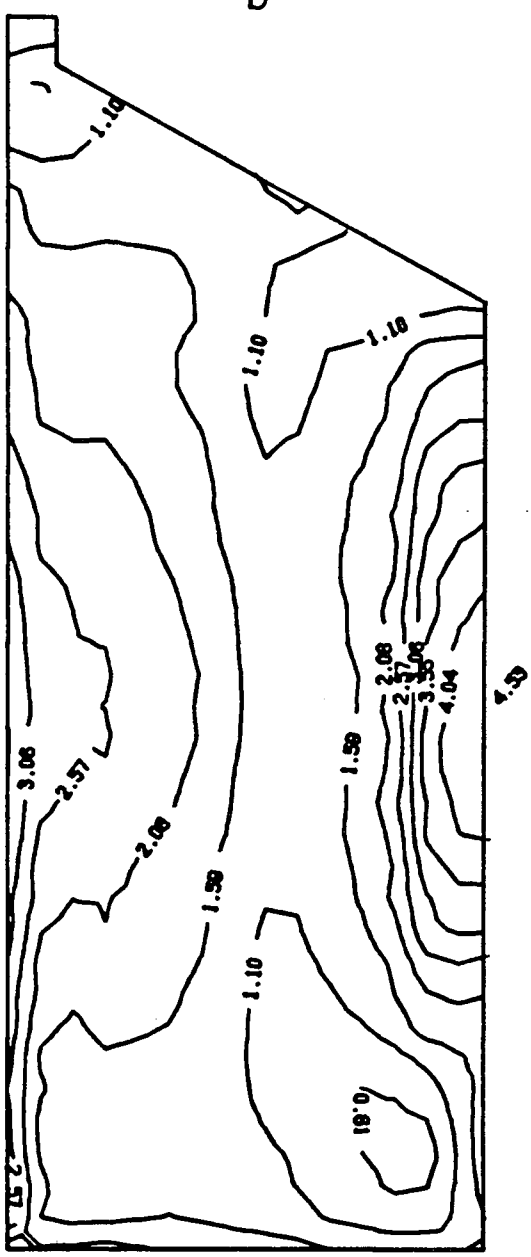
1.10
1.10
1.10
3.06
2.57
2.08
1.59
1.59
2.08
2.57
3.06
3.55
4.04
4.53
1.10
0.81
2.57

c

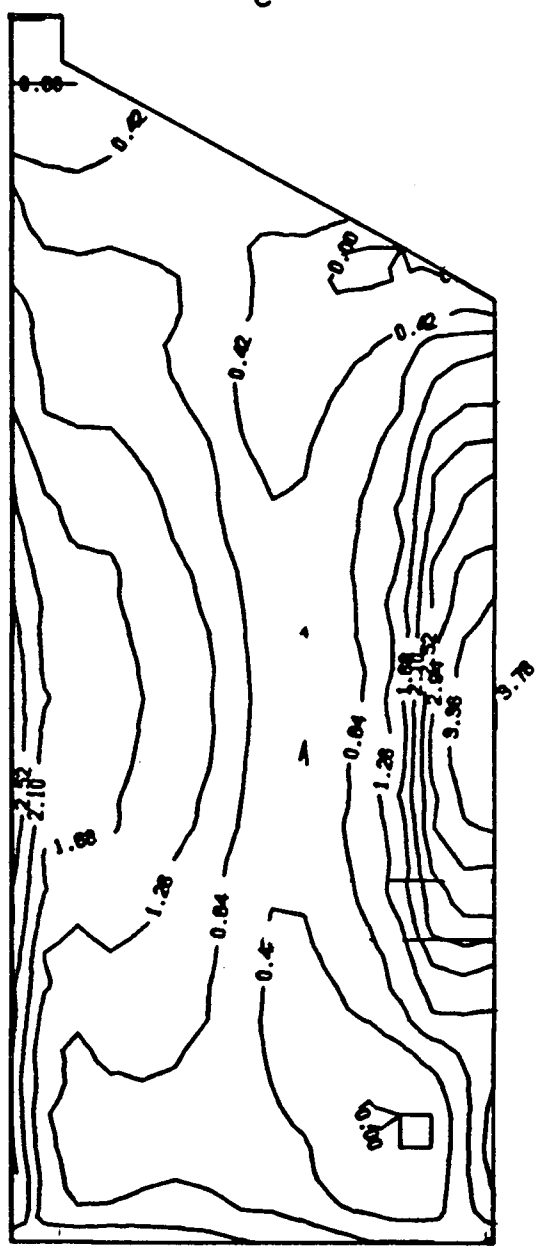
0.00
0.42
0.00
0.42
0.42
2.52
2.10
1.68
1.28
0.84
0.84
1.28
1.68
2.10
2.52
2.94
3.36
3.78
0.00

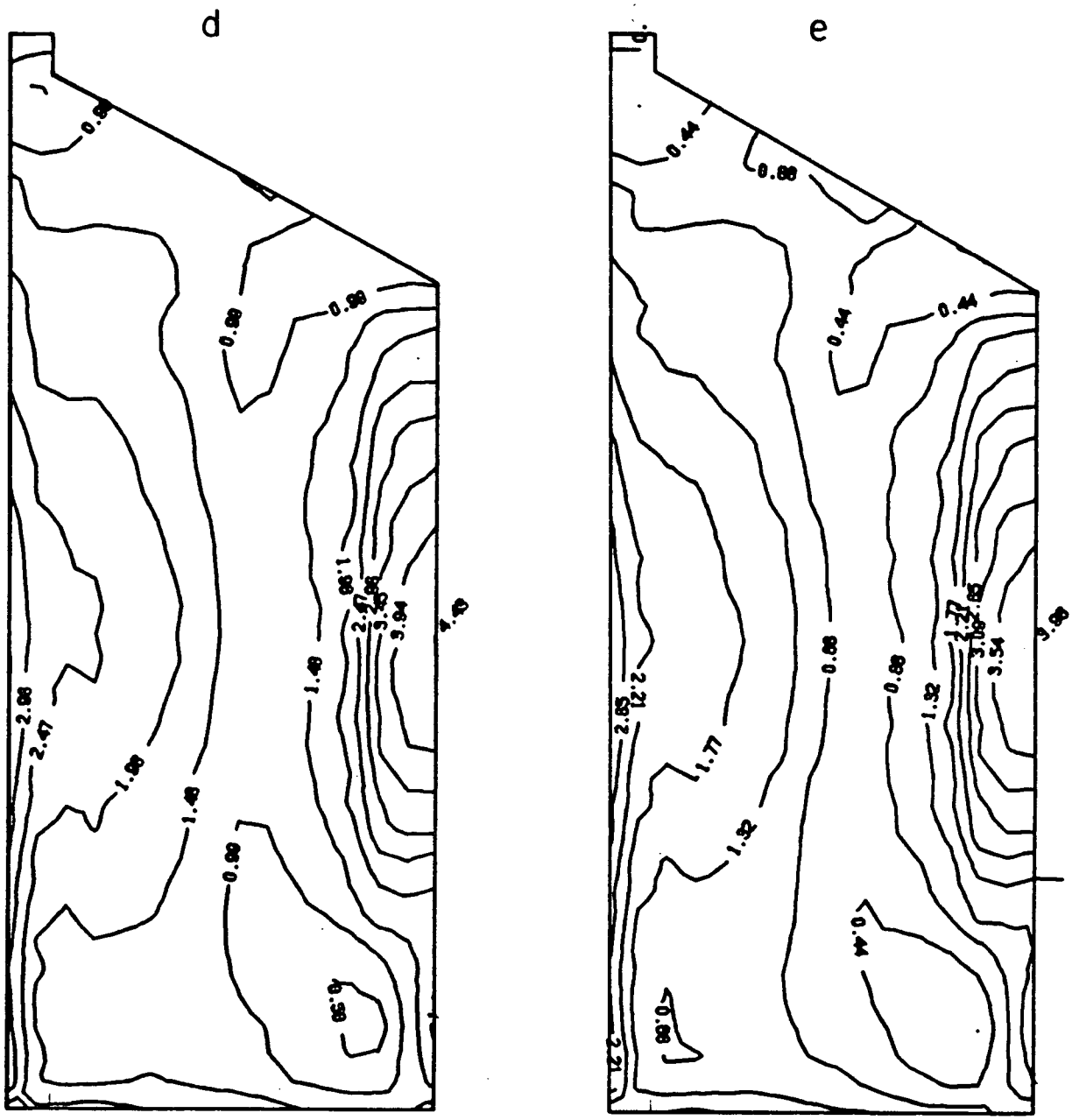

XIII.5.1.1 G/2

(a) Temperature and Von Mises Stress
(b) MRSS ; (c) MRSS-CRSS (Yield) ;
(d) MRSS-CRSS (MB) ; (e) MRSS-CRSS (MBTe) .

a

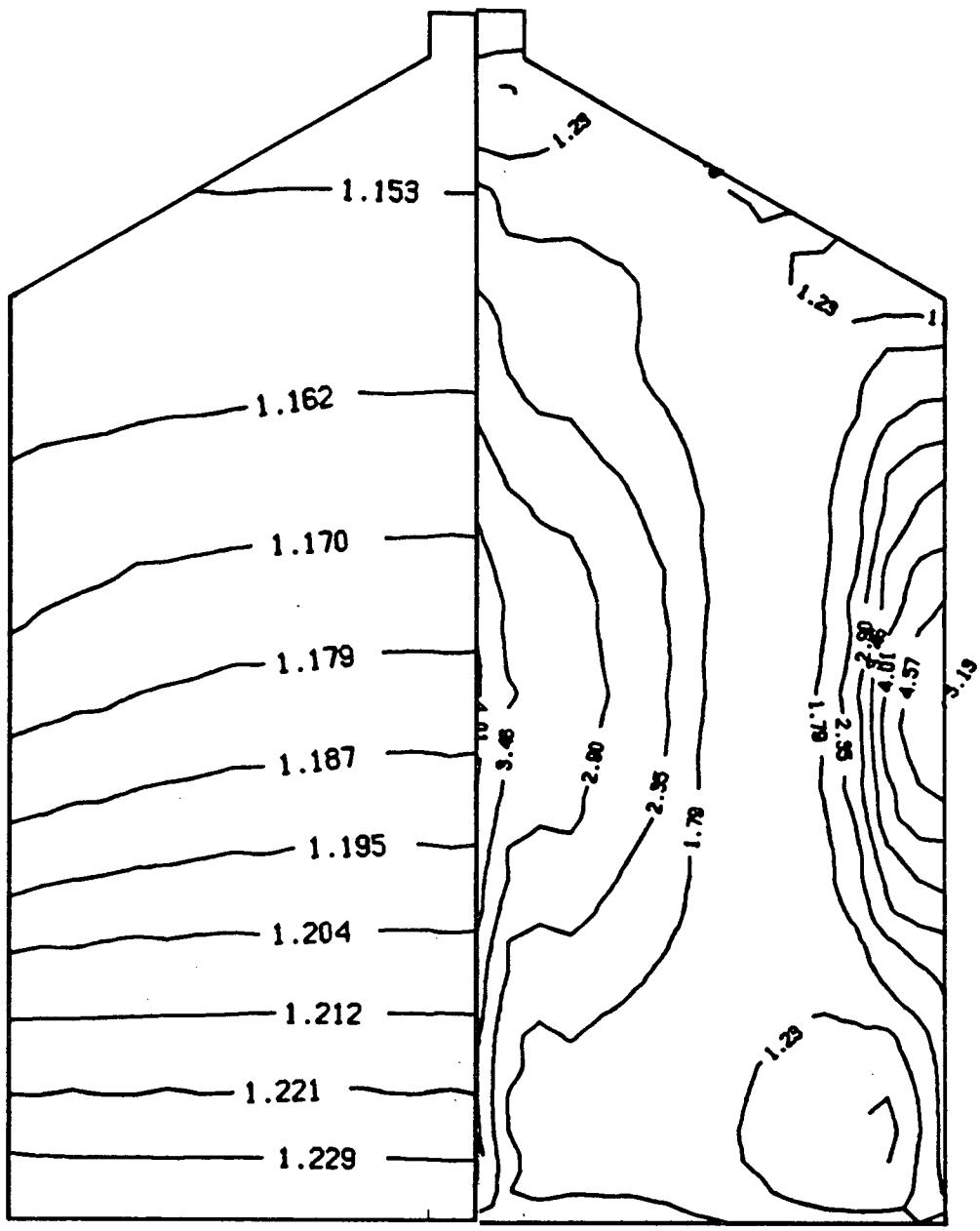
1.153
1.162
1.170
1.179
1.187
1.195
1.204
1.212
1.221
1.229
1.23
1.23
1.23
3.48
2.80
2.35
1.79
1.79
2.35
2.80
4.01
4.57
3.19

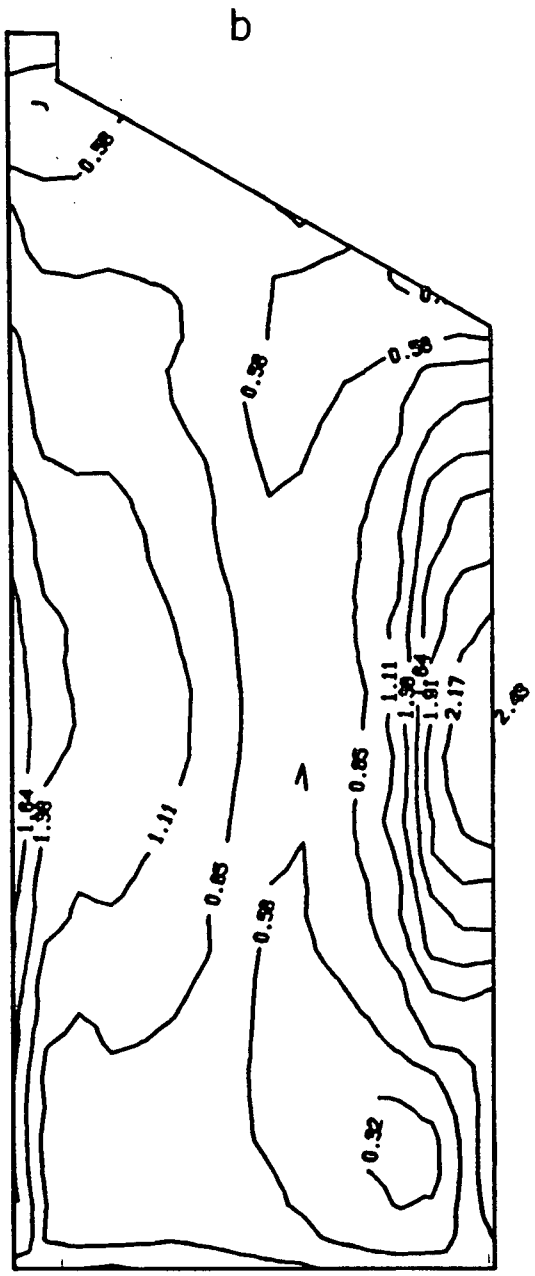
b
0.58
0.58
0.58
1.11
0.65
0.58
0.32
0.65
1.11
1.64
1.38
1.91
2.17
2.49

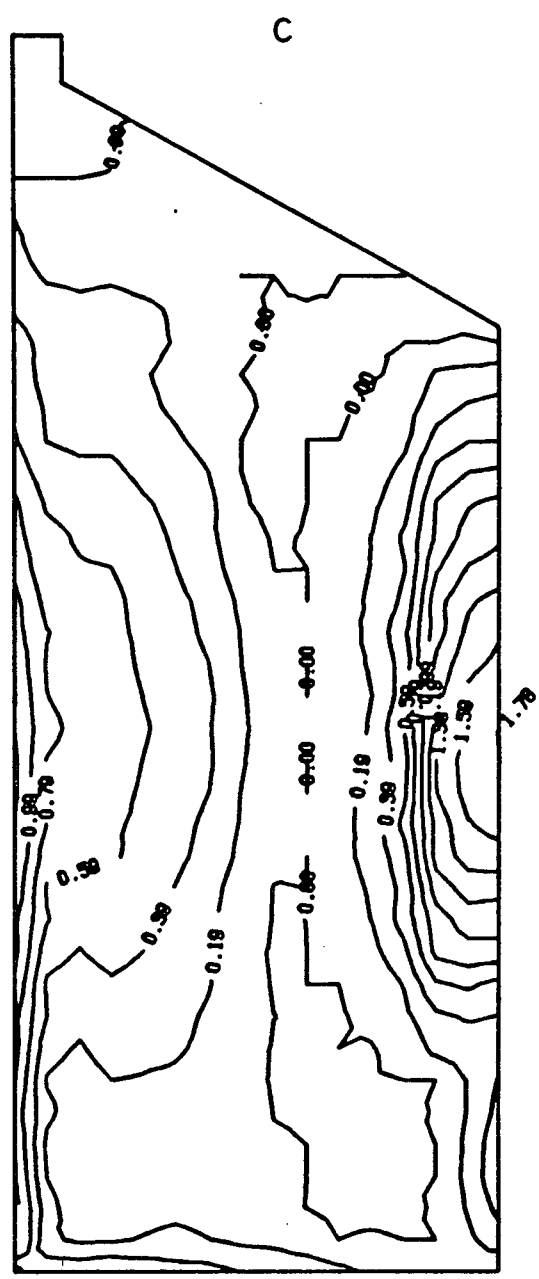
c
0.00
0.00
0.00
0.00
0.19
0.39
0.19
0.39
0.59
0.79
1.59
1.78

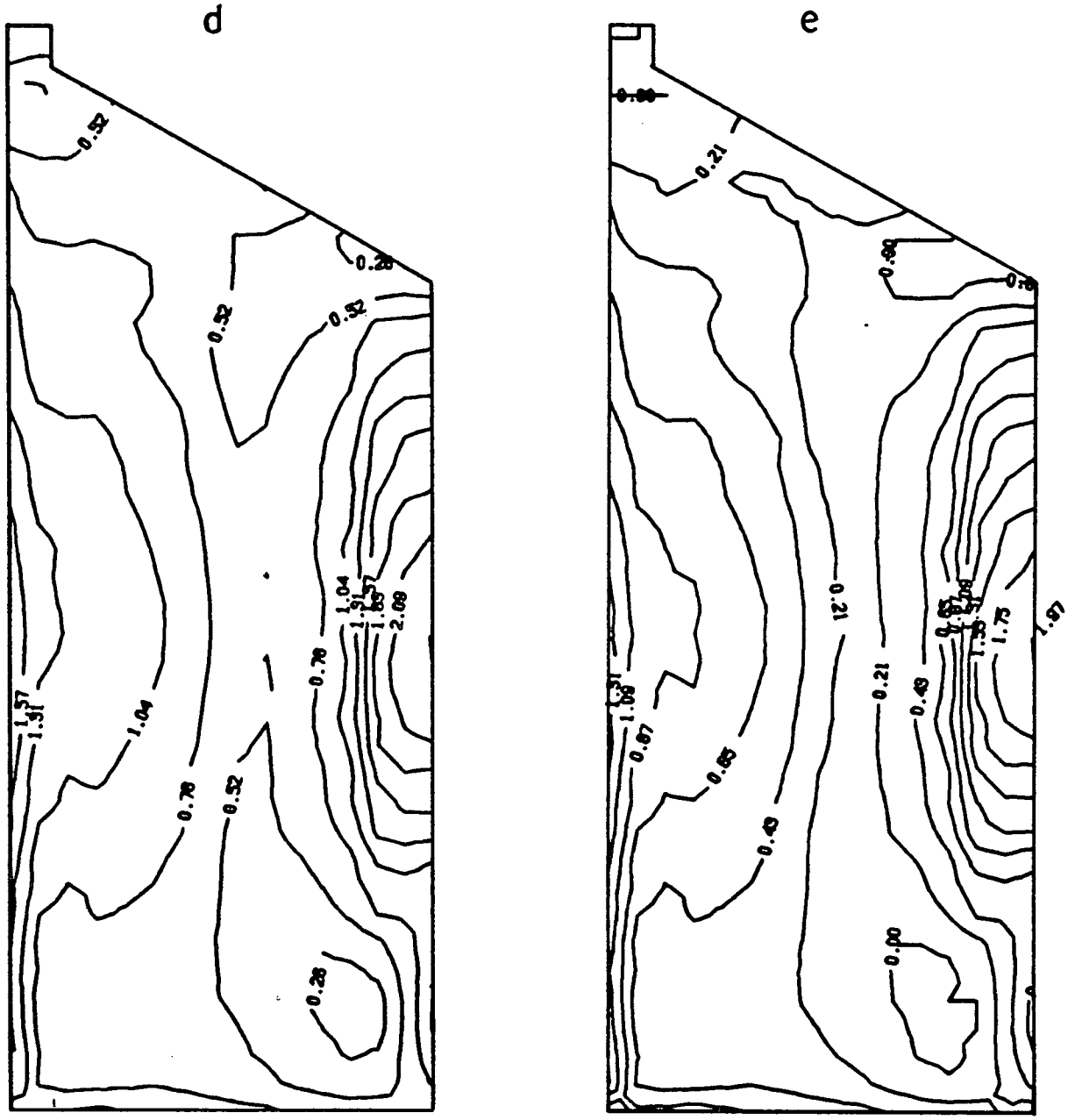

XIII.5.1.2 G/4

(a) Temperature and Von Mises Stress
(b) MRSS ; (c) MRSS-CRSS (Yield) ;
(d) MRSS-CRSS (MB) ; (e) MRSS-CRSS (MBTe) .

a

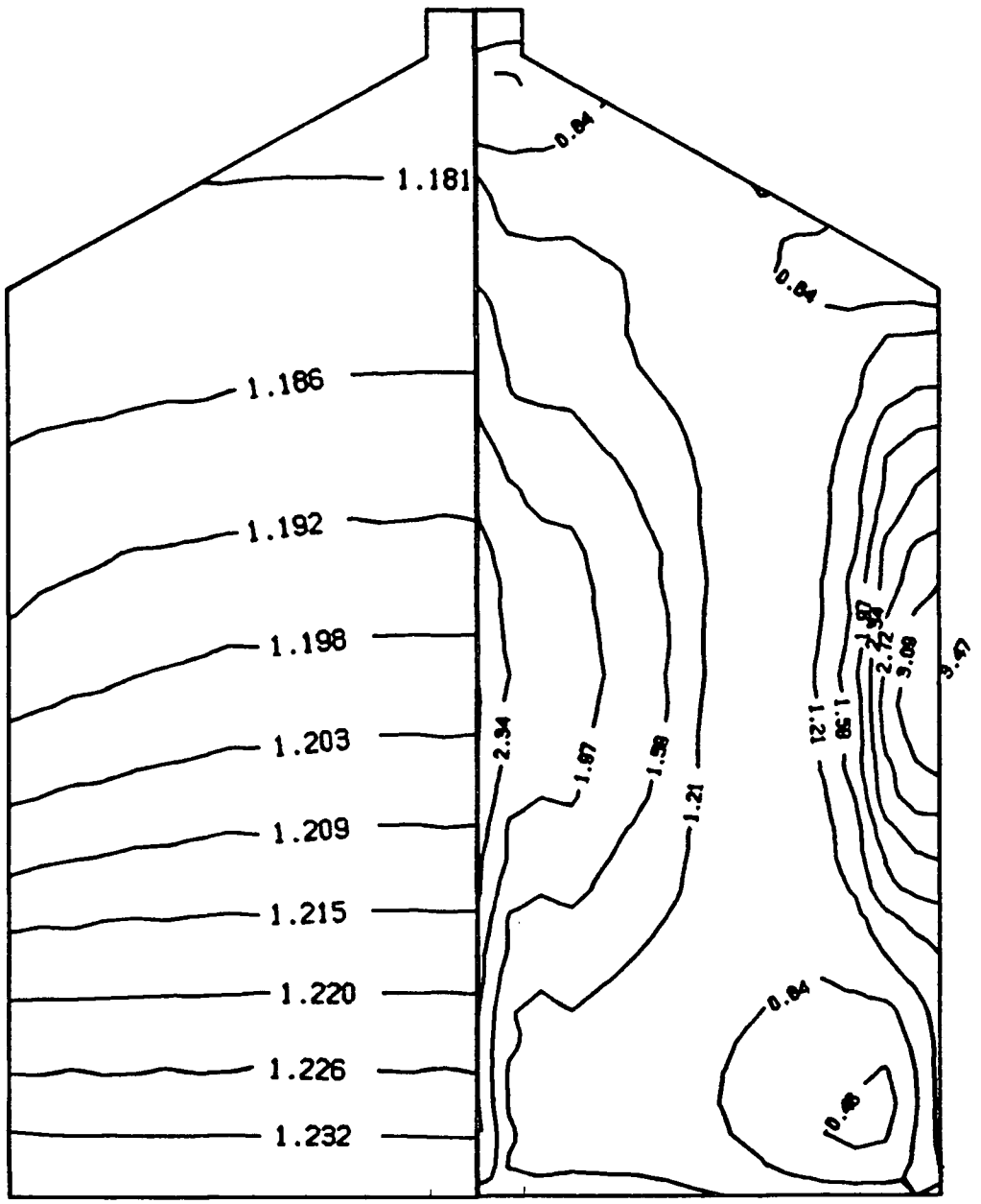
1.181
1.186
1.192
1.198
1.203
1.209
1.215
1.220
1.226
1.232
0.84
0.84
2.34
1.97
1.58
1.21
0.84
0.48

b

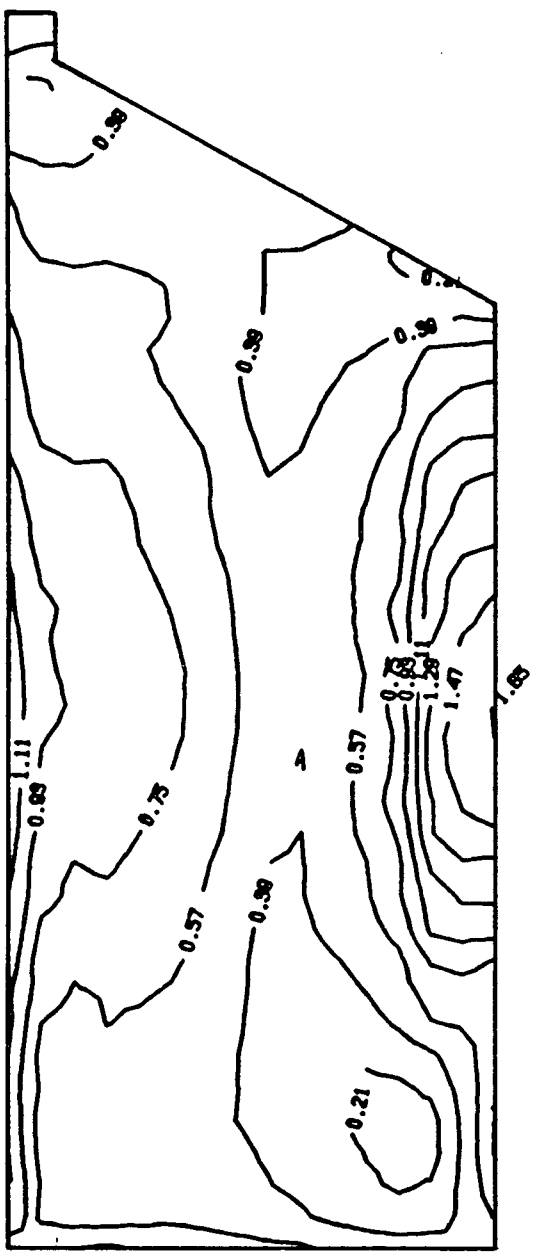
0.39
0.39
0.39
1.11
0.93
0.75
0.57
0.57
0.39
0.21
1.47
1.65

c

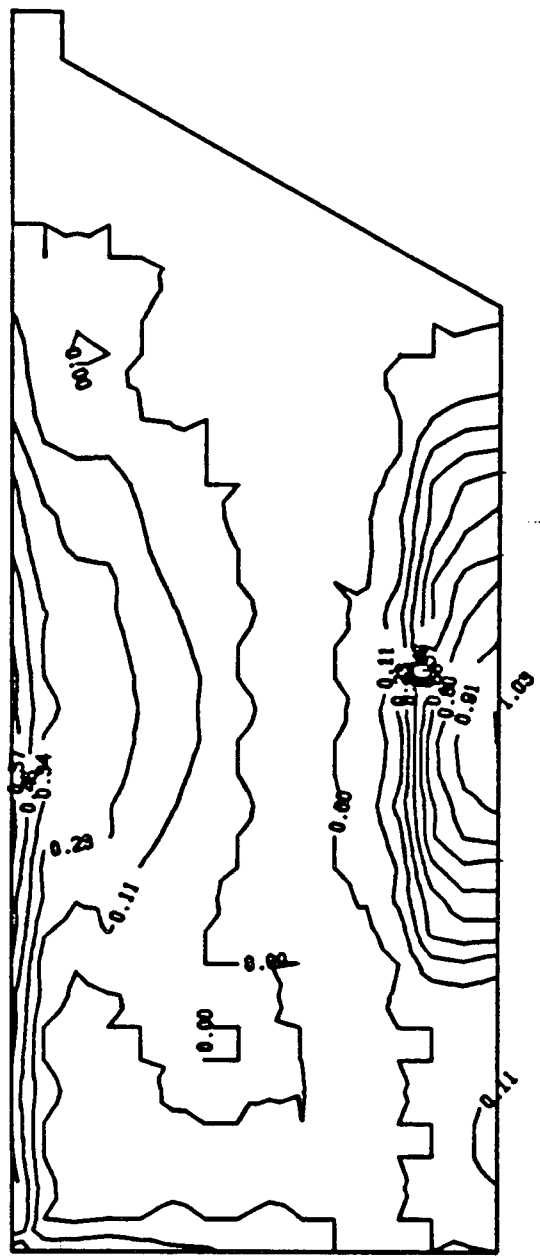
0.00
0.23
0.11
0.00
0.00
0.11
0.91
1.03
0.11

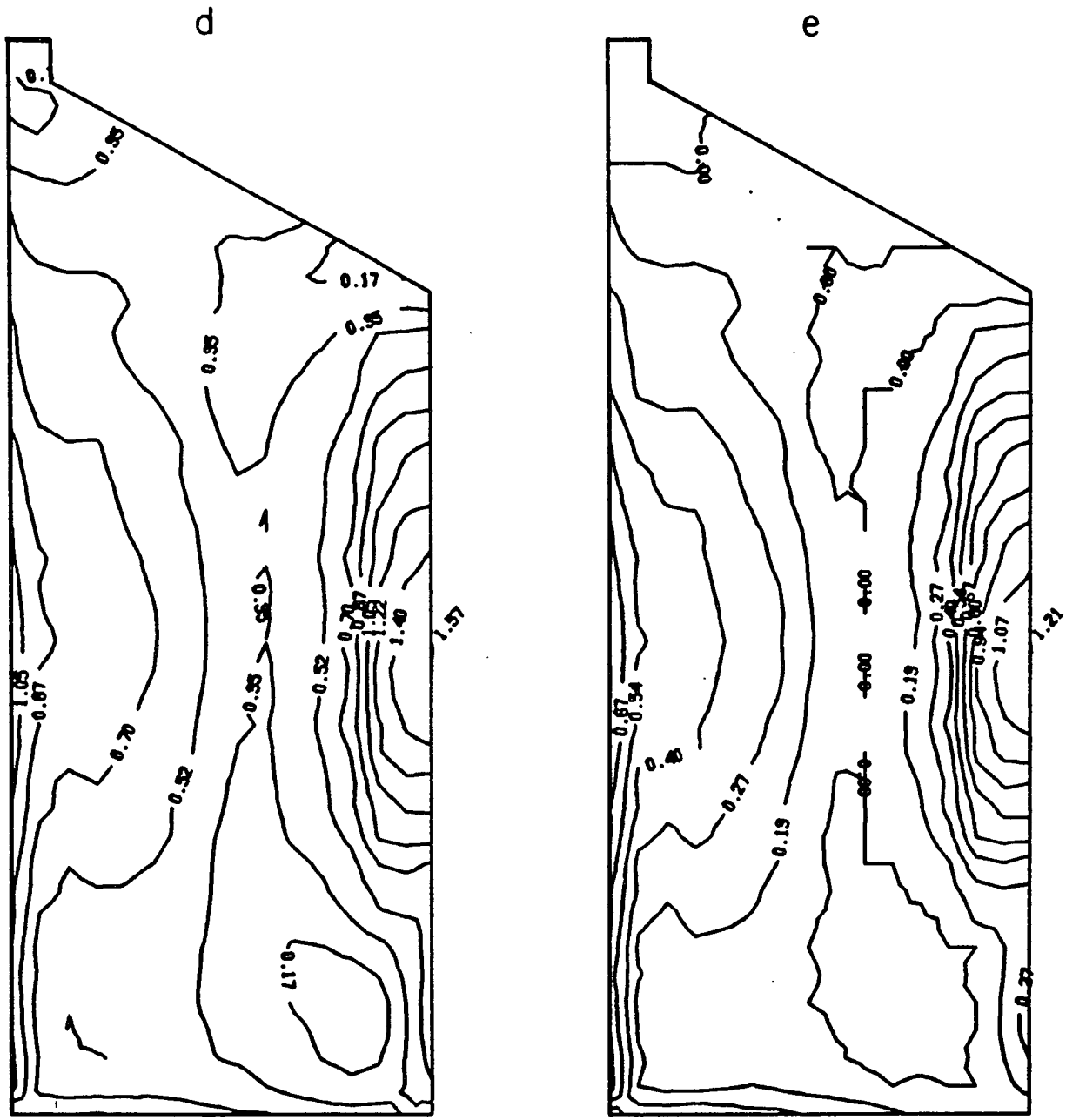

XIII.5.1.3 G/6

(a) Temperature and Von Mises Stress
(b) MRSS ; (c) MRSS-CRSS (Yield) ;
(d) MRSS-CRSS (MB) ; (e) MRSS-CRSS (MBTe) .

a

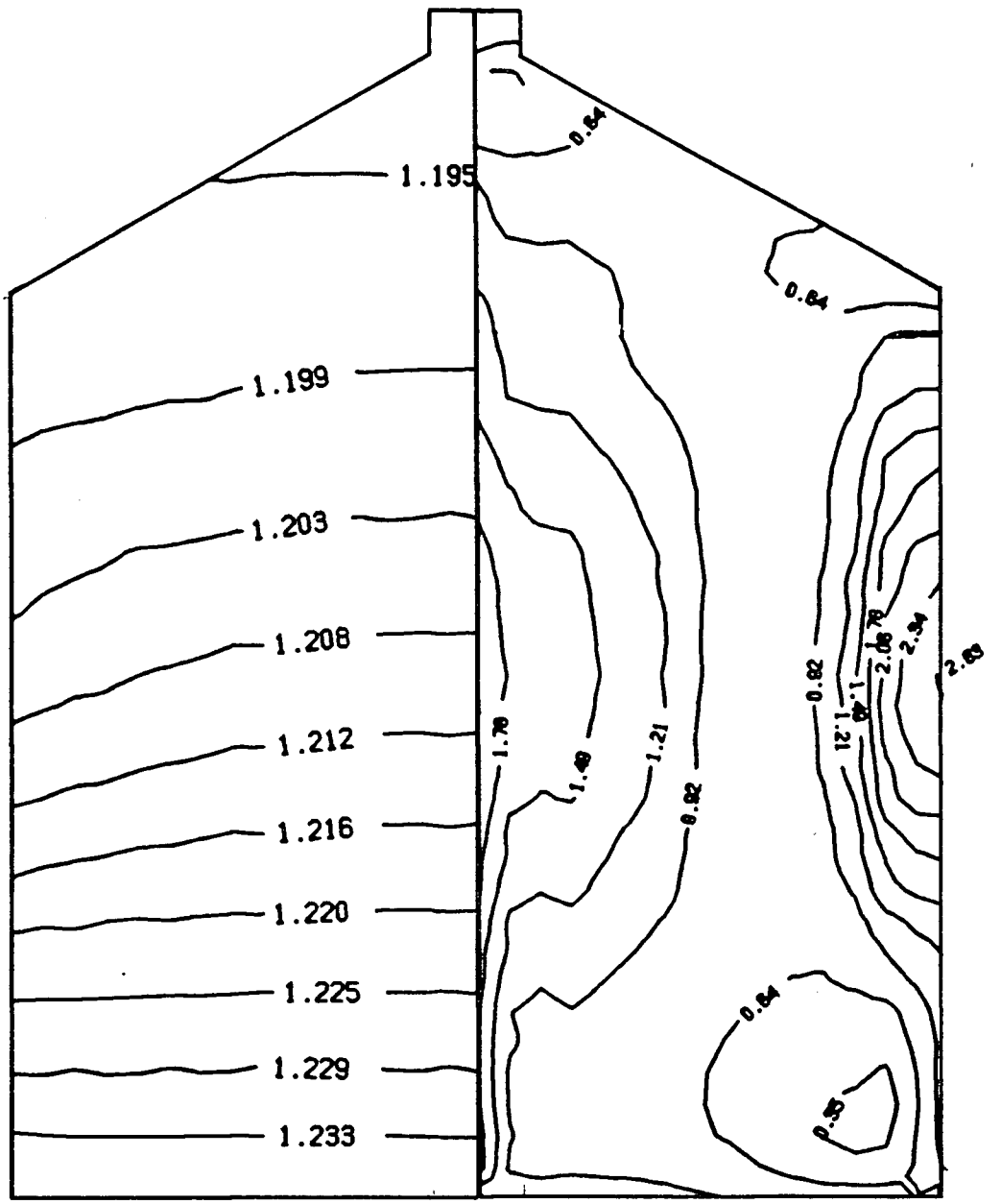
1.195
1.199
1.203
1.208
1.212
1.216
1.220
1.225
1.229
1.233
0.84
0.84
1.70
1.49
1.21
0.82
0.82
1.21
1.70
2.08
2.34
2.60
0.84
0.55

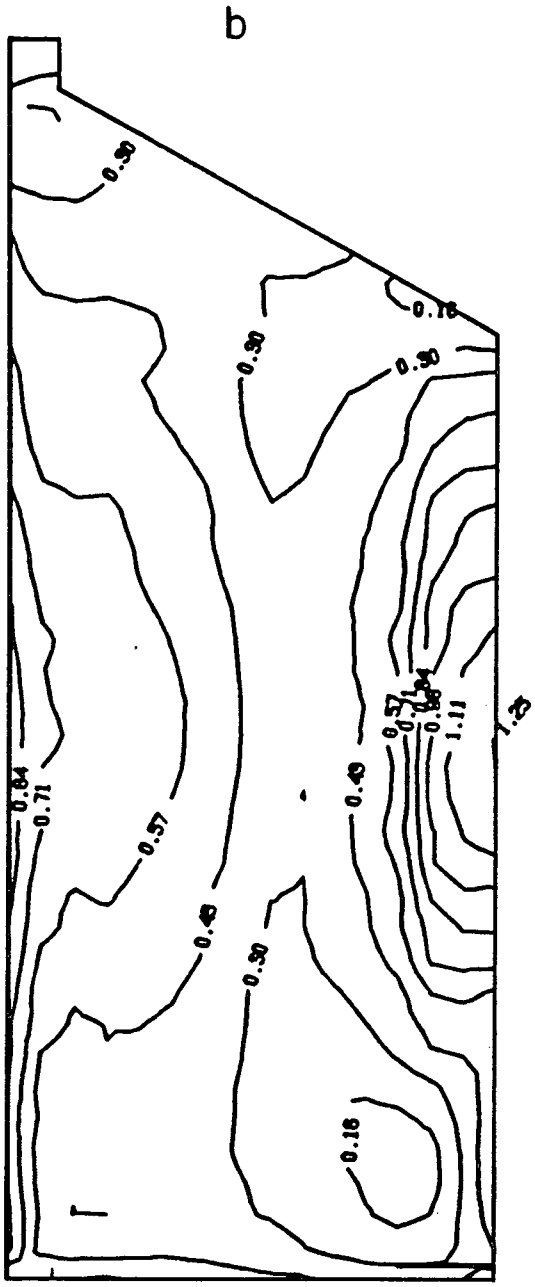
b
0.30
0.16
0.30
0.30
0.84
0.71
0.57
0.49
0.49
0.30
0.16
1.11
1.25

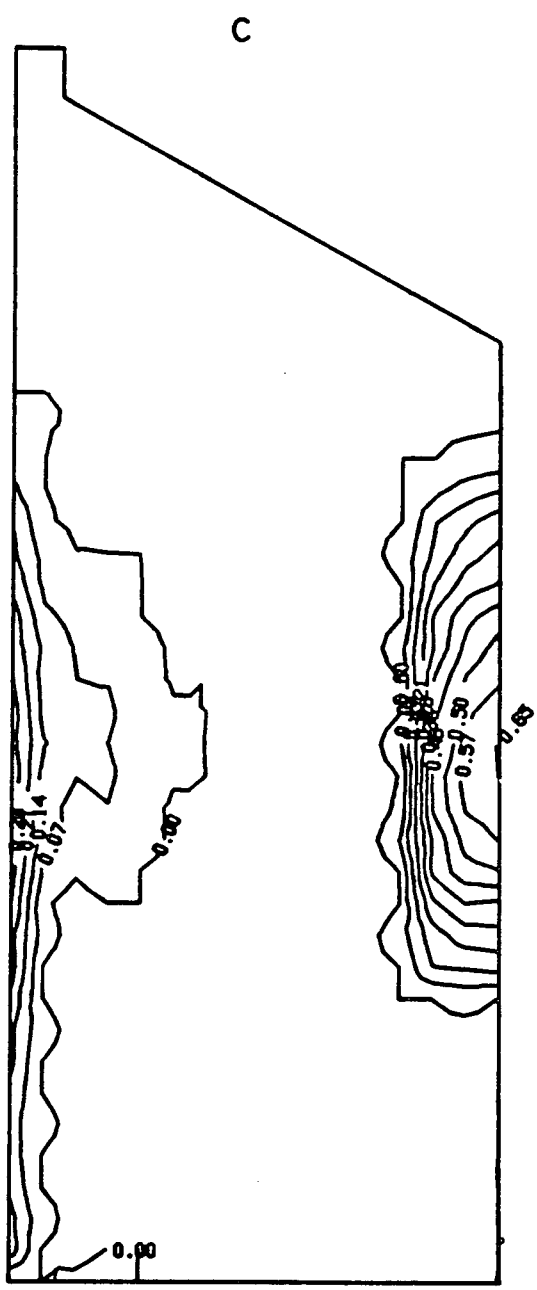
c
0.00
0.00
0.57
0.63

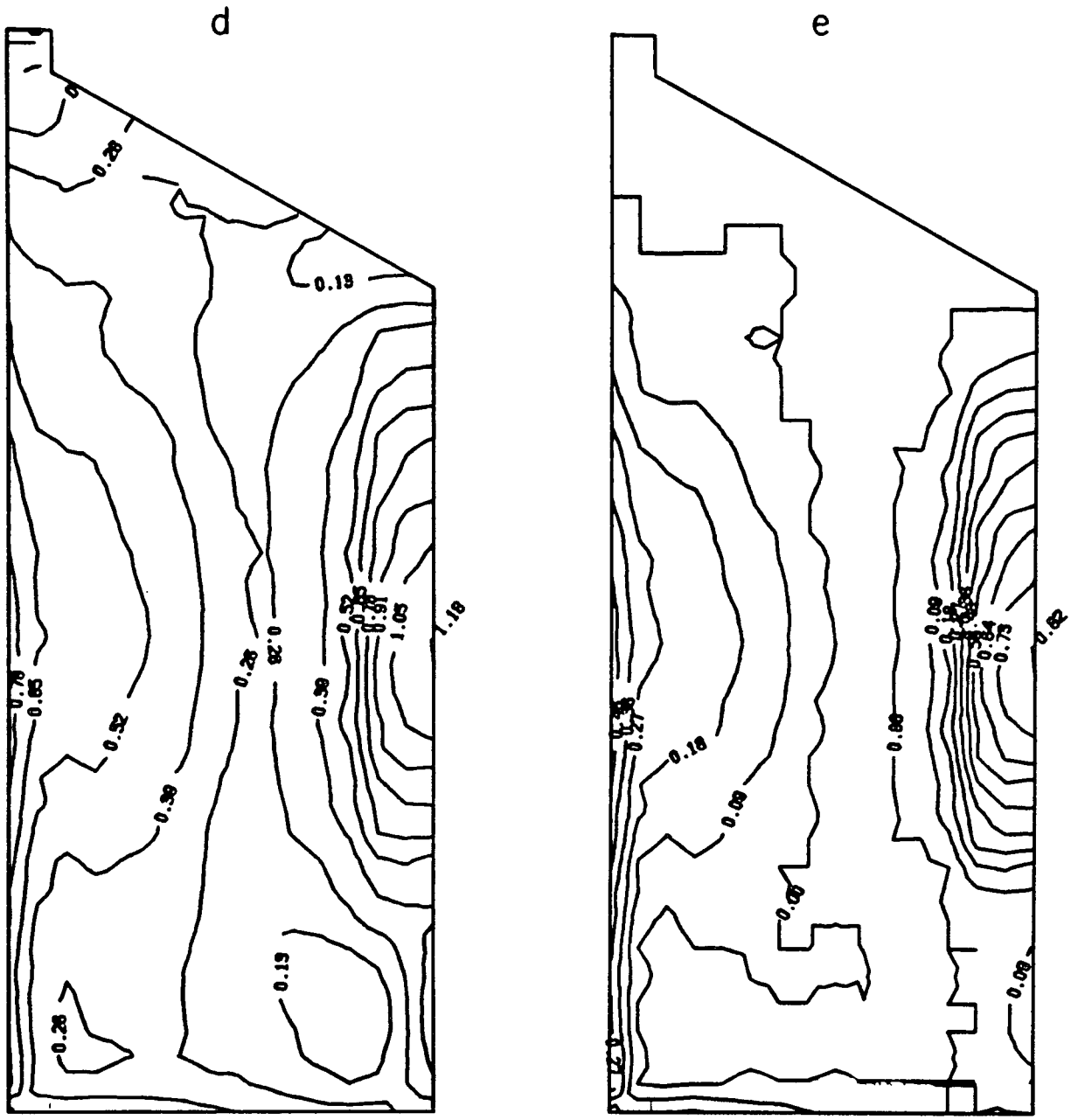

XIII.5.1.4 G/8

(a) Temperature and Von Mises Stress
(b) MRSS ; (c) MRSS-CRSS (Yield) ;
(d) MRSS-CRSS (MB) ; (e) MRSS-CRSS (MBTe) .

a

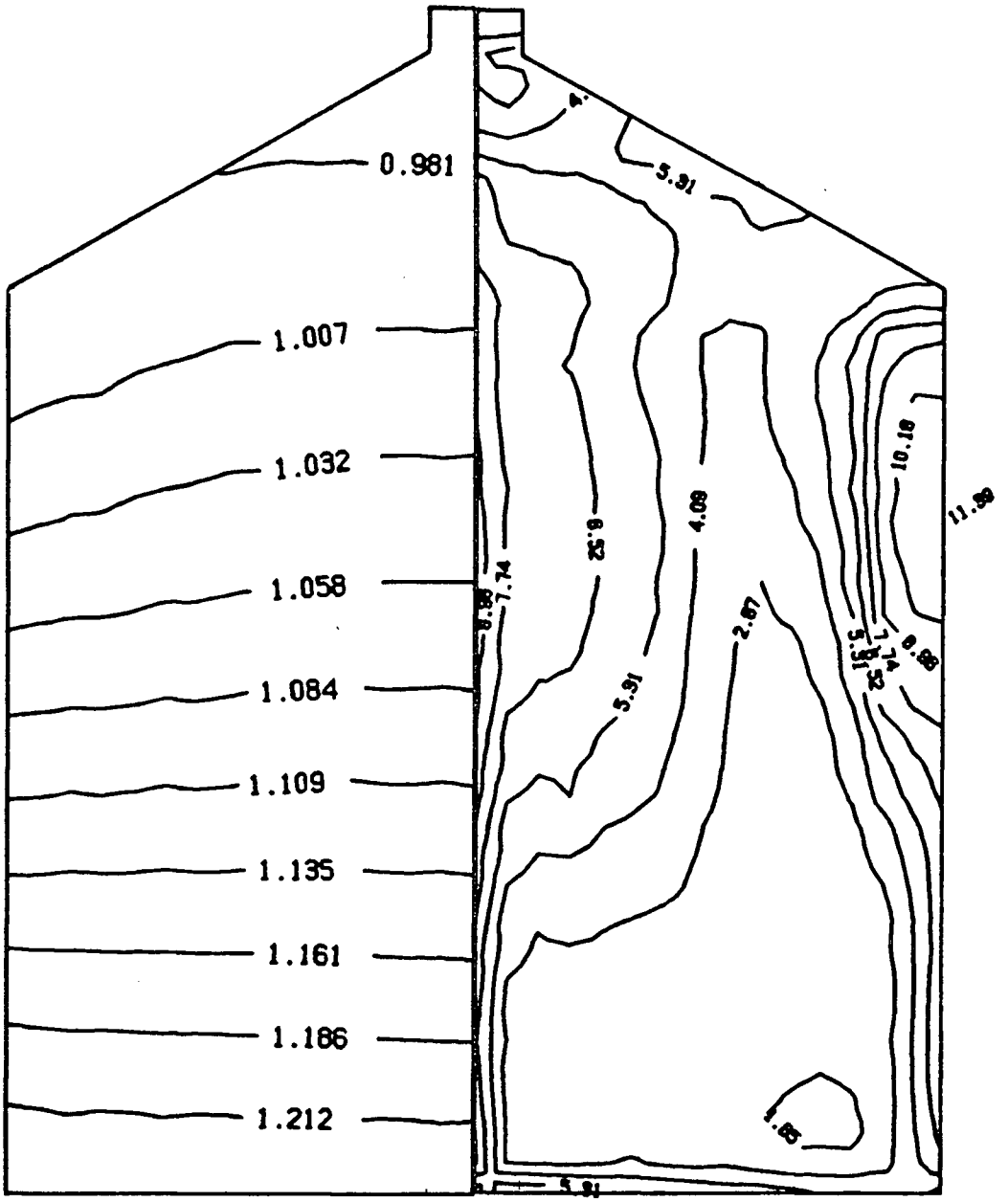
0.981
1.007
1.032
1.058
1.084
1.109
1.135
1.161
1.186
1.212
5.31
4.09
2.87
10.18
11.89
7.74
6.52
5.31

b

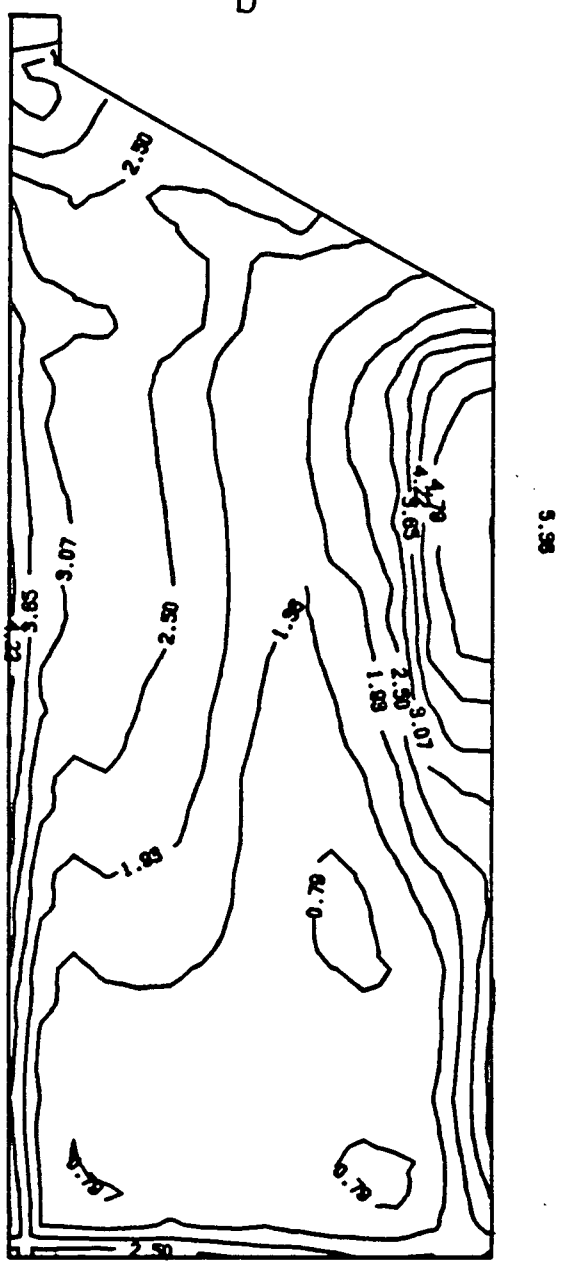

c

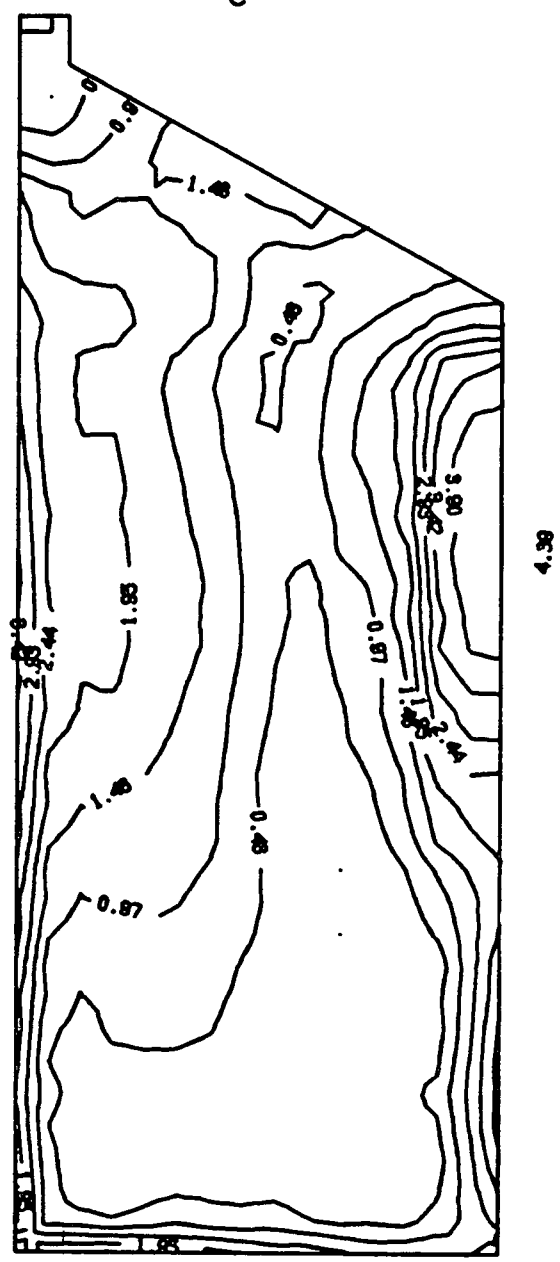

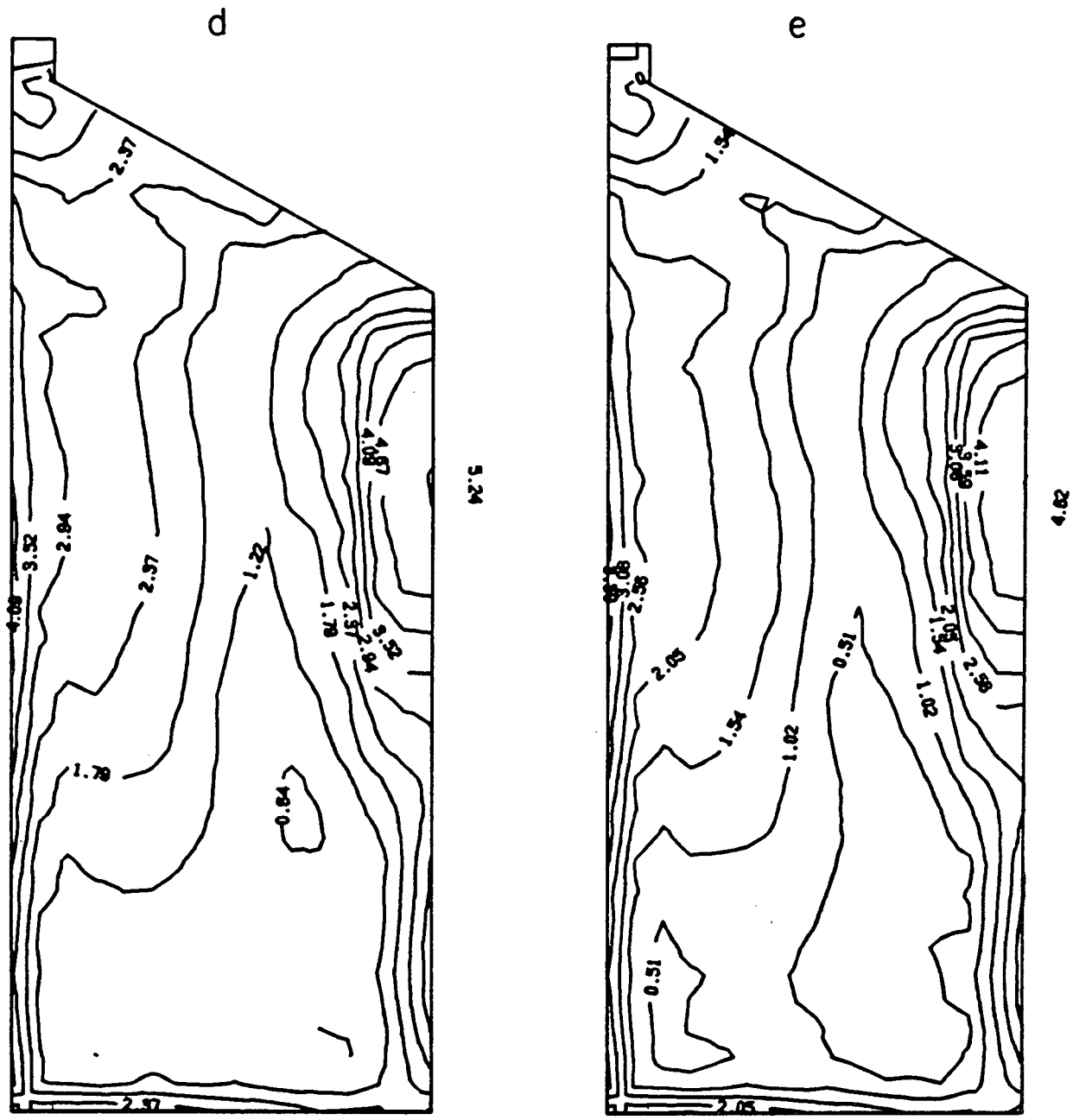

XIII.5.2.1 G

(a) Temperature and Von Mises Stress
(b) MRSS ; (c) MRSS-CRSS (Yield) ;
(d) MRSS-CRSS (MB) ; (e) MRSS-CRSS (MBTe) .

a

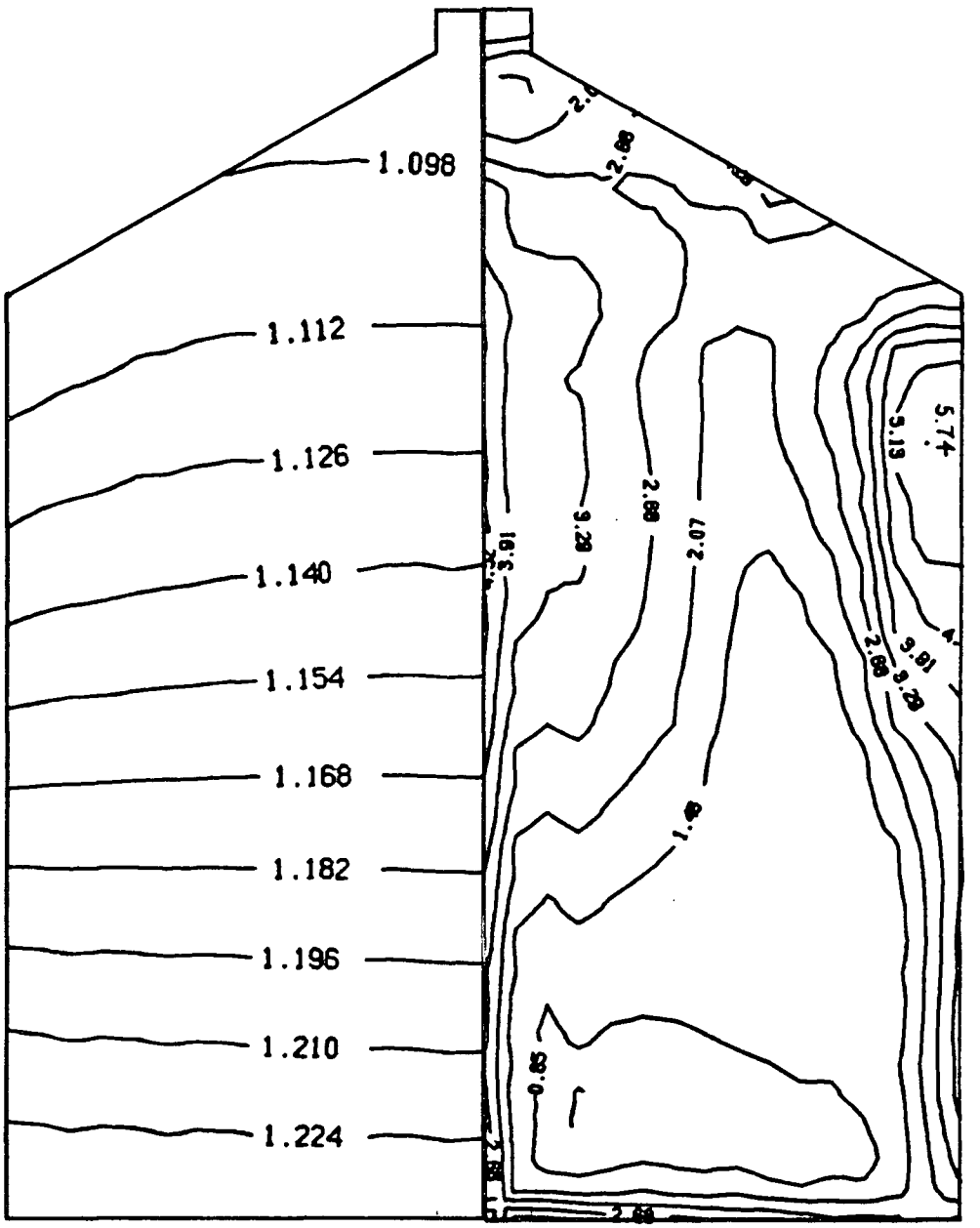
1.098
1.112
1.126
1.140
1.154
1.168
1.182
1.196
1.210
1.224
2.88
3.29
2.88
2.07
5.74
5.13
3.81
3.29
2.88
1.48
0.85
2.88

b

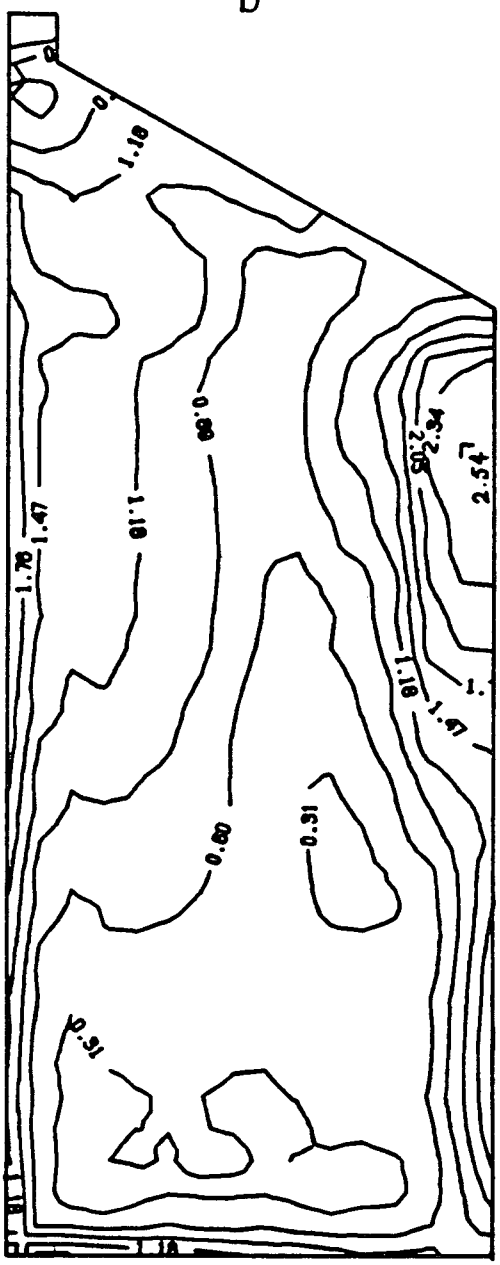

c

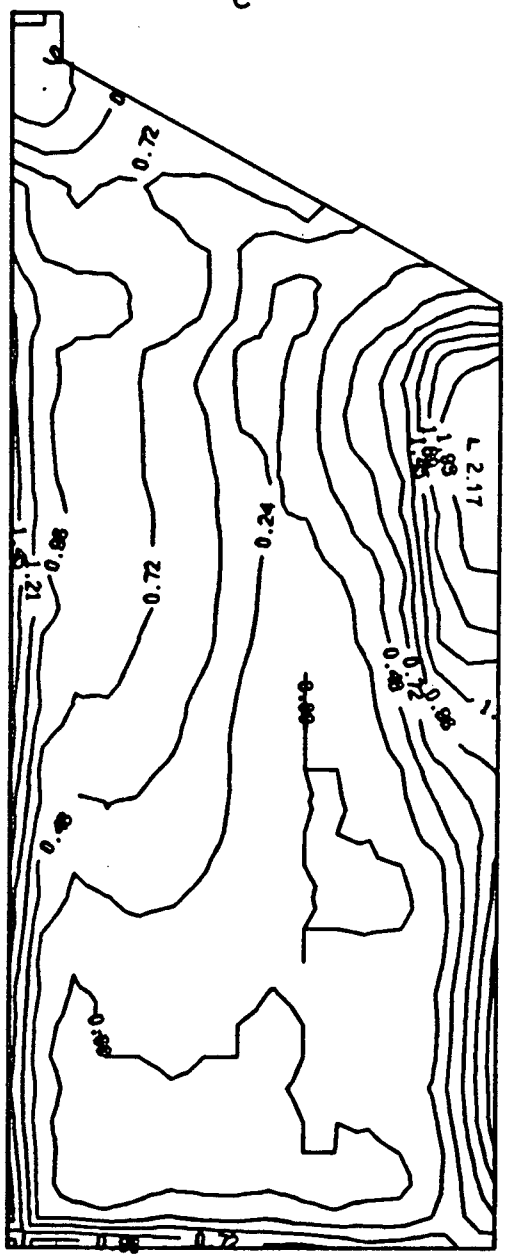

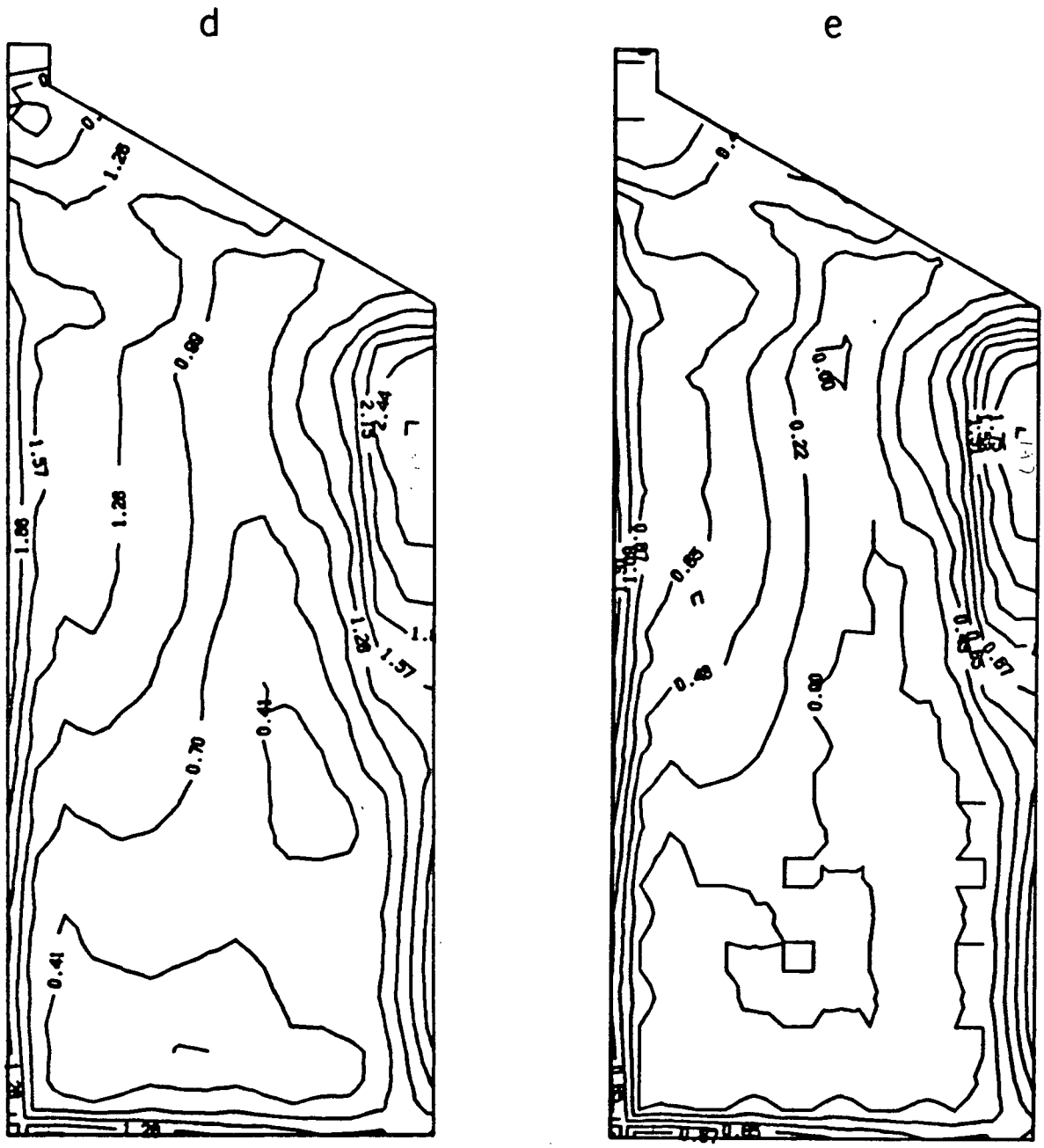

XIII.5.2.2 G/2

(a) Temperature and Von Mises Stress
(b) MRSS ; (c) MRSS-CRSS (Yield) ;
(d) MRSS-CRSS (MB) ; (e) MRSS-CRSS (MBTe) .

a

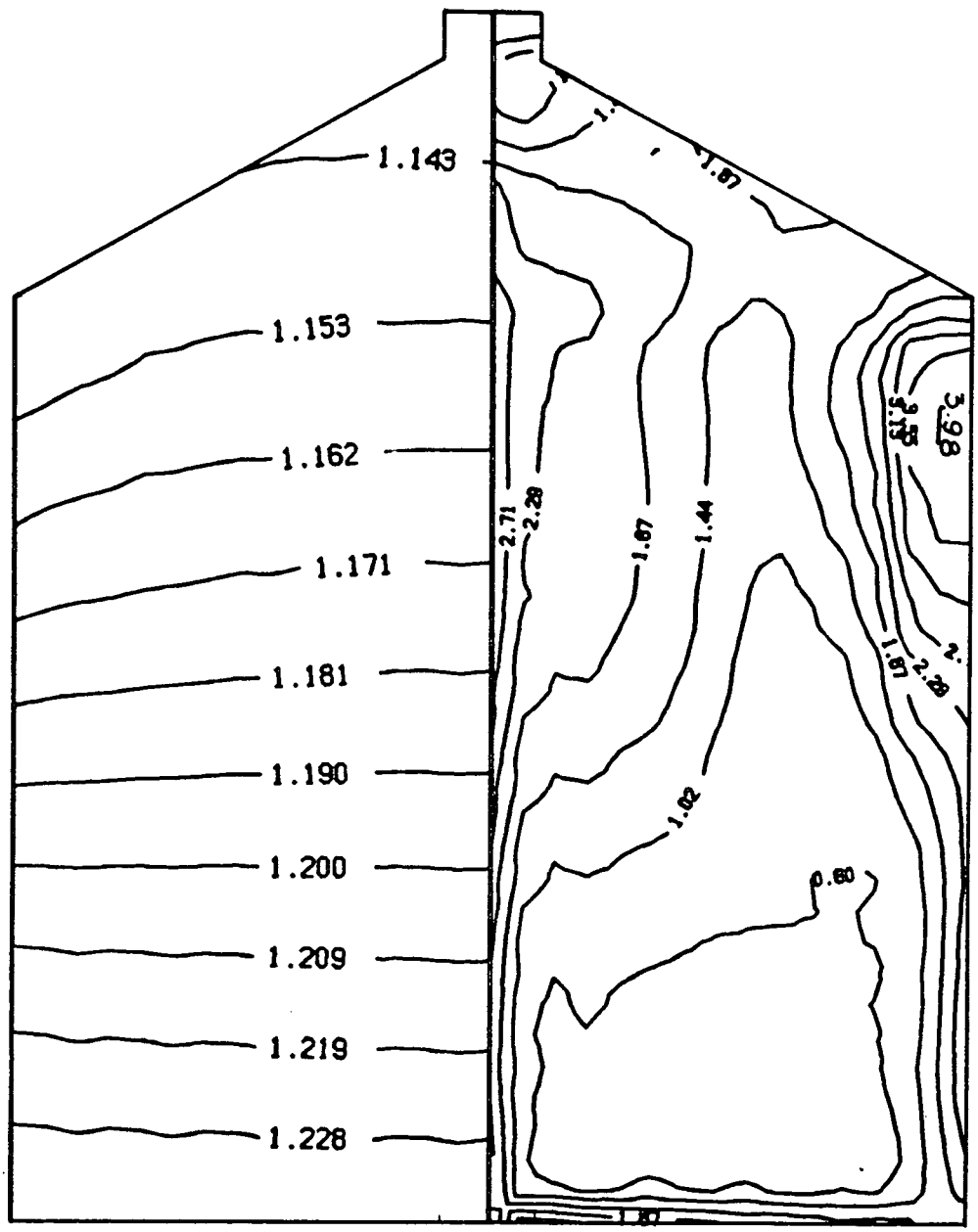
1.143
1.153
1.162
1.171
1.181
1.190
1.200
1.209
1.219
1.228
2.71
2.29
1.87
1.44
1.02
0.60

b

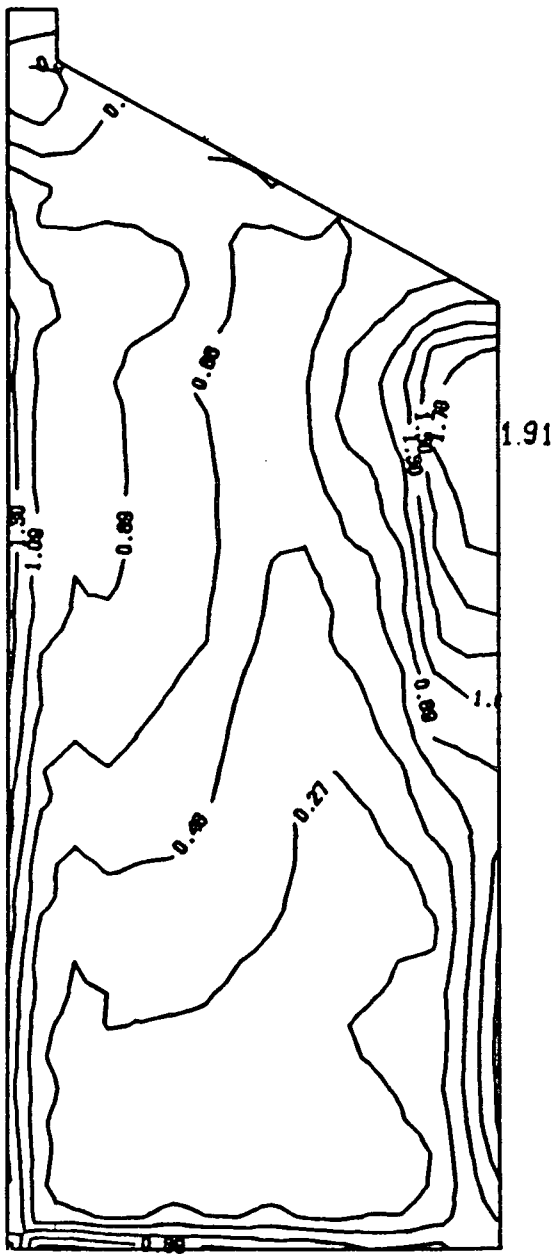

c

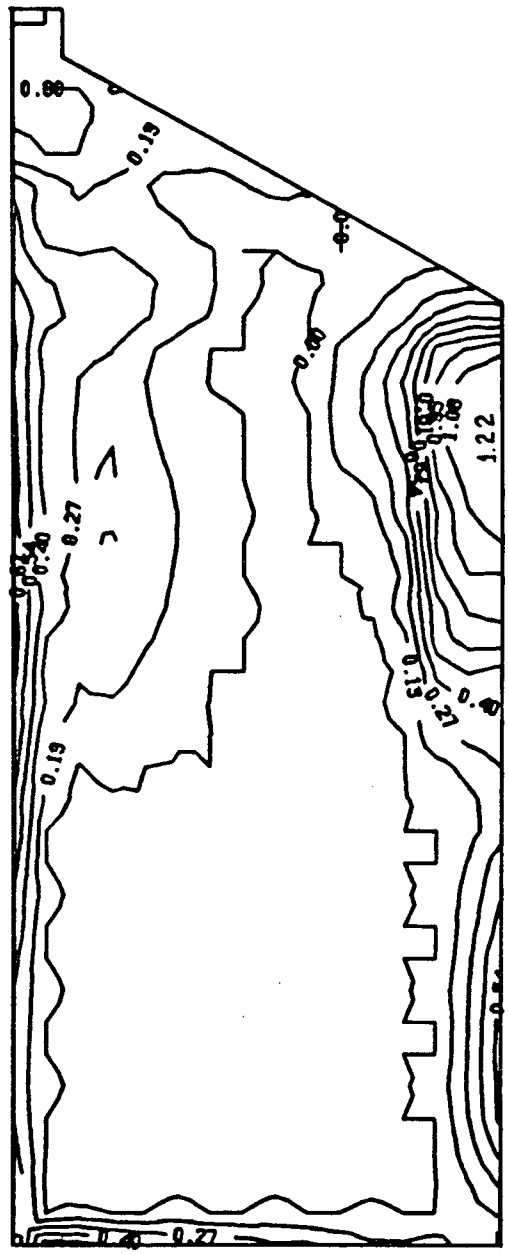

XIII.5.2.3 G/3

(a) Temperature and Von Mises Stress
(b) MRSS ; (c) MRSS-CRSS (Yield) ;
(d) MRSS-CRSS (MB) ; (e) MRSS-CRSS (MBTe) .

a

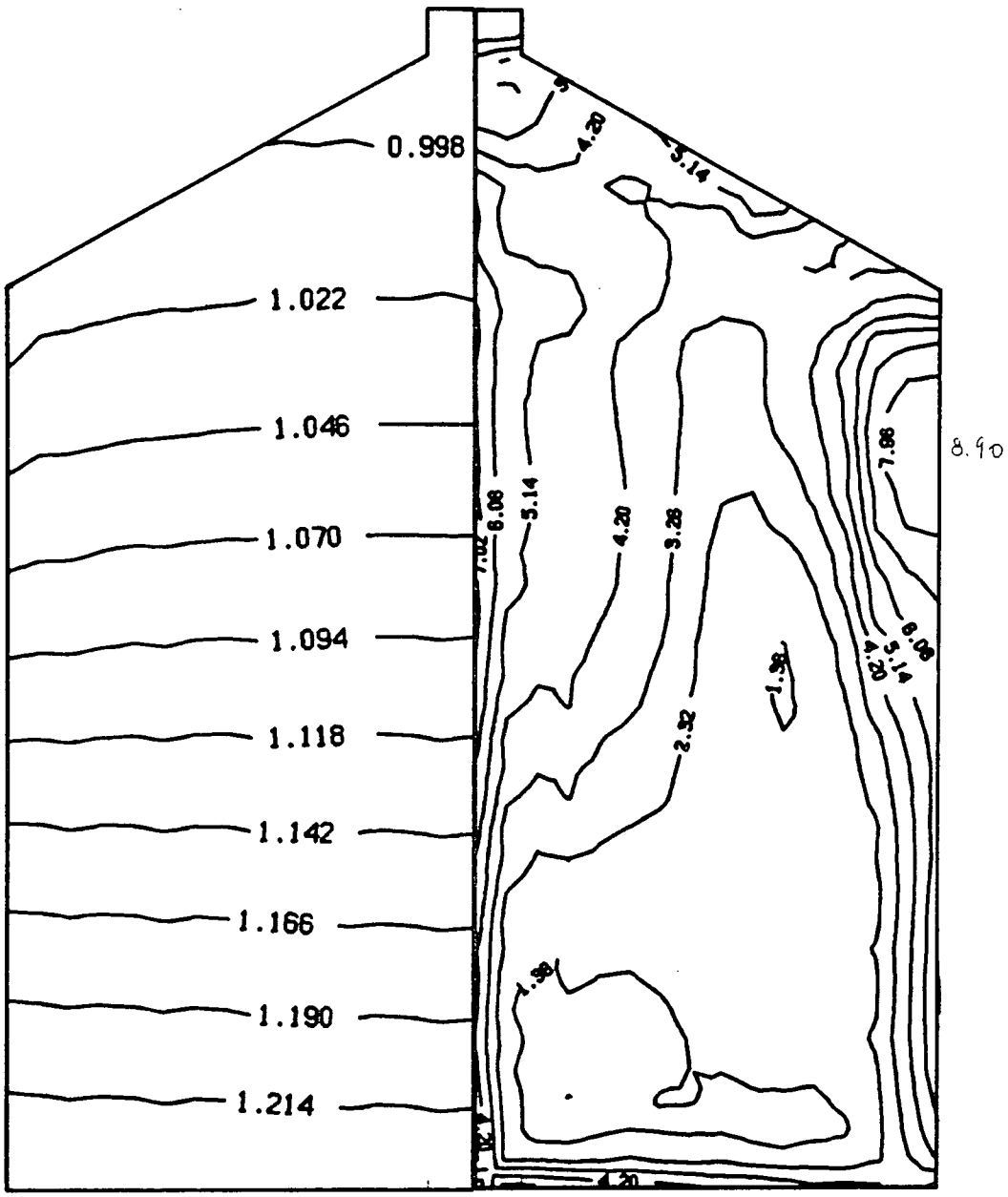
0.998
1.022
1.046
1.070
1.094
1.118
1.142
1.166
1.190
1.214
4.20
5.14
8.90
7.88
6.08
5.14
4.20
3.26
2.32
1.38
1.38
4.20

b

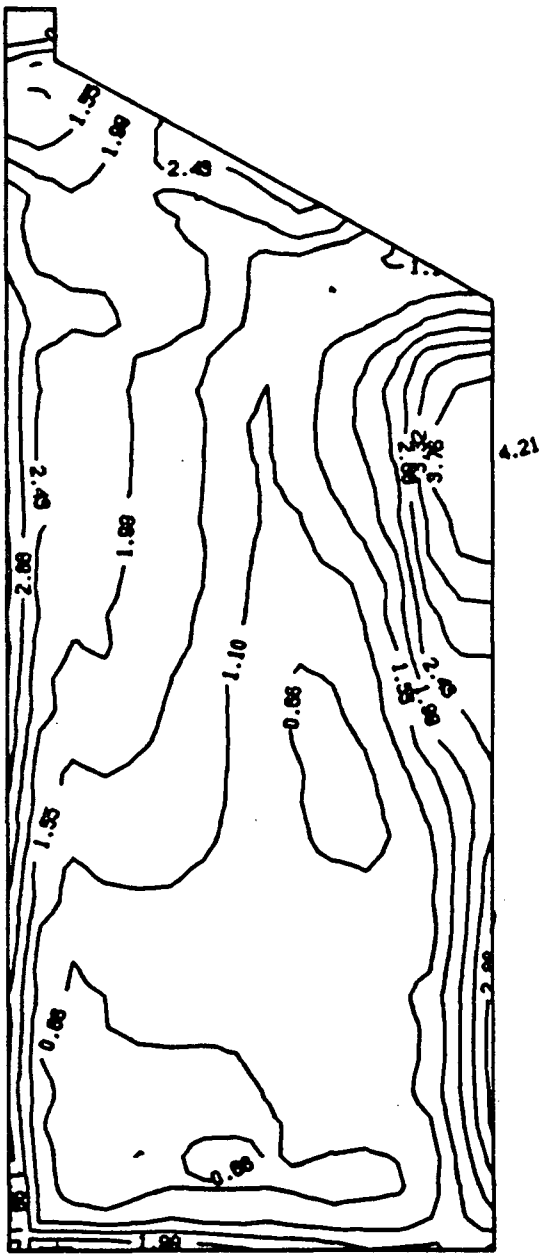

c

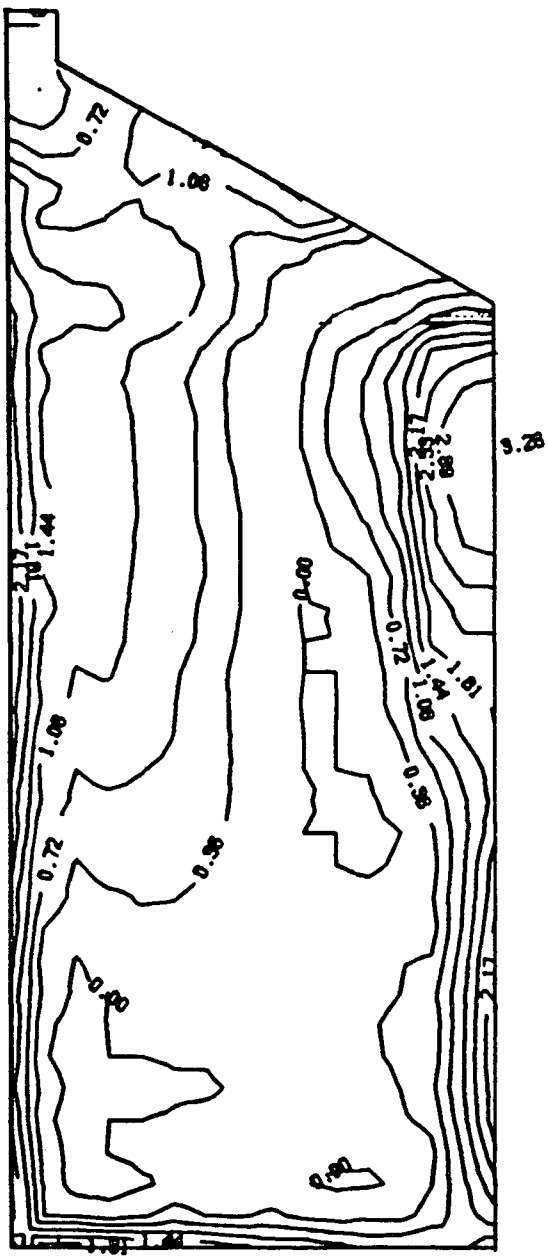

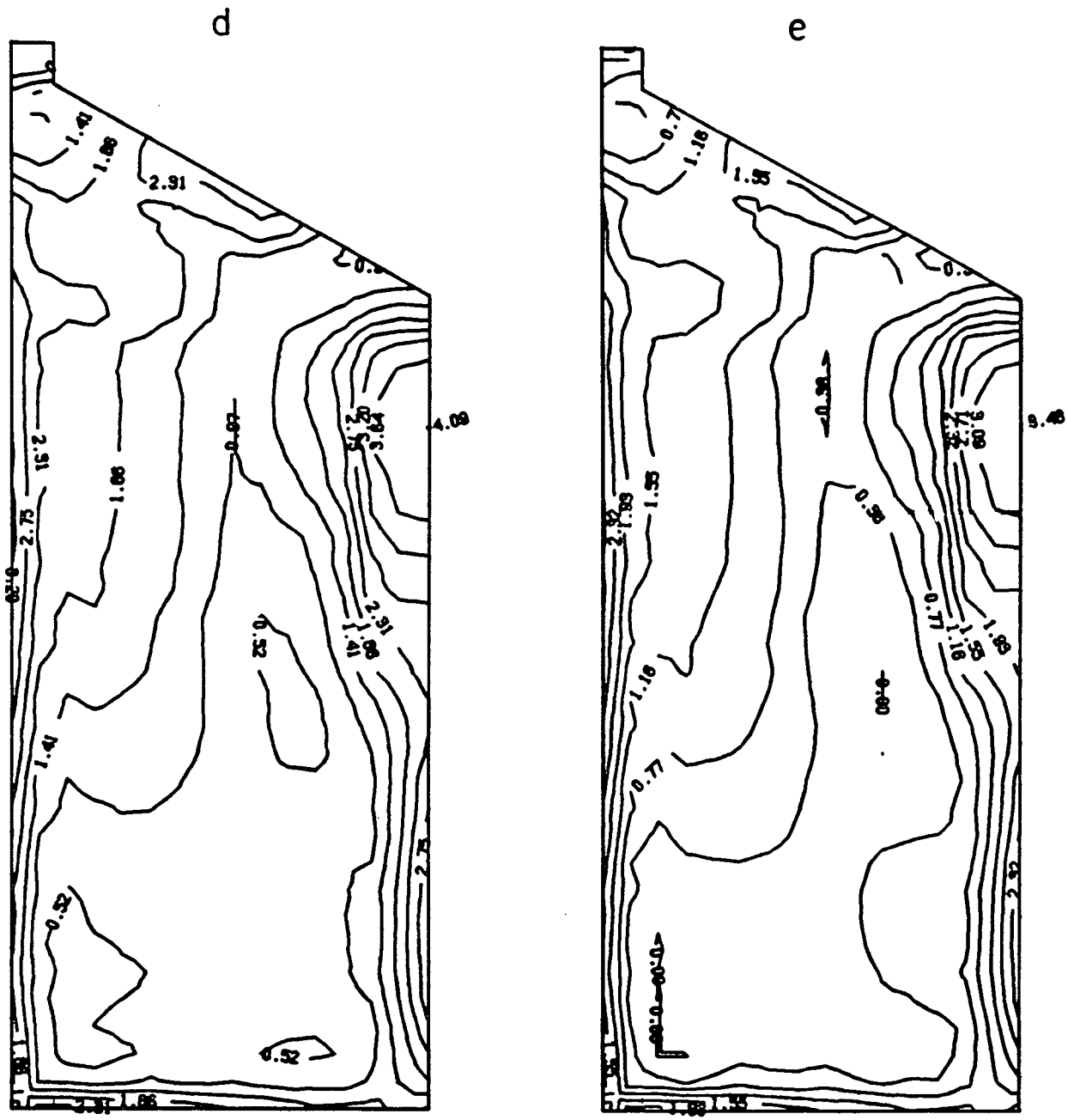

XIII.5.3.1 G

(a) Temperature and Von Mises Stress
(b) MRSS ; (c) MRSS-CRSS (Yield) ;
(d) MRSS-CRSS (MB) ; (e) MRSS-CRSS (MBTe) .

a

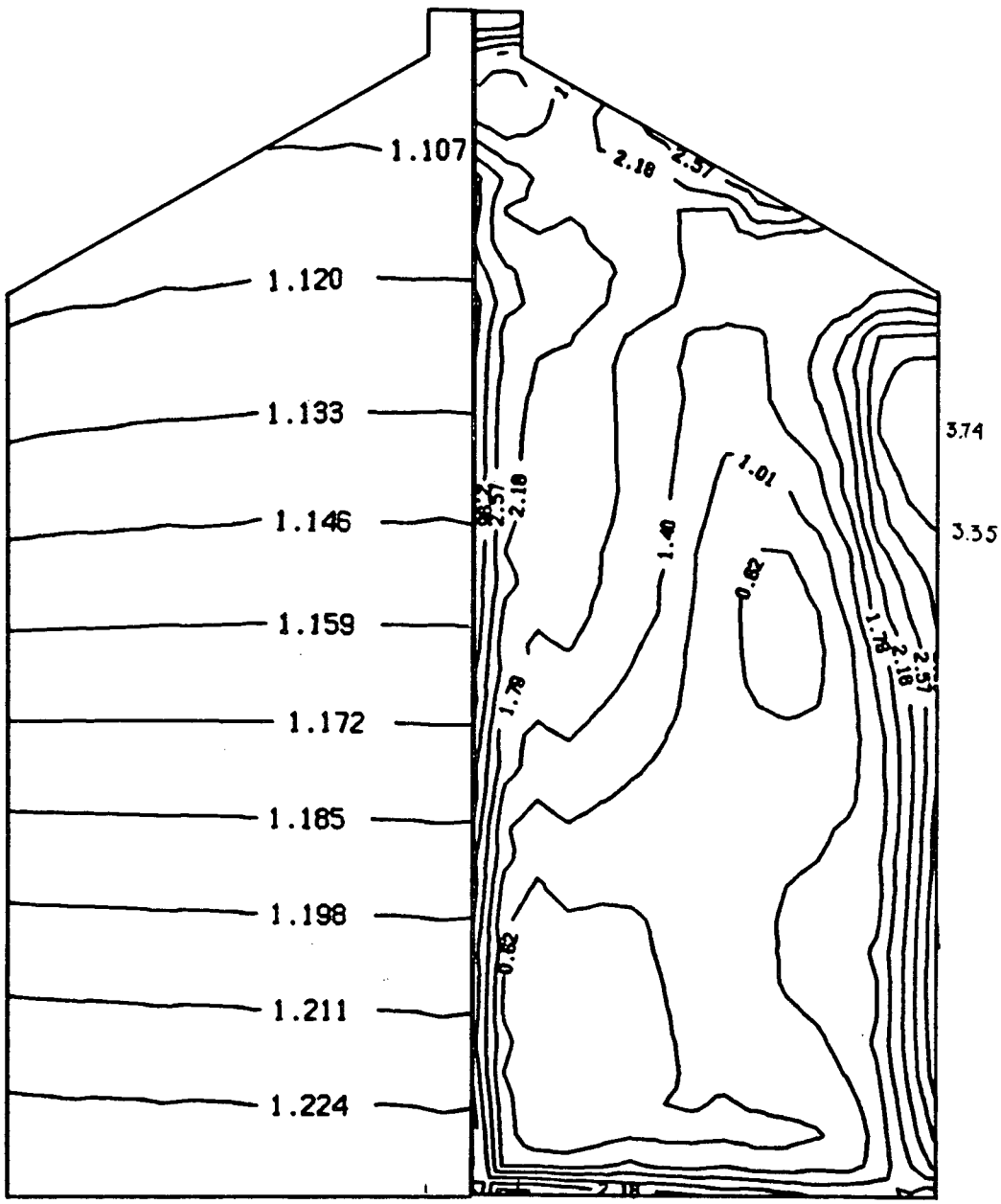
1.107
1.120
1.133
1.146
1.159
1.172
1.185
1.198
1.211
1.224
2.18
2.57
1.01
1.78
3.74
3.35

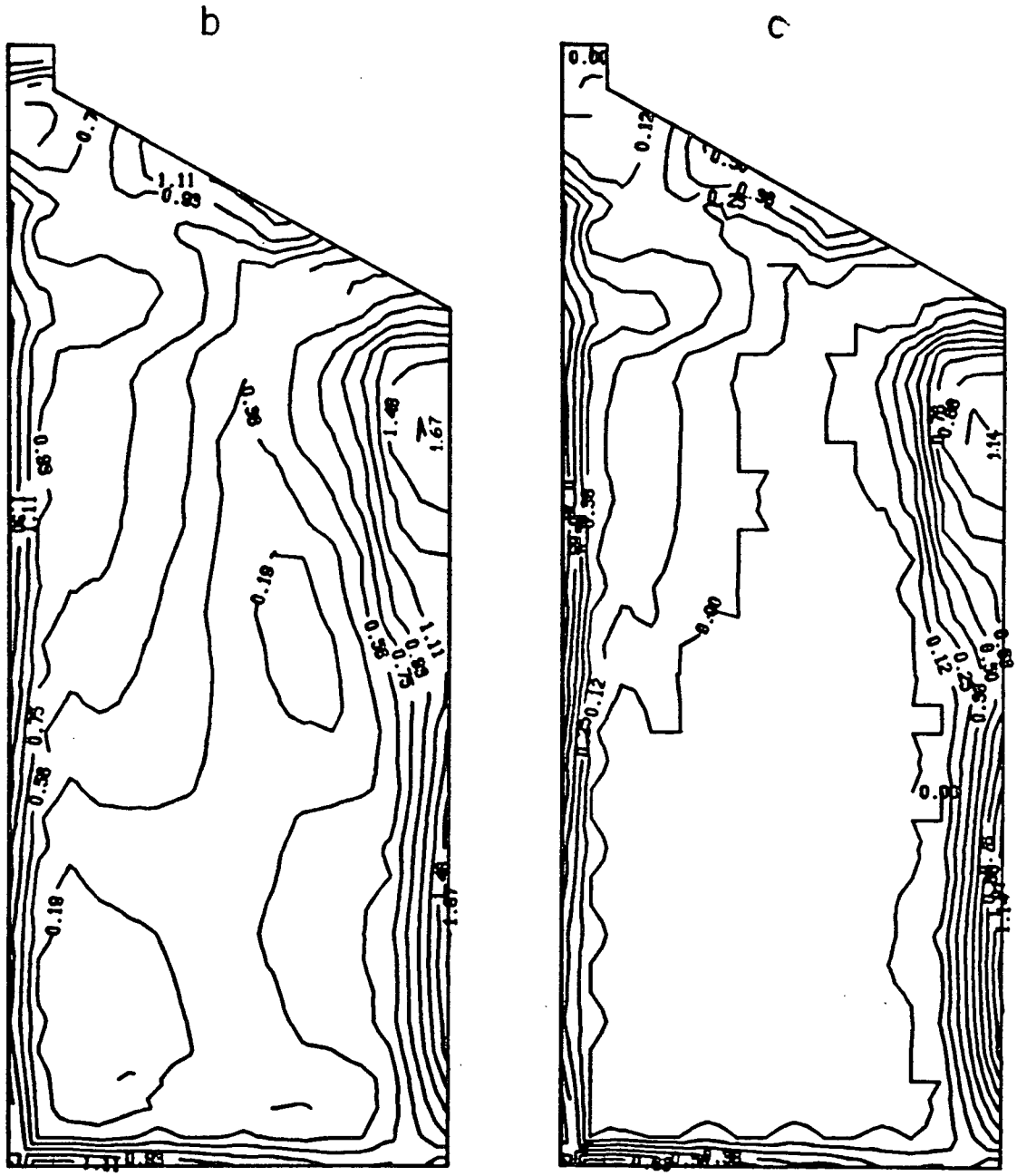

XIII.5.3.2 G/2
(a) Temperature and Von Mises Stress
(b) MRSS ; (c) MRSS-CRSS (Yield) ;

a

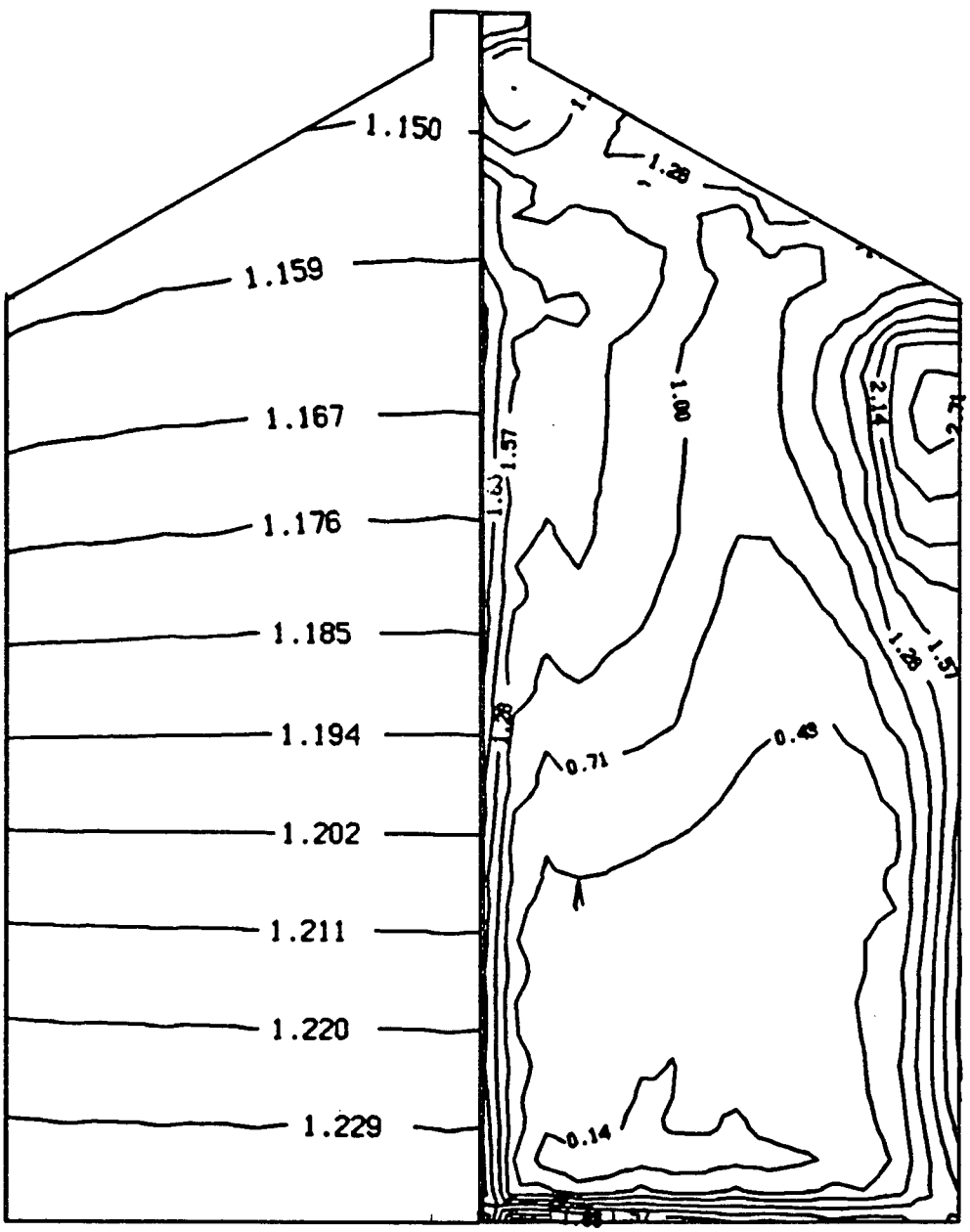
1.150
1.159
1.167
1.176
1.185
1.194
1.202
1.211
1.220
1.229
1.28
1.57
1.00
2.14
1.28
1.57
0.71
0.43
0.14

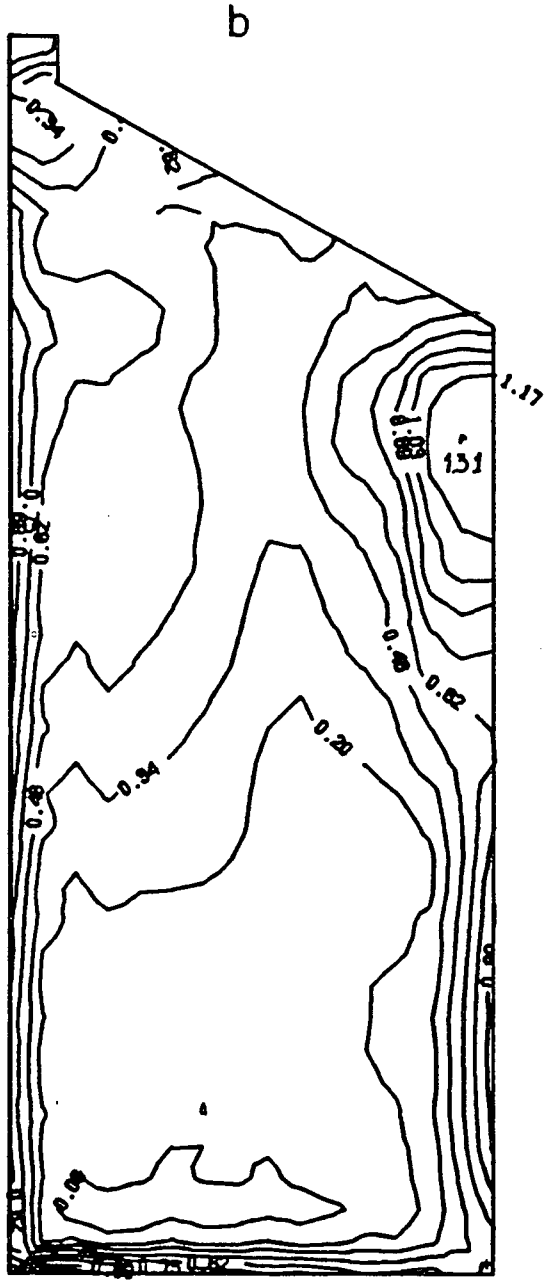
b
1.17
1.31
0.34
0.20

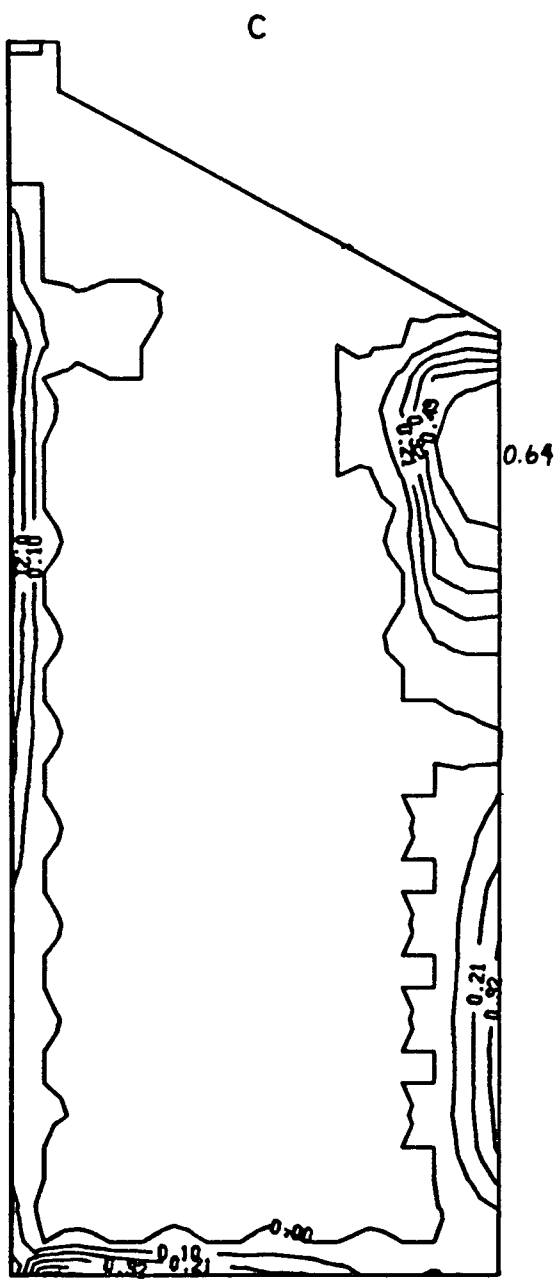
c
0.64
0.21

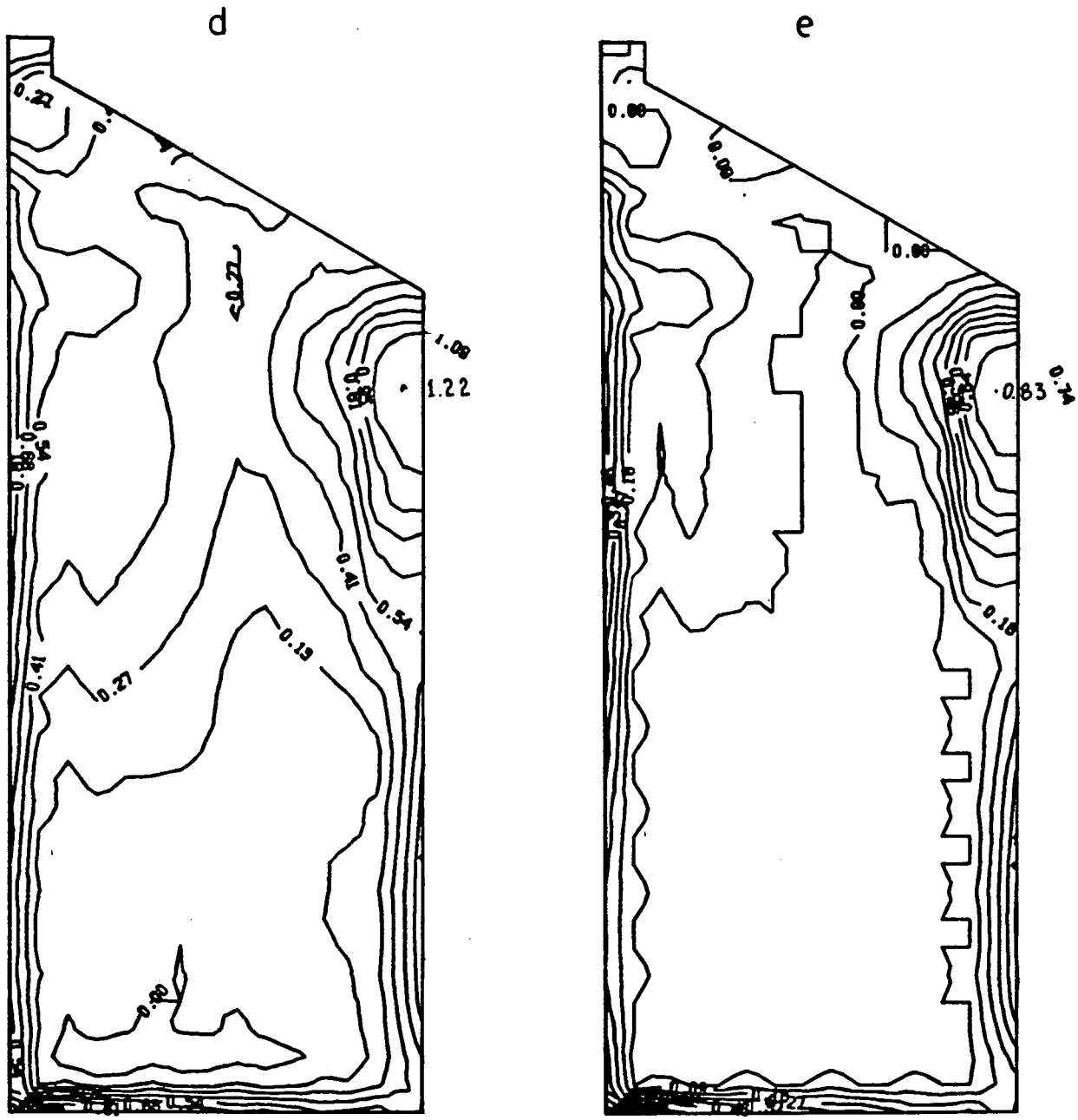

XIII.5.3.3 G/3
(a) Temperature and Von Mises Stress
(b) MRSS ; (c) MRSS-CRSS (Yield) ;
(d) MRSS-CRSS (MB) ; (e) MRSS-CRSS (MBTe) .

XIII.6 Thermal Conditions R, 40 mm
CL, 80 mm ; CA, 30° ; AP, 30 atm.

XIII.6.1 B,21 mm

XIII.6.1.1 G/4
(a) Temperature and Von Mises Stress
(b) MRSS ; (c) MRSS-CRSS (Yield) ;
(d) MRSS-CRSS (MB) ; (e) MRSS-CRSS (MBTe) .

XIII.6.1.2 G/8
(a) Temperature and Von Mises Stress
(b) MRSS ; (c) MRSS-CRSS (Yield) ;
(d) MRSS-CRSS (MB) ; (e) MRSS-CRSS (MBTe) .

XIII.6.2 B, 40 mm

XIII.6.2.1 G
(a) Temperature and Von Mises Stress
(b) MRSS ; (c) MRSS-CRSS (Yield) ;
(d) MRSS-CRSS (MB) ; (e) MRSS-CRSS (MBTe) .

XIII.6.2.2 G/2
(a) Temperature and Von Mises Stress
(b) MRSS ; (c) MRSS-CRSS (Yield) ;
(d) MRSS-CRSS (MB) ; (e) MRSS-CRSS (MBTe) .

XIII.6.2.3 G/3
(a) Temperature and Von Mises Stress
(b) MRSS ; (c) MRSS-CRSS (Yield) ;
(d) MRSS-CRSS (MB) ; (e) MRSS-CRSS (MBTe) .

XIII.6.2.4 G/5
(a) Temperature and Von Mises Stress
(b) MRSS ; (c) MRSS-CRSS (Yield) ;
(d) MRSS-CRSS (MB) ; (e) MRSS-CRSS (MBTe) .

XIII.6.3 B, 50 mm

XIII.6.3.1 G

XIII.6.3.1.1 CL, 60 mm
(a) Temperature ; (b) Von Mises Stress
(c) MRSS ; (d) MRSS-CRSS (Yield) ;
(e) MRSS-CRSS (MB) ; (f) MRSS-CRSS (MBTe) .

XIII.6.3.1.2 CL, 80 mm
(a) Temperature and Von Mises Stress
(b) MRSS ; (c) MRSS-CRSS (Yield) ;
(d) MRSS-CRSS (MB) ; (e) MRSS-CRSS (MBTe) .

XIII.6.3.2 G/3
(a) Temperature and Von Mises Stress
(b) MRSS ; (c) MRSS-CRSS (Yield) ;
(d) MRSS-CRSS (MB) ; (e) MRSS-CRSS (MBTe) .

XIII.6.3.3 G/5
(a) Temperature and Von Mises Stress
(b) MRSS ; (c) MRSS-CRSS (Yield) ;
(d) MRSS-CRSS (MB) ; (e) MRSS-CRSS (MBTe) .

a

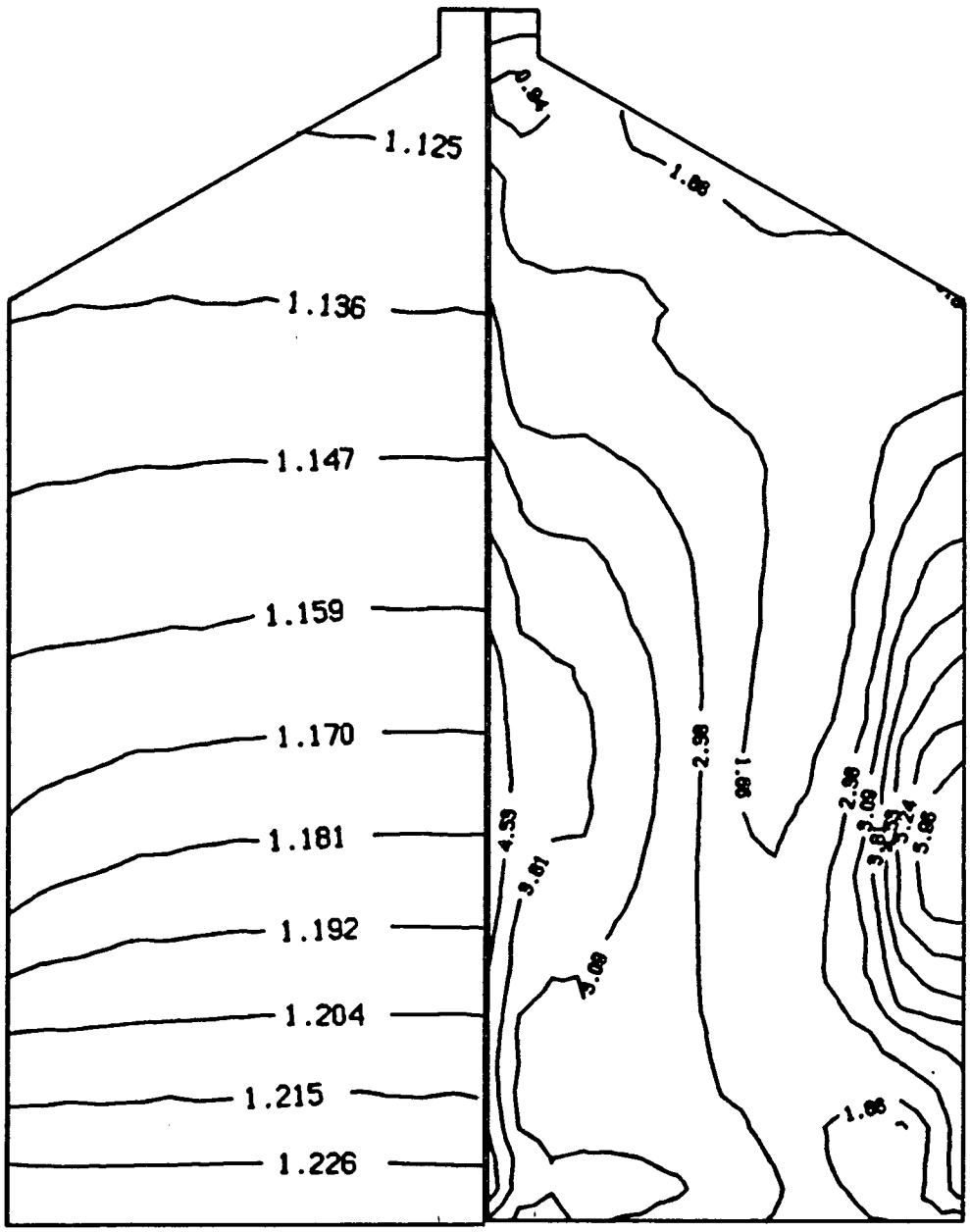
1.125
1.136
1.147
1.159
1.170
1.181
1.192
1.204
1.215
1.226
0.94
1.88
2.98
1.88
4.53
3.61
3.09
2.98
3.09
3.81
3.24
5.98
1.88

b

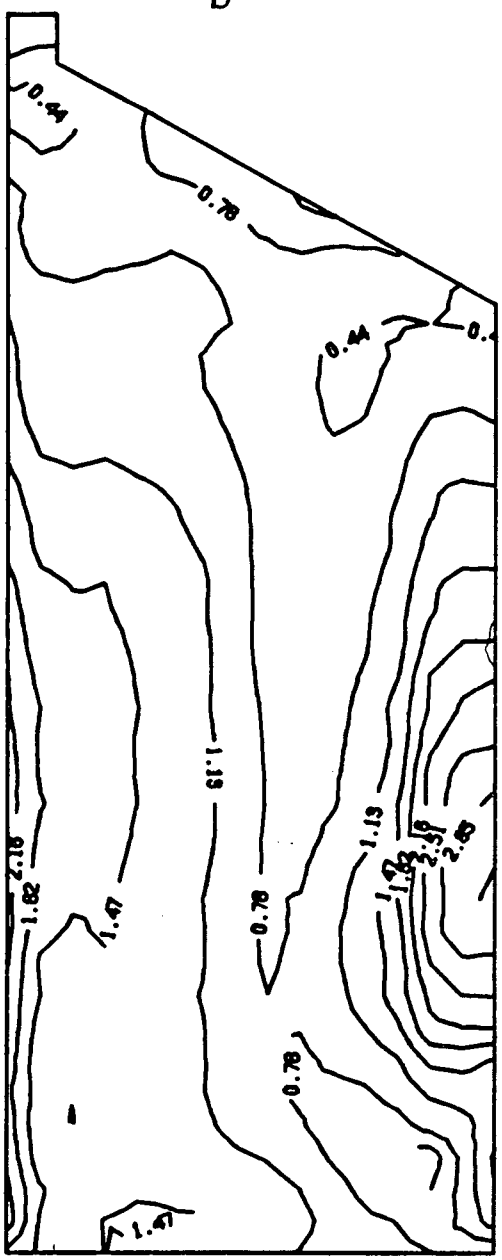
0.44
0.78
0.44
1.13
0.78
1.13
1.47
1.62
2.16
2.51
2.85
0.78
1.47

c

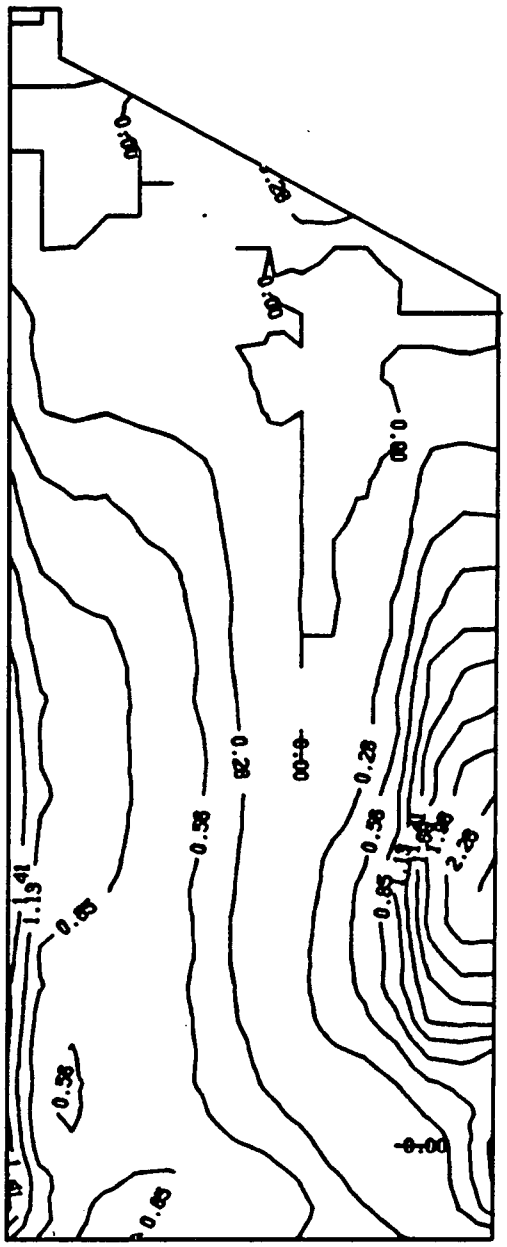
0.00
0.28
0.00
0.00
0.28
0.28
0.58
0.58
0.85
1.13
1.41
0.85
0.58
0.85
2.28
0.00

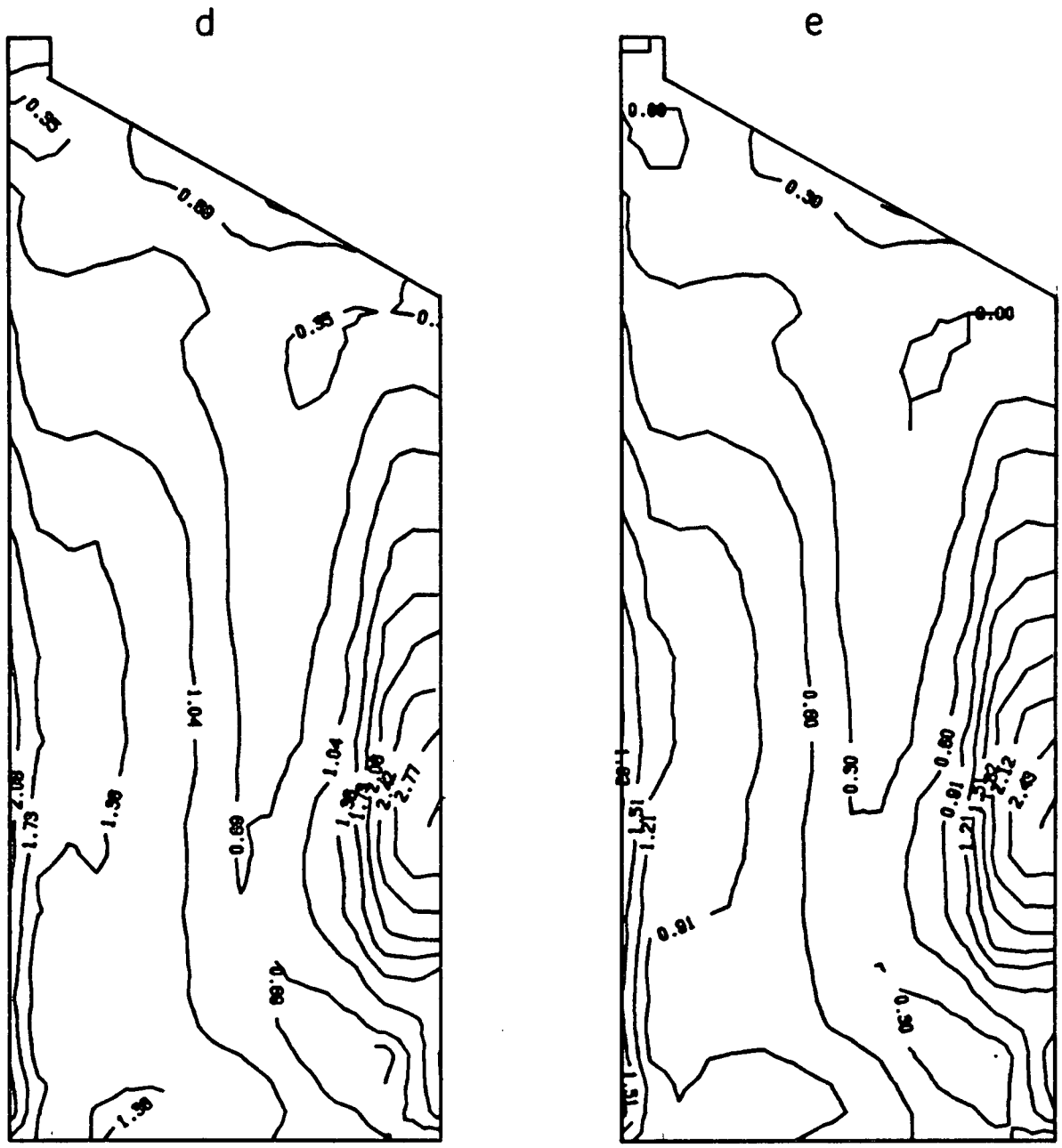

XIII.6.1.1 G/4
(a) Temperature and Von Mises Stress
(b) MRSS ; (c) MRSS-CRSS (Yield) ;
(d) MRSS-CRSS (MB) ; (e) MRSS-CRSS (MBTe) .

a

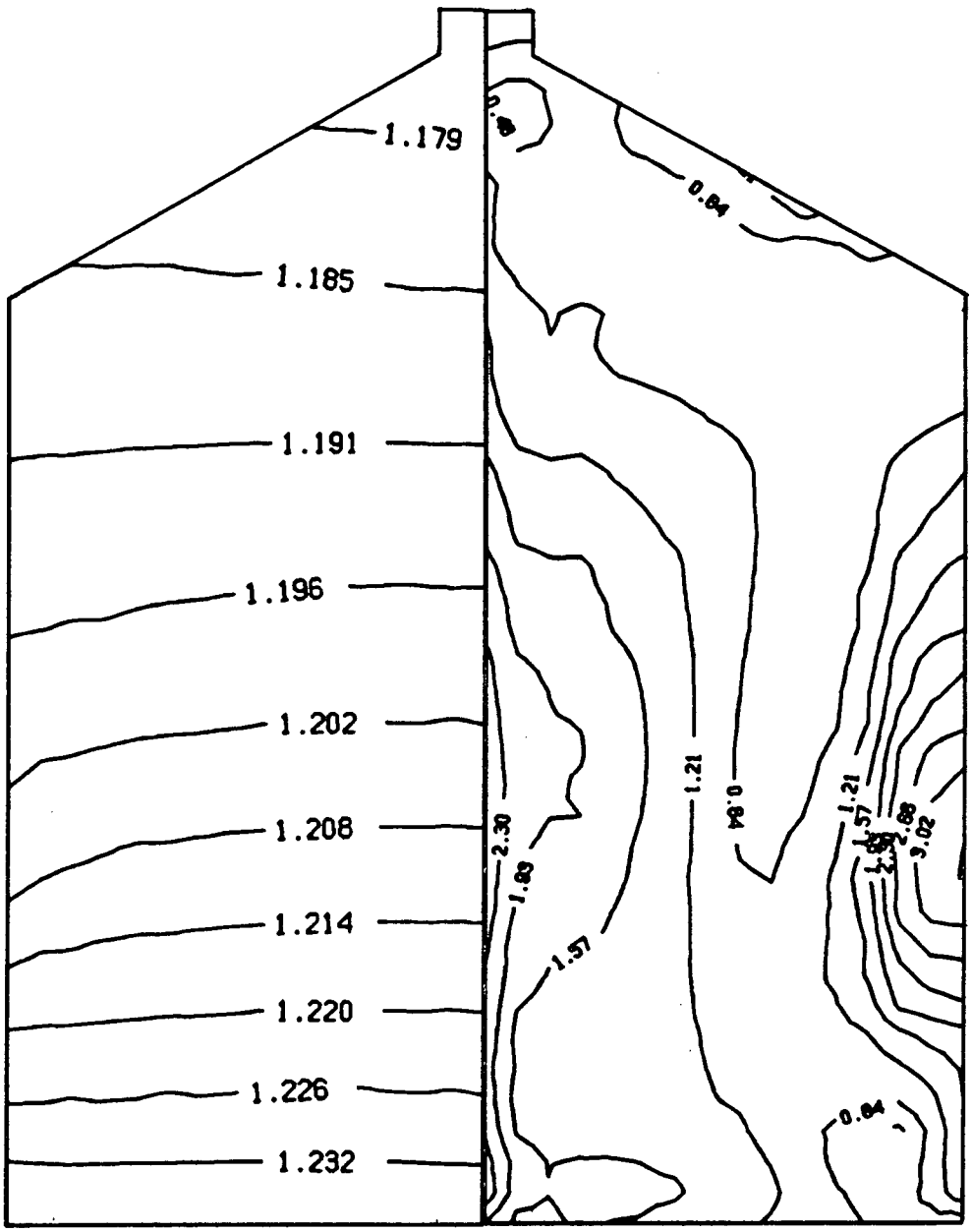
1.179
1.185
1.191
1.196
1.202
1.208
1.214
1.220
1.226
1.232
0.84
2.30
1.89
1.57
1.21
0.84
1.57
1.21
3.02
0.84

b

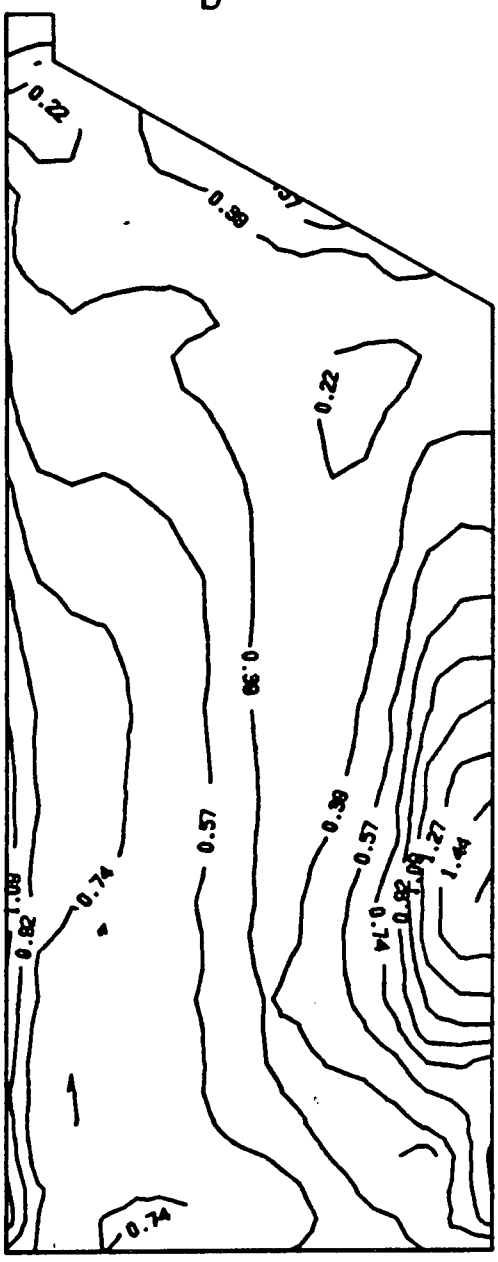
0.22
0.39
0.22
0.39
0.57
0.39
0.57
0.74
0.82
1.09
0.74
0.74
1.27
1.44

c

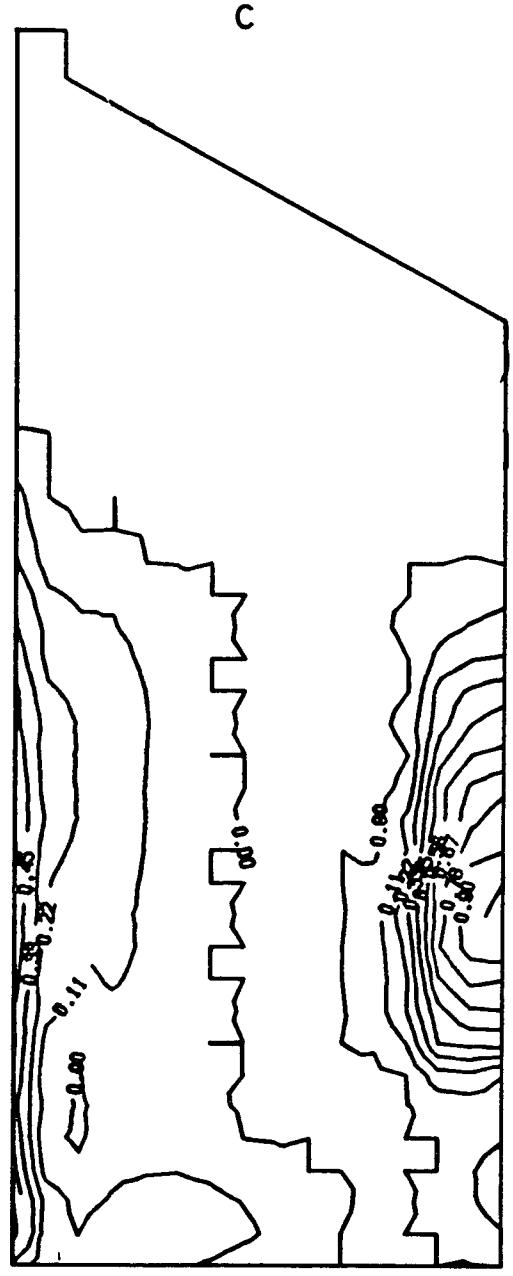
0.00
0.00
0.22
0.11
0.00

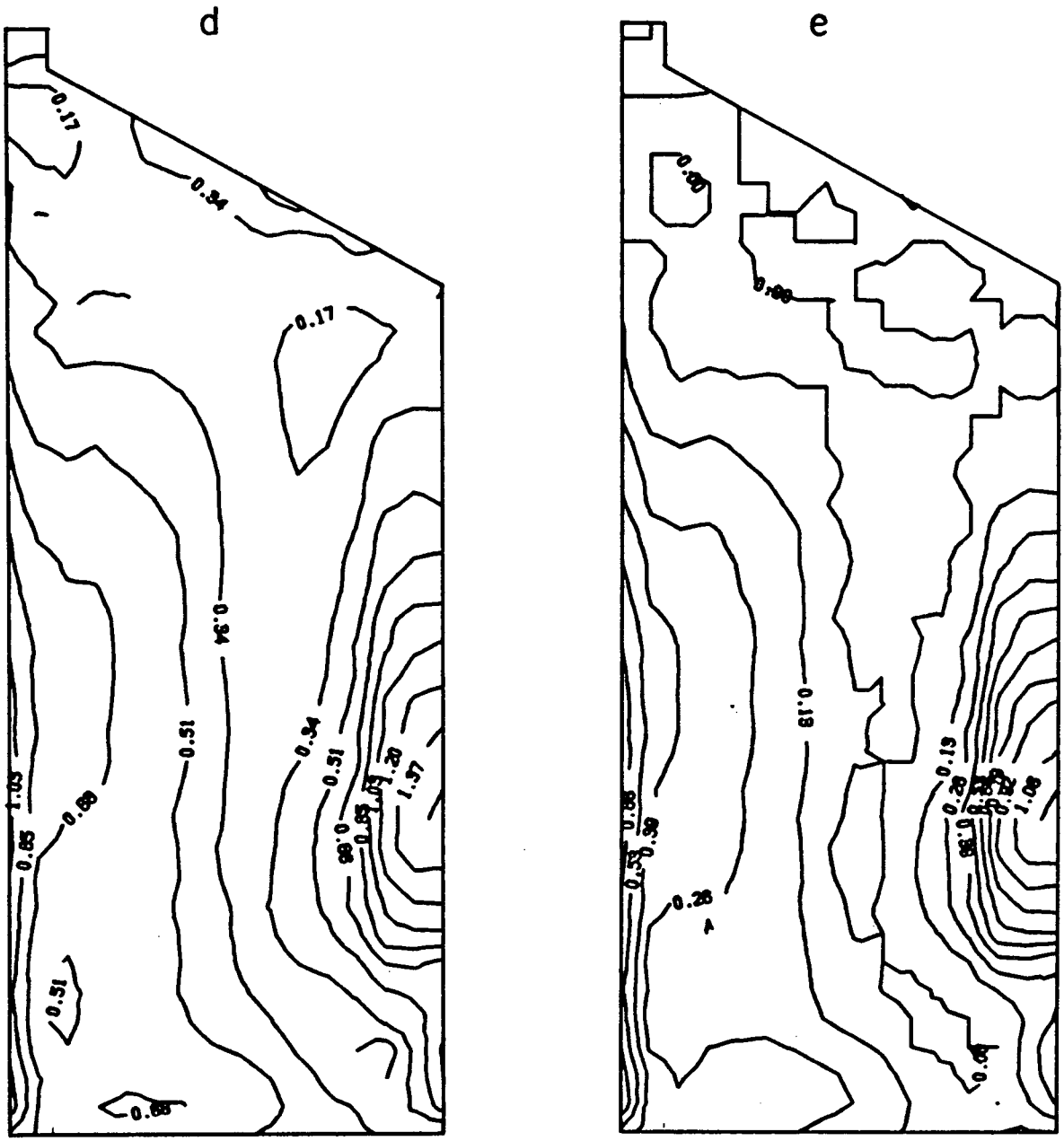

XIII.6.1.2 G/8
(a) Temperature and Von Mises Stress
(b) MRSS ; (c) MRSS-CRSS (Yield) ;
(d) MRSS-CRSS (MB) ; (e) MRSS-CRSS (MBTe) .

a

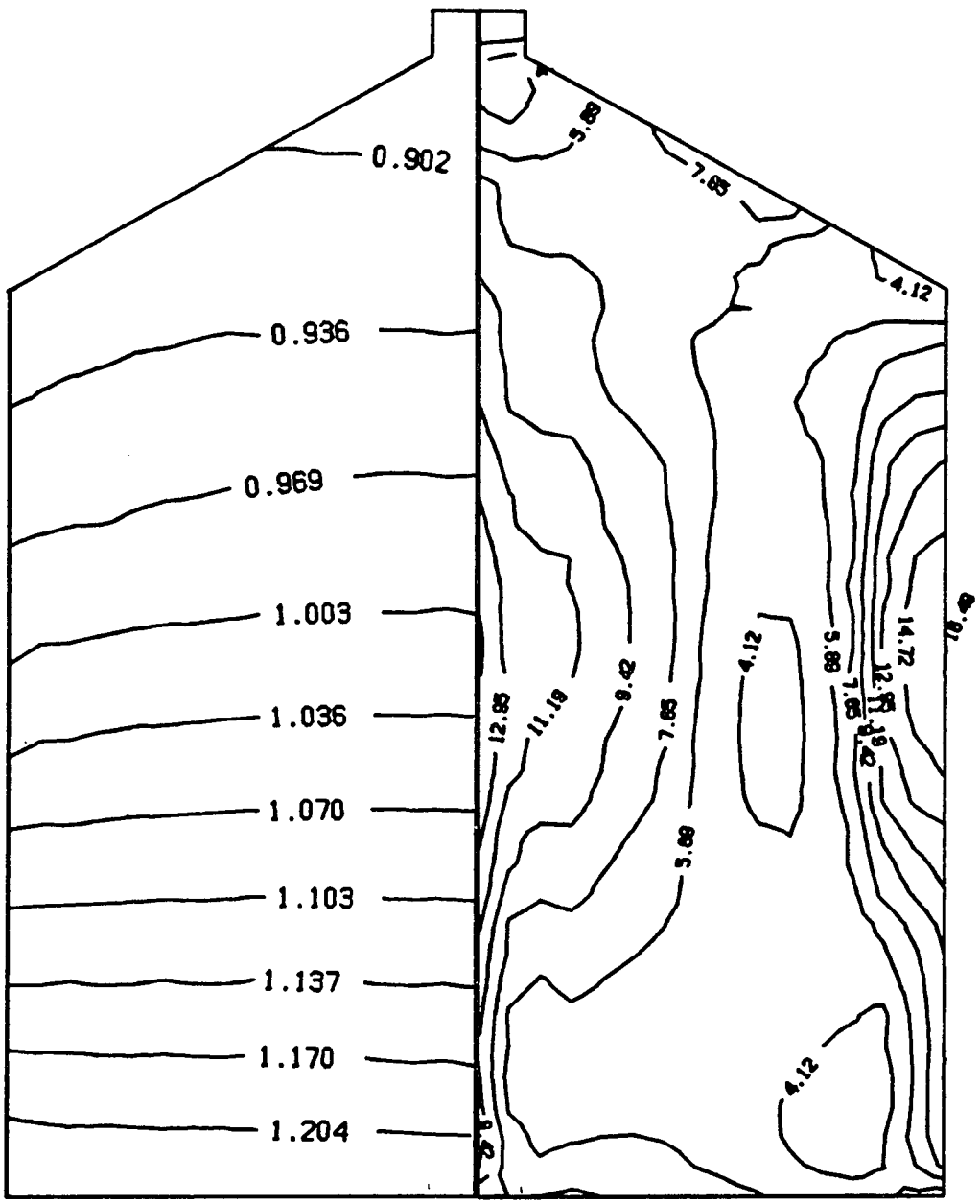
0.902
0.936
0.969
1.003
1.036
1.070
1.103
1.137
1.170
1.204
5.88
7.85
4.12
12.85
11.19
9.42
14.72

b

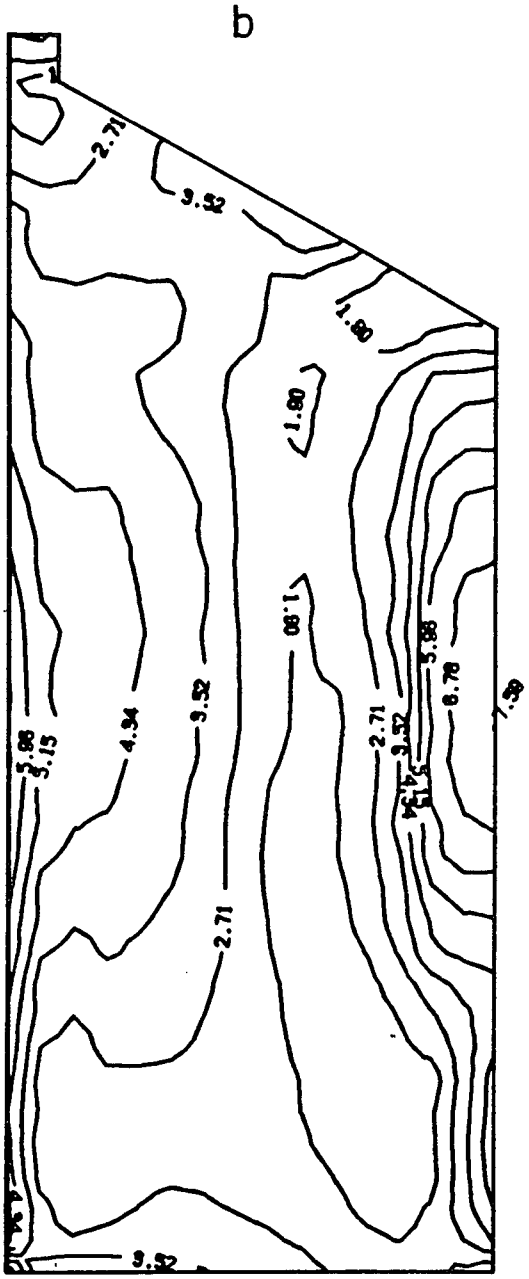
2.71
3.52
1.80
1.80
1.80
5.98
3.15
4.34
3.52
2.71
2.71
3.52
5.98
6.78
7.59
3.52

c

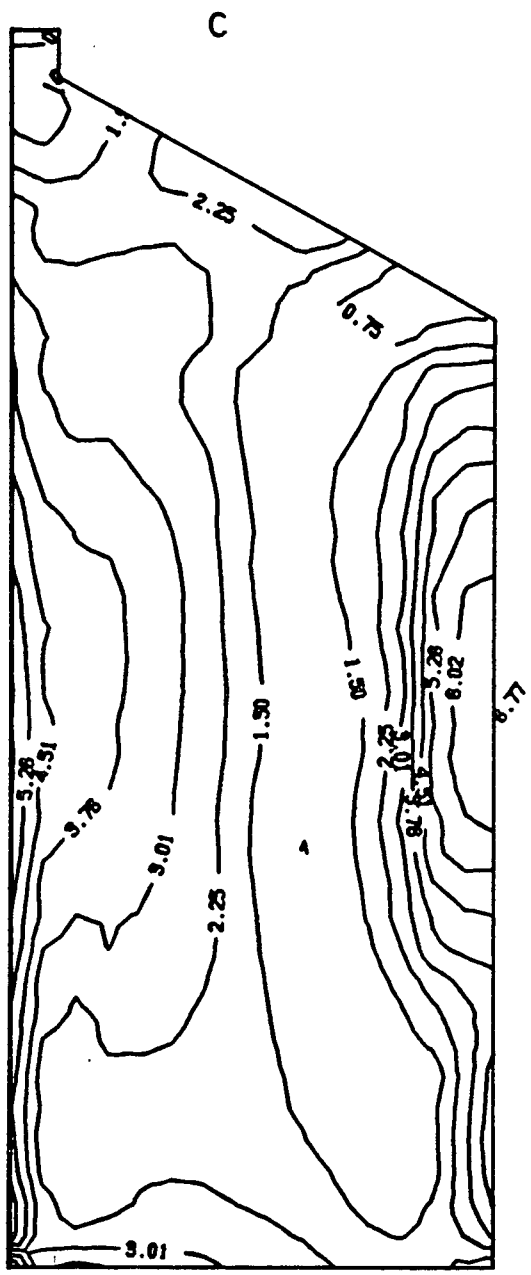
2.25
0.75
1.50
1.50
5.26
4.51
3.78
3.01
2.25
5.26
6.02
3.01

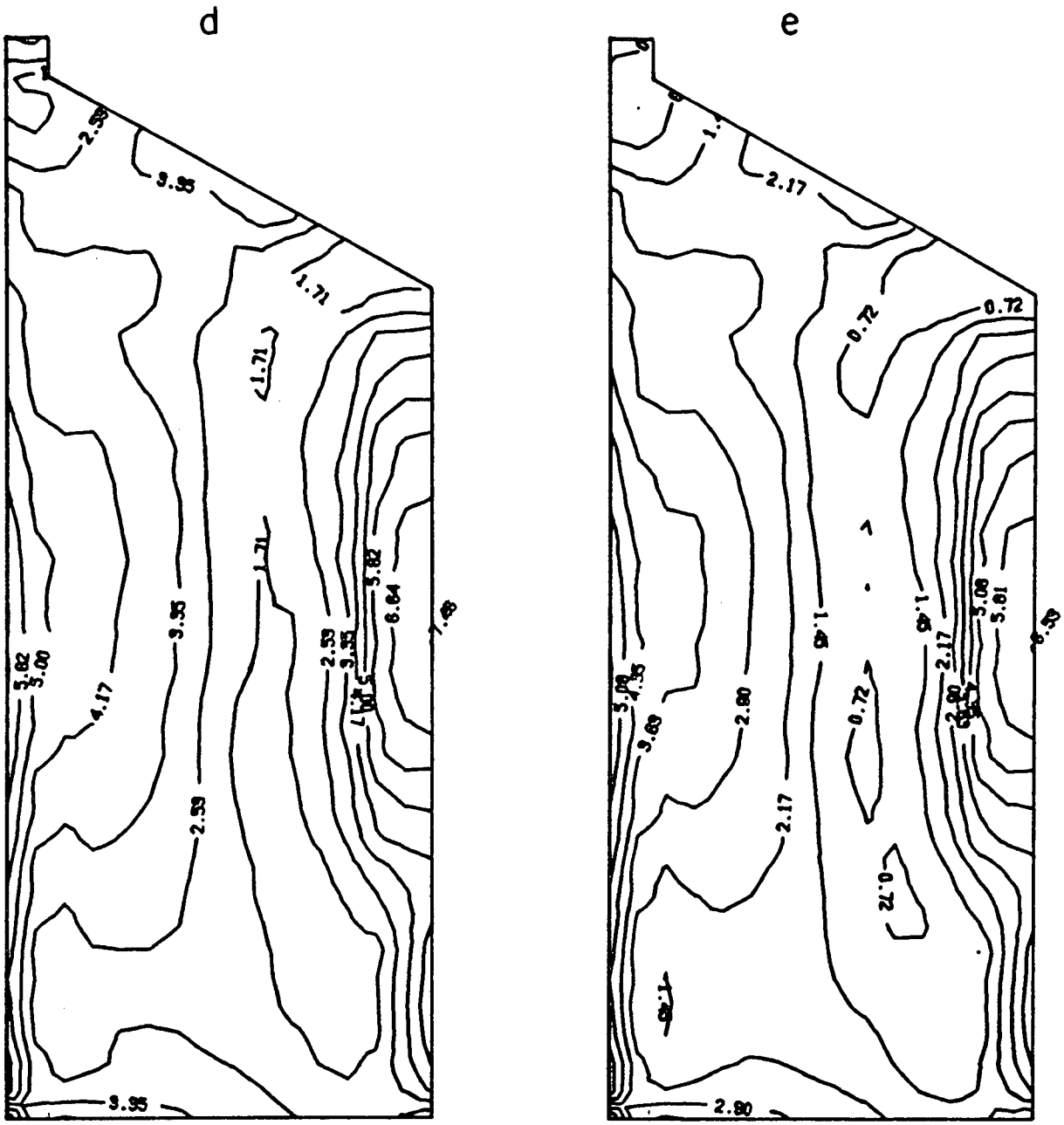

XIII.6.2.1 G
(a) Temperature and Von Mises Stress
(b) MRSS ; (c) MRSS-CRSS (Yield) ;
(d) MRSS-CRSS (MB) ; (e) MRSS-CRSS (MBTe) .

a

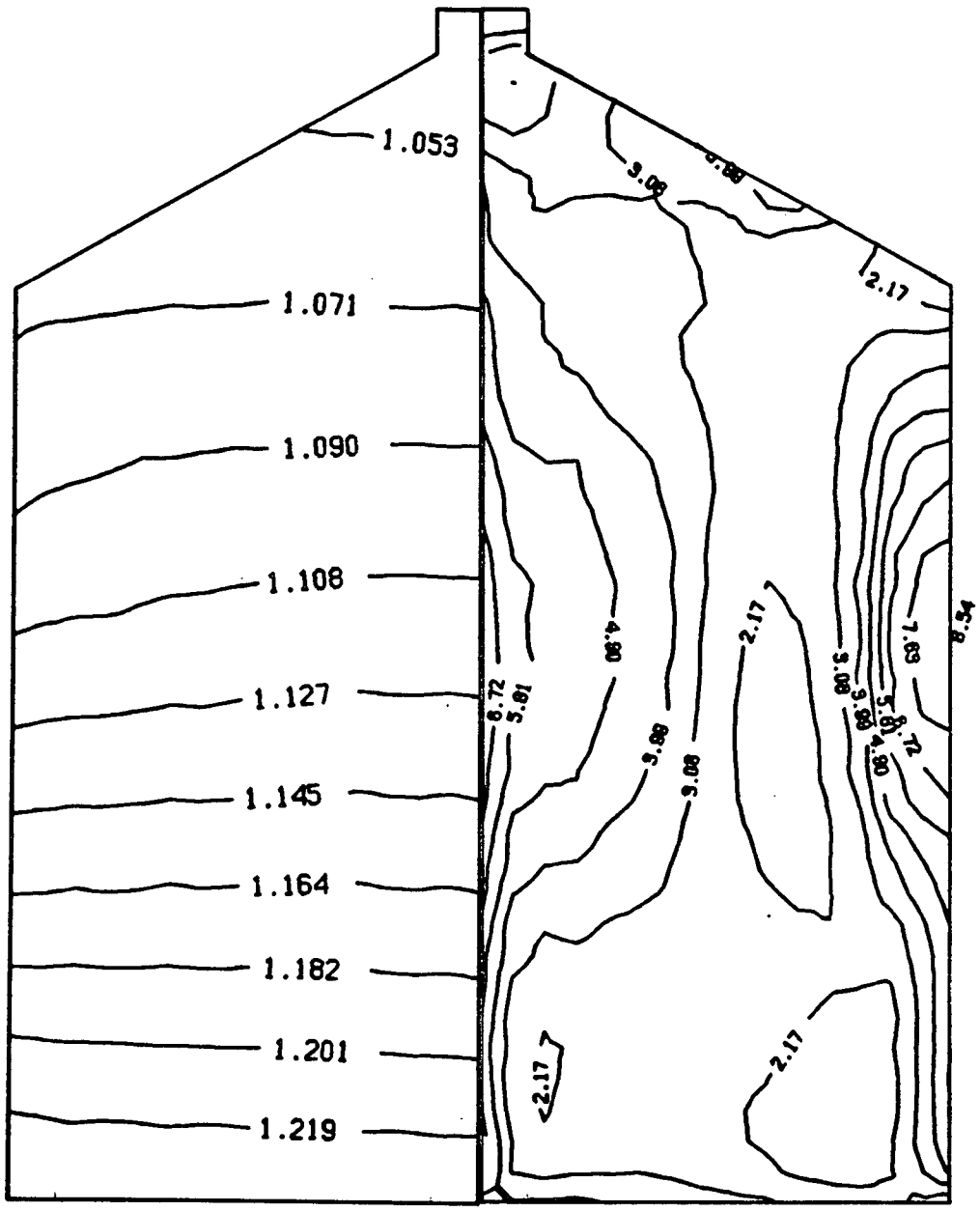
1.053
1.071
1.090
1.108
1.127
1.145
1.164
1.182
1.201
1.219
3.08
2.17
4.90
6.72
5.81
3.99
3.08
2.17
3.08
3.99
5.81
4.90
6.72
7.63
8.54
2.17
2.17

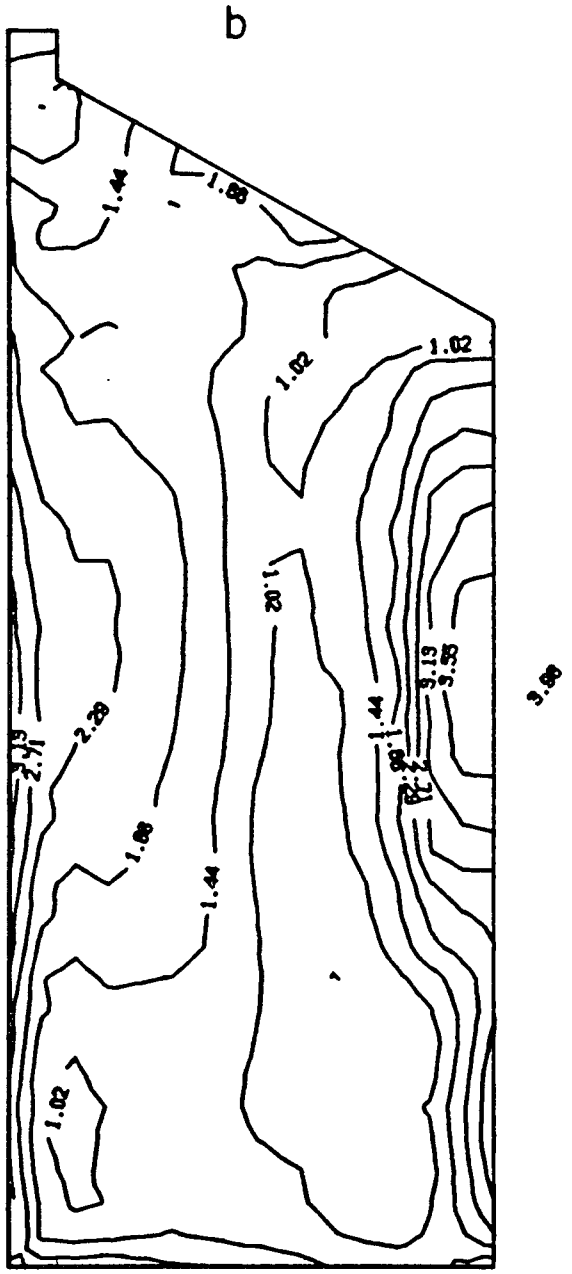
b
1.44
1.88
1.02
1.02
1.02
1.44
1.44
1.88
1.02
2.29
2.71
3.19
3.55
3.98

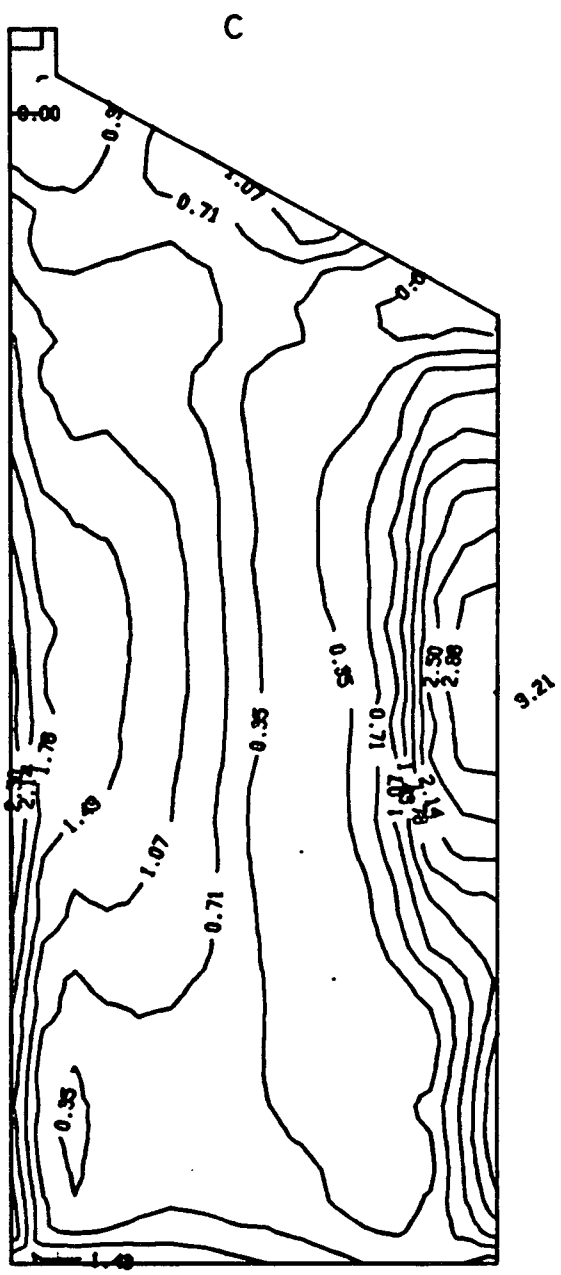
c
0.00
0.71
1.07
0.35
0.71
1.07
0.71
0.35
2.50
2.88
3.21

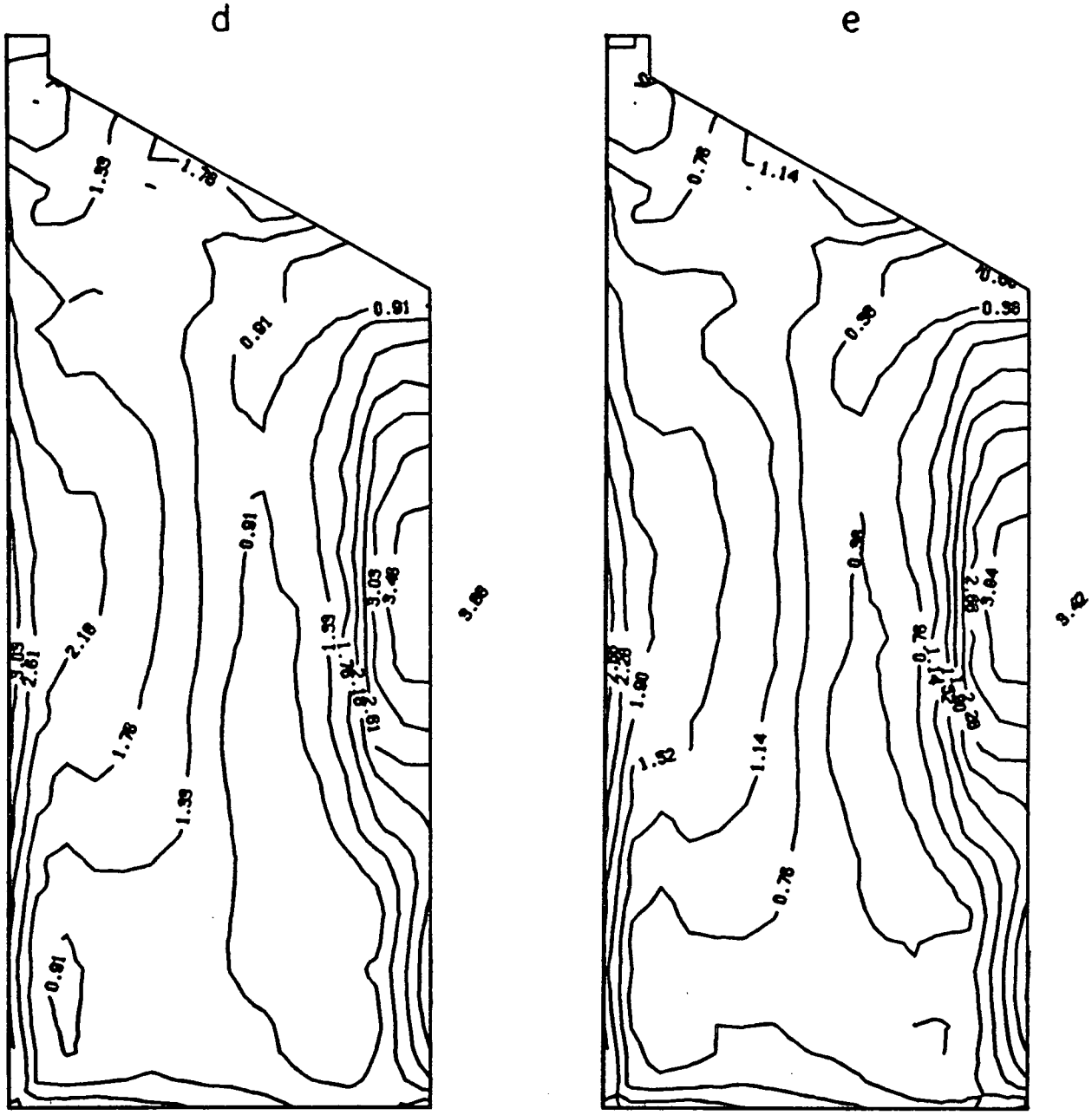

XIII.6.2.2 G/2

(a) Temperature and Von Mises Stress
(b) MRSS ; (c) MRSS-CRSS (Yield) ;
(d) MRSS-CRSS (MB) ; (e) MRSS-CRSS (MBTe) .

a

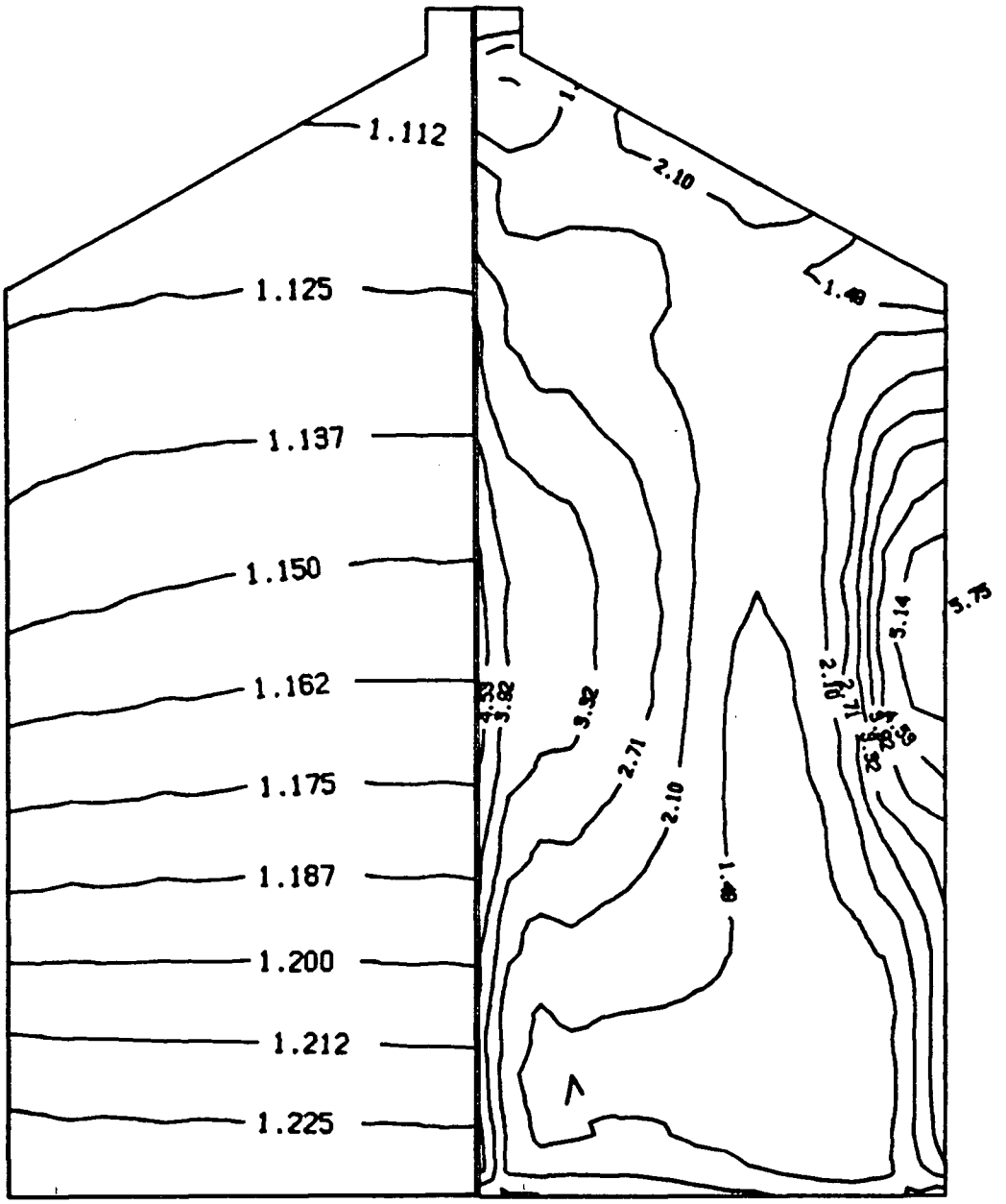
1.112
1.125
1.137
1.150
1.162
1.175
1.187
1.200
1.212
1.225
2.10
1.48
5.75
5.14
3.32
2.71
2.10
1.48

b

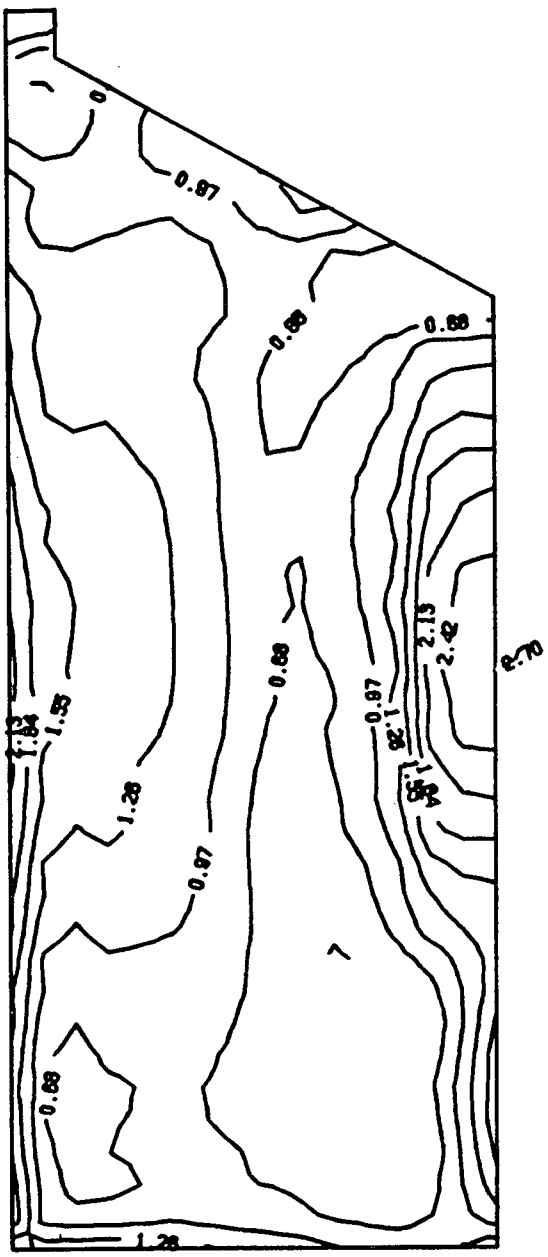
0.97
0.68
0.68
2.13
2.42
2.70
0.97
1.26
1.55
1.84
1.26
0.97
0.68
1.26

c

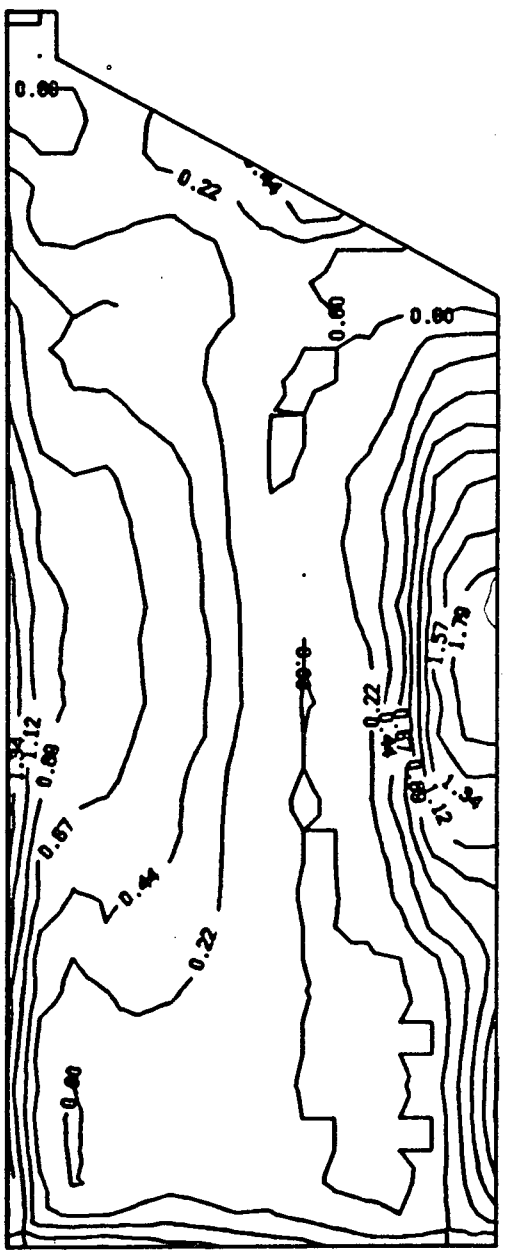
0.22
0.60
0.60
1.57
1.79
0.22
1.34
1.12
0.67
0.44
0.22
0.60

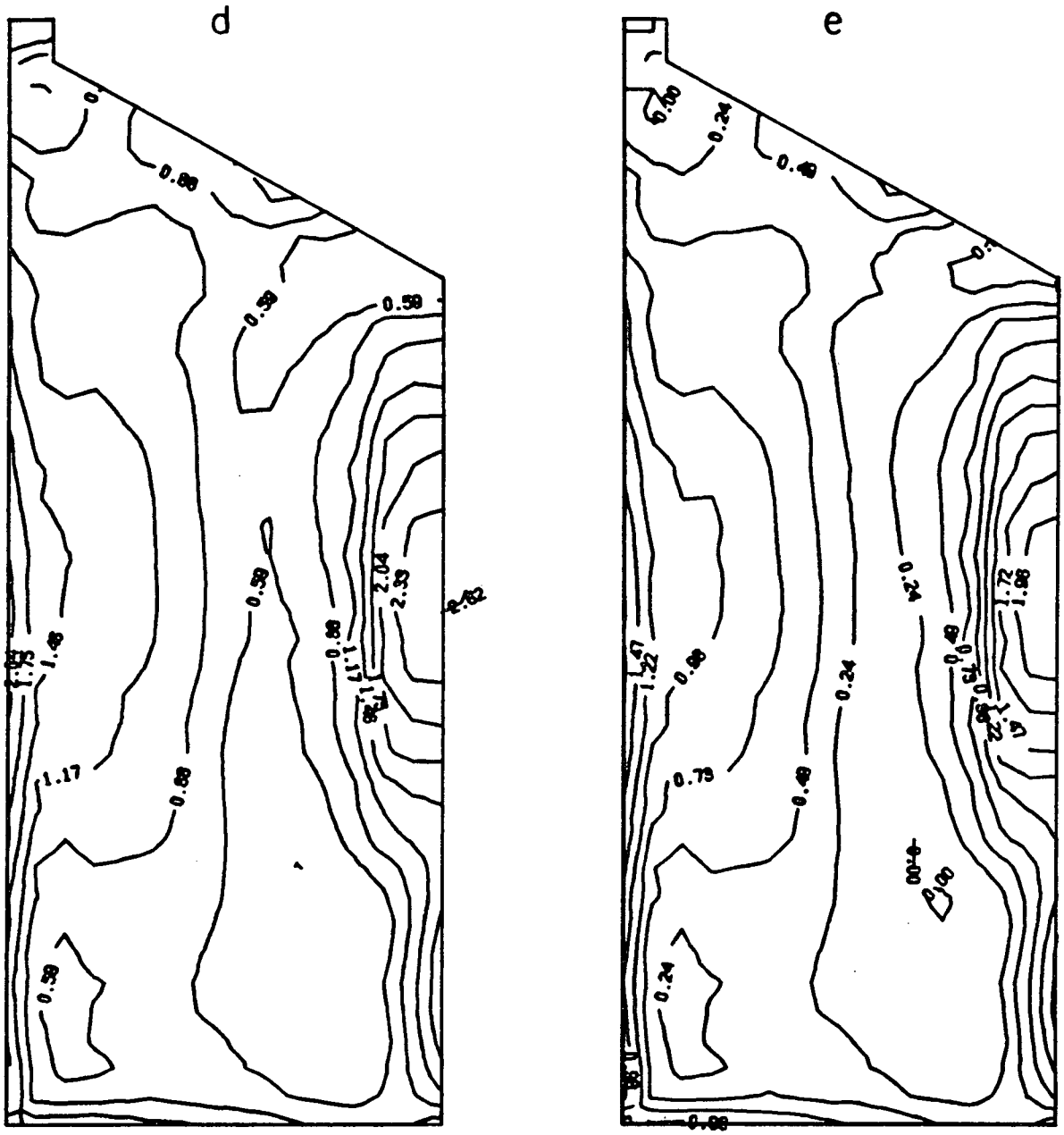

XIII.6.2.3 G/3
(a) Temperature and Von Mises Stress
(b) MRSS ; (c) MRSS-CRSS (Yield) ;
(d) MRSS-CRSS (MB) ; (e) MRSS-CRSS (MBTe) .

a

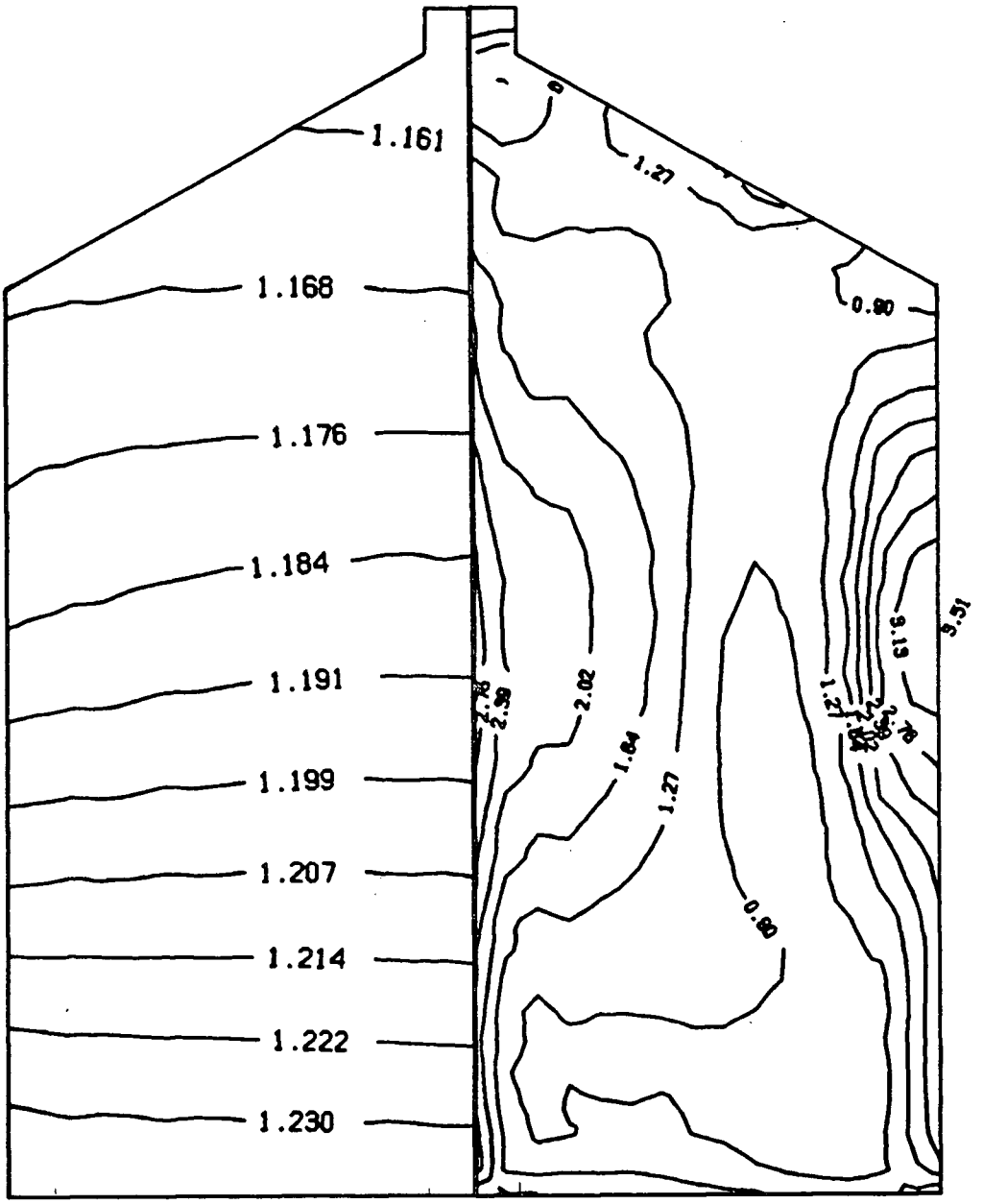
1.161
1.168
1.176
1.184
1.191
1.199
1.207
1.214
1.222
1.230
0
1.27
0.80
2.02
1.84
1.27
0.80
5.51

b
c
0.00
0.11
0.22
0.41
0.59
0.77
0.94
1.12
1.29
1.47

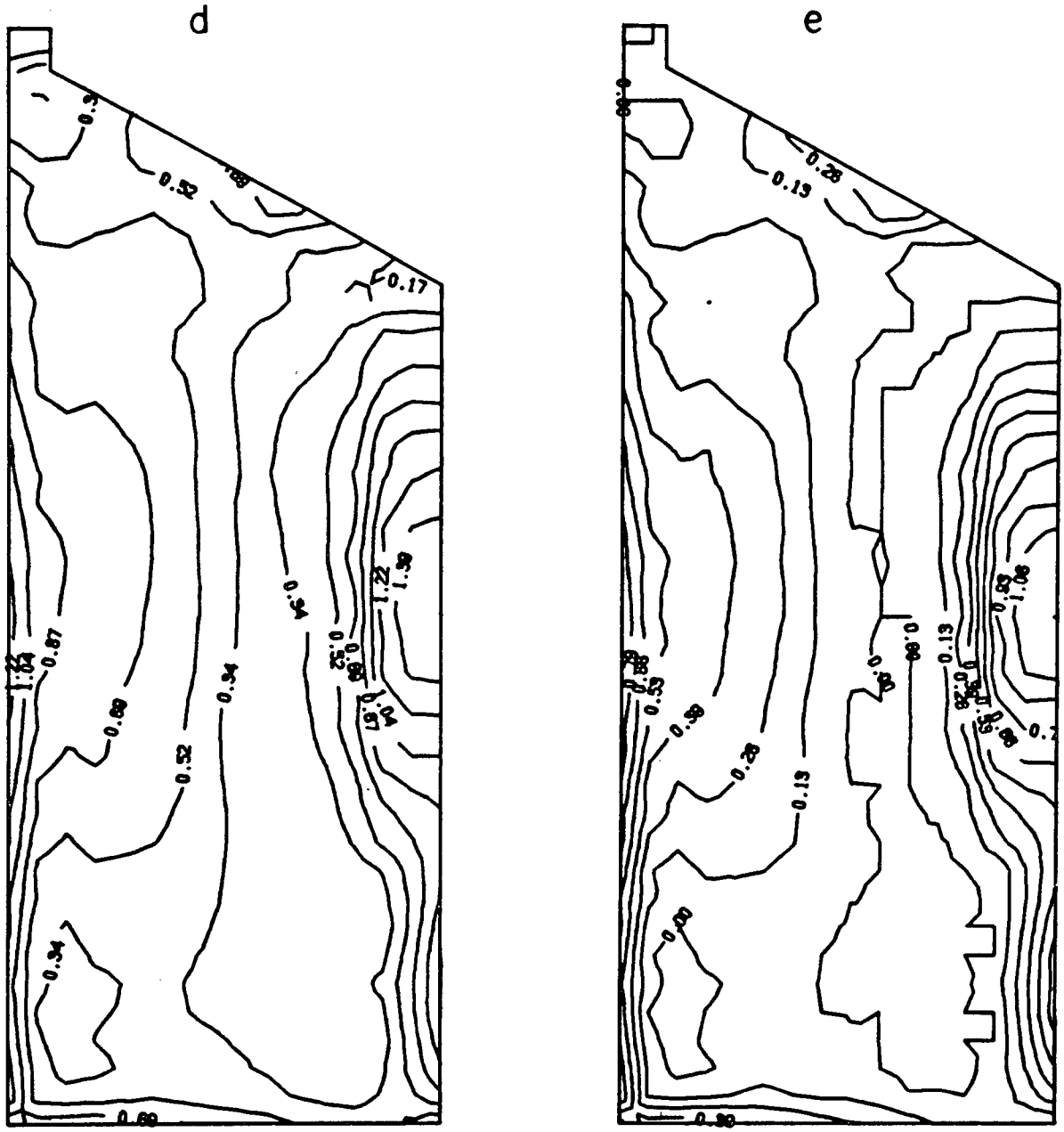

XIII.6.2.4 G/5
(a) Temperature and Von Mises Stress
(b) MRSS ; (c) MRSS-CRSS (Yield) ;
(d) MRSS-CRSS (MB) ; (e) MRSS-CRSS (MBTe) .

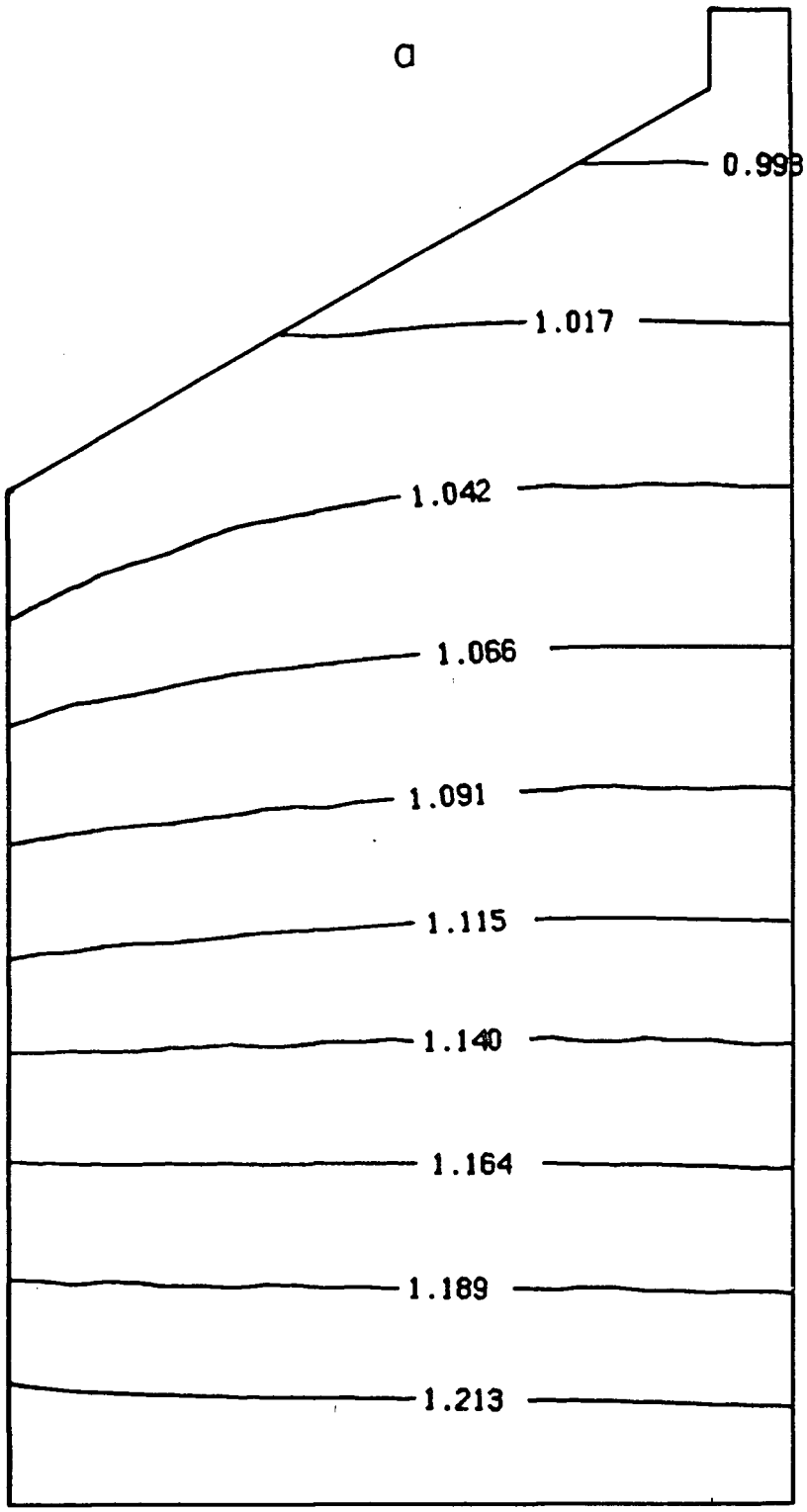
a
0.993
1.017
1.042
1.066
1.091
1.115
1.140
1.164
1.189
1.213

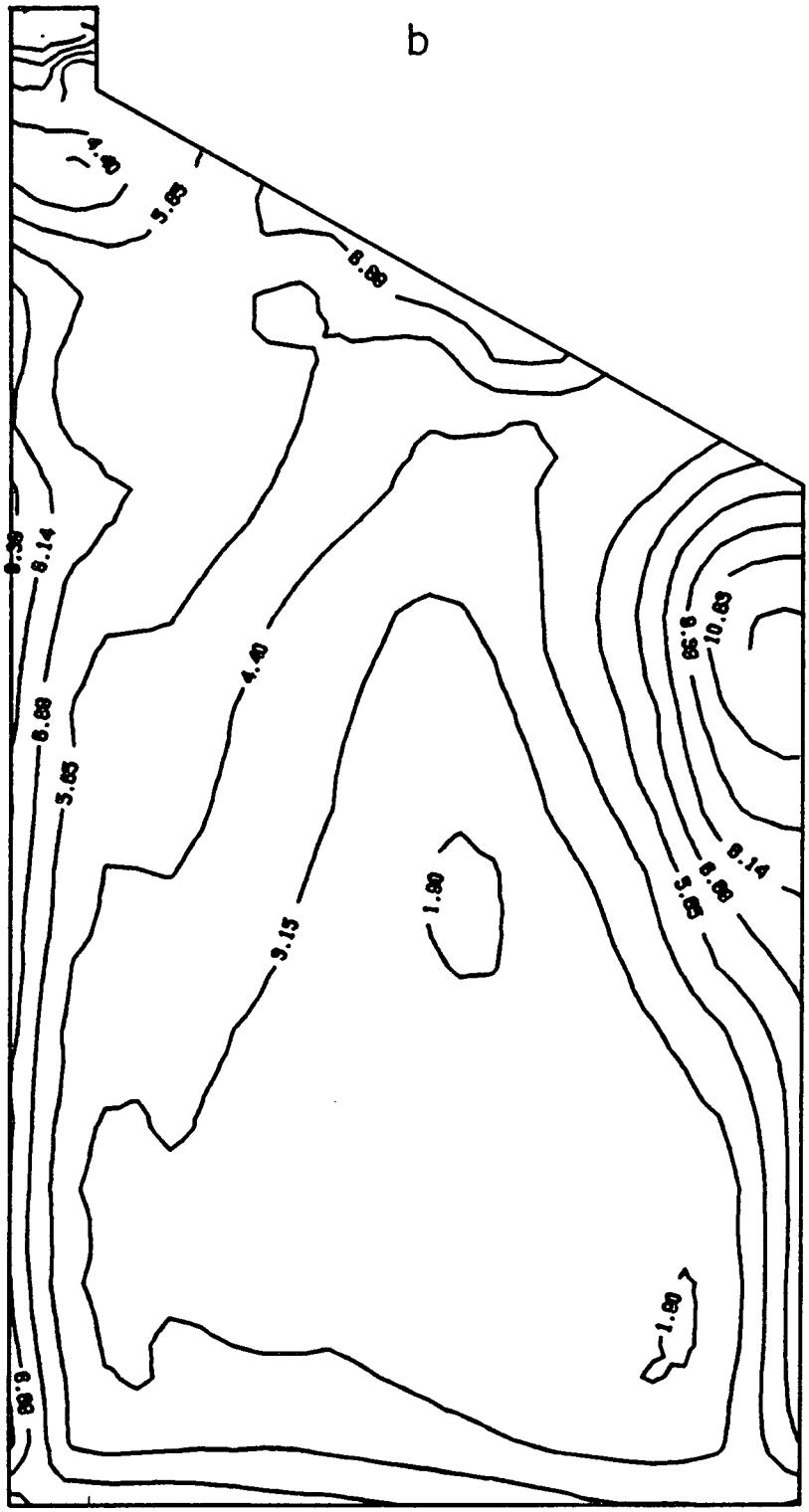
b
4.40
5.65
6.88
8.14
6.88
5.65
4.40
9.15
1.90
1.90
8.14
6.88
5.65
10.63
6.88

C

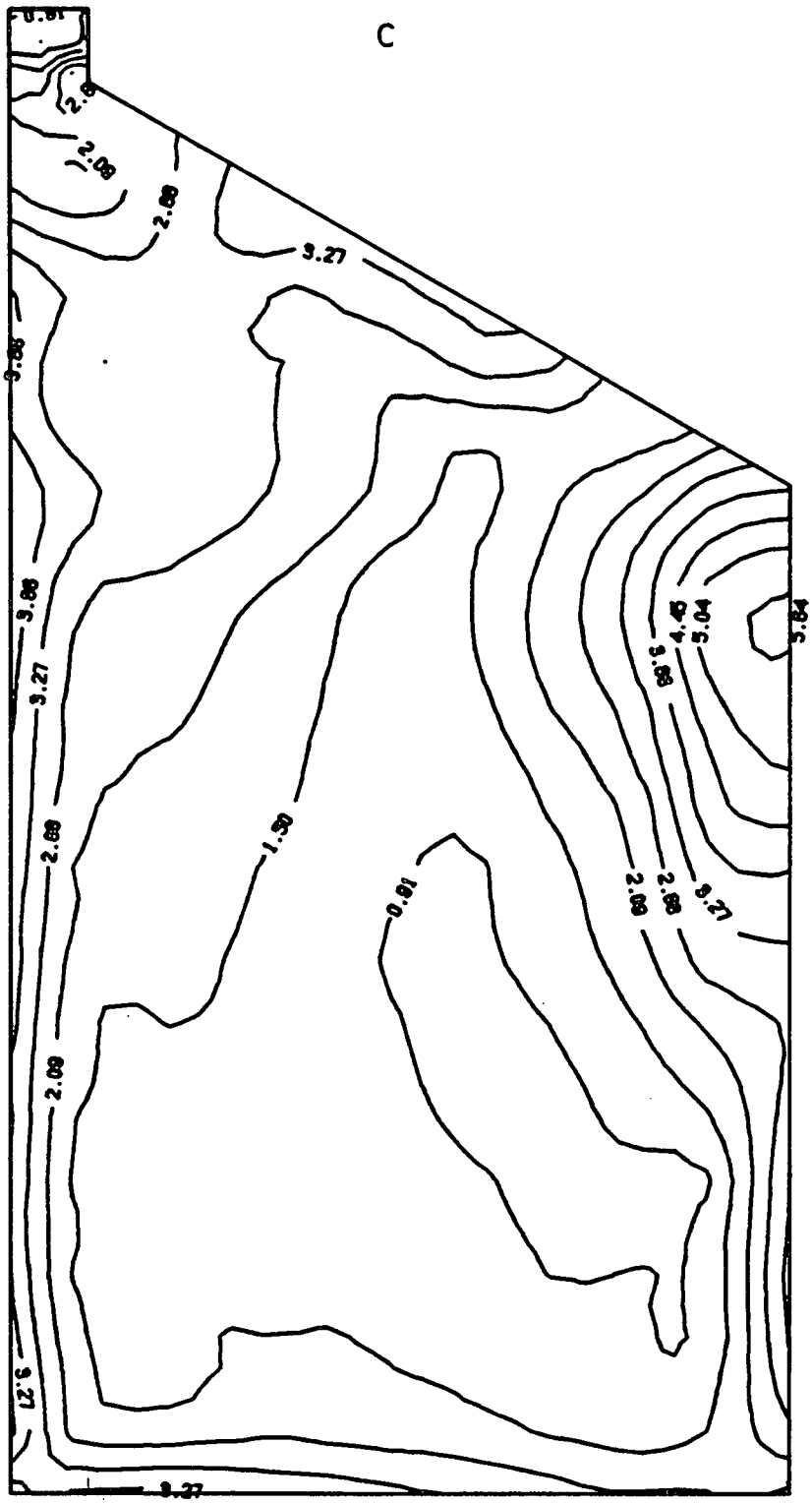

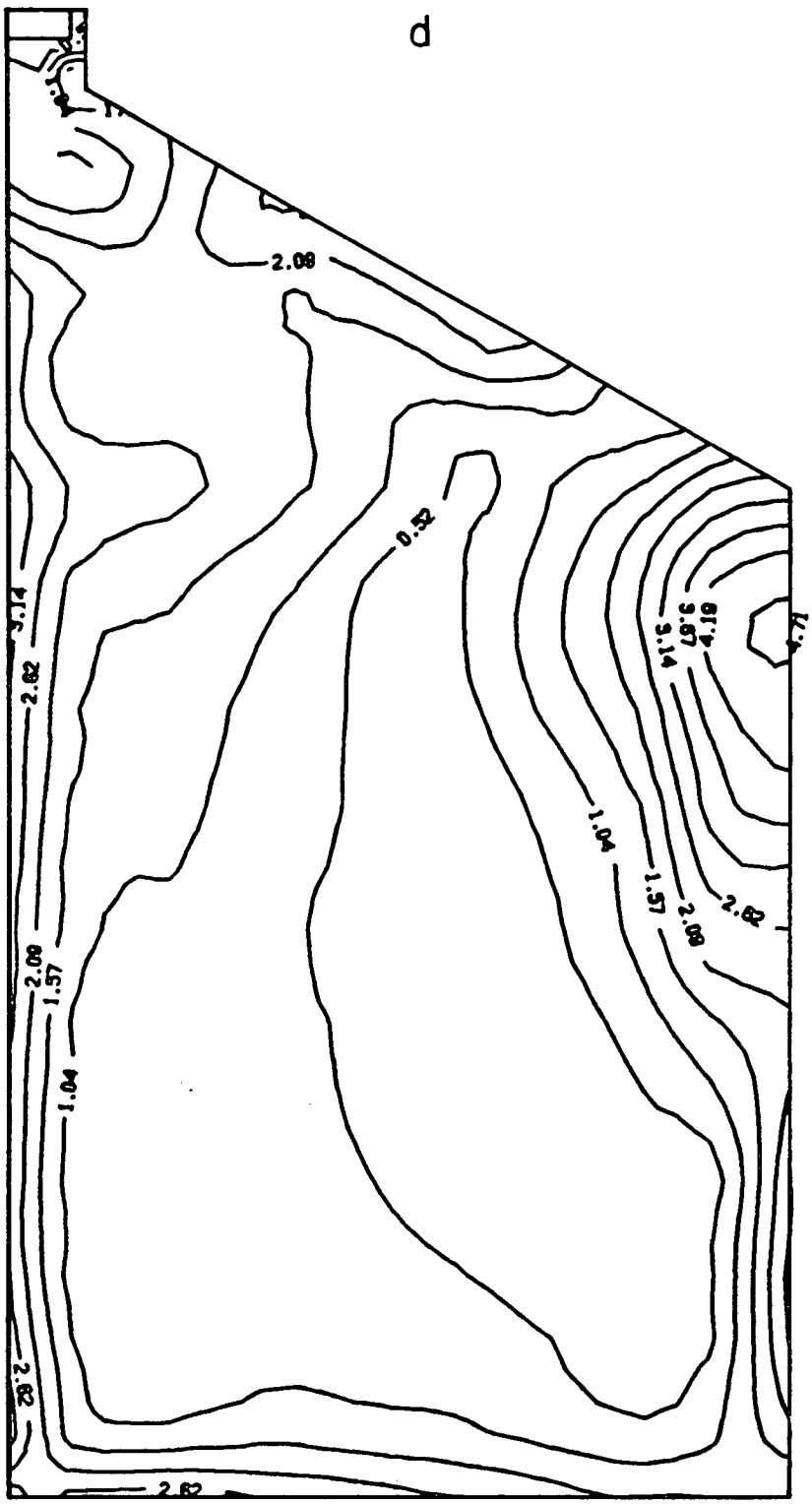
d
2.09
0.52
3.14
2.62
2.09
1.57
1.04
2.62
2.62
1.04
1.57
2.09
2.62
3.14
3.67
4.19
4.71

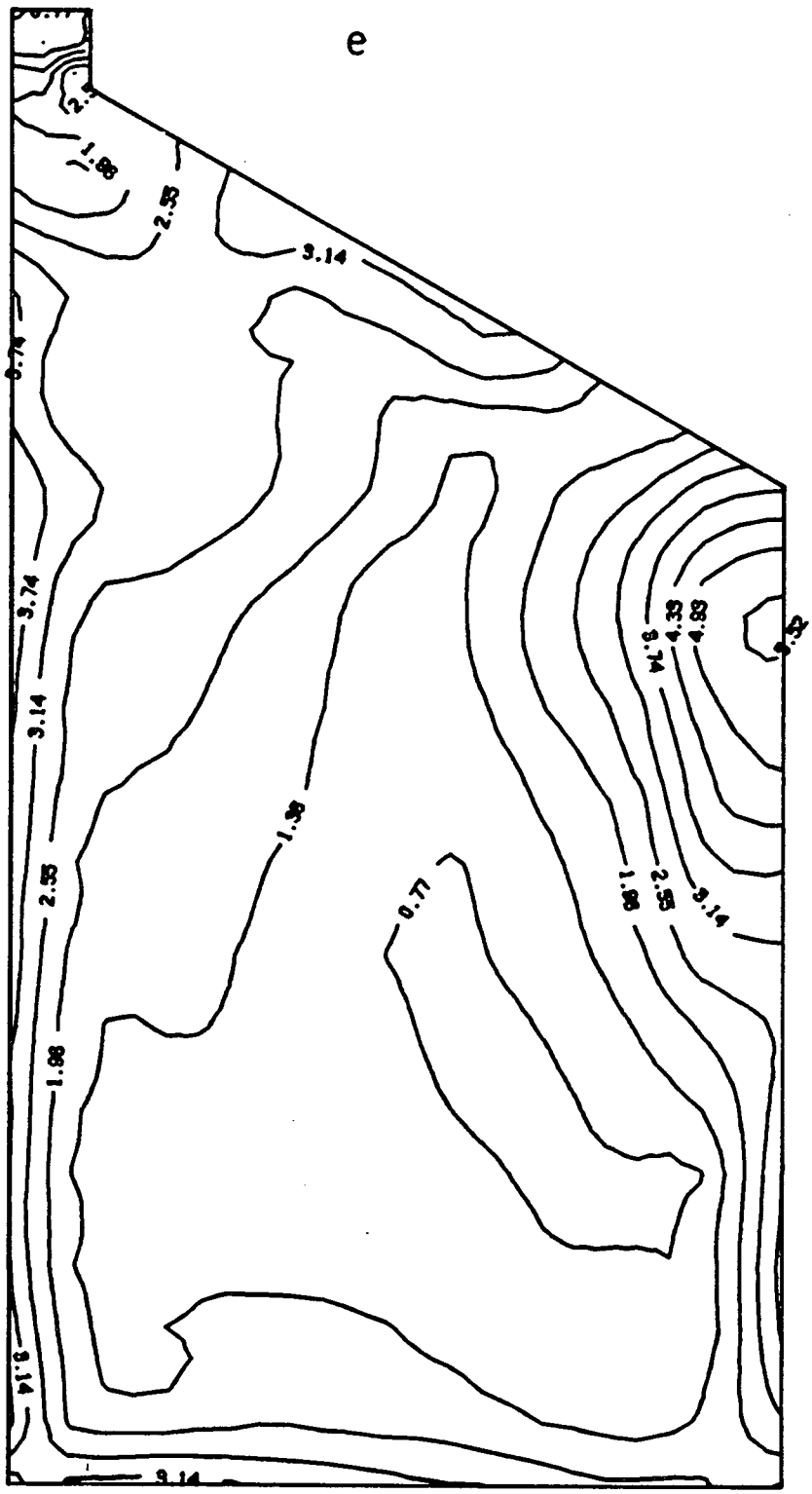
e
0.74
1.98
2.55
3.14
3.74
3.14
2.55
1.98
0.77
1.98
2.55
3.14
4.33
4.93
3.14
3.14

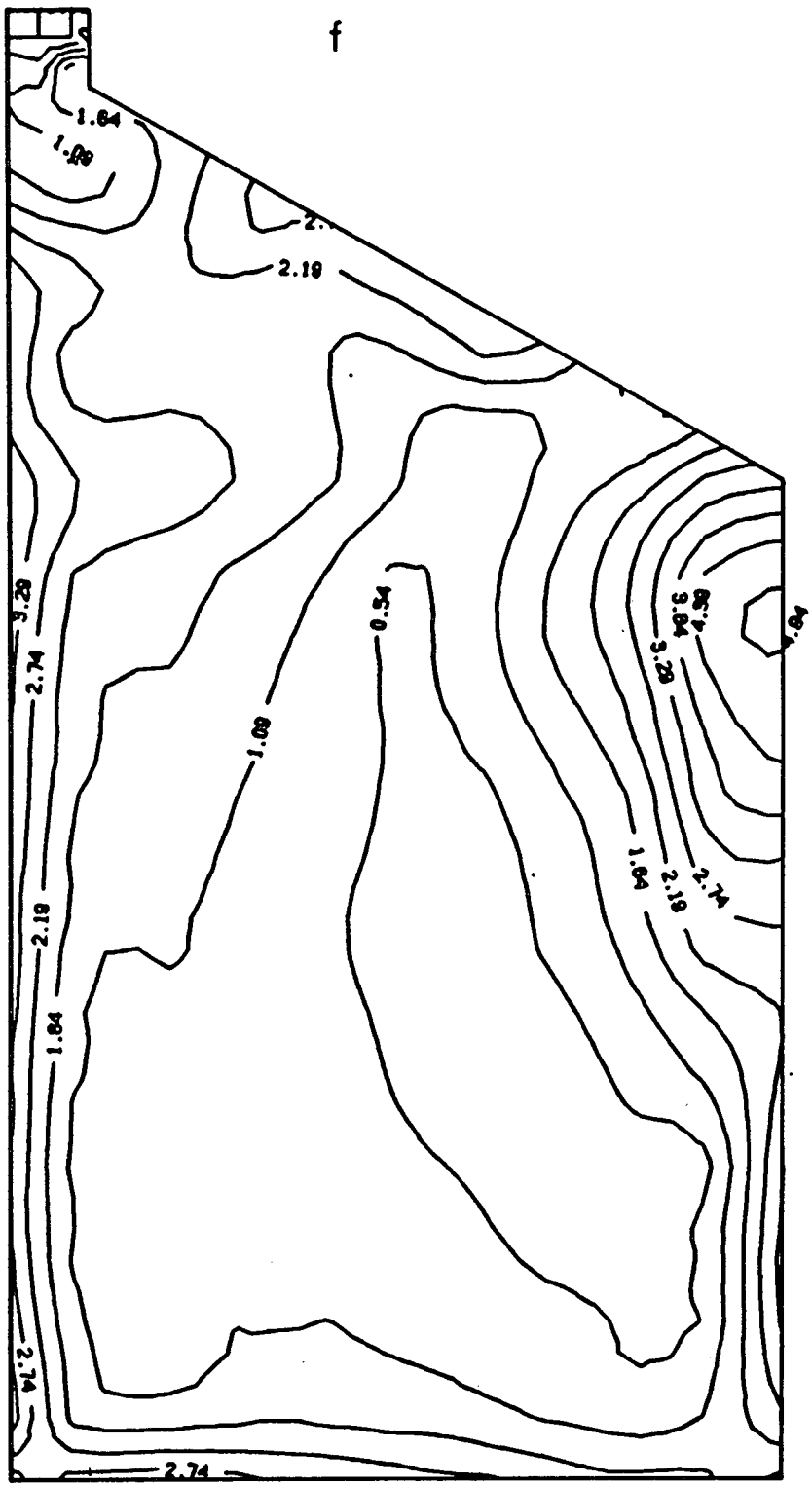

XIII.6.3.1.1 CL, 60 mm
(a) Temperature ; (b) Von Mises Stress
(c) MRSS ; (d) MRSS-CRSS (Yield) ;
(e) MRSS-CRSS (MB) ; (f) MRSS-CRSS (MBTe) .

a

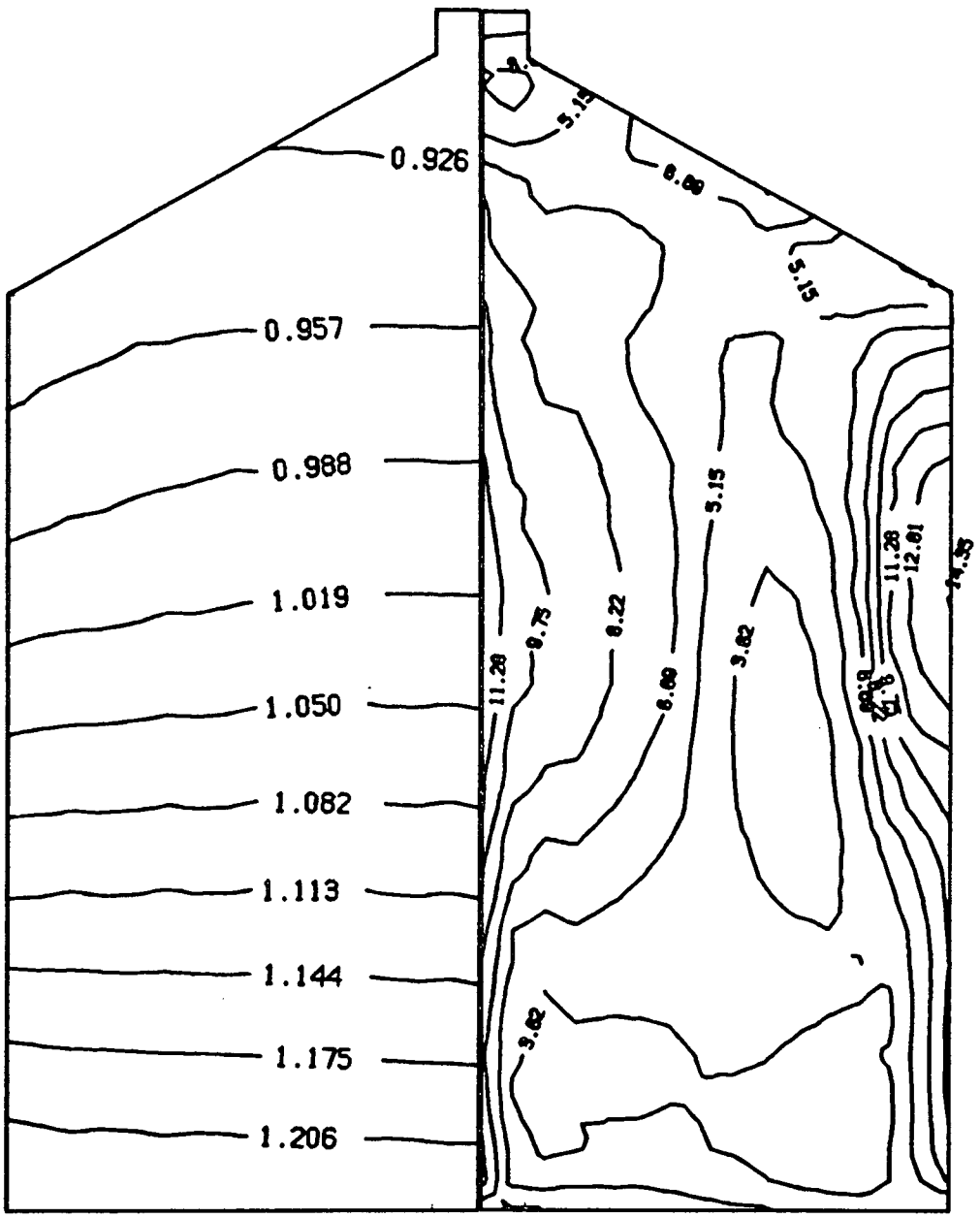
0.926
0.957
0.988
1.019
1.050
1.082
1.113
1.144
1.175
1.206
5.15
6.69
5.15
5.15
11.28
9.75
8.22
6.69
3.82
11.28
12.81
14.35
3.82

b

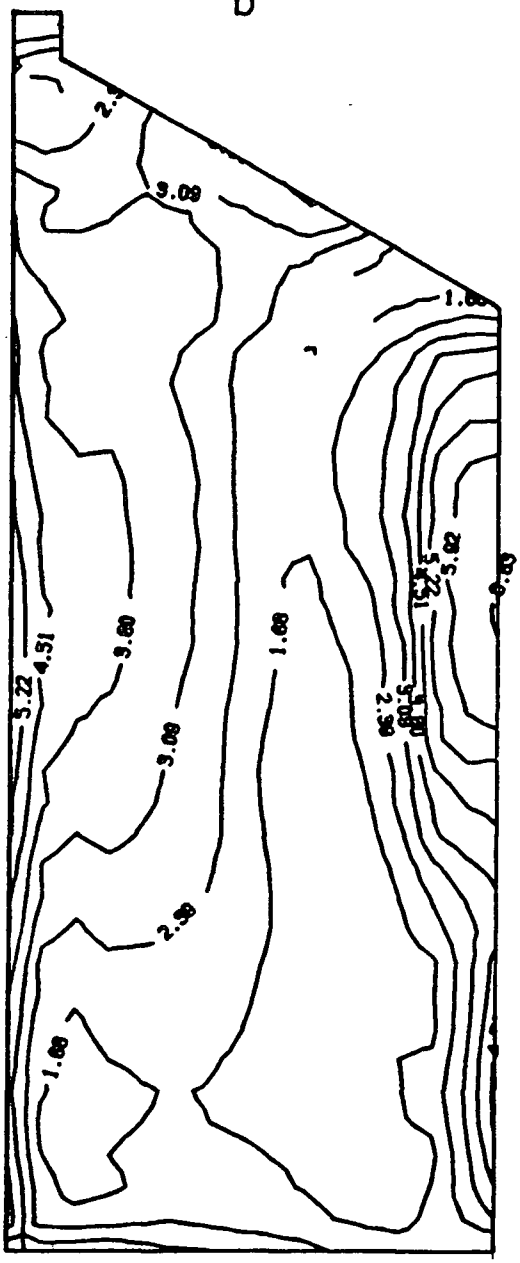
3.09
5.22
4.51
3.80
3.09
1.68
2.38
1.68
5.92
0.83

c

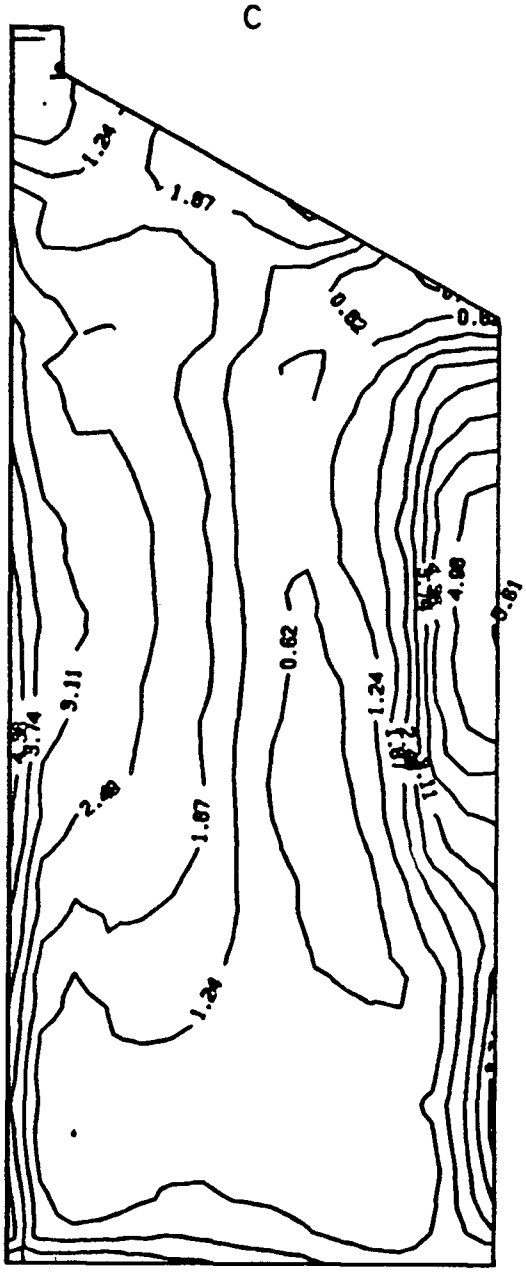
1.24
1.87
0.62
3.11
2.48
1.87
1.24
0.62
1.24
4.98
0.61

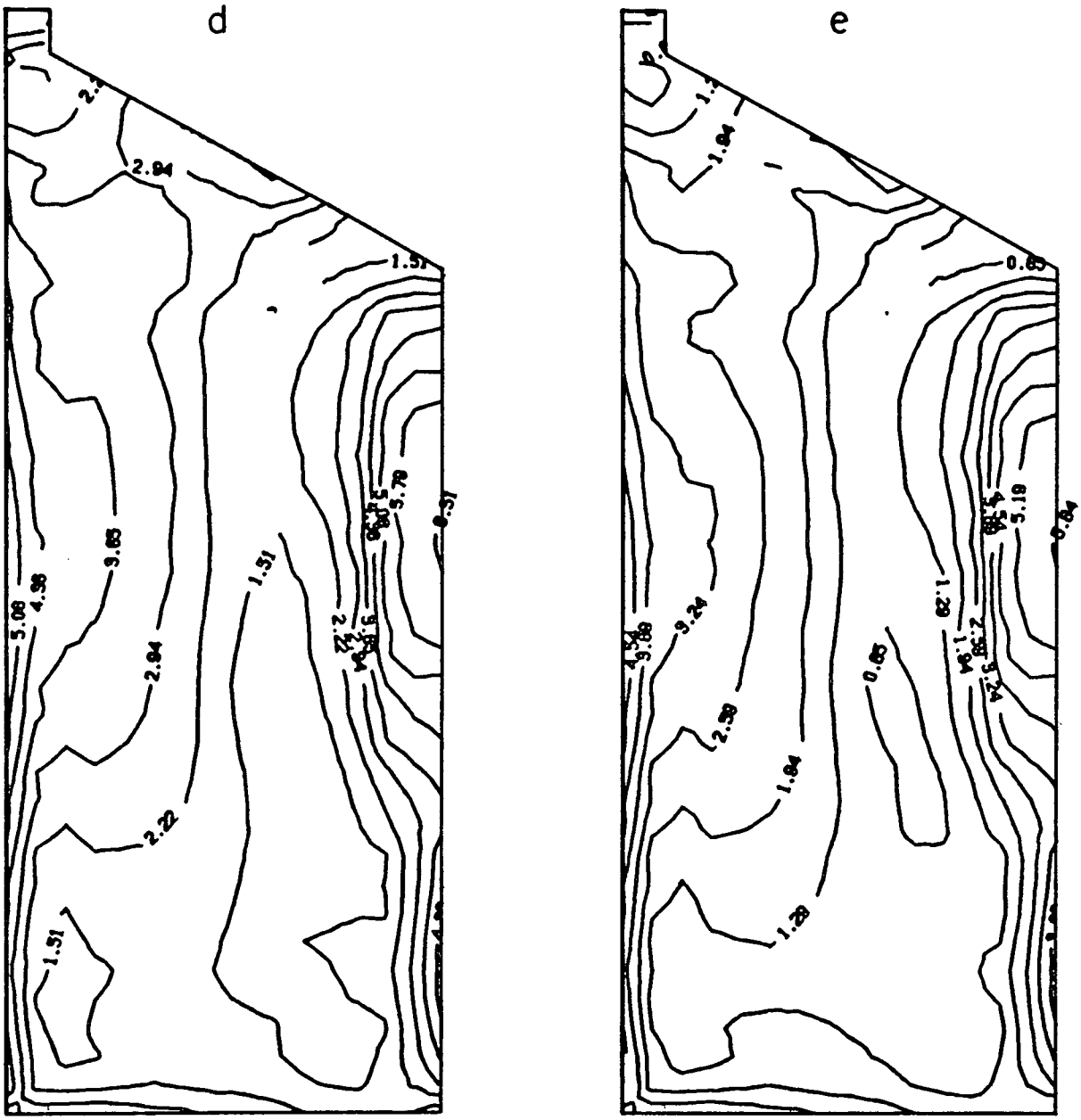

XIII.6.3.1.2 CL, 80 mm
(a) Temperature and Von Mises Stress
(b) MRSS ; (c) MRSS-CRSS (Yield) ;
(d) MRSS-CRSS (MB) ; (e) MRSS-CRSS (MBTe) .

a

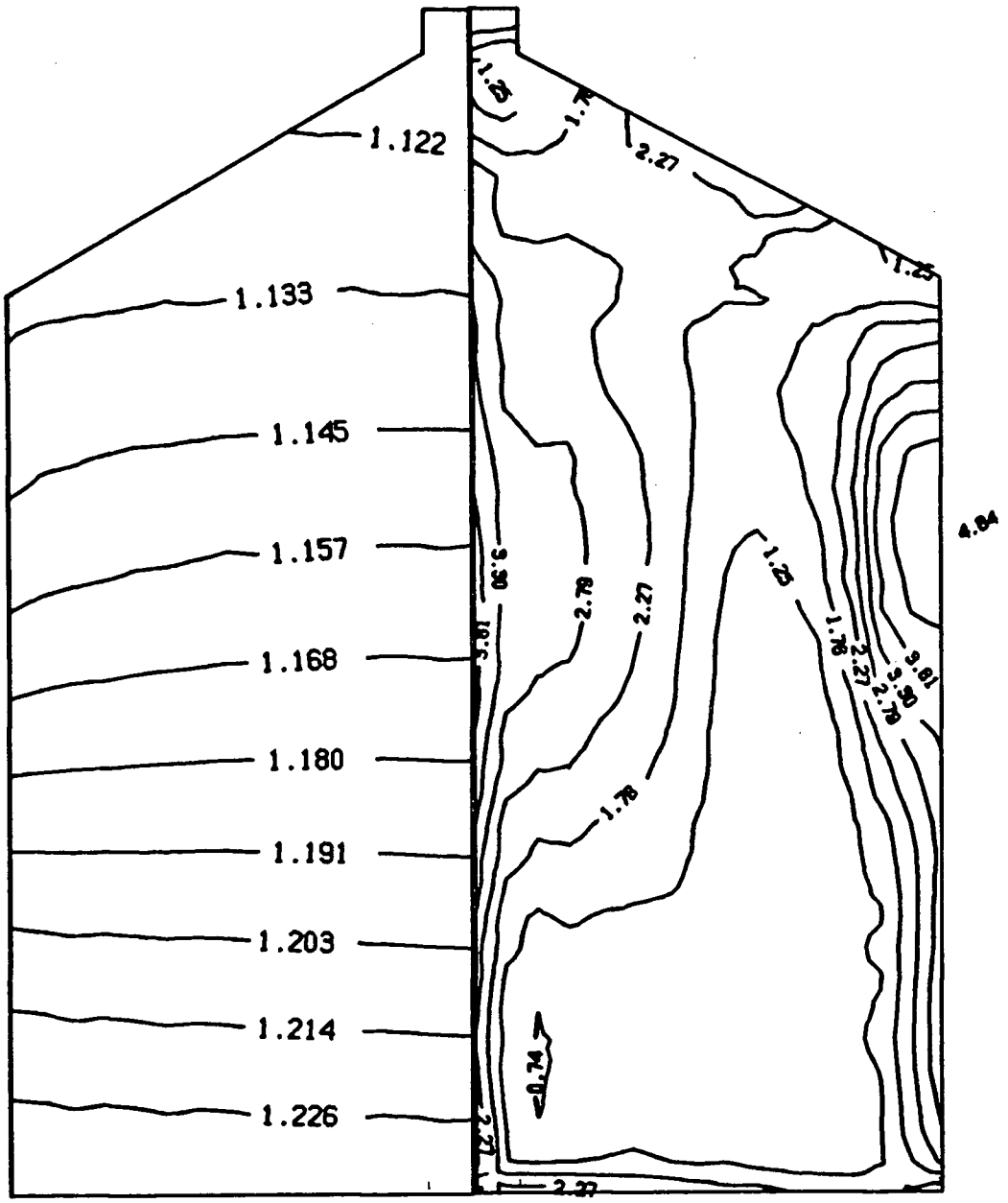
1.122
1.133
1.145
1.157
1.168
1.180
1.191
1.203
1.214
1.226
1.25
1.76
2.27
1.25
4.84
3.30
3.61
2.79
2.27
1.25
1.76
2.27
2.79
3.30
3.61
1.78
0.74
2.27
2.27

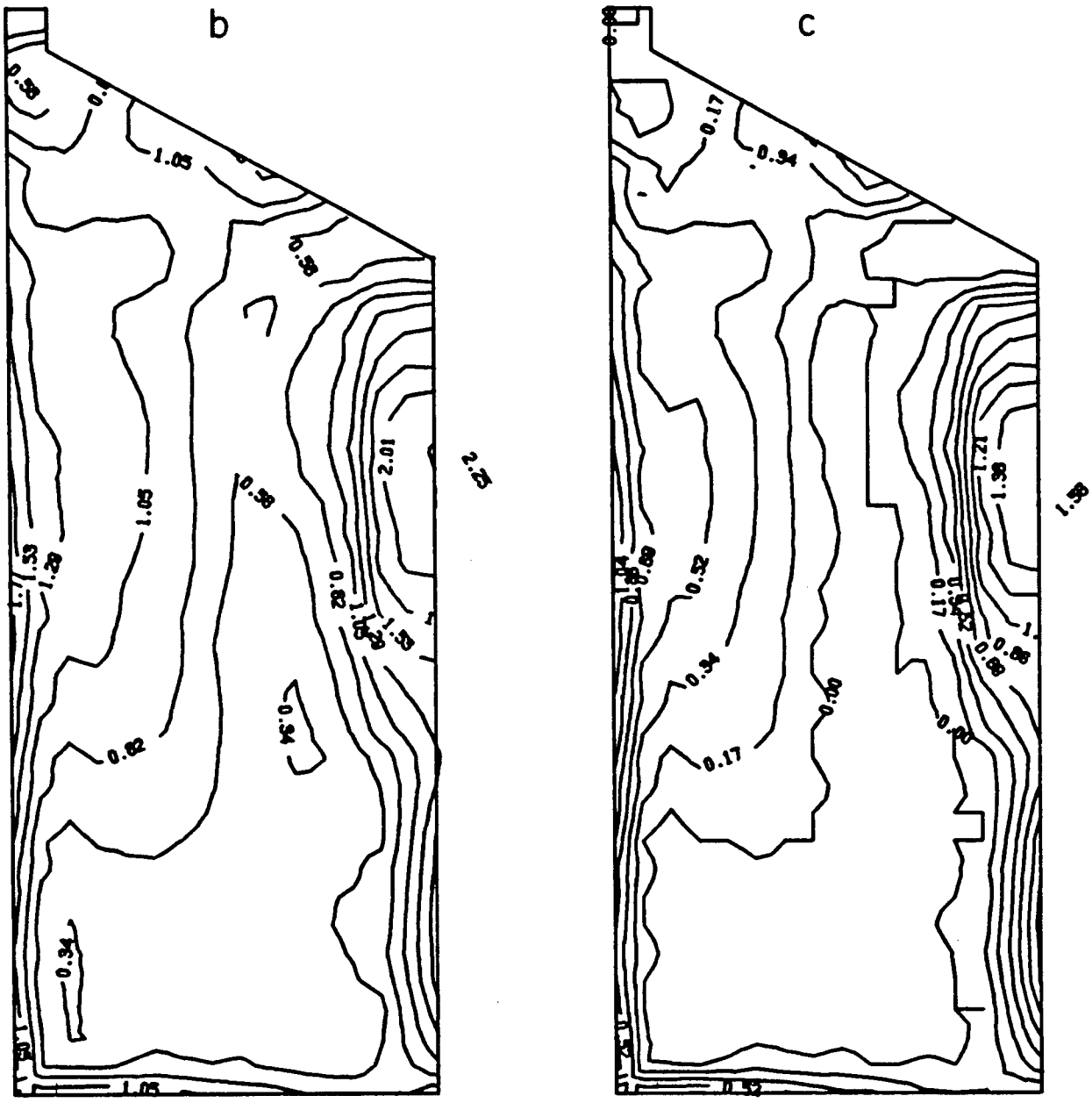
b
c
1.05
0.58
2.01
2.25
1.29
1.53
0.82
0.34
0.17
0.52
0.00
1.21
1.38
1.58

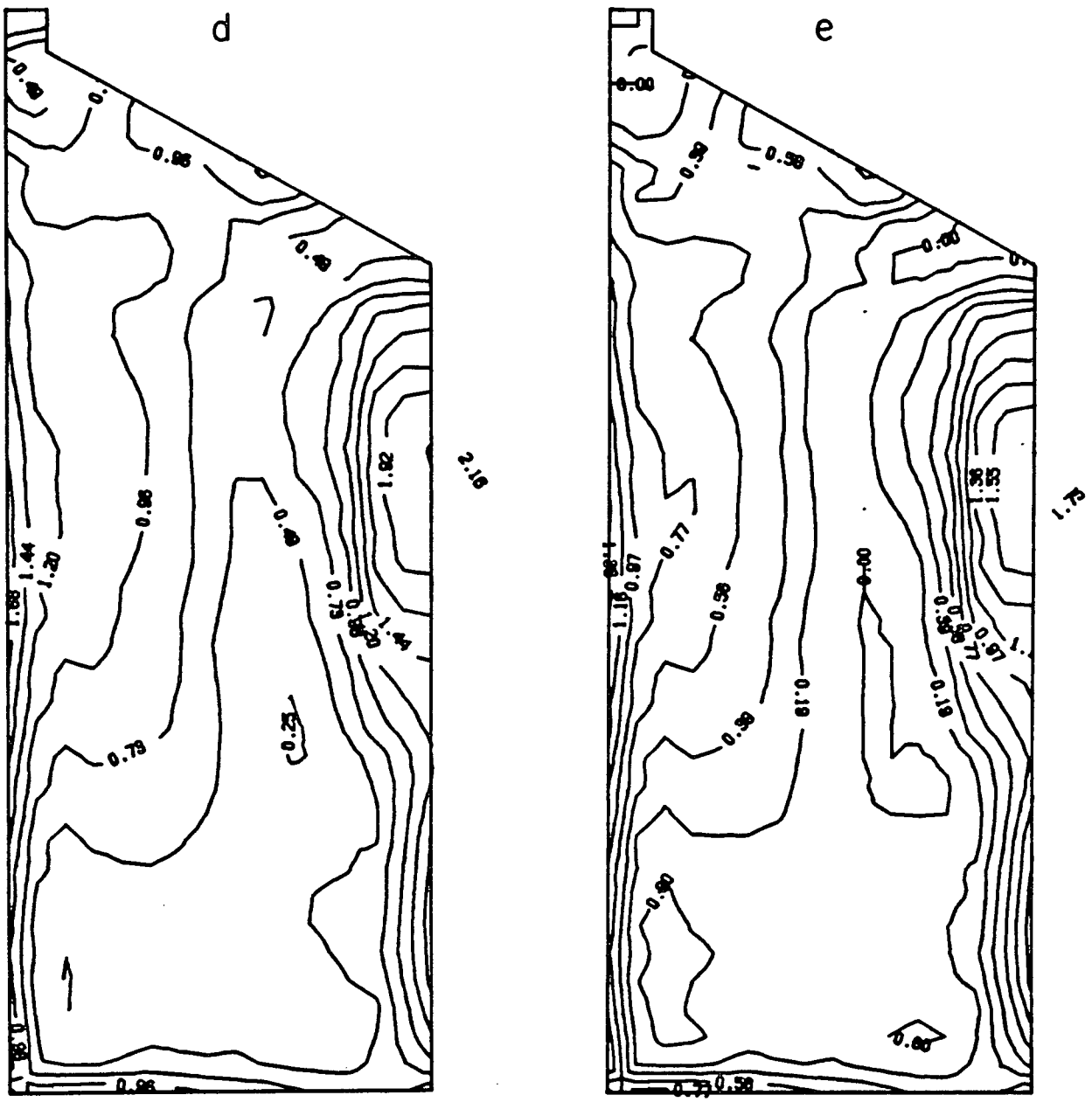

XIII.6.3.2 G/3
(a) Temperature and Von Mises Stress
(b) MRSS ; (c) MRSS-CRSS (Yield) ;
(d) MRSS-CRSS (MB) ; (e) MRSS-CRSS (MBTe) .

a

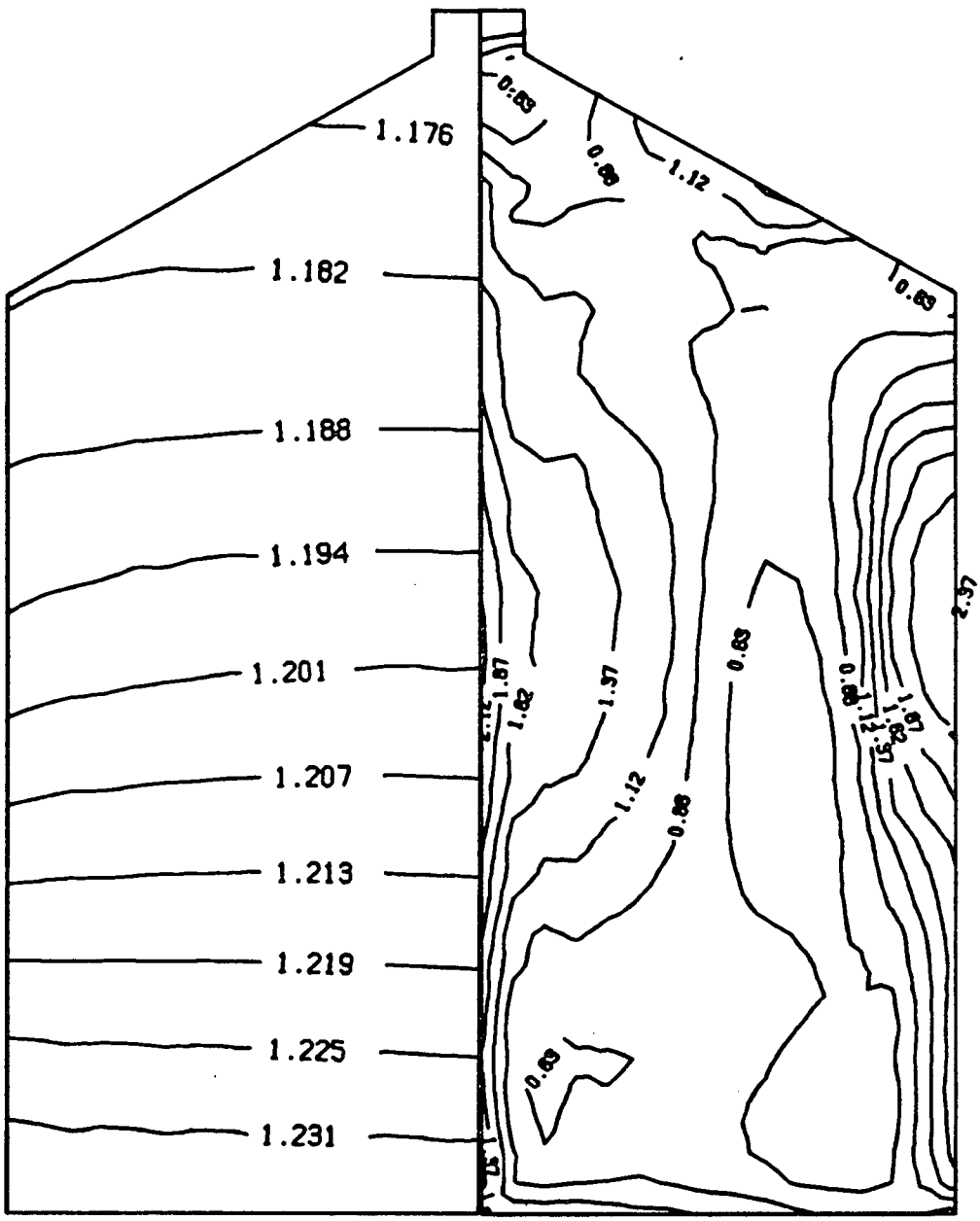
1.176
1.182
1.188
1.194
1.201
1.207
1.213
1.219
1.225
1.231
0.63
0.88
1.12
0.63
1.87
1.62
1.37
0.63
1.12
0.88
0.63
2.37

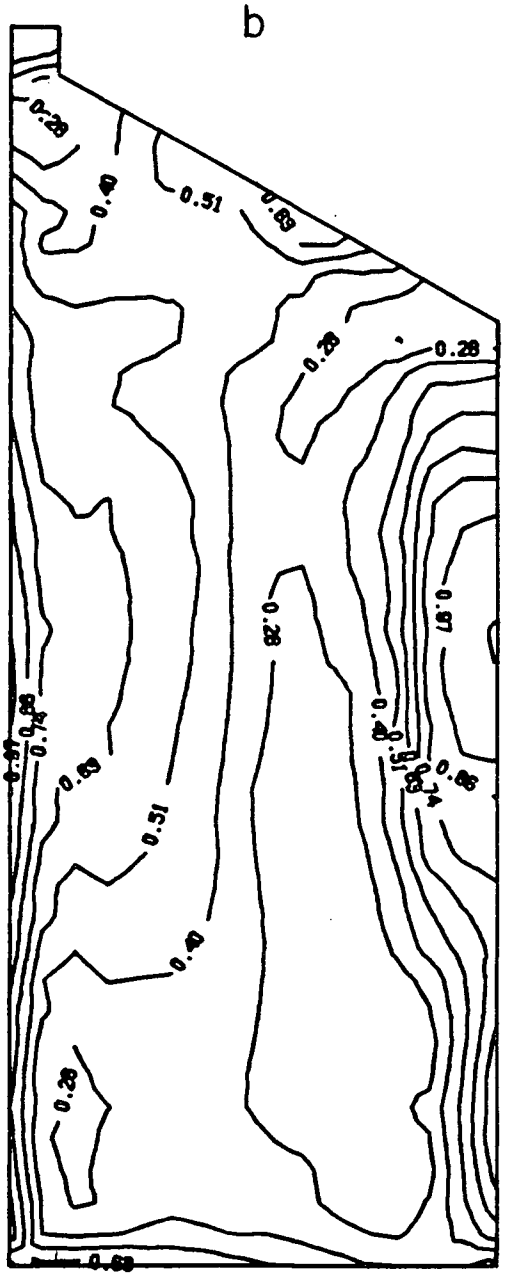
b
0.28
0.40
0.51
0.69
0.28
0.28
0.28
0.97
0.86
0.74
0.69
0.51
0.40
0.28
0.68

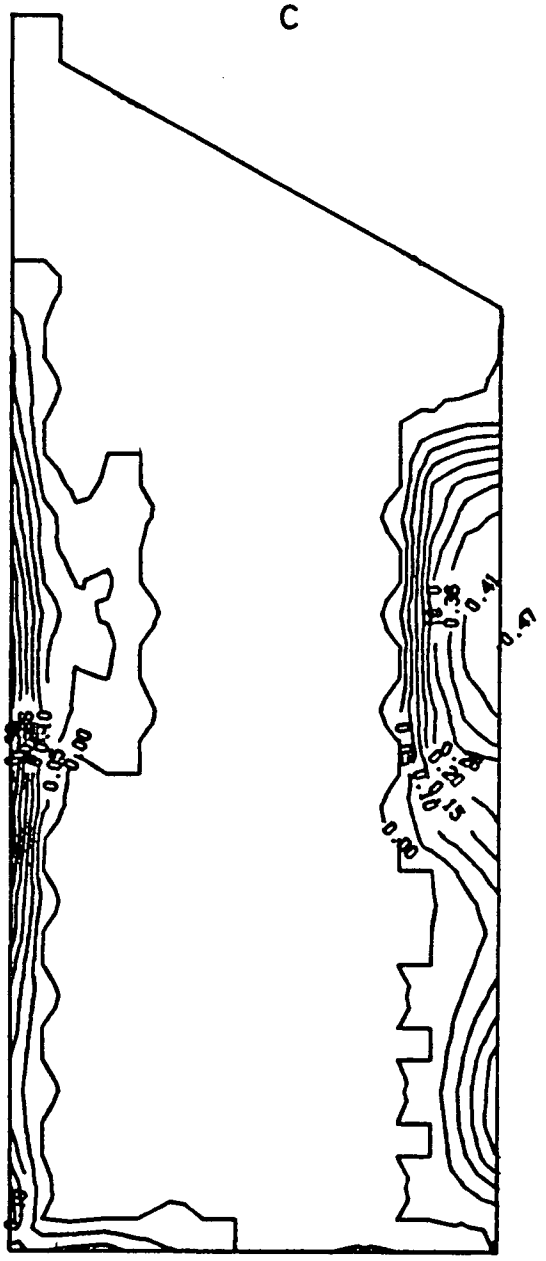
c
0.41
0.47
0.00
0.00

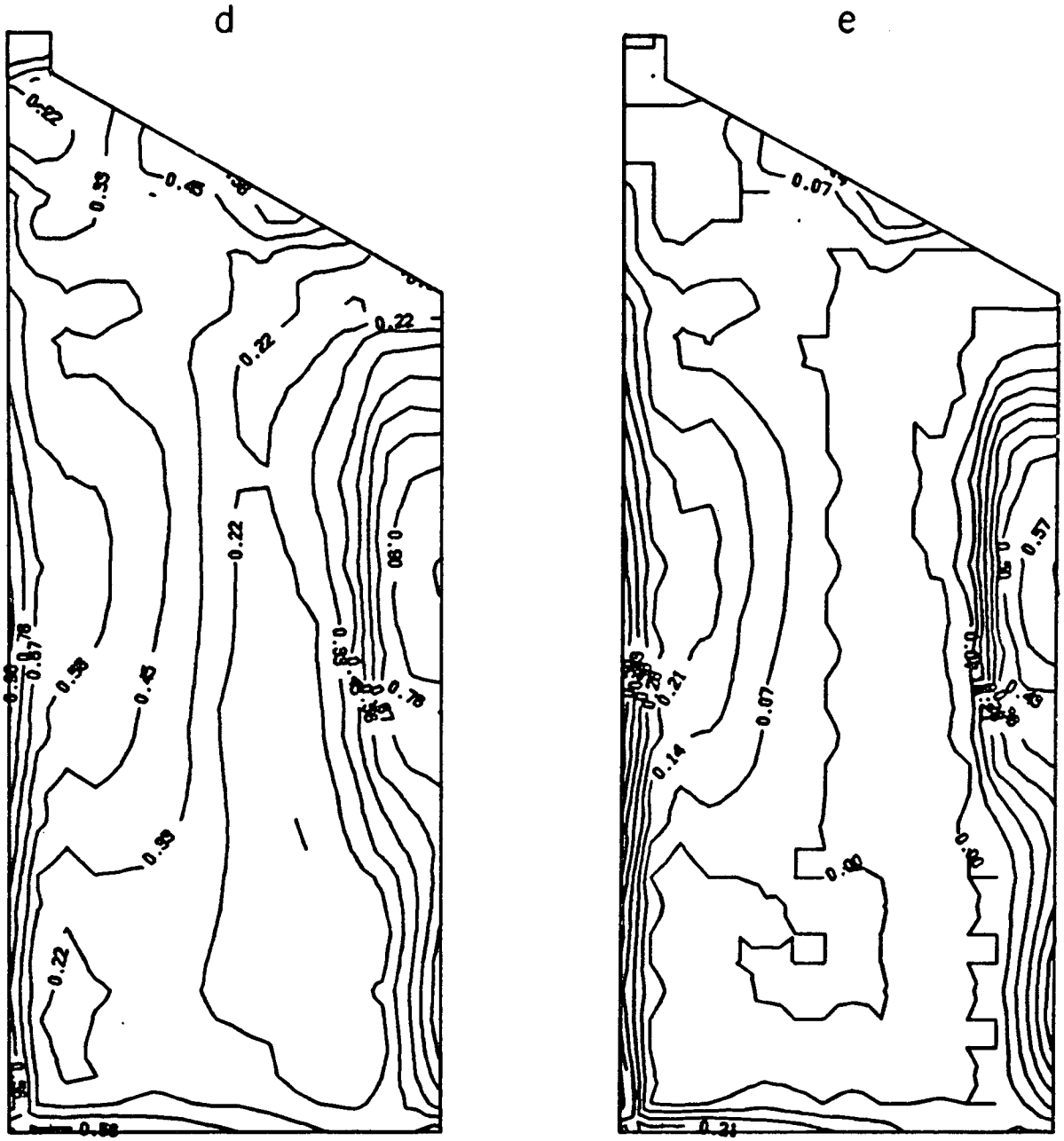

XIII.6.3.3 G/5

(a) Temperature and Von Mises Stress
(b) MRSS ; (c) MRSS-CRSS (Yield) ;
(d) MRSS-CRSS (MB) ; (e) MRSS-CRSS (MBTe) .

XIII.7 Argon Pressure, 2 atmospheres.
R, 27.5 mm ; CL, 55 mm ; CA, 30° ; B, 21 mm .

XIII.7.1 G
(a) Temperature and Von Mises Stress
(b) MRSS ; (c) MRSS-CRSS (Yield) ;
(d) MRSS-CRSS (MB) ; (e) MRSS-CRSS (MBTe) .

XIII.7.2 G/2
(a) Temperature and Von Mises Stress
(b) MRSS ; (c) MRSS-CRSS (Yield) ;
(d) MRSS-CRSS (MB) ; (e) MRSS-CRSS (MBTe) .

XIII.7.3 G/4
(a) Temperature and Von Mises Stress
(b) MRSS ; (c) MRSS-CRSS (Yield) ;
(d) MRSS-CRSS (MB) ; (e) MRSS-CRSS (MBTe) .

XIII.7.4 G/6
(a) Temperature and Von Mises Stress
(b) MRSS ; (c) MRSS-CRSS (Yield) ;
(d) MRSS-CRSS (MB) ; (e) MRSS-CRSS (MBTe) .

a

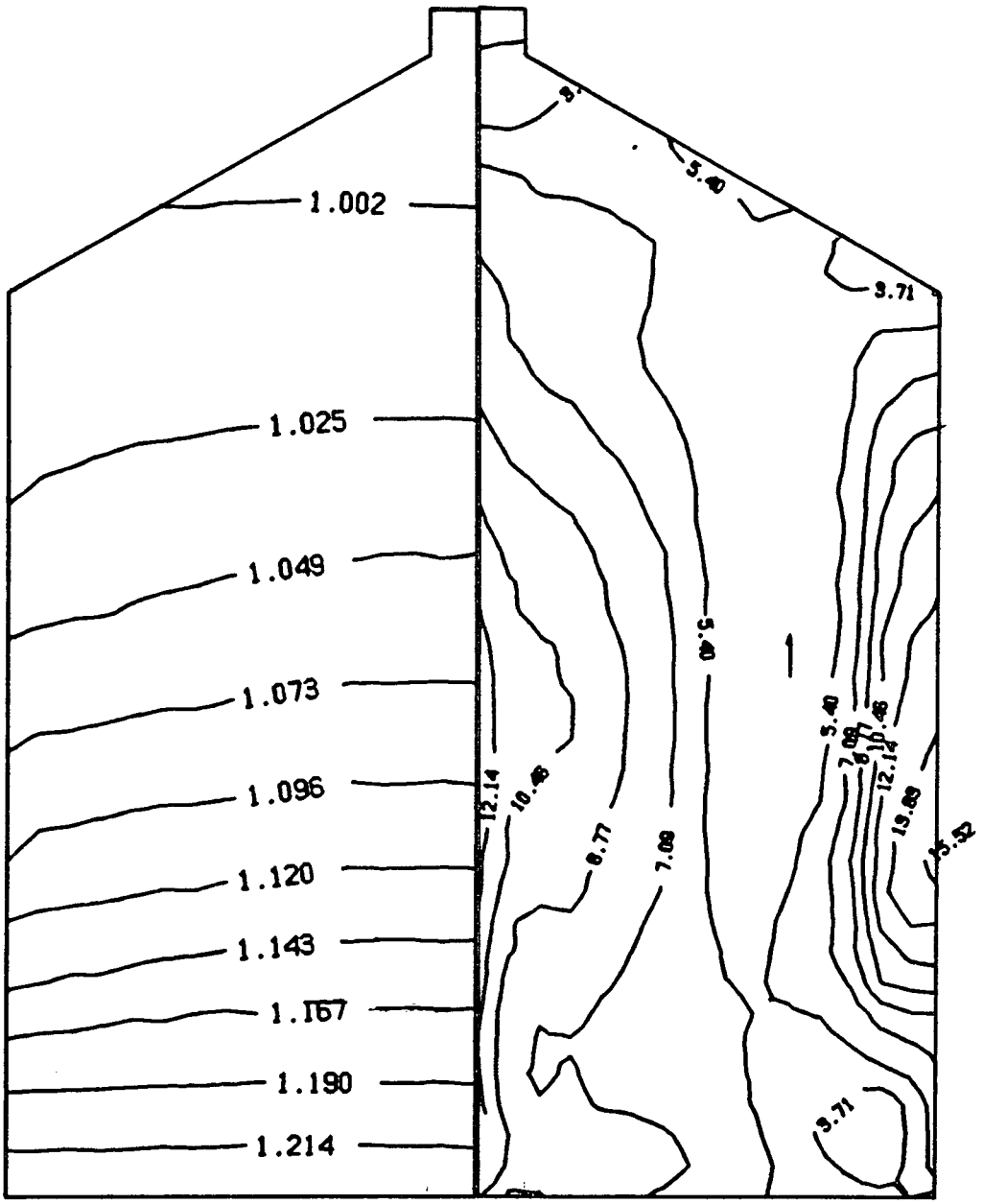
1.002
1.025
1.049
1.073
1.096
1.120
1.143
1.167
1.190
1.214
5.40
9.71
5.40
12.14
10.48
6.77
7.08
5.40
7.08
10.48
12.14
13.80
15.52
9.71

b

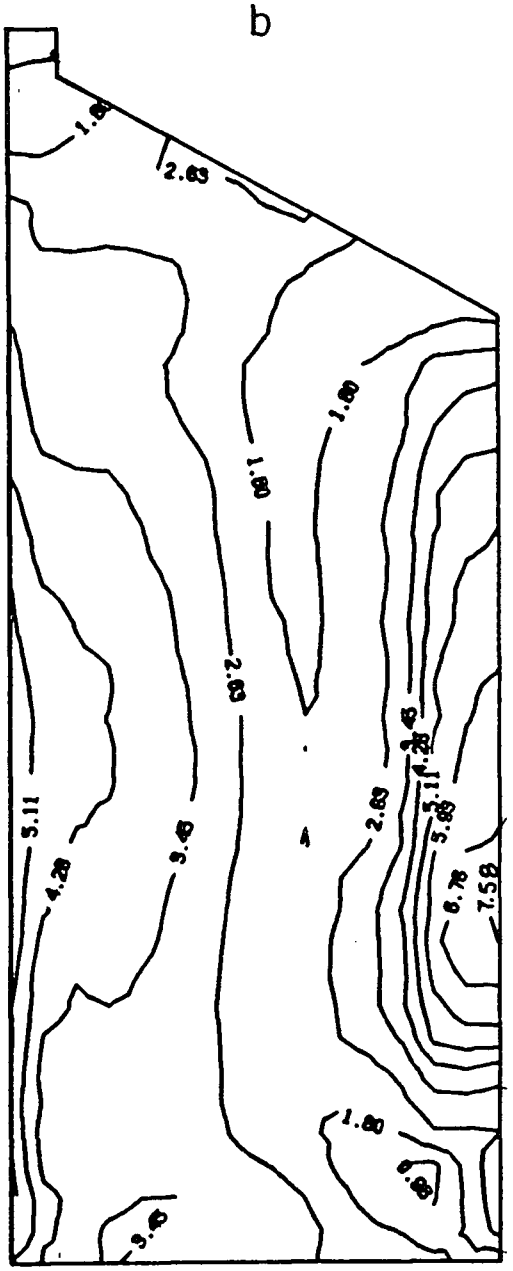
1.88
2.63
1.88
2.63
5.11
4.28
3.45
2.63
1.88
5.11
5.63
6.78
7.53
1.88
3.45

c

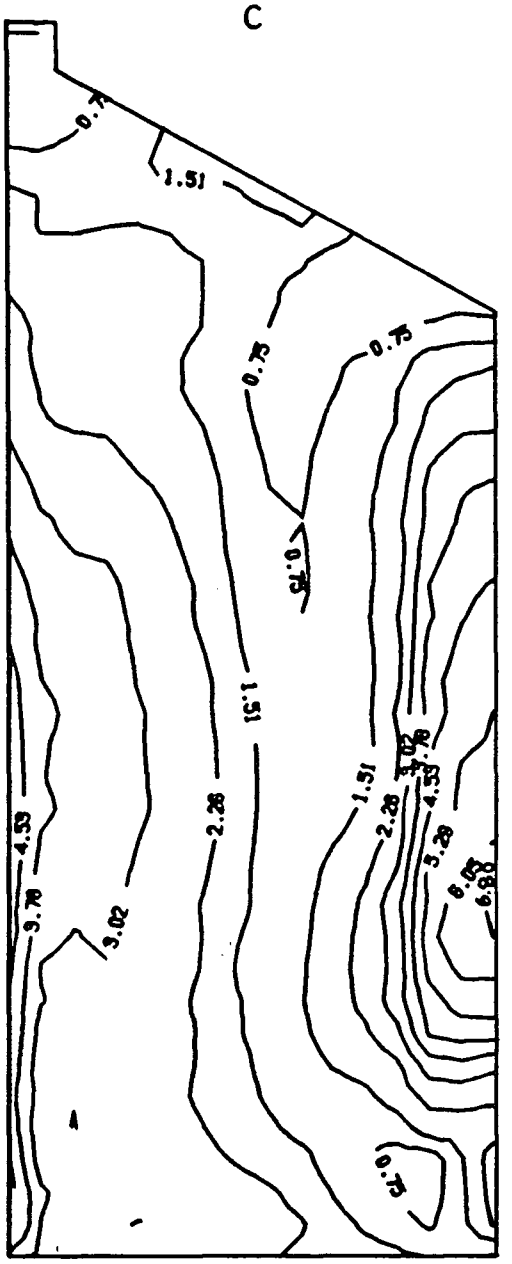
0.75
1.51
0.75
0.75
0.75
1.51
4.53
3.78
3.02
2.26
1.51
2.26
3.78
4.53
3.78
6.05
6.80
0.75

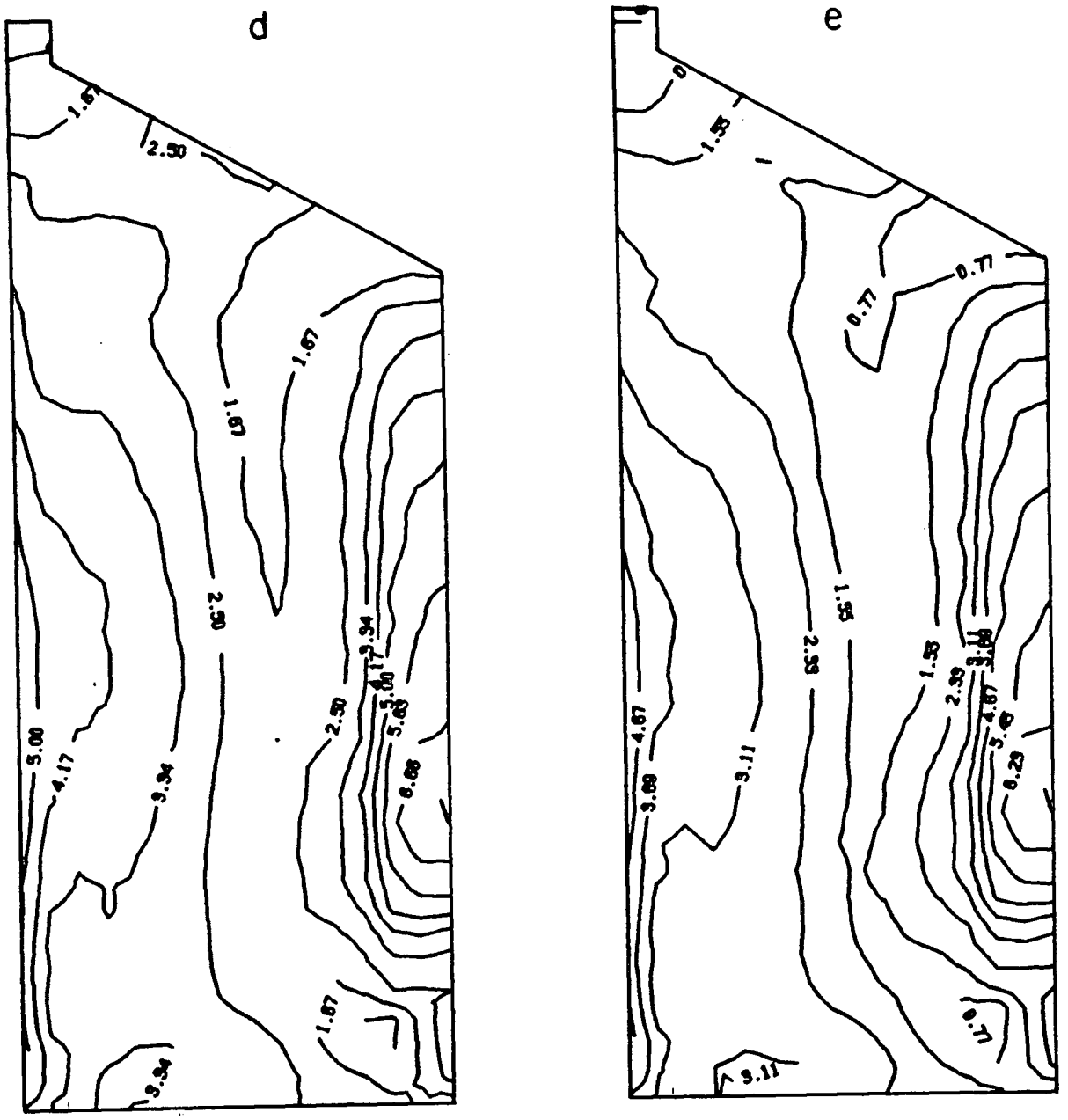

XIII.7.1 G

(a) Temperature and Von Mises Stress
(b) MRSS ; (c) MRSS-CRSS (Yield) ;
(d) MRSS-CRSS (MB) ; (e) MRSS-CRSS (MBTe) .

a

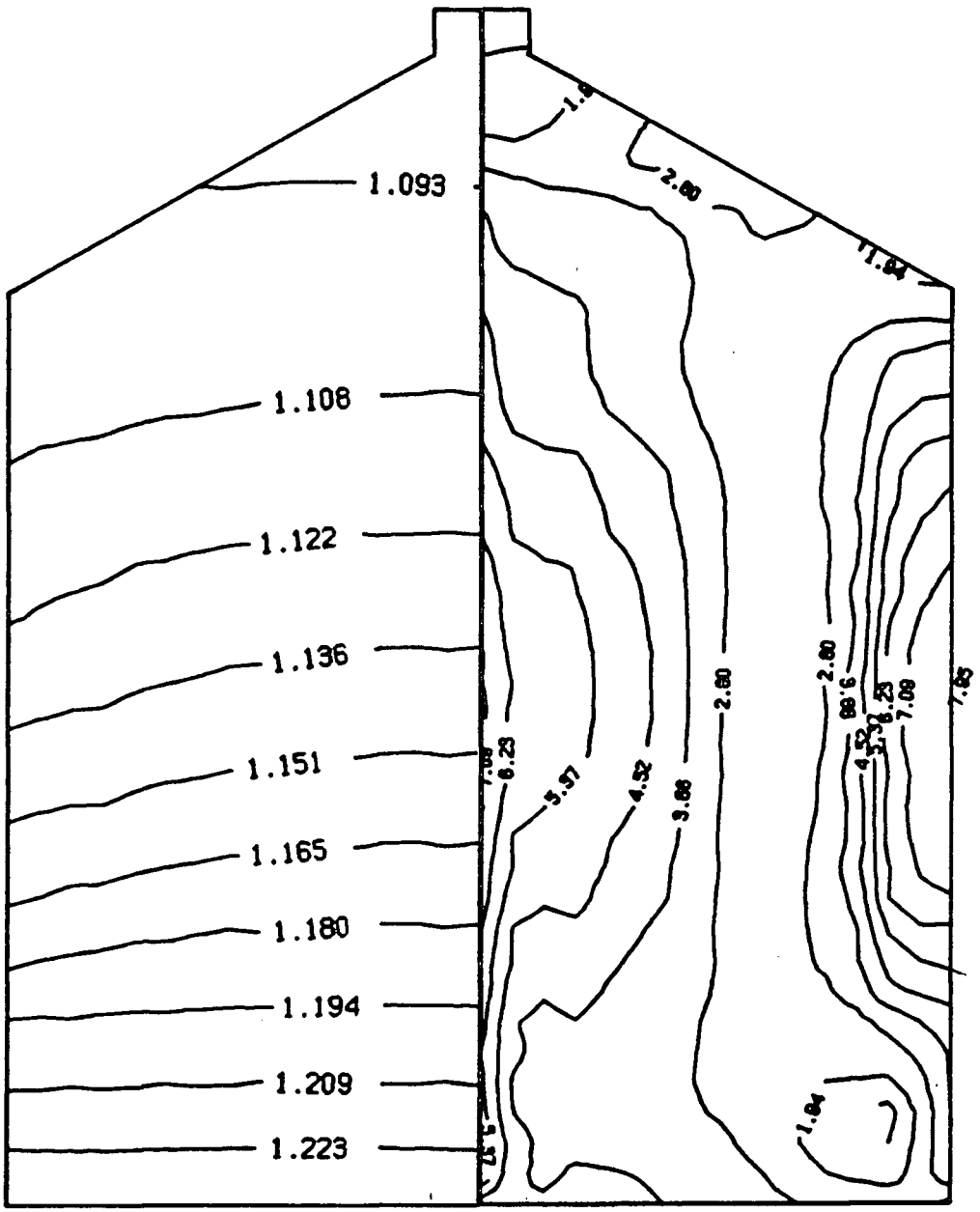
1.093
1.108
1.122
1.136
1.151
1.165
1.180
1.194
1.209
1.223
2.80
1.94
6.23
5.37
4.52
3.66
2.80
2.80
7.09
7.95
1.94

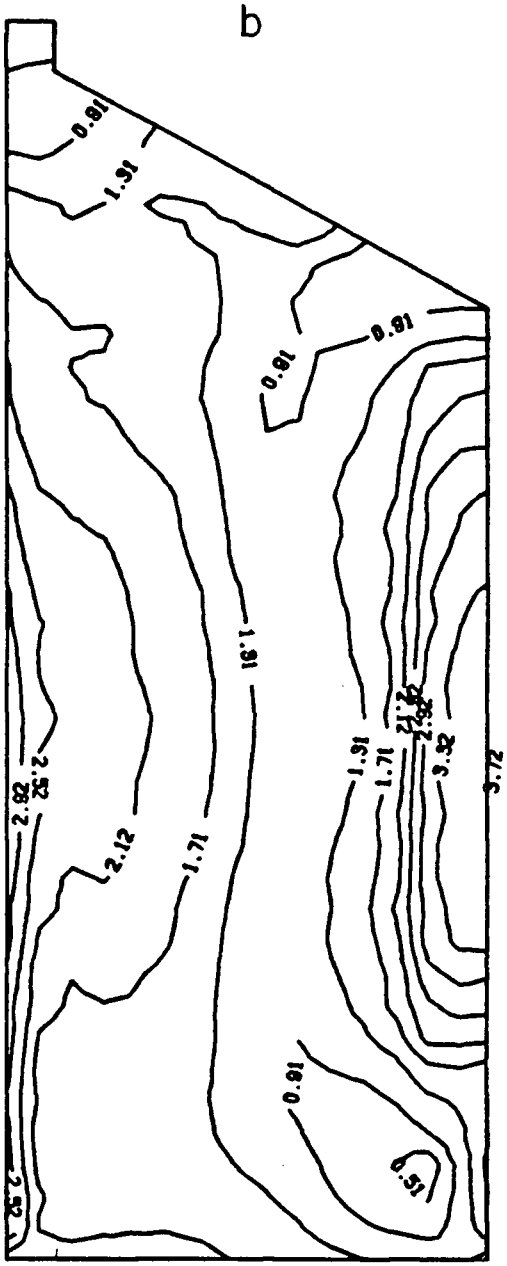
b
0.91
1.31
0.91
0.91
1.31
1.31
1.71
2.92
2.52
2.12
1.71
3.32
3.72
0.91
0.51

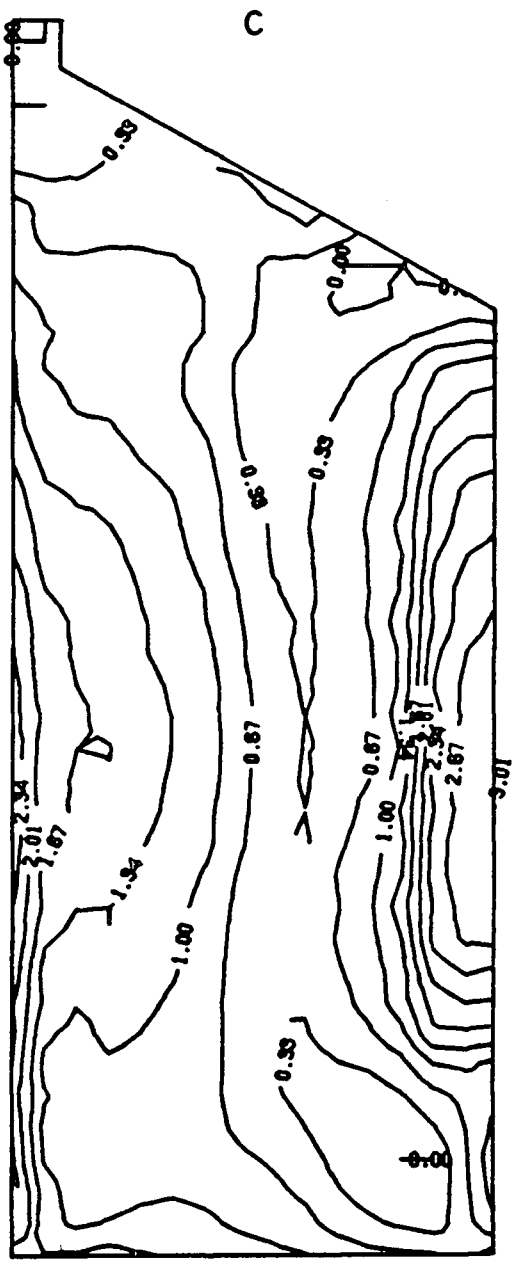
c
0.33
0.00
0.33
0.33
0.67
0.67
1.00
2.34
2.01
1.67
1.34
1.00
2.67
3.01
0.33
-0.00

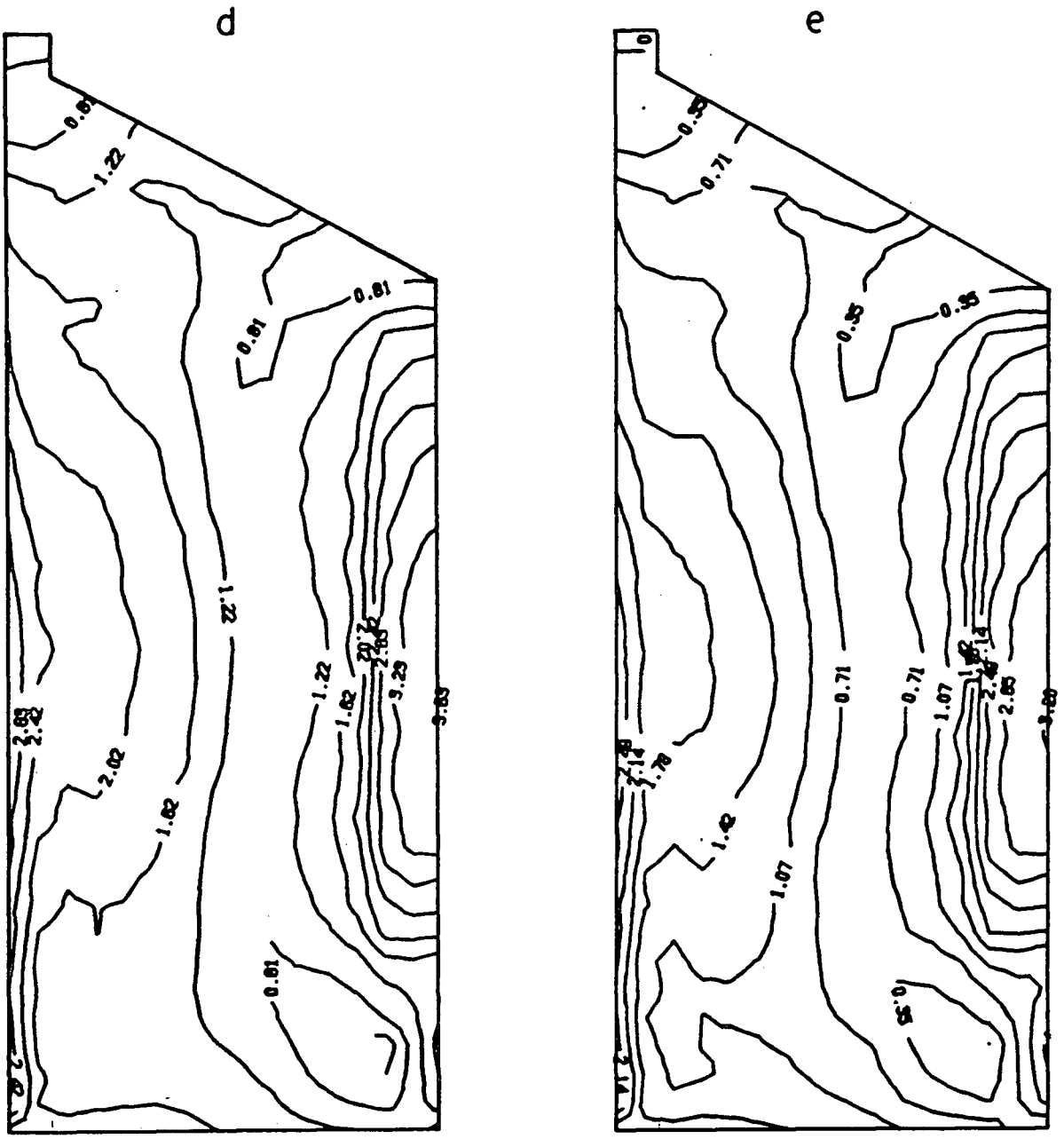

XIII.7.2 G/2
(a) Temperature and Von Mises Stress
(b) MRSS ; (c) MRSS-CRSS (Yield) ;
(d) MRSS-CRSS (MB) ; (e) MRSS-CRSS (MBTe) .

a

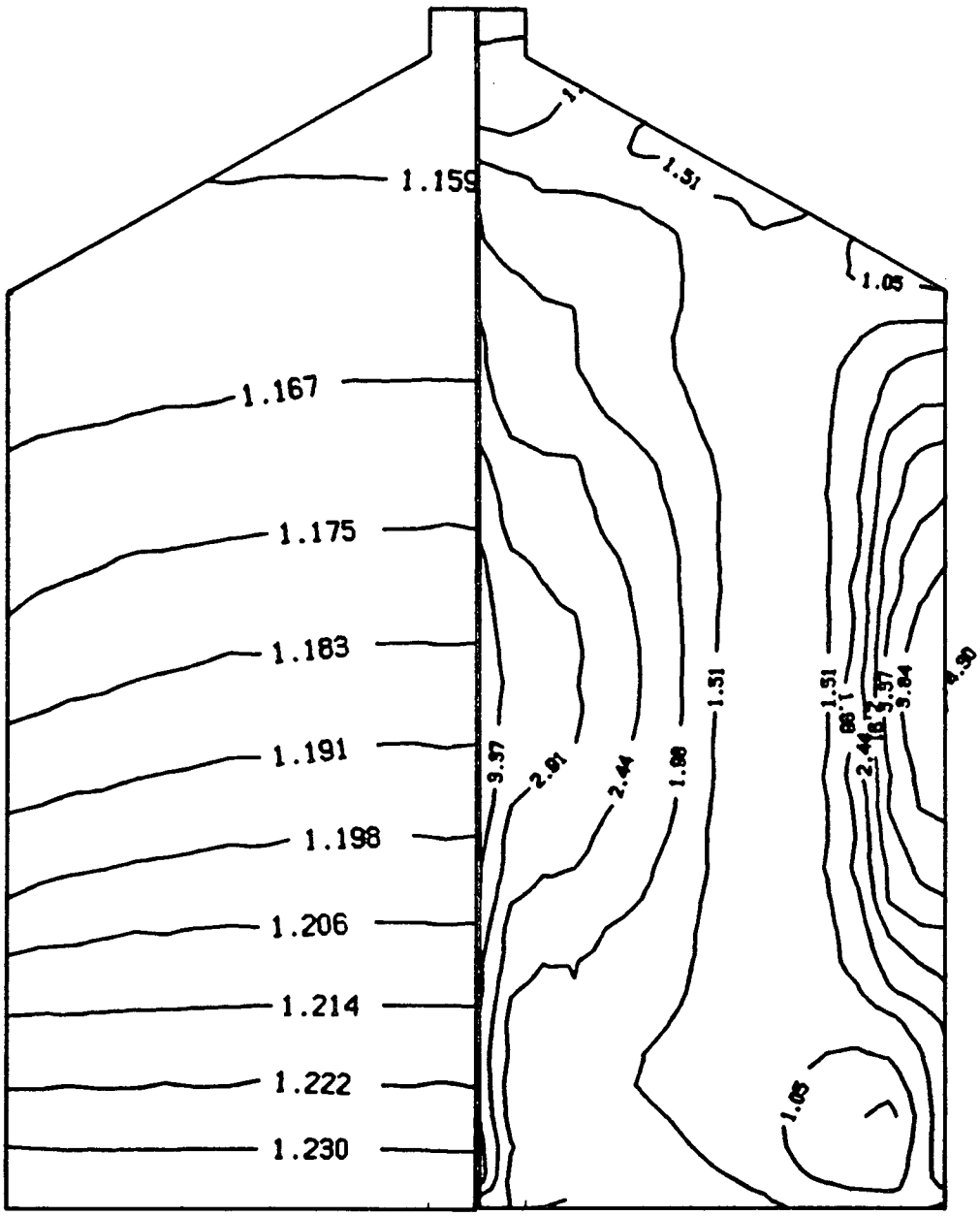
1.159
1.167
1.175
1.183
1.191
1.198
1.206
1.214
1.222
1.230
1.51
1.05
9.37
2.91
2.44
1.98
1.51
1.51
1.05

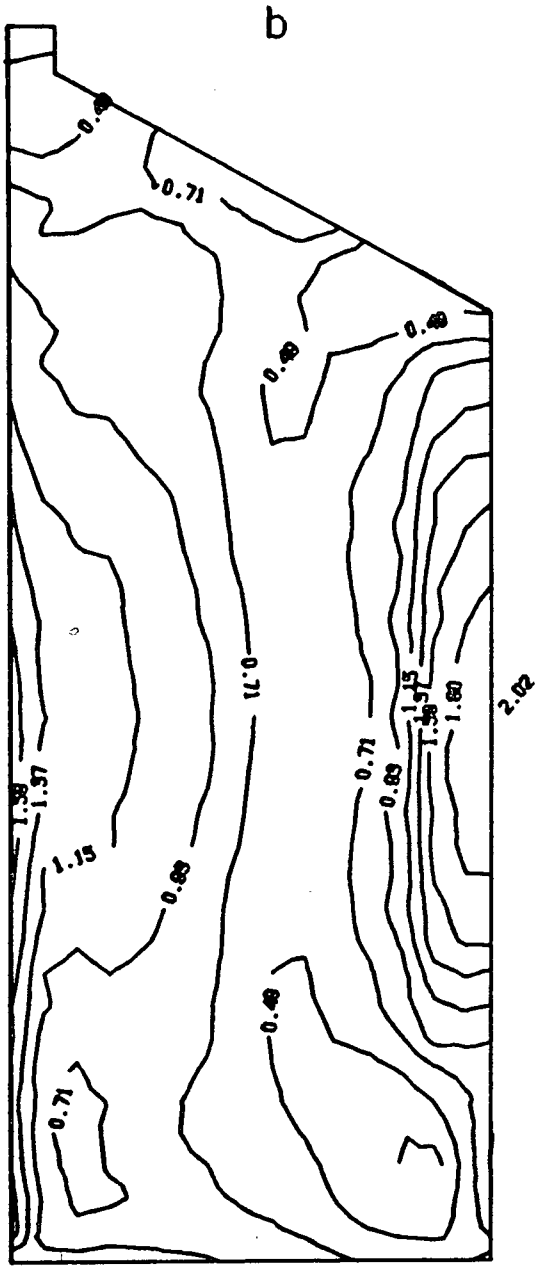
b
0.71
0.49
0.49
0.71
1.57
1.15
0.83
0.49
0.71
0.71
1.15
1.57
1.80
2.02

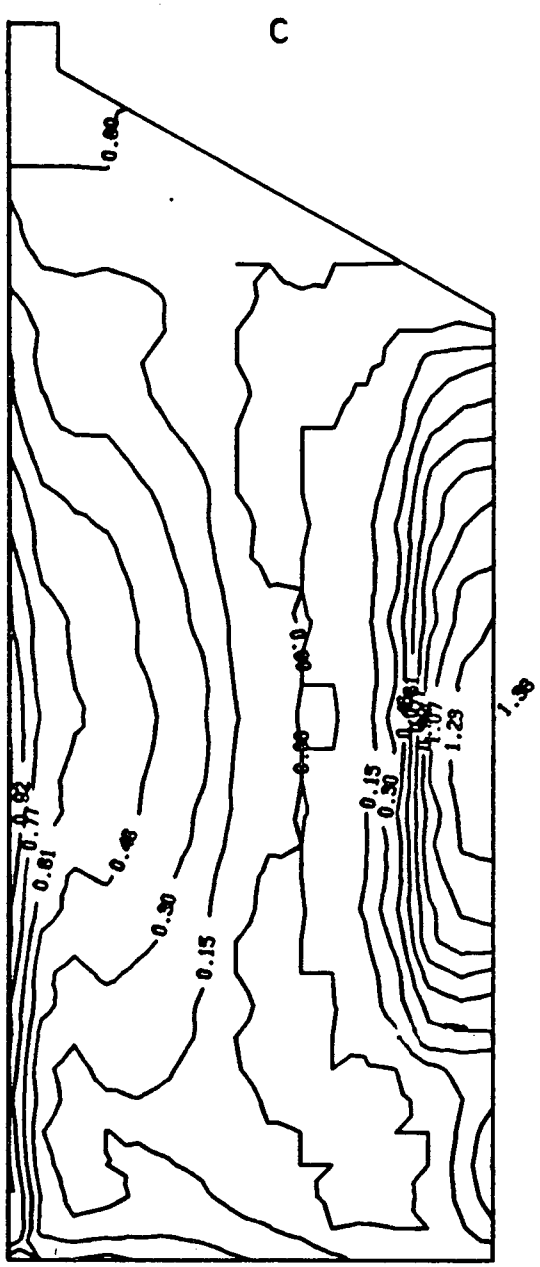
c
0.80
0.61
0.49
0.30
0.15
0.15
0.30
1.23
1.38

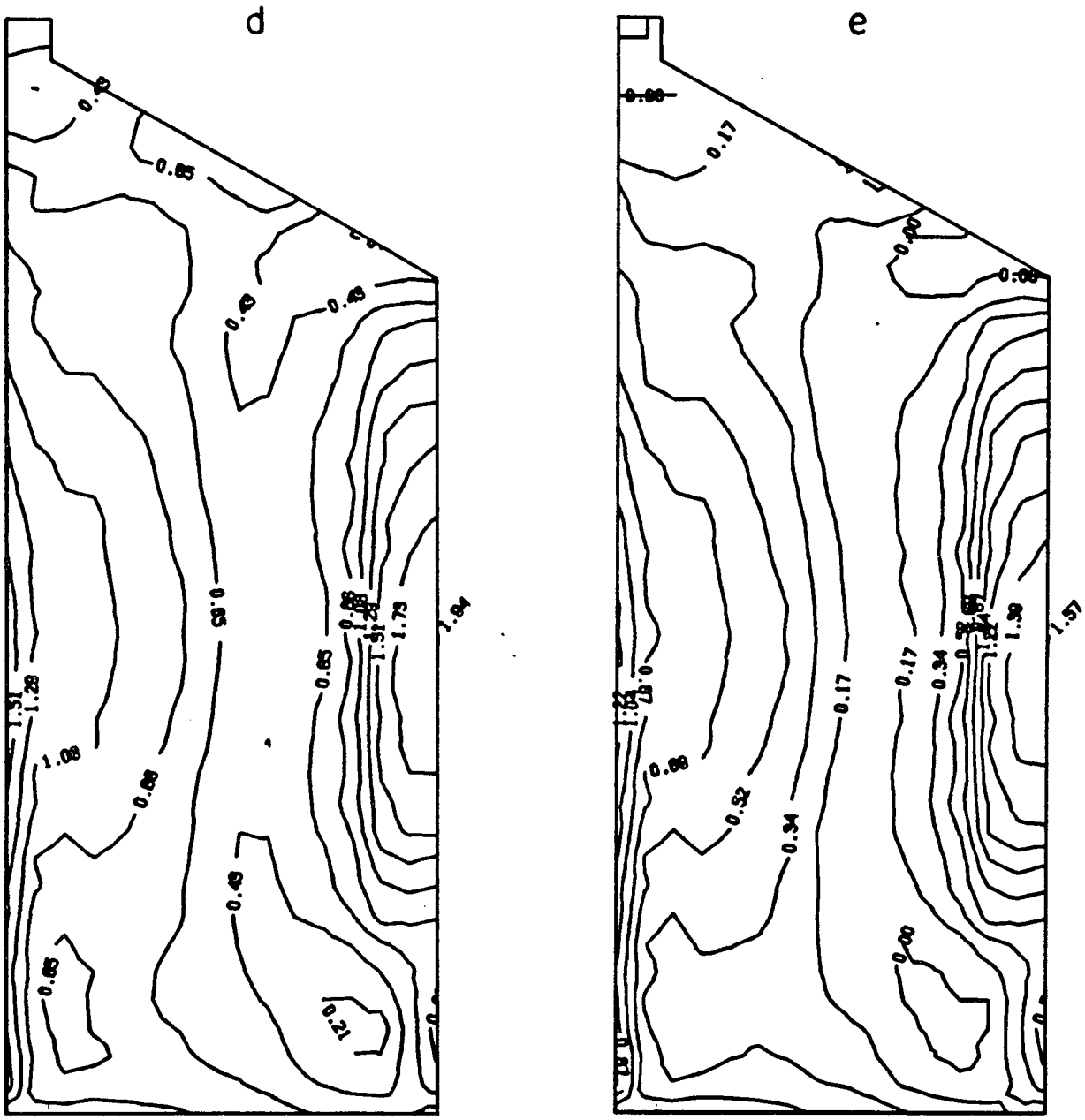

XIII.7.3 G/4

(a) Temperature and Von Mises Stress
(b) MRSS ; (c) MRSS-CRSS (Yield) ;
(d) MRSS-CRSS (MB) ; (e) MRSS-CRSS (MBTe) .

a

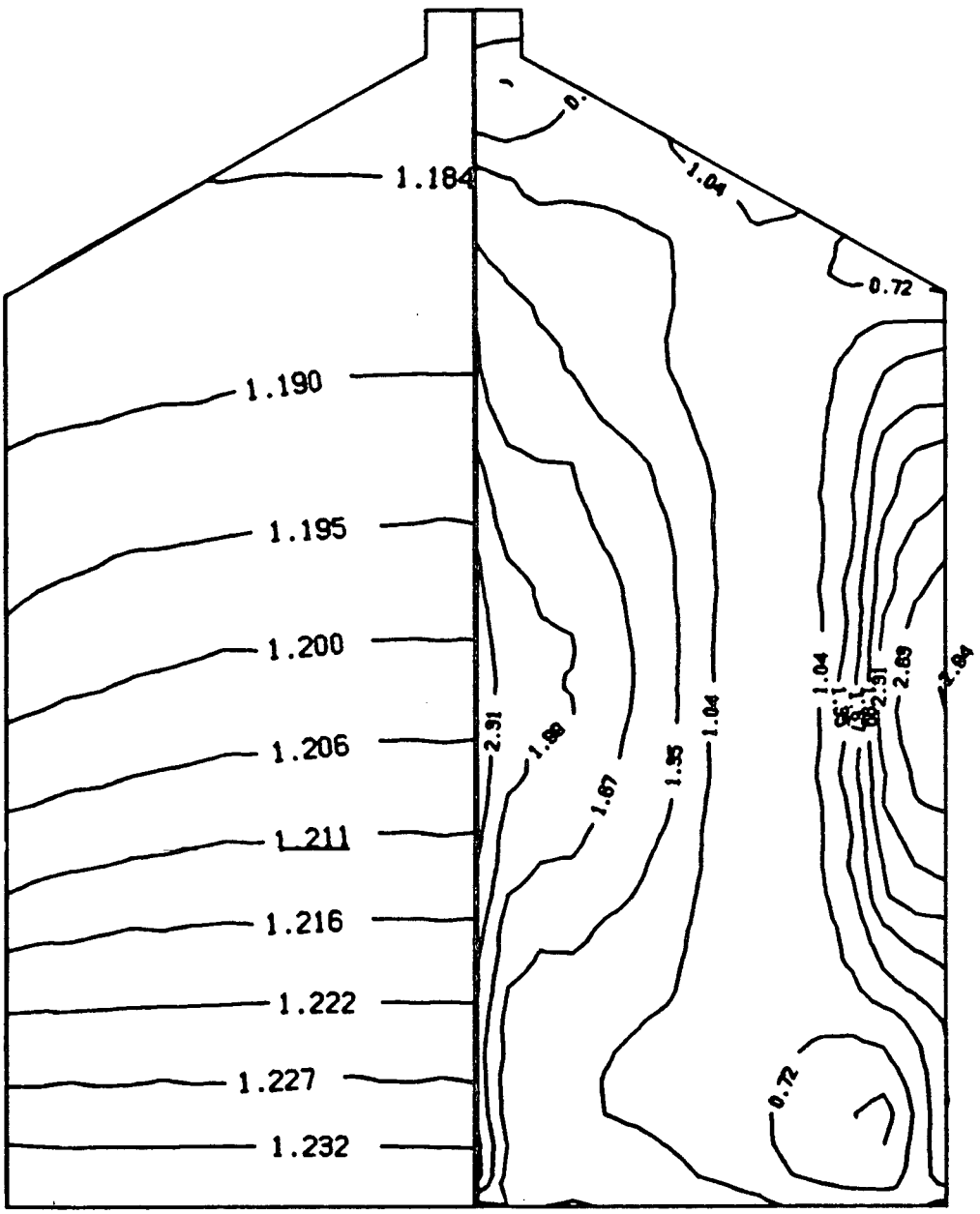
1.184
1.190
1.195
1.200
1.206
1.211
1.216
1.222
1.227
1.232
0.72
1.04
2.31
1.67
1.35
2.89

b

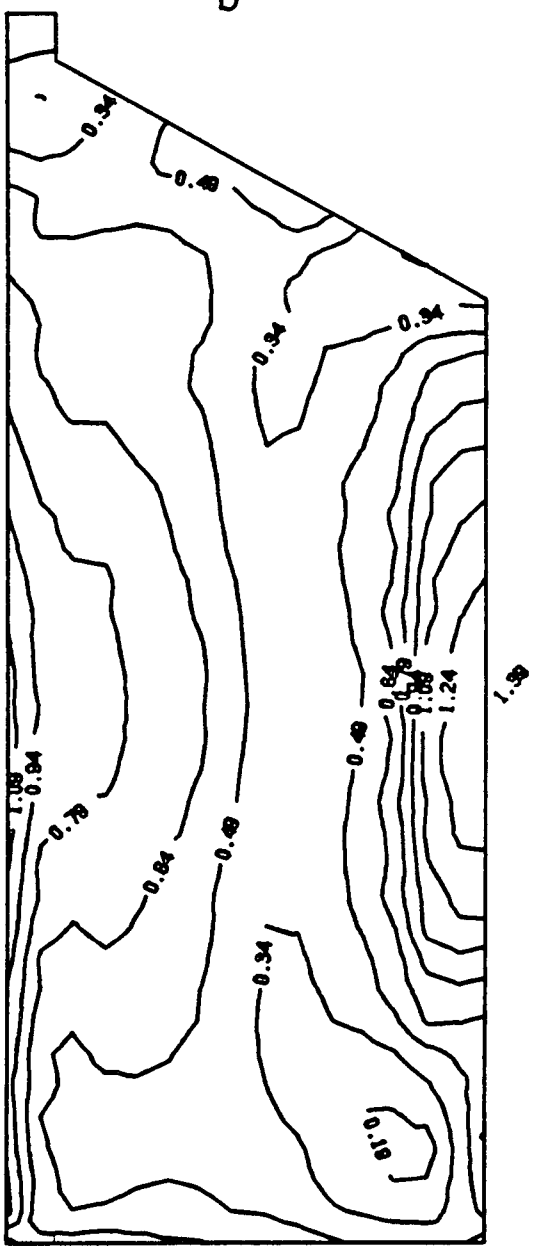

c

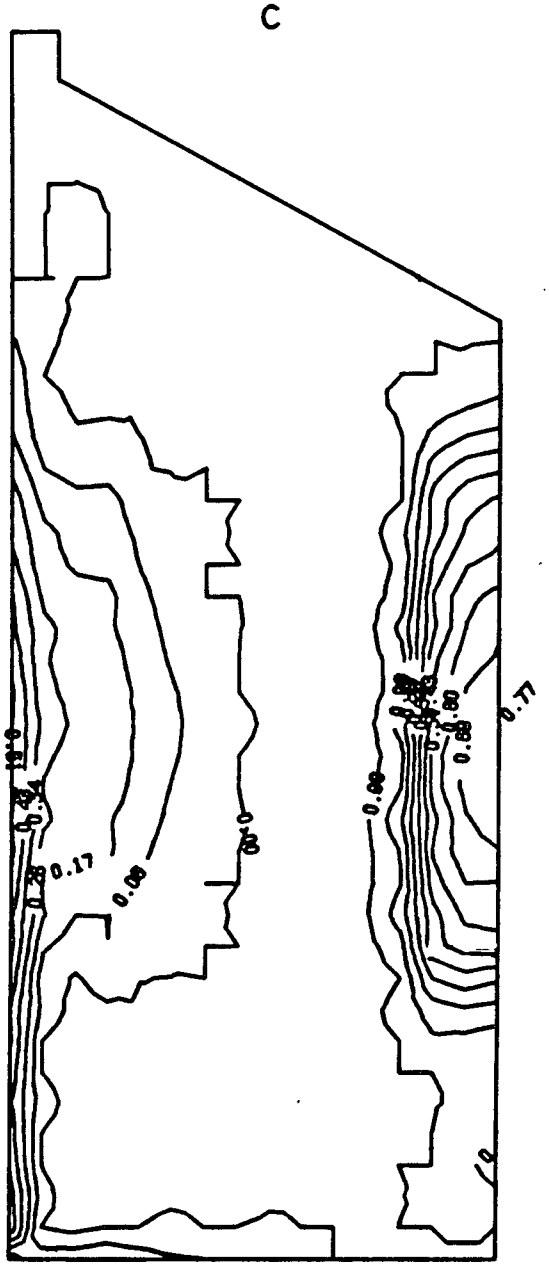

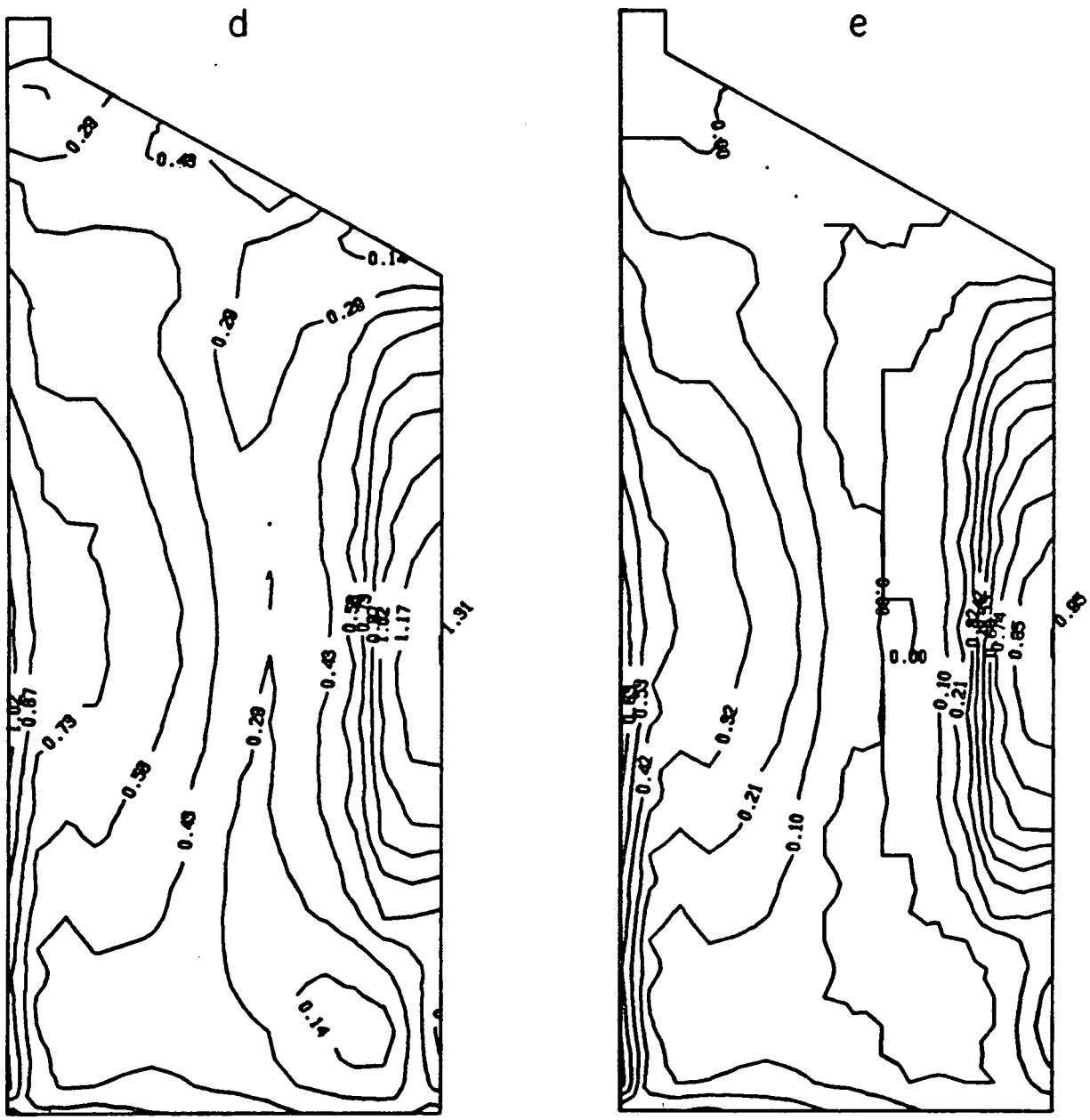

XIII.7.4 G/6

(a) Temperature and Von Mises Stress
(b) MRSS ; (c) MRSS-CRSS (Yield) ;
(d) MRSS-CRSS (MB) ; (e) MRSS-CRSS (MBTe) .

XIII.8 Curvature of the Solid/Liquid Interface
CA, 30° ; AP, 30 atm.

XIII.8.1 Convex Interface

XIII.8.1.1 B, 21 mm ; G .

XIII.8.1.1.1 R, 27.5 mm

XIII.8.1.1.1.1 CL, 27.5 mm
(a) Temperature and Von Mises Stress
(b) MRSS ; (c) MRSS-CRSS (Yield) ;
(d) MRSS-CRSS (MB) ; (e) MRSS-CRSS (MBTe) .

XIII.8.1.1.1.2 CL, 55 mm

XIII.8.1.1.1.2.1 (a) Temperature and Von Mises Stress
(b) MRSS ; (c) MRSS-CRSS (Yield) ;
(d) MRSS-CRSS (MB) ; (e) MRSS-CRSS (MBTe) .

XIII.8.1.1.1.2.2 MRSS-CRSS (Yield) in cross-sections at distances from the interface of
(a) 11 mm ; (b) 24.75 mm ; (c) 38.5 mm ;
(d) 52.25 mm ;

XIII.8.1.1.1.3 CL, 82.5 mm

XIII.8.1.1.1.3.1 (a) Temperature and Von Mises Stress
(b) MRSS ; (c) MRSS-CRSS (Yield) ;
(d) MRSS-CRSS (MB) ; (e) MRSS-CRSS (MBTe) .

XIII.8.1.1.1.3.2 MRSS-CRSS (Yield) in cross-sections at (along the axis) distances from the interface of
(a) 11 mm ; (b) 24.75 mm ; (c) 38.5 mm ;
(d) 52.5 mm ; (e) 66 mm .

XIII.8.1.1.2 R, 40.0 mm ; B, 21 mm ; G ; CL, 80 mm .

XIII.8.1.1.2.1 (a) Temperature and Von Mises Stress
(b) MRSS ; (c) MRSS-CRSS (Yield) ;
(d) MRSS-CRSS (MB) ; (e) MRSS-CRSS (MBTe) .

XIII.8.1.1.2.2 MRSS-CRSS (Yield) in cross-sections at distances (along the axis) from the interface of
(a) 16 mm ; (b) 36 mm ; (c) 56 mm .

XIII.8.1.2 B, 50 mm ; R, 2.75 mm

XIII.8.1.2.1 G

XIII.8.1.2.1.1 (a) Temperature and Von Mises Stress
(b) MRSS ; (c) MRSS-CRSS (Yield) ;
(d) MRSS-CRSS (MB) ; (e) MRSS-CRSS (MBTe) .

XIII.8.1.2.1.2 MRSS-CRSS (Yield) in cross-sections at distances (along the axis) from the interface of (a) 11 mm ; (b) 36 mm ; (c) 56 mm ; (d) 76 mm.

XIII.8.1.2.2. G/3

XIII.8.1.2.2.1 (a) Temperature and Von Mises Stress (b) MRSS ; (c) MRSS-CRSS (Yield) ; (d) MRSS-CRSS (MB) ; (e) MRSS-CRSS (MBTe) .

XIII.8.1.2.2.2 MRSS-CRSS (Yield) in cross-sections at distances (along the axis) from the interface of (a) 11 mm ; (b) 36 mm ; (c) 56 mm ; (d) 76 mm.

XIII.8.2 Concave Interface
B,21 mm ; G .

XIII.8.2.1 R, 27.5 mm ; CL, 55 mm .

XIII.8.2.1.1 (a) Temperature and Von Mises Stress (b) MRSS ; (c) MRSS-CRSS (Yield) ; (d) MRSS-CRSS (MB) ; (e) MRSS-CRSS (MBTe) .

XIII.8.2.1.2 MRSS-CRSS (Yield) in cross-sections at distances (along the axis) from the interface of (a) 2.75 mm ; (b) 16.5 mm ; (c) 30.25 mm ; (d) 44 mm .

XIII.8.2.2 R, 40 mm ; CL,80 mm .

XIII.8.2.2.1 (a) Temperature and Von Mises Stress (b) MRSS ; (c) MRSS-CRSS (Yield) ; (d) MRSS-CRSS (MB) ; (e) MRSS-CRSS (MBTe) .

XIII.8.2.2.2 MRSS-CRSS (Yield) in cross-sections at distances (along the axis) from the interface of (a) 2.75 mm ; (b) 16.5 mm ; (c) 30.25 mm ; (d) 44 mm .

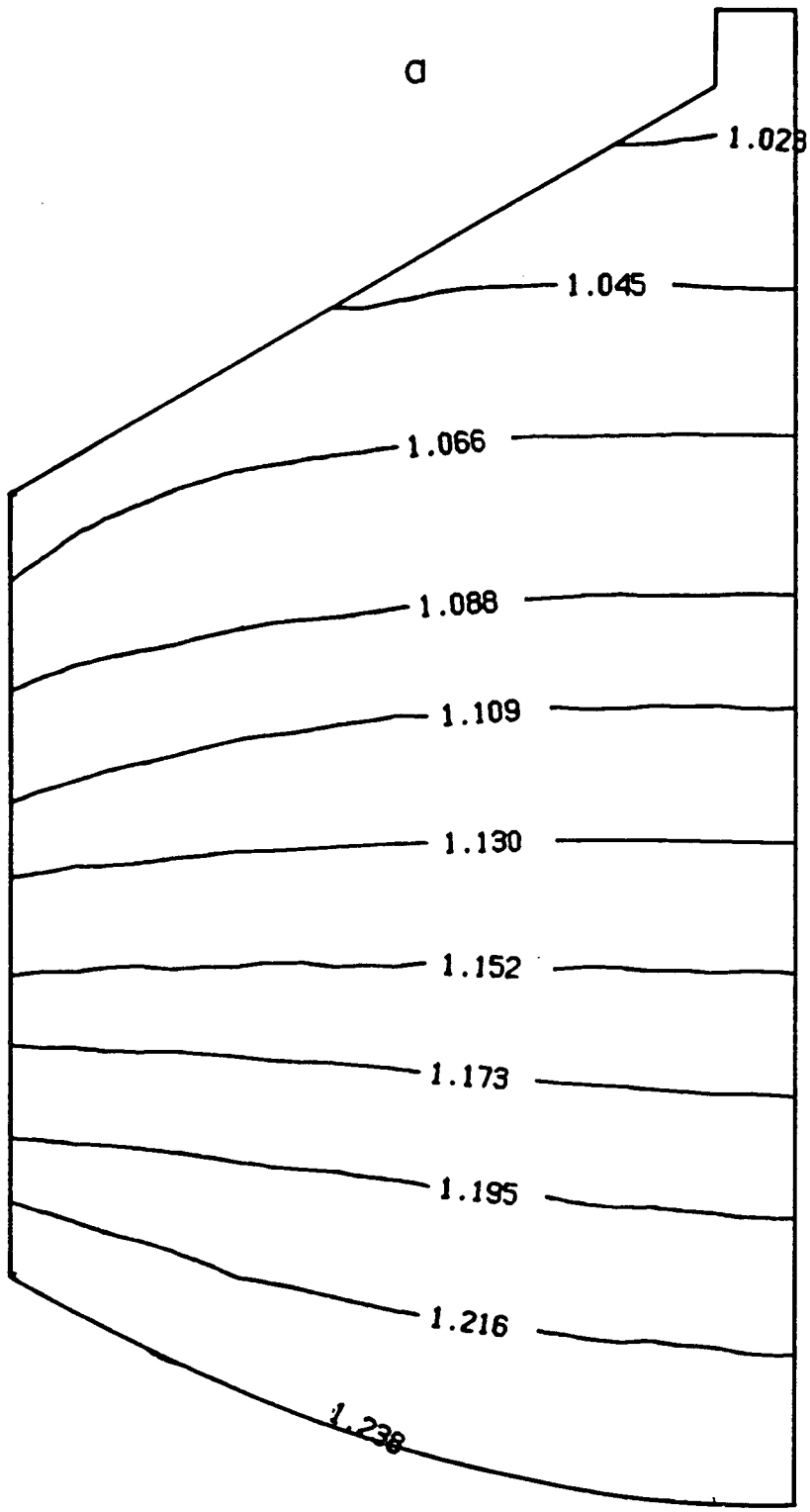
a
1.028
1.045
1.066
1.088
1.109
1.130
1.152
1.173
1.195
1.216
1.238

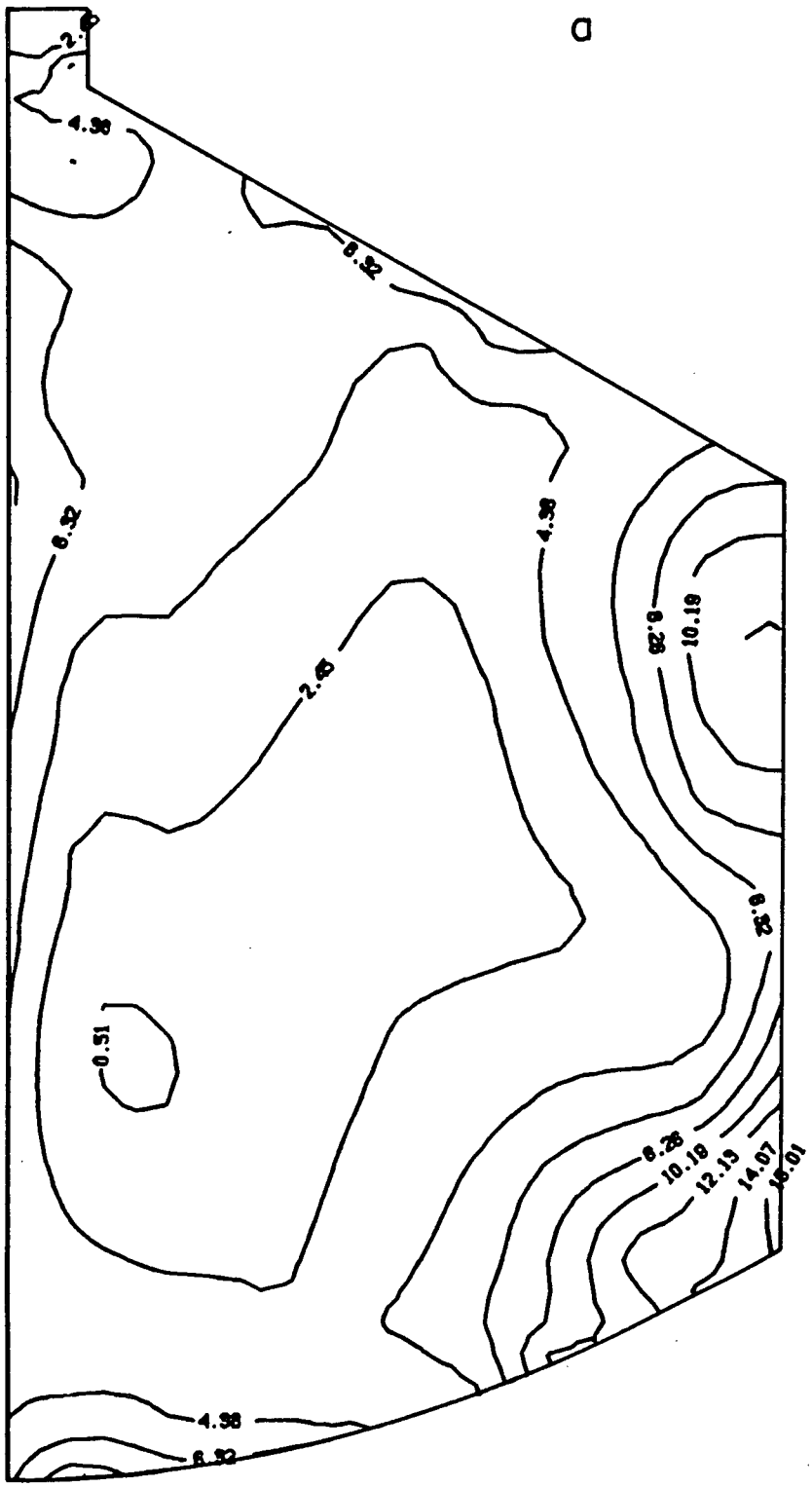
a
4.38
8.32
8.32
4.38
2.45
8.26
10.19
8.32
0.51
8.26
10.19
12.13
14.07
16.01
4.38
8.32

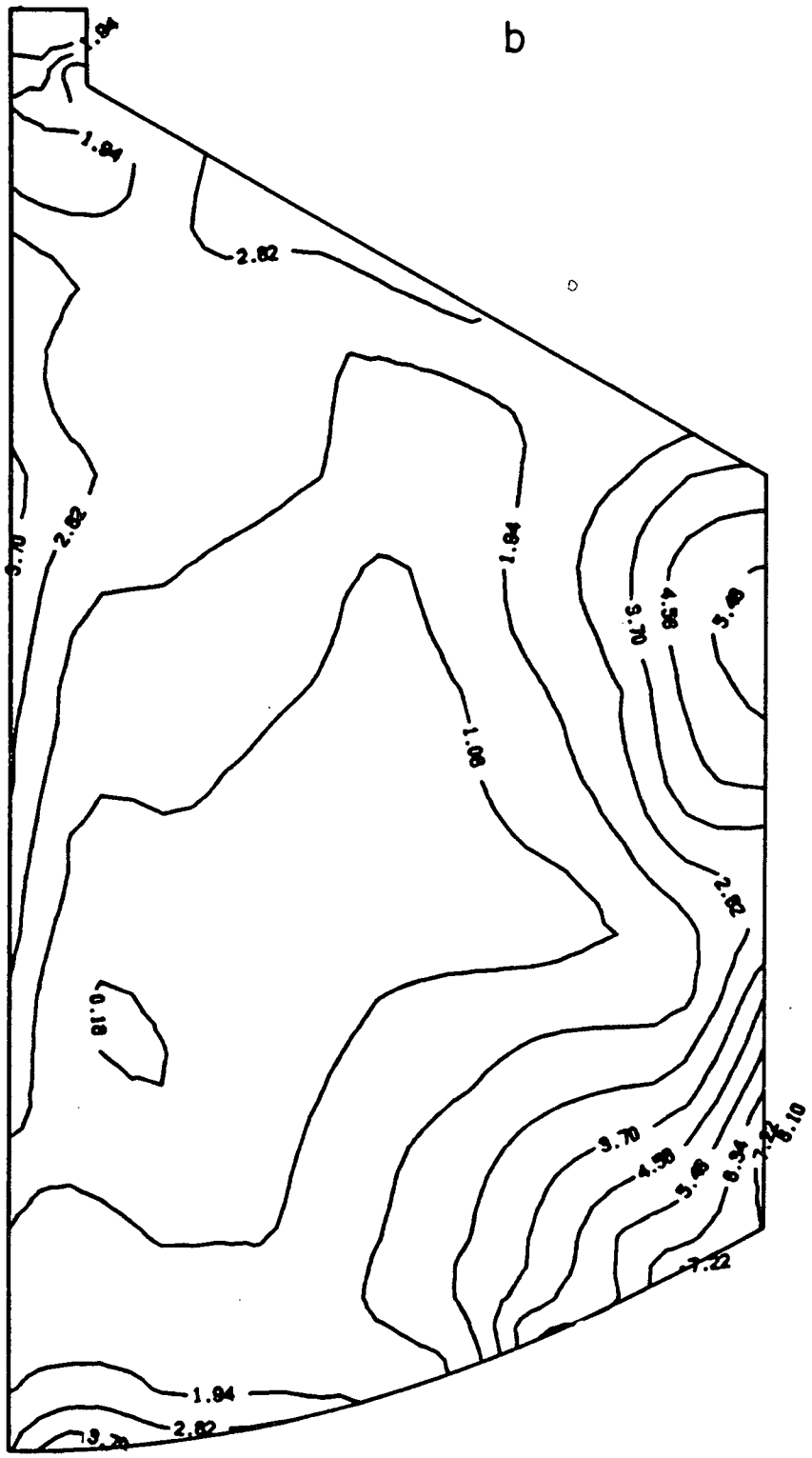
b
1.94
2.82
3.70
2.82
1.94
3.70
4.58
5.48
1.08
2.82
0.18
3.70
4.58
5.48
6.34
7.22
8.10
7.22
1.94
2.82
3.70

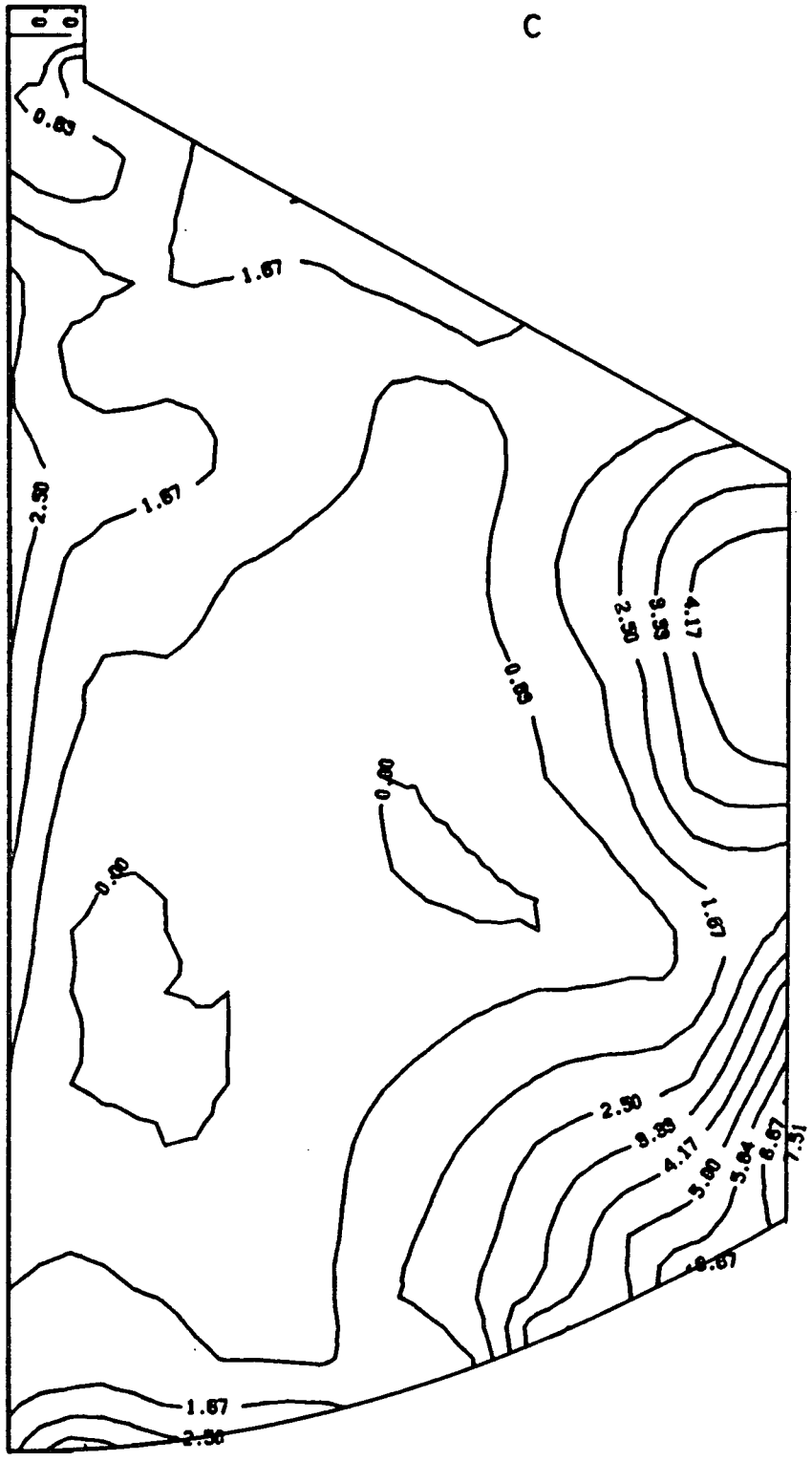
C
0.83
1.67
2.50
1.67
0.83
0.00
0.00
1.67
2.50
3.33
4.17
5.00
5.84
6.67
7.51
1.67
2.50

d

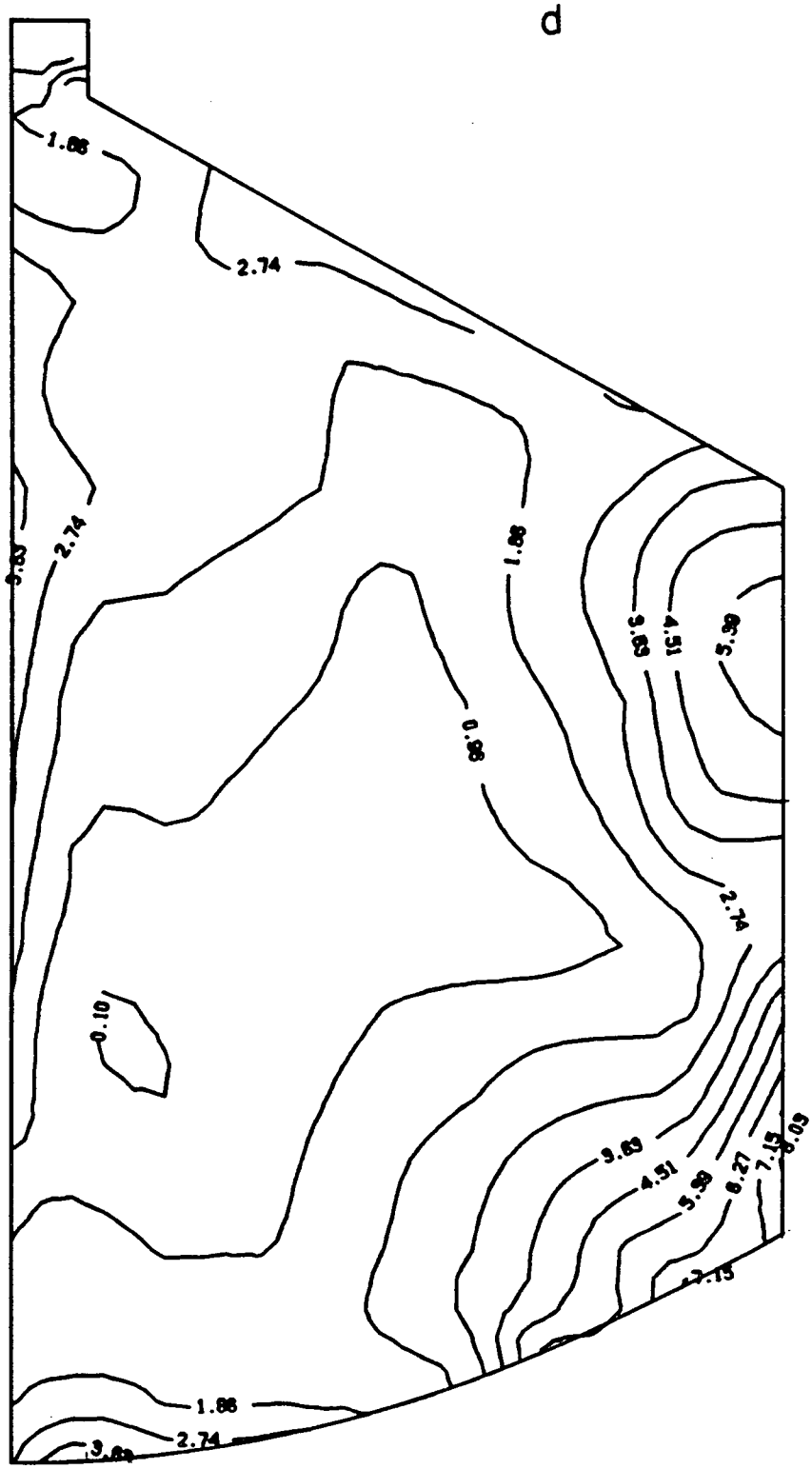
1.88
2.74
2.74
1.88
3.89
4.51
5.90
0.86
2.74
0.10
3.89
4.51
5.90
8.27
7.15
8.09
7.15
1.88
2.74
3.89

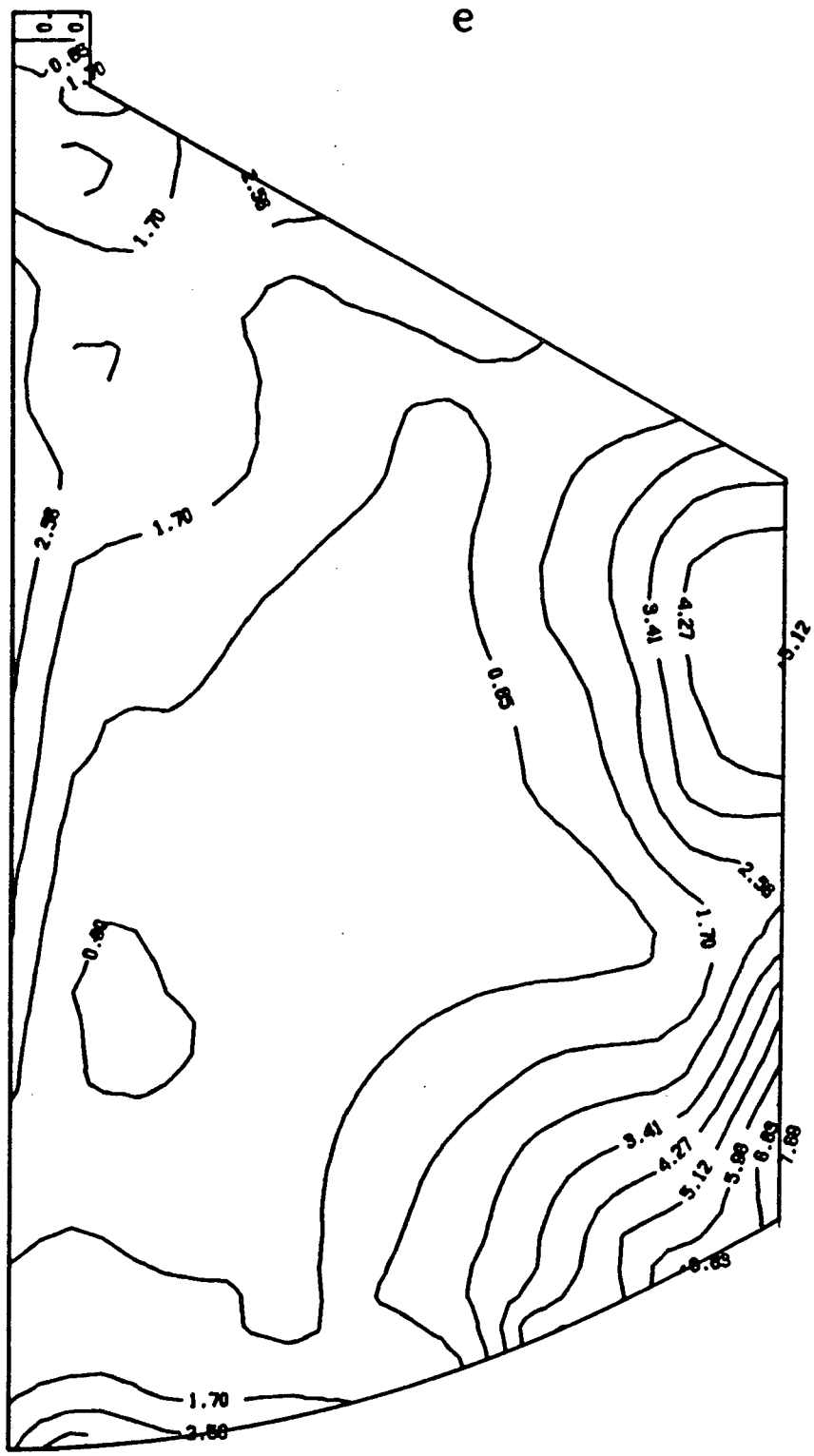

XIII.8.1.1.1.1 CL, 27.5 mm
(a) Temperature and Von Mises Stress
(b) MRSS ; (c) MRSS-CRSS (Yield) ;
(d) MRSS-CRSS (MB) ; (e) MRSS-CRSS (MBTe) .

a

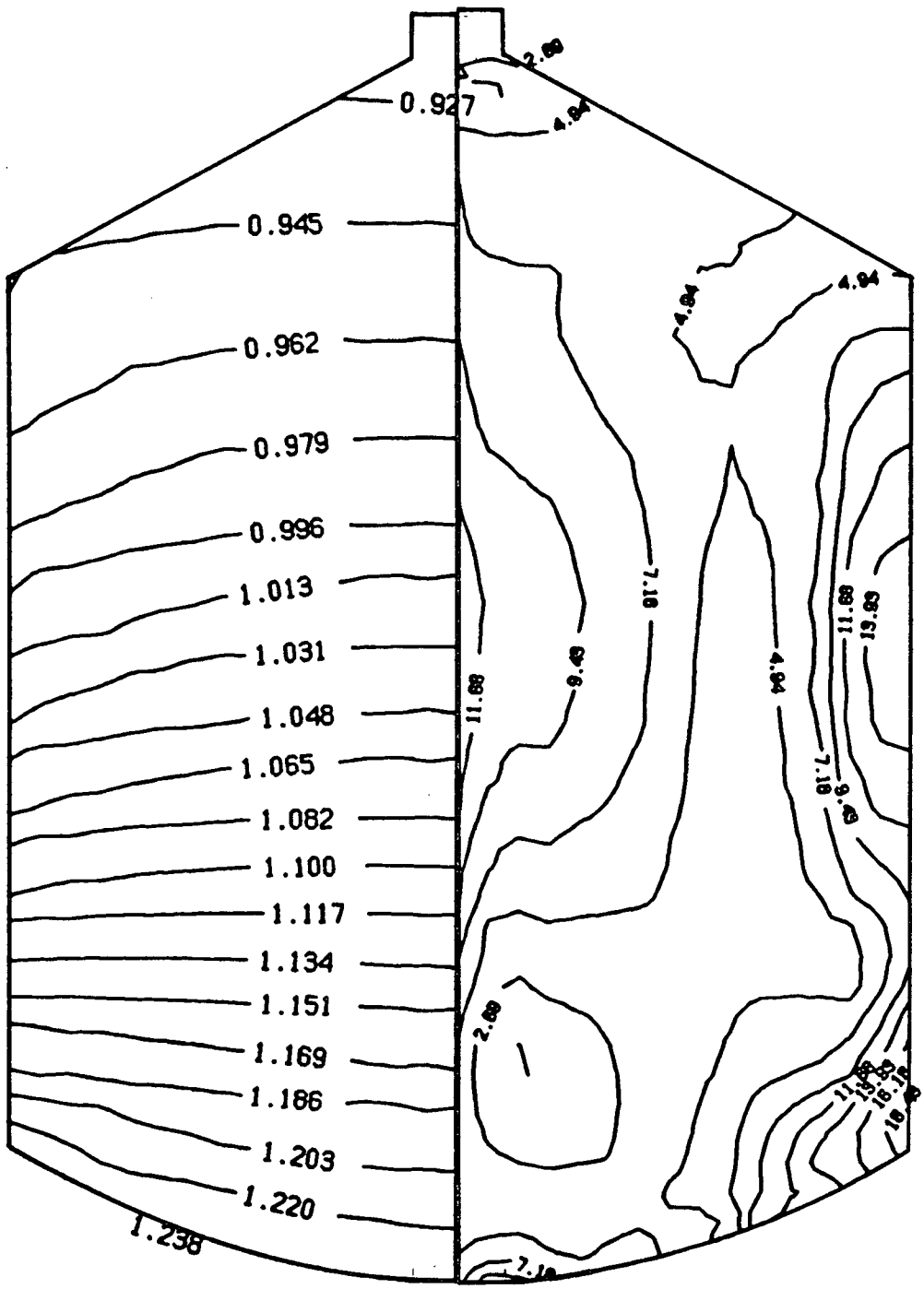
0.927
0.945
0.962
0.979
0.996
1.013
1.031
1.048
1.065
1.082
1.100
1.117
1.134
1.151
1.169
1.186
1.203
1.220
1.238
2.89
4.94
7.18
9.43
11.68
13.93
16.18

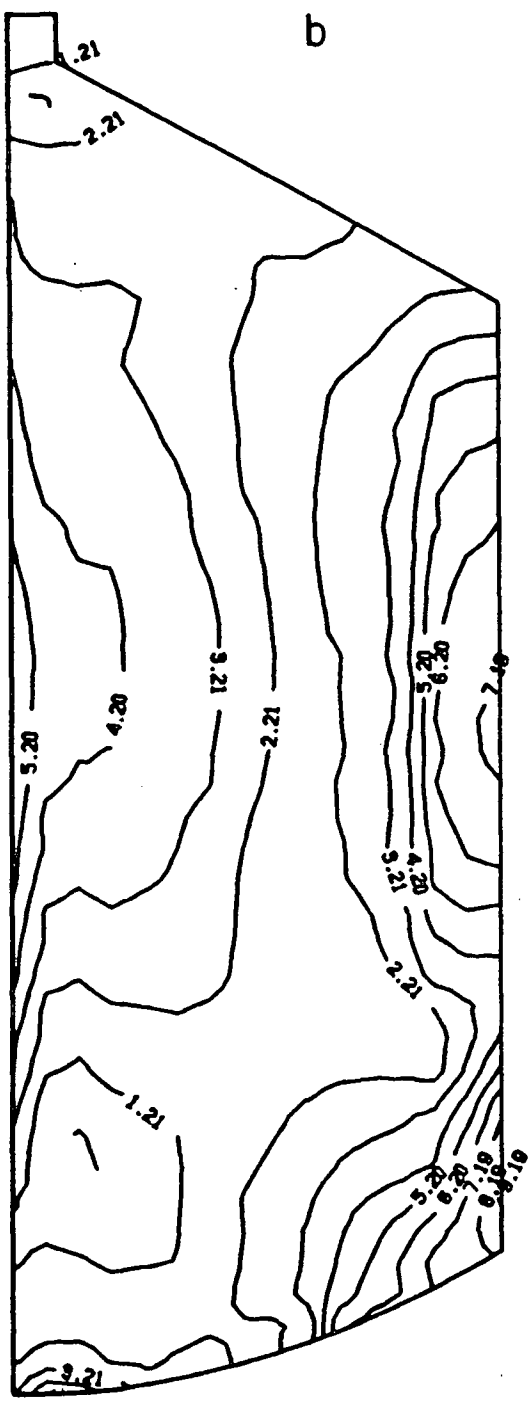
b
.21
2.21
5.20
4.20
3.21
2.21
5.20
6.20
7.19
3.21
4.20
2.21
1.21
3.21

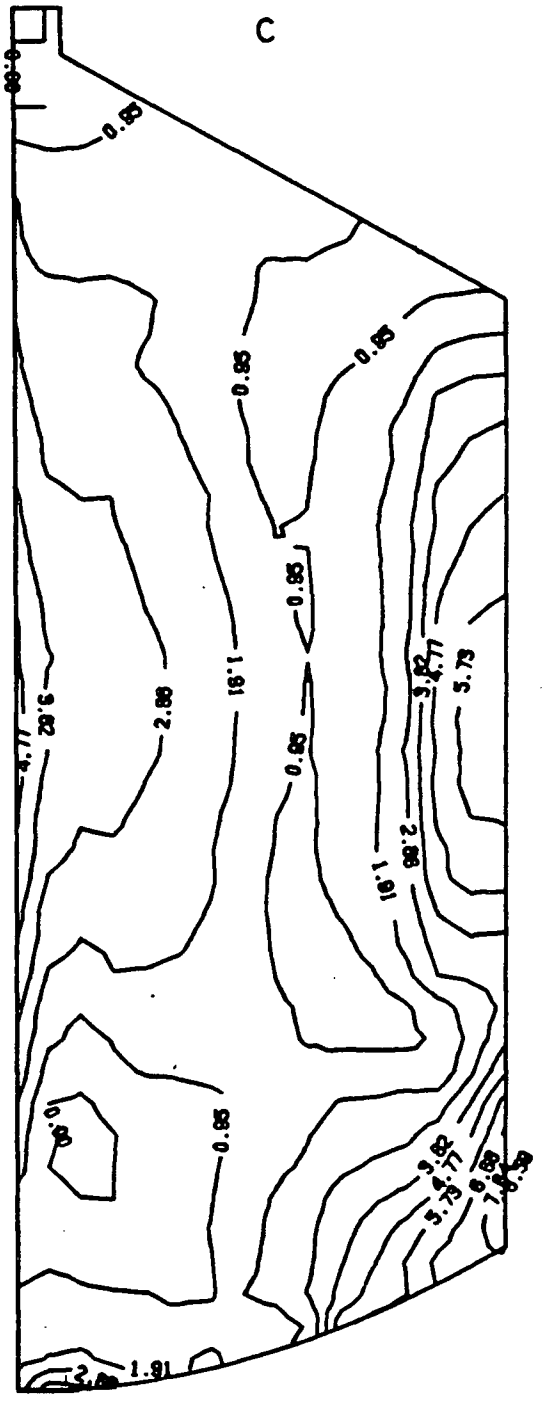
c
0.00
0.95
0.95
0.95
0.95
0.95
2.86
1.91
3.82
4.77
5.73
2.86
1.91
0.00
0.95
3.82
4.77
5.73
1.91

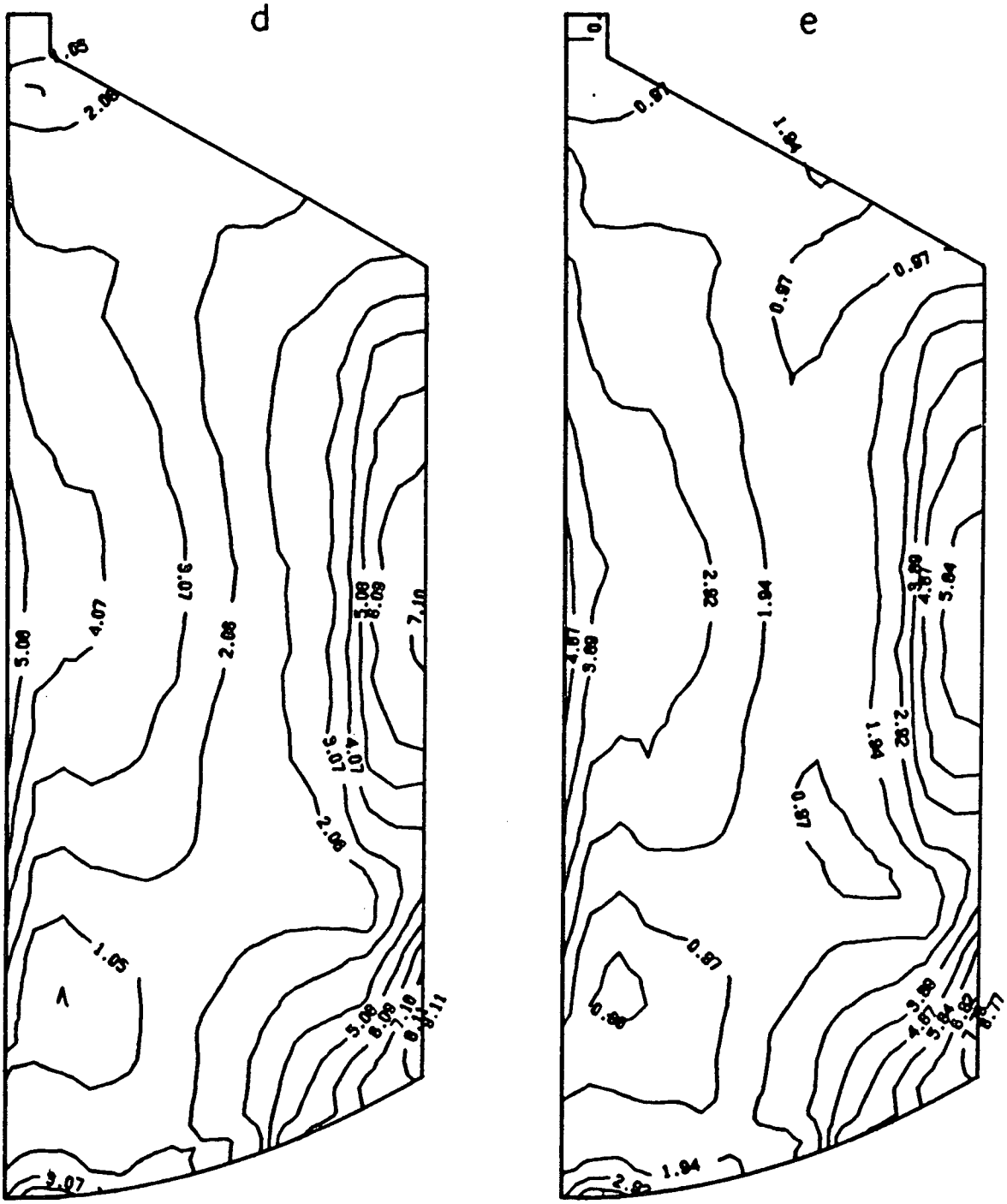

XIII.8.1.1.1.2.1 (a) Temperature and Von Mises Stress
(b) MRSS ; (c) MRSS-CRSS (Yield) ;
(d) MRSS-CRSS (MB) ; (e) MRSS-CRSS (MBTe) .

a

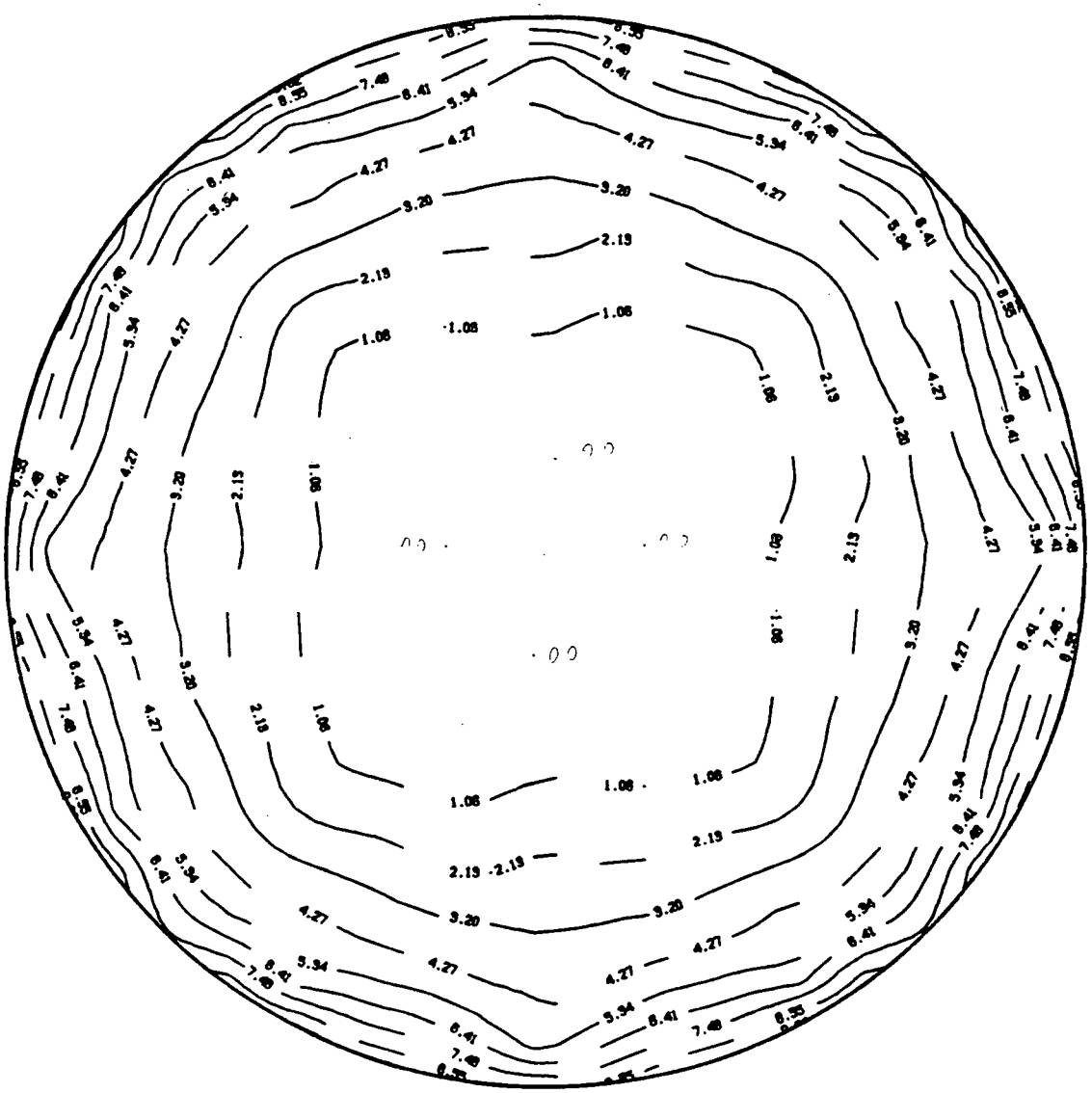

b

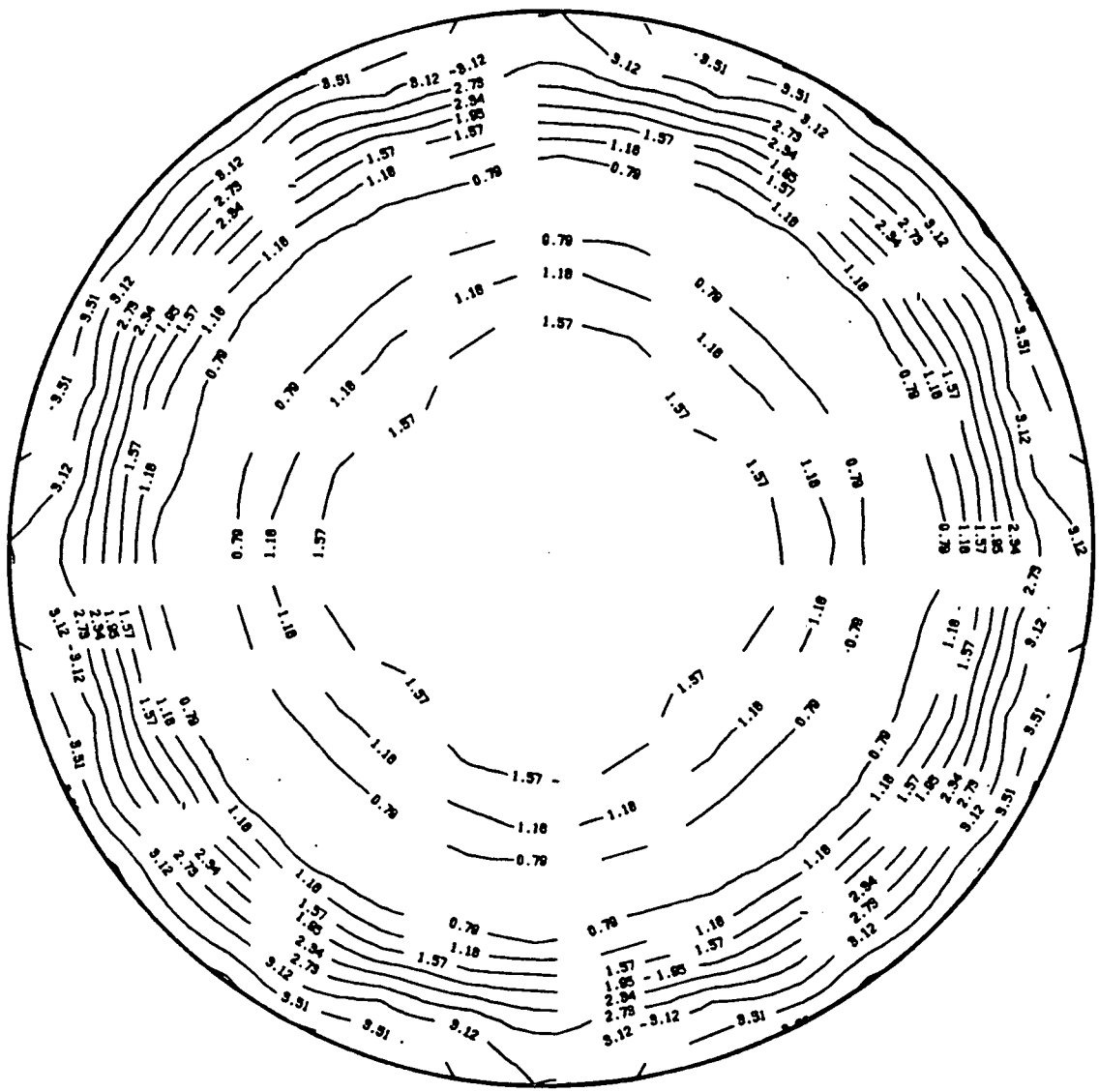

C

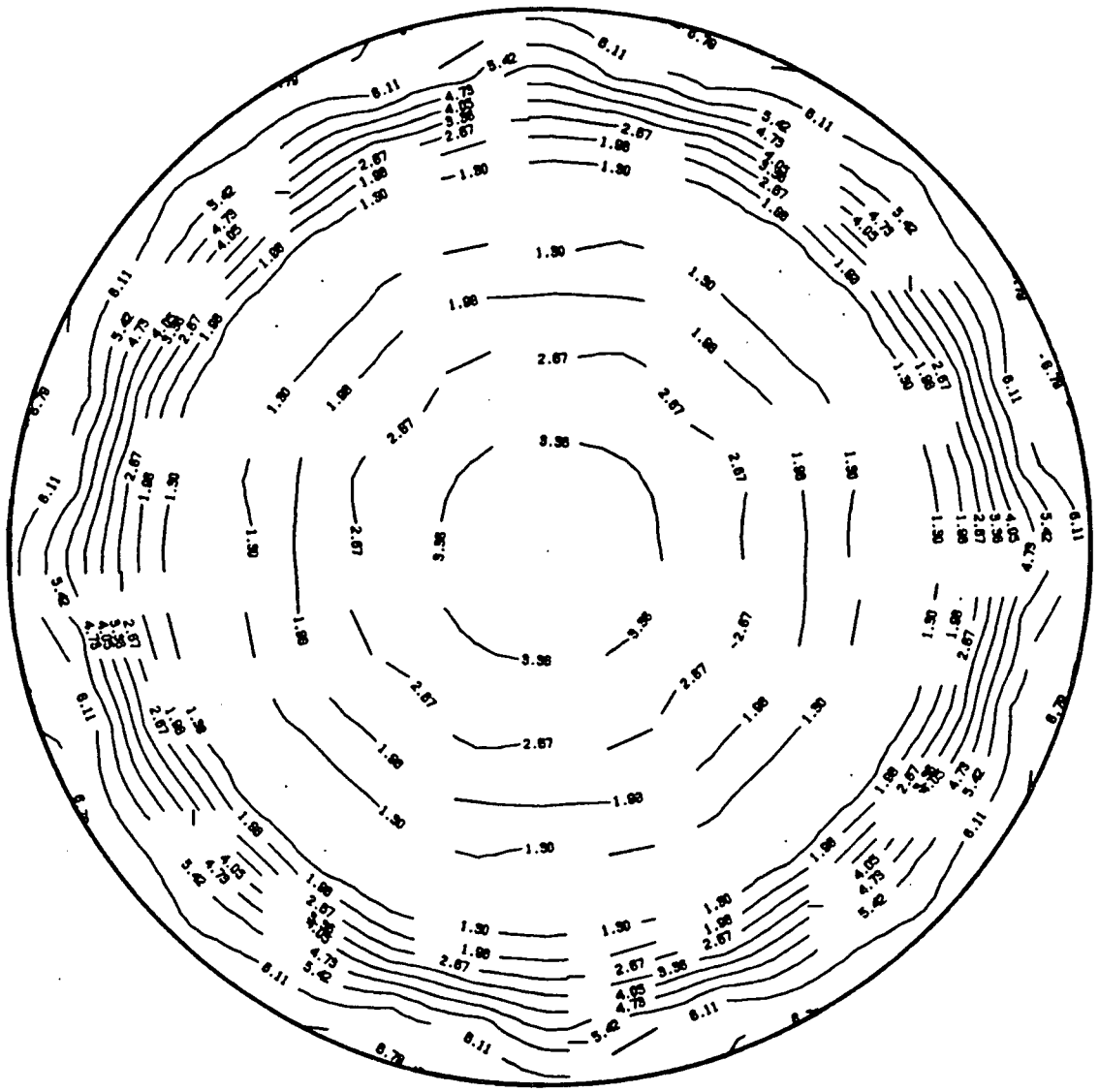

d

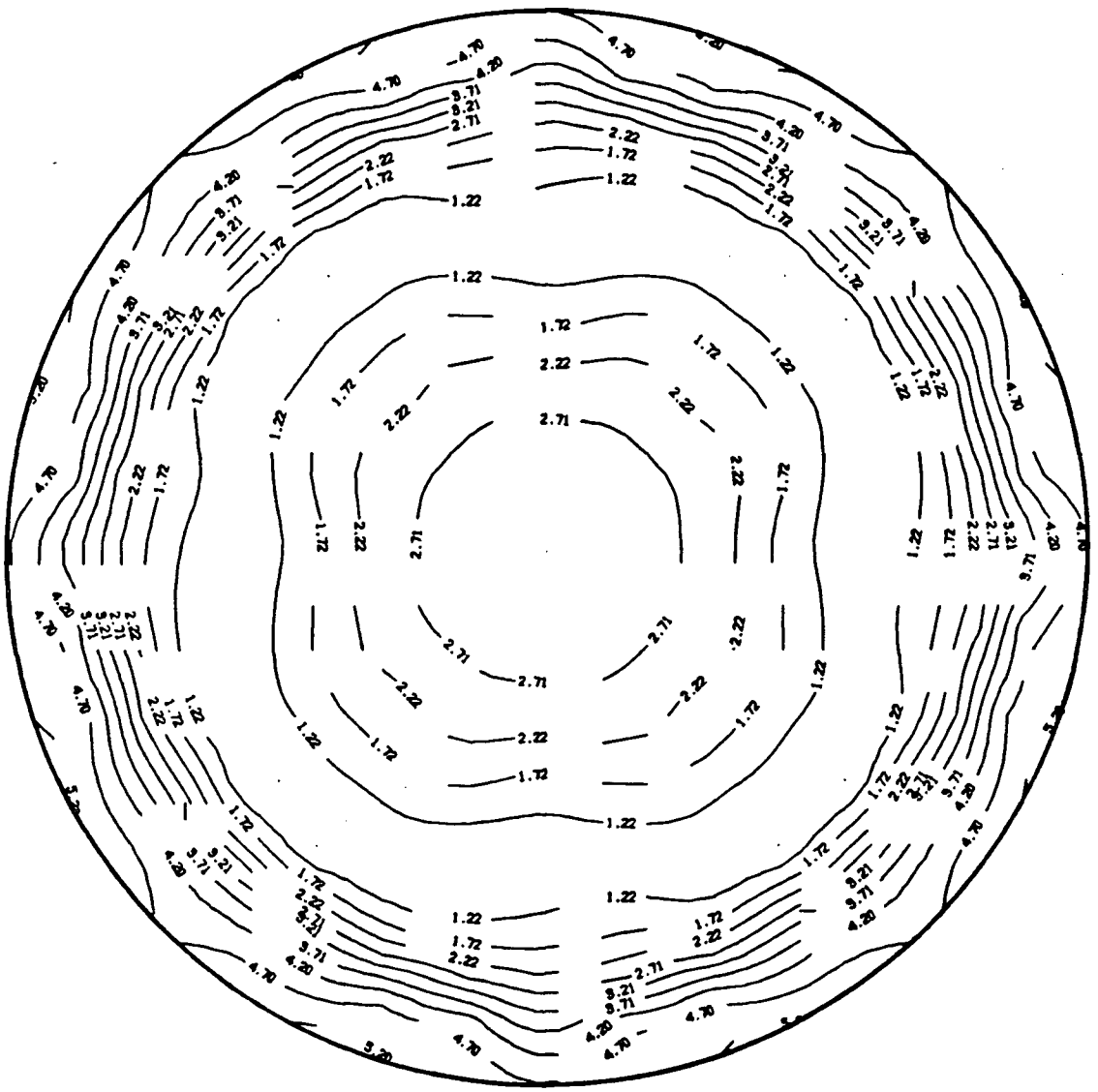

XIII.8.1.1.1.2.2 MRSS-CRSS (Yield) in cross-sections at distances from the interface of (a) 11 mm ; (b) 24.75 mm ; (c) 38.5 mm ; (d) 52.25 mm ;

a

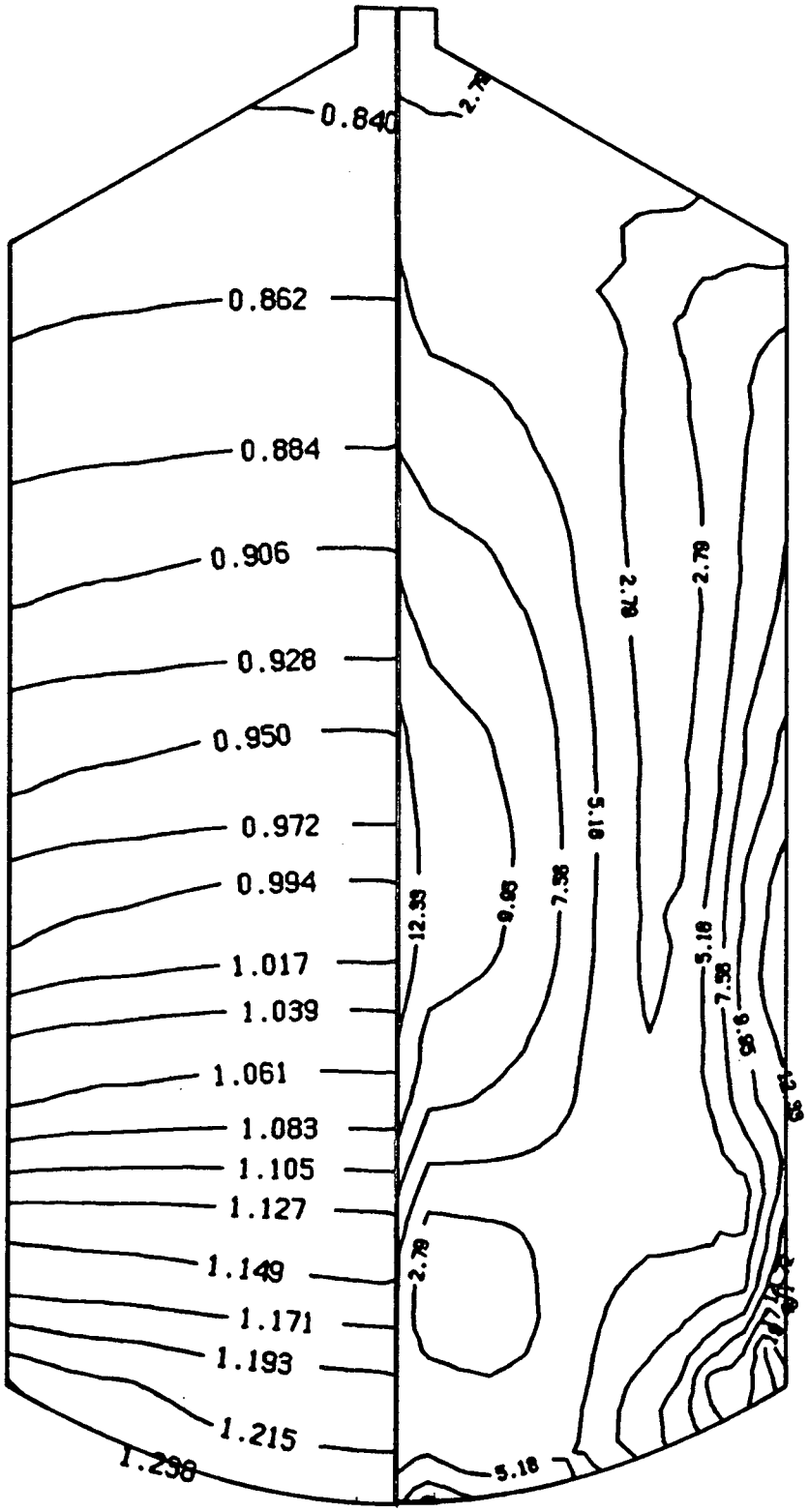
0.840
0.862
0.884
0.906
0.928
0.950
0.972
0.994
1.017
1.039
1.061
1.083
1.105
1.127
1.149
1.171
1.193
1.215
1.236
2.78
5.18
7.58
9.85
12.39

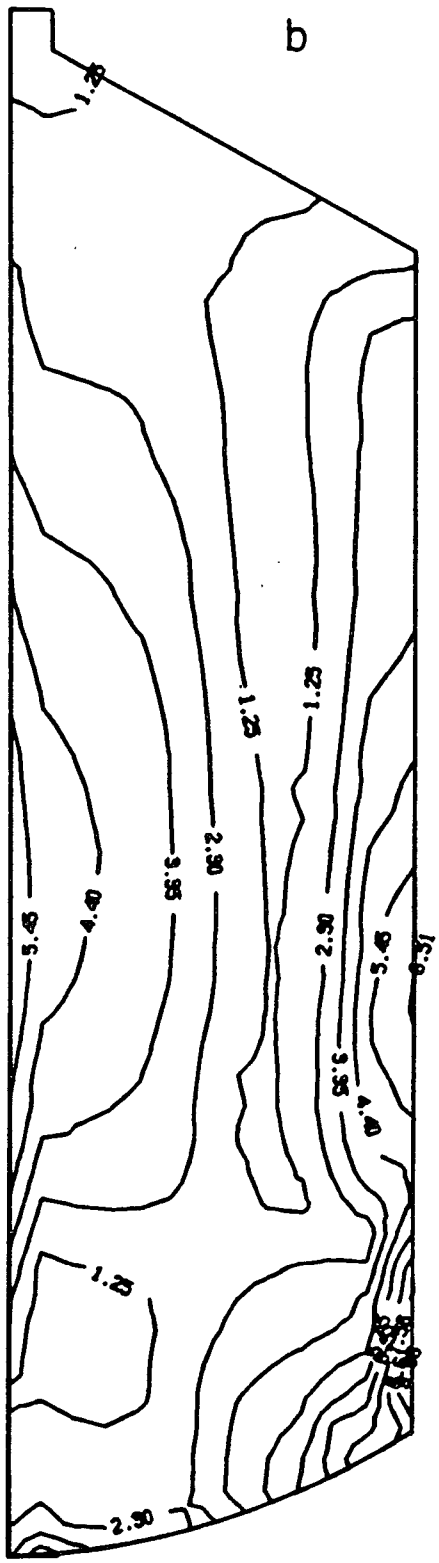
b
1.25
1.25
2.50
3.75
5.00
5.00
3.75
2.50
1.25
1.25
2.50

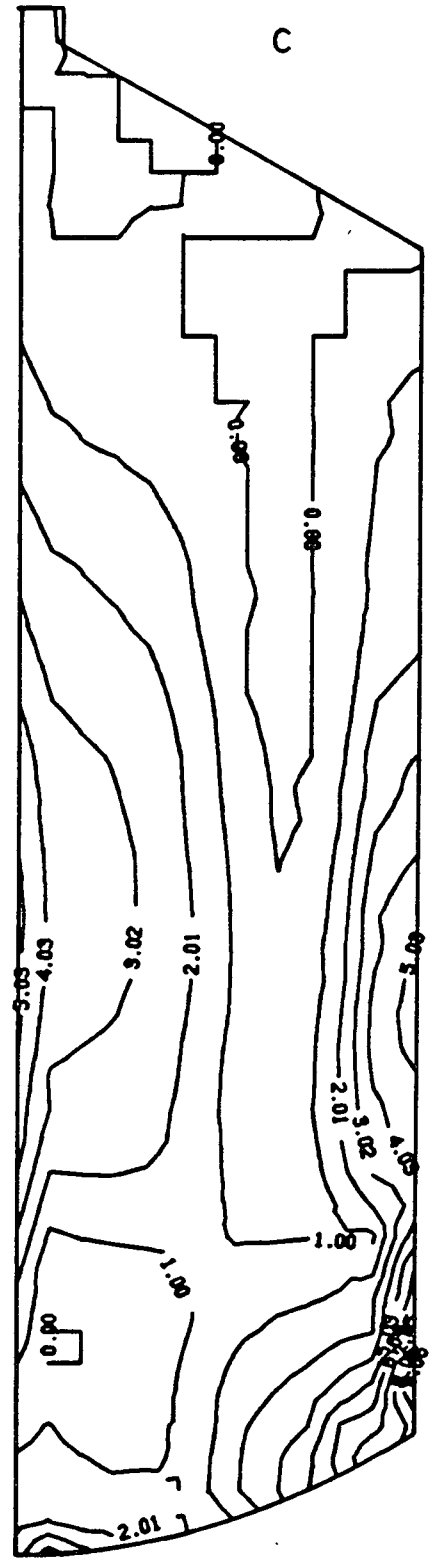
c
0.00
0.00
0.00
1.00
2.01
3.02
4.03
5.03
5.03
4.03
3.02
2.01
1.00
1.00
0.00
2.01

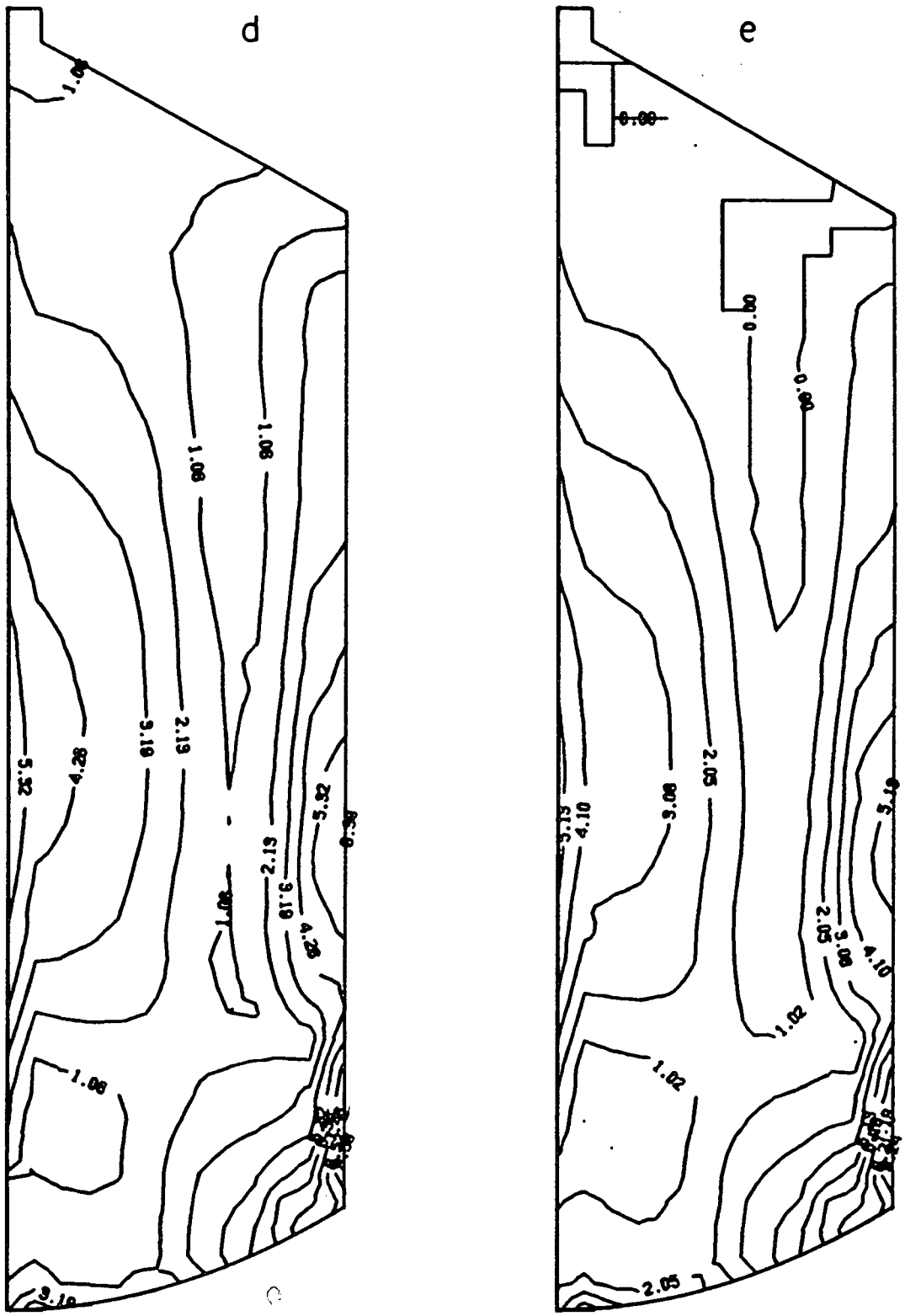

XIII.8.1.1.1.3.1 (a) Temperature and Von Mises Stress
(b) MRSS ; (c) MRSS-CRSS (Yield) ;
(d) MRSS-CRSS (MB) ; (e) MRSS-CRSS (MBTe) .

a

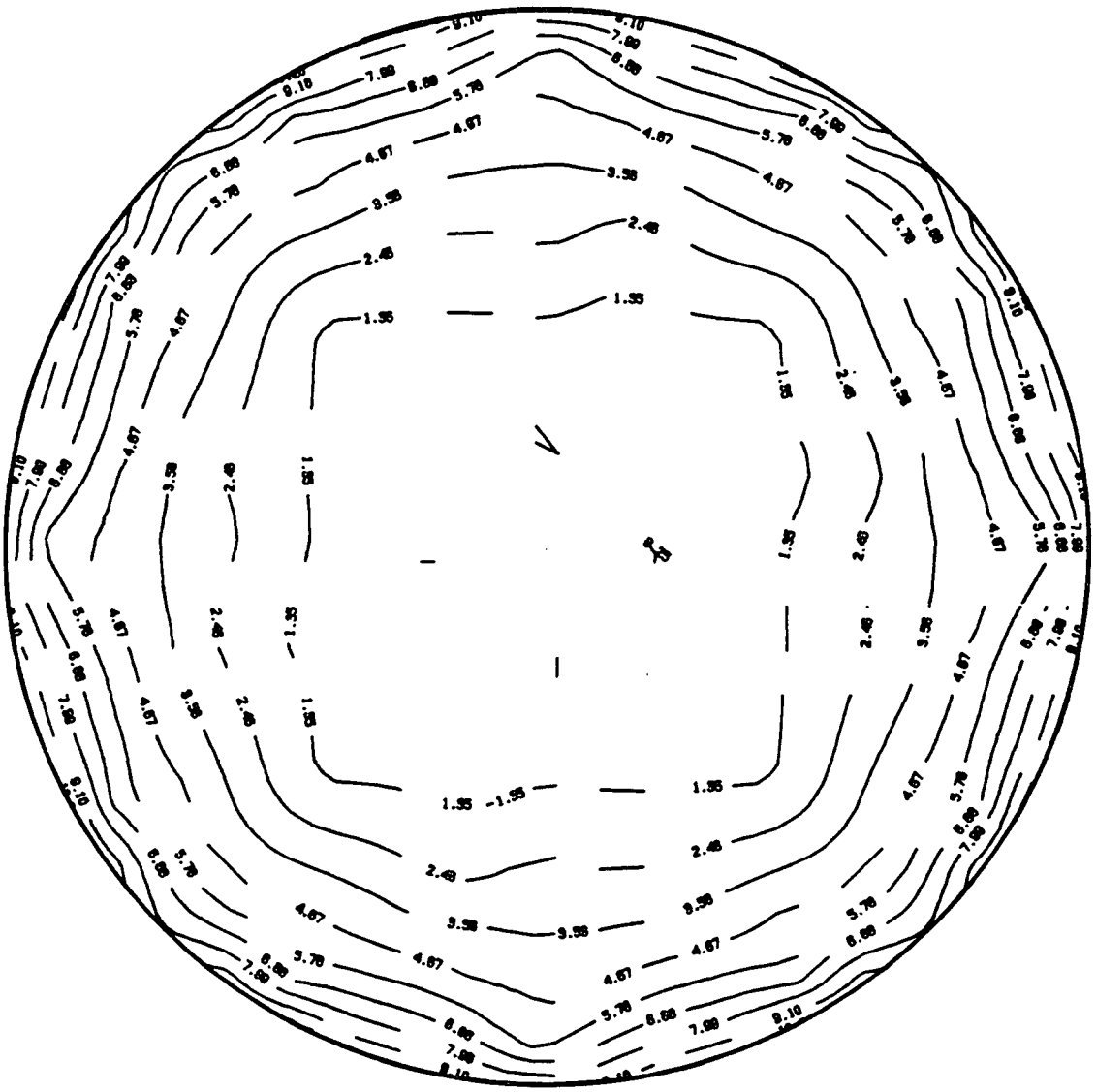

b

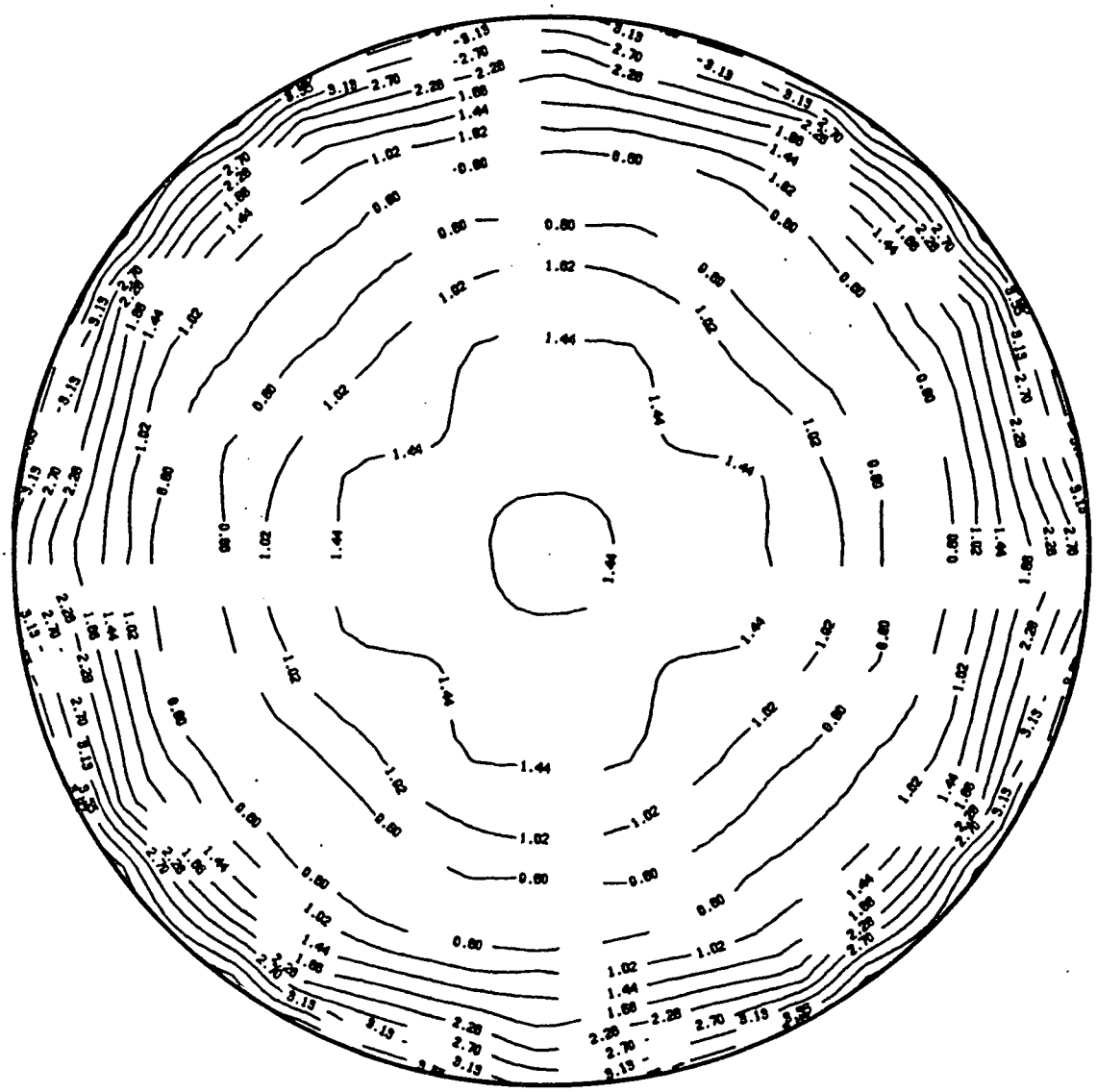

C

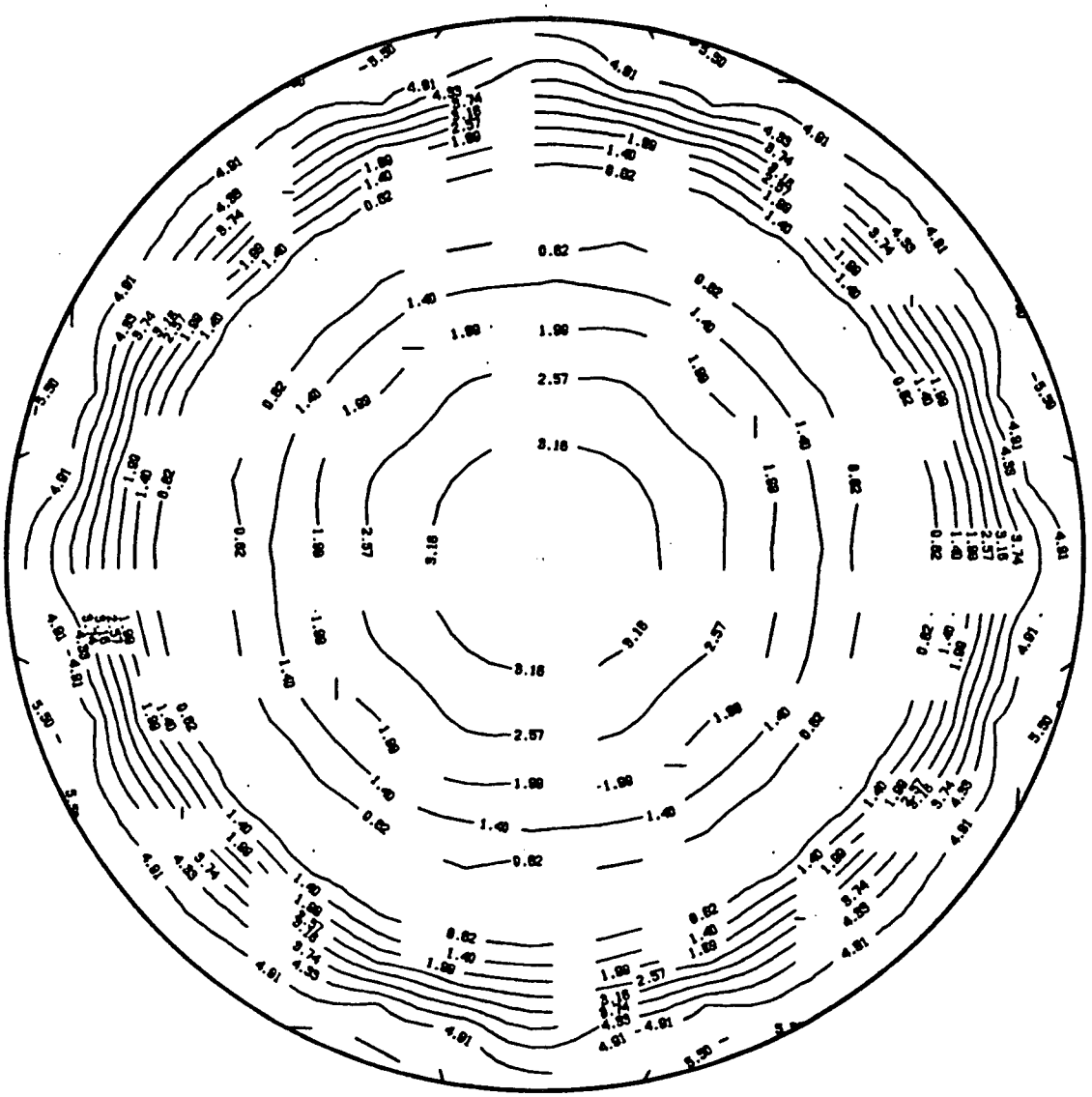

d

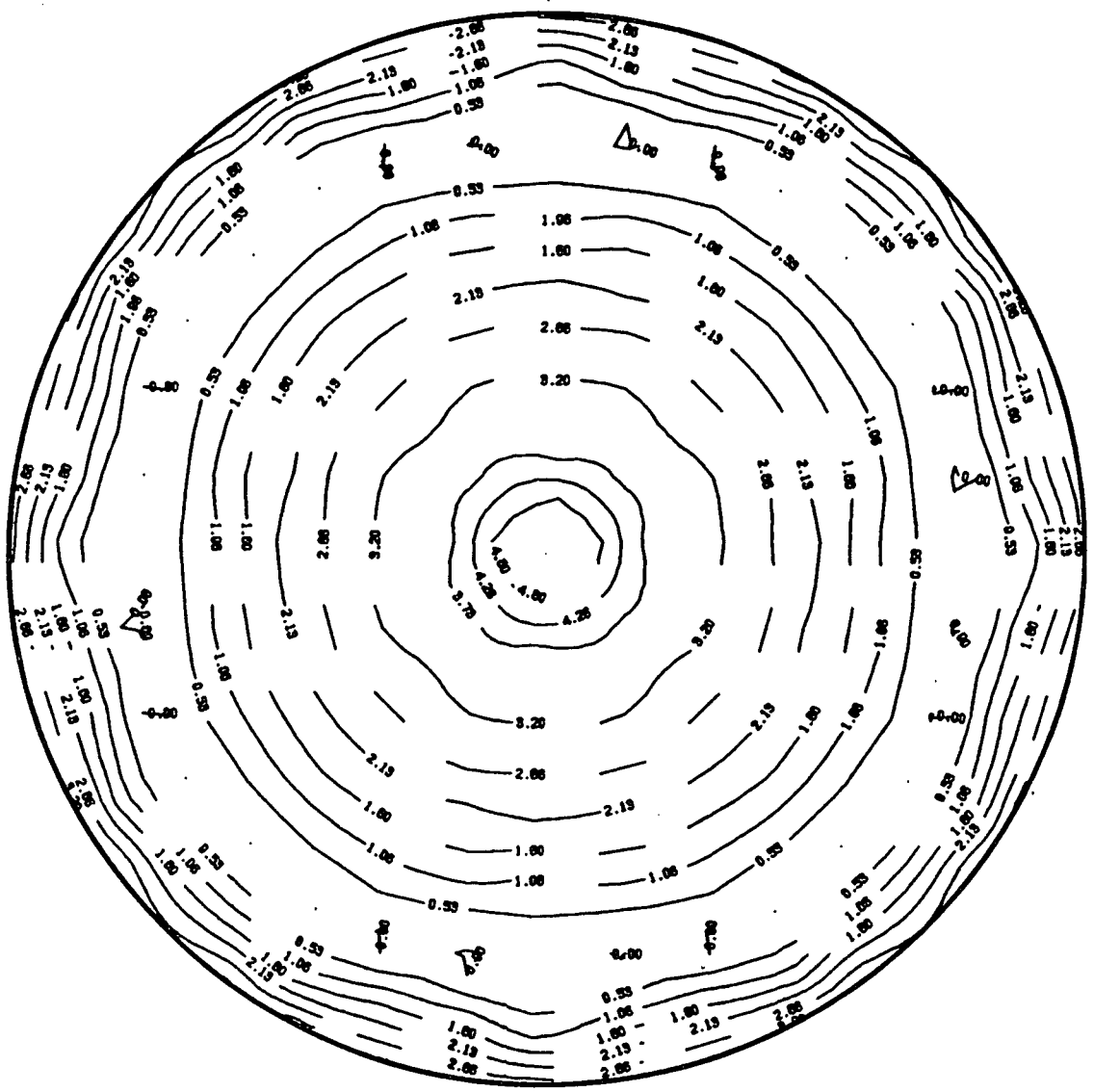

e

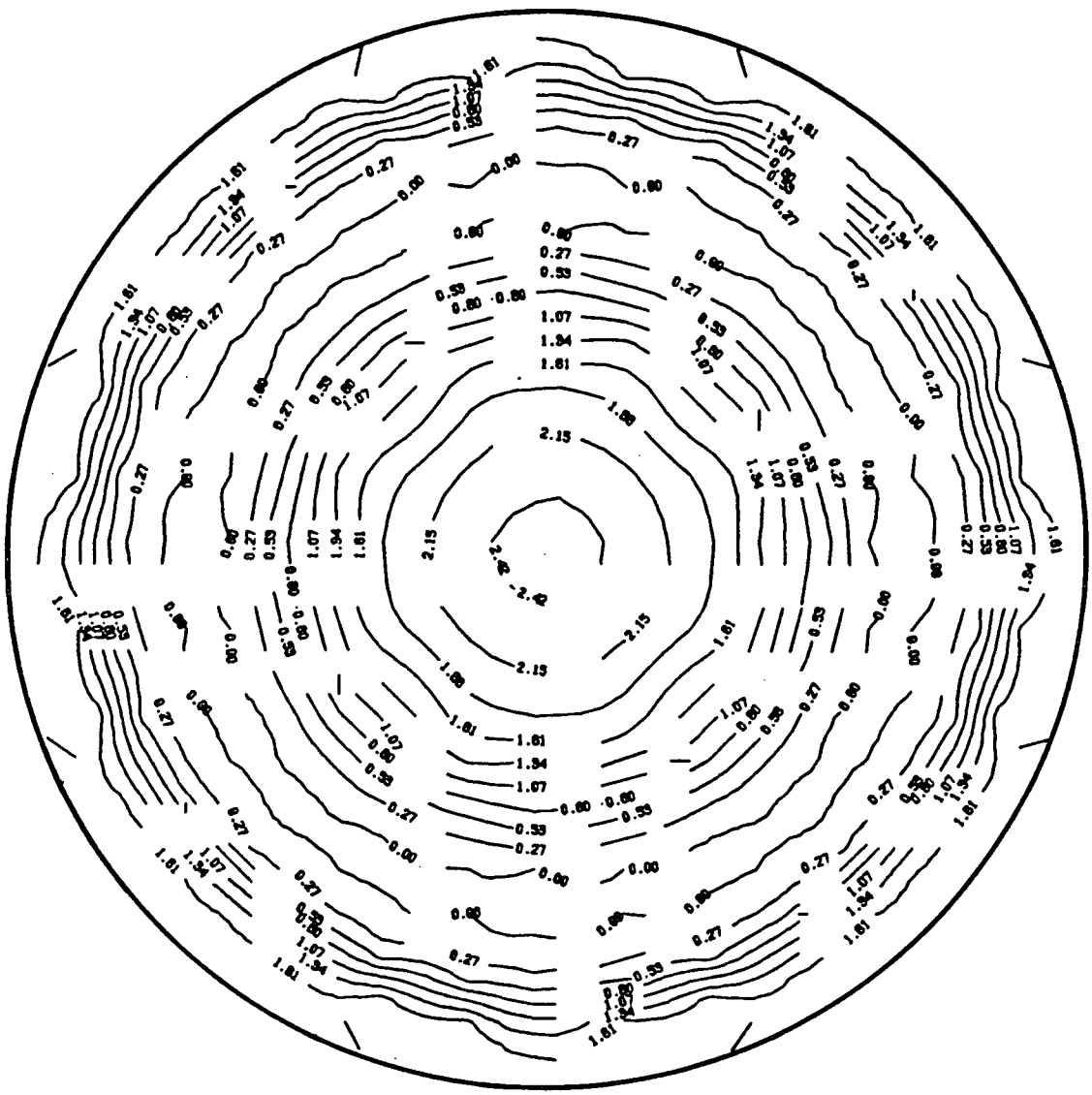

XIII.8.1.1.1.3.2 MRSS-CRSS (Yield) in cross-sections at (along the axis) distances from the interface of (a) 11 mm ; (b) 24.75 mm ; (c) 38.5 mm ; (d) 52.5 mm ; (e) 66 mm .

a

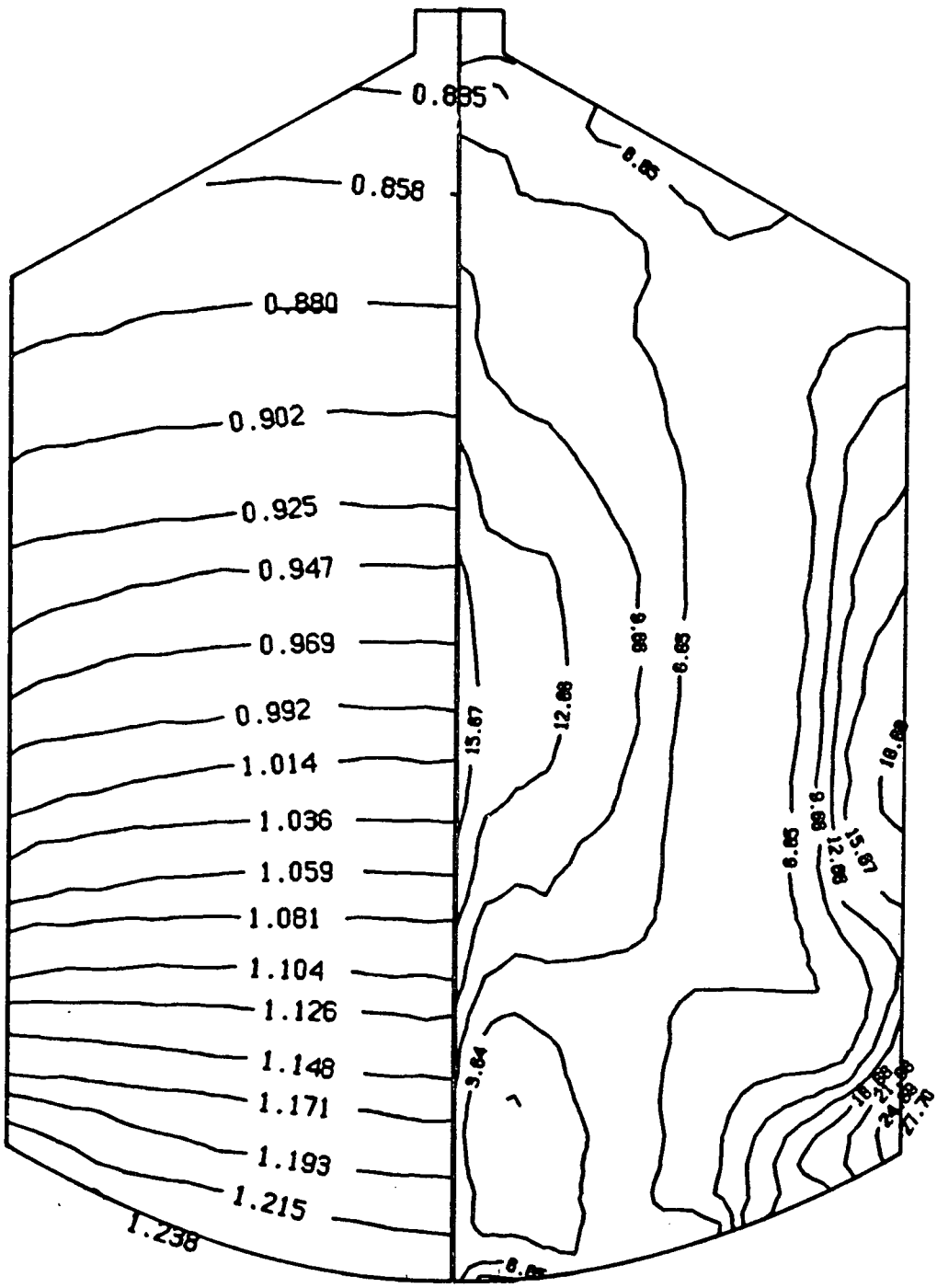
0.835
0.858
0.880
0.902
0.925
0.947
0.969
0.992
1.014
1.036
1.059
1.081
1.104
1.126
1.148
1.171
1.193
1.215
1.238
8.85
6.85
9.68
12.68
15.67
18.68
3.64
21.68
24.68
27.70

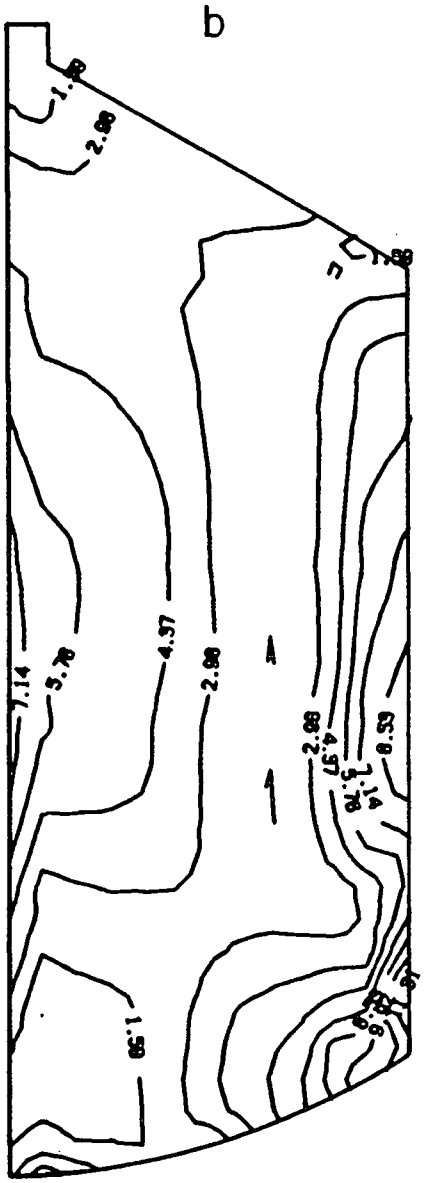
b
7.14
5.78
4.37
2.98
1.59

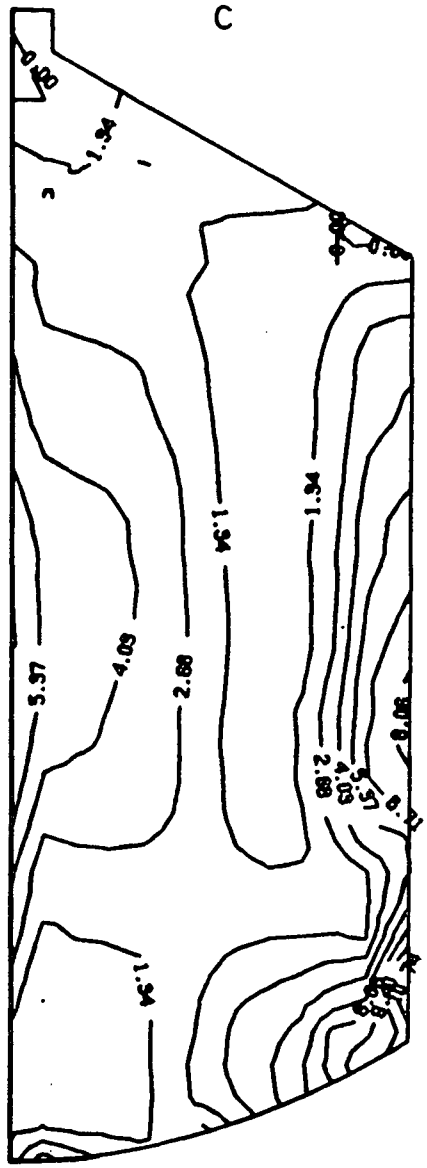
c
1.34
5.37
4.03
2.68

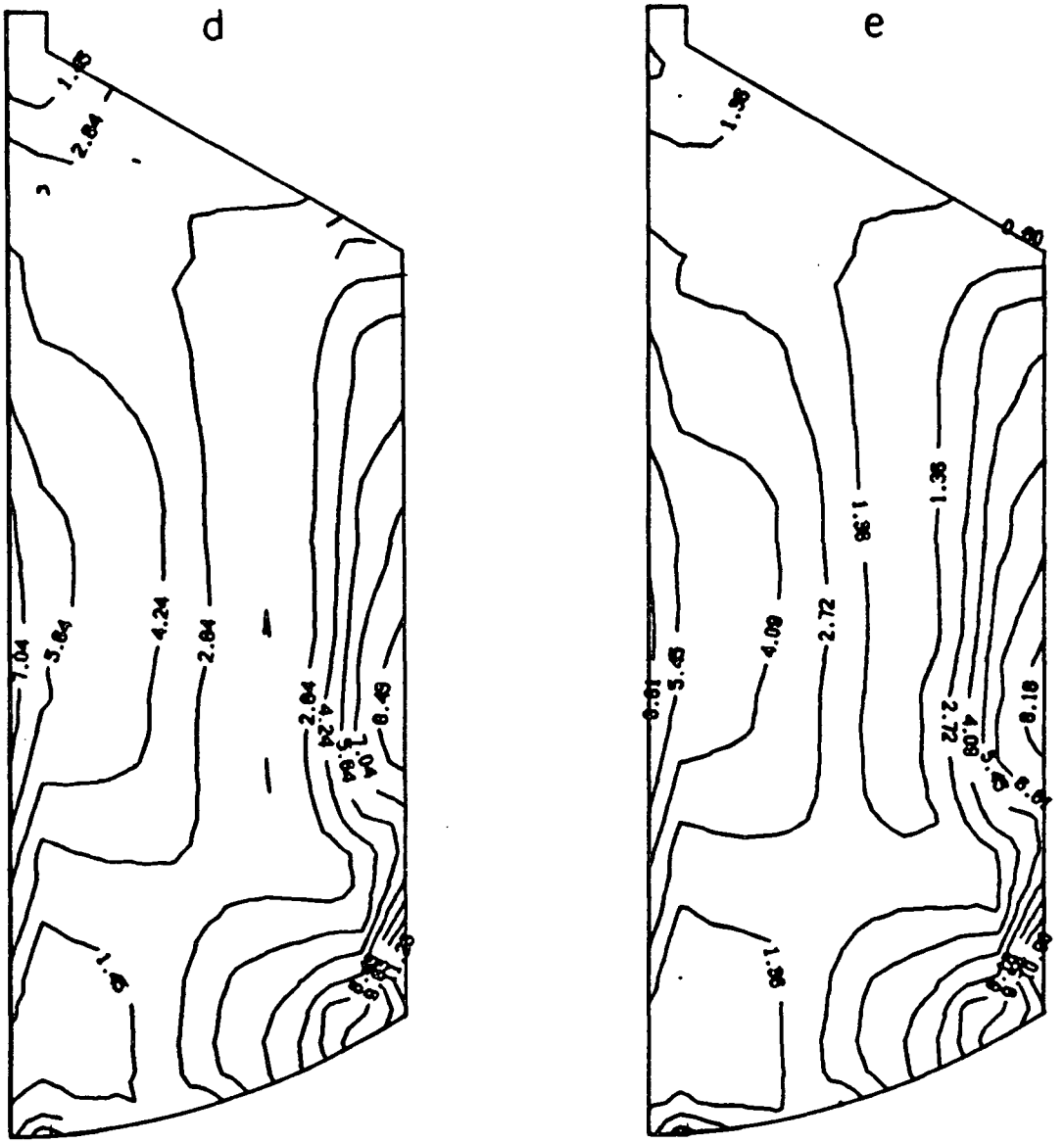

XIII.8.1.1.2.1 (a) Temperature and Von Mises Stress
(b) MRSS ; (c) MRSS-CRSS (Yield) ;
(d) MRSS-CRSS (MB) ; (e) MRSS-CRSS (MBTe) .

a

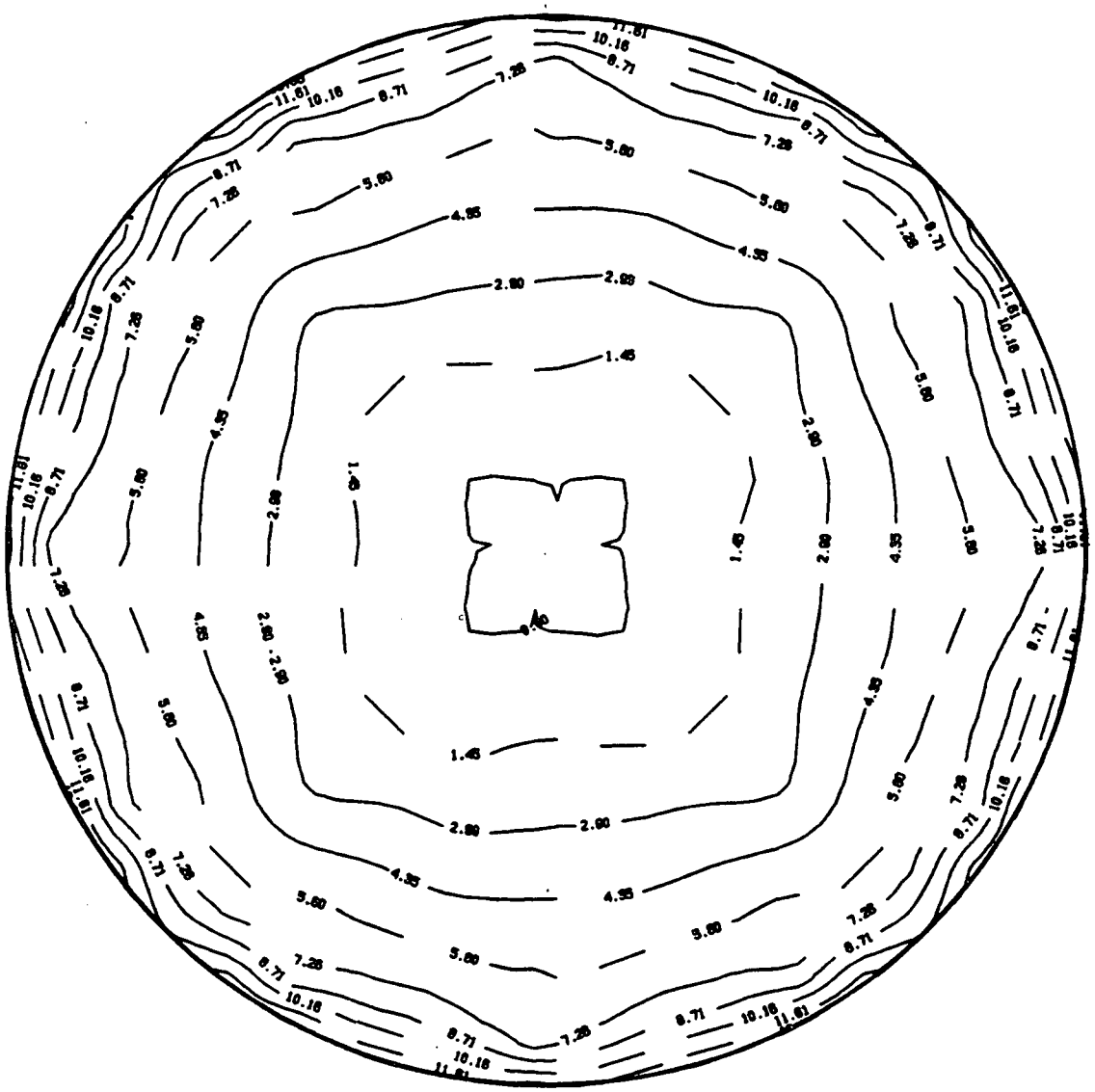

b

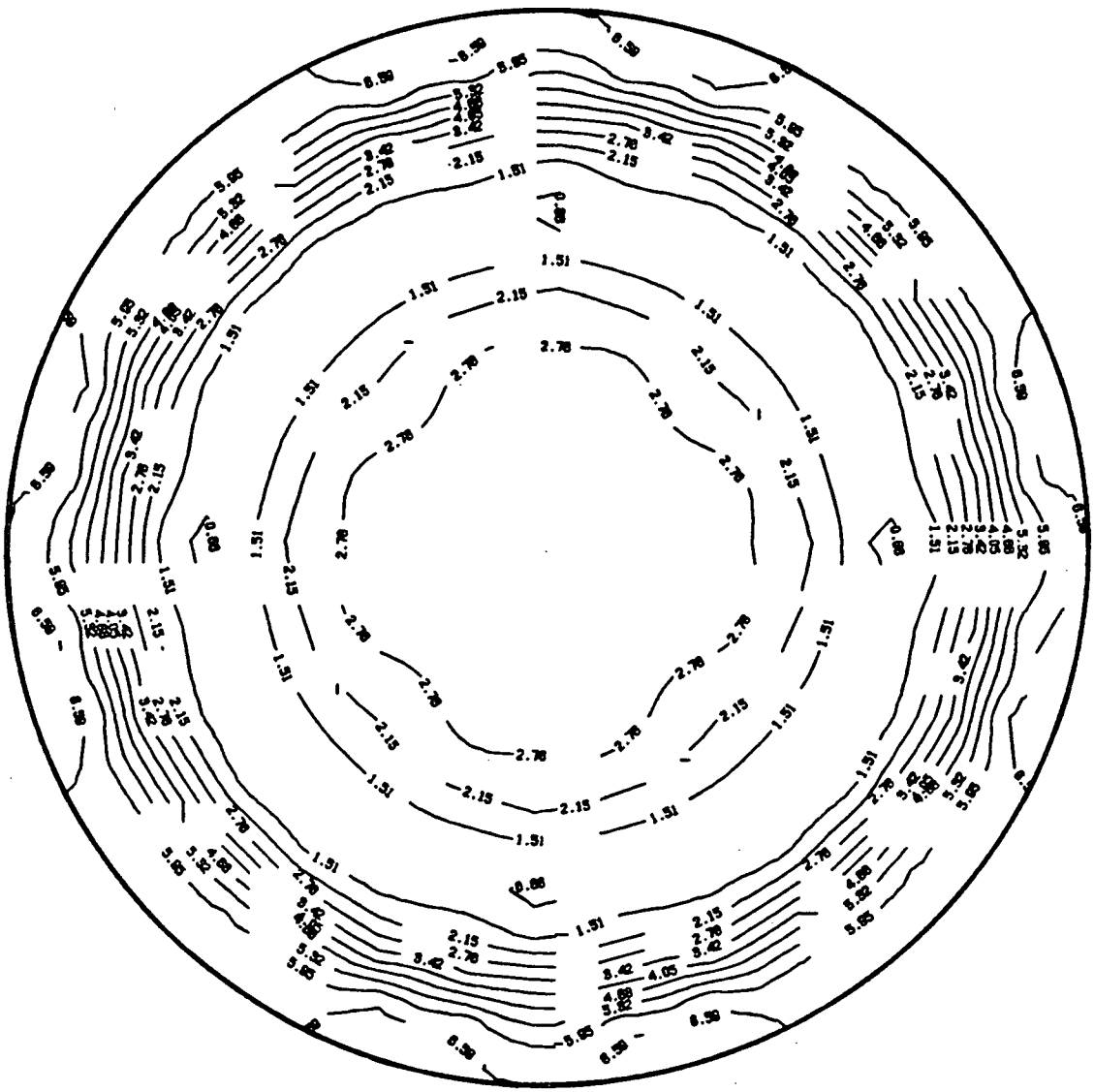

C

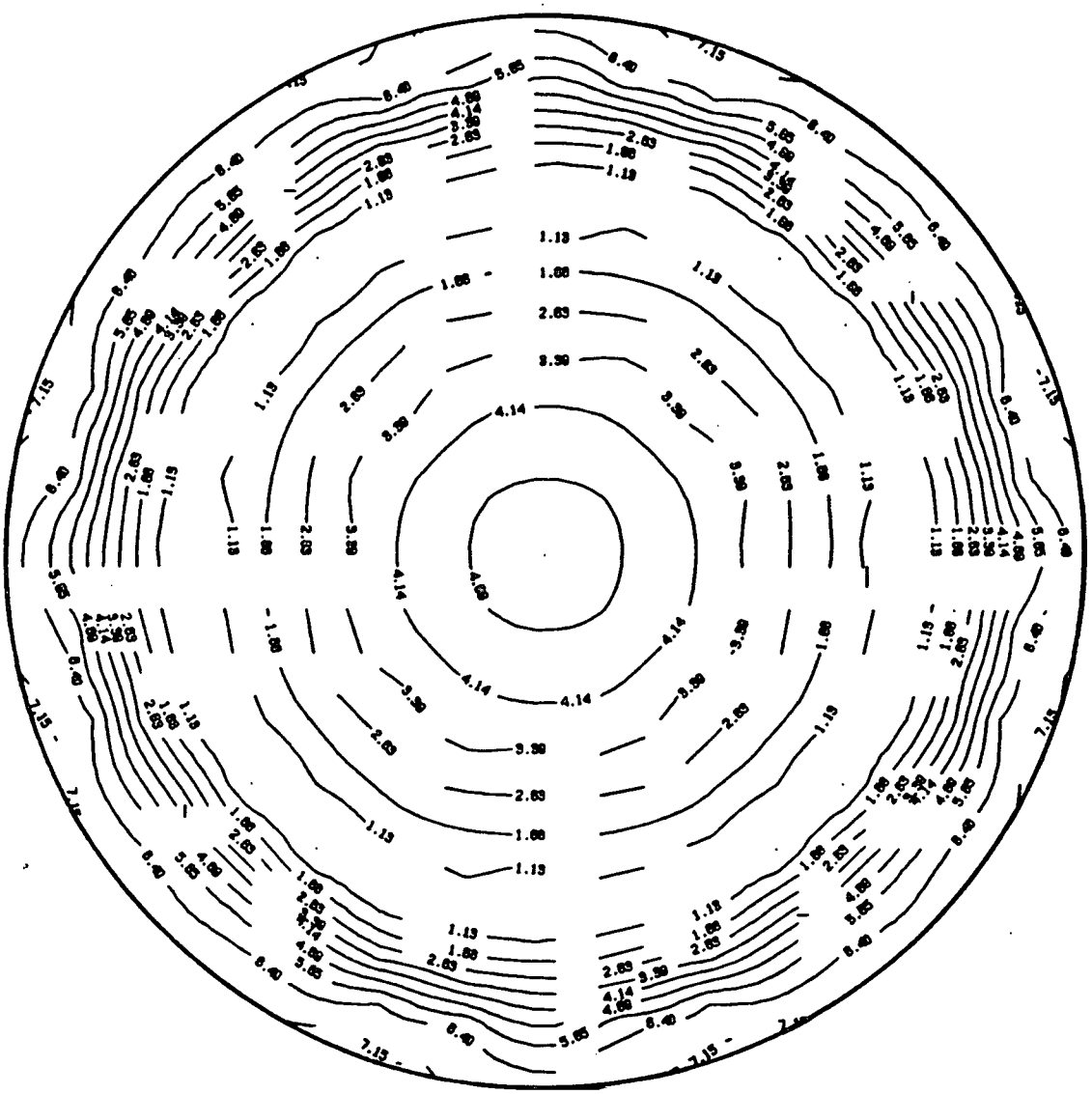

d

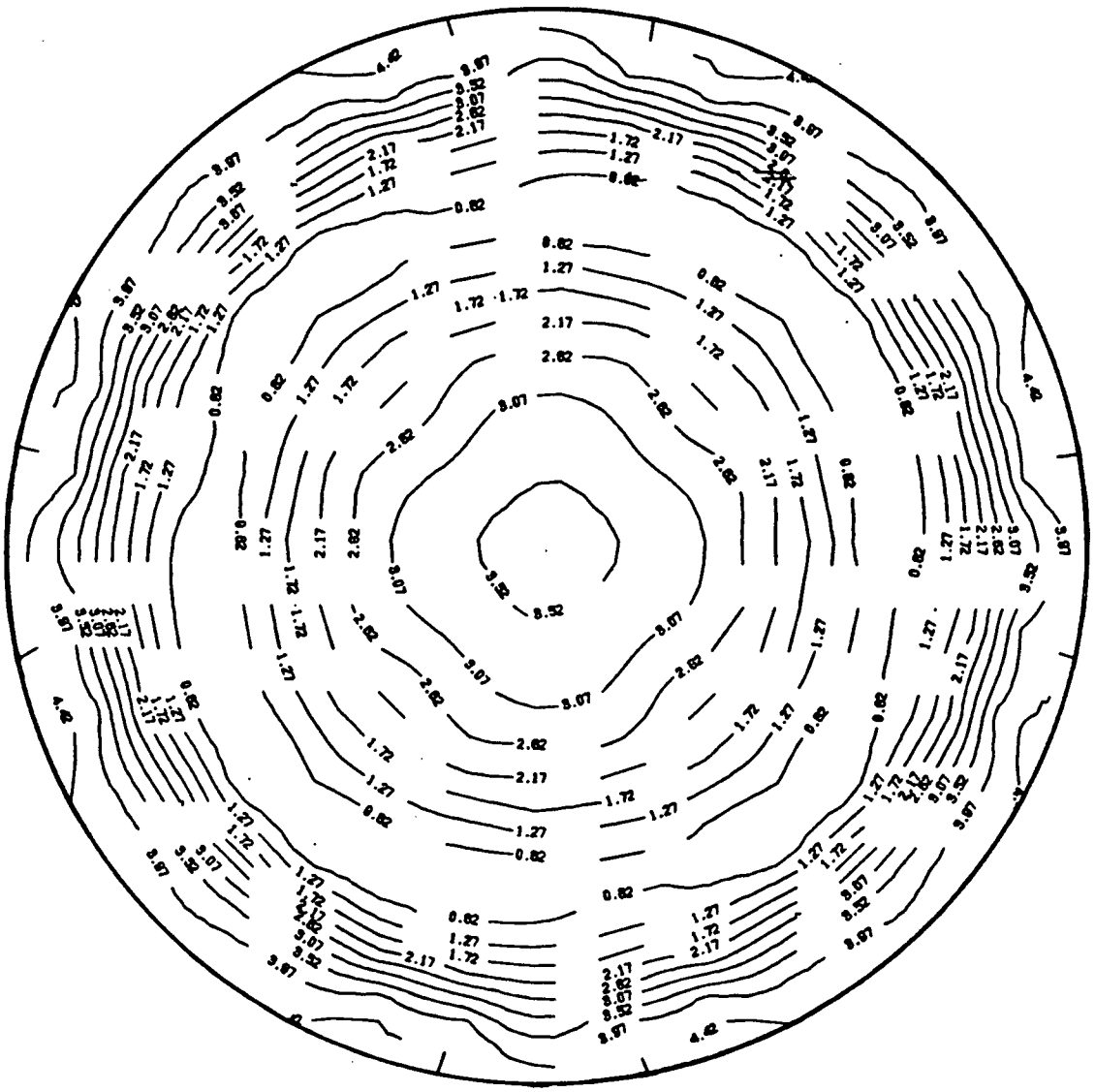

XIII.8.1.1.2.2 MRSS-CRSS (Yield) in cross-sections at distances (along the axis) from the interface of (a) 16 mm ; (b) 36 mm ; (c) 56 mm .

a

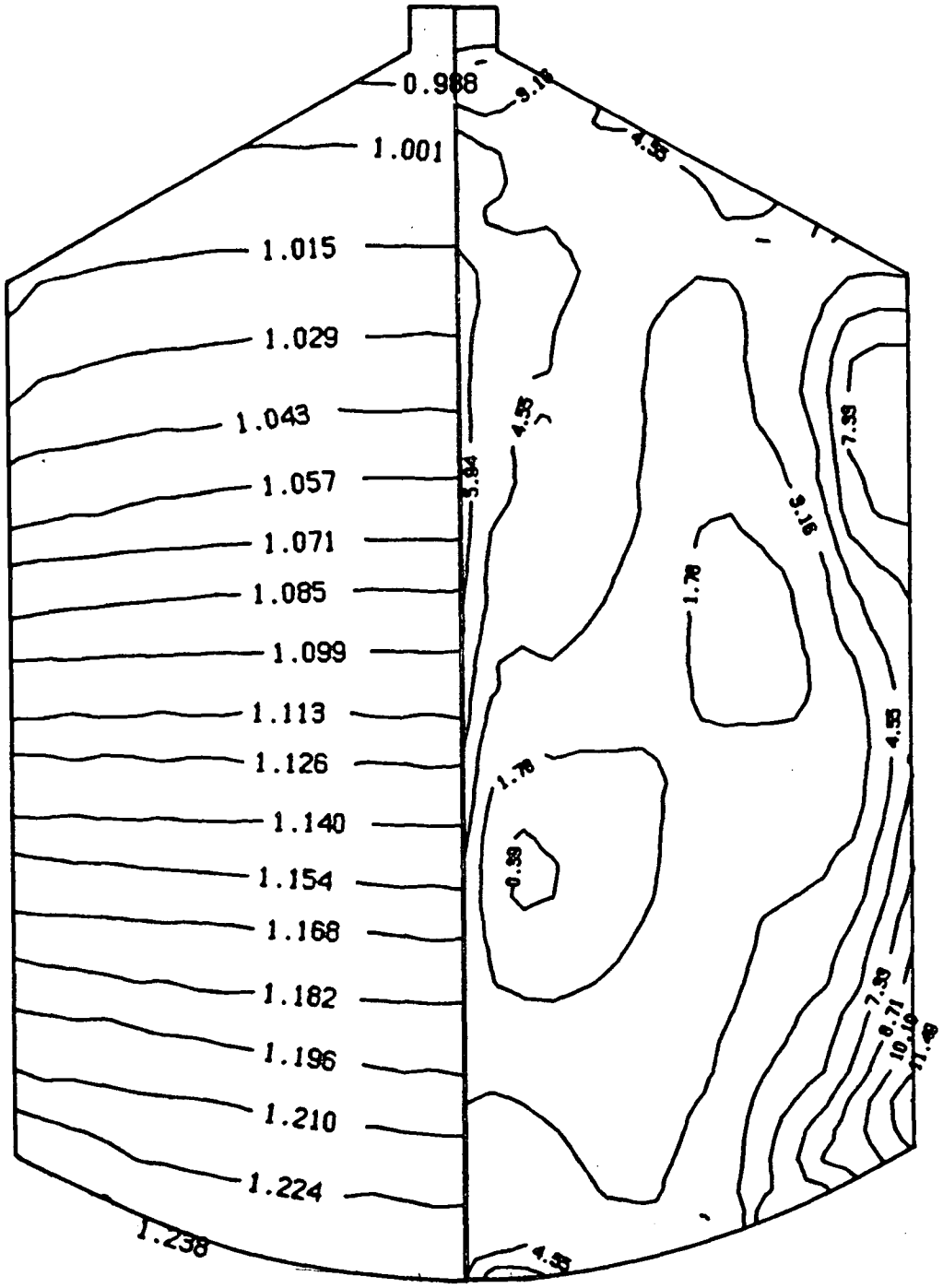
0.988
1.001
1.015
1.029
1.043
1.057
1.071
1.085
1.099
1.113
1.126
1.140
1.154
1.168
1.182
1.196
1.210
1.224
1.238
4.55
5.94
3.16
1.78
7.33
0.99
6.71
10.10
11.49

b
c
1.91
2.50
1.32
0.73
0.14
3.10
3.69
4.28
4.87
5.48
1.08
0.54
0.00
1.82
2.16
2.71
3.25
3.79
4.33
4.88

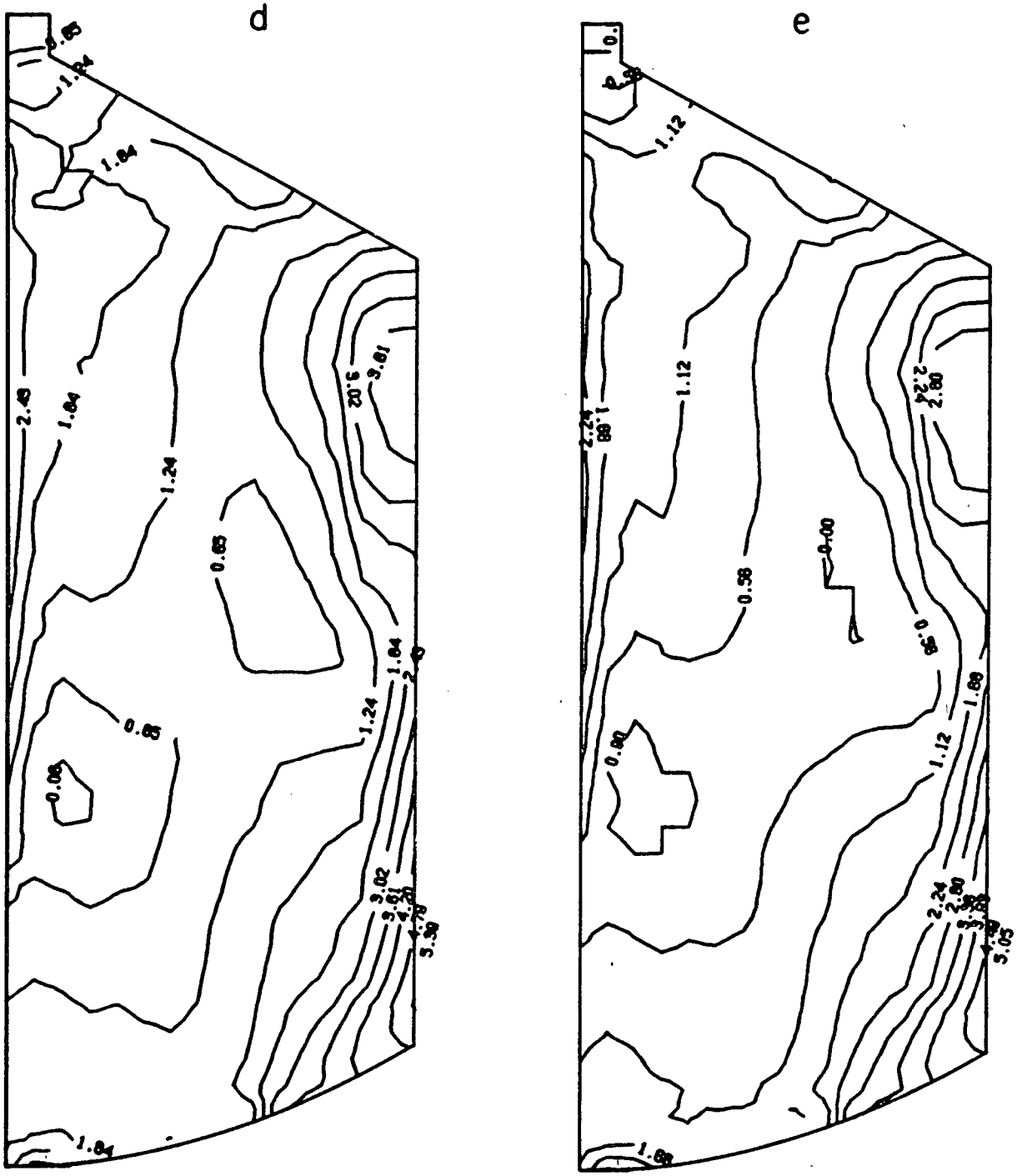

XIII.8.1.2.1.1 (a) Temperature and Von Mises Stress
(b) MRSS ; (c) MRSS-CRSS (Yield) ;
(d) MRSS-CRSS (MB) ; (e) MRSS-CRSS (MBTe) .

a

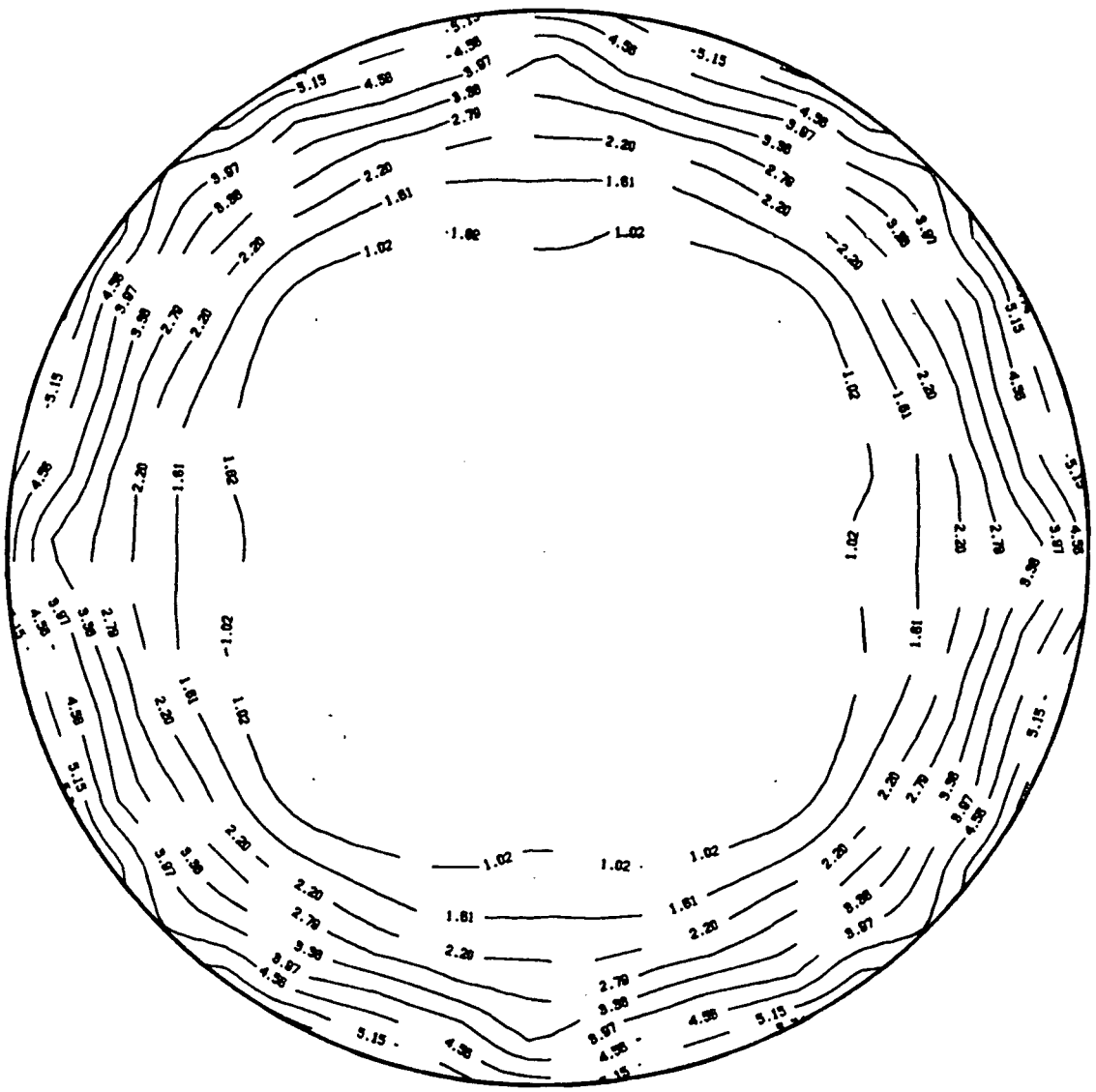

b

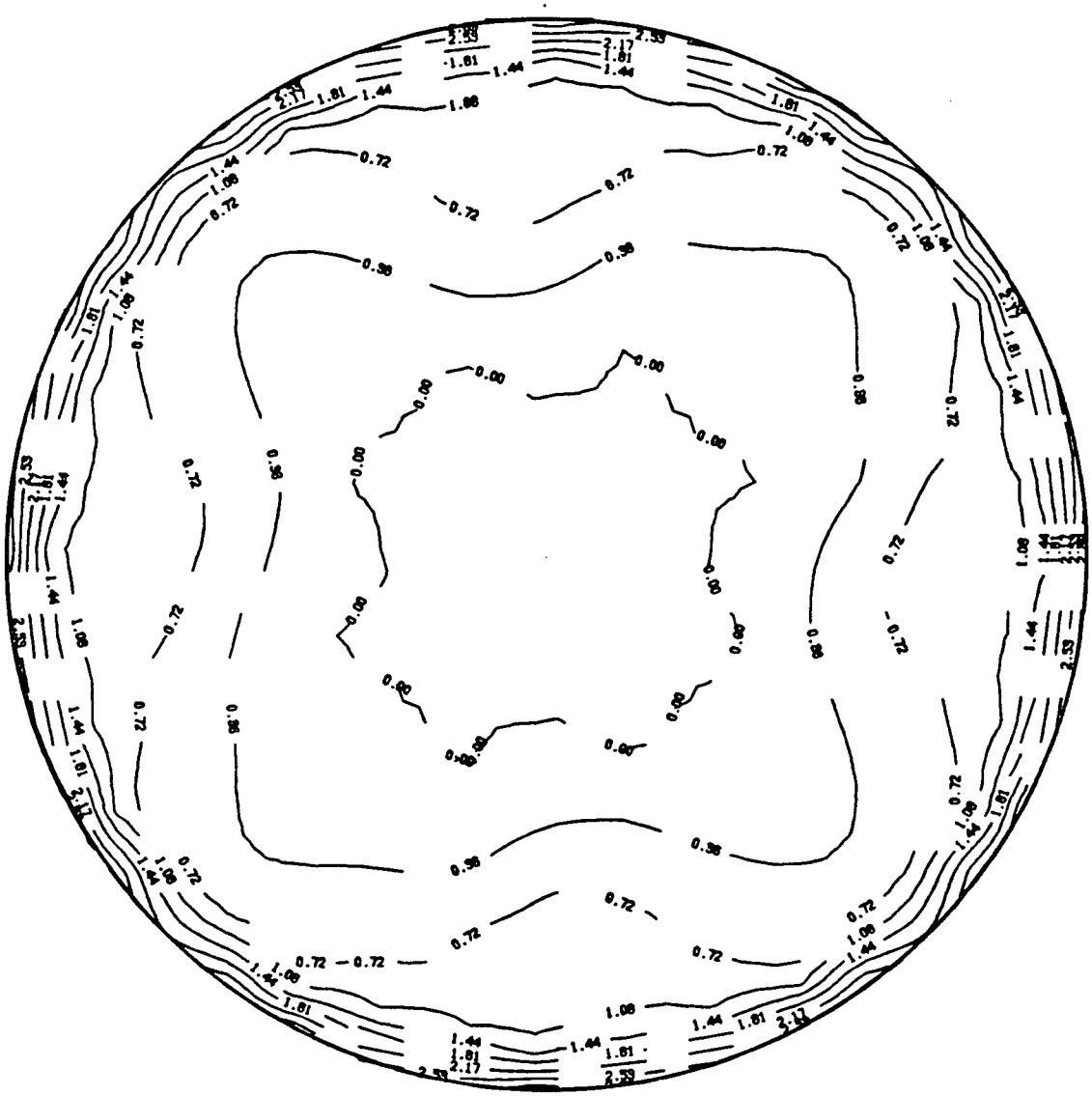

C

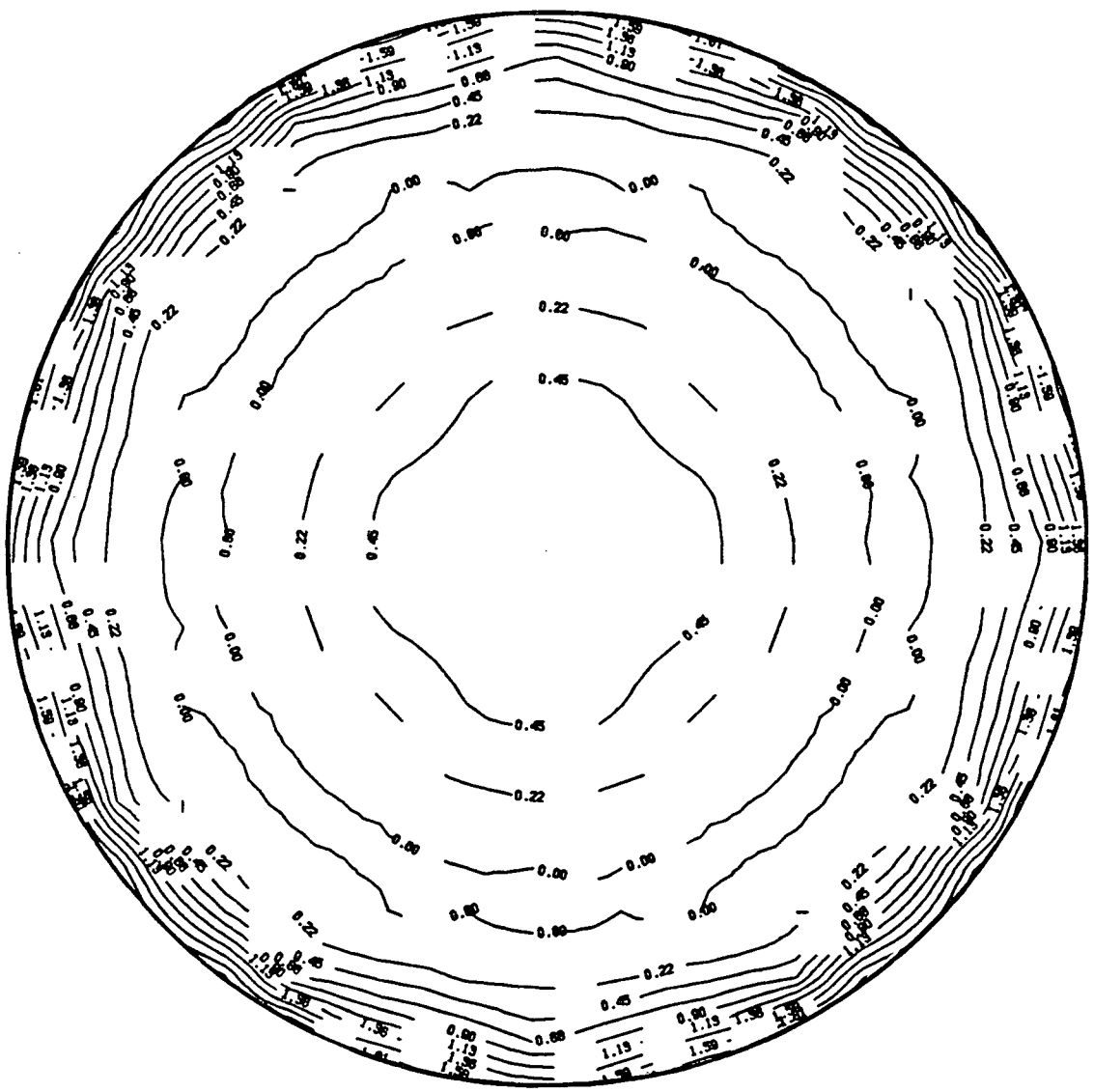

d

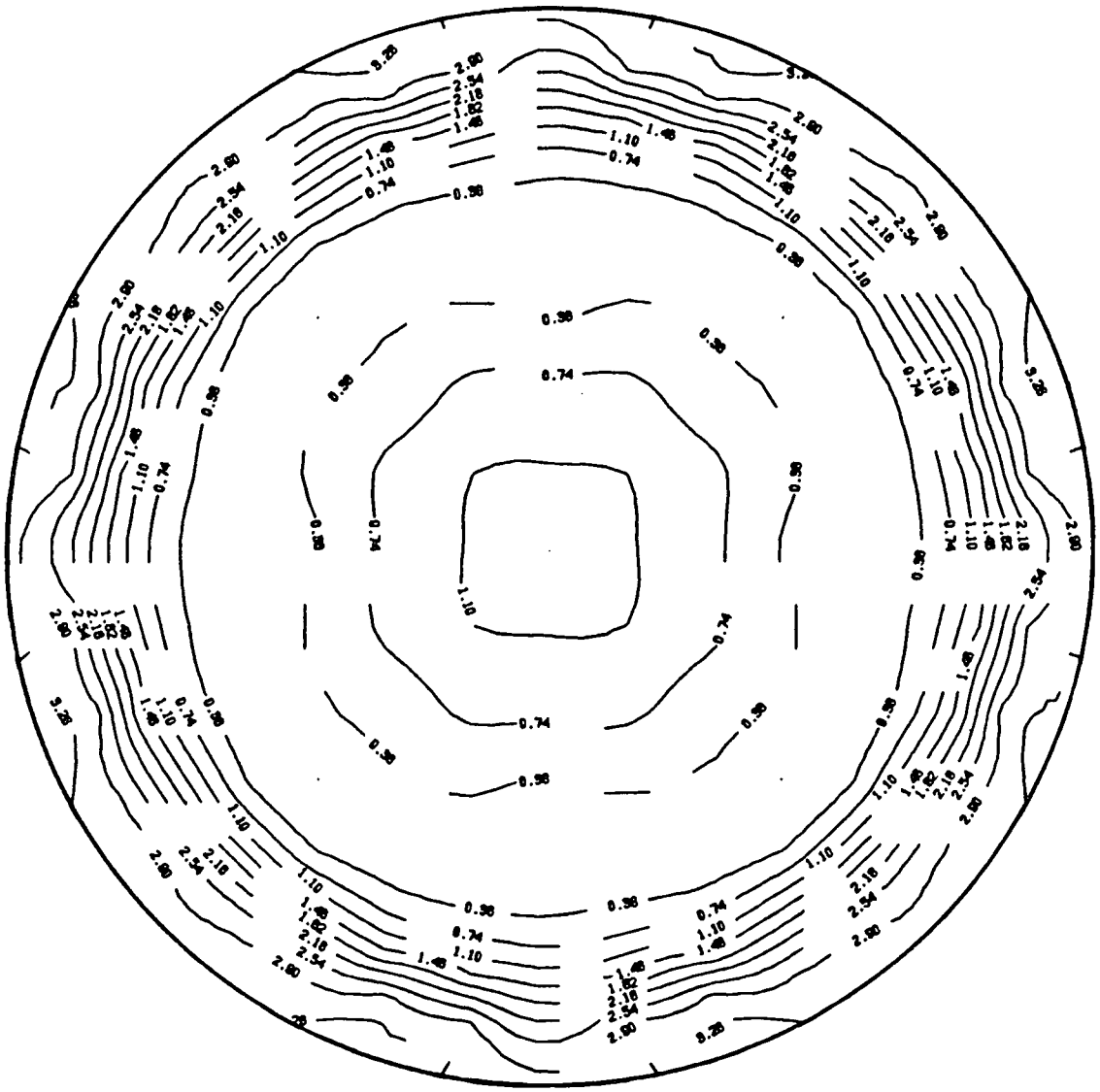

XIII.8.1.2.1.2 MRSS-CRSS (Yield) in cross-sections at distances (along the axis) from the interface of (a) 11 mm ; (b) 36 mm ; (c) 56 mm ; (d) 76 mm.

a

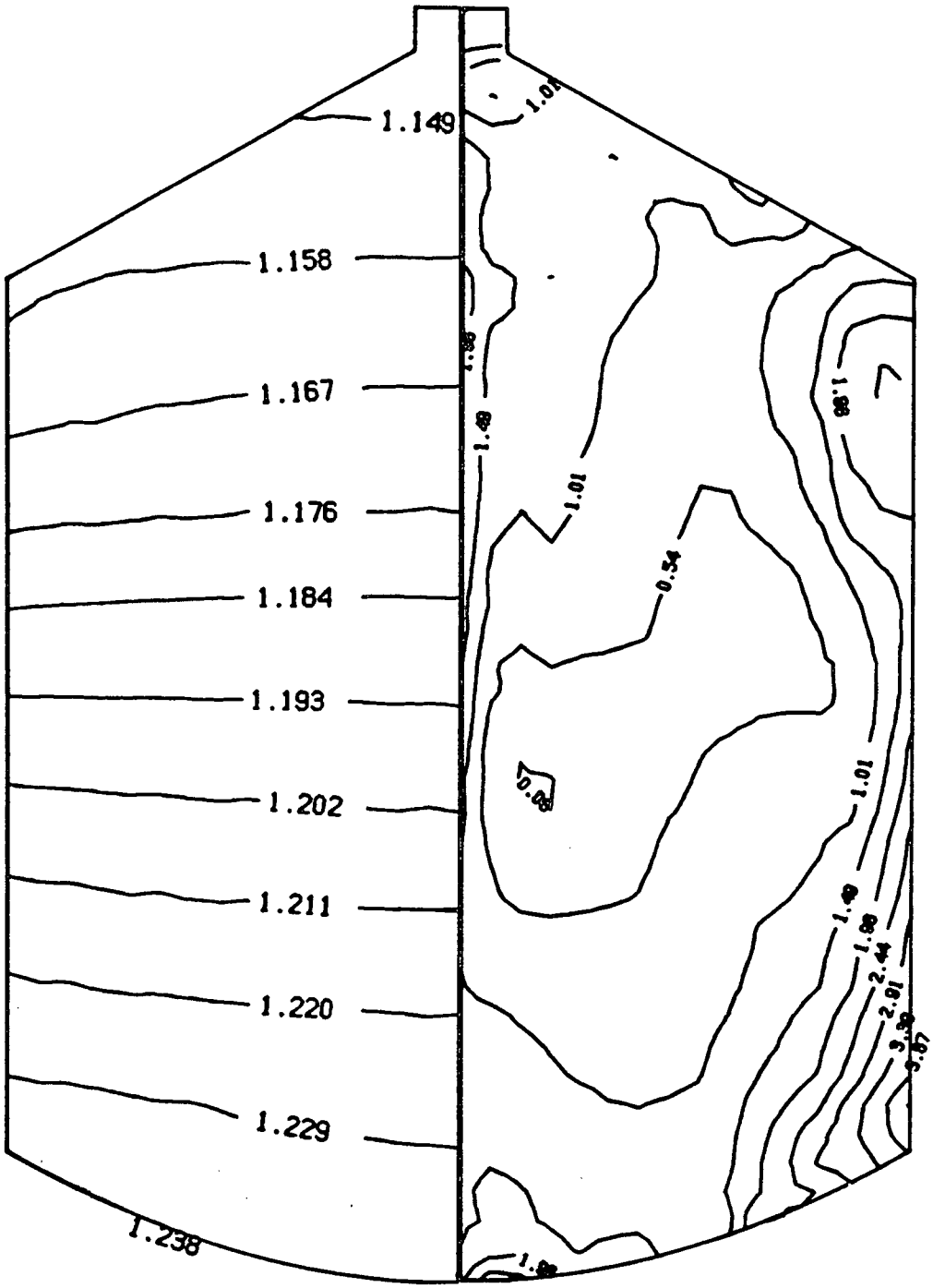
1.149
1.158
1.167
1.176
1.184
1.193
1.202
1.211
1.220
1.229
1.238
1.01
1.49
1.01
0.54
1.01
1.49
1.98
2.44
2.91
3.39
3.87

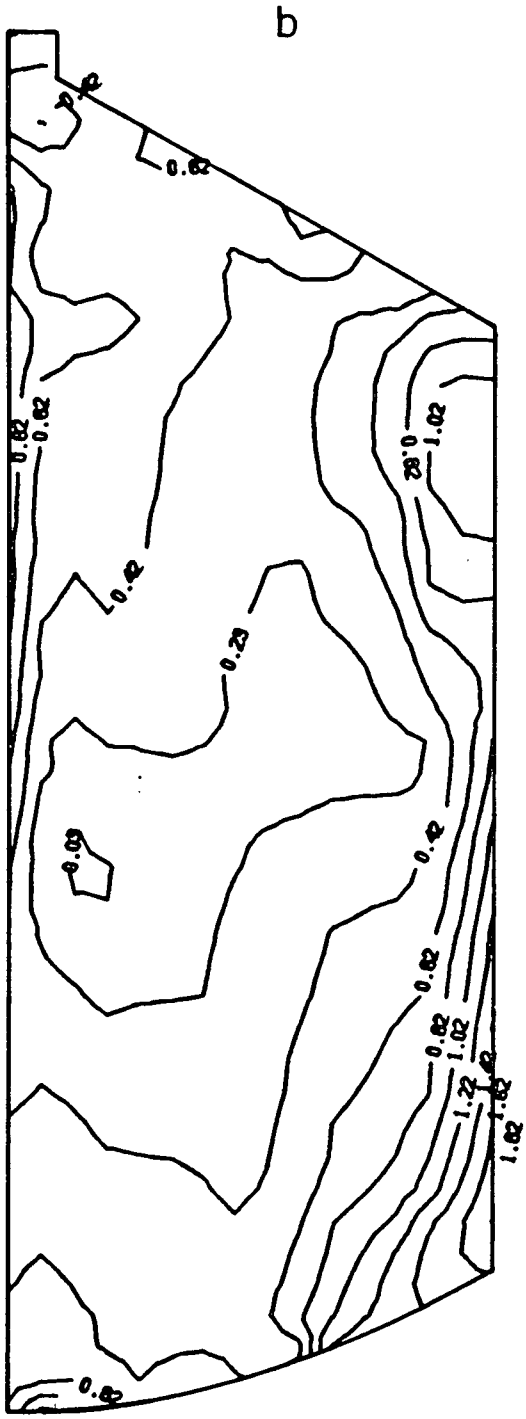
b
0.62
0.62
0.62
0.42
0.29
0.09
0.42
0.62
0.62
1.02
1.22
1.82
1.82
0.62

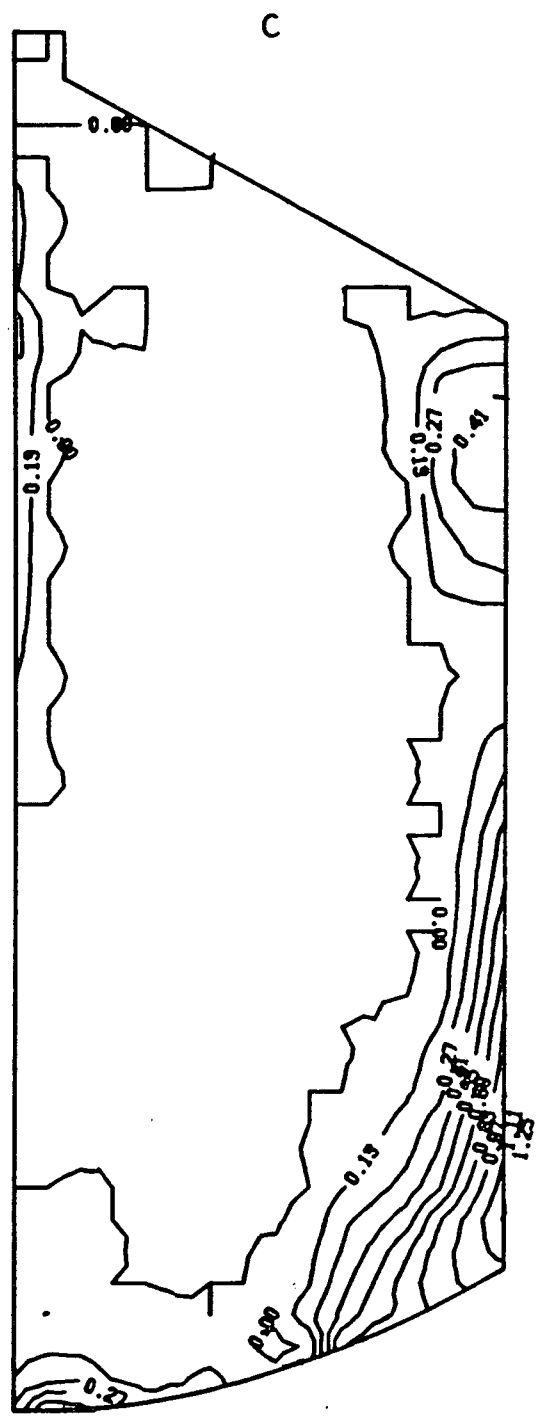
c
0.19
0.27
0.41
0.19
0.27

XIII.8.1.2.2.1 (a) Temperature and Von Mises Stress
(b) MRSS ; (c) MRSS-CRSS (Yield) ;
(d) MRSS-CRSS (MB) ; (e) MRSS-CRSS (MBTe) .

a

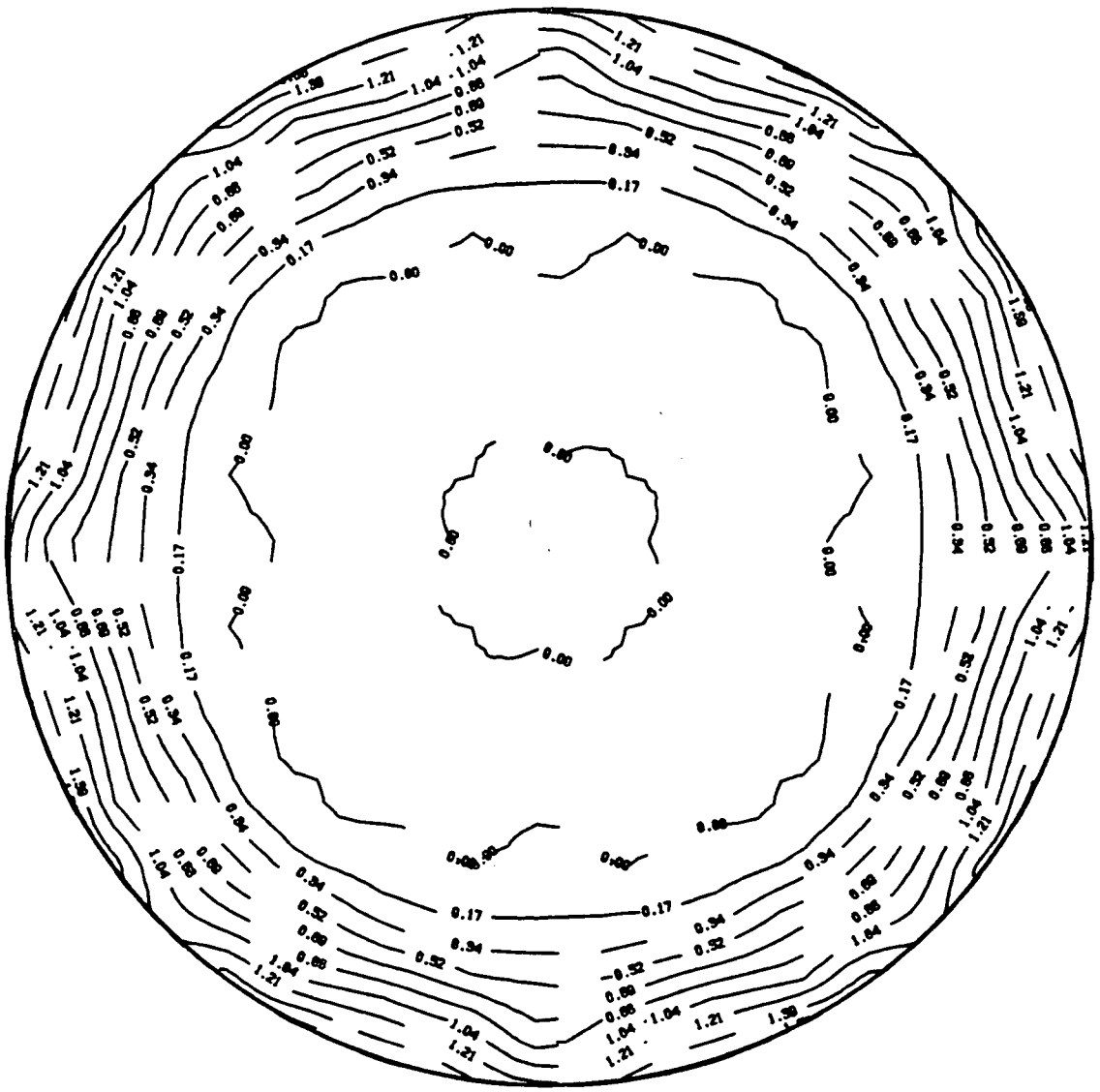

b

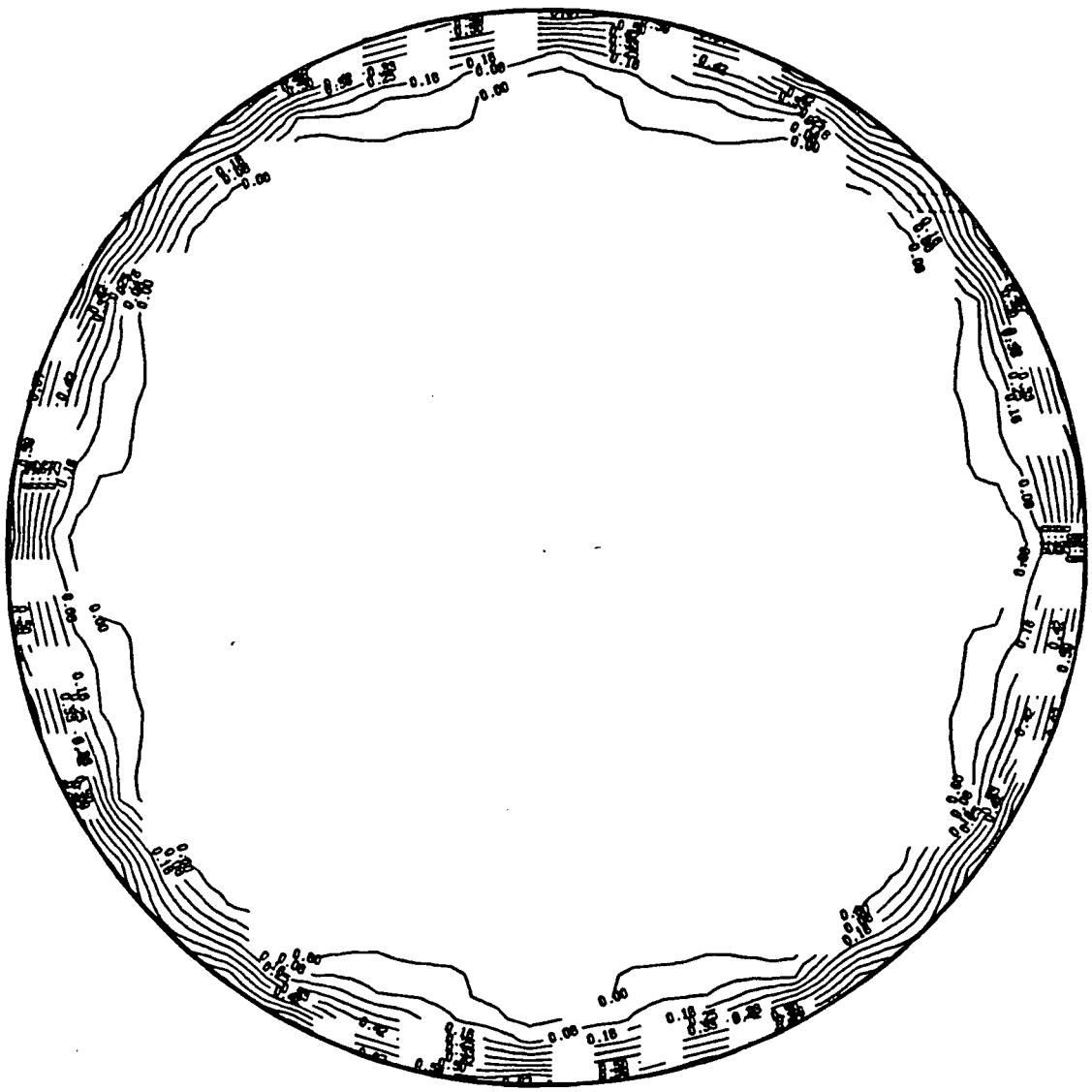

C

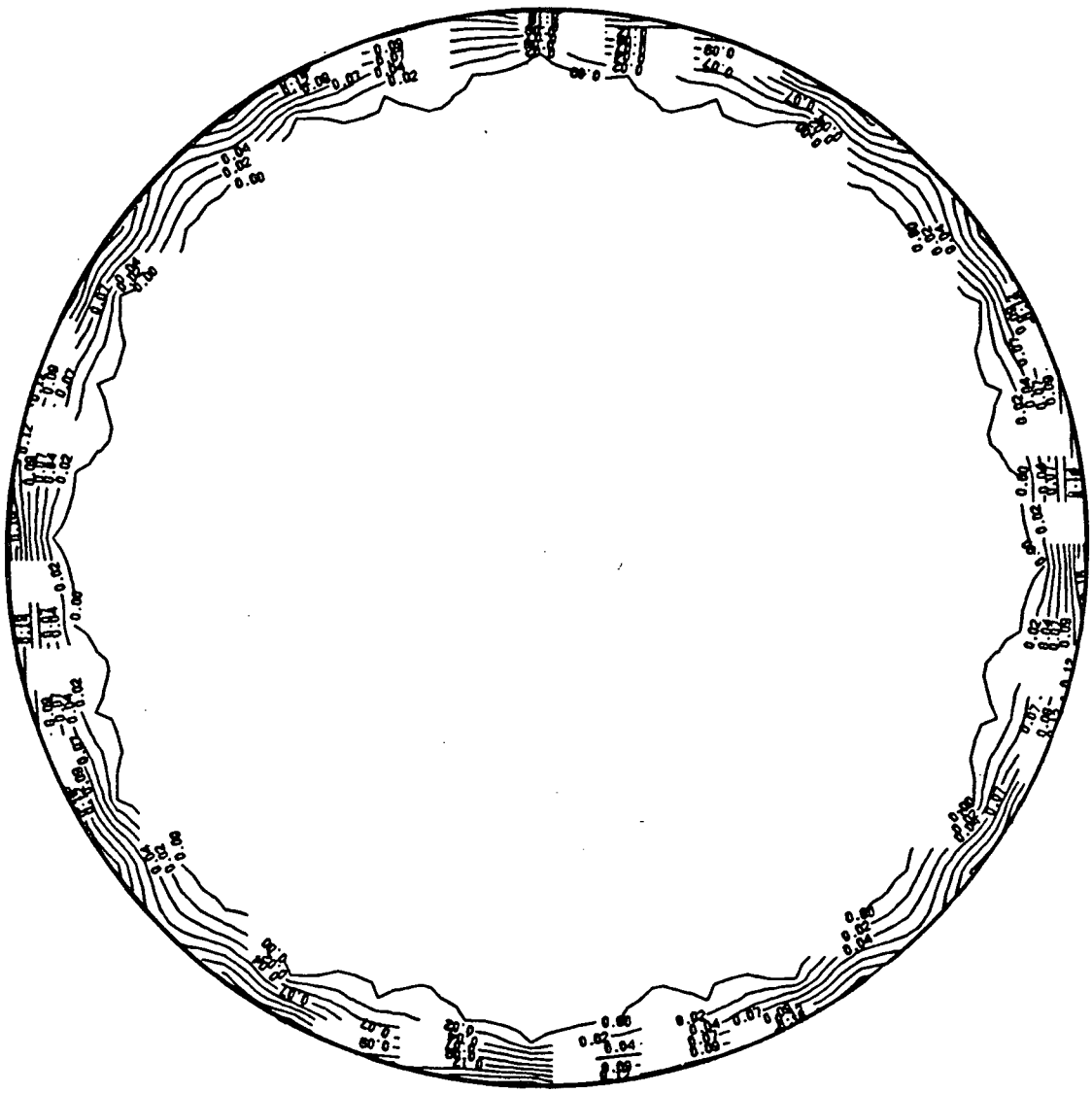

d

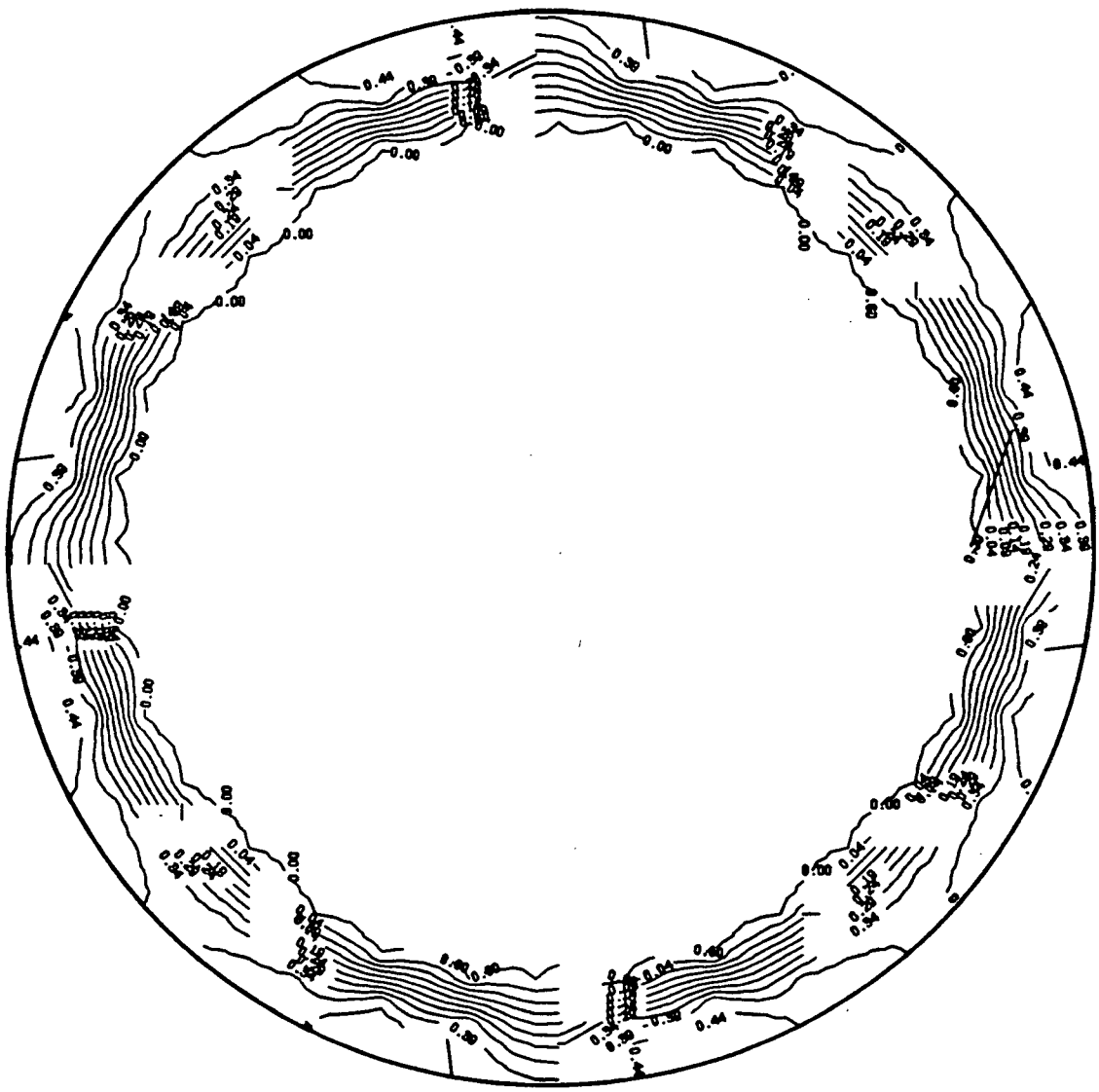

XIII.8.1.2.2.2 MRSS-CRSS (Yield) in cross-sections at distances (along the axis) from the interface of (a) 11 mm ; (b) 36 mm ; (c) 56 mm ; (d) 76 mm.

a

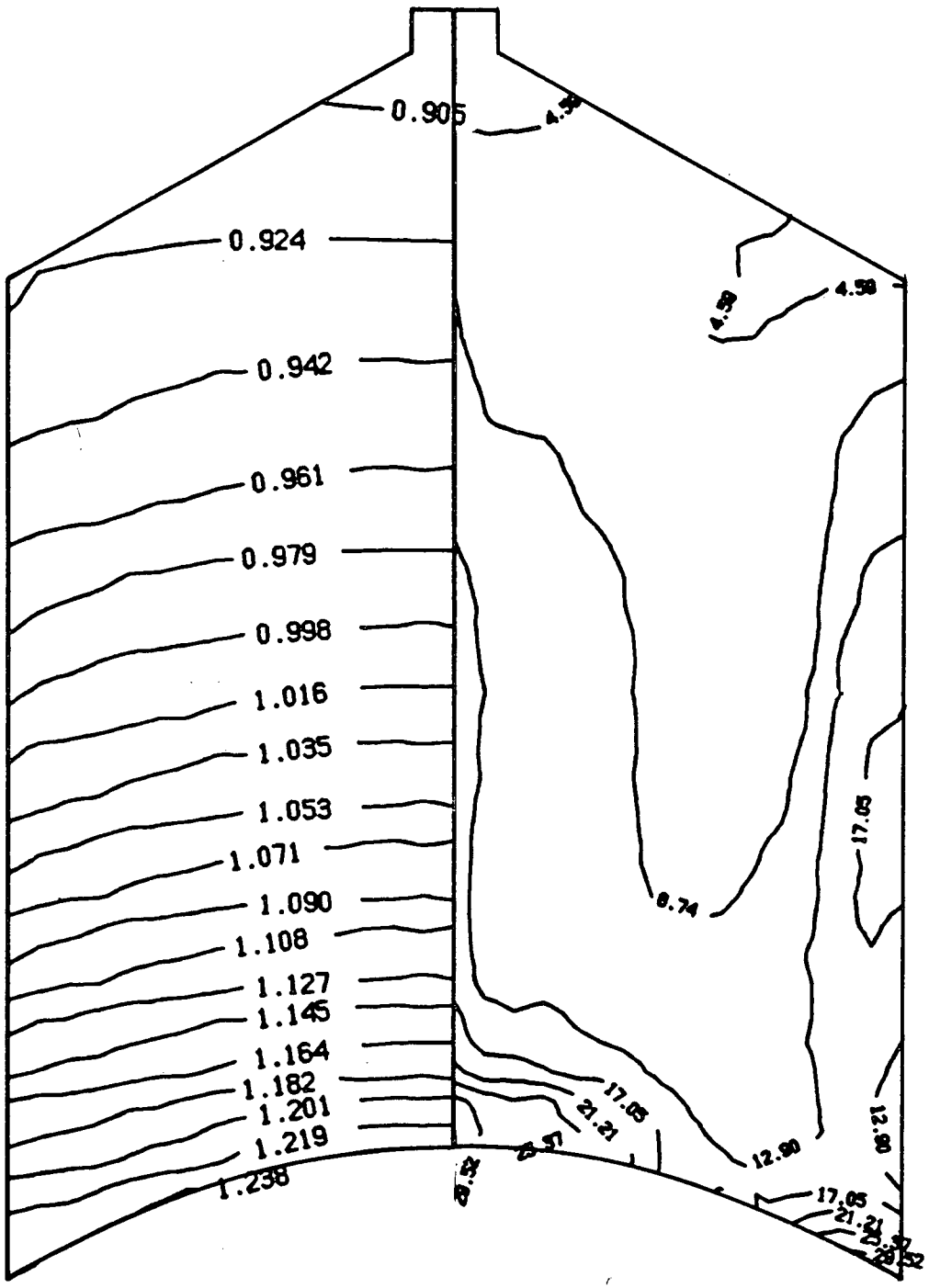
0.905
0.924
0.942
0.961
0.979
0.998
1.016
1.035
1.053
1.071
1.090
1.108
1.127
1.145
1.164
1.182
1.201
1.219
1.238
4.58
8.74
12.90
17.05
21.21

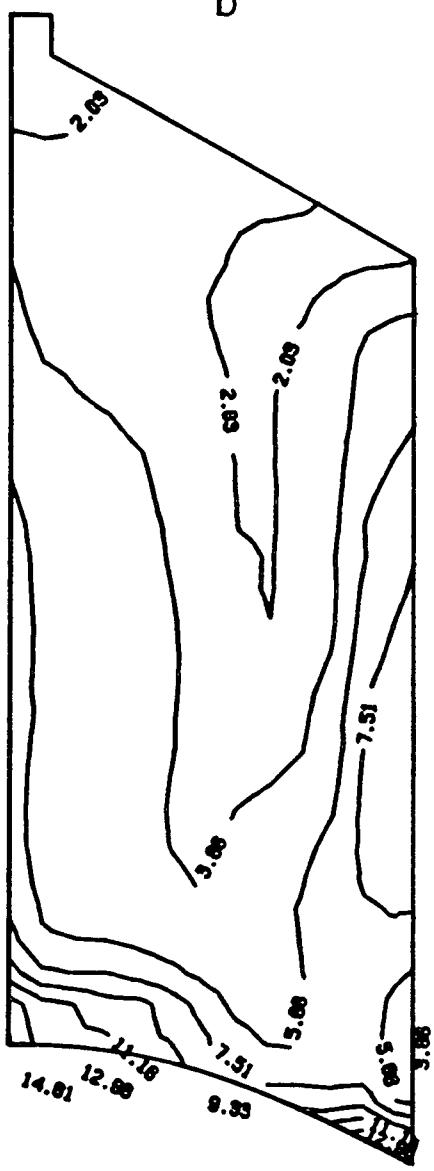
b
2.03
2.03
2.03
3.88
7.51
5.88
7.51
11.16
14.81
12.98
9.33
5.88
3.88

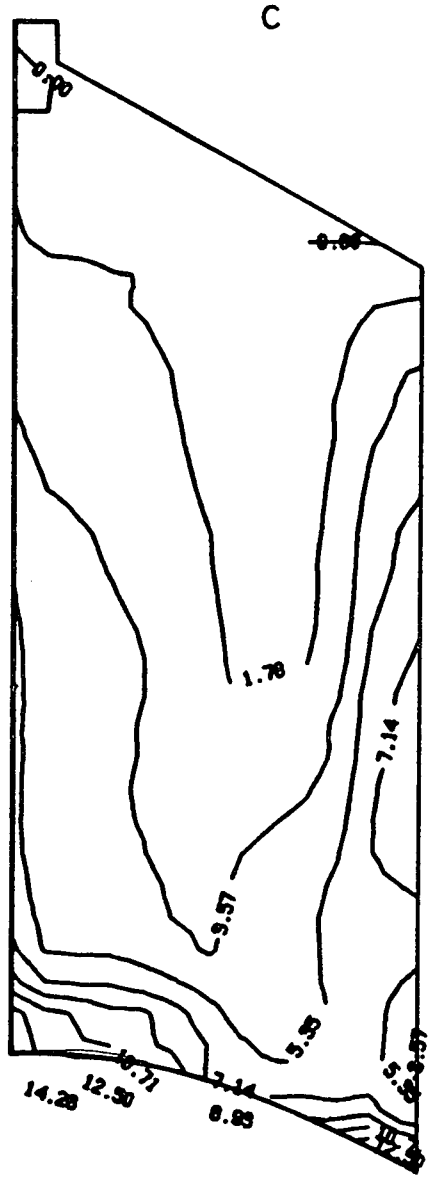
c
0.00
0.00
1.78
7.14
3.57
5.35
10.71
14.28
12.50
8.93
7.14

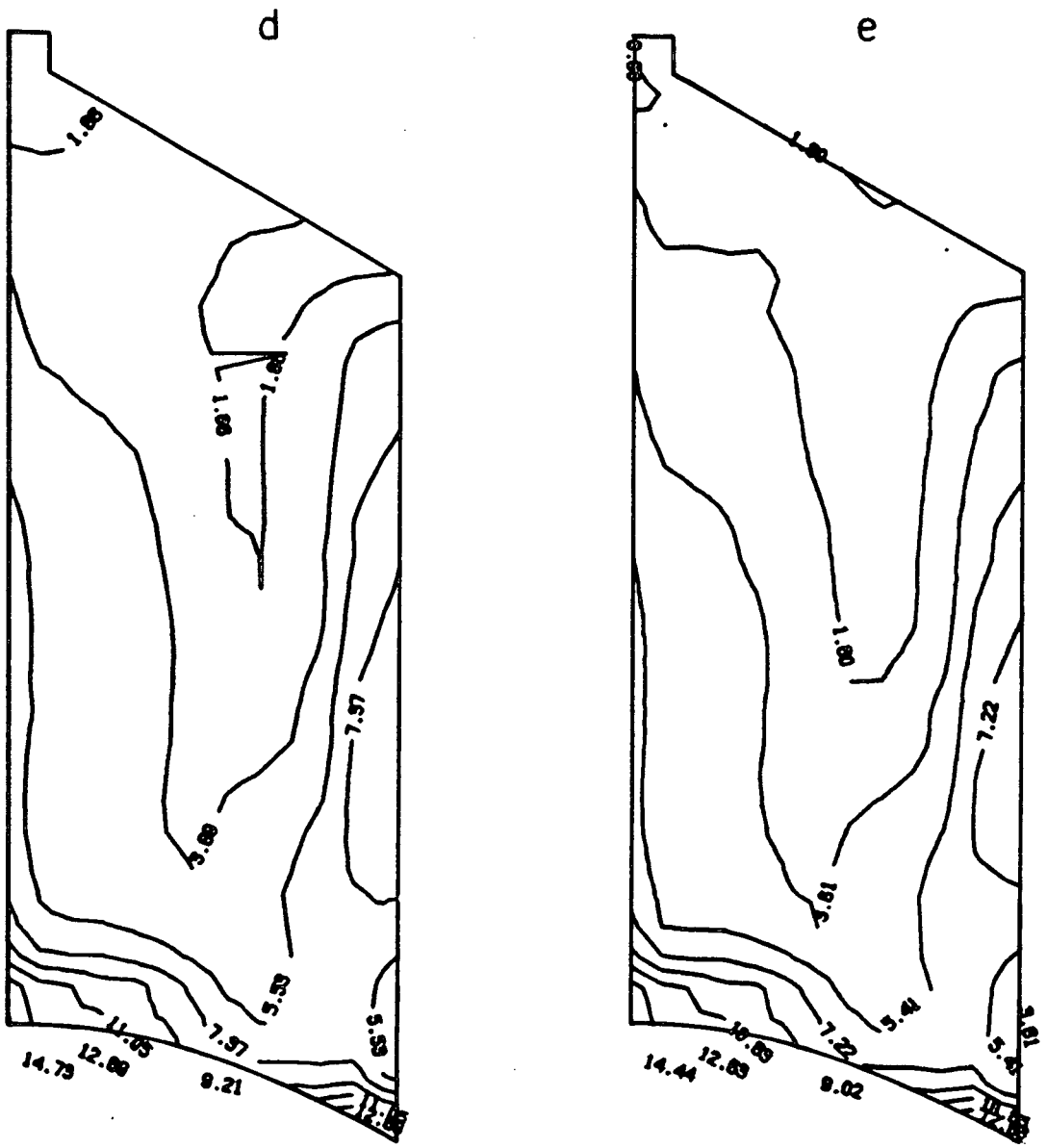

XIII.8.2.1.1 (a) Temperature and Von Mises Stress
(b) MRSS ; (c) MRSS-CRSS (Yield) ;
(d) MRSS-CRSS (MB) ; (e) MRSS-CRSS (MBTe) .

a

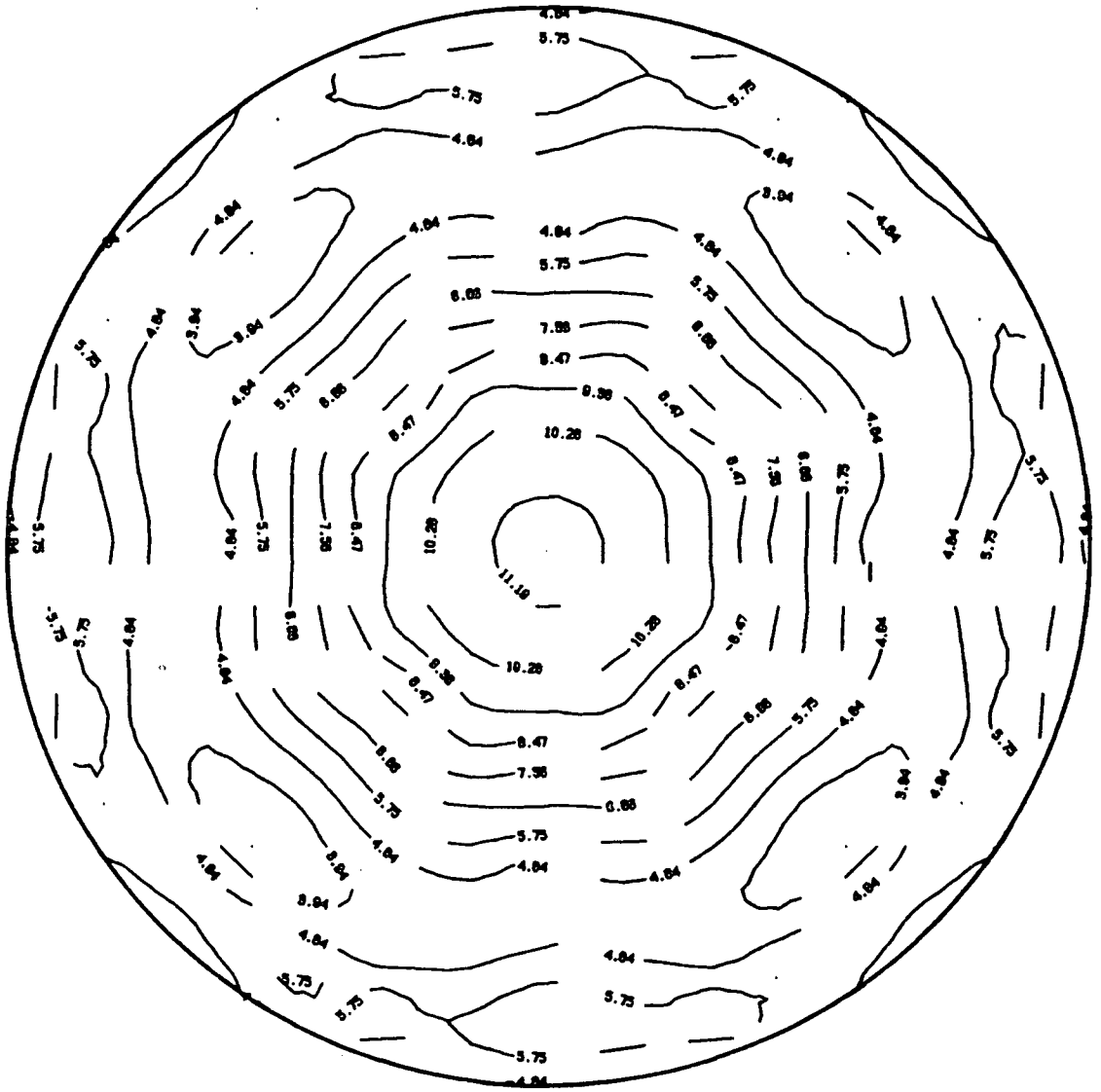

b

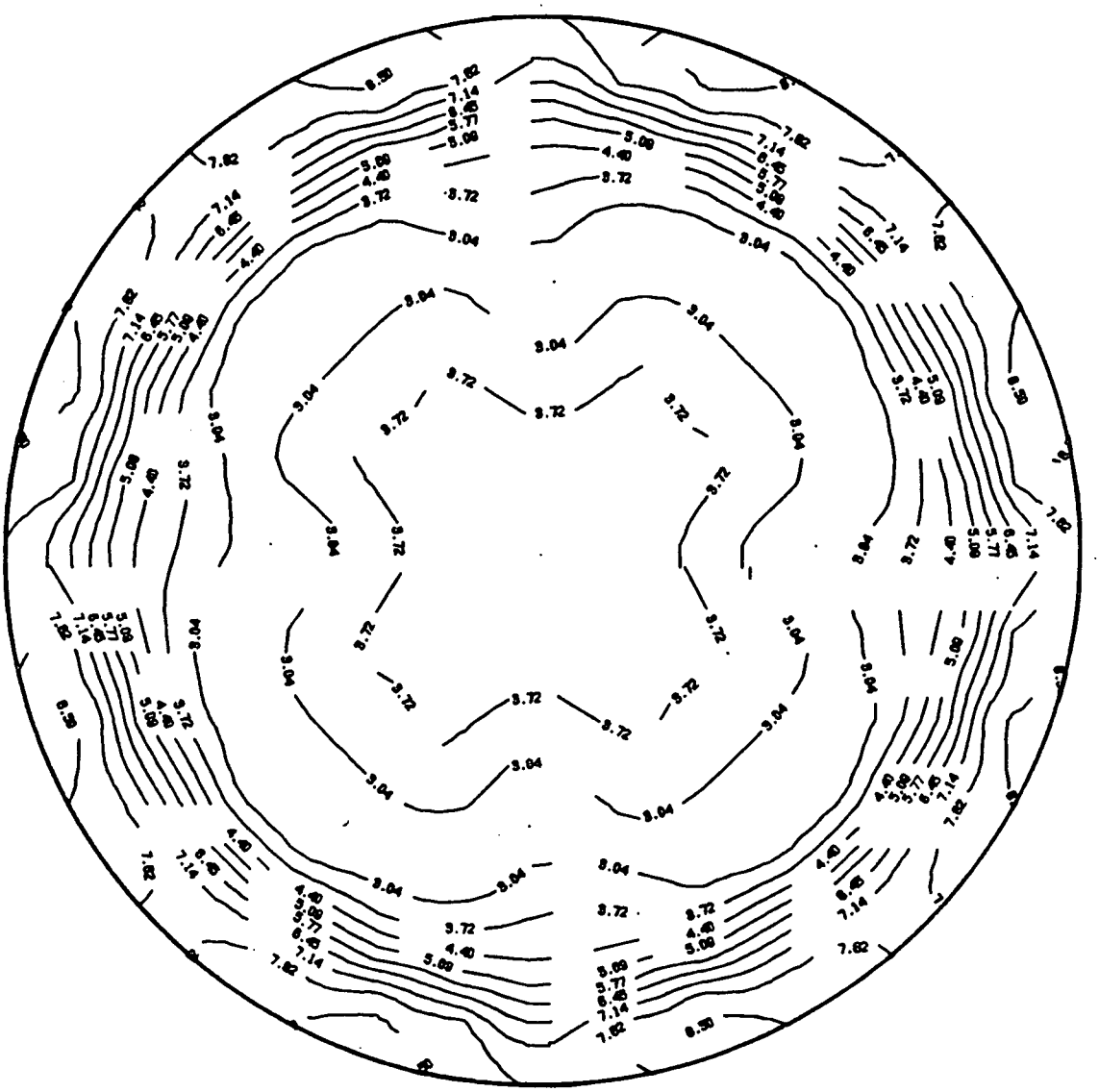

C

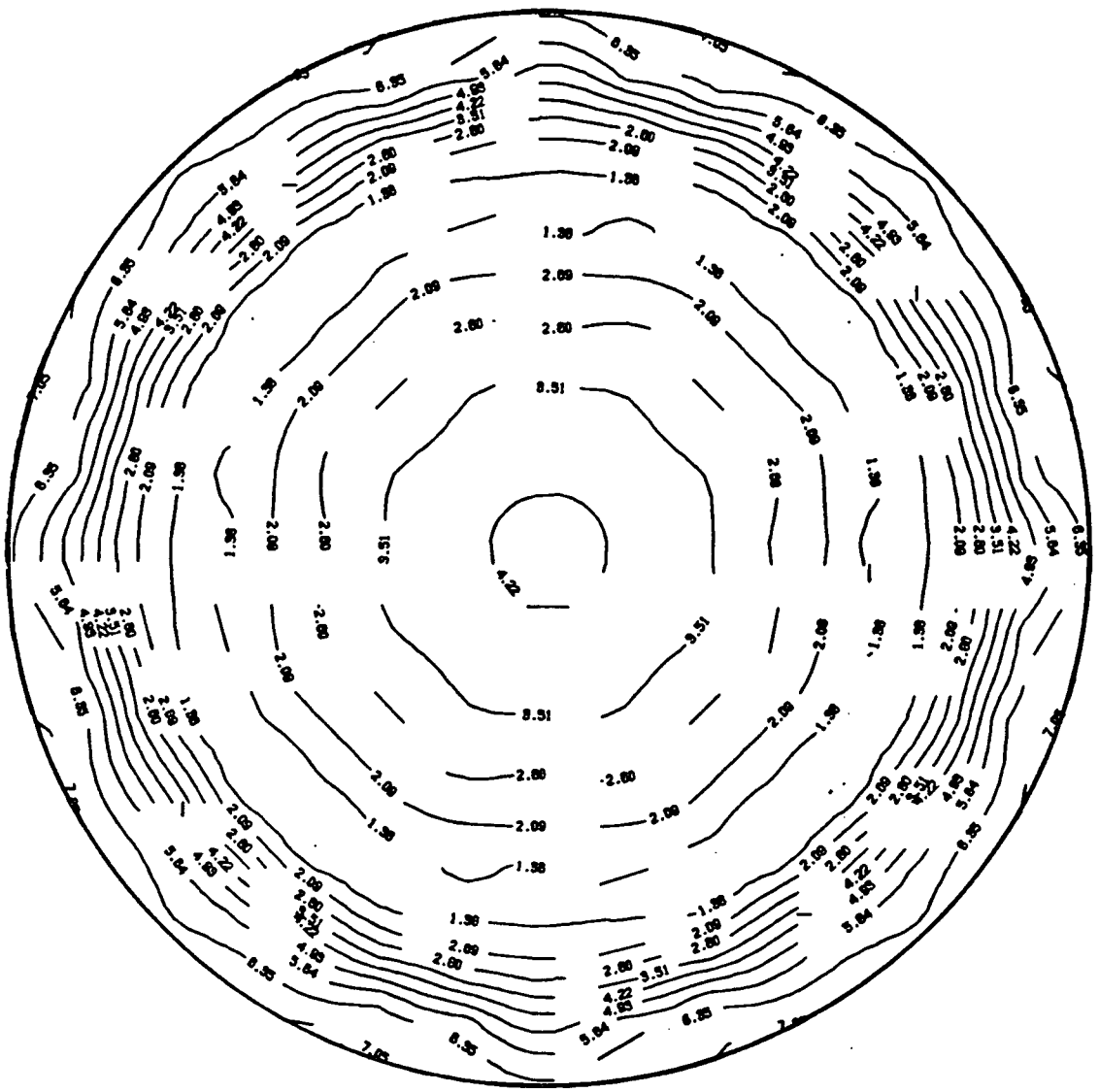

d

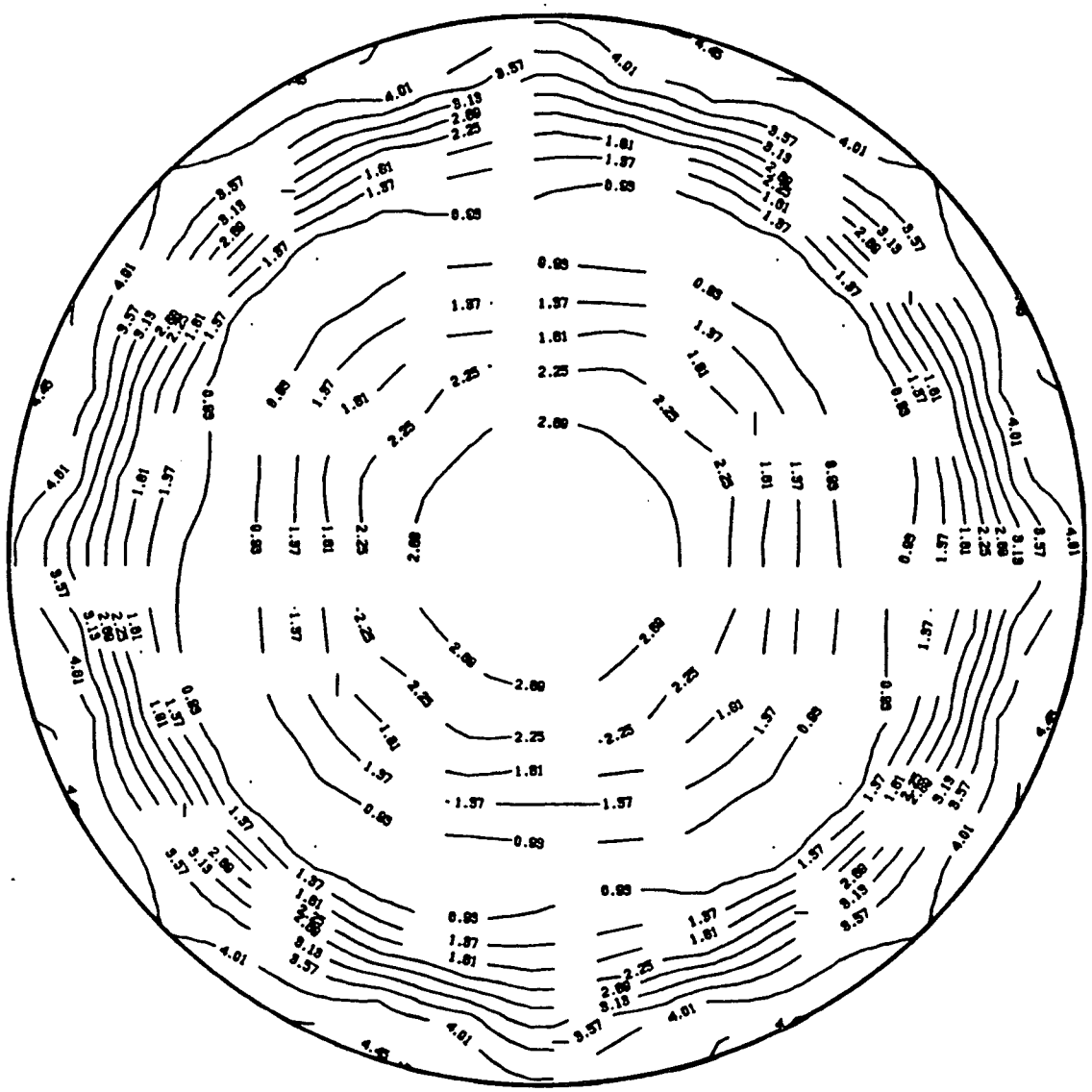

XIII.8.2.1.2 MRSS-CRSS (Yield) in cross-sections at distances (along the axis) from the interface of (a) 2.75 mm ; (b) 16.5 mm ; (c) 30.25 mm ; (d) 44 mm .

a

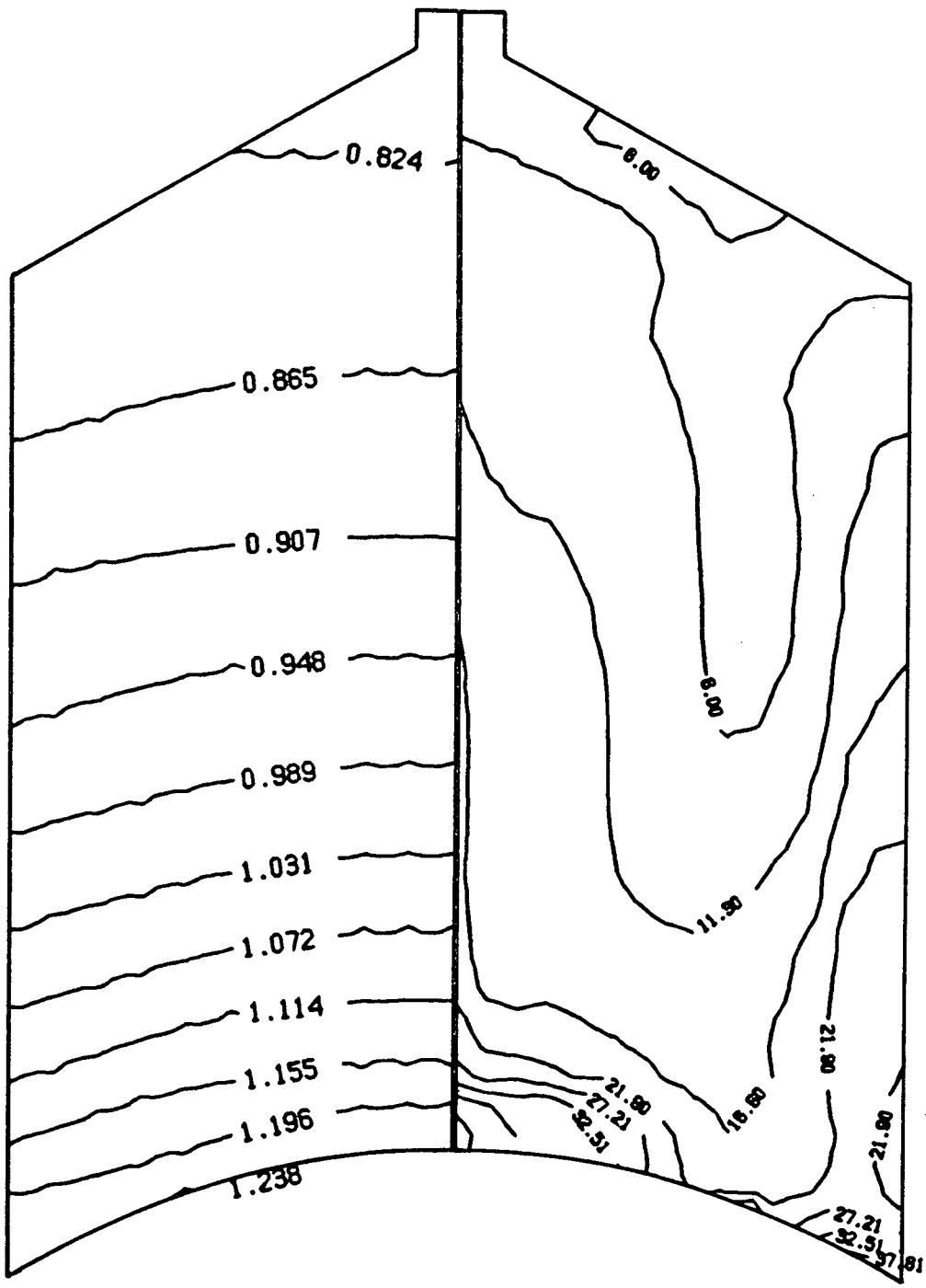
0.824
0.865
0.907
0.948
0.989
1.031
1.072
1.114
1.155
1.196
1.238
6.00
6.00
11.90
21.90
16.80
21.90
27.21
32.51
21.90
27.21
32.51
37.81

43.11

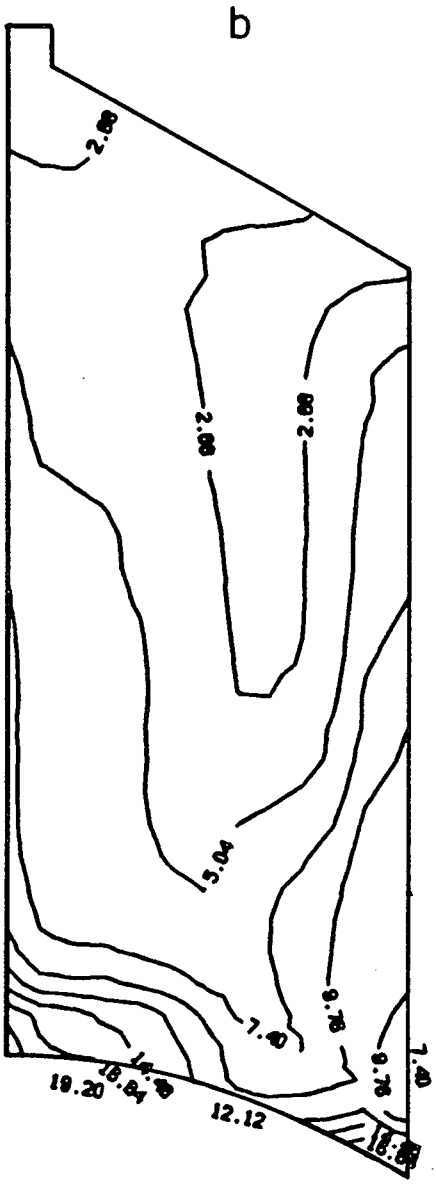
b
2.88
2.88
5.04
7.40
9.76
19.20
12.12

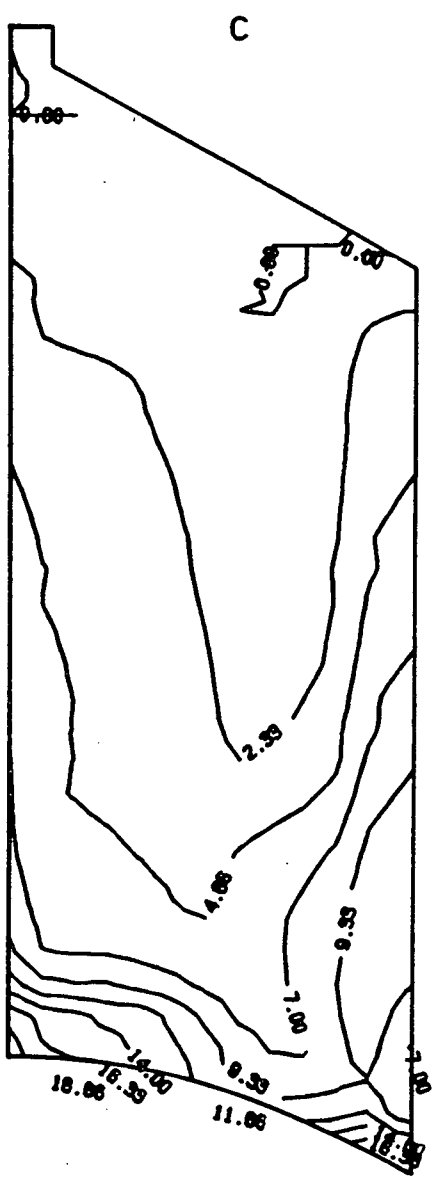
c
0.00
0.00
2.59
4.68
7.00
9.33
16.33
11.66

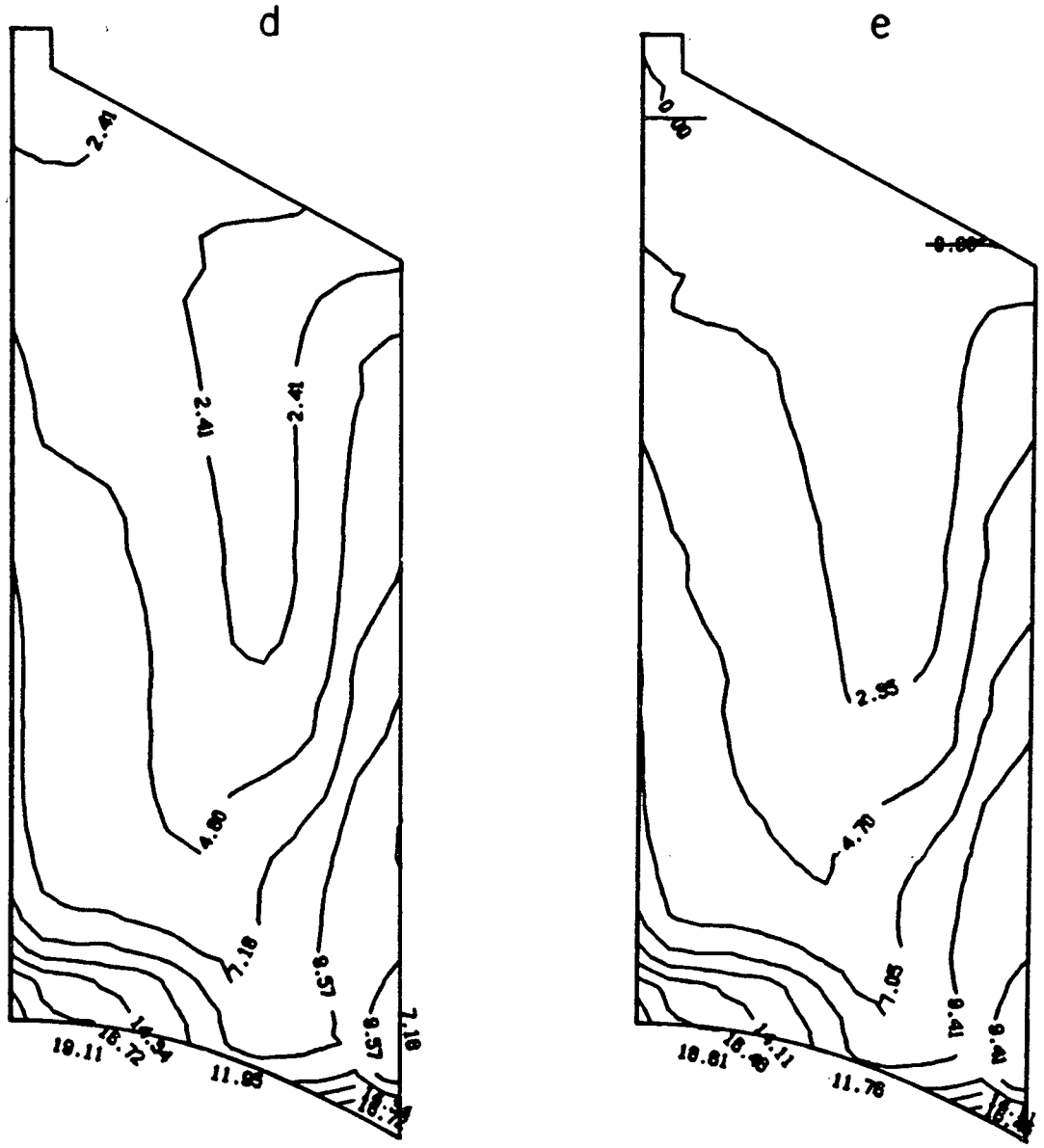

XIII.8.2.2.1 (a) Temperature and Von Mises Stress
(b) MRSS ; (c) MRSS-CRSS (Yield) ;
(d) MRSS-CRSS (MB) ; (e) MRSS-CRSS (MBTe) .

a

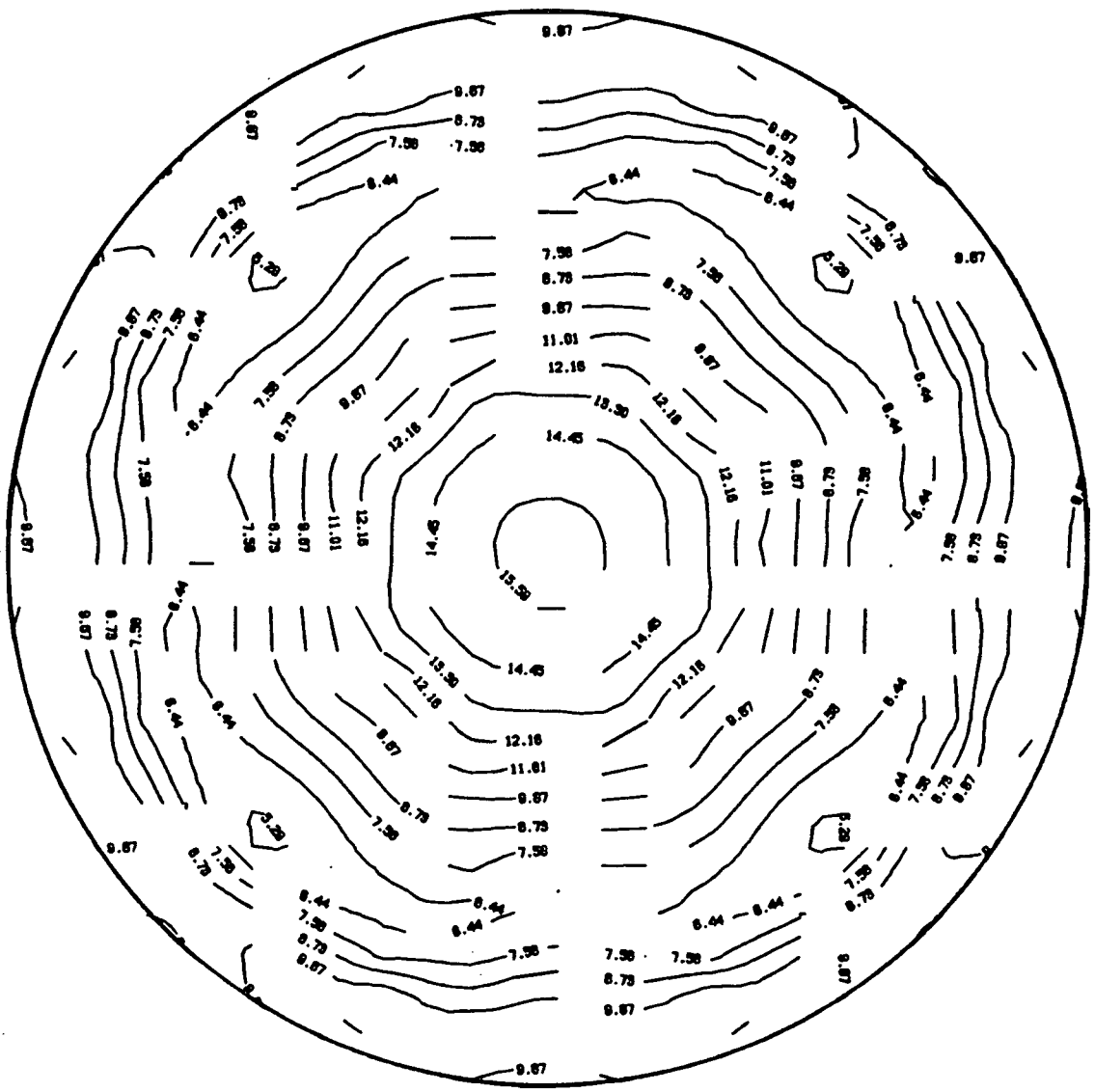

b

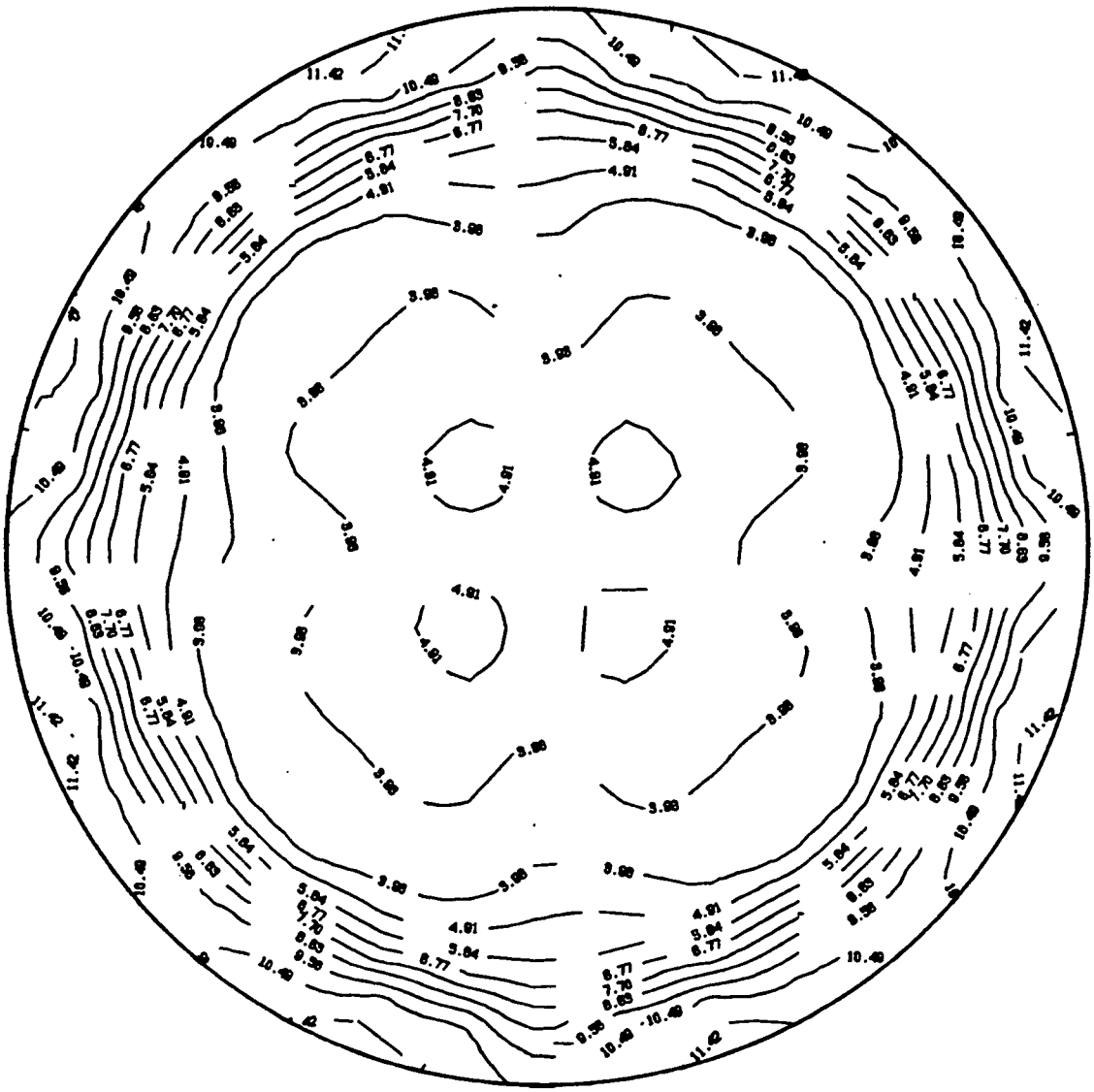

C

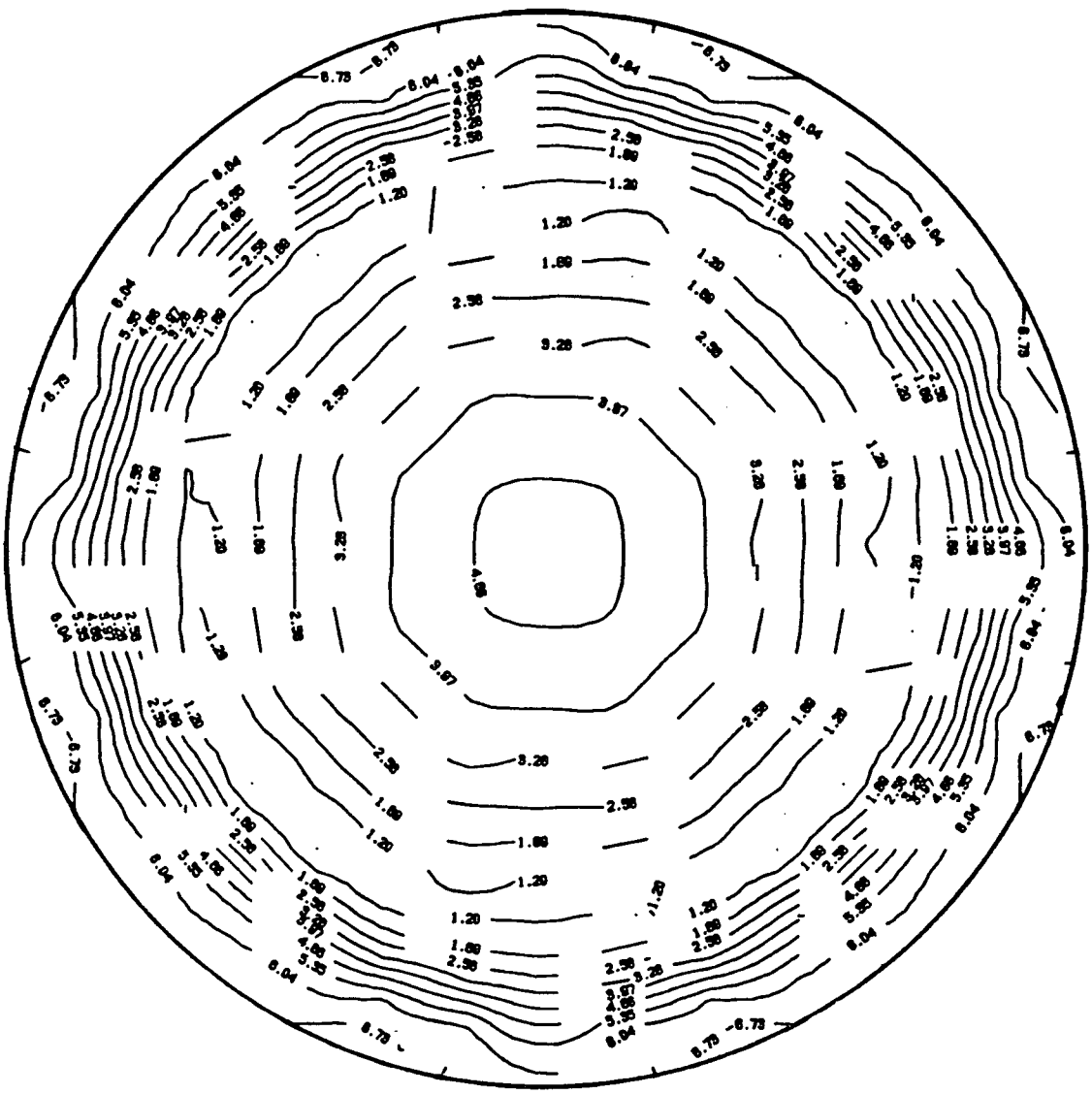

d

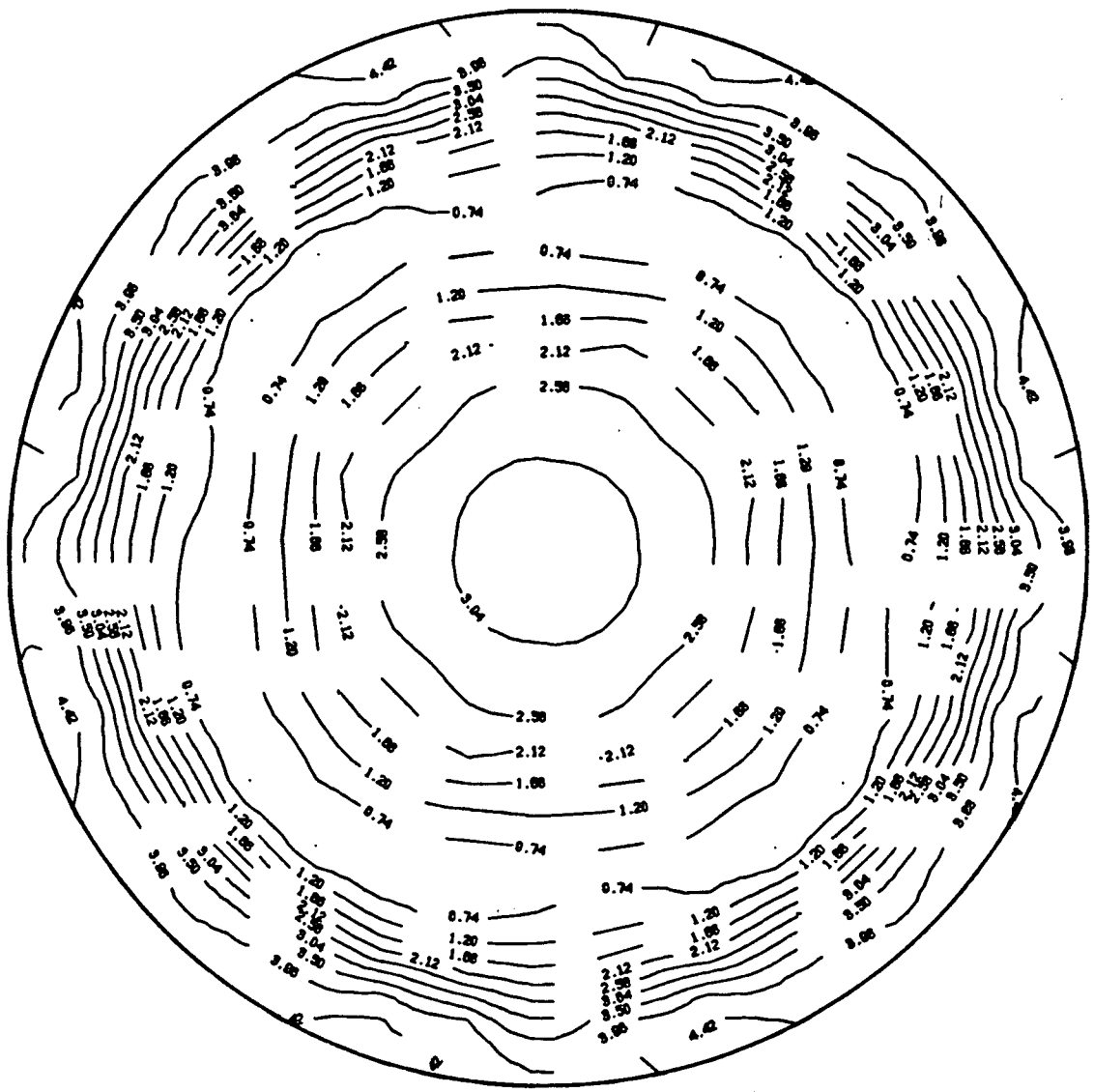

XIII.8.2.2.2 MRSS-CRSS (Yield) in cross-sections at distances (along the axis) from the interface of (a) 2.75 mm ; (b) 16.5 mm ; (c) 30.25 mm ; (d) 44 mm .

APPENDIX XIV

TEMPERATURE AND STRESS PLOTS FROM THE COMPUTER PROGRAMS OUTPUT (COOLING)

Units are, 10^{3o}C for the temperatures and MPa for the stresses. R, 27.5 mm ; CL, 110 mm .

XIV.1 Ambient Temperature 800°C, Argon

XIV.1.1 Initial Gradient GC

XIV.1.1.1 Time 10 seconds

XIV.1.1.1.1 (a) Temperature ; (b) Von Mises Stress
(c) MRSS ; (d) MRSS-CRSS (Yield) ;
(e) MRSS-CRSS (MB) ; (f) MRSS-CRSS (MBTe) .

XIV.1.1.1.2 MRSS-CRSS (Yield) in cross-sections at a distance from the interface of :
(a) 2.75 mm ; (b) 8.25 mm ; (c) 16.5 mm ;
(d) 25.5 mm .

XIV.1.1.1 Time 10 seconds

XIV.1.1.1.1 (a) Temperature ; (b) Von Mises Stress
(c) MRSS ; (d) MRSS-CRSS (Yield) ;
(e) MRSS-CRSS (MB) ; (f) MRSS-CRSS (MBTe) .

XIV.1.1.1.2 MRSS-CRSS (Yield) in cross-sections at a distance from the interface of :
(a) 2.75 mm ; (b) 8.25 mm ; (c) 16.5 mm ;
(d) 27.5 mm .

XIV.1.1.2 Time 20 seconds
(a) Temperature ; (b) Von Mises Stress
(c) MRSS ; (d) MRSS-CRSS (Yield) ;
(e) MRSS-CRSS (MB) ; (f) MRSS-CRSS (MBTe) .

XIV.1.1.3 Time 60 seconds
(a) Temperature ; (b) Von Mises Stress
(c) MRSS ; (d) MRSS-CRSS (Yield) ;
(e) MRSS-CRSS (MB) ; (f) MRSS-CRSS (MBTe) .

XIV.1.1.4 Time 300 seconds
(a) Temperature ; (b) Von Mises Stress
(c) MRSS ; (d) MRSS-CRSS (Yield) ;
(e) MRSS-CRSS (MB) ; (f) MRSS-CRSS (MBTe) .

XIV.1.2 Initial Gradient GC/2 ; Time 10 seconds .

XIV.1.2.1 (a) Temperature ; (b) Von Mises Stress
(c) MRSS ; (d) MRSS-CRSS (Yield) ;
(e) MRSS-CRSS (MB) ; (f) MRSS-CRSS (MBTe) .

XIV.1.2.2 MRSS-CRSS (Yield) in cross-sections at a distance from the interface of :
(a) 2.75 mm ; (b) 8.25 mm ; (c) 16.5 mm ;
(d) 27.5 mm .

XIV.1.3 Initial Gradient GC/4

XIV.1.3.1 Time 10 seconds

XIV.1.3.1.1 (a) Temperature ; (b) Von Mises Stress
(c) MRSS ; (d) MRSS-CRSS (Yield) ;
(e) MRSS-CRSS (MB) .

XIV.1.3.1.2 MRSS-CRSS (Yield) in cross-sections at a distance from the interface of :
(a) 2.75 mm ; (b) 8.25 mm ; (c) 16.5 mm ;
(d) 27.5 mm .

XIV.1.3.2 Time 20 seconds
(a) Temperature ; (b) Von Mises Stress
(c) MRSS ; (d) MRSS-CRSS (Yield) ;
(e) MRSS-CRSS (MBTe) .

XIV.1.3.3 Time 60 seconds
(a) Temperature ; (b) Von Mises Stress
(c) MRSS ; (d) MRSS-CRSS (Yield) ;
(e) MRSS-CRSS (MB) ; (f) MRSS-CRSS (MBTe) .

a

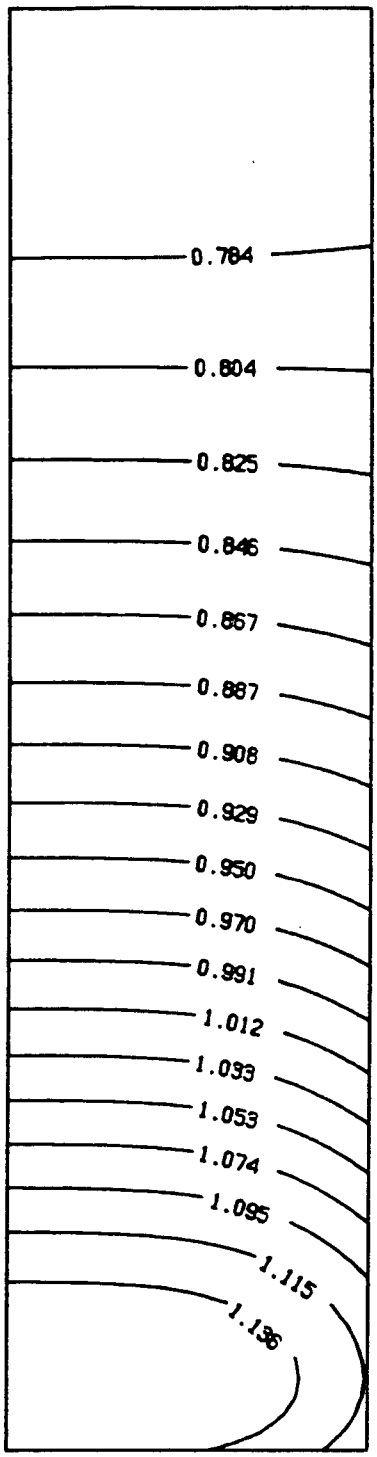
0.784
0.804
0.825
0.846
0.867
0.887
0.908
0.929
0.950
0.970
0.991
1.012
1.033
1.053
1.074
1.095
1.115
1.136

b

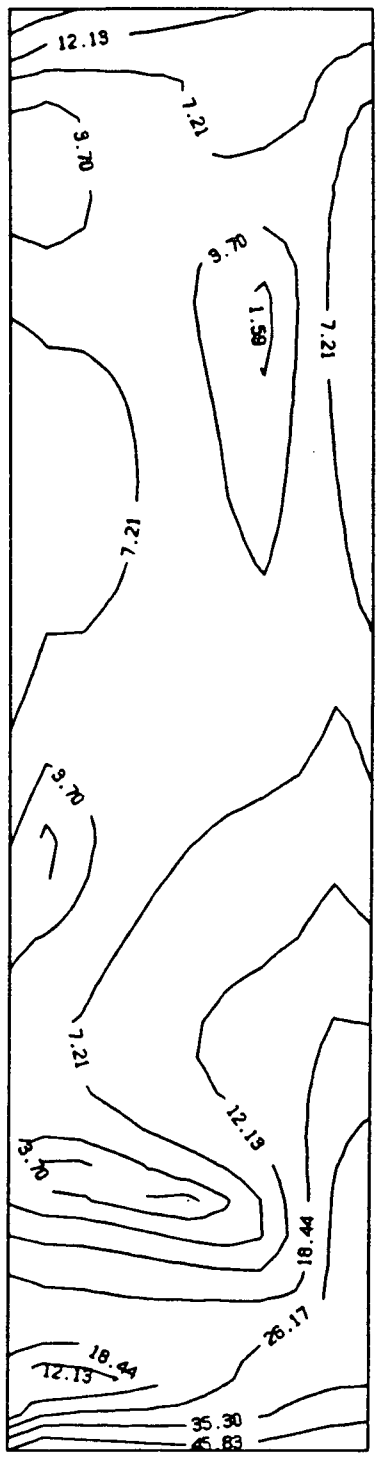
12.13
7.21
9.70
9.70
1.59
7.21
7.21
9.70
7.21
12.13
9.70
18.44
26.17
18.44
12.13
35.30

c

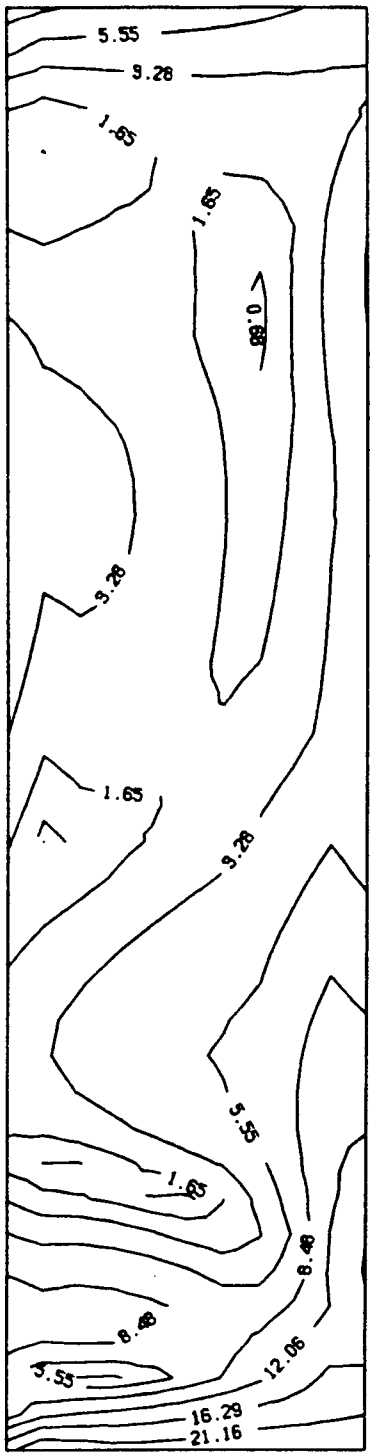
5.55
3.28
1.65
1.65
0.80
3.28
1.65
3.28
5.55
1.65
8.48
8.48
5.55
12.06
16.29
21.16

d

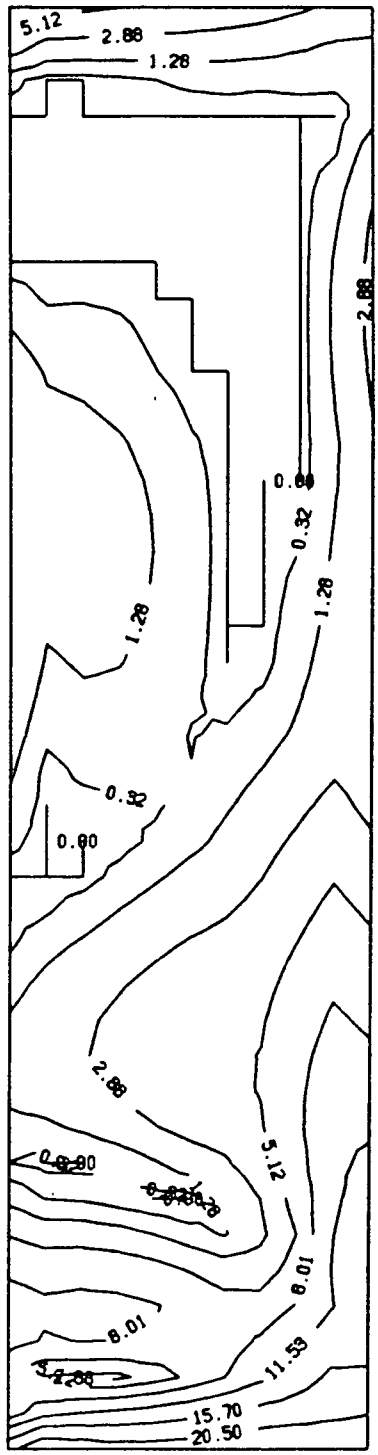
5.12
2.88
1.28
2.88
0.80
0.32
1.28
1.28
0.32
0.80
2.88
5.12
8.01
8.01
11.53
15.70
20.50

e

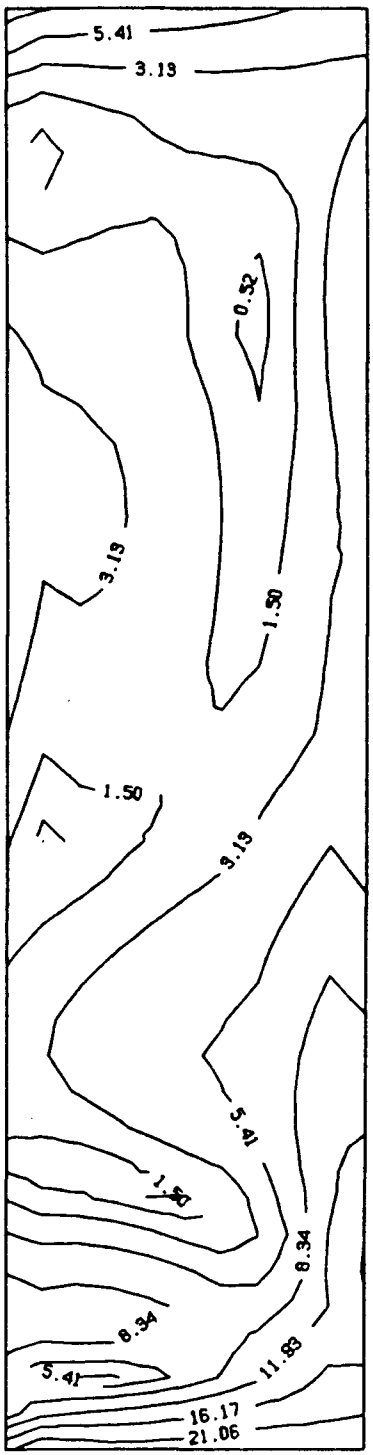

f

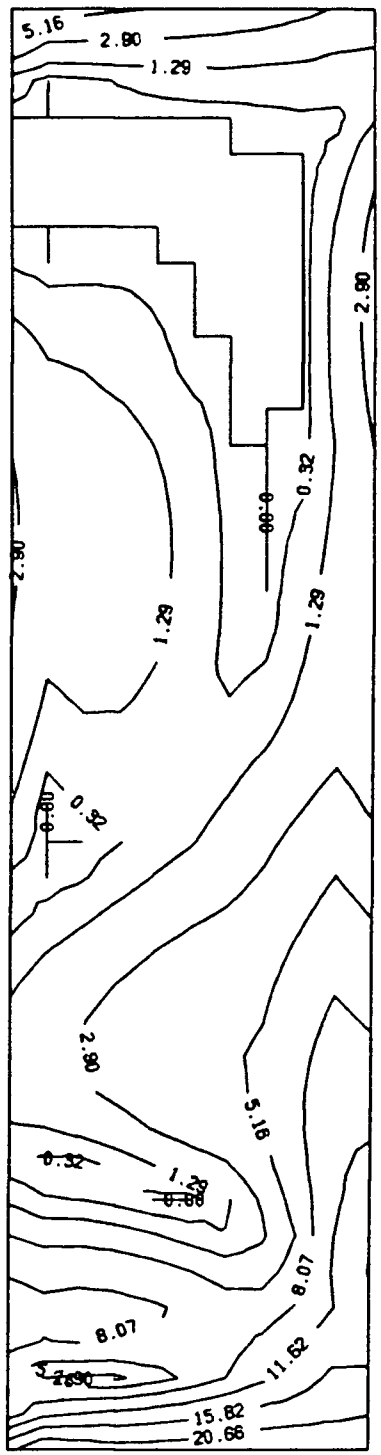

XIV.1.1.1.1 (a) Temperature ; (b) Von Mises Stress
(c) MRSS ; (d) MRSS-CRSS (Yield) ;
(e) MRSS-CRSS (MB) ; (f) MRSS-CRSS (MBTe) .

a

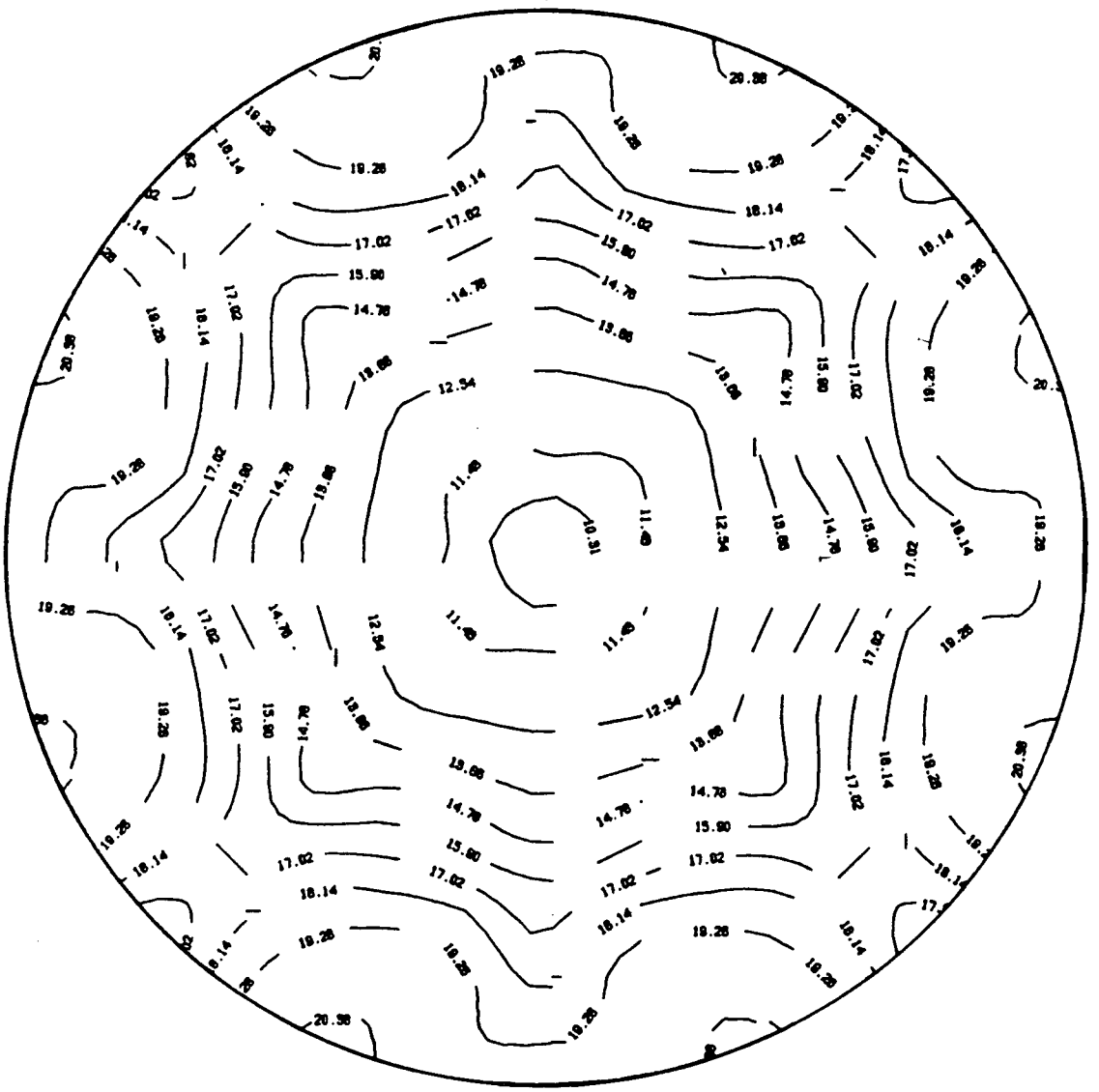

b

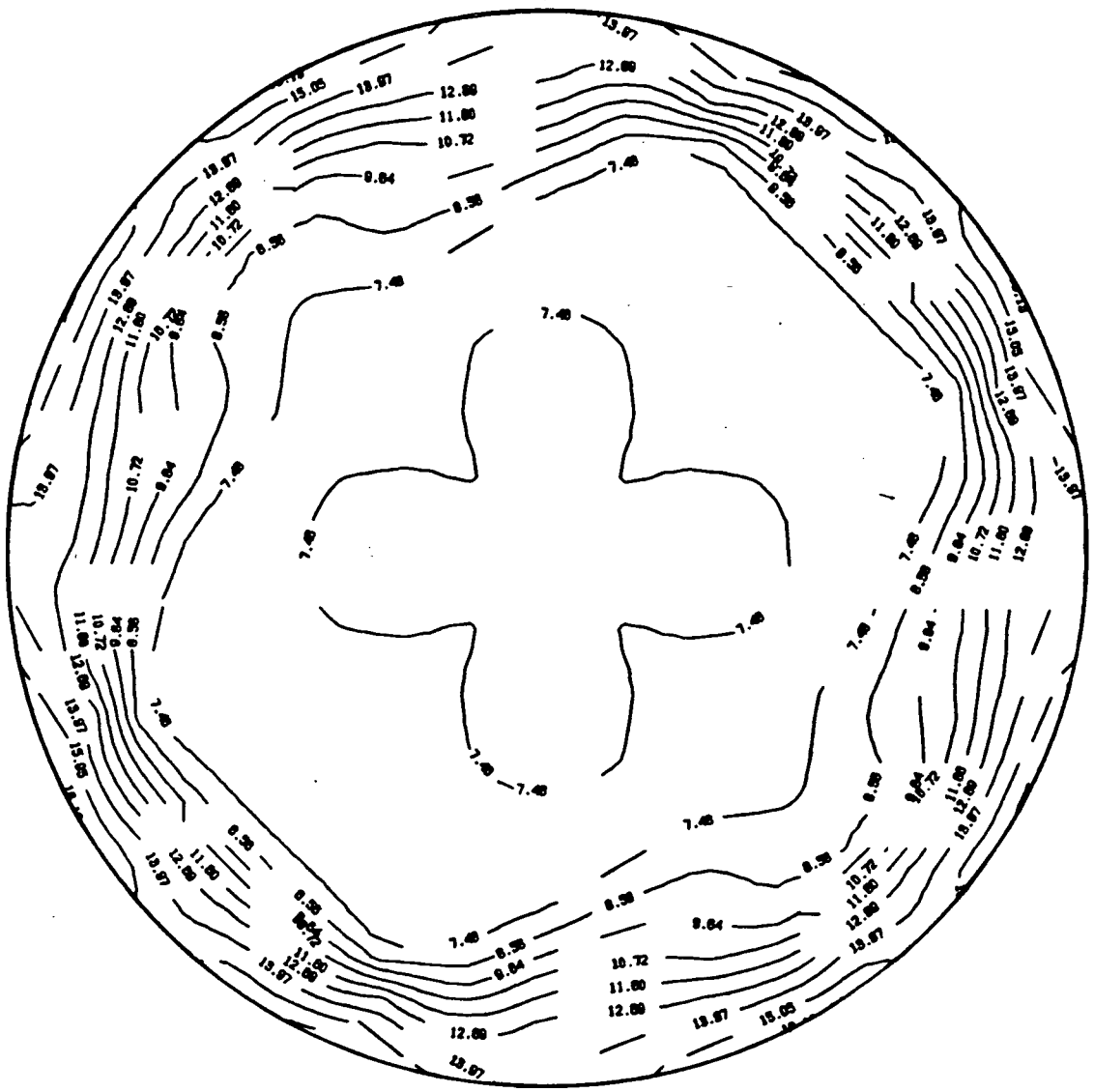

C

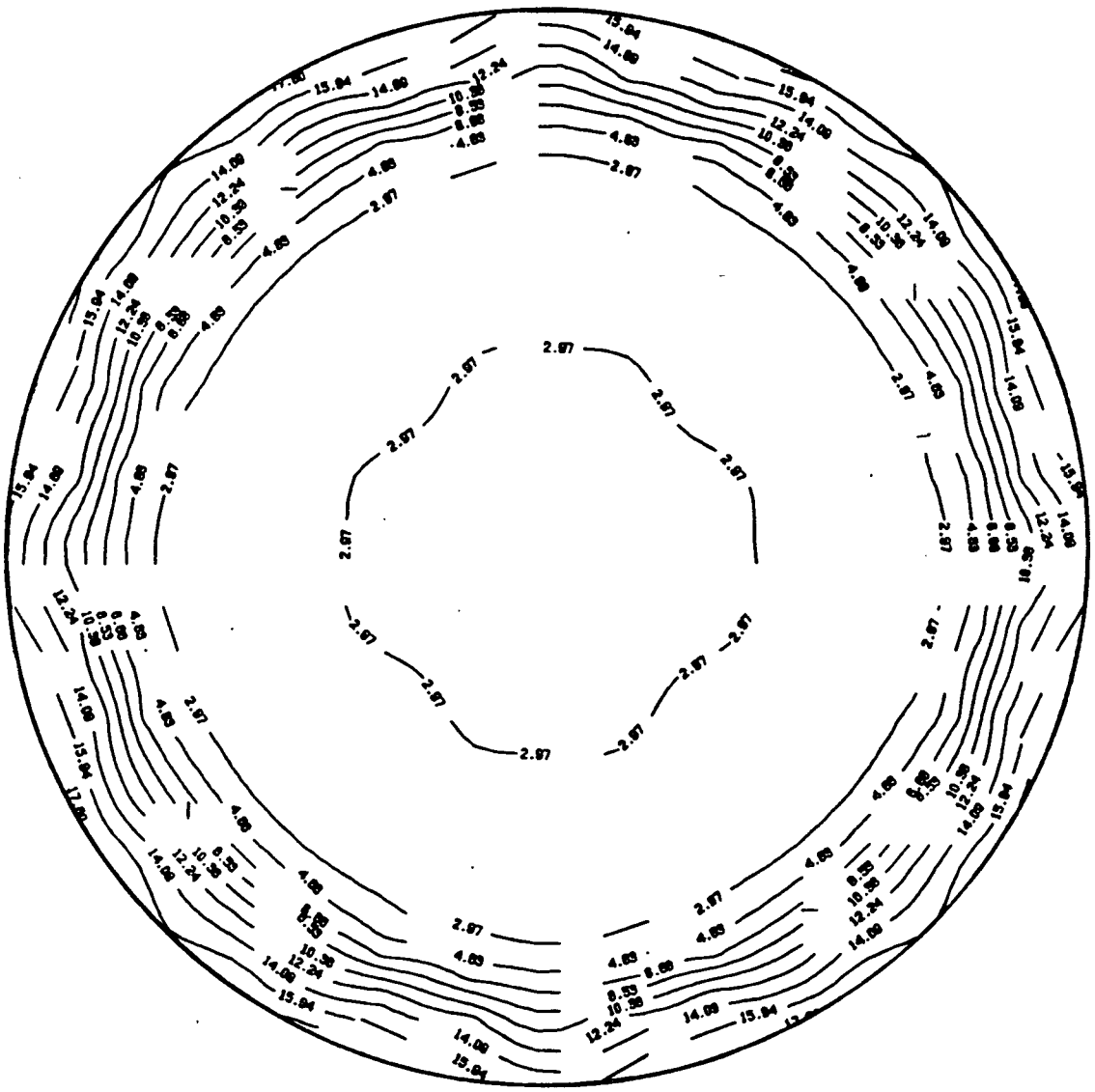

d

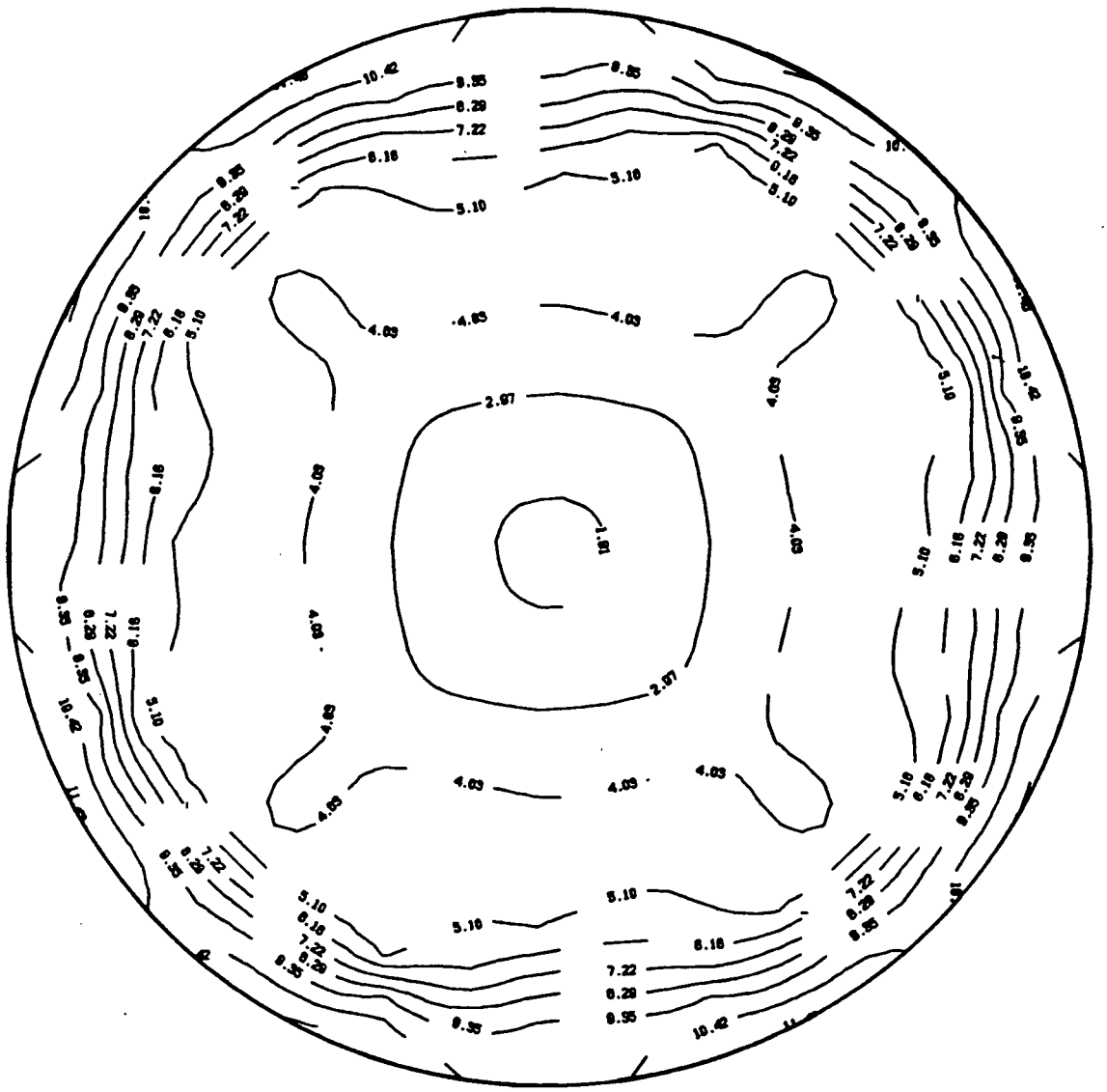

XIV.1.1.1.2 MRSS-CRSS (Yield) in cross-sections at a distance from the interface of :
(a) 2.75 mm ; (b) 8.25 mm ; (c) 16.5 mm ;
(d) 25.5 mm .

a

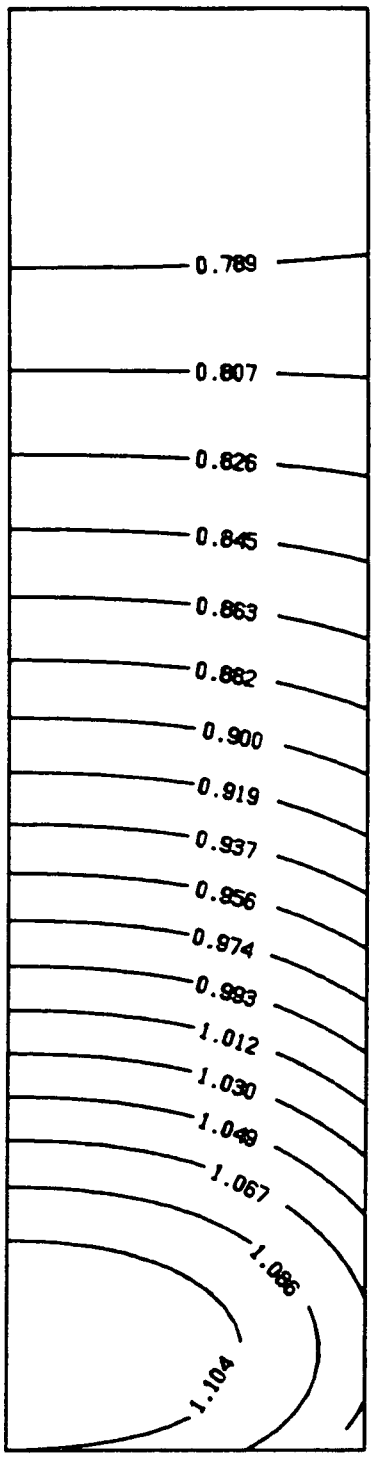
0.789
0.807
0.826
0.845
0.863
0.882
0.900
0.919
0.937
0.956
0.974
0.993
1.012
1.030
1.049
1.067
1.086
1.104

b

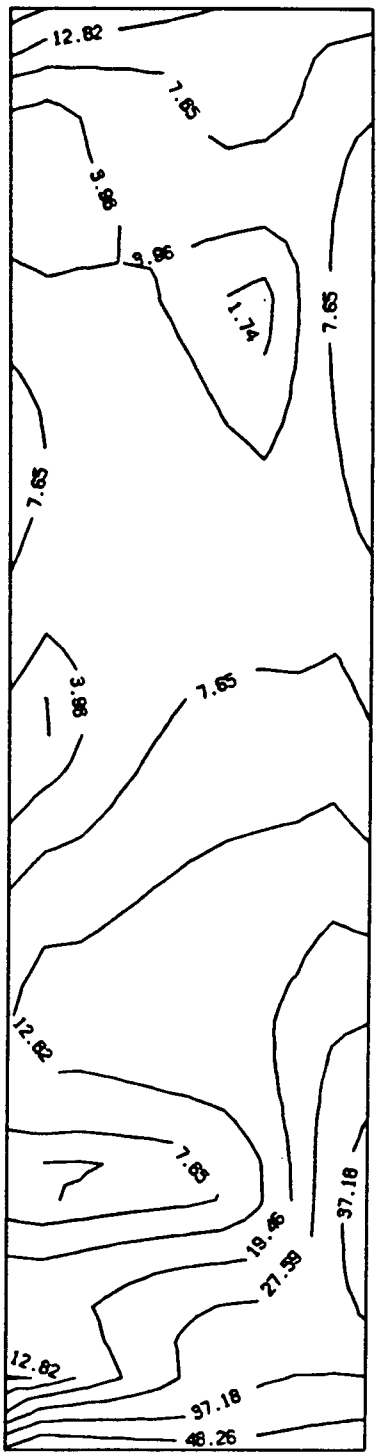
12.82
7.65
3.88
9.96
1.74
7.65
7.65
3.88
7.65
12.82
7.65
19.46
27.59
37.18
12.82
97.18
48.26

c

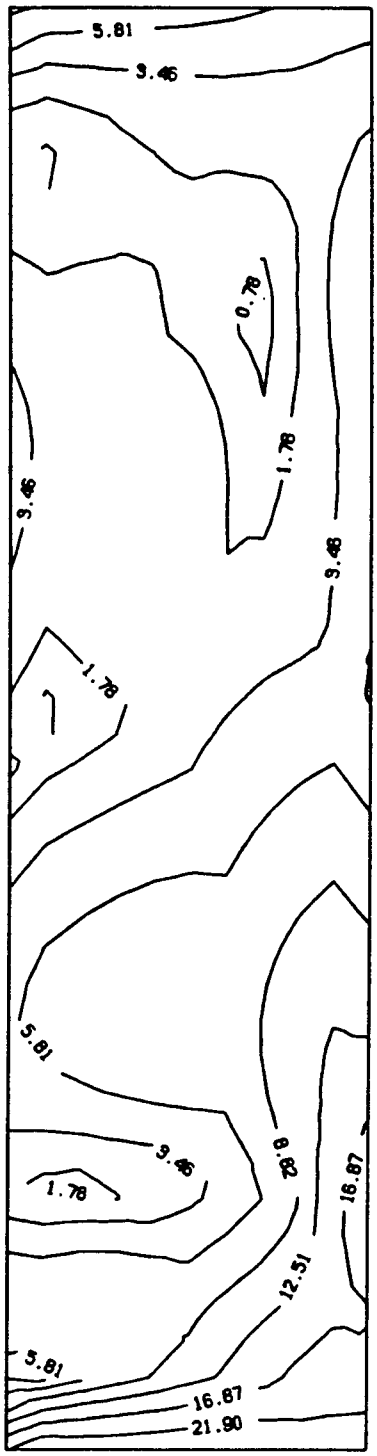
5.81
9.46
0.78
1.78
9.46
9.46
1.78
5.81
9.46
1.78
8.82
16.87
12.51
5.81
16.87
21.90

d

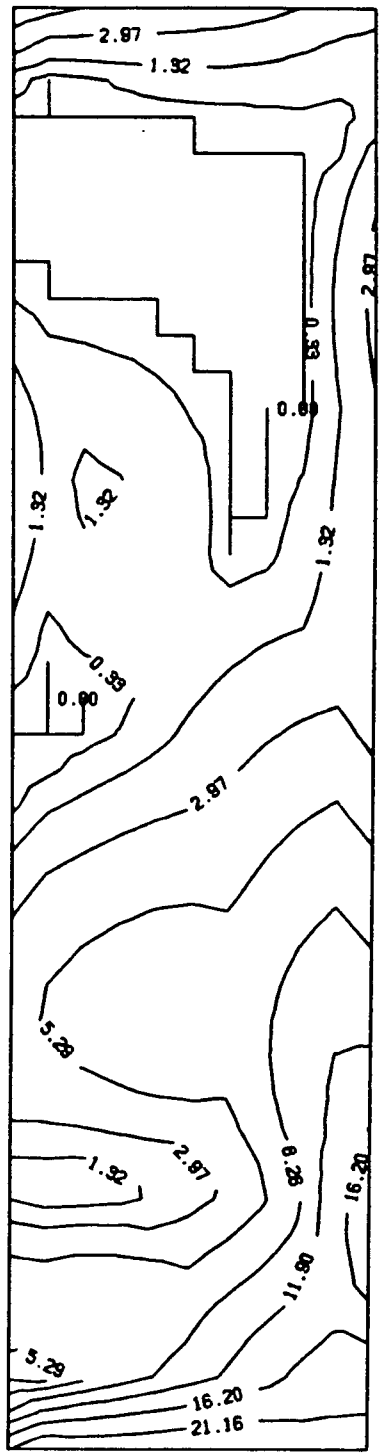
2.97
1.92
0.93
0.80
1.92
1.92
1.92
0.93
0.80
2.97
5.29
2.97
1.92
8.28
16.20
11.90
5.29
16.20
21.16

e

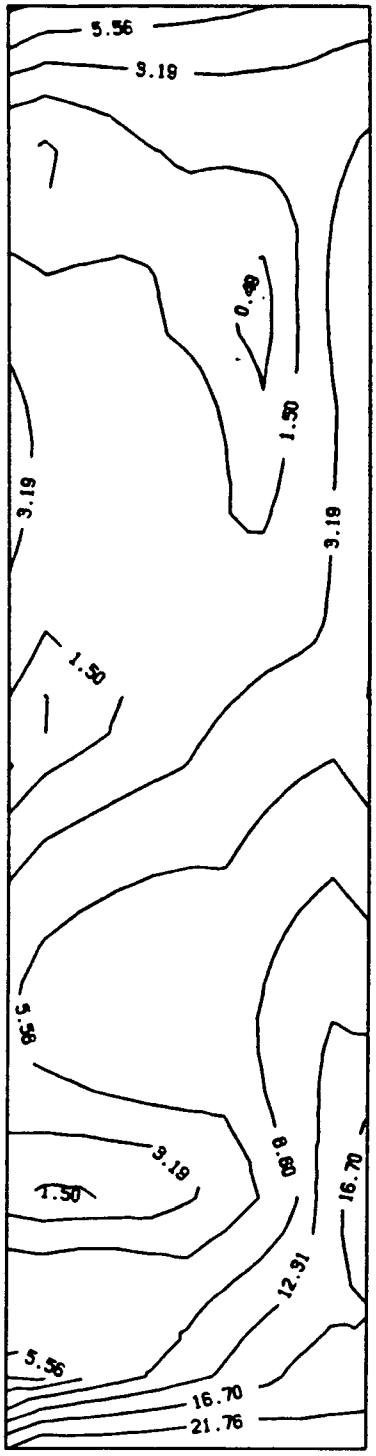

f

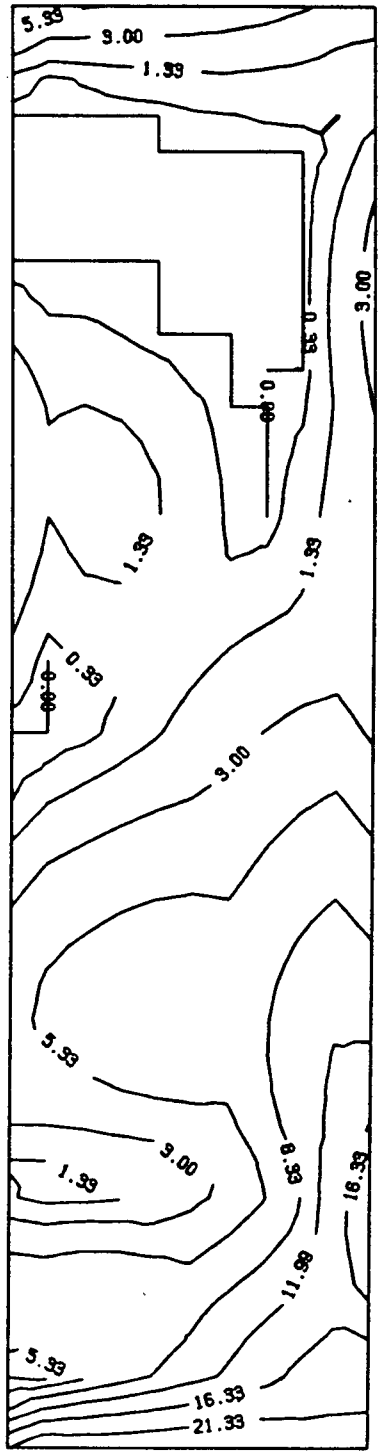

XIV.1.1.2 Time 20 seconds
(a) Temperature ; (b) Von Mises Stress
(c) MRSS ; (d) MRSS-CRSS (Yield) ;
(e) MRSS-CRSS (MB) ; (f) MRSS-CRSS (MBTe) .

a

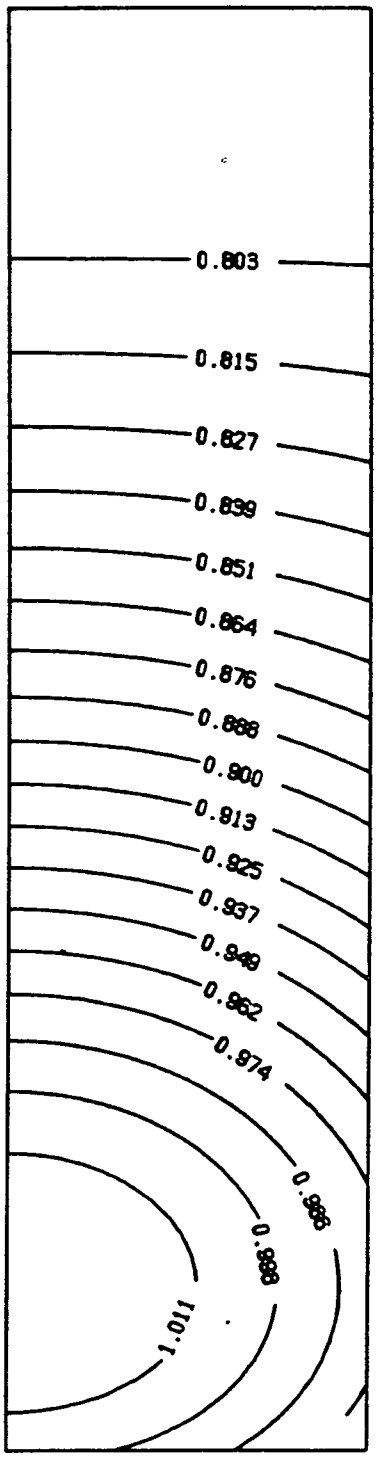
0.803
0.815
0.827
0.839
0.851
0.864
0.876
0.888
0.900
0.913
0.925
0.937
0.949
0.962
0.974
0.986
0.998
1.011

b

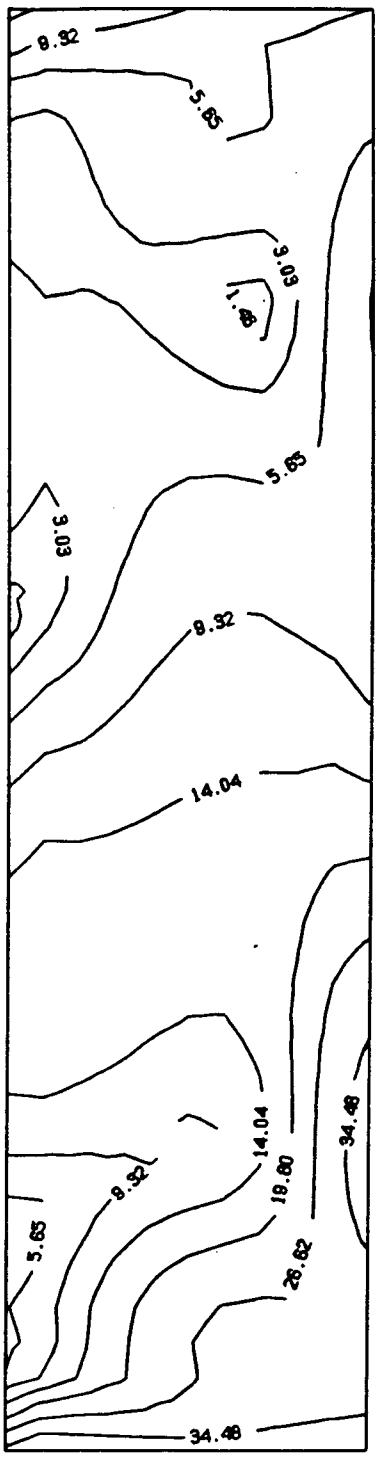
9.32
5.65
3.03
1.48
5.65
3.03
9.32
14.04
14.04
19.80
34.48
9.32
5.65
26.62
34.48

c

4.24
2.58
0.00
1.99
2.58
1.58
4.24
6.37
6.37
8.99
15.61
2.58
4.24
12.06
15.61

d

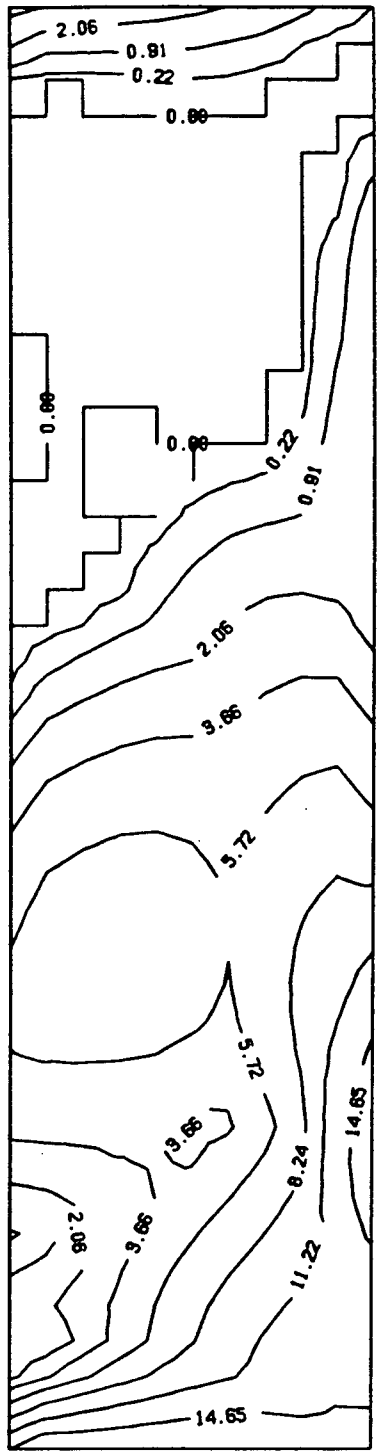
2.06
0.91
0.22
0.00
0.00
0.00
0.22
0.91
2.06
3.66
5.72
5.72
3.66
8.24
14.65
2.06
3.66
11.22
14.65

e

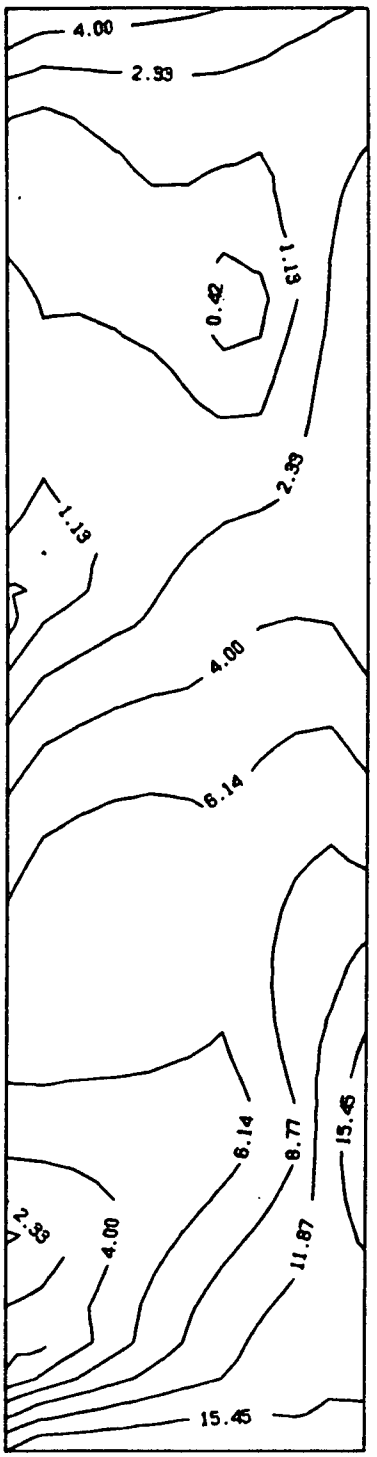

f

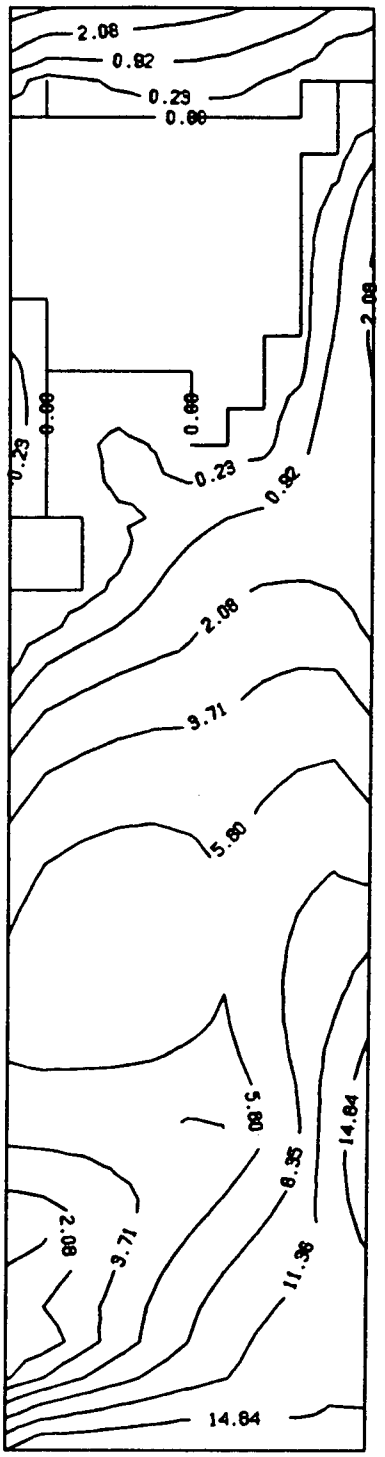

XIV.1.1.3 Time 60 seconds
(a) Temperature ; (b) Von Mises Stress
(c) MRSS ; (d) MRSS-CRSS (Yield) ;
(e) MRSS-CRSS (MB) ; (f) MRSS-CRSS (MBTe) .

a

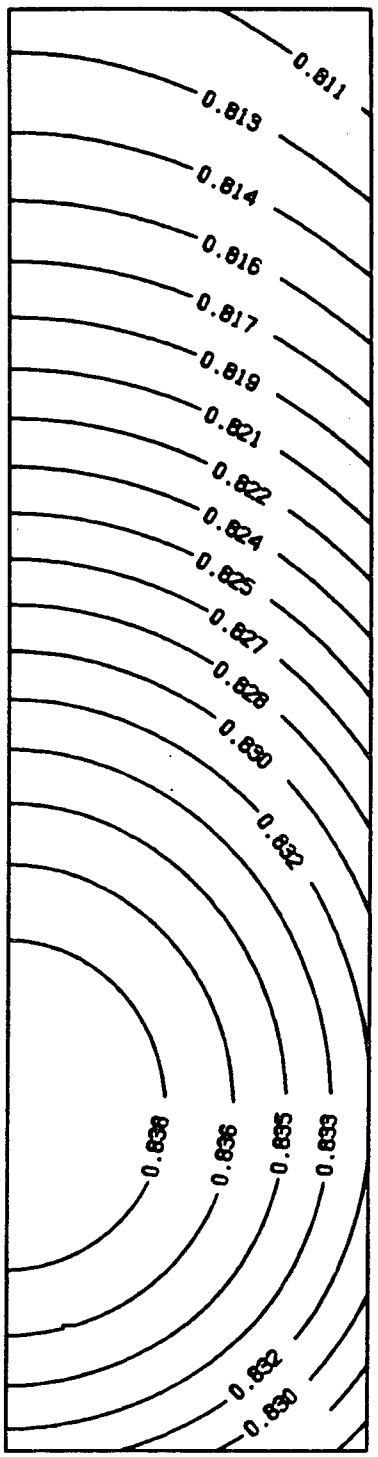
0.811
0.813
0.814
0.816
0.817
0.819
0.821
0.822
0.824
0.825
0.827
0.828
0.830
0.832
0.833
0.835
0.836
0.838
0.832
0.830

b

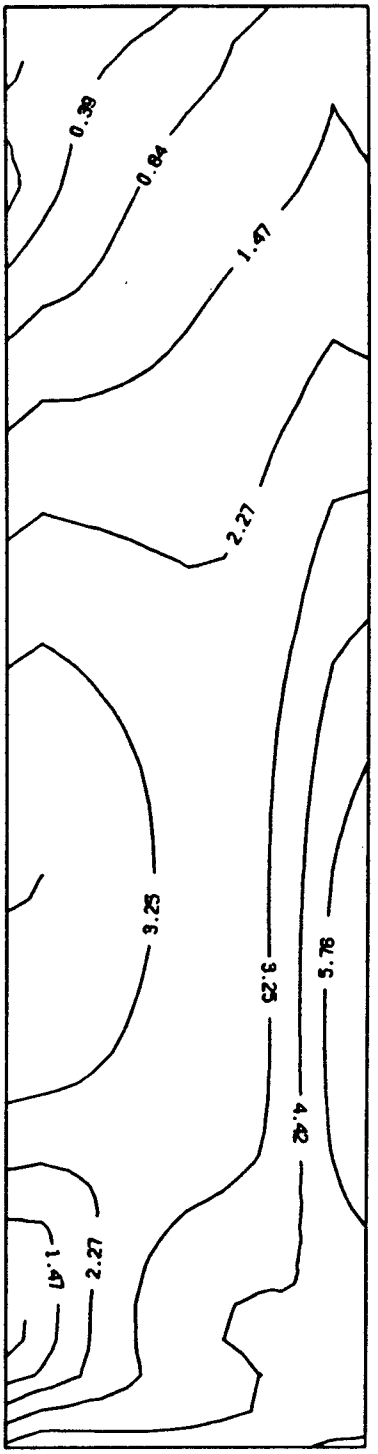
0.38
0.64
1.47
2.27
3.23
5.78
4.42
3.23
2.27
1.47

c

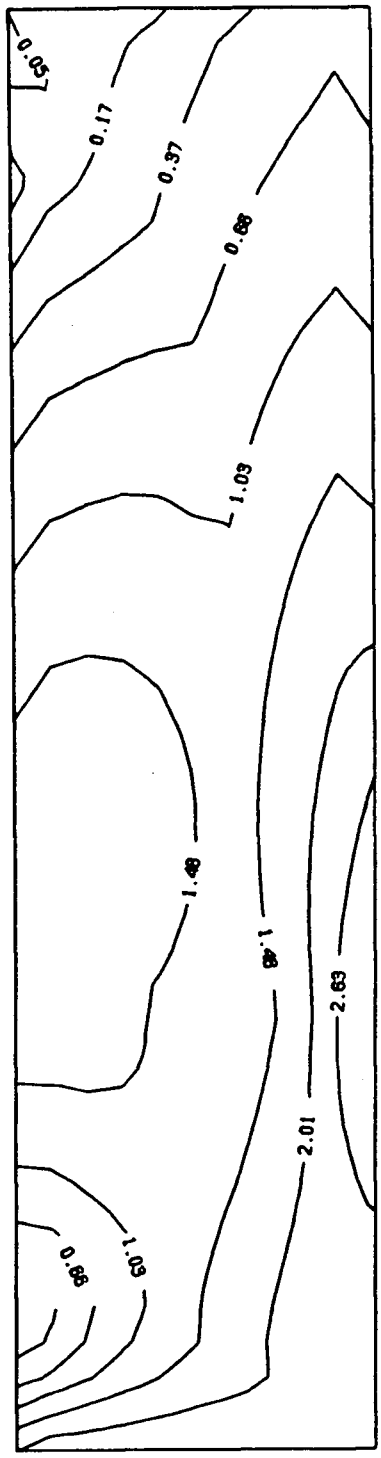

d

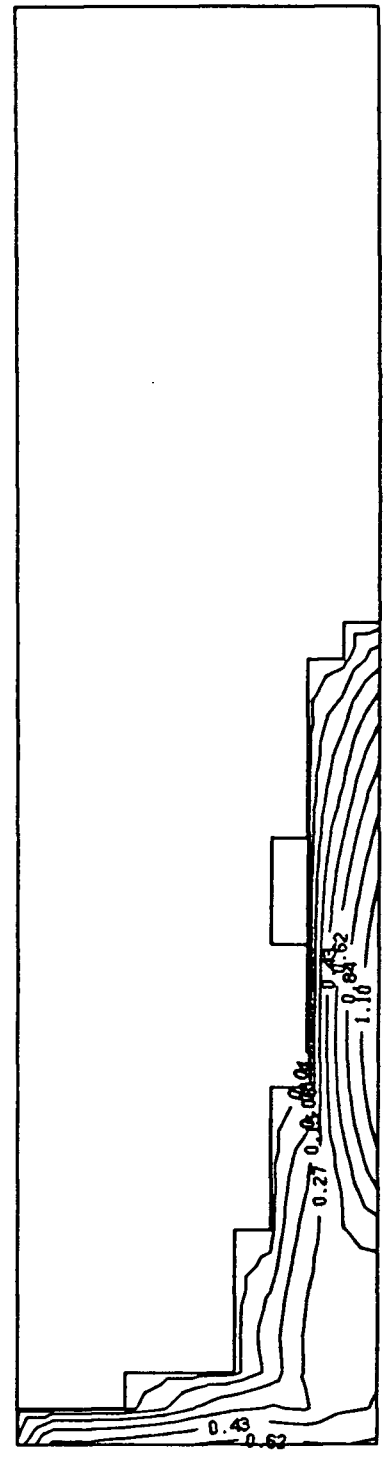

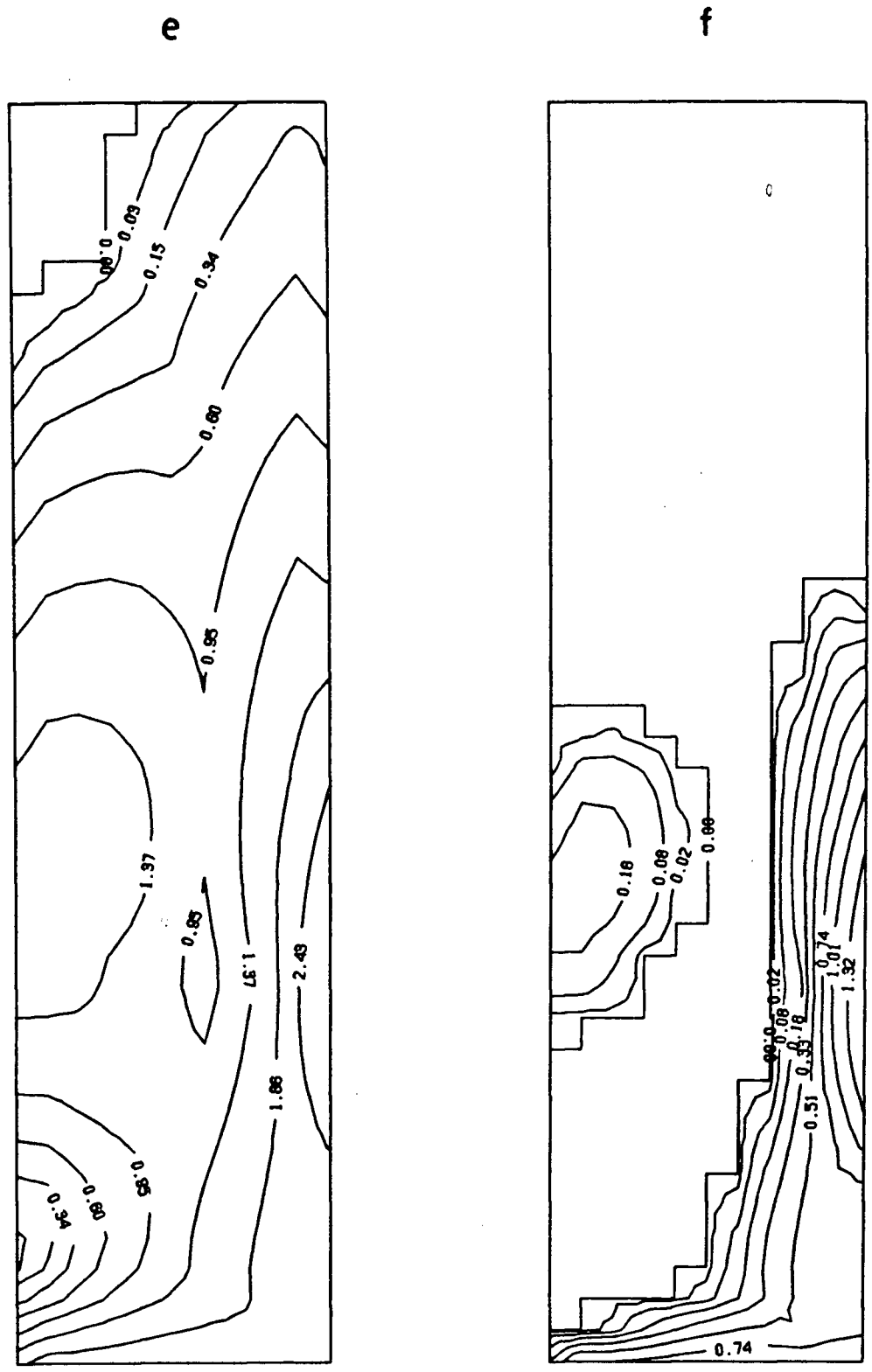

XIV.1.1.4 Time 300 seconds
(a) Temperature ; (b) Von Mises Stress
(c) MRSS ; (d) MRSS-CRSS (Yield) ;
(e) MRSS-CRSS (MB) ; (f) MRSS-CRSS (MBTe) .

a

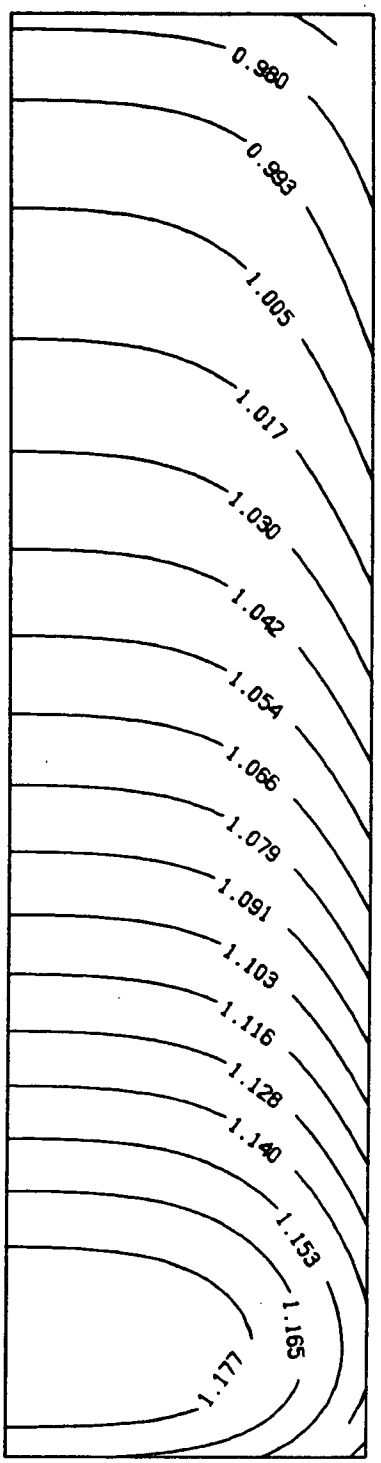
0.980
0.993
1.005
1.017
1.030
1.042
1.054
1.066
1.079
1.091
1.103
1.116
1.128
1.140
1.153
1.165
1.177

b

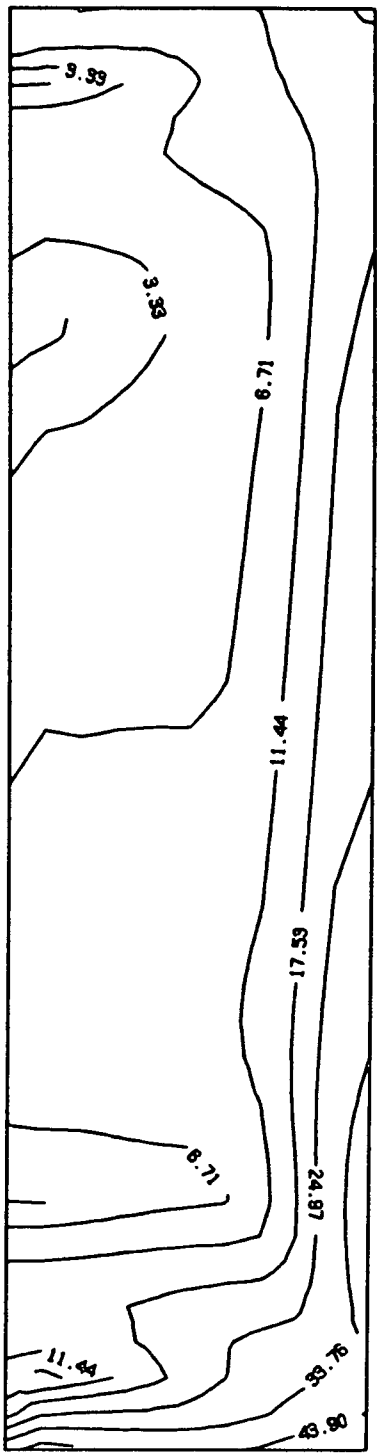
3.93
6.71
11.44
17.59
24.97
33.76
43.90

c

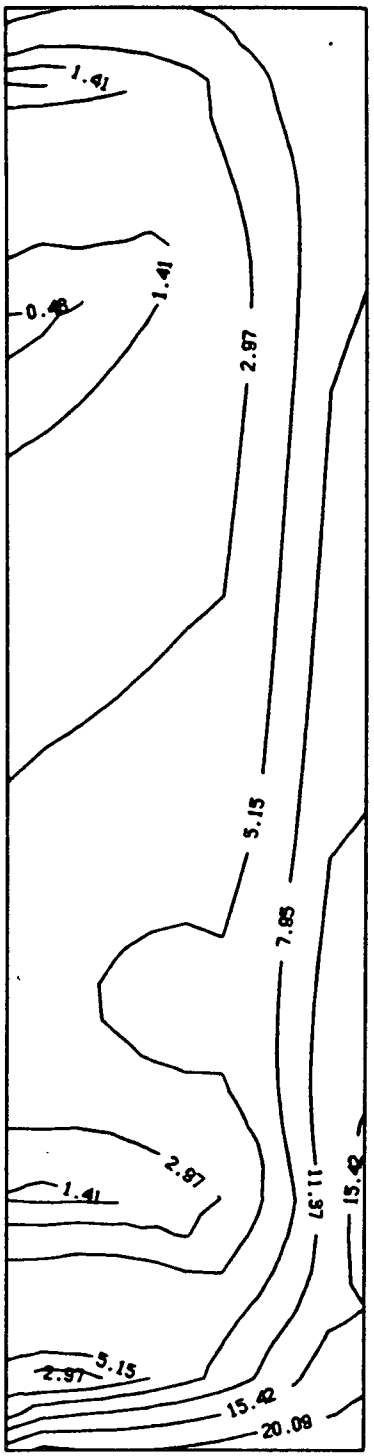
1.41
1.41
0.48
2.97
5.15
7.85
11.97
15.42
2.87
1.41
5.15
2.97
15.42
20.09

d

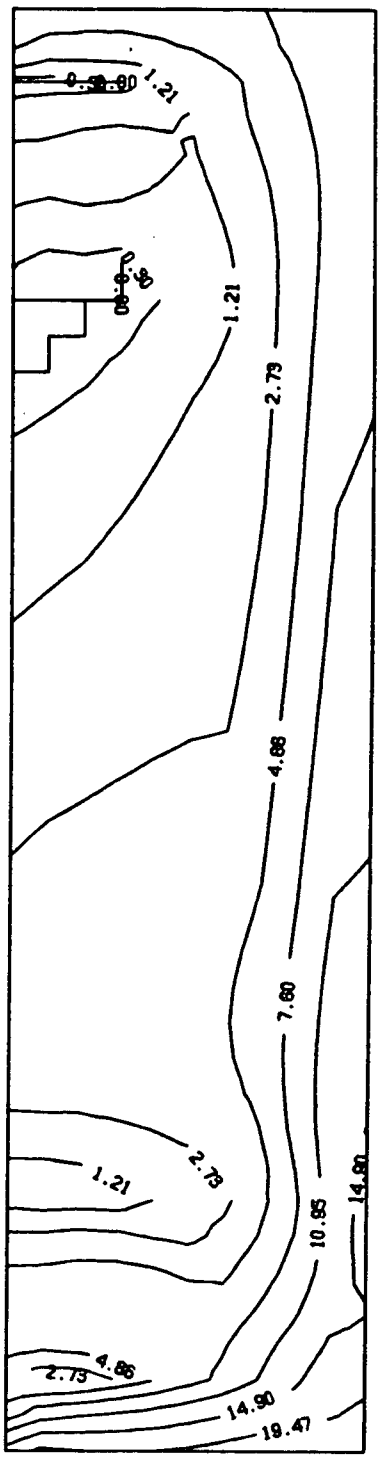
1.21
0.80
0.80
1.21
2.79
4.88
7.60
10.95
14.90
1.21
2.73
4.88
2.73
14.90
19.47

e

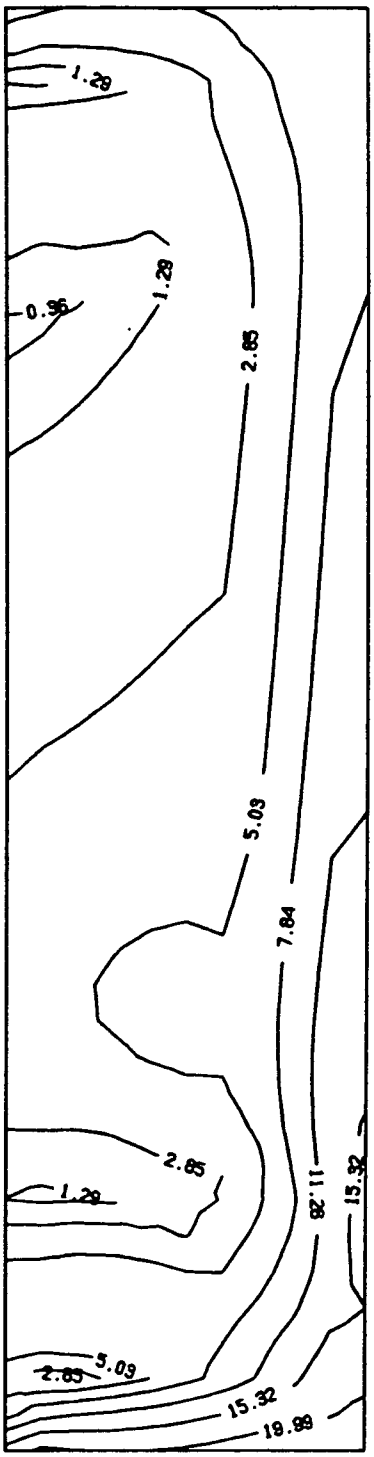

f

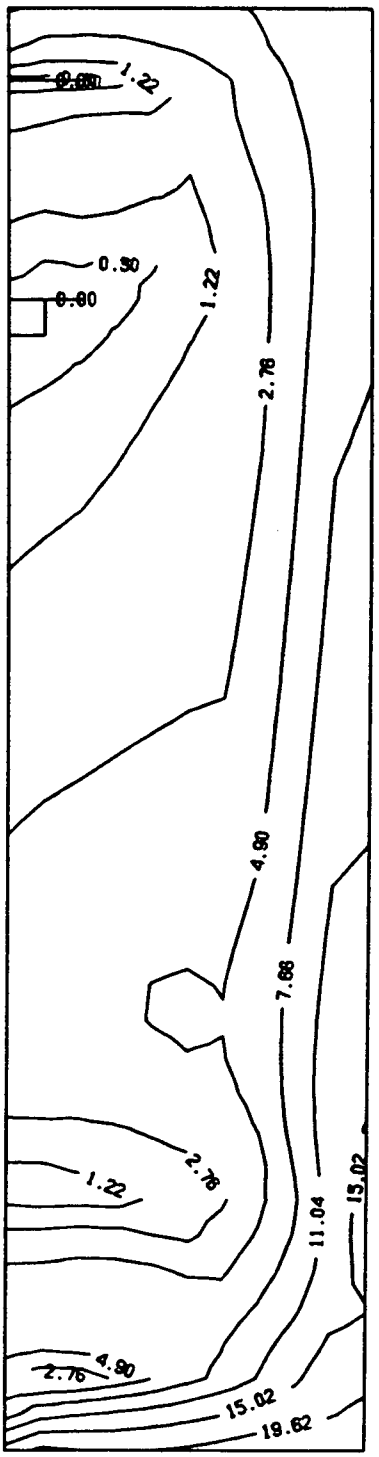

XIV.1.2.1 (a) Temperature ; (b) Von Mises Stress
(c) MRSS ; (d) MRSS-CRSS (Yield) ;
(e) MRSS-CRSS (MB) ; (f) MRSS-CRSS (MBTe) .

a

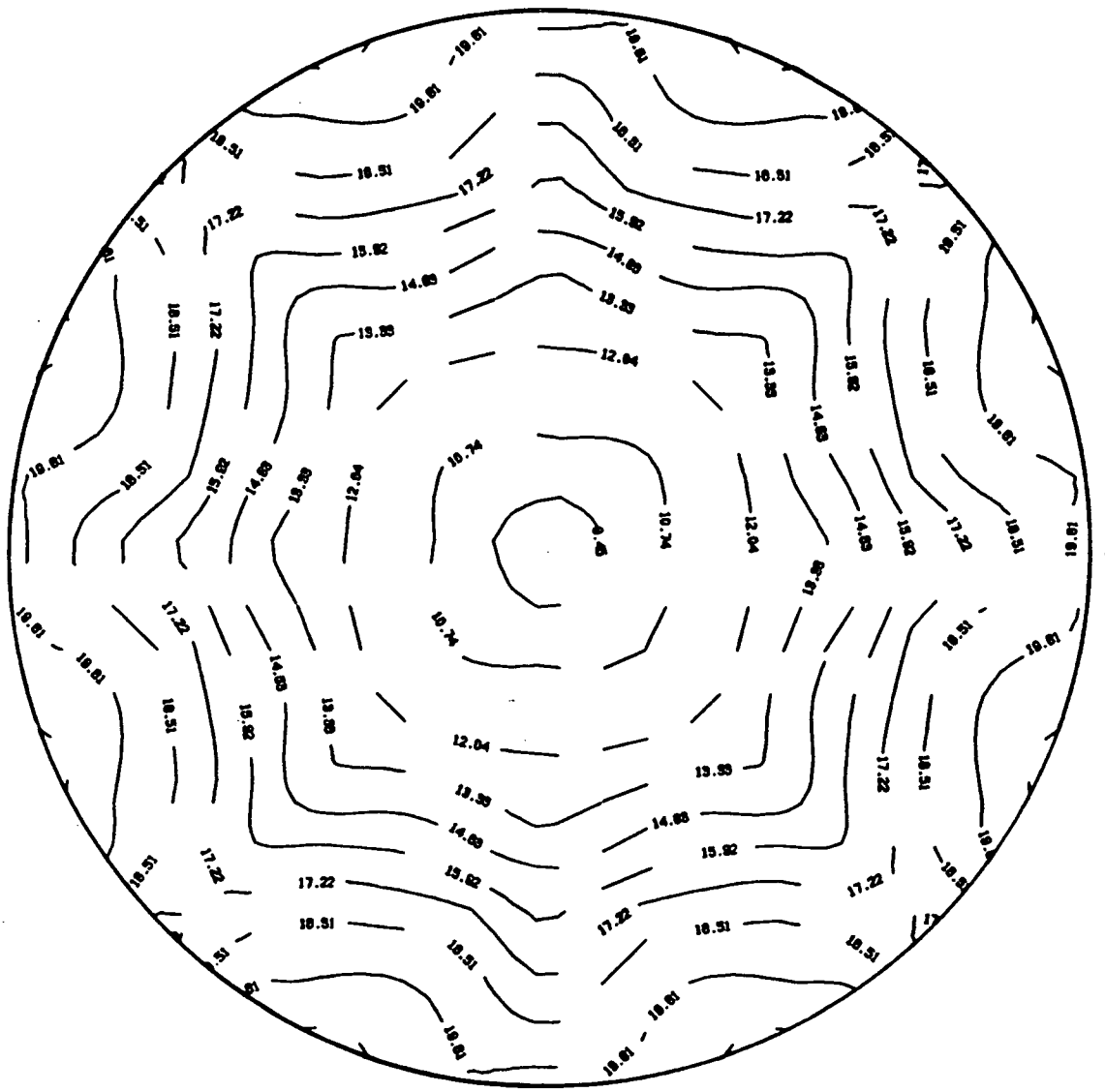

b

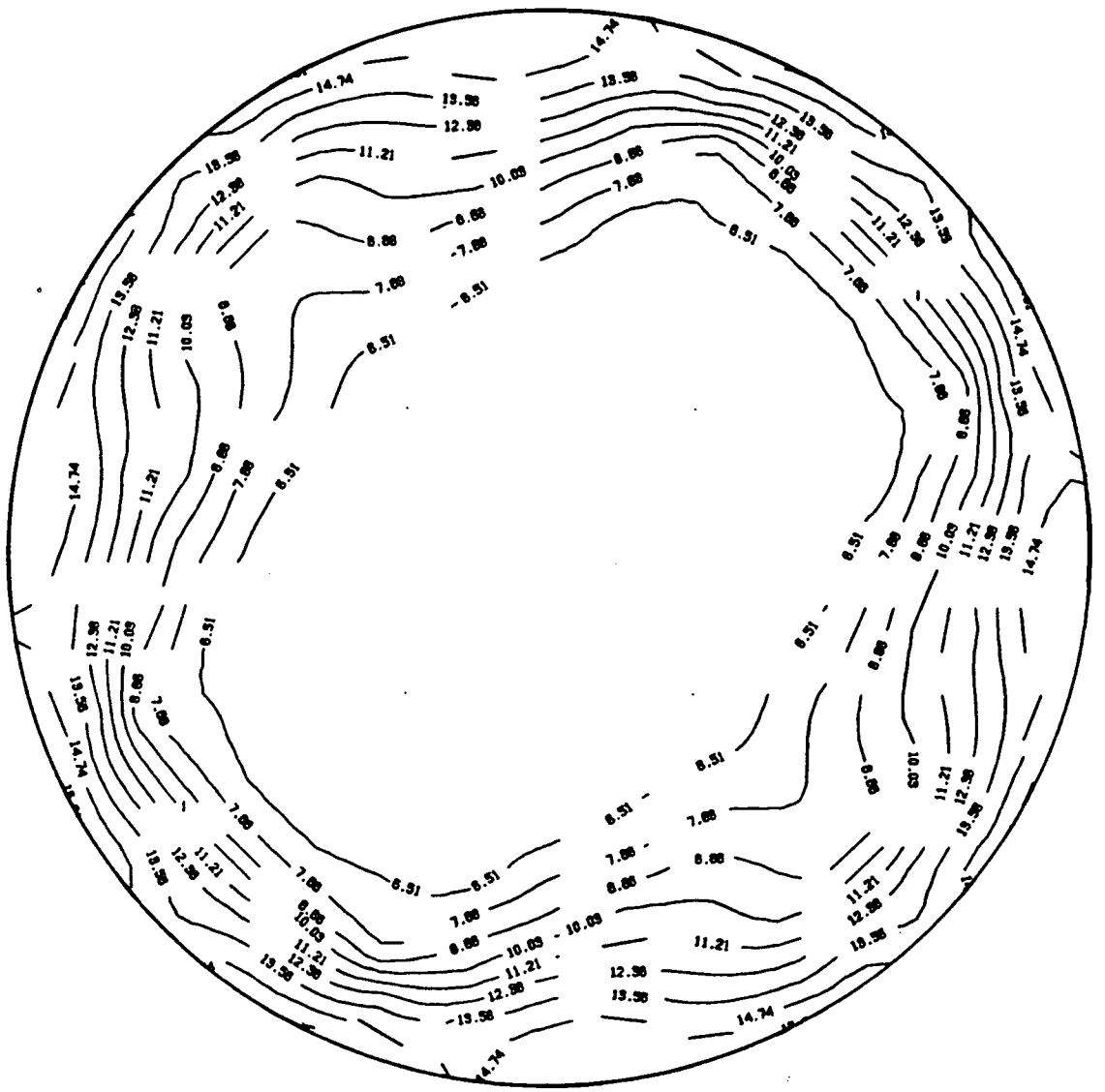

C

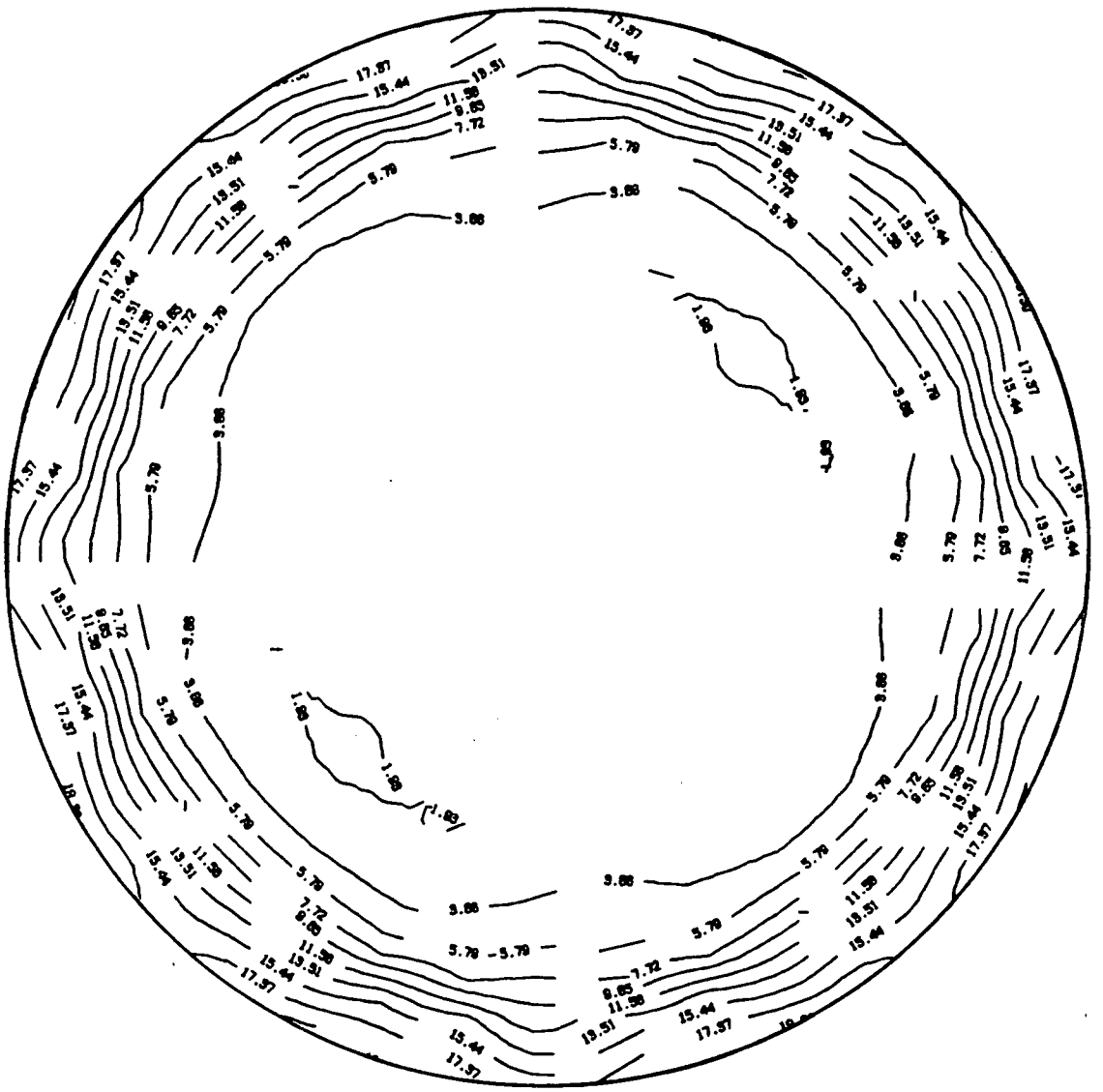

d

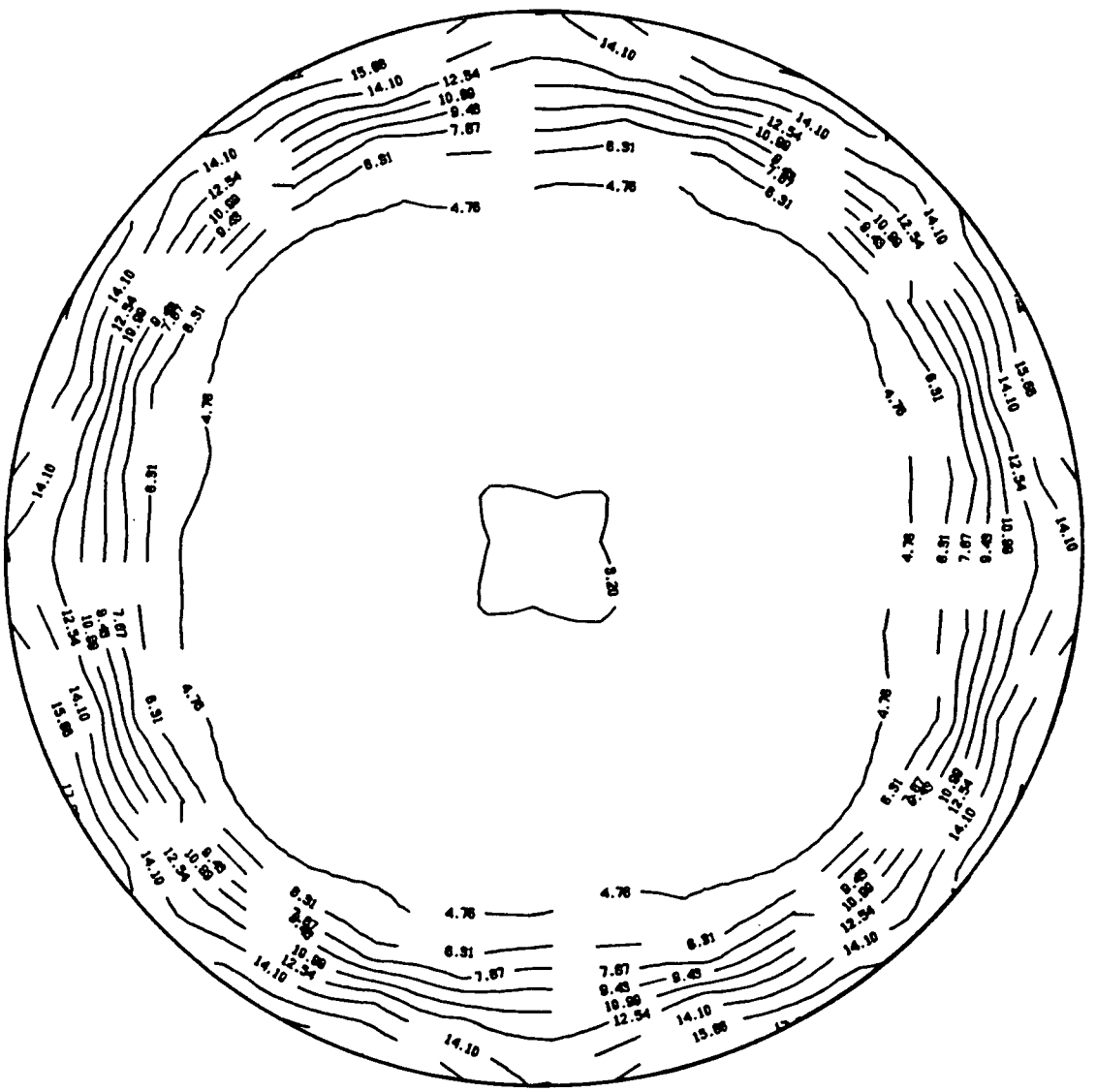

XIV.1.2.2 MRSS-CRSS (Yield) in cross-sections at a distance from the interface of :
(a) 2.75 mm ; (b) 8.25 mm ; (c) 16.5 mm ;
(d) 27.5 mm .

a

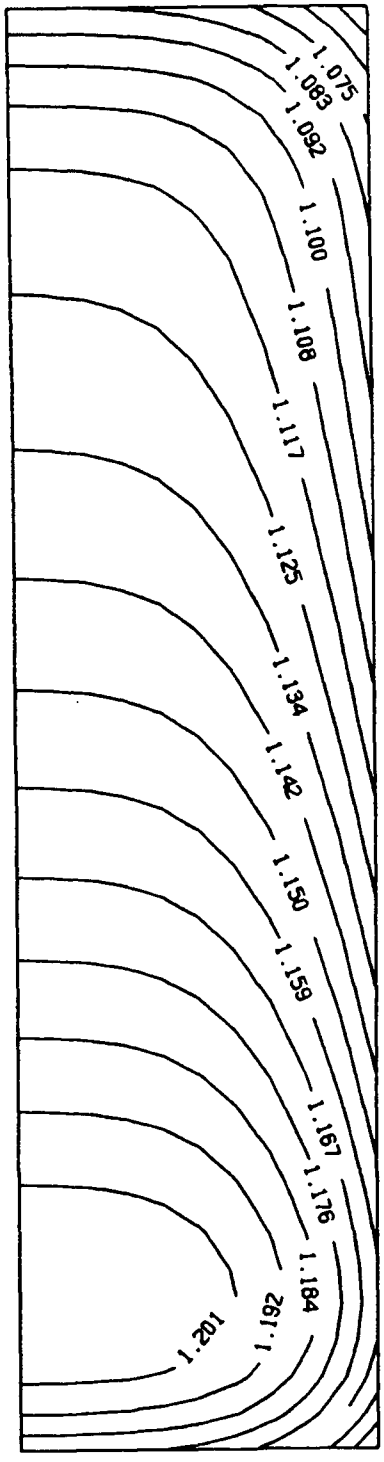
1.075
1.083
1.092
1.100
1.108
1.117
1.125
1.134
1.142
1.150
1.159
1.167
1.176
1.184
1.192
1.201

b

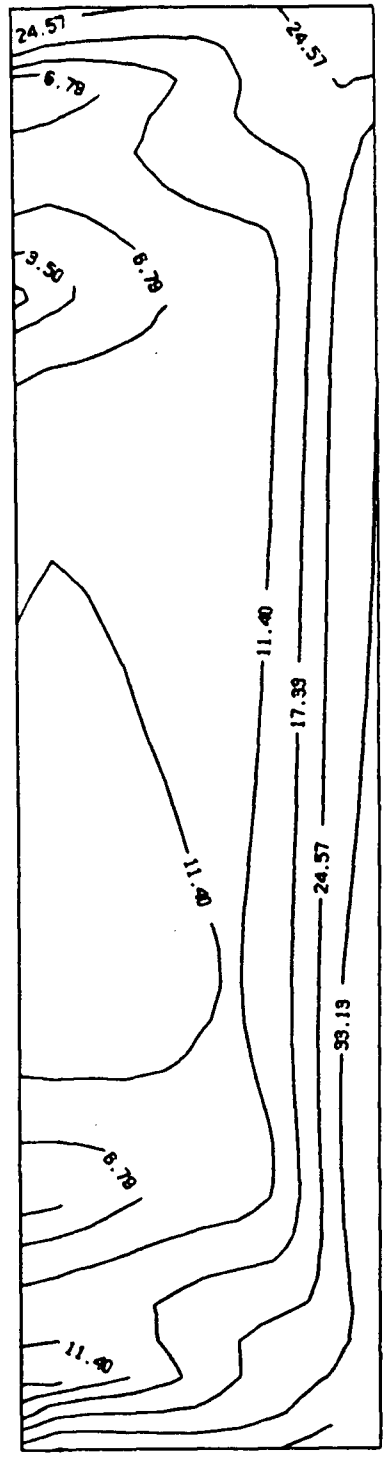
24.57
24.57
6.78
6.78
3.50
11.40
17.39
24.57
33.13
11.40
6.78
11.40

c

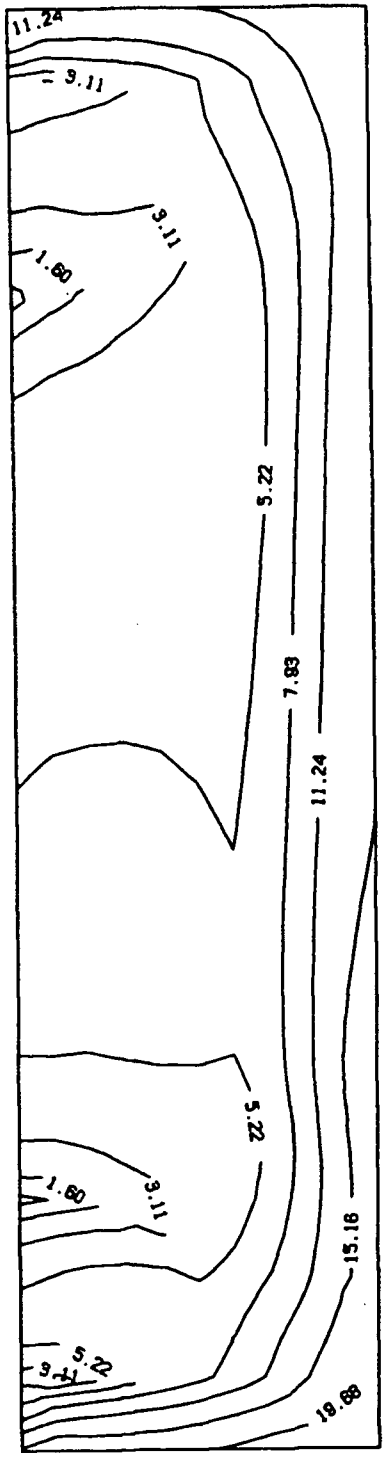
11.24
3.11
3.11
1.60
5.22
7.83
11.24
5.22
1.60
3.11
15.16
5.22
3.11
19.68

d

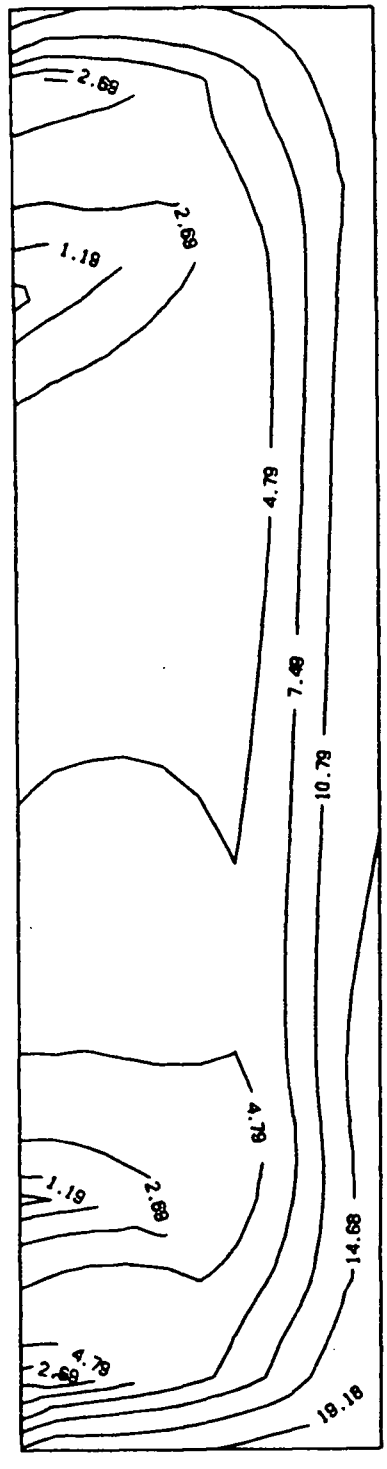
2.69
2.69
1.18
4.79
7.49
10.79
4.79
1.19
2.69
14.68
2.69
4.79
19.18

e

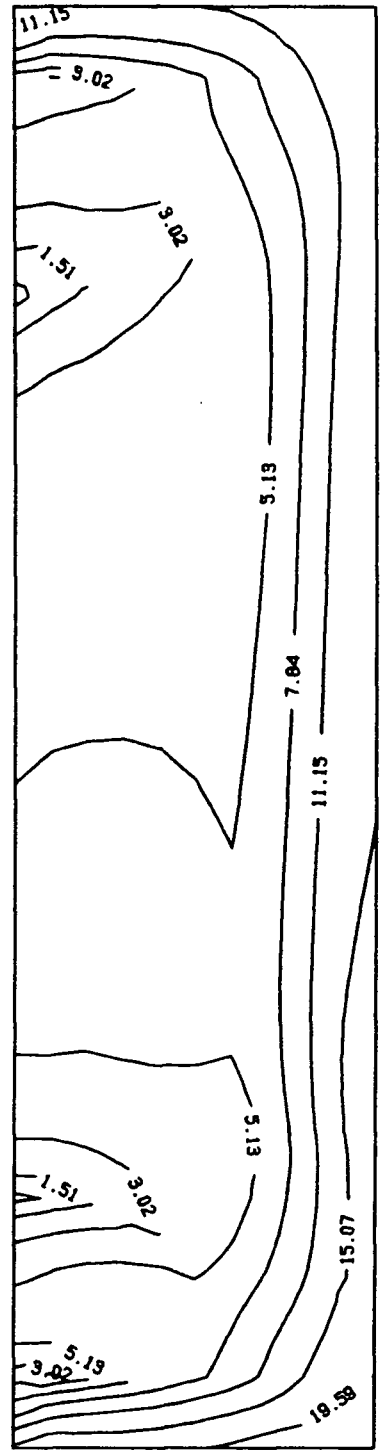

XIV.1.3.1.1 (a) Temperature ; (b) Von Mises Stress
(c) MRSS ; (d) MRSS-CRSS (Yield) ;
(e) MRSS-CRSS (MB) .

a

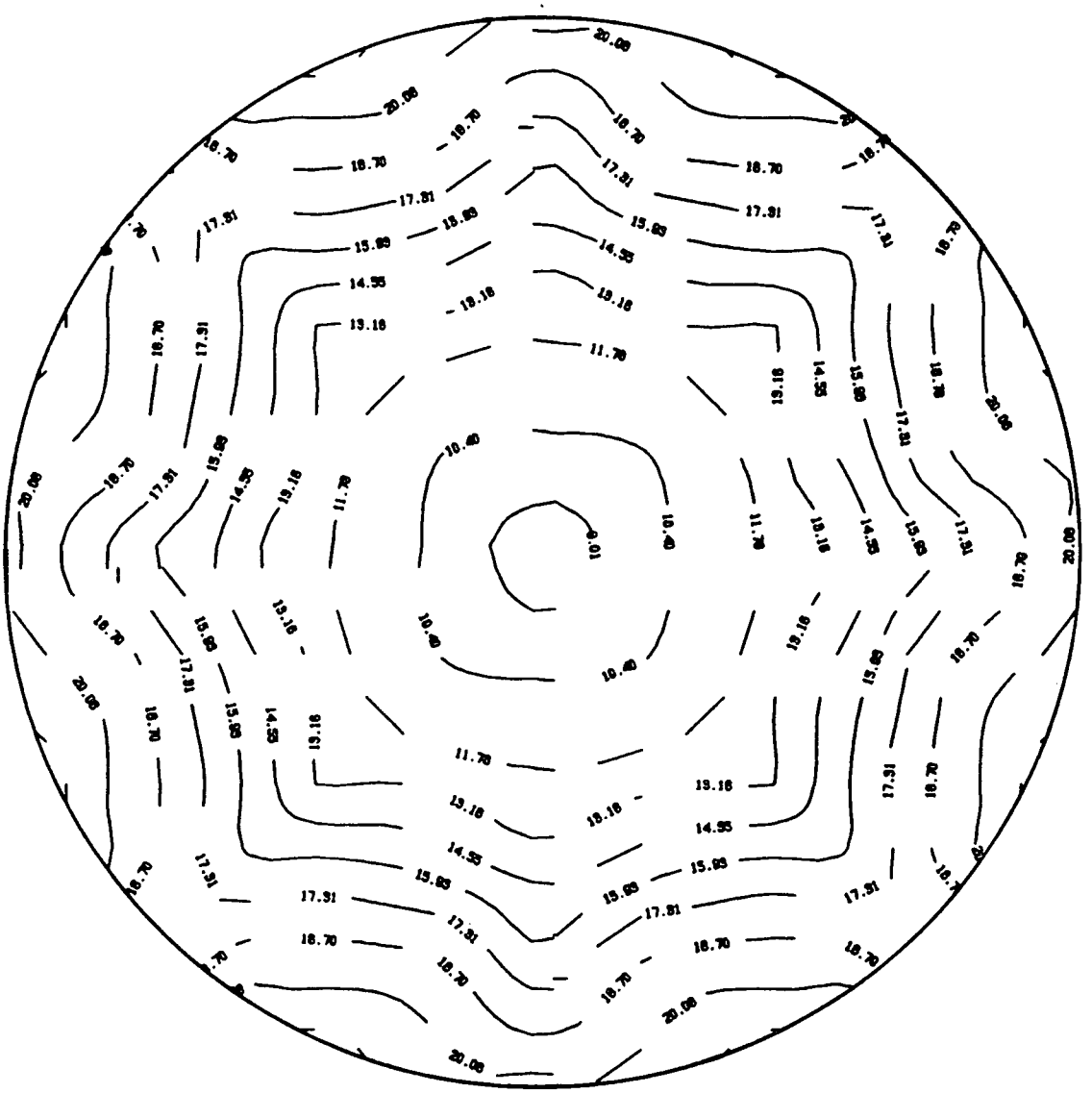

b

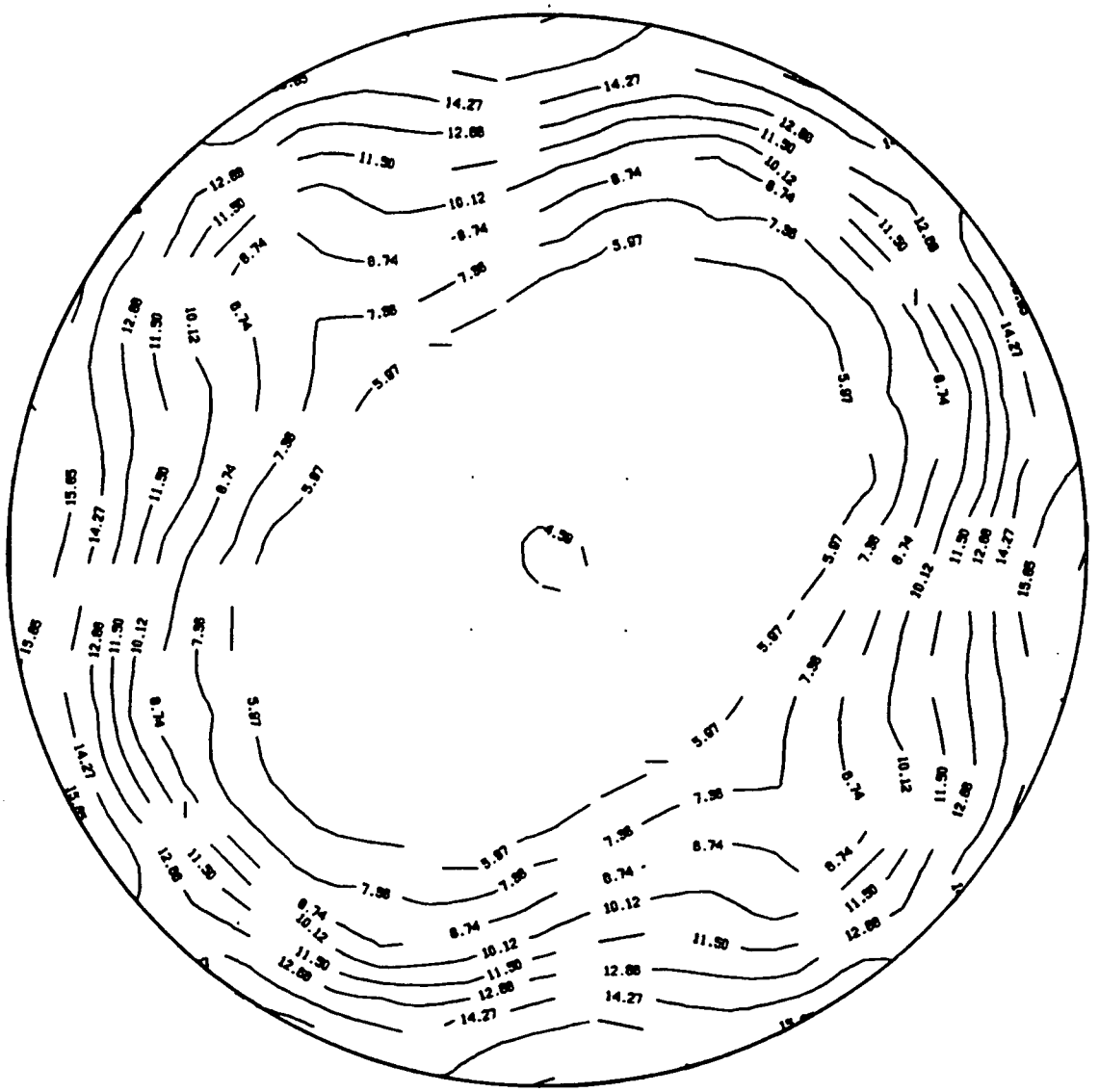

C

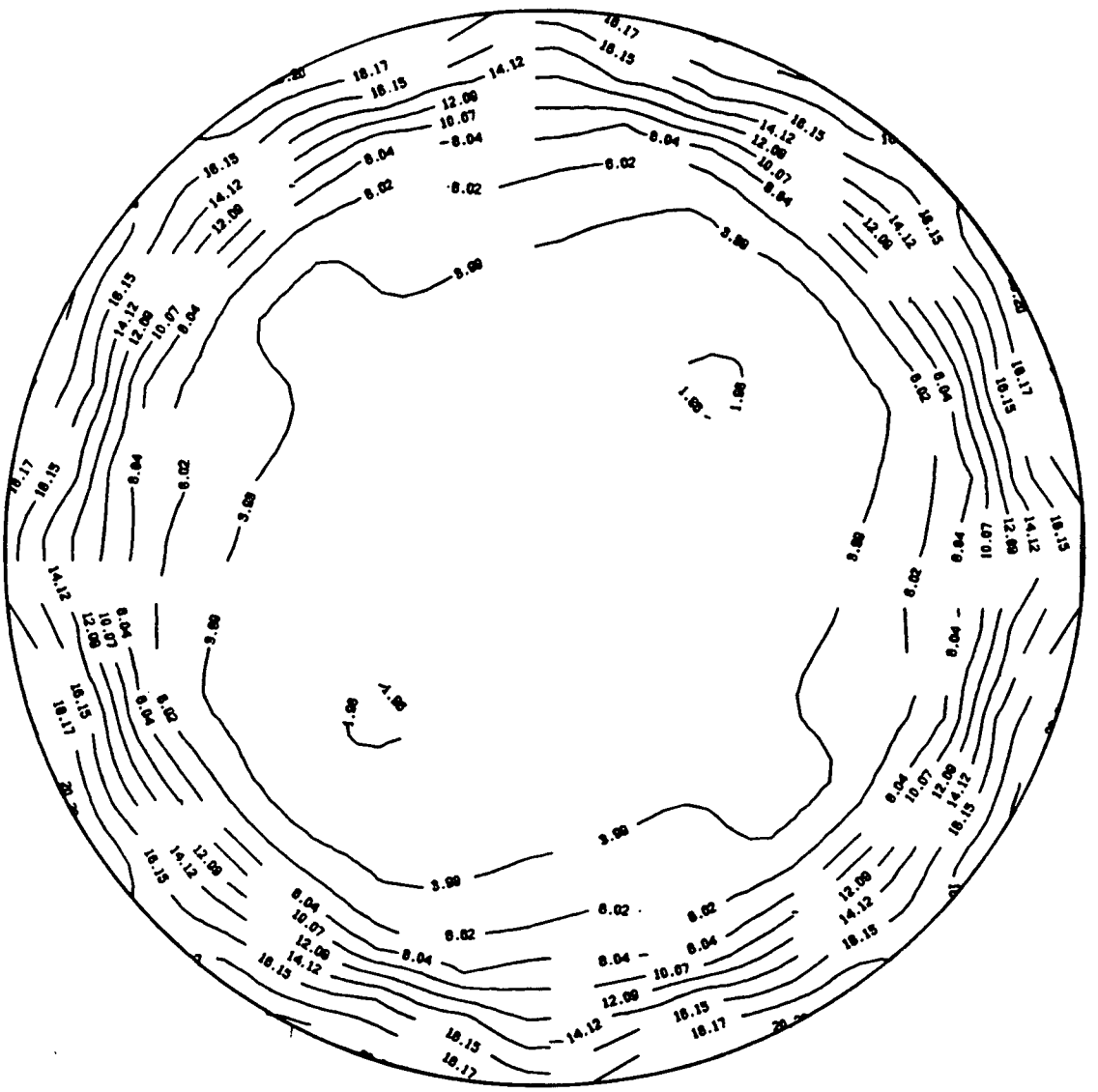

d

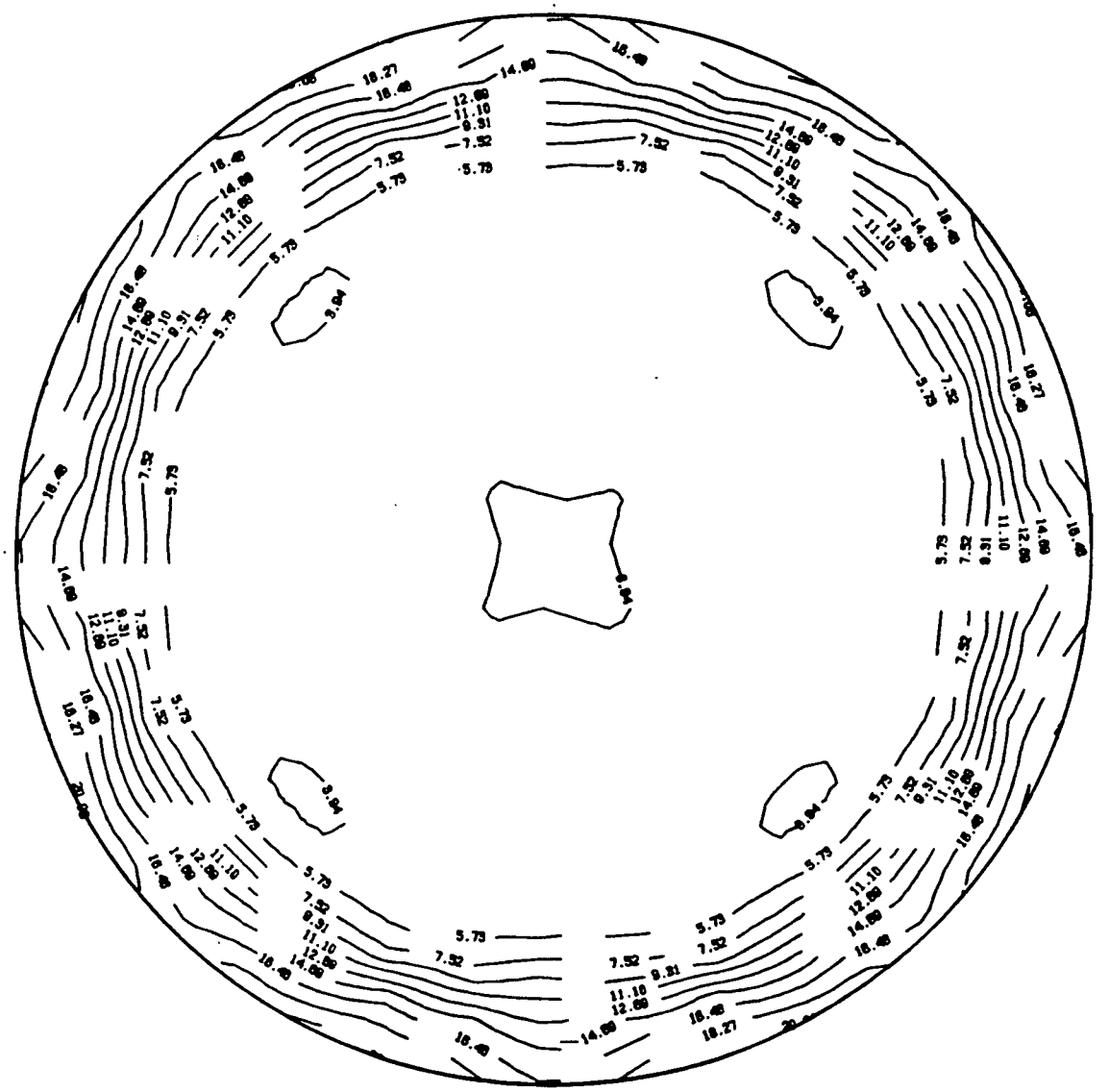

XIV.1.3.1.2 MRSS-CRSS (Yield) in cross-sections at a distance from the interface of :
(a) 2.75 mm ; (b) 8.25 mm ; (c) 16.5 mm ;
(d) 27.5 mm .

a

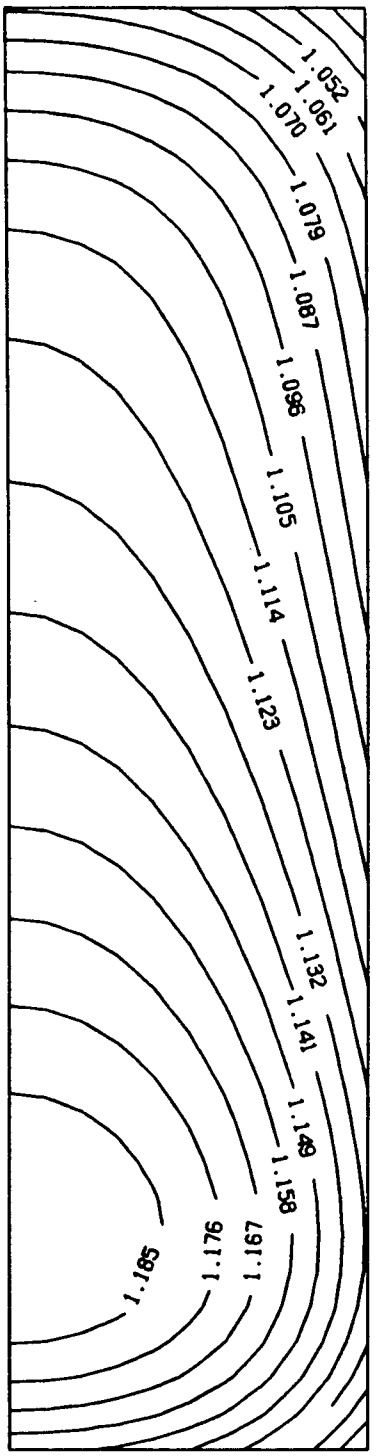
1.052
1.061
1.070
1.079
1.087
1.096
1.105
1.114
1.123
1.132
1.141
1.149
1.158
1.167
1.176
1.185

b

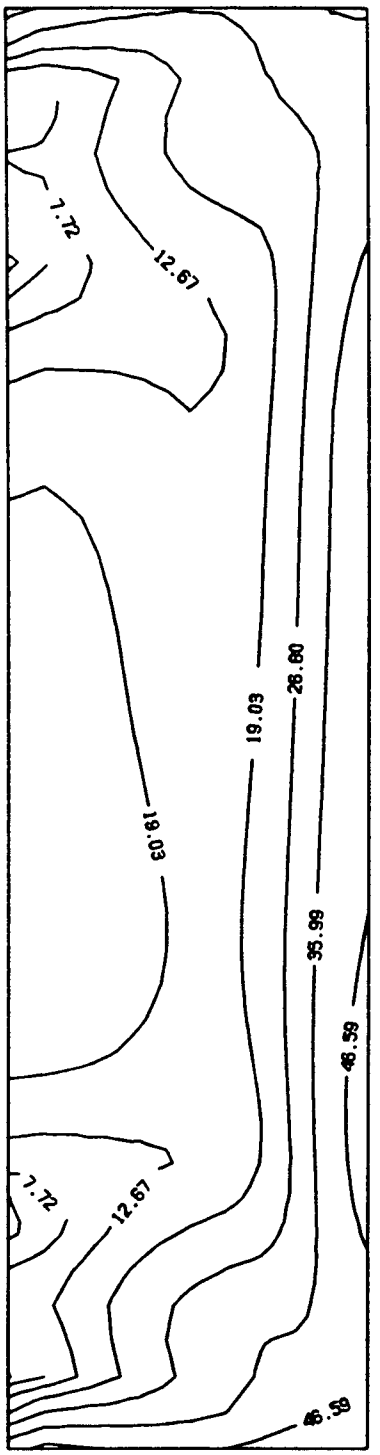
7.72
12.67
19.03
28.80
35.99
46.59
7.72
12.67
19.03

c

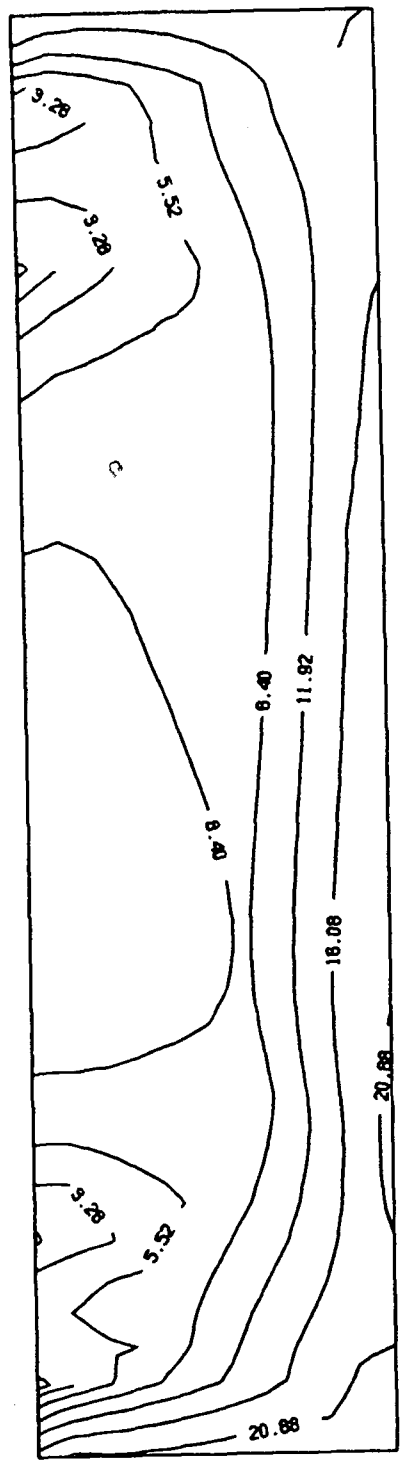
3.28
5.52
3.28
8.40
11.92
16.08
20.88
3.28
5.52
20.88

d

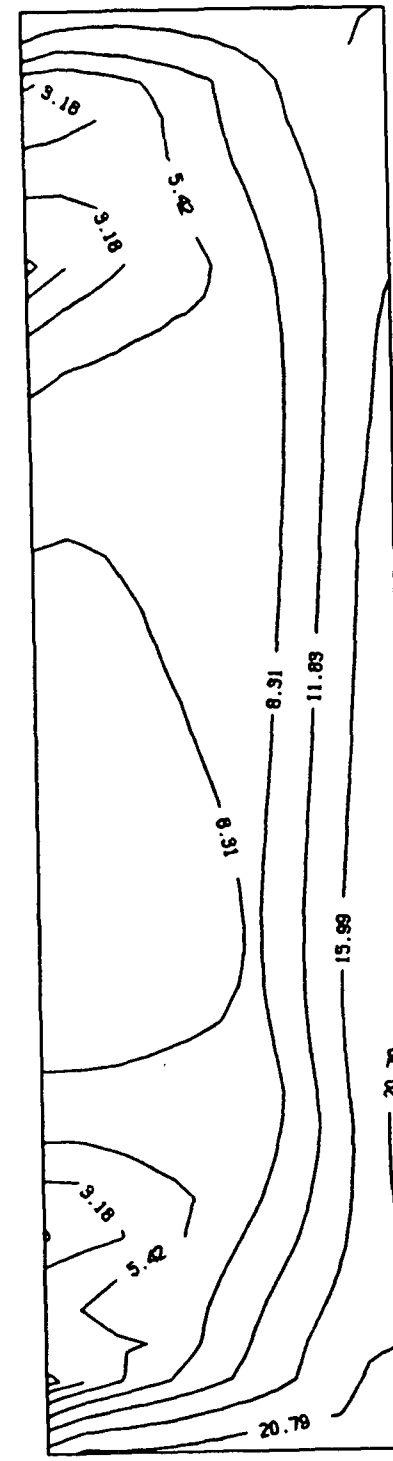
3.18
5.42
3.18
8.91
11.83
15.99
20.79
3.18
5.42
20.79

e

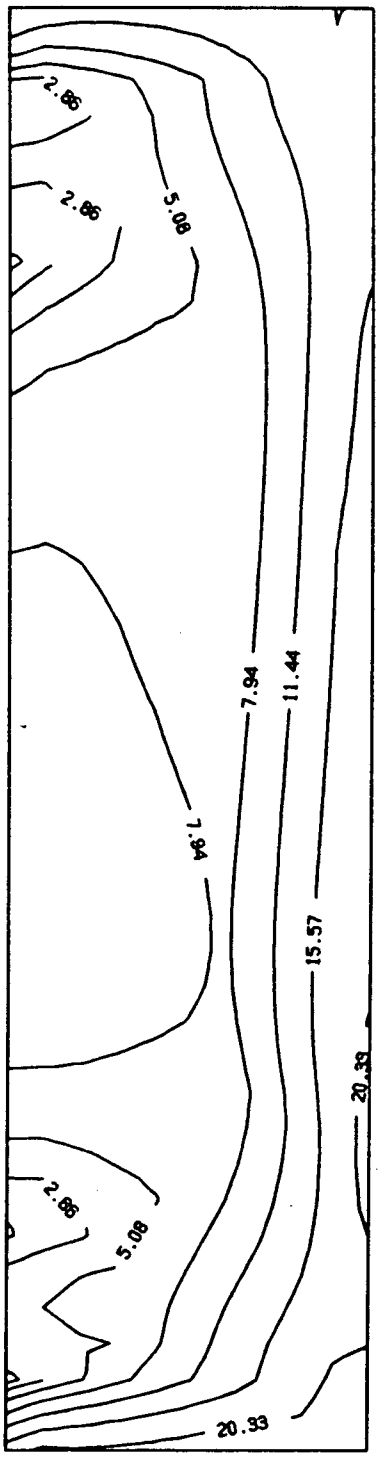

XIV.1.3.2 Time 20 seconds
(a) Temperature ; (b) Von Mises Stress
(c) MRSS ; (d) MRSS-CRSS (Yield) ;
(e) MRSS-CRSS (MBTe) .

a

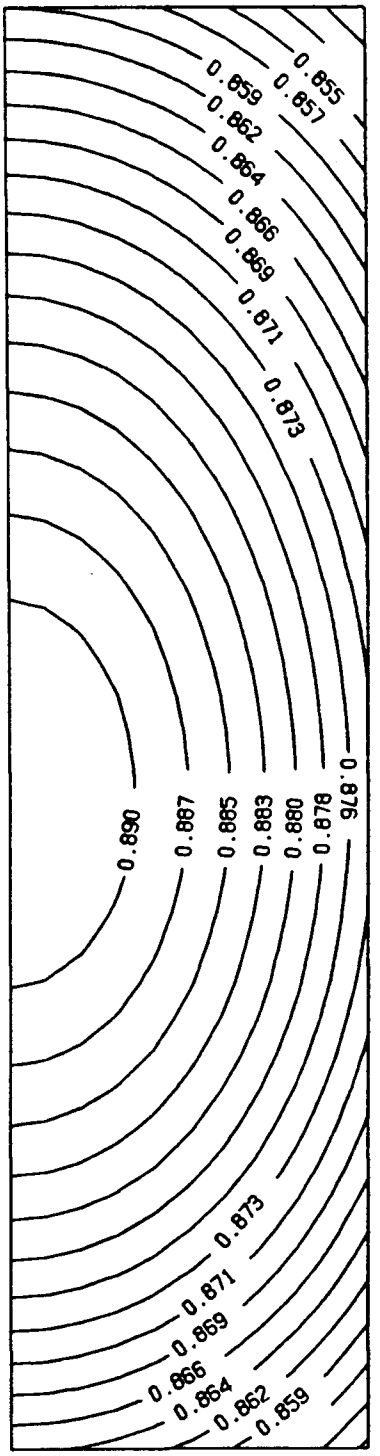
0.855
0.857
0.859
0.862
0.864
0.866
0.869
0.871
0.873
0.876
0.878
0.880
0.883
0.885
0.887
0.890
0.873
0.871
0.869
0.866
0.864
0.862
0.859

b

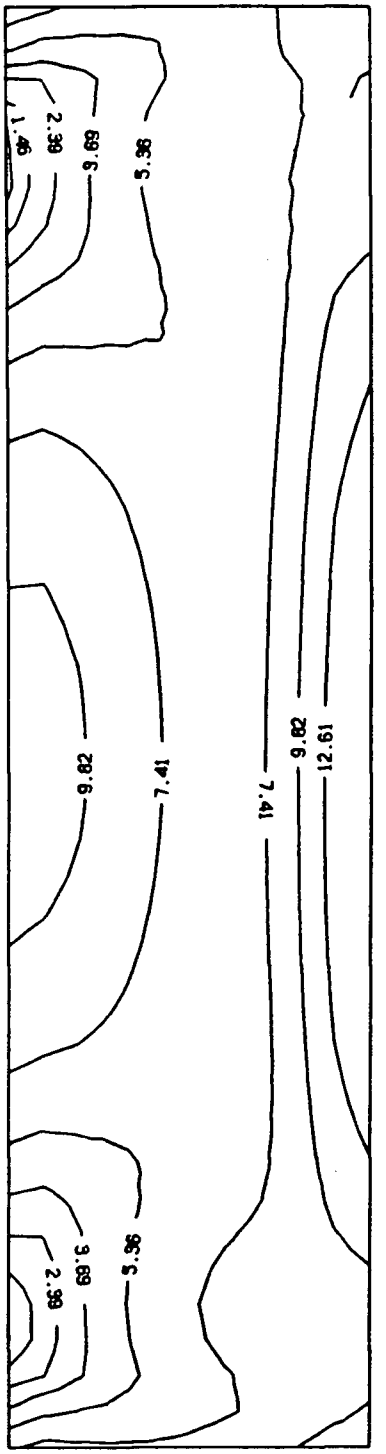
1.46
2.39
3.69
5.36
9.82
7.41
7.41
9.82
12.61
5.36
3.69
2.39

0.98
1.55
2.30
4.30
9.22
9.22
4.30
5.55
0.98
1.55
2.30
9.22

c

0.26
0.59
1.05
1.65
2.37
3.23
4.22
0.26
0.59
1.05
1.65
2.37

d

e

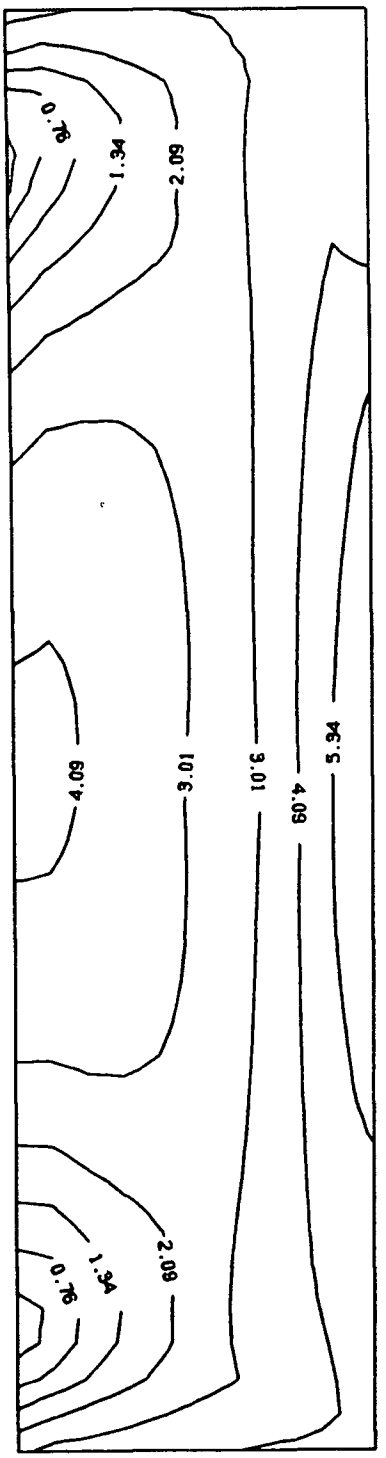

f

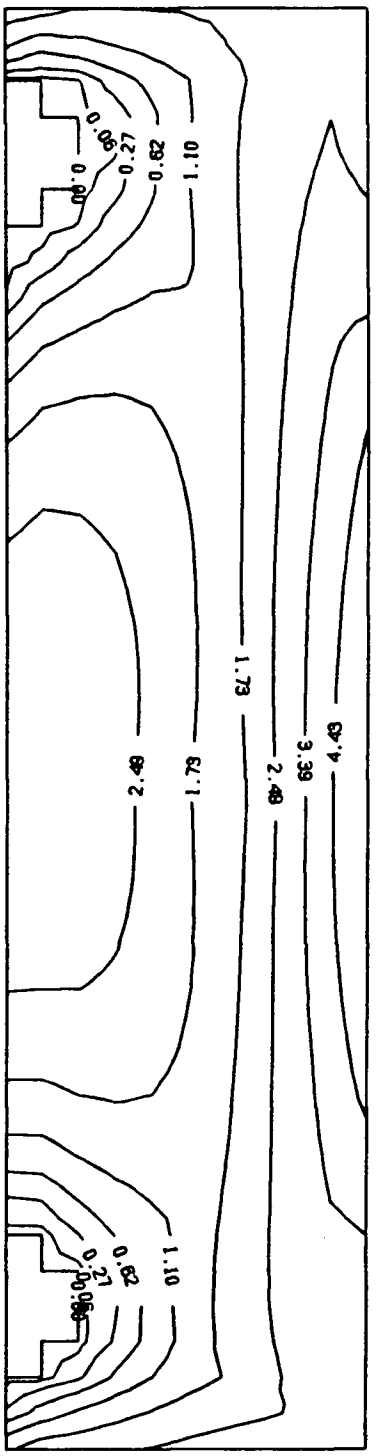

XIV.1.3.3 Time 60 seconds
(a) Temperature ; (b) Von Mises Stress
(c) MRSS ; (d) MRSS-CRSS (Yield) ;
(e) MRSS-CRSS (MB) ; (f) MRSS-CRSS (MBTe) .

XIV.2 Ambient Temperature 1000°C

XIV.2.1 Boron Oxide

XIV.2.1.1 Initial Gradient GC

XIV.2.1.1.1 Time 5 seconds

XIV.2.1.1.1.1 (a) Temperature ; (b) Von Mises Stress
(c) MRSS ; (d) MRSS-CRSS (Yield) ;
(e) MRSS-CRSS (MB) ; (f) MRSS-CRSS (MBTe) .

XIV.2.1.1.1.2 MRSS-CRSS (Yield) in cross-sections at a distance from the interface of :
(a) 2.75 mm ; (b) 8.25 mm ; (c) 16.5 mm ;
(d) 27.5 mm .

XIV.2.1.1.2 Time 10 seconds

XIV.2.1.1.2.1 (a) Temperature ; (b) Von Mises Stress
(c) MRSS ; (d) MRSS-CRSS (Yield) ;
(e) MRSS-CRSS (MB) ; (f) MRSS-CRSS (MBTe) .

XIV.2.1.1.2.2 MRSS-CRSS (Yield) in cross-sections at a distance from the interface of :
(a) 2.75 mm ; (b) 8.25 mm ; (c) 16.5 mm ;
(d) 27.5 mm .

XIV.2.1.1.3 Time 20 seconds

XIV.2.1.1.3.1 (a) Temperature ; (b) Von Mises Stress
(c) MRSS ; (d) MRSS-CRSS (Yield) ;
(e) MRSS-CRSS (MB) ; (f) MRSS-CRSS (MBTe) .

XIV.2.1.1.3.2 MRSS-CRSS (Yield) in cross-sections at a distance from the interface of :
(a) 2.75 mm ; (b) 8.25 mm ; (c) 16.5 mm ;
(d) 27.5 mm .

XIV.2.1.1.4 Time 60 seconds
(a) Temperature ; (b) Von Mises Stress
(c) MRSS ; (d) MRSS-CRSS (Yield) ;
(e) MRSS-CRSS (MB) ; (f) MRSS-CRSS (MBTe) .

XIV.2.1.2 Initial Gradient GC/2 ; Time 10 seconds .
(a) Temperature ; (b) Von Mises Stress
(c) MRSS ; (d) MRSS-CRSS (Yield) ;
(e) MRSS-CRSS (MB) ; (f) MRSS-CRSS (MBTe) .

XIV.2.1.3 Initial Gradient GC/4

XIV.2.1.3.1 Time 10 seconds

XIV.2.1.3.1.1 (a) Temperature ; (b) Von Mises Stress
(c) MRSS ; (d) MRSS-CRSS (Yield) ;
(e) MRSS-CRSS (MB) ; (f) MRSS-CRSS (MBTe) .

XIV.2.1.3.1.2 MRSS-CRSS (Yield) in cross-sections at a distance from the interface of :
(a) 2.75 mm ; (b) 8.25 mm ; (c) 16.5 mm ;
(d) 27.5 mm .

XIV.2.1.3.2 Time 20 seconds

XIV.2.1.3.2.1 (a) Temperature ; (b) Von Mises Stress
(c) MRSS ; (d) MRSS-CRSS (Yield) ;
(e) MRSS-CRSS (MB) ; (f) MRSS-CRSS (MBTe) .

XIV.2.1.3.2.2 MRSS-CRSS (Yield) in cross-sections at a distance from the interface of :
(a) 2.75 mm ; (b) 8.25 mm ; (c) 16.5 mm ;
(d) 27.5 mm .

XIV.2.2 Argon

XIV.2.2.1 Initial Gradient GC

XIV.2.2.1.1 Time 5 seconds
(a) Temperature ; (b) Von Mises Stress
(c) MRSS ; (d) MRSS-CRSS (Yield) ;
(e) MRSS-CRSS (MB) ; (f) MRSS-CRSS (MBTe) .

XIV.2.2.1.2 Time 10 seconds

XIV.2.2.1.2.1 (a) Temperature ; (b) Von Mises Stress
(c) MRSS ; (d) MRSS-CRSS (Yield) ;
(e) MRSS-CRSS (MB) ; (f) MRSS-CRSS (MBTe) .

XIV.2.2.1.2.2 MRSS-CRSS (Yield) in cross-sections at a distance from the interface of :
(a) 2.75 mm ; (b) 8.25 mm ; (c) 16.5 mm ;
(d) 27.5 mm .

XIV.2.2.1.3 Time 20 seconds
(a) Temperature ; (b) Von Mises Stress
(c) MRSS ; (d) MRSS-CRSS (Yield) ;
(e) MRSS-CRSS (MB) ; (f) MRSS-CRSS (MBTe) .

XIV.2.2.1.4 Time 60 seconds

XIV.2.2.1.4.1 (a) Temperature ; (b) Von Mises Stress
(c) MRSS ; (d) MRSS-CRSS (Yield) ;
(e) MRSS-CRSS (MB) ; (f) MRSS-CRSS (MBTe) .

XIV.2.2.1.4.2 MRSS-CRSS (Yield) in cross-sections at a distance from the interface of :
(a) 2.75 mm ; (b) 8.25 mm ; (c) 16.5 mm ;
(d) 27.5 mm .

XIV.2.2.1.5 Time 300 seconds
(a) Temperature ; (b) Von Mises Stress
(c) MRSS ; (d) MRSS-CRSS (MB) .

XIV.2.2.2 Initial Gradient GC/2

XIV.2.2.2.1 Time 10 seconds

XIV.2.2.2.1.1 (a) Temperature ; (b) Von Mises Stress
(c) MRSS ; (d) MRSS-CRSS (Yield) ;
(e) MRSS-CRSS (MB) ; (f) MRSS-CRSS (MBTe) .

XIV.2.2.2.1.2 MRSS-CRSS (Yield) in cross-sections at a distance from the interface of :
(a) 2.75 mm ; (b) 8.25 mm ; (c) 16.5 mm ;
(d) 27.5 mm .

XIV.2.2.2.2 Time 20 seconds

XIV.2.2.2.2.1 (a) Temperature ; (b) Von Mises Stress
(c) MRSS ; (d) MRSS-CRSS (Yield) ;
(e) MRSS-CRSS (MB) ; (f) MRSS-CRSS (MBTe) .

XIV.2.2.2.2.2 MRSS-CRSS (Yield) in cross-sections at a distance from the interface of :
(a) 2.75 mm ; (b) 8.25 mm ; (c) 16.5 mm ;
(d) 27.5 mm .

XIV.2.2.2.3 Time 60 seconds

XIV.2.2.2.3.1 (a) Temperature ; (b) Von Mises Stress
(c) MRSS ; (d) MRSS-CRSS (Yield) ;
(e) MRSS-CRSS (MB) ; (f) MRSS-CRSS (MBTe) .

XIV.2.2.2.3.2 MRSS-CRSS (Yield) in cross-sections at a distance from the interface of :
(a) 2.75 mm ; (b) 8.25 mm ; (c) 16.5 mm ;
(d) 27.5 mm .

XIV.2.2.3 Initial Gradient GC/4

XIV.2.2.3.1 Time 10 seconds

XIV.2.2.3.1.1 (a) Temperature ; (b) Von Mises Stress
(c) MRSS ; (d) MRSS-CRSS (Yield) ;
(e) MRSS-CRSS (MB) ; (f) MRSS-CRSS (MBTe) .

XIV.2.2.3.1.2 MRSS-CRSS (Yield) in cross-sections at a distance from the interface of :
(a) 2.75 mm ; (b) 8.25 mm ; (c) 16.5 mm ;
(d) 27.5 mm .

XIV.2.2.3.2 Time 60 seconds

XIV.2.2.3.2.1 (a) Temperature ; (b) Von Mises Stress
(c) MRSS ; (d) MRSS-CRSS (Yield) ;
(e) MRSS-CRSS (MB) ; (f) MRSS-CRSS (MBTe) .

XIV.2.2.3.2.2 MRSS-CRSS (Yield) in cross-sections at a distance from the interface of :
(a) 2.75 mm ; (b) 8.25 mm ; (c) 16.5 mm ;
(d) 27.5 mm .

a

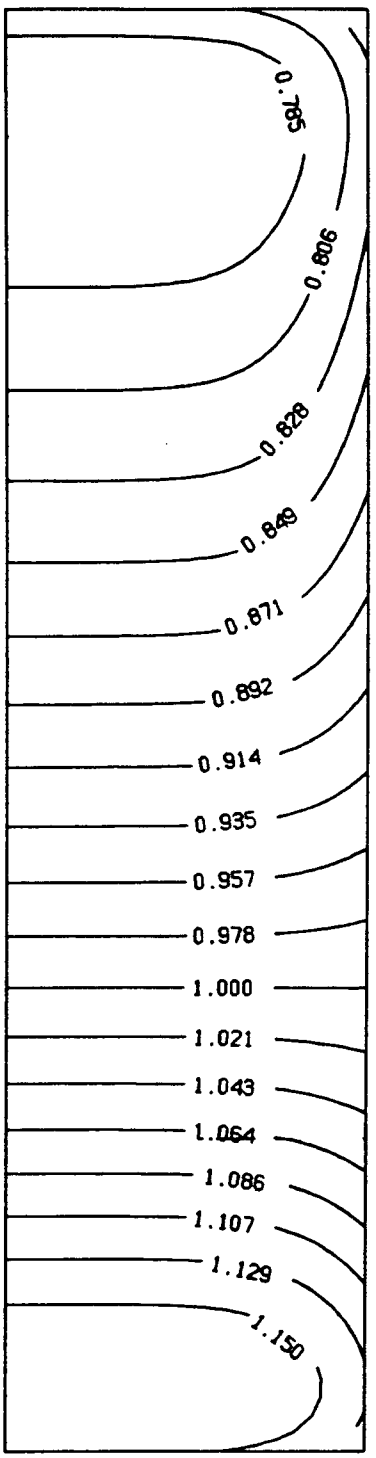
0.785
0.806
0.828
0.849
0.871
0.892
0.914
0.935
0.957
0.978
1.000
1.021
1.043
1.064
1.086
1.107
1.129
1.150

b

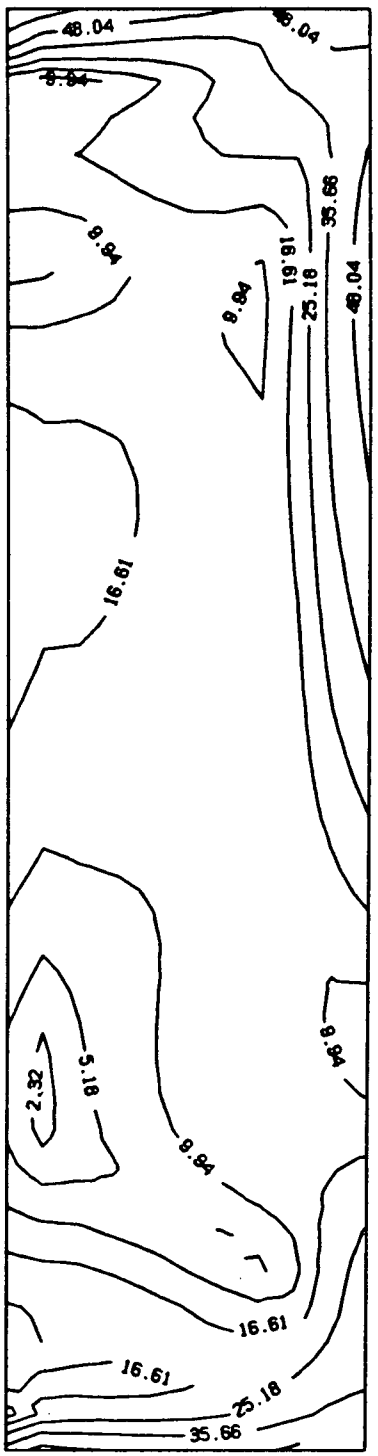
48.04
48.04
9.84
35.66
9.84
19.91
25.18
48.04
9.84
16.61
9.84
2.32
5.18
9.84
16.61
16.61
25.18
35.66

c

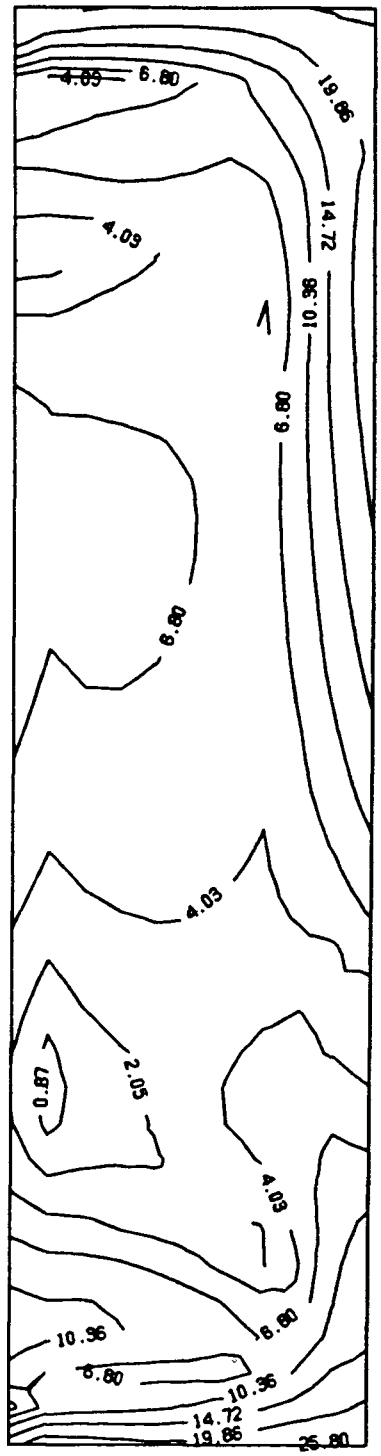
4.09
6.80
19.86
14.72
10.36
6.80
6.80
4.03
0.87
2.05
4.03
10.36
6.80
10.36
14.72
19.86
25.80

d

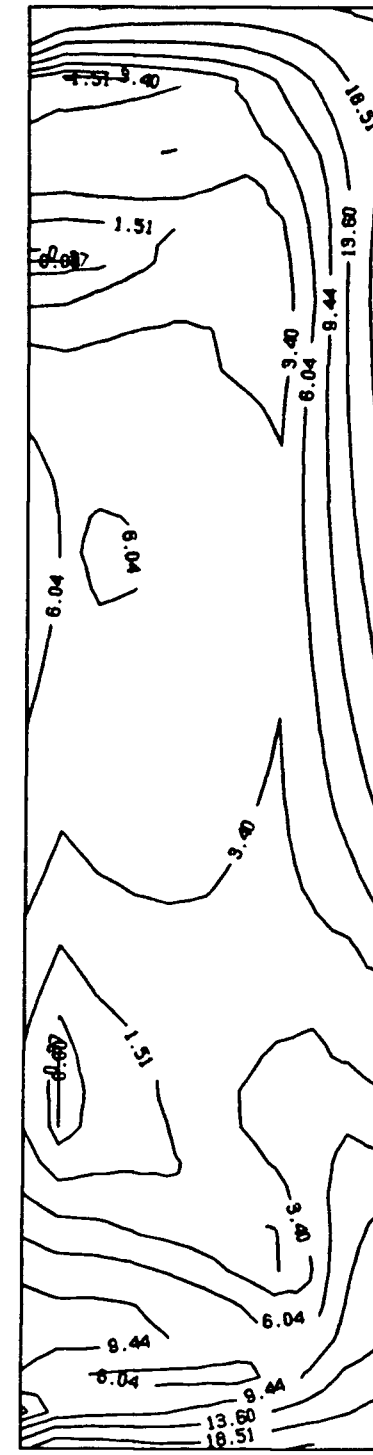
1.51
3.40
18.51
19.80
9.44
6.04
3.40
6.04
6.04
3.40
1.51
3.40
6.04
9.44
9.44
13.60
18.51

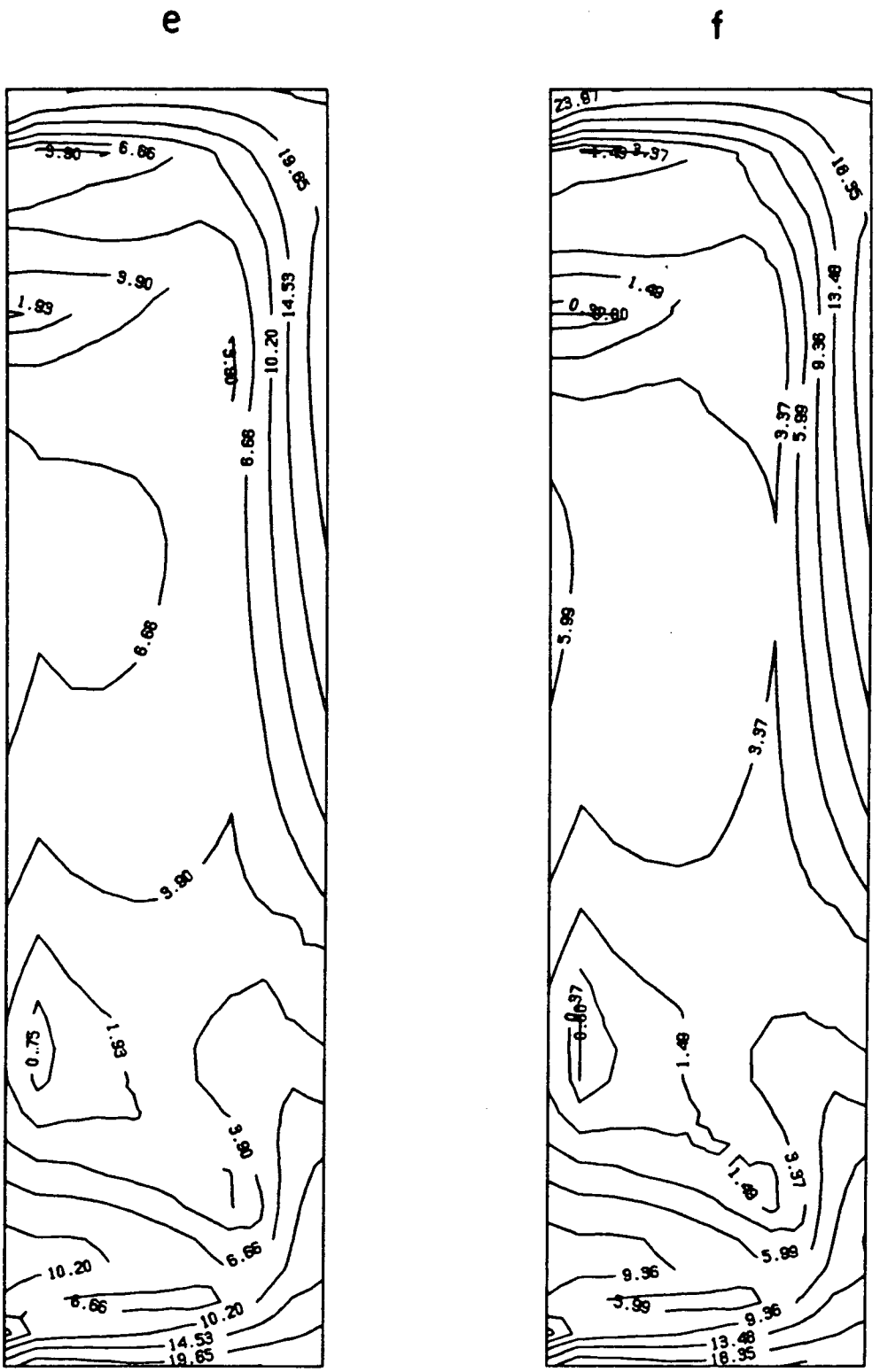

XIV.2.1.1.1.1 (a) Temperature ; (b) Von Mises Stress
(c) MRSS ; (d) MRSS-CRSS (Yield) ;
(e) MRSS-CRSS (MB) ; (f) MRSS-CRSS (MBTe) .

a

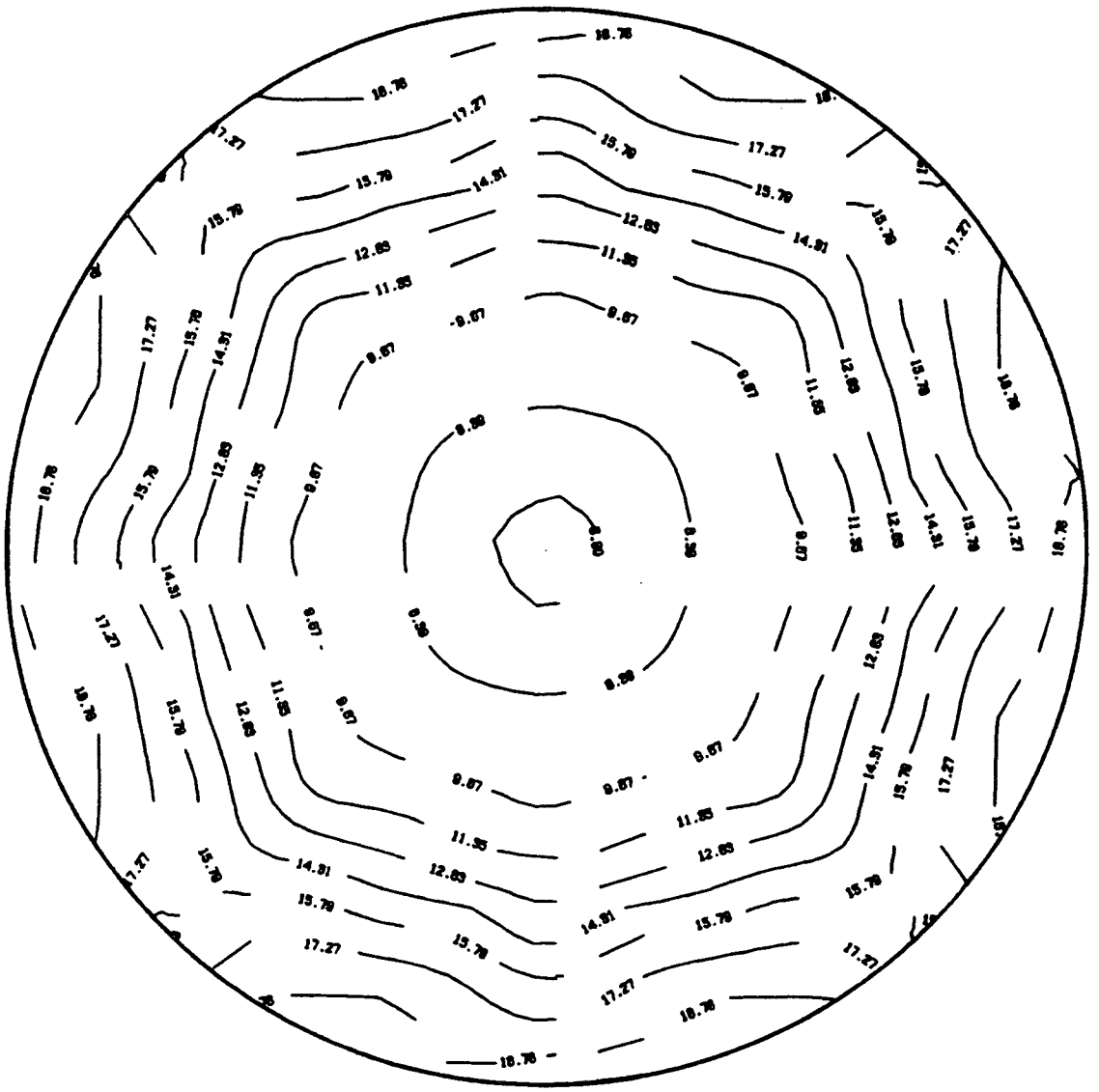

b

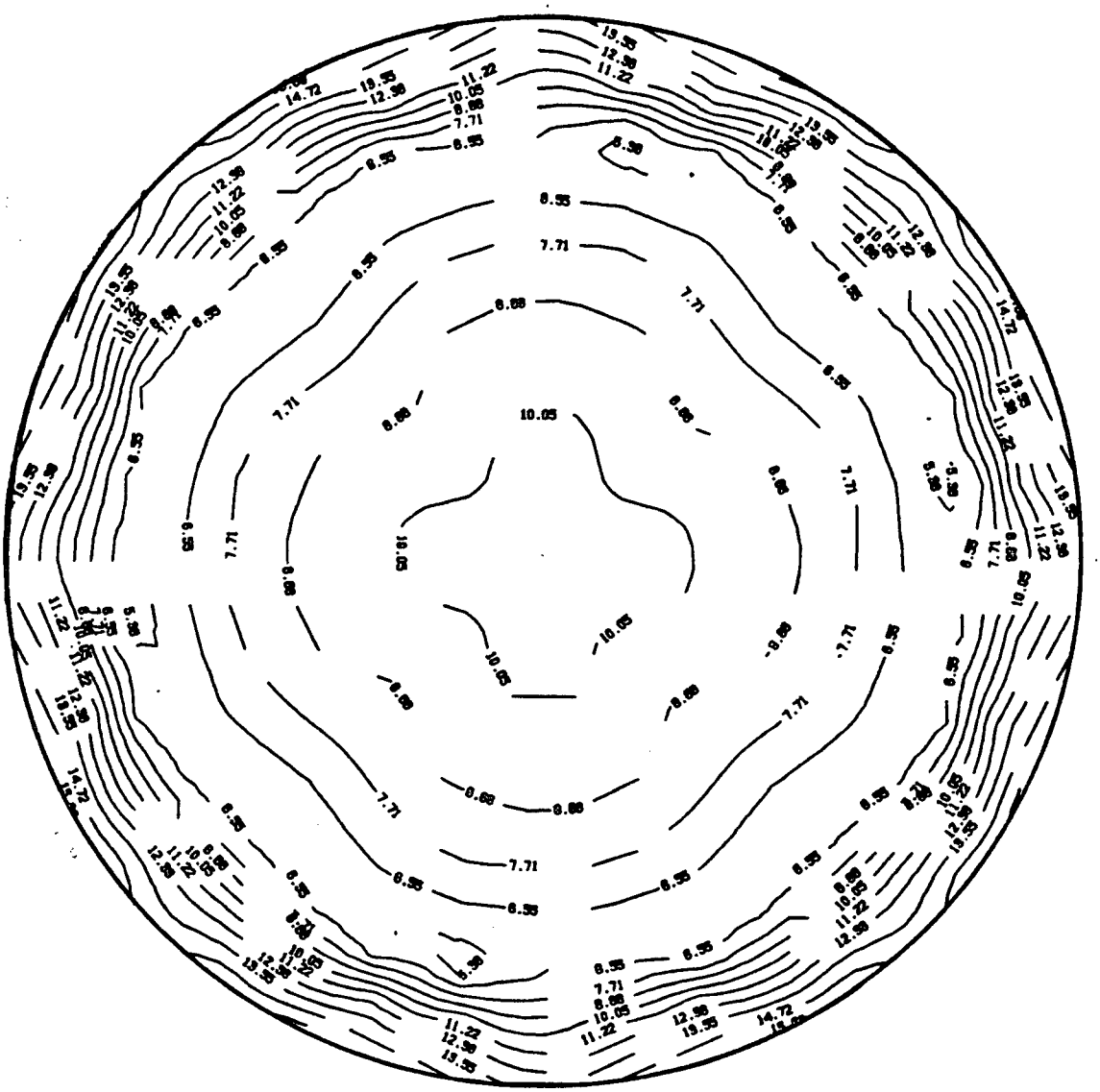

C

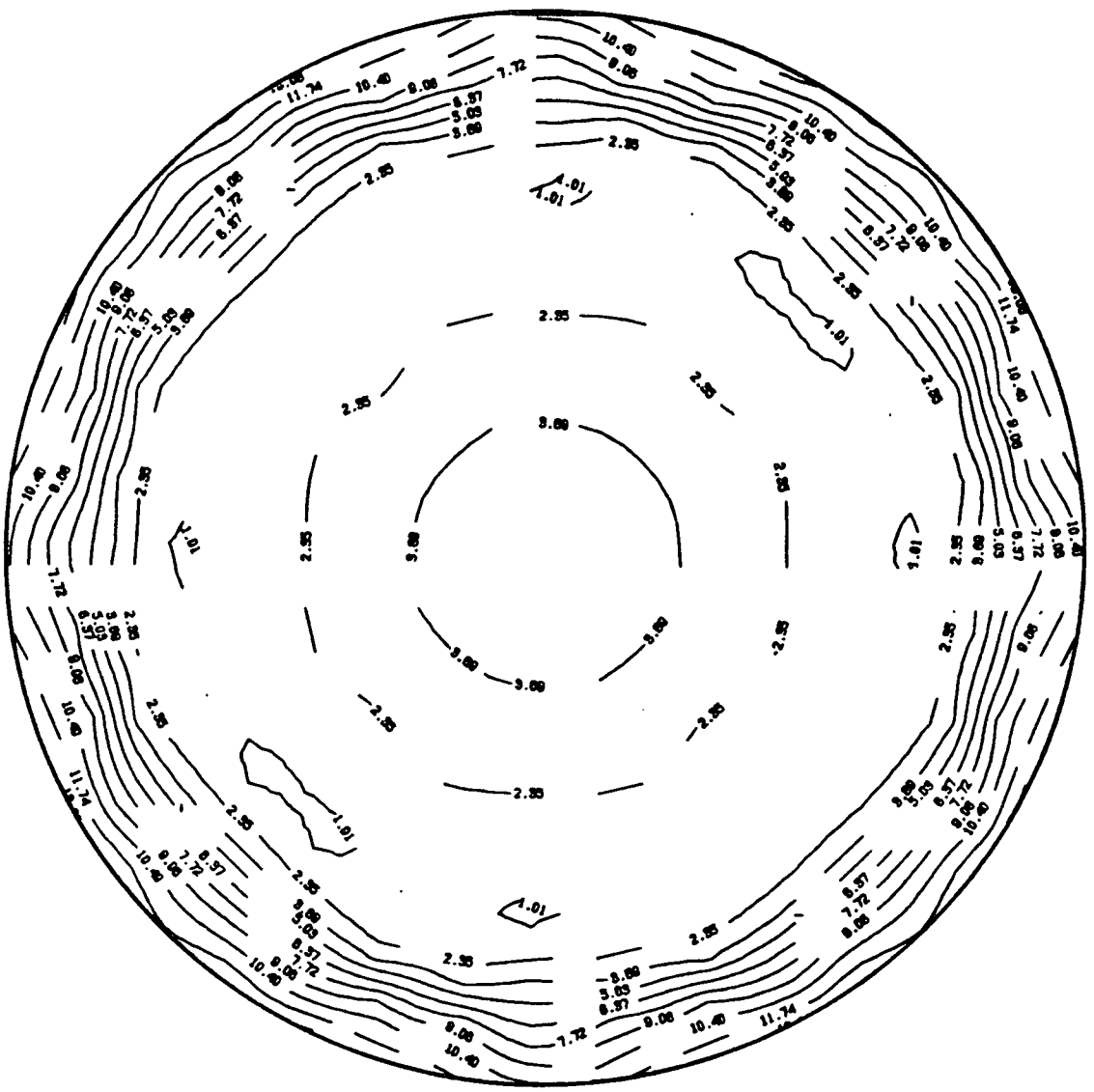

d

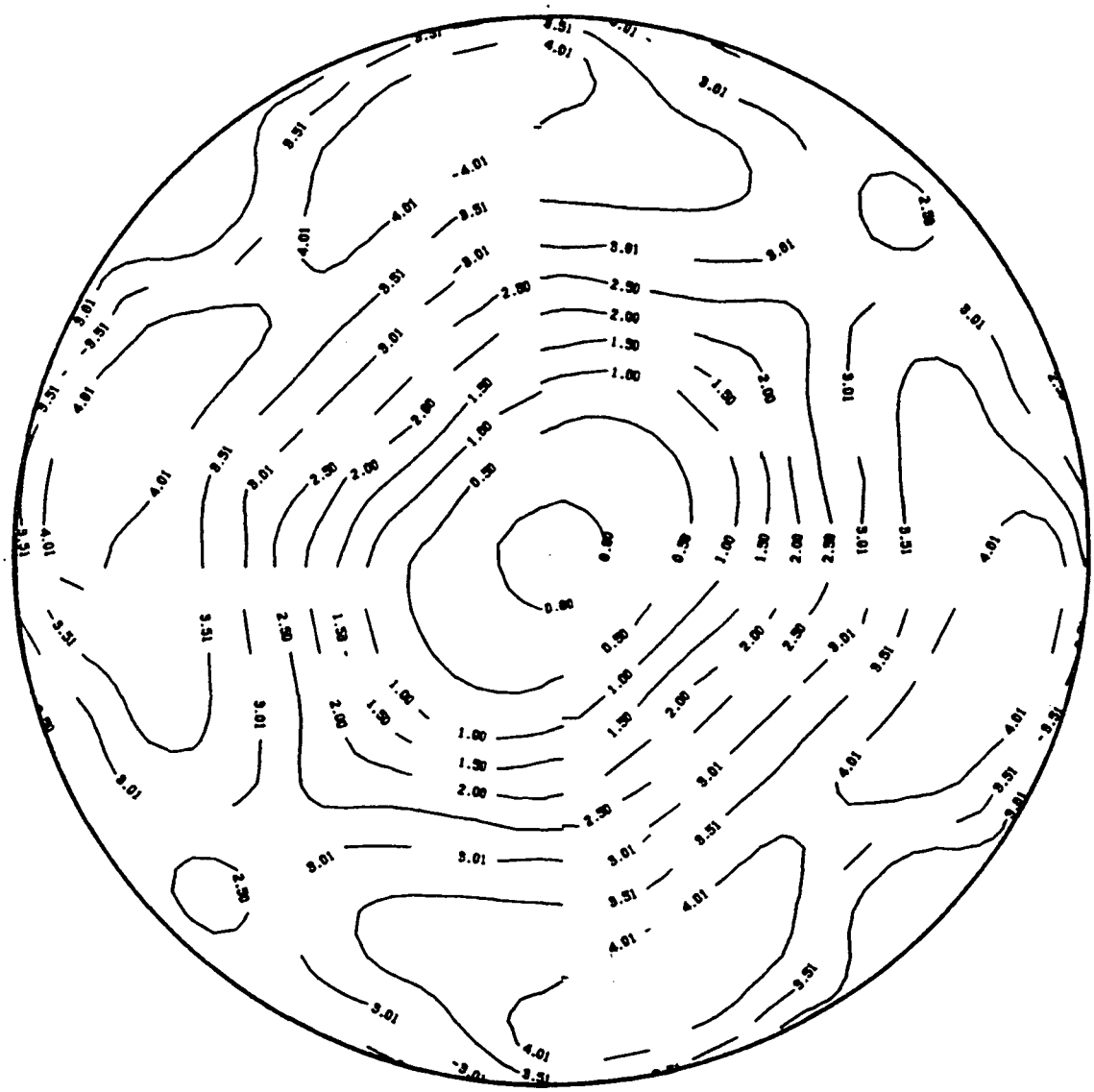

XIV.2.1.1.1.2 MRSS-CRSS (Yield) in cross-sections at a distance from the interface of :
(a) 2.75 mm ; (b) 8.25 mm ; (c) 16.5 mm ;
(d) 27.5 mm .

a

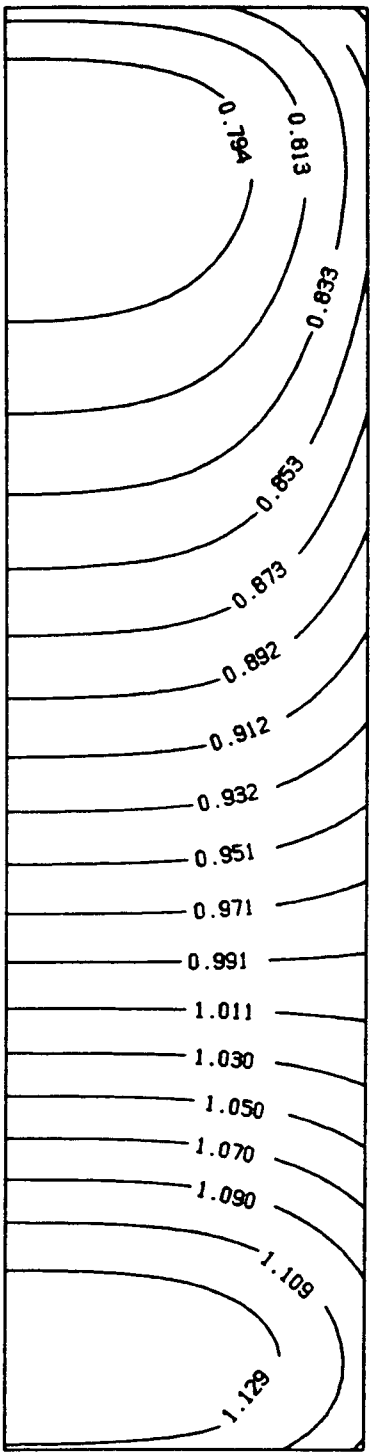
0.794
0.813
0.833
0.853
0.873
0.892
0.912
0.932
0.951
0.971
0.991
1.011
1.030
1.050
1.070
1.090
1.109
1.129

b

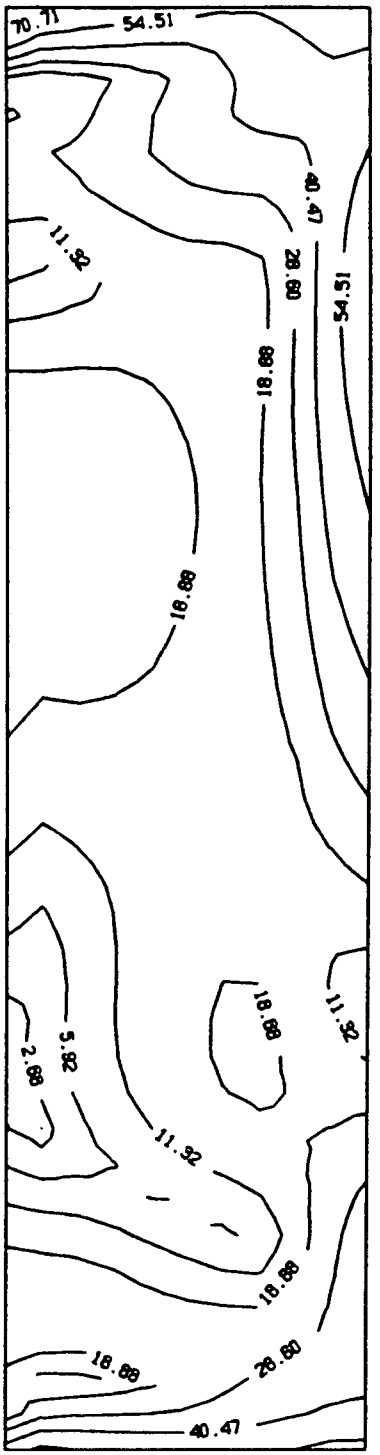
54.51
40.47
28.80
18.88
11.92
5.92
2.88

c

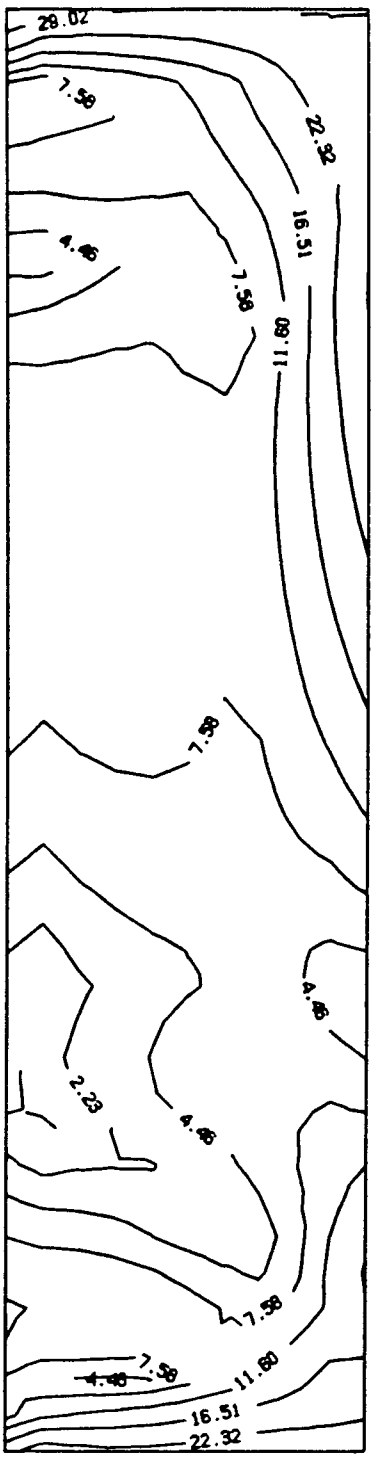
28.02
7.58
22.32
16.51
4.46
7.58
11.80
7.58
4.46
2.23
4.46
7.58
7.58
4.46
11.80
16.51
22.32

d

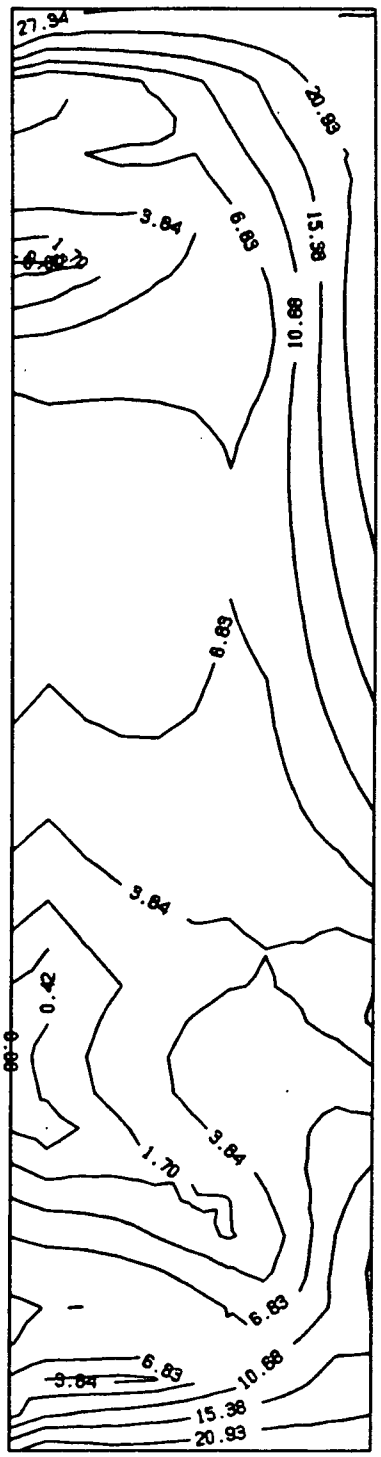
27.94
20.93
3.84
6.83
15.38
10.68
6.83
3.84
0.42
0.00
1.70
3.84
6.83
6.83
3.84
10.68
15.38
20.93

e

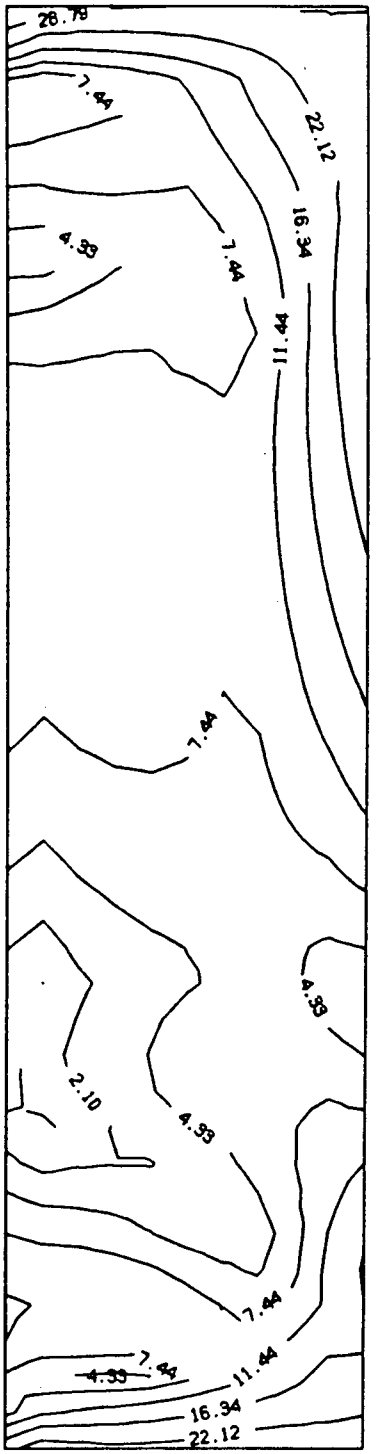

f

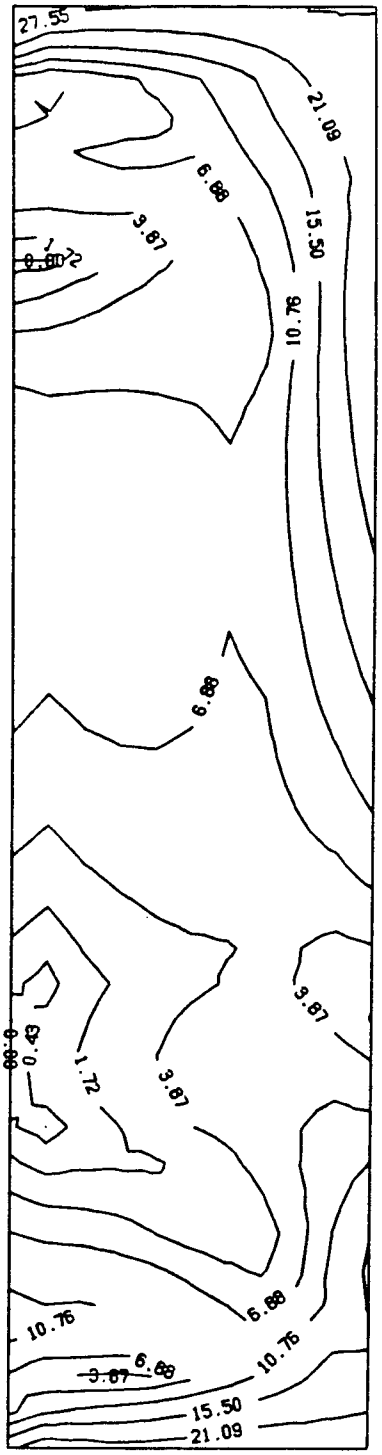

XIV.2.1.1.2.1 (a) Temperature ; (b) Von Mises Stress
(c) MRSS ; (d) MRSS-CRSS (Yield) ;
(e) MRSS-CRSS (MB) ; (f) MRSS-CRSS (MBTe) .

a

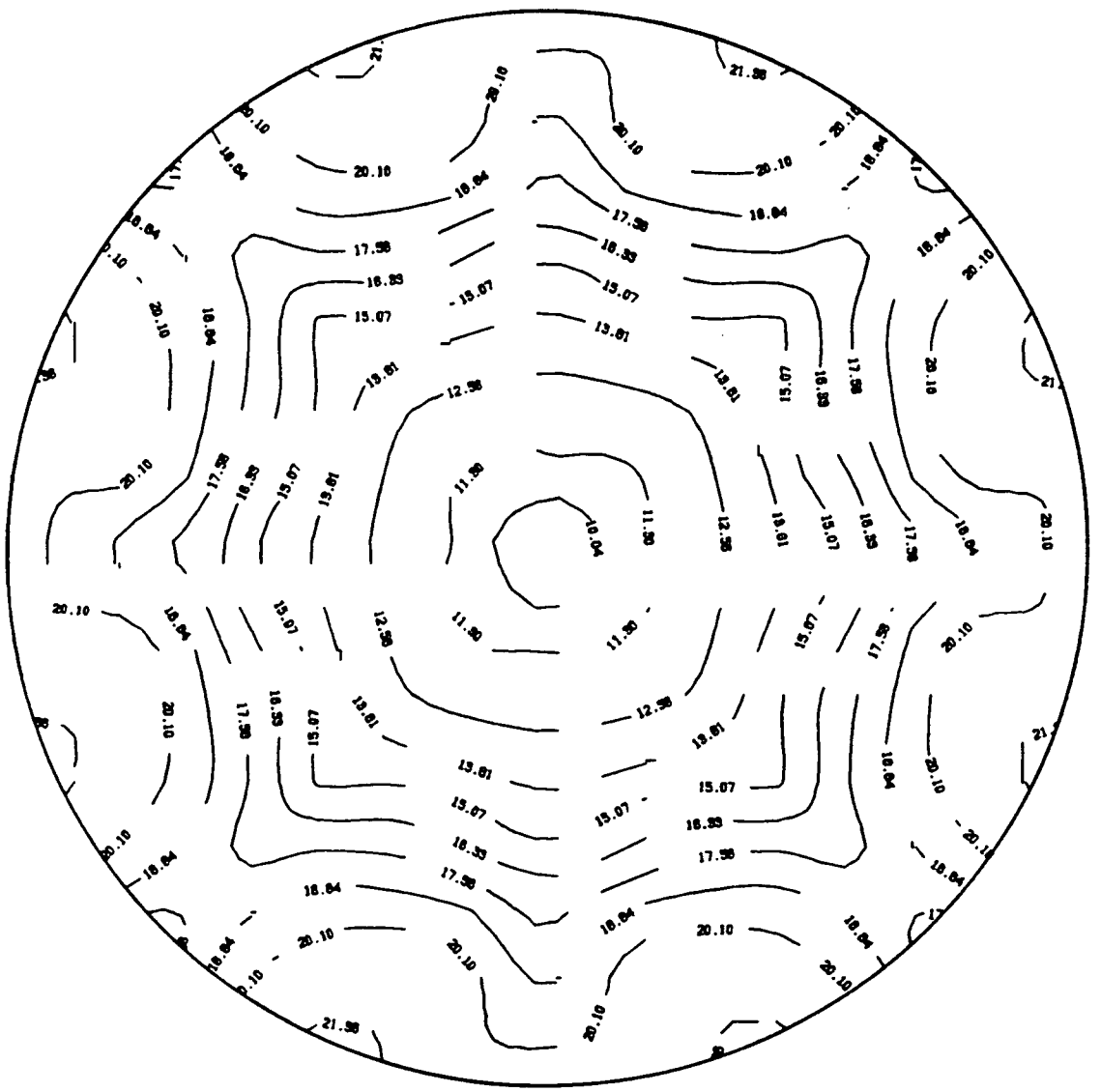

b

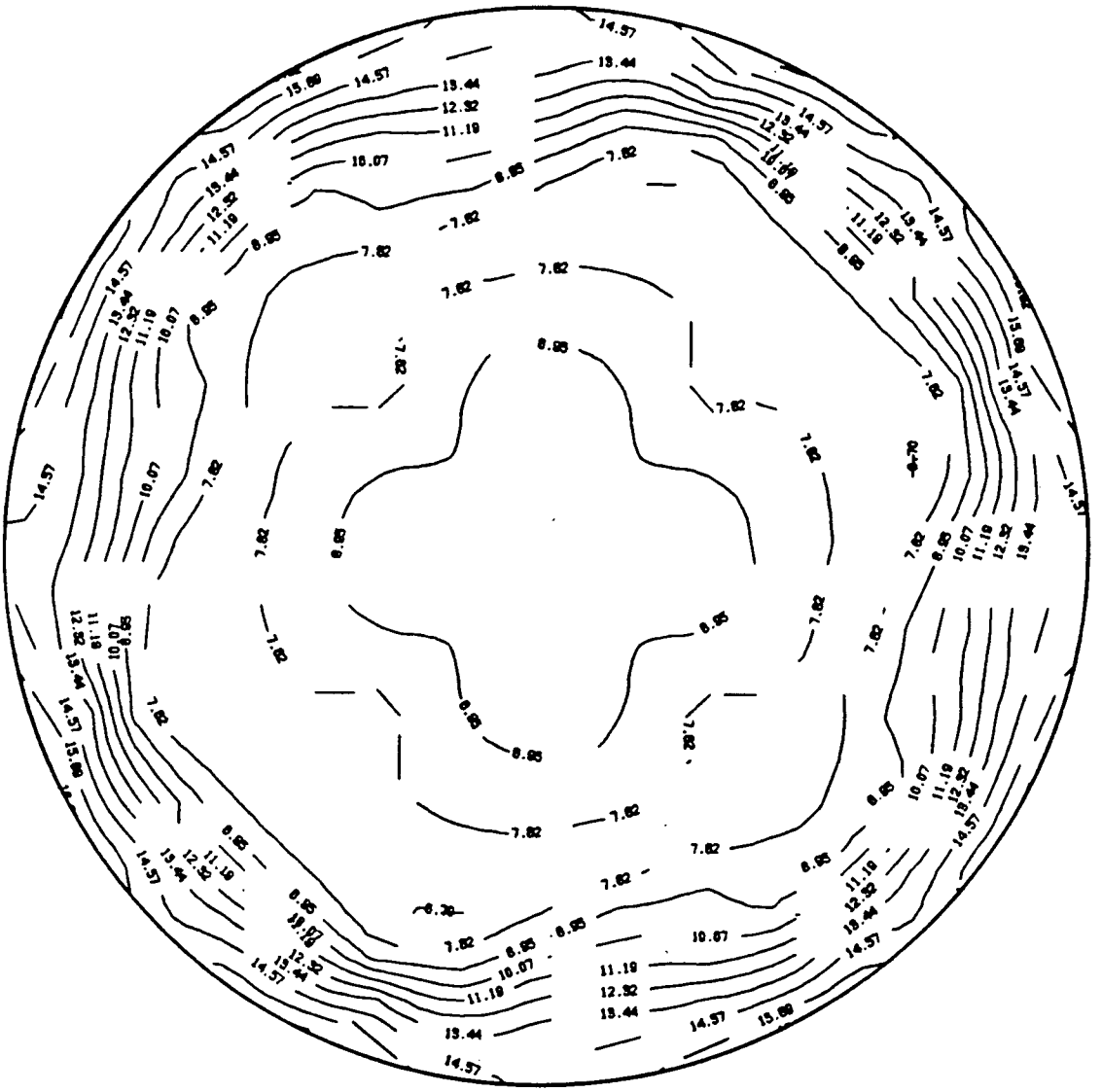

C

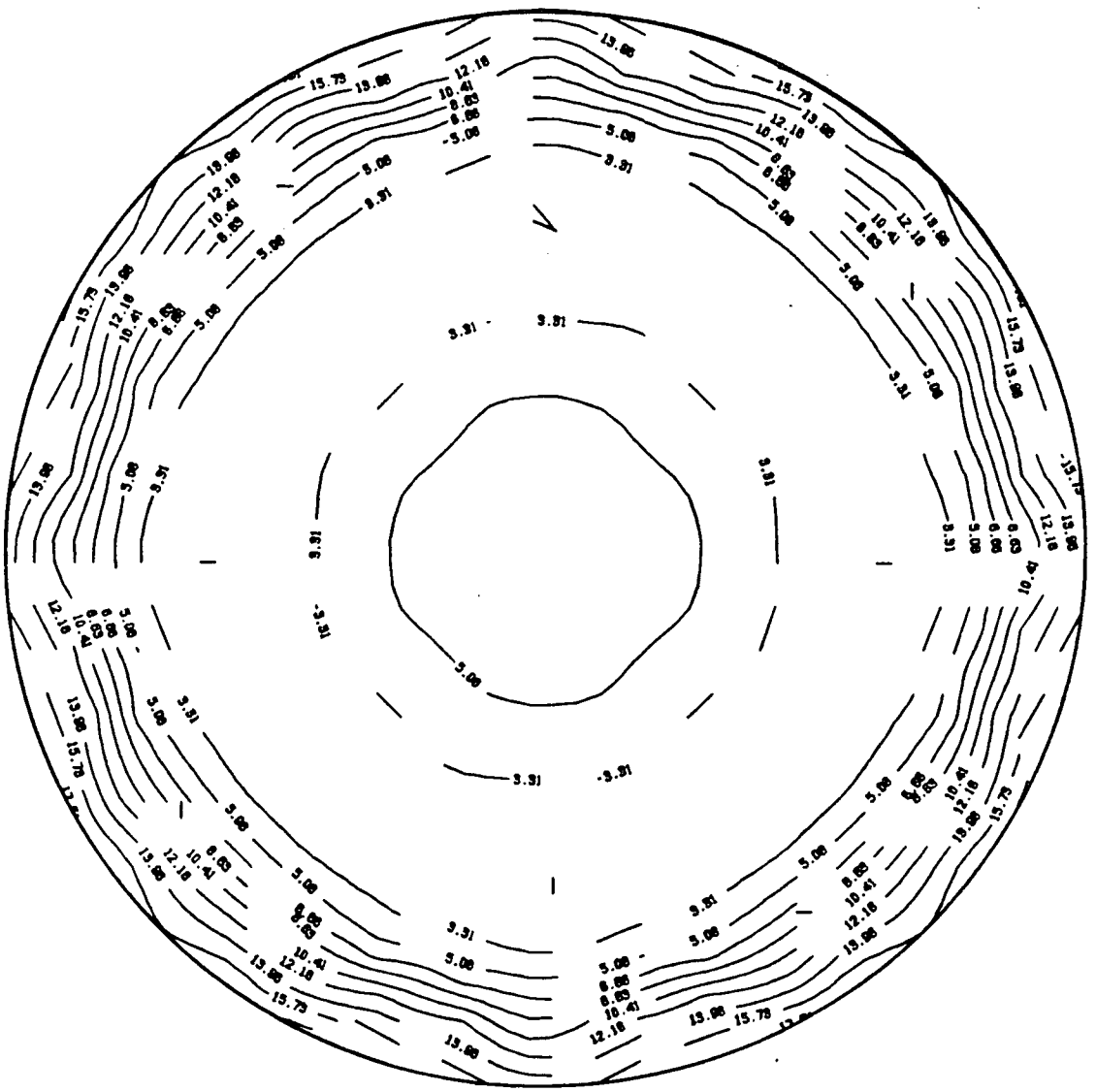

d

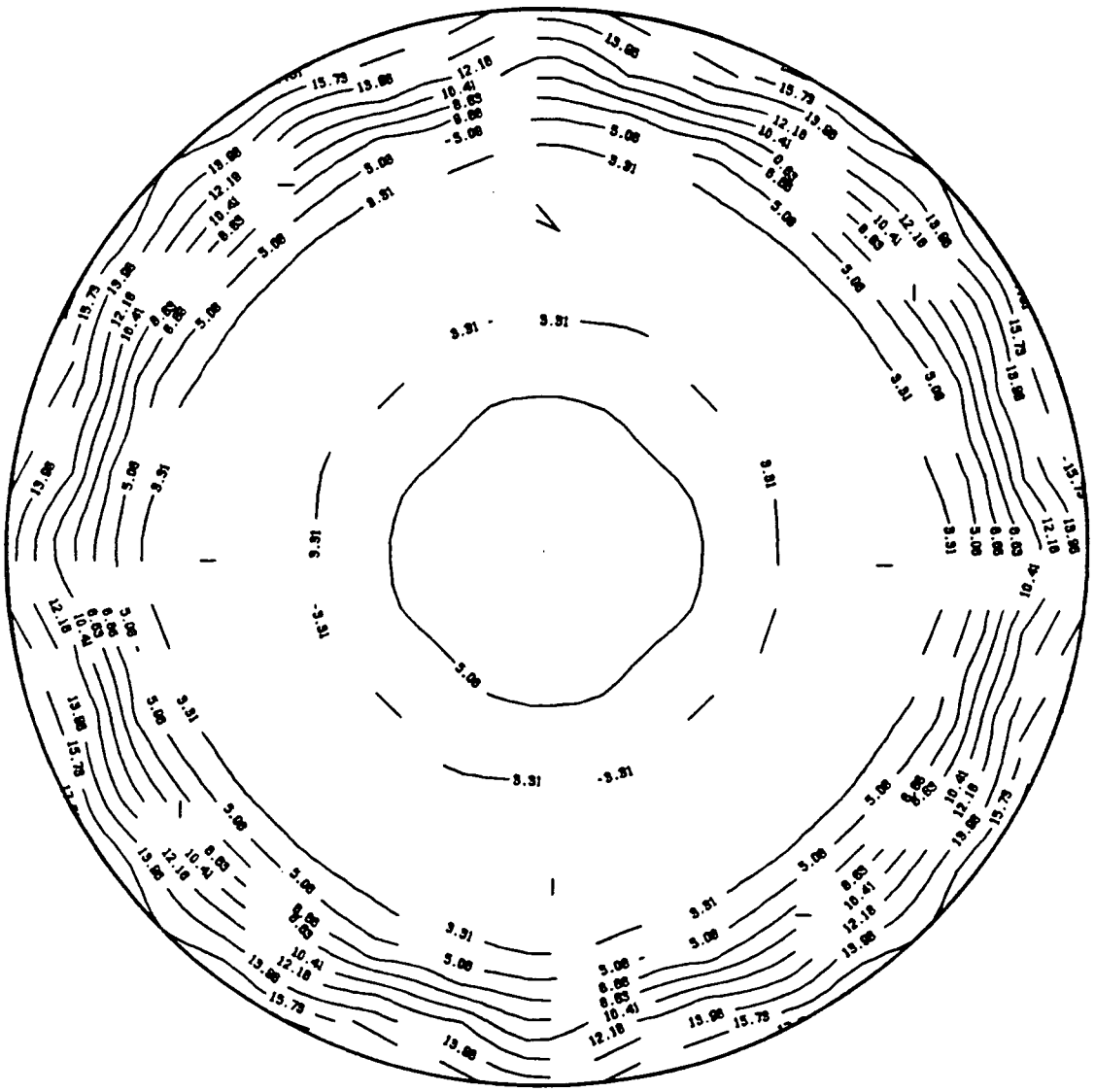

XIV.2.1.1.2.2 MRSS-CRSS (Yield) in cross-sections at a distance from the interface of :
(a) 2.75 mm ; (b) 8.25 mm ; (c) 16.5 mm ;
(d) 27.5 mm .

a

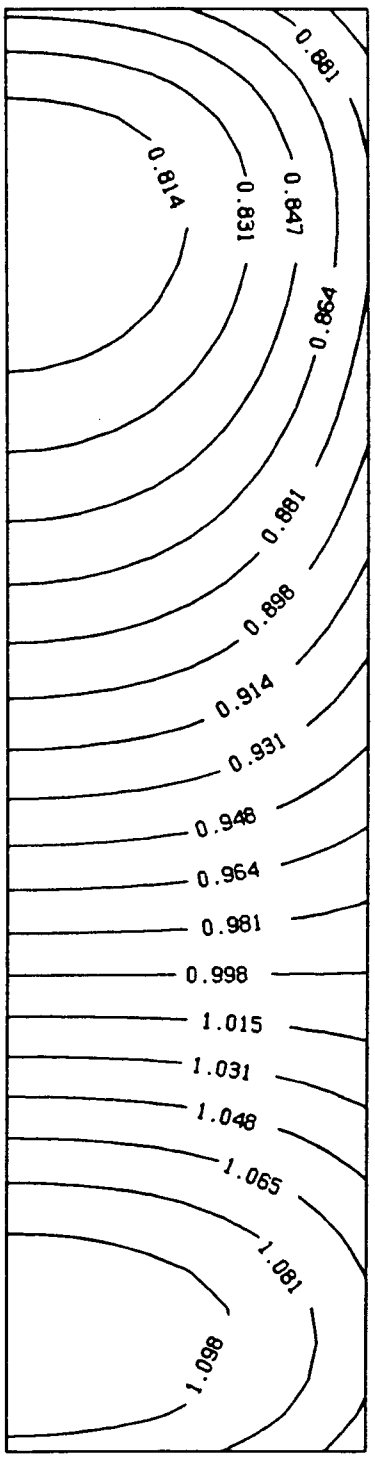
0.881
0.814
0.831
0.847
0.864
0.881
0.898
0.914
0.931
0.948
0.964
0.981
0.998
1.015
1.031
1.048
1.065
1.081
1.098

b

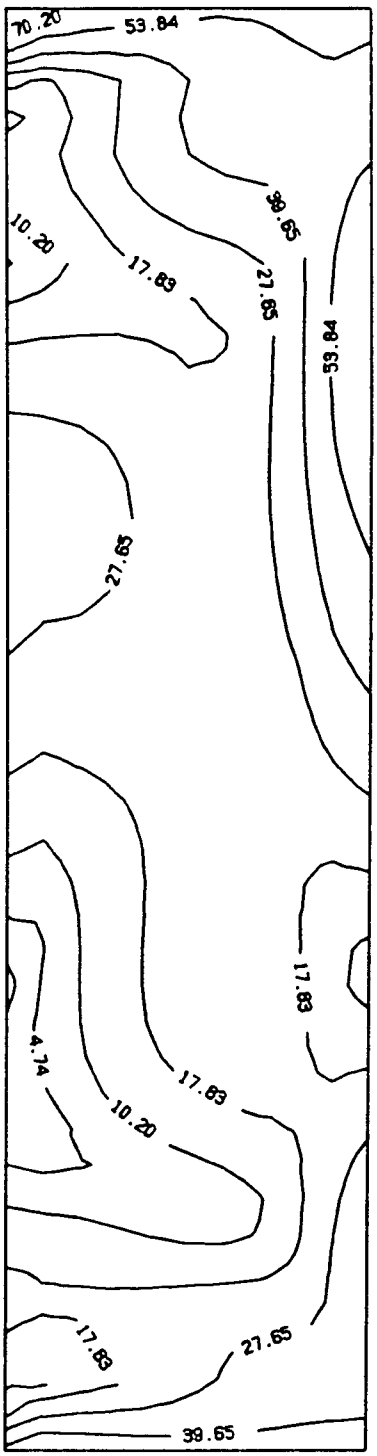
70.20
53.84
39.65
10.20
17.83
27.65
53.84
27.65
17.83
4.74
17.83
10.20
17.83
27.65
39.65

c

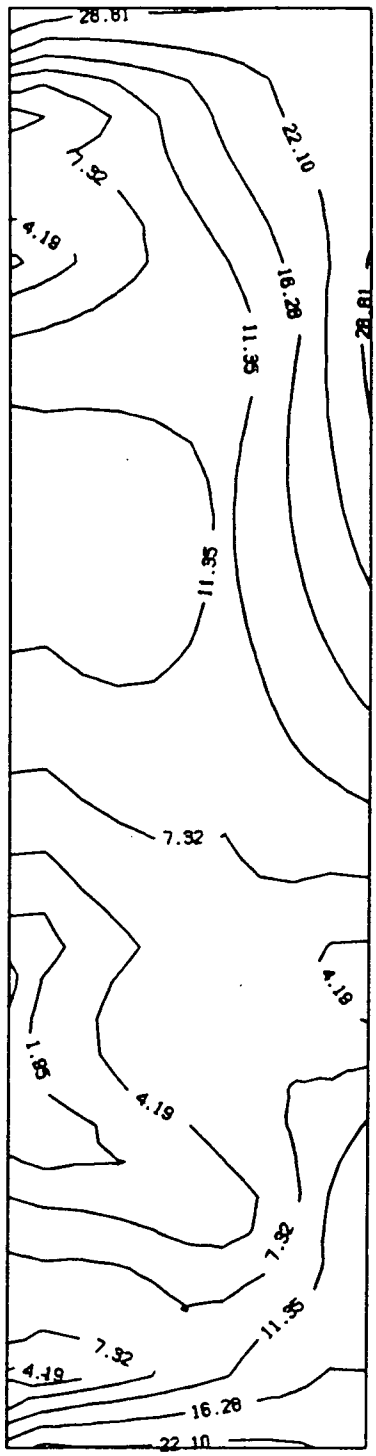
28.81
22.10
18.28
11.35
7.32
4.19
1.85
4.19
7.32
11.35
16.28
22.10

d

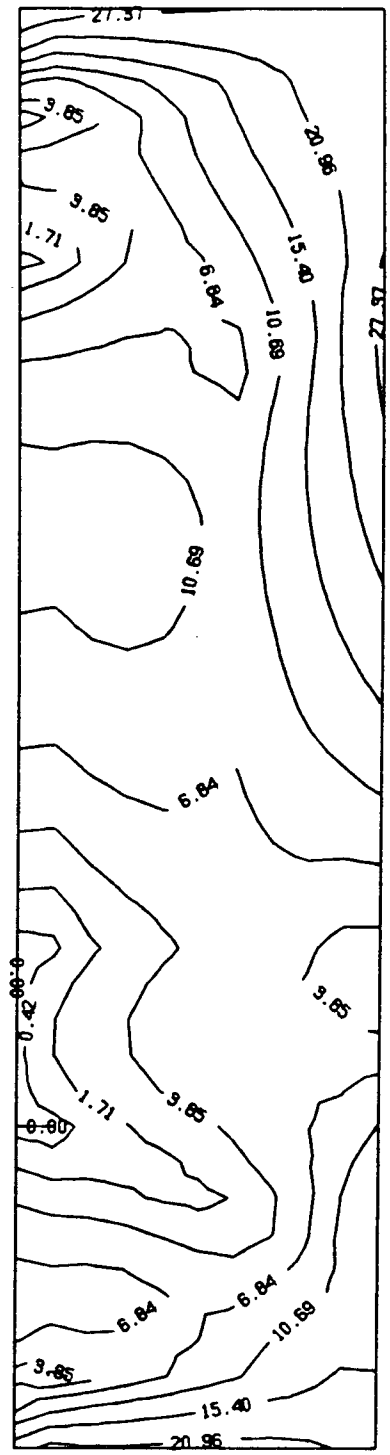
27.37
20.96
15.40
10.69
6.84
3.85
1.71
0.00
0.42
1.71
3.85
6.84
10.69
15.40
20.96

e

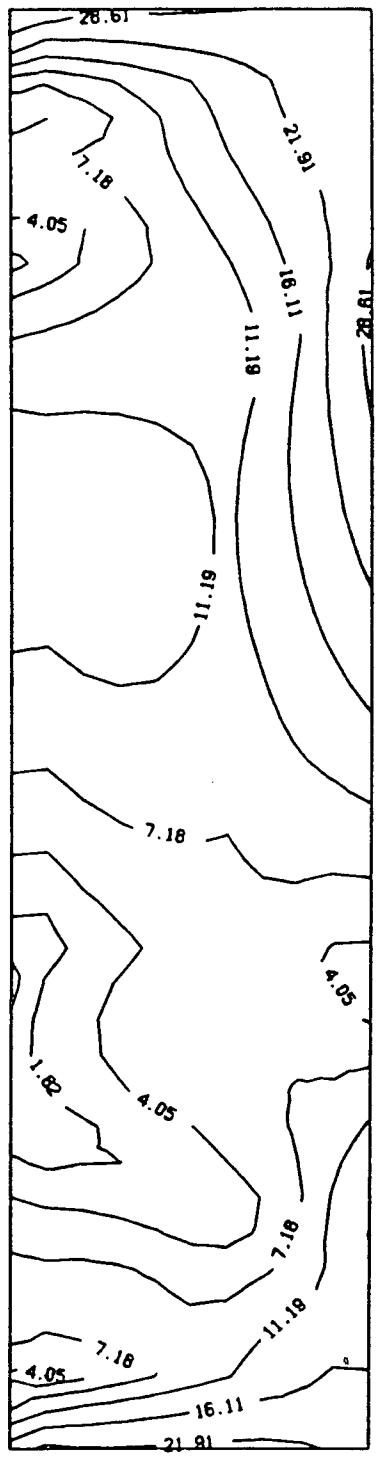

f

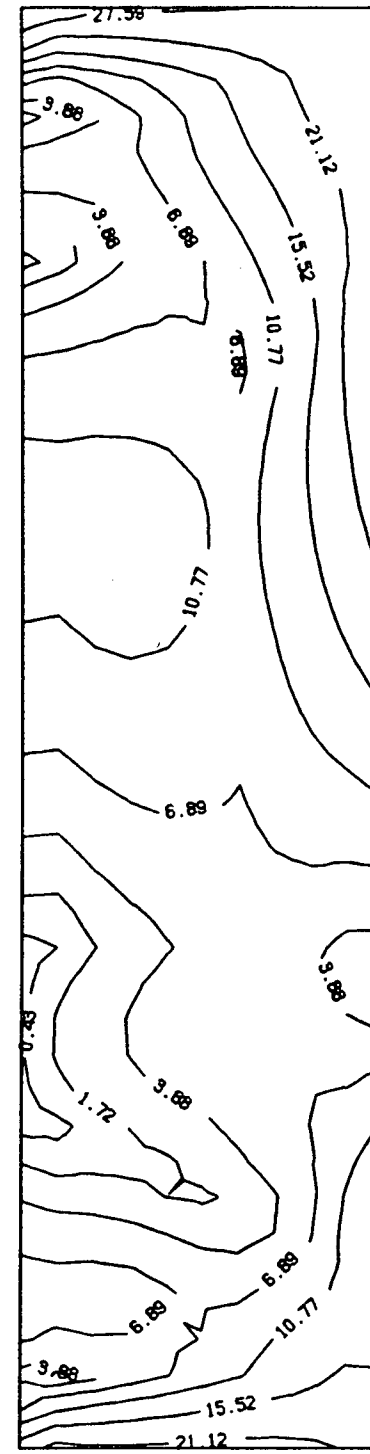

XIV.2.1.1.3.1 (a) Temperature ; (b) Von Mises Stress
(c) MRSS ; (d) MRSS-CRSS (Yield) ;
(e) MRSS-CRSS (MB) ; (f) MRSS-CRSS (MBTe) .

a

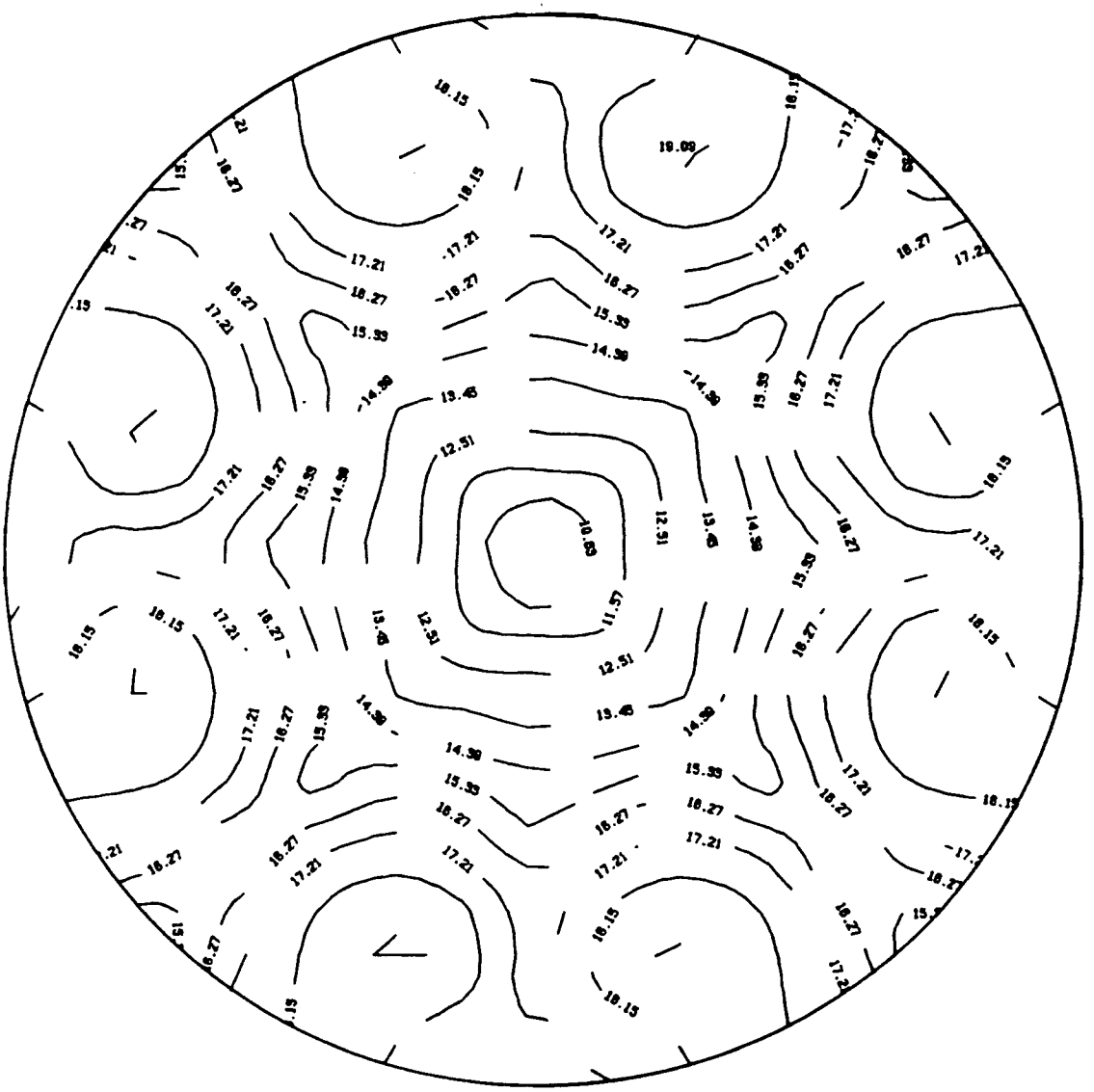

b

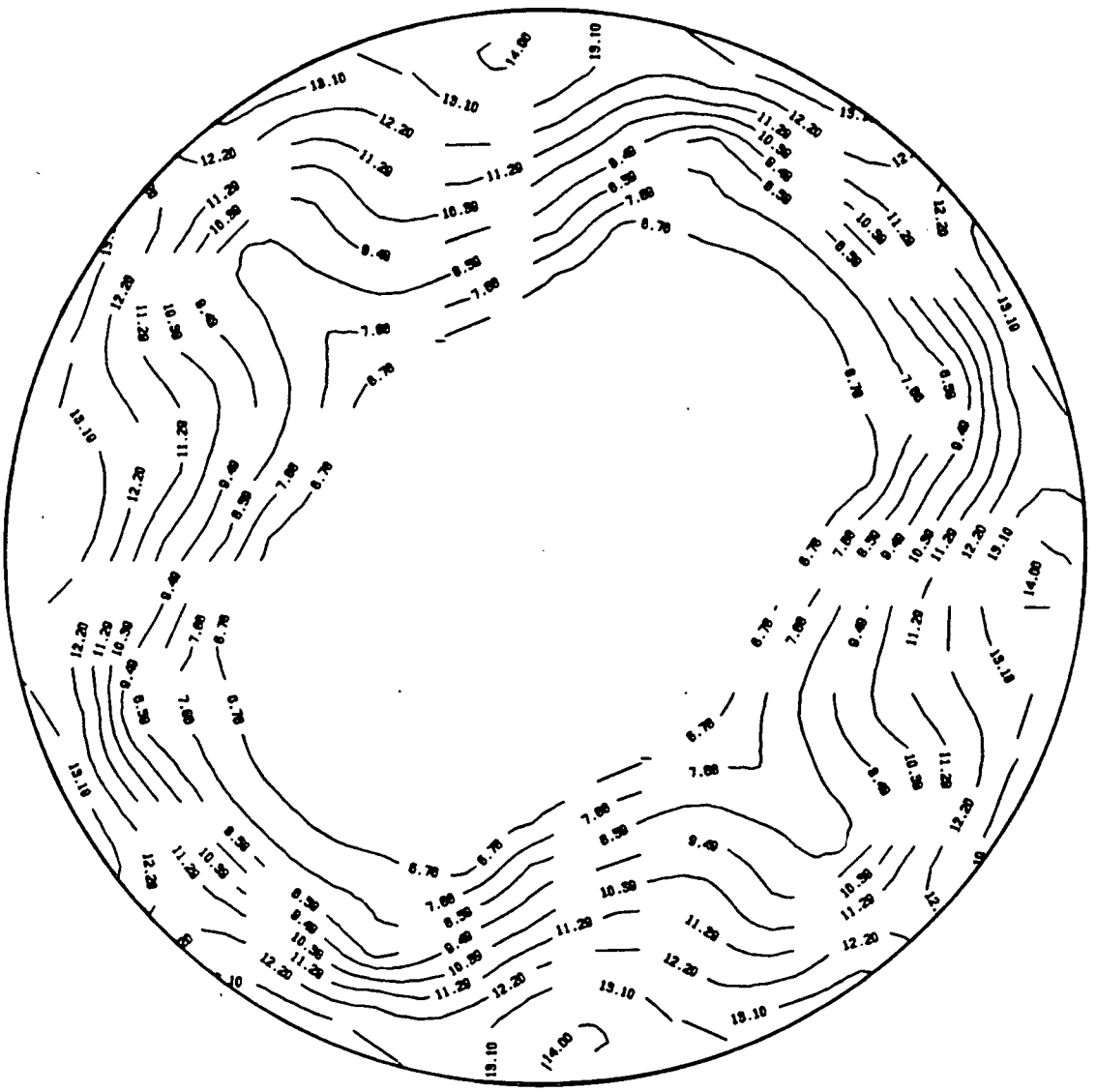

C

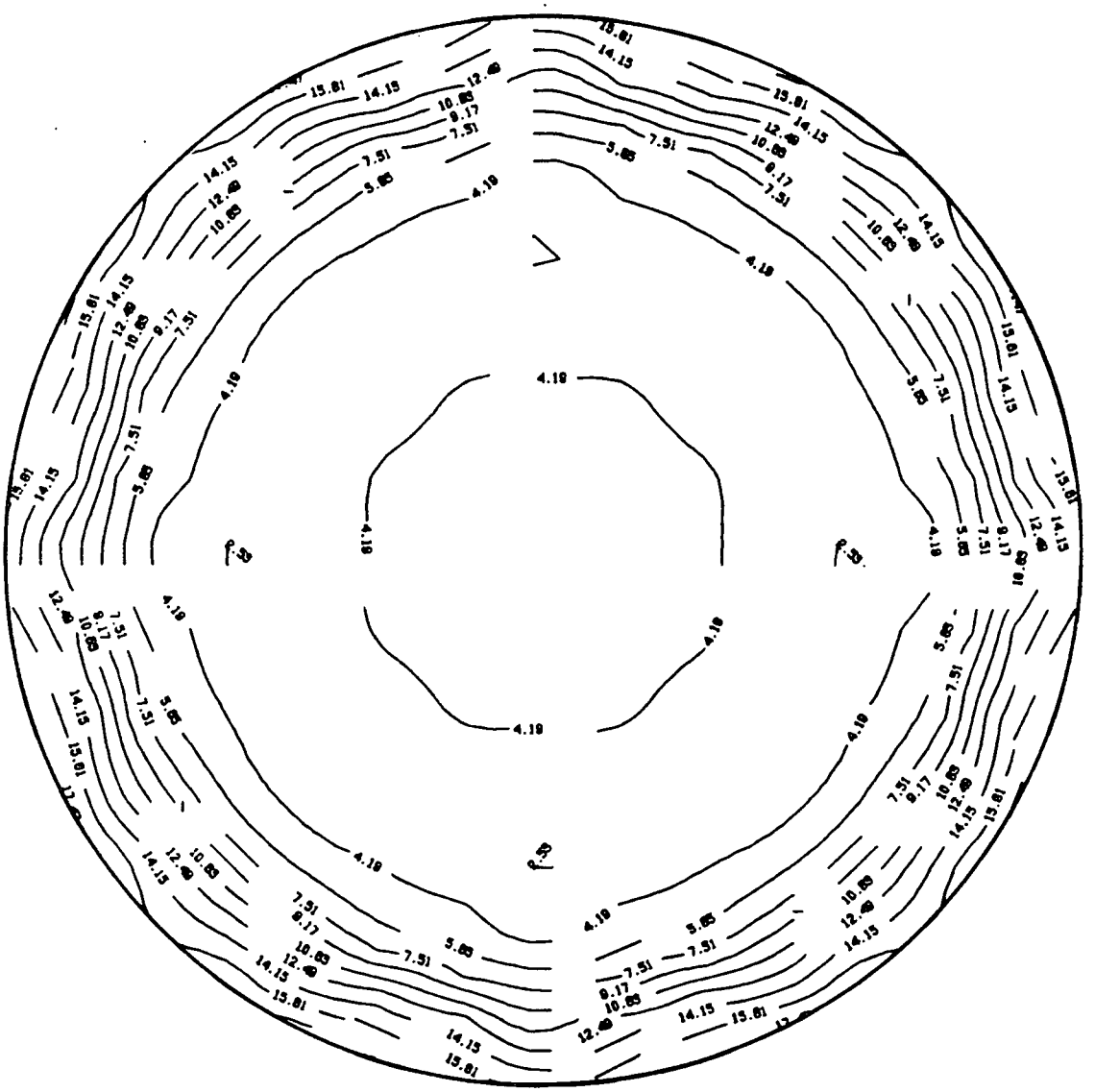

d

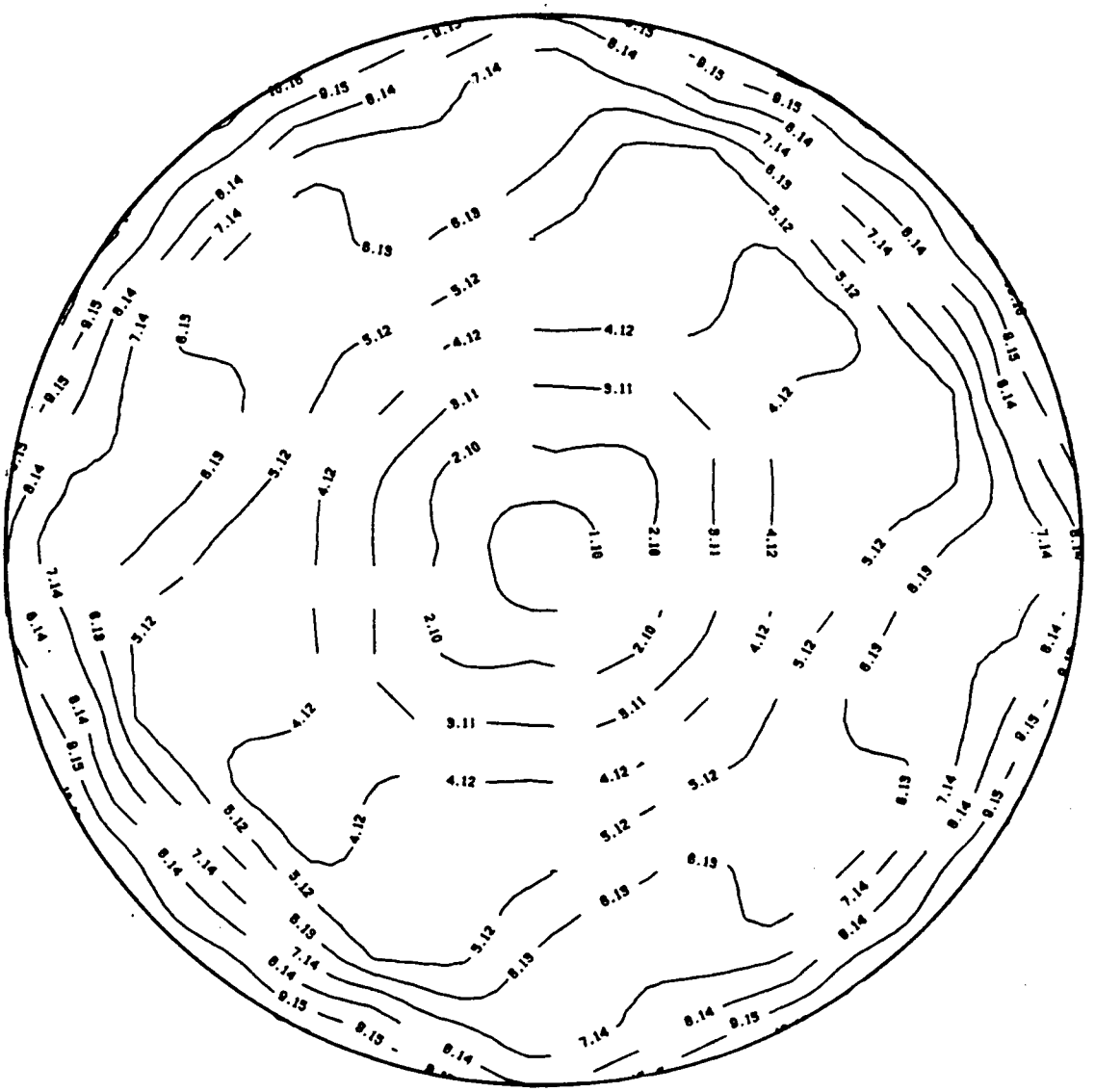

XIV.2.1.1.3.2 MRSS-CRSS (Yield) in cross-sections at a distance from the interface of :
(a) 2.75 mm ; (b) 8.25 mm ; (c) 16.5 mm ;
(d) 27.5 mm .

a

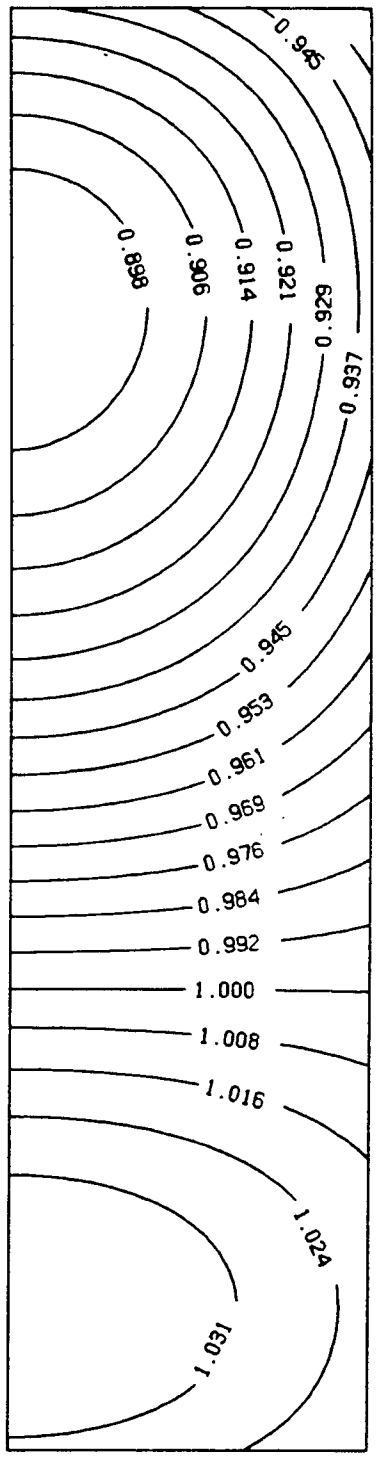
0.945
0.898
0.906
0.914
0.921
0.929
0.937
0.945
0.953
0.961
0.969
0.976
0.984
0.992
1.000
1.008
1.016
1.024
1.031

b

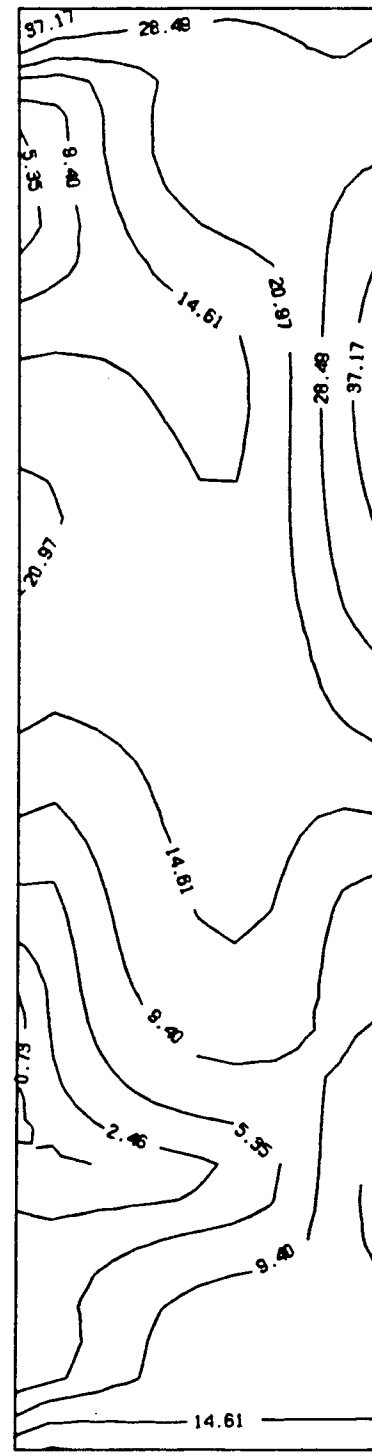
97.17
28.48
5.55
9.40
14.61
20.97
28.48
37.17
20.97
14.61
9.40
0.13
2.46
5.55
9.40
14.61

c

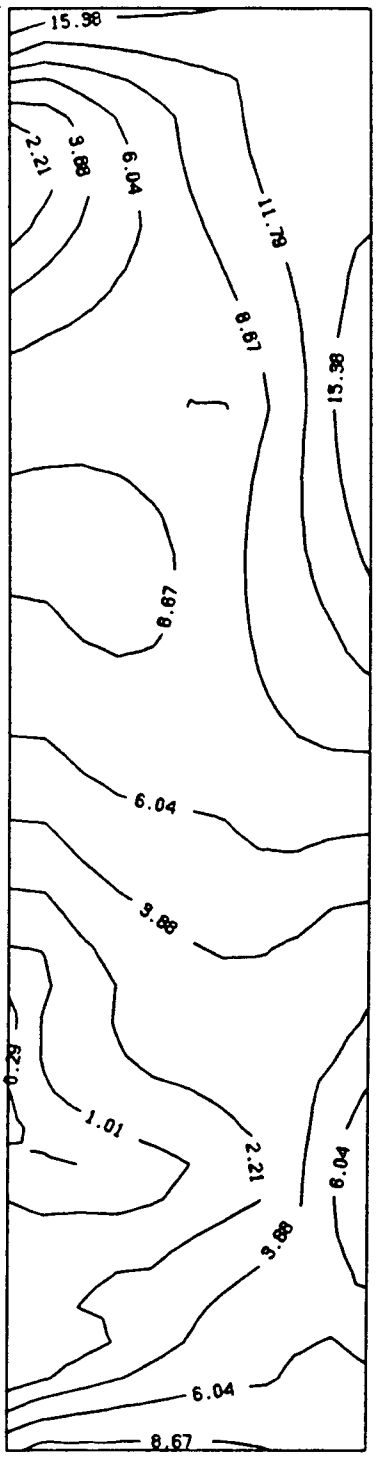
15.98
11.79
8.67
15.38
6.04
3.88
2.21
8.67
6.04
3.88
1.01
2.21
8.04
3.88
6.04
8.67

d

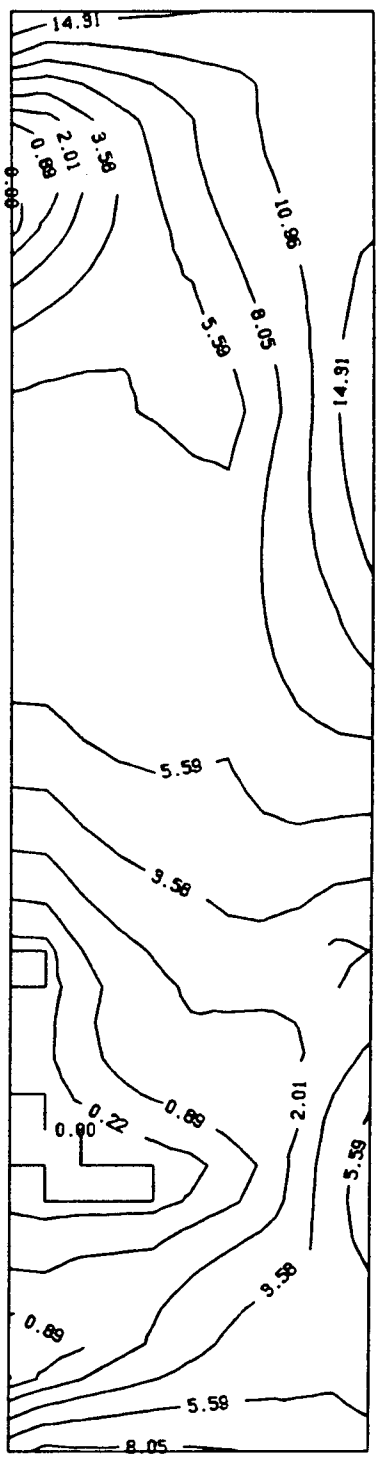
14.91
10.96
8.05
14.91
5.59
3.58
2.01
0.89
0.00
5.59
3.58
0.89
0.00
2.01
5.59
3.58
0.89
5.58
8.05

e

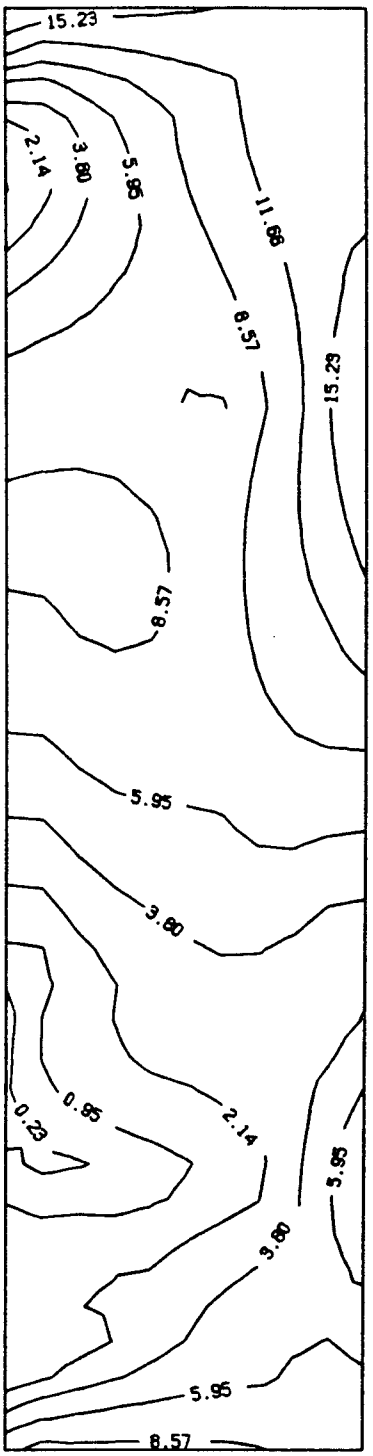

f

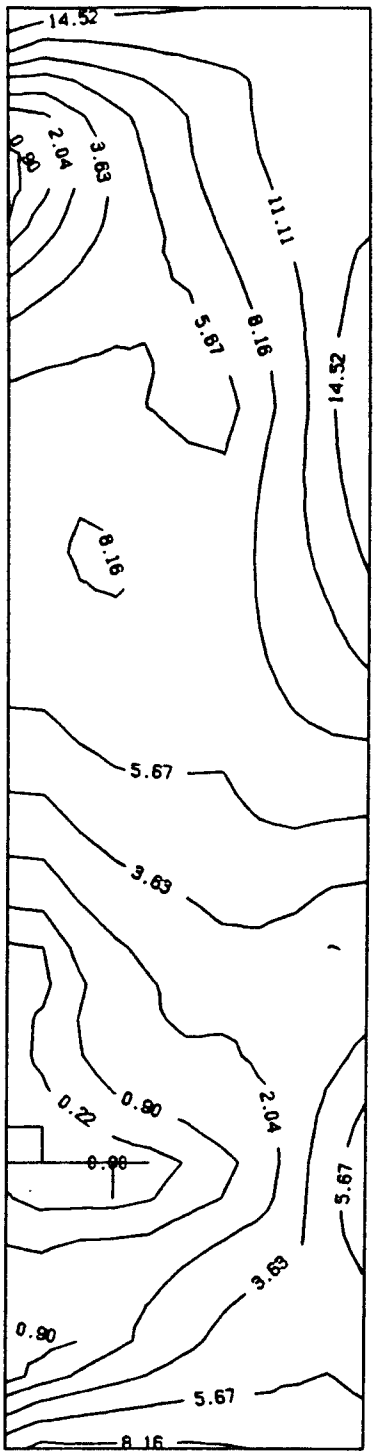

XIV.2.1.1.4 Time 60 seconds
(a) Temperature ; (b) Von Mises Stress
(c) MRSS ; (d) MRSS-CRSS (Yield) ;
(e) MRSS-CRSS (MB) ; (f) MRSS-CRSS (MBTe) .

a

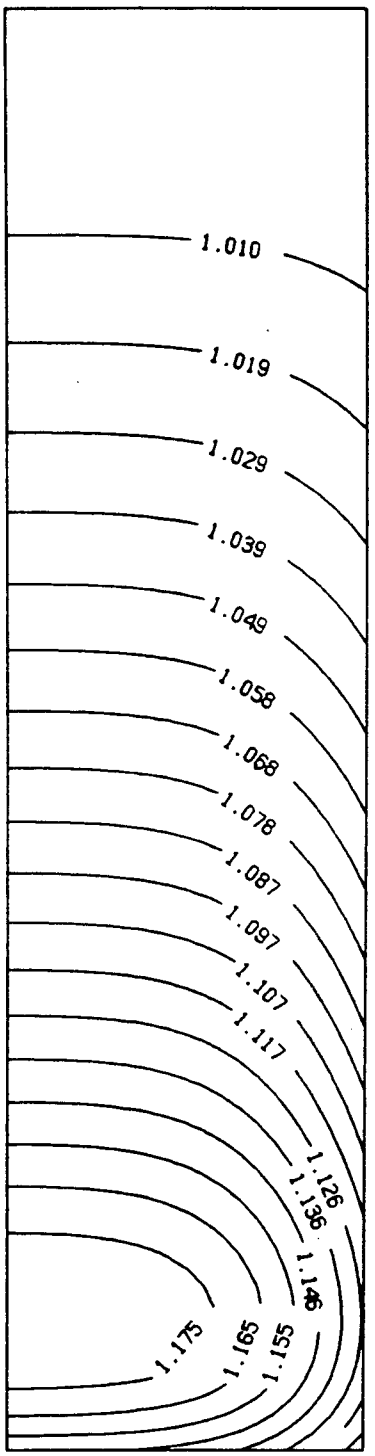
1.010
1.019
1.029
1.039
1.049
1.058
1.068
1.078
1.087
1.097
1.107
1.117
1.126
1.136
1.146
1.155
1.165
1.175

b

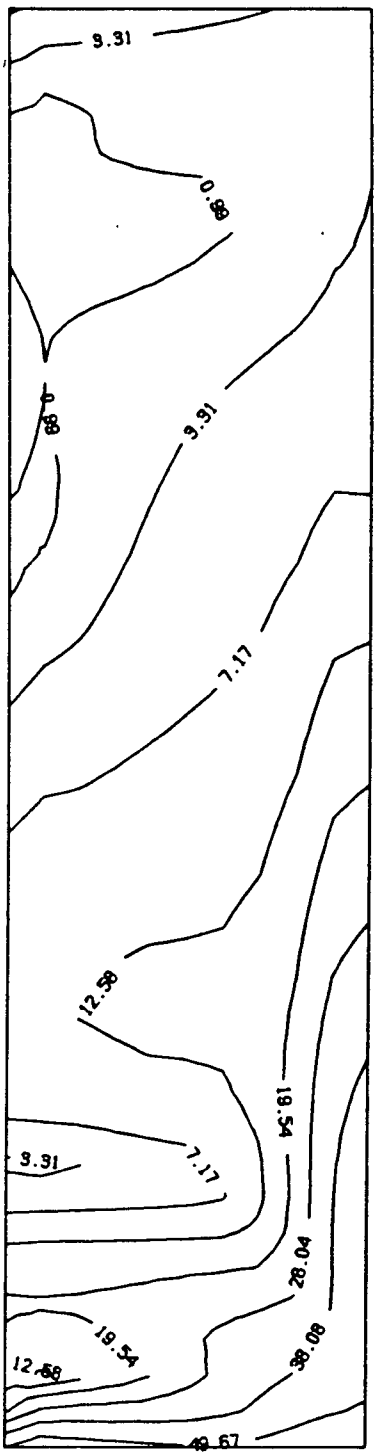
9.31
0.00
9.31
7.17
12.58
18.54
3.31
7.17
28.04
19.54
38.08
12.58
49.67

c

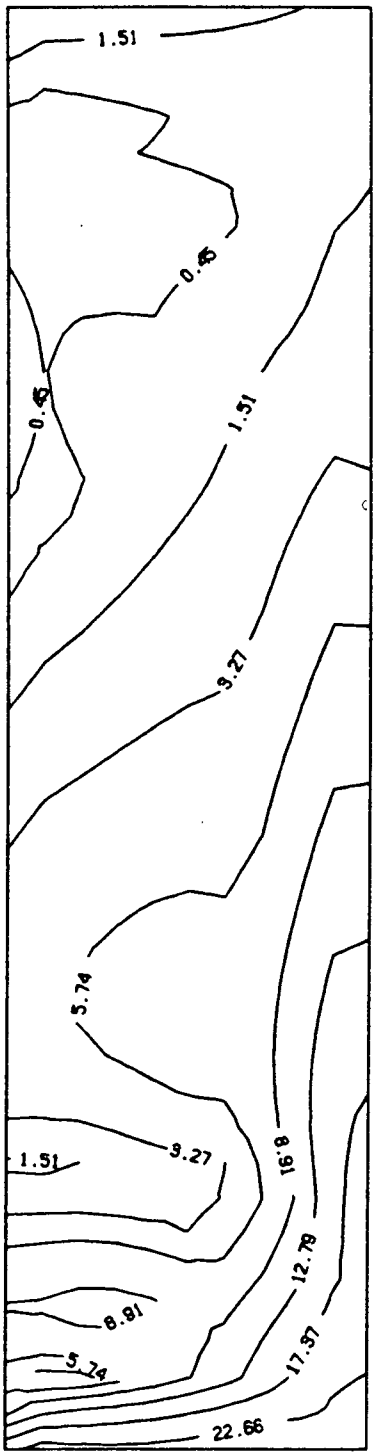
1.51
0.45
0.45
1.51
3.27
5.74
1.51
3.27
16.8
12.79
8.91
5.74
17.57
22.66

d

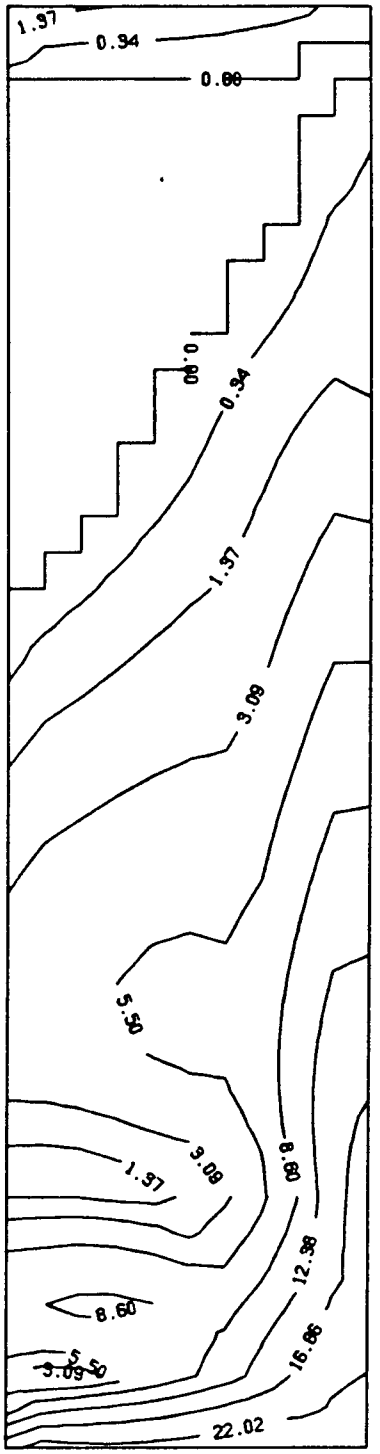
1.97
0.94
0.00
0.00
0.94
1.97
3.09
5.50
1.97
3.09
8.60
5.50
3.09
8.60
12.38
16.66
22.02

e

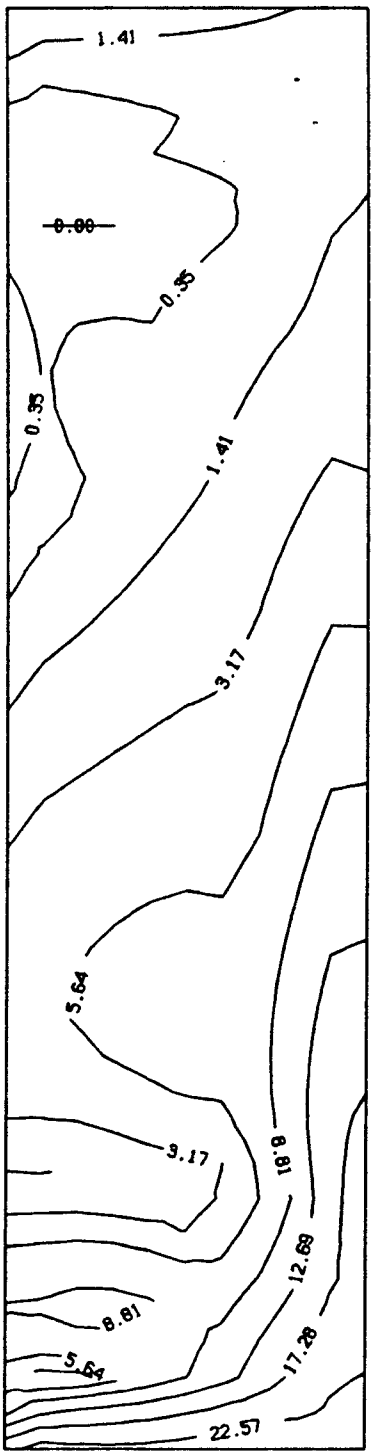

f

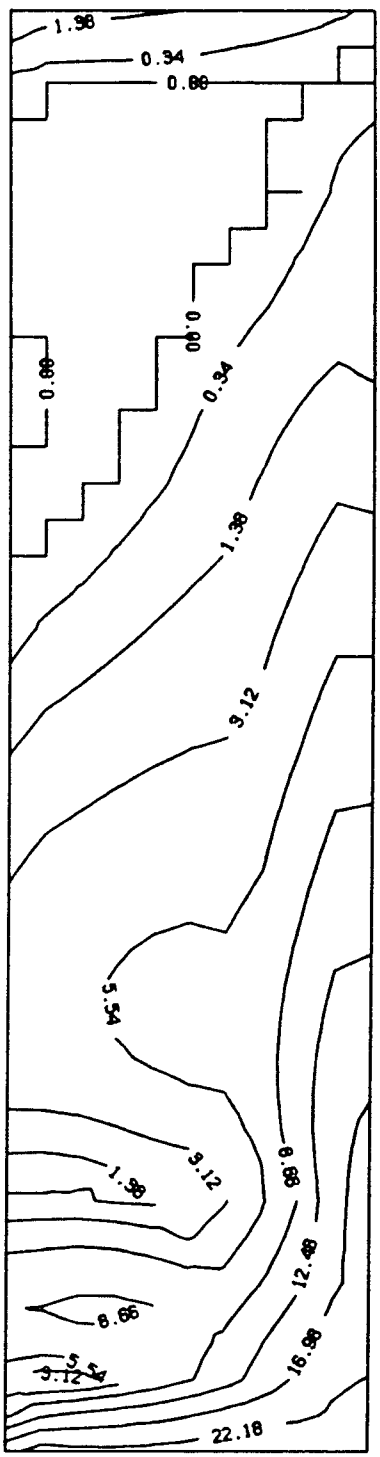

XIV.2.1.2 Initial Gradient GC/2 ; Time 10 seconds .
(a) Temperature ; (b) Von Mises Stress
(c) MRSS ; (d) MRSS-CRSS (Yield) ;
(e) MRSS-CRSS (MB) ; (f) MRSS-CRSS (MBTe) .

a

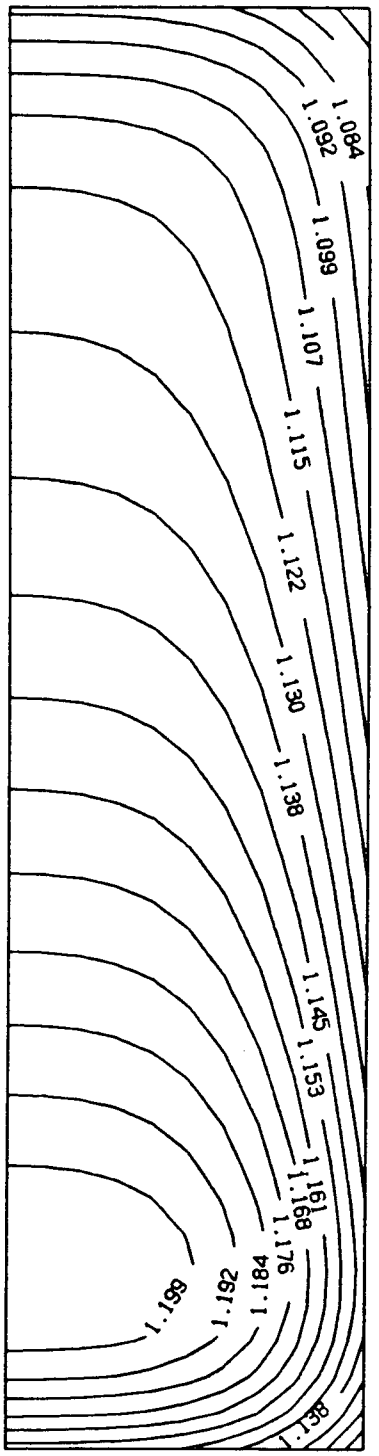
1.084
1.092
1.099
1.107
1.115
1.122
1.130
1.138
1.145
1.153
1.161
1.168
1.176
1.184
1.192
1.199

b

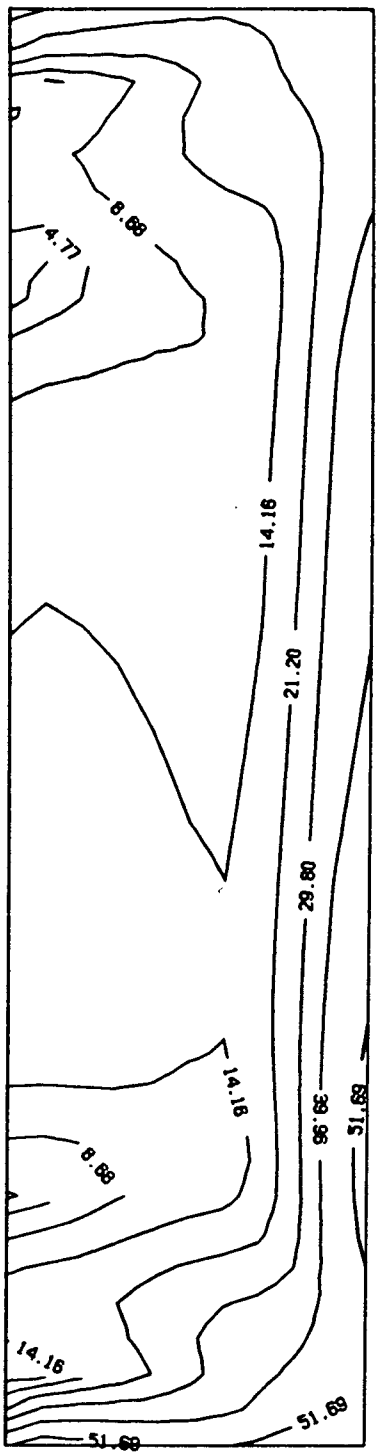
4.77
8.88
14.18
21.20
29.80
39.96
51.69
14.18
8.88
14.16
51.68
51.69

c

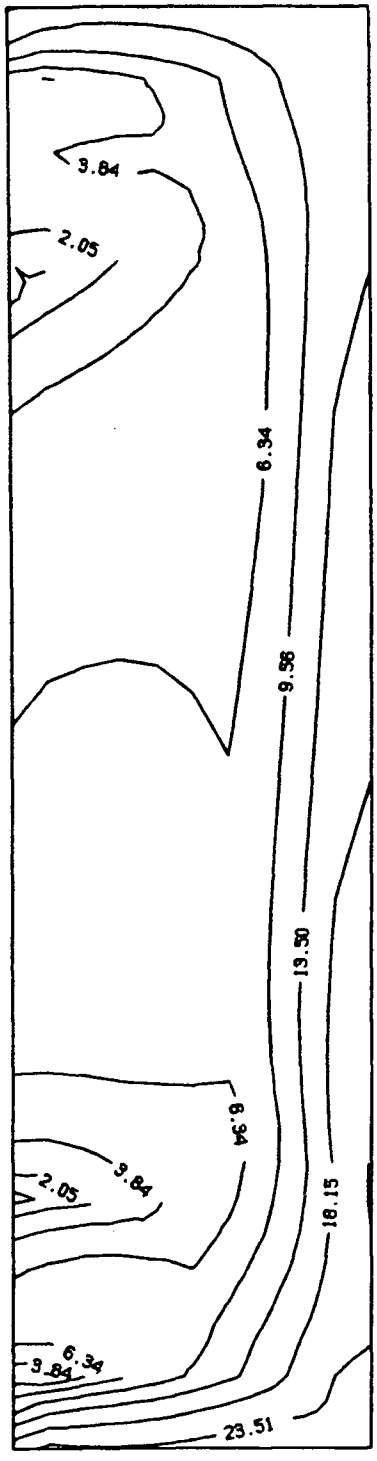

d

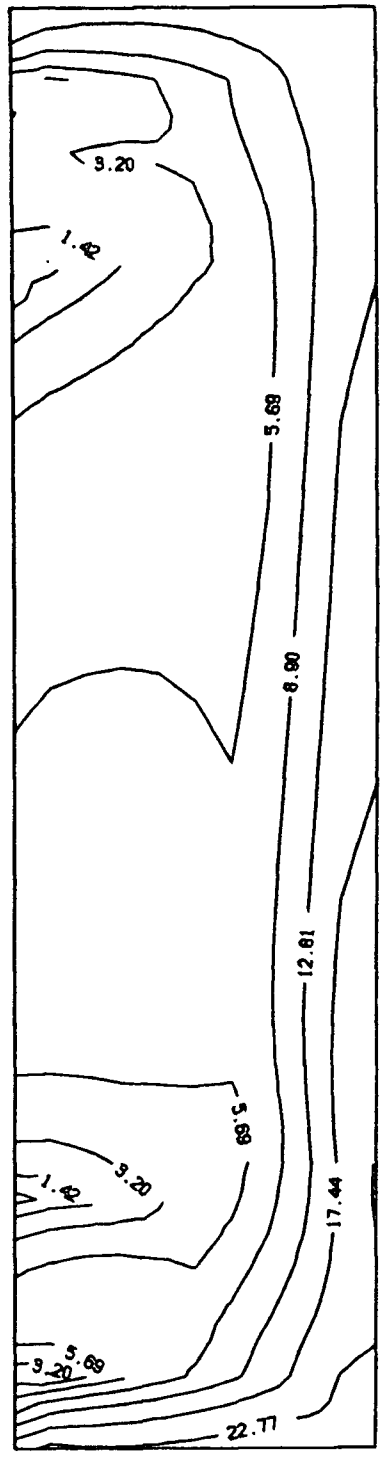

e

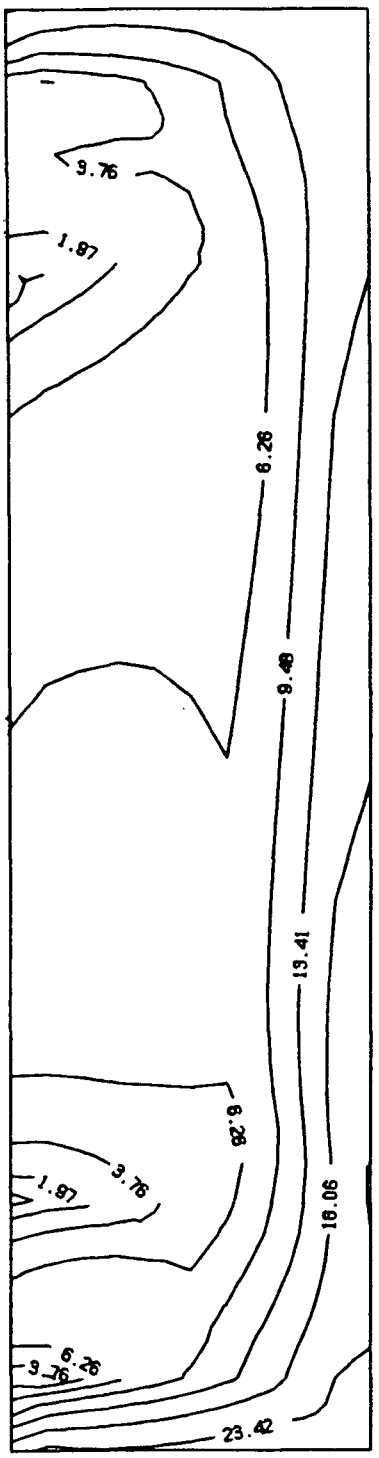

f

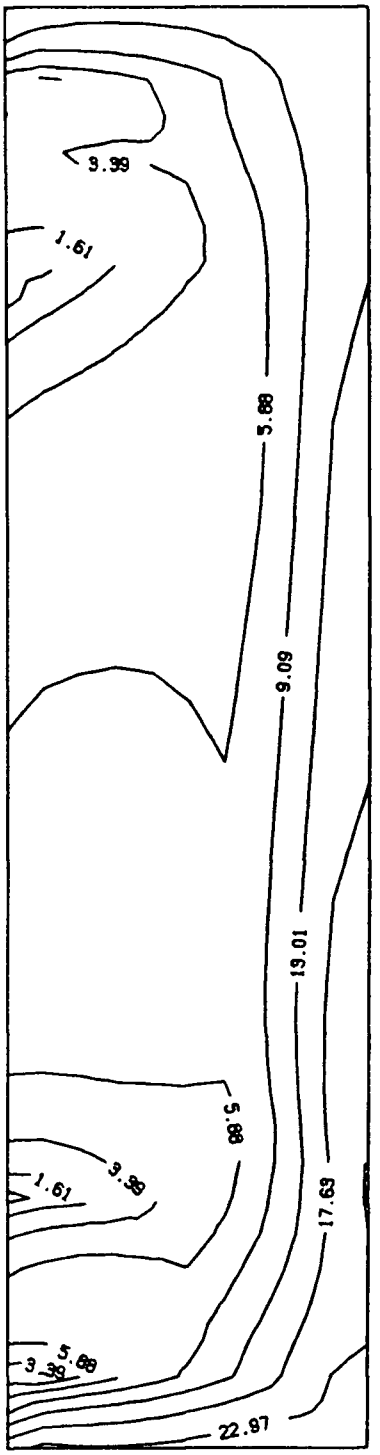

XIV.2.1.3.1.1 (a) Temperature ; (b) Von Mises Stress
(c) MRSS ; (d) MRSS-CRSS (Yield) ;
(e) MRSS-CRSS (MB) ; (f) MRSS-CRSS (MBTe) .

a

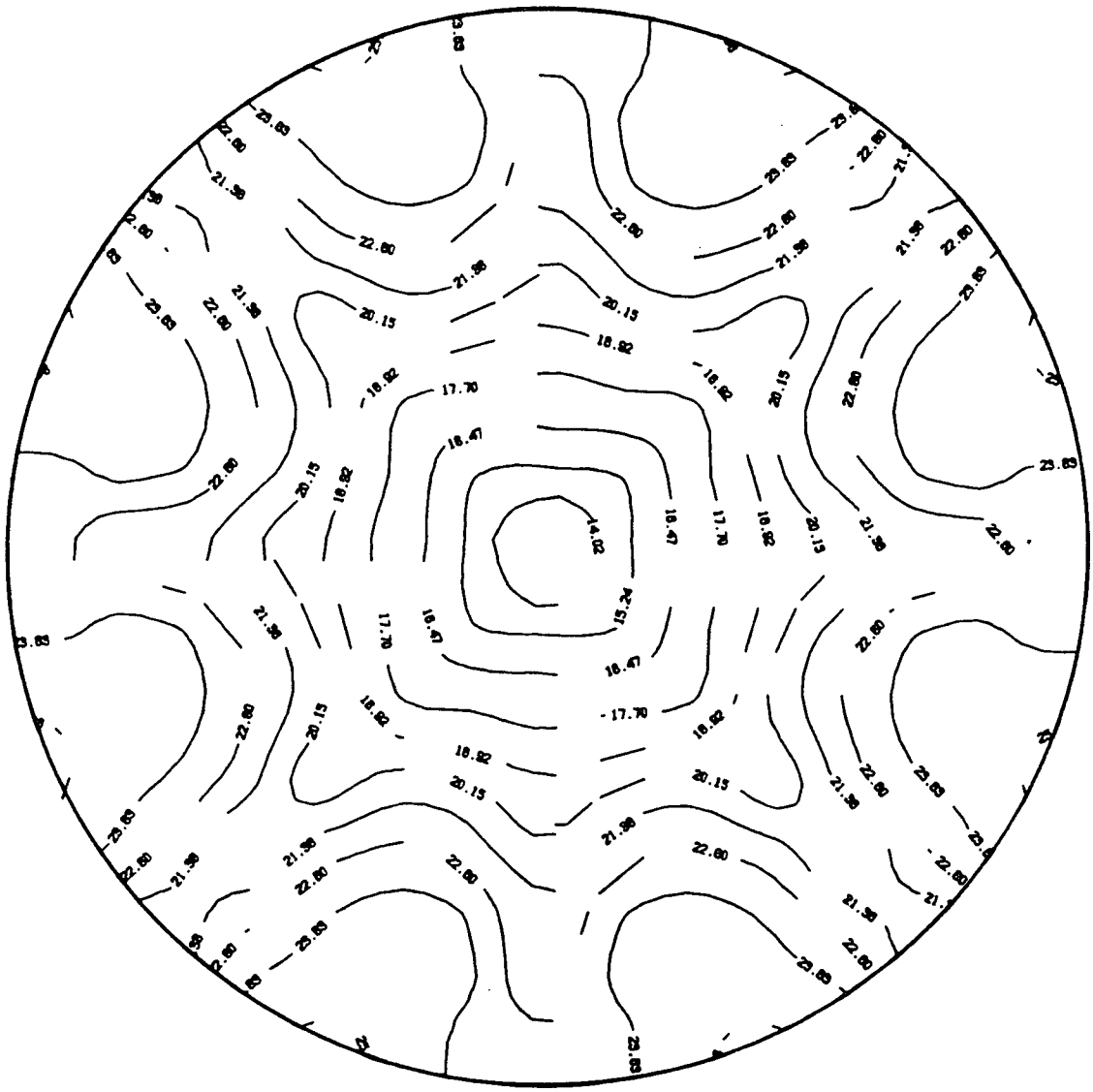

b

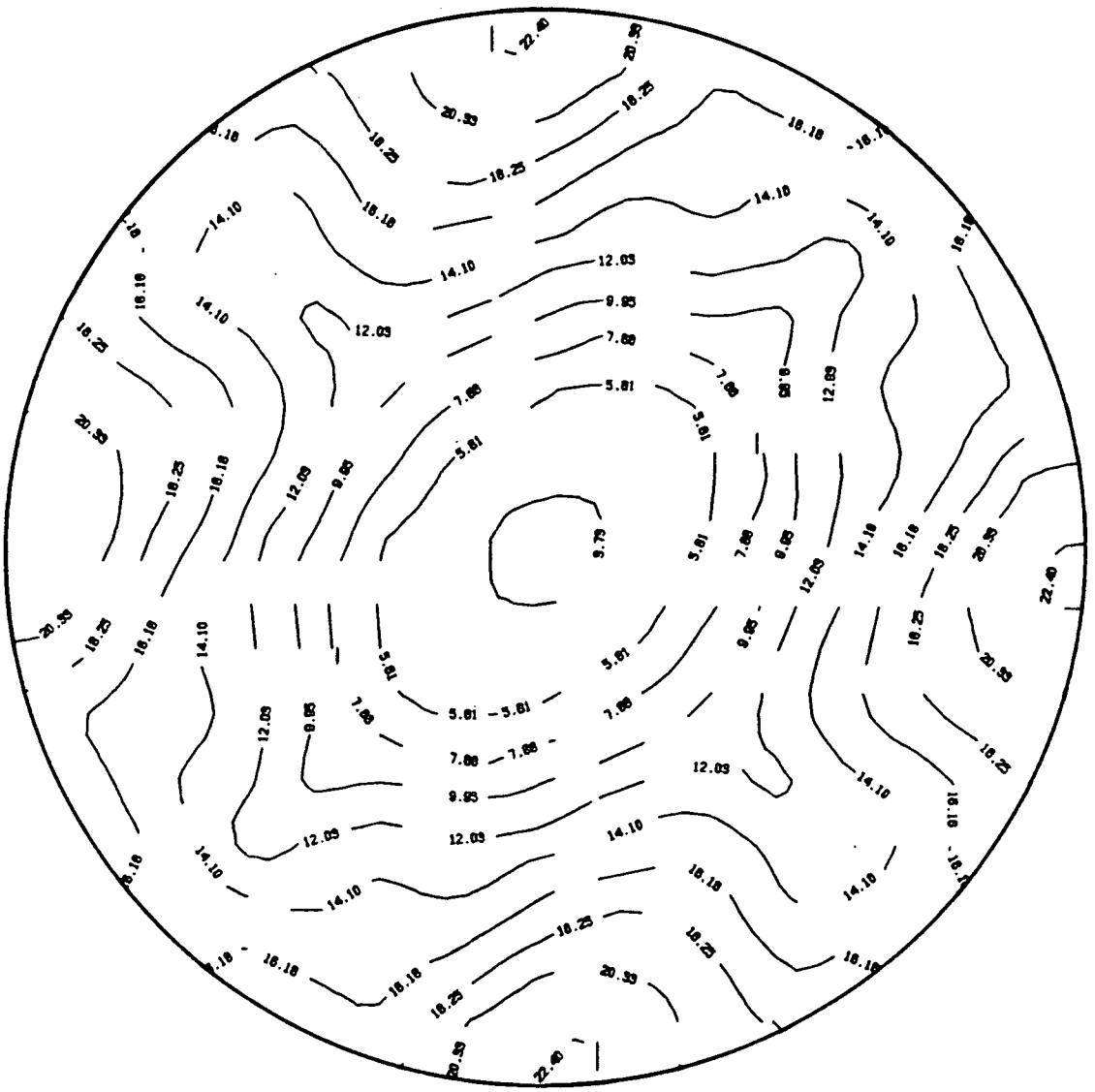

C

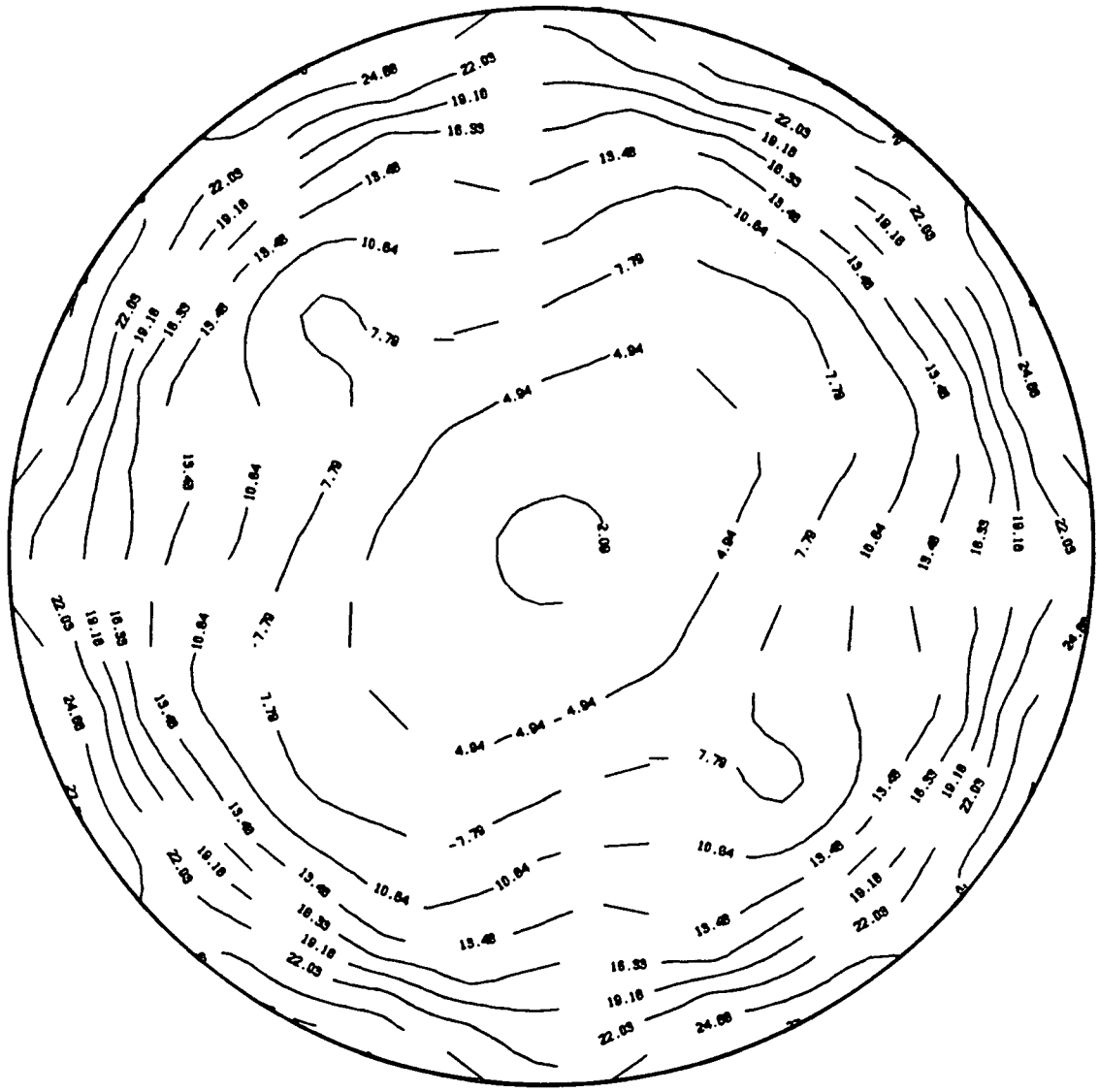

d

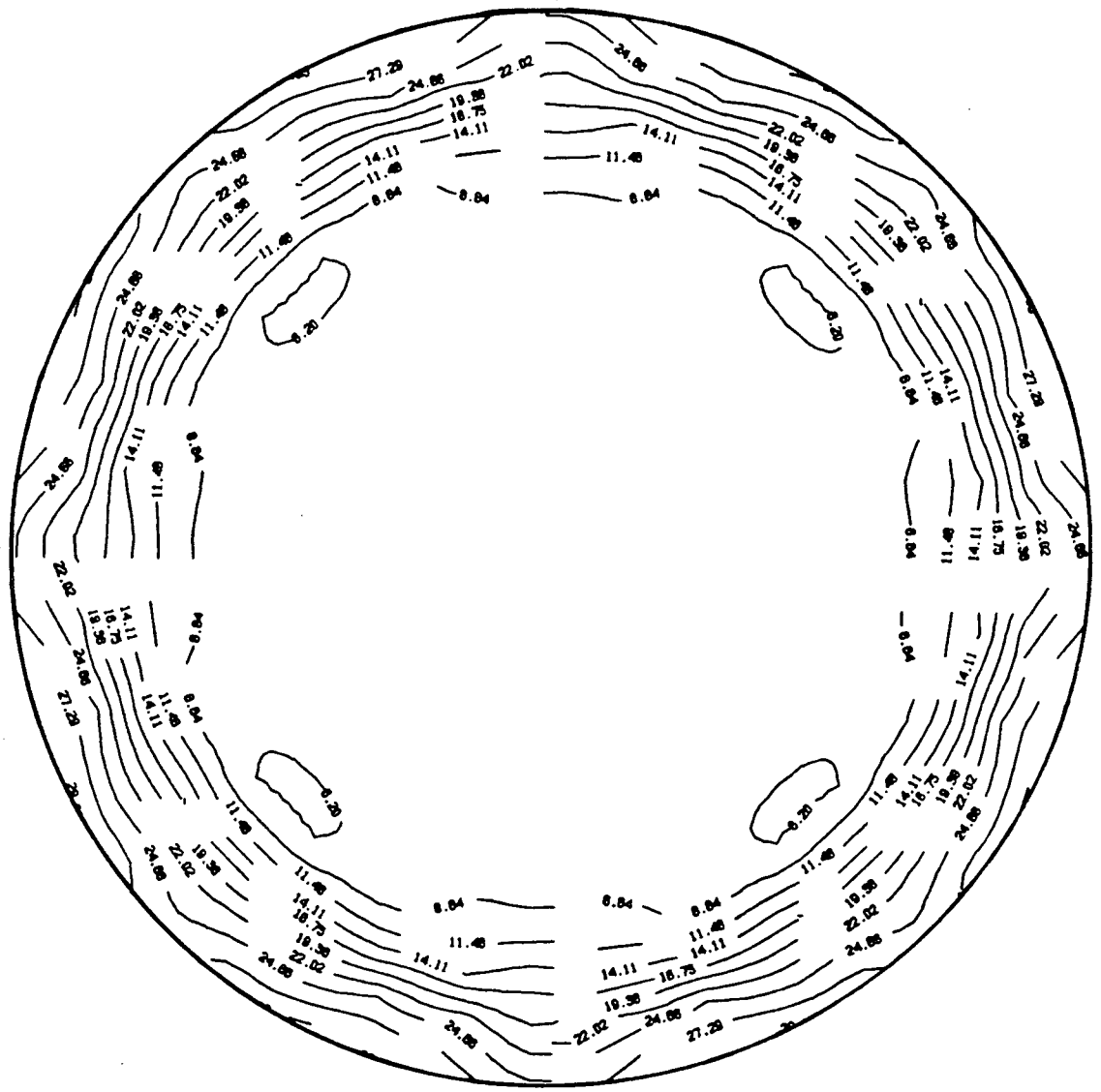

XIV.2.1.3.1.2 MRSS-CRSS (Yield) in cross-sections at a distance from the interface of :
(a) 2.75 mm ; (b) 8.25 mm ; (c) 16.5 mm ;
(d) 27.5 mm .

a

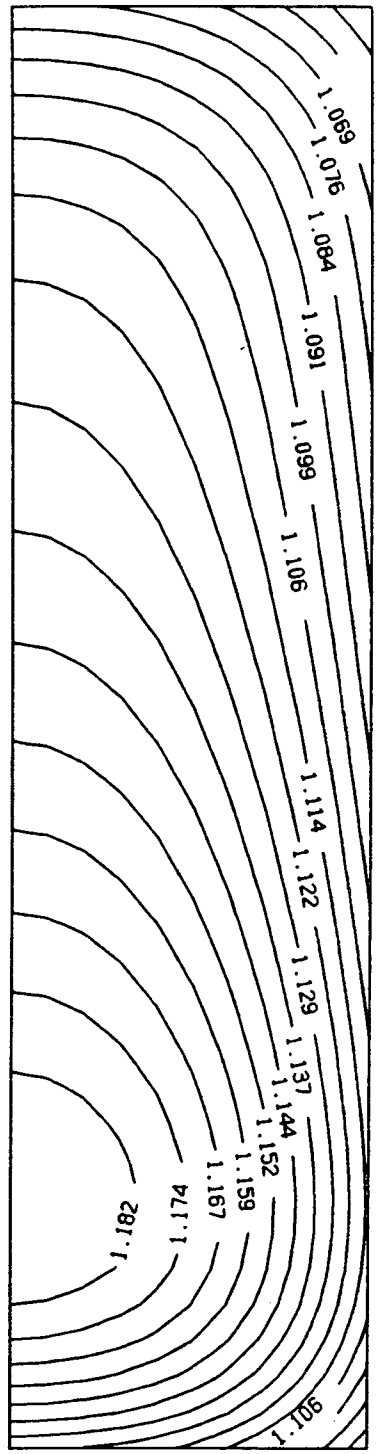
1.069
1.076
1.084
1.091
1.099
1.106
1.114
1.122
1.129
1.137
1.144
1.152
1.159
1.167
1.174
1.182
1.106

b

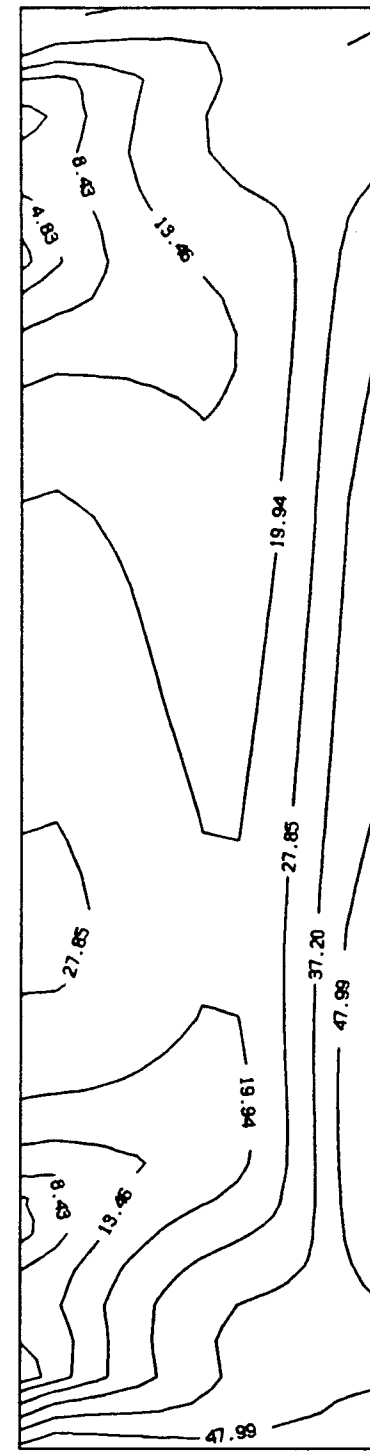
4.83
8.43
13.46
19.94
27.85
37.20
47.99
27.85
19.94
8.43
13.46
47.99

c

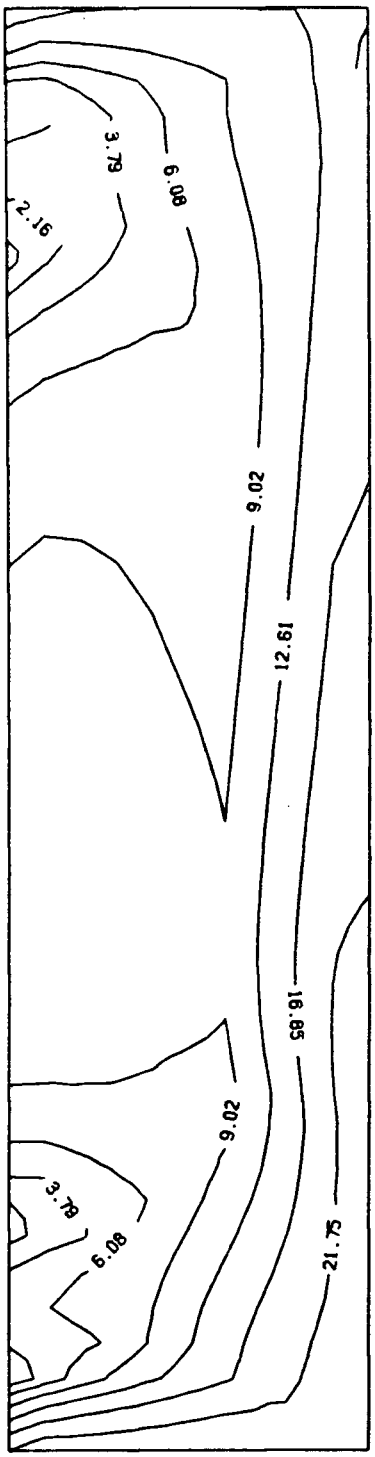
2.16
3.79
6.08
9.02
12.61
16.85
21.75
3.79
6.08
9.02

d

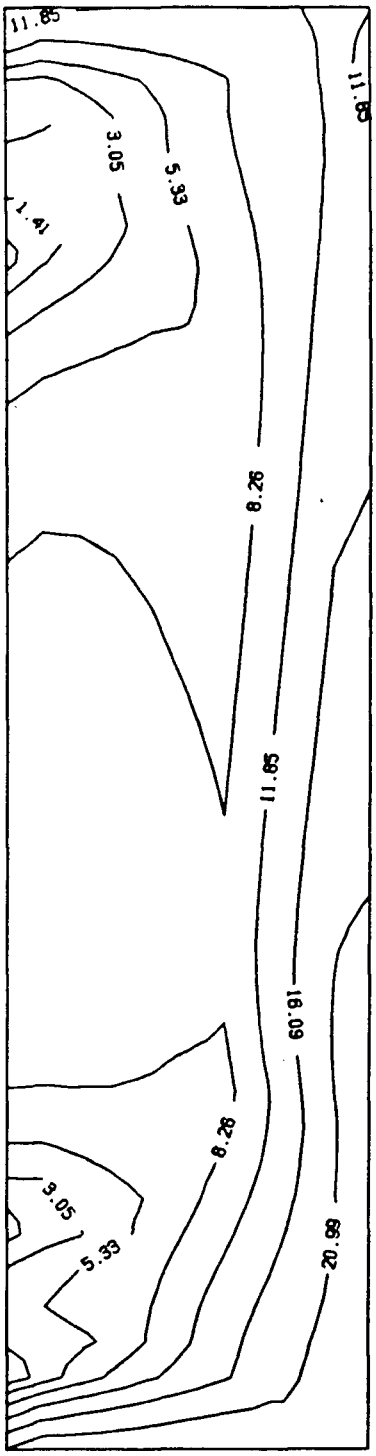
1.41
3.05
5.93
8.26
11.85
16.09
20.99
9.05
5.33
8.26
11.85

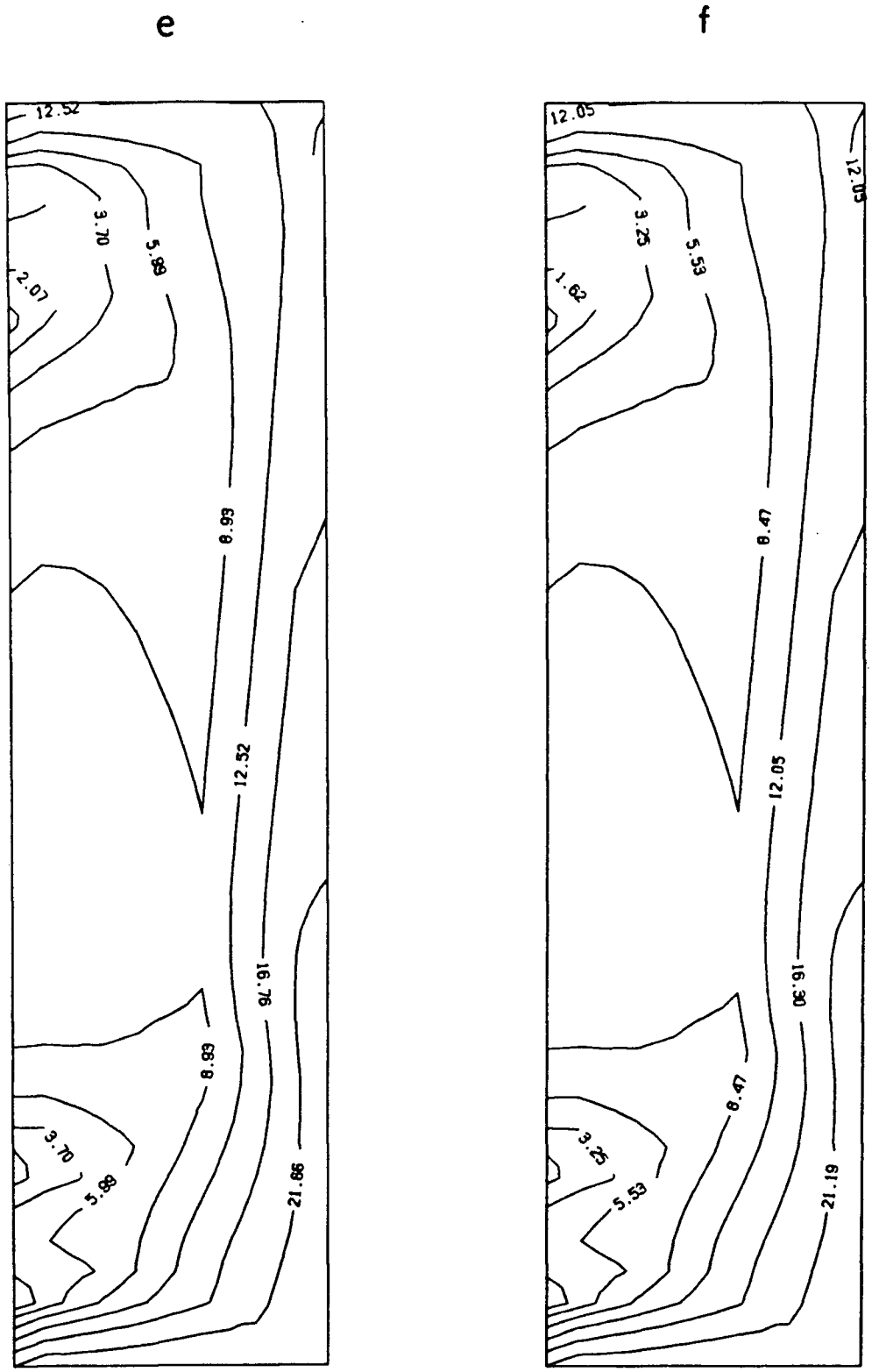

XIV.2.1.3.2.1 (a) Temperature ; (b) Von Mises Stress
(c) MRSS ; (d) MRSS-CRSS (Yield) ;
(e) MRSS-CRSS (MB) ; (f) MRSS-CRSS (MBTe) .

a

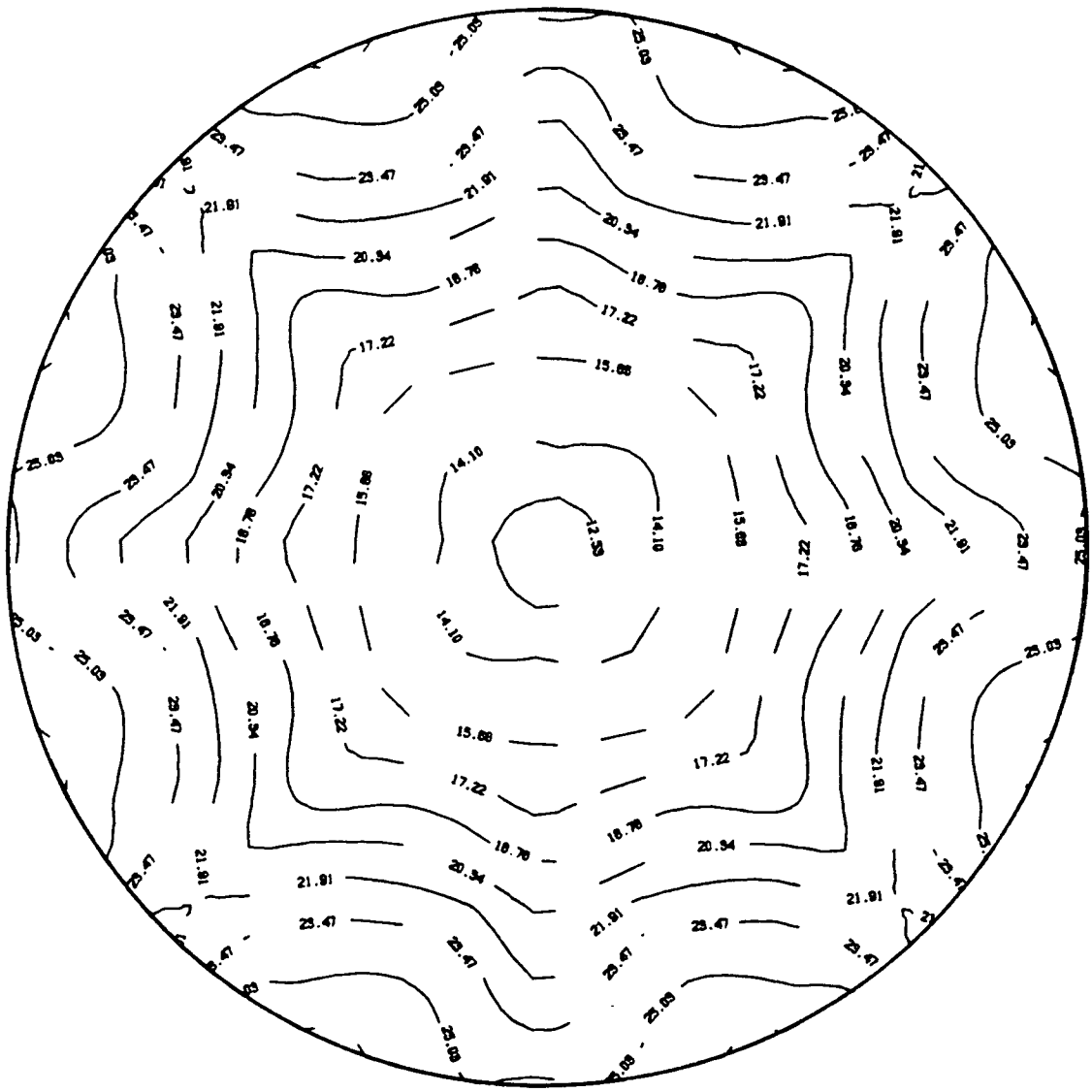

b

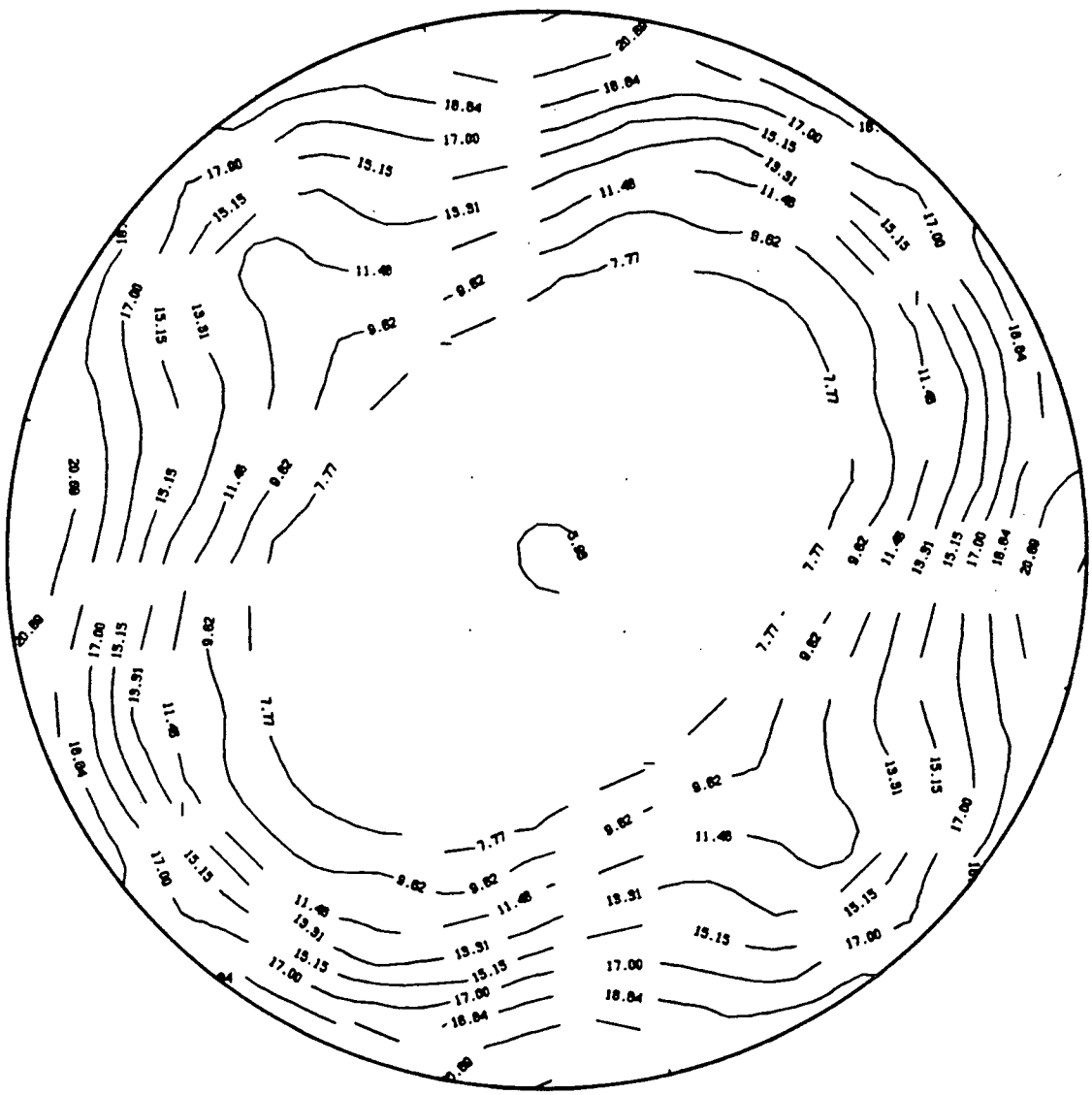

C

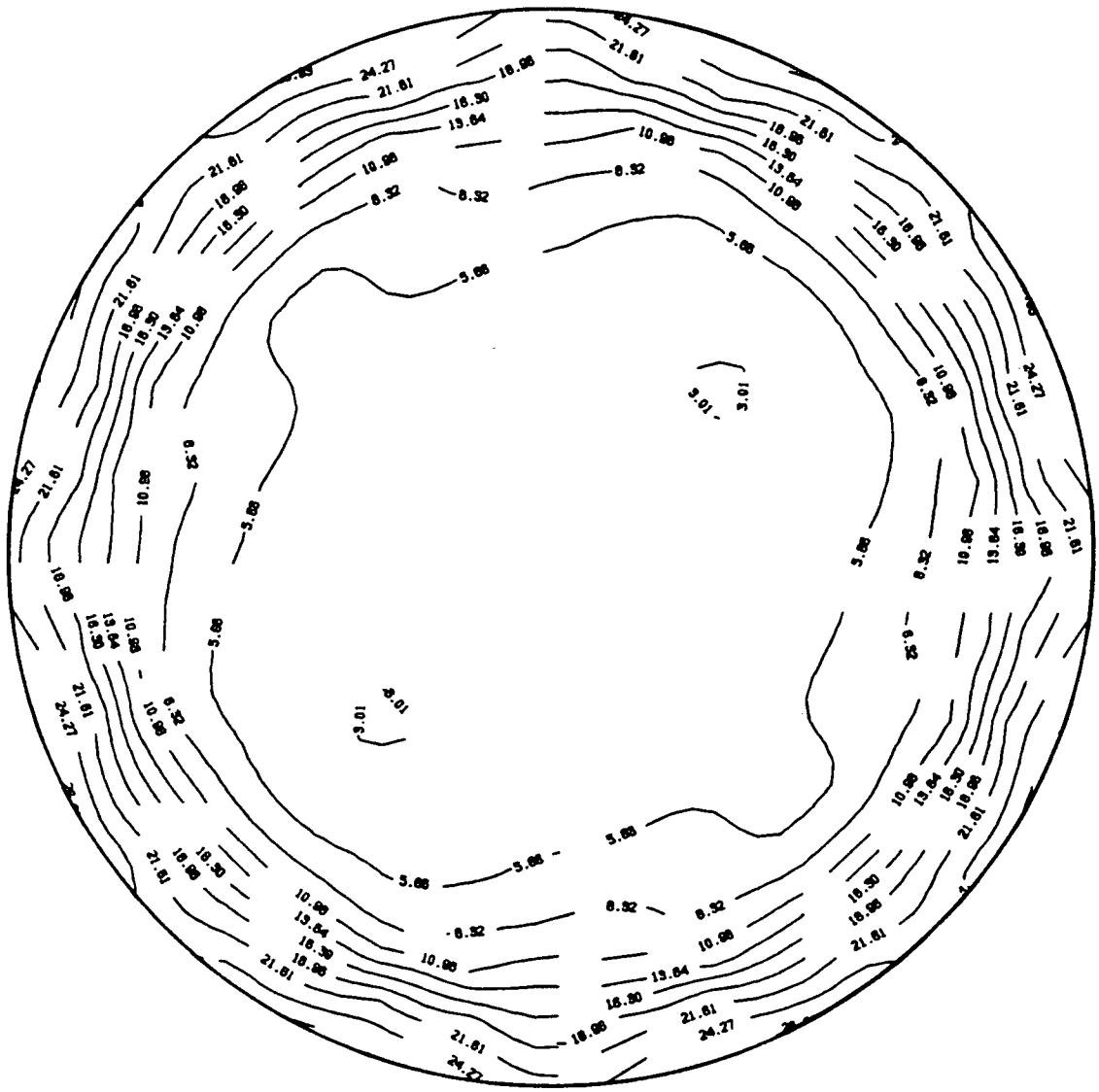

d

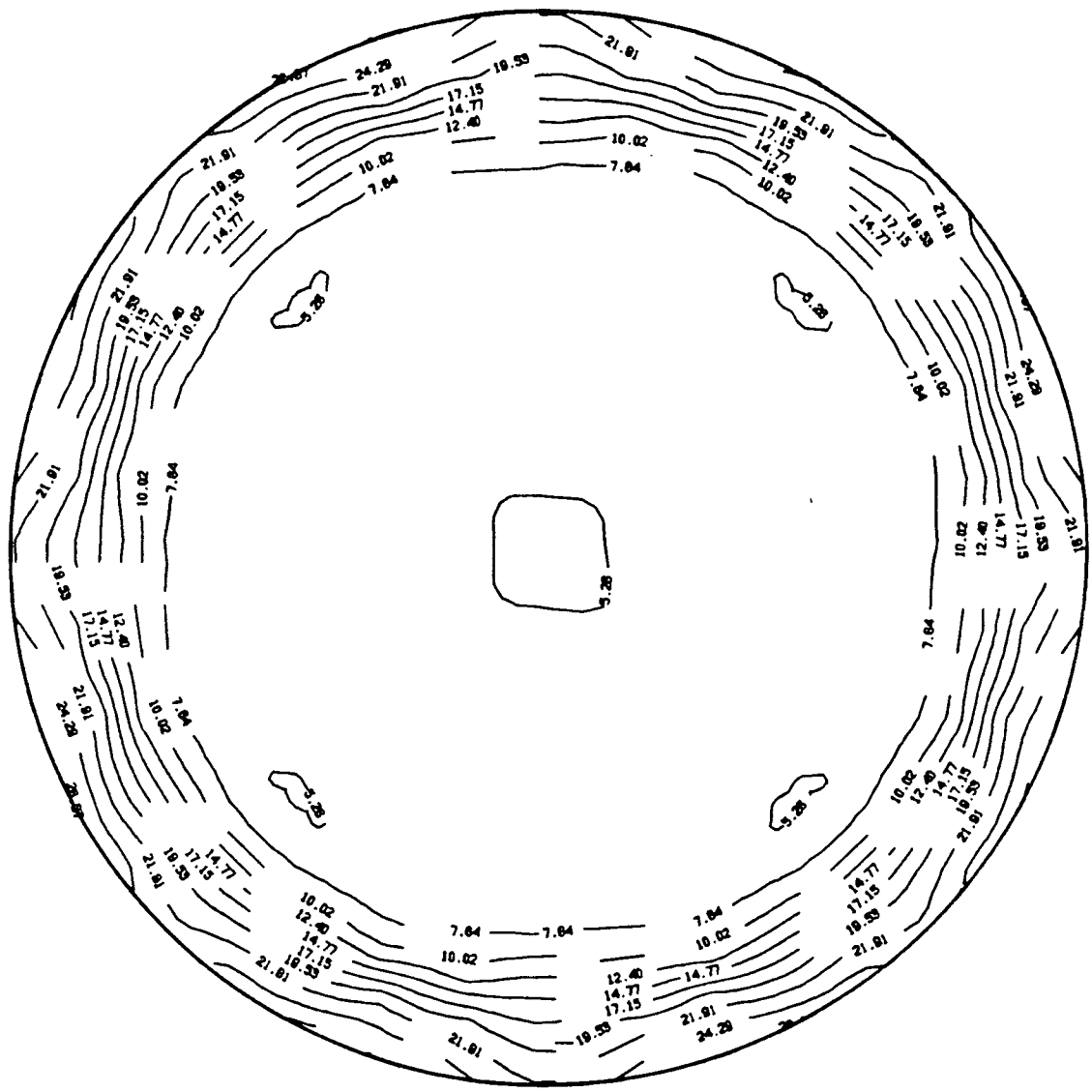

XIV.2.1.3.2.2 MRSS-CRSS (Yield) in cross-sections at a distance from the interface of :
(a) 2.75 mm ; (b) 8.25 mm ; (c) 16.5 mm ;
(d) 27.5 mm .

a

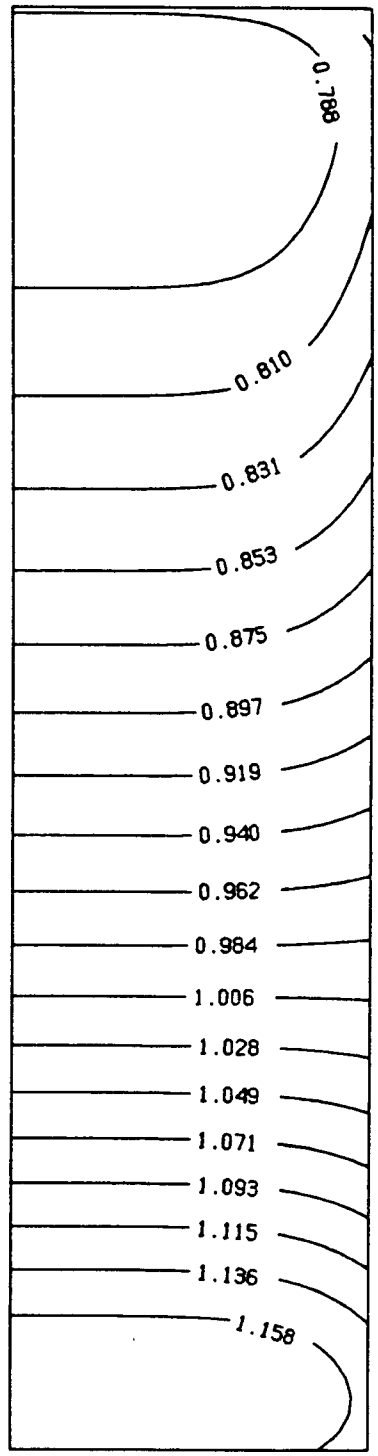
0.788
0.810
0.831
0.853
0.875
0.897
0.919
0.940
0.962
0.984
1.006
1.028
1.049
1.071
1.093
1.115
1.136
1.158

b

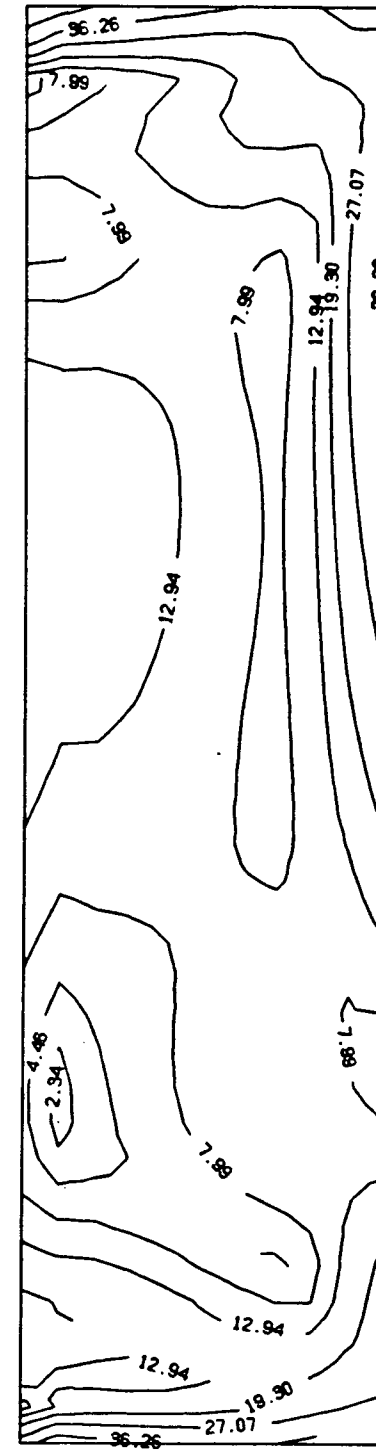
96.26
7.89
7.88
27.07
19.30
12.94
7.99
12.94
4.48
2.34
7.88
7.88
12.94
12.94
19.30
27.07
96.26

c

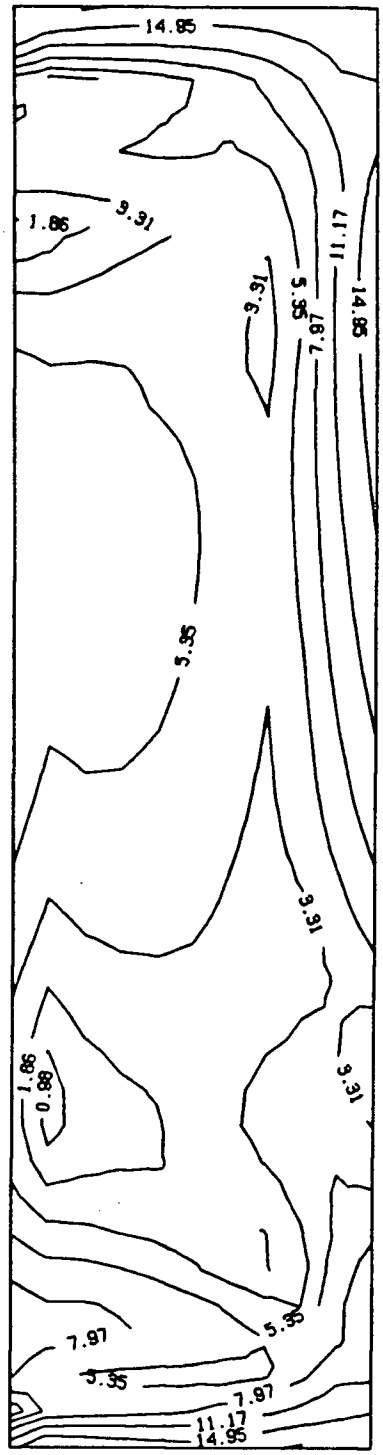
14.85
1.86
3.91
3.91
5.95
7.97
11.17
14.85
5.95
3.91
1.86
0.98
3.91
7.97
5.35
5.95
7.97
11.17
14.95

d

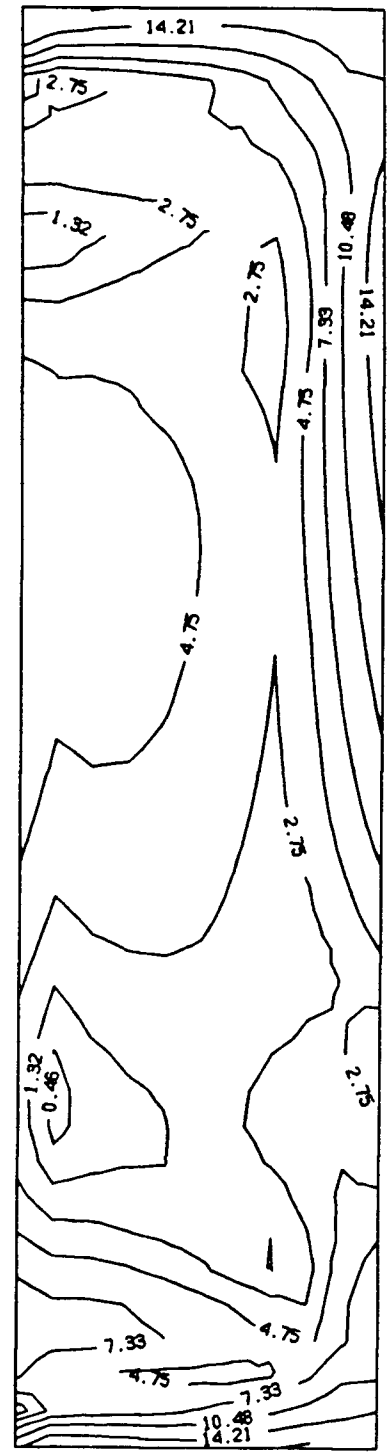
14.21
2.75
1.32
2.75
2.75
7.33
10.48
14.21
4.75
4.75
2.75
1.32
0.46
2.75
4.75
7.33
4.75
7.33
10.48
14.21

e

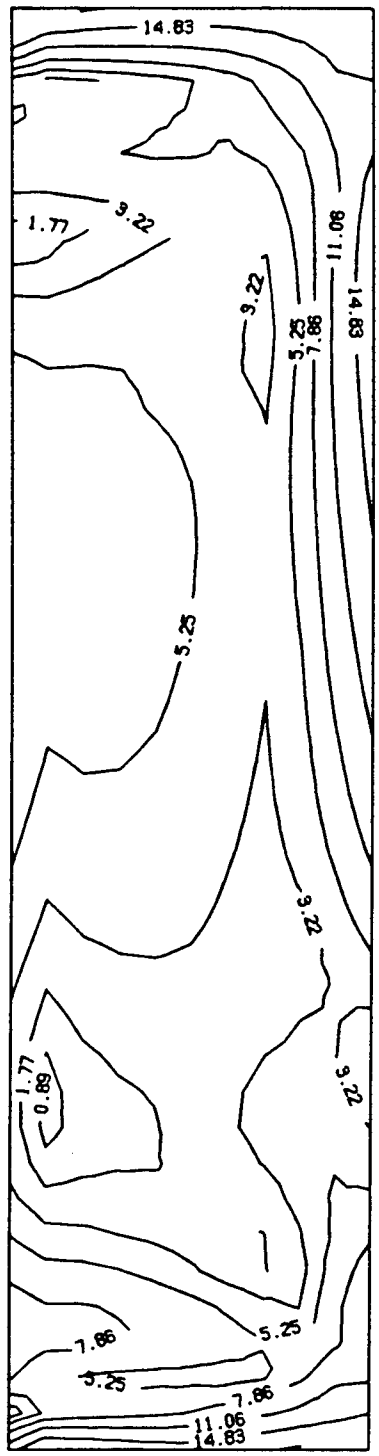

f

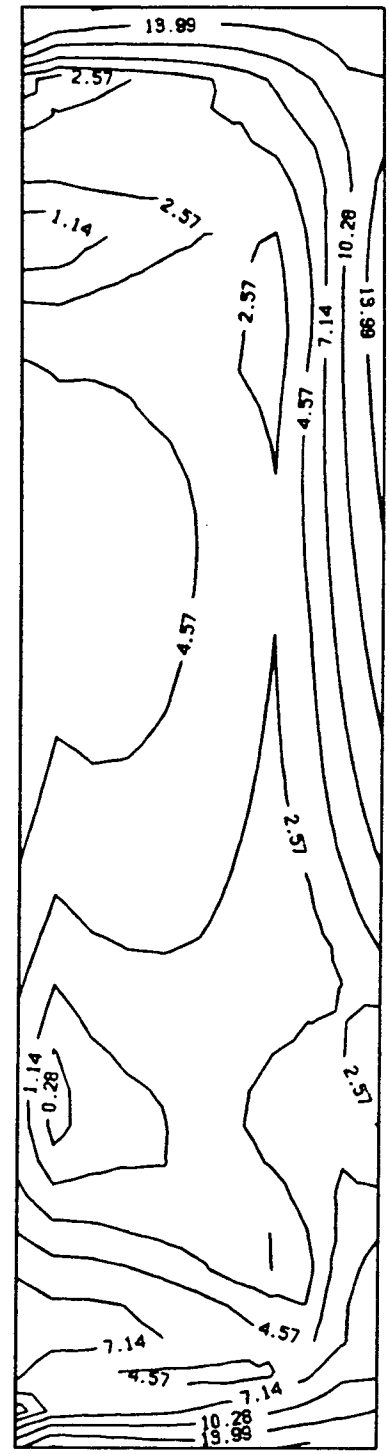

XIV.2.2.1.1 Time 5 seconds
(a) Temperature ; (b) Von Mises Stress
(c) MRSS ; (d) MRSS-CRSS (Yield) ;
(e) MRSS-CRSS (MB) ; (f) MRSS-CRSS (MBTe) .

a

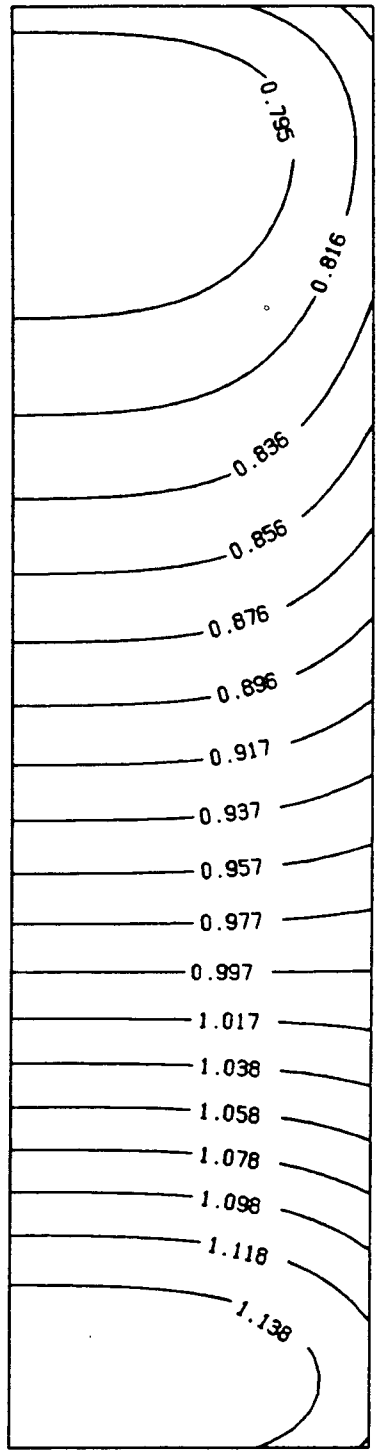
0.795
0.816
0.836
0.856
0.876
0.896
0.917
0.937
0.957
0.977
0.997
1.017
1.038
1.058
1.078
1.098
1.118
1.138

b

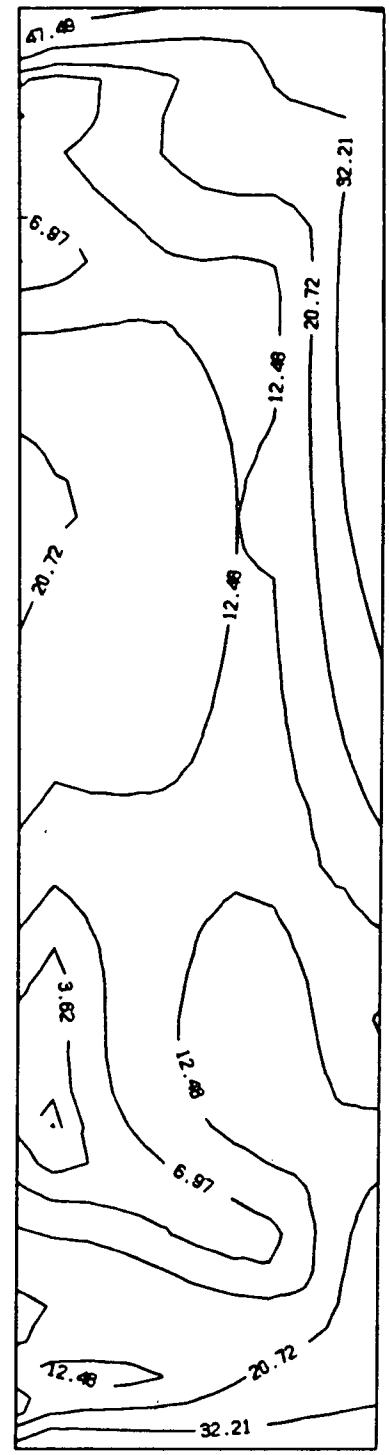
47.48
32.21
6.97
20.72
12.48
20.72
12.48
3.62
12.48
6.97
12.48
20.72
32.21

e

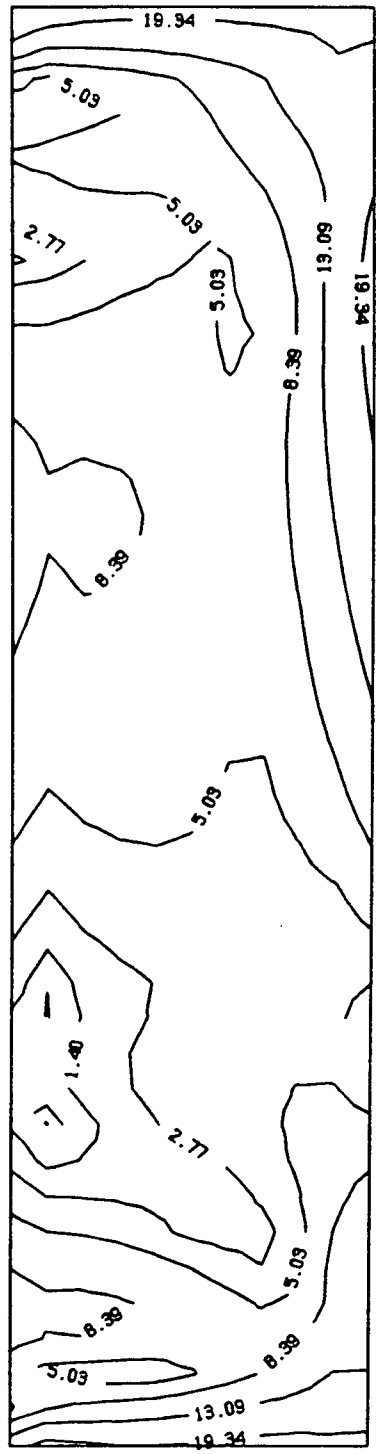

f

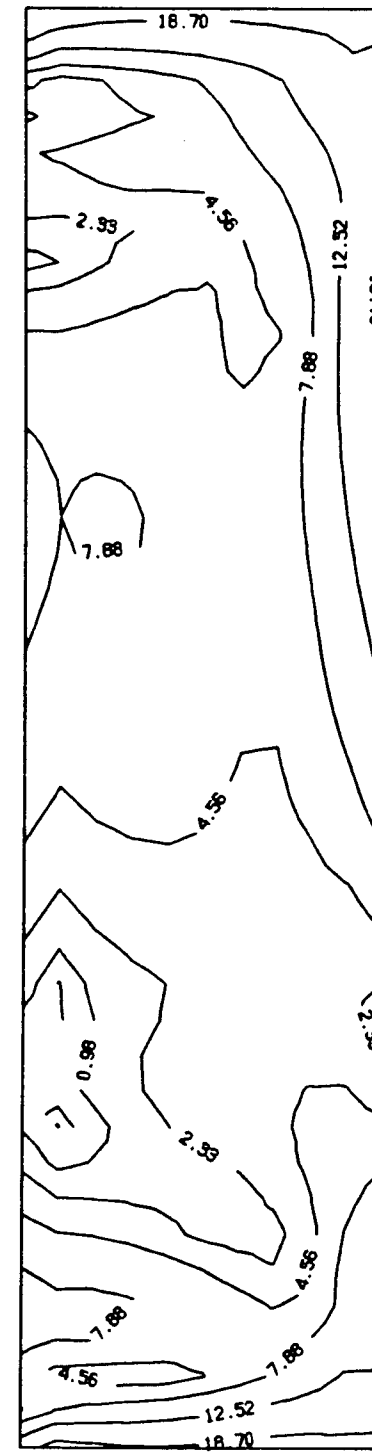

XIV.2.2.1.2.1 (a) Temperature ; (b) Von Mises Stress
(c) MRSS ; (d) MRSS-CRSS (Yield) ;
(e) MRSS-CRSS (MB) ; (f) MRSS-CRSS (MBTe) .

c

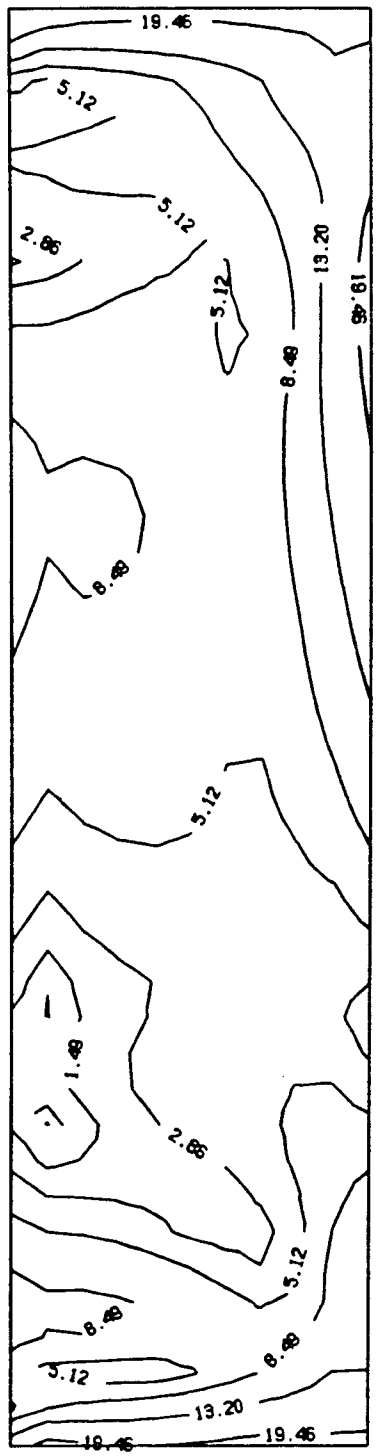
19.46
5.12
5.12
2.86
5.12
13.20
19.46
8.49
8.49
5.12
1.49
2.86
5.12
8.49
8.49
5.12
13.20
19.46
19.46

d

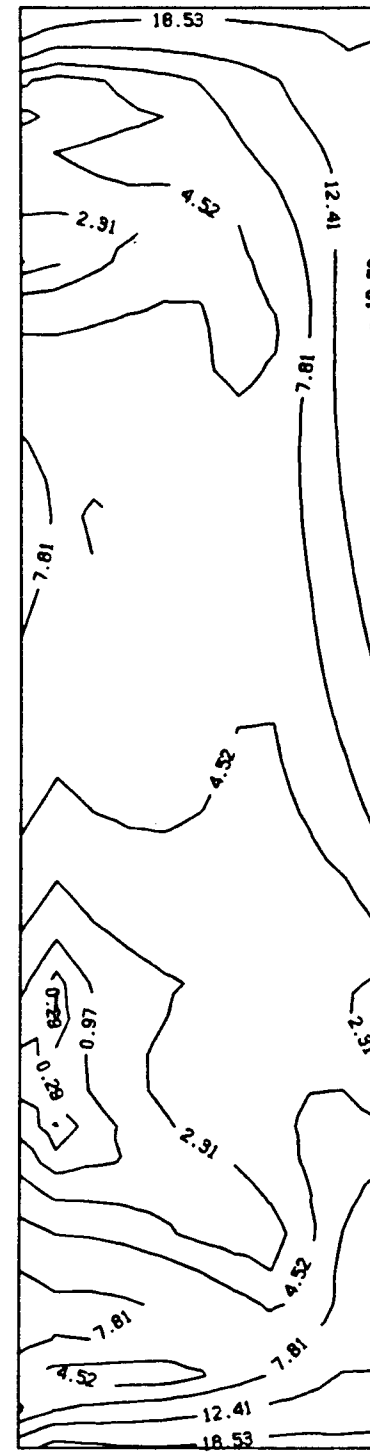
18.53
4.52
2.91
12.41
18.53
7.81
7.81
4.52
0.29
0.97
0.29
2.91
2.91
4.52
7.81
7.81
4.52
12.41
18.53

a

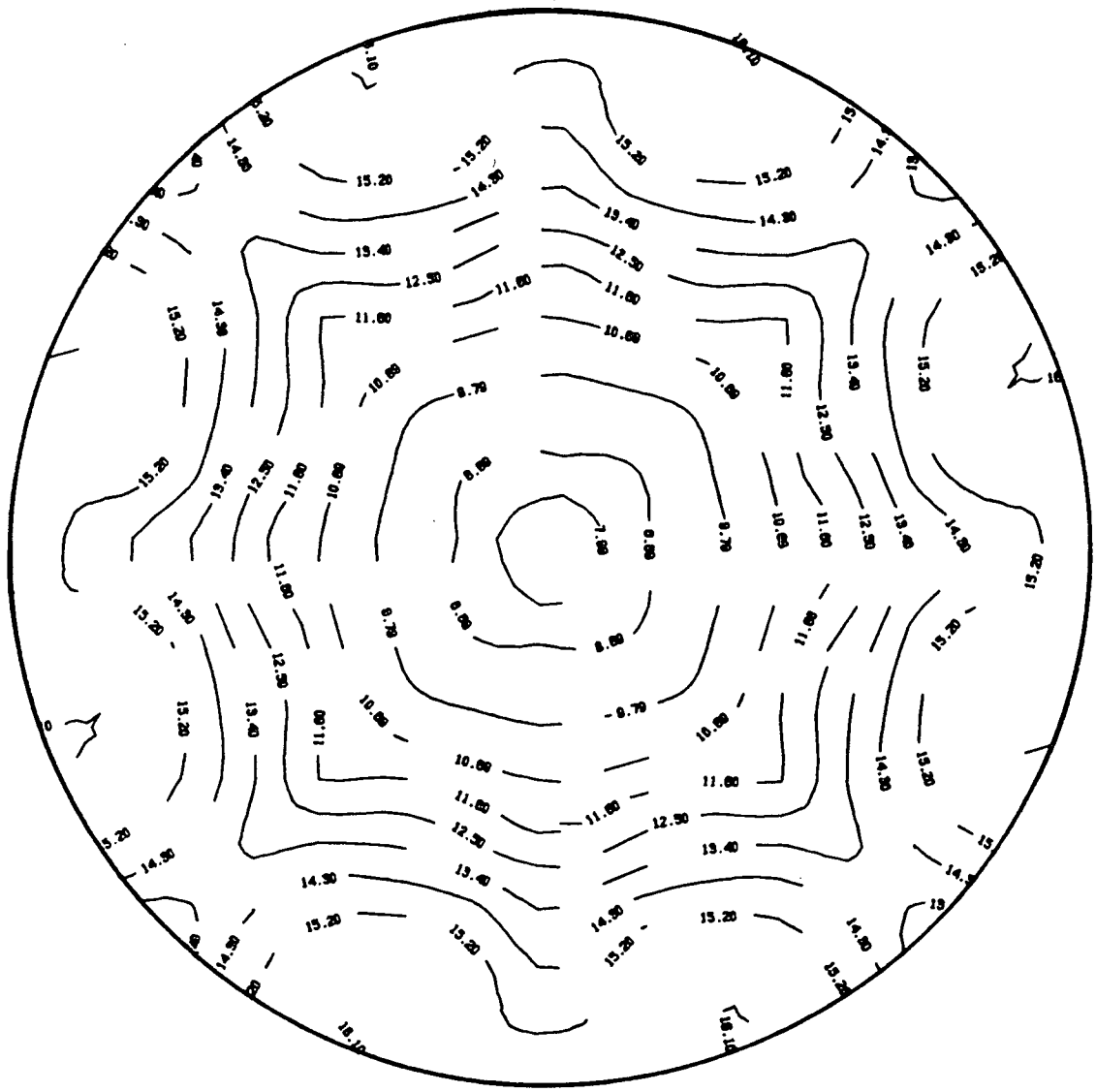

b

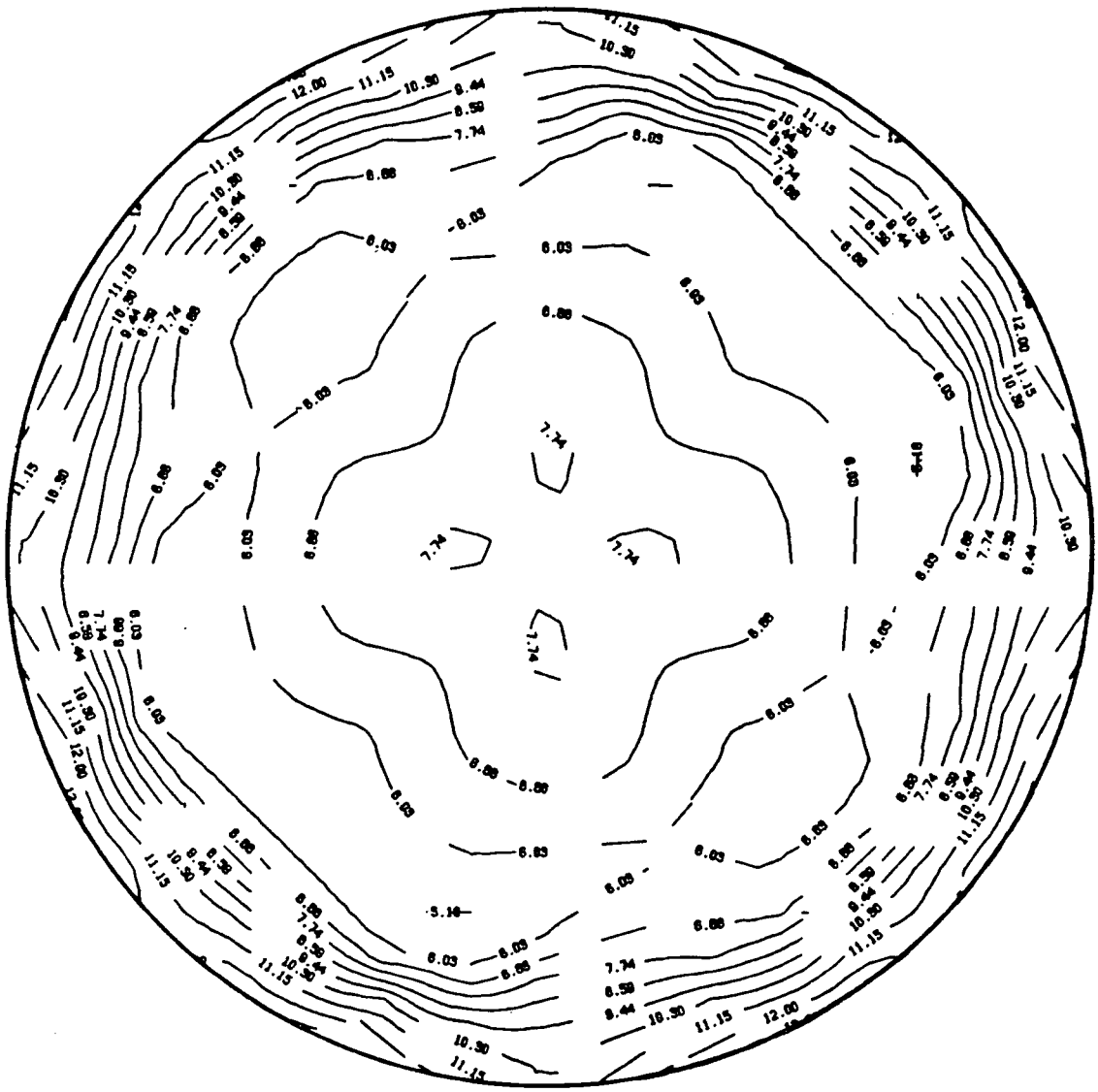

C

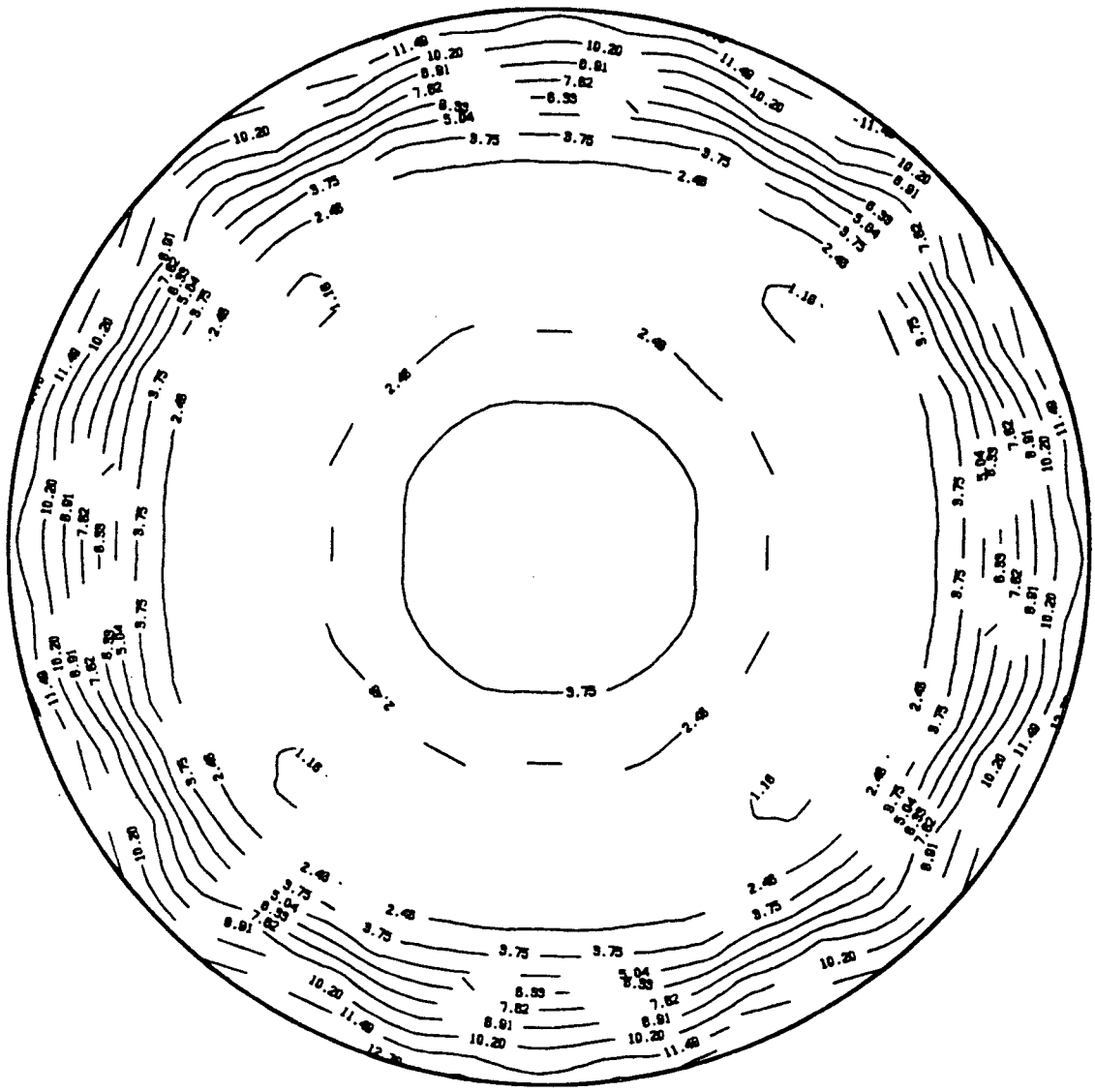

d

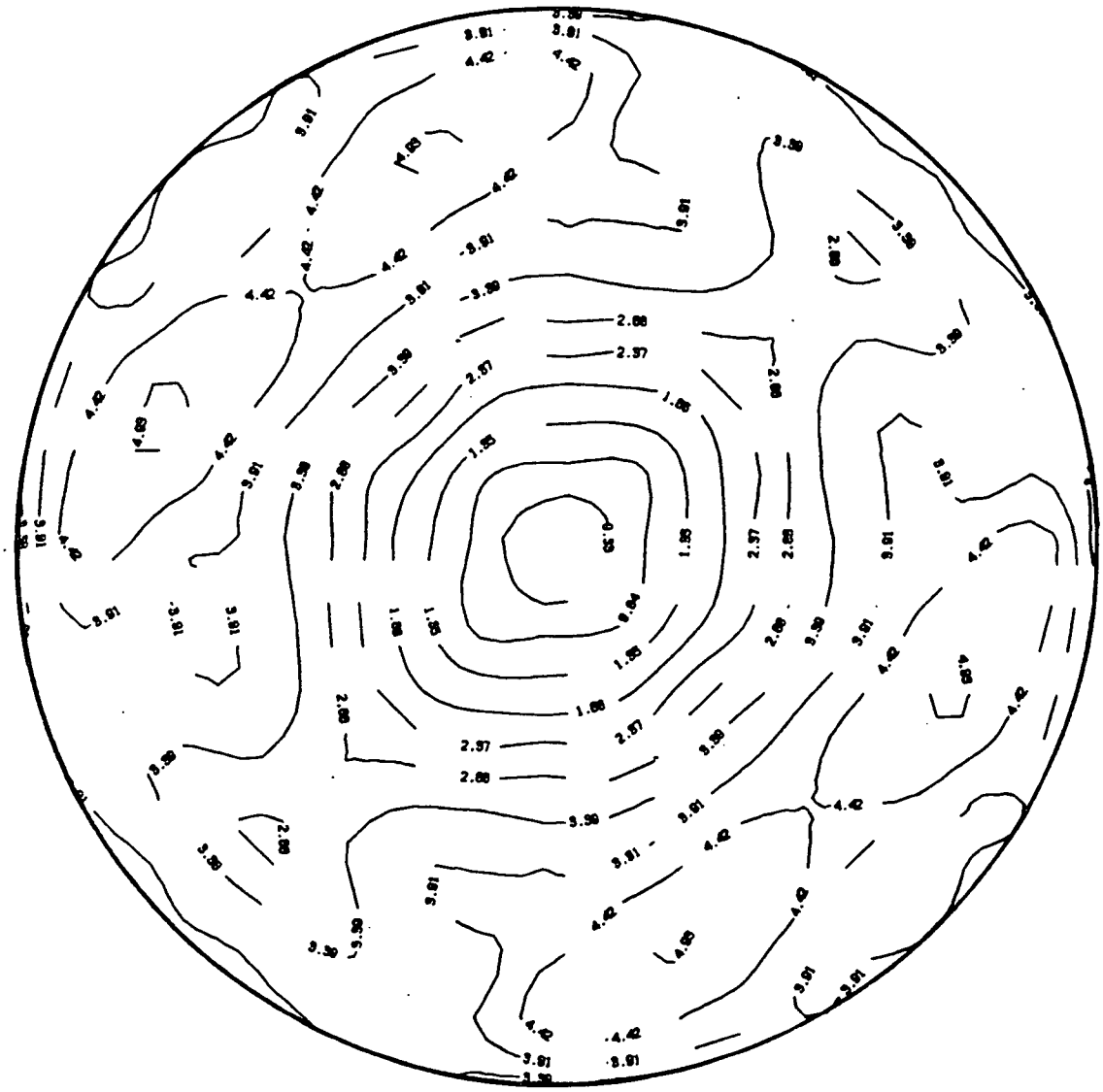

XIV.2.2.1.2.2 MRSS-CRSS (Yield) in cross-sections at a distance from the interface of :
(a) 2.75 mm ; (b) 8.25 mm ; (c) 16.5 mm ;
(d) 27.5 mm .

a

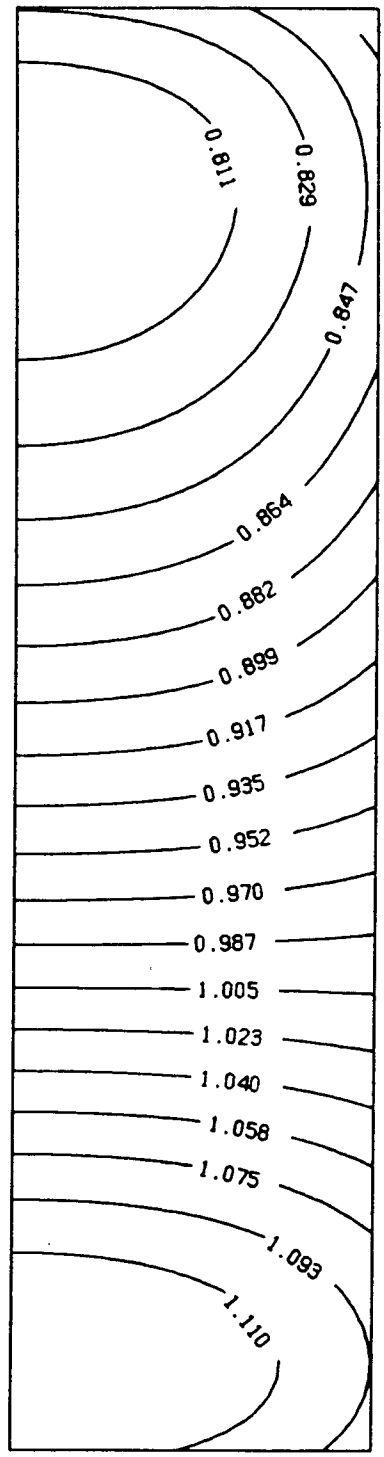
0.811
0.829
0.847
0.864
0.882
0.899
0.917
0.935
0.952
0.970
0.987
1.005
1.023
1.040
1.058
1.075
1.093
1.110

b

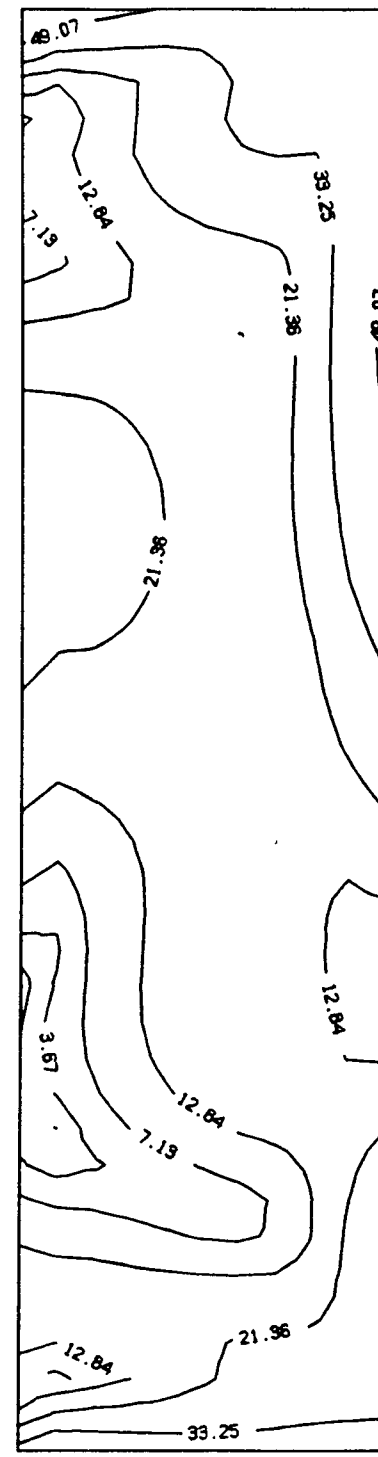
48.07
12.84
39.25
7.13
21.36
48.07
21.36
12.84
3.67
12.84
7.13
21.36
12.84
33.25

c

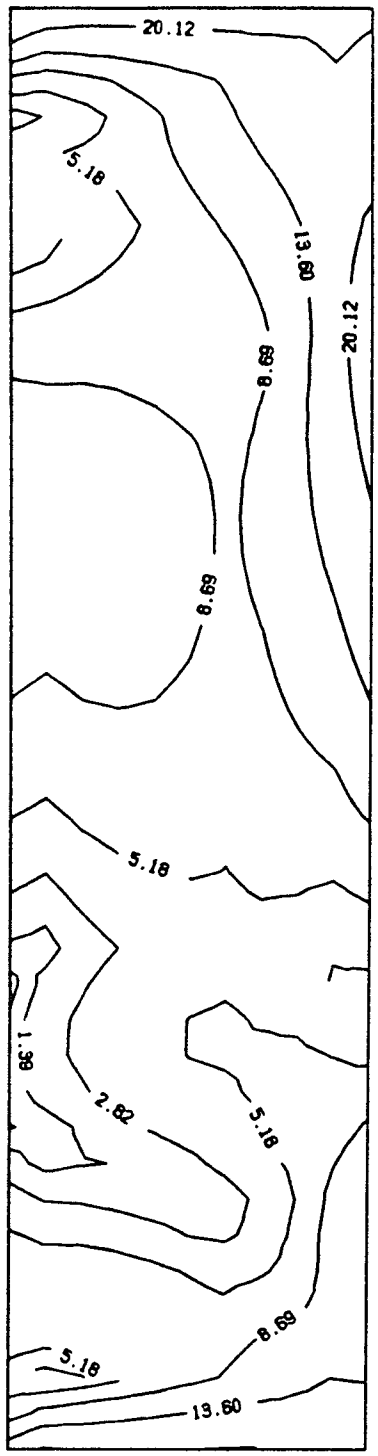
20.12
5.18
13.80
8.69
20.12
8.69
5.18
1.38
2.82
5.18
5.18
8.69
13.80

d

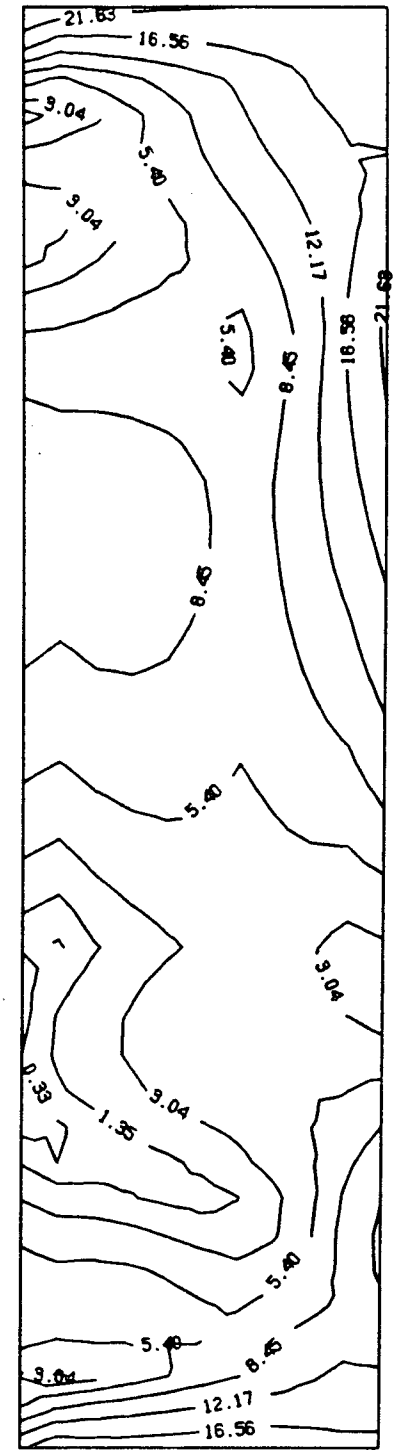
21.63
16.56
9.04
5.40
9.04
12.17
5.40
8.45
18.38
21.63
8.45
5.40
9.04
0.33
1.35
9.04
5.40
5.40
8.45
12.17
16.56

e

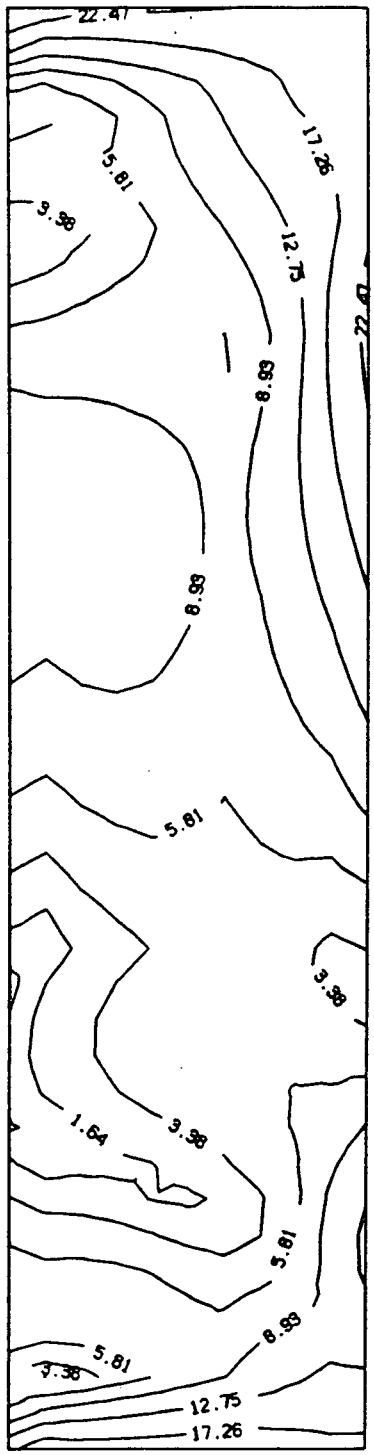

f

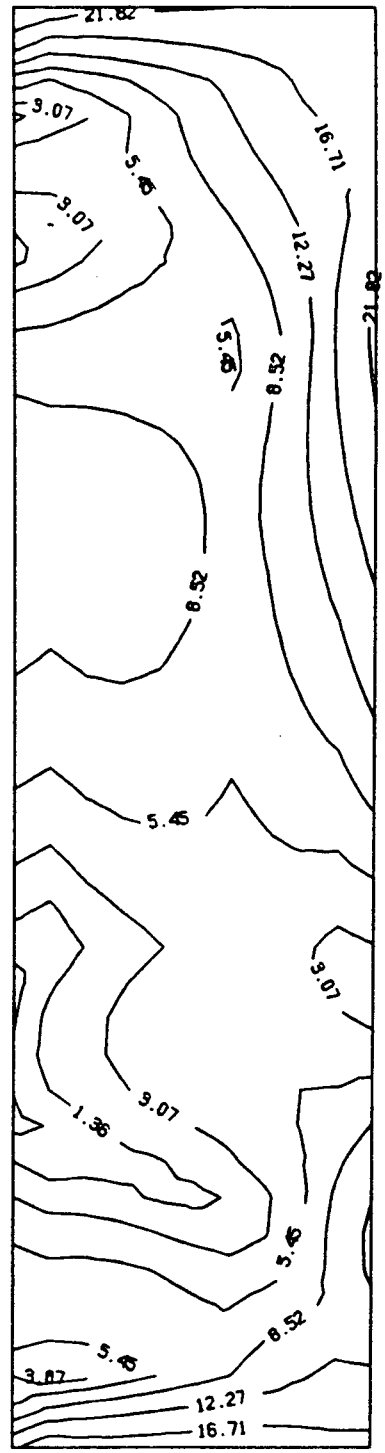

XIV.2.2.1.3 Time 20 seconds
(a) Temperature ; (b) Von Mises Stress
(c) MRSS ; (d) MRSS-CRSS (Yield) ;
(e) MRSS-CRSS (MB) ; (f) MRSS-CRSS (MBTe) .

a

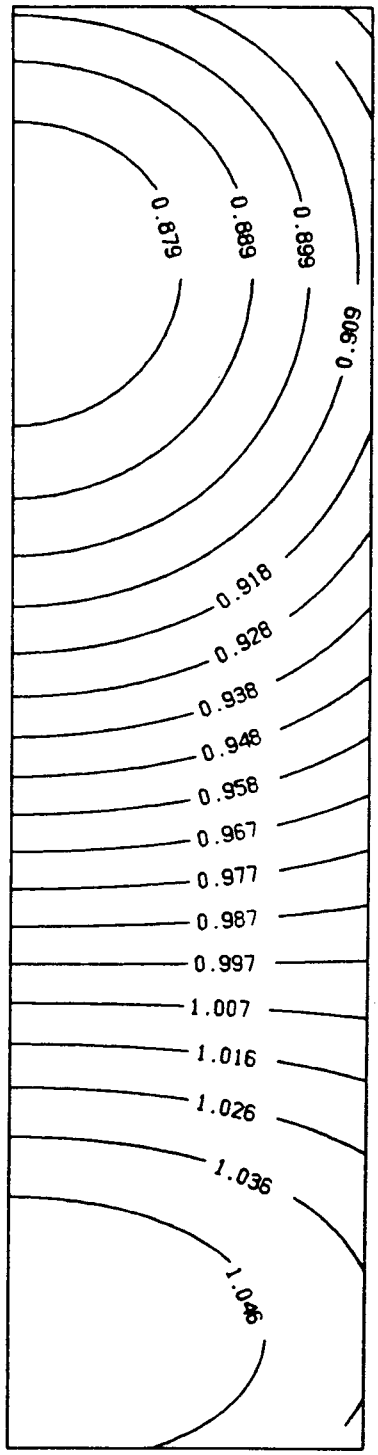
0.879
0.889
0.899
0.909
0.918
0.928
0.938
0.948
0.958
0.967
0.977
0.987
0.997
1.007
1.016
1.026
1.036
1.046

b

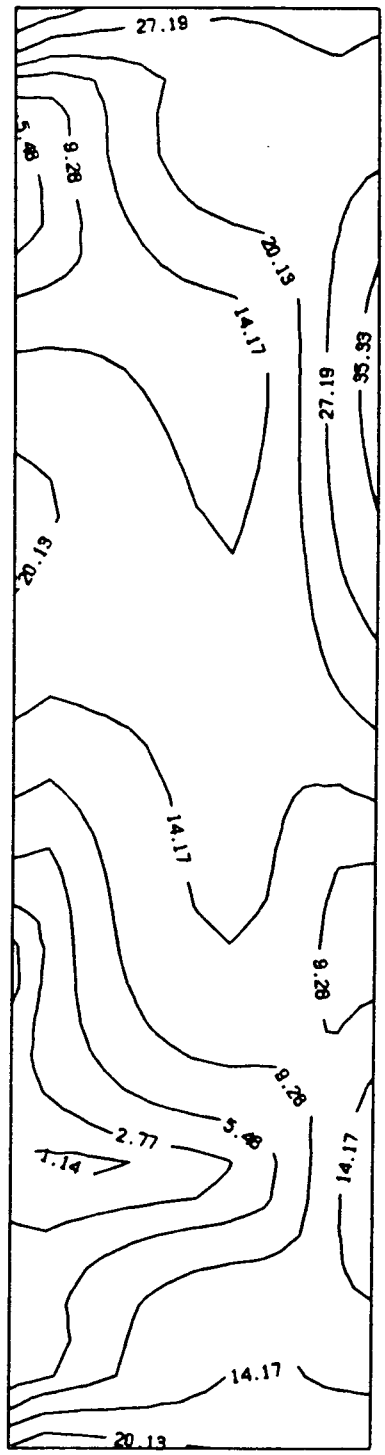
27.19
5.48
9.28
20.13
14.17
27.19
35.93
20.13
14.17
9.28
9.28
5.48
2.77
1.14
14.17
14.17
20.13

c

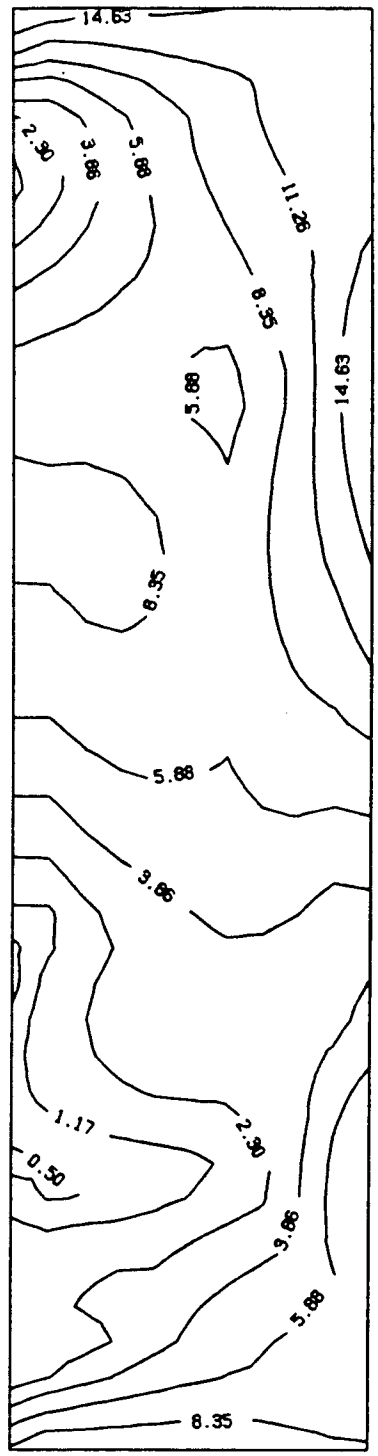

d

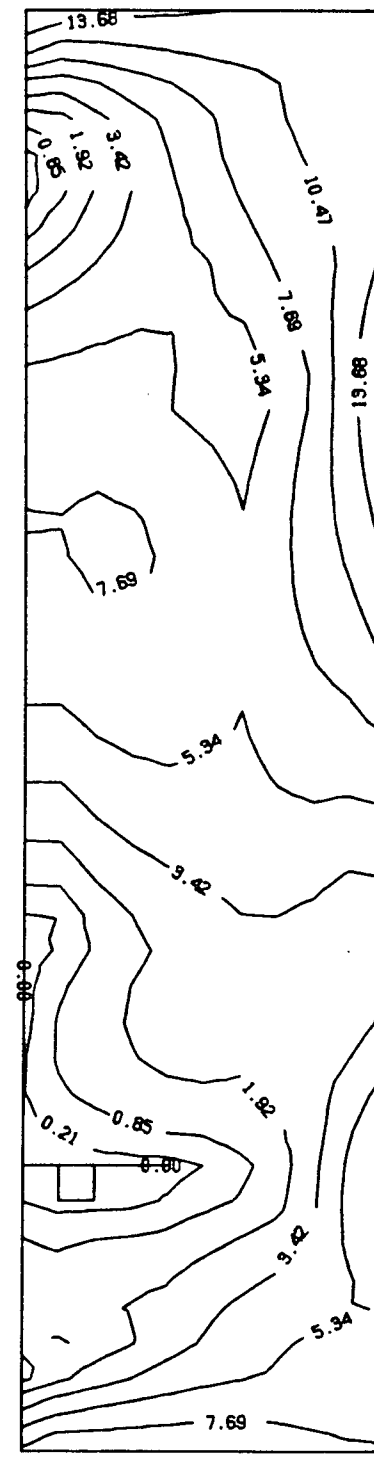

XIV.2.2.1.4.1 (a) Temperature ; (b) Von Mises Stress
(c) MRSS ; (d) MRSS-CRSS (Yield) ;

a

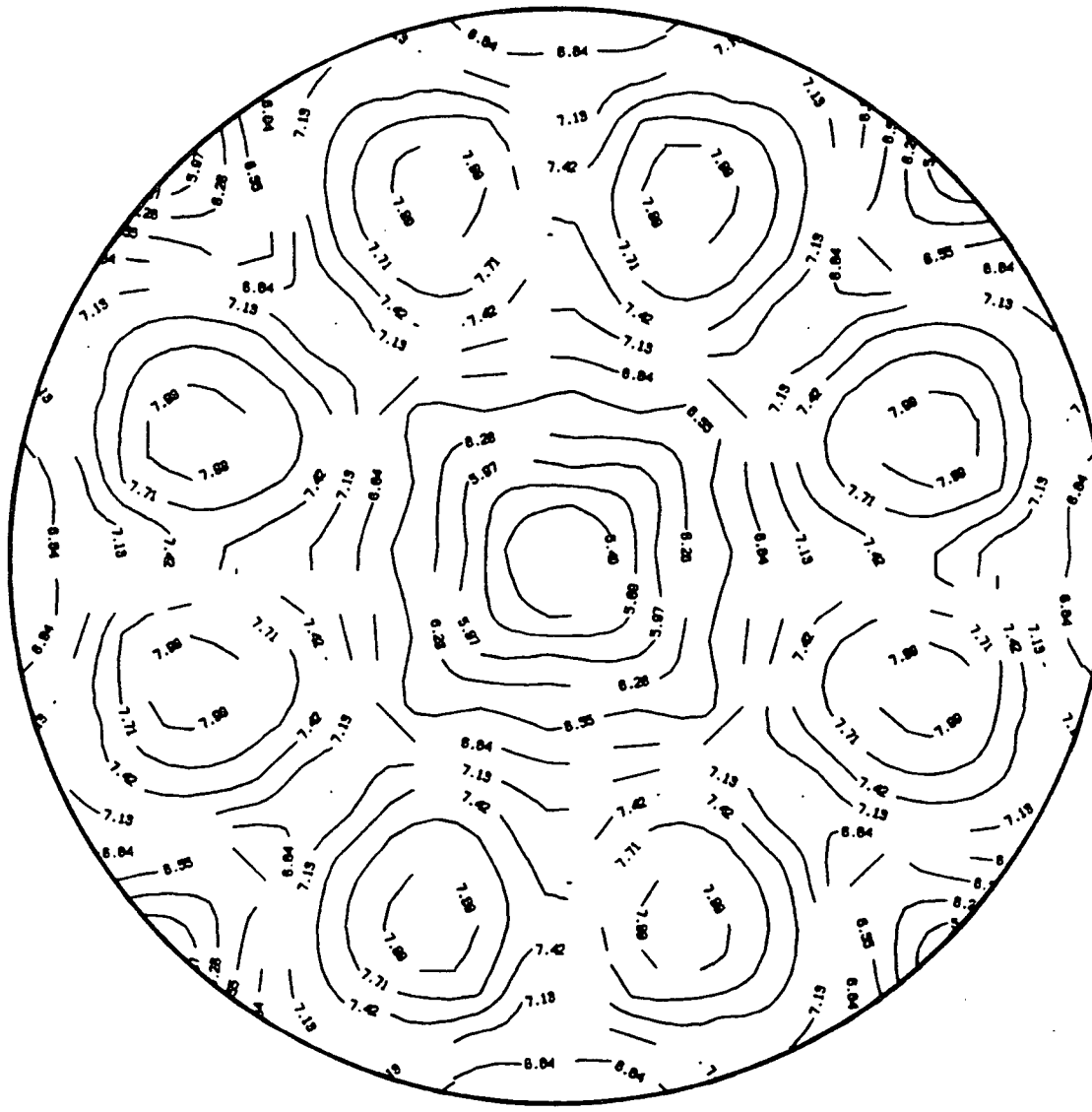

b

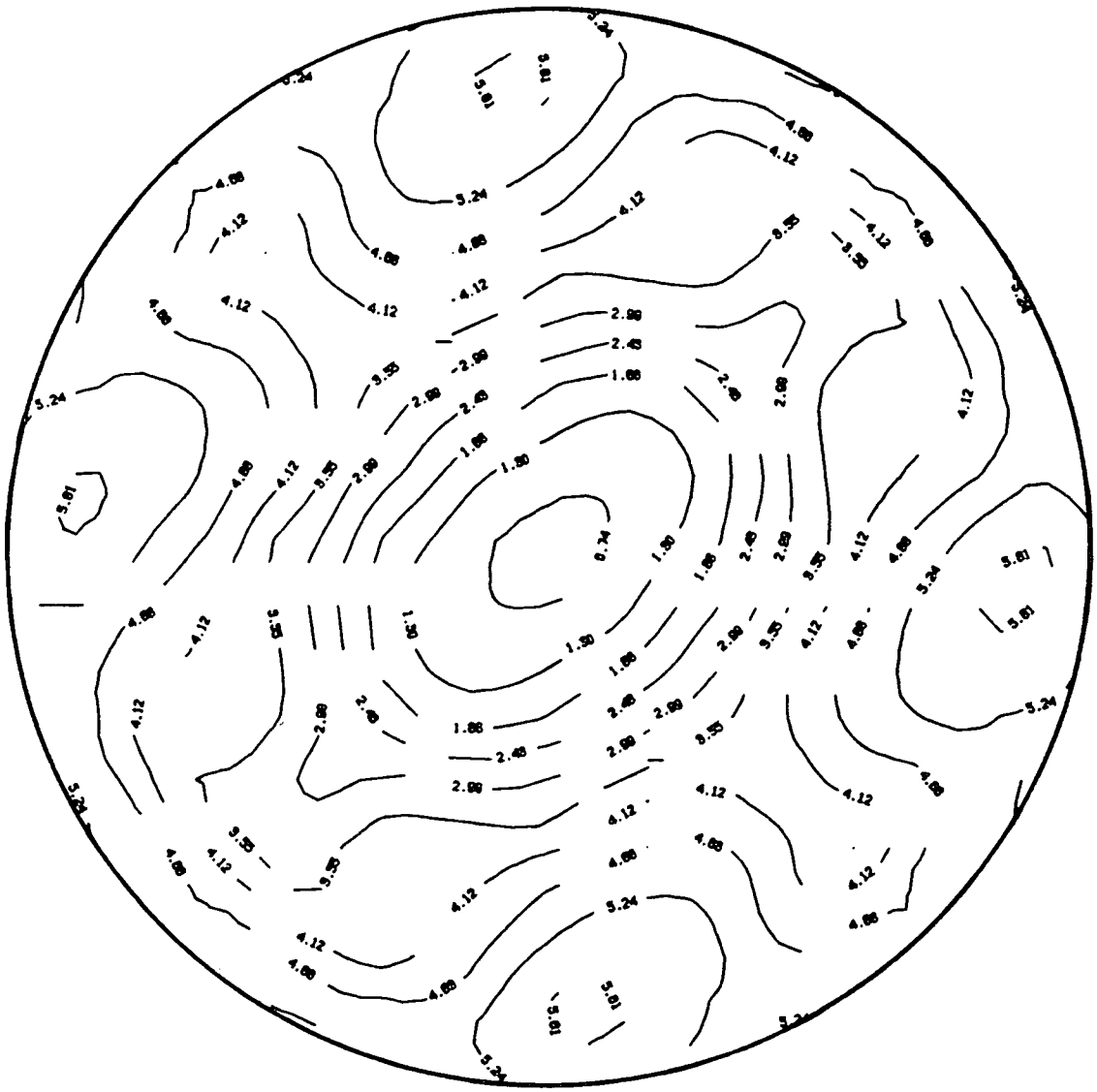

C

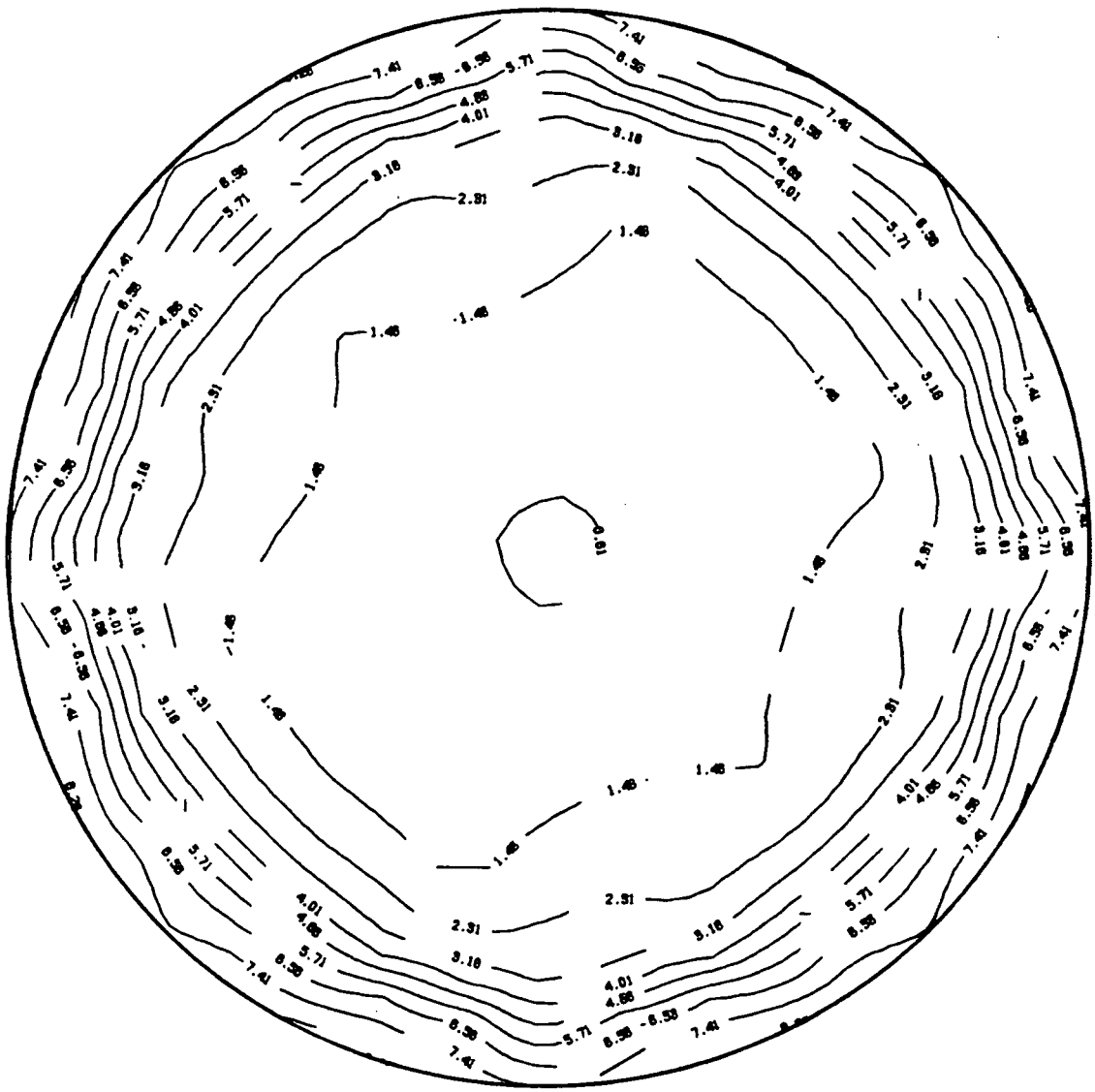

d

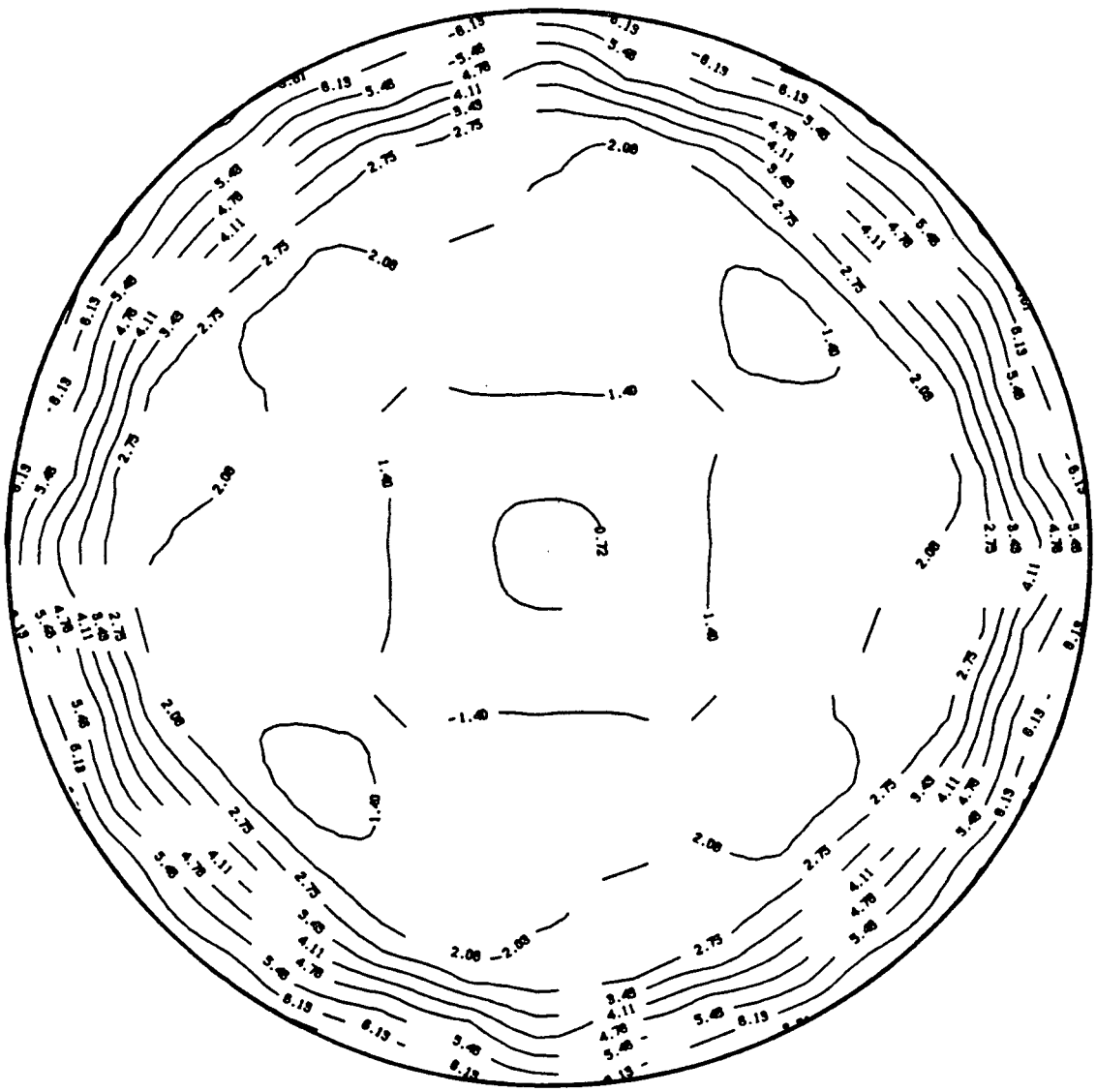

XIV.2.2.1.4.2 MRSS-CRSS (Yield) in cross-sections at a distance from the interface of :
(a) 2.75 mm ; (b) 8.25 mm ; (c) 16.5 mm ;
(d) 27.5 mm .

a

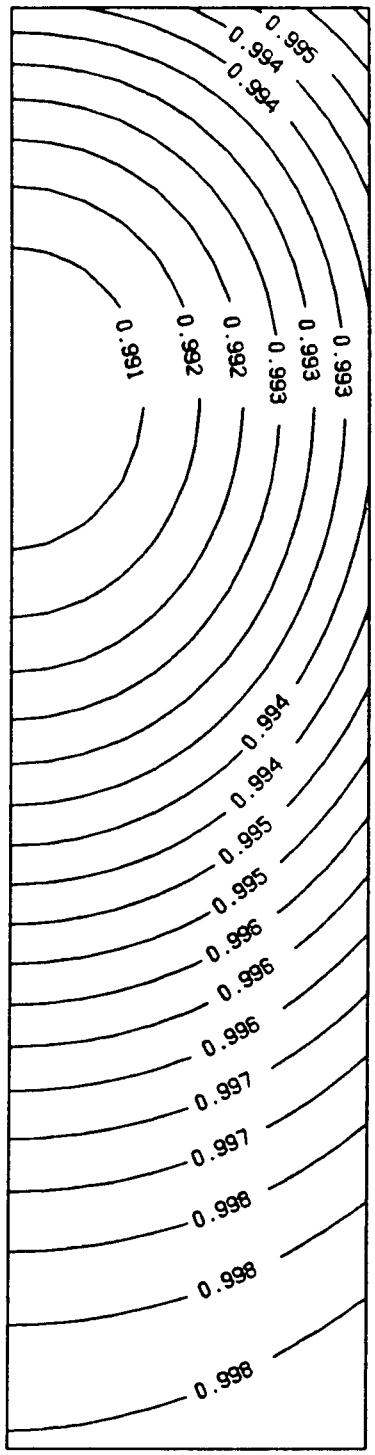
0.991
0.992
0.992
0.993
0.993
0.993
0.994
0.994
0.994
0.995
0.995
0.995
0.996
0.996
0.996
0.996
0.997
0.997
0.998
0.998
0.998

b

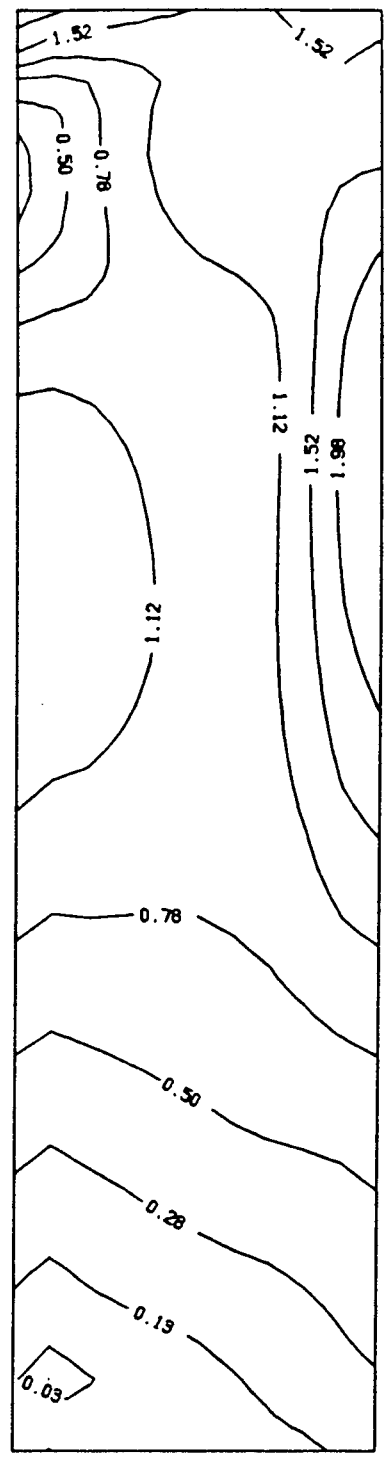
1.52
1.52
0.50
0.78
1.12
1.52
1.98
1.12
0.78
0.50
0.28
0.13
0.03

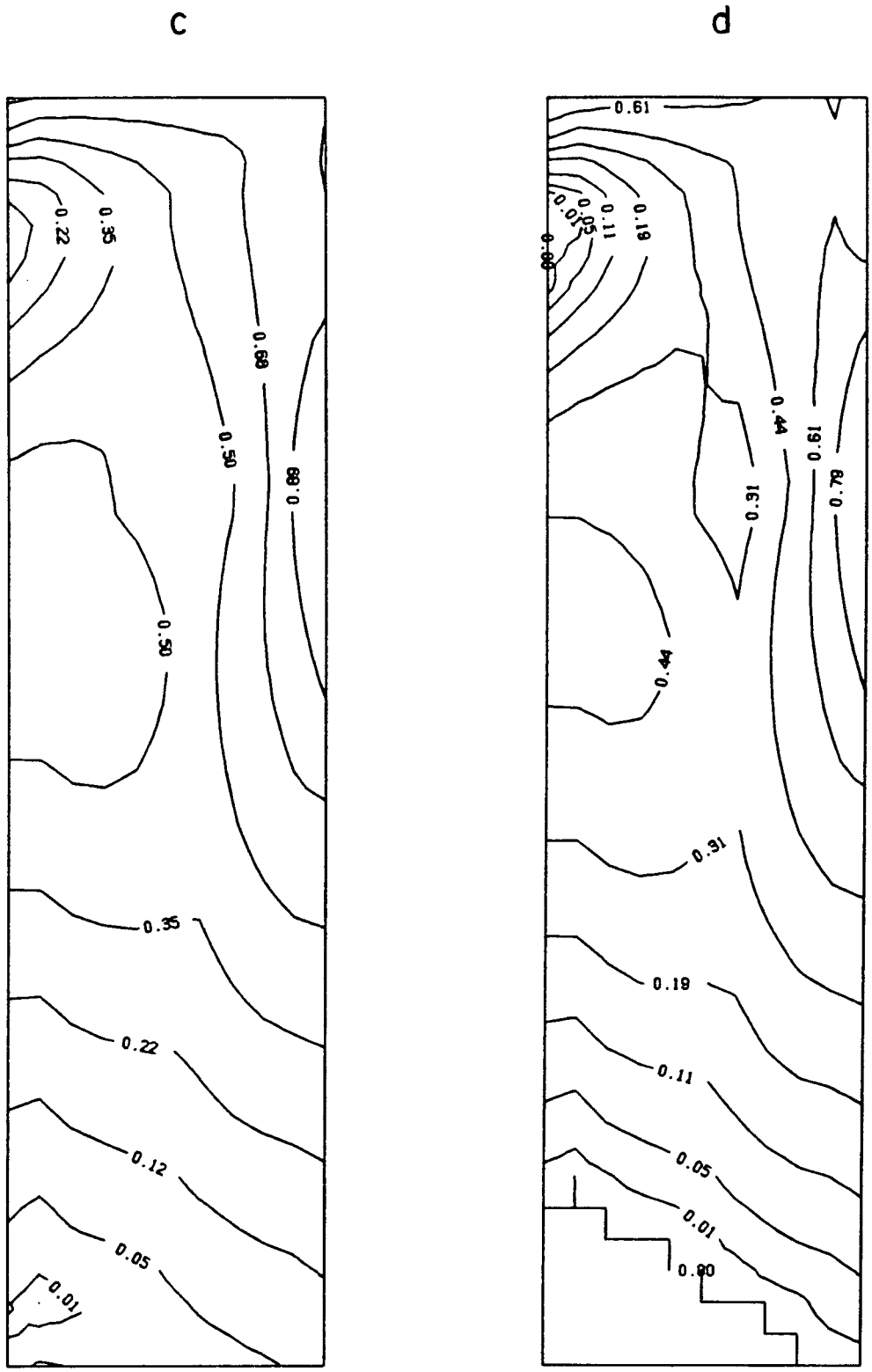

XIV.2.2.1.5 Time 300 seconds
(a) Temperature ; (b) Von Mises Stress
(c) MRSS ; (d) MRSS-CRSS (MB) .

a

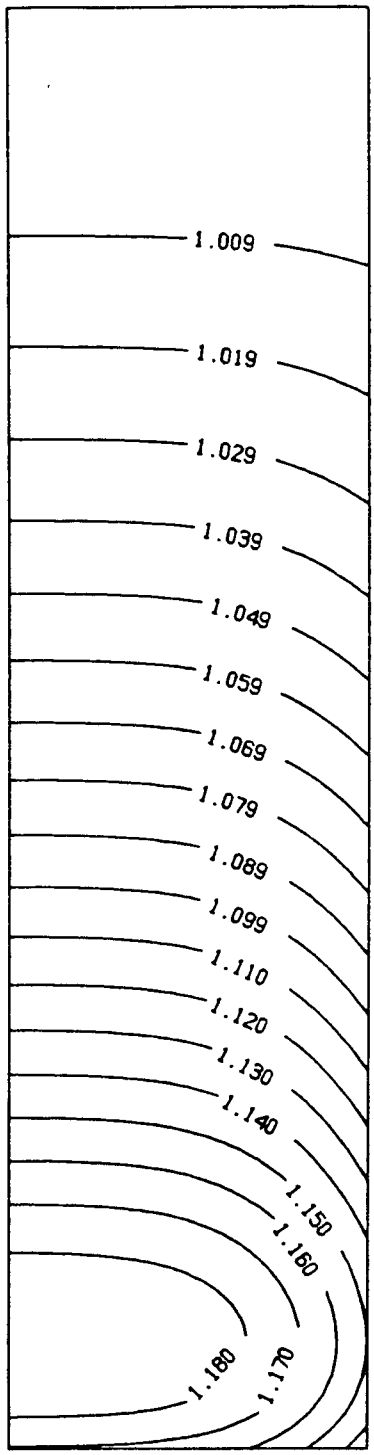
1.009
1.019
1.029
1.039
1.049
1.059
1.069
1.079
1.089
1.099
1.110
1.120
1.130
1.140
1.150
1.160
1.170
1.180

b

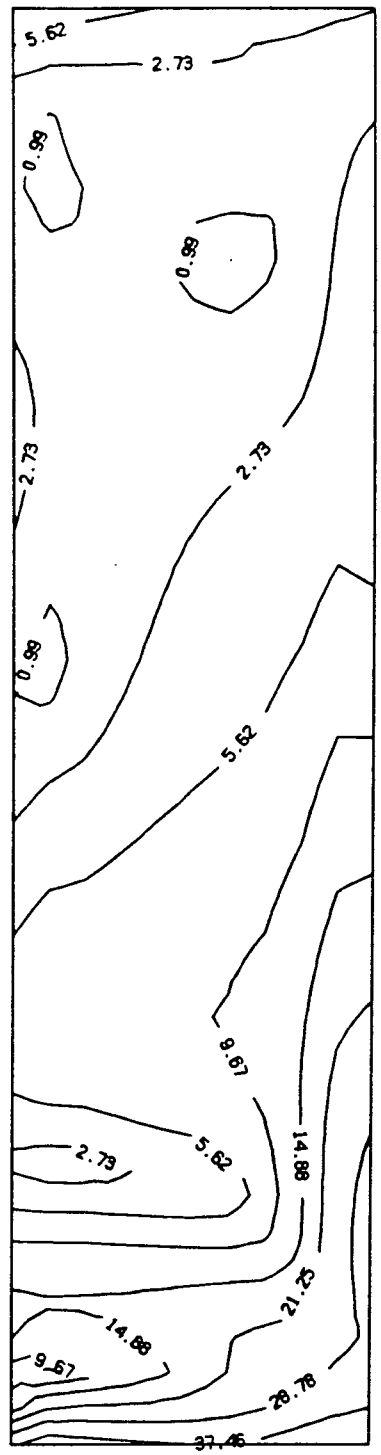
5.62
2.73
0.99
0.99
2.73
2.73
0.99
5.62
9.67
2.73
5.62
14.88
14.88
21.25
9.67
28.78
37.46

c

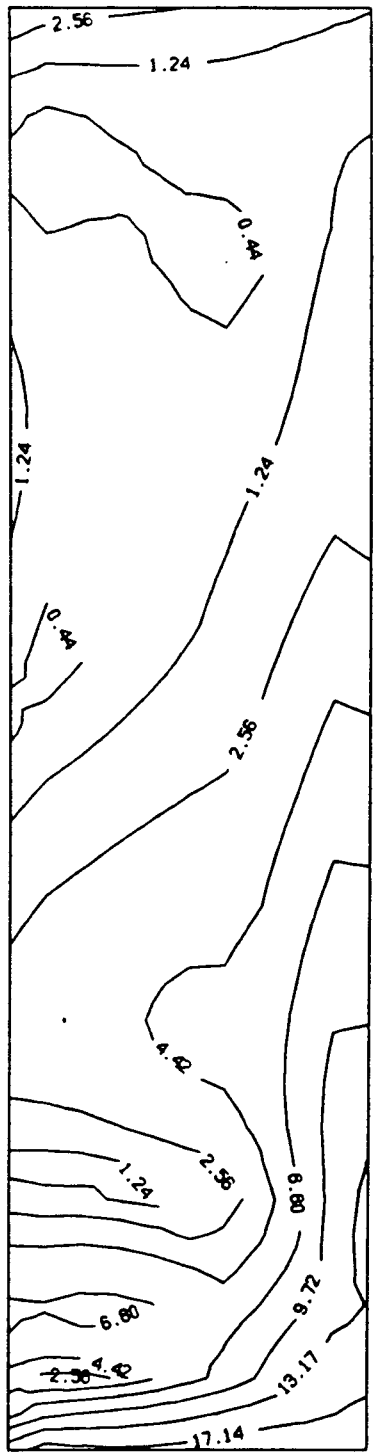
2.56
1.24
0.44
1.24
1.24
0.44
2.56
4.40
2.56
1.24
8.00
9.72
6.80
4.40
2.56
13.17
17.14

d

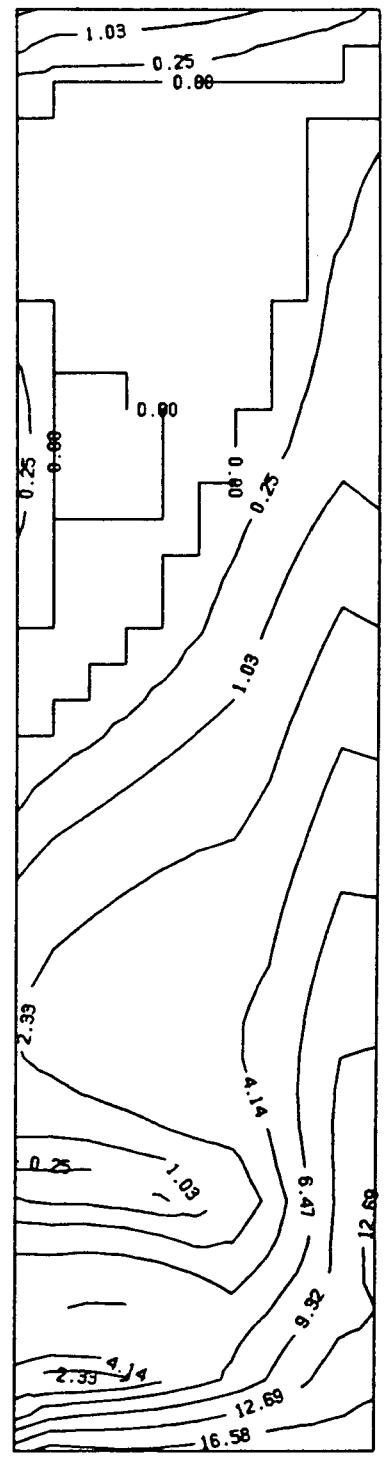
1.03
0.25
0.00
0.00
0.25
0.00
0.00
0.25
1.03
2.39
4.14
0.25
1.03
6.47
12.69
9.32
4.14
2.39
12.69
16.58

e

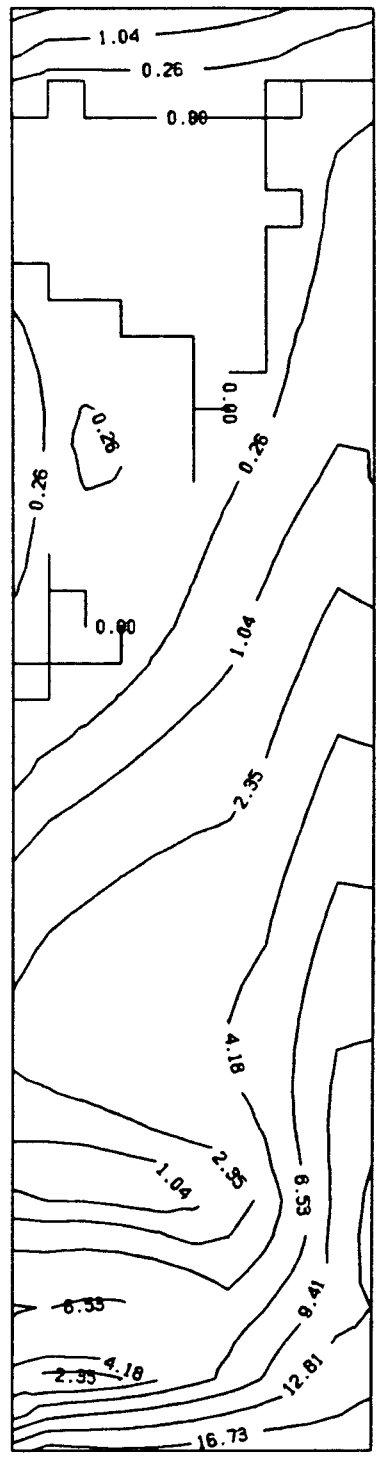

XIV.2.2.2.1.1 (a) Temperature ; (b) Von Mises Stress
(c) MRSS ; (d) MRSS-CRSS (Yield) ;
(e) MRSS-CRSS (MBTe) .

a

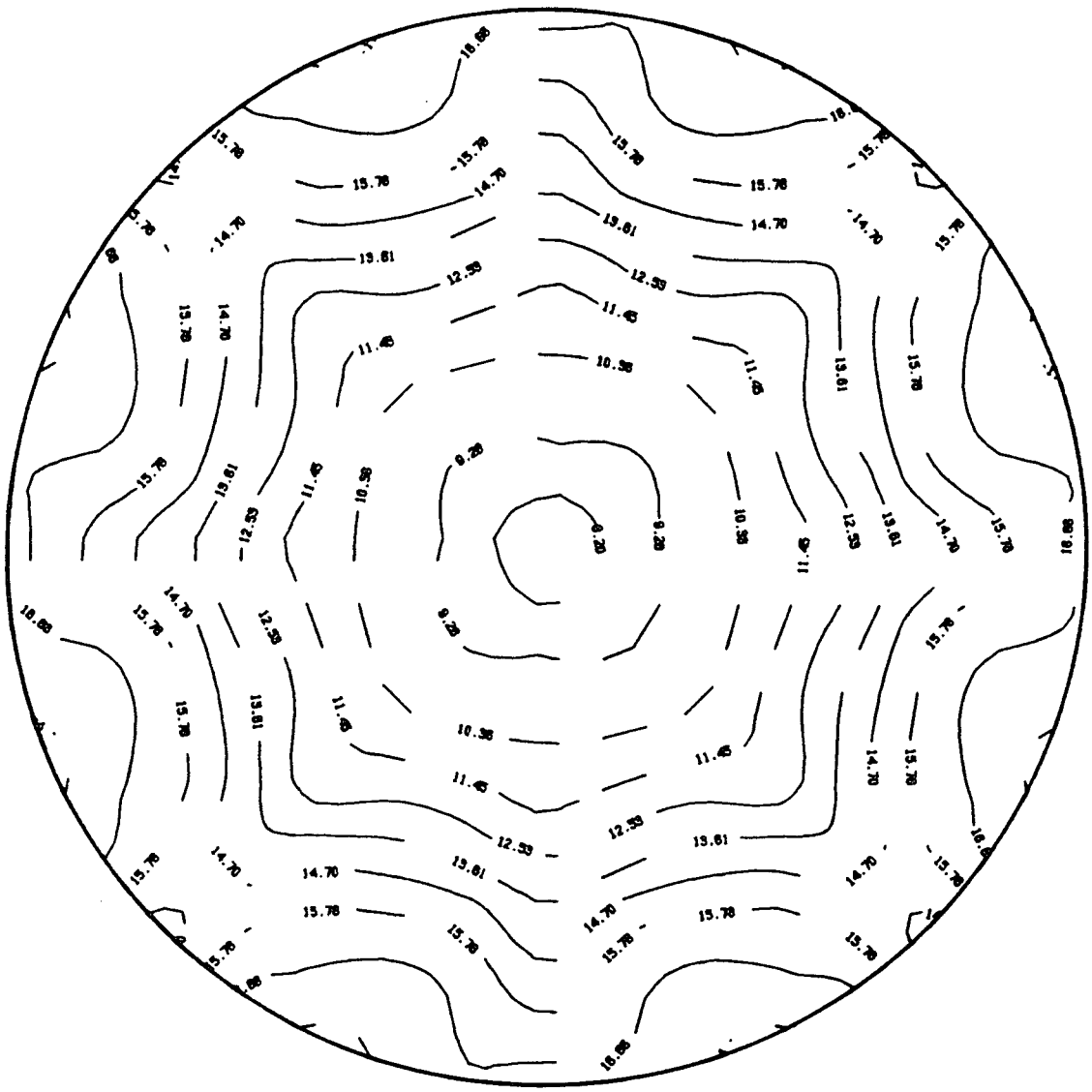

b

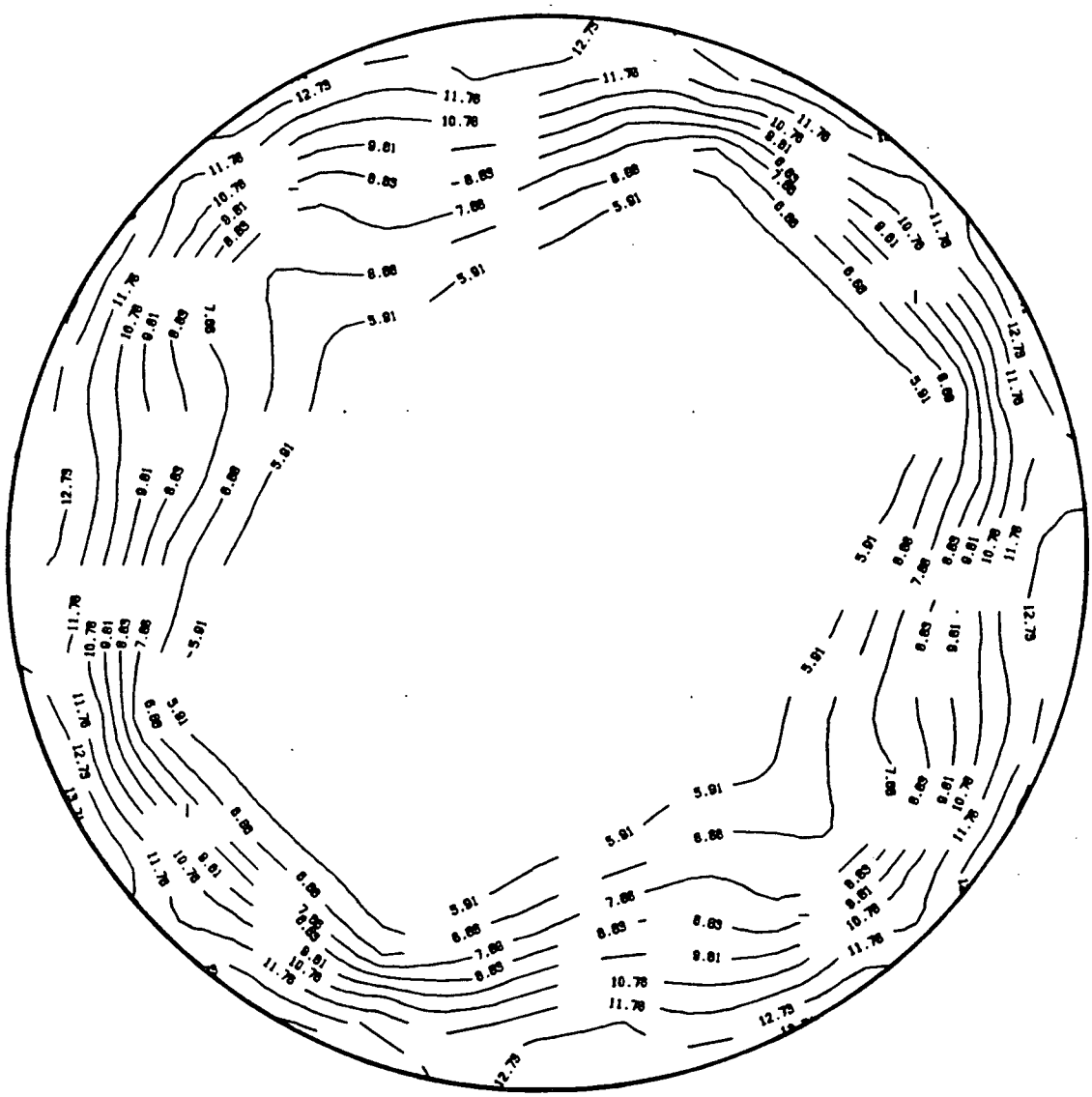

C

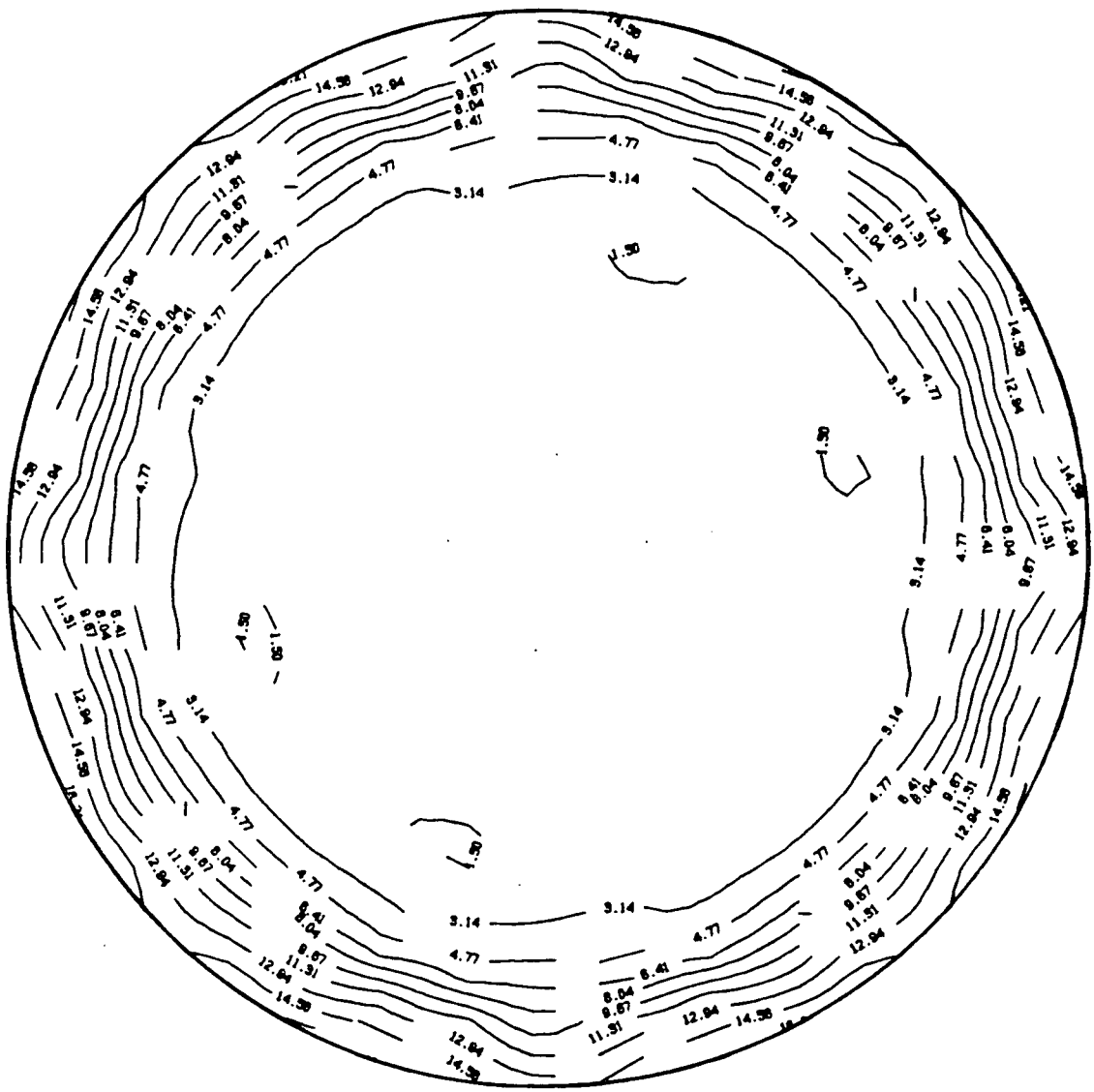

d

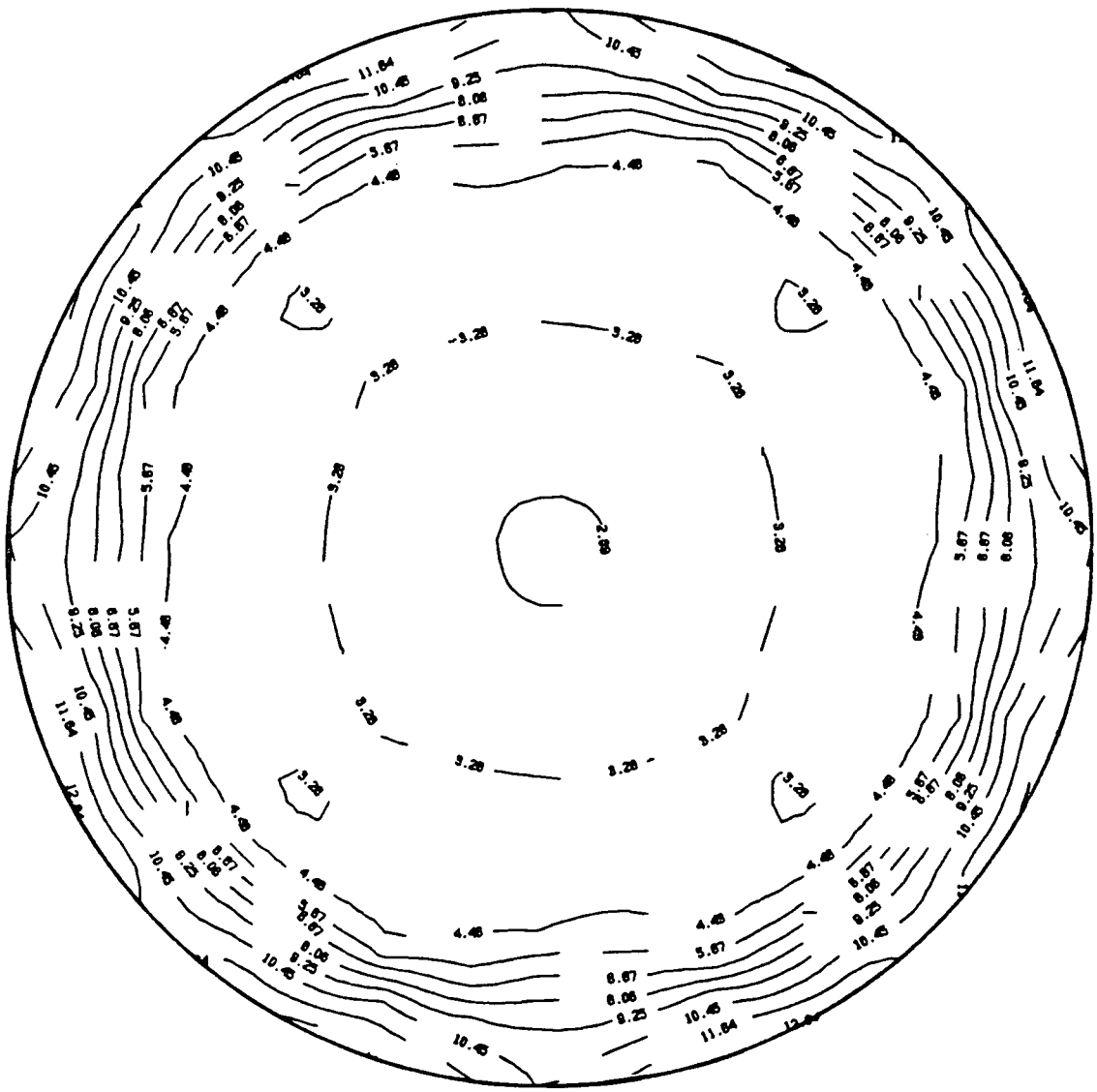

XIV.2.2.2.1.2 MRSS-CRSS (Yield) in cross-sections at a distance from the interface of :
(a) 2.75 mm ; (b) 8.25 mm ; (c) 16.5 mm ;
(d) 27.5 mm .

a

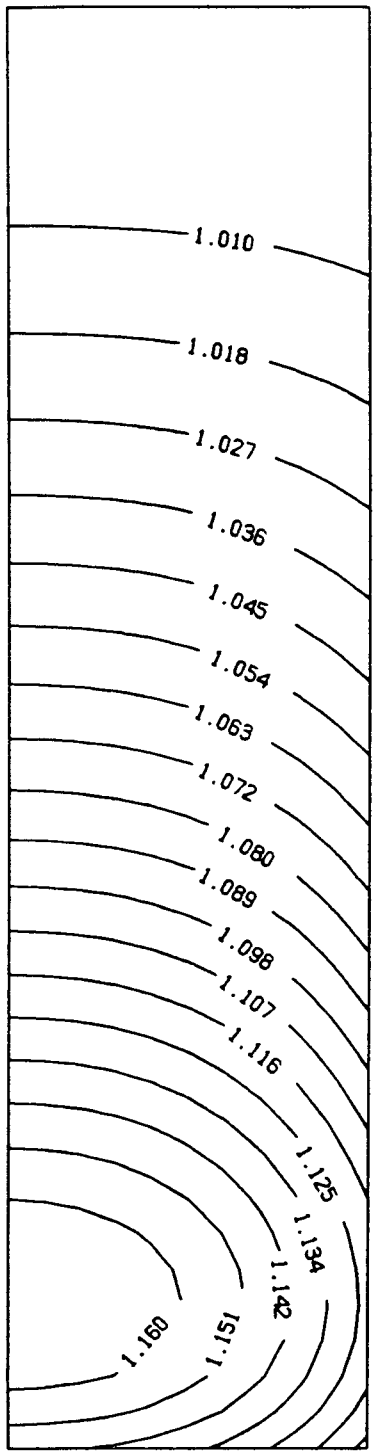
1.010
1.018
1.027
1.036
1.045
1.054
1.063
1.072
1.080
1.089
1.098
1.107
1.116
1.125
1.134
1.142
1.151
1.160

b

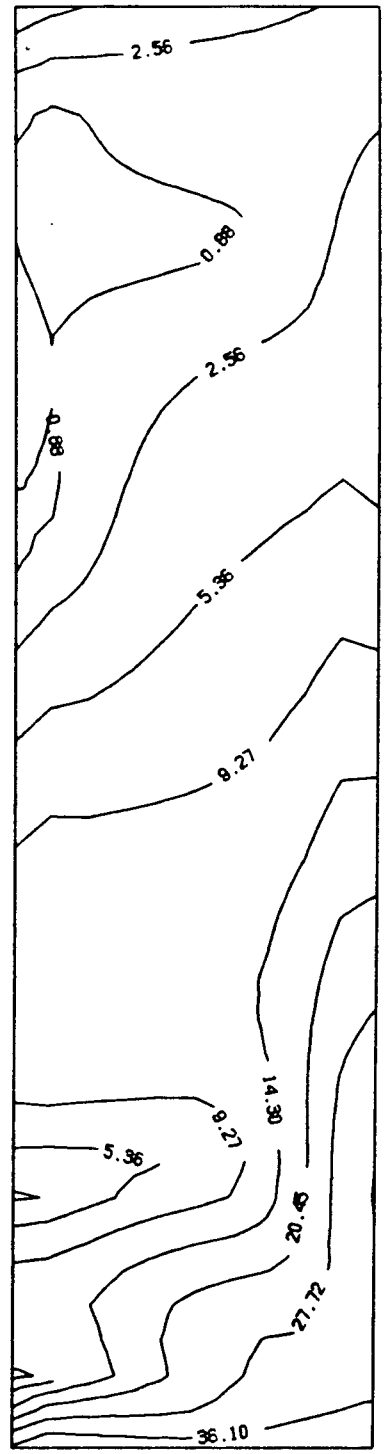
2.56
0.88
2.56
0.88
5.36
8.27
14.30
8.27
5.36
20.45
27.72
36.10

c

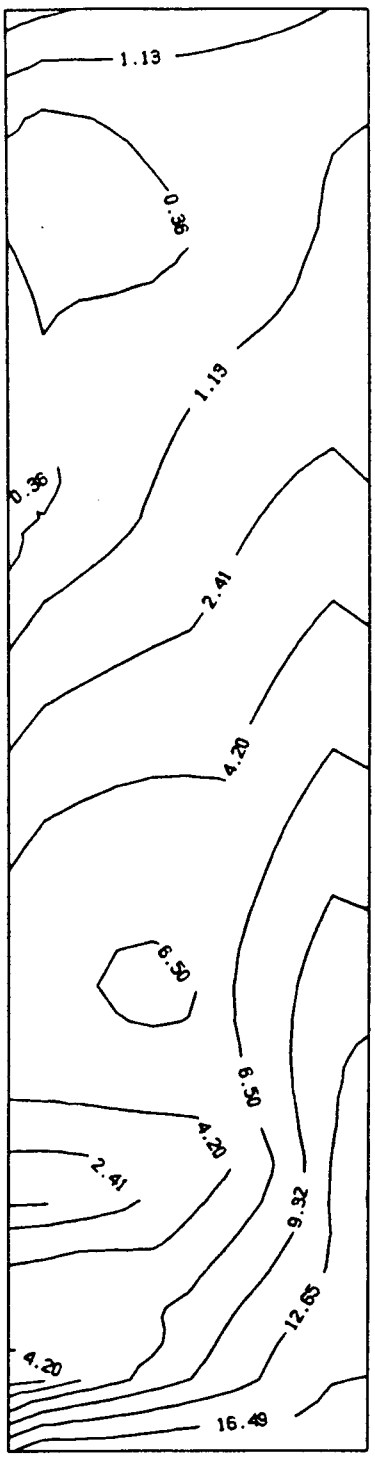
1.13
0.36
1.13
0.36
2.41
4.20
6.50
6.50
4.20
2.41
9.32
12.65
4.20
16.49

d

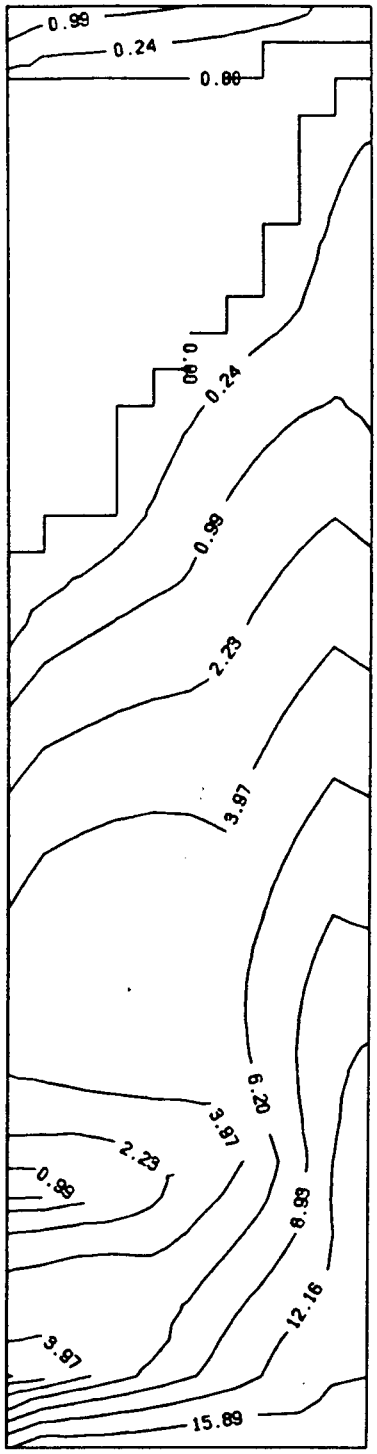
0.99
0.24
0.00
0.00
0.24
0.99
2.23
3.97
6.20
3.97
2.23
0.88
8.89
12.16
3.97
15.89

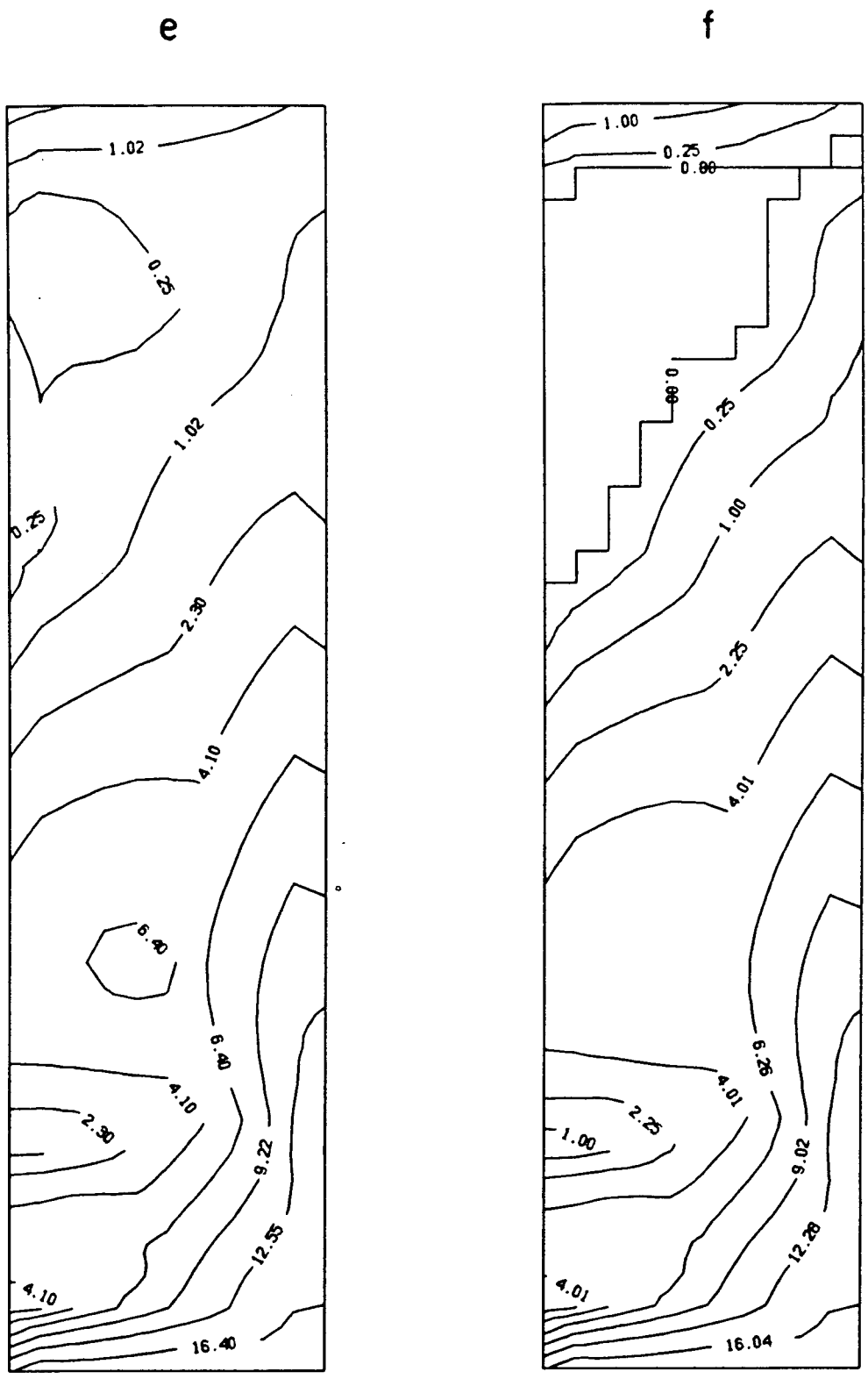

XIV.2.2.2.2.1 (a) Temperature ; (b) Von Mises Stress
(c) MRSS ; (d) MRSS-CRSS (Yield) ;
(e) MRSS-CRSS (MB) ; (f) MRSS-CRSS (MBTe) .

a

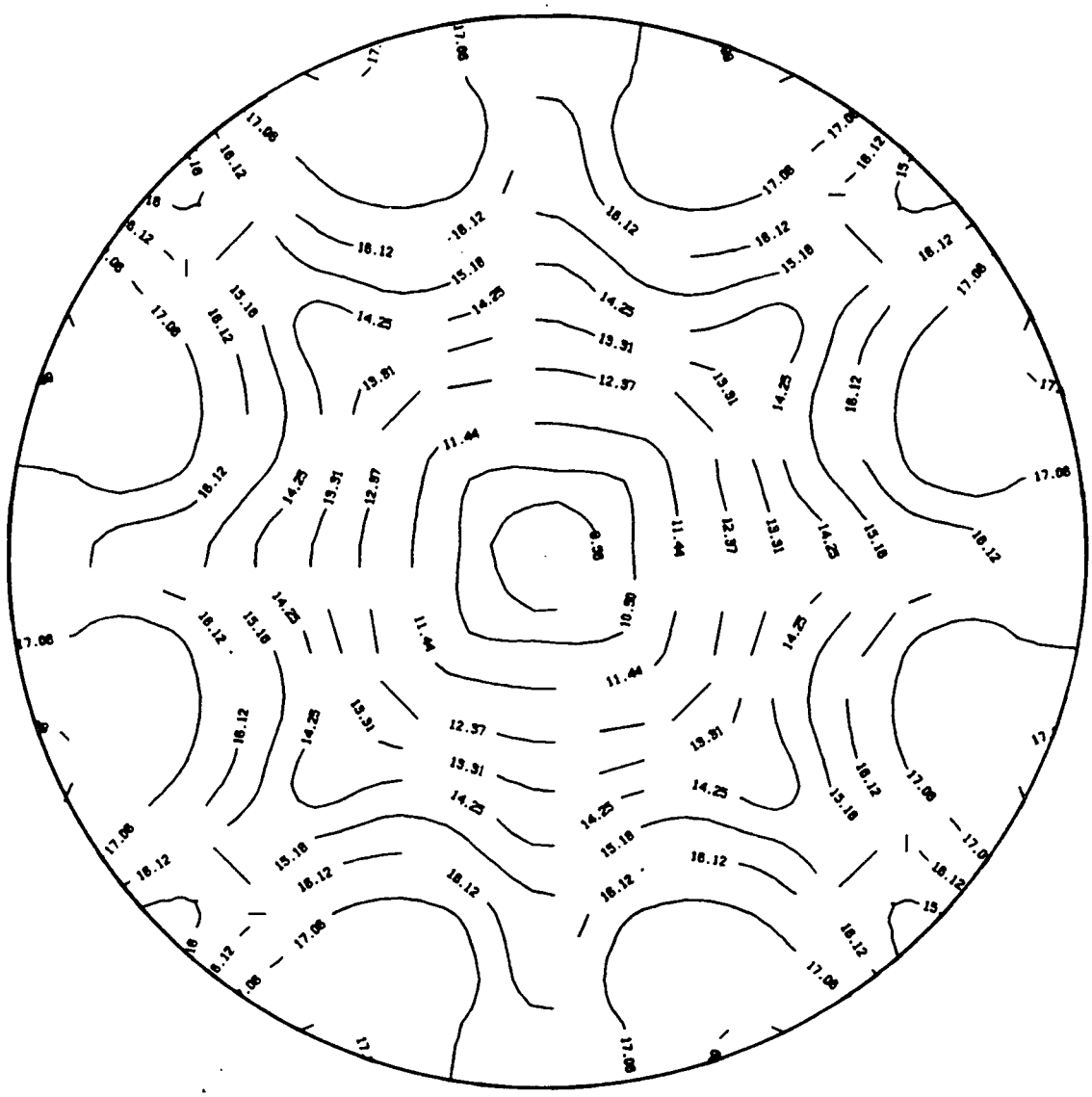

b

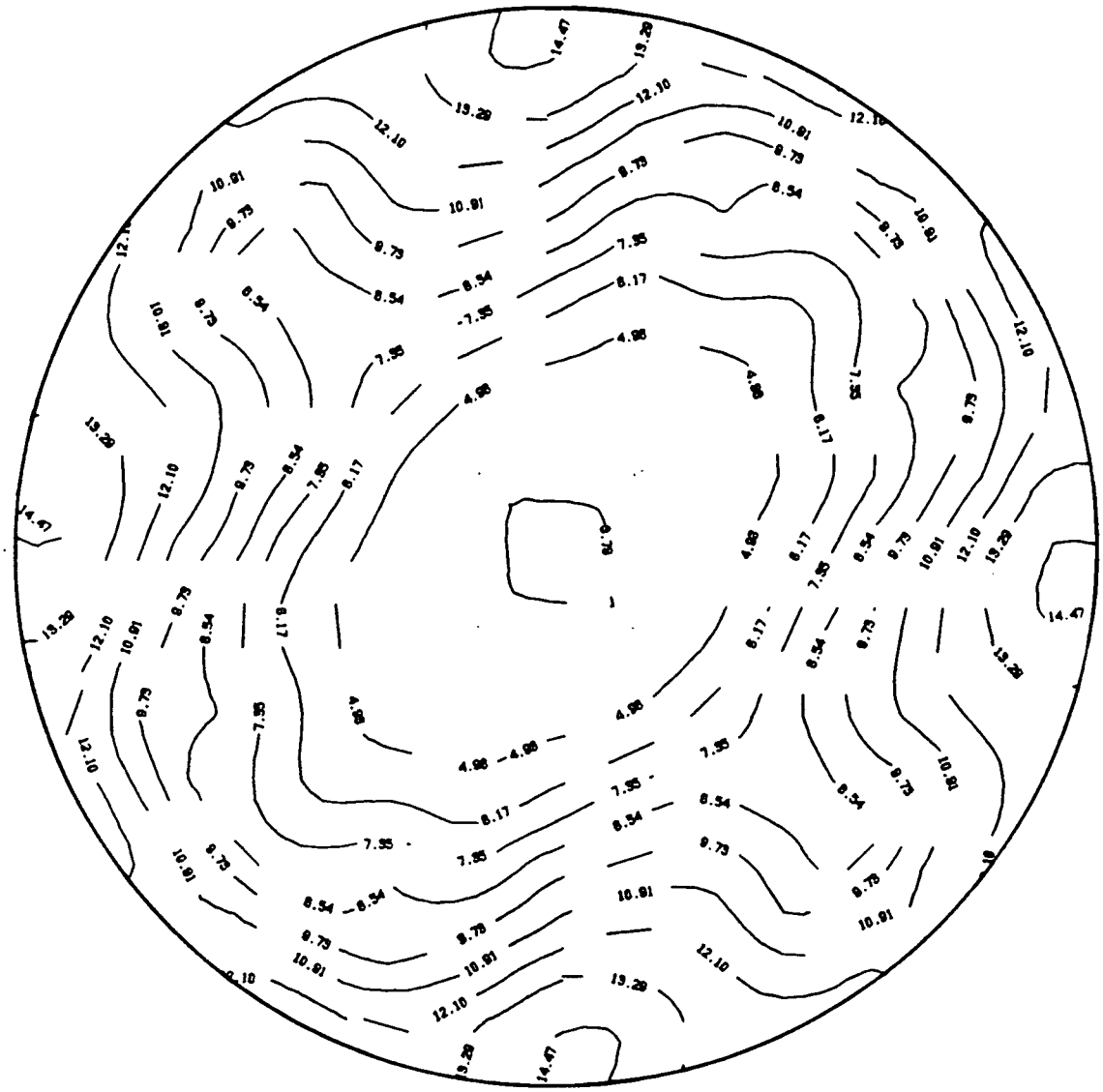

C

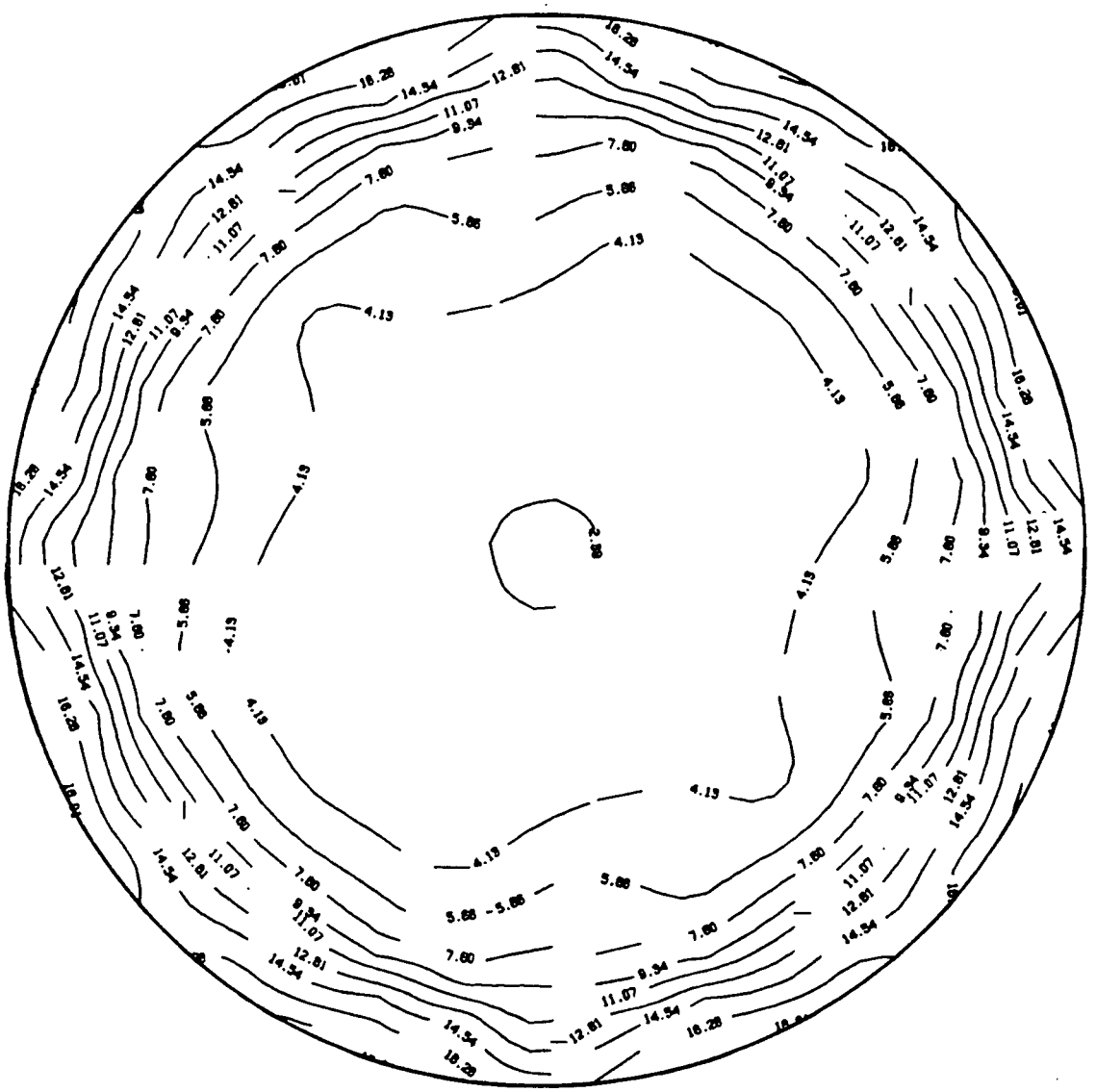

d

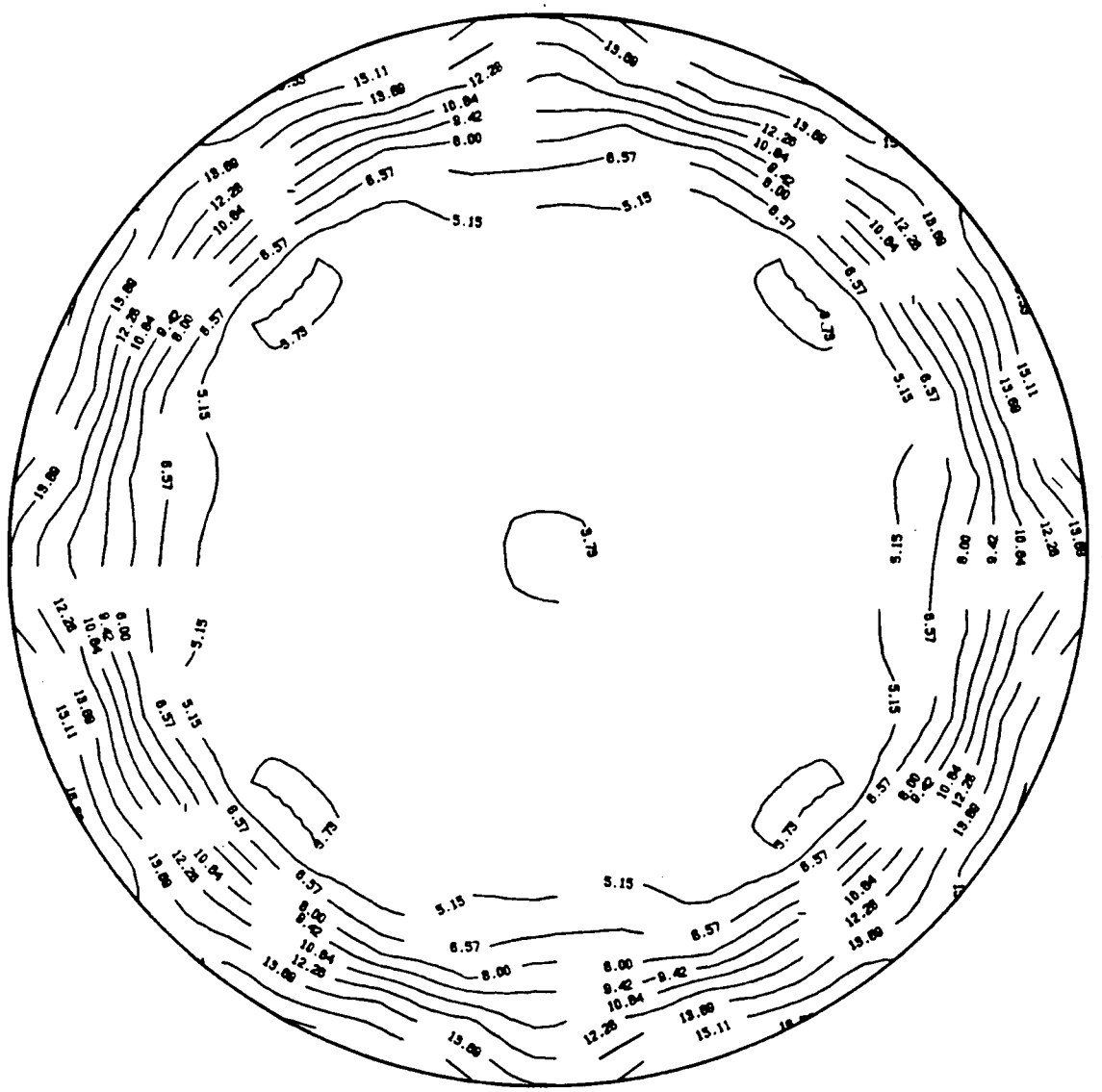

XIV.2.2.2.2.2 MRSS-CRSS (Yield) in cross-sections at a distance from the interface of :
(a) 2.75 mm ; (b) 8.25 mm ; (c) 16.5 mm ;
(d) 27.5 mm .

a

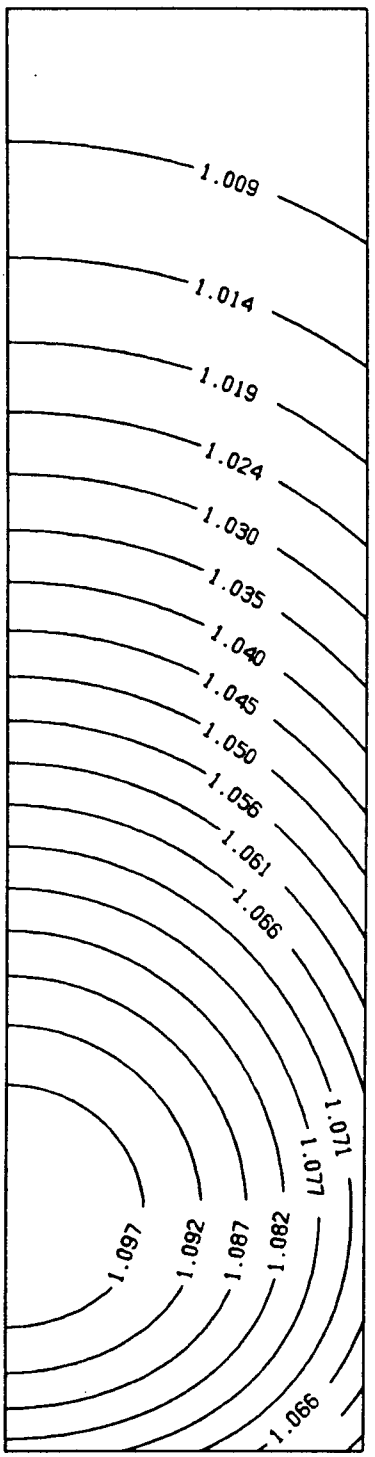
1.009
1.014
1.019
1.024
1.030
1.035
1.040
1.045
1.050
1.056
1.061
1.066
1.071
1.077
1.097
1.092
1.087
1.082
1.066

b

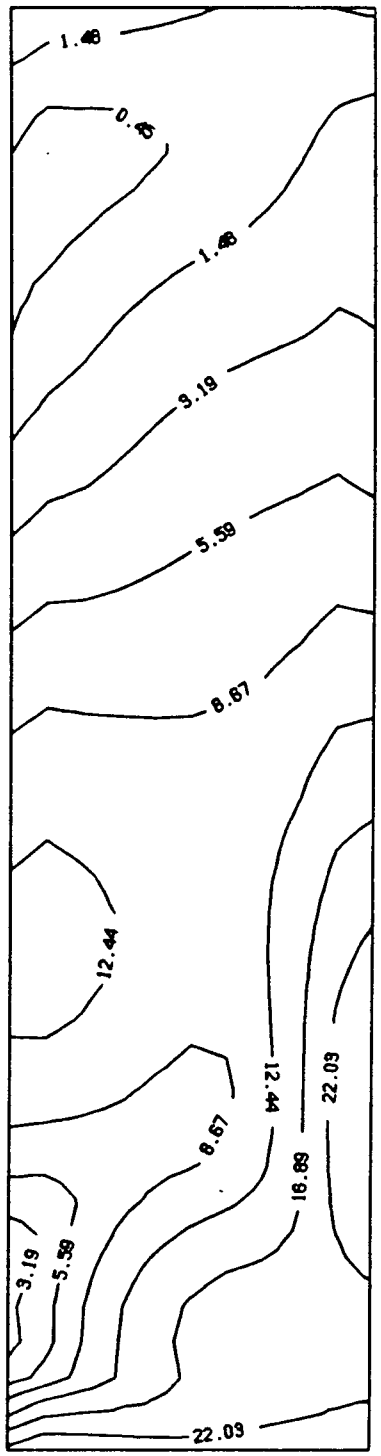
1.48
0.45
1.48
3.19
5.59
8.87
12.44
12.44
22.03
8.87
16.89
3.19
5.59
22.03

c

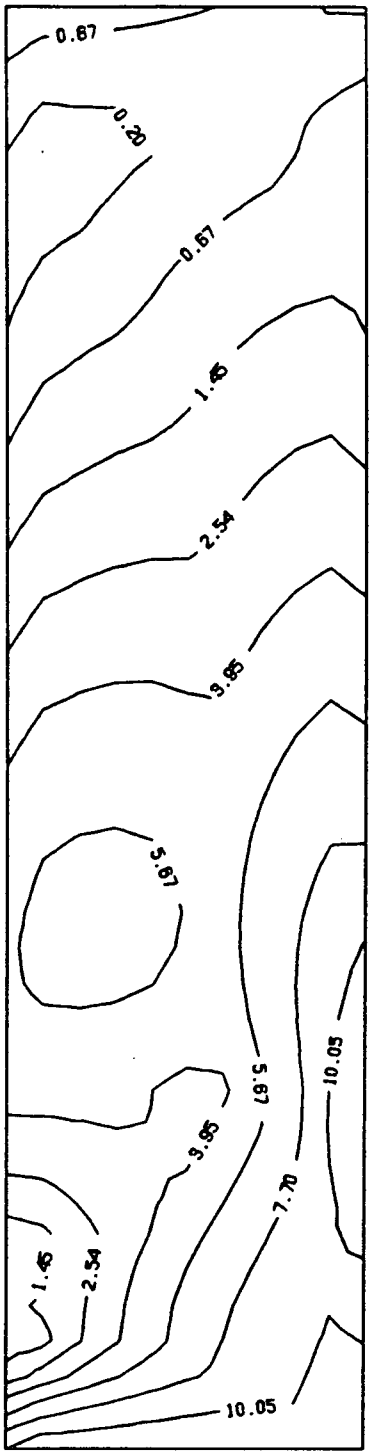
0.67
0.20
0.67
1.45
2.54
3.85
5.67
5.67
10.05
3.85
7.70
1.45
2.54
10.05

d

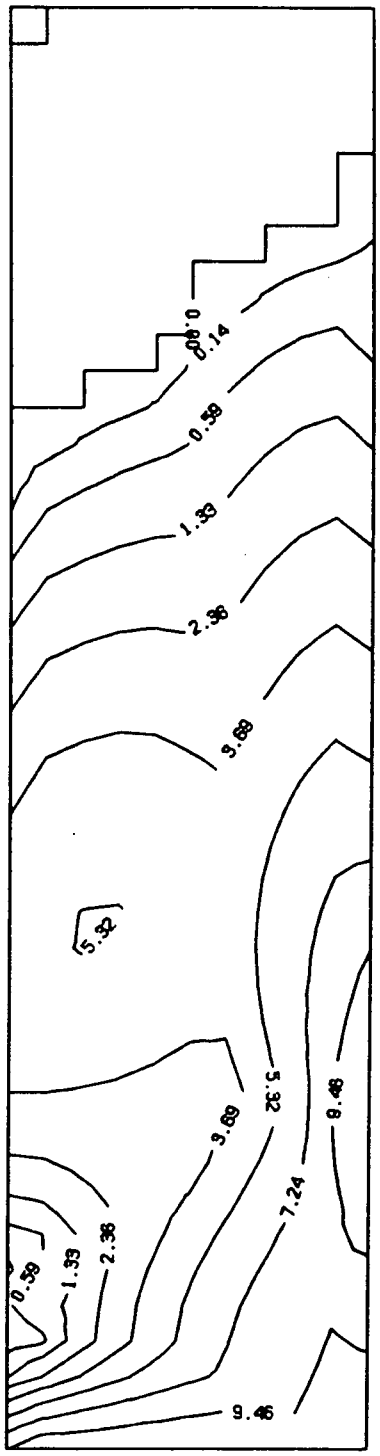
0.00
0.14
0.59
1.33
2.36
3.68
5.32
5.32
3.69
8.48
7.24
0.59
1.33
2.36
9.46

e

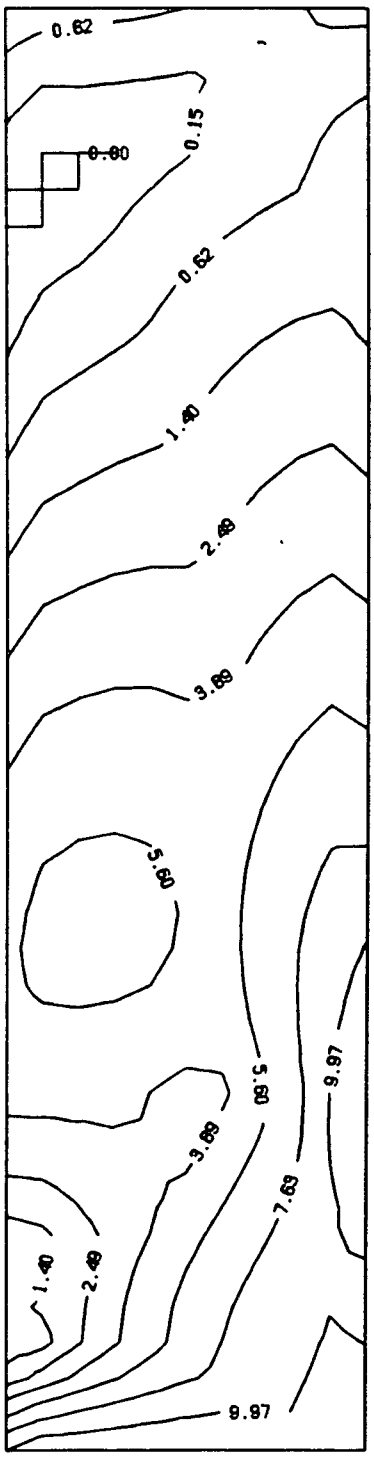

f

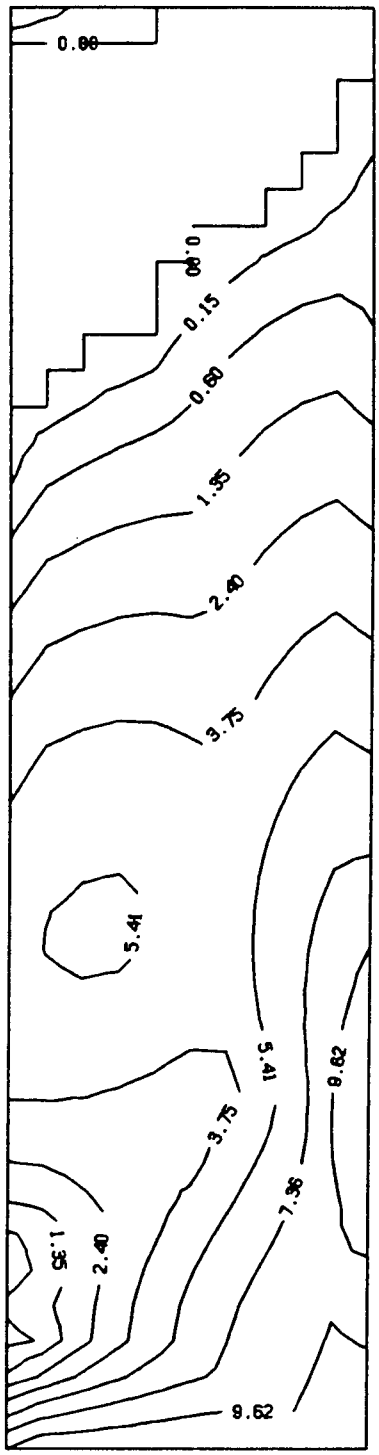

XIV.2.2.2.3.1 (a) Temperature ; (b) Von Mises Stress
(c) MRSS ; (d) MRSS-CRSS (Yield) ;
(e) MRSS-CRSS (MB) ; (f) MRSS-CRSS (MBTe) .

a

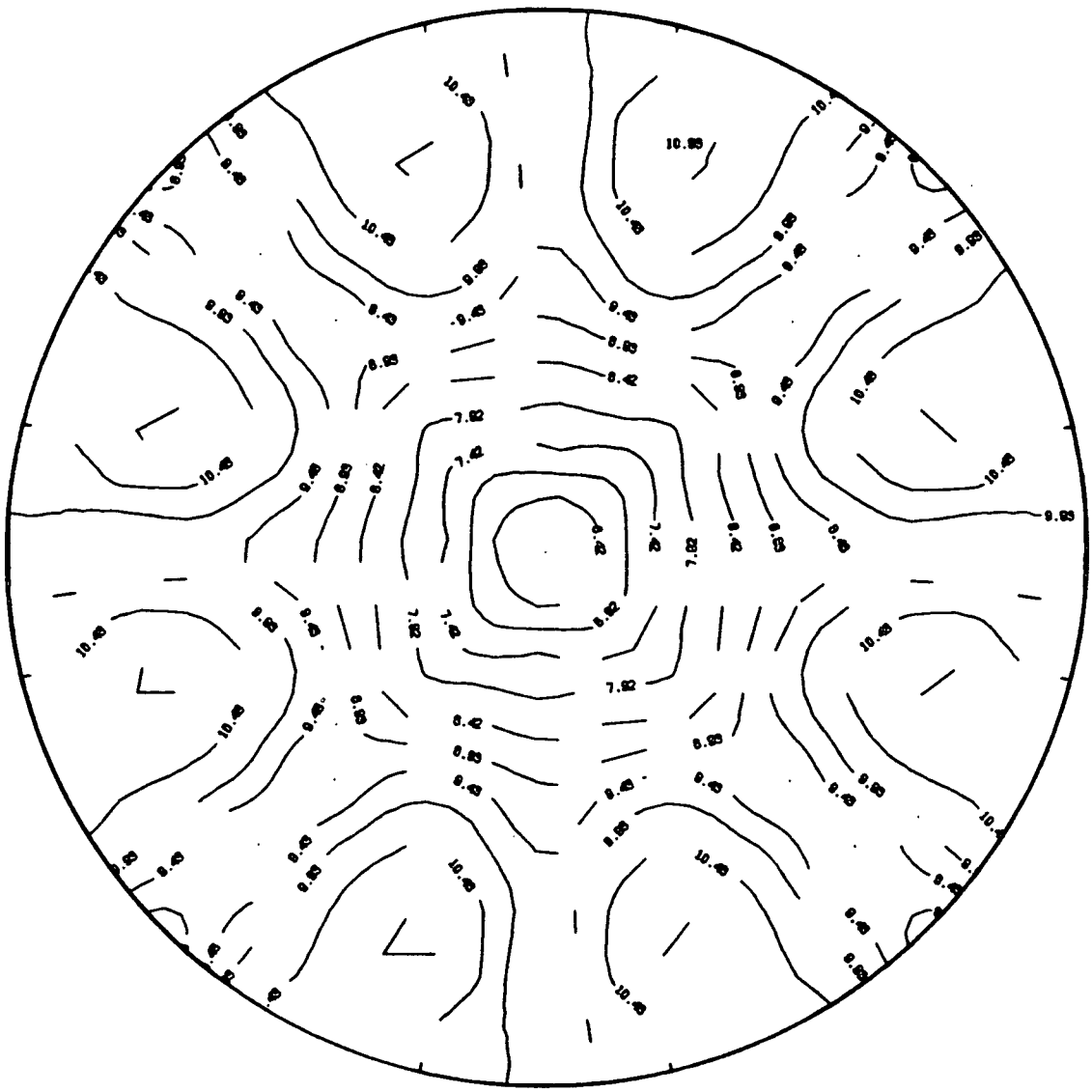

b

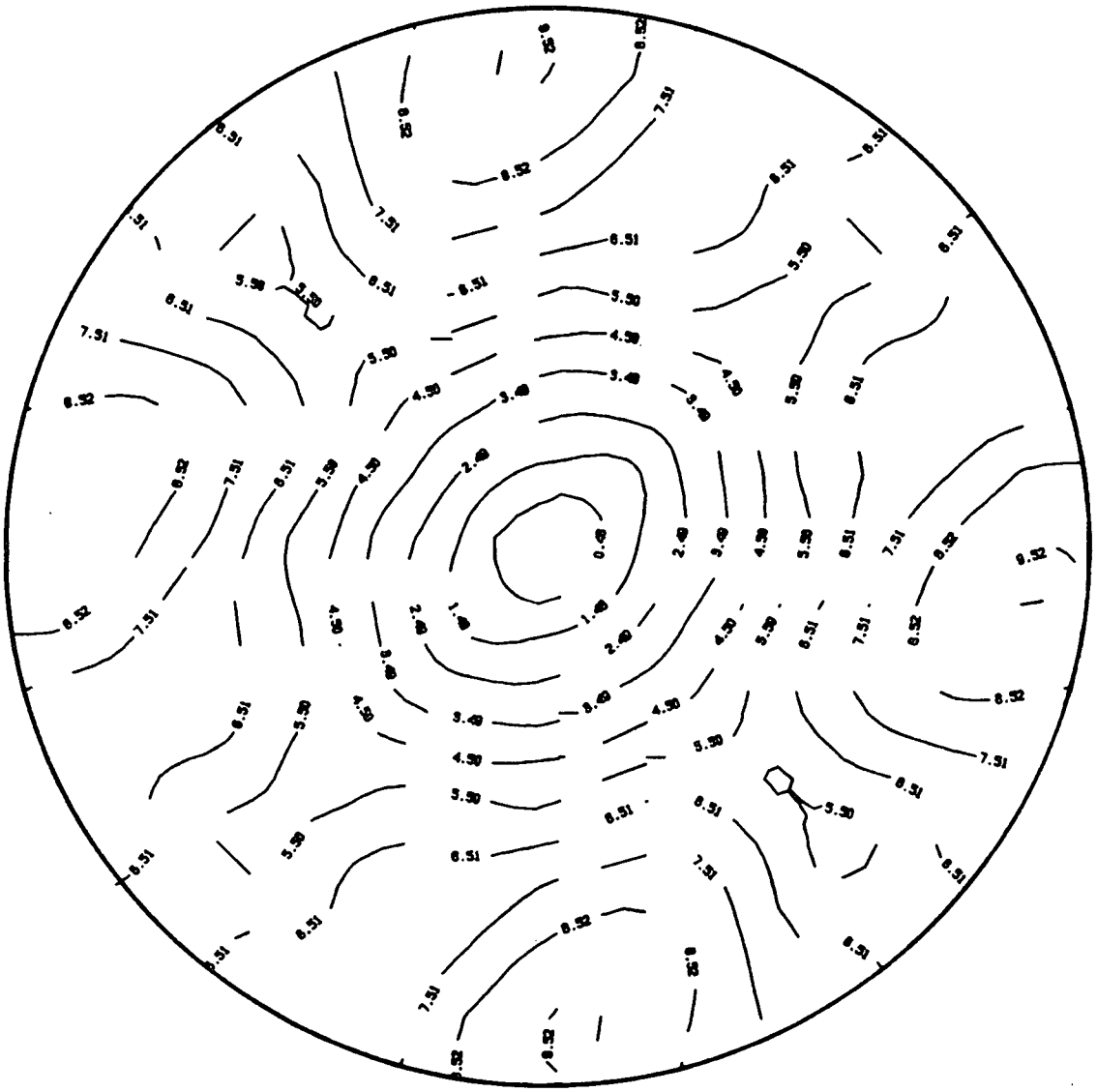

C

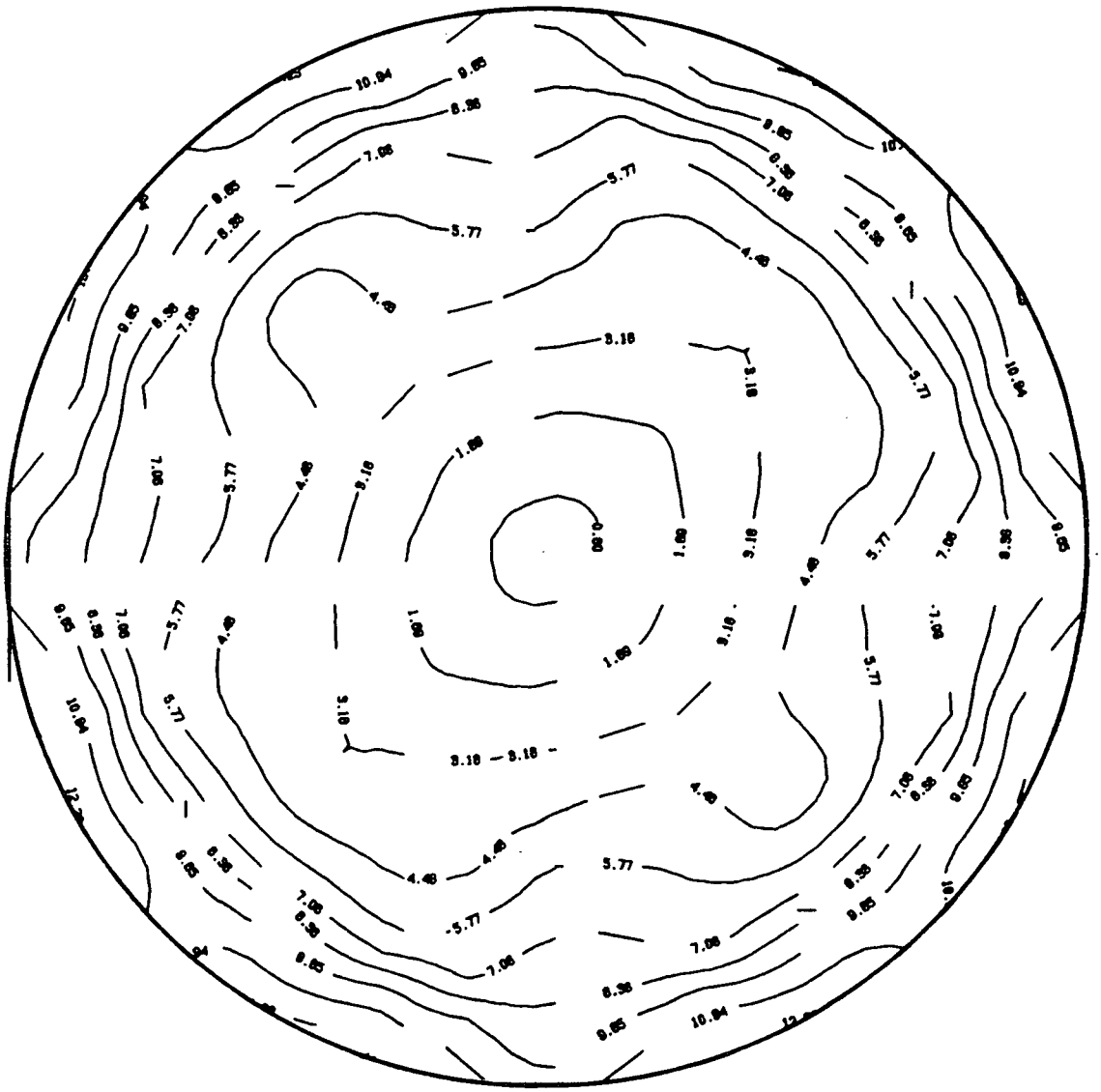

d

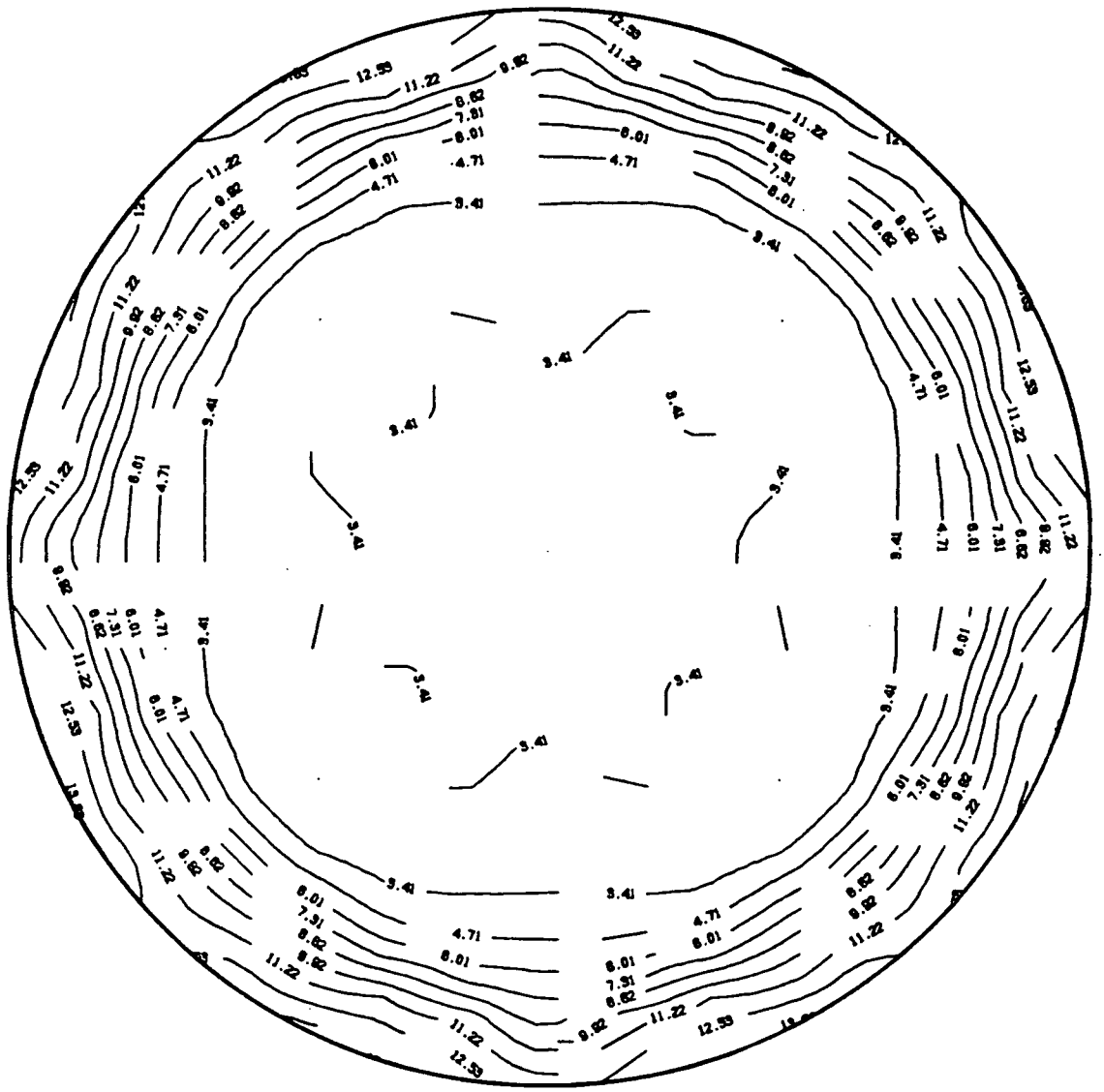

XIV.2.2.2.3.2 MRSS-CRSS (Yield) in cross-sections at a distance from the interface of :
(a) 2.75 mm ; (b) 8.25 mm ; (c) 16.5 mm ;
(d) 27.5 mm .

a

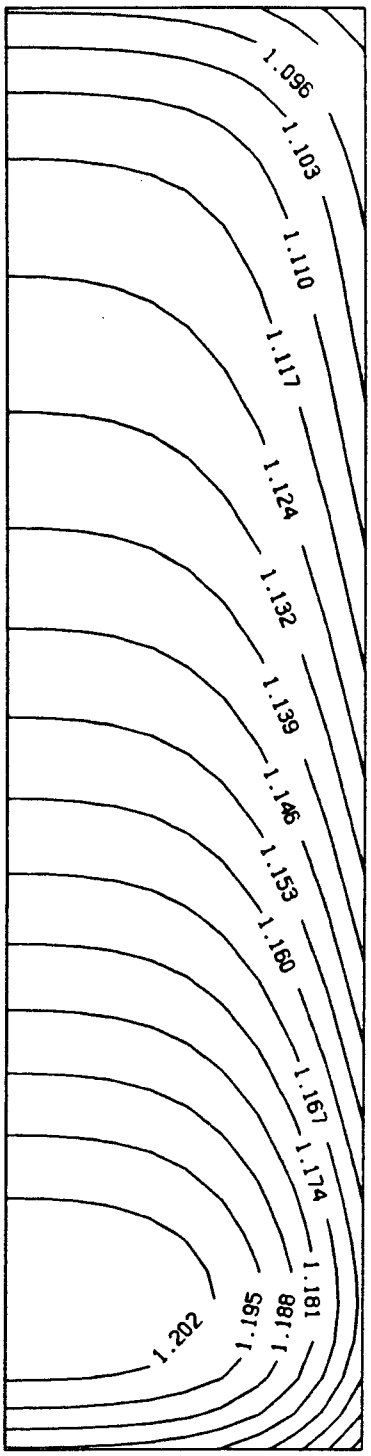
1.096
1.103
1.110
1.117
1.124
1.132
1.139
1.146
1.153
1.160
1.167
1.174
1.181
1.188
1.195
1.202

b

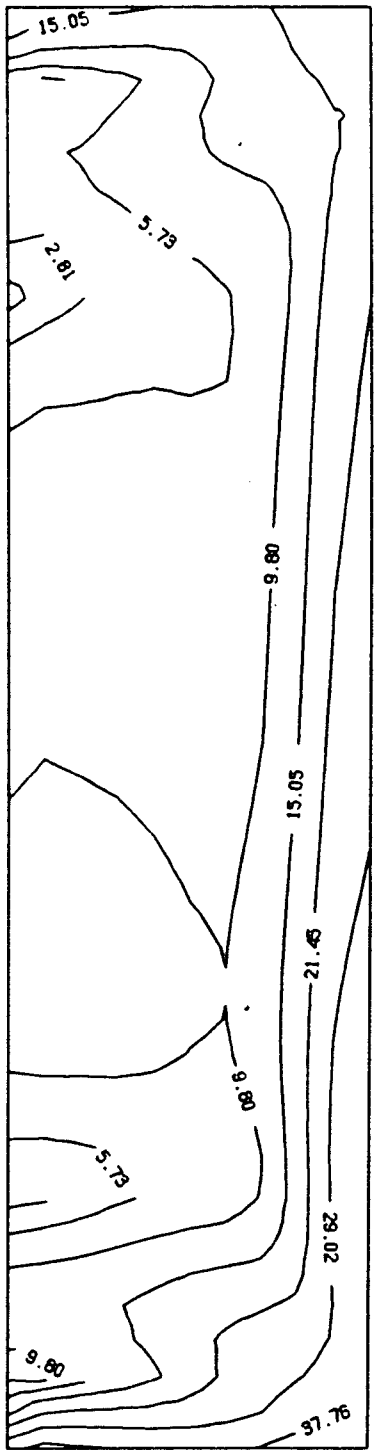
15.05
5.73
2.81
9.80
15.05
21.45
9.80
5.73
29.02
9.80
37.76

c

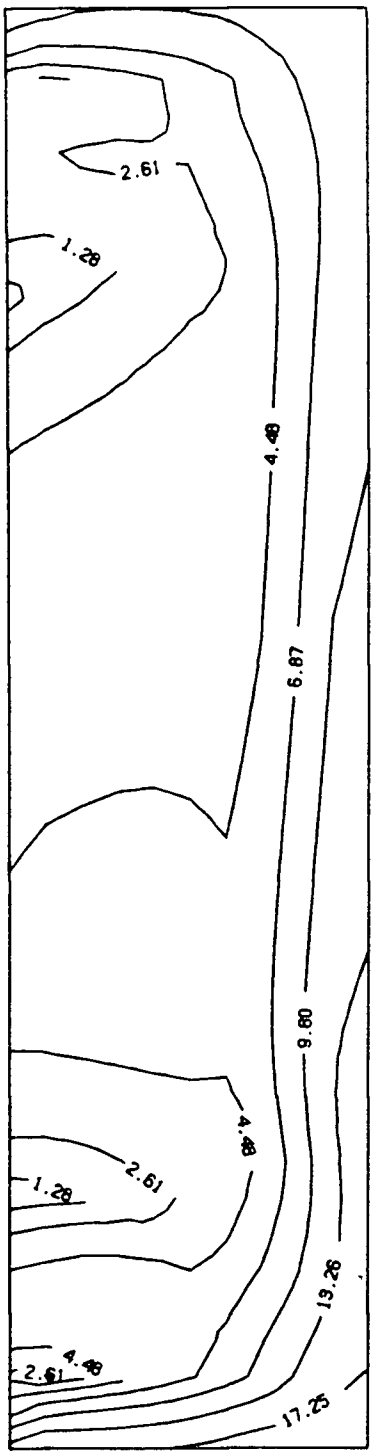
2.61
1.28
4.48
6.87
9.80
4.48
2.61
1.28
19.26
4.48
2.61
17.25

d

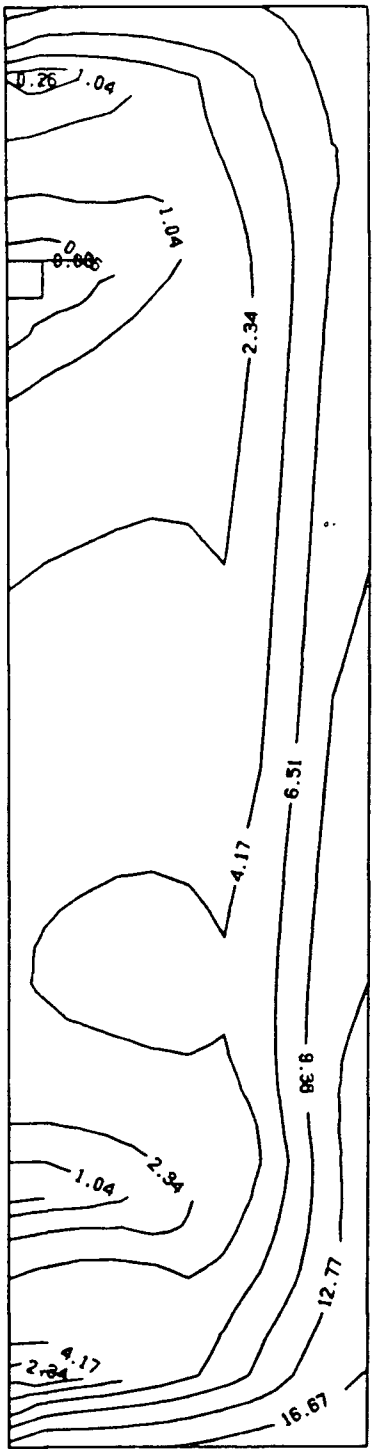
0.26
1.04
1.04
0.000
2.34
6.51
4.17
9.38
2.34
1.04
12.77
4.17
2.34
16.67

e

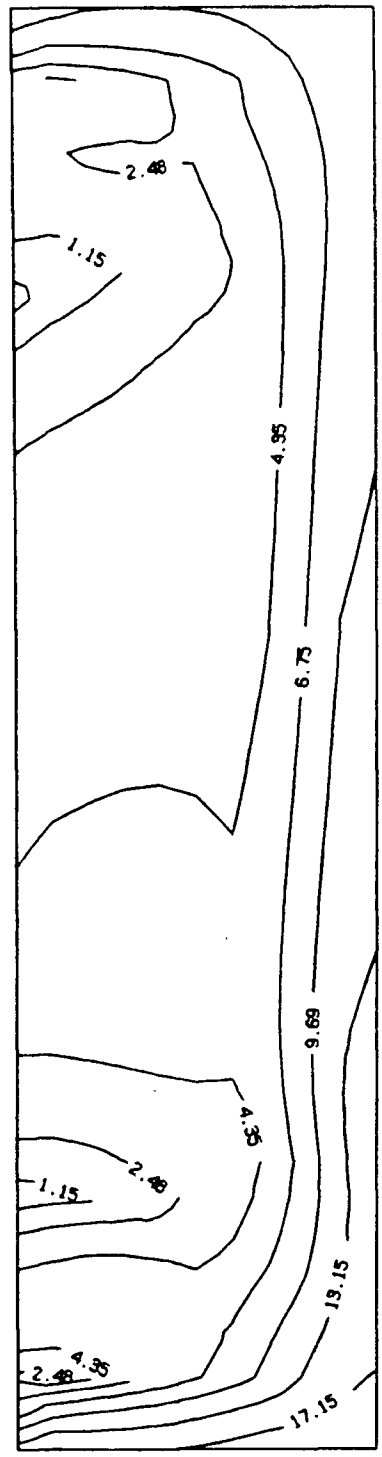

f

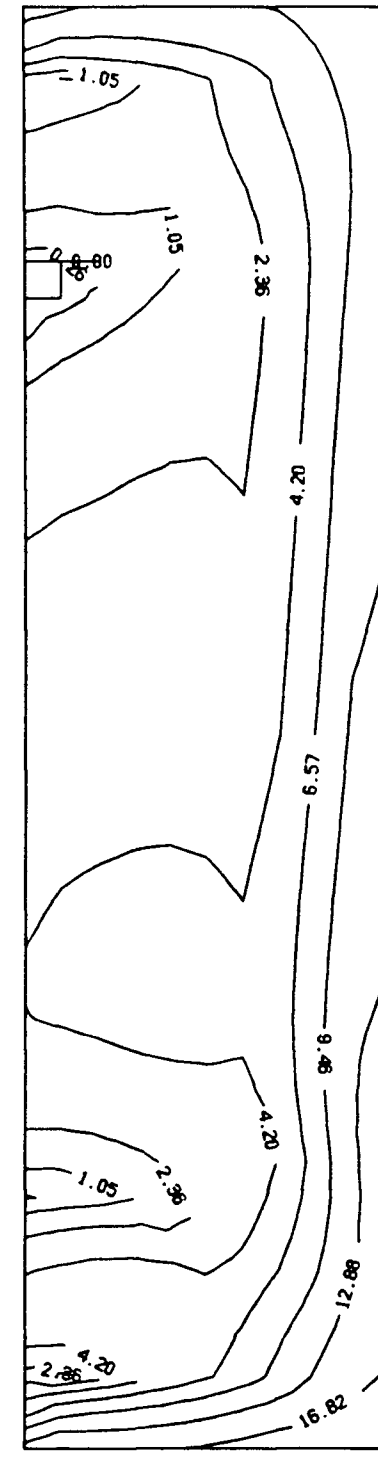

XIV.2.2.3.1.1 (a) Temperature ; (b) Von Mises Stress
(c) MRSS ; (d) MRSS-CRSS (Yield) ;
(e) MRSS-CRSS (MB) ; (f) MRSS-CRSS (MBTe) .

a

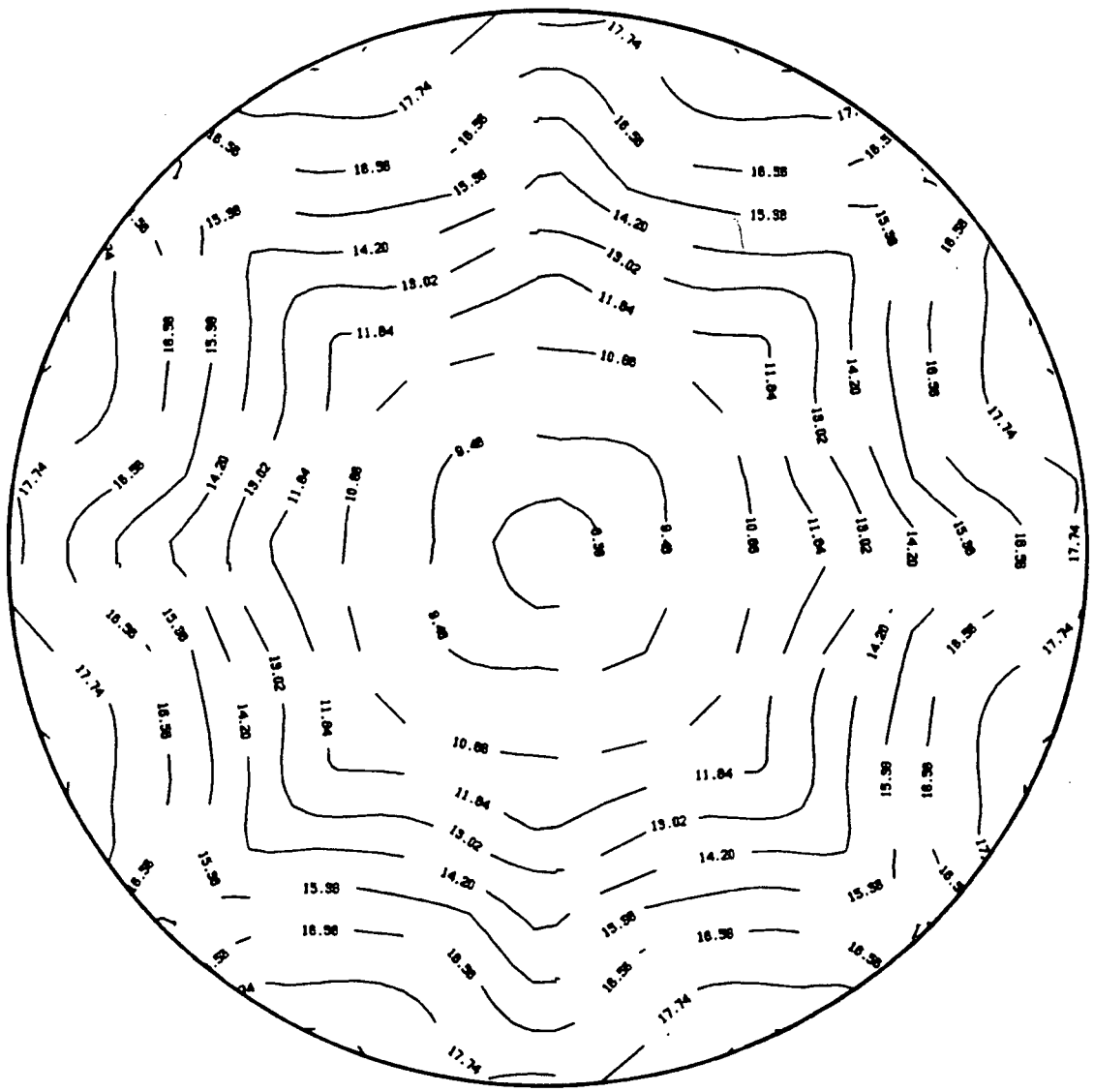

b

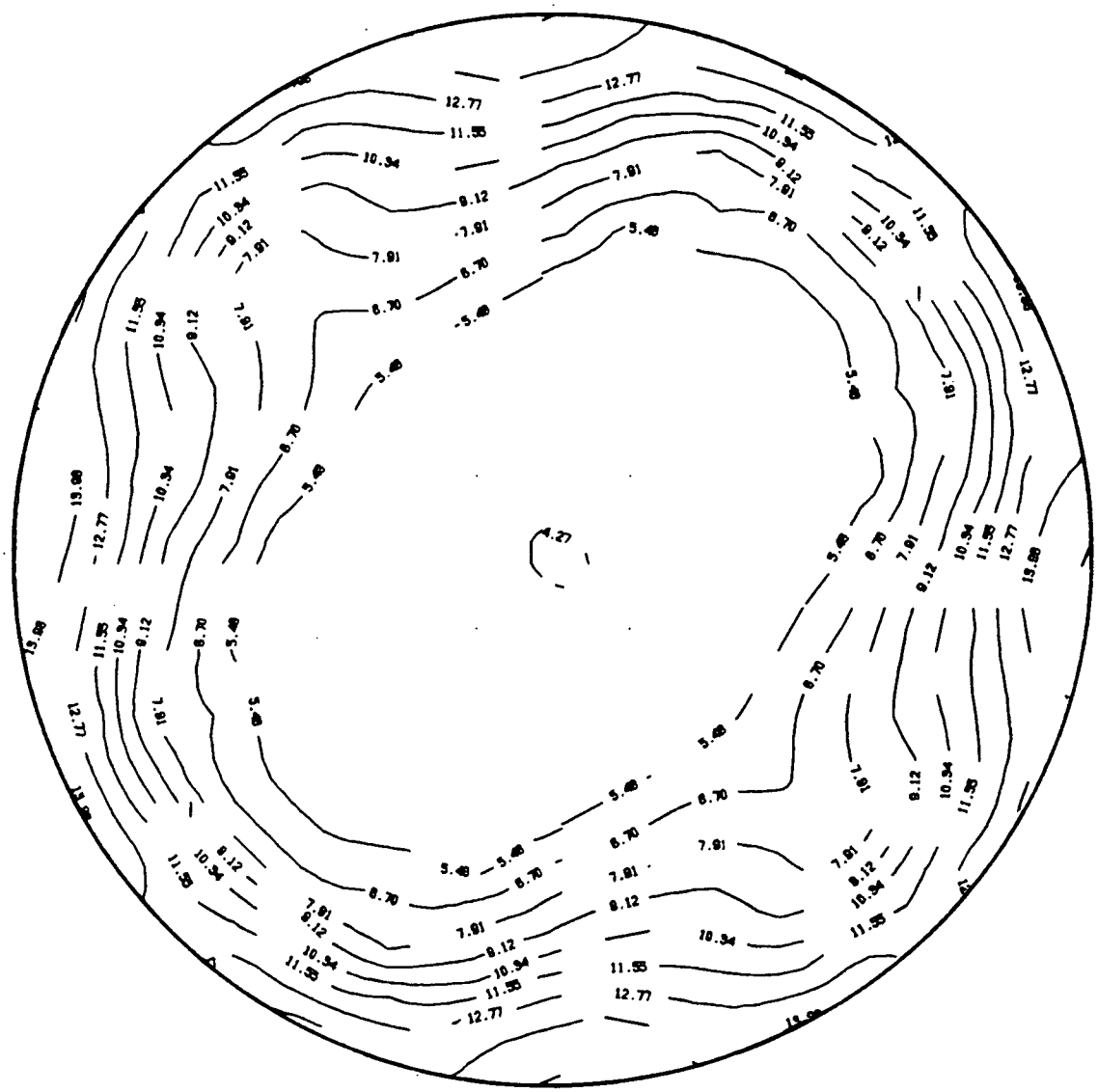

C

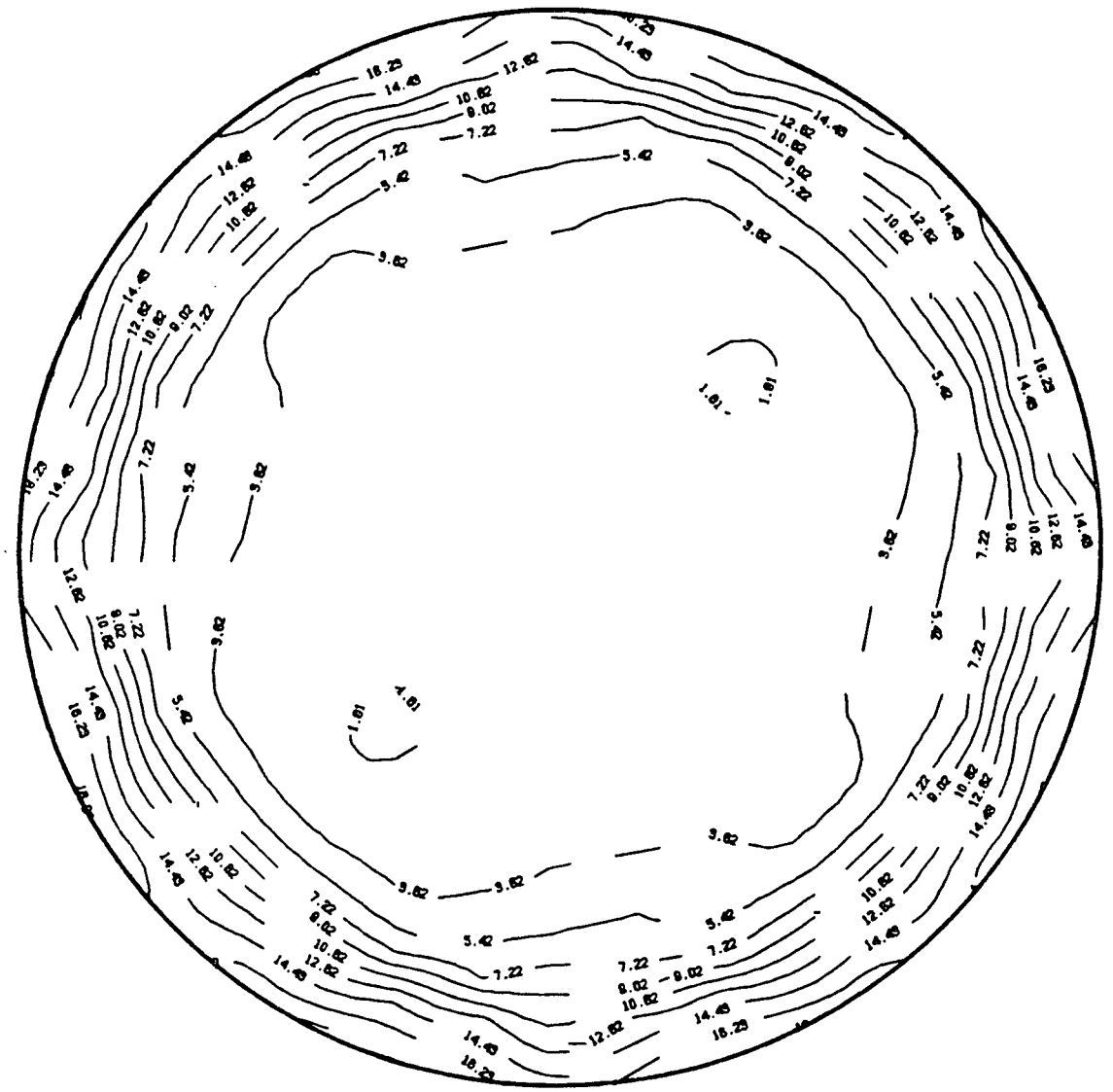

d

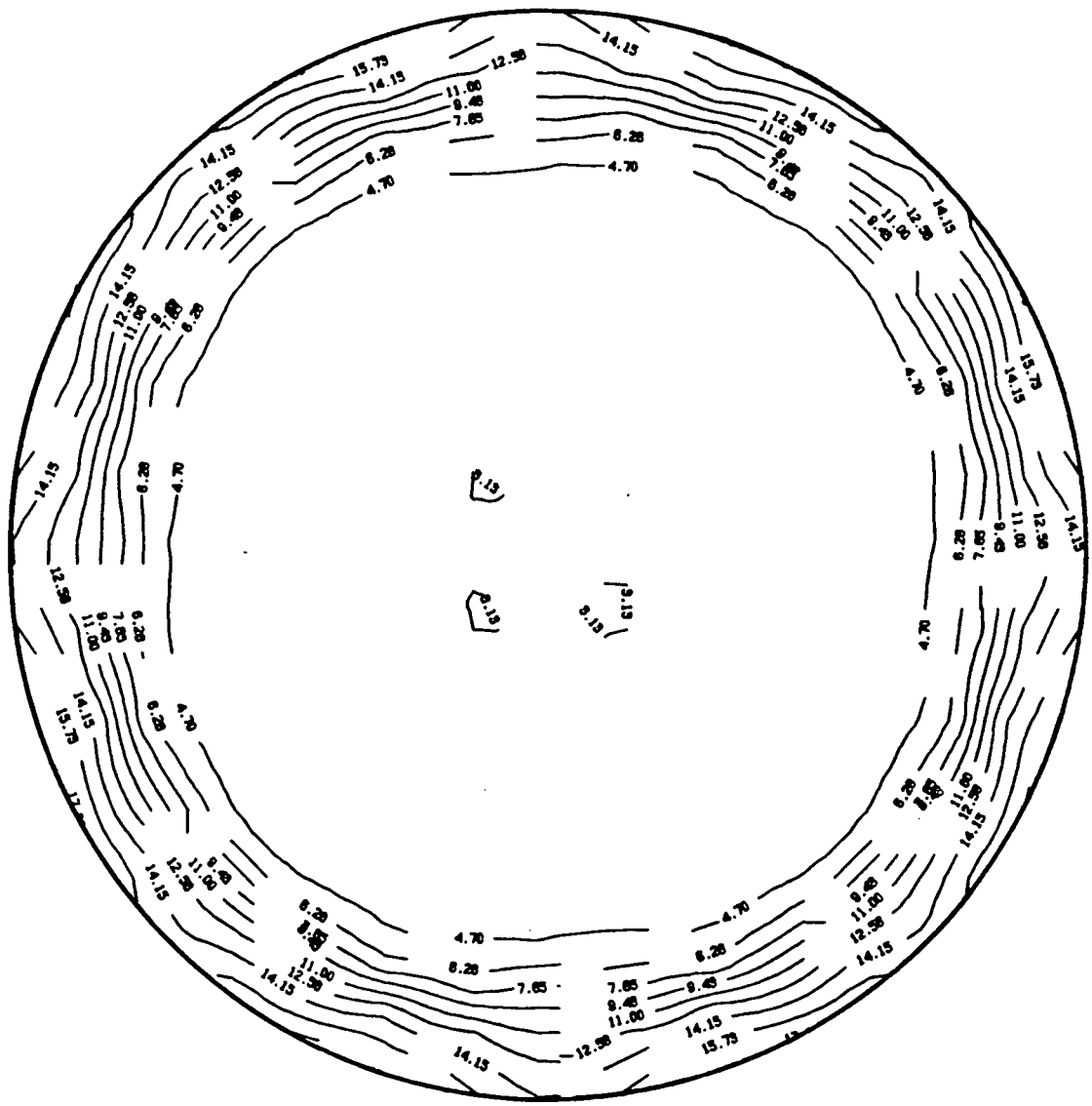

XIV.2.2.3.1.2 MRSS-CRSS (Yield) in cross-sections at a distance from the interface of :
(a) 2.75 mm ; (b) 8.25 mm ; (c) 16.5 mm ;
(d) 27.5 mm .

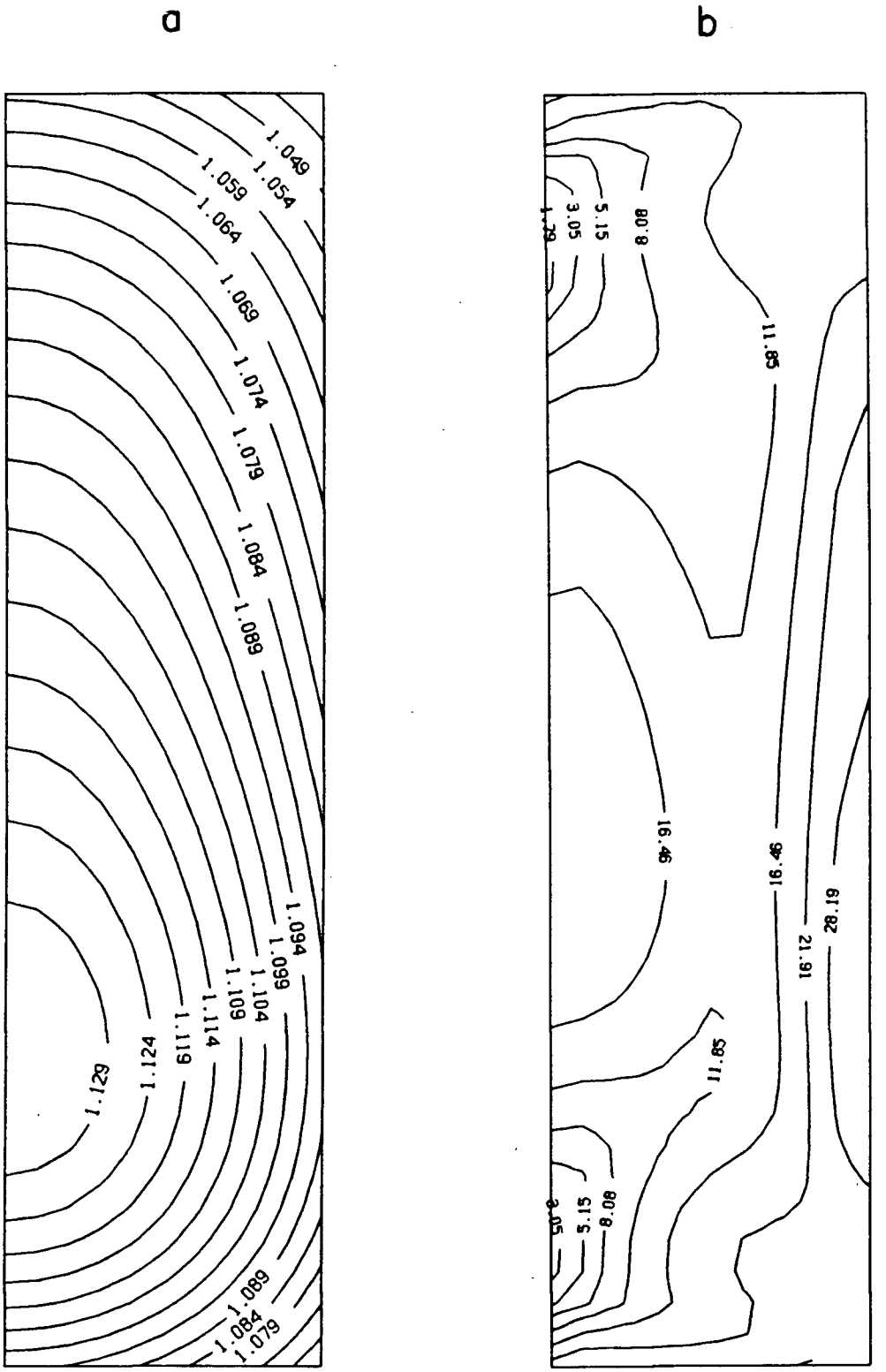
a
1.049
1.054
1.059
1.064
1.069
1.074
1.079
1.084
1.089
1.094
1.099
1.104
1.109
1.114
1.119
1.124
1.129
b
3.05
5.15
8.08
11.85
16.46
16.91
28.19
11.85
5.15
8.08

c

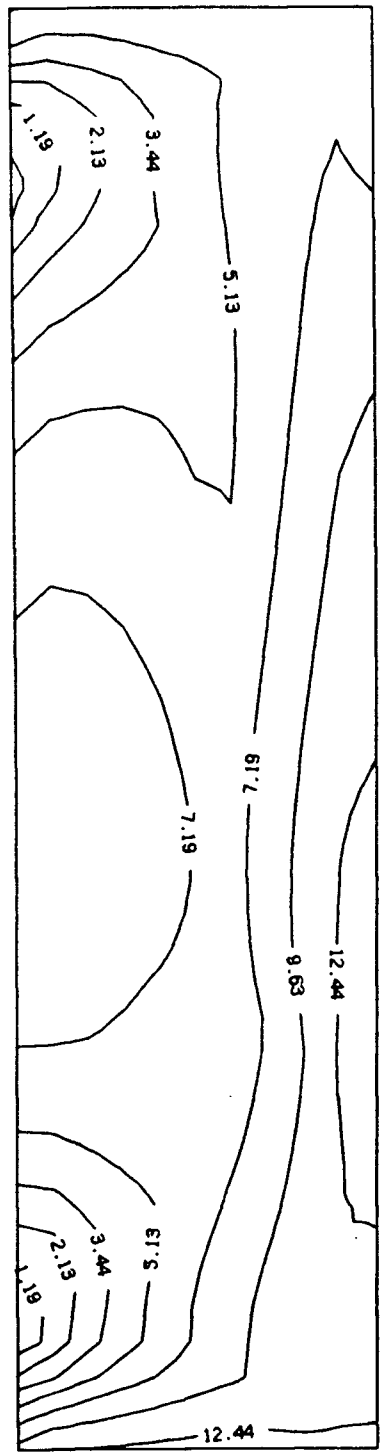
1.19
2.13
3.44
5.13
7.19
9.63
12.44
12.44
9.63
7.19
5.13
3.44
2.13
1.19

d

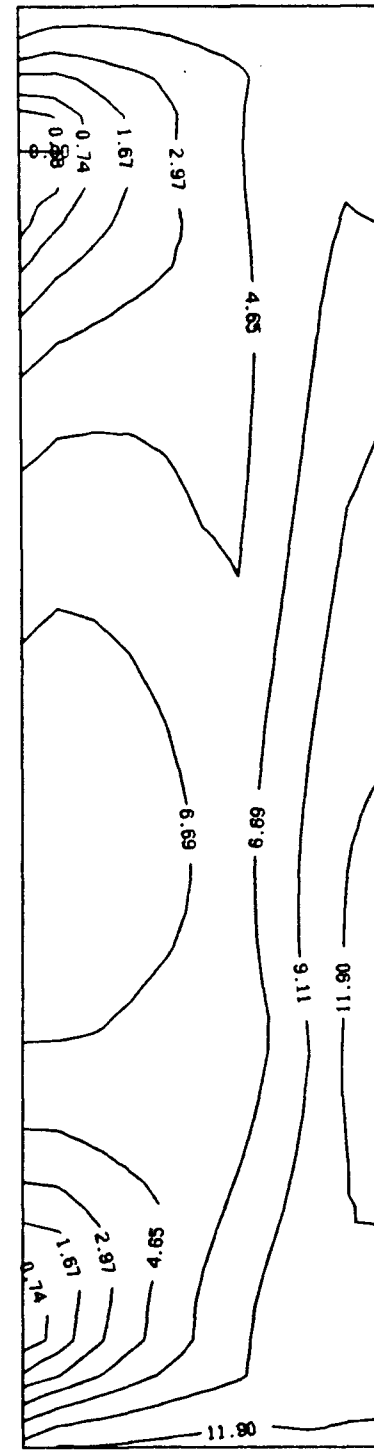
0.74
1.67
2.97
4.63
6.69
9.11
11.80
11.80
9.11
6.69
4.63
2.97
1.67
0.74

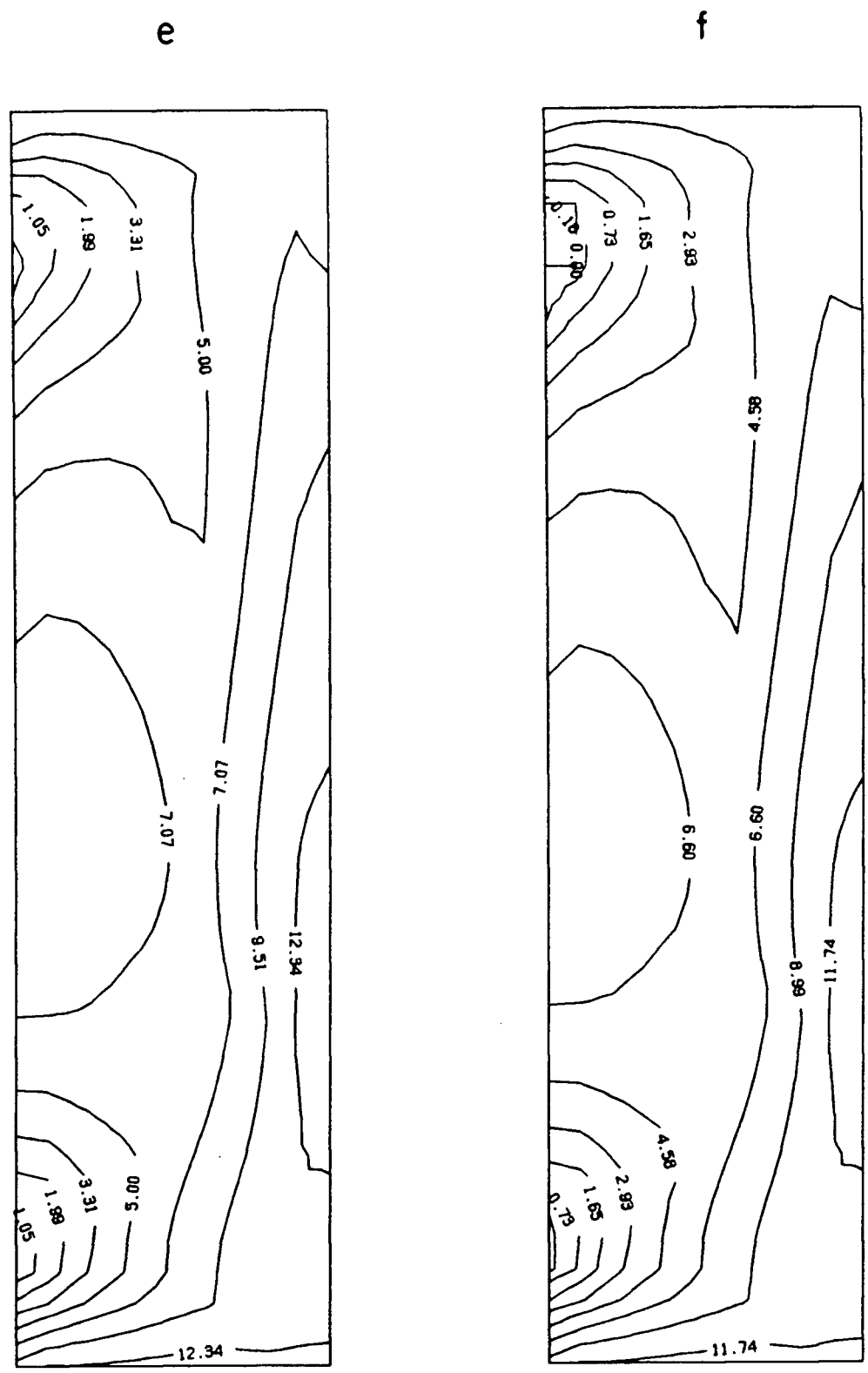

XIV.2.2.3.2.1 (a) Temperature ; (b) Von Mises Stress
(c) MRSS ; (d) MRSS-CRSS (Yield) ;
(e) MRSS-CRSS (MB) ; (f) MRSS-CRSS (MBTe) .

a

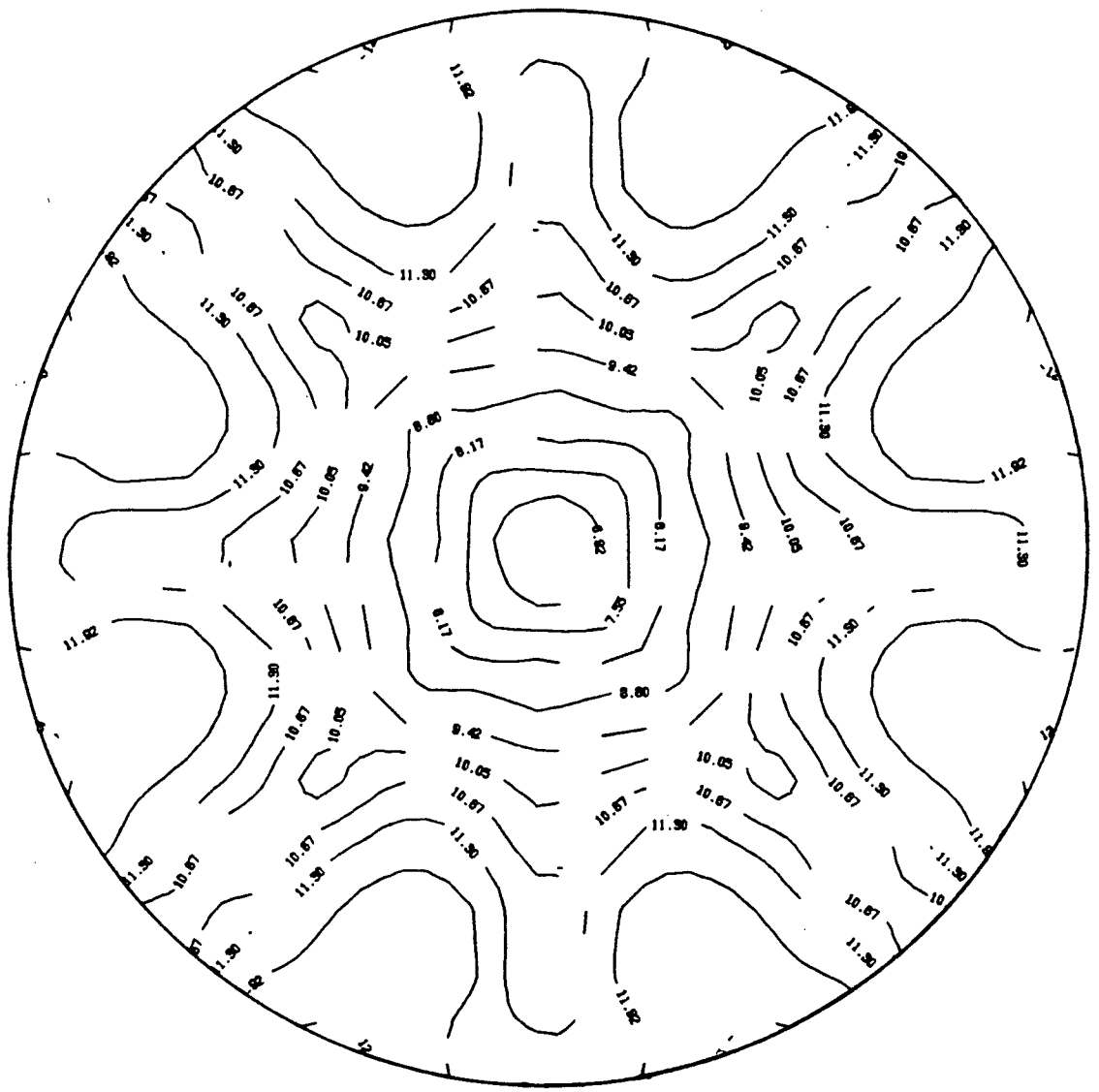

b

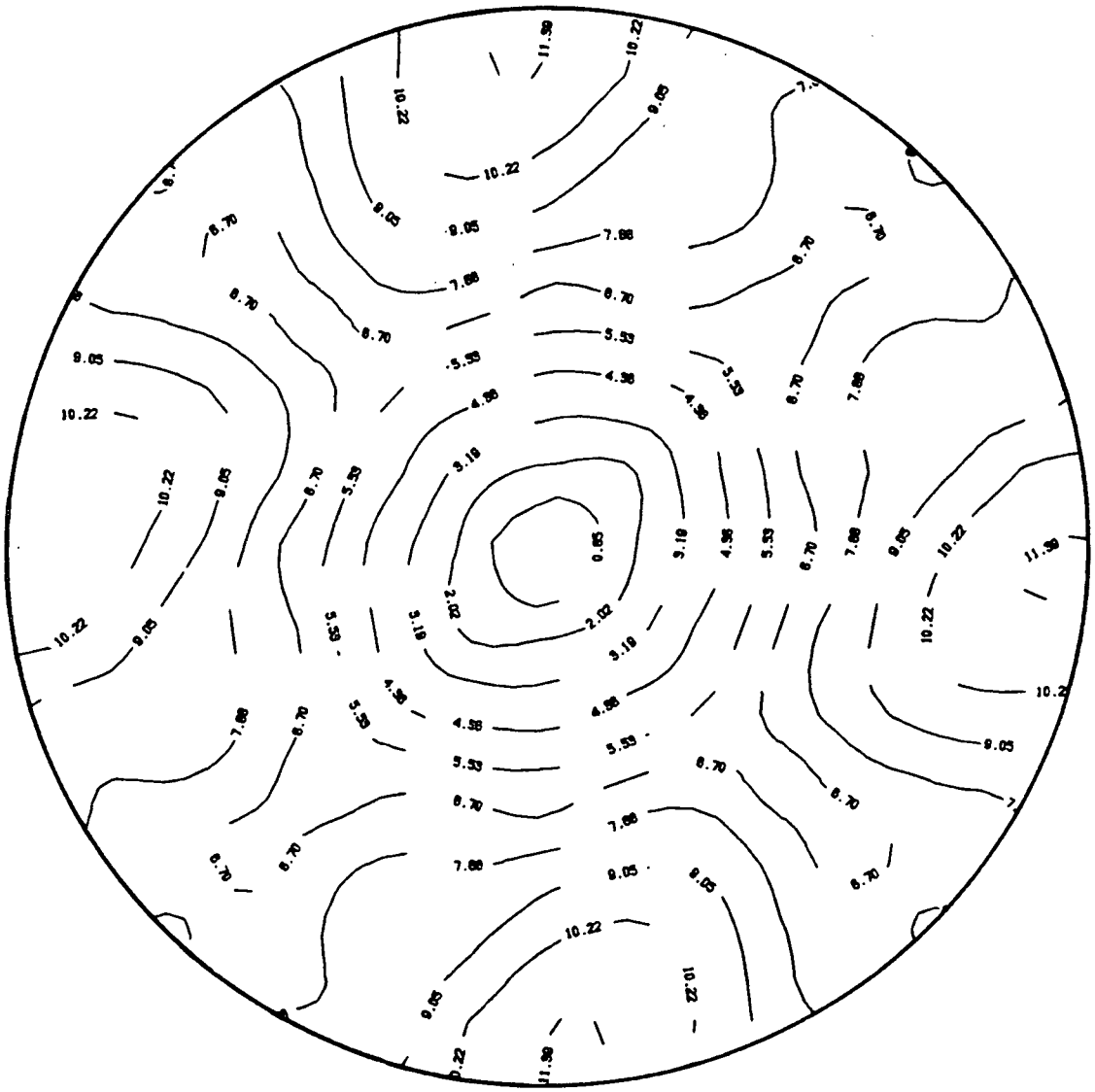

C

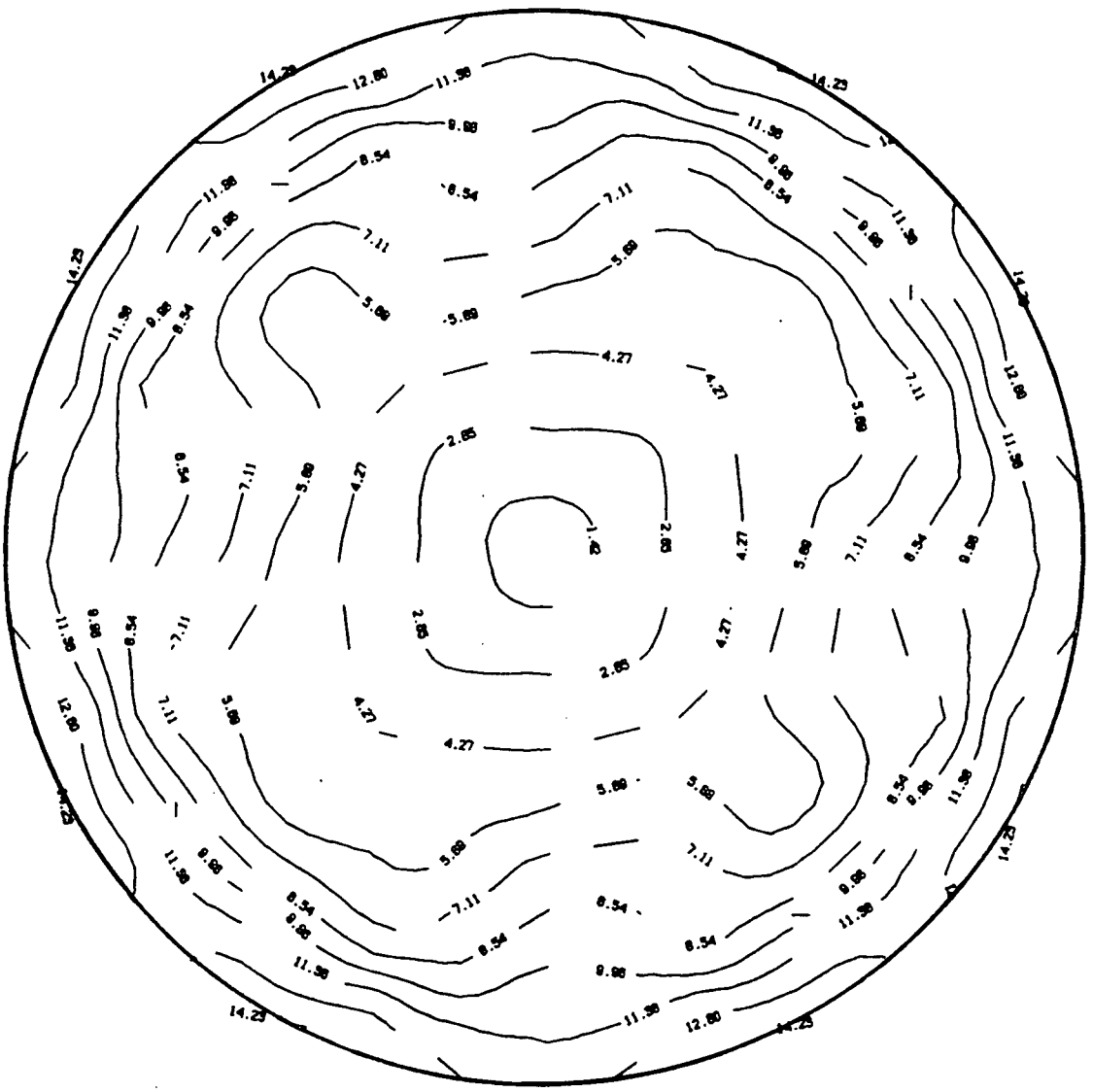

d

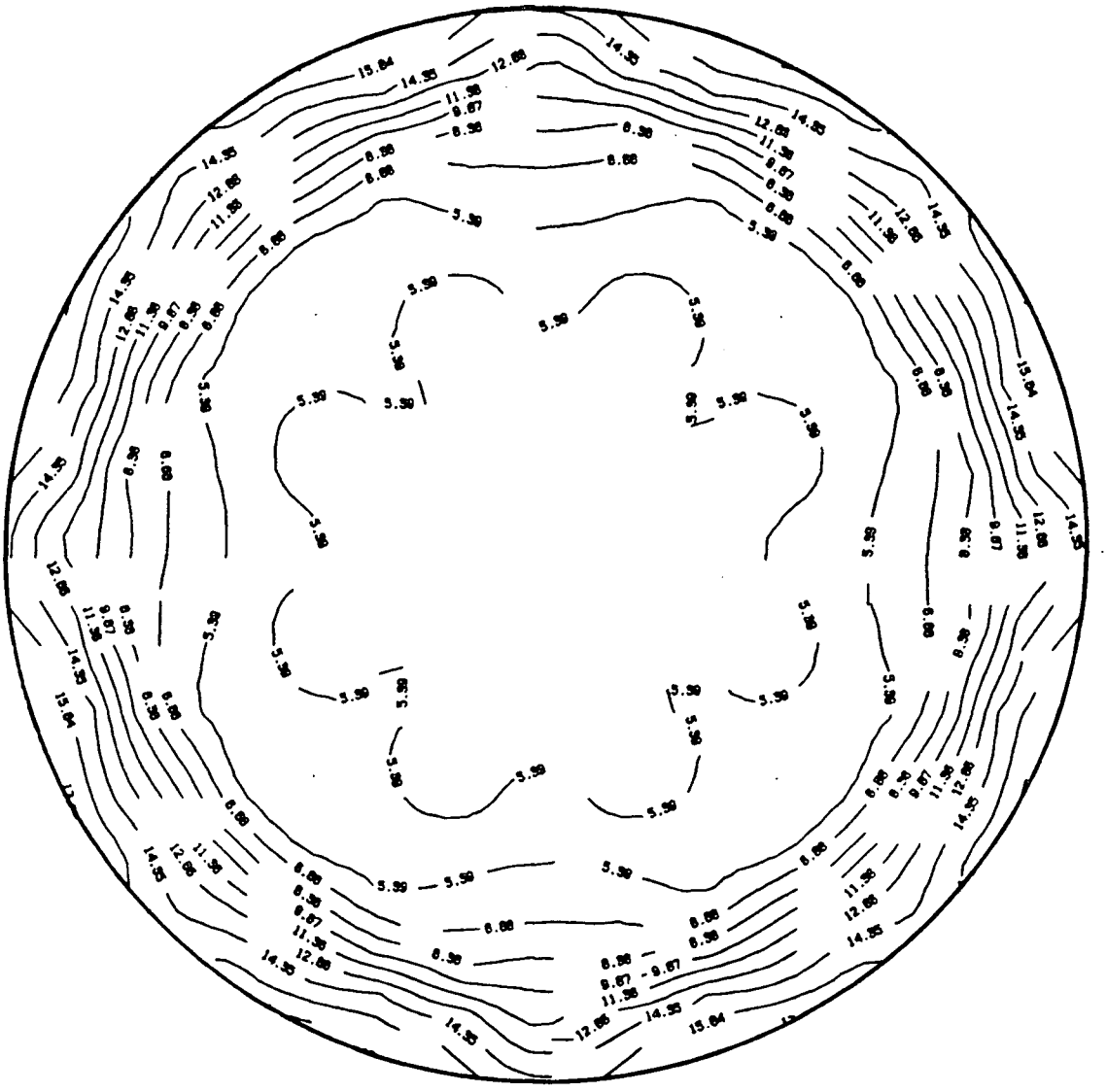

XIV.2.2.3.2.2 MRSS-CRSS (Yield) in cross-sections at a distance from the interface of :
(a) 2.75 mm ; (b) 8.25 mm ; (c) 16.5 mm ; (d) 27.5 mm .